Doctoral Thesis

Multi-Core Fiber and Optical Supersymmetry: Theory and Applications

Andrés Macho Ortiz

Supervisor // Prof. Dr. Roberto Llorente Sáez

June 2019, Valencia (Spain)

UNIVERSITAT POLITÈCNICA DE VALÈNCIA

DEPARTAMENTO DE COMUNICACIONES

UNIVERSITAT POLITÈCNICA DE VALÈNCIA

Multi-Core Fiber and Optical Supersymmetry: Theory and Applications

Andrés Macho Ortiz

Supervisor: Prof. Dr. Roberto Llorente Sáez

Doctoral Thesis

submitted for the degree of
Doctor of Philosophy in Telecommunication Engineering

June 2019, Valencia (Spain)

amachor@ntc.upv.es
Ph.D. Thesis, Nanophotonics Technology Center
UNIVERSITAT POLITÈCNICA DE VALÈNCIA

Cover design by © Pablo Piñeiro Mato 2018
Cover photo by iStock.com/Flashworks

First printing, May 2019 (deposit)
Second printing, June 2019 (defense)

A mis padres Jesús y Teresa
y a mi hermana Ángela

"*Science is shaped by ignorance. Great questions themselves evolve, of course, because their answers spawn new and better questions in turn*"

David Gross

Agradecimientos

Me enfrento a los renglones aún en blanco de esta sección sabiendo que son, sin duda, los más difíciles de toda la memoria. Echando un vistazo hacia atrás a todos estos años de doctorado, una lluvia de recuerdos desempaña mi mente y, de repente, comienza a pasearse por mi cabeza todo ese público incondicional que, con ánimo incansable, ha estado año tras año apoyándome, siguiendo cada bache y cada pequeño triunfo a lo largo del inicio de mi carrera profesional.

Son muchas las personas que me han acompañado durante esta exigente etapa y que directa o indirectamente han contribuido a que hoy me encuentre escribiendo estas líneas con las que echo el cierre a mi tesis doctoral.

Merecen copar estas primeras líneas las dos personas que son los principales culpables de los resultados conseguidos en esta tesis: Carlos García-Meca y Francisco Javier Fraile-Peláez. El gran intelecto de ambos solo es superado por su gran calidad humana. A Carlitos tengo que agradecerle la dedicación y paciencia sin límites que me ha prestado durante todo el doctorado, incluso cuando estaba saturado de trabajo e imprevistos familiares. Aún recuerdo ese día a principios de Junio de 2016 cuando llegó de comer y me dijo: "Apunta un trabajo brutal que podemos hacer de supersimetría: supersimetría en el tiempo, factorizando la derivada temporal en vez de la espacial"... ¡Boom!, me explotó la cabeza. Qué talento, qué capacidad. A Javier tengo que agradecerle que sea un catedrático singular. Qué paciencia ha mostrado alguien de su categoría con un alumno que no conocía, y que para colmo le mandaba desarrollos teóricos plagados de errores. De ambos he podido aprender los hábitos básicos para poder trabajar en el mundo de lo teórico.

A mis padres, Jesús y Teresa, pilares fundamentales en mi vida. Sin ellos jamás hubiese podido conseguir lo que he logrado hasta ahora. Todos y cada uno de sus valores constituyen un gran ejemplo a seguir, no solo para mí, sino también para mi hermana y todo el resto de mi familia. Y precisamente es a mi hermana, Ángela, la persona a la que se me hace más difícil poder plasmar en una sola frase todo el cariño que la tengo. Es un auténtico ejemplo de esfuerzo, dedicación y constancia de trabajo.

A mis queridas primas Teresa, Sofía y Patrizia; a mis abuelos Andrés, José, Lala y Tata; y a mis tíos Andrés, Conchi, Ángel, Loli, Pepe, Mariví, Carmen, Patrizia, Marino y Santiago. Son los culpables de que adore escaparme a Zamora en cuanto puedo coger vacaciones. El cariño y alegría que transmiten a los demás es imposible de compensar en un solo párrafo. Teniendo una familia así es muy fácil sentirse orgulloso de ellos.

Me gustaría también agradecer el apoyo que me han dado durante todos estos cuatro años, y prácticamente durante gran parte de mi vida, a mis grandes amigos: Nacho, Carlos, Piña, Primo, Vivi, Apa, Guille, Mario, Cazallas, Buades, Edu, Kike, Adolfo, Miki, Felipe, Jaime ... Cada uno ha puesto su granito de arena en esta travesía y da tranquilidad saber que en el futuro podré seguir contando con ellos. Un futuro en el que espero que Vivi aprenda a jugar de verdad al pádel y consiga pasar de "Iniciación++".

A los compañeros de levantamiento de hierros en Valencia, Álvaro y Jose. Dos amistades nuevas de las que merecen realmente la pena conservar. A pesar del cachondeo que nos traemos todos los días en el gimnasio, Álvarito me ha sorprendido por su espíritu crítico cuando me preguntaba por temas de ciencia.

A mi amigos y verdaderos pilares del NTC: Sergio, Álvaro, Luis, Mario, Kike, Pau y Julio. De todos los trabajos que hemos publicado, el mejor de ellos, sin duda, ha sido el grupo de Cinemaniacos. Espero que algún día Sergio y Álvaro puedan superar el trauma de ver ganar al Madrid 13 Champions, y que Luis acepte de una vez que siempre pierda Vegeta. Tampoco me puedo olvidar del resto de compañeros del NTC: Margue, Alba, Ángela, Anita, Fran, Andrea, Diego, Alex, Carles, Bea, David Zurita y Antoine. Ha sido un placer trabajar a vuestro lado.

A mi supervisor, Roberto Llorente Sáez, quien me ha brindado la oportunidad de poder realizar la tesis en el NTC con una beca FPI y me ha guiado a nivel profesional y personal durante el doctorado mostrando una paciencia digna de elogiar ante mi ansia de trabajo. También quiero agradecerle a María Morant Pérez la paciencia y dedicación que mostró conmigo en los inicios.

I wish to thank Dr. Rodrigo Amezcua-Correa and Prof. Demetrios Christodoulides for giving me the opportunity of doing research on multi-core fibers and optical supersymmetry in a short-term scholar visiting at CREOL (The College of Optics & Photonics, University of Central Florida, United States of America). The help of two great experts like them really allowed me to improve my knowledge on these topics. Special thanks also go to Steffen, María, Natalia, Zahoora, Juan Carlos, Enrique, Selim and Sergi for their support and help during my stay in Orlando.

My deepest gratitude is also due to the group of experts that formed the dissertation evaluation committee: Prof. Adolfo Cartaxo (Instituto de Telecomunicações, Portugal), Prof. Pedro Chamorro (Universidad de Valladolid, Spain), and Prof. Stuart Walker (University of Essex, United Kingdom).

A Don Jesús Medina Campo, profesor de Matemáticas del colegio Nuestra Señora del Buen Consejo, de quien tengo un especial recuerdo. Gracias a él se despertó mi afán de investigación, me enseñó a estudiar con carácter crítico, a ir siempre un poco más allá y tener curiosidad por intentar comprobar hasta lo más evidente, o como él diría "lo más trivial".

Finalmente, me gustaría cerrar los agradecimientos asignando estas últimas líneas a un gran amigo y referente científico en el que fijarme, al Profesor Miguel Ángel Muriel Fernández. Miguel me ha dedicado su tiempo siempre que lo he requerido. Su guía y consejos han sido fundamentales para afrontar una de las etapas más exigentes a nivel académico y fue el principal responsable de que acabara en Valencia haciendo la tesis, algo por lo que le estaré eternamente agradecido.

Resumen

A DÍA DE HOY, las redes de comunicaciones de fibra óptica están alcanzando su capacidad límite debido al rápido crecimiento de la demanda de datos en la última década, generado por el auge de los teléfonos inteligentes, las tabletas, las redes sociales, la provisión de servicios en la nube, las transmisiones en streaming y las comunicaciones máquina-a-máquina. Con el fin de solventar dicho problema, se ha propuesto incrementar la capacidad límite de las redes ópticas mediante el reemplazo de la fibra óptica clásica por la *fibra óptica multinúcleo* (MCF, acrónimo en inglés de multi-core fiber), la cual es capaz de integrar la capacidad de varias fibras ópticas clásicas en su estructura ocupando prácticamente la misma sección transversal que éstas.

Sin embargo, explotar todo el potencial de una fibra MCF requiere entender en profundidad los fenómenos electromagnéticos que aparecen en este tipo de fibras cuando guiamos luz a través de ellas. Así pues, en la *primera parte* de la tesis se analizan teóricamente estos fenómenos electromagnéticos y, posteriormente, se estudia la viabilidad de la tecnología MCF en distintos tipos de redes ópticas de transporte, específicamente, en aquellas que hacen uso de transmisiones *radio-sobre-fibra*. Estos resultados pueden ser de gran utilidad para las futuras generaciones móviles 5G y Beyond-5G en las próximas décadas.

Adicionalmente, con el fin de expandir las funcionalidades básicas de las fibras MCF, esta tesis explora nuevas estrategias de diseño de las mismas utilizando la analogía existente entre las ecuaciones que rigen la mecánica cuántica y el electromagnetismo. Con esta idea en mente, en la *segunda parte* de la tesis se propone diseñar una nueva clase de fibras MCF usando las matemáticas de la *supersimetría*, surgida en el seno de la teoría de cuerdas y de la teoría cuántica de campos como un marco teórico de trabajo que permite unificar las interacciones fundamentales de la naturaleza (la nuclear fuerte, la nuclear débil, el electromagnetismo y la gravedad). Girando en torno a esta idea surgen las fibras MCF supersimétricas, las cuales nos permiten procesar la información de los usuarios durante la propia propagación de la luz a través de ellas, reduciendo así la complejidad del procesado de datos del usuario en recepción.

Finalmente, esta tesis se completa introduciendo un cambio de paradigma que permite diseñar dispositivos fotónicos disruptivos. Demostramos que la supersimetría de mecánica cuántica no relativista, propuesta como una serie de transformaciones matemáticas restringidas al *dominio espacial*, se puede extender también al *dominio del tiempo*, al menos dentro del marco de trabajo de la fotónica. Como resultado de nuestras investigaciones, demostramos que la supersimetría temporal puede convertirse en una plataforma prometedora para la fotónica integrada ya que nos permite diseñar nuevos dispositivos ópticos versátiles y ultra-compactos que pueden jugar un papel clave en los procesadores del futuro.

Asimismo, con el fin de hacer los resultados principales de esta tesis doctoral lo más generales posibles, se detalla cómo poder extrapolarlos a otros campos de la física como acústica y mecánica cuántica.

Resum

Avui en dia, les xarxes de comunicacions de fibra òptica estan aconseguint la seua capacitat límit a causa del ràpid creixement de la demanda de dades duante l'última dècada, generat per l'auge dels telèfons intel · ligents, les tablets, les xarxes socials, la provisió de servicis en la núvol, les transmissions en streaming i les comunicacions màquina-a-màquina. Per a resoldre el dit problema, s'ha proposat incrementar la capacitat límit de les xarxes òptiques per mitjà del reemplaçament de la fibra òptica clàssica per la fibra òptica multinúcleo (MCF, acrònim en anglés de multi-core fiber), la qual és capaç d'integrar la capacitat de diverses fibres òptiques clàssiques en la seua estructura ocupant pràcticament la mateixa secció transversal que estes.

Tanmateix, explotar tot el potencial d'una fibra MCF requereix entendre en profunditat els fenòmens electromagnètics que apareixen en aquestes fibres quan guiem llum a través d'elles. Així, doncs, en la *primera part* de la tesi analitzem teòricament aquests fenòmens electromagnètics i, posteriorment, estudiem la viabilitat de la tecnologia MCF en distints tipus de xarxes òptiques de transport, específicament, en aquelles que fan ús de transmissions *ràdio-sobre-fibra*. Estos resultats poden ser de gran utilitat per a les futures generacions mòbils 5G i Beyond-5G en les pròximes dècades.

Addicionalment, a fi d'expandir les funcionalitats bàsiques de les fibres MCF, esta tesi explora noves estratègies de disseny de les mateixes utilitzant l'analogia existent entre les equacions que regixen la mecànica quàntica i l'electromagnetisme. Amb aquesta idea en ment, en la *segona part* de la tesi proposem dissenyar una nova classe de fibres MCF usant les matemàtiques de la *supersimetria*, sorgida en el si de la teoria de cordes i de la teoria quàntica de camps com un marc teòric de treball que permet unificar les interaccions fonamentals de la natura (la nuclear forta, la nuclear feble, l'electromagnetisme i la gravetat). Al voltant d'aquesta idea sorgeixen les fibres MCF supersimètriques, les quals ens permeten processar la informació dels usuaris durant la pròpia propagació de la llum a través d'elles, reduint així la complexitat del processament de dades de l'usuari a recepció.

Finalment, esta tesi es completa introduint un canvi de paradigma que permet dissenyar dispositius fotónicos disruptius. Demostrem que la supersimetria de mecànica quàntica no relativista, proposta com una sèrie de transformacions matemàtiques restringides al *domini espacial*, es pot estendre també al *domini del temps*, almenys dins del marc de treball de la fotónica. Com resultat de les nostres investigacions, demostrem que la supersimetria temporal pot convertir-se en una plataforma prometedora per a la fotònica integrada ja que ens permet dissenyar nous dispositius òptics versàtils i ultracompactes que poden jugar un paper clau en els processadors del futur.

Per tal de fer els resultats principals d'aquesta tesi doctoral el més generals possibles, es detalla com poder extrapolar-los a altres camps de la física com ara la acústica i la mecànica quàntica.

Abstract

To date, communication networks based on optical fibers are rapidly approaching their capacity limit as a direct consequence of the increment of the data traffic demand in the last decade due to the ubiquity of smartphones, tablets, social networks, cloud computing applications, streaming services including video and gaming, and machine-to-machine communications. In such a scenario, a new class of optical fiber which is able to integrate the capacity of several classical optical fibers approximately in the same transverse section as that of the original one, the *multi-core fiber* (MCF), has been recently proposed to overcome the capacity limits of current optical networks.

However, the possibility of exploiting the full potential of an MCF requires to deeply understand the electromagnetic phenomena that can be observed when guiding light in this optical medium. In this vein, in the *first part* of this thesis, we analyze theoretically these phenomena and, next, we study the suitability of the MCF technology in optical transport networks using *radio-over-fiber* transmissions. These findings could be of great utility for 5G and Beyond-5G cellular technology in the next decades.

In addition, the close connection between the mathematical framework of quantum mechanics and electromagnetism becomes a great opportunity to explore ground-breaking design strategies of these new fibers that allow us to expand their basic functionalities. Revolving around this idea, in the *second part* of this thesis we propose to design a new class of MCFs using the mathematics of *supersymmetry* (SUSY), emerged within the context of string and quantum field theory as a means to unify the basic interactions of nature (strong, electroweak, and gravitational interactions). Interestingly, a supersymmetric MCF will allow us, not only to propagate the light, but also to process the information of users during propagation.

Finally, we conclude this thesis by introducing a paradigm shift that allows us to design disruptive optical devices. We demonstrate that the basic ideas of SUSY in non-relativistic quantum mechanics, restricted to the *space domain* to clarify unsolved questions about SUSY in string and quantum field theory, can also be extended to the *time domain*, at least within the framework of photonics. In this way, it is shown that temporal supersymmetry may serve as a key tool to judiciously design versatile and ultra-compact optical devices enabling a promising new platform for integrated photonics.

For the sake of completeness, we indicate how to extrapolate the main results of this thesis to other fields of physics, such as acoustics and quantum mechanics.

Contents

Introduction and objectives

Since the early 1970s, optical fiber has sparked a breakthrough in communications given that it has significantly increased the data transmission capacity of communication networks. However, in the last decade, the emergence of smartphones, tablets, social networks, cloud computing applications, streaming services including video and gaming, and machine-to-machine communications has accelerated the growth of the data traffic demand. To date, communication networks based on optical fibers are rapidly approaching their capacity limit (see Chapter 1).

In such circumstances, *space-division multiplexing* (SDM) has been proposed in recent years to overcome the capacity limits of current optical networks. Specifically, the concept of SDM leads to a new generation of optical communication systems using new types of optical fibers and multiplexing techniques. The most attractive approach is the *multi-core fiber* (MCF). An MCF is able to integrate the capacity of several classical optical fibers approximately in the same transverse section. In this way, MCFs allow us to increase the data transmission capacity of our communication networks. Moreover, MCF technology emerges as a great opportunity to uncover novel applications in other branches of science such as medicine and astronomy, for instance, to develop respectively new endoscopic techniques and to detect exoplanets, as discussed in Chapter 1.

Unfortunately, the possibility of exploiting the full benefits of an MCF is not as straightforward as initially foreseen. The propagation of light through this medium involves new electromagnetic phenomena that cannot be observed in classical optical fibers. These phenomena modify the features of the propagated light and, consequently, they should be investigated in detail to exploit the complete capacity of MCFs. In this vein, in the *first part* of this thesis, concretely in Chapters 2-4, we analyze theoretically the main propagation impairments of this new optical medium. Next, using these results, we study in Chapter 5 the suitability of the MCF technology in optical transport networks using *radio-over-fiber* transmissions. These findings could be of great utility for 5G and Beyond-5G optical transport networks in the near future and in the next decades.

In addition, the close connection between the laws of quantum mechanics and electromagnetism becomes a great opportunity to explore ground-breaking design strategies of these SDM fibers that allow us to expand their basic functionalities. In such a scenario, the mathematics of *supersymmetry* (SUSY), emerged in string and quantum field theory as a means to unify the strong, electroweak, and gravitational interactions, are explored in the *second part* of this thesis to design a new class of MCFs: the supersymmetric MCF (see Chapters 6 and 7). Interestingly, this kind of fibers will allow us, not only to propagate the light, but also to process the information of users during propagation. This opens up the possibility of enabling privileged communications in future SDM systems, reducing at the same time the complexity of the digital signal processor at the receiver.

Next, motivated by the exotic ideas of SUSY in non-relativistic quantum mechanics, restricted to the *space domain*, we contemplate the possibility of extending its foundations to the *time domain*, at least within the framework of photonics. We conclude this thesis revolving around this idea in Chapter 8. In this way, we show that temporal SUSY may serve as a unique tool to judiciously design ultra-compact, reconfigurable and polarization-independent optical devices which define a promising platform for integrated photonics.

Finally, in Chapter 9, we highlight the main results of this thesis, we indicate how to extrapolate them to other branches of physics such as acoustics and quantum mechanics, and we discuss the ongoing and future work.

Chapters and scientific contributions

This thesis has contributed with different scientific publications in several international journals, international conferences and in a book chapter. The list of publications is detailed on page 313. Here, we summarize in Table I the relation of each thesis chapter with the corresponding scientific publications.

Chapters	**Journals**	**Books**	**Conferences**
Chapter 1	-	Book 1	Conf. 9
Chapter 2	Papers 1, 2, 3	-	Conf. 8, 9
Chapter 3	Papers 1, 4	-	Conf. 10
Chapter 4	Papers 6, 9†	-	Conf. 10
Chapter 5	Papers 2, 5	-	Conf. 1-7
Chapter 6	Paper 10†	-	-
Chapter 7	Paper 7	-	Conf. 11
Chapter 8	Papers 8†, 10†	-	-
Chapter 9	Paper 9†	-	-

Table I. Relation between thesis chapters and scientific publications. [†: Paper submitted]

Collaborations

This thesis has been developed in collaboration with Prof. Francisco Javier Fraile-Peláez from Universidad de Vigo (Chapters 3 and 4), Dr. Carlos García-Meca from Universitat Politècnica de València (Chapters 3, 4, 6, 7 and 8), and Dra. María Morant Pérez from Universitat Politècnica de València (Chapters 2, 3 and 5).

Prof. Demetrios Christodoulides and Dr. Rodrigo Amezcua-Correa from CREOL, The College of Optics & Photonics at University of Central Florida, are also acknowledged for their thoughtful discussions and recommendations that greatly contributed to the results of Chapter 8.

Funding

This work was supported by the Spanish F.P.I. Grant BES-2013-062952 and by the Spanish Plan projects: MINECO/FEDER UE MODAL TEC2012-38558-C02-01, MINECO/FEDER UE XCORE TEC2015-70858-C2-1-R, AEI/FEDER UE JIN TEC2015-73581, HIDRASENSE RTC-2014-2232-3, and GVA AICO/18 NXTIC.

Formalism and notation

Before delving into the theory of multi-core fibers and supersymmetry, let us briefly discuss some basic notes about the formalism and notation employed in this thesis:

- *Slowly-varying function.* This concept applies, for instance, to the refractive index profile in gradual-index fibers. Given a complex-valued function $f : \mathbb{R}^n \to \mathbb{C}$, we will say that f has a slowly-varying evolution in the x_i variable if, by definition, $\delta_i f(\boldsymbol{x}) \ll |f(\boldsymbol{x})|$ in $\delta x_i \sim x_{\mathrm{R}}$, where $\delta_i f(\boldsymbol{x}) := |f(\boldsymbol{x}) - f(\boldsymbol{x} + \delta x_i \hat{u}_i)|$ and x_{R} is a positive-real value of reference. Thus $(\partial/\partial x_i \equiv \partial_i)$:
$$\frac{\delta_i f(\boldsymbol{x})}{\delta x_i} \ll \frac{|f(\boldsymbol{x})|}{x_{\mathrm{R}}} \Rightarrow |\partial_i f(\boldsymbol{x})| \ll \frac{|f(\boldsymbol{x})|}{x_{\mathrm{R}}}.$$

In addition, bearing in mind the slowly-varying nature of the above function in the $\hat{u}_i$ direction, we can also assume that if $|\partial_i f(\boldsymbol{x})| < |f(\boldsymbol{x})|$, then $\left|\partial_i^2 f(\boldsymbol{x})\right| < |\partial_i f(\boldsymbol{x})|$. As a result, we conclude that:

$$|\partial_i f(\boldsymbol{x})| \ll \frac{|f(\boldsymbol{x})|}{x_{\mathrm{R}}} \Rightarrow \left|\partial_i^2 f(\boldsymbol{x})\right| \ll \frac{1}{x_{\mathrm{R}}} |\partial_i f(\boldsymbol{x})| \ll \frac{1}{x_{\mathrm{R}}^2} |f(\boldsymbol{x})| .$$

Finally, note that x_i may also describe a time variable.

- The *real representation* or *real wave function* of a field will be denoted by using a calligraphic notation. As an example, the real representation of the electric field strength will be written as $\boldsymbol{\mathcal{E}}(\boldsymbol{r}, t)$.

- We define the *one-dimensional temporal Fourier transform* as:

$$\boldsymbol{\mathcal{E}}(\boldsymbol{r}, t) := \frac{1}{2\pi} \int_{-\infty}^{\infty} \widetilde{\boldsymbol{\mathcal{E}}}(\boldsymbol{r}, \omega) \exp(j\omega t) \, \mathrm{d}\omega;$$
$$\widetilde{\boldsymbol{\mathcal{E}}}(\boldsymbol{r}, \omega) := \int_{-\infty}^{\infty} \boldsymbol{\mathcal{E}}(\boldsymbol{r}, t) \exp(-j\omega t) \, \mathrm{d}t,$$

using a tilde to denote the Fourier-transformed functions. In this context, $\boldsymbol{\mathcal{E}}^+$ and $\boldsymbol{\mathcal{E}}^-$ account for the positive and negative frequencies of the spectrum, respectively:

$$\boldsymbol{\mathcal{E}}(\boldsymbol{r}, t) = \boldsymbol{\mathcal{E}}^-(\boldsymbol{r}, t) + \boldsymbol{\mathcal{E}}^+(\boldsymbol{r}, t) = \frac{1}{2\pi} \int_{-\infty}^{0} \widetilde{\boldsymbol{\mathcal{E}}}(\boldsymbol{r}, \omega) \exp(j\omega t) \, \mathrm{d}\omega + \frac{1}{2\pi} \int_{0}^{\infty} \widetilde{\boldsymbol{\mathcal{E}}}(\boldsymbol{r}, \omega) \exp(j\omega t) \, \mathrm{d}\omega.$$

Taking into account that $\boldsymbol{\mathcal{E}}$ is real, then $\widetilde{\boldsymbol{\mathcal{E}}}(\boldsymbol{r}, \omega) = \widetilde{\boldsymbol{\mathcal{E}}}^*(\boldsymbol{r}, -\omega)$ and, consequently $\boldsymbol{\mathcal{E}}^- = (\boldsymbol{\mathcal{E}}^+)^*$. Therefore, $\boldsymbol{\mathcal{E}} = 2\mathrm{Re}\left\{\boldsymbol{\mathcal{E}}^+\right\}$.

- The *analytic representation* or *analytic signal* $\boldsymbol{E}(\boldsymbol{r}, t)$ is defined as the complex function which contains only the positive frequencies of $\boldsymbol{\mathcal{E}}(\boldsymbol{r}, t)$. More specifically, $\boldsymbol{E}(\boldsymbol{r}, t)$ is defined via its 1D temporal Fourier transform as:

$$\widetilde{\boldsymbol{E}}(\boldsymbol{r}, \omega) := \begin{cases} 2\widetilde{\boldsymbol{\mathcal{E}}}(\boldsymbol{r}, \omega) & \omega > 0 \\ \widetilde{\boldsymbol{\mathcal{E}}}(\boldsymbol{r}, 0) & \omega = 0 \\ 0 & \omega < 0 \end{cases}.$$

Interestingly, it can be shown that $\boldsymbol{E}(\boldsymbol{r}, t) = \boldsymbol{\mathcal{E}}(\boldsymbol{r}, t) + j\check{\boldsymbol{\mathcal{E}}}(\boldsymbol{r}, t)$ where $\check{\boldsymbol{\mathcal{E}}}$ is the Hilbert transform of $\boldsymbol{\mathcal{E}}$.[1] Hence, $\boldsymbol{\mathcal{E}} = \mathrm{Re}\{\boldsymbol{E}\}$, which leads to the relation $\boldsymbol{E} = 2\boldsymbol{\mathcal{E}}^+$. The analytic representation of a signal was introduced by Dennis Gabor in 1946 [1]. In the monochromatic regime (Chapter 2), we will write the analytic representation of the electric field strength as $\boldsymbol{E}(\boldsymbol{r}, t) = \boldsymbol{E}_{\omega_0}(\boldsymbol{r}) \exp(j\omega_0 t)$, where $\boldsymbol{E}_{\omega_0}$ is the *complex amplitude*. In this way, the real representation can be expressed as:

$$\boldsymbol{\mathcal{E}}(\boldsymbol{r}, t) = \mathrm{Re}\left\{\boldsymbol{E}_{\omega_0}(\boldsymbol{r}) \exp(j\omega_0 t)\right\} = \frac{1}{2}\left[\boldsymbol{E}_{\omega_0}(\boldsymbol{r}) \exp(j\omega_0 t) + \boldsymbol{E}_{-\omega_0}(\boldsymbol{r}) \exp(-j\omega_0 t)\right],$$

with $\boldsymbol{E}_{-\omega_0} = (\boldsymbol{E}_{\omega_0})^*$. In optical media operating in the monochromatic regime but perturbed by temporal fluctuations of the refractive index (Chapter 3), and in the quasi-monochromatic regime (Chapter 4), $\boldsymbol{E}_{\omega_0}$ is also assumed to be time-dependent to describe the slowly-varying temporal perturbations of the medium or the slowly-varying temporal evolution of a pulse.

[1] The simplest example is the harmonic function $\exp(j\omega t) = \cos(\omega t) + j\sin(\omega t)$, where $\sin(\omega t)$ is the Hilbert transform of $\cos(\omega t)$.

- We define the *two-dimensional Fourier transform* as (Chapter 8):

$$\boldsymbol{\mathcal{E}}(\boldsymbol{r},t) := \frac{1}{4\pi^2}\int_{-\infty}^{\infty}\int_{-\infty}^{\infty}\widetilde{\boldsymbol{\mathcal{E}}}(k,\omega;\boldsymbol{r}_{\mathrm{T}})\exp(-j\boldsymbol{k}\cdot\boldsymbol{r})\exp(j\omega t)\,\mathrm{d}k\mathrm{d}\omega;$$
$$\widetilde{\boldsymbol{\mathcal{E}}}(k,\omega;\boldsymbol{r}_{\mathrm{T}}) := \int_{-\infty}^{\infty}\int_{-\infty}^{\infty}\boldsymbol{\mathcal{E}}(\boldsymbol{r},t)\exp(j\boldsymbol{k}\cdot\boldsymbol{r})\exp(-j\omega t)\,\mathrm{d}r_{\mathrm{L}}\mathrm{d}t,$$

  where the vector position $\boldsymbol{r} = \boldsymbol{r}_{\mathrm{T}} + \boldsymbol{r}_{\mathrm{L}} = \boldsymbol{r}_{\mathrm{T}} + r_{\mathrm{L}}\hat{u}_{\mathrm{L}}$ is described as a function of the transversal ($\boldsymbol{r}_{\mathrm{T}}$) and parallel vectors ($\boldsymbol{r}_{\mathrm{L}}$) to the propagation direction of the electromagnetic energy ($\hat{u}_{\mathrm{L}}$). We contemplate two different scenarios: (*i*) the spatial scattering and (*ii*) the temporal scattering. In both cases, a reflected and a transmitted wave can be observed as a result of the interaction of an incident wave with a localized refractive index variation in space $[n(\boldsymbol{r})]$ or in time $[n(t)]$. In the former scenario, $\boldsymbol{\mathcal{E}}^{+}$ and $\boldsymbol{\mathcal{E}}^{-}$ will be respectively associated with the description of the positive and negative *frequencies* of the spectrum:

$$\begin{aligned}\boldsymbol{\mathcal{E}}(\boldsymbol{r},t) = \boldsymbol{\mathcal{E}}^{-}(\boldsymbol{r},t) + \boldsymbol{\mathcal{E}}^{+}(\boldsymbol{r},t) &= \frac{1}{4\pi^2}\int_{k=-\infty}^{\infty}\int_{\omega=-\infty}^{0}\widetilde{\boldsymbol{\mathcal{E}}}(k,\omega;\boldsymbol{r}_{\mathrm{T}})\exp(-j\boldsymbol{k}\cdot\boldsymbol{r})\exp(j\omega t)\,\mathrm{d}\omega\mathrm{d}k\\ &+ \frac{1}{4\pi^2}\int_{k=-\infty}^{\infty}\int_{\omega=0}^{\infty}\widetilde{\boldsymbol{\mathcal{E}}}(k,\omega;\boldsymbol{r}_{\mathrm{T}})\exp(-j\boldsymbol{k}\cdot\boldsymbol{r})\exp(j\omega t)\,\mathrm{d}\omega\mathrm{d}k.\end{aligned}$$

  In the latter scenario, $\boldsymbol{\mathcal{E}}^{+}$ and $\boldsymbol{\mathcal{E}}^{-}$ will be respectively associated with the description of the positive and negative *wave numbers* of the spectrum:

$$\begin{aligned}\boldsymbol{\mathcal{E}}(\boldsymbol{r},t) = \boldsymbol{\mathcal{E}}^{-}(\boldsymbol{r},t) + \boldsymbol{\mathcal{E}}^{+}(\boldsymbol{r},t) &= \frac{1}{4\pi^2}\int_{k=-\infty}^{0}\int_{\omega=-\infty}^{\infty}\widetilde{\boldsymbol{\mathcal{E}}}(k,\omega;\boldsymbol{r}_{\mathrm{T}})\exp(-j\boldsymbol{k}\cdot\boldsymbol{r})\exp(j\omega t)\,\mathrm{d}\omega\mathrm{d}k\\ &+ \frac{1}{4\pi^2}\int_{k=0}^{\infty}\int_{\omega=-\infty}^{\infty}\widetilde{\boldsymbol{\mathcal{E}}}(k,\omega;\boldsymbol{r}_{\mathrm{T}})\exp(-j\boldsymbol{k}\cdot\boldsymbol{r})\exp(j\omega t)\,\mathrm{d}\omega\mathrm{d}k.\end{aligned}$$

  In both cases, taking into account that $\boldsymbol{\mathcal{E}}$ is real, then $\widetilde{\boldsymbol{\mathcal{E}}}(k,\omega;\boldsymbol{r}_{\mathrm{T}}) = \widetilde{\boldsymbol{\mathcal{E}}}^{*}(-k,-\omega;\boldsymbol{r}_{\mathrm{T}})$ and, consequently $\boldsymbol{\mathcal{E}}^{-} = (\boldsymbol{\mathcal{E}}^{+})^{*}$. That is, $\boldsymbol{\mathcal{E}} = 2\mathrm{Re}\{\boldsymbol{\mathcal{E}}^{+}\}$.

- Bearing in mind that $\boldsymbol{\mathcal{E}}^{+}$ and $\boldsymbol{\mathcal{E}}^{-}$ have a different definition in the spatial and temporal scattering problems, the *analytic representation* (or analytic signal) $\boldsymbol{E}(\boldsymbol{r},t)$ must be defined in a different way in each case. Specifically, in the spatial scattering problem $\boldsymbol{E}(\boldsymbol{r},t)$ only describes the positive frequencies of $\boldsymbol{\mathcal{E}}(\boldsymbol{r},t)$ via its 2D Fourier transform:

$$\widetilde{\boldsymbol{E}}(k,\omega;\boldsymbol{r}_{\mathrm{T}}) := \begin{cases}2\widetilde{\boldsymbol{\mathcal{E}}}(k,\omega;\boldsymbol{r}_{\mathrm{T}}) & \omega > 0\\ \widetilde{\boldsymbol{\mathcal{E}}}(k,0;\boldsymbol{r}_{\mathrm{T}}) & \omega = 0\\ 0 & \omega < 0\end{cases},$$

  and in the temporal scattering $\boldsymbol{E}(\boldsymbol{r},t)$ only describes the positive wave numbers of $\boldsymbol{\mathcal{E}}(\boldsymbol{r},t)$:

$$\widetilde{\boldsymbol{E}}(k,\omega;\boldsymbol{r}_{\mathrm{T}}) := \begin{cases}2\widetilde{\boldsymbol{\mathcal{E}}}(k,\omega;\boldsymbol{r}_{\mathrm{T}}) & k > 0\\ \widetilde{\boldsymbol{\mathcal{E}}}(0,\omega;\boldsymbol{r}_{\mathrm{T}}) & k = 0\\ 0 & k < 0\end{cases}.$$

  However, note that in both cases $\boldsymbol{\mathcal{E}} = \mathrm{Re}\{\boldsymbol{E}\}$ and $\boldsymbol{E} = 2\boldsymbol{\mathcal{E}}^{+}$.

- A Helmholtz equation is a second-order homogeneous partial differential equation (PDE) of the form:

$$\left(\triangle + k^2\right)\phi(\boldsymbol{r}) = 0,$$

  where $\triangle$ is the Laplacian operator, k is a real number, and ϕ is a scalar field. In coherence with the mathematical literature of PDEs [2–6], we will also refer to a Helmholtz equation when:

  - k is a function. In such a case, the PDE is usually termed as a Helmholtz equation with variable coefficients.
  - The right-hand side of the above equation is not null, in which case the PDE is referred to as a non-homogeneous Helmholtz equation.

- In the second part of this thesis, we will usually refer to non-relativistic quantum mechanics simply as quantum mechanics. In fact, the non-relativistic quantum-mechanical version of supersymmetry is simply termed as supersymmetric quantum mechanics in the literature.

- In order to use a more economical notation, we will usually denote the limit of a real or complex-valued function f at $x \to a$ as:

$$\lim_{x \to a} f(x) \equiv f(x \to a).$$

This page was intentionally left blank.

Part I

Multi-core Optical Fiber: Theoretical Analysis and Transmission Performance

Chapter 1

Space-division multiplexing and multi-core fiber

1.1 Introduction

Optical fiber has sparked a new paradigm in communications as it has significantly increased the Shannon capacity of communication networks based on metallic waveguides [7]. Nowadays, the data traffic carried on access and backbone networks is easily covered thanks to the development of the optical fiber technology in the second half of the last century [8]. Figure 1 depicts the evolution of the system capacity per optical fiber along with the underlying technologies employed during the past four decades.

The birth of optical communications in the early 1970s produced an explosive growth in the data traffic capacity [9]. In 1975, the first commercial fiber-optic cable system was developed operating at 45 Mb/s. Two years later, in 1977, General Telephone and Electronics sent the first live telephone traffic in Long Beach (California) using an optical fiber with a bit rate capacity of 6 Mb/s. Since these early systems were initially limited by multi-mode dispersion, the single-mode regime was revealed as a fundamental feature to improve the system performance. At this first stage, the bit rate was progressively increased by using on-off keying (OOK) modulation formats and time-division multiplexed (TDM) transmissions. Unfortunately, the propagation distance of these systems was limited by the fiber losses.

In order to overcome this issue, optical amplification was developed in the early 1990s [8]. Specifically, erbium-doped fiber amplifiers (EDFA) and wavelength-division multiplexed (WDM) optical transmissions enabled to increase not only the propagation distance, but also the bit rate per fiber from tens of Gb/s to few Tb/s [10]. During the next decade, the communication bandwidth demand was economically covered in access and backbone networks by EDFA&WDM systems using OOK signals and direct detection. Since the early 2000s, the efforts of the scientific community were focused on increasing the spectral efficiency of optical networks to cover the data traffic demand. Advanced modulation formats and coherent detection became a highly desirable technical advancement [11]. In particular, the use of coherent optical receivers with the combination of digital signal processing (DSP) algorithms has led to increase the long transmission distances and high spectral efficiencies required for current commercial optical networks [8].

However, in the last decade, the emergence of smartphones, tablets, social networks, cloud computing, streaming transmissions and machine-to-machine (M2M) communications has accelerated the growth of the data traffic. To date, in spite of the fact that the data traffic demand is easily covered by WDM systems using single-mode single-core fibers (SM-SCFs[1]), recent works indicate that these WDM systems are rapidly approaching their Shannon capacity [12]. Aimed to overcome this channel capacity limit, *space-division multiplexing* (SDM) has been proposed in recent years [13].

[1] SM-SCFs are also termed as single-mode fibers (SMFs) in the literature.

The term *optical SDM* refers to multiplexing techniques that establish multiple spatially distinguishable data paths through a single or multiple parallel waveguides. This concept was originally conceived in the decade of 1980 [14]. Unfortunately, the technology underneath optical SDM was immature and extremely expensive, especially in the manufacturing process. Nevertheless, the fabrication methods have been extensively developed in the last decade reducing the manufacturing cost of the SDM technology [8, 15]. In such a scenario, new types of optical fibers supporting SDM transmissions have been proposed [13]. In the next section, we will review the main SDM optical waveguides, focusing our attention especially on optical fibers comprising several cores in a single cladding, the so-called *multi-core fiber*.

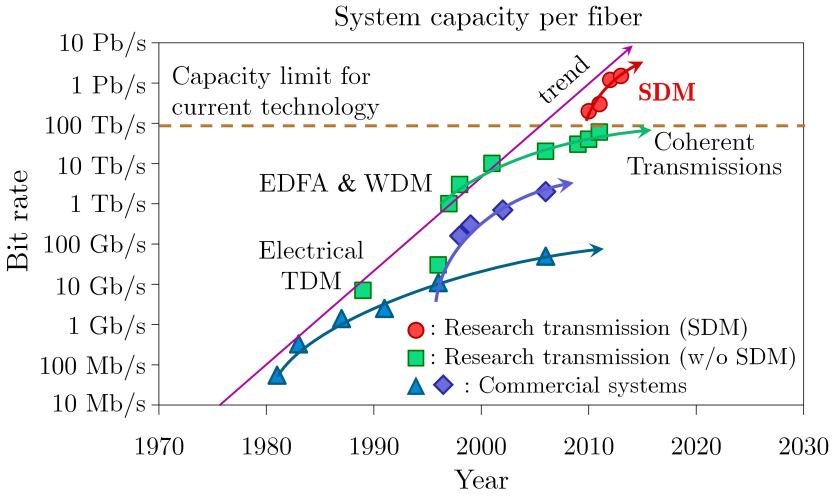

Figure 1.1. Historic evolution and growth trend of the system capacity per optical fiber in research and commercial systems [16].

1.2 Space-division multiplexing in optical communications: technical approaches

An SDM transmission comprising multiple individual spatial light paths can be performed by using diverse technical approaches. Figure 1.2 depicts the cross-sectional area of different optical waveguides proposed for realizing SDM. Specifically, although we have shown fiber designs with a compact cladding, the same concepts here discussed can also be applied to microstructured optical fibers [13].

Single-core fiber. A single-core fiber (SCF) with a normalized frequency set to guide several modes can be employed to perform mode-division multiplexing (MDM) [Fig. 1.2(a)]. In such a scenario, each mode is an individual data path [16]. Typically, since MDM transmissions have significant mode-coupling and differential mode group delay (DMGD), we can observe inter-symbol interference in these systems. To mitigate this physical impairment, DSP based on multiple-input multiple-output (MIMO) techniques is required at the receiver [17], as in wireless systems with multipath interference and multiple antennas at the transmitter and receiver.

In general, fiber manufacturing imperfections and external environmental factors such as floor vibrations may increase the mode-coupling among the different SCF modes. In such circumstances, the MIMO DSP complexity is found to be directly proportional to the total DMGD of the link [17]. This inherently implies that, unless there is a breakthrough in MIMO algorithms, multi-mode SCFs (MM-SCFs[2]) are unsuitable for future real-deployed long-haul SDM transmissions due to the high

[2]MM-SCFs are also referred to as multi-mode fibers (MMFs).

complexity required by the DSP at the receiver. Recent results have been reported by using MM-SCFs with a low number of modes, termed as *few-mode fibers* (FMFs), with a reduced DMGD [18] and on-line MIMO processing [19].

Fiber bundle. Early attempts to realize SDM were by means of the fiber bundle [13]. A fiber bundle is composed of physically independent SCFs operating in the single-mode or multi-mode regime [Fig. 1.2(b)]. In the former case, the fundamental mode of each SCF is an individual data path. In the latter case, the data paths are composed by the different guided modes of each fiber of the bundle. In both cases, the total number of distinguishable data paths is found to be the number of guided modes/fiber $\times$ the number of fibers. Thus, this SDM solution may combine two levels of spatial multiplexing.

In this scenario, the cable operators have the possibility of re-using the current SCF installations, but with a reduced core density given that this SDM solution includes a different cladding per core. This entails a minimum integration level in the SDM system due to the requirement of using independent network devices per core such as transmitters, amplifiers and receivers among other examples. Along this line, it should be noted that the installation of independent optical fiber amplifiers requires a different pumped laser per amplifier, which poses an incremental energy cost in the SDM network, especially in long-haul transmissions [20]. In addition, the high cross-sectional area of each cladding implies a reduced spatial efficiency. This increases the installation cost [8,13], the visual impact, and becomes a fundamental drawback in SDM applications which require a high spatial efficiency, such as in biomedical images, astronomy or satellite communications among others (see Section 1.4). On the other hand, an SCF bundle inherits the dissimilar thermal properties of each individual fiber, which may give rise to a different bit error rate (BER) in each SDM channel [21]. Cable operators such as Telefónica I+D are investigating this SDM solution as a first step to migrate from the current SCF-WDM networks to the SDM technology [22].

Multi-core fiber. The natural proposal of an SDM waveguide is the multi-core fiber (MCF). An optical MCF comprises an array of physically distinct cores in a single cladding [Fig. 1.2(c)]. As in the fiber bundle, an MCF may combine two levels of spatial multiplexing. The total number of data paths is the number of cores $\times$ the number of guided modes/core. However, the core density is found to be much higher than in the fiber bundle. More broadly, the high core density of this proposal allows us to increase the integration level in peripheral network devices of the SDM system. As a simple example, let us consider an MCF with N cores and M guided modes per core. The corresponding SDM transmission only requires a single transmitter and a single receiver with $N \times M$ spatial data paths. In addition, a given optical fiber amplifier of the network should be able to amplify the $N \times M$ channels using a single pumped laser. Hence, an MCF system implies a higher integration level and a lower energy consumption than the SDM solutions discussed before. In this scenario, MCF transmitters, receivers and amplifiers have been extensively researched in recent years [13, 20].

The aforementioned features would also be of special interest in data centers, with an increasing scalability of the channel capacity and a substantial reduction in space and energy cost [23]. On the other hand, in the next decades, MCF technology could also provide a lower installation cost, an easier civil construction and a smaller visual impact than the current SCF bundles [8].

As shown in Fig. 1.3 and we will see in more detail in the next section, there are different types of MCFs. Remarkably, MCFs with similar cores and operating in the single-mode regime, the so-called *homogeneous single-mode* MCFs, are of special interest in optical communications given that the differential group delay between two different data paths is found to be lower in these fibers than in an SM-SCF bundle [21] or in any other SDM proposal. Consequently, these MCFs allow us to increase the current channel capacity of our optical networks by exploiting six signal dimensions (time, wavelength, amplitude, phase, polarization and space) through spatial multi-dimensional modulation formats and guaranteeing at the same time a reduced DSP complexity at the receiver [24]. For these reasons, the first part of this thesis is mainly focused on the analysis of the single-mode regime of this new kind of optical fibers.

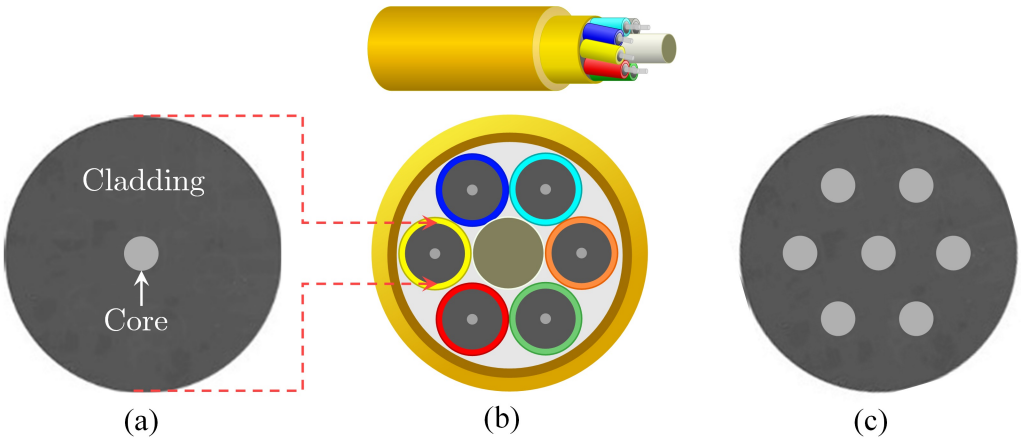

Figure 1.2. Different optical fibers for realizing SDM transmissions. (a) Single-core fiber (SCF). An SCF only supports SDM transmissions when operating in the multi-mode regime. Each mode can be employed as an individual light path performing mode-division multiplexing (MDM). (b) Fiber bundle composed of physically independent SCFs. This solution allows us to re-use the current fiber installations with a reduced core density and minimum integration levels in the optical network (transmitters, receivers, amplifiers and additional optical devices). (c) Multi-core fiber (MCF) comprising several cores in a single cladding. Each core can support a single or several guided modes (see next section). MCFs allows us to reach high integration levels in the optical network. Although we have shown the typical cross-sectional area of classical silica fibers with a compact cladding, the same concepts can be applied to microstructured optical fibers [13].

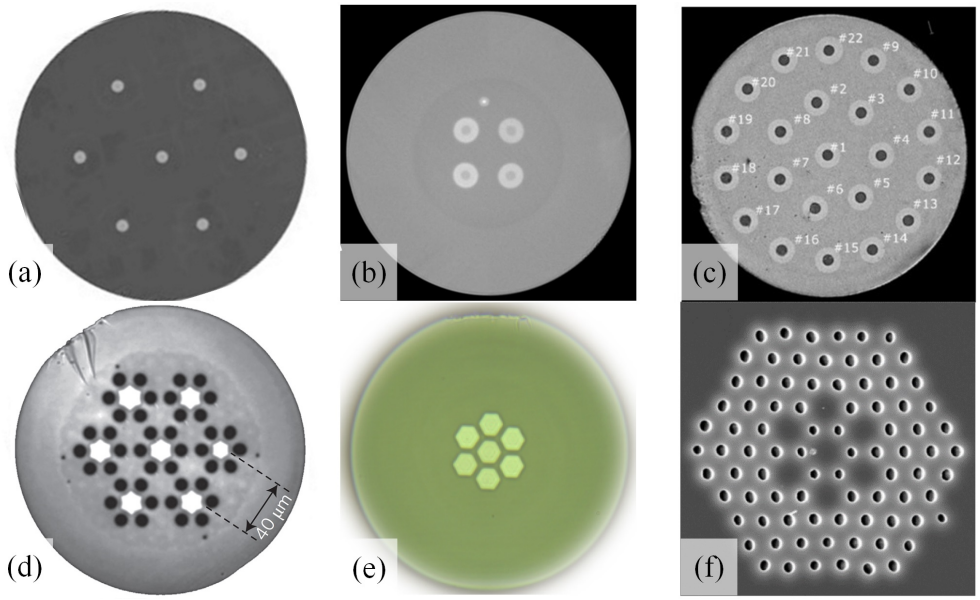

Figure 1.3. Cross-section microscope image of fabricated MCFs. (a) 7-core homogeneous single-mode MCF (reproduced from Ref. [25] © 2017 Fibercore), (b) 4-core coupled-core MCF (reproduced from Ref. [26] © 2016 Optical Society of America), (c) 22-core trench-assisted single-mode MCF (reproduced from Ref. [27] © 2015 IEEE), (d) 7-core hole-assisted few-mode MCF (reproduced from Ref. [28] © 2014 Springer Nature), (e) 7-core multi-mode MCF with hexagonal shaped cores (reproduced from Ref. [29] © 2015 IEEE), (f) 7-core photonic crystal fiber (reproduced from Ref. [30] © 2013 IOPscience).

1.3 Multi-core fiber types

MCF designs can be classified in different categories according to diverse fiber parameters and characteristics. Table 1.1 shows the usual MCF designs employed for optical transmissions, laser and sensing applications:

1. The refractive index profile of each core allows us to differentiate between step-index (SI) and gradual-index (GI) MCFs. In the former case, the refractive index profile of all cores has a step between two constant values at the interfaces that separate the cores and cladding regions. However, in the latter case, an MCF is referred to as a GI-MCF if at least one core has a continuous refractive index profile. Along this line, we can make a distinction with a third type of MCF: a trench- or hole-assisted MCF (TA-MCF or HA-MCF). A TA- or HA-MCF has a multi-step refractive index profile to reduce the mode-coupling (inter-core crosstalk) between the linearly-polarized (LP) modes of adjacent cores [31]. Specifically, in a HA-MCF, the multi-step index profile is fabricated by performing holes around the cores in the cladding region.

2. A single-mode MCF (SM-MCF) supports only the LP_{01} mode group in each core. In contrast, if a given core guides several LP mode groups, the fiber is known as a multi-mode MCF (MM-MCF). Moreover, an MCF supporting only the first three or four LP mode groups (LP_{01}, LP_{11}, LP_{21}, LP_{02}) is usually termed as a few-mode MCF (FM-MCF) [16, 28].[3]

3. Attending to the spatial homogeneity of the MCF structure, we can make a distinction between a homogeneous MCF (HO-MCF) or a heterogeneous MCF (HE-MCF). In the former case, all cores present the same refractive index profile and, in the latter case, the MCF comprises at least one core with a different refractive index profile.[4]

4. The core-to-core distance is one of the main fiber parameters which determinates the inter-core crosstalk level among the LP modes of each core. Usually, if the core-to-core distance between two homogeneous cores a and b (d_{ab}) is lower than seven times[5] the core radius R_0, the MCF operates in the strong-coupling regime and supports supermodes[6] [33]. In such a case, the MCF is referred to as a coupled-core MCF (CC-MCF). On the contrary, in the weak-coupling regime, supermodes cannot be generated and each core is considered as an individual light path. This fiber design is termed as uncoupled-core MCF (UC-MCF). Recent works have been reported with a mixed design based on coupled and uncoupled cores [34, 35].

5. If the intrinsic linear birefringence of each core $\Delta n = |n_x - n_y|$ is lower than 10^{-7}, the MCF is referred to as a lowly-birefringent MCF (LB-MCF). Otherwise, if $\Delta n > 10^{-7}$ in a given core, the MCF is known as a highly-birefringent MCF (HB-MCF). In general, an HB-MCF comprises elliptical or panda cores for polarization-maintaining applications [36, 37].

6. Additional MCF designs involve: photonic crystal MCFs [13], dispersion-shifted cores [38], selective-inscribed Bragg gratings [39] and hexagonal shaped cores [40], among others.

---

[3] In a weakly-guiding fiber, an LP_{mn} mode group without azimuthal variation ($m = 0$) includes 1 LP mode and 2 polarized core modes (2 polarizations). In contrast, an LP_{mn} mode group with azimuthal variation ($m > 0$) involves 2 LP modes and 4 different polarized core modes (2 LP modes × 2 polarizations). See Ref. [32] for more details.

[4] Two cores a and b have a different refractive index profile if $n_a(r_a) \neq n_b(r_b)$, where $r_{a(b)}$ is the local radial coordinate of each core. Hence, two SI cores have a different refractive index profile if $n_a(r_a = 0) \neq n_b(r_b = 0)$ or they have a different core radius.

[5] The condition $d_{ab} < 7R_0$ is only an approximation which is found to be valid in the third transmission window, in the single-mode regime and with $R_0 \sim 4$ μm. In general, the criterion to reach the strong-coupling regime in a given MCF depends on additional fiber parameters such as the refractive index profile and the wavelength of the optical carrier, among others.

[6] A *supermode* can be defined as an exact eigenmode of the MCF structure which cannot be regarded as a mere linear combination of the core modes in isolated conditions, i.e., when each core is completely uncoupled from the others. In this way, supermodes can only be generated in the strong-coupling regime.

MCF classification	Type 1	Type 2	Figure/Comments
Refractive index profile	Step-Index SI-MCF	Gradual-Index GI-MCF	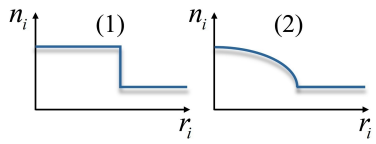
Modal regime	Single-mode SM-MCF	Multi-mode MM-MCF	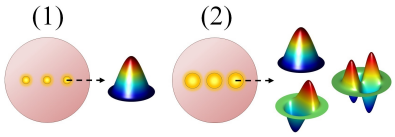
Spatial homogeneity	Homogeneous cores HO-MCF	Heterogeneous cores HE-MCF	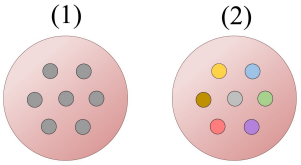
Core-to-core distance (d_{ab})	Uncoupled cores ($d_{ab} \geq 7 \cdot R_0$) UC-MCF	Coupled cores ($d_{ab} < 7 \cdot R_0$) CC-MCF	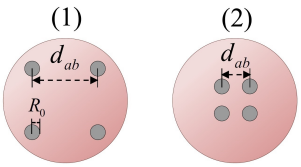
Intrinsic linear birefringence	Lowly-birefringent cores LB-MCF	Highly-birefringent cores HB-MCF	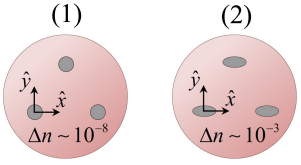
Others	(1) Trench-assisted MCF (TA-MCF), (2) Hole-assisted MCF (HA-MCF), (3) Mixed MCF design with coupled and uncoupled cores, (4) Dispersion-shifted MCF (DS-MCF), (5) MCF Bragg gratings, (6) Hexagonal shaped cores		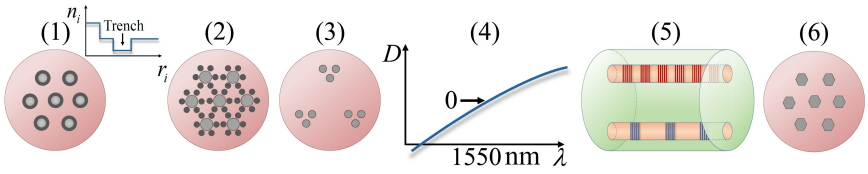

Table 1.1. Classification of multi-core fiber types [BOOK 1].

Once the MCF cross-section design is established, the specific fabrication method is of key importance for the final optical transmission performance. MCF fabrication processes have been refined and optimized in the last years as a byproduct of an intensive research work [15, 41–43]. MCF fabrication can be addressed by microstructured *stack-and-draw* technology [43], a flexible technology which allows us to fabricate very different fibers on the same machinery. Unfortunately, MCF manufacturing is a complex process with nonlinear results on the process parameters. In particular, some rods or capillaries configurations may be technically difficult to draw into the designed form, which results in an MCF with higher crosstalk levels than in the theoretical design. In this scenario, it is necessary to investigate the linear and nonlinear MCF propagation taking into account these MCF manufacturing imperfections ($\equiv$ intrinsic perturbations) along with the external ($\equiv$ extrinsic) medium perturbations (see Section 1.5).

1.4 Current and emerging applications of multi-core fiber

Once we have reviewed the fundamentals of optical SDM and the different MCF types, we will discuss in this section the main applications and opportunities of the MCF technology not only in photonics, but also in other branches of science such as medicine and experimental physics.

1.4.1 Backbone and access optical networks using multi-core fiber

SDM systems using MCFs have been extensively investigated in recent years targeting to overcome the exponential growth of data traffic in backbone and access networks [8, 12, 13]. The first laboratory MCF transmission was demonstrated in May 2010 [44]. Zhu and co-workers used an SI-SM-HO-UC-LB-7CF with a hexagonal lattice. A novel network configuration was proposed for passive optical network (PON) based on a bidirectional parallel transmission at 1310 nm and 1490 nm using a tapered MCF connector (TMC) for injecting and extracting the optical signals in the MCF.

Year	Ref.	Fiber type	Cores × LP mode groups	Distance (km)	Channel rate (Gb/s)	WDM channels per core	SE (b/s/Hz)	Total capacity (Tb/s)
2011	[45]	SM-MCF	7×1	2688	128	10	15	7
2012	[46]	SM-MCF	12×1	52	456	222	91.40	1012
2013	[47]	SM-MCF	19×1	10.1	172	100	30.50	305
2013	[48]	SM-MCF	19×1	10.1	100	125	33.60	210
2014	[28]	FM-MCF	7×2	1	5103	50	102	200
2015	[49]	SM-MCF	7×1	2520	128	73	20	51
2015	[50]	FM-MCF	36×2	5.5	107	40	108	432
2015	[51]	FM-MCF	12×2	527	40	20	94.32	24
2015	[52]	FM-MCF	19×4	9.8	40	8	345	29
2016	[53]	FM-MCF	19×4	9.8	60	360	456	2050
2017	[54]	SM-MCF	32×1	205.6	768	46	217.6	1001
2018	[55]	FM-MCF	19×4	11.3	144	739	1099.9	10160

Table 1.2. Summary of progress in MCF transmissions in recent years. The MCF type indicates only the modal regime (additional characteristics of the MCF involving the index profile, the spatial homogeneity, the core-to-core distance and the birefringence can be found in the corresponding reference). The channel rate includes polarization-division multiplexing and the overhead for forward error correction (FEC). The spectral efficiency (SE) and total capacity exclude the FEC overhead [BOOK 1].

A set of MCF experiments were reported since 2011. Scaling in capacity demonstrations, Refs. [46–48] should be mentioned. In [48] the authors demonstrated a 210 Tb/s self-homodyne transmission system using distributed feedback (DFB) lasers and a 19-core TA-SM-HO-UC-LB-MCF. Sakaguchi et al. reported in [47] a record capacity of 305 Tb/s over 10.1 km using the same MCF as in [48], with an average value of crosstalk of −32 dB at 1550 nm. The authors also fabricated a 19-channel SDM multiplexer/demultiplexer using free-space optics with low insertion losses and low additional crosstalk. As another interesting example, Takara et al. reported in [46] 1.01 Pb/s transmission over 52 km with the highest aggregate spectral efficiency of 91.4 b/s/Hz by using a one-ring-structured 12-core TA-SM-HO-UC-LB-MCF. They generated 222 WDM channels

of 456 Gb/s PDM-32QAM-SC-FDM signals[7] with 50-GHz spacing in the C and L bands. Thanks to the significant efforts performed in the design and fabrication of MCFs, the demonstration of long-haul SDM transmissions based on MCFs have shown an impressive progress in terms of capacity, reach, and spectral efficiency, as detailed in Table 1.2.

On the other hand, cloud radio-access network (C-RAN) systems should also deal with this huge future capacity demand in the next-generation wireless systems, i.e., 5G cellular technology and Beyond-5G [56, 57]. According to some telecom equipment manufacturers, it is expected that 5G cellular networks will be required to provide 1000 times higher mobile data traffic in 2025 as compared with 2013, including flexibility and adaptability solutions to maximize the energy efficiency of the network [58, 59]. In this context, a new radio-access model supporting massive data uploading will also be required including additional transport facilities in the physical layer.

Fronthaul connectivity performed by radio-over-fiber (RoF) transmission using single-input single-output (SISO), MIMO, sub-Nyquist sampling, and ultra-wideband signals exceeding 400 MHz bandwidth has been proposed for the 5G cellular generation [57, 60–62]. The required channel capacity is further extended in the case of Beyond-5G systems, where a massive number of antennas operating in MIMO configuration should be connected by using RoF. To overcome the massive increment in the data capacity demand, MCF has been recently proposed by Prof. Roberto Llorente and coworkers as a suitable medium for LTE-Advanced (LTE-A) MIMO fronthaul systems [63–65].

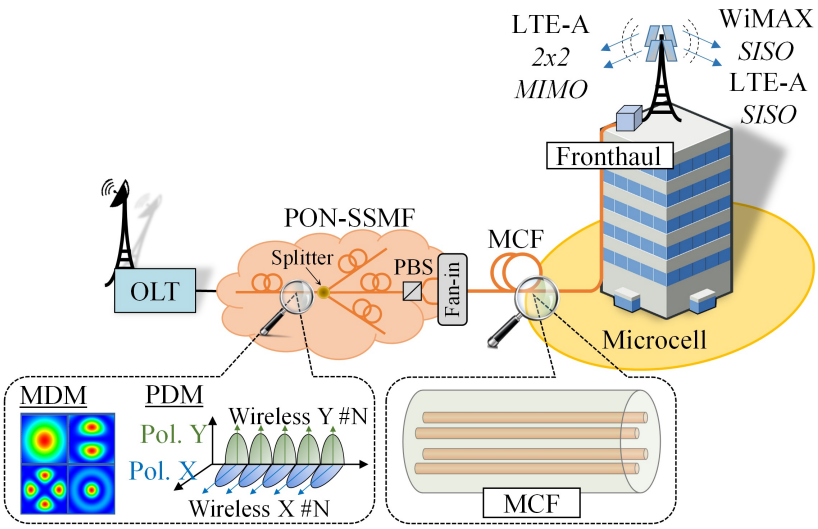

Figure 1.4. Next-generation optical fronthaul system using an MCF operating with a converged fiber-wireless PON including optical polarization-division multiplexing (PDM) and mode-division multiplexing (MDM) transmissions [BOOK 1].

MCFs open up attractive possibilities in RoF systems as different wireless signals can be simultaneously transmitted over the same optical wavelengths and electrical frequencies in different cores of the optical waveguide to provide multi-wireless service using a single laser at the transmitter. Thus, MCF technology can be proposed as an alternative to the classical SM-SCF [also termed in the literature as standard single-mode fiber (SSMF)] to provide fronthaul connectivity using multiple wavelength channels with multiple lasers. Additionally, MCFs with high core density are suitable for connecting large phase array antennas performing multi-user MIMO processing. Furthermore, network operators can offer a dynamic and scalable capacity in the next cellular generation due to the aggregated channel capacity provided by the MCF technology. Moreover, the possibility of combining MCF-RoF transmissions with additional multiplexing techniques such as TDM, WDM, PDM and MDM should be considered. Figure 1.4 depicts the proposed fronthaul

[7] PDM: Polarization-Division Multiplexing, QAM: Quadrature Amplitude Modulation, SC: Single Carrier, FDM: Frequency-Division Multiplexing.

provision applied to converged fiber wireless PON including PDM to provide connectivity between the SSMF and MCF media.

Interestingly, [65] investigates: (*i*) the tolerance of fully-standard LTE-A signals in MIMO and SISO configurations to the random crosstalk fluctuations, and (*ii*) the demonstration of fronthaul provision of both LTE-A and WiMAX signals using a 150-m SI-SM-HO-UC-LB-4CF. In order to reduce the random fluctuations of the error vector magnitude (EVM) induced by the inter-core crosstalk, the core interleaving nonlinear stimulation (CINLS) has been proposed to mismatch the propagation constant of adjacent core modes reducing the temporal and spectral EVM fluctuations of the MCF-RoF transmissions (see Chapter 5).

1.4.2 Signal processing

The potential application of the MCF technology is not only restricted to SDM transmissions. The inherent capability of an MCF to modify the propagated signals allows us to investigate a myriad of new applications for ultra-high capacity SDM transmissions and microwave photonics (MWP) based on signal processing techniques. As we will see, the basic concept of MCF signal processing is a far richer scope than initially foreseen.

In particular, in MWP, the use of MCFs to implement signal processing functionalities was firstly proposed by Gasulla and Capmany in [66]. In this work, the authors investigated the suitability of these new fibers to perform true-time delay lines (TTDLs), optical beamforming, optical filtering and arbitrary waveform generation using heterogeneous cores. These applications have been extensively researched in [38, 39, 67–70] with different MCF designs and experimental set-ups. As an attractive example, it should be remarked the proposal reported in [39, 68], where the inscription of selective Bragg gratings in a homogeneous MCF it was first introduced in [68] and later experimentally verified in [39] to achieve compact fiber-based TTDL without using heterogeneous cores. Along this line, other MWP applications such as optical beamforming can also be performed by using homogeneous cores, as described in [71]. In this work, Llorente and co-workers proposed a compact all-fiber beamformer based on an N-core homogeneous MCF.

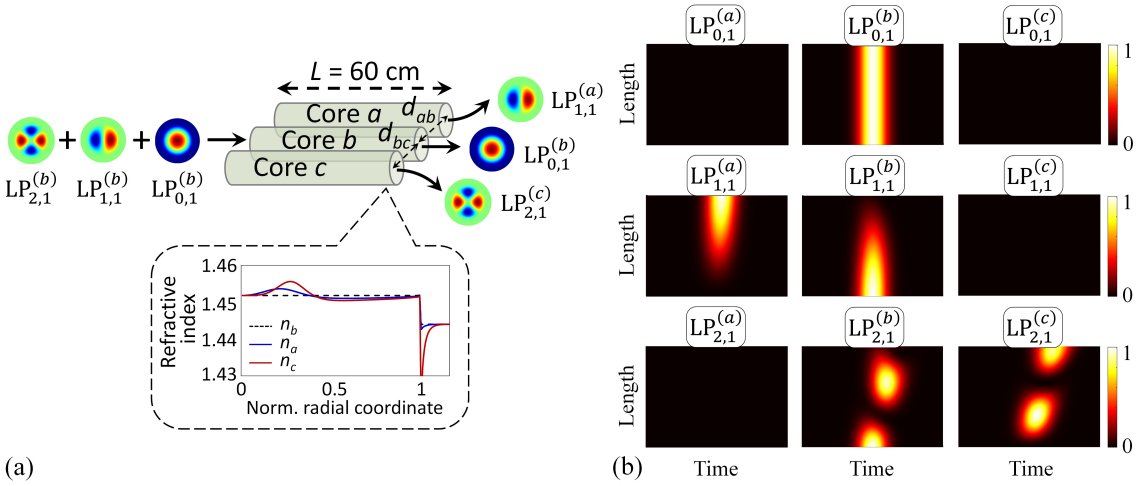

Figure 1.5. Modal (de)multiplexer based on a 60-cm 3-core MCF [74]. (a) Schematic structure of the optical device. (b) A 10 ps Gaussian pulse propagating through the: LP_{01}, LP_{11} and LP_{21} modes of the cores *a*, *b*, and *c*. Unlike in conventional demultiplexers, the mode-coupling between adjacent cores implies no mode conversion: the modes are *truly* demultiplexed.

Otherwise, MCF signal processing also refers to additional applications and functionalities such as pulse shaping, dispersion engineering, mode conversion and mode filtering applications. Remarkably, the engineering of the refractive index profile allows us to implement these fashion

features in MCF media. In this scenario, a fascinating proposal originally conceived within the framework of string and quantum field theory [72] was profitably extrapolated to photonics to design SCFs and MCFs [73, 74]: the supersymmetry (SUSY). Strikingly, one-dimensional SUSY allows us to perform the aforementioned MWP applications. The specific details can be found in Chapter 7. As an interesting example (among other applications), we include here the description of a true mode (de)multiplexer (M-MUX/DEMUX) using a 3-core MCF. Figure 1.5 shows the optical device and its functionality.

The device is designed using a 60-cm MCF comprising three cores a, b and c with a core-to-core distance of 55 μm and a core radius of 25 μm operating in the third transmission window at 1550 nm [Fig. 1.5(a)]. The index profile of the cores a and c was calculated by using SUSY isospectral transformations. The index profile of the core b was taken to be the step-index profile. The mode (de)multiplexer operates as follows. A 10-ps Gaussian optical pulse is launched to the central core b, first in the LP_{01} mode, and later in the LP_{11} and LP_{21} modes with a peak power of 0 dBm to operate in the linear regime of the MCF. The numerical simulation was performed by using a beam propagation method. Figure 1.5(b) shows the numerical results of the optical pulse propagating through each LP mode in the M-DEMUX. It is worth noting that, in contrast with conventional mode (de)multiplexing strategies [75–77], a true mode demultiplexing is demonstrated for each LP mode. At the device output, the pulse launched into the LP_{11} mode of the core b is found in the LP_{11} mode of the core a, the pulse launched into the LP_{01} mode of the core b is found in the same mode and core, and the pulse launched into the LP_{21} mode of the core b can be observed in the LP_{21} mode of the core c. Moreover, pulse shaping and dispersion engineering functionalities can be incorporated into the proposed device (see Chapter 7 for more details).

1.4.3 Multi-core fiber lasers, amplifiers and optical sensors

All-fiber designs of optical lasers, amplifiers and sensors using MCFs have been extensively investigated in recent years [78–88]. In particular, the multi-mode interference (MMI) which can be observed through a chain SMF-MCF-SMF is widely employed in lasers, amplifiers and optical sensors to improve the performance of classical designs based on SCFs [81, 86].

As one can expect, the basic concept of an active MCF is the natural evolution for the cladding-pumped rare-earth-doped fibers. The classical design using a single core offers an excellent combination of high efficiency and beam quality. However, high output powers are limited by the stimulation of nonlinear effects. In that case, the increment of the mode field area is the obvious solution to decrease the nonlinear effects. In this scenario, active MCFs offer the possibility of reducing the fiber nonlinearities using a coupled-core design to generate supermodes with large mode field area [78, 82]. Moreover, note that the gain medium is split at discrete regions (cores) inside the cladding and, therefore, the thermal dissipation is higher than in the classical single-core design. As a result, higher output powers can be achieved in MCF media [82]. On the other hand, in contrast with an SCF bundle, an N-core MCF laser/amplifier only requires a single pumped laser for N optical paths, with the corresponding energy cost reduction for the network operators [83, 84].

In this topic, an intense research work has been developed in the last decade [8, 13]. To date, most CC-MCF lasers/amplifiers operate in the in-phase supermode combining high brightness and near-diffraction limited far field profile. The selection of the in-phase supermode can be performed by using diverse methods such as phase-locking and Talbot cavities [79]. As an example, a monolithic fiber laser using a CC-MCF with highly- and lowly-reflective fiber Bragg gratings (HR/LR-FBG) is shown in Fig. 1.6(a) [81]. The MCF segment is located between the HR-FBG and the LR-FBG creating an active cavity, where the MMI allows us to obtain a high-contrast spectral modulation. In addition, the uniform illumination of the cores is achieved by performing a cladding-pumped scheme. Remarkably, this design demonstrates the direct correlation between the MMI in few-mode SCF systems and in the laser operation when multiple supermodes oscillate simultaneously. Following a similar approach, additional MCF laser and amplifier designs have been proposed in [80, 82]. Nevertheless, in long-haul SDM transmissions, the usual design is the multi-core erbium-doped-fiber-amplifier based on a cladding-pumped scheme [83, 84].

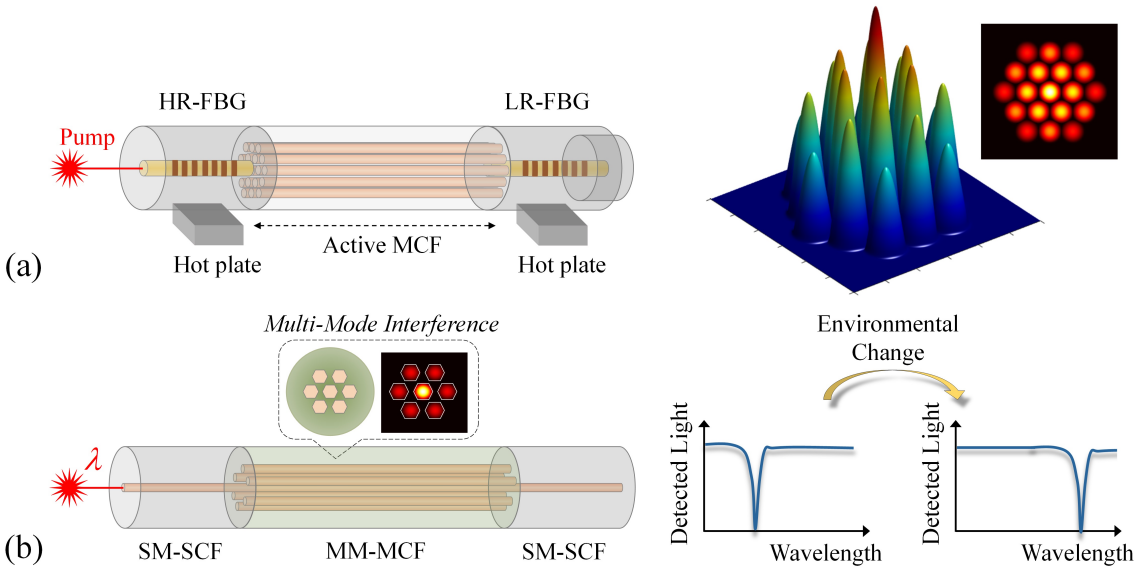

Figure 1.6. MCF laser and optical sensor operating on the principle of multi-mode interference [BOOK 1]. (a) MCF laser comprising a highly- and lowly-reflective fiber Bragg grating (HR/LR-FBG) [81]. (b) MCF optical sensor with hexagonal shaped cores [86].

On the other hand, MCF sensors are also based on a similar concept as in the laser of the previous example [see Fig. 1.6(b)]. The sensor comprises two SMFs spliced to a short MCF segment with hexagonal shaped cores. The operating principle within the MCF segment is the MMI, which induces a deep peak on the transmission spectrum. An external environmental change shifts the spectral position of the minimum. As a specific example, let us consider a temperature change. When increasing the temperature, the thermal expansion of the MCF medium will increase the refractive index of silica cores and, consequently, the peak will be shifted to a longer wavelength [86].

In the past, fiber optic sensors using SCFs have been widely discussed for sensing in a broad range of industrial and scientific applications to measure temperature, force, liquid level, and pressure, among other physical variables. Nowadays, the MCF technology allows us to design and fabricate new optical sensors providing accuracy, high resolution, compactness, stability, reproducibility and reliability [85–88].

1.4.4 Biomedical applications

Multi-core optical fibers have also been studied in recent years within the context of medicine for biomedical sensing and imaging applications [89–99]. Basically, biomedical sensors using MCFs are based on the MMI technique previously described. Thus, let us now focus our attention on biomedical imaging applications in the next paragraphs.

Nowadays, the main challenge in biomedical imaging is the study of cells in biological tissues. In this scenario, the multiphoton microscopy and adaptive optics become fundamental technologies because of their benefits in cellular resolution, high sensitivity, and high imaging rate [99]. In particular, the two photon excited fluorescence (TPEF) microscopy requires the use of adaptive optics to increase the imaging depth, in practice limited to 1 mm [100]. Remarkably, the so-called *lensless endoscope* is based on the TPEF microscopy and adaptive optics adding at the same time the use of an optical waveguide [99]. The waveguide should be capable of acquiring a multiphoton image of an object located at its tip. To this end, MCFs have been proposed as a necessary technology for the realization of ultrathin lensless endoscopes [89–99]. Figure 1.7 depicts different MCF types proposed for biomedical imaging along with a basic scheme of adaptive optics using a spatial light modulator (SLM).

In general, MCFs used for image transport require a high number of cores (> 100) with weak mode-coupling and low intermodal dispersion among cores. Therefore, the preferred design is an SI-SM-HO-CC-LB-MCF, in line with the MCF shown in Fig. 1.7(a). Examples of this MCF type fabricated for medical imaging purposes can be found in [90–92], with a core-to-core distance lower than 20 μm and inter-core crosstalk levels lower than $-20\,\mathrm{dB/m}$. In spite of the fact that the intermodal dispersion can be reduced with a homogeneous design, disordered MCFs based on the transverse Anderson localization [101] have been reported in [93] to improve the image transport quality [Fig. 1.7(b)]. Specifically, the transverse Anderson localization of light allows localized optical-beam-transport through a transversely disordered medium. Interestingly, in disordered multi-dielectric media, the resultant image quality can also be correctly described with perturbation theory (see Section 1.5). Disordered arranged cores with different radius may exhibit a high phase-mismatching between their optical modes. As a result, the inter-core crosstalk level between adjacent core modes is lower than in a homogeneous and periodically arranged design [Fig. 1.7(a)]. In a similar way, additional highly-density MCF designs could be investigated from the coupled local-mode theory using HB cores with a random orientation of the principal axes to minimize the inter-core crosstalk (see Chapter 3).

On the other hand, adaptive optics is required in the TPEF microscopy to recover the initial imaging of the biological tissue [Fig. 1.7(c)]. The advance on wavefront shapers composed by 2D SLMs and deformable mirrors have spurred the main evolution in ultrathin endoscopes [99]. Thompson et al. were the first to report imaging with a lensless endoscope based on a waveguide with multiple cores [89]. Later, in 2013, Andresen and co-workers realized a lensless endoscope employing an MCF similar to Fig. 1.7(a) with extremely low crosstalk between adjacent cores [90]. In the same line, additional works have been reported by combining MCF and MM-SCFs with adaptive optics [91, 92, 94–98]. At present, the major aim in lensless endoscopy using MCF media is to increase the core density guaranteeing a reduced mode-coupling and intermodal dispersion between neighboring cores [99].

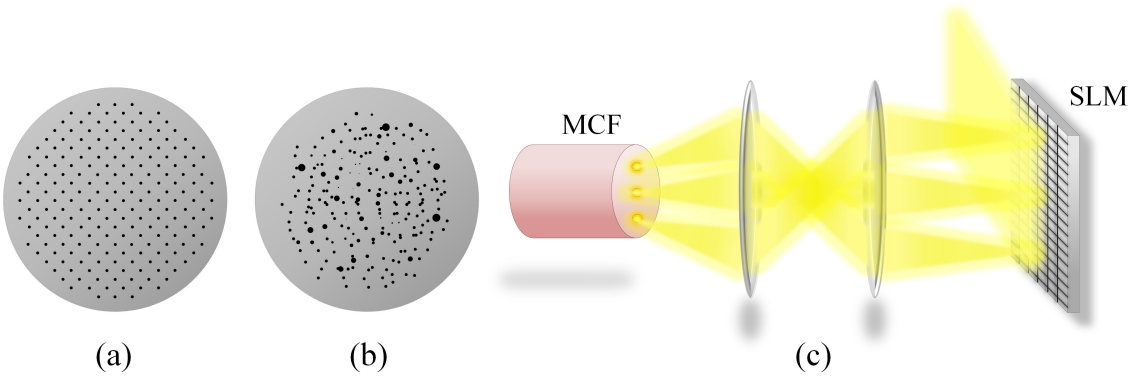

Figure 1.7. MCFs and adaptive optics for medical imaging [BOOK 1]. (a) MCF with periodically arranged cores [90], (b) disorder MCF based on transverse Anderson localization [93], and (c) wavefront shaping with a single spatial light modulator (SLM) for an MCF based lensless endoscope [91].

1.4.5 Opportunities in experimental physics

In the past, fiber-optical analogies have been widely investigated to use SCFs as an experimental platform for testing different physical phenomena in various fields, such as in quantum mechanics, general relativity or condensed matter physics, among others [93, 101–109]. In this context, MCFs are potential laboratories that could extend the possibilities offered by SCFs. In fact, a specific example of solid-state physics has already been discussed in the previous subsection, the Anderson effect, relying on the immobility of an electron in a disordered lattice [93, 101]. As Anderson localization involves an interfering phenomenon, this effect has been extended to optics. In [101], Anderson localization has been discussed in two-dimensional photonic lattices, and in [93] its

potential applications have been discussed for medical imaging using disordered MCFs, as detailed before. More broadly, additional strong disordered phenomena in optics such as the self-organized instability in MM-SCFs [107] can be generalized to MM-MCFs supporting supermodes.

Another interesting example can be found in fluid dynamics in the study of rogue waves on deep water. The giant oceanic rogue waves emerge from the sea induced by many different linear and nonlinear wave propagating effects [108]. Indeed, these nonlinear phenomena can be investigated from a fiber-optical analogy [109]. The nonlinear wave propagation on deep water and in SM-SCF media is described in both cases by a master equation: the nonlinear Schrödinger equation (NLSE), as shown in Fig. 1.8. It can be seen that both propagating equations have a similar form and, therefore, the theoretical results can be directly extrapolated from one field to another. Significantly, the emergence of rogue waves can be analytically studied from the solutions of the NLSE referred to as solitons on finite background (SFB) [110]. As a specific example, we include in Fig. 1.8 the Akhmediev breathers (ABs), the Peregrine soliton (PS) and the Kuznetsov-Ma (KM) solitons.[8] In a similar way, the coupled NLSEs (CNLSEs) have also been discussed in the literature to gain physical insight between interacting rogue waves [111–114]. In such a scenario, MCFs offer the possibility of investigating the collision of these nonlinear solutions by using the coupled local-mode theory reported in Chapters 3 and 4 of this thesis. In fact, MCFs can be employed to elucidate the underlying wave propagation phenomena of any physical system with propagating equations of the form of the CNLSEs, e.g., superposed nonlinear waves in coherently coupled Bose-Einstein condensates [114] or turbocharge applications in acoustics [115]. Remarkably, in acoustics, the coupled local-mode theory can play an essential role. Time-varying cylindrical acoustic ducts can be engineered with the same modal properties as optical MCFs. Therefore, the theory presented herein can also be employed to analyze the intermodal dispersion and the random medium perturbations in such acoustic systems [116].

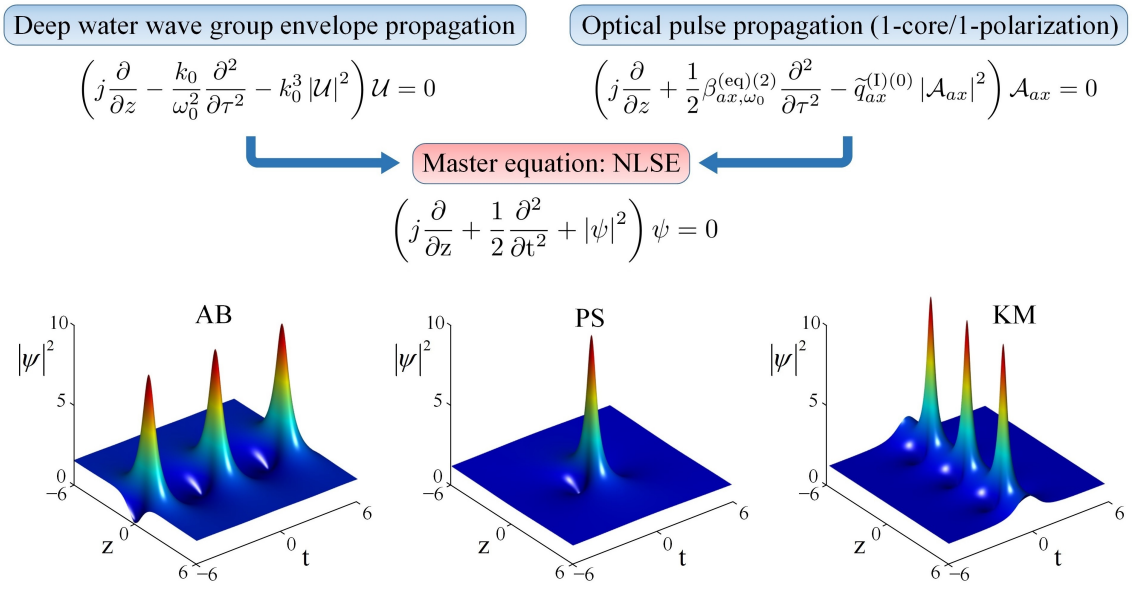

Figure 1.8. Analogy between fluid mechanics and optics. The NLSE describes the linear and nonlinear wave propagation in different physical systems. Analytic SFB solutions of the NLSE: Akhmediev breathers (ABs), the Peregrine soliton (PS) and the Kuznetsov-Ma (KM) solitons [BOOK 1].

[8] Many of these SFB solutions are termed in the literature as rogue waves. Nevertheless, the fundamental concept of rogue waves, emerging unexpectedly from the sea, requires additional statistical criteria only fulfilled by higher-order SFB solutions. In either case, the term rogue waves is commonly used for any analytic SFB solution of the NLSE.

On the other hand, additional exotic physical phenomena can also be explored in MCF media expanding the possibilities of SCFs. For example, an optical pulse propagating through an SCF establishes a moving medium analogous to a space-time geometry. Specifically, this gravitational approach was employed in [105] to demonstrate a fiber-optical analogy of the event horizon in a black hole. Along this line, additional gravitational anomalies could be investigated in an MCF when adjacent cores perturb the space-time geometry created by an optical pulse propagating in a given core of the fiber.

Finally, it is worth mentioning that MCFs are being explored in other branches of experimental physics such as in astronomy [117]. The main advantage of these new fibers is the reduced core-to-core distance which can be achieved in a single cladding. In particular, this property presents special interest to create spectroscopic maps of galaxies or detecting exoplanets due to the superior fill factor of MM-MCFs in comparison with other approaches, such as an MM-SCF or a fiber bundle of SM-SCFs.[9] The Sydney-AAO Multi-object Integral field spectrograph (SAMI) project [118], responsible of performing a large spatial spectroscopy of galaxies, pioneered the introduction of MCFs in astronomical observatories.

1.5 Linear and nonlinear wave propagation in multi-core fiber: perturbation theory

The propagation of electromagnetic waves in an MCF can be modeled from Maxwell's equations, the essence of classical electromagnetism. They are able to describe the structure of the electromagnetic field and the fundamental interactions between the electric field strength ($\boldsymbol{\mathcal{E}}$) and the magnetic induction ($\boldsymbol{\mathcal{B}}$). In their *fundamental* form, the macroscopic Maxwell equations read as follows (we use the real representation of the fields and the notation $\partial_t \equiv \partial/\partial t$):

$$\nabla \times \boldsymbol{\mathcal{E}}(\boldsymbol{r},t) = -\partial_t \boldsymbol{\mathcal{B}}(\boldsymbol{r},t); \tag{1.5.1}$$

$$c_0^2 \nabla \times \boldsymbol{\mathcal{B}}(\boldsymbol{r},t) = \frac{1}{\varepsilon_0}\boldsymbol{\mathcal{J}}(\boldsymbol{r},t) + \partial_t \boldsymbol{\mathcal{E}}(\boldsymbol{r},t); \tag{1.5.2}$$

$$\varepsilon_0 \nabla \cdot \boldsymbol{\mathcal{E}}(\boldsymbol{r},t) = \rho(\boldsymbol{r},t); \tag{1.5.3}$$

$$\nabla \cdot \boldsymbol{\mathcal{B}}(\boldsymbol{r},t) = 0, \tag{1.5.4}$$

where ρ and $\boldsymbol{\mathcal{J}}$ are the total charge and current densities, respectively.[10,11] Both terms include the free and bound charges and currents, i.e., $\rho = \rho_{\mathrm{f}} + \rho_{\mathrm{b}}$ and $\boldsymbol{\mathcal{J}} = \boldsymbol{\mathcal{J}}_{\mathrm{f}} + \boldsymbol{\mathcal{J}}_{\mathrm{b}}$ [119].

As is well known, the fields $\boldsymbol{\mathcal{E}}$ and $\boldsymbol{\mathcal{B}}$ are able to modify the charge distribution of a medium and induce currents in it. Such alterations act as new sources that generate additional electromagnetic fields. Therefore, it is necessary to know the electromagnetic response of the medium to model theoretically the different electromagnetic wave propagation phenomena. These field-matter interactions can be adequately described by defining two new *auxiliary* macroscopic fields, namely $\boldsymbol{\mathcal{D}}$ (electric displacement) and $\boldsymbol{\mathcal{H}}$ (magnetic field strength), which account for the macroscopic response of the medium charges and currents to the applied fields [120]. The connection between the fundamental and auxiliary fields is given through the so-called constitutive relations:

$$\boldsymbol{\mathcal{D}}(\boldsymbol{r},t) := \varepsilon_0 \boldsymbol{\mathcal{E}}(\boldsymbol{r},t) + \boldsymbol{\mathcal{P}}(\boldsymbol{r},t); \quad \boldsymbol{\mathcal{H}}(\boldsymbol{r},t) := \frac{1}{\mu_0}\boldsymbol{\mathcal{B}}(\boldsymbol{r},t) - \boldsymbol{\mathcal{M}}(\boldsymbol{r},t), \tag{1.5.5}$$

where $\boldsymbol{\mathcal{P}}$ and $\boldsymbol{\mathcal{M}}$ are the polarization and magnetization fields, and basically describe the density of electric and magnetic dipole moments, respectively.

In an MCF, a multi-dielectric medium, the free charges and currents are found to be null, $\rho = \rho_{\mathrm{b}} = -\nabla \cdot \boldsymbol{\mathcal{P}}$, $\boldsymbol{\mathcal{J}} = \boldsymbol{\mathcal{J}}_{\mathrm{b}} = \partial_t \boldsymbol{\mathcal{P}}$, $\boldsymbol{\mathcal{M}} = \boldsymbol{0}$ and Eqs. (1.5.1)-(1.5.4) are reduced to:

[9] The fill factor is defined as the ratio $\sum_k S_k / S_{\mathrm{T}}$, where S_k is the transversal area of a given core k and S_{T} is the total transversal area of the waveguide. Typically, in MM-SCFs (105/125) the fill factor is of the order of 0.7. Using an MM-SCF or a fiber bundle of SM-SCFs a lot of dead space cannot be observed.

[10] All the fields appearing in Eqs. (1.5.1)-(1.5.4) are volume-averaged quantities, expressed in S.I. units.

[11] $c_0 = 1/\sqrt{\varepsilon_0 \mu_0}$ is the speed of light in vacuum. ε_0 and μ_0 are respectively the electric permittivity and the magnetic permeability in vacuum.

$$\nabla \times \boldsymbol{\mathcal{E}}(\boldsymbol{r},t) = -\partial_t \boldsymbol{\mathcal{B}}(\boldsymbol{r},t); \tag{1.5.6}$$
$$\nabla \times \boldsymbol{\mathcal{H}}(\boldsymbol{r},t) = \partial_t \boldsymbol{\mathcal{D}}(\boldsymbol{r},t); \tag{1.5.7}$$
$$\nabla \cdot \boldsymbol{\mathcal{D}}(\boldsymbol{r},t) = 0; \tag{1.5.8}$$
$$\nabla \cdot \boldsymbol{\mathcal{B}}(\boldsymbol{r},t) = 0. \tag{1.5.9}$$

A rigorous electromagnetic analysis of the linear and nonlinear wave propagation in an MCF should be performed by solving Eqs. (1.5.6)-(1.5.9) in each dielectric region of the fiber (cores+cladding) and then applying the boundary conditions at the different core-cladding interfaces. Unfortunately, the calculation of the exact MCF eigenmodes using the previous equations involves a high degree of complexity and, usually, they should be numerically solved. In this vein, in order to study analytically the wave propagation phenomena in MCF media, *perturbation theory* is commonly employed.

Perturbation theory comprises mathematical methods for finding an approximate solution to a non-exactly solvable problem from the exact solution of a simpler problem than the original one [121]. Perturbation theory was originally conceived and developed by Lagrange and Laplace in the 18th century within the context of astronomy to analyze the *perturbation* in the orbit of a planet of our solar system induced by other planets or celestial bodies. Later, in 20th century, these mathematical methods were extended to other fields of physics such as quantum mechanics [122], string theory [123] and electromagnetism [124]. In particular, perturbation theory was firstly applied to optical waveguides by Snyder, Marcuse and Kogelnik in the early 1970's [125]. In the late 1990s and early 2000s, the interest in this theory has been revitalized thanks to the field of nanophotonics to study, among other notable examples, Fano resonances in photonic crystal slabs [126], optical resonators [127] and MCFs [128].

In MCF media, our goal is to model analytically the wave propagation phenomena in each core taking into account the mode-coupling effects from adjacent cores. In this context, perturbation theory alleviates the theoretical work by approximating the exact MCF eigenmodes as a linear combination of the isolated core modes. That is, the modes of each core are calculated from the classical modal analysis of an SCF [32] by considering isolated cores. In the next chapters, we will use perturbation theory to analyze the main propagation impairments in SM-MCFs. Figure 1.9 shows a flowchart of this method. Starting from Maxwell's equations, our goal is to derive a set of coupled first-order differential equations in terms of the complex envelopes of the polarized core modes[12] by performing the following steps:

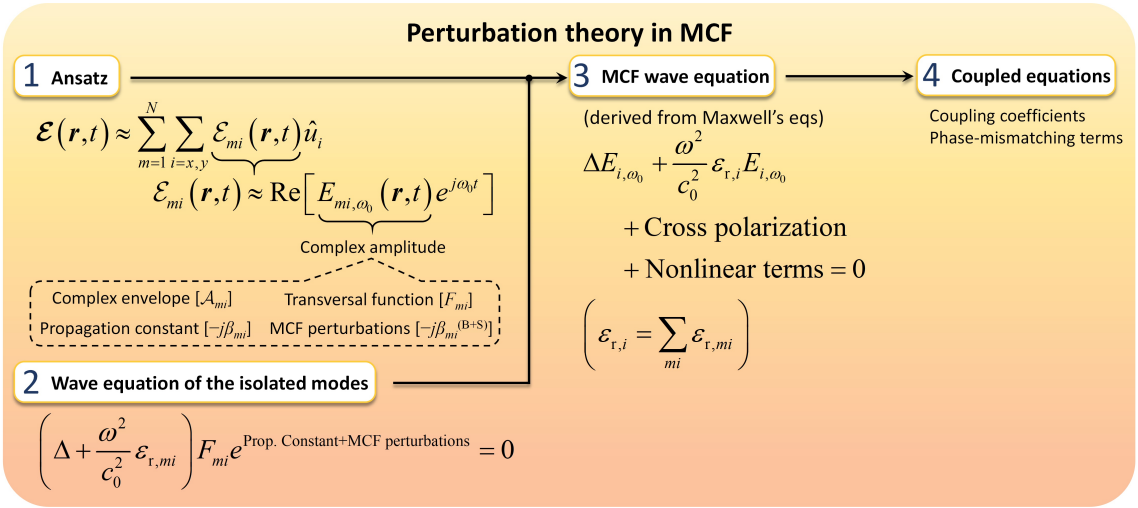

Figure 1.9. Flowchart of perturbation theory applied to SM-MCF media [BOOK 1].

[12] In an N-core SM-MCF, a polarized core mode mi refers to the $\mathrm{LP}_{01,mi}$ mode associated with core m and polarization axis i, with $(m,i) \in \{1,...,N\} \times \{x,y\}$.

1. First, we should propose the ansatz of the global electric field strength ($\boldsymbol{\mathcal{E}}$) of the MCF structure following the assumption of perturbation theory [124]: the exact electric field strength is approximated by a linear combination of the mi polarized core modes considering isolated cores, that is, assuming that the geometry of each core m is not perturbed by the presence of adjacent cores ($\boldsymbol{\mathcal{E}} \simeq \sum_{mi} \mathcal{E}_{mi}\hat{u}_i$).[13] In general, we will assume weakly-guiding cores and, consequently, the longitudinal component of $\boldsymbol{\mathcal{E}}$ can be neglected. At the same time, we should decouple the rapidly and the slowly-varying temporal and longitudinal changes of $\mathcal{E}_{mi}$. The rapidly-varying *temporal* changes are decoupled by using the slowly-varying complex amplitude approximation with $\mathcal{E}_{mi} \simeq \mathrm{Re}\{E_{mi,\omega_0}(\boldsymbol{r},t)\exp(j\omega_0 t)\}$, where E_{mi,ω_0} is the complex amplitude and ω_0 is the angular frequency of the optical carrier.[14] In a similar way, the rapidly-varying *longitudinal* variations are decoupled by writing E_{mi,ω_0} as a function of the complex envelopes $\mathcal{A}_{mi}(z,t)$, i.e., $E_{mi,\omega_0}(\boldsymbol{r},t) = f(\mathcal{A}_{mi}(z,t))$. Thus, $\mathcal{A}_{mi}$ comprises the slowly-varying longitudinal and temporal variations of $\mathcal{E}_{mi}$. Along these same lines, note that although $\mathcal{E}_{mi}$ and E_{mi,ω_0} are written assuming isolated conditions of the core m, $\mathcal{A}_{mi}$ should be assumed longitudinal dependent to describe, not only the usual longitudinal distortions of the optical pulses in SCFs,[15] but also the longitudinal fluctuations induced by the *coupled* power from adjacent cores. Moreover, E_{mi,ω_0} also involves fundamental information such as the ideal[16] propagation constant ($-j\beta_{mi}$), the transversal eigenfunction (F_{mi}) and the MCF perturbations (bending, twisting and additional spatial and temporal fiber birefringent effects) encoded by the phase function $\beta_{mi}^{(\mathrm{B+S})}(z;t)$.[17]

2. Each polarized core mode mi is written by assuming isolated conditions of each core. Hence, F_{mi} and β_{mi} can be expressed as indicated in [32] for the LP_{01} mode of an SM-SCF. Moreover, taking into account that the nonlinear effects are not included either the modal solution of [32] or in $\beta_{mi}^{(\mathrm{B+S})}$, thus the eigenfunction $F_{mi}\exp(-j(\beta_{mi}+\beta_{mi}^{(\mathrm{B+S})})z)$ must satisfy the linear wave equation depicted in the second step of Fig. 1.9 in $\delta z \sim \lambda_m = \lambda_0/n_m$, where λ_0 is the wavelength of the optical carrier in vacuum, $n_m := (n_{mx}+n_{my})/2$ and $\{n_{mi}\}_{i=x,y}$ are the principal refractive indexes of core m at ω_0.[18]

3. In the third step, the wave equation of the MCF should be derived from Maxwell's equations for the complex amplitudes E_{mi,ω_0} by including the cross- and nonlinear-polarization terms.

4. Finally, we derive the coupled equations of the complex envelopes by inserting the results of the first and second step in the MCF wave equation of the third step. At this point, we should assume the slowly-varying complex envelope approximation (SVEA), that is, $\delta_z\mathcal{A}_{mi} \ll |\mathcal{A}_{mi}|$ in $\delta z \sim \lambda_m$ and $\delta_t\mathcal{A}_{mi} \ll |\mathcal{A}_{mi}|$ in $\delta t \sim 2\pi/\omega_0$.[19] More specifically:

$$\left|\partial_z^2\mathcal{A}_{mi}\right| \ll k_m\left|\partial_z\mathcal{A}_{mi}\right| \ll k_m^2\left|\mathcal{A}_{mi}\right|; \quad \left|\partial_t^2\mathcal{A}_{mi}\right| \ll \omega_0\left|\partial_t\mathcal{A}_{mi}\right| \ll \omega_0^2\left|\mathcal{A}_{mi}\right|, \tag{1.5.10}$$

with $k_m = 2\pi/\lambda_m$. Thus, we can assume that $\partial_z^2\mathcal{A}_{mi} \simeq 0$ in $\delta z \sim \lambda_m$ and $\partial_t^2\mathcal{A}_{mi} \simeq 0$ in $\delta t \sim 2\pi/\omega_0$.[20]

[13] Since the electric field strength and the magnetic induction can be expressed in identical form, we will use the former field for our theoretical discussions with straightforward extrapolation of the results to the magnetic induction by using the intrinsic impedance of each dielectric region.

[14] In general, we should consider several optical carriers to model the wave propagation in WDM-SDM systems using SM-MCFs. However, the interchannel nonlinearities (cross-phase modulation and four-wave mixing) should only be taken into account for optical pulses with a temporal width higher than 50 ps (see Chapter 4 for more details). Therefore, the assumption of a single optical carrier will allow us to simplify the theoretical discussions of the major physical impairments in SM-MCFs.

[15] For instance, chromatic dispersion and polarization-mode dispersion among other phenomena.

[16] The ideal propagation constant is the *unperturbed* propagation constant, that is, without including medium perturbations.

[17] In the introduction of the next chapter, we will describe in more detail the different spatial and temporal MCF perturbations.

[18] In LB cores, $n_{mx} = n_{my} \equiv n_m$. However, in HB cores, $n_{mx} \neq n_{my}$.

[19] We define $\delta_z\mathcal{A}_{mi} := |\mathcal{A}_{mi}(z,t) - \mathcal{A}_{mi}(z+\delta z,t)|$ and $\delta_t\mathcal{A}_{mi} := |\mathcal{A}_{mi}(z,t) - \mathcal{A}_{mi}(z,t+\delta t)|$. It should be noted that we will use the linear operators δ_z and δ_t along this thesis with different functions, such as the refractive index, the MCF bending radius and the MCF twist rate among others.

[20] Later, in Chapter 4, we will discuss the approximations $\partial_z^2\mathcal{A}_{mi} \simeq 0$ and $\partial_t^2\mathcal{A}_{mi} \simeq 0$ in more detail (see page 129).

Along these lines, an additional comment should be taken into account for future theoretical discussions in relation with the optical power of each polarized core mode. Specifically, the optical power propagated by a polarized core mode mi (P_{mi}) should be calculated by integrating the time average of the Poynting vector ($\boldsymbol{\mathcal{S}}_{mi} = \boldsymbol{\mathcal{E}}_{mi} \times \boldsymbol{\mathcal{H}}_{mi}$) in a period of the optical carrier and in an *infinite* cross-sectional area of core m. In particular, P_{mi} can be expressed as a function of the complex envelope as follows:[21]

$$P_{mi}(z,t) = \iint \langle \boldsymbol{\mathcal{E}}_{mi} \times \boldsymbol{\mathcal{H}}_{mi} \rangle \cdot \hat{u}_z \mathrm{d}x\mathrm{d}y = \mathscr{C}_{mi}^{(\mathrm{P})} \left| \mathcal{A}_{mi}(z,t) \right|^2, \tag{1.5.11}$$

where:[22]

$$\mathscr{C}_{mi}^{(\mathrm{P})} := \frac{1}{2\eta_m} \iint F_{mi}^2(x,y)\, \mathrm{d}x\mathrm{d}y, \tag{1.5.12}$$

being $\eta_m = \eta_0/n_m \simeq 120\pi/n_m$ the intrinsic impedance of core m at ω_0. For the sake of simplicity, we set $\mathscr{C}_{mi}^{(\mathrm{P})} \equiv 1$ in our theoretical discussions. Nonetheless, the exact value of $\mathscr{C}_{mi}^{(\mathrm{P})}$ (in m^2/Ω) must be considered when using the coupled-mode equations of this thesis to estimate the exact value of P_{mi} (in watts).

On the other hand, the error assumed by approximating the MCF supermodes as $\boldsymbol{\mathcal{E}} \simeq \sum_{mi} \mathcal{E}_{mi} \hat{u}_i$ depends on several fiber parameters: the core-to-core distance, the refractive index difference among cores and cladding, or the frequency of the optical carrier among others. Hence, the limit of the coupled equations cannot be straightforwardly established through a general mathematical expression. Nonetheless, as discussed in [125], perturbation theory seems to be sufficiently accurate to describe the mode-coupling when the distance between parallel waveguides (i.e. our core-to-core distance in MCF) is much larger than the wavelength of the propagated waves.

In the following chapters, we will investigate the main physical impairments in SM-MCFs using the aforementioned perturbation theory. First, we will describe in Chapter 2 the crosstalk among cores by considering monochromatic electromagnetic fields and omitting polarization effects. Second, we will discuss in Chapter 3 the intra- and inter-core crosstalk by including polarization effects. And finally, in Chapter 4, we will analyze the intermodal dispersion and higher-order coupling and nonlinear effects which can be observed in the non-monochromatic regime, and more concretely, when propagating optical pulses through an MCF. For completeness, the multi-mode regime is also discussed at the end of Chapter 4.

[21] Note that the complex envelope is assumed to be constant in a period of the optical carrier. Thus, in this case, the time average operator only applies over the rapidly-varying exponential terms of the electromagnetic fields. Moreover, we omit the integration limits to use a more economical notation.

[22] From Eq. (1.5.12) the following remarks are in order:

- In the single-mode regime, F_{mi} is a real function, that is, $F_{mi} = F_{mi}^*$. In contrast, in the multi-mode regime, the term F_{mi}^2 must be replaced by $|F_{mi}|^2$.
- In GI-MCFs, η_m is found to be spatial dependent and, therefore, it must be included in the integrand.

This page was intentionally left blank.

Chapter 2

Linear and nonlinear inter-core crosstalk

2.1 Introduction

In multi-dielectric media, we can observe mode-coupling among adjacent dielectric regions. The continuity of the electromagnetic field in such media is the physical origin of the mode-coupling, referred to as inter-core crosstalk (IC-XT) in MCFs.

Concretely, in these fibers, the behavior of the IC-XT depends directly on the longitudinal and temporal medium perturbations, which may exhibit a deterministic or random nature. The longitudinal medium perturbations include macrobends, microbends, fiber twisting and intrinsic manufacturing imperfections [129]. The temporal medium perturbations are induced by external environmental factors, such as temperature variations and floor vibrations induced by human activity [130, 131]. All these fiber perturbations modify the propagation constant of the core modes and, consequently, the IC-XT behavior is found to be dependent on these perturbations.

Despite the fact that the intrinsic manufacturing imperfections have a deterministic nature, the remaining perturbations may present a random behavior and, therefore, the linear and nonlinear IC-XT may have a stochastic evolution in the time and space domains (along the longitudinal direction of the fiber, assumed the z-axis in this thesis). Hence, it is natural to ask how the probability distribution is in each domain.

The first IC-XT models have investigated this question focusing their efforts on the linear and single-mode regimes of the fiber and excluding the temporal perturbations of the medium [128–130, 132–136]. Specifically, these initial models have considered monochromatic electric fields, a single identical polarization in each core, and longitudinal fiber perturbations, included heuristically in the classical coupled-mode theory (CMT) [137]. These initial simplifications alleviate the mathematical work simplifying the deduction of the spatial distribution of the linear IC-XT, at least in a first approximation.

In this chapter, following a similar approach as in these initial works, we will investigate the *spatial* probability distribution of the IC-XT in the *nonlinear* regime of SM-MCFs and we will unify the theoretical description of this physical impairment in both power regimes with a simple and intuitive mathematical model. On the other hand, the impact of the MCF temporal perturbations on the linear and nonlinear IC-XT statistics will be discussed in the next chapter.

The chapter is structured as follows. In Section 2.2, the nonlinear CMT of the directional coupler (an ideal MCF without perturbations) is extended to bent and twisted SM-MCFs. From the newly derived CMT, the random longitudinal evolution of the linear and nonlinear IC-XT is demonstrated in Section 2.3. In this scenario, the analysis of the linear and nonlinear IC-XT spatial distributions is required to gain insight into the behavior of this optical impairment. To this end, we previously derive in Section 2.4 a set of coupled equations in terms of the average value of the optical power: the nonlinear coupled-power theory (CPT). Remarkably, the nonlinear CPT will

allow us to obtain the closed-form expressions of the mean and variance of the IC-XT spatial distribution in both linear and nonlinear regimes. Next, in Section 2.5, we will perform the statistical analysis in both power regimes discussing the probability density function, cumulative distribution function, mean and variance of the crosstalk. In Section 2.6, the experimental validation of our previous theoretical discussions is performed using a homogeneous four-core fiber (4CF). Finally, in Section 2.7, the main conclusions of this chapter are highlighted.

2.2 Coupled-mode theory for bent and twisted multi-core fiber

The classical CMT (derived from Maxwell's equations using the basic ideas of perturbation theory) was originally formulated for the linear directional coupler by Allan Snyder in 1972 [137]. Later, in 1982, the CMT was extended to the nonlinear regime by Jensen [138], which proposed the nonlinear directional coupler (NLDC) based on homogeneous rectangular waveguides for all-optical switching and signal processing applications. In this section, the goal is to extend the nonlinear CMT of Jensen to homogeneous and heterogeneous MCF media involving longitudinal perturbations. First, we will revisit the nonlinear CMT by considering a NLDC based on heterogeneous circular waveguides. Second, we will calculate the closed-form expressions of the mode-coupling coefficients for the step-index case. Next, we will discuss the exact solution of the nonlinear CMT pointing out the main differences with experimental measurements of IC-XT in real MCFs. Finally, we will resolve the discrepancy between theory and experiments by including heuristically the MCF longitudinal perturbations in the nonlinear coupled-mode equations.

2.2.1 Coupled-mode equations for ideal multi-core fiber

Consider a weakly-guiding 2-core SM-MCF with cores a and b and radius $R_{0,a}$ and $R_{0,b}$, respectively, a core-to-core distance d_{ab} and without longitudinal or temporal fiber perturbations (see Fig. 2.1). In order to describe the linear and nonlinear mode-coupling between the LP_{01} mode of each core, we assume monochromatic electric fields and the MCF is modeled as a lossless, nonlinear, isotropic, heterogeneous, time-invariant and non-dispersive multi-dielectric medium. In addition, a single polarization can also be assumed in each core mode (x-polarization) taking into account the isotropic nature of the optical medium and the *omission* of the fiber perturbations. Thus, from a point of view of perturbation theory, the real wave function of the global electric field strength of the MCF can be approximated to (step 1 of Fig. 1.9):

$$\begin{aligned}\boldsymbol{\mathcal{E}}(\boldsymbol{r},t) &\simeq \sum_{m=a,b} \mathcal{E}_m(\boldsymbol{r},t)\,\hat{u}_x = \sum_{m=a,b} \mathrm{Re}\left\{E_{m,\omega_0}(\boldsymbol{r})\exp(j\omega_0 t)\right\}\hat{u}_x \\ &= \sum_{m=a,b} \mathrm{Re}\left\{A_m(z)\,F_m(x,y,\omega_0)\exp(-j\beta_m(\omega_0)\,z)\exp(j\omega_0 t)\right\}\hat{u}_x, \end{aligned} \tag{2.2.1}$$

where ω_0 is the angular frequency of the optical carrier and E_{m,ω_0} is the complex amplitude of the electric field strength in the core $m = a, b$ comprising: the complex envelope A_m satisfying the SVEA,[1] the transversal Bessel function F_m [32] and the ideal phase constant β_m [i.e., the unperturbed phase constant (see footnote 16 on page 24)]. It should be noted that F_m and β_m depend on ω_0. However, since we are considering monochromatic electric fields, the frequency dependence will be omitted from now on, i.e., $F_m(x,y,\omega_0) \equiv F_m(x,y)$ and $\beta_m(\omega_0) \equiv \beta_m$.

Moreover, as indicated in step 2 of Fig. 1.9, each core mode is written by assuming isolated cores. Thus, F_m and β_m can be calculated from the classical modal solution of an SM-SCF, that is,

[1] Note that we have employed a different function for the complex envelope in Eq. (2.2.1) from the one used in Eq. (1.5.10). In this chapter, we will use the notation $A(z)$ to describe the complex envelope in the monochromatic regime (continuous waves). Later, in Chapter 3 (monochromatic regime with time-varying perturbations) and Chapter 4 (non-monochromatic regime), we will recover the notation $\mathcal{A}(z,t)$ to include the temporal dependence of the complex envelope.

F_m and β_m must satisfy the Helmholtz equation $[\triangle + k_0^2 \varepsilon_{\mathrm{r},m}(\boldsymbol{r})] F_m(x,y) \exp(-j\beta_m z) = 0$, where $k_0 = \omega_0/c_0$ and $\varepsilon_{\mathrm{r},m}$ is the relative electric permittivity[2] of the core m. Defining the *global* relative electric permittivity distribution of the MCF as $\varepsilon_{\mathrm{r}}(\boldsymbol{r}) := \varepsilon_{\mathrm{r},c}(\boldsymbol{r}) + \Delta\varepsilon_{\mathrm{r},a}(\boldsymbol{r}) + \Delta\varepsilon_{\mathrm{r},b}(\boldsymbol{r})$ (see Fig. 2.1), we found from the aforementioned Helmholtz equation that:

$$\left[\triangle_{\mathrm{T}} + k_0^2 \varepsilon_{\mathrm{r}}(\boldsymbol{r})\right] F_{a(b)}(x,y) = \left[k_0^2 \Delta\varepsilon_{\mathrm{r},b(a)}(\boldsymbol{r}) + \beta_{a(b)}^2\right] F_{a(b)}(x,y), \tag{2.2.2}$$

with $\triangle_{\mathrm{T}} := \partial_x^2 + \partial_y^2$ the transverse Laplacian operator.

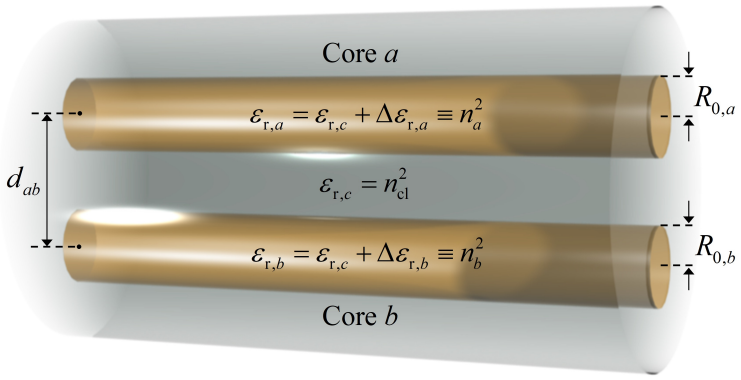

Figure 2.1. Heterogeneous 2-core MCF considered for theoretical discussions.

In step 3, the wave equation of the MCF should be derived from Maxwell's equations in terms of the complex amplitudes E_{m,ω_0} by including the nonlinear polarization terms.[3] As detailed in Appendix A2 on page 53, the nonlinear wave equation of the MCF is found to be:

$$\triangle E_{\omega_0}(\boldsymbol{r}) + k_0^2 \left[\varepsilon_{\mathrm{r}}(\boldsymbol{r}) + \gamma |E_{\omega_0}(\boldsymbol{r})|^2\right] E_{\omega_0}(\boldsymbol{r}) = 0, \tag{2.2.3}$$

where $E_{\omega_0} \simeq E_{a,\omega_0} + E_{b,\omega_0}$ and γ is the nonlinear coefficient of the fiber.

Finally, in step 4, we can find the coupled-mode equations by combining Eqs. (2.2.1) and (2.2.2) into Eq. (2.2.3). After some algebraic work and using the SVEA, we obtain:[4]

$$\begin{aligned} &F_a \exp(-j\beta_a z)\left(k_0^2 \Delta\varepsilon_{\mathrm{r},b} - j2\beta_a \frac{\mathrm{d}}{\mathrm{d}z}\right) A_a + F_b \exp(-j\beta_b z)\left(k_0^2 \Delta\varepsilon_{\mathrm{r},a} - j2\beta_b \frac{\mathrm{d}}{\mathrm{d}z}\right) A_b \\ &\quad + k_0^2 \gamma \Big\{ A_a |A_a|^2 F_a^3 \exp(-j\beta_a z) + A_b |A_b|^2 F_b^3 \exp(-j\beta_b z) \\ &\qquad + 2|A_a|^2 A_b F_a^2 F_b \exp(-j\beta_b z) + 2A_a |A_b|^2 F_a F_b^2 \exp(-j\beta_a z) \\ &\qquad + A_a^2 A_b^* F_a^2 F_b \exp\left[j(\beta_b - 2\beta_a) z\right] + A_a^* A_b^2 F_a F_b^2 \exp\left[j(\beta_a - 2\beta_b) z\right] \Big\} = 0. \end{aligned} \tag{2.2.4}$$

The coupled-mode equation modeling mode-coupling from core b to core a is found by multiplying Eq. (2.2.4) by $F_a \exp(j\beta_a z)$ and integrating in an infinite cross section of the MCF:

$$\begin{aligned} j\left[\frac{\mathrm{d}A_a}{\mathrm{d}z} + \chi_{a,b} \exp(-j\Delta\beta_{b,a} z) \frac{\mathrm{d}A_b}{\mathrm{d}z}\right] &= c_a A_a + \kappa_{a,b} \exp(-j\Delta\beta_{b,a} z) A_b + q_a^{(1)} |A_a|^2 A_a \\ &\quad + q_{a,b}^{(2)} \left[2A_a |A_b|^2 + A_a^* A_b^2 \exp(-j2\Delta\beta_{b,a} z)\right] \\ &\quad + q_{a,b}^{(3)} \left[2|A_a|^2 A_b \exp(-j\Delta\beta_{b,a} z) + A_a^2 A_b^* \exp(j\Delta\beta_{b,a} z)\right] \\ &\quad + q_{a,b}^{(4)} |A_b|^2 A_b \exp(-j\Delta\beta_{b,a} z), \end{aligned} \tag{2.2.5}$$

[2] In gradual-index refractive index profiles, $\varepsilon_{\mathrm{r},m}(\boldsymbol{r}) = n_m^2(\boldsymbol{r})$ is assumed slowly-varying in spatial variations of the order of $\overline{\lambda}_m = \lambda_0/\overline{n}_m$, where $\overline{n}_m := \langle n_m(\boldsymbol{r}) \rangle$ and $\langle\ \rangle$ denotes the ensemble average operator. Usually, these spatial variations only have radial dependence inside the core region.

[3] Note that the cross-polarization terms can be omitted when considering the MCF as an isotropic medium.

[4] For the sake of simplicity, the independent variables are omitted in some expressions of this thesis. In a similar way, in spite of the fact that the derivative of a differentiable function f should be written by using the differential as $\mathrm{d}f(z)(\mathrm{d}z)/\mathrm{d}z$, we will relax the notation writing $\mathrm{d}f(z)/\mathrm{d}z$ or $\mathrm{d}f/\mathrm{d}z$.

where $\Delta\beta_{b,a} := \beta_b - \beta_a$; $\chi_{a,b}$, c_a and $\kappa_{a,b}$ are the linear mode-coupling coefficients (MCCs); and $q_a^{(1)}$, $q_{a,b}^{(2)}$, $q_{a,b}^{(3)}$ and $q_{a,b}^{(4)}$ are the nonlinear MCCs (see below). A similar equation modeling mode-coupling from core a to core b can just be obtained by multiplying Eq. (2.2.4) by $F_b \exp(j\beta_b z)$.

2.2.2 Mode-coupling coefficients

The linear and nonlinear MCCs are defined as (all integrals apply over an infinite cross section):

$$\chi_{a,b} := \frac{\beta_b}{\beta_a N_a} \iint F_b(x,y)\, F_a(x,y)\, \mathrm{d}x\mathrm{d}y; \tag{2.2.6}$$

$$c_a := \frac{k_0^2}{2\beta_a N_a} \iint \Delta\varepsilon_{\mathrm{r},b}(\boldsymbol{r})\, F_a^2(x,y)\, \mathrm{d}x\mathrm{d}y; \tag{2.2.7}$$

$$\kappa_{a,b} := \frac{k_0^2}{2\beta_a N_a} \iint \Delta\varepsilon_{\mathrm{r},a}(\boldsymbol{r})\, F_b(x,y)\, F_a(x,y)\, \mathrm{d}x\mathrm{d}y; \tag{2.2.8}$$

$$q_a^{(1)} := \frac{k_0^2}{2\beta_a N_a} \iint \gamma F_a^4(x,y)\, \mathrm{d}x\mathrm{d}y; \tag{2.2.9}$$

$$q_{a,b}^{(2)} := \frac{k_0^2}{2\beta_a N_a} \iint \gamma F_b^2(x,y)\, F_a^2(x,y)\, \mathrm{d}x\mathrm{d}y; \tag{2.2.10}$$

$$q_{a,b}^{(3)} := \frac{k_0^2}{2\beta_a N_a} \iint \gamma F_b(x,y)\, F_a^3(x,y)\, \mathrm{d}x\mathrm{d}y; \tag{2.2.11}$$

$$q_{a,b}^{(4)} := \frac{k_0^2}{2\beta_a N_a} \iint \gamma F_b^3(x,y)\, F_a(x,y)\, \mathrm{d}x\mathrm{d}y, \tag{2.2.12}$$

with $N_a := \iint F_a^2(x,y)\, \mathrm{d}x\mathrm{d}y$. The MCCs describe the linear and nonlinear mode overlapping between the transversal functions F_m. The linear mode overlapping involves not only the cross-coupling effect ($\chi_{a,b}$ and $\kappa_{a,b}$), but also the self-overlapping (c_a) of the core modes. The nonlinear mode overlapping can be classified in two different categories: intra-core and inter-core. The former is related to the nonlinear self-coupling effect of the LP_{01} mode in each core, given by the MCC $q_a^{(1)}$ in core a. The latter is related to the nonlinear cross-coupling effects between the $\mathrm{LP}_{01,a}$ and $\mathrm{LP}_{01,b}$ modes, modeled by the MCCs $q_{a,b}^{(2)}$, $q_{a,b}^{(3)}$ and $q_{a,b}^{(4)}$. In step-index SM-MCFs, the MCCs can be calculated by using the following closed-form expressions (see Appendix B2, on page 54):

$$\chi_{a,b} \simeq \frac{2n_b}{n_a} \frac{J_0^2(u_a)}{[J_0^2(u_a) + J_1^2(u_a)]} \left[\frac{J_1(u_a)}{u_a J_0(u_a)} \frac{K_0(w_b d_{ab}/R_{0,b})}{K_0(w_b)} + \frac{R_{0,b}^2}{R_{0,a}^2} \frac{J_1(u_b)}{u_b J_0(u_b)} \frac{K_0(w_a d_{ab}/R_{0,a})}{K_0(w_a)} \right]; \tag{2.2.13}$$

$$c_a \simeq \frac{k_0 \mathrm{NA}_b^2}{2n_a} \frac{R_{0,b}^2}{R_{0,a}^2} \frac{J_0^2(u_a)}{[J_0^2(u_a) + J_1^2(u_a)]} \frac{K_0^2(w_a d_{ab}/R_{0,a})}{K_0^2(w_a)}; \tag{2.2.14}$$

$$\kappa_{a,b} \simeq \frac{k_0 \mathrm{NA}_a^2}{n_a} \frac{J_0(u_a)\, J_1(u_a)}{u_a [J_0^2(u_a) + J_1^2(u_a)]} \frac{K_0(w_b d_{ab}/R_{0,b})}{K_0(w_b)}; \tag{2.2.15}$$

$$q_a^{(1)} \simeq \frac{k_0 \gamma H_a^2}{8 n_a R_{0,a}^2} \frac{\left[1 - \exp\left(-4R_{0,a}^2/H_a^2\right)\right]}{J_0^2(u_a)\,[J_0^2(u_a) + J_1^2(u_a)]}; \tag{2.2.16}$$

$$q_{a,b}^{(2)} \simeq \frac{k_0 \gamma}{2n_a} \left\{ \frac{K_0^2(w_b d_{ab}/R_{0,b})}{K_0^2(w_b)} + \frac{R_{0,b}^2}{R_{0,a}^2} \frac{K_0^2(w_a d_{ab}/R_{0,a})}{K_0^2(w_a)} \frac{J_0^2(u_a)}{J_0^2(u_b)} \left[\frac{J_0^2(u_b) + J_1^2(u_b)}{J_0^2(u_a) + J_1^2(u_a)} \right] \right\}; \tag{2.2.17}$$

$$q_{a,b}^{(3)} \simeq \frac{k_0 \gamma H_a^2}{6 n_a R_{0,a}^2} \frac{K_0(w_b d_{ab}/R_{0,b})}{J_0(u_a)\, K_0(w_b)} \left[\frac{1 - \exp\left(-3R_{0,a}^2/H_a^2\right)}{J_0^2(u_a) + J_1^2(u_a)} \right]; \tag{2.2.18}$$

$$q_{a,b}^{(4)} \simeq \frac{k_0 \gamma H_b^2}{6 n_a R_{0,a}^2} \frac{J_0^2(u_a)}{J_0^3(u_b)} \frac{K_0(w_a d_{ab}/R_{0,a})}{K_0(w_a)} \left[\frac{1 - \exp\left(-3R_{0,b}^2/H_b^2\right)}{J_0^2(u_a) + J_1^2(u_a)} \right], \tag{2.2.19}$$

where $n_{a(b)}$ and $n_{\rm cl}$ are the refractive index of the core $a(b)$ and the cladding; $\mathrm{NA}_{a(b)} = \sqrt{n_{a(b)}^2 - n_{\rm cl}^2}$ is the numerical aperture; $H_{a(b)} \simeq R_{0,a(b)}(0.65 + 1.619V_{a(b)}^{-3/2} + 2.879V_{a(b)}^{-6})$ is the modal field radius of the $\mathrm{LP}_{01,a(b)}$ [139]; $R_{0,a(b)}$ is the core radius; $V_{a(b)} = k_0 R_{0,a(b)}\mathrm{NA}_{a(b)}$ is the normalized frequency; and $u_{a(b)}$ and $w_{a(b)}$ are the modal parameters [32]:

$$u_{a(b)} = \left(1+\sqrt{2}\right) V_{a(b)} / \left[1 + \left(4 + V_{a(b)}^4\right)^{1/4}\right]; \tag{2.2.20}$$

$$w_{a(b)} = \sqrt{V_{a(b)}^2 - u_{a(b)}^2}. \tag{2.2.21}$$

As was pointed out in [140], in homogeneous NLDCs with a distance between waveguides much higher than the waveguide width [in our case uncoupled homogeneous MCFs ($d_{ab} \gg 2R_0$)], $\kappa_{a,b}$ and $q_a^{(1)}$ are respectively the dominant linear and nonlinear MCCs, and the additional MCCs can be neglected due to the weakly-coupling conditions. Nonetheless, this result should be revisited in homogeneous and heterogeneous MCFs comprising coupled cores. As an example, let us consider a 2-core MCF with $R_{0,a} = R_{0,b} \equiv R_0 = 4$ μm, $n_b = 1.452$, $n_{\rm cl} = 1.444$, $\gamma = 1.5 \cdot 10^{-22}$ m^2/V^2 and $\lambda_0 = 1550$ nm. The linear MCCs $\chi_{a,b}$ and c_a, and the nonlinear MCCs $q_{a,b}^{(2)}$, $q_{a,b}^{(3)}$ and $q_{a,b}^{(4)}$ are respectively compared with the linear and nonlinear MCCs $\kappa_{a,b}$ and $q_a^{(1)}$. The ratios $\chi_{a,b}/\kappa_{a,b}$, $c_a/\kappa_{a,b}$, $q_{a,b}^{(2)}/q_a^{(1)}$, $q_{a,b}^{(3)}/q_a^{(1)}$ and $q_{a,b}^{(4)}/q_a^{(1)}$ are calculated using Eqs. (2.2.13)-(2.2.19).

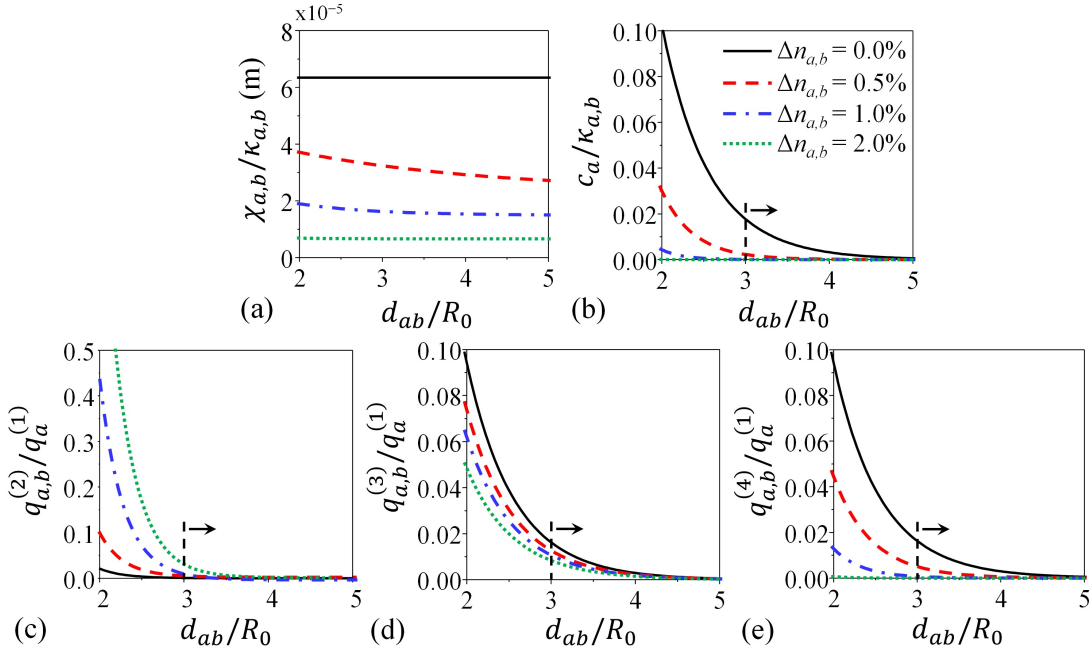

Figure 2.2. Comparison of the linear and nonlinear mode-coupling coefficients (MCCs) for different values of d_{ab}/R_0 and $\Delta n_{a,b}$. (a) $\chi_{a,b}/\kappa_{a,b}$, (b) $c_a/\kappa_{a,b}$, (c) $q_{a,b}^{(2)}/q_a^{(1)}$, (d) $q_{a,b}^{(3)}/q_a^{(1)}$ and (e) $q_{a,b}^{(4)}/q_a^{(1)}$.

Figure 2.2 shows the behavior of these ratios when varying d_{ab} and the index mismatching $\Delta n_{a,b} := (n_a - n_b)/n_b$. As can be seen, the MCCs $\chi_{a,b}$, c_a, $q_{a,b}^{(2)}$, $q_{a,b}^{(3)}$ and $q_{a,b}^{(4)}$ can be omitted in homogeneous and heterogeneous MCFs with $d_{ab} > 3R_0$. However, in coupled-core MCFs with $2R_0 < d_{ab} \leq 3R_0$, $\chi_{a,b}$ can be omitted but the MCCs c_a, $q_{a,b}^{(2)}$, $q_{a,b}^{(3)}$ and $q_{a,b}^{(4)}$ should be retained in the coupled-mode equations. These conclusions are found to be the same with $\Delta n_{a,b} < 0$. Moreover, in an MCF with $R_{0,a} \neq R_{0,b}$, the condition is found to be $d_{ab} > R_{0,a} + R_{0,b} + \max\{R_{0,a}, R_{0,b}\}$. Along this line, note that our Eq. (2.2.15) allows us to estimate the MCC $\kappa_{a,b}$ when cores with dissimilar radius are involved, a scenario which cannot be modeled with the closed-form expression of $\kappa_{a,b}$ reported by Snyder [137] and Okamoto [124].

2.2.3 Exact solution of the coupled-mode equations and discrepancy with experimental measurements in real multi-core fiber

In this section, let us perform a brief analysis of the coupled-mode equation (2.2.5). To this end, consider a simple case: an ideal homogeneous 2-core MCF with uncoupled cores ($d_{ab} \gg 3R_0$). In such a case, the coupled equations are reduced to the equations of the homogeneous NLDC with $\kappa_{a,b} = \kappa_{b,a} \equiv \kappa$, $q_a^{(1)} = q_b^{(1)} \equiv q$ and $\Delta\beta_{b,a} = 0$:

$$j\frac{\mathrm{d}A_a(z)}{\mathrm{d}z} = \kappa A_b(z) + q\left|A_a(z)\right|^2 A_a(z); \tag{2.2.22}$$

$$j\frac{\mathrm{d}A_b(z)}{\mathrm{d}z} = \kappa A_a(z) + q\left|A_b(z)\right|^2 A_b(z). \tag{2.2.23}$$

In [138], Jensen found the exact solution of this system of differential equations. Performing the transformation $A_{a(b)}(z) = a_{a(b)}(z)\exp(-j\varphi_{a(b)}(z))$, with $\left(a_{a(b)}, \varphi_{a(b)}\right) \in \mathcal{F}(\mathbb{R},\mathbb{R})^2$ and defining the parameters $P_\mathrm{T} := a_a^2(z) + a_b^2(z)$ and $\Gamma := 4a_a(z)a_b(z)\cos(\varphi_b(z) - \varphi_a(z)) - 2(q/\kappa)a_a^2(z)a_b^2(z)$, the solution in the cores a and b in terms of optical power is found to be:[5,6]

$$P_a(z) = \left|A_a(z)\right|^2 = P_\mathrm{T} - P_b(z); \tag{2.2.24}$$

$$P_b(z) = \left|A_b(z)\right|^2 = \frac{P_\mathrm{C}}{2} + \frac{\sigma\rho P_\mathrm{C}}{\sqrt{\sigma^2+\rho^2}}\mathrm{sd}\left(\kappa\sqrt{\sigma^2+\rho^2}\; z + F\left(\phi_0\middle|\, m\right)\middle|\, m\right), \tag{2.2.25}$$

with:

$$\sigma^2 = 4\frac{P_\mathrm{T}^2}{P_\mathrm{C}^2} - 2\left(1 - \frac{\Gamma}{P_\mathrm{C}}\right) + 2\sqrt{\frac{1-2\Gamma}{P_\mathrm{C}}}; \tag{2.2.26}$$

$$\rho^2 = -4\frac{P_\mathrm{T}^2}{P_\mathrm{C}^2} + 2\left(1 - \frac{\Gamma}{P_\mathrm{C}}\right) + 2\sqrt{\frac{1-2\Gamma}{P_\mathrm{C}}}; \tag{2.2.27}$$

$$m = \frac{\sigma^2}{\sigma^2+\rho^2}; \tag{2.2.28}$$

$$P_\mathrm{C} = 4\kappa/q; \tag{2.2.29}$$

$$\phi_0 = \arcsin\left\{\frac{[4P_b(0) - 2P_\mathrm{T}]}{\sigma}\sqrt{\frac{\sigma^2+\rho^2}{[4P_b(0) - 2P_\mathrm{T}]^2 + \rho^2 P_\mathrm{C}^2}}\right\}, \tag{2.2.30}$$

where $F(\phi_0|\, m)$ is an elliptic integral of the first kind, and $\mathrm{sd}(\theta|\, m)$ is a Jacobi elliptic function.

The parameter P_C is defined in [138] as the critical power of the NLDC, and describes the behavior of the coupled power between cores. If $P_a(0) = 0$ and $P_b(0) \ll P_\mathrm{C}$, then $m \ll 1$ and Eqs. (2.2.24) and (2.2.25) become:

$$P_{a(b)}(z) = P_b(0)\frac{1 \mp \cos(2\kappa z)}{2}, \tag{2.2.31}$$

with a coupling length of $L_\mathrm{C} = \pi/2k$. However, if $P_a(0) = 0$ and $P_b(0) \geq P_\mathrm{C}$, the mode-coupling shows a nonlinear response of the form:

$$P_{a(b)}(z) = P_b(0)\frac{1 \mp \mathrm{cn}(2\kappa z|\, m)}{2}, \tag{2.2.32}$$

where $m = P_b^2(0)/P_\mathrm{C}^2$ and $\mathrm{cn}(\theta|\, m)$ is a Jacobi elliptic function with fundamental period $4K(m)$, a simple zero in $K(m)$ and a simple pole in $jK(1-m)$, with K a complete elliptic integral of the first kind defined as $K(m) := F(\pi/2|\, m)$ [141].

[5] Note that $\mathrm{d}P_\mathrm{T}/\mathrm{d}z = \mathrm{d}\Gamma/\mathrm{d}z = 0$.

[6] Actually, the units of $\left|A_{a(b)}(z)\right|^2$ are $\mathrm{V}^2/\mathrm{m}^2$. However, let us remember that the optical power is found to be proportional to $\left|A_{a(b)}(z)\right|^2$ [see Eq. (1.5.11)]. We set the constant $\mathscr{C}_{a(b)}^{(\mathrm{P})} \equiv 1$ for simplicity in our theoretical discussions. The same remark applies to Section 2.4.

Figure 2.3 depicts Eq. (2.2.32) for different power launch levels [$P_{\mathrm{L}} := P_b(0)$] and setting the linear MCC $\kappa = 0.0072\,\mathrm{m}^{-1}$ and $L = 1\,\mathrm{km}$, where L is the MCF length.[7] As pointed out before, for power launch levels much lower than the critical power, the ideal MCF exchanges power between cores as the symmetric linear optical coupler [137] and the light is completely switched from core b to core a (e.g. $P_{\mathrm{L}}/P_{\mathrm{C}} = 0.5$, red line). In contrast, with power launch levels equal or higher than the critical power, the switching process is not complete (e.g. $P_{\mathrm{L}}/P_{\mathrm{C}} = 1.2$, purple line). The Kerr effect induces a phase-mismatching between the $\mathrm{LP}_{01,a}$ and $\mathrm{LP}_{01,b}$ modes ($\Delta\beta_{b,a} \neq 0$) and, consequently, the maximum value of the mode-coupling is significantly reduced.

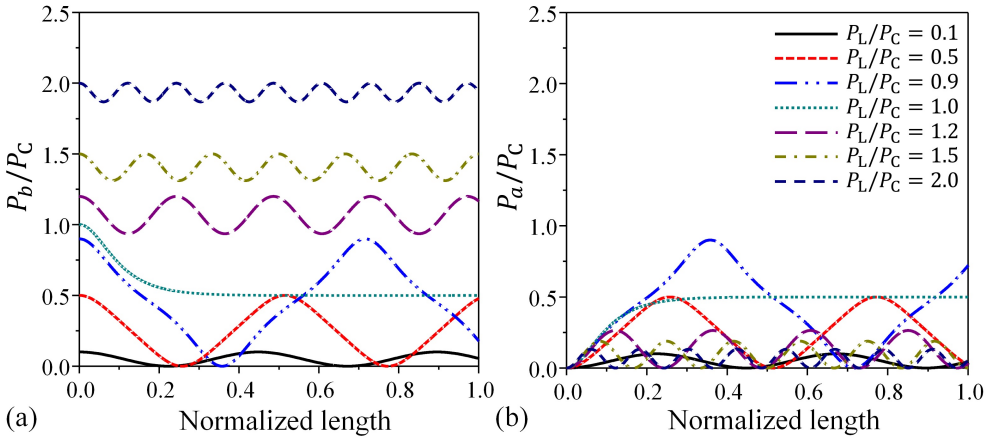

Figure 2.3. Longitudinal evolution of the coupled optical power in an ideal homogeneous 2-core MCF for different power launch levels in: (a) core b and (b) core a. (P_{L}: power launch, P_{C}: critical power).

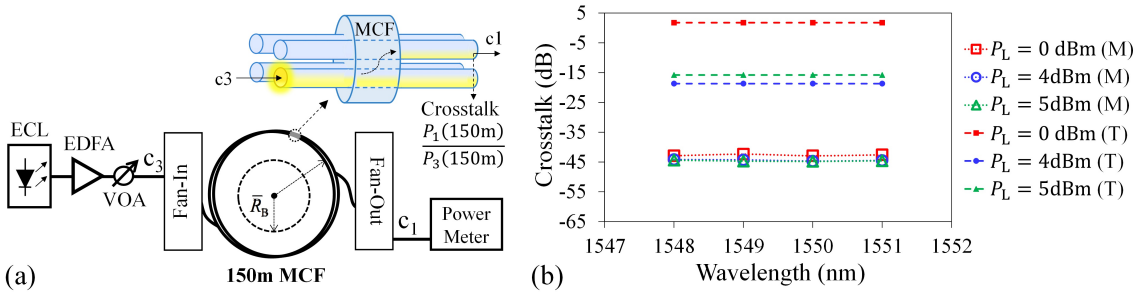

Figure 2.4. Measured (M) and theoretical (T) linear and nonlinear IC-XT in a homogeneous 4-core MCF Fibercore SM-4C1500(8.0/125). (a) Experimental set-up. (b) Inter-core crosstalk from core 3 to core 1. The theoretical estimation was performed by using Eq. (2.2.32).

Next, we compare these theoretical results with experimental measurements performed using a commercial MCF [Fibercore SM-4C1500(8.0/125)]. In particular, this fiber is an SI-SM-HO-UC-LB-MCF with 150 m of length and 4 cores distributed in a square lattice. Figure 2.4(a) shows the laboratory set-up. The MCF was spooled on a reel with an average value of the bending radius ($\overline{R}_{\mathrm{B}}$) and a twist rate of 67 cm and 4 turns/m, respectively. A tunable external cavity laser (ECL) at 1550 nm with a linewidth of 50 kHz was used along with an erbium-doped fiber amplifier (EDFA) to explore the nonlinear regime of the fiber. The EDFA gain was maximized to minimize the noise factor, which allows us to reduce the crosstalk averaging due to amplified spontaneous emission (ASE) noise [142]. A variable optical attenuator (VOA) was employed to modify the value of P_{L} taking into account the 2.2 dB of insertion loss of the 3D fan-in device. The optical power was injected into core 3 and measured in core 1 with an optical power meter (Newport 1931-C). It should be noted that the stimulated Brillouin scattering (SBS) does not reflect the power injected

[7] Specifically, the linear MCC κ was calculated from Eq. (2.2.15) taking $R_{0,a} = R_{0,b} = 4\ \mu\mathrm{m}$, $n_{\mathrm{cl}} = 1.444$, $n_a = n_b = 1.452$ and $d_{ab} = 35.2\,\mu\mathrm{m}$.

into the MCF when the condition $P_{\mathrm{L}} < P_{\mathrm{TH}}^{(\mathrm{SBS})}$ is satisfied, where $P_{\mathrm{TH}}^{(\mathrm{SBS})}$ is the SBS threshold power, estimated around 23.5 dBm in our MCF.[8]

Figure 2.4(b) depicts the comparison between the experimental measurements and the numerical estimations of the IC-XT for different wavelengths and P_{L} values. We used Eq. (2.2.32) with the same fiber parameters as in Fig. 2.3 to estimate the crosstalk, also including the constants $\mathscr{C}_a^{(\mathrm{P})}$ and $\mathscr{C}_b^{(\mathrm{P})}$ [Eq. (1.5.11)] to estimate the real optical power of each core mode at the MCF output. As can be seen, the measured results are in absolute *disagreement* with the calculated value of the IC-XT when using the classical nonlinear CMT. In addition, the parameter P_{C} cannot be estimated as $P_{\mathrm{C}} = (4\kappa/q)\,\mathscr{C}_b^{(\mathrm{P})}$ in real homogeneous MCFs given that this expression leads to a theoretical value around 15 dBm in this example. Nevertheless, as we will see in Section 2.6, the experimental work indicates that $P_{\mathrm{C}} \simeq 2$ dBm in silica MCFs. Therefore, at this point it is natural to ask why the theoretical estimations are in complete disagreement with the experimental measurements. The answer is found in the *MCF perturbations*.

2.2.4 The effect of the multi-core fiber perturbations: a heuristic modification of the coupled-mode theory

At the beginning of Subsection 2.2.1, we assumed an ideal MCF, i.e., without perturbations. Nonetheless, we found important discrepancies between theory and experiments given that the phase constants $\beta_{a(b)}$ are modified by the perturbations of the optical medium: the fiber bending, twisting, manufacturing imperfections, floor vibrations... Consequently, the phase-mismatching terms and the MCCs are wrongly estimated by using the ideal phase constants. Moreover, the fluctuation of the phase constants leads to the following fundamental questions about the initial considerations assumed in the MCF to derive the coupled-mode equations:

Isotropy. The medium perturbations, in particular the fiber bending and twisting, may induce linear and circular birefringence, respectively. Therefore, the initial assumption of considering the MCF as an *isotropic* medium seems to be inaccurate to describe the IC-XT in real-deployed MCF systems.

Time invariance. If external environmental factors induce physical changes in the MCF (e.g. temperature variations modifying the refractive index or floor vibrations inducing slight local changes in the bending radius and twist rate), we cannot assume a time-invariant system to describe the *constitutive relation* between the polarization and the electric field strength of the optical medium.

Ideal phase constants. Taking into account both longitudinal and temporal fiber perturbations, we cannot assume the ansatz of the electric field [Eq. (2.2.1)] with $\partial_z \beta_m = \partial_t \beta_m = 0$. In the same way, A_m and F_m will also be found longitudinal and temporal dependent due to these MCF fluctuations.

All in all, it is clear that the coupled-mode equations should be revisited to analyze the spatial and temporal behavior of the IC-XT. Thus, how can we tackle this problem by taking into account all these points with rigorous formalism? Although complex, this question will be solved in the next chapter. Now, in a first approximation, let us analyze the spatial behavior of the IC-XT by omitting the MCF temporal fluctuations and modifying heuristically the CMT [Eq. (2.2.5)].

[8] The threshold power of the SBS can be estimated in silica fibers as $P_{\mathrm{TH}}^{(\mathrm{SBS})} \simeq 21 A_{\mathrm{eff}}/(g_{\mathrm{B}} L_{\mathrm{eff}})$ [139], where A_{eff} is the effective area of the LP_{01} mode, g_{B} is the SBS gain and L_{eff} is the effective interaction length. In short fiber distances where the optical attenuation can be neglected, we can approximate $L_{\mathrm{eff}} \simeq L$. In our 150-m MCF, assuming $A_{\mathrm{eff}} \simeq 80\,\mu\mathrm{m}^2$ and $g_{\mathrm{B}} = 5 \cdot 10^{-11}$ m/W at 1550 nm, we find that $P_{\mathrm{TH}}^{(\mathrm{SBS})} \simeq 23.5$ dBm.

To this end, we replace the phase constant β_m of a given core m by the equivalent phase constant $\beta_m^{(\mathrm{eq})} := \beta_m + \beta_m^{(\mathrm{B+S})}$, with $\beta_m^{(\mathrm{B+S})}$ accounting for the longitudinal medium fluctuations in a short fiber segment where these perturbations can be assumed spatially invariant.[9] The superindexes 'B' and 'S' indicate, respectively, the phase perturbation induced by the fiber *bending* and additional *structural* longitudinal fluctuations of the medium (microbends, fiber twisting and manufacturing imperfections). Therefore, the phase-mismatching terms $\exp(\pm j\Delta\beta_{b,a}z)$ of Eq. (2.2.5) should be replaced by $\exp(\pm j\Delta\beta_{b,a}^{(\mathrm{eq})}z)$ in the MCF segment, where $\Delta\beta_{b,a}^{(\mathrm{eq})} := \beta_b^{(\mathrm{eq})} - \beta_a^{(\mathrm{eq})}$.

Now, if we consider the complete MCF length, the phase-mismatching terms must include the accumulative differential phase changes of $\beta_{a(b)}^{(\mathrm{eq})}$ along the different fiber segments. Hence, we should rewrite the exponential terms as $\exp(\pm j\int_0^z \Delta\beta_{b,a}^{(\mathrm{eq})}(\xi)\,\mathrm{d}\xi)$. Thus, defining the phase function:

$$\phi_m(z) := \int_0^z \beta_m^{(\mathrm{eq})}(\xi)\,\mathrm{d}\xi = \beta_m z + \int_0^z \beta_m^{(\mathrm{B+S})}(\xi)\,\mathrm{d}\xi, \tag{2.2.33}$$

with $m \in \{a,b\}$ and $\phi_m \in \mathcal{F}(\mathbb{R},\mathbb{R})$, Eq. (2.2.5) becomes:[10]

$$\begin{aligned} j\frac{\mathrm{d}A_a(z)}{\mathrm{d}z} &= c_a A_a(z) + \kappa_{a,b}\exp\left(-j\Delta\phi_{b,a}(z)\right)A_b(z) + q_a^{(1)}\left|A_a(z)\right|^2 A_a(z) \\ &+ q_{a,b}^{(2)}\left[2A_a(z)\left|A_b(z)\right|^2 + A_a^*(z)\,A_b^2(z)\exp\left(-j2\Delta\phi_{b,a}(z)\right)\right] \\ &+ q_{a,b}^{(3)}\left[2\left|A_a(z)\right|^2 A_b(z)\exp\left(-j\Delta\phi_{b,a}(z)\right) + A_a^2(z)\,A_b^*(z)\exp\left(j\Delta\phi_{b,a}(z)\right)\right] \\ &+ q_{a,b}^{(4)}\left|A_b(z)\right|^2 A_b(z)\exp\left(-j\Delta\phi_{b,a}(z)\right), \end{aligned} \tag{2.2.34}$$

with $\Delta\phi_{b,a} := \phi_b - \phi_a$ and neglecting the MCC $\chi_{a,b}$ as discussed before. From now on, we will refer to Eq. (2.2.34) as the *modified CMT*.

At this point, one can argue about whether the MCCs should also be assumed spatial dependent along the z-axis. In general, as we will verify experimentally in Section 2.6, the theoretical estimation of the IC-XT will be sufficiently accurate by using Eq. (2.2.34) with constant MCCs when omitting polarization effects and the temporal perturbations of the MCF. Furthermore, the use of constant MCCs allows us to minimize the computational time of Eq. (2.2.34).

2.3 Longitudinal evolution of inter-core crosstalk

Once we have presented the modified CMT, we will be able to investigate the evolution of the linear and nonlinear IC-XT along the MCF length. We will analyze to different scenarios: (*i*) constant and (*ii*) random bending and twisting conditions. Both situations can be described by using Eq. (2.2.34) along with the *equivalent refractive index model* (ERIM) of Hayashi [133]. Specifically, Hayashi and coworkers proposed the ERIM to calculate analytically the phase functions ϕ_m with constant bending and twisting conditions. In that case, ϕ_m can be calculated as [129]:

$$\phi_m(z) = \int_0^z \beta_m^{(\mathrm{eq})}(\xi)\,\mathrm{d}\xi = k_0\int_0^z n_m^{(\mathrm{eq})}(\xi; R_\mathrm{B}, f_\mathrm{T})\,\mathrm{d}\xi; \tag{2.3.1}$$

$$n_m^{(\mathrm{eq})}(z; R_\mathrm{B}, f_\mathrm{T}) \simeq n_m\left[1 + \frac{d_m}{R_\mathrm{B}}\cos\left(2\pi f_\mathrm{T} z + \theta_m + \theta_0\right)\right], \tag{2.3.2}$$

[9] Given that we will use the CMT to analyze the impact of $\beta_m^{(\mathrm{B+S})}$ on the IC-XT, the own concept of the complex envelope $A_{a(b)}(z)$ requires to use the SVEA in $\delta z \sim \lambda_{a(b)} = \lambda_0/n_{a(b)}$. Therefore, the minimum segment length which should be assumed must be higher than $\lambda_{a(b)}$. This assumption is coherent with real MCFs [129]: the fiber bending and twisting are found to be invariant in longitudinal distances of the order of $\lambda_{a(b)} \sim \mu$m.

[10] Note that Eq. (2.2.34) is obtained by modifying heuristically Eq. (2.2.5). This strategy is mathematically questionable. Firstly, the phase constants $\beta_{a(b)}$ are assumed invariant to derive the coupled equations [Eq. (2.2.5)] and, secondly, we assume that the MCF perturbations modify the phase constants in Eq. (2.2.5). Furthermore, these perturbations may induce anisotropic effects, but we only consider a single polarization per core. We will address these issues in the next chapter.

where R_{B} is the bending radius, f_{T} is the twist rate, d_m is the Euclidean distance of core m to the MCF center, θ_m is the offset of the twist angle of core m (measured from the MCF reference axis), and θ_0 is the offset of the twist angle of the MCF reference axis at $z = 0$ [see Fig. 2.5(a)]. In weakly-guiding GI-MCFs, we can replace n_m by $\max\{n_m(r)\}$.

Remarkably, the ERIM can also be employed in the case in which R_{B} and f_{T} vary randomly along the MCF, as reported by Macho et al., in [143]. In that case, the MCF length should be divided into a series of segments where R_{B} and f_{T} can be assumed constant in each one. Thus, in a given l-th segment (located between the points z_l and z_{l+1}), the phase function ϕ_m can be calculated in a given z point as:[11]

$$\begin{aligned}\phi_m(z) &= \int_{z_l}^{z} \beta_m^{(\mathrm{eq})}(\xi)\,\mathrm{d}\xi = k_0 \int_{z_l}^{z} n_m^{(\mathrm{eq})}(\xi; R_{\mathrm{B},l}, f_{\mathrm{T},l})\,\mathrm{d}\xi \\ &\simeq k_0 n_m (z - z_l) + \frac{k_0 n_m d_m}{2\pi f_{\mathrm{T},l} R_{\mathrm{B},l}} \left[\sin(2\pi f_{\mathrm{T},l} z + \theta_m + \theta_0) - \sin(2\pi f_{\mathrm{T},l} z_l + \theta_m + \theta_0)\right], \quad (2.3.3)\end{aligned}$$

with $R_{\mathrm{B},l}$ and $f_{\mathrm{T},l}$ the values of R_{B} and f_{T} in the l-th segment. If $f_{\mathrm{T},l} \cdot (z_{l+1} - z_l) \simeq 0$, then we can approximate $\phi_m(z) \simeq k_0 n_m^{(\mathrm{eq})}(z; R_{\mathrm{B},l}, f_{\mathrm{T},l}) \cdot (z - z_l)$.

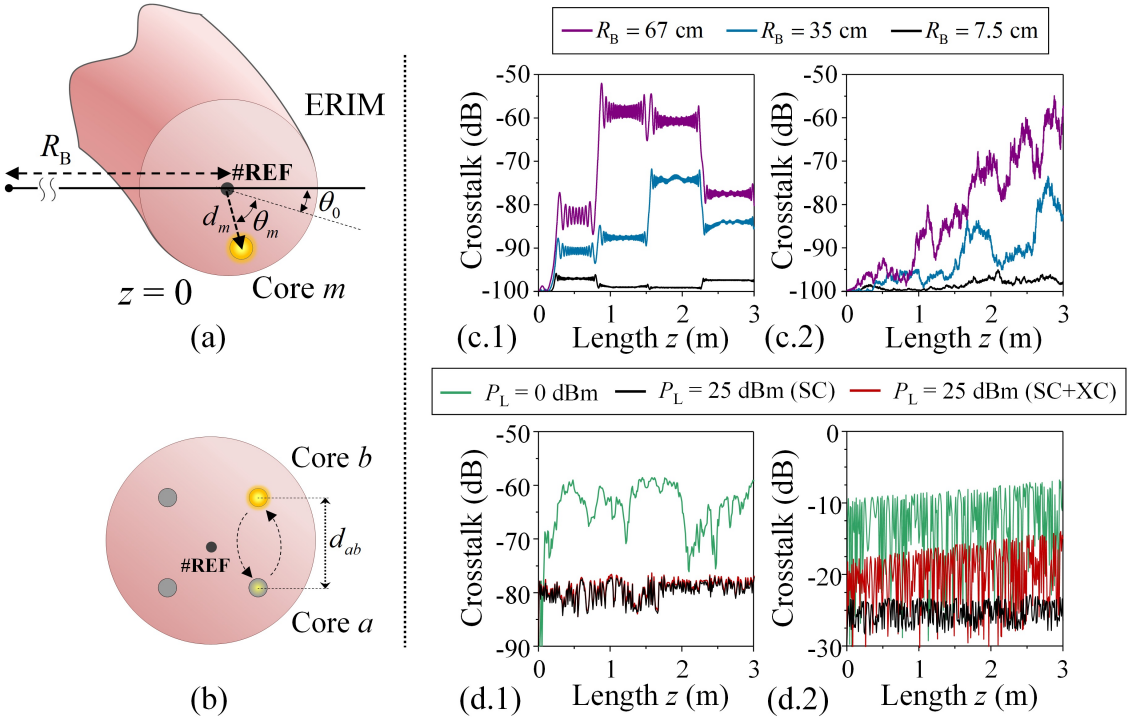

Figure 2.5. Longitudinal evolution of the linear and nonlinear IC-XT. (a) Equivalent refractive index model. (b) Simulated 4-core MCF (only the cores a and b have been considered in the numerical calculations). (c) Linear IC-XT with (c.1) deterministic and (c.2) random fiber bending and twisting conditions. (d) Comparison of the linear and nonlinear IC-XT for different power launch levels (P_{L}) and different core-to-core distances (d_{ab}) considering: (d.1) $d_{ab} = 10R_0$ and (d.2) $d_{ab} = 2.5R_0$. The fiber bending and twisting are described in the main text. [Green line: $P_{\mathrm{L}} = 0$ dBm. Black line: $P_{\mathrm{L}} = 25$ dBm simulating only the nonlinear self-coupling effect (SC) neglecting the nonlinear MCCs $q_{a,b}^{(2)}$, $q_{a,b}^{(3)}$ and $q_{a,b}^{(4)}$ in Eq. (2.2.34). Red line: $P_{\mathrm{L}} = 25$ dBm simulating the nonlinear self- and cross-coupling effects (SC+XC) retaining all the nonlinear MCCs in Eq. (2.2.34)].

[11] We assumed $f_{\mathrm{T},l} \neq 0$ in the second line of Eq. (2.3.3).

As a first simple example, we simulate the longitudinal evolution of the linear IC-XT in a homogeneous 4-core MCF with: $R_0 = 4$ μm, $n_{a(b)} = 1.452$, $n_{\rm cl} = 1.444$, $d_{ab} = 35.2\mu$m and $\lambda_0 = 1550$ nm. The core distribution is shown in Fig. 2.5(b). The fiber twisting is fixed to $f_{\rm T} = 1\,$turn/m and the bending radius was evaluated for three different constant values with $R_{\rm B} \in \{7.5, 35, 67\}$ cm. We solve numerical the modified CMT [Eq. (2.2.34)] by assuming as initial conditions $A_a\,(z=0) = 0$ and $A_b\,(z=0) = \sqrt{P_{\rm L}}$, with $P_{\rm L} = 0\,$dBm to evaluate the linear regime.[12] The crosstalk from core b to core a is defined as $XT_{a,b} := P_a(z=L)/P_b(z=L)$, where $L = 3\,$m is the simulated length. Figure 2.5(c.1) depicts the numerical results. *Discrete deterministic changes* can be observed in the longitudinal evolution of the IC-XT at every phase-matching point, i.e., the $z_{\rm PM}$ points along the MCF length where $\Delta n_{b,a}^{(\rm eq)}(z = z_{\rm PM}) = 0$. These results are in line with [133]. However, the IC-XT behavior is found to be absolutely different when varying randomly $R_{\rm B}$ and $f_{\rm T}$.

In the next example, we consider the same MCF of the first example but assuming $R_{\rm B}$ and $f_{\rm T}$ randomly varying along 20 different fiber segments following a normal distribution (N) of $R_{\rm B} = {\rm N}(\mu \in \{7.5, 35, 67\}, \sigma^2 = 2)\,$cm and $f_{\rm T} = {\rm N}(\mu = 1, \sigma^2 = 0.1)\,$turns/m. In this case, the phase-matching points are randomly distributed along the MCF length and, consequently, the crosstalk presents *quasi-discrete random changes* [Fig. 2.5(c.2)]. The quasi-discrete nature seems to be continuous due to the reduced distance between adjacent phase-matching points. In addition, we can note that the higher the bending radius, the higher the average value of the IC-XT.

Next, we analyze the nonlinear IC-XT in a heterogeneous 4-core MCF with the same core distribution as in the previous examples and fiber parameters: $R_0 = 4$ μm, $n_a = 1.46$, $n_b = 1.45$, $n_{\rm cl} = 1.444$, $\gamma = 1.5 \cdot 10^{-22}$ m^2/V^2 and $\lambda_0 = 1550$ nm. Two different core-to-core distances were evaluated with $d_{ab} = 10R_0$ and $d_{ab} = 2.5R_0$ to analyze both UC- and CC-MCF designs, respectively. In this case, the bending radius was taken to be constant with $R_{\rm B} = 50\,$cm, but the twist rate is assumed randomly varying along 20 different fiber segments following a normal distribution of $f_{\rm T} = {\rm N}(\mu = 1, \sigma^2 = 0.1)\,$turns/m. Equation (2.2.34) was numerically solved by assuming as initial conditions $A_a\,(z=0) = 0$ and $A_b\,(z=0) = \sqrt{P_{\rm L}}$, with $P_{\rm L} \in \{0, 25\}\,$dBm to compare the IC-XT behavior in the linear and nonlinear regimes. The numerical results are depicted in Fig. 2.5(d.1) and (d.2) for the UC-MCF and CC-MCF, respectively. The green line describes the longitudinal evolution of the linear crosstalk, the black line depicts the longitudinal evolution of the nonlinear crosstalk when simulating only the nonlinear self-coupling effect neglecting the MCCs $q_{a,b}^{(2)}$, $q_{a,b}^{(3)}$ and $q_{a,b}^{(4)}$ in Eq. (2.2.34), and the red line shows the nonlinear crosstalk retaining all the nonlinear MCCs in Eq. (2.2.34).

As can be seen, the crosstalk has a random evolution in the linear and nonlinear regime along the MCF length as a direct consequence of the random twisting conditions of the fiber. Specifically, in the nonlinear regime, the crosstalk is found to be lower than in the linear regime because of the additional phase-mismatching induced in core a by the Kerr effect. Furthermore, it should be noted that we cannot observe any difference in the crosstalk evolution when the nonlinear cross-coupling effects are simulated in UC-MCFs [Fig. 2.5(d.1)]. In contrast, in CC-MCFs with a reduced d_{ab} value ($d_{ab} < 3R_0$), the nonlinear cross-coupling effects (modeled by the MCCs $q_{a,b}^{(2)}$, $q_{a,b}^{(3)}$ and $q_{a,b}^{(4)}$) should be retained in Eq. (2.2.34), as was pointed out in Fig. 2.2 and is confirmed in Fig. 2.5(d.2). Remarkably, the numerical solution shows that the nonlinear cross-coupling effects increase the nonlinear crosstalk in CC-MCFs.

As demonstrated above, the linear and nonlinear IC-XT shows a random nature along the MCF length inherited from the random bending and twisting conditions of the optical medium. In such a scenario, a statistical analysis of the linear and nonlinear spatial distribution of the IC-XT is required. Interestingly, the modified CMT allows us to estimate the spatial distribution of the crosstalk performing a Monte Carlo simulation of Eq. (2.2.34) by assuming $R_{\rm B}$ and $f_{\rm T}$ as random processes which fluctuate along different fiber segments. In each l-th segment, $R_{{\rm B},l}$ and

[12] Actually, $A_b\,(z=0)$ should be calculated as a function of $P_{\rm L}$ as $A_b\,(z=0) = \sqrt{P_{\rm L}/\mathscr{C}_b^{(\rm P)}}$. However, we take $\mathscr{C}_b^{(\rm P)} \equiv 1$ for simplicity in the numerical simulations. Note that the value of the IC-XT does not depend on the constants $\mathscr{C}_a^{(\rm P)}$ and $\mathscr{C}_b^{(\rm P)}$. In homogeneous cores $\mathscr{C}_a^{(\rm P)} = \mathscr{C}_b^{(\rm P)}$ and in heterogeneous cores we can assume $\mathscr{C}_a^{(\rm P)} \simeq \mathscr{C}_b^{(\rm P)}$ with weakly-guiding conditions.

$f_{\mathrm{T},l}$ can be modeled as continuous random variables whose values will be modified in each Monte Carlo iteration. Then, the probability density function, mean and variance of the crosstalk can be numerically estimated if $R_{\mathrm{B},l}$ and $f_{\mathrm{T},l}$ are adequately randomized in each segment.

However, a Monte Carlo simulation of Eq. (2.2.34) requires a high computational time due to the complex exponential terms. In this context, it would be of great interest to investigate closed-form expressions which allow us to estimate the spatial statistics of the crosstalk without performing numerical simulations. To this end, we should previously derive in the next section a set of coupled equations in terms optical power: the coupled-power theory (CPT). Remarkably, the CPT will allow us to obtain in Section 2.5 the closed-form expressions of the mean and variance of the IC-XT.

2.4 Coupled-power theory for bent and twisted multi-core fiber

The analytic estimation of the crosstalk by using the modified CMT involves a high degree of complexity. In addition, we are rarely interested in the exact phases and amplitudes of the individual core modes to perform a statistical analysis of this physical impairment. For most practical purposes, it would be sufficient to know the average value of the coupled power from adjacent cores. In this scenario, the coupled-power theory (CPT) will allow us to describe the mode-coupling in terms of the average power of each core mode.

The CPT was originally proposed by Dietrich Marcuse for MM-SCFs omitting their nonlinear nature [144]. Recently, Masanori Koshiba extended this theory to SM-MCFs to investigate the IC-XT in the linear regime [128]. Unfortunately, the CPT has not been formulated by considering the nonlinear effects, a fundamental requisite to analyze the behavior of the IC-XT mean when the Kerr nonlinearities are stimulated in the optical medium. In this section, we will extend the CPT to SM-MCFs operating in the nonlinear regime, which allows us to unify this theory in both power regimes. Furthermore, in order to simplify the mathematical discussions, we will consider the usual fiber design criterion $d_{ab} > 3R_0$ in high-capacity MCF-SDM transmissions using uncoupled and coupled cores [8, 16, 31].

In the linear regime and omitting the fiber losses, the IC-XT from core b to core a can be expressed as a function of the average optical power as [128]:

$$\frac{\mathrm{d}\overline{P}_a(z)}{\mathrm{d}z} = h_{a,b}\left[\overline{P}_b(z) - \overline{P}_a(z)\right], \tag{2.4.1}$$

where $h_{a,b}$ is the linear power-coupling coefficient describing the average value of the linear crosstalk per unit of length (see below) and $\overline{P}_{a(b)}$ is the average power of the core $a(b)$, defined as:

$$\overline{P}_{a(b)}(z) := \left\langle P_{a(b)}(z)\right\rangle = \left\langle \left|A_{a(b)}(z)\right|^2\right\rangle = \frac{1}{2L_{\mathrm{C}}(z)}\int_{z-L_{\mathrm{C}}(z)}^{z+L_{\mathrm{C}}(z)} \left|A_{a(b)}(\tau)\right|^2 \mathrm{d}\tau, \tag{2.4.2}$$

with $L_{\mathrm{C}}(z)$ the coupling length between the cores a and b (see Section 2.2.3). From the above equations the following considerations are in order:

- In ideal MCFs (i.e. optical couplers) the coupling length is found to be constant (see Fig. 2.3). However, in real MCFs with longitudinal random perturbations, L_{C} is found to be longitudinal dependent (see Fig. 2.5). Hence, $\overline{P}_{a(b)}$ inherits the longitudinal dependence and the random nature from L_{C}.
- In the weak-coupling regime (UC-MCFs), the crosstalk variance is much lower than the crosstalk mean (see Section 2.5). In such a case, we can assume that $P_{a(b)}(z)$ is approximately constant in $\delta z \sim L_{\mathrm{C}}$. Consequently, in a given z_0 point $\overline{P}_{a(b)}(z_0+\delta z) \simeq P_{a(b)}(z_0+\delta z)$ in $\delta z \sim L_{\mathrm{C}}(z_0)$. This approximation will be used later to discuss the crosstalk mean from the CPT.

- As was pointed out before in footnote 6, the units of $\left|A_{a(b)}\left(z\right)\right|^2$ are $\mathrm{V}^2/\mathrm{m}^2$. Nonetheless, we will use the same terminology as in the literature and we will refer to $P_{a(b)}$ as the optical power of the core $a(b)$. This mathematical inconsistency is solved by taking $\mathscr{C}_{a(b)}^{(\mathrm{P})} \equiv 1$ in Eq. (1.5.11) to simplify the theoretical discussions.

Now, focusing our attention on the nonlinear regime, it should be noted that the nonlinear coupling effects must be included in Eq. (2.4.1) and, therefore, the derivation of the coupled-power equations from the CMT should be revisited. Along this line, it should be remember that, as demonstrated in Sections 2.2.2 and 2.3, the predominant nonlinear effect in uncoupled- and coupled-core SM-MCFs with $d_{ab} > 3R_0$ is the nonlinear self-coupling effect, modeled by the MCC $q_a^{(1)}$ in Eq. (2.2.34). In such conditions, Eq. (2.2.34) can reduced to:

$$j\frac{\mathrm{d}}{\mathrm{d}z}\mathbf{A}\left(z\right) = \mathbf{M}\left(z\right)\cdot\mathbf{A}\left(z\right), \tag{2.4.3}$$

with $\mathbf{A}\left(z\right) := \left[A_a\left(z\right), A_b\left(z\right)\right]^{\mathrm{T}}$ and the $\mathbf{M}$ matrix defined as:

$$\mathbf{M}\left(z\right) := \mathbf{q}\cdot\mathbf{P}\left(z\right) + \exp\left(j\int_0^z \mathbf{b}^{(\mathrm{eq})}\left(\xi\right)\mathrm{d}\xi\right)\cdot\mathbf{k}\cdot\exp\left(-j\int_0^z \mathbf{b}^{(\mathrm{eq})}\left(\xi\right)\mathrm{d}\xi\right), \tag{2.4.4}$$

where $\mathbf{q} := \mathrm{diag}\left(q_a^{(1)}, q_b^{(1)}\right)$, $\mathbf{b}^{(\mathrm{eq})} := \mathrm{diag}\left(\beta_a^{(\mathrm{eq})}, \beta_b^{(\mathrm{eq})}\right)$, $\mathbf{P}\left(z\right) := \mathrm{diag}\left(P_a\left(z\right), P_b\left(z\right)\right)$ and:

$$\mathbf{k} := \begin{bmatrix} 0 & \kappa_{a,b} \\ \kappa_{b,a} & 0 \end{bmatrix}. \tag{2.4.5}$$

Considering that Eq. (2.4.3) describes the mode-coupling between modes of different cores, we can assume crosstalk values much lower than 0 dB. In such a case, Eq. (2.4.3) admits a first-order solution of the form:

$$\mathbf{A}\left(z\right) \simeq \left(\mathbf{I} - j\int_0^z \mathbf{M}\left(\xi\right)\mathrm{d}\xi\right)\cdot\mathbf{A}\left(0\right), \tag{2.4.6}$$

where $\mathbf{I}$ is the identity matrix. Thus, analyzing an MCF segment located between the points z_1 and z_2, with $|z_2 - z_1|$ larger than the correlation length of the MCF random perturbations,[13] the longitudinal evolution of the complex envelopes can be described as $\mathbf{A}(z_2) \simeq \mathbf{T}\cdot\mathbf{A}(z_1)$, where $\mathbf{T}$ is the 2x2 matrix:

$$\mathbf{T} := \mathbf{I} - j\int_{z_1}^{z_2} \mathbf{M}\left(\xi\right)\mathrm{d}\xi \equiv \begin{bmatrix} T_{a,a} & T_{a,b} \\ T_{b,a} & T_{b,b} \end{bmatrix}. \tag{2.4.7}$$

It can be noted that $T_{a,b}$ describes the linear IC-XT from core b to core a, and $T_{a,a}$ models the linear propagation and the nonlinear self-coupling effect of the $\mathrm{LP}_{01,a}$ mode. A similar description applies to $T_{b,a}$ and $T_{b,b}$ coefficients. In particular, $T_{a,b}$ is found to be:

$$\begin{aligned} T_{a,b} &= -j\kappa_{a,b}\int_{z_1}^{z_2} \exp\left(-j\int_{z_1}^{z} \Delta\beta_{b,a}^{(\mathrm{eq})}\left(\xi\right)\mathrm{d}\xi\right)\mathrm{d}z \\ &= -j\kappa_{a,b}\int_{z_1}^{z_2} f_{b,a}\left(z\right)\exp\left(-j\Delta\beta_{b,a}\left(z - z_1\right)\right)\mathrm{d}z, \end{aligned} \tag{2.4.8}$$

where $f_{b,a}$ is assumed an ergodic and strict-sense stationary spatial random process modeling the longitudinal random perturbations:[14]

$$f_{b,a}\left(z\right) := \exp\left(-j\int_{z_1}^{z} \Delta\beta_{b,a}^{(\mathrm{B+S})}\left(\xi\right)\mathrm{d}\xi\right), \tag{2.4.9}$$

[13] This condition is required to analyze an ergodic fiber segment.

[14] We assume $f_{b,a}$ as an ergodic and strict-sense stationary random process for simplicity. However, in real deployed MCF systems, the bending radius could have a different random distribution in different z points. Moreover, if we include the temporal perturbations of the fiber, $f_{b,a}\left(z;t\right)$ cannot be assumed as an ergodic and strict-sense stationary random process in the z variable if these temporal perturbations induce a different random distribution of $\Delta\beta_{b,a}^{(\mathrm{B+S})}\left(z;t\right)$ in different z points. In such a case, the spatial average of $f_{b,a}$ could be found different from the corresponding statistical average.

and $T_{a,a}$ takes the form:

$$T_{a,a} = 1 - jq_a^{(1)} \int_{z_1}^{z_2} P_a(z)\,\mathrm{d}z, \tag{2.4.10}$$

with the first term of the RHS accounting for the linear propagation and the second term modeling the self-coupling effect.

Remarkably, the power-coupling coefficients required to model the linear and the nonlinear coupling can be derived from these coefficients. In particular, the linear power-coupling coefficient $h_{a,b}$ can be calculated from $T_{a,b}$ as follows:

$$\begin{aligned} h_{a,b} &= \frac{\left\langle |T_{a,b}|^2 \right\rangle}{z_2 - z_1} = \frac{\left\langle T_{a,b} T_{a,b}^* \right\rangle}{z_2 - z_1} = \frac{\kappa_{a,b}^2}{z_2 - z_1} \int_{x=z_1}^{z_2} \int_{y=z_1}^{z_2} \left\langle f_{b,a}(x)\, f_{b,a}^*(y) \right\rangle \exp\left(j\Delta\beta_{b,a}(y-x)\right) \mathrm{d}y\mathrm{d}x \\ &= \frac{\kappa_{a,b}^2}{z_2 - z_1} \int_{x=z_1}^{z_2} \int_{y=z_1}^{z_2} R_{b,a}^{(f)}(y-x) \exp\left(j\Delta\beta_{b,a}(y-x)\right) \mathrm{d}y\mathrm{d}x \qquad [\tau \equiv y - x] \\ &= \frac{\kappa_{a,b}^2}{z_2 - z_1} \int_{x=z_1}^{z_2} \int_{\tau=z_1-x}^{z_2-x} R_{b,a}^{(f)}(\tau) \exp\left(j\Delta\beta_{b,a}\tau\right) \mathrm{d}\tau\mathrm{d}x, \end{aligned} \tag{2.4.11}$$

with $R_{b,a}^{(f)}$ the autocorrelation function[15] (ACF) of $f_{b,a}$. Now, considering the correlation length of $f_{b,a}$ much lower than the segment length, the spatial frequencies of $R_{b,a}^{(f)}$ are well described in the fiber segment and, consequently, we can extend the second integral on the full line ($-\infty < \tau < \infty$). As a result, using the Wiener-Khinchin theorem [145], we obtain:

$$h_{a,b} \simeq \kappa_{a,b}^2 \int_{-\infty}^{\infty} R_{b,a}^{(f)}(\tau) \exp\left(j\Delta\beta_{b,a}\tau\right) \mathrm{d}\tau = \kappa_{a,b}^2 S_{b,a}^{(f)}\left(\upsilon = \frac{\Delta\beta_{b,a}}{2\pi}\right), \tag{2.4.12}$$

where $S_{b,a}^{(f)}$ is the power spectral density (PSD) of $f_{b,a}$ and υ is the spatial frequency.[16] Note that this result is in line with [31]. However, in contrast to [128], it is not necessary to include the deterministic part of $\Delta\beta_{b,a}^{(\mathrm{B+S})}$ along with $\Delta\beta_{b,a}$ in Eq. (2.4.12).

Moreover, following a similar strategy, the nonlinear power-coupling coefficient h_a can be written in the MCF segment as ($q_a^{(1)} \equiv q_a$):

$$\begin{aligned} h_a &= \frac{\left\langle |T_{a,a}|^2 - 1 \right\rangle}{z_2 - z_1} = \frac{q_a^2}{z_2 - z_1} \int_{x=z_1}^{z_2} \int_{y=z_1}^{z_2} \left\langle P_a(x)\, P_a(y) \right\rangle \mathrm{d}y\mathrm{d}x \\ &= \frac{q_a^2}{z_2 - z_1} \int_{x=z_1}^{z_2} \int_{y=z_1}^{z_2} R_a(y-x)\,\mathrm{d}y\mathrm{d}x \qquad [\tau \equiv y - x] \\ &= \frac{q_a^2}{z_2 - z_1} \int_{x=z_1}^{z_2} \int_{\tau=z_1-x}^{z_2-x} R_a(\tau)\,\mathrm{d}\tau\mathrm{d}x, \end{aligned} \tag{2.4.13}$$

with R_a the ACF of the real spatial random process P_a. As before, considering the correlation length of P_a much lower than the segment length, we can assume that the PSD of P_a (S_a) is well-defined in the fiber segment. Hence, Eq. (2.4.13) is reduced to:

$$h_a \simeq q_a^2 \int_{-\infty}^{\infty} R_a(\tau)\,\mathrm{d}\tau = q_a^2 S_a(\upsilon = 0). \tag{2.4.14}$$

---

[15] Since $f_{b,a}$ is a strict-sense stationary random process, then $R_{b,a}^{(f)}$ is a Hermitian function.

[16] In a spatial random process $\{X(z), z \in D\}$, where $D \subset \mathbb{R}$, the PSD is defined as the *spatial* Fourier transform of the ACF, that is, $S^{(X)}(\upsilon) = \int_{-\infty}^{\infty} R^{(X)}(z) \exp(j2\pi\upsilon z)\,\mathrm{d}z$. In contrast, in a temporal random process $\{X(t), t \in T\}$, where $T \subset \mathbb{R}$, the PSD is defined as the *temporal* Fourier transform of the ACF, that is, $S^{(X)}(f) = \int_{-\infty}^{\infty} R^{(X)}(t) \exp(-j2\pi f t)\,\mathrm{d}t$ [145]. Although the sign convention is commonly changed in the space and time domain, we could also use the same convention in both Fourier transforms.

Finally, taking into account that the nonlinear self-coupling effect reduces the power coupling between cores (as demonstrated in previous sections), Eq. (2.4.1) is heuristically modified in the nonlinear regime as follows:

$$\frac{\mathrm{d}\overline{P}_a(z)}{\mathrm{d}z} = h_{a,b}^{(\mathrm{eq})}\left[\overline{P}_b(z) - \overline{P}_a(z)\right], \tag{2.4.15}$$

with:

$$h_{a,b}^{(\mathrm{eq})} = h_{a,b} - h_a = \kappa_{a,b}^2 S_{b,a}^{(f)}\left(\frac{\Delta\beta_{b,a}}{2\pi}\right) - q_a^2 S_a(0). \tag{2.4.16}$$

A similar expression is found in terms of $\mathrm{d}\overline{P}_b(z)/\mathrm{d}z$ by exchanging the corresponding subindexes in the above equations. As we will see in the next section, Eq. (2.4.15) will allow us to derive the closed-form expressions of the crosstalk mean in both linear and nonlinear regimes.

Now, let us take a closer look at Eq. (2.4.15) by assuming as initial conditions $\overline{P}_a(z=0) = P_{\mathrm{L}}$ and $\overline{P}_b(z=0) = 0$. In a first approximation and considering that $\overline{P}_a(z)$ is approximately constant along the z-axis in the nonlinear regime (see Fig. 2.5, black line), we can replace the nonlinear power-coupling coefficient h_a by $Lq_a^2\overline{P}_a^2(z)$, where L is the MCF length. In addition, note that $\overline{P}_a(z) + \overline{P}_b(z) = P_{\mathrm{L}}$ when assuming the MCF as a lossless medium and, therefore, we found that $\overline{P}_a'(z) = -\overline{P}_b'(z)$. Hence, the coupled-power equations are only symmetric in the linear regime. Along this line, it should be remarked that $h_{a,b}^{(\mathrm{eq})} > 0$. In particular, this condition allows us to infer the maximum value of P_{L} where the nonlinear CPT provides a non-divergent solution: $P_{\mathrm{L},max} = \sqrt{h_{a,b}/(Lq_a^2)}$.

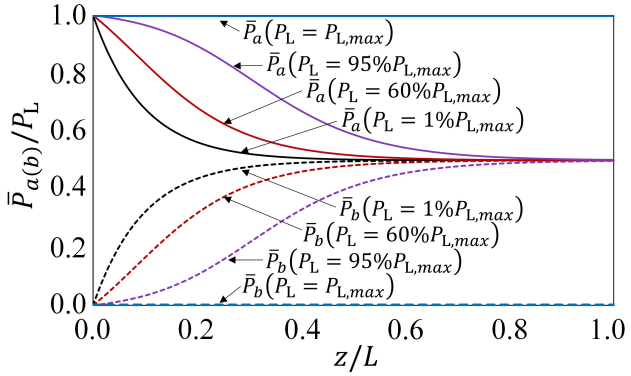

Figure 2.6. Normalized solution of the nonlinear coupled-power theory considering different optical power launch levels (P_{L}) [CONF 6].

Figure 2.6 shows the normalized solution of the nonlinear CPT considering a lossless homogeneous 2-core MCF with $h_{a,b} = h_{b,a} = 5.2 \cdot 10^{-5}$ m^{-1}, $q_a = 2.7 \cdot 10^{-13}$ m/V^2 and $L = 150$ km. The value of P_{L} ranges from 0% to 100% of the maximum power $P_{\mathrm{L},max}$. As can be seen, the higher the power launch level, the higher the fiber length required to reach the same solution as in the linear regime (black line). When the Kerr effect is stimulated with high power levels, the nonlinear self-coupling effect reduces the power exchange between cores. However, after several kilometers and excluding the attenuation effects, the power of the excited core is reduced due to the power transferred to the adjacent core. In such a situation, the stimulation of the Kerr effect is reduced in the excited core a and the solution of the nonlinear CPT tends to the same solution as the linear CPT of Marcuse [144, 146].

On the other hand, if we incorporate the fiber attenuation to this scenario, we should take into account that the Kerr effect will cease to be stimulated after several kilometers in the excited core a. As an example, if we assume a critical power P_{C} in silica fibers around ~ 2 dBm (see Section 2.5), a power attenuation coefficient of $\alpha = 0.2$ dB/km, and $P_{\mathrm{L}} = 5$ dBm; the IC-XT will operate in the nonlinear regime for MCF distances around ~ 15 km. More explicitly, the length of the nonlinear interaction (L_{NL}) can be calculated as $L_{\mathrm{NL}} = (P_{\mathrm{L}} - P_{\mathrm{C}})/\alpha$.

To summarize, the nonlinear CPT allows us to achieve a deeper understanding of the longitudinal evolution of the *average* value of the IC-XT in both linear and nonlinear power regimes. Especially, this feature will be exploited in the next section to infer the connection of the IC-XT mean with the power launch level.

2.5 Statistical analysis of inter-core crosstalk

In this section, we perform the statistical analysis of the IC-XT in both linear and nonlinear regimes when a single core or multiple cores are excited at the MCF input. First, we will investigate the single-core excitation and, later, we will extend the model to the multi-core excitation by performing a simple transformation of random variables.

2.5.1 Single-core excitation

Let us consider a 2-core MCF with cores a and b, where only the core b is excited at the MCF input with an optical power P_{L}. Moreover, in order to simplify the mathematical discussions, the spatial random distribution of the linear and nonlinear IC-XT is discussed for UC-MCFs with quasi-constant bending and twisting conditions ($\delta_z R_{\mathrm{B}} \ll \overline{R}_{\mathrm{B}}$ and $\delta_z f_{\mathrm{T}} \ll \overline{f}_{\mathrm{T}}$)[17] operating in the *phase-matching region*, i.e., with an average value of the bending radius satisfying that $\Delta n_{b,a}^{(\mathrm{eq})}$ becomes null at different z points along the MCF length [see Eq. (2.3.2)]. These points are referred to as the phase-matching points, as mentioned on page 37. The number of phase-matching points will be denoted as N_{L} and N_{NL} in the linear and nonlinear regime, respectively. In general, in homogeneous SM-MCFs $N_{\mathrm{L(NL)}} \neq 0$, but in the heterogeneous case, the phase-matching points can only be observed in the phase-matching region. For instance, if the core b is located at the MCF center, this corresponds to an $\overline{R}_{\mathrm{B}}$ value lower than the threshold value R_{pk} [31, 129]:

$$\overline{R}_{\mathrm{B}} < R_{\mathrm{pk}} \simeq \frac{d_{ab} n_a}{|\Delta n_{b,a}|}. \tag{2.5.1}$$

These initial conditions facilitate the derivation of the crosstalk distribution from the modified CMT. In such circumstances, since the crosstalk shows a *quasi-discrete* longitudinal random evolution (Fig. 2.5), Eq. (2.2.34) can be solved by using a discrete first-order solution (see below). And, despite the fact that we have restricted our discussion to UC-MCFs operating in the phase-matching region, interestingly, in the phase-mismatching region of these fibers, the crosstalk distribution is found to be the same [31]. Nonetheless, in CC-MCFs, the analysis of the crosstalk distribution requires to use a different formalism [147, 148], which is out of the scope of this work.

Specifically, the random variable (r.v.) of the IC-XT from core b to core a is defined as the ratio of the optical power in core a to the optical power in core b at the MCF output when only core b is excited at the MCF input:

$$X_{a,b}^{\mathrm{L(NL)}} := \frac{P_a\left(z = L\right)}{P_b\left(z = L\right)}, \tag{2.5.2}$$

with the superindex 'L' or 'NL' indicating the power regime (L: linear, NL: nonlinear). In the phase-matching region and in the weak-coupling regime, assuming $N_{\mathrm{L(NL)}}$ phase-matching points along the MCF length (denoted by the discrete variable $\mathrm{z_P}$), we can approximate Eq. (2.5.2) to:[18]

$$X_{a,b}^{\mathrm{L(NL)}} \simeq \frac{P_a\left[\mathrm{z_P} = N_{\mathrm{L(NL)}}\right]}{P_b\left[\mathrm{z_P} = N_{\mathrm{L(NL)}}\right]} \simeq \frac{\overline{P}_a\left[\mathrm{z_P} = N_{\mathrm{L(NL)}}\right]}{\overline{P}_b\left[\mathrm{z_P} = N_{\mathrm{L(NL)}}\right]}, \tag{2.5.3}$$

where the overbar denotes the average power (see Section 2.4).

[17] The linear operator δ_z was defined in Chapter 1, on page 24.

[18] Writing $P_a\left(z\right)$ and $P_a\left(\mathrm{z_P}\right)$ simultaneously is a "sloppy" yet not so rare habit in the literature, just as writing $n\left(\omega\right)$ and $n\left(\lambda\right)$, for example. Obviously, it is mathematically wrong to use the same function name, P_a, for two *different* functions. However, we relax the notation indicating the quasi-discrete nature of the second function as $P_a\left[\mathrm{z_P}\right]$. The same remark applies to the P_b, $\overline{P}_a$, $\overline{P}_b$, $\Delta\phi_{b,a}$, A_a and A_b functions in this section.

2.5.1.1 Linear regime

Here, we perform a brief review of the main results reported by Hayashi and co-workers in the linear regime [31]. The specific details of the mathematical derivations are not included in this work. The reader can find the complete discussions in the corresponding references. In particular, these results will be used later to derive the crosstalk distribution in the nonlinear regime.

Considering crosstalk values much lower than 0 dB, we can write a discrete first-order solution of the modified CMT [Eq. (2.2.34)] as a function of the phase-matching points as follows:

$$\begin{aligned} A_a\left[\mathrm{z_P}=N_\mathrm{L}\right] &\simeq A_a\left[\mathrm{z_P}=N_\mathrm{L}-1\right]-jK_{a,b}A_b\left[\mathrm{z_P}=N_\mathrm{L}-1\right]\exp\left(-j\Delta\phi_{b,a}\left[\mathrm{z_P}=N_\mathrm{L}\right]\right) \\ &\simeq A_a\left[\mathrm{z_P}=0\right]-jK_{a,b}\sum_{l=1}^{N_\mathrm{L}}A_b\left[\mathrm{z_P}=l-1\right]\exp\left(-j\Delta\phi_{b,a}\left[\mathrm{z_P}=l\right]\right), \end{aligned} \tag{2.5.4}$$

neglecting the nonlinear effects and modeling the quasi-discrete changes of the linear IC-XT with the MCC $K_{a,b}$ [133]:

$$|K_{a,b}|=\sqrt{\frac{2\pi\kappa_{a,b}\overline{R}_\mathrm{B}}{\beta_a d_{ab}\overline{f}_\mathrm{T}}}. \tag{2.5.5}$$

Since $A_a\left[0\right]=0$ and $A_b\left[l-1\right]\simeq A_b\left[N_\mathrm{L}\right]$ when omitting the optical attenuation[19] in the weak-coupling regime, the r.v. $X_{a,b}^\mathrm{L}$ can be expressed as:

$$X_{a,b}^\mathrm{L}=\left|K_{a,b}\sum_{l=1}^{N_\mathrm{L}}\exp\left(-j\Delta\phi_{b,a}\left[l\right]\right)\right|^2. \tag{2.5.6}$$

In order to infer the distribution of $X_{a,b}^\mathrm{L}$ from the above equation, we should analyze the whole of the contributions of the $\mathrm{LP}_{01,b}$ mode to the crosstalk *observed* in the core a. In real MCFs, with an underlying anisotropic nature inherited from the medium perturbations, this requires to consider two polarizations and two different real solutions per polarization in Eq. (2.5.6): the sine and cosine solutions of the exponential term. Consequently, if we assume that the coupled power from the $\mathrm{LP}_{01,b}$ mode is adequately randomized in these four solutions of the $\mathrm{LP}_{01,a}$ mode, the r.v. $X_{a,b}^\mathrm{L}$ is found to be the linear combination of four independent and identically distributed r.v.'s, that is, $X_{a,b}^\mathrm{L}=\sum_{i=1}^{4}X_i$ with:

$$X_i=\frac{1}{4}X_{a,b}^\mathrm{L}=\left|\sum_{l=1}^{N_\mathrm{L}}\frac{K_{a,b}}{2}\exp\left(-j\Delta\phi_{b,a}\left[l\right]\right)\right|^2. \tag{2.5.7}$$

Equation (2.5.7) involves a sequence of independent and identically distributed r.v.'s, each one with zero mean and variance $|K_{a,b}|^2/4$. Hence, using the Central Limit Theorem [145], we infer that the r.v. X_i is the square of a normal distribution (N) with zero mean and variance $N_\mathrm{L}|K_{a,b}|^2/4$. Therefore:

$$X_{a,b}^\mathrm{L}\sim\mathrm{N}^2\left(0,N_\mathrm{L}\frac{|K_{a,b}|^2}{4}\right)+\mathrm{N}^2\left(0,N_\mathrm{L}\frac{|K_{a,b}|^2}{4}\right)+\mathrm{N}^2\left(0,N_\mathrm{L}\frac{|K_{a,b}|^2}{4}\right)+\mathrm{N}^2\left(0,N_\mathrm{L}\frac{|K_{a,b}|^2}{4}\right). \tag{2.5.8}$$

Now, taking into account that a non-standard normal distribution $\mathrm{N}\left(0,\sigma^2\right)$ can be expressed as a function of the standard normal distribution as $\sigma\cdot\mathrm{N}\left(0,1\right)$, it is straightforward to demonstrate that $\mathrm{N}^2\left(0,\sigma^2\right)=\sigma^2\cdot\mathrm{N}^2\left(0,1\right)$ [145]. Thus, we find that $X_{a,b}^\mathrm{L}$ is a chi-squared distribution with four degrees of freedom (d.f.):

$$X_{a,b}^\mathrm{L}\sim N_\mathrm{L}\frac{|K_{a,b}|^2}{4}\left[\mathrm{N}^2\left(0,1\right)+\mathrm{N}^2\left(0,1\right)+\mathrm{N}^2\left(0,1\right)+\mathrm{N}^2\left(0,1\right)\right]\equiv N_\mathrm{L}\frac{|K_{a,b}|^2}{4}\chi_4^2. \tag{2.5.9}$$

[19] Note that the MCF has been assumed as a lossless multi-dielectric medium in this chapter. In any case, the main conclusions of this section are found to be valid when the power losses are included in the theoretical analysis.

From the last linear relation of r.v.'s, the expressions of the probability density function (p.d.f.), cumulative distribution function (c.d.f.), mean and variance of the linear IC-XT can be derived:

$$f_{X^{\mathrm{L}}_{a,b}}(x_{\mathrm{L}}) = \frac{4x_{\mathrm{L}}}{N_{\mathrm{L}}^2 |K_{a,b}|^4} \exp\left(-\frac{2x_{\mathrm{L}}}{N_{\mathrm{L}} |K_{a,b}|^2}\right) u(x_{\mathrm{L}}); \tag{2.5.10}$$

$$F_{X^{\mathrm{L}}_{a,b}}(x_{\mathrm{L}}) = \int_{-\infty}^{x_{\mathrm{L}}} f_{X^{\mathrm{L}}_{a,b}}(y)\,\mathrm{d}y = \left[1 - \left(1 + \frac{2x_{\mathrm{L}}}{N_{\mathrm{L}} |K_{a,b}|^2}\right) \exp\left(-\frac{2x_{\mathrm{L}}}{N_{\mathrm{L}} |K_{a,b}|^2}\right)\right] u(x_{\mathrm{L}}); \tag{2.5.11}$$

$$\mu_{\mathrm{L}} = E\left[X^{\mathrm{L}}_{a,b}\right] = N_{\mathrm{L}} |K_{a,b}|^2; \tag{2.5.12}$$

$$\sigma^2_{\mathrm{L}} = E\left[\left(X^{\mathrm{L}}_{a,b}\right)^2\right] - E^2\left[X^{\mathrm{L}}_{a,b}\right] = N_{\mathrm{L}}^2 \frac{|K_{a,b}|^4}{2}; \qquad \left(\sigma^2_{\mathrm{L}} = \mu^2_{\mathrm{L}}/2\right), \tag{2.5.13}$$

where u is the unit step function and E is the expectation operator.

Unfortunately, the number of phase-matching points is usually unknown and, consequently, the crosstalk distribution cannot be analytically estimated from the above expressions. This issue was solved by Hayashi and Koshiba in [129,134]. Remarkably, these authors derived a closed-form expression for the mean of the linear IC-XT as a function of the fiber parameters for different MCF cases. Here, we remark two basic examples. In a heterogeneous MCF with small bending radius satisfying that $\overline{R}_{\mathrm{B}} < R_{\mathrm{pk}}$, μ_{L} can be estimated using Eq. (26) of [129]:

$$\mu_{\mathrm{L}} \simeq \frac{2\kappa^2_{a,b} L}{k_0 \sqrt{\left(n_a d_{ab}/\overline{R}_{\mathrm{B}}\right)^2 - \Delta n^2_{b,a}}}, \tag{2.5.14}$$

and for large bending radius with $\overline{R}_{\mathrm{B}} \gg R_{\mathrm{pk}}$, μ_{L} can be estimated from Eq. (21) of [134]:

$$\mu_{\mathrm{L}} \simeq \frac{2\kappa^2_{a,b} l_c L}{1 + \left(k_0 \Delta n_{b,a} l_c\right)^2}, \tag{2.5.15}$$

with l_c the correlation length of the ACF modeling the MCF structural fluctuations (microbending, fiber twisting and manufacturing imperfections). Equations (2.5.14) and (2.5.15) were derived from the linear CPT and the ERIM by assuming the core b at the MCF center. Thus, the error of these expressions increases when using them to estimate μ_{L} between non-central cores of the MCF. Nonetheless, in such a case, this error can be neglected given that it is usually lower than the crosstalk variance, as we have experimentally verified in Section 2.6.

On the other hand, it is interesting to remark the behavior of the mean with $\overline{R}_{\mathrm{B}}$ in a heterogeneous SM-MCF. We include an illustrative example in Fig. 2.7. In the phase-matching region, μ_{L} increases with $\overline{R}_{\mathrm{B}}$. However, in the phase-mismatching region, μ_{L} is reduced when $\overline{R}_{\mathrm{B}}$ increases due to the effect of the structural fluctuations inducing an additional phase-mismatching $\Delta\beta^{(\mathrm{S})}_{b,a}$ between the core modes [134].

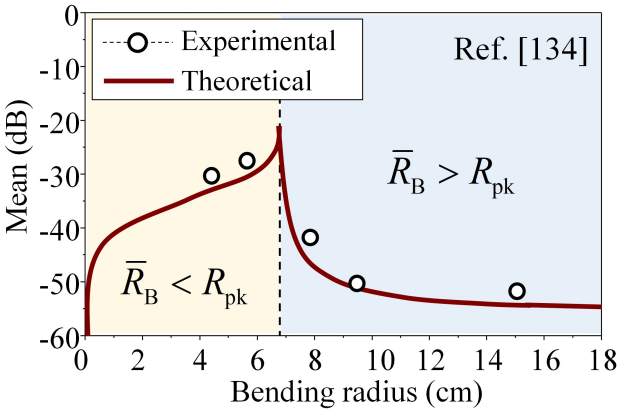

Figure 2.7. Mean of the linear IC-XT as a function of the average value of the bending radius ($\overline{R}_{\mathrm{B}}$) [134].

2.5.1.2 Nonlinear regime

Once we have reviewed the distribution of the linear IC-XT, we detail the original results of our investigations, focused on the nonlinear regime. Remarkably, the distribution of the nonlinear IC-XT can also be found following a similar approach as in the previous section. Hence, the starting point is a discrete first-order solution of the modified nonlinear CMT [Eq. (2.2.34)] restricted to UC-MCFs with N_{NL} phase-matching points along the fiber length:

$$\begin{aligned} A_a\left[\mathrm{z_P}=N_{\mathrm{NL}}\right] \simeq A_a\left[\mathrm{z_P}=N_{\mathrm{NL}}-1\right] - jK_{a,b}A_b\left[\mathrm{z_P}=N_{\mathrm{NL}}-1\right]\exp\left(-j\Delta\phi_{b,a}\left[\mathrm{z_P}=N_{\mathrm{NL}}\right]\right) \\ - jq_a^{(1)}L_{N_{\mathrm{NL}}-1}\left|A_a\left[\mathrm{z_P}=N_{\mathrm{NL}}-1\right]\right|^2 A_a\left[\mathrm{z_P}=N_{\mathrm{NL}}-1\right], \end{aligned} \tag{2.5.16}$$

where $L_{N_{\mathrm{NL}}-1}$ is the fiber length between the last two phase-matching points. The last equation is a recurrence relation which allows us to relate the input an the output of the core a ($q_a^{(1)} \equiv q_a$):

$$A_a\left[N_{\mathrm{NL}}\right] \simeq A_a\left[0\right] - j\sum_{l=1}^{N_{\mathrm{NL}}} q_a L_{l-1}\left|A_a\left[l-1\right]\right|^2 A_a\left[l-1\right] + K_{a,b}A_b\left[l-1\right]\exp\left(-j\Delta\phi_{b,a}\left[l\right]\right). \tag{2.5.17}$$

In the same way as in the linear regime, $A_a\left[0\right]=0$ and $A_b\left[l-1\right] \simeq A_b\left[N_{\mathrm{NL}}\right]$. Furthermore, in the nonlinear regime, we can also assume that $A_a\left[l\right]$ is approximately similar in each phase-matching point. In this manner, we can approximate:

$$\sum_{l=1}^{N_{\mathrm{NL}}} L_{l-1}\left|A_a\left[l-1\right]\right|^2 A_a\left[l-1\right] \simeq L\left|A_a\left[N_{\mathrm{NL}}\right]\right|^2 A_a\left[N_{\mathrm{NL}}\right], \tag{2.5.18}$$

and Eq. (2.5.17) becomes:

$$A_a\left[N_{\mathrm{NL}}\right] \simeq -jq_aL\left|A_a\left[N_{\mathrm{NL}}\right]\right|^2 A_a\left[N_{\mathrm{NL}}\right] - jK_{a,b}A_b\left[N_{\mathrm{NL}}\right]\sum_{l=1}^{N_{\mathrm{NL}}}\exp\left(-j\Delta\phi_{b,a}\left[l\right]\right). \tag{2.5.19}$$

Therefore, the ratio of the complex envelopes at the MCF output is found to be:

$$\frac{A_a\left[N_{\mathrm{NL}}\right]}{A_b\left[N_{\mathrm{NL}}\right]} \simeq \frac{-j}{1+jq_aL\left|A_a\left[N_{\mathrm{NL}}\right]\right|^2}K_{a,b}\sum_{l=1}^{N_{\mathrm{NL}}}\exp\left(-j\Delta\phi_{b,a}\left[l\right]\right), \tag{2.5.20}$$

and consequently, the r.v. modeling the nonlinear IC-XT from core b to core a [see Eq. (2.5.3)] can be expressed as a function of the linear IC-XT [Eq. (2.5.6)] as follows:

$$X_{a,b}^{\mathrm{NL}} \simeq \frac{1}{1+q_a^2L^2P_{\mathrm{L}}^2\left(X_{a,b}^{\mathrm{NL}}\right)^2}X_{a,b}^{\mathrm{L}} \;\Rightarrow\; X_{a,b}^{\mathrm{L}} \simeq q_a^2L^2P_{\mathrm{L}}^2\left(X_{a,b}^{\mathrm{NL}}\right)^3 + X_{a,b}^{\mathrm{NL}}, \tag{2.5.21}$$

where we have approximated $\left|A_a\left[N_{\mathrm{NL}}\right]\right|^2 \simeq P_{\mathrm{L}}X_{a,b}^{\mathrm{NL}}$.

Surprisingly, we have found a cubic relation between the r.v.'s $X_{a,b}^{\mathrm{L}}$ and $X_{a,b}^{\mathrm{NL}}$, denoted as $X_{a,b}^{\mathrm{L}} = h\left(X_{a,b}^{\mathrm{NL}}\right)$. Specifically, h is a bijective and positive-real function given that $X_{a,b}^{\mathrm{NL}} \geq 0$. This point allows us to use the one-to-one transformation of the corresponding p.d.f.'s [145]:

$$f_{X_{a,b}^{\mathrm{NL}}}\left(x_{\mathrm{NL}}\right) = f_{X_{a,b}^{\mathrm{L}}}\left(x_{\mathrm{L}}=h\left(x_{\mathrm{NL}}\right)\right)\left|\frac{\mathrm{d}h\left(x_{\mathrm{NL}}\right)}{\mathrm{d}x_{\mathrm{NL}}}\right|, \tag{2.5.22}$$

with $f_{X_{a,b}^{\mathrm{L}}}$ given by Eq. (2.5.10) with $N_{\mathrm{L}} \to N_{\mathrm{NL}}$ because of the r.v. $X_{a,b}^{\mathrm{L}}$ is now calculated with N_{NL} phase-matching points in Eq. (2.5.21). Hence, the p.d.f. of the nonlinear IC-XT is:

$$f_{X_{a,b}^{\mathrm{NL}}}\left(x_{\mathrm{NL}}\right) = \frac{\left(12L^4q_a^4P_{\mathrm{L}}^4x_{\mathrm{NL}}^5 + 16L^2q_a^2P_{\mathrm{L}}^2x_{\mathrm{NL}}^3 + 4x_{\mathrm{NL}}\right)}{N_{\mathrm{NL}}^2\left|K_{a,b}\right|^4}\exp\left(-\frac{2L^2q_a^2P_{\mathrm{L}}^2x_{\mathrm{NL}}^3 + 2x_{\mathrm{NL}}}{N_{\mathrm{NL}}\left|K_{a,b}\right|^2}\right)u\left(x_{\mathrm{NL}}\right). \tag{2.5.23}$$

Bearing in mind the low nonlinear nature of silica MCFs ($q_a \sim 10^{-13}\,\mathrm{m/V^2}$), Eq. (2.5.23) can be reduced to:

$$f_{X_{a,b}^{\mathrm{NL}}}(x_{\mathrm{NL}}) \simeq \frac{4x_{\mathrm{NL}}}{N_{\mathrm{NL}}^2 |K_{a,b}|^4} \exp\left(-\frac{2x_{\mathrm{NL}}}{N_{\mathrm{NL}} |K_{a,b}|^2}\right) u(x_{\mathrm{NL}}). \tag{2.5.24}$$

In general, the number of phase-matching points will be modified with the power launch level (see below). In this vein, the nonlinear effects can be modeled by the parameter N_{NL} in the p.d.f. Specifically, Eq. (2.5.24) indicates that the nonlinear IC-XT is also a chi-squared distribution with 4 d.f.'s. Nonetheless, to complete the statistical analysis we should calculate the closed-form expressions of the c.d.f., mean and variance of the nonlinear IC-XT.

It is straightforward to derive the c.d.f. from Eq. (2.5.11) taking into account that h and h^{-1} are monotonic increasing functions with $x_{\mathrm{L(NL)}} > 0$:

$$\begin{aligned} F_{X_{a,b}^{\mathrm{NL}}}(x_{\mathrm{NL}}) &= P\left(X_{a,b}^{\mathrm{NL}} \leq x_{\mathrm{NL}}\right) = P\left(h^{-1}\left(X_{a,b}^{\mathrm{L}}\right) \leq x_{\mathrm{NL}}\right) = P\left(X_{a,b}^{\mathrm{L}} \leq h(x_{\mathrm{NL}})\right) = F_{X_{a,b}^{\mathrm{L}}}(h(x_{\mathrm{NL}})) \\ &= \left[1 - \left(1 + \frac{2L^2 q_a^2 P_{\mathrm{L}}^2 x_{\mathrm{NL}}^3 + 2x_{\mathrm{NL}}}{N_{\mathrm{NL}} |K_{a,b}|^2}\right) \exp\left(-\frac{2L^2 q_a^2 P_{\mathrm{L}}^2 x_{\mathrm{NL}}^3 + 2x_{\mathrm{NL}}}{N_{\mathrm{NL}} |K_{a,b}|^2}\right)\right] u(x_{\mathrm{NL}}) \\ &\simeq \left[1 - \left(1 + \frac{2x_{\mathrm{NL}}}{N_{\mathrm{NL}} |K_{a,b}|^2}\right) \exp\left(-\frac{2x_{\mathrm{NL}}}{N_{\mathrm{NL}} |K_{a,b}|^2}\right)\right] u(x_{\mathrm{NL}}), \end{aligned} \tag{2.5.25}$$

and since $X_{a,b}^{\mathrm{NL}} \sim \left(N_{\mathrm{NL}} |K_{a,b}|^2 / 4\right) \chi_4^2$, the mean and variance can be approximated to:

$$\mu_{\mathrm{NL}} \simeq N_{\mathrm{NL}} |K_{a,b}|^2; \tag{2.5.26}$$

$$\sigma_{\mathrm{NL}}^2 \simeq \frac{\mu_{\mathrm{NL}}^2}{2} = N_{\mathrm{NL}}^2 |K_{a,b}|^4 / 2. \tag{2.5.27}$$

As in the linear regime, it can be noted that the distribution of the nonlinear crosstalk cannot be analytically estimated from the above expressions given that N_{NL} is unknown. Nevertheless, we can solve this issue by inferring a closed-form expression of μ_{NL} as a function of the fiber parameters. At this point, we should recover the nonlinear CPT derived in Section 2.4. In this way, we can estimate the average value of the optical power of core a from Eq. (2.4.15) as follows:

$$\overline{P}_a(z = L) = \overline{P}_a(z = 0) + \int_0^L h_{a,b}^{(\mathrm{eq})} \left[\overline{P}_b(z) - \overline{P}_a(z)\right] \mathrm{d}z. \tag{2.5.28}$$

Thus, μ_{NL} can be calculated in the weak-coupling regime as $[\overline{P}_a(0) = 0]$:

$$\begin{aligned} \mu_{\mathrm{NL}} &= E\left[X_{a,b}^{\mathrm{NL}}\right] = E\left[\frac{P_a(z = L)}{P_b(z = L)}\right] \simeq E\left[\frac{\overline{P}_a(z = L)}{\overline{P}_b(z = L)}\right] \\ &= E\left[\frac{1}{\overline{P}_b(L)} \int_0^L h_{a,b}^{(\mathrm{eq})} \left[\overline{P}_b(z) - \overline{P}_a(z)\right] \mathrm{d}z\right] \\ &= E\left[\frac{1}{\overline{P}_b(L)} \int_0^L h_{a,b} \left[\overline{P}_b(z) - \overline{P}_a(z)\right] \mathrm{d}z\right] - E\left[\frac{1}{\overline{P}_b(L)} \int_0^L q_a^2 S_a(0) \left[\overline{P}_b(z) - \overline{P}_a(z)\right] \mathrm{d}z\right]. \end{aligned} \tag{2.5.29}$$

The former term of the RHS is the mean of the linear crosstalk (μ_{L}) and the latter term accounts for the nonlinear self-coupling effect. Concretely, in the nonlinear and weak-coupling regimes, we can perform the approximation $\overline{P}_b(z) - \overline{P}_a(z) \simeq \overline{P}_b(z) \simeq P_{\mathrm{L}}$. Hence:

$$\begin{aligned} \mu_{\mathrm{NL}} &\simeq \mu_{\mathrm{L}} - L q_a^2 P_{\mathrm{L}} E\left[\frac{S_a(0)}{\overline{P}_b(L)}\right] = \mu_{\mathrm{L}} - L q_a^2 P_{\mathrm{L}} E\left[\frac{1}{\overline{P}_b(L)} \int_{-\infty}^{\infty} R_a(\tau) \mathrm{d}\tau\right] \\ &= \mu_{\mathrm{L}} - L q_a^2 P_{\mathrm{L}} E\left[\frac{1}{\overline{P}_b(L)} \int_{-\infty}^{\infty} \langle P_a(z) P_a(z + \tau)\rangle \mathrm{d}\tau\right]. \end{aligned} \tag{2.5.30}$$

Since P_a is an ergodic process (as can be directly deduced by using the modified CMT keeping in mind that $f_{b,a}$ is ergodic, indicated on page 39), the spatial averages are equal to the statistical averages. Accordingly, Eq. (2.5.30) can be rewritten as:[20]

$$\begin{aligned}\mu_{\mathrm{NL}} &\simeq \mu_{\mathrm{L}} - Lq_a^2 P_{\mathrm{L}} E\left[\frac{1}{\overline{P}_b(L)}\int_{-\infty}^{\infty} E\left[P_a(z)\,P_a(z+\tau)\right]\mathrm{d}\tau\right] \\ &= \mu_{\mathrm{L}} - Lq_a^2 P_{\mathrm{L}} E\left[\frac{P_a(z)}{\overline{P}_b(L)}\int_{-\infty}^{\infty} P_a(z+\tau)\,\mathrm{d}\tau\right]. \end{aligned} \tag{2.5.31}$$

As demonstrated numerically in Section 2.3, the fluctuation of the crosstalk decreases in the nonlinear regime [see Fig. 2.5(d)]. In this scenario, the random fluctuations of the coupled power are minimized and, therefore, we can approximate $P_a(z)/\overline{P}_b(L) \simeq \mu_{\mathrm{NL}}$. As a result, Eq. (2.5.31) becomes:

$$\begin{aligned}\mu_{\mathrm{NL}} &\simeq \mu_{\mathrm{L}} - Lq_a^2 P_{\mathrm{L}}\mu_{\mathrm{NL}} E\left[\int_{-\infty}^{\infty} P_a(z+\tau)\,\mathrm{d}\tau\right] = \mu_{\mathrm{L}} - Lq_a^2 P_{\mathrm{L}}\mu_{\mathrm{NL}} E\left[\int_{-\infty}^{\infty} P_a(x)\,\mathrm{d}x\right] \\ &= \mu_{\mathrm{L}} - Lq_a^2 P_{\mathrm{L}}\mu_{\mathrm{NL}}\int_{-\infty}^{\infty}\overline{P}_a(x)\,\mathrm{d}x \simeq \mu_{\mathrm{L}} - Lq_a^2 P_{\mathrm{L}}\mu_{\mathrm{NL}}\widetilde{\mathcal{P}}_a(\upsilon=0), \end{aligned} \tag{2.5.32}$$

where we have performed the dummy variable transformation $x \equiv z+\tau$ and $\widetilde{\mathcal{P}}_a$ is the spatial Fourier transform of $\overline{P}_a$.

In general, $\widetilde{\mathcal{P}}_a(0)$ depends on different physical parameters such as the power launch level or the fiber length. Nonetheless, as verified experimentally in Section 2.6, $q_a^2\widetilde{\mathcal{P}}_a(0)$ can be approximated by a positive-real constant ρ when assuming a slowly-varying evolution of $\widetilde{\mathcal{P}}_a(0)$ with the power launch level. From this assumption, we surprisingly find a linear relation between the linear and nonlinear crosstalk mean: $\mu_{\mathrm{L}} \simeq (1+\rho L P_{\mathrm{L}})\,\mu_{\mathrm{NL}}$. Moreover, since $\sigma^2_{\mathrm{L(NL)}} = \mu^2_{\mathrm{L(NL)}}/2$ and $N_{\mathrm{L(NL)}} = \mu_{\mathrm{L(NL)}}/|K_{a,b}|^2$, we can relate the mean, variance and the number of phase-matching points of both power regimes using the following relations:

$$\mu_{\mathrm{NL}} \simeq \frac{\mu_{\mathrm{L}}}{1+\rho L P_{\mathrm{L}}}; \quad \sigma^2_{\mathrm{NL}} \simeq \frac{\sigma^2_{\mathrm{L}}}{(1+\rho L P_{\mathrm{L}})^2}; \quad N_{\mathrm{NL}} \simeq \frac{N_{\mathrm{L}}}{1+\rho L P_{\mathrm{L}}}. \tag{2.5.33}$$

It is worth mentioning that Eqs. (2.5.33) allow us to estimate the statistical parameters of the crosstalk as a function of the fiber bending and twisting parameters when using the correct expression of μ_{L} from Refs. [129, 134]. Remarkably, σ^2_{NL} and N_{NL} can also be estimated from μ_{L} as:

$$\sigma^2_{\mathrm{NL}} \simeq \frac{\mu^2_{\mathrm{L}}}{2(1+\rho L P_{\mathrm{L}})^2}; \quad N_{\mathrm{NL}} \simeq \frac{\mu_{\mathrm{L}}}{|K_{a,b}|^2(1+\rho L P_{\mathrm{L}})}. \tag{2.5.34}$$

On the other hand, it is noticeable that Eqs. (2.5.33) should be employed when $P_{\mathrm{L}} \geq P_{\mathrm{C}}$. In real MCFs, the critical power cannot be estimated by using a similar mathematical discussion as in the NLDC of Jensen [138] due to the MCF random perturbations. Nevertheless, we can estimate the threshold power between the linear and nonlinear regimes considering that the fiber nonlinearities are stimulated when applying an electric field comparable to the characteristic atomic electric field strength ($\mathcal{E}_{\mathrm{A}}$). In silica media, $\mathcal{E}_{\mathrm{A}}$ is of the order of $\sim 10^5$ V/m [149]. In such circumstances and assuming an effective area of the LP_{01} mode of $A_{\mathrm{eff}} \simeq 80\,\mu\mathrm{m}^2$ with $\lambda_0 = 1550$ nm, the critical power is found to be around 2 dBm [150]:

$$P_{\mathrm{C}} = \frac{1}{2}\varepsilon_0 c_0 A_{\mathrm{eff}}\mathcal{E}^2_{\mathrm{A}} \simeq 1.58\ \mathrm{mW} \equiv 2\ \mathrm{dBm}. \tag{2.5.35}$$

[20] The identity of the second line in Eq. (2.5.31) is performed by using the linear property of the expectation operator.

2.5.2 Multi-core excitation

The previous subsection unifies the statistical analysis of the IC-XT in the linear and nonlinear regimes but assuming that a single core is excited at $z = 0$. Outstandingly, if we now assume that multiple cores are illuminated at the MCF input, the previous analysis can also be used to study the crosstalk distribution in both power regimes. In particular, this is straightforward to demonstrate when the illuminated cores are *homogeneous*.

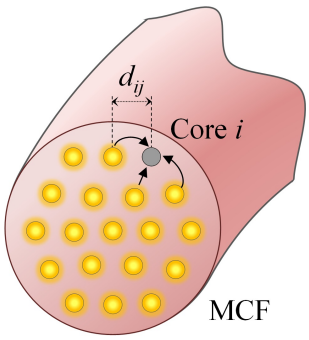

Figure 2.8. N-core MCF operating in multi-core excitation. The crosstalk in the unexcited core i is mainly increased by the coupled power from adjacent cores [143].

Let us assume an N-core UC-MCF with $N-1$ cores excited at $z = 0$. As depicted in Fig. 2.8, the mode-coupling between the unexcited core i and the non-adjacent cores can be neglected. In such a case, if we assume that the crosstalk is only increased by M adjacent cores ($M < N$), the crosstalk in core i can be modeled by the r.v. Y defined as:[21]

$$Y := \frac{P_i\left(z=L\right)}{\sum_{j=1}^{M} P_j\left(z=L\right)}. \tag{2.5.36}$$

The total power P_i can be expressed as a function of the coupled power from each adjacent core j to core i ($P_{i,j}$) at each z point, i.e., $P_i = \sum_{j=1}^{M} P_{i,j}$. Operating in the weak-coupling regime, if we consider adjacent homogeneous cores with the same distance to core i and $P_1\left(z=0\right) \simeq P_2\left(z=0\right) \simeq \ldots \simeq P_M\left(z=0\right)$, we can assume that the terms $P_{i,j}\left(z=L\right)$ are of the same order of magnitude, i.e., $P_{i,1}\left(z=L\right) \sim P_{i,2}\left(z=L\right) \sim \ldots \sim P_{i,M}\left(z=L\right)$. Hence, $P_i\left(z=L\right)$ can be roughly approximated as $P_i\left(z=L\right) \simeq M \cdot P_{i,j}\left(z=L\right)$ and, consequently, the r.v. Y can be expressed as:

$$\frac{1}{Y} = \frac{\sum_{j=1}^{M} P_j\left(z=L\right)}{P_i\left(z=L\right)} = \sum_{j=1}^{M} \frac{P_j\left(z=L\right)}{P_i\left(z=L\right)} \simeq \sum_{j=1}^{M} \frac{P_j\left(z=L\right)}{M \cdot P_{i,j}\left(z=L\right)} = \frac{1}{M}\sum_{j=1}^{M} \frac{1}{X_{i,j}}, \tag{2.5.37}$$

where $X_{i,j}$ are r.v.'s accounting for the one-to-one IC-XT from core $j \in \{1,\ldots,M\}$ to core i. Once we have expressed the global IC-XT as a function of the one-to-one IC-XT, we can find the p.d.f. of Y by performing a series of mathematical transformations between different auxiliary r.v.'s.

Firstly, we define the r.v. $Z_{i,j} := 1/X_{i,j}$. The corresponding p.d.f. can be written as:

$$f_{Z_{i,j}}\left(z_{i,j}\right) = f_{X_{i,j}}\left(x_{i,j} = \frac{1}{z_{i,j}}\right)\left|\frac{\mathrm{d}}{\mathrm{d}z_{i,j}}\left(\frac{1}{z_{i,j}}\right)\right| = \frac{1}{z_{i,j}^2} f_{X_{i,j}}\left(\frac{1}{z_{i,j}}\right), \tag{2.5.38}$$

where $f_{X_{i,j}}\left(x_{i,j}\right)$ is given by Eq. (2.5.10) in the linear regime and Eq. (2.5.23) in the nonlinear regime. Secondly, we define a new r.v. $W := \sum_{j=1}^{M} Z_{i,j}$, with a p.d.f. of the form:[22]

[21] We omit the superindex 'L' and 'NL' in the r.v.'s of this section. The theoretical discussion is the same in both power regimes.

[22] In weakly-coupling conditions, the r.v.'s $\{X_{i,j}\}_{j=1}^{M}$ can be regarded as *independent* r.v.'s if we neglect the fluctuation of the terms $\{P_j\}_{j=1}^{M}$ induced by mode-coupling among the illuminated cores. In such circumstances, $\{Z_{i,j}\}_{j=1}^{M}$ are also independent r.v.'s. This can be directly verified by demonstrating that the joint p.d.f. of $\{Z_{i,j}\}_{j=1}^{M}$ can be written as a function of the product of the marginal p.d.f.'s by using Eq. (4.31) of [145].

$$f_W(w) = f_{Z_{i,1}}(w) * \ldots * f_{Z_{i,M}}(w) = \left[\frac{1}{w^2} f_{X_{i,1}}\left(\frac{1}{w}\right)\right] * \ldots * \left[\frac{1}{w^2} f_{X_{i,M}}\left(\frac{1}{w}\right)\right], \tag{2.5.39}$$

where $*$ is the convolution operation. Thirdly, we introduce a new auxiliary r.v. $U := 1/W$, with p.d.f.:

$$f_U(u) = f_W\left(w = \frac{1}{u}\right)\left|\frac{\mathrm{d}}{\mathrm{d}u}\left(\frac{1}{u}\right)\right| = \frac{1}{u^2}\left\{\left[u^2 f_{X_{i,1}}(u)\right] * \ldots * \left[u^2 f_{X_{i,M}}(u)\right]\right\}. \tag{2.5.40}$$

Finally, the p.d.f. of the r.v. $Y = M \cdot U$ is found from the above equation:

$$f_Y(y) = f_U\left(u = \frac{y}{M}\right)\left|\frac{\mathrm{d}}{\mathrm{d}y}\left(\frac{y}{M}\right)\right| = \frac{1}{M^{2M-1}y^2}\left\{\left[y^2 f_{X_{i,1}}\left(\frac{y}{M}\right)\right] * \ldots * \left[y^2 f_{X_{i,M}}\left(\frac{y}{M}\right)\right]\right\}. \tag{2.5.41}$$

As inferred from Eq. (2.5.41), in uncoupled-core homogeneous MCFs operating in multi-core excitation, the crosstalk distribution (f_Y) can be estimated from the crosstalk distribution associated to the single-core excitation ($f_{X_{i,j}}$). As we will verify experimentally in the next section, f_Y can also be identified as a chi-squared distribution with a number of degrees of freedom which may be higher than 4 due to the $M-1$ convolution operations. However, in some cases, the crosstalk distribution in multi-core excitation can also be approximated, with low error, by a chi-squared distribution with only 4 degrees of freedom, as recently reported in [430].

In addition, the crosstalk variance may also be increased in multi-core excitation as a result of the convolution operation (see below Fig. 2.11). Alternatively, we can also explain the increment of the crosstalk variance by means of a physical interpretation of the multi-core excitation. Specifically, we can observe a higher crosstalk variance than in the single-core excitation scenario because of the higher number of phase-matching points induced in core i by the simultaneous excitation of adjacent cores.

On the other hand, a further theoretical analysis is required to estimate the crosstalk distribution when operating in multi-core excitation in heterogeneous MCFs or in homogeneous MCFs with cores illuminated by different optical power levels. In such circumstances, the assumption $P_{i,j}(z=L) \sim P_{i,k}(z=L)$ [with $j \neq k$ and $(j,k) \in \{1,\ldots M\}^2$] performed in previous page does not hold. In such scenarios, the work reported in [430] by T. M. F. Alves could be of valuable interest to estimate the crosstalk distribution.

2.6 Experimental measurements

Laboratory set-up. In order to validate the theoretical analysis reported in previous sections, experimental measurements are performed using a commercial homogeneous MCF [Fibercore SM-4C1500(8.0/125)]. In particular, we analyze the crosstalk statistics as a function of the optical power launch level by considering both single-core and multi-core excitations. The experimental set-up is shown in Fig. 2.9 for both scenarios. The laser, optical amplifier, MCF and optical power meter are the same as in Fig. 2.4. The statistical analysis of the crosstalk in single-core excitation is evaluated from core 3 to core 1 with two different bending radius configurations of 67 and 100 cm. The multi-core excitation is evaluated from cores 2, 3 and 4 to core 1 with a bending radius of 100 cm. The twist rate is selected around 4 turns/m. In all the analyzed cases, the bending and twisting conditions are averaged quantities.

Measurement method. In single-core excitation, the optical power launched into the core 3 (P_{L}) was increased from -3 dBm to 18 dBm. The EDFA gain was maximized to minimize the noise factor, which allows us to reduce the crosstalk averaging due to the ASE noise [142]. The VOA was employed to modify the value of P_{L} taking into account the 2.2 dB of insertion loss of the 3D fan-in device. Accordingly, the value of the optical power at the VOA output was varying

from −0.8 dBm to 20.2 dBm. The IC-XT distribution was estimated for each P_{L} value by using the wavelength sweeping method [133] ranging the optical carrier from 1550 to 1580 nm with a step of 10 pm between consecutive samples. Specifically, the wavelength sweeping method modifies the value of the optical carrier (λ_0) to change the random process $\beta^{(\mathrm{eq})}(z)$ along the MCF length in each core mode. Remarkably, it should be noted that each iteration of the wavelength sweeping method restarts the random process $\beta^{(\mathrm{eq})}(z)$ in each core mode, in complete analogy with an iteration of a Monte Carlo simulation.

On the other hand, the crosstalk distribution in multi-core excitation was experimentally evaluated by injecting 0 dBm of optical power in cores 2, 3 and 4 simultaneously. Three different 50/50 optical splitters and VOAs were employed to balance the optical power injected into each core. We verified that the splitting ratio of the optical splitters remained unchanged when sweeping the laser wavelength.

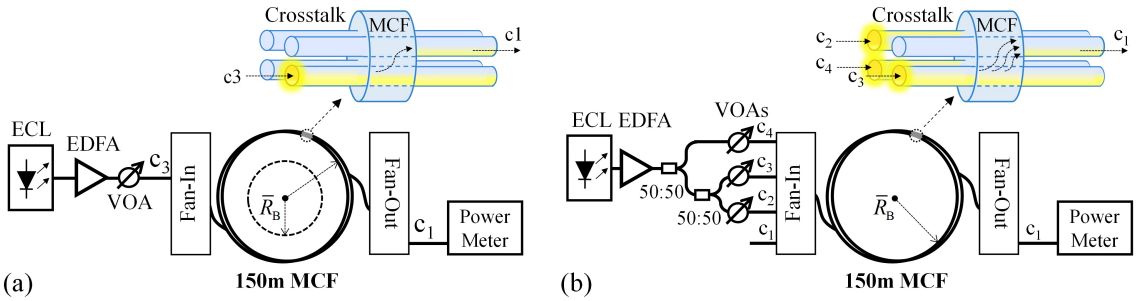

Figure 2.9. Experimental set-up employed to analyze the crosstalk statistics in: (a) single-core excitation, (b) multi-core excitation [143].

Results. Figure 2.10 shows the measured results of the crosstalk statistics when operating in single-core excitation. Figures 2.10 (a) and (b) depict the evolution of the c.d.f. and p.d.f. of the crosstalk considering three different power launch levels $P_{\mathrm{L}} \in \{0, 9, 15\}$ dBm for the bending radius configuration of 100 cm. As can be seen, the higher the power launch level, the higher the similitude of the c.d.f. with the unit step function and the p.d.f. with the Dirac delta function. Furthermore, we can note that the measured p.d.f.'s and c.d.f.'s satisfy the closed-form expressions given by Eqs. (2.5.23) and (2.5.25), respectively. The analytic estimation of these functions was performed by calculating the MCCs $\kappa_{1,3}$ and $K_{1,3}$ from Eqs. (2.2.8) and (2.5.5) using the fiber parameters: $n_1 = n_3 = 1.452$, $n_{\mathrm{cl}} = 1.444$, $R_0 = 4$ μm, $\lambda_0 = 1550$ nm and $d_{13} = 35.2$ μm. In particular, we find $\kappa_{1,3} = 0.0072$ m^{-1}, $K_{1,3} = 5.13 \cdot 10^{-4}$ with $\overline{R}_{\mathrm{B}} = 67$ cm and $K_{1,3} = 6.27 \cdot 10^{-4}$ with $\overline{R}_{\mathrm{B}} = 100$ cm. The number of phase-matching points in the linear and nonlinear regime (N_{L} and N_{NL}) can be estimated by combining Eqs. (2.5.12), (2.5.14) and (2.5.34) with $\rho = 1/2$.

Figures 2.10 (c), (d) and (e) depict the measured IC-XT mean, variance and the number of phase-matching points as a function of the optical power launched into core 3. In the linear regime, the crosstalk statistical parameters are found to be constant with P_{L}. However, in the nonlinear regime, the Kerr effect mismatches the phase constant of the core modes as P_{L} increases and, therefore, the homogeneous MCF becomes heterogeneous. As a result, the mean, variance and the number of phase-matching points are found to be monotonic decreasing functions with P_{L}. Accordingly, $X^{\mathrm{NL}}_{1,3}(z; P_{\mathrm{L}})$ may also present temporal fluctuations if the power launch conditions are temporally modified, which occurs, for instance, when propagating optical pulses through the MCF.

The statistical parameters of the crosstalk can be estimated in both linear and nonlinear power regimes by using two different strategies: (*i*) performing a Monte Carlo simulation of the modified CMT and, (*ii*) using the closed-form expressions derived in the previous section. These two strategies were validated in both power regimes with the experimental results.

Firstly, a Monte Carlo simulation was performed using Eq. (2.2.34) over 500 iterations for each power launch level considering longitudinal Gaussian random fluctuations in the bending radius and twist rate around $\sim 1\,\text{cm}$ and $\sim 0.2\,\text{turns/m}$, respectively. The random fluctuations of these fiber parameters induce stochastic variations in the equivalent refractive index of each core of the order of $\sim 10^{-6}$. The power launch level was increased from $-3\,\text{dBm}$ to $18\,\text{dBm}$. It can be noted from Figs. 2.10(c)-(e) that the Monte Carlo simulation fits correctly with the experimental measurements for each bending radius configuration. These results validate the modified CMT of Section 2.2.4.

Secondly, we estimate analytically the crosstalk mean, variance and the number of phase-matching points from Eqs. (2.5.12), (2.5.13), (2.5.14) and (2.5.33) with $\rho = 1/2$. We can note that the theoretical estimations of the crosstalk statistical parameters are in good agreement with the experimental measurements in both linear and nonlinear regimes. Along this line, it should be remarked that the critical power P_C is found to be constant around 2 dBm when varying the average value of the bending radius, as predicted by Eq. (2.5.35).

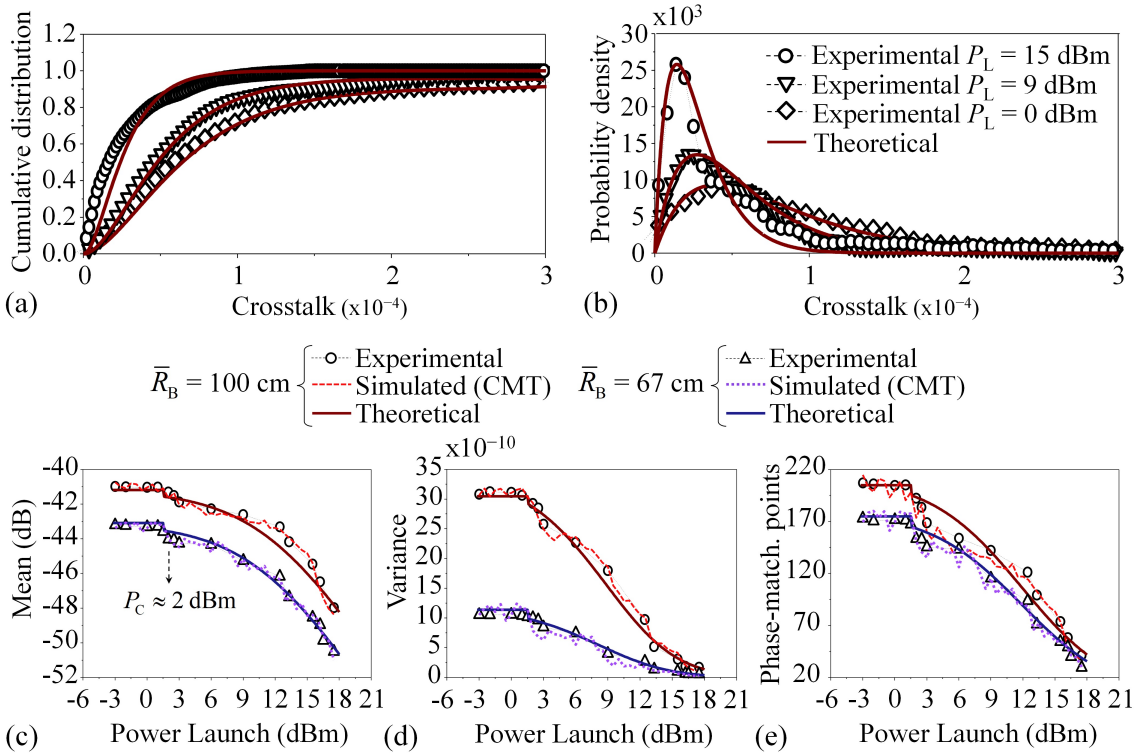

Figure 2.10. Experimental results of the crosstalk statistics in single-core excitation from core 3 to core 1. (a) cumulative distribution function, (b) probability density function, (c) mean, (d) variance and (e) number of phase-matching points [143].

In multi-core excitation, the crosstalk distribution should be analytically estimated from Eq. (2.5.41) by considering only the excited adjacent cores. Hence, if we illuminate the cores 2, 3 and 4 at the MCF input, the crosstalk in core 1 should be calculated by excluding the mode-coupling from core 4. It can be noted from Fig. 2.11 that the measured p.d.f. of the crosstalk fits correctly to Eq. (2.5.41) when using Eq. (2.5.10) to estimate the individual distributions $f_{X_{1,2}}$ and $f_{X_{1,3}}$ with $N_L = 136$ and 206, respectively. The individual p.d.f.'s were estimated with a different number of phase-matching points given that the mean of the r.v.'s $X_{1,2}$ and $X_{1,3}$ are found to be different. In line with our theoretical discussions, the p.d.f. of the crosstalk in multi-core excitation is identified as a chi-squared distribution χ^2_s with $s > 4$ (degrees of freedom) due to the increment of the crosstalk variance induced by the convolution operation. A chi-squared

distribution with 4 d.f. is inset in Fig. 2.11 for comparison. The crosstalk variance in core 1 is increased from $3.1 \cdot 10^{-9}$ to $5.7 \cdot 10^{-9}$ when cores 2, 3 and 4 are simultaneously excited at the MCF input.

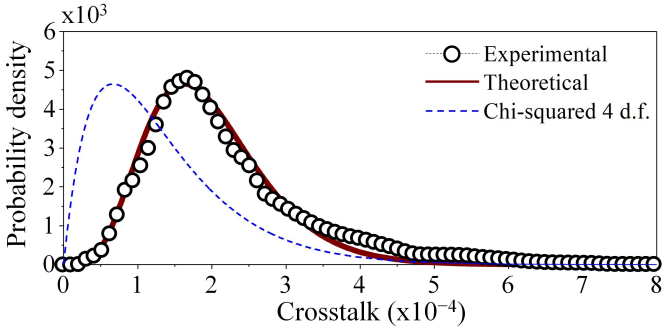

Figure 2.11. Probability density function of the IC-XT when operating in three-core excitation [143].

2.7 Conclusions

In this chapter, we have reported the theoretical unification of the linear and nonlinear IC-XT in SM-MCFs perturbed by longitudinal random fluctuations (macrobending, microbending, fiber twisting and additional manufacturing imperfections) by using perturbation methods. In order to estimate the crosstalk when an MCF is excited with low and high optical power levels, the coupled-mode and coupled-power theories were extended to the nonlinear regime. Remarkably, the nonlinear coupled-mode theory allows us to estimate numerically the random behavior of the crosstalk in MCFs with coupled and uncoupled cores. Along this line, we found that the linear self-coupling and nonlinear cross-coupling effects can be neglected when the core-to-core distance is higher than three times the core radius. On the other hand, the nonlinear coupled-power theory allows us to reduce the computational time of the coupled-mode theory describing the crosstalk behavior as a function of the average value of the coupled power, a fundamental feature that is subsequently used to estimate analytically the crosstalk mean.

Using both coupled-mode and coupled-power theories, we unified the statistical analysis of the IC-XT in both power regimes. The closed-form expressions of the cumulative distribution function, probability density function, mean and variance of the crosstalk were derived and discussed by considering two different scenarios: the single-core and multi-core excitation. Specifically, the spatial distribution of the IC-XT is identified as a chi-squared distribution with 4 degrees of freedom in single-core excitation. In multi-core excitation, the degrees of freedom are increased as a direct consequence of the accumulative crosstalk from adjacent cores, modeled by means of a convolution operation of the individual crosstalk distributions.

The theoretical analysis was experimentally validated using a commercial homogeneous MCF [Fibercore SM-4C1500(8.0/125)]. As inferred from our theoretical discussions, the experimental results confirm that the nonlinear self-coupling effect mismatches the propagation constants of the core modes reducing the number of phase-matching points along the MCF length. As a result, the mode-coupling is reduced and the mean and variance of the chi-squared distribution decreases as the power launch level is increased. In such a scenario, the threshold power between the linear and nonlinear regimes was experimentally measured around $\sim 2\,$dBm of power launch for silica MCFs.

Appendix A2: Nonlinear wave equation

Combining Faraday's and Ampère's laws [Eqs. (1.5.6) and (1.5.7)] applying the curl operator in the former, we obtain the following nonlinear wave equation for the real representation of the electric field strength:

$$\triangle \boldsymbol{\mathcal{E}}\left(\boldsymbol{r},t\right)-\frac{1}{c_0^2}\partial_t^2\boldsymbol{\mathcal{E}}\left(\boldsymbol{r},t\right)=\mu_0\partial_t^2\boldsymbol{\mathcal{P}}^{(1)}\left(\boldsymbol{r},t\right)+\mu_0\partial_t^2\boldsymbol{\mathcal{P}}^{(3)}\left(\boldsymbol{r},t\right), \tag{A2.1}$$

where $\boldsymbol{\mathcal{P}}^{(1)}$ and $\boldsymbol{\mathcal{P}}^{(3)}$ are the linear and nonlinear polarizations of the MCF, respectively. Note that we have neglected the term $\nabla(\nabla\cdot(\boldsymbol{\mathcal{P}}^{(1)}+\boldsymbol{\mathcal{P}}^{(3)}))$ in the previous equation considering slowly-varying refractive index profiles[23] and isotropic MCFs [$\nabla(\nabla\cdot\boldsymbol{\mathcal{P}}^{(1)})\simeq\mathbf{0}$] exhibiting a low nonlinear nature [$\nabla(\nabla\cdot\boldsymbol{\mathcal{P}}^{(3)})\simeq\mathbf{0}$], in line with our assumptions in Section 2.2.1. The linear and nonlinear polarizations can be written as a function of their complex amplitudes as:

$$\boldsymbol{\mathcal{P}}^{(1)}\left(\boldsymbol{r},t\right)=\mathrm{Re}\left\{P_{\omega_0}^{(1)}\left(\boldsymbol{r}\right)\exp\left(j\omega_0 t\right)\right\}\hat{u}_x; \tag{A2.2}$$

$$\boldsymbol{\mathcal{P}}^{(3)}\left(\boldsymbol{r},t\right)\simeq\mathrm{Re}\left\{P_{\omega_0}^{(3)}\left(\boldsymbol{r}\right)\exp\left(j\omega_0 t\right)\right\}\hat{u}_x, \tag{A2.3}$$

where the nonlinear polarization in $3\omega_0$ was omitted taking into account that the phase-matching condition in this nonlinear term is not satisfied in silica fibers [139]. In the monochromatic regime, the complex amplitude of the linear and nonlinear polarizations can be expressed as [139]:[24]

$$P_{\omega_0}^{(1)}\left(\boldsymbol{r}\right)=\varepsilon_0\chi_{xx}^{(1)}\left(\boldsymbol{r}\right)E_{\omega_0}\left(\boldsymbol{r}\right); \tag{A2.4}$$

$$P_{\omega_0}^{(3)}\left(\boldsymbol{r}\right)=\frac{3}{4}\varepsilon_0\chi_{xxxx}^{(3)}\left|E_{\omega_0}\left(\boldsymbol{r}\right)\right|^2E_{\omega_0}\left(\boldsymbol{r}\right), \tag{A2.5}$$

where $E_{\omega_0}\simeq E_{a,\omega_0}+E_{b,\omega_0}$, and $\chi_{xx}^{(1)}$ and $\chi_{xxxx}^{(3)}$ are components of the first- and third-order electric susceptibility tensors, respectively. It should be noted that $\chi_{xx}^{(1)}$ is assumed spatially dependent to describe the refractive index profile of the MCF, but $\chi_{xxxx}^{(3)}$ is assumed to be constant taking into account the low nonlinear nature of silica. Finally, defining $\varepsilon_{\mathrm{r}}\left(\boldsymbol{r}\right):=1+\chi_{xx}^{(1)}\left(\boldsymbol{r}\right)$, $\gamma:=(3/4)\chi_{xxxx}^{(3)}$ and using Eqs. (A2.2)-(A2.5) in Eq. (A2.1), we obtain Eq. (2.2.3).

[23] That is, $\delta_r n\ll n$ in $\delta r\sim\lambda_0/n$, where $\delta_r n:=|n\left(r\right)-n\left(r+\delta r\right)|$.

[24] For optical frequencies well below the electronic and nuclear transitions, the nonlinear polarization can be considered instantaneous with the incident electric field. Thus, in the monochromatic regime, Eq. (A2.5) can be found from the nonlinear constitutive relation in the time domain [139]:

$$\mathcal{P}_i^{(3)}\left(\boldsymbol{r},t\right)=\varepsilon_0\chi_{ijkl}^{(3)}\mathcal{E}_j\left(\boldsymbol{r},t\right)\mathcal{E}_k\left(\boldsymbol{r},t\right)\mathcal{E}_l\left(\boldsymbol{r},t\right).$$

Appendix B2: Mode-coupling coefficients in step-index multi-core fiber

The closed-form expressions of the MCCs given by Eqs. (2.2.13)-(2.2.19) are derived by assuming step-index cores.[25] It can be noted that the MCCs depend on the general term $\iint F_b^k F_a^s \mathrm{d}S_\infty$, with $(k,s) \in \{0,1,2,3,4\}^2$ and $\mathrm{d}S_\infty = \mathrm{d}x\mathrm{d}y$ being the differential surface of the cross section of the MCF. In particular, this integral can be expressed by using a different cylindrical coordinate system in each core as follows (see Fig. B2.1):

$$\begin{aligned}\iint F_b^k F_a^s \mathrm{d}S_\infty &= \oiint F_b^k F_a^s \mathrm{d}S_a + \oiint F_b^k F_a^s \mathrm{d}S_b + I_{\mathrm{cl}}^{(k,s)} \\ &= \oiint F_b^k\left(r,\varphi\right) F_a^s\left(r,\varphi\right) r\mathrm{d}r\mathrm{d}\varphi + \oiint F_b^k\left(r',\varphi'\right) F_a^s\left(r',\varphi'\right) r'\mathrm{d}r'\mathrm{d}\varphi' + I_{\mathrm{cl}}^{(k,s)}, \quad \text{(B2.1)}\end{aligned}$$

where $I_{\mathrm{cl}}^{(k,s)} = \iint F_b^k F_a^s \mathrm{d}S_{\mathrm{cl}}$ describes the mode overlapping in the cladding.

Figure B2.1 depicts the spatial modal distribution of the $\mathrm{LP}_{01,a}$ and $\mathrm{LP}_{01,b}$ core modes in the cross section of the 2-core fiber. The cores a and b are respectively described by the reference systems $R = \{O; \{\hat{r}, \hat{\varphi}, \hat{z}\}\}$ and $R' = \{O'; \{\hat{r}', \hat{\varphi}', \hat{z}'\}\}$, connected by the following relations:

$$r' = \sqrt{r^2 + d_{ab}^2 - 2d_{ab} r\cos\varphi}; \quad \text{(B2.2)}$$

$$\tan\varphi' = \frac{r\sin\varphi}{r\cos\varphi - d_{ab}}; \quad \text{(B2.3)}$$

$$z' = z. \quad \text{(B2.4)}$$

Note that both reference systems can be approximately related as $r' \simeq r - d_{ab}$ when $\varphi \to 0$. In Cartesian coordinates, this condition is fulfilled when $|y| = |y'| \ll R_{0,a(b)}$, i.e., the cross-sectional area where is located the evanescent field of the cores (see Fig. B2.1). In particular, this approximation allows us to easily calculate the mode overlapping between adjacent cores. Using the analytic expression of [32] for the LP_{01} mode in step-index SM-SCFs, Eq. (B2.1) can be approximated to:

$$\begin{aligned}\iint F_b^k F_a^s \mathrm{d}S_\infty &\simeq \int_r\int_\varphi \frac{K_0^k\left(\frac{w_b}{R_{0,b}}\left(r-d_{ab}\right)\right)}{K_0^k\left(w_b\right)} \frac{J_0^s\left(\frac{u_a}{R_{0,a}}r\right)}{J_0^s\left(u_a\right)} r\mathrm{d}r\mathrm{d}\varphi \\ &+ \int_{r'}\int_{\varphi'} \frac{J_0^k\left(\frac{u_b}{R_{0,b}}r'\right)}{J_0^k\left(u_b\right)} \frac{K_0^s\left(\frac{w_a}{R_{0,a}}\left(r'+d_{ab}\right)\right)}{K_0^s\left(w_a\right)} r'\mathrm{d}r'\mathrm{d}\varphi' + I_{\mathrm{cl}}^{(k,s)} \\ &\simeq 2\pi\left[\frac{K_0^k\left(w_b d_{ab}/R_{0,b}\right)}{K_0^k\left(w_b\right)J_0^s\left(u_a\right)}\int_0^{R_{0,a}} J_0^s\left(\frac{u_a}{R_{0,a}}r\right) r\mathrm{d}r\right. \\ &\left. + \frac{K_0^s\left(w_a d_{ab}/R_{0,a}\right)}{J_0^k\left(u_b\right)K_0^s\left(w_a\right)}\int_0^{R_{0,b}} J_0^k\left(\frac{u_b}{R_{0,b}}r'\right) r'\mathrm{d}r'\right] + I_{\mathrm{cl}}^{(k,s)}. \quad \text{(B2.5)}\end{aligned}$$

Similar to [137], the modified Bessel function of second kind (K_0) has been approximated to its value in the center of the adjacent core due to the low slope of this function with $r, r' > R_{0,a(b)}$. As can be seen, the integrals in the RHS of Eq. (B2.5) can be directly solved with $k, s \leq 2$. Nonetheless, in the cases $k, s > 2$, the Gaussian approximation of J_0 is employed with $r, r' \leq R_{0,a(b)}$:

$$J_0^{s(k)}\left(\frac{u_{a(b)}}{R_{0,a(b)}}r\right) \simeq \exp\left(-r^2/H_{a(b)}^2\right)^{s(k)}, \quad \text{(B2.6)}$$

[25] In gradual-index MCFs, the MCCs should be numerically calculated. However, in trench- or hole-assisted MCFs with step-index cores, the closed-form expressions presented herein can be revisited by using a similar approach as in [151].

where $H_{a(b)}$ is the modal field radius of the $\mathrm{LP}_{01,a(b)}$ mode [139]. Moreover, the denominator of the MCCs can be approximated to:

$$N_a = \iint F_a^2 \mathrm{d}S_\infty \simeq \oiint F_a^2 \mathrm{d}S_a = \int_0^{R_{0,a}} \int_0^{2\pi} \frac{J_0^2\left(\frac{u_a}{R_{0,a}} r\right)}{J_0^2\left(u_a\right)} r \mathrm{d}r \mathrm{d}\varphi$$
$$= \pi R_{0,a}^2 \left[1 + \frac{J_1^2\left(u_a\right)}{J_0^2\left(u_a\right)}\right], \tag{B2.7}$$

assuming highly-confined modes, with $\oiint F_a^2 \mathrm{d}S_a \gg \iint F_a^2 \mathrm{d}S_{\mathrm{cl}}$.

On the other hand, it should be noted that the optical power required to stimulate the Kerr effect in the cladding is around $\sim 30\,\mathrm{dBm}$ when assuming a modal effective area of $80\,\mu\mathrm{m}$ [152]. Therefore, considering optical power levels lower than 30 dBm, we can assume that the third-order nonlinear polarization is not stimulated in the cladding. In other words, a silica MCF is equivalent to an MCF where the nonlinear nature is only restricted to the cores, with $\gamma\left(\boldsymbol{r}\right)$ spatially dependent and null in the cladding. As a result, we can safely assume $I_{\mathrm{cl}}^{(k,s)} \simeq 0$ in the nonlinear MCCs. Furthermore, in $q_a^{(1)}$, we have neglected the term K_0^4 taking into account that $\oiint F_a^4 \mathrm{d}S_a \gg \oiint F_a^4 \mathrm{d}S_b$; in $q_{a,b}^{(3)}$, we have neglected the term $\oiint F_b F_a^3 \mathrm{d}S_b$ given that $\oiint F_b F_a^3 \mathrm{d}S_a \gg \oiint F_b F_a^3 \mathrm{d}S_b$; and in $q_{a,b}^{(4)}$, we have omitted the integral $\oiint F_b^3 F_a \mathrm{d}S_a$ considering that $\oiint F_b^3 F_a \mathrm{d}S_b \gg \oiint F_b^3 F_a \mathrm{d}S_a$. Likewise, since $\Delta\varepsilon_{\mathrm{r},a}\left(\boldsymbol{r}\right)$ and $\Delta\varepsilon_{\mathrm{r},b}\left(\boldsymbol{r}\right)$ are found to be null in the cladding and in adjacent cores, Eq. (B2.5) should be restricted to the corresponding region to calculate the MCCs c_a and $\kappa_{a,b}$. Finally, assuming $\beta_a \simeq k_0 n_a$ (weakly-guiding MCF) and using Eqs. (B2.5)-(B2.7), the closed-form expressions of the linear and nonlinear MCCs are derived.

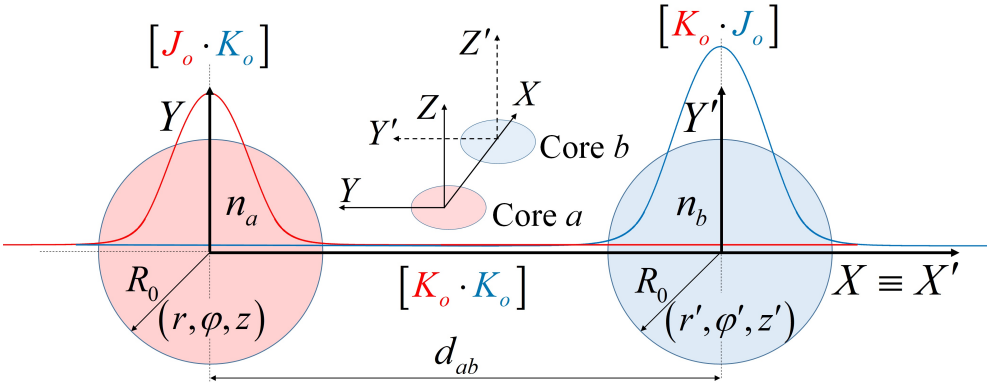

Figure B2.1. Transversal functions F_a and F_b in the cross section of the MCF [143].

This page was intentionally left blank.

Chapter 3

Longitudinal and temporal birefringence effects

3.1 Introduction

In the preceding chapter, we have investigated the probability distribution of the inter-core crosstalk (IC-XT) in MCFs by assuming important simplifications in these media that should be carefully revisited for the complete understanding of this physical impairment. Specifically: (*i*) we have omitted the optical attenuation, the anisotropic nature and the temporal fluctuations of the MCF, and (*ii*) the longitudinal perturbations have been heuristically inserted in the coupled-mode theory. As a result, we have found a set of coupled-mode equations with important limitations to describe crucial aspects such as the time-varying behavior of the IC-XT and intra-core coupling effects.

In the literature of this topic, we also find several fundamental limitations in the mathematical models preceding our work. In [153–156], the intra-core and inter-core coupling effects of SM-MCFs have been investigated by using the Manakov equations, where the longitudinal MCF perturbations have been described by assuming unperturbed ideal modes and the temporal MCF perturbations have been omitted. These temporal perturbations have been analyzed in [157, 158], but omitting the intra-core effects and using a similar heuristic formalism as in Chapter 2 to model the medium fluctuations.

In order to solve these problems, in this chapter we describe the longitudinal and temporal birefringence effects of MCFs using a more rigorous formalism than in previous works. In particular, we develop a coupled local-mode theory (CLMT) inserting both longitudinal and temporal MCF perturbations along with the anisotropic nature of the fiber in Maxwell's equations. As a result, we obtain an accurate theoretical model able to predict the different types of crosstalk between the polarized core modes in SM-MCFs: (*i*) the intra-core crosstalk (iC-XT) which describes the mode-coupling between orthogonal polarizations in a given core; (*ii*) the direct inter-core crosstalk (DIC-XT) modeling the mode-coupling between the same polarization axis in different cores; and (*iii*) the cross inter-core crosstalk (XIC-XT) involving mode-coupling between orthogonal polarizations in different cores. To complete our study, we perform extensive experimental measurements on a 4-core MCF, which are found to be in good agreement with numerical simulations of the proposed CLMT. Remarkably, we will demonstrate that the spatial and temporal IC-XT fluctuations have identical distributions when the temporal perturbations are only induced by slight floor vibrations due to human activity and the temperature conditions are found to be constant.

The chapter is structured as follows. In Section 3.2, the CLMT is derived from Maxwell's equations. In Section 3.3, a numerical method to implement the CLMT is proposed. Next, in Section 3.4, extensive numerical simulations of the temporal and longitudinal evolution of the linear birefringence and its impact on the iC-, DIC- and XIC-XT are reported considering both lowly- and highly-birefringent cores. The experimental validation of the CLMT is performed in Section 3.5. Finally, in Section 3.6, the main conclusions of this chapter are highlighted.

3.2 Coupled local-mode theory

In this section, we report the coupled local-mode theory (CLMT) for SM-MCF media modeling the intra-core and inter-core coupling effects between the polarized core modes (PCMs) when operating in the monochromatic regime and considering both temporal and longitudinal birefringent effects. The theory presented herein is a general model which can be applied to SM-MCFs comprising: coupled or uncoupled cores, lowly- or highly-birefringent cores, trench- or hole-assisted cladding and gradual- or step-index profiles.

To this end, let us consider a weakly-guiding SM-MCF with two cores a and b with longitudinal and temporal perturbations. As depicted in Fig. 3.1, each core m (with $m \in \{a, b\}$) can be modeled as a series of birefringent segments with a different time-varying retardation and random orientation of the local principal axes. Therefore, the first-order electric susceptibility tensor $\chi_{ij}^{(1)}$ of the MCF can slightly fluctuate in time and along the fiber length, as a consequence of external perturbations such as bending, twisting, floor vibrations and temperature variations, as well as due to manufacturing imperfections. As a result, in each segment of a given core m, the propagation constant of the PCMs $\mathrm{LP}_{01,mx}$ and $\mathrm{LP}_{01,my}$ presents a different value due to the mentioned slight changes and, therefore, the transversal function of each PCM mi (with $i \in \{x, y\}$) will also be modified.

In order to analyze theoretically this scenario, the MCF of the previous example should be considered as a multi-dielectric, lossy, nonlinear, anisotropic, heterogeneous, time-varying and temporally dispersive medium. Nevertheless, note that we cannot observe temporally dispersive effects when assuming incident monochromatic fields.

In addition, we introduce here the concept of *local mode* in perturbation theory. A local mode is defined as an eigenfunction in a short core segment in which the perturbations of the ideal phase constant and the transversal eigenfunction of the LP_{01} mode are approximately constant in both orthogonal polarizations. Hence, each core and PCM can be modeled as a series of birefringent segments and local modes where the longitudinal and temporal MCF perturbations are approximately invariant but can fluctuate between adjacent segments, as shown in Fig. 3.1. In this way, in contrast with Chapter 2, where the longitudinal MCF perturbations are heuristically inserted in the coupled-mode equations assuming ideal modes, we will be able to include both longitudinal and temporal medium perturbations from the ansatz of perturbation theory (step 1 of Fig. 1.9) considering the global electric field strength of the MCF as a linear combination of the local modes of each core. The resulting coupled local-mode equations will include space- and time-varying exponential terms and mode-coupling coefficients. This formalism will allow us to describe accurately the impact of the different longitudinal and temporal fiber random perturbations on the crosstalk among the PCMs.

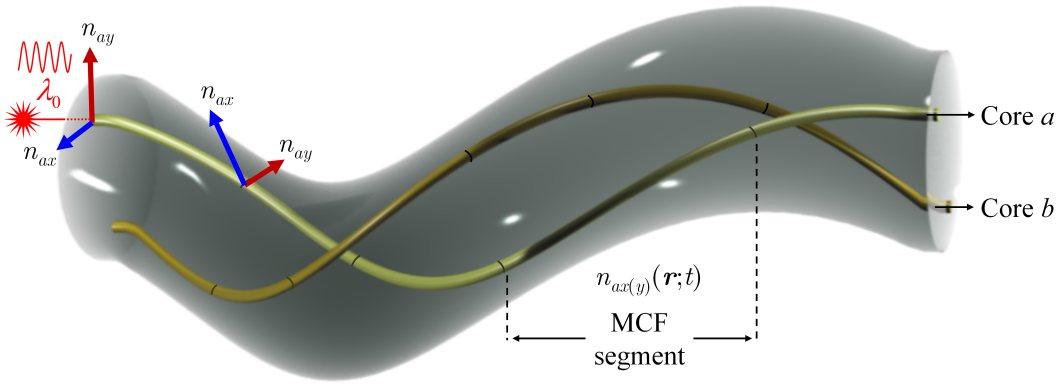

Figure 3.1. Multi-core fiber comprising different birefringent segments in cores a and b with random orientation and longitudinal and temporal fluctuations in the principal refractive indexes of each core $n_{ai}(\boldsymbol{r};t)$ and $n_{bi}(\boldsymbol{r};t)$, with $i \in \{x, y\}$. The spatial dependence of n_{ai} and n_{bi} also includes the radial dependence of the refractive index profile in gradual-index MCFs [131].

3.2.1 Multi-core fiber local modes

Our initial goal is to include the MCF random perturbations in step 1 of perturbation theory (see Fig. 1.9). Hence, in contrast with Chapter 2, we should propose the ansatz of the electric field strength of the MCF by taking into account these perturbations. In this way, assuming monochromatic electric fields with both orthogonal polarizations and slowly-varying amplitude functions, the exact real wave function of the global electric field strength of the MCF ($\boldsymbol{\mathcal{E}}$) can be approximated as a linear combination of the electric field strength of each PCM mi ($\mathcal{E}_{mi}$) considering isolated cores, that is, assuming that the geometry of each core m is not perturbed by the presence of adjacent cores:

$$\boldsymbol{\mathcal{E}}\left(\boldsymbol{r},t\right)\simeq\sum_{m=a,b}\sum_{i=x,y}\mathcal{E}_{mi}\left(\boldsymbol{r},t\right)\hat{u}_i=\sum_{m=a,b}\sum_{i=x,y}\mathrm{Re}\left\{E_{mi,\omega_0}\left(\boldsymbol{r};t\right)\exp\left(j\omega_0 t\right)\right\}\hat{u}_i, \tag{3.2.1}$$

where E_{mi,ω_0} is the complex amplitude of the PCM mi including the longitudinal and temporal birefringence fluctuations, ω_0 is the angular frequency of the optical carrier and $\hat{u}_i$ is the transverse unit vector. Note that Eq. (3.2.1) allows us to decouple the rapid temporal oscillation of the optical carrier from the slow temporal evolution of the complex amplitudes induced by the time-varying fluctuations of the MCF.

The theoretical model we propose entails as an essential prerequisite to describe the fiber perturbations in E_{mi,ω_0}. Thus, the complex amplitude is expressed as follows:

$$E_{mi,\omega_0}\left(\boldsymbol{r};t\right)=A_{mi}\left(z;t\right)F_{mi}\left(x,y,\omega_0;z,t\right)\exp\left(-j\Phi_{mi}\left(z,\omega_0;t\right)\right), \tag{3.2.2}$$

where A_{mi} is the complex envelope, F_{mi} is the transversal eigenfunction of the PCM mi and Φ_{mi} is the complex phase function of the PCM mi defined as:

$$\Phi_{mi}\left(z,\omega_0;t\right):=\phi_{mi}\left(z,\omega_0;t\right)-j\frac{1}{2}\alpha\left(\omega_0\right)z, \tag{3.2.3}$$

with α the power attenuation coefficient of the MCF modeling optical absorption generated from Rayleigh scattering and assumed similar in each PCM,[1] and ϕ_{mi} the real phase function involving the longitudinal and temporal MCF perturbations:

$$\phi_{mi}\left(z,\omega_0;t\right):=\int_0^z\beta_{mi}^{(\mathrm{eq})}\left(\xi,\omega_0;t\right)\mathrm{d}\xi=\beta_{mi}\left(\omega_0\right)z+\int_0^z\beta_{mi}^{(\mathrm{B+S})}\left(\xi,\omega_0;t\right)\mathrm{d}\xi, \tag{3.2.4}$$

with $\beta_{mi}^{(\mathrm{eq})}$ the equivalent phase constant of each local mode of the PCM mi, which comprises the ideal phase constant β_{mi} and the phase perturbation $\beta_{mi}^{(\mathrm{B+S})}$ induced by macrobends (B) and additional longitudinal and temporal fiber structural fluctuations (S). In addition, it should be remarked for future mathematical discussions that (we use the notation $\partial_z=\partial/\partial z$):

$$\partial_z\Phi_{mi}=\beta_{mi}^{(\mathrm{eq})}-j\tfrac{1}{2}\alpha;\quad\partial_z^2\Phi_{mi}=\partial_z\beta_{mi}^{(\mathrm{eq})};\quad\left(\partial_z\Phi_{mi}\right)^2\simeq\left(\beta_{mi}^{(\mathrm{eq})}\right)^2-j\alpha\beta_{mi}^{(\mathrm{eq})}. \tag{3.2.5}$$

Equations (3.2.1)-(3.2.4) allow us to describe the longitudinal and temporal MCF perturbations in the electric field strength of the MCF. Along this line, the following considerations on the above equations are in order:

- The longitudinal and temporal MCF perturbations define the birefringent segments and the local modes in each PCM mi. These fiber perturbations are included in E_{mi,ω_0} via the functions A_{mi}, F_{mi} and Φ_{mi}. Given that the longitudinal and temporal MCF perturbations modify the ideal phase constant β_{mi} as indicated by Eq. (3.2.4), F_{mi} and A_{mi} should also be assumed longitudinal and temporal dependent in order to satisfy Maxwell's equations in the

[1] The optical attenuation induced by the resonant frequencies of fused silica can be neglected when the optical carrier is located in the third transmission window.

MCF segments. Specifically, the local mode $F_{mi}\exp(-j\Phi_{mi})$ should satisfy the Helmholtz equation in each birefringent segment of the core m:

$$\left(\triangle + k_0^2\varepsilon_{\mathrm{r},mi}\left(\boldsymbol{r},\omega_0;t\right)\right)F_{mi}(x,y,\omega_0;z,t)\exp\left(-j\Phi_{mi}\left(z,\omega_0;t\right)\right)=0, \tag{3.2.6}$$

where $\varepsilon_{\mathrm{r},mi}$ is the relative electric permittivity in the core m and polarization axis i [see below Eqs. (3.2.14) and (3.2.18)]. In particular, the above equation is step 2 of perturbation theory depicted in Fig. 1.9.

- The longitudinal and temporal changes induced in $\beta_{mi}^{(\mathrm{eq})}$ by the medium perturbations are assumed to be slowly-varying in comparison with the spatial and temporal duration of a cycle of the optical carrier in each core, i.e., in $\delta z \sim \lambda_m$ and $\delta t \sim 2\pi/\omega_0$.[2] In such circumstances, the optical power reflected due to the longitudinal and temporal changes of $\beta_{mi}^{(\mathrm{eq})}$ can be neglected.

- The semicolon symbol is used to separate explicitly the longitudinal and temporal changes induced by the MCF perturbations. As an example, the slowly-varying longitudinal and temporal fluctuations of the transversal local eigenfunction $F_{mi}(x,y,\omega_0;z,t)$ are explicitly separated by the semicolon symbol from the transversal changes given by the well-known Bessel functions [32].

- The phase of the local modes is given by the complex function Φ_{mi} in each MCF segment. Therefore, considering that the local modes must satisfy Eq. (3.2.6), F_{mi} should also be assumed a complex function. Nevertheless, keeping in mind that the imaginary part of Φ_{mi} (modeling the optical absorption) is much lower than the real part ϕ_{mi} (accounting for the ideal phase constant along with the fiber perturbations), we assume F_{mi} as a real function from now on. However, note that in the multi-mode regime, F_{mi} should be considered as a complex function to include the azimuthal order of the corresponding LP mode group.

- Since we are assuming monochromatic electric fields, we cannot model dispersive effects among the PCMs. Nonetheless, we will discuss the non-monochromatic regime in the next chapter by considering pulsed waves. In this way, we will be able to include the chromatic dispersion and higher-order dispersive effects in the coupled local-mode equations.

3.2.2 Coupled-wave equations

In step 3 of perturbation theory, the wave equation of the MCF should be derived from Maxwell's equations for the complex amplitudes E_{mi,ω_0}. We start by combining Faraday's and Ampère's laws [Eqs. (1.5.6) and (1.5.7)] applying the curl operator. Thus, using the constitutive relations given by Eq. (1.5.5), the nonlinear wave equation of the electric field strength is found as:

$$\triangle\boldsymbol{\mathcal{E}}\left(\boldsymbol{r},t\right)-\frac{1}{c_0^2}\partial_t^2\boldsymbol{\mathcal{E}}\left(\boldsymbol{r},t\right)=\mu_0\partial_t^2\boldsymbol{\mathcal{P}}^{(1)}\left(\boldsymbol{r},t\right)+\mu_0\partial_t^2\boldsymbol{\mathcal{P}}^{(3)}\left(\boldsymbol{r},t\right), \tag{3.2.7}$$

where $\boldsymbol{\mathcal{P}}^{(1)}$ and $\boldsymbol{\mathcal{P}}^{(3)}$ are the linear and nonlinear polarization of the MCF, respectively. Note that we have neglected the term $\nabla(\nabla\cdot(\boldsymbol{\mathcal{P}}^{(1)}+\boldsymbol{\mathcal{P}}^{(3)}))$ in Eq. (3.2.7) considering slowly-varying refractive index profiles[3] and the low birefringent and nonlinear nature of silica MCFs (including also the case HB-MCF), in line with the assumptions performed in the classical modal analysis of SCFs with an LB or HB design [139, 150, 159–161]. Unfortunately, this approximation has not been rigorously verified in the literature. For the above reason, we include in Appendix A3 (on page 82) a numerical verification of this point in LB- and HB-MCFs.

[2] As was pointed out in Chapter 1, note that the wavelength of the optical carrier is found to be different in each core (λ_m). In particular, $\lambda_m = \lambda_0/n_m$, where λ_0 is the wavelength of the optical carrier in vacuum, $n_m := (n_{mx}+n_{my})/2$ and $\{n_{mi}\}_{i=x,y}$ are the principal refractive indexes of core m at ω_0. In LB cores, $n_{mx}=n_{my}\equiv n_m$. However, in HB cores, $n_{mx}\neq n_{my}$.

[3] That is, $\delta_r n_{mi} \ll n_{mi}$ in $\delta r \sim \lambda_m$, where $\delta_r n_{mi} := |n_{mi}(r) - n_{mi}(r+\delta r)|$.

Our goal is to rewrite Eq. (3.2.7) in terms of the complex amplitudes of the electric field strength. Hence, we should take into account that we can write $\boldsymbol{\mathcal{E}}$, $\boldsymbol{\mathcal{P}}^{(1)}$ and $\boldsymbol{\mathcal{P}}^{(3)}$ as:

$$\boldsymbol{\mathcal{E}}\left(\boldsymbol{r},t\right)=\sum_{i=x,y}\mathrm{Re}\left\{E_{i,\omega_0}\left(\boldsymbol{r};t\right)\exp\left(j\omega_0 t\right)\right\}\hat{u}_i; \tag{3.2.8}$$

$$\boldsymbol{\mathcal{P}}^{(1)}\left(\boldsymbol{r},t\right)=\sum_{i=x,y}\mathrm{Re}\left\{P^{(1)}_{i,\omega_0}\left(\boldsymbol{r};t\right)\exp\left(j\omega_0 t\right)\right\}\hat{u}_i; \tag{3.2.9}$$

$$\boldsymbol{\mathcal{P}}^{(3)}\left(\boldsymbol{r},t\right)\simeq\sum_{i=x,y}\mathrm{Re}\left\{P^{(3)}_{i,\omega_0}\left(\boldsymbol{r};t\right)\exp\left(j\omega_0 t\right)\right\}\hat{u}_i, \tag{3.2.10}$$

where $E_{i,\omega_0}\simeq\sum_m E_{mi,\omega_0}$, and $P^{(1)}_{i,\omega_0}$ and $P^{(3)}_{i,\omega_0}$ are the complex amplitudes of $\boldsymbol{\mathcal{P}}^{(1)}$ and $\boldsymbol{\mathcal{P}}^{(3)}$, respectively. Note that the complex amplitude $P^{(3)}_{i,3\omega_0}$ of the nonlinear polarization in $3\omega_0$ was omitted taking into account that the phase-matching condition in this nonlinear term is not satisfied in silica fibers [139]. In this scenario, the complex amplitude of the linear and nonlinear polarizations can be expressed using the Einstein summation convention as (see page 86):

$$P^{(1)}_{i,\omega_0}\left(\boldsymbol{r};t\right)=\varepsilon_0\chi^{(1)}_{ij}\left(\boldsymbol{r},\omega_0;t\right)E_{j,\omega_0}\left(\boldsymbol{r};t\right); \tag{3.2.11}$$

$$P^{(3)}_{i,\omega_0}\left(\boldsymbol{r};t\right)=\frac{3}{4}\varepsilon_0\chi^{(3)}_{ijkl}E_{j,\omega_0}\left(\boldsymbol{r};t\right)E_{k,\omega_0}\left(\boldsymbol{r};t\right)E_{l,-\omega_0}\left(\boldsymbol{r};t\right), \tag{3.2.12}$$

where the first-order electric susceptibility tensor $\chi^{(1)}_{ij}$ is assumed to be spatial[4] and temporal dependent due to the MCF perturbations, and the third-order susceptibility $\chi^{(3)}_{ijkl}$ is assumed to be constant taking into account the low nonlinear nature of silica fibers. Moreover, $\chi^{(3)}_{ijkl}$ can be expressed in silica fibers as follows [159]:

$$\chi^{(3)}_{ijkl}=\chi_{\mathrm{NL}}\left(\frac{1-f_{\mathrm{R}}}{3}\right)\left(\delta_{ij}\delta_{kl}+\delta_{ik}\delta_{jl}+\delta_{il}\delta_{jk}\right), \tag{3.2.13}$$

where δ_{ij} is the Kronecker delta function, $\chi_{\mathrm{NL}}=2.6\cdot10^{-22}$ m^2/V^2 at the wavelength of 1550 nm and $f_{\mathrm{R}}=0.245$. In the next chapter, the role of the constant f_{R} will be described in detail. Furthermore, we define:

$$\varepsilon_{\mathrm{r},i}\left(\boldsymbol{r},\omega_0;t\right):=1+\chi^{(1)}_{ii}\left(\boldsymbol{r},\omega_0;t\right); \tag{3.2.14}$$

$$\sigma\left(\boldsymbol{r},\omega_0;t\right):=\chi^{(1)}_{xy}\left(\boldsymbol{r},\omega_0;t\right). \tag{3.2.15}$$

The real part of these parameters gives information about the material dispersion and the MCF perturbations, and the imaginary part accounts for the optical absorption of the medium. Bearing in mind that $\mathrm{Im}\left\{\chi^{(1)}_{ij}\right\}\sim\alpha/k_0$ in silica when the optical carrier is located in the third transmission window [149], the imaginary part of $\varepsilon_{\mathrm{r},i}$ and σ can be neglected. Moreover, assuming that the MCF can be regarded as a time-invariant medium in time intervals of the order of $\delta t\sim2\pi/\omega_0$, we can infer from the Poynting theorem that $\chi^{(1)}_{xy}=\chi^{(1)}_{yx}$ [162]. Finally, taking into account that $E_{i,-\omega_0}=E^*_{i,\omega_0}$, the coupled-wave equations of the MCF are found:

$$\triangle E_{x,\omega_0}+k_0^2\left(\varepsilon_{\mathrm{r},x}E_{x,\omega_0}+\sigma E_{y,\omega_0}\right)+k_0^2\gamma\left[\left(\left|E_{x,\omega_0}\right|^2+\frac{2}{3}\left|E_{y,\omega_0}\right|^2\right)E_{x,\omega_0}+\frac{1}{3}E^2_{y,\omega_0}E_{x,-\omega_0}\right]=0; \tag{3.2.16}$$

$$\triangle E_{y,\omega_0}+k_0^2\left(\varepsilon_{\mathrm{r},y}E_{y,\omega_0}+\sigma E_{x,\omega_0}\right)+k_0^2\gamma\left[\left(\left|E_{y,\omega_0}\right|^2+\frac{2}{3}\left|E_{x,\omega_0}\right|^2\right)E_{y,\omega_0}+\frac{1}{3}E^2_{x,\omega_0}E_{y,-\omega_0}\right]=0, \tag{3.2.17}$$

where $\gamma\left(\omega_0\right):=\left(3/4\right)\chi_{\mathrm{NL}}\left(1-f_{\mathrm{R}}\right)=1.5\cdot10^{-22}$ m^2/V^2 with $\lambda_0=1550$ nm.

[4]The longitudinal dependence of $\chi^{(1)}_{ij}$ allows us to describe the MCF longitudinal birefringence effects and the transversal dependence describes the intrinsic variations of the refractive index profile in gradual-index MCFs.

3.2.3 Coupled local-mode equations

Once we have derived the coupled-wave equations of the MCF, we can obtain the coupled local-mode equations in step 4 of perturbation theory by inserting Eq. (3.2.2) into Eqs. (3.2.16) and (3.2.17). However, we should previously discuss some questions related to the MCF birefringence and local modes.

First, we should describe the relative electric permittivity given by Eq. (3.2.14) and accounting for the linear birefringence in each polarization axis:

$$\begin{aligned}\varepsilon_{\mathrm{r},i}\left(\boldsymbol{r},\omega_0;t\right) &= \varepsilon_{\mathrm{r},ci}\left(\boldsymbol{r},\omega_0;t\right)+\Delta\varepsilon_{\mathrm{r},ai}\left(\boldsymbol{r},\omega_0;t\right)+\Delta\varepsilon_{\mathrm{r},bi}\left(\boldsymbol{r},\omega_0;t\right)\\ &= \begin{cases}\boldsymbol{r}\equiv\text{core } a & \varepsilon_{\mathrm{r},ai}\left(\boldsymbol{r},\omega_0;t\right)=\varepsilon_{\mathrm{r},ci}\left(\boldsymbol{r},\omega_0;t\right)+\Delta\varepsilon_{\mathrm{r},ai}\left(\boldsymbol{r},\omega_0;t\right)\equiv\left(n_{ai}^{(\mathrm{eq})}\right)^2\\ \boldsymbol{r}\equiv\text{cladding} & \varepsilon_{\mathrm{r},ci}\left(\boldsymbol{r},\omega_0;t\right)\equiv n_{\mathrm{cl}}^2\\ \boldsymbol{r}\equiv\text{core } b & \varepsilon_{\mathrm{r},bi}\left(\boldsymbol{r},\omega_0;t\right)=\varepsilon_{\mathrm{r},ci}\left(\boldsymbol{r},\omega_0;t\right)+\Delta\varepsilon_{\mathrm{r},bi}\left(\boldsymbol{r},\omega_0;t\right)\equiv\left(n_{bi}^{(\mathrm{eq})}\right)^2\end{cases},\end{aligned} \tag{3.2.18}$$

where $\varepsilon_{\mathrm{r},ai}$, $\varepsilon_{\mathrm{r},bi}$ and $\varepsilon_{\mathrm{r},ci}$ are the relative electric permittivity in the cores a, b and in the cladding, respectively; and $\Delta\varepsilon_{\mathrm{r},ai}$ and $\Delta\varepsilon_{\mathrm{r},bi}$ are the difference between the relative electric permittivity of the cladding and those of cores a and b, respectively. Since $\varepsilon_{\mathrm{r},ai}$ and $\varepsilon_{\mathrm{r},bi}$ give information about the MCF perturbations in each core and polarization axis, the root square value is defined as the *equivalent refractive index*, i.e., $n_{ai}^{(\mathrm{eq})}:=\sqrt{\varepsilon_{\mathrm{r},ai}}$ and $n_{bi}^{(\mathrm{eq})}:=\sqrt{\varepsilon_{\mathrm{r},bi}}$. The concept of the equivalent refractive index was introduced in Chapter 2 with the ERIM (see page 35), but following a heuristic formalism and omitting the polarization effects and time-varying fluctuations of the MCF. In this chapter, we introduce this concept from Maxwell's equations and we will complete the ERIM by including the aforementioned effects in Section 3.3. Moreover, the circular birefringence is given by:

$$\sigma\left(\boldsymbol{r},\omega_0;t\right)=\begin{cases}\boldsymbol{r}\equiv\text{core } a & \sigma_a\left(\boldsymbol{r},\omega_0;t\right)=\chi_{a,xy}^{(1)}\left(\boldsymbol{r},\omega_0;t\right)\\ \boldsymbol{r}\equiv\text{cladding} & \sigma_c\left(\boldsymbol{r},\omega_0;t\right)=\chi_{c,xy}^{(1)}\left(\boldsymbol{r},\omega_0;t\right)\\ \boldsymbol{r}\equiv\text{core } b & \sigma_b\left(\boldsymbol{r},\omega_0;t\right)=\chi_{b,xy}^{(1)}\left(\boldsymbol{r},\omega_0;t\right)\end{cases}. \tag{3.2.19}$$

Second, it should be noted that Eq. (3.2.6) allows us to obtain two fundamental relations to describe the MCF perturbations in the coupled local-mode equations. As can be deduced from the numerical model described in Section 3.3, $\partial_z F_{mi}\simeq\partial_z^2 F_{mi}\simeq 0$ in $\delta z\sim\lambda_m$. As a result, the following expressions emerge from Eq. (3.2.6):

$$\left(\triangle_{\mathrm{T}}+k_0^2\varepsilon_{\mathrm{r},i}\right)F_{ai}=\left[k_0^2\Delta\varepsilon_{\mathrm{r},bi}+\left(\beta_{ai}^{(\mathrm{eq})}\right)^2+j\left(\partial_z-\alpha\right)\beta_{ai}^{(\mathrm{eq})}\right]F_{ai}; \tag{3.2.20}$$

$$\left(\triangle_{\mathrm{T}}+k_0^2\varepsilon_{\mathrm{r},i}\right)F_{bi}=\left[k_0^2\Delta\varepsilon_{\mathrm{r},ai}+\left(\beta_{bi}^{(\mathrm{eq})}\right)^2+j\left(\partial_z-\alpha\right)\beta_{bi}^{(\mathrm{eq})}\right]F_{bi}, \tag{3.2.21}$$

with $\triangle_{\mathrm{T}}:=\partial_x^2+\partial_y^2$ the transverse Laplacian operator.

Now, at this point we can start with the derivation of the coupled local-mode equations by combining Eqs. (3.2.2), (3.2.16) and (3.2.17). After some algebraic work and using the SVEA along with Eqs. (3.2.5), (3.2.20) and (3.2.21), we obtain the next coupled equations:

$$
\begin{aligned}
&k_0^2\Delta\varepsilon_{\mathrm{r},bx}F_{ax}\exp\left(-j\phi_{ax}\right)A_{ax}-\left(j2\beta_{ax}^{(\mathrm{eq})}+\alpha\right)F_{ax}\exp\left(-j\phi_{ax}\right)\partial_z A_{ax}\\
&\quad+k_0^2\Delta\varepsilon_{\mathrm{r},ax}F_{bx}\exp\left(-j\phi_{bx}\right)A_{bx}-\left(j2\beta_{bx}^{(\mathrm{eq})}+\alpha\right)F_{bx}\exp\left(-j\phi_{bx}\right)\partial_z A_{bx}\\
&\quad+k_0^2\sigma\left[A_{ay}F_{ay}\exp\left(-j\phi_{ay}\right)+A_{by}F_{by}\exp\left(-j\phi_{by}\right)\right]\\
&\quad+k_0^2\gamma\exp\left(-\alpha z\right)\left\{\begin{array}{l}
A_{ax}\left|A_{ax}\right|^2F_{ax}^3\exp\left(-j\phi_{ax}\right)\\
+A_{bx}\left|A_{bx}\right|^2F_{bx}^3\exp\left(-j\phi_{bx}\right)\\
+2\left|A_{ax}\right|^2A_{bx}F_{ax}^2F_{bx}\exp\left(-j\phi_{bx}\right)\\
+2A_{ax}\left|A_{bx}\right|^2F_{ax}F_{bx}^2\exp\left(-j\phi_{ax}\right)\\
+A_{ax}^2A_{bx}^*F_{ax}^2F_{bx}\exp\left[-j\left(2\phi_{ax}-\phi_{bx}\right)\right]\\
+A_{ax}^*A_{bx}^2F_{ax}F_{bx}^2\exp\left[-j\left(2\phi_{bx}-\phi_{ax}\right)\right]
\end{array}\right\}\\
&\quad+\frac{2}{3}k_0^2\gamma\exp\left(-\alpha z\right)\left\{\begin{array}{l}
A_{ax}\left|A_{ay}\right|^2F_{ax}F_{ay}^2\exp\left(-j\phi_{ax}\right)\\
+A_{bx}\left|A_{by}\right|^2F_{bx}F_{by}^2\exp\left(-j\phi_{bx}\right)\\
+\left|A_{ay}\right|^2A_{bx}F_{ay}^2F_{bx}\exp\left(-j\phi_{bx}\right)\\
+A_{ax}\left|A_{by}\right|^2F_{ax}F_{by}^2\exp\left(-j\phi_{ax}\right)\\
+A_{ax}A_{ay}^*A_{by}F_{ax}F_{ay}F_{by}\exp\left[-j\left(\phi_{ax}-\phi_{ay}+\phi_{by}\right)\right]\\
+A_{ay}A_{bx}A_{by}^*F_{ay}F_{bx}F_{by}\exp\left[-j\left(\phi_{ay}+\phi_{bx}-\phi_{by}\right)\right]\\
+A_{ax}A_{ay}A_{by}^*F_{ax}F_{ay}F_{by}\exp\left[-j\left(\phi_{ax}+\phi_{ay}-\phi_{by}\right)\right]\\
+A_{ay}^*A_{bx}A_{by}F_{ay}F_{bx}F_{by}\exp\left[-j\left(\phi_{bx}+\phi_{by}-\phi_{ay}\right)\right]
\end{array}\right\}\\
&\quad+\frac{1}{3}k_0^2\gamma\exp\left(-\alpha z\right)\left\{\begin{array}{l}
A_{ax}^*A_{ay}^2F_{ax}F_{ay}^2\exp\left[-j\left(2\phi_{ay}-\phi_{ax}\right)\right]\\
+A_{ay}^2A_{bx}^*F_{ay}^2F_{bx}\exp\left[-j\left(2\phi_{ay}-\phi_{bx}\right)\right]\\
+A_{ax}^*A_{by}^2F_{ax}F_{by}^2\exp\left[-j\left(2\phi_{by}-\phi_{ax}\right)\right]\\
+A_{bx}^*A_{by}^2F_{bx}F_{by}^2\exp\left[-j\left(2\phi_{by}-\phi_{bx}\right)\right]\\
+2A_{ax}^*A_{ay}A_{by}F_{ax}F_{ay}F_{by}\exp\left[-j\left(\phi_{ay}+\phi_{by}-\phi_{ax}\right)\right]\\
+2A_{ay}A_{bx}^*A_{by}F_{ay}F_{bx}F_{by}\exp\left[-j\left(\phi_{ay}-\phi_{bx}+\phi_{by}\right)\right]
\end{array}\right\}=0;
\end{aligned}
\tag{3.2.22}
$$

$$
\begin{aligned}
&k_0^2\Delta\varepsilon_{\mathrm{r},by}F_{ay}\exp\left(-j\phi_{ay}\right)A_{ay}-\left(j2\beta_{ay}^{(\mathrm{eq})}+\alpha\right)F_{ay}\exp\left(-j\phi_{ay}\right)\partial_z A_{ay}\\
&\quad+k_0^2\Delta\varepsilon_{\mathrm{r},ay}F_{by}\exp\left(-j\phi_{by}\right)A_{by}-\left(j2\beta_{by}^{(\mathrm{eq})}+\alpha\right)F_{by}\exp\left(-j\phi_{by}\right)\partial_z A_{by}\\
&\quad+k_0^2\sigma\left[A_{ax}F_{ax}\exp\left(-j\phi_{ax}\right)+A_{bx}F_{bx}\exp\left(-j\phi_{bx}\right)\right]\\
&\quad+k_0^2\gamma\exp\left(-\alpha z\right)\left\{\begin{array}{l}
A_{ay}\left|A_{ay}\right|^2F_{ay}^3\exp\left(-j\phi_{ay}\right)\\
+A_{by}\left|A_{by}\right|^2F_{by}^3\exp\left(-j\phi_{by}\right)\\
+2\left|A_{ay}\right|^2A_{by}F_{ay}^2F_{by}\exp\left(-j\phi_{by}\right)\\
+2A_{ay}\left|A_{by}\right|^2F_{ay}F_{by}^2\exp\left(-j\phi_{ay}\right)\\
+A_{ay}^2A_{by}^*F_{ay}^2F_{by}\exp\left[-j\left(2\phi_{ay}-\phi_{by}\right)\right]\\
+A_{ay}^*A_{by}^2F_{ay}F_{by}^2\exp\left[-j\left(2\phi_{by}-\phi_{ay}\right)\right]
\end{array}\right\}\\
&\quad+\frac{2}{3}k_0^2\gamma\exp\left(-\alpha z\right)\left\{\begin{array}{l}
A_{ay}\left|A_{ax}\right|^2F_{ay}F_{ax}^2\exp\left(-j\phi_{ay}\right)\\
+A_{by}\left|A_{bx}\right|^2F_{by}F_{bx}^2\exp\left(-j\phi_{by}\right)\\
+\left|A_{ax}\right|^2A_{by}F_{ax}^2F_{by}\exp\left(-j\phi_{by}\right)\\
+A_{ay}\left|A_{bx}\right|^2F_{ay}F_{bx}^2\exp\left(-j\phi_{ay}\right)\\
+A_{ay}A_{ax}^*A_{bx}F_{ay}F_{ax}F_{bx}\exp\left[-j\left(\phi_{ay}-\phi_{ax}+\phi_{bx}\right)\right]\\
+A_{ax}A_{by}A_{bx}^*F_{ax}F_{by}F_{bx}\exp\left[-j\left(\phi_{ax}+\phi_{by}-\phi_{bx}\right)\right]\\
+A_{ay}A_{ax}A_{bx}^*F_{ay}F_{ax}F_{bx}\exp\left[-j\left(\phi_{ay}+\phi_{ax}-\phi_{bx}\right)\right]\\
+A_{ax}^*A_{by}A_{bx}F_{ax}F_{by}F_{bx}\exp\left[-j\left(\phi_{by}+\phi_{bx}-\phi_{ax}\right)\right]
\end{array}\right\}\\
&\quad+\frac{1}{3}k_0^2\gamma\exp\left(-\alpha z\right)\left\{\begin{array}{l}
A_{ay}^*A_{ax}^2F_{ay}F_{ax}^2\exp\left[-j\left(2\phi_{ax}-\phi_{ay}\right)\right]\\
+A_{ax}^2A_{by}^*F_{ax}^2F_{by}\exp\left[-j\left(2\phi_{ax}-\phi_{by}\right)\right]\\
+A_{ay}^*A_{bx}^2F_{ay}F_{bx}^2\exp\left[-j\left(2\phi_{bx}-\phi_{ay}\right)\right]\\
+A_{by}^*A_{bx}^2F_{by}F_{bx}^2\exp\left[-j\left(2\phi_{bx}-\phi_{by}\right)\right]\\
+2A_{ay}^*A_{ax}A_{bx}F_{ay}F_{ax}F_{bx}\exp\left[-j\left(\phi_{ax}+\phi_{bx}-\phi_{ay}\right)\right]\\
+2A_{ax}A_{by}^*A_{bx}F_{ax}F_{by}F_{bx}\exp\left[-j\left(\phi_{ax}-\phi_{by}+\phi_{bx}\right)\right]
\end{array}\right\}=0.
\end{aligned}
\tag{3.2.23}
$$

The coupled local-mode equations can be found by multiplying Eqs. (3.2.22) and (3.2.23) by the corresponding terms $F_{mi}\exp(j\phi_{mi})$ and integrating in an infinite cross-sectional area of the MCF. As an example, the coupled local-mode equation modeling the mode-coupling from the PCMs ay, bx and by to the PCM ax is found to be:

$$
\begin{aligned}
j\left[1-j\alpha/\left(2\beta_{ax}^{(\mathrm{eq})}\right)\right]\partial_z A_{ax} &= c_{ax}A_{ax} + m_{ax,ay}\exp\left(-j\Delta\phi_{ay,ax}\right)A_{ay} + \eta_{ax,by}\exp\left(-j\Delta\phi_{by,ax}\right)A_{by} \\
&+\exp\left(-j\Delta\phi_{bx,ax}\right)\left\{\kappa_{ax,bx}-\left[j+\alpha/\left(2\beta_{bx}^{(\mathrm{eq})}\right)\right]\chi_{ax,bx}\partial_z\right\}A_{bx} \\
&+\exp\left(-\alpha z\right)\left\{\begin{array}{l}
q_{ax}^{(1)}\left|A_{ax}\right|^2 A_{ax} + q_{ax,bx}^{(2)}\left[2A_{ax}\left|A_{bx}\right|^2 + A_{ax}^{*}A_{bx}^{2}\exp\left(-j2\Delta\phi_{bx,ax}\right)\right] \\
+q_{ax,bx}^{(3)}\left[2\left|A_{ax}\right|^2 A_{bx}\exp\left(-j\Delta\phi_{bx,ax}\right) + A_{ax}^{2}A_{bx}^{*}\exp\left(j\Delta\phi_{bx,ax}\right)\right] \\
+q_{ax,bx}^{(4)}\left|A_{bx}\right|^2 A_{bx}\exp\left(-j\Delta\phi_{bx,ax}\right) \\
+g_{ax,ay}^{(1)}\left[\frac{2}{3}A_{ax}\left|A_{ay}\right|^2 + \frac{1}{3}A_{ax}^{*}A_{ay}^{2}\exp\left(-j2\Delta\phi_{ay,ax}\right)\right] \\
+g_{ax,b}^{(2)}\left[\begin{array}{l}\frac{2}{3}A_{bx}\left|A_{by}\right|^2\exp\left(-j\Delta\phi_{bx,ax}\right) \\ +\frac{1}{3}A_{bx}^{*}A_{by}^{2}\exp\left(-j\Delta\phi_{by,ax}\right)\exp\left(-j\Delta\phi_{by,bx}\right)\end{array}\right] \\
+g_{ax,b}^{(3)}\left[\frac{2}{3}A_{ax}\left|A_{by}\right|^2 + \frac{1}{3}A_{ax}^{*}A_{by}^{2}\exp\left(-j2\Delta\phi_{by,ax}\right)\right] \\
+g_{ax,b}^{(4)}\left[\begin{array}{l}\frac{4}{3}A_{ay}\exp\left(-j\Delta\phi_{ay,ax}\right)\mathrm{Re}\left\{A_{bx}A_{by}^{*}\exp\left(-j\Delta\phi_{bx,by}\right)\right\} \\ +\frac{2}{3}A_{ay}^{*}A_{bx}A_{by}\exp\left(-j\Delta\phi_{bx,ax}\right)\exp\left(-j\Delta\phi_{by,ay}\right)\end{array}\right] \\
+g_{ax,b}^{(5)}\left[\begin{array}{l}\frac{2}{3}\left|A_{ay}\right|^2 A_{bx}\exp\left(-j\Delta\phi_{bx,ax}\right) \\ +\frac{1}{3}A_{ay}^{2}A_{bx}^{*}\exp\left(-j\Delta\phi_{ay,ax}\right)\exp\left(-j\Delta\phi_{ay,bx}\right)\end{array}\right] \\
+g_{ax,b}^{(6)}\left[\begin{array}{l}\frac{4}{3}A_{ax}\mathrm{Re}\left\{A_{ay}^{*}A_{by}\exp\left(-j\Delta\phi_{by,ay}\right)\right\} \\ +\frac{2}{3}A_{ax}^{*}A_{ay}A_{by}\exp\left(-j\Delta\phi_{ay,ax}\right)\exp\left(-j\Delta\phi_{by,ax}\right)\end{array}\right]
\end{array}\right\},
\end{aligned}
\tag{3.2.24}
$$

where c_{ax}, $m_{ax,ay}$, $\eta_{ax,by}$, $\kappa_{ax,bx}$, $\chi_{ax,bx}$, $q_{ax}^{(1)}$, $q_{ax,bx}^{(2,3,4)}$, $g_{ax,ay}^{(1)}$ and $g_{ax,b}^{(2,\ldots,6)}$ are the mode-coupling coefficients (MCCs) defined in the next section; and the phase-mismatching functions $\Delta\phi_{mi,nj}$ are defined as $\Delta\phi_{mi,nj} := \phi_{mi} - \phi_{nj}$, $\forall\,(mi,nj) \in \{ax, ay, bx, by\}^2$.

The theoretical model is completed by three additional coupled equations which can be obtained just by exchanging the corresponding subindexes in Eq. (3.2.24). Remarkably, the coupled local-mode equations allow us to describe accurately the linear and nonlinear crosstalk among the PCMs by including the longitudinal and temporal MCF birefringent effects in the MCCs and phase-mismatching functions. Despite the fact that these equations have complicated expressions, we will be able to simplify them by analyzing the predominant MCCs.

3.2.4 Mode-coupling coefficients

The linear MCCs are defined as (all integrals apply over an infinite cross-sectional area):

$$\chi_{ax,bx}\left(z,\omega_0;t\right) := \frac{\beta_{bx}^{(\mathrm{eq})}}{\beta_{ax}^{(\mathrm{eq})}N_{ax}}\iint F_{bx}F_{ax}\mathrm{d}x\mathrm{d}y; \tag{3.2.25}$$

$$c_{ax}\left(z,\omega_0;t\right) := \frac{k_0^2}{2\beta_{ax}^{(\mathrm{eq})}N_{ax}}\iint \Delta\varepsilon_{\mathrm{r},bx}F_{ax}^2\mathrm{d}x\mathrm{d}y; \tag{3.2.26}$$

$$m_{ax,ay}\left(z,\omega_0;t\right) := \frac{k_0^2}{2\beta_{ax}^{(\mathrm{eq})}N_{ax}}\iint \sigma F_{ay}F_{ax}\mathrm{d}x\mathrm{d}y; \tag{3.2.27}$$

$$\kappa_{ax,bx}\left(z,\omega_0;t\right) := \frac{k_0^2}{2\beta_{ax}^{(\mathrm{eq})}N_{ax}}\iint \Delta\varepsilon_{\mathrm{r},ax}F_{bx}F_{ax}\mathrm{d}x\mathrm{d}y; \tag{3.2.28}$$

$$\eta_{ax,by}\left(z,\omega_0;t\right) := \frac{k_0^2}{2\beta_{ax}^{(\mathrm{eq})}N_{ax}}\iint \sigma F_{by}F_{ax}\mathrm{d}x\mathrm{d}y, \tag{3.2.29}$$

and the nonlinear MCCs:

$$q_{ax}^{(1)}\left(z,\omega_0;t\right) := \frac{k_0^2}{2\beta_{ax}^{(\mathrm{eq})}N_{ax}} \iint \gamma F_{ax}^4 \mathrm{d}x\mathrm{d}y; \tag{3.2.30}$$

$$q_{ax,bx}^{(2)}\left(z,\omega_0;t\right) := \frac{k_0^2}{2\beta_{ax}^{(\mathrm{eq})}N_{ax}} \iint \gamma F_{bx}^2 F_{ax}^2 \mathrm{d}x\mathrm{d}y; \tag{3.2.31}$$

$$q_{ax,bx}^{(3)}\left(z,\omega_0;t\right) := \frac{k_0^2}{2\beta_{ax}^{(\mathrm{eq})}N_{ax}} \iint \gamma F_{bx} F_{ax}^3 \mathrm{d}x\mathrm{d}y; \tag{3.2.32}$$

$$q_{ax,bx}^{(4)}\left(z,\omega_0;t\right) := \frac{k_0^2}{2\beta_{ax}^{(\mathrm{eq})}N_{ax}} \iint \gamma F_{bx}^3 F_{ax} \mathrm{d}x\mathrm{d}y; \tag{3.2.33}$$

$$g_{ax,ay}^{(1)}\left(z,\omega_0;t\right) := \frac{k_0^2}{2\beta_{ax}^{(\mathrm{eq})}N_{ax}} \iint \gamma F_{ay}^2 F_{ax}^2 \mathrm{d}x\mathrm{d}y; \tag{3.2.34}$$

$$g_{ax,b}^{(2)}\left(z,\omega_0;t\right) := \frac{k_0^2}{2\beta_{ax}^{(\mathrm{eq})}N_{ax}} \iint \gamma F_{bx} F_{by}^2 F_{ax} \mathrm{d}x\mathrm{d}y; \tag{3.2.35}$$

$$g_{ax,b}^{(3)}\left(z,\omega_0;t\right) := \frac{k_0^2}{2\beta_{ax}^{(\mathrm{eq})}N_{ax}} \iint \gamma F_{by}^2 F_{ax}^2 \mathrm{d}x\mathrm{d}y; \tag{3.2.36}$$

$$g_{ax,b}^{(4)}\left(z,\omega_0;t\right) := \frac{k_0^2}{2\beta_{ax}^{(\mathrm{eq})}N_{ax}} \iint \gamma F_{ay} F_{bx} F_{by} F_{ax} \mathrm{d}x\mathrm{d}y; \tag{3.2.37}$$

$$g_{ax,b}^{(5)}\left(z,\omega_0;t\right) := \frac{k_0^2}{2\beta_{ax}^{(\mathrm{eq})}N_{ax}} \iint \gamma F_{ay}^2 F_{bx} F_{ax} \mathrm{d}x\mathrm{d}y; \tag{3.2.38}$$

$$g_{ax,b}^{(6)}\left(z,\omega_0;t\right) := \frac{k_0^2}{2\beta_{ax}^{(\mathrm{eq})}N_{ax}} \iint \gamma F_{ay} F_{by} F_{ax}^2 \mathrm{d}x\mathrm{d}y, \tag{3.2.39}$$

with $N_{ax}\left(z,\omega_0;t\right) := \iint F_{ax}^2 \mathrm{d}x\mathrm{d}y$. Note that the definition of the nonlinear MCCs $g^{(1,\ldots,6)}$ is different from the one that we reported in [131].

A significant reduction of the complexity of Eq. (3.2.24) can be performed by analyzing the predominant MCCs. The linear MCCs $\chi_{ax,bx}$, c_{ax} and $\kappa_{ax,bx}$ are identical to the linear MCCs of Chapter 2 [Eqs. (2.2.13)-(2.2.15)] when omitting polarization effects. In such a scenario, it was observed that $\chi_{ax,bx}$ can be neglected, $\kappa_{ax,bx}$ is found to be the predominant linear MCC and c_{ax} should only be retained when the core-to-core distance d_{ab} is lower than three times the core radius R_0 (assuming the same value in both cores). However, two new linear MCCs appear when including polarization effects, $m_{ax,ay}$ and $\eta_{ax,by}$, accounting for the iC-XT and XIC-XT, respectively. In order to investigate whether these coefficients should be retained in the coupled local-mode equations, we compare the ratios $m_{ax,ay}/\kappa_{ax,bx}$ and $\eta_{ax,by}/\kappa_{ax,bx}$ following a similar mathematical discussion as in Section 2.2.2.

To this end, let us assume a straight SI-SM-HO-LB-MCF[5] with a constant twist rate f_{T} and without temporal birefringence. In such circumstances, the ratios $m_{ax,ay}/\kappa_{ax,bx}$ and $\eta_{ax,by}/\kappa_{ax,bx}$ are found to be only longitudinal dependent and are maximized. In addition, as can be deduced from the ERIM detailed in the next section, $\left\langle n_{ai}^{(\mathrm{eq})}\left(\boldsymbol{r},\omega_0\right)\right\rangle \simeq \left\langle n_{bi}^{(\mathrm{eq})}\left(\boldsymbol{r},\omega_0\right)\right\rangle \equiv n_a$ and $F_{mx} \simeq F_{my}$ $\forall\left(i,m\right) \in \{x,y\}\times\{a,b\}$, where n_a is the material refractive index of core a at ω_0 and $\langle\ \rangle$ is the spatial average operator in the longitudinal direction. As a result, the spatial average of the aforementioned ratios can be calculated from Eqs. (3.2.27)-(3.2.29) using a similar derivation as in Appendix B2:

$$\left\langle \frac{m_{ax,ay}\left(z,\omega_0\right)}{\kappa_{ax,bx}\left(z,\omega_0\right)} \right\rangle \simeq \frac{\sigma_a}{2\left(n_a^2-n_{\mathrm{cl}}^2\right)} \frac{u_a\left[J_0^2\left(u_a\right)+J_1^2\left(u_a\right)\right]}{J_0\left(u_a\right)J_1\left(u_a\right)} \frac{K_0\left(w_b\right)}{K_0\left(w_b d_{ab}/R_0\right)}; \tag{3.2.40}$$

$$\left\langle \frac{\eta_{ax,by}\left(z,\omega_0\right)}{\kappa_{ax,bx}\left(z,\omega_0\right)} \right\rangle \simeq \frac{2\sigma_a}{n_a^2-n_{\mathrm{cl}}^2}, \tag{3.2.41}$$

[5] See Table 1.1 on page 14.

where $\sigma_a = \pi R_0 f_T n_a^4 |p_{11} - p_{12}|$ is a constant value in this case (see next section for more details), p_{11} and p_{12} are components of the photo-elastic tensor ($|p_{11} - p_{12}| = 0.149$) [163], n_{cl} is the material refractive index of the cladding at ω_0, and u_a and w_b are modal parameters given by Eqs. (2.2.20) and (2.2.21). As an example, the ratios given by the above equations are calculated with $R_0 = 4$ μm, $n_{a(b)} = 1.452$, $n_{cl} = 1.444$ and $\lambda_0 = 1550$ nm.

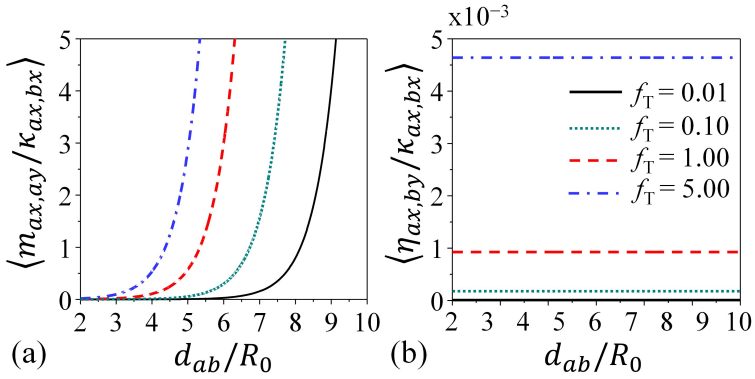

Figure 3.2. Comparison of the linear mode-coupling coefficients (MCCs) $m_{ax,ay}$ and $\eta_{ax,by}$ with $\kappa_{ax,bx}$ using the spatial average ratios given by Eqs. (3.2.40) and (3.2.41) for different values of d_{ab}/R_0 and f_T (in turns/m). (a) $\langle m_{ax,ay}/\kappa_{ax,bx}\rangle$ and (b) $\langle \eta_{ax,by}/\kappa_{ax,bx}\rangle$ [131].

Figure 3.2 shows the behavior of the calculated ratios for different values of d_{ab}/R_0 and f_T (in turns/m). As can be seen from Fig. 3.2(a), the MCC $m_{ax,ay}$ should be maintained in the coupled local-mode equations, since this MCC is usually of the same order of magnitude or higher than $\kappa_{ax,bx}$. As expected, the higher the twist rate value, the higher the mode-coupling between the x and y polarizations in a given core. Nonetheless, as depicted in Fig. 3.2(b), the linear MCC $\eta_{ax,by}$ can be neglected for any value of d_{ab}. Remarkably, the XIC-XT will depend directly on the iC-XT of both cores, as will be verified in the next sections. These conclusions are found to be identical when repeating this analysis in heterogeneous MCFs.

On the other hand, it should be noted that the nonlinear MCCs $q_{ax}^{(1)}$ and $g_{ax,ay}^{(1)}$ account for the nonlinear self-coupling in core a, and $q_{ax,bx}^{(2,3,4)}$ and $g_{ax,b}^{(2,\ldots,6)}$ describe the nonlinear cross-coupling effects between cores a and b. As was demonstrated in Chapter 2 (see Sections 2.2.2 and 2.3), these nonlinear cross-coupling effects can be neglected when $d_{ab} > 3R_0$.

Consequently, assuming an N-core MCF with a core-to-core distance satisfying this condition, performing a transformation of the complex envelopes of the form $A_{mi}(z;t) \equiv \mathcal{A}_{mi}(z;t)\exp(\alpha z/2)$, and taking into account that $\alpha \ll \beta_{mi}^{(eq)}$; Eq. (3.2.24) becomes:

$$j\left(\partial_z + \frac{\alpha}{2}\right)\mathcal{A}_{ax} = m_{ax,ay}\exp\left(-j\Delta\phi_{ay,ax}\right)\mathcal{A}_{ay} + \sum_{m\neq a}^{N}\kappa_{ax,mx}\exp\left(-j\Delta\phi_{mx,ax}\right)\mathcal{A}_{mx} + \left(q_{ax}^{(1)}|\mathcal{A}_{ax}|^2 + \frac{2}{3}g_{ax,ay}^{(1)}|\mathcal{A}_{ay}|^2\right)\mathcal{A}_{ax} + \frac{1}{3}g_{ax,ay}^{(1)}\exp\left(-j2\Delta\phi_{ay,ax}\right)\mathcal{A}_{ax}^{*}\mathcal{A}_{ay}^{2}. \tag{3.2.42}$$

Once we have derived the CLMT, it is natural to ask if we can infer from Eq. (3.2.42) a closed-form expression to estimate the mean of the different crosstalk types, in the same way as the discussion performed in Chapter 2 for the linear and nonlinear IC-XT without polarization effects. The answer is investigated in Appendix B3, on page 88. Now, let us describe the numerical method required to simulate the CLMT.

3.3 Numerical method: equivalent refractive index model

The numerical simulation of the coupled local-mode equations requires to complete the ERIM of Chapter 2 by including polarization effects and time-varying fiber perturbations. In this way, the equivalent refractive index $n_{mi}^{(\mathrm{eq})}$ of each PCM mi [defined in Eq. (3.2.18)] will allow us to calculate the phase functions and the linear and nonlinear MCCs of Eq. (3.2.42) by considering both longitudinal and temporal MCF perturbations. As a byproduct, we will be able to analyze the longitudinal and temporal behavior of the crosstalk between the different PCMs of an MCF. Figure 3.3 depicts the numerical model, detailed hereafter:

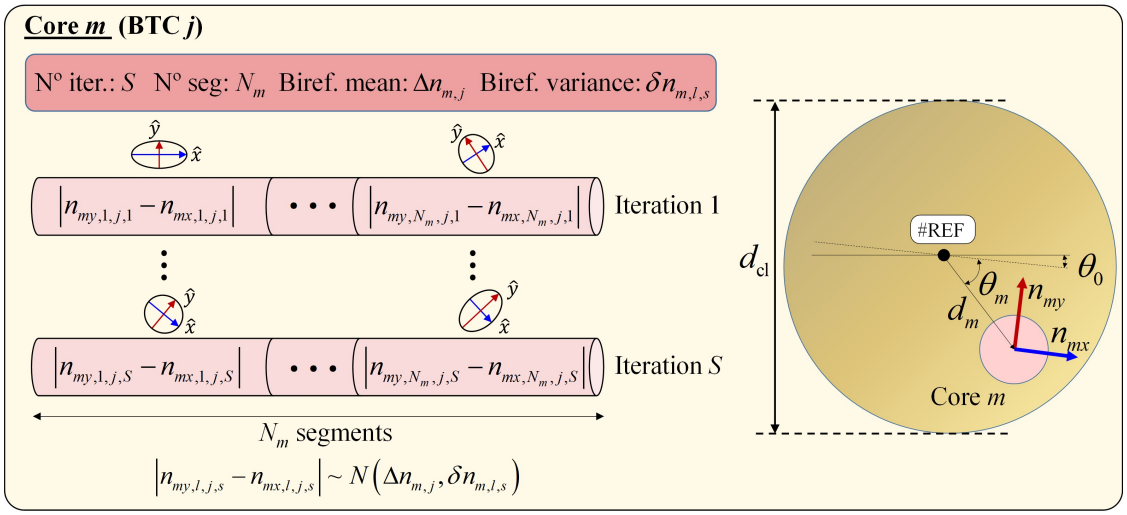

Figure 3.3. Equivalent refractive index model of the CLMT [131].

- Firstly, the MCF length is assumed to be composed by different birefringent segments in each core. Each birefringent segment of a given core m is denoted by the subindex l, with $l \in \{1, \ldots, N_m\}$. The orientation of the local principal axes between adjacent segments will be changed via the σ_m function [see below Eq. (3.3.12)].

- Secondly, we should define the time scale over which the linear birefringence of the MCF can be assumed to be constant, i.e., the *birefringence temporal change* (BTC) unit. Specifically, the BTC unit should be higher than $2\pi/\omega_0$ in this model. In our case, we will consider a BTC unit of one day, although it could be of the order of several minutes according to the experimental observations reported in [158]. The numeration of each BTC will be described by the subindex $j \in \mathbb{N}$.

- Thirdly, in contrast to Chapter 2, we now assume that the bending radius (R_{B}) and twist rate (f_{T}) can fluctuate, not only along the z-axis, but also in time due to the slight changes induced by the floor vibrations. Hence, we have now two random processes with two variables each one, $R_{\mathrm{B}}(z;t)$ and $f_{\mathrm{T}}(z;t)$, which will be assumed ergodic and strict-sense stationary in z and t for simplicity.[6] In such circumstances, the temporal changes of R_{B} and f_{T} along the fiber length can be modeled by a different iteration s of a Monte Carlo simulation ($s \in \{1, \ldots S\}$). Interestingly, a Monte Carlo simulation is not far removed from the reality: the floor vibrations induce slight local changes in R_{B} and f_{T} along the fiber length, which corresponds in particular to different Monte Carlo iterations. Thus, the random processes

[6] This assumption should be specifically revisited in access networks, where R_{B} and f_{T} may have different random distributions in different z points. Furthermore, an external environmental change may also induce a different random distribution of R_{B} and f_{T} in different time intervals. However, our assumption is in line with our experimental work and allows us to facilitate the comprehension of the main results of this chapter.

$R_{\mathrm{B}}(z;t)$ and $f_{\mathrm{T}}(z;t)$ can be modeled in a given l-th segment and s-th iteration by the random variables $R_{\mathrm{B},l,s}$ and $f_{\mathrm{T},l,s}$.[7] Concretely, the Monte Carlo method will be of great utility to analyze the temporal evolution of the crosstalk mean between PCMs in different BTCs.

- Along these same lines, note that there are two different time scales (both higher than $2\pi/\omega_0$) related to the temporal MCF perturbations: slower than the BTC unit (denoted by the subindex j) and faster than the BTC unit (denoted by the subindex s). In general, the temporal fluctuations of the former time scale are induced by temperature changes of the optical medium and the latter are induced by floor vibrations (see below Section 3.5).

- Moreover, a fundamental remark which has not been observed in the IC-XT literature about the bending radius distribution should be discussed. As detailed in Appendix C3 (see page 92), the fiber twisting may induce a bending effect in each core (except maybe when the core is located at the MCF center). As can be seen from Fig. C3.2, in highly-twisted MCFs ($\overline{f}_{\mathrm{T}} \geq 6$ turns/m), the core bending effect induced by the fiber twisting ($R_{\mathrm{BT},m}$) should also be included in $n_{mi}^{(\mathrm{eq})}$. However, the effects of $R_{\mathrm{BT},m}$ on $n_{mi}^{(\mathrm{eq})}$ can be neglected when $\overline{f}_{\mathrm{T}} < 6$ turns/m. In general, a reduced average value of the twist rate allows us to minimize the probability of damaging the MCF. In this vein, we can safely assume that $\overline{f}_{\mathrm{T}} < 6$ turns/m in future real deployed MCF systems. For this reason, we will not consider $R_{\mathrm{BT},m}$ in our numerical model.

All in all, the phase function ϕ_{mi} can be calculated as a function of $n_{mi}^{(\mathrm{eq})}$ as follows [see Eq. (3.2.4)]:

$$\phi_{mi}(z,\omega_0;t) = \int_0^z \beta_{mi}^{(\mathrm{eq})}(\xi,\omega_0;t)\,\mathrm{d}\xi = k_0 \int_0^z n_{mi}^{(\mathrm{eq})}(\xi,\omega_0;t)\,\mathrm{d}\xi; \tag{3.3.1}$$

$$n_{mi}^{(\mathrm{eq})}(z,\omega_0;t) \simeq n_{mi}(z,\omega_0;t)\left[1+\frac{d_m}{R_{\mathrm{B}}(z;t)}\cos\left(2\pi f_{\mathrm{T}}(z;t)\,z+\theta_0+\theta_m\right)\right], \tag{3.3.2}$$

where $n_{mi}(z,\omega_0;t)$ describes the temporal fluctuation of the intrinsic linear birefringence along the MCF length; θ_0 is the offset of the twist angle of the MCF reference axis at $z=0$; θ_m is the offset of the twist angle of the core m measured from the MCF reference axis; and d_m is the Euclidean distance of the core m to the MCF center (see Fig. 3.3).

The above expressions can be rewritten in the l-th birefringent segment, j-th BTC and s-th iteration using the random variables and random processes detailed before:

$$\phi_{mi,l,j,s}(z,\omega_0) = \int_{z_l}^z \beta_{mi,l,j,s}^{(\mathrm{eq})}(\xi,\omega_0)\,\mathrm{d}\xi = k_0 \int_{z_l}^z n_{mi,l,j,s}^{(\mathrm{eq})}(\xi,\omega_0)\,\mathrm{d}\xi; \tag{3.3.3}$$

$$n_{mi,l,j,s}^{(\mathrm{eq})}(z,\omega_0) \simeq n_{mi,l,j,s}(\omega_0)\left[1+\frac{d_m}{R_{\mathrm{B},l,s}}\cos\left(2\pi f_{\mathrm{T},l,s} z+\theta_0+\theta_m\right)\right], \tag{3.3.4}$$

where $n_{mi,l,j,s}(\omega_0)$ is the random variable which describes the temporal fluctuation of the intrinsic linear birefringence in the l-th birefringent segment. In particular, the intrinsic linear birefringence in the l-th birefringent segment, j-th BTC and s-th iteration is given by the random variable $|n_{my,l,j,s}(\omega_0) - n_{mx,l,j,s}(\omega_0)|$, calculated from a Gaussian random process $\mathrm{N}\left(\mu(\omega_0;t),\sigma^2(z,\omega_0;t)\right)$ along the MCF length. The mean $\mu(\omega_0;t) = \Delta n_{m,j}(\omega_0)$ is the longitudinal average value of the intrinsic linear birefringence in core m the j-th BTC at ω_0. The value of $\Delta n_{m,j}(\omega_0)$ can be measured in each BTC by using the wavelength sweeping method (see Section 3.5 for more details). Typically, $\Delta n_{m,j}(\omega_0) \sim 10^{-7}$ in LB-cores and $\Delta n_{m,j}(\omega_0) \sim 10^{-4}$ in HB-cores. The variance $\sigma^2(z,\omega_0;t) = \delta n_{m,l,s}(\omega_0)$ includes the photo-elastic effect in the l-th segment [164]:

$$\delta n_{m,l,s}(\omega_0) \simeq \xi + 0.011 n_m^3 d_{\mathrm{cl}}^2 / R_{\mathrm{B},l,s}^2, \tag{3.3.5}$$

[7] Consequently, we can expect that the spatial IC-XT distribution measured using the wavelength sweeping method (see Chapter 2) will be in good agreement with the temporal IC-XT distribution experimentally measured at $z=L$ with constant temperature conditions (see Section 3.5). Note that both measurement techniques are in complete analogy with a Monte Carlo simulation. In the former case, each spectral sample modifies the value of the optical carrier restarting the random process $\phi_{mi}^{(\mathrm{eq})}(z,\omega_0;t)$, and in the latter case, the floor vibrations restart the same random process by changing the value of the random variables $R_{\mathrm{B},l,s}$ and $f_{\mathrm{T},l,s}$.

where $\xi = 10^{-8}$, $d_{\rm cl}$ is the cladding diameter, $n_m := (n_{mx} + n_{my})/2$, and n_{mx} and n_{my} are the principal refractive indexes in core m at ω_0.[8] In LB-cores, $n_m = n_{mx} = n_{my}$. The parameter ξ is included in the ERIM to describe the intrinsic longitudinal fluctuations of the linear birefringence between adjacent segments, induced by the intrinsic manufacture imperfections. Finally, the value $n_{mi,l,j,s}(\omega_0)$ is calculated as:

$$n_{mi,l,j,s}(\omega_0) \sim n_{mi}(\omega_0) \pm \frac{1}{2}\mathrm{N}\left(\Delta n_{m,j}(\omega_0), \delta n_{m,l,s}(\omega_0)\right), \tag{3.3.6}$$

with '+' if $i = y$ and '−' if $i = x$.

In spite of the fact that the above expressions assume step-index profiles, in weakly-guiding GI-MCFs we can replace n_{mi} by $\max\{n_{mi}(r)\}$ in Eq. (3.3.6). Moreover, although we have considered $R_{\rm B}(z;t)$ and $f_{\rm T}(z;t)$ as strict-sense stationary random processes in both variables, in a real deployed MCF system the environmental factors could induce longitudinal and temporal changes in their statistical distribution. In such a case, we should replace $R_{{\rm B},l,s}$ and $f_{{\rm T},l,s}$ by the random variables $R_{{\rm B},l,j,s}$ and $f_{{\rm T},l,j,s}$, respectively. These new random variables should be modeled by different distributions when changing the value of l and j, according to the real external conditions of the MCF system.

On the other hand, the mode-coupling coefficients can be calculated numerically by using Eqs. (3.2.25)-(3.2.39). To this end, the transversal local eigenfunction $F_{mi}(x, y, \omega_0; z, t)$ can be calculated by using the closed-form expressions detailed in [32] for the LP_{01} mode along with the ERIM. More specifically, using a local polar coordinate system (r, φ, z) in the core m, F_{mi} can be written in the l-th birefringent segment, j-th BTC and s-th iteration as:

$$F_{mi,l,j,s}(r, \omega_0; z) = \begin{cases} J_0\left(\frac{u_{mi,l,j,s}(z,\omega_0)}{R_{0,m}} r\right) / J_0\left(u_{mi,l,j,s}(z,\omega_0)\right); & r \le R_{0,m} \\ K_0\left(\frac{w_{mi,l,j,s}(z,\omega_0)}{R_{0,m}} r\right) / K_0\left(w_{mi,l,j,s}(z,\omega_0)\right); & r > R_{0,m} \end{cases}, \tag{3.3.7}$$

where $R_{0,m}$ is the radius[9] of core m and $u_{mi,l,j,s}(z,\omega_0)$ and $w_{mi,l,j,s}(z,\omega_0)$ are random processes accounting for the classical modal parameters u and w of the LP_{01} mode in core m and polarization axis i:

$$u_{mi,l,j,s}(z,\omega_0) = \left(1+\sqrt{2}\right) V_{mi,l,j,s}(z,\omega_0) \Big/ \left[1 + \left(4 + V^4_{mi,l,j,s}(z,\omega_0)\right)^{1/4}\right]; \tag{3.3.8}$$

$$w_{mi,l,j,s}(z,\omega_0) = \sqrt{V^2_{mi,l,j,s}(z,\omega_0) - u^2_{mi,l,j,s}(z,\omega_0)}, \tag{3.3.9}$$

where $V_{mi,l,j,s}(z,\omega_0)$ is the random process modeling the normalized frequency $V_{mi}(z,\omega_0;t)$:

$$V_{mi,l,j,s}(z,\omega_0) = \frac{\omega_0}{c_0} R_{0,m} C_{{\rm F},m} \sqrt{\left(n^{(\rm eq)}_{mi,l,j,s}(z,\omega_0)\right)^2 - n^2_{\rm cl}}. \tag{3.3.10}$$

In the last equation, $n_{\rm cl}$ is the cladding refractive index and $C_{{\rm F},m}$ is an auxiliary parameter referred to as the correction factor of core m, included in Eq. (3.3.10) to calculate the correct value of the normalized frequency when using the nominal value of $R_{0,m}$. In real MCFs, the core radius has longitudinal variations along the fiber length due to manufacturing imperfections. Hence, the average value of $R_{0,m}$ can be found to be different from the nominal value indicated in the MCF datasheet. In order to consider these core radius imperfections, the constant $C_{{\rm F},m}$ should be calculated by using the cut-off wavelength of each core ($\lambda_{{\rm C},m}$) as a reference:

$$C_{{\rm F},m} = \frac{2.405\lambda_{{\rm C},m}}{2\pi R_{0,m}\sqrt{n^2_m - n^2_{\rm cl}}}. \tag{3.3.11}$$

[8] Actually, we should use the *effective* principal refractive indexes $n_{{\rm eff},mi}$ instead of n_{mi}. However, we approximate $n_{{\rm eff},mi} \simeq n_{mi}$ in weakly-guiding SM-MCFs with $V_{mi} \sim 2$ to simplify the calculations. This approximation should be revisited in the multi-mode regime.

[9] In elliptical cores, $R_{0,m} = (R_{0,mx} + R_{0,my})/2$.

In our case, the correction factor is found to be $C_{\mathrm{F},m} \simeq 0.9$ when assuming $\lambda_{\mathrm{C},m} = 1410$ nm, $R_{0,m} = 4$ μm, $n_m = 1.452$ and $n_{\mathrm{cl}} = 1.444$ according to the datasheet of the commercial MCF Fibercore SM-4C1500(8.0/125). Using Eqs. (3.3.7)-(3.3.11) it is straightforward to verify that $\partial_z F_{mi} \simeq \partial_z^2 F_{mi} \simeq 0$ in $\delta z \sim \lambda_m$ for usual average values of f_{T} and R_{B} in laboratory MCF transmissions [45–55], in line with our initial assumptions indicated before in Eq. (3.2.20).

An additional fundamental remark should be made from Fig. 3.3. As mentioned before, the local orientation of the principal axes fluctuates between adjacent birefringent segments. In particular, this is modeled through the longitudinal dependence of the first-order susceptibility tensor $\chi_{ij}^{(1)}$. The diagonal terms are modified when varying $n_{mi}^{(\mathrm{eq})}$, and the off-diagonal terms are given by the σ function [Eq. (3.2.19)], which can be calculated in a given core m as [165]:

$$\sigma_m\left(\boldsymbol{r},\omega_0;t\right) = \pi R_{0,m} f_{\mathrm{T}}\left(z;t\right) n_m^4 \left|p_{11}-p_{12}\right|, \tag{3.3.12}$$

where p_{11} and p_{12} are components of the photo-elastic tensor ($p_{12}-p_{11}=0.149$ [163]). As a result, the orientation of the principal axes of each birefringent segment is changed as a consequence of the longitudinal fluctuations of the twist rate. For short MCF distances, a low variance of the f_{T} distribution seems to be sufficiently accurate to describe the MCF birefringence, as it is experimentally demonstrated in Section 3.5. Nonetheless, when large MCF distances of several kilometers are involved, the orientation of the principal axes should be adequately randomized by increasing the variance of the f_{T} distribution to include the intrinsic circular birefringence of each core, or combining this approach with additional strategies such as the phase plates [155,166,167]. In this fashion, the computational time may also be reduced by inserting phase plates between birefringent segments and reducing the variance of the f_{T} distribution.

In addition, in order to reduce the computational time of the numerical simulations in step-index MCFs, the MCCs of Eq. (3.2.42) can also be calculated by combining the closed-form expressions of Chapter 2 [Eqs. (2.2.15) and (2.2.16)] and the ERIM. Thus, the next random processes can be employed in each l-th birefringent segment, j-th BTC and s-th iteration to calculate the MCCs (we omit the independent variables due to space restrictions):

$$m_{ax,ay,l,j,s} \simeq \frac{\pi}{2} k_0 \left|p_{11}-p_{12}\right| f_{\mathrm{T},l,s} R_{0,a} \frac{n_a^4}{n_{ax,l,j,s}^{(\mathrm{eq})}}; \tag{3.3.13}$$

$$\kappa_{ax,bx,l,j,s} \simeq 2k_0 \frac{\left(n_{ax,l,j,s}^{(\mathrm{eq})} - n_{\mathrm{cl}}\right) J_0\left(u_{ax,l,j,s}\right) J_1\left(u_{ax,l,j,s}\right)}{u_{ax,l,j,s}\left[J_0^2\left(u_{ax,l,j,s}\right)+J_1^2\left(u_{ax,l,j,s}\right)\right]} \frac{K_0\left(w_{bx,l,j,s} d_{ab}/R_{0,b}\right)}{K_0\left(w_{bx,l,j,s}\right)}; \tag{3.3.14}$$

$$q_{ax,l,j,s}^{(1)} \simeq g_{ax,ay,l,j,s}^{(1)} \simeq \frac{1}{8} k_0 \frac{\gamma H_{ax,l,j,s}^2}{R_{0,a}^2 n_{ax,l,j,s}^{(\mathrm{eq})}} \frac{\left[1-\exp\left(-4R_{0,a}^2/H_{ax,l,j,s}^2\right)\right]}{J_0^2\left(u_{ax,l,j,s}\right)\left[J_0^2\left(u_{ax,l,j,s}\right)+J_1^2\left(u_{ax,l,j,s}\right)\right]}, \tag{3.3.15}$$

with $H_{ax,l,j,s} = R_{0,a}(0.65+1.619V_{ax,l,j,s}^{-3/2}+2.879V_{ax,l,j,s}^{-6})$ and $\gamma = 1.5\cdot 10^{-22}$ m^2/V^2 in silica fibers.

Finally, it should be taken into account that the Kerr effect could also be modeled in ϕ_{mi} as a modal perturbation of the LP_{01} mode by including the nonlinear changes of the material refractive index in $n_{mi}^{(\mathrm{eq})}$. Nonetheless, this approach could increase the computational time of the CLMT, since the nonlinear changes of the refractive index depend on the absolute square of the complex envelopes. It is a less time-consuming approach to model the nonlinear effects only by the nonlinear MCCs.

3.4 Numerical simulations

In this section, we study the impact of the temporal and longitudinal MCF birefringent effects on the mean of the iC-XT, DIC-XT and XIC-XT. The numerical analysis of the crosstalk between the PCMs was performed in line with the MCF simulation model detailed in the previous section. Two different 150-m homogeneous 2-core MCFs comprising LB and HB cores were considered in the numerical simulations, as depicted in Fig. 3.4. The number of simulated segments and the

temporal average value of $\Delta n_{m,j}$ is indicated in Table 3.1 by the parameter $\langle \Delta n_{m,j} \rangle$ for each core $m \in \{a, b\}$.[10] In order to compare the simulation results with the experimental measurements of the next section, we have considered a BTC unit of one day and we have assumed the cores a and b with different $\langle \Delta n_{m,j} \rangle$ and a different number of segments in the LB-MCF case. Furthermore, as we will also verify experimentally, the higher the value of $\langle \Delta n_{m,j} \rangle$ in a given core m, the lower the number of segments N_m that should be considered. Additional MCF parameters were employed: $d_{ab} = 36$ μm, $d_{\text{cl}} = 125$ μm, $R_{0,a} = R_{0,b} = 4$ μm, $n_a = n_b = 1.452$, $n_{\text{cl}} = 1.444$, $\theta_0 = 0$ and $\lambda_0 = 2\pi c_0/\omega_0 = 1550$ nm. In an HB-core m with elliptical shape, $R_{0,m}$ is the average value of the minor and major axis dimensions, $n_{mx} = n_m - 0.5\,\langle \Delta n_{m,j} \rangle$ and $n_{my} = n_m + 0.5\,\langle \Delta n_{m,j} \rangle$.

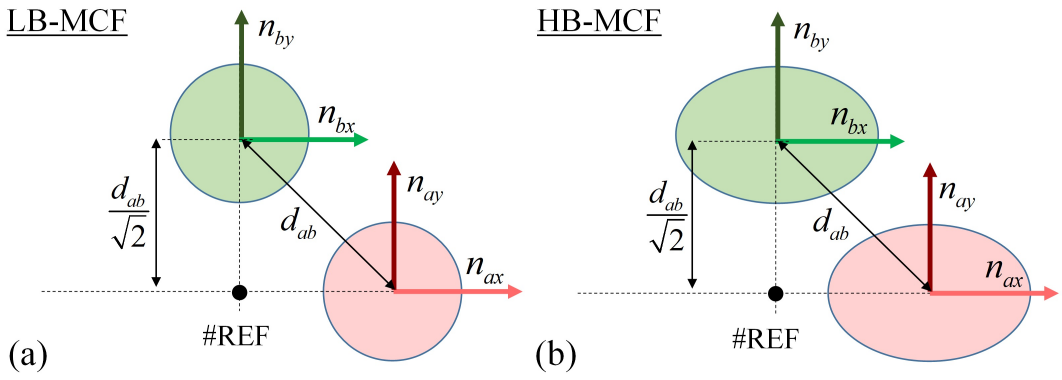

Figure 3.4. Schematic cross-sectional area of the simulated MCFs: (a) lowly-birefringent (LB) cores and (b) highly-birefringent (HB) cores [131].

2-core MCF parameters	Number of segments N_m		Linear birefringence average value $\langle \Delta n_{m,j} \rangle$	
Cores	LB	HB	LB	HB
a	8	1	$5{\cdot}10^{-7}$	$4{\cdot}10^{-4}$
b	6	1	$1.2{\cdot}10^{-6}$	$4{\cdot}10^{-4}$

Table 3.1. Number of birefringent segments (N_m) and longitudinal and temporal average value of the intrinsic linear birefringence ($\langle \Delta n_{m,j} \rangle$) of each core [131].

Figure 3.5 shows the simulation results of the iC-XT, DIC-XT and XIC-XT mean between the PCMs of the LB-MCF when varying $\Delta n_{a,j}$ and $\Delta n_{b,j}$ throughout a 10 BTCs, that is, in a 10-day period ($j \in \{1, \ldots, 10\}$). According to Chapter 2, the crosstalk mean from a PCM ξ to a PCM ν is defined as $\mu_{\nu,\xi}(t) := E\left[P_\nu(z = L; t)/P_\xi(z = L; t)\right]$, where L is the MCF length and $(\nu, \xi) \in \{ax, ay, bx, by\}^2$. The Monte Carlo method was performed over 100 iterations ($S = 100$) considering a constant bending radius of $R_{\text{B}} = 100$ cm. In addition, two different twist rate Gaussian distributions of $f_{\text{T}} = \text{N}(0.05, 0.02)$ and $f_{\text{T}} = \text{N}(1, 0.02)$ turns/m were simulated along the MCF length (i.e., the random variable $f_{\text{T},l,s}$ is calculated from these distributions in each l-th birefringent segment and s-th iteration). The simulation results are shown in Figs. 3.5(a1)-(c1) and Figs. 3.5(a2)-(c2) for each twist rate distribution, respectively (we denote the average value of the twist rate as $\overline{f}_{\text{T}}$). The temporal evolution of $\Delta n_{a,j}$ and $\Delta n_{b,j}$ (the longitudinal average value of the intrinsic linear birefringence of each core the j-th day) is assumed as a Gaussian distribution with mean $\langle \Delta n_{m,j} \rangle$ and variance 10^{-7} [see Figs. 3.5(a1) and (a2)]. Note that we have considered a similar temporal evolution of $\Delta n_{a,j}$ and $\Delta n_{b,j}$, in line with the experimental results of the next section.

[10] In this section, we will omit the dependence of the fiber parameters with ω_0 for the sake of simplicity.

As seen from Figs. 3.5(a1) and (a2), the higher the value of $\Delta n_{m,j}$, the lower the iC-XT mean observed in a given core m. The main reason for this comes from the higher phase-mismatching between the intra-core PCMs $\mathrm{LP}_{01,mx}$ and $\mathrm{LP}_{01,my}$. If $\Delta n_{m,j}$ increases, the phase-mismatching between both orthogonal polarizations increases reducing the iC-XT mean. Furthermore, increasing the value of $\overline{f}_{\mathrm{T}}$ from 0.05 to 1 turns/m, the iC-XT mean is also increased in both cores due to the increment of the circular birefringence, as it is observed when comparing the iC-XT levels in Figs. 3.5(b1) and (b2). In this second case, as the global birefringence (linear+circular) increases and prevails over the temporal fluctuation of $\Delta n_{m,j}$ ($\sim 10^{-7}$), the temporal fluctuation of the iC-XT mean decreases. This is confirmed in Fig. 3.5(b2) with a minimal excursion of 2 dB in the iC-XT mean.

On the other hand, as depicted in Figs. 3.5(c1) and (c2), the XIC-XT mean presents the same temporal evolution as the iC-XT mean. This indicates that the XIC-XT is mainly generated by the intra-core mode-coupling, as it was pointed out before. It should be noted the XIC-XT mean is lower than the DIC-XT mean when the iC-XT mean of both cores is lower than 0 dB. However, increasing $\overline{f}_{\mathrm{T}}$ from 0.05 to 1 turns/m, the iC-XT mean increases higher than 0 dB in the core a the 1st, 3rd,5th, 6th and 8th days. As a result, the XIC-XT mean is higher than the DIC-XT these days, as shown in Fig. 3.5(c2).

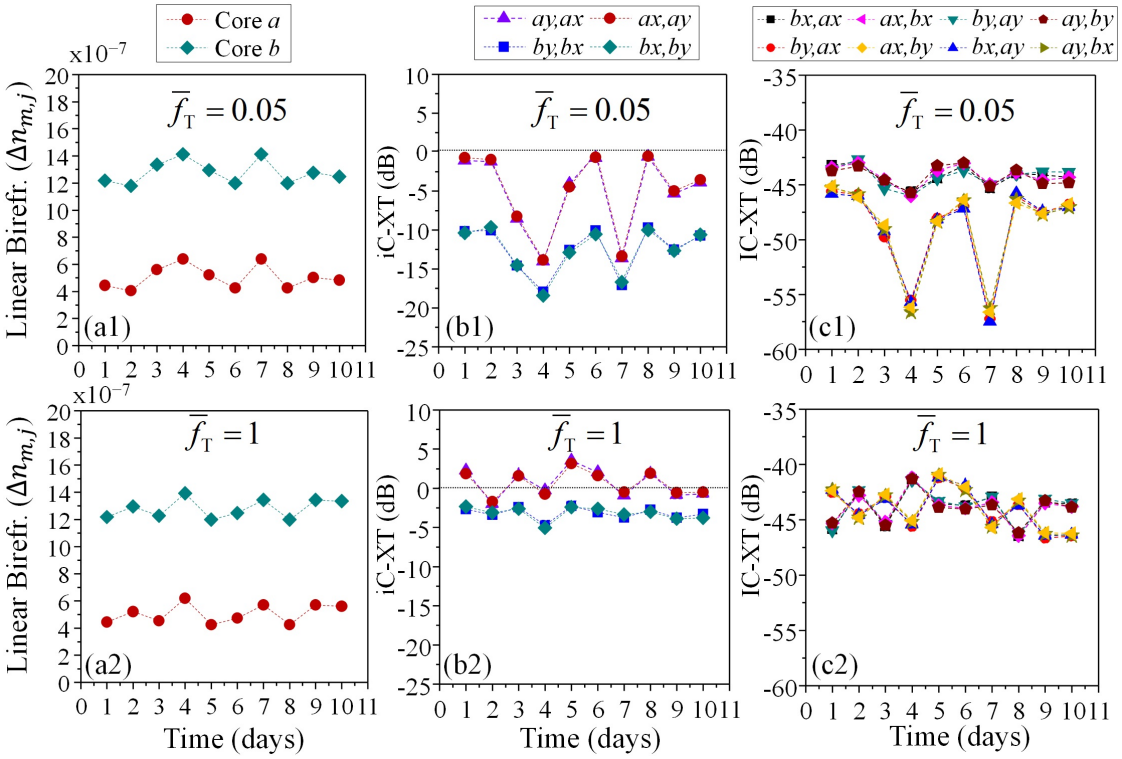

Figure 3.5. Simulation results of the crosstalk behavior between the PCMs in a 150-m 2-core MCF with lowly-birefringent cores, considering the temporal fluctuation of the linear birefringence of each core with a twist rate average value of $\overline{f}_{\mathrm{T}} = 0.05$ and 1 turns/m: (a) Simulated temporal evolution of the linear birefringence in the cores a and b throughout a 10-day period; (b) intra-core crosstalk ; and (c) direct and cross inter-core crosstalk. (iC-XT: intra-core crosstalk, IC-XT: inter-core crosstalk) [131].

Figure 3.6 shows the simulated results considering the 150-m HB-MCF of Fig. 3.4(b), with $\langle \Delta n_{m,j} \rangle = 4 \cdot 10^{-4}$ in both cores (see Table 3.1). The crosstalk behavior in the HB-MCF was also calculated over 100 iterations assuming the same bending and twisting conditions as in the LB-MCF. Figures 3.6(a1)-(c1) and Figs. 3.6(a2)-(c2) show the simulated results for each twist rate distribution. It should be noted from Figs. 3.6(a1) and (a2) that we cannot observe a significant temporal variation of $\Delta n_{m,j}$, since it was assumed to be of the same order of magnitude as that in

the LB cores ($\sim 10^{-7}$), much lower than $\langle \Delta n_{m,j} \rangle = 4 \cdot 10^{-4}$ in this case. Therefore, the temporal evolution of the iC-XT mean was found approximately similar in both cores with a maximal excursion of 1 dB, approximately. In addition, note that the iC-XT mean is much lower than in the LB cores due to a higher phase-mismatching between the intra-core PCMs. Increasing $\overline{f}_{\mathrm{T}}$ from 0.05 to 1 turns/m, the iC-XT mean increases from −33 dB to −20 dB, as shown in Figs. 3.6(b1) and (b2). The XIC-XT is found to be much lower than the DIC-XT for both $\overline{f}_{\mathrm{T}}$ values due to the low average value and temporal fluctuation of iC-XT in both cores [Figs. 3.6(c1) and (c2)]. Nevertheless, when $\overline{f}_{\mathrm{T}}$ increases from 0.05 to 1 turns/m, the difference between the DIC-XT and the XIC-XT mean is reduced from 30 to 17 dB due to the increment of the iC-XT mean in both cores.

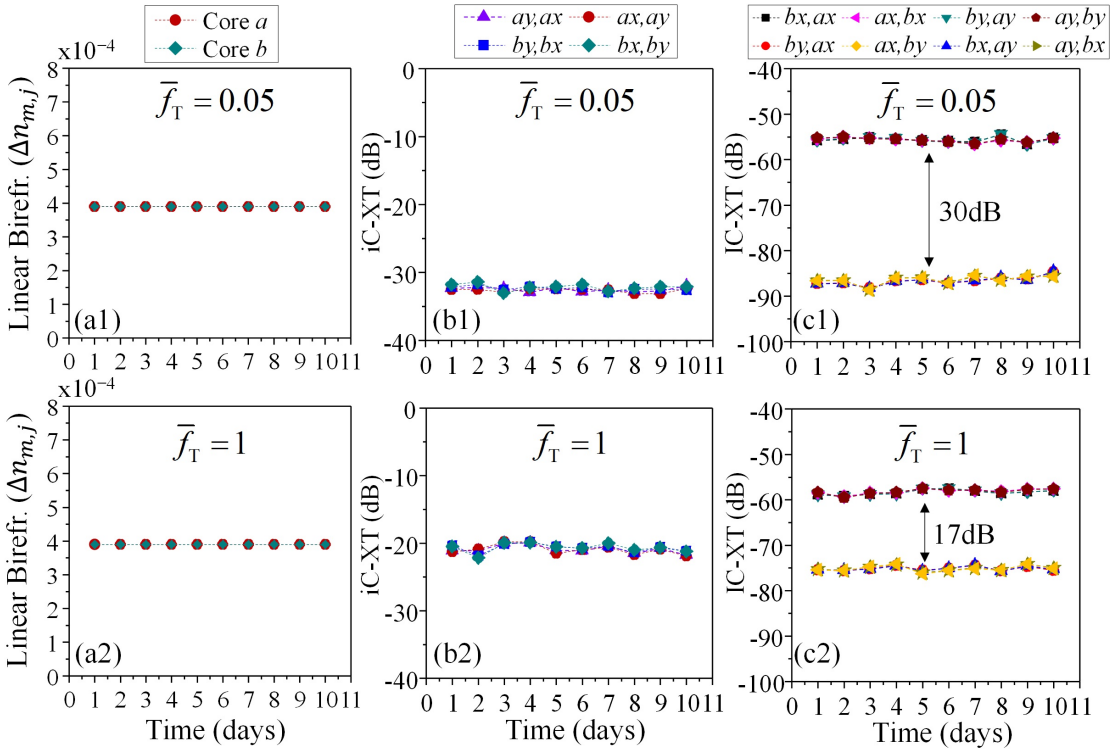

Figure 3.6. Simulation results of the crosstalk behavior between the PCMs in a 150-m 2-core MCF with highly-birefringent cores, considering the temporal fluctuation of the linear birefringence of each core with a twist rate average value of $\overline{f}_{\mathrm{T}} = 0.05$ and 1 turns/m: (a) Simulated temporal evolution of the linear birefringence in the cores *a* and *b* throughout a 10-day period; (b) intra-core crosstalk; and (c) direct and cross inter-core crosstalk. (iC-XT: intra-core crosstalk, IC-XT: inter-core crosstalk) [131].

An additional comment on the results of Figs. 3.5 and 3.6 is in order. It should be noted that, in a given numerical simulation, the different cases of DIC-XT and XIC-XT have approximately the same mean. As an example, the XIC-XT mean between the PCMs *ax-by* is similar to the XIC-XT mean between the PCMs *ay-bx*. This is to be expected given that $|\Delta\phi_{ax,by}| \simeq |\Delta\phi_{ay,bx}|$ when cores with similar ellipticity are involved, as can be verified from the ERIM.

In order to further analyze the longitudinal MCF random perturbations induced by the fiber bending and twisting conditions, a multi-parameter simulation of the CLMT was performed over $S = 80$ Monte Carlo iterations considering a 2-m LB-MCF with cores *a* and *b* comprising a single birefringent segment with $\langle \Delta n_{a,j} \rangle = \langle \Delta n_{b,j} \rangle = 10^{-7}$. The additional MCF parameters such as the cores and cladding material refractive index are found to be the same as in the previous examples. Furthermore, the temporal fluctuation of the linear birefringence was omitted in this simulation. The numerical results are shown in Fig. 3.7.

Figure 3.7 depicts the mean of the: iC-XT *ay-ax* (similar to *by-bx* when assuming cores with a linear birefringence of the same order of magnitude), DIC-XT *bx-ax* and XIC-XT *by-ax* when changing the bending and twisting conditions of the fiber. As it can be noted from Fig. 3.7(a), we cannot observe intra-core mode-coupling between *ay-ax* with $f_{\mathrm{T}} = 0$ in only 2 m of fiber length. Macrobending increases the phase-mismatching between the PCMs *ax* and *ay* without inducing iC-XT due to the photo-elastic effect [164]. As a result, significant XIC-XT cannot be observed for short MCF lengths when $f_{\mathrm{T}} \to 0$, as in the case of Fig. 3.7(c). Nevertheless, an average level of DIC-XT between −100 and −50 dB can be seen from Fig. 3.7(b) in non-twisting conditions depending on the bending radius. In addition, the higher the twist rate and the bending radius, the higher the iC-XT, DIC-XT and XIC-XT mean due to the reduction of the phase-mismatching between the different PCMs. Note that the mean of the DIC-XT and XIC-XT is balanced when the iC-XT mean reaches the value of 0 dB in Fig. 3.7(a). Therefore, MCF twisting can be proposed as a potential strategy for birefringence management to balance the inter-core crosstalk between the different PCMs for short MCF distances. For MCF distances of several kilometers, the iC-XT mean will be increased due to the circular birefringence induced by fiber manufacturing imperfections. This intrinsic circular birefringence may be simulated by increasing the variance of the f_{T} distribution or by inserting phase plates between birefringent segments [167], as commented before.

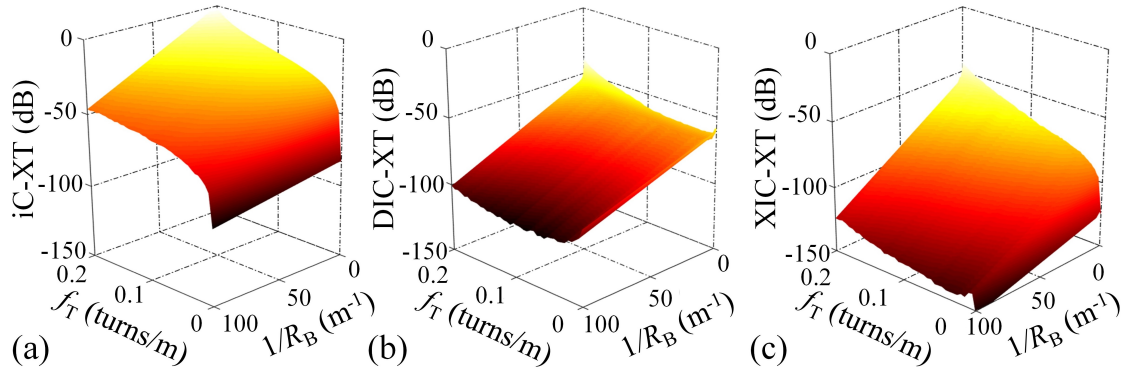

Figure 3.7. Multi-parameter simulation of the crosstalk between PCMs varying the bending radius (R_{B}) and twist rate (f_{T}) parameters in a 2-m homogeneous 2-core MCF with LB cores. (a) intra-core crosstalk mean *ay-ax*, (b) direct inter-core crosstalk mean *bx-ax*, and (c) cross inter-core crosstalk mean *by-ax* [131].

Finally, we analyze the crosstalk behavior between the PCMs when operating in the nonlinear regime. To this end, we simulated a 2-core LB-MCF with parameters: $L = 5\,\mathrm{m}$, $f_{\mathrm{T}} = 0.08\,\mathrm{turns/m}$, $R_{\mathrm{B}} = 100\,\mathrm{cm}$, $N_m = 2$, $S = 80$ and a constant linear birefringence of $\langle \Delta n_{m,j} \rangle = \Delta n_{m,j} = 10^{-7}$ in each core *a* and *b*. The additional MCF parameters are found to be the same as in the previous examples. The power launch level injected into the PCM *ax* was increased from 0 to 140 dBm. The behavior of the mean of the iC-XT (*ay-ax*), DIC-XT (*bx-ax*) and XIC-XT (*by-ax*) is shown in Fig. 3.8.

It should be noted from Fig. 3.8(a) that the iC-XT mean remains almost unchanged for a power launch level $P_{\mathrm{L}} = P_{ax}(z = 0)$ lower than 140 dBm. In contrast, considering a hypothetical condition of $P_{\mathrm{L}} > 140$ dBm (omitting the SBS and silica fiber burning effects), the iC-XT mean increases due to the additional birefringence induced by the nonlinear polarization. Moreover, the mean of the DIC-XT and XIC-XT is reduced as P_{L} increases due to the additional phase-mismatching induced by the Kerr effect between the PCMs, as was extensively discussed in Chapter 2. However, an additional consideration can be pointed out from these results. The difference between the DIC-XT and XIC-XT mean is constant when the nonlinear birefringence can be neglected, specifically when $P_{\mathrm{L}} < 140$ dBm [Fig. 3.8(a)]. Nevertheless, considering higher power launch levels, the nonlinear fiber birefringence increases the iC-XT mean (as commented above) and, therefore, the difference between the DIC-XT and XIC-XT mean is reduced from 5 to 2.6 dB [Fig. 3.8(b)].[11]

[11] These *unrealistic* power launch levels have been simulated only for the academic value of the conclusions.

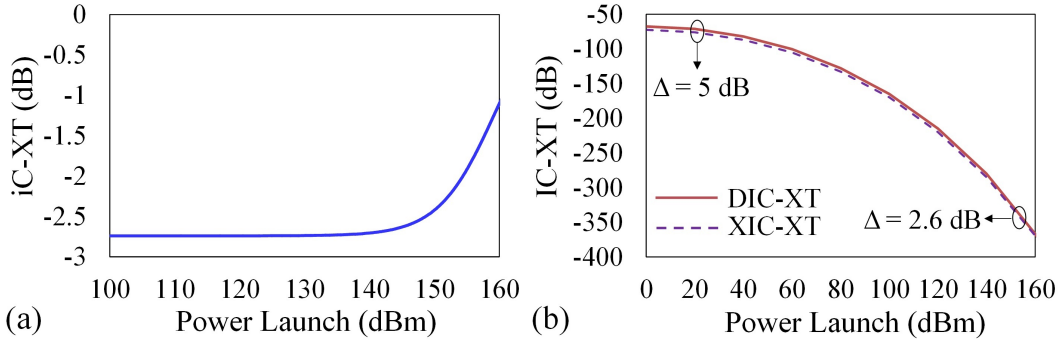

Figure 3.8. Numerical results of the nonlinear crosstalk as a function of the optical power injected into the PCM *ax* in a homogeneous 5-m 2-core LB-MCF: (a) nonlinear iC-XT mean between *ay*-*ax*, and (b) nonlinear DIC-XT and XIC-XT mean between *bx*-*ax* and *by*-*ax* [131].

3.5 Experimental measurements

The experimental work is focused on the analysis of the temporal MCF perturbations, specifically, floor vibrations induced by human activity and environmental temperature excursions.[12] Floor vibrations modify the value of the bending radius and twist rate along the fiber length, and an environmental temperature fluctuation may induce changes in the intrinsic linear birefringence of each core. In this section, we study experimentally the impact of such perturbations on the crosstalk between the PCMs. In addition, we validate the theoretical analysis of previous sections.

3.5.1 Floor vibrations

Floor vibrations induced by human activity inside a room emerge from walking and machinery. This kind of vibrations may involve frequencies ranging from few Hz to several KHz [168]. Despite the fact that these floor vibrations are usually not perceptible for humans, the crosstalk is extremely sensitive to this temporal perturbation of the optical medium, especially when the MCF is without the inner and external coating. In such circumstances, the bending radius and twist rate of the MCF vary in time and along the fiber length due to these vibrations. As a result, we can observe a random behavior of the crosstalk in the space and time domain.

Remarkably, we will demonstrate here that, with *constant temperature* conditions, the temporal IC-XT distribution observed at the MCF output is found to be the same as its spatial distribution, measured in Chapter 2 using the wavelength sweeping method. The reason was pointed out before. Both measurement techniques are in complete analogy with a Monte Carlo simulation where each iteration obtains a random sample of the random process $\phi_{mi}^{(\mathrm{eq})}$ in each PCM. In the time domain, the floor vibrations restart the random process $\phi_{mi}^{(\mathrm{eq})}$ by modifying temporally the value of $R_{\mathrm{B},l}$ and $f_{\mathrm{T},l}$ in each l-th birefringent segment, i.e., each temporal change of these parameters is similar to a Monte Carlo iteration. In the space domain, each spectral sample of the wavelength sweeping method modifies the value of the optical carrier restarting the random process $\phi_{mi}^{(\mathrm{eq})}$, i.e., each change of λ_0 corresponds to a Monte Carlo iteration. If the temperature conditions are invariant and the frequency of the floor vibrations is approximately constant, the distribution of $\phi_{mi}^{(\mathrm{eq})}$ and the IC-XT are found to be the same in z and t. In this scenario, the statistical analysis of the IC-XT can be restricted to the space domain and the main results of Chapter 2 can be extrapolated to study the temporal distribution of the IC-XT.

To illustrate this, we omit the polarization effects in this subsection for simplicity and we measure the temporal variations of the IC-XT from core 3 to core 1 of the Fibercore SM-4C1500(8.0/125)

[12] There are temporal perturbations of our system (transmitter+MCF+receiver), such as polarization fluctuations of the laser, which cannot be considered MCF perturbations, but can modify the statistical parameters of the IC-XT. Concretely, the impact of the polarization fluctuations of the laser on the IC-XT has been studied in [130].

at $z = L = 150$ m during 16 hours with quasi-constant temperature conditions in the laboratory room ($T \sim 24.5\,^{\circ}$C, maximal excursion of $0.5\,^{\circ}$C). The experimental set-up is found to be exactly the same as in Fig. 2.9(a), but using a constant optical carrier of $\lambda_0 = 1550$ nm. Figure 3.9(a) shows the temporal evolution of the linear and nonlinear IC-XT. We can note that the nonlinear IC-XT is found to be much lower than the linear IC-XT due to the additional phase-mismatching induced by the Kerr effect between the LP_{01} mode of cores 1 and 3, in line with our observations in Chapter 2. Next, we compare the p.d.f. measured from the temporal evolution of the IC-XT and the p.d.f. measured using the wavelength sweeping method between 1550 and 1580 nm [Figs. 3.9(b) and (c)]. As expected, we obtain the same p.d.f. from both measurement techniques (t-method and λ-method) verifying that the temporal perturbations induced by the floor vibrations do not change the spatial distribution of the IC-XT. Nonetheless, these conclusions could be found different in real deployed MCF systems where R_B and f_T cannot be regarded as strict-sense stationary random processes in z and t. Additional experimental work is required to improve our understanding about this question.

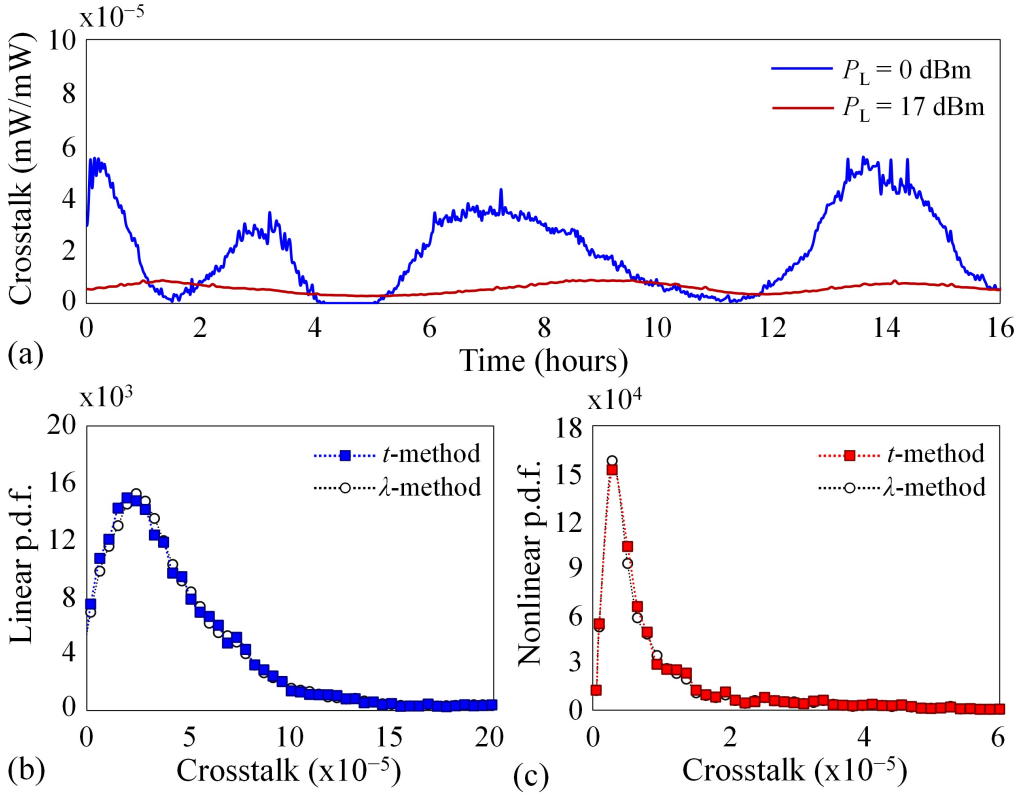

Figure 3.9. (a) Measured temporal evolution of the IC-XT induced by core 3 in core 1 at $z = 150$ m of the commercial MCF Fibercore SM-4C1500(8.0/125) considering different optical power launch (P_L) levels in core 3. The rapidly-varying temporal excursions of the IC-XT are found to be faster than 1 ms. Probability density function (p.d.f.) of the IC-XT in the (b) linear and (c) nonlinear regime estimated from the temporal profile (t-method) and from the wavelength sweeping method (λ-method).[13]

[13]It can be noted that the p.d.f. of the linear IC-XT [Fig. 3.9(b)] presents a non-zero value at the origin of the crosstalk-axis. The reason can be found in the temporal evolution of the linear IC-XT between the fourth and fifth hours [see Fig. 3.9(a), blue line]. In this time interval, the IC-XT reached an experimental value lower than the minimum detectable power of the photodiode of the power meter (around −100 dBm). Since the same event took place when measuring the p.d.f. of the linear IC-XT by using the λ-method, both p.d.f.'s were found to be in excellent agreement in Fig. 3.9(b). Along this line, it should be remarked that the impact of this zero-crosstalk interval observed in Fig. 3.9(a) was irrelevant to estimate experimentally the crosstalk distribution in the linear regime. The decorrelation time (half-width at $1/e$ of the autocorrelation function of the IC-XT) was found to be much higher (around 11 hours) than this zero-crosstalk interval.

3.5.2 Temperature fluctuation

Environmental temperature fluctuation induces changes in the linear birefringence of each core (see below). In such conditions, the crosstalk becomes a non-stationary random process in the time variable. For this reason, we introduced in the numerical model the concept of the BTC unit: the time scale over which the linear birefringence of the MCF and the crosstalk mean between the PCMs can be assumed time-invariant functions. Therefore, our goal is to investigate the BTC unit and analyze the impact of the temperature fluctuations on the crosstalk mean between the PCMs, a fundamental problem so far unexplored in the literature.

Laboratory set-up. A tunable continuous-wave[14] external cavity laser (CW-ECL) at 1550 nm with a linewidth of 50 kHz was used along with two polarization controllers (PC_1 and PC_2). The first polarization controller (PC_1) was employed to align the polarization axes of the ECL and the polarization beam splitter (PBS) in a back-to-back (B2B) connection, as detailed in Fig. 3.10. A polarization analyzer (Optellios PS2300) was used to verify that the output light of the PC_1 was linearly polarized along the x-axis by maximizing the upper branch of the PBS in the B2B connection. The second polarization controller (PC_2) was inserted to modify the polarization launched into a given core of the MCF. The additional EDFA followed by a variable optical attenuator (VOA) was employed only for the nonlinear crosstalk analysis between the PCMs. A 3D fan in/fan-out device with 2.2 dB insertion losses was employed in order to inject and extract the optical power launched into a 150-m homogeneous 4-core MCF [Fibercore SM 4C1500(8.0/125)] spooled on a reel inside a methacrylate box with an average value of the bending radius and twist rate of 100 cm and 1 turns/m, respectively. In addition, the laboratory room was isolated and the air cushions were inflated in our active optical table to minimize the floor vibrations induced by human activity.

The crosstalk behavior between the PCMs of cores 1 and 3 was analyzed in the linear and nonlinear regime by injecting into a given PCM an optical power launch level of 0 dBm and 6 dBm, respectively. In the nonlinear regime, the EDFA gain was maximized in order to reduce the crosstalk averaging due to ASE noise, as recommended in [142], and the power launch was controlled by the VOA. The optical power of the two PCMs ($LP_{01,mx}$ and $LP_{01,my}$) of a given core m (with $m \in \{1, 3\}$) was separated with the PBS and measured with a power meter comprising two different channels (Thorlabs PM320E).

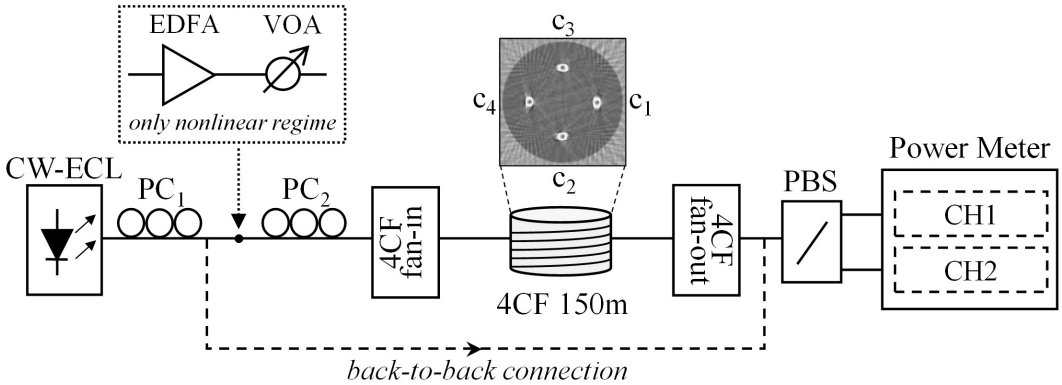

Figure 3.10. Experimental set-up for the intra- and inter-core crosstalk evaluation between the PCMs of cores 1 and 3 of a 4-core MCF [Fibercore SM-4C1500(8.0/125)], considering the temporal fluctuations of the linear birefringence induced by temperature excursions of the laboratory room [131].

[14] We employed a continuous-wave source with a reduced linewidth to minimize the impact of the dispersive effects of the propagated optical signal on the temporal dependence of the crosstalk [158].

Measurement method. The mean of the linear and nonlinear iC-XT, DIC-XT and XIC-XT between the PCMs of cores 1 and 3 was estimated by using the wavelength sweeping method from 1540 to 1590 nm with 5 pm step. The ECL was previously tested to confirm that the polarization remains unchanged when sweeping the laser wavelength. Interestingly, it should be noted that the wavelength sweeping method can also be used to estimate the value of the linear birefringence and the first-order polarization-mode dispersion (PMD) of each core, as detailed in [169]. Here, we will focus on the analysis of linear birefringence. The first-order PMD will be discussed in Appendix D3 (see page 94).

It was experimentally verified that the linear birefringence of each core ($\Delta n_{m,j}$) remained unchanged during more than 10 hours. As a result, we selected a BTC unit of one day and we performed measurements during several consecutive days in different months (see Fig. 3.11).

Results. Figure 3.11 shows the temporal fluctuation of the average temperature in the laboratory room, the temporal fluctuation of the linear birefringence ($\Delta n_{m,j}$) in cores 1 and 3, and its impact on the crosstalk mean between the PCMs. Specifically, we measured six consecutive days in October 2015, four consecutive days in January 2016, and five consecutive days in March 2016.

As shown in Fig. 3.11(a), the higher the average temperature is, the higher the intrinsic linear birefringence measured in each core. In particular, cores 1 and 3 have a different temporal average value of the linear birefringence, estimated in $\langle \Delta n_{1,j} \rangle = 4.9 \cdot 10^{-7}$ and $\langle \Delta n_{3,j} \rangle = 1.2 \cdot 10^{-6}$, respectively. It can be noted that the temporal average value of the linear birefringence is found to be approximately constant in each core the three measured months because of the average temperature is similar ($\sim 25\,^{\circ}$C). Moreover, although $\langle \Delta n_{1,j} \rangle \neq \langle \Delta n_{3,j} \rangle$, the temporal evolution of the linear birefringence presents a similar shape in both cores, in line with our assumptions in Section 3.4. This point is a fundamental difference between an MCF and an SCF bundle. In an SCF bundle, in general, the linear birefringence of each fiber may have a different temporal evolution [21] and, therefore, the compensation of the PMD should be performed by using individual digital signal processing in each fiber.

Furthermore, as depicted in Figs. 3.11(b) and (c), the higher the linear birefringence in a given core, the lower the mean of the iC-XT. In this scenario, it should be noted that the iC-XT in core 3 is lower than in core 1 due to a higher phase-mismatching between orthogonal polarizations. In line with the simulations of Section 3.4, the iC-XT mean has a lower temporal fluctuation in the more birefringent core (i.e. core 3) given that $\langle \Delta n_{3,j} \rangle \sim 10^{-6}$ is much higher than the order of its temporal fluctuation, around 10^{-7}. Along these lines, we can also observe from Figs. 3.11(d) that the temporal evolution of the XIC-XT mean presents the same behavior as the iC-XT mean, indicating that the XIC-XT depends directly on the iC-XT of both cores. As a result, the DIC-XT is higher than the XIC-XT when the iC-XT is lower than 0 dB in both cores, as it was observed the 3^{rd} and 4^{th} days (October 2015), the 7^{th} day (January 2016), and the 13^{th} and 14^{th} days (March 2016). In addition, note that the experimental measurements fit correctly with the numerical simulation of the CLMT when using the ERIM with the parameters indicated in Table 3.1 for the LB-MCF with $N_1 \equiv N_a = 8$, $N_3 \equiv N_b = 6$, $\Delta n_{1,j} \equiv \Delta n_{a,j}$ and $\Delta n_{3,j} \equiv \Delta n_{b,j}$. Therefore, we conclude that the more birefringent a given core is, the lower the number of segments that should be assumed to simulate the crosstalk by using the CLMT, as commented before.

On the other hand, the nonlinear crosstalk between the PCMs $1y$-$1x$, $3y$-$3x$, $3x$-$1x$ and $3y$-$1x$ was also measured the 5^{th}, 6^{th} and 15^{th} days with a power level of 6 dBm launched into the corresponding PCM, taking into account the insertion losses of 2.2 dB of the 3D fan-in device. As it was previously observed in Section 3.4, the iC-XT mean has the same value in the nonlinear regime taking into account that the nonlinear birefringence can be neglected for realistic optical power launch levels lower than 40 dBm. In addition, the DIC-XT and XIC-XT mean is reduced around 1 dB keeping constant the difference between both inter-core crosstalk types as a direct consequence of the constant behavior of the iC-XT mean in the nonlinear regime.

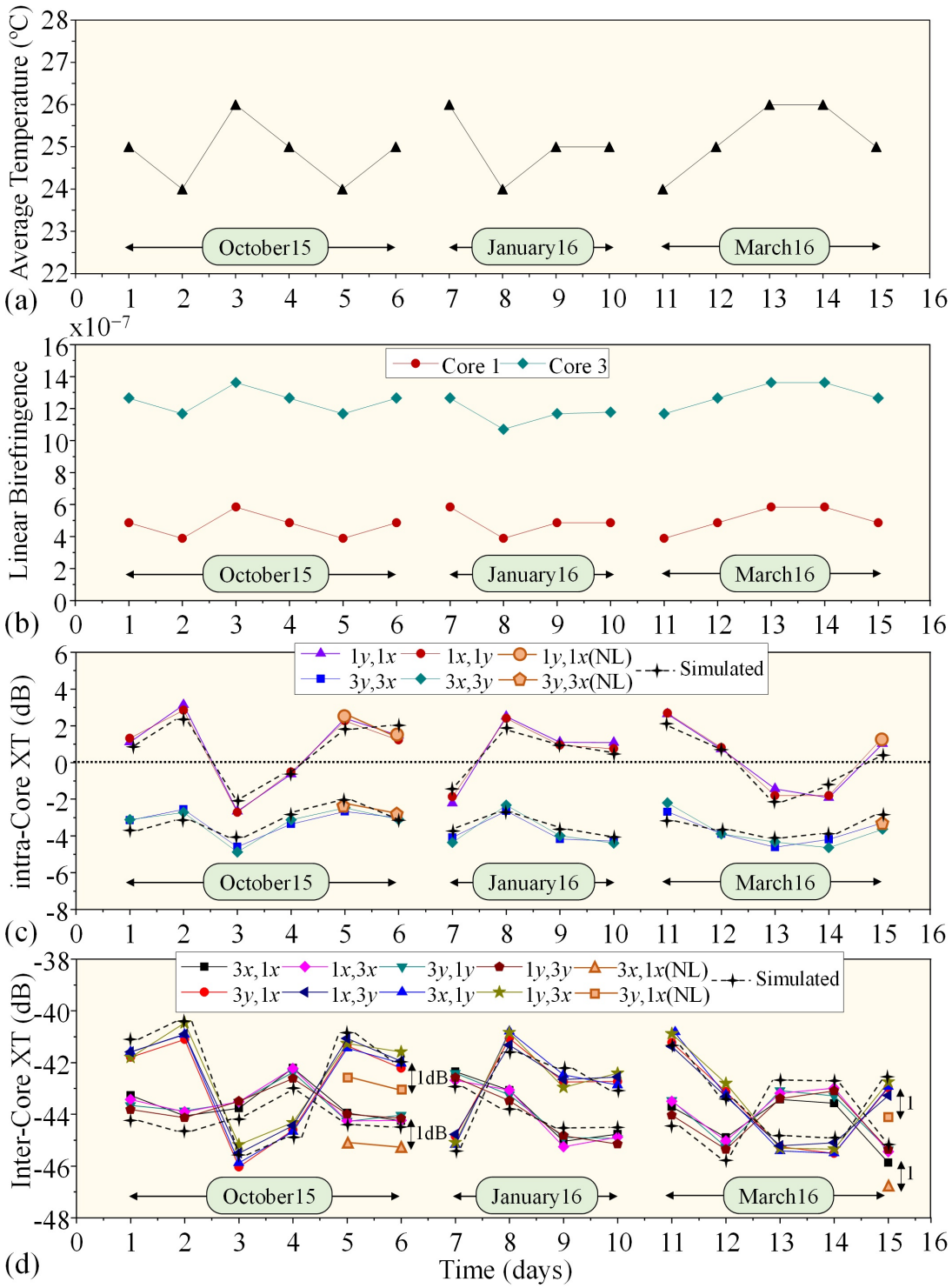

Figure 3.11. Experimental results of the temporal evolution of the linear birefringence over different days and months of a 150 m 4-core MCF, and corresponding intra- and inter-core crosstalk mean between cores 1 and 3. A power launch level of $P_{\mathrm{L}} = 0$ dBm was used in the linear regime (NL: nonlinear regime with $P_{\mathrm{L}} = 6$ dBm). (a) Average temperature of the laboratory room, (b) linear birefringence $\Delta n_{m,j}$ of cores 1 and 3, (c) intra-core crosstalk $1x$-$1y$ and $3x$-$3y$, and (d) direct- and cross-inter-core crosstalk $1i$-$3j$ with $(i,j) \in \{x,y\}^2$ [131].

Moreover, although the crosstalk analysis between the PCMs is restricted only to cores 1 and 3, the linear birefringence $\Delta n_{m,j}$ was also measured in cores 2 and 4 (see Appendix D3). Specifically, we found that $\langle \Delta n_{2,j} \rangle \simeq \langle \Delta n_{4,j} \rangle \simeq 7 \cdot 10^{-7}$. In such a scenario, we also analyzed the average value of the iC-XT mean of each core as a function of $\langle \Delta n_{m,j} \rangle$. Figure 3.12 shows the simulated results of the iC-XT mean evolution when increasing the value of $\langle \Delta n_{m,j} \rangle$ in a given core m considering 80 Monte Carlo iterations and the same fiber parameters as the simulation of the 2-core LB-MCF depicted in Fig. 3.5. The bending radius and twist rate were assumed with the same value as in the experimental set-up, with $R_{\mathrm{B}} = 100$ cm and $f_{\mathrm{T}} = 1$ turns/m, neglecting the random fluctuations of these parameters taking into account that $\delta_z R_{\mathrm{B}} \simeq \delta_z f_{\mathrm{T}} \simeq 0$ (see the definition of the linear operator δ_z on page 24). It can be noted that the iC-XT mean is reduced when $\langle \Delta n_{m,j} \rangle$ increases inducing a higher phase-mismatching between orthogonal polarizations. Furthermore, it was confirmed that the simulated results are in good agreement with the experimental measurements of each core, validating the theoretical analysis reported in previous sections.

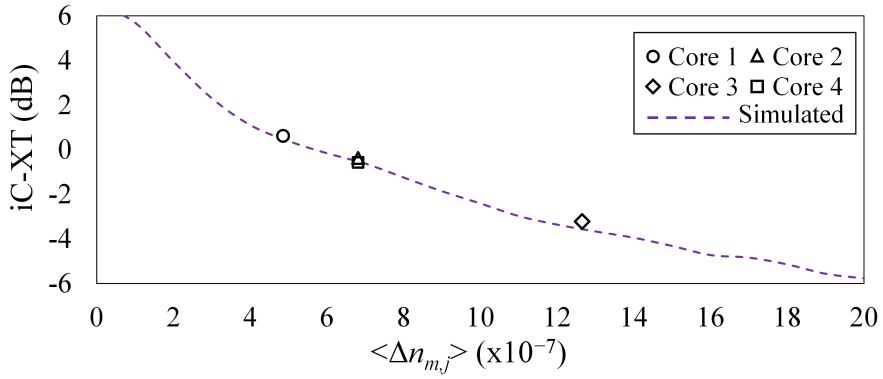

Figure 3.12. Experimental measurements and simulated results of the evolution of the intra-core crosstalk (iC-XT) mean with the longitudinal and temporal average value of the intrinsic linear birefringence $\langle \Delta n_{m,j} \rangle$. Solid points: measured data of cores 1, 2, 3, 4 of the 4-core MCF employed in the experimental work. Dashed line: simulation results using the CLMT [131].

The experimental analysis reported in this section addresses a non-real deployed MCF system with quasi-constant bending and twisting conditions. For real deployed MCF systems, the results presented herein should be revisited by considering higher fiber distances and a random bending radius and twist rate along the fiber length. Likewise, the PMD and the dispersive effects of the optical medium should also be investigated in this scenario. To this end, the CLMT will be extended to the non-monochromatic regime in the next chapter.

3.6 Conclusions

In this chapter, we have reported the theoretical and experimental analysis of the intra- and inter-core crosstalk behavior in SM-MCF by including the temporal and longitudinal birefringence perturbations of the optical medium. In order to propose an accurate analytical model with a lower computational time than numerical simulations of Maxwell's equations based on FDTD (Finite-Difference Time-Domain) calculations, the coupled local-mode theory (CLMT) was derived from Maxwell's equations by using perturbation theory. As a result, both temporal and longitudinal MCF birefringence perturbations were included with a rigorous formalism in the phase functions and mode-coupling coefficients (MCCs) of the polarized core modes (PCMs). The theoretical analysis shows that the MCC modeling the cross inter-core crosstalk (XIC-XT) can be neglected, which indicates that the XIC-XT depends directly on the intra-core crosstalk (iC-XT) mean observed in the cores of the MCF, as it was verified numerically and experimentally.

In addition, the simulation model of the CLMT was proposed by using the equivalent refractive index model (ERIM) of Chapter 2, which was completed by including polarization effects and the

time-varying fiber perturbations. Our numerical simulations, comprising lowly-birefringent and highly-birefringent cores, indicate that the higher is the linear birefringence in a given core, the lower is the value and the temporal fluctuation of the iC-XT mean. Furthermore, the XIC-XT mean follows the same temporal evolution as the iC-XT mean, which indicates that the XIC-XT is mainly generated due to intra-core mode-coupling effects. As a result, the XIC-XT mean is lower than the direct inter-core crosstalk (DIC-XT) mean when the iC-XT mean of both cores is found to be lower than 0 dB. Both DIC-XT and XIC-XT are balanced when the iC-XT mean reaches the value of 0 dB in each core. Hence, MCF twisting was proposed as a birefringence management strategy in short MCF distances to balance the DIC-XT and XIC-XT. However, when higher MCF distances of several kilometers are considered, the iC-XT mean increases reducing the difference between the mean of the DIC-XT and XIC-XT. In nonlinear regime, it was observed that the nonlinear iC-XT mean remains unchanged when the power level launched into a given PCM increases (assuming realistic values lower than 40 dBm). In contrast, the DIC-XT and XIC-XT mean is reduced showing a similar evolution. Outstandingly, these results can be used to design highly-birefringent MCFs with a random orientation of the principal axes of each core to reduce the mode-coupling between the PCMs of the fiber. This concept is similar to the crosstalk behavior in disordered MCFs, exhibiting transverse Anderson localization [93].

For completeness, extensive experimental measurements were performed using a homogeneous 4-core MCF with constant and time-varying temperature conditions. In the former case, we demonstrated that the spatial and temporal IC-XT random fluctuations have identical distributions when the temporal perturbations are only induced by slight floor vibrations. In the latter case, we demonstrated that environmental temperature fluctuation induces changes in the linear birefringence of each core modifying the mean and variance of the iC-XT and IC-XT distributions. Specifically, we performed experimental measurements in several consecutive days of three different months. Our experimental results pointed out that the linear birefringence of each cores is found to be approximately constant during more than 10 hours. In addition, we observed that, in contrast to a fiber bundle, the temporal evolution of the linear birefringence is found to be similar in different cores of our MCF.

Along these lines, it should be remarked that the time scale over which the linear birefringence of the MCF can be assumed to be constant [i.e. the birefringence temporal change (BTC) unit] is difficult to estimate theoretically. Note that the time-varying temperature conditions will mainly depend on the geographic region. The experimental work of this chapter was performed in Valencia (Spain). In particular, this geographic region presents a reduced temperature contrast between day and night. In this way, we observed constant birefringent conditions in a long time interval. Thus, we cannot extrapolate these experimental results as general conclusions to any real deployed MCF scenario. In our personal opinion, the analysis of the crosstalk temporal distribution requires additional experimental work in different geographic regions with diverse climatic conditions.

Appendix A3: Notes on the coupled-wave equations

In this appendix, we discuss several fundamental aspects on the nonlinear coupled-wave equations derived in Subsection (3.2.2). Firstly, we will discuss the omission of the term $\nabla(\nabla\cdot(\boldsymbol{\mathcal{P}}^{(1)}+\boldsymbol{\mathcal{P}}^{(3)}))$ in the nonlinear fiber wave equation [Eq. (3.2.7)] and, secondly, we will take a closer look at the constitutive relations Eq. (3.2.11) and (3.2.12).

A3.1 Analysis of the term $\nabla(\nabla\cdot(\boldsymbol{\mathcal{P}}^{(1)}+\boldsymbol{\mathcal{P}}^{(3)}))$

The *exact* nonlinear wave equation of an SCF or an MCF reads as follows:

$$\left(\triangle-\frac{1}{c_0^2}\partial_t^2\right)\boldsymbol{\mathcal{E}}\left(\boldsymbol{r},t\right)=\mu_0\partial_t^2\boldsymbol{\mathcal{P}}^{(1)}\left(\boldsymbol{r},t\right)+\mu_0\partial_t^2\boldsymbol{\mathcal{P}}^{(3)}\left(\boldsymbol{r},t\right)-\frac{1}{\varepsilon_0}\nabla\left(\nabla\cdot\left(\boldsymbol{\mathcal{P}}^{(1)}+\boldsymbol{\mathcal{P}}^{(3)}\right)\right), \quad \text{(A3.1)}$$

where $\boldsymbol{\mathcal{E}}$, $\boldsymbol{\mathcal{P}}^{(1)}$ and $\boldsymbol{\mathcal{P}}^{(3)}$ are respectively the electric field strength, and the linear and nonlinear polarizations of the fiber. In the photonics literature, the approximation $\nabla(\nabla\cdot(\boldsymbol{\mathcal{P}}^{(1)}+\boldsymbol{\mathcal{P}}^{(3)}))\simeq\mathbf{0}$ is usually performed without including any mathematical proof or numerical verification [139,150, 159–161].

Here, we will discuss if the *source* $\varepsilon_0^{-1}\nabla(\nabla\cdot(\boldsymbol{\mathcal{P}}^{(1)}+\boldsymbol{\mathcal{P}}^{(3)}))$ can be neglected in the RHS of the above equation when considering optical fibers with a lowly-birefringent (LB) or a highly-birefringent (HB) design. In the following, we will first discuss the linear term $\varepsilon_0^{-1}\nabla(\nabla\cdot\boldsymbol{\mathcal{P}}^{(1)})$ for the LB and HB cases and next, we will analyze the nonlinear term $\varepsilon_0^{-1}\nabla(\nabla\cdot\boldsymbol{\mathcal{P}}^{(3)})$.

Linear polarization (LB case)

In an isotropic step-index fiber, the constitutive relation between $\boldsymbol{\mathcal{E}}$ and $\boldsymbol{\mathcal{P}}^{(1)}$ can be written in a given dielectric region (cores or cladding) as $\boldsymbol{\mathcal{P}}^{(1)}\left(\boldsymbol{r},t\right)=\varepsilon_0\chi^{(1)}\boldsymbol{\mathcal{E}}\left(\boldsymbol{r},t\right)$, with the first-order electric susceptibility being a scalar and omitting the temporally dispersive effects for simplicity. In such circumstances, the fields $\boldsymbol{\mathcal{E}}$ and $\boldsymbol{\mathcal{P}}^{(1)}$ are parallel and $\nabla\cdot\boldsymbol{\mathcal{P}}^{(1)}=0$ as can be deduced from the Gauss's law $\nabla\cdot\boldsymbol{\mathcal{D}}=0$. In isotropic gradual-index fibers, $\boldsymbol{\mathcal{P}}^{(1)}\left(\boldsymbol{r},t\right)=\varepsilon_0\chi^{(1)}\left(r\right)\boldsymbol{\mathcal{E}}\left(\boldsymbol{r},t\right)$ and $\nabla\cdot\boldsymbol{\mathcal{P}}^{(1)}\neq0$. However, we can safely assume slowly-varying radial variations of $\chi^{(1)}$, that is, $\delta_r\chi^{(1)}\ll\chi^{(1)}$ in $\delta r\sim\lambda$ and $\delta_r\chi^{(1)}:=\left|\chi^{(1)}(r)-\chi^{(1)}(r+\delta r)\right|$. In this vein, we can approximate $\nabla\cdot\boldsymbol{\mathcal{P}}^{(1)}\simeq0$ in $\delta r\sim\lambda$.

Nonetheless, in real step-index or gradual-index fibers, we should also consider the effect of the *longitudinal fiber perturbations* (macrobends, microbends, fiber twisting and manufacturing imperfections) in the term $\nabla\cdot\boldsymbol{\mathcal{P}}^{(1)}$. Specifically, a longitudinal fiber perturbation will induce an anisotropic response in $\boldsymbol{\mathcal{P}}^{(1)}$ due to the photo-elastic effect [164]. Consequently, we should analyze the impact of this anisotropic response on the term $\varepsilon_0^{-1}\nabla(\nabla\cdot\boldsymbol{\mathcal{P}}^{(1)})$ of Eq. (A3.1).

As a first example, consider a step-index LB core with an incident monochromatic electric field strength $\boldsymbol{\mathcal{E}}\left(\boldsymbol{r},t\right)=\mathrm{Re}\left\{\boldsymbol{E}_{\omega_0}\left(\boldsymbol{r}\right)\exp\left(j\omega_0t\right)\right\}$ with a complex amplitude of the form:[15]

$$\boldsymbol{E}_{\omega_0}\left(\boldsymbol{r}\right)=\left(a\hat{u}_x+b\hat{u}_y\right)F\left(x,y\right)\exp\left(-j\beta z\right), \quad \text{(A3.2)}$$

and $(a,b)\in\mathbb{R}^2$. Now, let us assume a given perturbation at $z=z_{\mathrm{P}}$. The complex amplitude of the linear polarization $\boldsymbol{P}_{\omega_0}^{(1)}$ generated by this perturbation obeys the expression:[16]

$$\boldsymbol{P}_{\omega_0}^{(1)}\left(x,y,z_{\mathrm{P}}\right)=\varepsilon_0\left\{\begin{array}{l}\left[\chi_{xx}^{(1)}\left(z_{\mathrm{P}}\right)a+\chi_{xy}^{(1)}\left(z_{\mathrm{P}}\right)b\right]\hat{u}_x\\+\left[\chi_{xy}^{(1)}\left(z_{\mathrm{P}}\right)a+\chi_{yy}^{(1)}\left(z_{\mathrm{P}}\right)b\right]\hat{u}_y\end{array}\right\}F\left(x,y\right)\exp\left(-j\beta z_{\mathrm{P}}\right). \quad \text{(A3.3)}$$

It should be remarked that we have only modeled the fiber perturbation in the tensor $\chi_{ij}^{(1)}$. Here, we assume that F and β are longitudinal invariant functions to facilitate the analysis.

[15] We omit the dependence of F and β with ω_0 to use a more economical notation.

[16] Note that $\chi_{xy}^{(1)}=\chi_{yx}^{(1)}$ as discussed on page 61.

In particular, we will analyze the anisotropic response induced by the fiber perturbation in two different ways:

1. From the misalignment angle between $\boldsymbol{P}_{\omega_0}^{(1)}$ and $\boldsymbol{E}_{\omega_0}$, given by the Θ function:

$$\Theta\left(a,b\right) := \left|\arctan\left(\frac{\chi_{xy}^{(1)}\left(z_{\mathrm{P}}\right)a + \chi_{yy}^{(1)}\left(z_{\mathrm{P}}\right)b}{\chi_{xx}^{(1)}\left(z_{\mathrm{P}}\right)a + \chi_{xy}^{(1)}\left(z_{\mathrm{P}}\right)b}\right) - \arctan\left(\frac{b}{a}\right)\right|. \tag{A3.4}$$

   We will assume that the fiber perturbation inducing the linear birefringence is a macrobend.[17] In this scenario, we will consider that the macrobend modifies only the principal y-axis[18] as $\chi_{yy}^{(1)}\left(z_{\mathrm{P}}\right) = \chi_{xx}^{(1)} + \Delta\chi^{(1)}\left(z_{\mathrm{P}}\right)$, where $\Delta\chi^{(1)}$ can be calculated from the ERIM [Eq. (3.3.5)] or using the birefringent model reported in [165]:[19]

$$\Delta\chi^{(1)}\left(z_{\mathrm{P}}\right) \simeq C_{\mathrm{f}} n_{\mathrm{co}} \frac{d_{\mathrm{cl}}^2}{R_{\mathrm{B}}^2}, \tag{A3.5}$$

   with $C_{\mathrm{f}} \simeq 0.022 n_{\mathrm{co}}^3$ in silica fibers and n_{co} the material refractive index of the LB core. Moreover, we will assume that the circular birefringence $\chi_{xy}^{(1)}\left(z_{\mathrm{P}}\right)$ is induced by an external constant twist rate f_{T}. Hence, $\chi_{xy}^{(1)}\left(z_{\mathrm{P}}\right)$ can be calculated from the ERIM as [Eq. (3.3.12)]:

$$\chi_{xy}^{(1)}\left(z_{\mathrm{P}}\right) = \pi R_0 f_{\mathrm{T}} n_{\mathrm{co}}^4 \left|p_{11} - p_{12}\right|, \tag{A3.6}$$

   where $|p_{11} - p_{12}| = 0.149$ in the case of fused silica.

2. From the ratio of sources $\left|\varepsilon_0^{-1}\nabla(\nabla\cdot\boldsymbol{\mathcal{P}}^{(1)})\right| / \left|\mu_0\partial_t^2\boldsymbol{\mathcal{P}}^{(1)}\right|$ at $z = z_{\mathrm{P}}$, which can be calculated by using the complex amplitude $\boldsymbol{P}_{\omega_0}^{(1)}$ as:

$$\mathcal{R}^{(1)}\left(x,y;z_{\mathrm{P}}\right) := \frac{\left|\varepsilon_0^{-1}\nabla\left(\nabla\cdot\boldsymbol{P}_{\omega_0}^{(1)}\left(x,y,z_{\mathrm{P}}\right)\right)\right|}{\left|\mu_0\omega_0^2\boldsymbol{P}_{\omega_0}^{(1)}\left(x,y,z_{\mathrm{P}}\right)\right|}. \tag{A3.7}$$

In order to verify if $\nabla(\nabla\cdot\boldsymbol{\mathcal{P}}^{(1)})$ can be neglected in Eq. (A3.1), it is suitable to analyze a critical case with a reduced value of R_{B} and a high twist rate, e.g., $R_{\mathrm{B}} = 1$ cm and $f_{\mathrm{T}} = 5$ turns/m. In such circumstances, taking $n_{\mathrm{co}} = 1.452$, $R_0 = 4$ μm and $d_{\mathrm{cl}} = 125$ μm, we found that $\Delta\chi^{(1)} \simeq 1.5\cdot10^{-5}$ and $\chi_{xy}^{(1)} \simeq 4.2\cdot10^{-5}$.

Figure A3.1(a) shows Eq. (A3.4) for different values of a and b. We can observe that the maximum misalignment angle between $\boldsymbol{P}_{\omega_0}^{(1)}$ and $\boldsymbol{E}_{\omega_0}$ is around $2.2\cdot10^{-3}$ degrees when a or b are null. In such a case, the ratio $\mathcal{R}^{(1)}$ is found to be lower than 2% with $\sqrt{x^2+y^2} < R_0$ and $\lambda_0 = 2\pi c_0/\omega_0 = 1550$ nm [see Fig. A3.1(b)].

Linear polarization (HB case)

In the next example, we analyze the HB case. To this end, let us assume an incident monochromatic electric field strength $\boldsymbol{\mathcal{E}}\left(\boldsymbol{r},t\right) = \mathrm{Re}\left\{\boldsymbol{E}_{\omega_0}\left(\boldsymbol{r}\right)\exp\left(j\omega_0 t\right)\right\}$ in a step-index HB core with:

$$\boldsymbol{E}_{\omega_0}\left(\boldsymbol{r}\right) = aF_x\left(x,y\right)\exp\left(-j\beta_x z\right)\hat{u}_x + bF_y\left(x,y\right)\exp\left(-j\beta_y z\right)\hat{u}_y, \tag{A3.8}$$

and $(a,b) \in \mathbb{R}^2$. For simplicity, let us assume $F_x \simeq F_y$ and $\beta_y = \beta_x + \Delta\beta$ renaming $\beta_x \equiv \beta$. In this way, Eq. (A3.8) is reduced to:

$$\boldsymbol{E}_{\omega_0}\left(\boldsymbol{r}\right) \simeq \left[a\hat{u}_x + b\exp\left(-j\Delta\beta z\right)\hat{u}_y\right]F\left(x,y\right)\exp\left(-j\beta z\right). \tag{A3.9}$$

[17] The contribution of microbends and manufacturing imperfections to the linear birefringence can be omitted if we consider a bending radius inducing a linear birefringence much higher than 10^{-7}.

[18] We set the reference system $\{O;\{\hat{u}_x,\hat{u}_y,\hat{u}_z\}\}$ in line with the principal axes established by the macrobend.

[19] Equation (A3.5) is retrieved from Eq. (13) of [165] taking into account that $\Delta\chi^{(1)}\left(z_{\mathrm{P}}\right) \simeq 2n_{\mathrm{co}}\Delta n\left(z_{\mathrm{P}}\right)$ and assuming to be null the rate of the axis deformation induced by the macrobend ($\zeta = 0$).

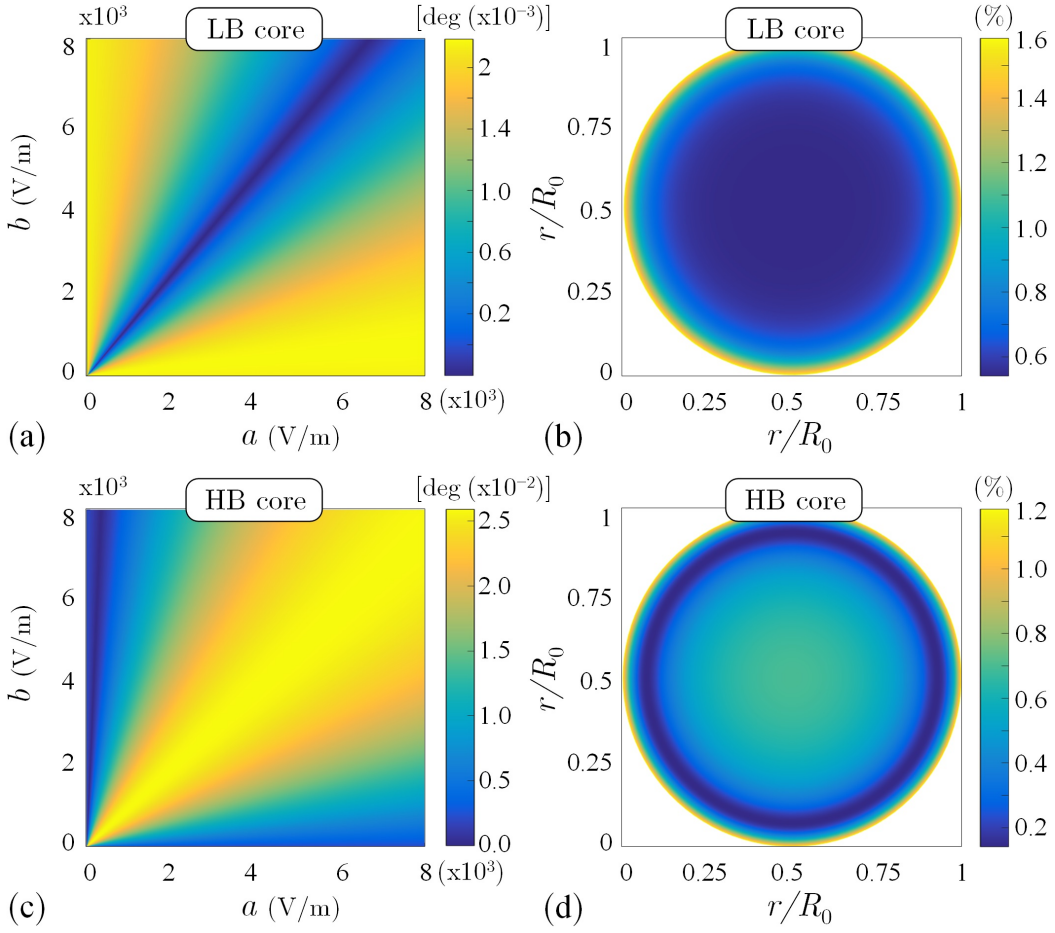

Figure A3.1. Analysis of the term $\varepsilon_0^{-1}\nabla(\nabla\cdot\boldsymbol{\mathcal{P}}^{(1)})$ in the nonlinear wave equation [Eq. (A3.1)] considering lowly-birefringent (LB) and highly-birefringent (HB) cores. LB case: (a) Eq. (A3.4) and (b) Eq. (A3.7). HB case: (c) Eq. (A3.4) and (d) Eq. (A3.7).

Once again, if we consider a fiber perturbation at $z = z_{\mathrm{P}}$, the complex amplitude of the linear polarization $\boldsymbol{P}_{\omega_0}^{(1)}$ takes the form:

$$\boldsymbol{P}_{\omega_0}^{(1)}(x,y,z_{\mathrm{P}}) \simeq \varepsilon_0 \left\{ \begin{array}{l} \left[\chi_{xx}^{(1)}(z_{\mathrm{P}})\, a + \chi_{xy}^{(1)}(z_{\mathrm{P}})\, b \exp\left(-j\Delta\beta z_{\mathrm{P}}\right)\right]\hat{u}_x \\ + \left[\chi_{xy}^{(1)}(z_{\mathrm{P}})\, a + \chi_{yy}^{(1)}(z_{\mathrm{P}})\, b \exp\left(-j\Delta\beta z_{\mathrm{P}}\right)\right]\hat{u}_y \end{array} \right\} F(x,y)\exp\left(-j\beta z_{\mathrm{P}}\right). \tag{A3.10}$$

Let us assume $z_{\mathrm{P}} \sim \lambda$ to simplify the numerical calculations. In such a case, $\exp\left(-j\Delta\beta z_{\mathrm{P}}\right) \simeq 1$ and Eq. (A3.10) is reduced to Eq. (A3.3). In this way, we can study the anisotropic response of the linear polarization in an HB core by using the same expressions as in the LB core [Eqs. (A3.4) and (A3.7)] but now considering the intrinsic linear birefringence of the HB core, of the order of $\Delta\chi^{(1)} \sim 10^{-3}$. The circular birefringence will be assumed of the same order of magnitude as in the LB case ($\chi_{xy}^{(1)} \simeq 4.2\cdot 10^{-5}$), induced by a twist rate of 5 turns/m.

Figure A3.1(c) depicts Eq. (A3.4) for different values of a and b. Now, the maximum misalignment angle between $\boldsymbol{P}_{\omega_0}^{(1)}$ and $\boldsymbol{E}_{\omega_0}$ is found around $2.5\cdot 10^{-2}$ degrees when $a = b$. In this case, $\mathcal{R}^{(1)}$ is found to be lower than 1.5% with $\sqrt{x^2+y^2} < R_0$ and $\lambda_0 = 1550$ nm [see Fig. A3.1(d)]. In spite of the fact that the maximum value of $\mathcal{R}^{(1)}$ is lower than in the LB case, note that its average value is increased around 0.1% in the HB core. In any case, we finally conclude that the source $\varepsilon_0^{-1}\nabla(\nabla\cdot\boldsymbol{\mathcal{P}}^{(1)})$ can be neglected in the nonlinear wave equation when LB and HB cores are involved in the theoretical analysis.

Nonlinear polarization

In general, the nonlinear effects of an optical fiber have an anisotropic response with the incident electric field [149]. In order to analyze the impact of their anisotropic nature in the nonlinear wave equation [Eq. (A3.1)], let us now assume an incident monochromatic electric field strength $\boldsymbol{\mathcal{E}}(\boldsymbol{r},t)=\mathrm{Re}\left\{\boldsymbol{E}_{\omega_0}(\boldsymbol{r})\exp(j\omega_0 t)\right\}$ in a step-index LB core of the form:[20]

$$\boldsymbol{E}_{\omega_0}(\boldsymbol{r})=(a\hat{u}_x+jb\hat{u}_y)\,F(x,y)\exp(-j\beta z)\,, \tag{A3.11}$$

and $(a,b)\in\mathbb{R}^2$. The optical power launched at $z=0$ is found to be $P_{\mathrm{L}}=\mathscr{C}^{(\mathrm{P})}\left(a^2+b^2\right)$, where:

$$\mathscr{C}^{(\mathrm{P})}:=\frac{1}{2\eta_{\mathrm{co}}}\iint F^2(x,y)\,\mathrm{d}x\mathrm{d}y, \tag{A3.12}$$

and $\eta_{\mathrm{co}}=\eta_0/n_{\mathrm{co}}\simeq 120\pi/n_{\mathrm{co}}$. In this case, we will assume that $\boldsymbol{P}^{(1)}_{\omega_0}(\boldsymbol{r})=\varepsilon_0\left(n^2_{\mathrm{co}}-1\right)\boldsymbol{E}_{\omega_0}(\boldsymbol{r})$, i.e., $\nabla\cdot\boldsymbol{P}^{(1)}_{\omega_0}=0$ to analyze only the anisotropic response of the global polarization $\boldsymbol{\mathcal{P}}=\boldsymbol{\mathcal{P}}^{(1)}+\boldsymbol{\mathcal{P}}^{(3)}$ induced by the nonlinear effects. Concretely, using Eq. (3.2.12), the complex amplitude of $\boldsymbol{\mathcal{P}}^{(3)}$ takes the form:

$$\boldsymbol{P}^{(3)}_{\omega_0}(\boldsymbol{r})=\varepsilon_0\gamma\left[a\left(a^2+\frac{1}{3}b^2\right)\hat{u}_x+jb\left(b^2+\frac{1}{3}a^2\right)\hat{u}_y\right]F^3(x,y)\exp(-j\beta z)\,, \tag{A3.13}$$

with $\gamma=1.5\cdot 10^{-22}\ \mathrm{m}^2/\mathrm{V}^2$ in the third transmission window. As a result, in a transversal plane of the fiber the fields $\boldsymbol{\mathcal{E}}$, $\boldsymbol{\mathcal{P}}^{(1)}$ and $\boldsymbol{\mathcal{P}}^{(3)}$ describe ellipses with the axes aligned with our reference system $\{O;\{\hat{u}_x,\hat{u}_y,\hat{u}_z\}\}$ and with an ellipticity given respectively by the angles:

$$\Psi_{\mathcal{E}}=\Psi_{\mathcal{P}^{(1)}}=\arctan\left(\frac{b}{a}\right); \tag{A3.14}$$

$$\Psi_{\mathcal{P}^{(3)}}=\arctan\left(\frac{b\left(b^2+\frac{1}{3}a^2\right)}{a\left(a^2+\frac{1}{3}b^2\right)}\right). \tag{A3.15}$$

Consequently, we can observe that the nonlinear polarization has an anisotropic response given that, in general, $\Psi_{\mathcal{P}^{(3)}}\neq\Psi_{\mathcal{E}}$. In this scenario, the complex amplitude $\boldsymbol{P}_{\omega_0}$ of $\boldsymbol{\mathcal{P}}$ is found to be:

$$\boldsymbol{P}_{\omega_0}(\boldsymbol{r})=\varepsilon_0\left\{\begin{array}{l} a\left[\left(n^2_{\mathrm{co}}-1\right)+\gamma F^2(x,y)\left(a^2+\frac{1}{3}b^2\right)\right]\hat{u}_x \\ +b\left[\left(n^2_{\mathrm{co}}-1\right)+\gamma F^2(x,y)\left(b^2+\frac{1}{3}a^2\right)\right]\hat{u}_y \end{array}\right\}F(x,y)\exp(-j\beta z)\,. \tag{A3.16}$$

Thus, the difference between the ellipticity of the ellipses described by $\boldsymbol{\mathcal{E}}$ and $\boldsymbol{\mathcal{P}}$ is:

$$\Delta\Psi(x,y;a,b)=\left|\arctan\left(\frac{b\left[\left(n^2_{\mathrm{co}}-1\right)+\gamma F^2(x,y)\left(b^2+\frac{1}{3}a^2\right)\right]}{a\left[\left(n^2_{\mathrm{co}}-1\right)+\gamma F^2(x,y)\left(a^2+\frac{1}{3}b^2\right)\right]}\right)-\arctan\left(\frac{b}{a}\right)\right|. \tag{A3.17}$$

The anisotropic response of the nonlinear effects should be investigated at each (x,y) point of $\mathbb{R}^2$ by analyzing $\Delta\Psi$ for the specific values of a and b where this function is maximized. In order to simplify the problem, let us analyze the point $(x,y)=(0,0)$, where we can expect that the nonlinear effects are maximized for the LP_{01} mode group. Therefore, Eq. (A3.17) is reduced to the function $\Delta\psi(a,b):=\Delta\Psi(0,0;a,b)$, with $\Delta\psi\in\mathcal{F}\left(\mathbb{R}^2,\mathbb{R}^+\right)$.

Figure A3.2(a) indicates that $\Delta\psi=0$ when $a=0$ (linear polarization), $b=0$ (linear polarization) or $a=b$ (circular polarization).[21] Nevertheless, the nonlinear birefringence is maximized by taking $b=a/2$ or $a=b/2$, which corresponds with an elliptical polarization in the incident electric field with $\Psi_{\mathcal{E}}=27^{\mathrm{o}}$ and 63^{o}, respectively. Next, we calculate the value of $\Delta\psi$ as a function of P_{L}

[20] In the nonlinear regime, we only report the LB case for the sake of simplicity. The HB case was also discussed in our personal study finding the same conclusions as in the LB case.

[21] Here, we refer to the *linear polarization* as the linear trajectory described by $\boldsymbol{\mathcal{E}}$ in a transversal plane of the fiber. The context should avoid any confusion with $\boldsymbol{\mathcal{P}}^{(1)}$.

by taking $b = a/2$. As can be seen from Fig. A3.2(b), the difference of the ellipticity between $\boldsymbol{\mathcal{E}}$ and $\boldsymbol{\mathcal{P}}$ reaches its maximum value $\Delta\psi_{\max} \simeq 12^{\circ}$ for optical powers higher than 140 dBm. Nonetheless, considering realistic optical power launch levels lower than 40 dBm, $\Delta\psi \sim 10^{-8}$ degrees, much lower than the misalignment angle between $\boldsymbol{\mathcal{E}}$ and $\boldsymbol{\mathcal{P}}^{(1)}$ in the previous numerical examples.

For completeness, we analyze the ratio of the nonlinear sources:

$$\mathcal{R}^{(3)}\left(x, y; P_{\mathrm{L}}\right) := \frac{\left|\varepsilon_0^{-1}\nabla\left(\nabla\cdot\boldsymbol{P}_{\omega_0}^{(3)}\left(x, y, z=0; P_{\mathrm{L}}\right)\right)\right|}{\left|\mu_0\omega_0^2\boldsymbol{P}_{\omega_0}^{(3)}\left(x, y, z=0; P_{\mathrm{L}}\right)\right|}. \tag{A3.18}$$

We evaluated the above ratio by considering a hypothetical optical power of $P_{\mathrm{L}} = 140$ dBm. In that case, the maximum value of $\mathcal{R}^{(3)}$ was observed near the cladding ($\sqrt{x^2+y^2} \to R_0$) with $\mathcal{R}^{(3)} < 3\%$. Therefore, for realistic values of P_{L} ($\ll 140$ dBm), we can safely assume that the term $\varepsilon_0^{-1}\nabla(\nabla\cdot\boldsymbol{\mathcal{P}}^{(3)})$ can be omitted in Eq. (A3.1). In conclusion, in all the analyzed cases, the source $\varepsilon_0^{-1}\nabla(\nabla\cdot(\boldsymbol{\mathcal{P}}^{(1)}+\boldsymbol{\mathcal{P}}^{(3)}))$ can be neglected in the nonlinear wave equation, in line with the classical assumption usually indicated in the optical fiber literature [139, 150, 159–161].

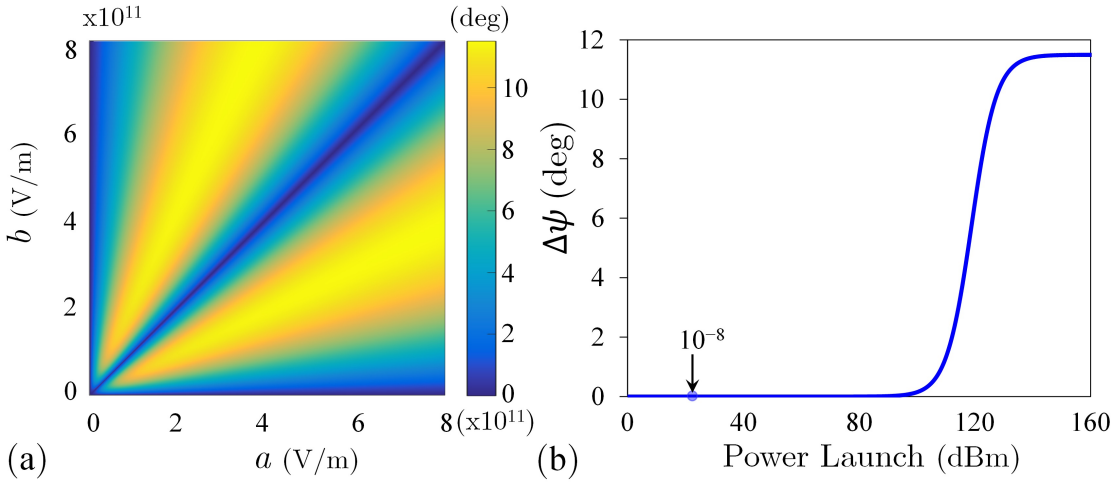

Figure A3.2. Analysis of the term $\varepsilon_0^{-1}\nabla(\nabla\cdot\boldsymbol{\mathcal{P}}^{(3)})$ in the nonlinear wave equation [Eq. (A3.1)]. (a) Behavior of the $\Delta\psi$ function with the parameters a and b. (b) Evolution of $\Delta\psi$ with the optical power launch level when $b = a/2$.

A3.2 Linear and nonlinear constitutive relations $\mathcal{P}$-$\mathcal{E}$

The constitutive relation between the linear polarization $\boldsymbol{\mathcal{P}}^{(1)}$ and $\boldsymbol{\mathcal{E}}$ in an anisotropic, heterogeneous, time-varying and temporally dispersive dielectric medium is given by the expression:

$$\mathcal{P}_i^{(1)}\left(\boldsymbol{r}, t\right) = \varepsilon_0 \int_{-\infty}^{\infty} \chi_{ij}^{(1)}\left(\boldsymbol{r}, t, \tau\right)\mathcal{E}_j\left(\boldsymbol{r}, \tau\right)\mathrm{d}\tau, \tag{A3.19}$$

where $\chi_{ij}^{(1)}$ is the first-order electric susceptibility tensor accounting for the linear and circular birefringence of the MCF in the time domain. Concretely, $\varepsilon_0\chi_{ij}^{(1)}\left(\boldsymbol{r}, t, \tau\right)$ is the time-varying impulse response of the system, i.e., the response of the system at time t for a homogeneous input at time τ of the form $\mathcal{E}_j\left(\boldsymbol{r}, t\right) = \delta\left(t-\tau\right)$. If we assume that the temporal birefringence is approximately constant in $\delta t \sim \langle T\rangle \sim \lambda_{\max}/c_0$, with $\lambda_{\max} := \max\left\{\lambda_m\right\}_m$, the linear and time-varying system can be regarded as a linear and time-invariant system in a time interval of the order of $\langle T\rangle$:

$$\mathcal{P}_i^{(1)}\left(\boldsymbol{r}, t\right) \simeq \varepsilon_0 \int_{\langle T\rangle} \chi_{ij}^{(1)}\left(\boldsymbol{r}, t-\tau\right)\mathcal{E}_j\left(\boldsymbol{r}, \tau\right)\mathrm{d}\tau. \tag{A3.20}$$

Thus, applying a short-time Fourier transform ($\mathcal{F}_{\mathrm{T}}$) in a temporal window $\mathscr{W}(t)$ defined in a time interval $\delta t \sim \langle T \rangle$, Eq. (A3.20) can be expressed in the frequency domain as (we use a tilde to denote the Fourier-transformed fields):[22]

$$\widetilde{\mathcal{P}}_i^{(1)}(\boldsymbol{r},\omega;t) = \varepsilon_0 \widetilde{\chi}_{ij}^{(1)}(\boldsymbol{r},\omega;t)\,\widetilde{\mathcal{E}}_j(\boldsymbol{r},\omega;t)\,, \tag{A3.21}$$

where:

$$\begin{aligned}\widetilde{\chi}_{ij}^{(1)}(\boldsymbol{r},\omega;t) = \mathcal{F}_{\mathrm{T}}\left[\chi_{ij}^{(1)}(\boldsymbol{r},t)\right] :&= \int_{-\infty}^{\infty} \chi_{ij}^{(1)}(\boldsymbol{r},\tau)\,\mathscr{W}(\tau - t)\exp(-j\omega\tau)\,\mathrm{d}\tau \\ &= \int_{t-T/2}^{t+T/2} \chi_{ij}^{(1)}(\boldsymbol{r},\tau)\exp(-j\omega\tau)\,\mathrm{d}\tau,\end{aligned} \tag{A3.22}$$

and:

$$\widetilde{\mathcal{E}}_j(\boldsymbol{r},\omega;t) = \mathcal{F}_{\mathrm{T}}\left[\mathcal{E}_j(\boldsymbol{r},t)\right] = \mathrm{Re}\left\{2\pi E_{j,\omega_0}(\boldsymbol{r};t)\,\delta(\omega-\omega_0)\right\}; \tag{A3.23}$$

$$\widetilde{\mathcal{P}}_i^{(1)}(\boldsymbol{r},\omega;t) = \mathcal{F}_{\mathrm{T}}\left[\mathcal{P}_i^{(1)}(\boldsymbol{r},t)\right] = \mathrm{Re}\left\{2\pi P_{i,\omega_0}^{(1)}(\boldsymbol{r};t)\,\delta(\omega-\omega_0)\right\}. \tag{A3.24}$$

At this point, remember that $\mathrm{Im}\left\{\widetilde{\chi}_{ij}^{(1)}\right\} \simeq 0$ in silica when the optical carrier is located in the third transmission window. Therefore, using Eqs. (A3.23) and (A3.24) in Eq. (A3.21), taking into account that:

$$\widetilde{\chi}_{ij}^{(1)}(\boldsymbol{r},\omega;t)\,\delta(\omega-\omega_0) = \widetilde{\chi}_{ij}^{(1)}(\boldsymbol{r},\omega_0;t)\,\delta(\omega-\omega_0)\,, \tag{A3.25}$$

and renaming $\widetilde{\chi}_{ij}^{(1)}(\boldsymbol{r},\omega_0;t) \equiv \chi_{ij}^{(1)}(\boldsymbol{r},\omega_0;t)$,[23] we finally obtain Eq. (3.2.11). Now, it is obvious why the dispersive nature of the MCF cannot be observed in the monochromatic regime.

On the other hand, the nonlinear constitutive relation given by Eq. (3.2.12) can be derived from the constitutive relation between the nonlinear polarization $\boldsymbol{\mathcal{P}}^{(3)}$ and $\boldsymbol{\mathcal{E}}$ in the time domain:

$$\mathcal{P}_i^{(3)}(\boldsymbol{r},t) = \varepsilon_0 \chi_{ijkl}^{(3)} \mathcal{E}_j(\boldsymbol{r},t)\,\mathcal{E}_k(\boldsymbol{r},t)\,\mathcal{E}_l(\boldsymbol{r},t)\,. \tag{A3.26}$$

It can be noted that the nonlinear response of $\boldsymbol{\mathcal{P}}^{(3)}$ is assumed instantaneous with $\boldsymbol{\mathcal{E}}$ because the delay response induced by the electronic and nuclear transitions of silica atoms can be omitted when the incident electric field is a continuous wave [159]. In this context, using Eqs. (3.2.8) and (3.2.10) along with the intrinsic permutation symmetry of $\chi_{ijkl}^{(3)}$, we find Eq. (3.2.12).

[22] We can safely assume that the short-time Fourier transform and the classical Fourier transform share the same mathematical properties in $\delta t \sim \langle T \rangle$ given that we have assumed slowly-varying temporal changes of the optical medium. The same remark applies to Chapter 4.

[23] Writing $\chi_{ij}^{(1)}(\boldsymbol{r},t)$ and $\chi_{ij}^{(1)}(\boldsymbol{r},\omega_0;t)$ simultaneously is a sloppy notation. Although it is mathematically wrong to use the same function $\chi_{ij}^{(1)}$ to describe two *different* functions, let us relax the notation to employ exclusively the tilde in the frequency domain.

Appendix B3: Coupled local-power theory

The numerical estimation of the crosstalk mean between PCMs by using the CLMT requires a high computational time. In such circumstances, it is natural to ask if we can derive a closed-form expression to estimate the crosstalk mean between two given PCMs of the MCF. The answer requires to investigate previously a set of coupled equations in terms of the *average power* of the local modes by using a first-order solution of the CLMT. Therefore, our first goal is to analyze the suitability of a first-order solution of Eq. (3.2.42) to estimate the mean of the iC-XT, DIC-XT and XIC-XT.

To this end, let us consider an SM-2CF with cores a and b, $d_{ab} > 3R_0$, and operating in the linear regime. In such a scenario, the mode-coupling from the PCM k to the PCM i can be modeled by the following equation when omitting the fiber losses and the interaction with other PCMs:

$$j\partial_z \mathcal{A}_i(z;t) = \Upsilon_{i,k}(z,\omega_0;t)\exp\left(-j\Delta\phi_{k,i}(z,\omega_0;t)\right)\mathcal{A}_k(z;t), \tag{B3.1}$$

where $\Upsilon_{i,j}$ is the MCC and $(i,k) \in \{ax,ay,bx,by\}^2$. Equation (B3.1) allows us to describe the iC-XT, DIC-XT and XIC-XT by replacing $\Upsilon_{i,k}$ by the corresponding linear MCC (see Section 3.2.4). Hence, in a fiber segment located between the points z_1 and z_2, with $|z_2 - z_1|$ larger than the correlation length of the fiber longitudinal perturbations and sufficiently short to assume the MCC approximately constant along the segment, a first-order solution of Eq. (B3.1) can be written as $\mathcal{A}_i(z_2;t) \simeq T_{i,k}(\omega_0;t)\,\mathcal{A}_k(z_1;t)$, with:

$$\begin{aligned} T_{i,k}(\omega_0;t) &= -j\int_{z_1}^{z_2} \Upsilon_{i,k}(\xi,\omega_0;t)\exp\left(-j\Delta\phi_{k,i}(\xi,\omega_0;t)\right)\mathrm{d}\xi \\ &\simeq -j\Upsilon_{i,k}(z_1,\omega_0;t)\int_{z_1}^{z_2}\exp\left(-j\Delta\phi_{k,i}(\xi,\omega_0;t)\right)\mathrm{d}\xi. \end{aligned} \tag{B3.2}$$

Unfortunately, Eq. (B3.2) cannot be employed to estimate the iC-XT in LB-MCFs due to the high mode-coupling between orthogonal PCMs of the same core. In this scenario, the rapid variations of the iC-XT along the fiber length cannot be estimated from a first-order solution of Eq. (B3.1). As an example, we show in Fig. B3.1(a) the random longitudinal evolution of the iC-XT between the PCMs *ax-ay* along 40 m of the same MCF simulated in Fig. 3.5(b2) for the second day, with an iC-XT mean of −2.5 dB.

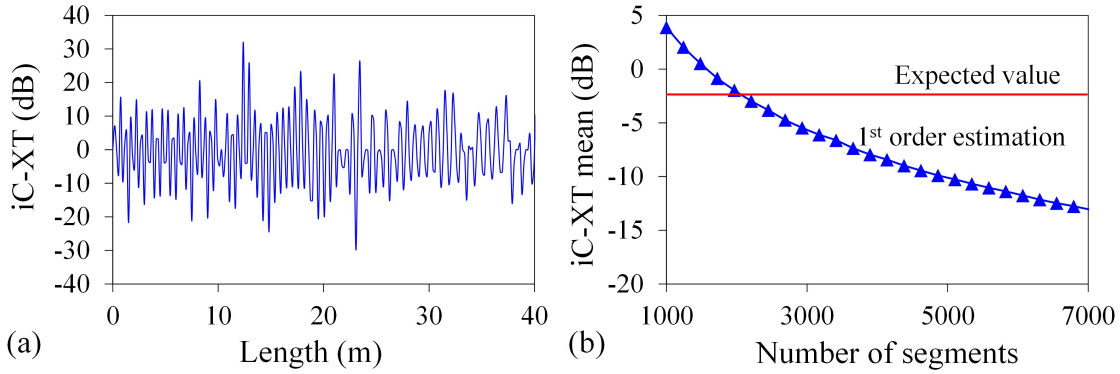

Figure B3.1. (a) Longitudinal evolution of the iC-XT between the PCMs *ax-ay* calculated from the CLMT. (b) Numerical estimation of the iC-XT mean at $z = 150$ m by using a first-order solution of the CLMT. Each point corresponds to a different Monte Carlo simulation with 100 iterations.

As seen, the use of a first-order solution of the CLMT to describe these rapidly-varying fluctuations may be inaccurate. This is confirmed in Fig. B3.1(b), where the iC-XT mean of this example is calculated at $z = 150$ m by using the same numerical method of Section 3.3 but now applying a first-order estimation of the CLMT [Eq. (B3.2)]. Each birefringent segment is

divided in several small fiber segments where the first-order solution of the CLMT is applied. We performed different Monte Carlo simulations of 100 iterations each one varying the total number of small fiber segments along the MCF length from 1000 to 7000. Each Monte Carlo simulation corresponds to a different point in Fig. B3.1(b). It can be noted that, despite the fact that we use a high number of segments, the numerical solution does not converge to the expected value of $-2.5\,\mathrm{dB}$. The reason is found in the rapid variations and the high variance of the iC-XT. Consequently, we cannot investigate a closed-form expression to estimate the iC-XT from a coupled-power theory which requires to use a first-order solution of the CLMT. In a similar way, Eq. (B3.2) cannot be employed to estimate the DIC-XT in MCFs with coupled cores due to the high mean and variance of this crosstalk type.

Nevertheless, the use of Eq. (B3.2) could be an attractive strategy in HB-MCFs with uncoupled cores. In this scenario, the mean and variance of the iC-XT, DIC-XT and XIC-XT are significantly reduced in comparison with the lowly-birefringent and coupled-core cases. In this vein, the corresponding mean of each crosstalk may be estimated from a first-order solution of the CLMT. As a byproduct, we can investigate a set of coupled equations in terms of the average power of the local modes, the so-called *coupled local-power theory* (CLPT); and later, the corresponding closed-form expressions to estimate the crosstalk mean between the PCMs can be derived from the CLPT, which could be of extreme utility to engineer the crosstalk in HB-MCFs comprising uncoupled cores.

In order to estimate analytically the crosstalk between the PCMs i and k, it would be sufficient to know the average value of the coupled power. To this end, we introduce here the concept of *local power*, defined as the power[24] of a local mode, i.e., $P_{i(k)}(z;t) = \left|\mathcal{A}_{i(k)}(z;t)\right|^2$. Proceeding in a similar manner as in Chapter 2 (see page 38), we define the average value of P_i as:

$$\overline{P}_i(z;t) := \langle P_i(z;t)\rangle = \frac{1}{2L_{\mathrm{C}}(z;t)} \int_{z-L_{\mathrm{C}}(z;t)}^{z+L_{\mathrm{C}}(z;t)} \left|\mathcal{A}_i(\tau;t)\right|^2 \mathrm{d}\tau, \tag{B3.3}$$

where $L_{\mathrm{C}}(z;t)$ is the coupling length between the PCMs involved in the theoretical analysis, in our case, the PCMs i and k. The coupling length is the minimum fiber distance required to observe the maximum coupled power between both PCMs when a single PCM is excited at the MCF input and assuming an MCF without perturbations. In such circumstances, this parameter is found to be constant. However, in real MCFs, L_{C} and $\overline{P}_i$ inherit the longitudinal and temporal dependence of the medium perturbations. Furthermore, taking into account that in MCFs with $d_{ab} > 3R_0$ the crosstalk variance is much lower than the crosstalk mean (see Chapter 2), we can safely assume that $P_i(z;t)$ is approximately constant in $\delta z \sim L_{\mathrm{C}}$. Thus, in a given z_0 point $\overline{P}_i(z_0+\delta z;t) \simeq P_i(z_0+\delta z;t)$ in $\delta z \sim L_{\mathrm{C}}(z_0;t)$. Later, we will use this approximation to derive the closed-form expression of the crosstalk mean between the PCMs i and k.

Our goal is to derive a partial differential equation modeling the longitudinal evolution of $\overline{P}_i$. To this end, we will use a first-order solution of the CLMT by selecting an MCF segment close to the origin ($z_1 \equiv 0$ and $z_2 \equiv z$) with a length satisfying the same conditions as in Eq. (B3.2). Hence, this equation can be restated as:

$$T_{i,k}(\omega_0;t) \simeq -j\Upsilon_{i,k}(0,\omega_0;t) \int_0^z f_{k,i}(\xi,\omega_0;t) \exp\left(-j\Delta\beta_{k,i}(\omega_0)\,\xi\right) \mathrm{d}\xi, \tag{B3.4}$$

with:

$$f_{k,i}(z,\omega_0;t) := \exp\left(-j\int_0^z \Delta\beta_{k,i}^{(\mathrm{B+S})}(\xi,\omega_0;t)\,\mathrm{d}\xi\right). \tag{B3.5}$$

Note that $f_{k,i}$ can only be assumed as an ergodic and strict-sense stationary random process in the z variable in time intervals where the temporal perturbations do not induce changes in its statistical distribution along the MCF segment. Accordingly, we can write:

[24] Actually, $P_{i(k)} = \mathscr{C}_{i(k)}^{(\mathrm{P})}\left|\mathcal{A}_{i(k)}(z;t)\right|^2$ where $\mathscr{C}_{i(k)}^{(\mathrm{P})}$ is given by Eq. (1.5.12). Nonetheless, we take $\mathscr{C}_{i(k)}^{(\mathrm{P})} \equiv 1$ for simplicity.

$$\begin{aligned}\partial_z \overline{P}_i(z;t) &= \partial_z \langle P_i(z;t)\rangle = \partial_z \langle \mathcal{A}_i(z;t)\,\mathcal{A}_i^*(z;t)\rangle \\ &= \langle \partial_z\mathcal{A}_i(z;t)\,\mathcal{A}_i^*(z;t) + \mathcal{A}_i(z;t)\,\partial_z\mathcal{A}_i^*(z;t)\rangle \\ &= \langle -j\Upsilon_{i,k}(z,\omega_0;t)\exp\left(-j\Delta\phi_{k,i}(z,\omega_0;t)\right)\mathcal{A}_k(z;t)\,\mathcal{A}_i^*(z;t) + \text{c.c.}\rangle \\ &\simeq -j\Upsilon_{i,k}(z,\omega_0;t)\exp\left(-j\Delta\beta_{k,i}(\omega_0)\,z\right)\langle f_{k,i}(z,\omega_0;t)\,\mathcal{A}_k(z;t)\,\mathcal{A}_i^*(z;t)\rangle + \text{c.c.}, \quad \text{(B3.6)}\end{aligned}$$

with the abbreviation c.c. indicating the complex conjugate terms of the RHS. Now, applying a first-order solution in $\mathcal{A}_k(z;t)$ and $\mathcal{A}_i^*(z;t)$ as detailed before, neglecting the terms $\Upsilon_{i,k}^3$ due to the weak mode-coupling conditions, assuming that $f_{k,i}$ is adequately randomized[25] along the MCF segment, and performing a similar mathematical discussion as in Chapter 2 (see page 40) to derive the linear power-coupling coefficient, it is tedious but straightforward to demonstrate that Eq. (B3.6) can be reduced to:[26]

$$\partial_z \overline{P}_i(z;t) = h_{i,k}(z,\omega_0;t)\left[\overline{P}_k(z;t) - \overline{P}_i(z;t)\right], \quad \text{(B3.7)}$$

where $h_{i,k}$ is the linear power-coupling coefficient:

$$h_{i,k}(z,\omega_0;t) = \Upsilon_{i,k}^2(z,\omega_0;t)\,S_{k,i}^{(f)}\left(\upsilon = \frac{\Delta\beta_{k,i}(\omega_0)}{2\pi};t\right), \quad \text{(B3.8)}$$

with $S_{k,i}^{(f)}$ the power spectral density (PSD) of $f_{k,i}$ and υ the spatial frequency.[27] It is worthy to note that, in contrast to the CPT of Chapter 2, the CLPT includes space- and time-varying power-coupling coefficients.

Outstandingly, the mean of the iC-XT and DIC-XT can be analytically estimated in HB-MCFs from Eq. (B3.8) taking into account that $\overline{P}_i(z=0;t) = 0$, $\overline{P}_k(z;t) \gg \overline{P}_i(z;t)$, and $\overline{P}_k$ and $h_{i,k}$ have an average value much higher than their random fluctuations along the MCF length:[28]

$$\mu_{i,k}(\omega_0;t) = E\left[\frac{P_i(z=L;t)}{P_k(z=L;t)}\right] \simeq E\left[\frac{\overline{P}_i(z=L;t)}{\overline{P}_k(z=L;t)}\right] \simeq L h_{i,k}(z=L,\omega_0;t). \quad \text{(B3.9)}$$

The iC-XT mean can be calculated as in SCFs, that is, assuming a Gaussian PSD [145]:

$$S_{k,i}^{(f)}(\upsilon;t) = \sqrt{\pi} l_{k,i}(t)\exp\left[-\left(\pi l_{k,i}(t)\,\upsilon\right)^2\right]. \quad \text{(B3.10)}$$

In addition, it is noticeable that the random behavior of the DIC-XT is mainly induced by the random bending and twisting conditions of the MCF. Thus, in coherence with [31], we calculate the DIC-XT by using an exponential ACF [145], which corresponds to a Lorentzian PSD:

$$S_{k,i}^{(f)}(\upsilon;t) = \frac{2l_{k,i}(t)}{1+\left(2\pi l_{k,i}(t)\,\upsilon\right)^2}. \quad \text{(B3.11)}$$

In both cases, $l_{k,i}$ is the correlation length of the random process $f_{k,i}$, which can also vary in time due to the temporal perturbations of the medium.

[25] That is, $\langle f_{k,i}(z,\omega_0;t)\rangle = 1$, see the final note at the end of this appendix.

[26] A similar mathematical discussion of this section can also be found in Chapter 5 of [146] for MM-SCFs operating in the linear regime and omitting their temporal perturbations, i.e., modeling the optical medium as a linear and time-invariant (LTI) system.

[27] The PSD is calculated as $S_{k,i}^{(f)}(\upsilon;t) = \int_{-\infty}^{\infty} R_{k,i}^{(f)}(z,\omega_0;t)\exp(j\upsilon z)\,\mathrm{d}z$, where $R_{k,i}^{(f)}$ is the autocorrelation function (ACF) defined as $R_{k,i}^{(f)}(z,\omega_0;t) := \left\langle f_{k,i}(x,\omega_0;t)\,f_{k,i}^*(x+z,\omega_0;t)\right\rangle$. The dependence of the PSD with ω_0 is implicit in the spatial frequency $\upsilon \propto \Delta\beta_{k,i}(\omega_0)$.

[28] Note that we can write $\overline{P}_i(z=L;t)$ from Eq. (B3.7) as $\overline{P}_i(z=L;t) = \int_0^L h_{i,k}(z,\omega_0;t)\left[\overline{P}_k(z;t) - \overline{P}_i(z;t)\right]\mathrm{d}z$. Moreover, the expectation operator only applies on the z variable.

However, the XIC-XT cannot be directly estimated from the CLPT because of the linear MCC modeling the XIC-XT in Eq. (B3.1), i.e.$\Upsilon_{i,k} \equiv \eta_{i,k}$, is negligible (see Fig. 3.2). As demonstrated in this chapter, the XIC-XT depends directly on the iC-XT of the cores propagating the PCMs i and k. This is not the case for the iC-XT and DIC-XT, which can be roughly estimated from the MCCs $m_{i,k}$ and $\kappa_{i,k}$ by omitting additional interactions with other PCMs of the fiber. Obviously, these considerations should be revisited when the estimation of the DIC-XT requires to consider the mode-coupling with other adjacent cores, e.g., in HB-MCFs with coupled cores.

Specifically, the XIC-XT can be calculated from the DIC-XT and the global IC-XT observed in both polarizations. As an example, the crosstalk mean between the PCMs ax and by can be found from the relation:

$$\begin{aligned}\mu_{ax,by}(\omega_0;t) &= E\left[\frac{P_{ax}(z=L;t)}{P_{by}(z=L;t)}\right] = E\left[\frac{P_a(z=L;t)-P_{ay}(z=L;t)}{P_{by}(z=L;t)}\right] \\ &= \mu_{a,by}(\omega_0;t) - \mu_{ay,by}(\omega_0;t)\,. \end{aligned} \tag{B3.12}$$

The term $\mu_{a,by}$ is the crosstalk mean observed in both polarizations of the core a when only the PCM by is stimulated at the MCF input. Thus, $\mu_{a,by} \equiv \mu_{a,b}$, which can be estimated from Eqs. (2.5.14) or (2.5.15). Furthermore, $\mu_{ay,by}$ can be calculated by combining Eqs. (B3.8), (B3.9) and (B3.11).

This theoretical model must be completed in future works by estimating the correlation lengths of the different crosstalk types as a function of MCF parameters such as the material refractive index of each core, the core-to-core distance, or the average value of the bending radius and twist rate, among others. In this way, we will be able to engineer the crosstalk in HB-MCFs without requiring numerical simulations.

Additional note on the derivation of the CLPT

It is important to remark that the derivation of the CLPT requires that $f_{k,i}$ is found to be adequately randomized along the MCF segment. This implies to assume that $\langle f_{k,i}(z,\omega_0;t)\rangle = 1$, with the possibility of retaining the deterministic part of $\Delta\beta_{k,i}^{(\mathrm{B+S})}$ in the definition of $f_{k,i}$. As a result, in contrast to [128], the linear power-coupling coefficient of the CPT of Chapter 2 [Eq. (2.4.12)] and the CLPT [Eq. (B3.8)] can be calculated without the necessity of including the deterministic part of $\Delta\beta_{k,i}^{(\mathrm{B+S})}$ along with the ideal phase-mismatching $\Delta\beta_{k,i}$.

Let us be more specific. In the mathematical derivation of Eq. (B3.7) from Eq. (B3.6), we found a term of the form:

$$\mathrm{Im}\left\{\langle f_{k,i}(z,\omega_0;t)\rangle \langle |\mathcal{A}_i^*(0;t)|\,|\mathcal{A}_k(0;t)|\exp\left(j\Delta\varphi_{k,i}(0;t)\right)\rangle\right\}, \tag{B3.13}$$

where $\Delta\varphi_{k,i}$ is the phase of $\mathcal{A}_i^*(0;t)\,\mathcal{A}_k(0;t)$. As in [146], we can assume that $f_{k,i}(z,\omega_0;t)$ and $\mathcal{A}_{i(k)}(0;t)$ are uncorrelated given that the segment length has been selected higher than $l_{k,i}$. Hence, Eq. (B3.13) is reduce to:

$$\left\langle |\mathcal{A}_i^*(0;t)|\,|\mathcal{A}_k(0;t)|\sin\left(\Delta\varphi_{k,i}(0;t) - \int_0^z \Delta\beta_{k,i}^{(\mathrm{B+S})}(\xi,\omega_0;t)\,\mathrm{d}\xi\right)\right\rangle. \tag{B3.14}$$

Now, separating the deterministic ($\Delta B_{k,i}^{(\mathrm{B+S})}$) and the random part ($\delta\beta_{k,i}^{(\mathrm{B+S})}$) of the MCF perturbations as $\Delta\beta_{k,i}^{(\mathrm{B+S})}(z,\omega_0;t) = \Delta B_{k,i}^{(\mathrm{B+S})} + \delta\beta_{k,i}^{(\mathrm{B+S})}(z,\omega_0;t)$, Eq. (B3.14) can be rewritten as:

$$\left\langle |\mathcal{A}_i^*(0;t)|\,|\mathcal{A}_k(0;t)|\sin\left(\Delta\varphi_{k,i}(0;t) - \Delta B_{k,i}^{(\mathrm{B+S})} z - \int_0^z \delta\beta_{k,i}^{(\mathrm{B+S})}(\xi,\omega_0;t)\,\mathrm{d}\xi\right)\right\rangle, \tag{B3.15}$$

which is found to be null when considering that $\delta\beta_{k,i}^{(\mathrm{B+S})}$ is adequately randomized between 0 and 2π along the MCF segment. Therefore, the condition $\langle f_{k,i}(z,\omega_0;t)\rangle = 1$ does not require to impose that $\Delta B_{k,i}^{(\mathrm{B+S})} = 0$ in Eq. (B3.5) to derive the CLPT.

Appendix C3: Twisting-induced core bending effects

Let us consider a straight 4-core MCF ($R_{\mathrm{B}} = \infty$) with a constant twist rate f_{T}. As can be seen from Fig. C3.1, a non-central core (e.g. core a) has an intrinsic bending radius ($R_{\mathrm{BT},a}$) induced by the MCF twisting. Specifically, $R_{\mathrm{BT},a}$ will depend on f_{T} and the location of the core a. As an example, if the core a is located at the MCF center ($d_a = 0$), then $R_{\mathrm{BT},a} = R_{\mathrm{B}} = \infty$. However, $R_{\mathrm{BT},a} < \infty$ when $d_a \neq 0$ and, therefore, its effects should be included in the ERIM. In this appendix, we will analyze the case of the 4-core MCF depicted in Fig. C3.1, we will demonstrate that $R_{\mathrm{BT},a}$ should be considered when $f_{\mathrm{T}} \geq 6$ turns/m, and we will indicate the modification of the ERIM to include this birefringent effect in $n_{mi}^{(\mathrm{eq})}$.

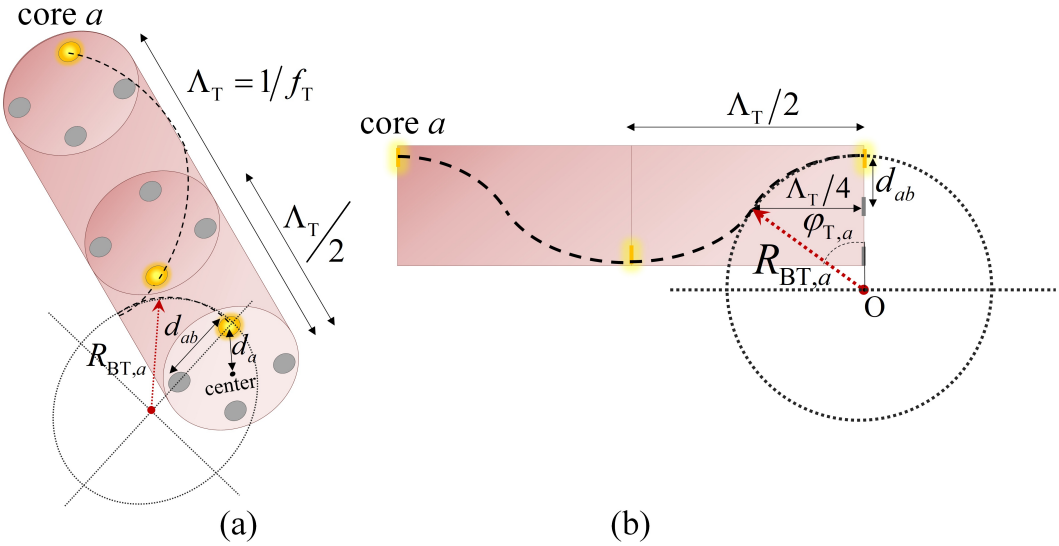

Figure C3.1. Core bending induced by the MCF twisting. (a) 3D image and (b) lateral view.

Firstly, we should derive the mathematical relation between $R_{\mathrm{BT},a}$, f_{T}, and $d_a = d_{ab}/\sqrt{2}$ in the 4-core MCF. As can be inferred from Fig. C3.1(b), we can write:

$$\sin\varphi_{\mathrm{T},a} = \frac{\Lambda_{\mathrm{T}}/4}{R_{\mathrm{BT},a}}; \qquad \cos\varphi_{\mathrm{T},a} = \frac{R_{\mathrm{BT},a} - d_{ab}}{R_{\mathrm{BT},a}} \quad , \tag{C3.1}$$

where $\Lambda_{\mathrm{T}} = 1/f_{\mathrm{T}}$. Hence, from the relation $\sin^2\varphi_{\mathrm{T},a} + \cos^2\varphi_{\mathrm{T},a} = 1$, we obtain:

$$R_{\mathrm{BT},a} = \frac{1}{32 d_{ab} f_{\mathrm{T}}^2} + \frac{d_{ab}}{2}. \tag{C3.2}$$

In particular, Eq. (C3.2) is found to be valid only in the 4-core MCF of this example. Nevertheless, Eq. (C3.2) allows us to estimate the usual values of $R_{\mathrm{BT},a}$ when varying the twist rate in our commercial MCF [Fibercore SM-4C1500(8.0/125)]. Figure C3.2 shows the logarithm of $R_{\mathrm{BT},a}$ for different values of f_{T} and d_{ab}/R_0, where R_0 is the core radius. It can be noted that $R_{\mathrm{BT},a}$ decreases as f_{T} increases, with a quasi-flattened evolution with the ratio d_{ab}/R_0. Considering a usual twist rate value of $f_{\mathrm{T}} = 1$ turns/m, we find that $R_{\mathrm{BT},a} \sim 1000$ m, much higher than the usual values of R_{B} in a real deployed optical fiber system. Nonetheless, $R_{\mathrm{BT},a}$ should be included in the ERIM in highly-twisted MCFs with $f_{\mathrm{T}} \geq 6$ turns/m, where $R_{\mathrm{BT},a} < 10$ m.

In real MCFs, $R_{\mathrm{BT},a}$ also inherits the longitudinal and temporal random fluctuations of $f_{\mathrm{T}}(z;t)$ and $d_{ab}(z)$. In order to include this new birefringent effect in the ERIM, Eq. (3.3.2) should be restated as:

$$n_{mi}^{(\mathrm{eq})}(z,\omega_0;t) \simeq n_{mi}(z,\omega_0;t)\left[1 + \frac{d_m \cos\left(2\pi f_{\mathrm{T}}(z;t)\, z + \theta_0 + \theta_m\right)}{\min\left\{R_{\mathrm{B}}(z;t), R_{\mathrm{BT},m}(z;t)\right\}}\right]. \tag{C3.3}$$

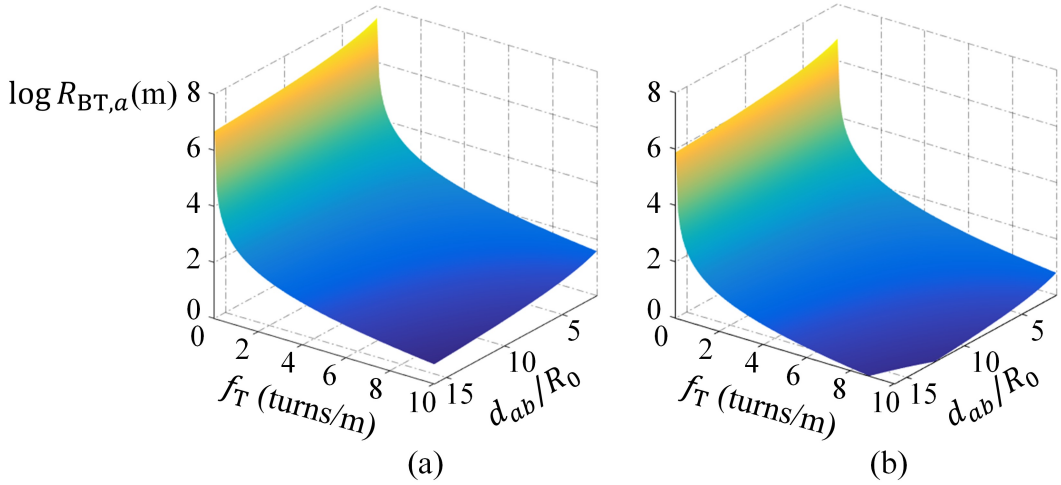

Figure C3.2. Bending radius induced in core a by the MCF twisting. (a) $R_0 = 4$ μm and (b) $R_0 = 25$ μm.

Appendix D3: Experimental characterization of first-order polarization-mode dispersion in multi-core fiber

As indicated in [169], the wavelength sweeping method also allows us to analyze the first-order polarization-mode dispersion (PMD) by measuring the differential group delay (DGD) between the orthogonal PCMs of a given core m. In spite of the fact that this analysis would be more suitable when analyzing the non-monochromatic regime (Chapter 4), we discuss the PMD in this chapter to compare the results with Fig. 3.11.

As discussed in previous sections, a real MCF can be modeled as a series of birefringent segments with a different time-varying retardation and random orientation of the local principal axes. In this scenario, the linear birefringence can also fluctuate in time due to the external temporal perturbations of the optical medium, such as temperature variations. As a result of these temporal excursions of the linear birefringence, the DGD and the first-order PMD will also vary in time.

In the photonics literature, the DGD of the LP_{01} mode is usually calculated by using two different definitions: (a) considering the absolute value of the difference between the group delays of the $\mathrm{LP}_{01,x}$ and $\mathrm{LP}_{01,y}$ modes (in ps, see e.g. [170, 171]), and (b) considering the absolute value of the difference between the group delays per unit of length of the $\mathrm{LP}_{01,x}$ and $\mathrm{LP}_{01,y}$ modes (in ps/km, see e.g. [172]). In this appendix, we will use the former definition. Consequently, taking into account the MCF perturbations, the DGD of the LP_{01} mode in core m ($\Delta T^{(\mathrm{G})}_{m,\omega_0}$) should be calculated as:

$$\Delta T^{(\mathrm{G})}_{m,\omega_0}(t) = \int_0^L \left| \beta^{(\mathrm{eq})(1)}_{my,\omega_0}(z;t) - \beta^{(\mathrm{eq})(1)}_{mx,\omega_0}(z;t) \right| \mathrm{d}z, \tag{D3.1}$$

where $\beta^{(\mathrm{eq})(1)}_{mi,\omega_0}(z;t) := \partial_\omega \beta^{(\mathrm{eq})}_{mi}(z, \omega = \omega_0; t)$. From the above expression, we can infer that $\Delta T^{(\mathrm{G})}_{m,\omega_0}$ is a time-varying random process. In particular, $\Delta T^{(\mathrm{G})}_{m,\omega_0}$ cannot be assumed as a strict-sense stationary random process due to the time-varying conditions of the temperature. Thus, our goal in this appendix is to analyze the temporal evolution of the statistical distribution of $\Delta T^{(\mathrm{G})}_{m,\omega_0}$ in our 4-core MCF.

The statistical distribution of the DGD in an SM-SCF is the well-known Maxwellian distribution [169]. Assuming a similar distribution in MCF media, the p.d.f. of $\Delta T^{(\mathrm{G})}_{m,\omega_0}$ can be expressed as follows:

$$f_{\Delta T^{(\mathrm{G})}_{m,\omega_0}}(\tau;t) = \frac{32}{\pi^2} \frac{\tau^2}{(\Delta\tau_m(t))^3} \exp\left[-\frac{4}{\pi} \left(\frac{\tau}{\Delta\tau_m(t)} \right)^2 \right], \tag{D3.2}$$

with $\Delta\tau_m(t) = E\left[\Delta T^{(\mathrm{G})}_{m,\omega_0}(t)\right]$. Note that $\Delta\tau_m$ is found to be a time-varying function because $\Delta T^{(\mathrm{G})}_{m,\omega_0}$ is not strict-sense stationary. Specifically, assuming a BTC unit of one day (in line with our experimental results of Section 3.5), the value of $\Delta\tau_m$ the j-th BTC will be directly proportional to $\Delta n_{m,j}$, that is, $\Delta\tau_{m,j} \propto \Delta n_{m,j}$. In fact, the higher the linear birefringence, the higher will be the mean of the DGD distribution. In the same way, the variance will also be found directly proportional to $\Delta n_{m,j}$.

Interestingly, $\Delta\tau_{m,j}$ can be estimated by using the wavelength sweeping method as [169]:

$$\Delta\tau_{m,j}\,[\mathrm{ps}] \simeq 1.37 \cdot 10^{-6} N_{m,j} \frac{\lambda_{\mathrm{start}}\,[\mathrm{nm}]\,\lambda_{\mathrm{stop}}\,[\mathrm{nm}]}{|\lambda_{\mathrm{stop}}\,[\mathrm{nm}] - \lambda_{\mathrm{start}}\,[\mathrm{nm}]|}, \tag{D3.3}$$

where $N_{m,j}$ is the number of extrema, and λ_{start} and λ_{stop} are the initial and final wavelengths of the measured optical spectrum, respectively. Along these lines, it should be remarked that the step of the wavelength sweeping method $\Delta\lambda$ must satisfy the condition $\Delta\lambda\,[\mathrm{nm}] < \min\{1/\Delta\tau_{m,j}\,[\mathrm{ps}]\}_j$ in order to measure correctly the number of extrema. Assuming LB cores with $\Delta\tau_{m,j}$ expected to be lower than 5 ps in our MCF, the selected wavelength step of $\Delta\lambda = 5$ pm satisfies this condition in our experimental set-up.

We analyzed the temporal evolution of the DGD in the same days and months as in Fig. 3.11. Figure D3.1(a) shows the measured transmission spectra of the $LP_{01,x}$ and $LP_{01,y}$ modes in cores 1 and 3 the 12^{th} day (March 2016). We can observe that the number of extrema is higher in core 3 than in core 1. Therefore, we conclude that core 3 has a higher linear birefringence and a higher DGD than core 1, as pointed out in Section 3.5.

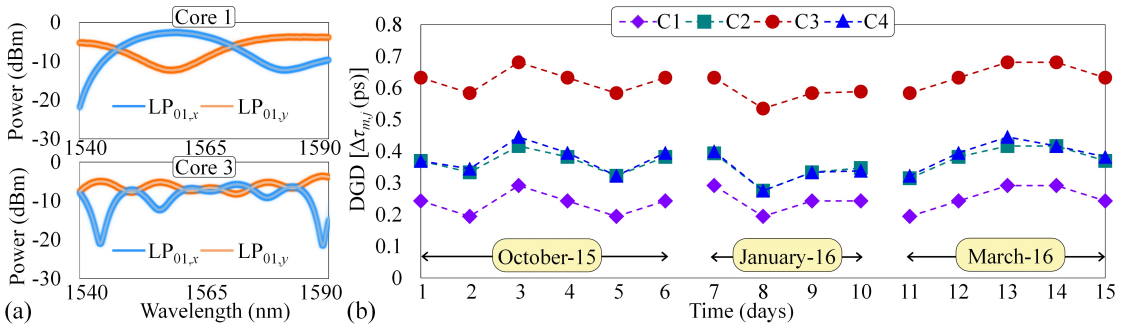

Figure D3.1. (a) Measured transmission spectra of the $LP_{01,x}$ and $LP_{01,y}$ modes in core 1 and core 3 the 12^{th} day (March 2016). (b) Temporal evolution of the DGD in cores 1, 2, 3 and 4 considering several consecutive days in three different months [CONF 10].

From the measured spectra in the four cores of our MCF, we can estimate the DGD mean and distribution in each core and day as indicated previously. The temporal evolution of $\Delta\tau_{m,j}$ (with $m \in \{1,2,3,4\}$ and $j \in \{1,\ldots,15\}$) is detailed in Fig. D3.1(b). We can observe that the average value of the DGD ($\langle\Delta\tau_{m,j}\rangle$) in each core considering the three measured months is found to be: 0.24 ps, 0.36 ps, 0.62 ps and 0.37 ps in cores 1, 2, 3, and 4, respectively. Specifically, core 3 presents a higher DGD than cores 1, 2 and 4. However, although we observe cores with different average value of the DGD, it should be noted that the temporal evolution of $\Delta\tau_{m,j}$ has a similar shape in the four cores, in line with our conclusions in Section 3.5.

Finally, the DGD distribution is shown in Fig. D3.2. Figure D3.2(a) shows the p.d.f. of the DGD calculated from Eq. (D3.2) by replacing $\Delta\tau_m(t)$ by $\langle\Delta\tau_{m,j}\rangle$. Figures D3.2(b)-(e) depict the temporal evolution of the DGD distribution in cores 1, 2, 3 and 4, respectively. From these results we can note that the Maxwellian distribution of core 3 has a higher mean and variance, which allows us to verify that the linear birefringence of this core is higher than in cores 1, 2 and 4. It can also be observed that cores 2 and 4 present a DGD distribution with similar mean and variance. These results should be considered in digital signal processing techniques to compensate the PMD in SDM transmissions.

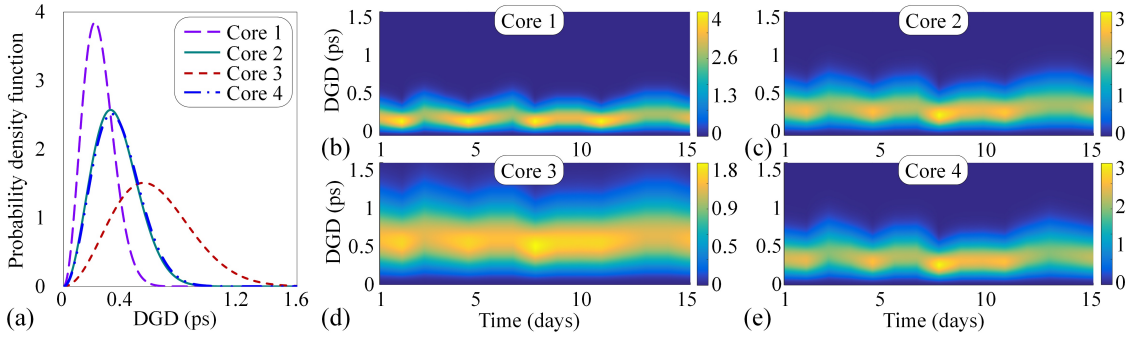

Figure D3.2. (a) Probability density function (p.d.f.) of the average value of the DGD in each core. Temporal evolution of the p.d.f. of the DGD spanning the fifteen measured days in: (b) core 1, (c) core 2, (d) core 3, and (e) core 4 [CONF 10].

This page was intentionally left blank.

Chapter 4

Ultra-short pulse propagation model using local modes

4.1 Introduction

The theoretical models of preceding chapters describe the optical propagation of monochromatic waves, i.e., harmonic functions with infinite duration. This idealization allows us to simplify the analysis of the propagation phenomena in MCFs. Nevertheless, a real electromagnetic propagation always involves non-monochromatic waves and, therefore, we should now consider this fundamental point by discussing the *non-monochromatic regime*.

In such a scenario, ultra-short pulses play a key factor to exploit the full potential of any optical fiber. In optical communications, for instance, ultra-short pulses allow us to increase the bit rate to deal with current data traffic demand and have been proposed for different applications such as supercontinuum light generation and optical combs suitable for WDM systems [28, 55, 173, 174]. In experimental physics, ultra-short optical pulses propagating in the nonlinear fiber regime have been employed to investigate important physical phenomena such as fiber optical analogues of Hawking radiation or rogue waves on deep water via the analysis of the nonlinear Schrödinger equation (NLSE) [105, 109]. In this way, MCFs may offer a physical platform to investigate the collision between the nonlinear solutions of these systems from a set of coupled NLSEs.

For the above reasons, it is important to have available a precise theoretical model encompassing all aspects of ultra-short pulse propagation in MCFs. In the picosecond regime, where higher-order dispersive and nonlinear effects can be neglected, the Manakov equations have been extended to MM-SCFs and MM-MCFs to analyze the nonlinear propagation of optical pulses wider than 1 ps by including polarization effects and the random longitudinal fiber perturbations, but omitting the temporal fluctuations of the medium and without any information of physical parameters such as the bending radius and the twist rate of the fiber [153–156]. Moreover, in the femtosecond regime, existing MCF propagation models exclude polarization effects and omit the temporal and longitudinal random perturbations of the fiber [175–184]. Since such perturbations modify the birefringence properties of the medium and the propagation constant of the core modes [131], they should be considered in real deployed MCF systems or in experimental physics studies using this kind of optical waveguides.

In order to include these realistic fiber conditions in the mathematical description of the propagation of femtosecond and picosecond optical pulses through an MCF, we present in this chapter a theoretical model based on the concept of local modes, in which the aforementioned spatial and temporal fiber perturbations and polarization effects are incorporated from the beginning in Maxwell's equations. And although we will focus our efforts on the single-mode regime, we will also discuss the multi-mode regime at the end of this chapter. Remarkably, as demonstrated analytically and numerically, the intermodal dispersion induced by these random perturbations between different fundamental polarized core modes (PCMs) $\mathrm{LP}_{01,mi}$ – where m indicates the core and i

the polarization axis – can become the major physical impairment in the single-mode regime of the fiber when propagating ultra-short optical pulses. In such a scenario, the intermodal dispersion, referred to as the *mode-coupling dispersion* (MCD) in this chapter, is induced not only by the mismatching between the propagation constants of the PCMs, but also by the frequency dependence of their mode overlapping. Remarkably, our results indicate that the random nature of the MCD, involving both dispersive effects and emerging from the fiber birefringence fluctuations, should be considered for future MCF designs, digital signal processing (DSP) techniques and optical soliton transmissions in advanced SDM systems using MCFs [8]. In addition, it is worth mentioning that this model is general and can also be applied to SCF media. In the following, we first describe the proposed model in general terms, and subsequently discuss the impact of the MCD, indicating different strategies to reduce its effects via the use of fiber perturbations.

4.2 Coupled local-mode theory for ultra-short optical pulses

Let us consider, for simplicity, a real weakly-guiding MCF operating in the single-mode regime. Later, in Appendix E4, we will also discuss the multi-mode regime (see page 142). The above optical medium can be considered as a multi-dielectric, lossy, nonlinear, anisotropic, heterogeneous, time-varying and temporally dispersive medium comprising longitudinal and temporal birefringent effects (see Chapter 3). In order to describe theoretically the propagation of ultra-short pulses in such optical media, we employ the concept of local modes presented in the previous chapter.

A *local mode* can be considered as an eigenfunction in a short core segment in which the perturbations of the ideal phase constant and the transversal function the LP_{01} mode are approximately constant in each polarization axis. Hence, each core can be modeled as a series of birefringent segments supporting local modes, in each of which the longitudinal and temporal MCF perturbations are approximately invariant but can fluctuate between adjacent segments (see Fig. 4.1). In this way, in contrast with previous works [153–156, 175–184], the fiber perturbations can be included from the beginning in Maxwell's equations. In Chapter 3, the coupled local-mode theory (CLMT) accounts for the MCF birefringence with a rigorous formalism, but considering monochromatic electromagnetic fields and omitting additional nonlinear effects such as the intrapulse stimulated Raman scattering. Consequently, the initial assumptions of the CLMT will be revisited here to develop a unified theory describing ultra-short pulse propagation in real MCFs. Interestingly, the theory presented herein is a general model which can be applied to SCFs and MCFs comprising: coupled or uncoupled cores, lowly- or highly-birefringent cores, trench- or hole-assisted cladding, and gradual- or step-index profiles.

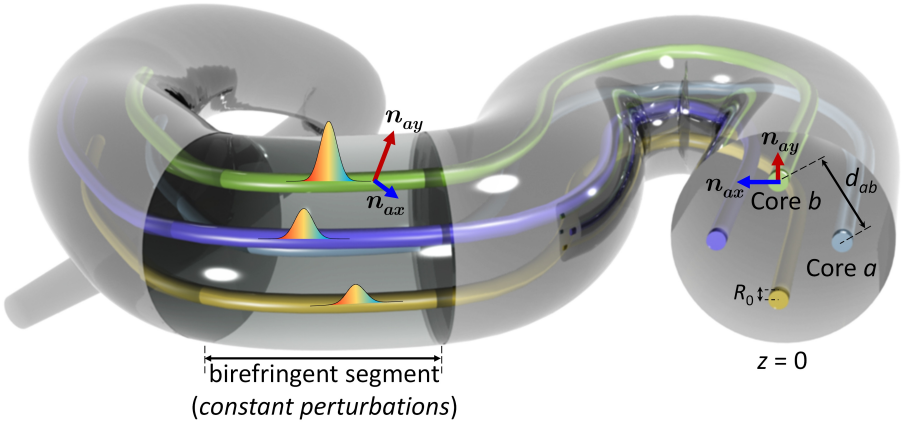

Figure 4.1. Multi-core fiber scenario of the proposed ultra-short pulse propagation model. Each core m propagates two polarized core modes (PCMs) $\mathrm{LP}_{01,mx}$ and $\mathrm{LP}_{01,my}$ through a series of birefringent segments with different principal axes. The longitudinal and time-varying transversal functions and phase constants of the PCMs are invariant in each segment. The PCMs of each birefringent segment define the fiber local modes. The number of birefringent segments may change between different cores [116].

4.2.1 Multi-core fiber local modes

We start following the same steps as in Chapter 3 using perturbation theory (see Fig. 1.9). Thus, our initial goal is to propose the ansatz of the electric field strength of the MCF by including the medium perturbations (step 1).

For the sake of simplicity, we assume only two cores a and b to derive the coupled local-mode equations and, later, we will generalize the model for an MCF comprising N cores. Again, we consider both orthogonal polarizations $i \in \{x, y\}$ in the LP_{01} mode of each core $m \in \{a, b\}$ and a single optical carrier with angular frequency ω_0. In general, we should consider multiple optical carriers to describe the pulse propagation in WDM-SDM systems using MCFs. Nevertheless, it should be taken into account that in a WDM transmission of ultra-short optical pulses the intrachannel pulse-to-pulse interactions are the predominant nonlinear effects and the interchannel nonlinearities[1] can be neglected [11]. In this vein, we assume a single optical carrier to facilitate the theoretical discussions.[2]

However, in contrast to the original version of the CLMT, we now assume *non-monochromatic* electric fields. In this way, the exact real wave function of the global electric field strength of the MCF ($\boldsymbol{\mathcal{E}}$) is approximated by using a linear combination of the non-monochromatic electric field strength of each PCM mi ($\mathcal{E}_{mi}$) considering isolated cores, i.e., assuming that the geometry of each core m is not perturbed by the presence of adjacent cores $\boldsymbol{\mathcal{E}}(\boldsymbol{r}, t) \simeq \sum_{mi} \mathcal{E}_{mi}(\boldsymbol{r}, t)\, \hat{u}_i$. At the same time, we should decouple the rapidly and the slowly-varying temporal and longitudinal changes of $\mathcal{E}_{mi}$. To this end, we use respectively the slowly-varying amplitude and envelope approximations as indicated below.[3] First, we separate the rapid and the slow *temporal* variations by employing the slowly-varying amplitude approximation:

$$\boldsymbol{\mathcal{E}}(\boldsymbol{r}, t) \simeq \sum_{m=a,b} \sum_{i=x,y} \mathcal{E}_{mi}(\boldsymbol{r}, t)\, \hat{u}_i \simeq \sum_{m=a,b} \sum_{i=x,y} \mathrm{Re}\left\{E_{mi,\omega_0}(\boldsymbol{r}, t) \exp(j\omega_0 t)\right\} \hat{u}_i, \tag{4.2.1}$$

where E_{mi,ω_0} is the complex amplitude of the electric field strength in the PCM mi satisfying that $\delta_t E_{mi,\omega_0} \ll |E_{mi,\omega_0}|$ in $\delta t \sim 2\pi/\omega_0$, where $\delta_t E_{mi,\omega_0} := |E_{mi,\omega_0}(\boldsymbol{r}, t) - E_{mi,\omega_0}(\boldsymbol{r}, t + \delta t)|$. It should be noted that the slowly-varying amplitude approximation, performed in the second approximation of the above equation, allows us to decouple the rapid temporal oscillation of the optical carrier from the slow temporal evolution of the complex amplitudes of the optical pulses. Therefore, the model proposed herein is valid *if and only if* Maxwell's equations are approximately satisfied when using Eq. (4.2.1). However, this assumption is not fulfilled if the pulse is too narrow, namely around the order of the period of the optical carrier or shorter. In such a case, the decomposition performed in Eq. (4.2.1) is no longer useful and the concept of the complex amplitude itself becomes unclear. In our case, the optical carrier lies in the third transmission window (around 193.1 THz), which sets the lower limit of applicability of the ansatz to pulses wider than ~ 10 fs (with a pulse bandwidth narrower than ~ 100 THz). In additional MCF applications which require the use of a different optical band, the validity of Eq. (4.2.1) can be easily tested by verifying that the pulse bandwidth is much lower than $\omega_0/2\pi$. Moreover, the upper limit of our model is found from the validity of assuming a single optical carrier, around ~ 50 ps taking into account that the interchannel nonlinearities should only be considered in a WDM system when using pulses wider than ~ 50 ps [11]. Consequently, the presented model will allow us to describe the propagation of pulses with a temporal width between 10 fs and 50 ps, not only in SM-MCF single-carrier transmissions, but also in WDM systems using these optical fibers. In SM-MCF WDM transmissions, the derived coupled local-mode equations should be numerically solved for each optical carrier of the WDM system.

[1] Cross-phase modulation (XPM) and four-wave mixing (FWM).

[2] In Appendix A4, on page 125, we explore the possibility of including multiple optical carriers in our ansatz.

[3] Note that in the monochromatic regime we only use the slowly-varying envelope approximation. Specifically, a solution of the form $\mathcal{E}_{mi}(\boldsymbol{r}, t) = \mathrm{Re}\{E_{mi,\omega_0}(\boldsymbol{r}) \exp(j\omega_0 t)\}$ is exact when assuming harmonic functions. This is not the case when E_{mi,ω_0} includes the temporal evolution of an optical pulse, where we should assume that $\delta_t E_{mi,\omega_0} \ll |E_{mi,\omega_0}|$ in $\delta t \sim 2\pi/\omega_0$ to satisfy Maxwell's equations.

The complex amplitude E_{mi,ω_0} is the key term of the proposed model, as it will encode the fiber perturbations and the optical pulses of the PCM mi, which comprises a series of local modes distributed along the different birefringent segments of the core m. All in all, the complex amplitude E_{mi,ω_0} is expressed as follows:

$$E_{mi,\omega_0}(\boldsymbol{r},t)=\frac{1}{2\pi}\int_{\mathfrak{B}_{\widetilde{\mathtt{A}}}}\widetilde{\mathtt{A}}_{mi}(z,\omega-\omega_0;t)\,F_{mi}(x,y,\omega;z,t)\exp\left(-j\Phi_{mi}(z,\omega;t)\right)\exp\left(j\,(\omega-\omega_0)\,t\right)\mathrm{d}\omega, \tag{4.2.2}$$

where $\widetilde{\mathtt{A}}_{mi}$ is the short-time Fourier transform (STFT) of the complex envelope in baseband (see below), $\mathfrak{B}_{\widetilde{\mathtt{A}}}$ is the bandwidth of $\widetilde{\mathtt{A}}_{mi}$, F_{mi} is the transversal eigenfunction of the PCM mi, and Φ_{mi} is the complex phase function of the PCM mi defined as:

$$\Phi_{mi}(z,\omega;t):=\phi_{mi}(z,\omega;t)-j\frac{1}{2}\alpha(\omega)\,z, \tag{4.2.3}$$

with α the power attenuation coefficient of the MCF modeling the optical absorption due to Rayleigh scattering and assumed similar in each PCM,[4] and ϕ_{mi} the real phase function involving the longitudinal and temporal MCF perturbations:

$$\phi_{mi}(z,\omega;t):=\int_0^z\beta_{mi}^{(\mathrm{eq})}(\xi,\omega;t)\,\mathrm{d}\xi=\beta_{mi}(\omega)\,z+\int_0^z\beta_{mi}^{(\mathrm{B+S})}(\xi,\omega;t)\,\mathrm{d}\xi, \tag{4.2.4}$$

with $\beta_{mi}^{(\mathrm{eq})}$ the equivalent phase constant involving the ideal phase constant β_{mi} and the phase perturbation $\beta_{mi}^{(\mathrm{B+S})}$ induced by macrobends (B) and additional longitudinal and temporal fiber structural fluctuations (S). In addition, it should be noted that:

$$\partial_z\Phi_{mi}=\beta_{mi}^{(\mathrm{eq})}-j\tfrac{1}{2}\alpha;\quad \partial_z^2\Phi_{mi}=\partial_z\beta_{mi}^{(\mathrm{eq})};\quad (\partial_z\Phi_{mi})^2\simeq\left(\beta_{mi}^{(\mathrm{eq})}\right)^2-j\alpha\beta_{mi}^{(\mathrm{eq})}. \tag{4.2.5}$$

Thus, the STFT ($\mathcal{F}_{\mathrm{T}}$) of Eqs. (4.2.1) and (4.2.2), calculated in a short-time interval of the order of the temporal pulse width T_{P}, is found to be:

$$\widetilde{\boldsymbol{\mathcal{E}}}(\boldsymbol{r},\omega;t)=\mathcal{F}_{\mathrm{T}}\left[\boldsymbol{\mathcal{E}}(\boldsymbol{r},t)\right]\simeq\frac{1}{2}\sum_{m=a,b}\sum_{i=x,y}\left[\widetilde{E}_{mi,\omega_0}(\boldsymbol{r},\omega-\omega_0;t)+\widetilde{E}_{mi,-\omega_0}(\boldsymbol{r},\omega+\omega_0;t)\right]\hat{u}_i; \tag{4.2.6}$$

$$\begin{aligned}\widetilde{E}_{mi,\omega_0}(\boldsymbol{r},\omega-\omega_0;t)&=\mathcal{F}_{\mathrm{T}}\left[E_{mi,\omega_0}(\boldsymbol{r},t)\exp(j\omega_0 t)\right]\\&=\widetilde{\mathtt{A}}_{mi}(z,\omega-\omega_0;t)\,F_{mi}(x,y,\omega;z,t)\exp\left(-j\Phi_{mi}(z,\omega;t)\right).\end{aligned} \tag{4.2.7}$$

At this point, we should decouple the rapidly- and slowly-varying *longitudinal* variations of the electric field by including the slow oscillations of Φ_{mi} along with $\widetilde{\mathtt{A}}_{mi}$. Hence, we should perform the following transformation of the complex envelope:

$$\widetilde{A}_{mi}(z,\omega-\omega_0;t):=\widetilde{\mathtt{A}}_{mi}(z,\omega-\omega_0;t)\exp\left[-j\left(\phi_{mi}(z,\omega;t)-\phi_{mi}(z,\omega_0;t)\right)\right]. \tag{4.2.8}$$

In this way, $\widetilde{A}_{mi}$ describes the slow temporal and longitudinal variations of $\mathcal{E}_{mi}$ thanks to Eqs. (4.2.1) and (4.2.8), respectively. Consequently, $\widetilde{E}_{mi,\omega_0}$ is rewritten as:

$$\widetilde{E}_{mi,\omega_0}(\boldsymbol{r},\omega-\omega_0;t)=\widetilde{A}_{mi}(z,\omega-\omega_0;t)\,F_{mi}(x,y,\omega;z,t)\exp\left(-j\phi_{mi}(z,\omega_0;t)-\frac{1}{2}\alpha(\omega)\,z\right). \tag{4.2.9}$$

[4] As discussed in Chapter 3, the optical attenuation induced by the resonant frequencies of fused silica can be neglected when the optical carrier is located in the third transmission window.

Furthermore, in order to preserve the temporal fiber birefringence fluctuations in $\widetilde{A}_{mi}$, the STFT is defined as:[5]

$$\widetilde{A}_{mi}\left(z,\Omega;t\right)=\mathcal{F}_{\mathrm{T}}\left[A_{mi}\left(z,t\right)\right]:=\int_{t-T_{\mathrm{P}}/2}^{t+T_{\mathrm{P}}/2}A_{mi}\left(z,\tau\right)\exp\left(-j\Omega\tau\right)\mathrm{d}\tau, \tag{4.2.10}$$

with A_{mi} satisfying the slowly-varying envelope approximation (SVEA) as discussed in Chapter 1 [see Eq. (1.5.10)].[6] Surprisingly, in spite of the fact that we assume $\delta_z A_{mi} \ll |A_{mi}|$ in $\delta z \sim \lambda_m$ and[7] $\delta_t A_{mi} \ll |A_{mi}|$ in $\delta t \sim 2\pi/\omega_0$, we found that both order criteria are violated for pulses near to the lower limit of our model (~ 10 fs), as discussed in Appendix B4, on page 129. Consequently, we cannot consider to be null $\partial_z^2 A_{mi}$ and $\partial_t^2 A_{mi}$ in $\delta z \sim \lambda_m$ and $\delta t \sim 2\pi/\omega_0$ with $T_{\mathrm{P}} \sim 10$ fs.

Equations (4.2.1)-(4.2.10) describe the ansatz employed in the first step of perturbation theory. Along these same lines, we should point out several considerations on the above equations:

- In contrast with previous short- and ultra-short pulse propagation models proposed for SCFs and MCFs [153–156, 175–186], the medium perturbations are included here in perturbation theory with rigorous formalism from Maxwell's equations. The longitudinal and temporal MCF perturbations define the birefringent segments and the local modes in each PCM mi. These fiber perturbations are included in E_{mi,ω_0} via the functions $\widetilde{\mathtt{A}}_{mi}$, F_{mi} and Φ_{mi}. Given that the longitudinal and temporal MCF perturbations modify the ideal phase constant β_{mi} as indicated in Eq. (4.2.4), F_{mi} and $\widetilde{\mathtt{A}}_{mi}$ should also be assumed longitudinal and temporal dependent in order to satisfy Maxwell's equations in the MCF segments. Specifically, the local mode $F_{mi}\exp(-j\Phi_{mi})$ should satisfy the Helmholtz equation in each birefringent segment of the core m and in each spectral component ω:

$$\left(\triangle+\frac{\omega^2}{c_0^2}\widetilde{\varepsilon}_{\mathrm{r},mi}\left(\boldsymbol{r},\omega;t\right)\right)F_{mi}\left(x,y,\omega;z,t\right)\exp\left(-j\Phi_{mi}\left(z,\omega;t\right)\right)=0, \tag{4.2.11}$$

  where $\widetilde{\varepsilon}_{\mathrm{r},mi}$ is the STFT of the relative electric permittivity in the core m and polarization axis i [see Eq. (4.2.25)]. In particular, the above equation is step 2 of perturbation theory.

- The longitudinal and temporal changes induced in $\beta_{mi}^{(\mathrm{eq})}$ by the medium perturbations are assumed to be slowly-varying in comparison with the spatial and temporal duration of a cycle of the optical carrier in each core, i.e., in $\delta z \sim \lambda_m$ and $\delta t \sim 2\pi/\omega_0$. In such circumstances, the optical power reflected due to the longitudinal and temporal changes of $\beta_{mi}^{(\mathrm{eq})}$ can be neglected.

- According to Chapter 3, the semicolon symbol is used to denote explicitly longitudinal and temporal changes induced by these MCF perturbations. As an illustrative example, the slowly-varying longitudinal and temporal fluctuations of the transversal local eigenfunction $F_{mi}(x,y,\omega;z,t)$ are explicitly separated by the semicolon symbol from the transversal changes.

- The phase of the local modes is given by the complex function Φ_{mi} in each MCF segment. Therefore, considering that the local modes must satisfy Eq. (4.2.11), F_{mi} should also be assumed as a complex function. Nevertheless, taking into account that the imaginary part of Φ_{mi} (modeling the optical absorption) is much lower than the real part ϕ_{mi} (accounting for the ideal phase constant along with the fiber perturbations), we assume F_{mi} as a real function from now on. In the multi-mode regime, F_{mi} should be considered as a complex

[5] The STFT should be defined as in Eq. (A3.22), i.e., using a temporal window function $\mathscr{W}$ to indicate explicitly the temporal dependence of $\widetilde{A}_{mi}$. Here, for the sake of simplicity, we describe $\mathscr{W}$ in the time interval of integration, i.e., $\tau \in [t - T_{\mathrm{P}}/2, t + T_{\mathrm{P}}/2]$. The same remark applies to additional STFTs of this chapter.

[6] Note that we use a different function for the complex envelope (A_{mi}) from the one used in Chapter 1 ($\mathcal{A}_{mi}$). However, the final expression of the coupled local-mode equations are given as a function of $\mathcal{A}_{mi}$. Both functions are connected in the frequency domain as $\widetilde{A}_{mi} = \widetilde{\mathcal{A}}_{mi}\exp(\alpha z/2)$, as indicated below.

[7] As discussed in previous chapters, the wavelength of the optical carrier is found to be different in each core m. Specifically, $\lambda_m = \lambda_0/n_m$ with $n_m := (n_{mx} + n_{my})/2$. See, e.g., page 60 for more details.

function to include the azimuthal order of the corresponding LP mode group (see Appendix E4, on page 142).

- The fiber perturbations are included in Eq. (4.2.2) without approximating $\Phi_{mi}(z,\omega;t)$ to $\Phi_{mi}(z,\omega_0;t)$. As a result, we can describe accurately the frequency dependence of the phase-mismatching between local modes including the fiber birefringent effects. This flexibility will allow us to investigate the behavior of the MCD in real SM-MCFs and the reduction of this optical impairment via the use of MCF perturbations.

4.2.2 Coupled-wave equations

In this subsection, according to step 3 of perturbation theory, the goal is to derive the coupled-wave equations of the complex amplitude E_{i,ω_0} of the global electric field strength $\boldsymbol{\mathcal{E}}$. That is, assuming $\boldsymbol{\mathcal{E}}$ of the form $\boldsymbol{\mathcal{E}}(\boldsymbol{r},t) \simeq \sum_{i=x,y} \mathrm{Re}\left\{E_{i,\omega_0}(\boldsymbol{r},t)\exp(j\omega_0 t)\,\hat{u}_i\right\}$, we can identify from Eq. (4.2.1) that $E_{i,\omega_0} \simeq \sum_m E_{mi,\omega_0}$. In the same way, the linear and nonlinear polarization $\boldsymbol{\mathcal{P}}^{(1)}$ and $\boldsymbol{\mathcal{P}}^{(3)}$ can also be expressed in terms of the corresponding complex amplitudes $P^{(1)}_{i,\omega_0}$ and $P^{(3)}_{i,\omega_0}$. Nonetheless, for simplicity, it is more convenient to discuss the coupled-wave equations in the frequency domain when analyzing non-monochromatic waves. Therefore, we should derive the coupled-wave equations of the MCF in terms of the STFTs of the aforementioned complex amplitudes.

In such a scenario, we start from the nonlinear wave equation (3.2.7) of Chapter 3, derived from the macroscopic Maxwell equations and reproduced here for clarity:

$$\left(\triangle - \frac{1}{c_0^2}\partial_t^2\right)\boldsymbol{\mathcal{E}}(\boldsymbol{r},t) = \mu_0\partial_t^2\boldsymbol{\mathcal{P}}^{(1)}(\boldsymbol{r},t) + \mu_0\partial_t^2\boldsymbol{\mathcal{P}}^{(3)}(\boldsymbol{r},t)\,. \tag{4.2.12}$$

Let us remember that we can neglect the term $\nabla(\nabla\cdot(\boldsymbol{\mathcal{P}}^{(1)}+\boldsymbol{\mathcal{P}}^{(3)}))$ in the above equation when considering slowly-varying refractive index profiles and the low birefringent and nonlinear nature of silica MCFs (including also the case HB-MCF), in line with our findings in Appendix A3, on page 82. Now, applying the STFT to Eq. (4.2.12) we obtain (see footnote 22 on page 87):

$$\left(\triangle + \frac{\omega^2}{c_0^2}\right)\widetilde{\boldsymbol{\mathcal{E}}}(\boldsymbol{r},\omega;t) = -\omega^2\mu_0\widetilde{\boldsymbol{\mathcal{P}}}^{(1)}(\boldsymbol{r},\omega;t) - \omega^2\mu_0\widetilde{\boldsymbol{\mathcal{P}}}^{(3)}(\boldsymbol{r},\omega;t)\,. \tag{4.2.13}$$

The field $\widetilde{\boldsymbol{\mathcal{E}}}$ can be expressed in terms of $\widetilde{E}_{i,\omega_0}$ (the STFT of E_{i,ω_0}) by using Eq. (4.2.6) and taking into account that $\widetilde{E}_{i,\omega_0} \simeq \sum_m \widetilde{E}_{mi,\omega_0}$. Moreover, $\widetilde{\boldsymbol{\mathcal{P}}}^{(1)}$ and $\widetilde{\boldsymbol{\mathcal{P}}}^{(3)}$ can be written in terms of their complex amplitude in the frequency domain as:

$$\begin{aligned}\widetilde{\boldsymbol{\mathcal{P}}}^{(k)}(\boldsymbol{r},\omega;t) &= \mathcal{F}_{\mathrm{T}}\left[\boldsymbol{\mathcal{P}}^{(k)}(\boldsymbol{r},t)\right] \simeq \mathcal{F}_{\mathrm{T}}\left[\sum_{i=x,y}\mathrm{Re}\left\{P^{(k)}_{i,\omega_0}(\boldsymbol{r},t)\exp(j\omega_0 t)\right\}\hat{u}_i\right]\\ &= \frac{1}{2}\sum_{i=x,y}\left[\widetilde{P}^{(k)}_{i,\omega_0}(\boldsymbol{r},\omega-\omega_0;t) + \widetilde{P}^{(k)}_{i,-\omega_0}(\boldsymbol{r},\omega+\omega_0;t)\right]\hat{u}_i;\quad k\in\{1,3\}\,,\end{aligned} \tag{4.2.14}$$

where the nonlinear polarization in $3\omega_0$ was omitted taking into account that the phase-matching condition in this nonlinear term is not satisfied in silica fibers [139]. Thus, Eq. (4.2.13) becomes:

$$\left(\triangle + \frac{\omega^2}{c_0^2}\right)\widetilde{E}_{i,\omega_0}(\boldsymbol{r},\omega-\omega_0;t) = -\omega^2\mu_0\widetilde{P}^{(1)}_{i,\omega_0}(\boldsymbol{r},\omega-\omega_0;t) - \omega^2\mu_0\widetilde{P}^{(3)}_{i,\omega_0}(\boldsymbol{r},\omega-\omega_0;t)\,. \tag{4.2.15}$$

Now, let us discuss the constitutive relation between $\widetilde{P}^{(1)}_{i,\omega_0}$ and $\widetilde{E}_{i,\omega_0}$. Considering the dispersive effects and the spatial and temporal random perturbations of the medium, the linear polarization in the time domain $\boldsymbol{\mathcal{P}}^{(1)}$ can be expressed as:

$$\boldsymbol{\mathcal{P}}^{(1)}(\boldsymbol{r},t) = \varepsilon_0\int_{-\infty}^{\infty}\boldsymbol{\chi}^{(1)}(\boldsymbol{r},t,\tau)\,\boldsymbol{\mathcal{E}}(\boldsymbol{r},\tau)\,\mathrm{d}\tau \simeq \varepsilon_0\int_{\langle T_{\mathrm{P}}\rangle}\boldsymbol{\chi}^{(1)}(\boldsymbol{r},t-\tau)\,\boldsymbol{\mathcal{E}}(\boldsymbol{r},\tau)\,\mathrm{d}\tau, \tag{4.2.16}$$

with ε_0 the electric permittivity in vacuum and $\boldsymbol{\chi}^{(1)}$ the first-order electric susceptibility tensor accounting for the linear and circular birefringence of the MCF. Note that $\boldsymbol{\chi}^{(1)}$ is assumed longitudinal and temporal dependent due to the MCF perturbations and the dispersive nature of silica. Rigorously, the linear polarization describes a linear time-varying system. However, at this point let us assume the pulse width T_{P} much shorter than the temporal birefringence fluctuations of the MCF.[8] Hence, the linear time-varying system described by $\boldsymbol{\mathcal{P}}^{(1)}$ can be regarded as a linear time-invariant system in a time interval of the order of T_{P}, as indicated in the approximation performed in Eq. (4.2.16). As a result, the constitutive relation of the linear polarization can be expressed in the frequency domain when applying the STFT as:

$$\widetilde{\boldsymbol{\mathcal{P}}}^{(1)}\left(\boldsymbol{r},\omega;t\right)=\varepsilon_0\widetilde{\boldsymbol{\chi}}^{(1)}\left(\boldsymbol{r},\omega;t\right)\widetilde{\boldsymbol{\mathcal{E}}}\left(\boldsymbol{r},\omega;t\right), \tag{4.2.17}$$

where:

$$\widetilde{\boldsymbol{\chi}}^{(1)}\left(\boldsymbol{r},\omega;t\right):=\mathcal{F}_{\mathrm{T}}\left[\boldsymbol{\chi}^{(1)}\left(\boldsymbol{r},t\right)\right]=\int_{t-T_{\mathrm{P}}/2}^{t+T_{\mathrm{P}}/2}\boldsymbol{\chi}^{(1)}\left(\boldsymbol{r},\tau\right)\exp\left(-j\omega\tau\right)\mathrm{d}\tau. \tag{4.2.18}$$

Thus, the complex amplitude of the linear polarization in the frequency domain is found to be (Einstein summation convention):

$$\widetilde{P}_{i,\omega_0}^{(1)}\left(\boldsymbol{r},\omega-\omega_0;t\right)=\varepsilon_0\widetilde{\chi}_{ij}^{(1)}\left(\boldsymbol{r},\omega;t\right)\widetilde{E}_{j,\omega_0}\left(\boldsymbol{r},\omega-\omega_0;t\right). \tag{4.2.19}$$

The real part of $\widetilde{\chi}_{ij}^{(1)}$ gives information about the material dispersion and the MCF perturbations, and the imaginary part accounts for the optical absorption of the medium [induced by Rayleigh scattering as well as the resonant frequencies of fused silica, located in the ultraviolet (68.4 nm and 116.2 nm) and infrared (9896.2 nm) bands]. In silica fibers operating in the third transmission window, optical absorption can be exclusively modeled by α and the imaginary part of $\widetilde{\chi}_{ij}^{(1)}$ can be neglected given that $\mathrm{Im}\left\{\chi_{ij}^{(1)}\right\}\sim\alpha/k_0$ [149].

Now, we still need to investigate the nonlinear polarization term $\widetilde{P}_{i,\omega_0}^{(3)}$ of Eq. (4.2.15). Nonetheless, the constitutive relation of the nonlinear polarization with the electric field strength involves a convolution operation in the frequency domain, increasing the complexity of the mathematical discussion of the coupled local-mode equations. Hence, we will maintain the term $\widetilde{P}_{i,\omega_0}^{(3)}$ in Eq. (4.2.15), which is reduced to:

$$\left(\triangle+\frac{\omega^2}{c_0^2}\right)\widetilde{E}_{i,\omega_0}\left(\boldsymbol{r},\omega-\omega_0;t\right)+\frac{\omega^2}{c_0^2}\widetilde{\chi}_{ij}^{(1)}\left(\boldsymbol{r},\omega;t\right)\widetilde{E}_{j,\omega_0}\left(\boldsymbol{r},\omega-\omega_0;t\right)=-\omega^2\mu_0\widetilde{P}_{i,\omega_0}^{(3)}\left(\boldsymbol{r},\omega-\omega_0;t\right). \tag{4.2.20}$$

Furthermore, considering that $\widetilde{\chi}_{yx}^{(1)}=\left(\widetilde{\chi}_{xy}^{(1)}\right)^*$ as can be deduced from the Poynting theorem by assuming the MCF as a time-invariant medium in $\delta t\sim 2\pi/\omega_0$ [162], defining:

$$\widetilde{\varepsilon}_{\mathrm{r},i}\left(\boldsymbol{r},\omega;t\right):=1+\widetilde{\chi}_{ii}^{(1)}\left(\boldsymbol{r},\omega;t\right); \tag{4.2.21}$$

$$\widetilde{\sigma}\left(\boldsymbol{r},\omega;t\right):=\widetilde{\chi}_{xy}^{(1)}\left(\boldsymbol{r},\omega;t\right), \tag{4.2.22}$$

and omitting the imaginary part of $\widetilde{\chi}_{ij}^{(1)}$ as indicated before, the coupled-wave equations are finally derived (the independent variables are omitted for the sake of simplicity from now on):

$$\triangle\widetilde{E}_{x,\omega_0}+\frac{\omega^2}{c_0^2}\left(\widetilde{\varepsilon}_{\mathrm{r},x}\widetilde{E}_{x,\omega_0}+\widetilde{\sigma}\widetilde{E}_{y,\omega_0}\right)=-\omega^2\mu_0\widetilde{P}_{x,\omega_0}^{(3)}; \tag{4.2.23}$$

$$\triangle\widetilde{E}_{y,\omega_0}+\frac{\omega^2}{c_0^2}\left(\widetilde{\varepsilon}_{\mathrm{r},y}\widetilde{E}_{y,\omega_0}+\widetilde{\sigma}\widetilde{E}_{x,\omega_0}\right)=-\omega^2\mu_0\widetilde{P}_{y,\omega_0}^{(3)}. \tag{4.2.24}$$

Note that, in contrast to Chapter 3, the coupled-wave equations given by Eqs. (4.2.23) and (4.2.24) are written in the frequency domain. As a result, the coupled local-mode equations should also be discussed in the frequency domain, and later, we will apply the inverse STFT to obtain the final expressions in the time domain.

[8] Typically, T_{P} is of the order of picoseconds or shorter and the faster temporal perturbations of the MCF, related with the floor vibrations, may be assumed of the order of milliseconds (see Chapter 3, on page 75).

4.2.3 Coupled local-mode equations

In step 4 of perturbation theory, we should finally derive the coupled local-mode equations by using our ansatz [Eq. (4.2.9)] along with Eq. (4.2.11) in the coupled-wave equations of the above subsection. Nevertheless, let us first indicate some relevant points about the MCF birefringence and local modes.

In particular, the relative electric permittivity distribution [Eq. (4.2.21)], modeling the intrinsic and extrinsic[9] linear birefringence can be written in each core and polarization axis as follows:

$$\begin{aligned}\widetilde{\varepsilon}_{\mathrm{r},i}\left(\boldsymbol{r},\omega;t\right) &= \widetilde{\varepsilon}_{\mathrm{r},ci}\left(\boldsymbol{r},\omega;t\right)+\Delta\widetilde{\varepsilon}_{\mathrm{r},ai}\left(\boldsymbol{r},\omega;t\right)+\Delta\widetilde{\varepsilon}_{\mathrm{r},bi}\left(\boldsymbol{r},\omega;t\right)\\ &= \begin{cases}\boldsymbol{r}\equiv\text{core } a & \widetilde{\varepsilon}_{\mathrm{r},ai}\left(\boldsymbol{r},\omega;t\right)=\widetilde{\varepsilon}_{\mathrm{r},ci}\left(\boldsymbol{r},\omega;t\right)+\Delta\widetilde{\varepsilon}_{\mathrm{r},ai}\left(\boldsymbol{r},\omega;t\right)\equiv\left(n_{ai}^{(\mathrm{eq})}\right)^2\\ \boldsymbol{r}\equiv\text{cladding} & \widetilde{\varepsilon}_{\mathrm{r},ci}\left(\boldsymbol{r},\omega;t\right)\\ \boldsymbol{r}\equiv\text{core } b & \widetilde{\varepsilon}_{\mathrm{r},bi}\left(\boldsymbol{r},\omega;t\right)=\widetilde{\varepsilon}_{\mathrm{r},ci}\left(\boldsymbol{r},\omega;t\right)+\Delta\widetilde{\varepsilon}_{\mathrm{r},bi}\left(\boldsymbol{r},\omega;t\right)\equiv\left(n_{bi}^{(\mathrm{eq})}\right)^2\end{cases},\end{aligned}\tag{4.2.25}$$

where $\widetilde{\varepsilon}_{\mathrm{r},ai}$, $\widetilde{\varepsilon}_{\mathrm{r},bi}$ and $\widetilde{\varepsilon}_{\mathrm{r},ci}$ are the relative electric permittivity in the cores a, b and in the cladding, respectively; and $\Delta\widetilde{\varepsilon}_{\mathrm{r},ai}$ and $\Delta\widetilde{\varepsilon}_{\mathrm{r},bi}$ are the difference between the relative electric permittivity of the cladding and those of cores a and b, respectively. As in Chapter 3, note that $\widetilde{\varepsilon}_{\mathrm{r},ai}$ and $\widetilde{\varepsilon}_{\mathrm{r},bi}$ give information about the MCF perturbations. More specifically, the root square value of these functions is defined as the *equivalent refractive index*, i.e., $n_{ai}^{(\mathrm{eq})}:=\sqrt{\widetilde{\varepsilon}_{\mathrm{r},ai}}$ and $n_{bi}^{(\mathrm{eq})}:=\sqrt{\widetilde{\varepsilon}_{\mathrm{r},bi}}$. In this vein, Eq. (4.2.25) allows us to introduce the concept of the equivalent refractive index using a rigorous formalism. In Appendix C4 (page 132), the equivalent refractive index model (ERIM) is described in more detail in the frequency domain. Likewise, the circular birefringence is given by:

$$\widetilde{\sigma}\left(\boldsymbol{r},\omega;t\right)=\begin{cases}\boldsymbol{r}\equiv\text{core } a & \widetilde{\sigma}_a\left(\boldsymbol{r},\omega;t\right)=\widetilde{\chi}_{a,xy}^{(1)}\left(\boldsymbol{r},\omega;t\right)\\ \boldsymbol{r}\equiv\text{cladding} & \widetilde{\sigma}_c\left(\boldsymbol{r},\omega;t\right)=\widetilde{\chi}_{c,xy}^{(1)}\left(\boldsymbol{r},\omega;t\right)\\ \boldsymbol{r}\equiv\text{core } b & \widetilde{\sigma}_b\left(\boldsymbol{r},\omega;t\right)=\widetilde{\chi}_{b,xy}^{(1)}\left(\boldsymbol{r},\omega;t\right)\end{cases}.\tag{4.2.26}$$

Note that the fiber parameters $\widetilde{\varepsilon}_{\mathrm{r},i}$ and $\widetilde{\sigma}$ are assumed real functions taking into account that we neglected the imaginary part of $\widetilde{\chi}_{ij}^{(1)}$ when operating in the third transmission window.

On the other hand, it is worthy to note that Eq. (4.2.11) allows us to obtain two fundamental relations to describe the chromatic dispersion along with the MCF perturbations. It is straightforward to derive these relations performing the next two steps. First, the complex phase function Φ_{mi} should be written as:

$$\begin{aligned}\Phi_{mi}\left(z,\omega;t\right) &= \int_0^z \beta_{mi}^{(\mathrm{eq})}\left(\xi,\omega;t\right)\mathrm{d}\xi-j\frac{1}{2}\alpha\left(\omega\right)z\\ &= \int_0^z\sum_{k=0}^{\infty}\frac{1}{k!}\left(\omega-\omega_0\right)^k\beta_{mi,\omega_0}^{(\mathrm{eq})(k)}\left(\xi;t\right)\mathrm{d}\xi-j\frac{1}{2}\alpha\left(\omega\right)z,\end{aligned}\tag{4.2.27}$$

with $\beta_{mi,\omega_0}^{(\mathrm{eq})(k)}\left(z;t\right):=\partial_\omega^k\beta_{mi}^{(\mathrm{eq})}\left(z,\omega=\omega_0;t\right)$. Second, we should approximate:[10]

$$\begin{aligned}\left(\beta_{mi}^{(\mathrm{eq})}\right)^2-\left(\beta_{mi,\omega_0}^{(\mathrm{eq})}\right)^2 &= \left(\beta_{mi}^{(\mathrm{eq})}+\beta_{mi,\omega_0}^{(\mathrm{eq})}\right)\left(\beta_{mi}^{(\mathrm{eq})}-\beta_{mi,\omega_0}^{(\mathrm{eq})}\right)\\ &\simeq 2\beta_{mi,\omega_0}^{(\mathrm{eq})}\left(\beta_{mi}^{(\mathrm{eq})}-\beta_{mi,\omega_0}^{(\mathrm{eq})}\right)=2\beta_{mi,\omega_0}^{(\mathrm{eq})}\sum_{k=1}^{\infty}\frac{1}{k!}\left(\omega-\omega_0\right)^k\beta_{mi,\omega_0}^{(\mathrm{eq})(k)}\\ &\equiv -j2\beta_{mi,\omega_0}^{(\mathrm{eq})}\mathfrak{D}_{mi}^{(\mathrm{eq})},\end{aligned}\tag{4.2.28}$$

where $\mathfrak{D}_{mi}^{(\mathrm{eq})}$ is the complex function defined as:

$$\mathfrak{D}_{mi}^{(\mathrm{eq})}\left(z,\omega;t\right):=\sum_{k=1}^{\infty}\frac{j}{k!}\left(\omega-\omega_0\right)^k\beta_{mi,\omega_0}^{(\mathrm{eq})(k)}\left(z;t\right).\tag{4.2.29}$$

[9] Macrobends and additional structural fluctuations modifying the value of $\widetilde{\varepsilon}_{\mathrm{r},i}$.

[10] From now on, the subindex ω_0 is used to indicate explicitly the value of the functions at $\omega=\omega_0$.

Thus, assuming that $\partial_z F_{mi} \simeq \partial_z^2 F_{mi} \simeq 0$ in $\delta z \sim \lambda_m$, we directly obtain from Eq. (4.2.11):[11]

$$\left(\triangle_{\mathrm{T}} + \frac{\omega^2}{c_0^2}\widetilde{\varepsilon}_{\mathrm{r},i}\right) F_{ai} = \left[\frac{\omega^2}{c_0^2}\Delta\widetilde{\varepsilon}_{\mathrm{r},bi} + \left(\beta_{ai,\omega_0}^{(\mathrm{eq})}\right)^2 - j2\beta_{ai,\omega_0}^{(\mathrm{eq})}\mathfrak{D}_{ai}^{(\mathrm{eq})} + j\left(\partial_z - \alpha\right)\beta_{ai}^{(\mathrm{eq})}\right] F_{ai}; \tag{4.2.30}$$

$$\left(\triangle_{\mathrm{T}} + \frac{\omega^2}{c_0^2}\widetilde{\varepsilon}_{\mathrm{r},i}\right) F_{bi} = \left[\frac{\omega^2}{c_0^2}\Delta\widetilde{\varepsilon}_{\mathrm{r},ai} + \left(\beta_{bi,\omega_0}^{(\mathrm{eq})}\right)^2 - j2\beta_{bi,\omega_0}^{(\mathrm{eq})}\mathfrak{D}_{bi}^{(\mathrm{eq})} + j\left(\partial_z - \alpha\right)\beta_{bi}^{(\mathrm{eq})}\right] F_{bi}, \tag{4.2.31}$$

with $\triangle_{\mathrm{T}} = \partial_x^2 + \partial_y^2$ the transversal Laplacian operator.

Now, at this point we can start with the derivation of the coupled local-mode equations by inserting Eq. (4.2.9) in the coupled-wave equations [Eqs. (4.2.23) and (4.2.24)]. As a result, after some algebraic work, retaining the second-order longitudinal derivatives of the complex envelopes considering that $\partial_z^2\widetilde{A}_{mi} \neq 0$ in $\delta z \sim \lambda_m$ for femtosecond optical pulses (see Appendix B4 on page 129) and using Eqs. (4.2.30) and (4.2.31), we obtain for the x-polarization axis ($i = x$):

$$\begin{aligned}
&\left[\frac{\omega^2}{c_0^2}\Delta\widetilde{\varepsilon}_{\mathrm{r},bx} - \left(j2\beta_{ax,\omega_0}^{(\mathrm{eq})} + \alpha - \partial_z\right)\mathfrak{D}_{ax}^{(\mathrm{eq})}\right] F_{ax}\exp\left(-j\phi_{ax,\omega_0}\right)\widetilde{A}_{ax} + F_{ax}\exp\left(-j\phi_{ax,\omega_0}\right)\partial_z^2\widetilde{A}_{ax} \\
&+\left[\frac{\omega^2}{c_0^2}\Delta\widetilde{\varepsilon}_{\mathrm{r},ax} - \left(j2\beta_{bx,\omega_0}^{(\mathrm{eq})} + \alpha - \partial_z\right)\mathfrak{D}_{bx}^{(\mathrm{eq})}\right] F_{bx}\exp\left(-j\phi_{bx,\omega_0}\right)\widetilde{A}_{bx} + F_{bx}\exp\left(-j\phi_{bx,\omega_0}\right)\partial_z^2\widetilde{A}_{bx} \\
&\quad - \left(j2\beta_{ax,\omega_0}^{(\mathrm{eq})} + \alpha\right) F_{ax}\exp\left(-j\phi_{ax,\omega_0}\right)\partial_z\widetilde{A}_{ax} - \left(j2\beta_{bx,\omega_0}^{(\mathrm{eq})} + \alpha\right) F_{bx}\exp\left(-j\phi_{bx,\omega_0}\right)\partial_z\widetilde{A}_{bx} \\
&\quad + \frac{\omega^2}{c_0^2}\widetilde{\sigma}\left[\widetilde{A}_{ay}F_{ay}\exp\left(-j\phi_{ay,\omega_0}\right) + \widetilde{A}_{by}F_{by}\exp\left(-j\phi_{by,\omega_0}\right)\right] = -\omega^2\mu_0\widetilde{P}_{x,\omega_0}^{(3)}\exp\left(\frac{1}{2}\alpha z\right).
\end{aligned} \tag{4.2.32}$$

A similar expression as Eq. (4.2.32) is obtained for the y-polarization axis by exchanging the subindexes x and y. As can be seen, the LHS of Eq. (4.2.32) describes the linear propagation and the RHS accounts for the nonlinear effects. Accordingly, the derivation of the coupled local-mode equations requires to investigate the constitutive relation between the complex amplitude of the nonlinear polarization and the electric field strength in the frequency domain.

To this end, we should start from the constitutive relation in the time domain. Therefore, at this point let us remember the expressions of the nonlinear polarization in the time and frequency domain as a function of the corresponding complex amplitudes:

$$\boldsymbol{\mathcal{P}}^{(3)}(\boldsymbol{r},t) = \sum_{i=x,y}\mathcal{P}_i^{(3)}(\boldsymbol{r},t)\,\hat{u}_i \simeq \sum_{i=x,y}\mathrm{Re}\left\{P_{i,\omega_0}^{(3)}(\boldsymbol{r},t)\exp\left(j\omega_0 t\right)\right\}\hat{u}_i; \tag{4.2.33}$$

$$\widetilde{\boldsymbol{\mathcal{P}}}^{(3)}(\boldsymbol{r},\omega;t) = \mathcal{F}_{\mathrm{T}}\left[\boldsymbol{\mathcal{P}}^{(3)}(\boldsymbol{r},t)\right] \simeq \sum_{i=x,y}\mathrm{Re}\left\{\widetilde{P}_{i,\omega_0}^{(3)}(\boldsymbol{r},\omega-\omega_0;t)\right\}\hat{u}_i, \tag{4.2.34}$$

with:

$$\widetilde{P}_{i,\omega_0}^{(3)}(\boldsymbol{r},\omega-\omega_0;t) = \mathcal{F}_{\mathrm{T}}\left[P_{i,\omega_0}^{(3)}(\boldsymbol{r},t)\exp\left(j\omega_0 t\right)\right], \tag{4.2.35}$$

and omitting the nonlinear polarization in $3\omega_0$, as indicated before. Hence, the nonlinear terms of Eq. (4.2.32) can be found analyzing the constitutive relation $\mathcal{P}$-$\mathcal{E}$ in the time domain and performing the STFT of the complex amplitudes.

In ultra-short optical pulses, the constitutive relation between the nonlinear polarization and the electric field strength should include the delay response of the electronic and nuclei structure of silica atoms when an electric field stimulates the optical medium. The most general expression to describe the third-order nonlinear response in silica media is to consider an output of a system: nonlinear, anisotropic, spatially homogeneous[12] and nondispersive, and temporally varying and

[11] The approximation $\partial_z F_{mi} \simeq \partial_z^2 F_{mi} \simeq 0$ in $\delta z \sim \lambda_m$ can be verified by using the ERIM (see Appendix C4).

[12] Although the nonlinear electric susceptibility can be found slightly different in each dielectric region of an MCF, we assume spatial homogeneity in $\chi_{ijkl}^{(3)}$ due to the low nonlinear nature of such optical media. In particular, note that $\chi_{ijkl}^{(3)} \sim 10^{-22}$ m^2/V^2 in the cores and cladding.

dispersive. In such circumstances, the constitutive relation can be written as (Einstein summation convention):

$$\mathcal{P}_i^{(3)}(\boldsymbol{r},t) = \varepsilon_0 \iiint_{\infty} \chi_{ijkl}^{(3)}(t,\tau_1,\tau_2,\tau_3)\,\mathcal{E}_j(\boldsymbol{r},\tau_1)\,\mathcal{E}_k(\boldsymbol{r},\tau_2)\,\mathcal{E}_l(\boldsymbol{r},\tau_3)\,\mathrm{d}\tau_1\mathrm{d}\tau_2\mathrm{d}\tau_3. \tag{4.2.36}$$

The temporally dispersive nature of the above equation allows us to describe the exact time delay induced by the electronic and nuclei response of silica atoms to the incident electric field. For optical frequencies well below the electronic transitions, the electronic contribution to the nonlinear polarization can be considered instantaneous. However, since nucleons (protons and neutrons) are considerably heavier than electrons, the nuclei motions have resonant frequencies much lower than the electronic transitions and, consequently, they should be retained in the constitutive relation. Specifically, *Raman scattering* is a well-known effect arising from the nuclear contribution to the nonlinear polarization. Therefore, considering ultra-short optical pulses wider than 1 fs, the electronic response can be assumed instantaneous and Eq. (4.2.36) can be reduced to [159]:

$$\begin{aligned}\mathcal{P}_i^{(3)}(\boldsymbol{r},t) &\simeq \mathcal{P}_i^{(3\mathrm{I})}(\boldsymbol{r},t) + \mathcal{P}_i^{(3\mathrm{R})}(\boldsymbol{r},t)\\ &= \varepsilon_0\chi_{ijkl}^{(3\mathrm{I})}\mathcal{E}_j(\boldsymbol{r},t)\,\mathcal{E}_k(\boldsymbol{r},t)\,\mathcal{E}_l(\boldsymbol{r},t) + \varepsilon_0\mathcal{E}_j(\boldsymbol{r},t)\int_{-\infty}^{\infty}\chi_{ijkl}^{(3\mathrm{R})}(t-\tau)\,\mathcal{E}_k(\boldsymbol{r},\tau)\,\mathcal{E}_l(\boldsymbol{r},\tau)\,\mathrm{d}\tau,\end{aligned} \tag{4.2.37}$$

where the first term of the RHS describes the instantaneous response (3I) accounting for the electron motions, and the second term describes the delayed response associated to the nuclei motions inducing Raman scattering (3R). The third-order electric susceptibility tensors of the above equation can be expressed in silica fibers as follows [187]:

$$\chi_{ijkl}^{(3\mathrm{I})} = \chi_{\mathrm{NL}}\left(\frac{1-f_{\mathrm{R}}}{3}\right)(\delta_{ij}\delta_{kl}+\delta_{ik}\delta_{jl}+\delta_{il}\delta_{jk}); \tag{4.2.38}$$

$$\chi_{ijkl}^{(3\mathrm{R})}(t) = \chi_{\mathrm{NL}}f_{\mathrm{R}}\left[h(t)\,\delta_{ij}\delta_{kl} + \frac{1}{2}u(t)\,(\delta_{ik}\delta_{jl}+\delta_{il}\delta_{jk})\right], \tag{4.2.39}$$

where δ_{ij} is the Kronecker delta function, $\chi_{\mathrm{NL}} = 2.6\cdot10^{-22}$ m^2/V^2 at the wavelength of 1550 nm, $f_{\mathrm{R}} = 0.245$ represents the fractional contribution of the delayed Raman response to the nonlinear polarization, and h and u functions describe the isotropic and anisotropic Raman response, respectively [187]:

$$h(t) = f_1\tau_1\left(\tau_1^{-2}+\tau_2^{-2}\right)\exp(-t/\tau_2)\sin(t/\tau_1); \tag{4.2.40}$$

$$u(t) = f_2\left(\frac{2\tau_3-t}{\tau_3^2}\right)\exp(-t/\tau_3) + \frac{f_3}{f_1}h(t), \tag{4.2.41}$$

with f_1, f_2, f_3, τ_1, τ_2 and τ_3 constants of the nonlinear medium satisfying the following relations:

$$\chi_{\mathrm{NL}}(1-f_{\mathrm{R}}) = \tfrac{4}{3}\varepsilon_0 c_0 n_{\mathrm{NL}} n_{\mathrm{MCF}}^2; \quad \textstyle\sum_{i=1}^{3} f_i = 1; \quad \int_{-\infty}^{\infty}\left(\chi_{ijkl}^{(3\mathrm{I})}\delta(t) + \chi_{ijkl}^{(3\mathrm{R})}(t)\right)\mathrm{d}t = \chi_{\mathrm{NL}}, \tag{4.2.42}$$

with n_{MCF} the average value of the material refractive index of the MCF and n_{NL} the nonlinear refractive index modeling the changes induced in n_{MCF} by the nonlinear polarization. In our case, we assume $n_{\mathrm{MCF}} \simeq 1.45$ and $n_{\mathrm{NL}} = 2.6\cdot10^{-20}$ m^2/W. From Eq. (4.2.42) and Ref. [187] we found: $f_1 = 0.75$, $f_2 = 0.21$, $f_3 = 0.04$, $\tau_1 = 12.2$ fs, $\tau_2 = 32$ fs, $\tau_3 = 96$ fs. Figure 4.2 depicts the isotropic and anisotropic Raman response functions considering $i = j = k = l = x$ in the third-order susceptibility tensor. As can be seen, the delay of the nonlinear polarization induced by the nuclei motions (Raman effect) should be included in the constitutive relation $\mathcal{P}$-$\mathcal{E}$ for optical pulses shorter than 200 fs, in line with Eq. (4.2.37). In addition, we can note that the isotropic Raman response predominates over the anisotropic response due to the molecular symmetry of the SiO_2.

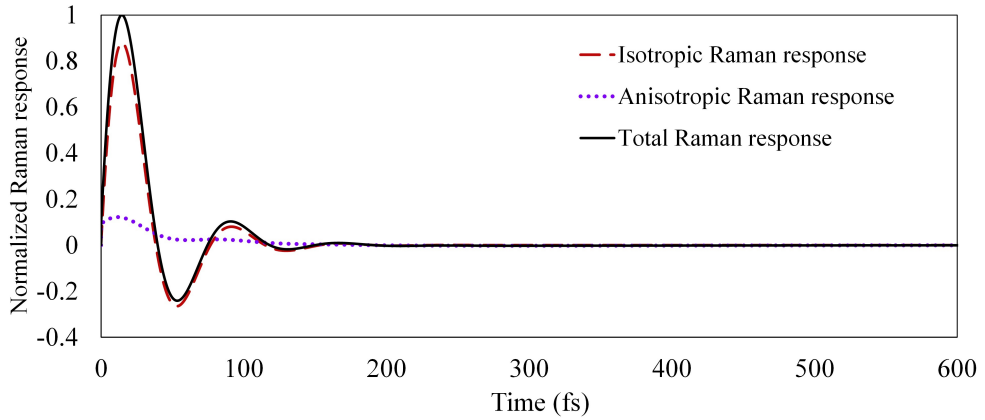

Figure 4.2. Normalized impulse response of the Raman scattering effect. Dashed line: isotropic response. Dotted line: anisotropic response. Solid line: total Raman response [116].

From Eqs. (4.2.33), (4.2.37) and (4.2.38), it is straightforward to obtain the complex amplitude of the instantaneous nonlinear polarization in the time domain for each polarization axis:

$$P_{x,\omega_0}^{(3\mathrm{I})} = \varepsilon_0 \gamma_\mathrm{I} \left[\left(\left| E_{x,\omega_0} \right|^2 + \frac{2}{3} \left| E_{y,\omega_0} \right|^2 \right) E_{x,\omega_0} + \frac{1}{3} E_{y,\omega_0}^2 E_{x,-\omega_0} \right]; \tag{4.2.43}$$

$$P_{y,\omega_0}^{(3\mathrm{I})} = \varepsilon_0 \gamma_\mathrm{I} \left[\left(\left| E_{y,\omega_0} \right|^2 + \frac{2}{3} \left| E_{x,\omega_0} \right|^2 \right) E_{y,\omega_0} + \frac{1}{3} E_{x,\omega_0}^2 E_{y,-\omega_0} \right], \tag{4.2.44}$$

where $\gamma_\mathrm{I} := (3/4)\, \chi_\mathrm{NL} \left(1 - f_\mathrm{R}\right) = 1.5 \cdot 10^{-22}$ m^2/V^2 at the wavelength of 1550 nm.

Furthermore, the complex amplitude of the nonlinear polarization modeling the nuclei motions (Raman response) can also be found using Eqs. (4.2.33), (4.2.37) and (4.2.39). As an example, the complex amplitude for the x-polarization is derived from these equations as:

$$\begin{aligned} P_{x,\omega_0}^{(3\mathrm{R})}(\boldsymbol{r},t) = \frac{1}{4}\varepsilon_0 \chi_\mathrm{NL} f_\mathrm{R} \Bigg\{ & 2E_{x,\omega_0}(\boldsymbol{r},t) \int_{-\infty}^{\infty} (h+u)(t-\tau) \left| E_{x,\omega_0}(\boldsymbol{r},\tau) \right|^2 \mathrm{d}\tau \\ & + 2E_{x,\omega_0}(\boldsymbol{r},t) \int_{-\infty}^{\infty} h(t-\tau) \left| E_{y,\omega_0}(\boldsymbol{r},\tau) \right|^2 \mathrm{d}\tau \\ & + 2E_{y,\omega_0}(\boldsymbol{r},t) \int_{-\infty}^{\infty} u(t-\tau)\, \mathrm{Re}\left[E_{x,\omega_0}(\boldsymbol{r},\tau)\, E_{y,-\omega_0}(\boldsymbol{r},\tau) \right] \mathrm{d}\tau \\ & + E_{x,-\omega_0}(\boldsymbol{r},t) \exp(-j2\omega_0 t) \int_{-\infty}^{\infty} (h+u)(t-\tau)\, E_{x,\omega_0}^2(\boldsymbol{r},\tau) \exp(j2\omega_0\tau)\, \mathrm{d}\tau \\ & + E_{x,-\omega_0}(\boldsymbol{r},t) \exp(-j2\omega_0 t) \int_{-\infty}^{\infty} h(t-\tau)\, E_{y,\omega_0}^2(\boldsymbol{r},\tau) \exp(j2\omega_0\tau)\, \mathrm{d}\tau \\ & + E_{y,-\omega_0}(\boldsymbol{r},t) \exp(-j2\omega_0 t) \int_{-\infty}^{\infty} u(t-\tau)\, E_{x,\omega_0}(\boldsymbol{r},\tau)\, E_{y,\omega_0}(\boldsymbol{r},\tau) \exp(j2\omega_0\tau)\, \mathrm{d}\tau \Bigg\}, \end{aligned} \tag{4.2.45}$$

including in this case the independent variables to clarify the mathematical discussion. In order to simplify Eq. (4.2.45), note that the last three terms of the RHS can be expressed in the general form:

$$E_{j,-\omega_0}(\boldsymbol{r},t) \exp(-j2\omega_0 t) \int_{-\infty}^{\infty} p(t-\tau)\, E_{k,\omega_0}(\boldsymbol{r},\tau)\, E_{l,\omega_0}(\boldsymbol{r},\tau) \exp(j2\omega_0\tau)\, \mathrm{d}\tau, \tag{4.2.46}$$

with $(j,k,l) \in \{x,y\}^3$ and the p function accounting for the h, u and $h+u$ functions. Now, performing a simple algebraic transformation of the convolution integral, Eq. (4.2.46) becomes:

$$
\begin{aligned}
&E_{j,-\omega_0}(\boldsymbol{r},t)\exp(-j2\omega_0 t)\int_{-\infty}^{\infty} p(t-\tau)\,E_{k,\omega_0}(\boldsymbol{r},\tau)\,E_{l,\omega_0}(\boldsymbol{r},\tau)\exp(j2\omega_0\tau)\,\mathrm{d}\tau \\
&\quad = E_{j,-\omega_0}(\boldsymbol{r},t)\exp(-j2\omega_0 t)\int_{-\infty}^{\infty} p(\tau)\,E_{k,\omega_0}(\boldsymbol{r},t-\tau)\,E_{l,\omega_0}(\boldsymbol{r},t-\tau)\exp(j2\omega_0(t-\tau))\,\mathrm{d}\tau \\
&\quad = E_{j,-\omega_0}(\boldsymbol{r},t)\int_{-\infty}^{\infty} p(\tau)\exp(-j2\omega_0\tau)\,E_{k,\omega_0}(\boldsymbol{r},t-\tau)\,E_{l,\omega_0}(\boldsymbol{r},t-\tau)\,\mathrm{d}\tau \\
&\quad = E_{j,-\omega_0}(\boldsymbol{r},t)\left[(p(t)\exp(-j2\omega_0 t))*(E_{k,\omega_0}(\boldsymbol{r},t)\,E_{l,\omega_0}(\boldsymbol{r},t))\right].
\end{aligned}
\tag{4.2.47}
$$

As can be noted, Eq. (4.2.47) involves a convolution of the *modulated* Raman response with the complex amplitudes of the electric field strength. Considering that the bandwidth of the Raman response (given by $p \in \{h, u, h+u\}$) is around 15 THz [139], centered at $-2\omega_0 \approx -380$ THz, and the bandwidth of the complex amplitudes is lower than 100 THz for ultra-short pulses wider than 10 fs (in baseband), the Fourier transform ($\mathcal{F}$) of the convolution is found to be null:[13]

$$
\begin{aligned}
&\mathcal{F}\left[(p(t)\exp(-j2\omega_0 t))*(E_{k,\omega_0}(\boldsymbol{r},t)\,E_{l,\omega_0}(\boldsymbol{r},t))\right] = \\
&\qquad = \frac{1}{2\pi}\widetilde{P}(\Omega+2\omega_0)\left[\widetilde{E}_{k,\omega_0}(\boldsymbol{r},\Omega)*\widetilde{E}_{l,\omega_0}(\boldsymbol{r},\Omega)\right] = 0,
\end{aligned}
\tag{4.2.48}
$$

and therefore, the last three terms of the RHS of Eq. (4.2.45) can be neglected. Finally, defining the f function as $f := h + u$ and the nonlinear constant $\gamma_{\mathrm{R}} := 0.5\chi_{\mathrm{NL}} f_{\mathrm{R}} = 3.2 \cdot 10^{-23}\ \mathrm{m^2/V^2}$ at the wavelength of 1550 nm, the complex amplitude of the nonlinear polarization modeling both electronic and nuclei responses is found at the x-polarization axis as:

$$
\begin{aligned}
P^{(3)}_{x,\omega_0}(\boldsymbol{r},t) = {} & \varepsilon_0\gamma_{\mathrm{I}}\left\{\left[|E_{x,\omega_0}(\boldsymbol{r},t)|^2 + \frac{2}{3}|E_{y,\omega_0}(\boldsymbol{r},t)|^2\right]E_{x,\omega_0}(\boldsymbol{r},t) + \frac{1}{3}E^2_{y,\omega_0}(\boldsymbol{r},t)\,E_{x,-\omega_0}(\boldsymbol{r},t)\right\} \\
& + \varepsilon_0\gamma_{\mathrm{R}}\left\{\begin{array}{l} E_{x,\omega_0}(\boldsymbol{r},t)\left[f(t)*|E_{x,\omega_0}(\boldsymbol{r},t)|^2 + h(t)*|E_{y,\omega_0}(\boldsymbol{r},t)|^2\right] \\ +E_{y,\omega_0}(\boldsymbol{r},t)\left[u(t)*\mathrm{Re}\left[E_{x,\omega_0}(\boldsymbol{r},t)\,E_{y,-\omega_0}(\boldsymbol{r},t)\right]\right] \end{array}\right\},
\end{aligned}
\tag{4.2.49}
$$

and similar for the y-polarization.

Once we have derived the complex amplitude of the nonlinear polarization in the time domain, Eq. (4.2.32) can be completed by using Eqs. (4.2.35) and (4.2.49). Along this line, note that γ_{I}, γ_{R} and F_{mi} are frequency-dependent functions. However, we can safely assume that the frequency dependence of these functions is much lower than their average value in the pulse bandwidth. Hence, Eq. (4.2.32) becomes:[14]

[13] In order to demonstrate that the convolution of Eq. (4.2.47) is found to be null, we use the Fourier transform ($\mathcal{F}$) instead of the STFT ($\mathcal{F}_{\mathrm{T}}$) because the temporal duration of p can be found higher than the temporal window function employed in the STFT. As a result, the temporal dependence of $\widetilde{E}_{k,\omega_0}$ and $\widetilde{E}_{l,\omega_0}$ dissapears in Eq. (4.2.48). Along this line, it should be noted that it is mathematically wrong to use the same functions to denote the Fourier transform and the STFT of E_{k,ω_0} and E_{l,ω_0}. Nonetheless, let us relax the notation for simplicity.

[14] For the sake of simplicity, the independent variables are only included in the convolution operation of the nonlinear terms.

$$\sum_{m=a,b}\left[\frac{\omega^2}{c_0^2}\left(\widetilde{\varepsilon}_{\mathrm{r},x}-\widetilde{\varepsilon}_{\mathrm{r},mx}\right)-\left(j2\beta_{mx,\omega_0}^{(\mathrm{eq})}+\alpha-\partial_z\right)\mathfrak{D}_{mx}^{(\mathrm{eq})}\right]F_{mx}\exp\left(-j\phi_{mx,\omega_0}\right)\widetilde{A}_{mx}$$
$$+F_{mx}\exp\left(-j\phi_{mx,\omega_0}\right)\partial_z^2\widetilde{A}_{mx}-\left(j2\beta_{mx,\omega_0}^{(\mathrm{eq})}+\alpha\right)F_{mx}\exp\left(-j\phi_{mx,\omega_0}\right)\partial_z\widetilde{A}_{mx}$$
$$+\frac{\omega^2}{c_0^2}\widetilde{\sigma}F_{my}\exp\left(-j\phi_{my,\omega_0}\right)\widetilde{A}_{my}$$
$$+\frac{\omega^2}{c_0^2}\gamma_{\mathrm{I}}\exp\left(-\alpha z\right)\begin{bmatrix}F_{mx}^3\exp\left(-j\phi_{mx,\omega_0}\right)\mathcal{F}_{\mathrm{T}}\left\{A_{mx}\left|A_{mx}\right|^2\exp\left(j\omega_0 t\right)\right\}\\+\frac{2}{3}F_{mx}F_{my}^2\exp\left(-j\phi_{mx,\omega_0}\right)\mathcal{F}_{\mathrm{T}}\left\{A_{mx}\left|A_{my}\right|^2\exp\left(j\omega_0 t\right)\right\}\\+\frac{1}{3}F_{mx}F_{my}^2\exp\left(-j\left(2\phi_{my,\omega_0}-\phi_{mx,\omega_0}\right)\right)\mathcal{F}_{\mathrm{T}}\left\{A_{mx}^*A_{my}^2\exp\left(j\omega_0 t\right)\right\}+...\end{bmatrix}$$
$$+\frac{\omega^2}{c_0^2}\gamma_{\mathrm{R}}\exp\left(-\alpha z\right)\begin{bmatrix}F_{mx}^3\exp\left(-j\phi_{mx,\omega_0}\right)\mathcal{F}_{\mathrm{T}}\left\{A_{mx}\left[f\left(t\right)*\left|A_{mx}\left(z,t\right)\right|^2\right]\exp\left(j\omega_0 t\right)\right\}\\+F_{mx}F_{my}^2\exp\left(-j\phi_{mx,\omega_0}\right)\mathcal{F}_{\mathrm{T}}\left\{A_{mx}\left[h\left(t\right)*\left|A_{my}\left(z,t\right)\right|^2\right]\exp\left(j\omega_0 t\right)\right\}\\+\frac{1}{2}F_{mx}F_{my}^2\exp\left(-j\phi_{mx,\omega_0}\right)\\\qquad\times\mathcal{F}_{\mathrm{T}}\left\{A_{my}\left[u\left(t\right)*\left(A_{mx}\left(z,t\right)A_{my}^*\left(z,t\right)\right)\right]\exp\left(j\omega_0 t\right)\right\}\\+\frac{1}{2}F_{mx}F_{my}^2\exp\left(-j\left(2\phi_{my,\omega_0}-\phi_{mx,\omega_0}\right)\right)\\\qquad\times\mathcal{F}_{\mathrm{T}}\left\{A_{my}\left[u\left(t\right)*\left(A_{mx}^*\left(z,t\right)A_{my}\left(z,t\right)\right)\right]\exp\left(j\omega_0 t\right)\right\}+...\end{bmatrix}=0, \tag{4.2.50}$$

and a similar expression is found for the y-polarization axis by exchanging the subindexes x and y in Eq. (4.2.50). As demonstrated in Chapter 2, note that the nonlinear terms involving cross-coupling effect among the PCMs of different cores can be neglected assuming an MCF with a core-to-core distance higher than three times the core radius, i.e., $d_{ab}>3R_0$. From Eq. (4.2.50), the coupled local-mode equation of each PCM mi in the frequency domain can be found by multiplying by $F_{mi}\exp(j\phi_{mi,\omega_0})$ and integrating in an infinite cross-sectional area of the MCF. As an example, the coupled local-mode equation of the PCM ax is found to be:

$$\begin{aligned}j\left(\partial_z+\mathfrak{D}_{ax}^{(\mathrm{eq})}\right)\widetilde{A}_{ax}&=\exp\left(-j\Delta\phi_{ay,ax}^{(0)}\right)\widetilde{m}_{ax,ay}\widetilde{A}_{ay}+\exp\left(-j\Delta\phi_{bx,ax}^{(0)}\right)\widetilde{\kappa}_{ax,bx}\widetilde{A}_{bx}\\&+\exp\left(-\alpha z\right)\left\{\widetilde{q}_{ax}^{(\mathrm{I})}\mathcal{F}_{\mathrm{T}}\left\{A_{ax}\left|A_{ax}\right|^2\exp\left(j\omega_0 t\right)\right\}\right.\\&+\frac{2}{3}\widetilde{g}_{ax,ay}^{(\mathrm{I})}\mathcal{F}_{\mathrm{T}}\left\{A_{ax}\left|A_{ay}\right|^2\exp\left(j\omega_0 t\right)\right\}\\&+\frac{1}{3}\exp\left(-j2\Delta\phi_{ay,ax}^{(0)}\right)\widetilde{g}_{ax,ay}^{(\mathrm{I})}\mathcal{F}_{\mathrm{T}}\left\{A_{ax}^*A_{ay}^2\exp\left(j\omega_0 t\right)\right\}\\&+\widetilde{q}_{ax}^{(\mathrm{R})}\mathcal{F}_{\mathrm{T}}\left\{A_{ax}\left[f\left(t\right)*\left|A_{ax}\left(z,t\right)\right|^2\right]\exp\left(j\omega_0 t\right)\right\}\\&+\widetilde{g}_{ax,ay}^{(\mathrm{R})}\mathcal{F}_{\mathrm{T}}\left\{A_{ax}\left[h\left(t\right)*\left|A_{ay}\left(z,t\right)\right|^2\right]\exp\left(j\omega_0 t\right)\right\}\\&+\frac{1}{2}\widetilde{g}_{ax,ay}^{(\mathrm{R})}\mathcal{F}_{\mathrm{T}}\left\{A_{ay}\left[u\left(t\right)*\left(A_{ax}\left(z,t\right)A_{ay}^*\left(z,t\right)\right)\right]\exp\left(j\omega_0 t\right)\right\}\\&+\frac{1}{2}\exp\left(-j2\Delta\phi_{ay,ax}^{(0)}\right)\widetilde{g}_{ax,ay}^{(\mathrm{R})}\times\\&\left.\times\ \mathcal{F}_{\mathrm{T}}\left\{A_{ay}\left[u\left(t\right)*\left(A_{ax}^*\left(z,t\right)A_{ay}\left(z,t\right)\right)\right]\exp\left(j\omega_0 t\right)\right\}\right\},\end{aligned} \tag{4.2.51}$$

where $\Delta\phi_{mi,nj}^{(0)}:=\phi_{mi,\omega_0}-\phi_{nj,\omega_0}$, $\forall\left(mi,nj\right)\in\{ax,ay,bx,by\}^2$; and the linear and nonlinear mode-coupling coefficients (MCCs) are defined in the frequency domain as (all integrals apply over an infinite cross-sectional area):

$$\widetilde{m}_{ax,ay}\left(z,\omega;t\right):=\frac{\omega^2}{2c_0^2\beta_{ax,\omega_0}^{(\mathrm{eq})}N_{ax}}\iint\widetilde{\sigma}F_{ay}F_{ax}\mathrm{d}x\mathrm{d}y; \tag{4.2.52}$$

$$\widetilde{\kappa}_{ax,bx}\left(z,\omega;t\right):=\frac{\omega^2}{2c_0^2\beta_{ax,\omega_0}^{(\mathrm{eq})}N_{ax}}\iint\Delta\widetilde{\varepsilon}_{\mathrm{r},ax}F_{bx}F_{ax}\mathrm{d}x\mathrm{d}y; \tag{4.2.53}$$

$$\widetilde{q}_{ax}^{(\mathrm{S})}\left(z,\omega;t\right):=\frac{\omega^2}{2c_0^2\beta_{ax,\omega_0}^{(\mathrm{eq})}N_{ax}}\iint\gamma_{\mathrm{S}}F_{ax}^4\mathrm{d}x\mathrm{d}y; \tag{4.2.54}$$

$$\widetilde{g}_{ax,ay}^{(\mathrm{S})}\left(z,\omega;t\right):=\frac{\omega^2}{2c_0^2\beta_{ax,\omega_0}^{(\mathrm{eq})}N_{ax}}\iint\gamma_{\mathrm{S}}F_{ay}^2F_{ax}^2\mathrm{d}x\mathrm{d}y;\quad\mathrm{S}\in\{\mathrm{I},\mathrm{R}\}, \tag{4.2.55}$$

with $N_{ax}\left(z,\omega;t\right):=\iint F_{ax}^2\mathrm{d}x\mathrm{d}y$. Note that the frequency dependence of the nonlinear MCCs also involves the nonlinear dispersion of γ_{I} and γ_{R}, induced by the frequency dependence of n_{NL}. In such a scenario, the function n_{NL} can be approximated by a first-order Taylor series expansion as $n_{\mathrm{NL}}\left(\omega\right)\simeq n_{\mathrm{NL}}^{(0)}+\left(\omega-\omega_0\right)n_{\mathrm{NL}}^{(1)}$, where $n_{\mathrm{NL}}^{(0)}=2.6\cdot10^{-20}$ m^2/W and $n_{\mathrm{NL}}^{(1)}=8.3\cdot10^{-24}$ ps $\cdot$ m^2/W in silica fibers [139, 163].

In general, additional MCCs appear in Eq. (4.2.51) modeling linear mode-coupling between the PCMs. Nevertheless, these MCCs can be neglected, as demonstrated in Chapter 3 for the monochromatic case [see Eq. (3.2.24)]. Now, redefining the complex envelopes in the frequency domain as $\widetilde{A}_{mi}:=\widetilde{\mathcal{A}}_{mi}\exp\left(\alpha z/2\right)$, assuming the attenuation coefficient α with low frequency dependence satisfying $\alpha\left(\omega_0\right)\gg\mathrm{d}\alpha\left(\omega=\omega_0\right)/\mathrm{d}\omega$, and defining the equivalent intra- and inter-core mode-coupling functions as:

$$\widetilde{M}_{ax,ay}^{(\mathrm{eq})}\left(z,\omega;t\right):=\exp\left(-j\Delta\phi_{ay,ax}\left(z,\omega_0;t\right)\right)\widetilde{m}_{ax,ay}\left(z,\omega;t\right); \tag{4.2.56}$$

$$\widetilde{K}_{ax,bx}^{(\mathrm{eq})}\left(z,\omega;t\right):=\exp\left(-j\Delta\phi_{bx,ax}\left(z,\omega_0;t\right)\right)\widetilde{\kappa}_{ax,bx}\left(z,\omega;t\right), \tag{4.2.57}$$

comprising the frequency dependence of the MCCs, Eq. (4.2.51) is reduced to:

$$\begin{aligned}
j\left(\partial_z+\mathfrak{D}_{ax}^{(\mathrm{eq})}+\frac{\alpha}{2}\right)\widetilde{\mathcal{A}}_{ax}=&\widetilde{M}_{ax,ay}^{(\mathrm{eq})}\widetilde{\mathcal{A}}_{ay}+\widetilde{K}_{ax,bx}^{(\mathrm{eq})}\widetilde{\mathcal{A}}_{bx}+\widetilde{q}_{ax}^{(\mathrm{I})}\mathcal{F}_{\mathrm{T}}\left\{\mathcal{A}_{ax}\left|\mathcal{A}_{ax}\right|^2\exp\left(j\omega_0t\right)\right\}\\
&+\frac{2}{3}\widetilde{g}_{ax,ay}^{(\mathrm{I})}\mathcal{F}_{\mathrm{T}}\left\{\mathcal{A}_{ax}\left|\mathcal{A}_{ay}\right|^2\exp\left(j\omega_0t\right)\right\}\\
&+\frac{1}{3}\exp(-j2\Delta\phi_{ay,ax}^{(0)})\widetilde{g}_{ax,ay}^{(\mathrm{I})}\mathcal{F}_{\mathrm{T}}\left\{\mathcal{A}_{ax}^*\mathcal{A}_{ay}^2\exp\left(j\omega_0t\right)\right\}\\
&+\widetilde{q}_{ax}^{(\mathrm{R})}\mathcal{F}_{\mathrm{T}}\left\{\mathcal{A}_{ax}\left[f\left(t\right)*\left|\mathcal{A}_{ax}\left(z,t\right)\right|^2\right]\exp\left(j\omega_0t\right)\right\}\\
&+\widetilde{g}_{ax,ay}^{(\mathrm{R})}\mathcal{F}_{\mathrm{T}}\left\{\mathcal{A}_{ax}\left[h\left(t\right)*\left|\mathcal{A}_{ay}\left(z,t\right)\right|^2\right]\exp\left(j\omega_0t\right)\right\}\\
&+\frac{1}{2}\widetilde{g}_{ax,ay}^{(\mathrm{R})}\mathcal{F}_{\mathrm{T}}\left\{\mathcal{A}_{ay}\left[u\left(t\right)*\left(\mathcal{A}_{ax}\left(z,t\right)\mathcal{A}_{ay}^*\left(z,t\right)\right)\right]\exp\left(j\omega_0t\right)\right\}\\
&+\frac{1}{2}\exp(-j2\Delta\phi_{ay,ax}^{(0)})\widetilde{g}_{ax,ay}^{(\mathrm{R})}\times\\
&\times\mathcal{F}_{\mathrm{T}}\left\{\mathcal{A}_{ay}\left[u\left(t\right)*\left(\mathcal{A}_{ax}^*\left(z,t\right)\mathcal{A}_{ay}\left(z,t\right)\right)\right]\exp\left(j\omega_0t\right)\right\}.
\end{aligned} \tag{4.2.58}$$

In order to derive the final expression of the coupled local-mode equation for the PCM ax in the time domain, we should perform the following Taylor series expansion at $\omega=\omega_0$ of the holomorphic functions (we denote the instantaneous and Raman nonlinear MCCs by the superindex $\mathrm{S}\in\{\mathrm{I},\mathrm{R}\}$):

$$\widetilde{M}_{ax,ay}^{(\mathrm{eq})}\left(z,\omega;t\right)=\sum_{n=0}^{\infty}\frac{1}{n!}\left(\omega-\omega_0\right)^n\partial_\omega^n\widetilde{M}_{ax,ay}^{(\mathrm{eq})}\left(z,\omega_0;t\right)\equiv\sum_{n=0}^{\infty}\frac{1}{n!}\left(\omega-\omega_0\right)^n\widetilde{M}_{ax,ay}^{(\mathrm{eq})(n)}; \tag{4.2.59}$$

$$\widetilde{K}_{ax,bx}^{(\mathrm{eq})}\left(z,\omega;t\right)=\sum_{n=0}^{\infty}\frac{1}{n!}\left(\omega-\omega_0\right)^n\partial_\omega^n\widetilde{K}_{ax,bx}^{(\mathrm{eq})}\left(z,\omega_0;t\right)\equiv\sum_{n=0}^{\infty}\frac{1}{n!}\left(\omega-\omega_0\right)^n\widetilde{K}_{ax,bx}^{(\mathrm{eq})(n)}; \tag{4.2.60}$$

$$\widetilde{q}_{ax}^{(\mathrm{S})}(z,\omega;t)=\sum_{n=0}^{\infty}\frac{1}{n!}(\omega-\omega_0)^n\,\partial_\omega^n\widetilde{q}_{ax}^{(\mathrm{S})}(z,\omega_0;t)\equiv\sum_{n=0}^{\infty}\frac{1}{n!}(\omega-\omega_0)^n\,\widetilde{q}_{ax}^{(\mathrm{S})(n)};\tag{4.2.61}$$

$$\widetilde{g}_{ax,ay}^{(\mathrm{S})}(z,\omega;t)=\sum_{n=0}^{\infty}\frac{1}{n!}(\omega-\omega_0)^n\,\partial_\omega^n\widetilde{g}_{ax,ay}^{(\mathrm{S})}(z,\omega_0;t)\equiv\sum_{n=0}^{\infty}\frac{1}{n!}(\omega-\omega_0)^n\,\widetilde{g}_{ax,ay}^{(\mathrm{S})(n)};\tag{4.2.62}$$

$$\alpha(\omega)\simeq\alpha(\omega_0)+(\omega-\omega_0)\left.\frac{\mathrm{d}\alpha(\omega)}{\mathrm{d}\omega}\right|_{\omega_0}\equiv\alpha^{(0)}+(\omega-\omega_0)\,\alpha^{(1)},\tag{4.2.63}$$

which can be expressed in the time domain by the next linear operators:

$$\begin{gathered}\widehat{\mathrm{M}}_{ax,ay}^{(\mathrm{eq})}(z;t):=\sum_{n=0}^{\infty}\frac{(-j)^n}{n!}\widetilde{M}_{ax,ay}^{(\mathrm{eq})(n)}\partial_t^n;\qquad\widehat{\mathrm{K}}_{ax,bx}^{(\mathrm{eq})}(z;t):=\sum_{n=0}^{\infty}\frac{(-j)^n}{n!}\widetilde{K}_{ax,bx}^{(\mathrm{eq})(n)}\partial_t^n;\\ \hat{\mathrm{q}}_{ax}^{(\mathrm{S})}(z;t):=\sum_{n=0}^{\infty}\frac{(-j)^n}{n!}\widetilde{q}_{ax}^{(\mathrm{S})(n)}\partial_t^n;\qquad\hat{\mathrm{g}}_{ax,ay}^{(\mathrm{S})}(z;t):=\sum_{n=0}^{\infty}\frac{(-j)^n}{n!}\widetilde{g}_{ax,ay}^{(\mathrm{S})(n)}\partial_t^n;\qquad\widehat{\alpha}:=\alpha^{(0)}-j\alpha^{(1)}\partial_t,\end{gathered}\tag{4.2.64}$$

and the complex function $\mathfrak{D}_{mi}^{(\mathrm{eq})}$ of the PCM mi is expressed in the time domain by the equivalent dispersion operator $\widehat{\mathrm{D}}_{mi}^{(\mathrm{eq})}$, which accounts for the frequency dependence of the ideal phase constant $\beta_{mi}(\omega)$ and the MCF perturbations $\beta_{mi}^{(\mathrm{B+S})}(z,\omega;t)$:

$$\widehat{\mathrm{D}}_{mi}^{(\mathrm{eq})}(z;t):=\sum_{n=1}^{\infty}\frac{(-j)^{n-1}}{n!}\beta_{mi,\omega_0}^{(\mathrm{eq})(n)}\partial_t^n.\tag{4.2.65}$$

Finally, applying the inverse STFT to Eq. (4.2.58) and considering an MCF comprising N cores, the final expression of the coupled local-mode equation for the PCM ax is derived in the time domain:

$$\begin{aligned}j\left(\partial_z+\widehat{\mathrm{D}}_{ax}^{(\mathrm{eq})}+\frac{1}{2}\widehat{\alpha}\right)\mathcal{A}_{ax}(z,t)&=\widehat{\mathrm{M}}_{ax,ay}^{(\mathrm{eq})}\mathcal{A}_{ay}(z,t)+\sum_{m\neq a}^{N}\widehat{\mathrm{K}}_{ax,mx}^{(\mathrm{eq})}\mathcal{A}_{mx}(z,t)\\&+\hat{\mathrm{q}}_{ax}^{(\mathrm{I})}\left(|\mathcal{A}_{ax}(z,t)|^2\,\mathcal{A}_{ax}(z,t)\right)+\frac{2}{3}\hat{\mathrm{g}}_{ax,ay}^{(\mathrm{I})}\left(|\mathcal{A}_{ay}(z,t)|^2\,\mathcal{A}_{ax}(z,t)\right)\\&+\frac{1}{3}\exp\left(-j2\Delta\phi_{ay,ax}^{(0)}(z;t)\right)\hat{\mathrm{g}}_{ax,ay}^{(\mathrm{I})}\left(\mathcal{A}_{ax}^{*}(z,t)\,\mathcal{A}_{ay}^{2}(z,t)\right)\\&+\hat{\mathrm{q}}_{ax}^{(\mathrm{R})}\left[\left(f(t)*|\mathcal{A}_{ax}(z,t)|^2\right)\mathcal{A}_{ax}(z,t)\right]\\&+\hat{\mathrm{g}}_{ax,ay}^{(\mathrm{R})}\left[\left(h(t)*|\mathcal{A}_{ay}(z,t)|^2\right)\mathcal{A}_{ax}(z,t)\right]\\&+\frac{1}{2}\hat{\mathrm{g}}_{ax,ay}^{(\mathrm{R})}\left\{\left[u(t)*\left(\mathcal{A}_{ax}(z,t)\,\mathcal{A}_{ay}^{*}(z,t)\right)\right]\mathcal{A}_{ay}(z,t)\right\}\\&+\frac{1}{2}\exp\left(-j2\Delta\phi_{ay,ax}^{(0)}(z;t)\right)\hat{\mathrm{g}}_{ax,ay}^{(\mathrm{R})}\times\\&\times\left\{\left[u(t)*\left(\mathcal{A}_{ax}^{*}(z,t)\,\mathcal{A}_{ay}(z,t)\right)\right]\mathcal{A}_{ay}(z,t)\right\}.\end{aligned}\tag{4.2.66}$$

The theoretical model is completed in the single-mode regime by $2N-1$ additional coupled equations for the PCMs $mi\neq ax$, which can be obtained just by exchanging the corresponding subindexes in the above equation. Later, in Appendix E4 (on page 142), we extend the CLMT to the multi-mode regime.

The proposed coupled local-mode equation presents new interesting terms when it is compared with previous ultra-short pulse propagation models in MCF [175–184]. Specifically, the linear operators of Eq. (4.2.66) are found to be longitudinal and temporal dependent, instead of being constant MCCs and unperturbed propagation constants. Thanks to these linear operators, our

model is able to describe accurately the linear and nonlinear propagation of each PCM and the linear and nonlinear MCD (also termed in the literature as intermodal dispersion) between different PCMs taking into consideration the longitudinal and temporal MCF perturbations.

It is worthy to note that the MCD is induced in each birefringent segment by two different dispersive effects when propagating femtosecond optical pulses through an MCF: (*i*) the frequency dependence of the local mismatching between the phase functions $\phi_{mi}\left(z,\omega;t\right)$ of the PCMs, referred to as the phase-mismatching dispersion (PhMD); and (*ii*) the frequency dependence of the mode overlapping between the PCMs, modeled by the MCCs and referred to as the coupling-coefficient dispersion (CCD). As an example, the PhMD between the PCMs ax and bx is given by the phase-mismatching function $\Delta\phi_{bx,ax}\left(z,\omega;t\right)$ and the CCD by the MCCs $\widetilde{\kappa}_{ax,bx}\left(z,\omega;t\right)$ and $\widetilde{\kappa}_{bx,ax}\left(z,\omega;t\right)$, both dispersive effects modeled by the operators $\widehat{\mathrm{D}}_{ax}^{(\mathrm{eq})}$, $\widehat{\mathrm{D}}_{bx}^{(\mathrm{eq})}$, $\widehat{\mathrm{K}}_{ax,bx}^{(\mathrm{eq})}$ and $\widehat{\mathrm{K}}_{bx,ax}^{(\mathrm{eq})}$ in the time domain. Along this line, note that the equivalent dispersion operators $\widehat{\mathrm{D}}_{ax}^{(\mathrm{eq})}$ and $\widehat{\mathrm{D}}_{bx}^{(\mathrm{eq})}$ describe not only the linear propagation of the PCMs ax and bx, but also the exact phase-mismatching $\Delta\phi_{bx,ax}\left(z,\omega;t\right)$ at each angular frequency ω at a given z point (see Subsection 4.3.2). Although the CCD has been previously reported considering ideal MCFs without birefringent effects, the CCD and the PhMD induced by these perturbations have been overlooked so far in the femtosecond regime [175–184]. However, the analysis of both physical impairments is essential to describe the propagation of ultra-short optical pulses in real MCFs perturbed by longitudinal and temporal birefringent effects. The first- and higher-order MCD induced by both dispersive effects will be further analyzed in the next sections.

Remarkably, the MCD can be observed in an SM-MCF between the PCMs of different cores (inter-core MCD) and between the PCMs of a single core (intra-core MCD). Note that the intra-core MCD is the well-known linear and nonlinear PMD. Hence, from now on, we will discuss the inter-core MCD (IMCD) involving mode-coupling between the PCMs of different cores.

4.3 Inter-core mode-coupling dispersion

Although the proposed model allows us to investigate a wide range of propagation phenomena in MCFs, our efforts are mainly focused on a deeper understanding of the IMCD induced by the fiber perturbations. In this section, we will take a closer look at the behavior of the IMCD in ideal and real MCFs, especially, when operating in the linear regime. To this end, and in order to gain physical insight, we will perform a theoretical discussion of the IMCD using Eq. (4.2.51) and omitting the optical power attenuation, the PMD (intra-core MCD), and the nonlinear effects. First, we will investigate the IMCD in ideal homogeneous MCFs (i.e. without fiber perturbations), and later, we will analyze the effects of the IMCD in real MCFs (i.e. with fiber perturbations) considering homogeneous and heterogeneous cores.

4.3.1 Ideal multi-core fiber

As a first example, let us consider an ideal homogeneous 2-core MCF (cores a and b) *without* longitudinal and temporal birefringent effects. In this scenario, if we omit the power attenuation, the PMD, the nonlinear effects and perform the transformation[15] of the complex envelopes $\widetilde{A}_{mi}(z,\omega-\omega_0)=\widetilde{\mathtt{A}}_{mi}(z,\omega-\omega_0)\exp[-j\left(\phi_{mi}\left(z,\omega\right)-\phi_{mi}\left(z,\omega_0\right)\right)]$ in the coupled local-mode equations of the PCMs ax and bx in the frequency domain [i.e. Eq. (4.2.51) for the PCM ax and the equivalent equation for the PCM bx], the following expressions are found:

$$j\partial_z\widetilde{\mathtt{A}}_{ax}\left(z,\omega-\omega_0\right)=\exp\left(-j\Delta\beta_{bx,ax}\left(\omega\right)z\right)\widetilde{\kappa}_{ax,bx}\left(\omega\right)\widetilde{\mathtt{A}}_{bx}\left(z,\omega-\omega_0\right); \tag{4.3.1}$$

$$j\partial_z\widetilde{\mathtt{A}}_{bx}\left(z,\omega-\omega_0\right)=\exp\left(+j\Delta\beta_{bx,ax}\left(\omega\right)z\right)\widetilde{\kappa}_{bx,ax}\left(\omega\right)\widetilde{\mathtt{A}}_{ax}\left(z,\omega-\omega_0\right). \tag{4.3.2}$$

[15]This transformation will allow us to discuss the IMCD from the complicated Eq. (4.2.51) with a simple and intuitive physical interpretation in ideal and real MCFs (see below). Furthermore, note that the temporal variation of $\widetilde{A}_{mi}$, $\widetilde{\mathtt{A}}_{mi}$ and ϕ_{mi} dissapears when omitting the temporal birefringence of the MCF. In such circumstances, we should work with the Fourier transform instead of using the STFT of the complex envelopes. Consequently, in Subsections 4.3.1 and 4.3.2, $\widetilde{A}_{mi}$ and $\widetilde{\mathtt{A}}_{mi}$ are actually the Fourier transform of A_{mi} and $\mathtt{A}_{mi}$, respectively.

It should be noted that, in ideal homogeneous MCFs, the phase-mismatching $\Delta\beta_{bx,ax}(\omega)$ between both PCMs becomes null considering that $\beta_{ax} = \beta_{bx}$, and the MCCs are found to be identical with $\widetilde{\kappa}_{ax,bx} = \widetilde{\kappa}_{bx,ax}$. In this way, Eqs. (4.3.1) and (4.3.2) indicate that an ideal homogeneous MCF is analogous to a symmetric optical coupler. Hence, assuming that only the PCM ax is excited at the MCF input, the solution of the previous equations is given by the expressions ($\Omega := \omega - \omega_0$):

$$\widetilde{\mathtt{A}}_{ax}(z,\Omega) = \cos\left(\widetilde{\kappa}(\Omega)\, z\right) \widetilde{\mathtt{A}}_{ax}(0,\Omega)\,; \qquad \widetilde{\mathtt{A}}_{bx}(z,\Omega) = -j\sin\left(\widetilde{\kappa}(\Omega)\, z\right) \widetilde{\mathtt{A}}_{ax}(0,\Omega)\,, \tag{4.3.3}$$

where the MCC $\widetilde{\kappa}$ is defined as $\widetilde{\kappa}(\Omega) := \widetilde{\kappa}_{ax,bx}(\Omega + \omega_0)$. The previous equations define two different linear and time-invariant (LTI) systems with the transfer functions H_{ax} and H_{bx} modeling the propagation of the complex envelopes $\widetilde{\mathtt{A}}_{mi}$ in the PCMs ax and bx:

$$H_{ax}(z,\Omega) := \frac{\widetilde{\mathtt{A}}_{ax}(z,\Omega)}{\widetilde{\mathtt{A}}_{ax}(0,\Omega)} = \cos\left(\widetilde{\kappa}(\Omega)\, z\right); \qquad H_{bx}(z,\Omega) := \frac{\widetilde{\mathtt{A}}_{bx}(z,\Omega)}{\widetilde{\mathtt{A}}_{ax}(0,\Omega)} = -j\sin\left(\widetilde{\kappa}(\Omega)\, z\right). \tag{4.3.4}$$

Now, in order to analyze the first-order CCD, let us perform a first-order Taylor series expansion of the MCC:

$$\widetilde{\kappa}(\Omega) \simeq \widetilde{\kappa}(\Omega = 0) + \Omega \left.\frac{\mathrm{d}\widetilde{\kappa}(\Omega)}{\mathrm{d}\Omega}\right|_{\Omega=0} \equiv \widetilde{\kappa}^{(0)} + \Omega\widetilde{\kappa}^{(1)}. \tag{4.3.5}$$

From Eqs. (4.3.4) and (4.3.5) it is straightforward to calculate the impulse response of each LTI system $h_{mx}(z,t) = \mathcal{F}^{-1}\left[H_{mx}(z,\Omega)\right]$ (with $m \in \{a,b\}$):

$$h_{ax}(z,t) = \frac{1}{2}\delta\left(t - \widetilde{\kappa}^{(1)}z\right)\exp\left(-j\widetilde{\kappa}^{(0)}z\right) + \frac{1}{2}\delta\left(t + \widetilde{\kappa}^{(1)}z\right)\exp\left(+j\widetilde{\kappa}^{(0)}z\right); \tag{4.3.6}$$

$$h_{bx}(z,t) = \frac{1}{2}\delta\left(t - \widetilde{\kappa}^{(1)}z\right)\exp\left(-j\widetilde{\kappa}^{(0)}z\right) - \frac{1}{2}\delta\left(t + \widetilde{\kappa}^{(1)}z\right)\exp\left(+j\widetilde{\kappa}^{(0)}z\right). \tag{4.3.7}$$

Consequently, we can note that the linear frequency dependence of the MCC (first-order CCD) induces the temporal splitting of the optical pulse in each PCM, according to the observations reported in [175]. Therefore, the first-order CCD can be observed in optical pulses with a temporal width T_{P} satisfying the condition $2\widetilde{\kappa}^{(1)}z \geq T_{\mathrm{P}}$. More specifically, the longitudinal evolution of an optical pulse launched into the PCM ax at $z = 0$ can be easily calculated by using Eqs. (4.3.6) and (4.3.7):

$$\begin{aligned}
\mathtt{A}_{ax}(z,t) &= \mathtt{A}_{ax}(0,t) * h_{ax}(z,t) \\
&= \frac{1}{2}\mathtt{A}_{ax}\left(0, t - \widetilde{\kappa}^{(1)}z\right)\exp\left(-j\widetilde{\kappa}^{(0)}z\right) + \frac{1}{2}\mathtt{A}_{ax}\left(0, t + \widetilde{\kappa}^{(1)}z\right)\exp\left(+j\widetilde{\kappa}^{(0)}z\right) \\
&\equiv \frac{1}{2}\mathtt{A}^{-}_{ax}\exp(-j\theta) + \frac{1}{2}\mathtt{A}^{+}_{ax}\exp(+j\theta)\,; \qquad (4.3.8) \\
\mathtt{A}_{bx}(z,t) &= \mathtt{A}_{ax}(0,t) * h_{bx}(z,t) \\
&= \frac{1}{2}\mathtt{A}_{ax}\left(0, t - \widetilde{\kappa}^{(1)}z\right)\exp\left(-j\widetilde{\kappa}^{(0)}z\right) - \frac{1}{2}\mathtt{A}_{ax}\left(0, t + \widetilde{\kappa}^{(1)}z\right)\exp\left(+j\widetilde{\kappa}^{(0)}z\right) \\
&\equiv \frac{1}{2}\mathtt{A}^{-}_{ax}\exp(-j\theta) - \frac{1}{2}\mathtt{A}^{+}_{ax}\exp(+j\theta)\,, \qquad (4.3.9)
\end{aligned}$$

and in terms of optical power (with $P_{mi} = |\mathtt{A}_{mi}|^2$):[16]

$$P_{ax}(z,t) = \frac{1}{4}\left|\mathtt{A}^{-}_{ax}\right|^2 + \frac{1}{4}\left|\mathtt{A}^{+}_{ax}\right|^2 + \frac{1}{4}\mathtt{A}^{-}_{ax}\left(\mathtt{A}^{+}_{ax}\right)^{*}\exp(-j2\theta) + \frac{1}{4}\left(\mathtt{A}^{-}_{ax}\right)^{*}\mathtt{A}^{+}_{ax}\exp(+j2\theta)\,; \tag{4.3.10}$$

$$P_{bx}(z,t) = \frac{1}{4}\left|\mathtt{A}^{-}_{ax}\right|^2 + \frac{1}{4}\left|\mathtt{A}^{+}_{ax}\right|^2 - \frac{1}{4}\mathtt{A}^{-}_{ax}\left(\mathtt{A}^{+}_{ax}\right)^{*}\exp(-j2\theta) - \frac{1}{4}\left(\mathtt{A}^{-}_{ax}\right)^{*}\mathtt{A}^{+}_{ax}\exp(+j2\theta)\,. \tag{4.3.11}$$

[16] Let us remember that we calculate the optical power in our theoretical discussions by setting $\mathscr{C}^{(\mathrm{P})}_{mi} \equiv 1$ for simplicity [see Eq. (1.5.11)].

If we assume MCF distances satisfying that $z \geq T_{\mathrm{P}}/2\widetilde{\kappa}^{(1)}$, thus $\mathtt{A}_{ax}^{-}\mathtt{A}_{ax}^{+} = 0$ and the third and fourth terms of Eqs. (4.3.10) and (4.3.11) become null obtaining a similar solution in each PCM ax and bx. The original pulse splits in four identical pulses with the 25% of the initial peak power:

$$P_{ax}(z,t) = P_{bx}(z,t) = \frac{1}{4}P_{ax}\left(0, t - \widetilde{\kappa}^{(1)}z\right) + \frac{1}{4}P_{ax}\left(0, t + \widetilde{\kappa}^{(1)}z\right). \tag{4.3.12}$$

Higher-order effects of the CCD induce an additional chirp in the complex envelope of the original pulse, as verified in Appendix D4 by performing numerical calculations of the CLMT [see Fig. D4.1(c)]. The CCD was previously investigated in symmetric optical couplers and ideal MCFs in [175–184]. Therefore, our model is in line with previous works when considering ideal conditions in homogeneous MCFs without including longitudinal and temporal birefringence perturbations or heterogeneous cores. In [182], the heterogeneous case was analyzed with a similar approach as in [175], i.e., modeling a two-core fiber as an ideal optical coupler by omitting the realistic perturbations of the medium. The power of our model and the original contribution of this chapter reveals itself when these realistic fiber conditions are considered.

On the other hand, an additional fundamental feature should be remarked from the above equations. Note that the same analysis can be performed to investigate the mode-coupling between two orthogonal PCMs of a given core (e.g. core a) assuming constant twisting conditions and omitting the intrinsic linear birefringence of the fiber. Concretely, the mode-coupling between the PCMs ax-ay can also be modeled by Eqs. (4.3.1) and (4.3.2) replacing the subindex bx by ay and the MCCs $\widetilde{\kappa}_{ax,bx}$ and $\widetilde{\kappa}_{bx,ax}$ by $\widetilde{m}_{ax,ay}$ and $\widetilde{m}_{ay,ax}$, respectively. Therefore, as can be deduced from the above considerations, the pulse splitting should also be observed between orthogonal PCMs of a given core. However, it is straightforward to verify using Eq. (4.2.52) and the ERIM detailed in Appendix C4 that $\partial_{\omega}\widetilde{m}_{ax,ay} \ll \widetilde{\kappa}^{(1)}$. Thus, we conclude that it is difficult to observe the CCD and the pulse splitting effect between orthogonal PCMs of a given core. The intra-core MCD is mainly induced in the linear fiber regime by the frequency dependence of the phase-mismatching $\Delta\phi_{ay,ax}(z,\omega;t)$, termed in the literature as the linear PMD.

4.3.2 Real multi-core fiber

Now, consider a short MCF segment in a time interval where the longitudinal and temporal fiber perturbations can be assumed to be constant.[17] In addition, in order to gain physical interpretation into the IMCD effects when the fiber birefringence is involved, let us assume once again only two PCMs ax and bx and perform the same transformation of the complex envelopes as in previous subsection in the corresponding coupled local-mode equations of the PCMs ax and bx in the frequency domain, that is, Eq. (4.2.51) for the PCM ax and the equivalent equation for the PCM bx. As a result, the following expressions are found:

$$j\partial_z\widetilde{\mathtt{A}}_{ax}(z,\omega-\omega_0) = \exp\left(-j\Delta\phi_{bx,ax}(z,\omega)\right)\widetilde{\kappa}_{ax,bx}(\omega)\,\widetilde{\mathtt{A}}_{bx}(z,\omega-\omega_0); \tag{4.3.13}$$

$$j\partial_z\widetilde{\mathtt{A}}_{bx}(z,\omega-\omega_0) = \exp\left(+j\Delta\phi_{bx,ax}(z,\omega)\right)\widetilde{\kappa}_{bx,ax}(\omega)\,\widetilde{\mathtt{A}}_{ax}(z,\omega-\omega_0), \tag{4.3.14}$$

where the frequency dependence of $\mathfrak{D}_{ax}^{(\mathrm{eq})}$ and $\mathfrak{D}_{bx}^{(\mathrm{eq})}$ is now described by the exponential terms, and the time dependence of the coupled local-mode equations disappears in the frequency domain when assuming a time-invariant optical medium. Furthermore, the phase-mismatching function can be approximated in the short MCF segment to $\Delta\phi_{bx,ax}(z,\omega) \simeq \Delta\beta_{bx,ax}^{(\mathrm{eq})}(\omega)\,z$ if we assume that $f_{\mathrm{T}}\cdot L_{\mathrm{seg}} \to 0$, where f_{T} is the twist rate and L_{seg} is the segment length. Hence, solving Eqs. (4.3.13) and (4.3.14) assuming that only the PCM ax is excited at the MCF input, we conclude that a real MCF with longitudinal birefringent effects can be modeled once again as two different LTI systems with the following transfer functions in baseband ($\Omega := \omega - \omega_0$):

[17] These initial assumptions allow us to investigate theoretically the IMCD in real MCFs comprising cores of different types: heterogeneous, homogeneous, coupled, uncoupled, lowly or highly-birefringent, trench- or hole-assisted, and with step- or gradual-index profiles.

$$H_{ax}(z,\Omega) := \frac{\widetilde{\mathtt{A}}_{ax}(z,\Omega)}{\widetilde{\mathtt{A}}_{ax}(0,\Omega)} = \exp\left(-j\frac{\Delta\beta^{(\mathrm{eq})}_{bx,ax}(\Omega+\omega_0)}{2}z\right)\times \\ \times\left[\cos\left(\widetilde{\eta}(\Omega)z\right)+j\frac{\Delta\beta^{(\mathrm{eq})}_{bx,ax}(\Omega+\omega_0)}{2\widetilde{\eta}(\Omega)}\sin\left(\widetilde{\eta}(\Omega)z\right)\right]; \tag{4.3.15}$$

$$H_{bx}(z,\Omega) := \frac{\widetilde{\mathtt{A}}_{bx}(z,\Omega)}{\widetilde{\mathtt{A}}_{ax}(0,\Omega)} = -j\frac{\widetilde{\kappa}_{bx,ax}(\Omega+\omega_0)}{\widetilde{\eta}(\Omega)}\exp\left(+j\frac{\Delta\beta^{(\mathrm{eq})}_{bx,ax}(\Omega+\omega_0)}{2}z\right)\sin\left(\widetilde{\eta}(\Omega)z\right), \tag{4.3.16}$$

where $\Delta\beta^{(\mathrm{eq})}_{bx,ax}$ is the mismatching of the equivalent phase constants between the PCMs ax and bx in the MCF segment, which includes the fiber perturbations and the intrinsic material index mismatching when the MCF comprises heterogeneous cores; and $\widetilde{\eta}(\Omega)$ is the complex function defined as:

$$\widetilde{\eta}(\Omega) := \left[\widetilde{\kappa}_{ax,bx}(\Omega+\omega_0)\widetilde{\kappa}_{bx,ax}(\Omega+\omega_0)+\left(\Delta\beta^{(\mathrm{eq})}_{bx,ax}(\Omega+\omega_0)\right)^2/4\right]^{1/2}. \tag{4.3.17}$$

Performing the next first-order Taylor series approximations $\Delta\beta^{(\mathrm{eq})}_{bx,ax} \simeq \Delta\beta^{(\mathrm{eq})(0)}_{bx,ax} + \Delta\beta^{(\mathrm{eq})(1)}_{bx,ax}\Omega$ and $\widetilde{\eta}(\Omega) \simeq \widetilde{\eta}^{(0)}+\widetilde{\eta}^{(1)}\Omega$ (with $\Delta\beta^{(\mathrm{eq})(n)}_{bx,ax} := \mathrm{d}^n\Delta\beta^{(\mathrm{eq})}_{bx,ax}(\Omega=0)/\mathrm{d}\Omega^n$ and $\widetilde{\eta}^{(n)} := \mathrm{d}^n\widetilde{\eta}(\Omega=0)/\mathrm{d}\Omega^n$), the transfer functions of the LTI systems are found to be proportional to:

$$H_{ax}(z,\Omega) \propto \exp\left(-j\frac{\Delta\beta^{(\mathrm{eq})(1)}_{bx,ax}}{2}z\Omega\right)\times \\ \times\left[\cos\left(\widetilde{\eta}^{(0)}z+\widetilde{\eta}^{(1)}z\Omega\right)+j\frac{\Delta\beta^{(\mathrm{eq})}_{bx,ax}(\Omega+\omega_0)}{2\widetilde{\eta}(\Omega)}\sin\left(\widetilde{\eta}^{(0)}z+\widetilde{\eta}^{(1)}z\Omega\right)\right]; \tag{4.3.18}$$

$$H_{bx}(z,\Omega) \propto -j\frac{\widetilde{\kappa}_{bx,ax}(\Omega+\omega_0)}{\widetilde{\eta}(\Omega)}\exp\left(+j\frac{\Delta\beta^{(\mathrm{eq})(1)}_{bx,ax}}{2}z\Omega\right)\sin\left(\widetilde{\eta}^{(0)}z+\widetilde{\eta}^{(1)}z\Omega\right). \tag{4.3.19}$$

From the above equations, we can directly infer the main implications of the IMCD:

- For ideal homogeneous cores without MCF perturbations ($\Delta\beta^{(\mathrm{eq})}_{bx,ax}=0$), it is straightforward to demonstrate that the impulse response of both LTI systems is reduced to Eqs. (4.3.6) and (4.3.7) with $\widetilde{\eta}\equiv\widetilde{\kappa}$. In other words, it is found to be proportional to the Dirac delta function $\delta(t\pm\widetilde{\eta}^{(1)}z)$. Therefore, the pulse splitting induced by the first-order CCD can be observed in both cores for an MCF length L satisfying the condition $L \geq T_{\mathrm{P}}/2\widetilde{\eta}^{(1)}$.

- The power of our model reveals itself when considering real homogeneous and heterogeneous MCFs with longitudinal and temporal birefringent effects inducing a local phase-mismatching $\Delta\beta^{(\mathrm{eq})}_{bx,ax}\neq 0$. In this case, the LTI systems introduce an additional group delay (with opposite sign in cores a and b) induced by the exponential terms of Eqs. (4.3.18) and (4.3.19) and, therefore, the impulse response is found to be proportional to $\delta(t\pm\widetilde{\eta}^{(1)}z\pm\Delta\beta^{(\mathrm{eq})(1)}_{bx,ax}z)$. Note that this effect is produced by the first-order PhMD, modeled by the term $\Delta\beta^{(\mathrm{eq})(1)}_{bx,ax}$, which accounts for the equivalent differential group delay between the PCMs ax and bx. Consequently, the pulse splitting and the group delay induced by the first-order CCD and the first-order PhMD inherit the possible random nature of $\widetilde{\eta}^{(1)}$ and $\Delta\beta^{(\mathrm{eq})(1)}_{bx,ax}$ along the MCF length (arising from the stochastic perturbations of the medium). In addition, the IMCD can also vary in time following the temporal fluctuations of the MCF perturbations that modify the value of $\widetilde{\eta}^{(1)}$ and $\Delta\beta^{(\mathrm{eq})(1)}_{bx,ax}$.

- The increment of the MCF perturbations given by $\left|\Delta\beta_{bx,ax}^{(\mathrm{eq})}\right|$ increases the group delay in the non-excited core b, but reduces the group delay in the excited core a. Note that the transfer function H_{ax} can be approximated to $H_{ax} \simeq 1$ if the absolute value of the equivalent phase-mismatching is much higher than the MCCs, as can be deduced from Eqs. (4.3.15) and (4.3.17). Consequently, the MCF perturbations can be used as a potential strategy of birefringence management to reduce the impact of the IMCD on the MCF transmission.

- As mentioned before, the CCD and the PhMD are induced by the frequency dependence of the MCCs and the local phase-mismatching $\Delta\beta_{bx,ax}^{(\mathrm{eq})}$, respectively. Thus, the second- and higher-order dispersive effects of the IMCD will introduce an additional chirp in the optical pulses, modifying their complex envelopes. In particular, although the higher-order PhMD is difficult to observe between orthogonal PCMs of a given core with similar dispersive parameters (also termed in the literature as the higher-order PMD), the higher-order PhMD becomes an important issue when PCMs of different cores are involved. In the same way, higher-order dispersive effects of the CCD will also modify the complex envelopes of the optical pulses.

- In spite of the fact that the LTI systems are only an approximate solution of the coupled local-mode equations in the linear regime of the fiber, their expressions also allow us to infer a fundamental behavior of the IMCD in the nonlinear regime. The Kerr effect will increase $\left|\Delta\beta_{bx,ax}^{(\mathrm{eq})}\right|$ reducing the mode-coupling between both PCMs, in line with the behavior of the nonlinear IC-XT experimentally observed in Chapter 2. Nonetheless, in general, the coupled local-mode equations [Eq. (4.2.66)] must be solved numerically to perform a complete analysis of the IMCD effects in the nonlinear regime. As we will see below, additional propagating effects will appear on the optical pulses induced by the MCF nonlinearities, which can only be observed when solving numerically the coupled local-mode equations.

These points are verified through extensive numerical calculations of the CLMT in the next section. As we will see, many interesting IMCD effects related to MCF perturbations that could not be addressed with previous femtosecond pulse propagation models [175–184] emerge when using the proposed theory.

4.4 Numerical simulations

In all the analyzed cases, we considered an MCF comprising a fiber length of $L = 40$ m and two cores a and b distributed in a square lattice with a core-to-core distance $d_{ab} = 26$ μm and a core radius $R_0 = 4$ μm, as depicted in Fig. 4.1. The wavelength of the optical carrier (λ_0) was selected to be in the third transmission window with $\lambda_0 = 1550$ nm. The peak power[18] of the optical pulses was taken to be 0 dBm to analyze the IMCD effects in the linear regime (Figs. 4.3, 4.4, 4.5 and 4.7) and 40.7 dBm to investigate the impact of the medium perturbations on a fundamental soliton (Fig. 4.6). The time variable was normalized by using the group delay of the PCM ax as a reference with $t_{\mathrm{N}} = (t - \beta_{ax}^{(1)} z)/T_{\mathrm{P}}$, where T_{P} is defined in this work as the full-width at $1/(2e)$ ($\sim 18\%$) of the peak power. In order to investigate the main effects of the IMCD, different fiber parameters are considered in each numerical example. The specific parameters of each simulation are detailed in Tables C4.1 and C4.2 of Appendix C4 (on page 136).

As a first simple example, we considered a homogeneous MCF with constant bending conditions. The material refractive index of the cores a and b and the cladding was selected to be $n_{a(b)} = 1.452$ and $n_{\mathrm{cl}} = 1.444$, respectively. Figure 4.3 shows the simulation results of the coupled local-mode equations when a 350-fs Gaussian optical pulse is launched into the PCM ax at $z = 0$. In this example, the linear birefringence is induced via the photo-elastic effect by three different constant bending radius $R_{\mathrm{B}} = \infty$, 10 cm and 1 cm, depicted in Figs. 4.3(a)-(c), respectively. Moreover, the

[18] In order to perform realistic numerical simulations of the CLMT, the power of the optical pulses was calculated as $P_{mi}(z,t) = \mathscr{C}_{mi}^{(\mathrm{P})} |\mathcal{A}_{mi}(z,t)|^2$, with the exact value of $\mathscr{C}_{mi}^{(\mathrm{P})}$ given by Eq. (1.5.12).

chromatic dispersion [also known as group-velocity dispersion (GVD)] and the PMD (induced by the intrinsic random linear and circular fiber birefringence) were omitted to isolate the effects of the first-order IMCD. In this way, the pulse is only propagated by the PCMs ax and bx.

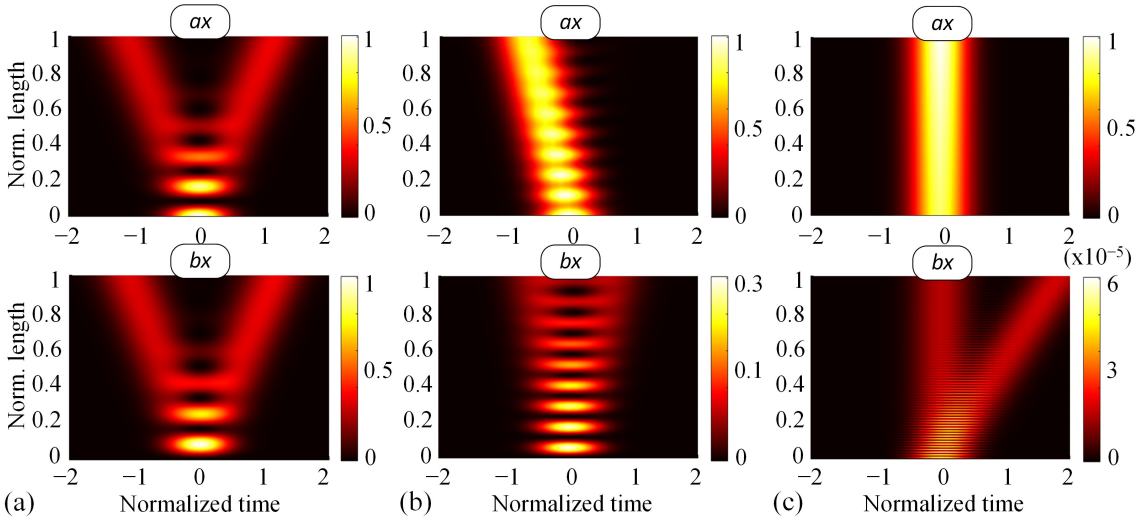

Figure 4.3. First-order IMCD with a constant macrobend. Simulation results of a 350-fs Gaussian optical pulse propagating through a 40-m homogeneous 2-core MCF (cores a and b) with three different constant bending radius: (a) $R_{\mathrm{B}} = \infty$, (b) $R_{\mathrm{B}} = 10$ cm and (c) $R_{\mathrm{B}} = 1$ cm. [Colorbar: normalized power] [116].

Figure 4.3(a) depicts the ideal homogeneous MCF, where the pulse splitting previously observed by Chiang [175] appears induced by the first-order CCD, in line with Eq. (4.3.12). Moreover, it can be observed from Figs. 4.3(b) and (c) that the lower the bending radius, the higher the phase-mismatching induced between the PCMs is. Therefore, an additional group delay appears in the optical pulse induced by the first-order PhMD, with opposite sign in the PCMs ax and bx. In particular, note that the group delay increases in core b when reducing the bending radius as a direct consequence of the impulse response $h_{bx}(t)$, which is proportional to the Dirac delta function $\delta(t \pm \widetilde{\eta}^{(1)} z \pm \Delta\beta_{bx,ax}^{(\mathrm{eq})(1)} z)$ (with $\Delta\beta_{bx,ax}^{(\mathrm{eq})(1)} < 0$ in this case). In contrast, the group delay decreases in core a when the bending radius is reduced [Fig. 4.3(c)]. As was pointed out previously, H_{ax} tends to 1 as $\left|\Delta\beta_{bx,ax}^{(\mathrm{eq})}\right|$ increases. Furthermore, the pulse splitting is reduced in both cores because of the reduction of the mode-coupling induced by the fiber bending. This shows that the MCF longitudinal perturbations (low values of the bending radius in this case) can be used to reduce the effect of the IMCD along the MCF length.

Another interesting potential effect of the first-order IMCD is related to the random birefringence that arises from a randomly-varying fiber bending radius. In this case, the effect of the first-order PhMD along with the CCD can also be observed when considering a high number of MCF birefringent segments where the bending radius fluctuates with a Normal distribution between adjacent segments. We simulate the MCF of the first example by considering a 250-fs Gaussian optical pulse and 50 birefringent segments with two different random distributions of the bending radius: $R_{\mathrm{B1}} = \mathrm{N}(\mu = 100, \sigma^2 = 40)$ cm and $R_{\mathrm{B2}} = \mathrm{N}(\mu = 10, \sigma^2 = 2)$ cm, where N is the normal distribution. The numerical results are shown in Figs. 4.4(a) and 4.4(b) for each bending radius distribution, respectively.

As can be seen from Fig. 4.4(a), the group delay and the pulse splitting present a random evolution in each core due to the stochastic nature of the MCF perturbations inducing a random differential group delay $\Delta\beta_{bx,ax}^{(\mathrm{eq})(1)}$ between the PCMs ax and bx, in line with our previous theoretical predictions. However, if the average value of the bending radius is reduced, the phase-mismatching between the core modes increases (see ERIM in Appendix C4) and, therefore, the pulse dispersion induced by the first-order PhMD decreases, as can be seen from Fig. 4.4(b) and 4.4(c). The comparison of the pulse dispersion at the MCF output in the PCM ax is shown in Fig. 4.4(c)

for each bending radius distribution, verifying that the IMCD is reduced with the second bending radius R_{B2}. It should be noted that, for higher fiber distances, although the intrinsic random linear birefringence of the MCF may increase the pulse distortion (via the PMD), small index differences induced in each core by the fiber fabrication process could reduce the IC-XT levels and the IMCD effects. On the other hand, in spite of the fact that the circular birefringence has been omitted in these simulations to isolate the effects of the IMCD, in Appendix D4 (page 137) we include additional simulations in which both linear and circular random birefringent effects are considered. As can be noted from Fig. D4.2, the circular birefringence only induces power exchange between orthogonal polarizations. Remarkably, we cannot observe an additional pulse distortion in this case taking into account that the PMD can be neglected in both cores when the intrinsic linear birefringence is omitted in the numerical simulations.

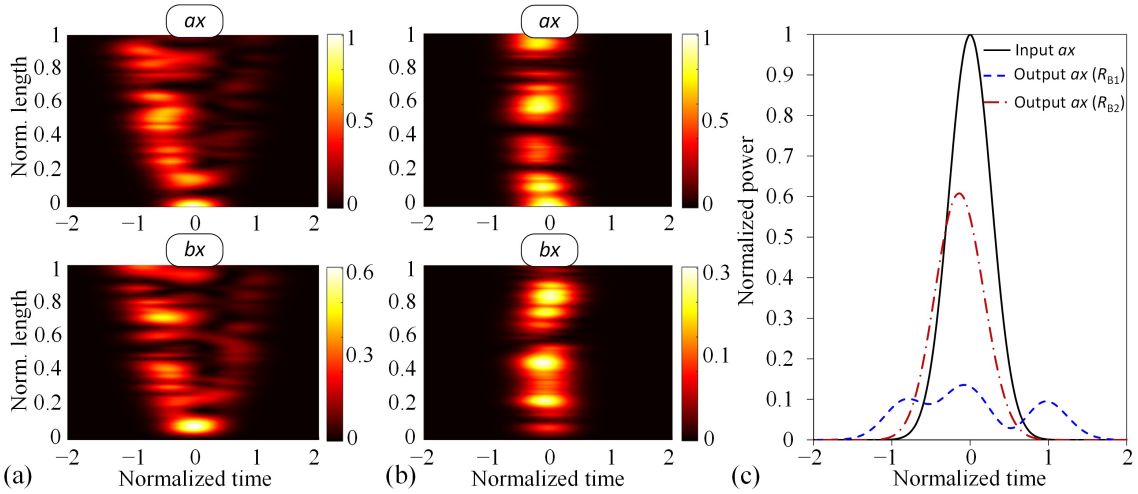

Figure 4.4. First-order IMCD with a random macrobend. Simulation results of a 250-fs Gaussian optical pulse propagating through a homogeneous 2-core MCF comprising 50 birefringent segments with random bending conditions. Two different normal distributions were considered for the numerical calculations in this example: (a) $R_{B1} = N(\mu = 100, \sigma^2 = 40)$ cm and (b) $R_{B2} = N(\mu = 10, \sigma^2 = 2)$ cm. (c) Pulse dispersion comparison at the MCF output for the PCM ax. [Colorbar: normalized power] [116].

In the next example, we compare the effects of the IMCD induced by the CCD and higher-order effects of the PhMD in homogeneous and heterogeneous MCFs. As detailed in the previous section, higher-order dispersive effects of the PhMD appear when considering a non-vanishing $\Delta\beta^{(l)}_{bx,ax}$ with $l \geq 2$. To investigate the additional chirp induced by the higher-order PhMD, a 200-fs Gaussian optical pulse was simulated in the same homogeneous MCF as in the previous examples, but with $\Delta\beta^{(1)}_{bx,ax} = 0.28$ ps/km, $\Delta\beta^{(2)}_{bx,ax} = 0.2$ ps^2/km and $\Delta\beta^{(3)}_{bx,ax} = 0$ ps^3/km (which are typical values induced by manufacturing imperfections [21,133,188]). A second heterogeneous MCF with $\Delta n = n_a - n_b = 0.002$, $\Delta\beta^{(1)}_{bx,ax} = 6.5$ ps/km, $\Delta\beta^{(2)}_{bx,ax} = 1$ ps^2/km and $\Delta\beta^{(3)}_{bx,ax} = 0.1$ ps^3/km was also simulated (dispersive parameters which can be found in a heterogeneous MCF design [69]). In both cases, the bending radius was assumed to vary randomly along 50 birefringent segments as a Normal distribution of $R_B = \mathrm{N}(\mu = 100, \sigma^2 = 40)$ cm. In order to illustrate the higher-order PhMD effects, the GVD is compensated in both cores along the MCF propagation using the dispersive parameters of a given PCM as a reference, in this case the PCM ax (the specific dispersive parameters and additional details of this simulation can be found in Table C4.2 of Appendix C4).

The simulation results are shown in Fig. 4.5, where we can observe the additional chirp induced by the second- and third-order PhMD ($\Delta\beta^{(2)}_{bx,ax}$ and $\Delta\beta^{(3)}_{bx,ax}$), which increases the temporal width of the pulse complex envelope in the PCMs ax and bx. Although $\Delta\beta^{(2)}_{bx,ax}$ and $\Delta\beta^{(3)}_{bx,ax}$ are lower in the homogeneous MCF [Fig. 4.5(a)] than in the heterogeneous MCF [Fig. 4.5(b)], the pulse distortion induced by the higher-order IMCD is significantly higher in the former case. In the

heterogeneous case, the second-order PhMD effects are reduced due to the increment of the intrinsic phase-mismatching $\Delta\beta_{bx,ax}(\omega_0)$ between the PCMs ax and bx. These results allow us to conclude that, in the femtosecond regime, the GVD compensation can be performed at the DSP by using the same digital filter for each PCM when heterogeneous cores and short MCF distances are involved ($L \leq L_{\mathrm{PhMD}} = T_{\mathrm{P}}^2 / \left|\Delta\beta_{bx,ax}^{(2)}\right|$, see below). Nonetheless, in homogeneous MCFs, while the criterion $L \leq L_{\mathrm{PhMD}}$ is fulfilled, $\Delta\beta_{bx,ax}(\omega_0) = 0$. Hence, the second-order PhMD induces a higher pulse distortion and the GVD compensation must be performed using a different digital filter per core, with the specific dispersive parameters of each one. In the case in which $L \ll L_{\mathrm{PhMD}}$ in homogeneous MCFs, the GVD compensation can also be performed by using the same digital filter for each core. Moreover, due to their low IC-XT levels, disordered MCFs exhibiting transverse Anderson localization [93] could also be proposed as a means to reduce the impact of the IMCD on some applications. In particular, disordered MCFs could be of extreme utility to improve the image quality in lensless endoscopy [92]. In Appendix D4, we also analyze in Figs. D4.3 and D4.4 the higher-order effects of the IMCD when including mode-coupling between orthogonal polarizations induced by the circular fiber birefringence. In both cases, we can observe a higher pulse distortion than in Fig. 4.5 when including the circular birefringence along with the PMD and the second-order PhMD.

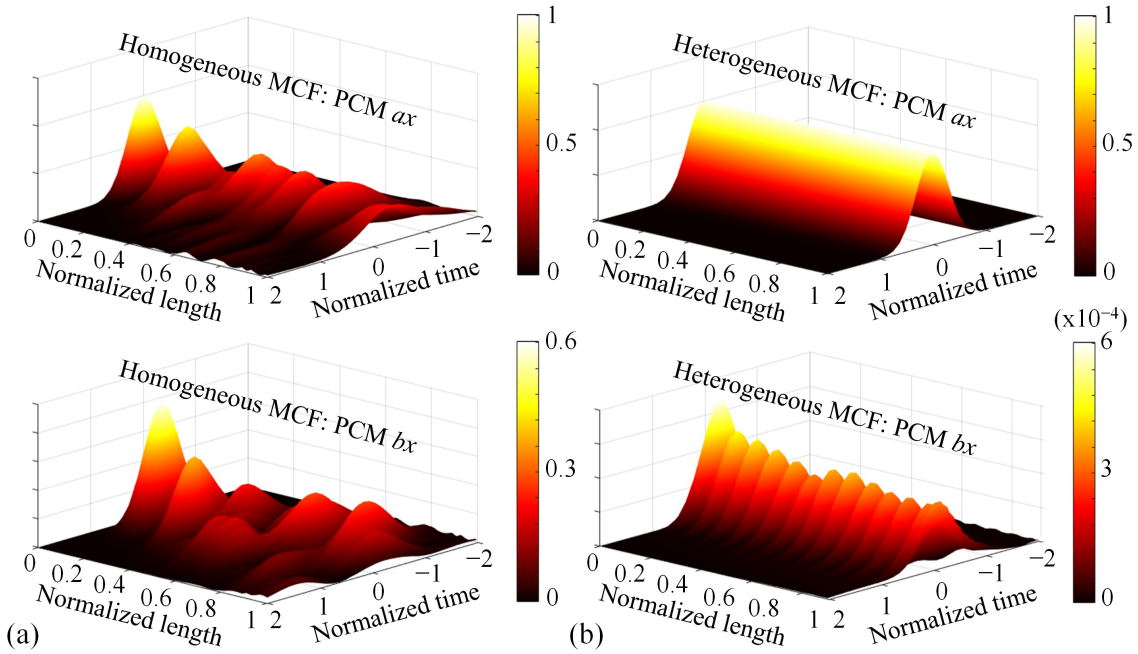

Figure 4.5. Higher-order IMCD in real homogeneous and heterogeneous MCFs. 200-fs Gaussian optical pulse propagated along a 40-m 2-core MCF in the PCMs ax and bx considering higher-order PhMD effects. (a) Homogeneous MCF. (b) Heterogeneous MCF with index difference $\Delta n = n_a - n_b = 0.002$. [Colorbar: normalized power] [116].

For completeness, the IMCD effects are also investigated in the nonlinear fiber regime along with the PMD (intra-core MCD). Remarkably, the impact of such perturbations on a bright soliton is analyzed. A 600-fs fundamental soliton ($\sim$ 350 fs full width at half maximum) was launched into the PCM ax of a dispersion-shifted homogeneous 2-core MCF with $n_a = n_b = 1.452$, $n_{\mathrm{cl}} = 1.444$, and usual first- and second-order GVD coefficients of $\beta^{(2)} = -1$ ps^2/km and $\beta^{(3)} = 0.1$ ps^3/km, respectively. The peak power (P_0) required to support the fundamental soliton is found to be 40.7 dBm considering a nonlinear refractive index of $n_{\mathrm{NL}} = 2.6 \cdot 10^{-20}$ m^2/W at 1550 nm. The fundamental soliton condition was numerically tested by omitting: the core b, the fiber birefringent effects, $\beta^{(3)}$, the self-steepening (induced by the frequency dependence of $\hat{\mathrm{q}}_{ax}^{(\mathrm{I})}$), and the intrapulse

Raman scattering inducing frequency shift in optical pulses shorter than 1 ps [Raman-induced frequency shift (RIFS) [139]].

Now, in order to simulate realistic MCF conditions, we include the core b, higher-order dispersive and nonlinear effects, and assume $\Delta\beta^{(1)}_{bx,ax} = 0.2$ ps/km and $\Delta\beta^{(2)}_{bx,ax} = 0.1$ ps^2/km induced by manufacturing imperfections (similar values for the y-polarization). In this case, we also include the intrinsic linear birefringence of the medium along with the linear and circular birefringence induced by the fiber bending and twisting conditions. We consider 50 birefringent segments along the MCF length, where the linear and circular birefringence fluctuate between adjacent segments. The circular birefringence is induced by a random twist rate f_{T} given by the Normal distribution $f_{\mathrm{T}} = \mathrm{N}(\mu = 0.1, \sigma^2 = 0.01)$ turns/m. The linear birefringence is induced by: (i) the random bending conditions with $R_{\mathrm{B}} = \mathrm{N}(\mu = 100, \sigma^2 = 40)$ cm, and (ii) the intrinsic linear birefringence of each core, fixed to $2 \cdot 10^{-7}$ in both cores a and b.

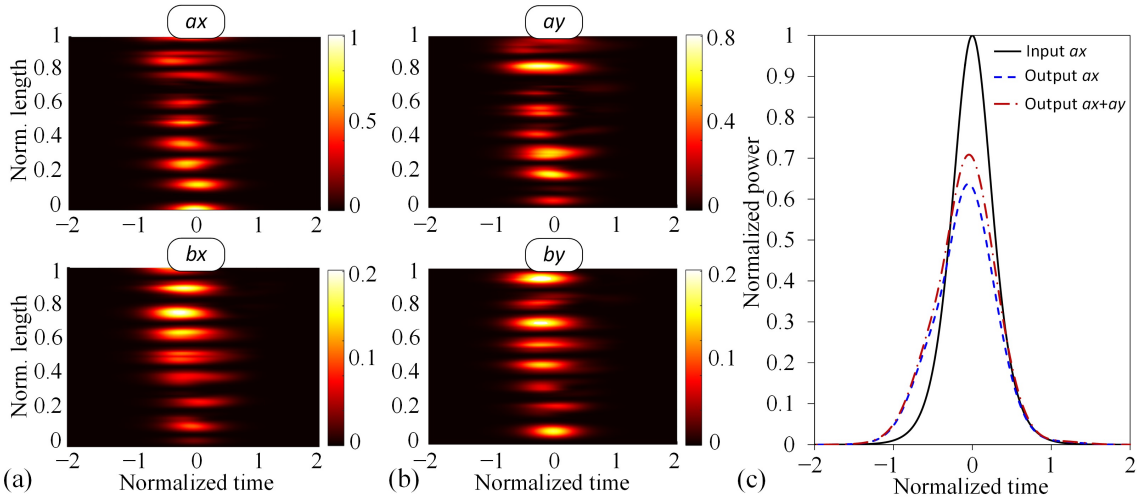

Figure 4.6. IMCD impact on optical solitons. (a) 600-fs fundamental soliton propagated along a 40-m 2-core dispersion-shifted homogeneous MCF in the PCMs ax, ay, bx, by considering first- and second-order IMCD effects. (b) Pulse shape comparison at the output of the core a. [Colorbar: normalized power] [116].

According to Fig. 4.6, we can observe that the soliton condition is broken along the MCF propagation. As discussed later, the second-order PhMD becomes one of the major physical impairments in coupled-core MCFs with a near-zero $\Delta\beta^{(2)}_{bx,ax}$ parameter. Thus, in the first propagation meters, the additional chirp induced by the second-order PhMD along with the first-order CCD increases the pulse width and reduces the peak power. As a result of the peak power reduction, the pulse width is increased along the MCF length and the soliton peak is shifted from its original position due to the first-order PhMD and the second-order GVD (induced by $\beta^{(3)}$). In this case, note that the effects of the RIFS and the self-steepening are difficult to observe with $T_{\mathrm{P}} = 600$ fs, $L = 40$ m, $\beta^{(2)} = -1$ ps^2/km and $P_0 \simeq 40$ dBm. Nevertheless, in optical pulses of few femtoseconds and in MCFs with a higher $\beta^{(2)}$ coefficient, the soliton distortion will be increased not only by the IMCD and the second-order GVD, but also by the RIFS and the self-steepening nonlinear effects.

So far, we have evaluated the longitudinal birefringent effects of the MCF, but omitting the temporal perturbations of the medium. However, as was indicated above, the IMCD can also fluctuate in time due to the temporal variation of the MCF birefringence modifying the value of the phase function $\phi_{mi}(z, \omega; t)$ in each PCM mi. Therefore, the random group delay induced by the first-order PhMD in each MCF segment may present a time-varying evolution.

To verify this statement, we perform a numerical simulation considering a time-varying intrinsic linear birefringence of the optical medium. Specifically, we simulate the homogeneous 2-core MCF of Fig. 4.5(a) but assuming a constant bending radius of $R_{\mathrm{B}} = 100$ cm and varying the intrinsic linear birefringence of each core over a 4-day period. The intrinsic linear birefringence was assumed to vary from day to day (BTC unit of 1 day, see page 67) following a normal distribution with

a different average value in each core, but with a similar temporal evolution, in line with the experimental work reported in Chapter 3 [see Fig. 4.7(a)]. Nonetheless, note that faster temporal changes of the linear birefringence can also be considered in each core. In any case, our previous discussion and the coupled local-mode equations are also found to be valid for faster time-varying birefringent conditions if these MCF fluctuations are approximately constant in time intervals of the order of T_{P}, as indicated above. Figure 4.7(b) shows the temporal dispersion of a 150 fs Gaussian optical pulse obtained each day at the MCF output for the PCM ax. As can be seen, the group delay and the pulse shape present random fluctuations in different days as a direct consequence of the temporal random group delay induced by the first-order PhMD and CCD in each MCF segment. From these results, it is clear that the time-varying effects of the IMCD should be taken into account to compensate for this physical impairment using DSP techniques in future SDM optical systems.

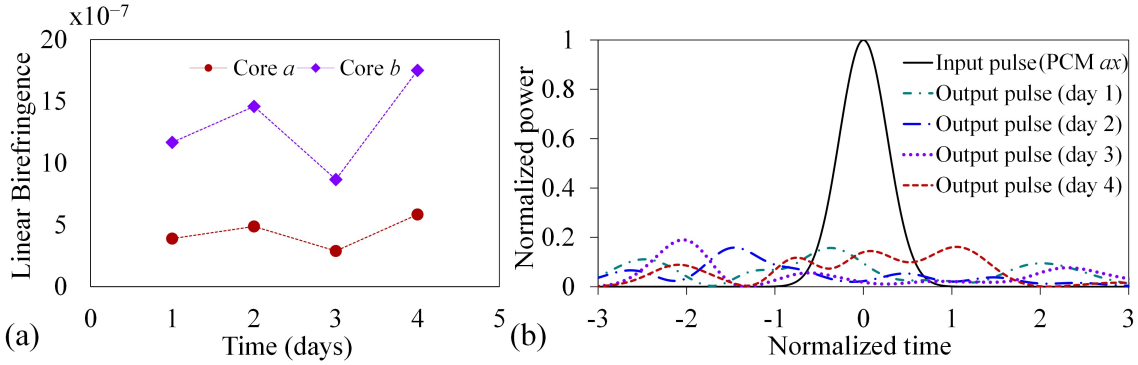

Figure 4.7. Time-varying IMCD. (a) Temporal evolution of the intrinsic linear birefringence assumed in cores a and b for the numerical calculations. (b) Corresponding optical pulse calculated in the PCM ax at the MCF output each simulated day [116].

Finally, once we know in general terms the effects of the IMCD in ultra-short optical pulses, we investigate the fiber length scales over which the dispersive effects of the IMCD should be considered in the pulse propagation phenomena when comparing this physical impairment with the first-order GVD. To this end, we compare the GVD, CCD and PhMD lengths considering an MCF without random perturbations, given by the expressions for the PCMs ax and bx (see page 141 for more details):

$$L_{\mathrm{GVD}} := T_{\mathrm{P}}^2 / \left|\beta_{ax}^{(2)}\right|; \quad L_{\mathrm{CCD}} := T_{\mathrm{P}} / \left(2\left|\tilde{\kappa}_{ax,bx}^{(1)}\right|\right); \quad L_{\mathrm{PhMD}} := T_{\mathrm{P}}^2 / \left|\Delta\beta_{bx,ax}^{(2)}\right|. \tag{4.4.1}$$

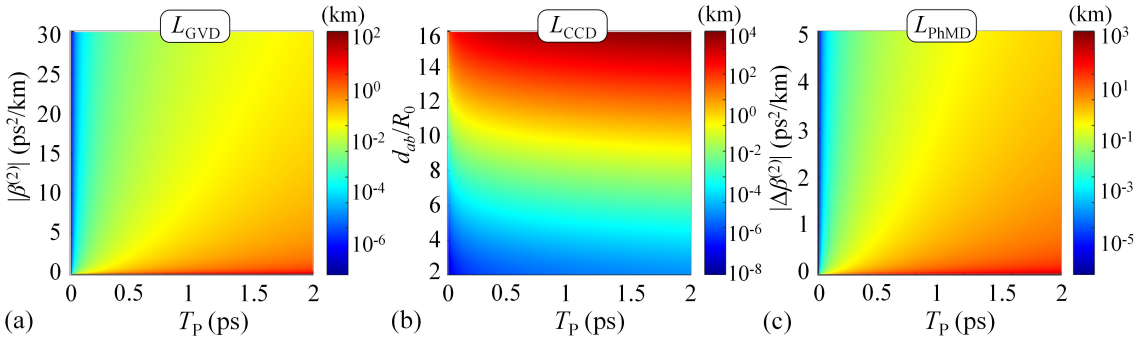

Figure 4.8. Dispersion length comparison. (a) Group-velocity dispersion (GVD) length, (b) coupling-coefficient dispersion (CCD) length, and (c) phase-mismatching dispersion (PhMD) length [116].

Figure 4.8 depicts the comparison of the GVD, CCD and PhMD dispersion lengths. As can be seen, the first-order GVD is expected to become the major physical impairment in MCFs where the mode-coupling effects are significantly reduced. This scenario should be considered in homogeneous uncoupled-core MCFs, i.e., with $\beta_{ax}^{(2)} \simeq \beta_{bx}^{(2)}$ and $d_{ab}/R_0 \geq 7$, or in heterogeneous MCFs with IC-XT levels lower than -30 dB [Fig. 4.5(b)]. Specific examples of these fibers can be found in [133, 189]. On the other hand, the IMCD becomes one of the major pulse distortion effects in MCFs operating in the strong-coupling regime ($d_{ab}/R_0 < 7$). In particular, femtosecond pulses propagating in coupled-core MCFs will be highly degraded by this optical impairment. In this scenario, the IMCD induced by the first-order CCD becomes the predominant impairment in coupled-core MCFs with homogeneous and lowly-dispersive cores, i.e., with $\beta_{ax}^{(2)} \simeq \beta_{bx}^{(2)} < 10$ ps^2/km. Nevertheless, the first-order GVD along with the IMCD induced by the second-order PhMD will be the predominant physical impairments in coupled-core MCFs with $\Delta\beta_{bx,ax}^{(2)} \neq 0$, especially when these fibers comprise homogeneous but non-identical cores with a near-zero $\Delta\beta_{bx,ax}^{(2)}$ parameter.

4.5 Conclusions

We have presented a general theory modeling the propagation of ultra-short optical pulses in real SM-MCFs perturbed by random longitudinal and temporal birefringent effects. The rigorous formalism here reported including the longitudinal and temporal fiber birefringent perturbations allows us to describe many interesting effects that could not be addressed with previous ultra-short pulse propagation models in the femtosecond regime [175–184]. Figure 4.9 shows a schematic comparison of our model with previous works.

As seen, these previous ultra-short pulse propagation models consider a single polarization, ideal cores and omit the fiber birefringent perturbations (see e.g. [175]). Therefore, these works can only describe the frequency dependence of the ideal mode-coupling coefficients, the CCD. Concretely, the first- and second-order CCD inducing pulse splitting and linear chirp were investigated from these models in the aforementioned references.

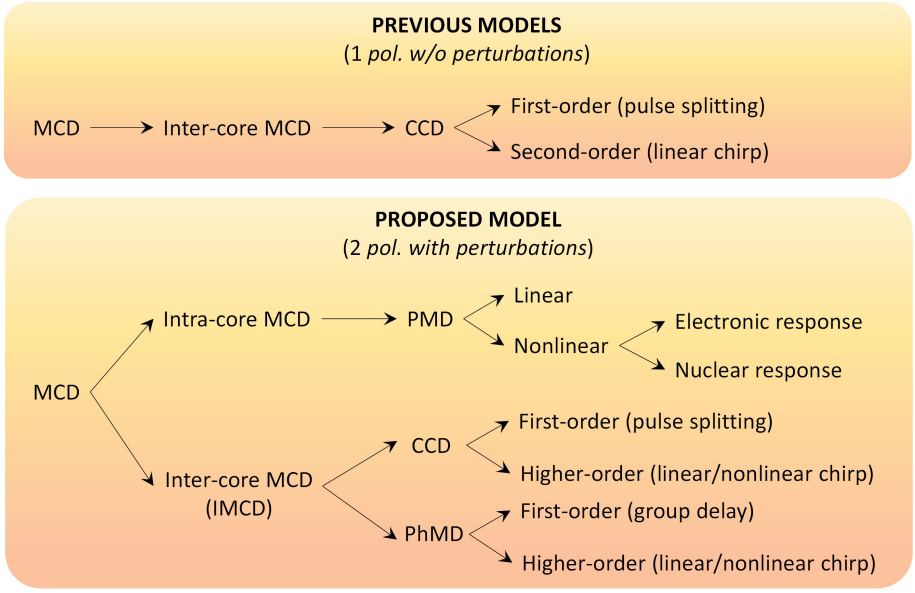

Figure 4.9. Schematic comparison of the MCD effects which can be analyzed with the proposed model and previous works [175–184] of femtosecond pulse propagation in MCFs. Considering a single polarization, ideal homogeneous cores and omitting the fiber perturbations, only the CCD can be modeled. However, including both orthogonal polarizations and the perturbations of the optical medium, the linear and nonlinear PMD along with the IMCD (CCD+PhMD) can be investigated [116].

Nevertheless, new dispersive effects induced by the mode-coupling among the fundamental core modes LP_{01} emerge when including two polarizations and the fiber perturbations in Maxwell's equations using the concept of local modes. Numerical calculations based on the developed theory reveal the existence of intermodal dispersion, referred to as the MCD in this work, induced by the random perturbations of the optical medium when operating in the linear and nonlinear fiber regimes. Specifically, in the femtosecond regime, the inter-core MCD (termed as IMCD) involves the frequency dependence of the mode overlapping and the phase-mismatching between the fiber local modes, dispersive effects referred to as the CCD and the PhMD, respectively. The CCD is completed in our model by including the fiber perturbations and higher-order dispersive effects inducing pulse splitting and nonlinear chirp. The PhMD, overlooked so far in previous models [175–184], emerges from: (*i*) the longitudinal and temporal fiber perturbations inducing a random group delay (first-order PhMD), and (*ii*) the intrinsic phase-mismatching between local modes inducing a deterministic group delay and a linear and nonlinear chirp (second- and higher-order PhMD). It is worth noting that the PhMD is analogous to the PMD observed in optical transmissions using SM-SCFs. Nonetheless, although the second-order PMD is difficult to observe in SM-SCF transmissions, the second-order PhMD is expected to become the predominant physical impairment (along with the first-order GVD) in coupled-core MCFs comprising homogeneous but non-identical cores with a near-zero $\Delta\beta^{(2)}_{bx,ax}$ parameter [see Fig. 4.5(a) and Fig. 4.8(c)]. In contrast, the CCD will be the predominant IMCD effect in coupled-core MCFs with low dispersive homogeneous cores [see Fig. 4.8(b)].

The potential implications of these effects evidenced by our model should be considered in the future to enhance the performance of MCFs for communication applications and to improve our understanding and control over MCF-based experimental physics. As an important example, the core-to-core distance of the MCFs employed in optical networks is being progressively reduced to increase the number of cores in a single cladding [8]. A reduced core-to-core distance will increase the IMCD and the pulse distortion, as discussed in Fig. 4.8. In this scenario, our results show that the increment of the MCF perturbations (increasing the average value of the linear birefringence via the photo-elastic effect and mismatching the phase constant of the local modes) is an effective birefringence management strategy to reduce the impact of the IMCD on the MCF. Remarkably, our results also indicate that the second-order PhMD induces a significant higher pulse distortion in real homogeneous MCFs (with similar but not identical dispersive parameters) than in heterogeneous MCFs, in spite of the fact that this kind of fibers exhibit a higher value of $\Delta\beta^{(2)}$ between adjacent cores. As a result, in heterogeneous MCFs, the digital compensation of the GVD in femtosecond optical pulses can be performed at the DSP using the same digital filter for each core when short propagation distances are involved ($L \leq L_{\mathrm{PhMD}}$).

Furthermore, note that in contrast with previous SCF and MCF models [153–156,175–186], our theory also includes the nonlinear PMD and the nonlinear IMCD that arises from the isotropic and anisotropic response of the nonlinear polarization considering both electronic and nuclei motion. In particular, our results show that the linear and nonlinear IMCD induced by the external fiber perturbations and manufacturing imperfections should also be taken into account when propagating femtosecond optical solitons in MCFs. More specifically, the random distortion and the pulse chirping emerging from the first- and second-order IMCD break the soliton condition along the MCF propagation (see Fig. 4.6). Hence, the proposed model allows us to investigate the impact of the linear and nonlinear birefringence induced by the fiber perturbations and higher-order nonlinear effects on optical solitons, rogue waves, and breathers [109].

The CLMT can be applied to design MCFs comprising cores of different manufacturing characteristics: homogeneous, heterogeneous, coupled, uncoupled, lowly- or highly-birefringent, trench- or hole-assisted, step- or gradual-index. Therefore, this general theory allows us to implement novel MCF designs operating in the single-mode regime with specific IMCD characteristics, which open new paths to explore in dispersion engineering and pulse shaping applications. However, additional nonlinear terms involving cross-coupling effects among the PCMs of different cores should be included for coupled-core MCFs with a core-to-core distance lower than three times the core radius, as discussed in Subsection 4.2.3. Nevertheless, in such a case, the accuracy of

this model (based on perturbation theory) may be reduced if the supermodes of the MCF do not meet the approximation performed in Eq. (4.2.1) when assuming that $\boldsymbol{\mathcal{E}} \simeq \sum_{mi} \mathcal{E}_{mi}\hat{u}_i$. Moreover, although the computational time of the coupled local-mode equations may increase considerably when large MCF distances are involved, it may be reduced by inserting phase plates [155, 167] between birefringent segments (see Appendix C4, on page 132 for more details).

Despite the fact that we have focused our analysis on the single-mode regime of the fiber, note that the extension of the CLMT to the multi-mode regime is straightforward when including additional LP mode groups in the global electric field of the MCF. In Appendix E4, on page 142, we discuss in detail the multi-mode regime. In such a scenario, it should be noted that Eqs. (4.3.15) and (4.3.16) can also be employed to analyze the impact of the intermodal dispersion between higher-order LP modes of the same core or different cores by calculating the appropriate value of the corresponding MCCs and phase-mismatching functions.

On the other hand, the CLMT can also be used to model the propagation of optical pulses in temporal waveguides (see Chapter 8, Appendix D8, page 290) and in dielectric planar spatial waveguides operating under the weakly-guiding approximation. In this last scenario, the CLMT could be of great utility in integrated photonics to analyze the pulse dispersion induced by the waveguide perturbations which may appear when the waveguide is integrated in ultra-compact optical devices.

Finally, it is worth mentioning that our model may also play an essential role in other branches of physics. As mentioned in the introduction, SCFs have been investigated as an experimental platform for testing diverse physical phenomena from various fields, including quantum mechanics, general relativity or condensed matter physics, among others, based on analogies of the fiber-optical nonlinear Schrödinger equation [102–109]. In a similar way, the CLMT can be employed to elucidate the underlying wave propagation phenomena of any physical system with propagating equations of the form of the coupled nonlinear Schrödinger equations, i.e., our coupled local-mode equations when higher-order coupling, dispersive and nonlinear effects are omitted. Hence, exotic physical phenomena such as superposed nonlinear waves in coherently coupled Bose-Einstein condensates [114], interacting rogue waves [111] or nonlinear ion-acoustic waves [190, 191] can be explored in MCF media expanding the possibilities of SCFs. In the same line, additional physical phenomena such as relativistic effects could also be analyzed using MCF media. Note that an optical pulse propagating through an SCF establishes a moving medium which corresponds to a space-time geometry. This gravitational approach was employed by Philbin and coworkers in [105] to demonstrate a fiber-optical analogy of the event horizon in a black hole using an ultra-short optical pulse of 70 fs. Therefore, additional gravitational phenomena could be investigated in MCFs when adjacent cores perturb the virtual space-time geometry created by a femtosecond optical pulse propagating in a given core of the fiber.

Appendix A4: Multiple optical carriers

The coupled local-mode equations developed in this chapter were derived from Maxwell's equations by assuming a single optical carrier taking into account that the XPM and FWM can be neglected for optical pulses shorter than 50 ps [11,192]. In this appendix, we lift this important limitation of our model by considering optical pulses wider than 50 ps. Our results could be of great interest to simulate the propagation of optical pulses in future transport networks using MCFs (Chapter 5).

For the sake of clarity, we start following a similar approach as in Section 4.2. We assume an N-core weakly-guiding MCF with both transversal components $i \in \{x, y\}$ in the LP_{01} mode of each core $m \in \{1, \ldots, N\}$ and Q optical carriers with angular frequency $\omega_q \in \{\omega_1, \ldots, \omega_Q\}$. Thus, approximating the global electric field strength of the MCF ($\boldsymbol{\mathcal{E}}$) as a linear combination of the electric field strength of each PCM mi ($\mathcal{E}_{mi}$) considering isolated cores, and decoupling the rapidly- and the slowly-varying temporal and longitudinal changes of $\mathcal{E}_{mi}$ by using respectively the slowly-varying amplitude (E_{mni,ω_q}) and envelope ($\widetilde{A}_{mi,\omega_q}$) functions, we can write in the *first* step of perturbation theory:

$$\boldsymbol{\mathcal{E}}(\boldsymbol{r},t) \simeq \sum_{m=1}^{N}\sum_{i=x,y} \mathcal{E}_{mi}(\boldsymbol{r},t)\,\hat{u}_i \simeq \sum_{m=1}^{N}\sum_{i=x,y}\sum_{q=1}^{Q} \mathrm{Re}\left\{E_{mi,\omega_q}(\boldsymbol{r},t)\exp(j\omega_q t)\right\}\hat{u}_i; \tag{A4.1}$$

$$\begin{aligned} E_{mi,\omega_q}(\boldsymbol{r},t) = \frac{1}{2\pi}\int_{\mathfrak{B}_{\tilde{A}}} \widetilde{A}_{mi,\omega_q}(z,\omega-\omega_q;t)\,F_{mi}(x,y,\omega;z,t)\times \\ \times\exp\left(-j\phi_{mi}(z,\omega_q;t)-\frac{1}{2}\alpha(\omega)z\right)\exp(j(\omega-\omega_q)t)\,\mathrm{d}\omega. \end{aligned} \tag{A4.2}$$

The description of each function included in the above equations is detailed in Subsection 4.2.1. Considering optical pulses wider than 50 ps, we can safely assume that $\alpha(\omega) \simeq \alpha(\omega_q)$ and $F_{mi}(x,y,\omega;z,t) \simeq F_{mi}(x,y,\omega_q;z,t)$ due to the reduced pulse bandwidth. Therefore, we can approximate the complex amplitude E_{i,ω_q} of the global electric field strength $\boldsymbol{\mathcal{E}}$ at the q-th optical carrier as follows:

$$\begin{aligned} E_{i,\omega_q}(\boldsymbol{r},t) &\simeq \sum_{m=1}^{N} E_{mi,\omega_q}(\boldsymbol{r},t) \\ &\simeq \sum_{m=1}^{N} A_{mi,\omega_q}(z,t)\,F_{mi}(x,y,\omega_q;z,t)\exp\left(-j\phi_{mi}(z,\omega_q;t)-\frac{1}{2}\alpha(\omega_q)z\right) \\ &\equiv \sum_{m=1}^{N} A_{mi,\omega_q}F_{mi,\omega_q}\exp\left(-j\phi_{mi,\omega_q}-\frac{1}{2}\alpha_{\omega_q}z\right), \end{aligned} \tag{A4.3}$$

using the subindex ω_q to indicate the explicit dependence of the functions F_{mi}, ϕ_{mi} and α with the angular frequency of the q-th optical carrier.

The *second* step of perturbation theory is the same as in the single-carrier case [see Eq. (4.2.11)]. Nonetheless, in the *third* step, we will find the main difference with the single-carrier case given that we must include the XPM and FWM by calculating the linear ($\boldsymbol{\mathcal{P}}^{(1)}$) and nonlinear polarizations ($\boldsymbol{\mathcal{P}}^{(3)}$) to derive the wave equation of the MCF. In this scenario, $\boldsymbol{\mathcal{P}}^{(1)}$ and $\boldsymbol{\mathcal{P}}^{(3)}$ can be written as follows ($k \in \{1,3\}$):[19]

$$\boldsymbol{\mathcal{P}}^{(k)}(\boldsymbol{r},t) \simeq \sum_{i=x,y} \mathcal{P}_i^{(k)}(\boldsymbol{r},t)\,\hat{u}_i \simeq \sum_{i=x,y}\sum_{q=1}^{C^{(k)}} \mathrm{Re}\left\{P_{i,\omega_q}^{(k)}(\boldsymbol{r},t)\exp(j\omega_q t)\right\}\hat{u}_i, \tag{A4.4}$$

where $C^{(k)}$ indicates the total number of optical carriers observed in the linear ($k = 1$) and nonlinear ($k = 3$) regimes. In the linear regime, $C^{(1)} = Q$. However, in the nonlinear regime, we

[19]The first approximation in Eq. (A4.4) omits $\mathcal{P}_z^{(k)}$ due to the weakly-guiding conditions.

should take into account the optical carriers generated by the FWM. Specifically, we know that $C^{(3)} = Q + \frac{1}{2}\left(Q^3 - Q^2\right)$ when considering the degenerate and non-degenerate FWM cases [192]. Along this line, the complex amplitude $P^{(3)}_{i,\omega_q}$ can be derived from the constitutive relation $\mathcal{P}$-$\mathcal{E}$ by omitting the Raman effect ($\mathcal{P}_i^{(3\mathrm{R})}$) due to the large temporal width of the optical pulses:

$$\mathcal{P}_i^{(3)}(\boldsymbol{r},t) = \mathcal{P}_i^{(3\mathrm{I})}(\boldsymbol{r},t) + \underbrace{\mathcal{P}_i^{(3\mathrm{R})}(\boldsymbol{r},t)}_{\simeq 0} \simeq \varepsilon_0 \chi^{(3\mathrm{I})}_{ijkl} \mathcal{E}_j(\boldsymbol{r},t)\,\mathcal{E}_k(\boldsymbol{r},t)\,\mathcal{E}_l(\boldsymbol{r},t)\,. \tag{A4.5}$$

Hence:

$$\begin{aligned}\mathcal{P}_i^{(3)}(\boldsymbol{r},t) &= \frac{1}{8}\varepsilon_0\chi^{(3\mathrm{I})}_{ijkl}\left[\sum_{n=1}^{Q} E_{j,\omega_n}(\boldsymbol{r},t)\exp(j\omega_n t) + \text{c.c.}\right]\left[\sum_{s=1}^{Q} E_{k,\omega_s}(\boldsymbol{r},t)\exp(j\omega_s t) + \text{c.c.}\right]\times \\ &\quad\times\left[\sum_{p=1}^{Q} E_{l,\omega_p}(\boldsymbol{r},t)\exp(j\omega_p t) + \text{c.c.}\right] \\ &\equiv \frac{1}{8}\varepsilon_0\chi^{(3\mathrm{I})}_{ijkl}\sum_{n,s,p=1}^{Q} E_{j,\pm\omega_n}E_{k,\pm\omega_s}E_{l,\pm\omega_p}\exp\left[j\left(\pm\omega_n\pm\omega_s\pm\omega_p\right)t\right],\end{aligned} \tag{A4.6}$$

where c.c. is the complex conjugate term and we have omitted the independent variables in the last line for simplicity. In particular, there are $8Q^3$ terms in the above equation. Replacing Eq. (A4.3) into Eq. (A4.6) and omitting the MCF perturbations at this point for the sake of clarity, we find that the nonlinear interaction is governed by the following phase condition in each PCM mi:

$$\beta_{mi}\left(\pm\omega_n\pm\omega_s\pm\omega_p\right) = \beta_{mj}\left(\pm\omega_n\right) + \beta_{mk}\left(\pm\omega_s\right) + \beta_{ml}\left(\pm\omega_p\right) - \Delta k_{mi}\left(\pm\omega_n\pm\omega_s\pm\omega_p\right), \tag{A4.7}$$

where Δk_{mi} accounts for the phase-mismatching between $P^{(3)}_{mi,\pm\omega_n\pm\omega_s\pm\omega_p}$ and the new electric field $E_{mi,\pm\omega_n\pm\omega_s\pm\omega_p}$ that is generated from this nonlinear wave-mixing. As is well known in nonlinear optics [150], in an interaction of the form given by Eq. (A4.6), the nonlinear terms which involve a high value of Δk_{mi} can be neglected. In silica fibers, this leads to retain only the terms with angular frequencies:

$$\begin{bmatrix} \omega_n+\omega_s-\omega_p \\ \omega_n-\omega_s+\omega_p \\ -\omega_n+\omega_s+\omega_p \end{bmatrix} + [\text{c.c.}]\,. \tag{A4.8}$$

As a result, Eq. (A4.6) can be reduced to:

$$\begin{aligned}\mathcal{P}_i^{(3)} &= \frac{1}{8}\varepsilon_0\sum_{n,s,p=1}^{Q}\left\{\begin{array}{l}\chi^{(3\mathrm{I})}_{ijkl}\left(-\omega_q;\omega_n,\omega_s,-\omega_p\right)E_{j,\omega_n}E_{k,\omega_s}E_{l,-\omega_p}\exp\left[j\left(\omega_n+\omega_s-\omega_p\right)t\right] \\ +\chi^{(3\mathrm{I})}_{ijkl}\left(-\omega_q;\omega_n,-\omega_s,\omega_p\right)E_{j,\omega_n}E_{k,-\omega_s}E_{l,\omega_p}\exp\left[j\left(\omega_n-\omega_s+\omega_p\right)t\right] \\ +\chi^{(3\mathrm{I})}_{ijkl}\left(-\omega_q;-\omega_n,\omega_s,\omega_p\right)E_{j,-\omega_n}E_{k,\omega_s}E_{l,\omega_p}\exp\left[j\left(-\omega_n+\omega_s+\omega_p\right)t\right] + \text{c.c.}\end{array}\right\} \\ &= \frac{3}{8}\varepsilon_0\sum_{n,s,p=1}^{Q}\chi^{(3\mathrm{I})}_{ijkl}\left(-\omega_q;\omega_n,\omega_s,-\omega_p\right)E_{j,\omega_n}E_{k,\omega_s}E_{l,-\omega_p}\exp\left[j\left(\omega_n+\omega_s-\omega_p\right)t\right] + \text{c.c.}\end{aligned} \tag{A4.9}$$

where $\omega_q = \omega_n + \omega_s - \omega_p$ and $q \in \left\{1,\ldots,C^{(3)}\right\}$. In Eq. (A4.9), we have performed the following two steps: (i) we have employed the intrinsic permutation symmetry of $\chi^{(3\mathrm{I})}_{ijkl}$; and (ii) we have performed the relabeling of the dummy indexes $k \leftrightarrow l$ and $s \leftrightarrow p$ in the second term, and $j \leftrightarrow l$ and $n \leftrightarrow p$ in the third term. Consequently, we find that $P^{(3)}_{i,\omega_q}$ must obey the relation:[20]

$$P^{(3)}_{i,\omega_q} = \frac{3}{4}\varepsilon_0\sum_{n,s,p}^{R_q}\chi^{(3\mathrm{I})}_{ijkl}\left(-\omega_q;\omega_n,\omega_s,-\omega_p\right)E_{j,\omega_n}E_{k,\omega_s}E_{l,-\omega_p}, \tag{A4.10}$$

[20]Here, we cannot write the summation starting from $n = s = p = 1$ if $q \neq 1$. For this reason, we omit the initial value of the indexes n, s, p.

with R_q indicating the number of nonlinear interactions of the form $\omega_q = \omega_n + \omega_s - \omega_p$ when varying $(n, s, p) \in \{1, \ldots, Q\}^3$. In general, the variable R_q is unknown since it depends on the specific value of the optical carriers employed in the MCF transmission.

Finally, in the *fourth* step of perturbation theory, we will be able to derive the sought coupled local-mode equations. Inserting Eq. (A4.3) into the corresponding coupled-wave equations, using Eq. (A4.10) and applying the SVEA, we find an equation for the x-polarization axis in the time domain of the form:[21]

$$\begin{aligned}\sum_{m=1}^{N}\Big[k_q^2\left(\varepsilon_{\mathrm{r},x,\omega_q}-\varepsilon_{\mathrm{r},mx,\omega_q}\right)-\left(j2\beta_{mx,\omega_q}^{(\mathrm{eq})}+\alpha_{\omega_q}\right)\widehat{\mathrm{D}}_{mxq}^{(\mathrm{eq})}\Big]F_{mx,\omega_q}\exp\left(-j\phi_{mx,\omega_q}\right)A_{mx,\omega_q}\\ -\left(j2\beta_{mx,\omega_q}^{(\mathrm{eq})}+\alpha_{\omega_q}\right)F_{mx,\omega_q}\exp\left(-j\phi_{mx,\omega_q}\right)\partial_z A_{mx,\omega_q}+k_q^2\sigma_{\omega_q}F_{my,\omega_q}\exp\left(-j\phi_{my,\omega_q}\right)A_{my,\omega_q}\\ +k_q^2\gamma_{\mathrm{I},\omega_q}\exp\left(-\alpha_{\omega_q}z\right)\mathcal{N}_{x,\omega_q}=0,\end{aligned} \tag{A4.11}$$

with $k_q = \omega_q/c_0$, $\widehat{\mathrm{D}}_{mxq}^{(\mathrm{eq})}$ the linear operator defined as:[22]

$$\widehat{\mathrm{D}}_{mxq}^{(\mathrm{eq})}(z;t) := \sum_{n=1}^{2}\frac{(-j)^{n-1}}{n!}\beta_{mx,\omega_q}^{(\mathrm{eq})(n)}\partial_t^n, \tag{A4.12}$$

$\beta_{mx,\omega_q}^{(\mathrm{eq})(n)}(z;t) := \partial_\omega^n\beta_{mx}^{(\mathrm{eq})}(z,\omega=\omega_q;t)$, $\gamma_{\mathrm{I},\omega_q} := \gamma_{\mathrm{I}}(\omega_q)$, and $\mathcal{N}_{x,\omega_q}$ accounting for the nonlinear terms. Omitting the nonlinear cross-coupling terms among cores by considering a core-to-core distance between two given cores a and b satisfying the condition $d_{ab} > R_{0,a}+R_{0,b}+\max\{R_{0,a},R_{0,b}\}$, where $R_{0,a(b)}$ is the radius of the core $a(b)$, we find that:

$$\begin{aligned}\mathcal{N}_{x,\omega_q}(z,t) = &\sum_{m=1}^{N}\sum_{n,s,p}^{R_q}A_{mx,\omega_n}A_{mx,\omega_s}A_{mx,\omega_p}^{*}F_{mx,\omega_n}F_{mx,\omega_s}F_{mx,\omega_p}\exp\left(-j\left(\phi_{mx,\omega_n}+\phi_{mx,\omega_s}-\phi_{mx,\omega_p}\right)\right)\\ &+\frac{1}{3}A_{mx,\omega_n}A_{my,\omega_s}A_{my,\omega_p}^{*}F_{mx,\omega_n}F_{my,\omega_s}F_{my,\omega_p}\exp\left(-j\left(\phi_{mx,\omega_n}+\phi_{my,\omega_s}-\phi_{my,\omega_p}\right)\right)\\ &+\frac{1}{3}A_{my,\omega_n}A_{mx,\omega_s}A_{my,\omega_p}^{*}F_{my,\omega_n}F_{mx,\omega_s}F_{my,\omega_p}\exp\left(-j\left(\phi_{my,\omega_n}+\phi_{mx,\omega_s}-\phi_{my,\omega_p}\right)\right)\\ &+\frac{1}{3}A_{my,\omega_n}A_{my,\omega_s}A_{mx,\omega_p}^{*}F_{my,\omega_n}F_{my,\omega_s}F_{mx,\omega_p}\exp\left(-j\left(\phi_{my,\omega_n}+\phi_{my,\omega_s}-\phi_{mx,\omega_p}\right)\right).\end{aligned} \tag{A4.13}$$

Exchanging the dummy indexes $n \leftrightarrow s$ in the third line and $n \leftrightarrow p$ in the fourth line,[23] Eq. (A4.13) is reduced to:

$$\begin{aligned}\mathcal{N}_{x,\omega_q}(z,t) = &\sum_{m=1}^{N}\sum_{n,s,p}^{R_q}A_{mx,\omega_n}A_{mx,\omega_s}A_{mx,\omega_p}^{*}F_{mx,\omega_n}F_{mx,\omega_s}F_{mx,\omega_p}\exp\left(-j\left(\phi_{mx,\omega_n}+\phi_{mx,\omega_s}-\phi_{mx,\omega_p}\right)\right)\\ &+\frac{2}{3}A_{mx,\omega_n}A_{my,\omega_s}A_{my,\omega_p}^{*}F_{mx,\omega_n}F_{my,\omega_s}F_{my,\omega_p}\exp\left(-j\left(\phi_{mx,\omega_n}+\phi_{my,\omega_s}-\phi_{my,\omega_p}\right)\right)\\ &+\frac{1}{3}A_{my,\omega_p}A_{my,\omega_s}A_{mx,\omega_n}^{*}F_{my,\omega_p}F_{my,\omega_s}F_{mx,\omega_n}\exp\left(-j\left(\phi_{my,\omega_p}+\phi_{my,\omega_s}-\phi_{mx,\omega_n}\right)\right).\end{aligned} \tag{A4.14}$$

[21] In Eq. (A4.11), we have omitted a linear operator of the form:

$$\widehat{\mathrm{Z}}_{mxq}^{(\mathrm{eq})}(z;t) := \sum_{n=1}^{2}\frac{(-j)^{n-1}}{n!}\partial_z\beta_{mx,\omega_q}^{(\mathrm{eq})(n)}(z;t)\,\partial_t^n,$$

because it would appear in the LHS of Eq. (A4.15) multiplied by the term $1/\left(2\beta_{ax,\omega_q}^{(\mathrm{eq})}\right) \simeq 0$.

[22] We use a second-order Taylor series expansion of $\beta_{mx}^{(\mathrm{eq})}$ around $\omega = \omega_q$ due to the reduced pulse bandwidth.

[23] Actually, we perform a double relabeling. For instance, the step $n \leftrightarrow s$ involves the relabeling $n \to s$ and $s \to n$.

Now, redefining $\alpha_{\omega_q} \equiv \alpha_q$, $A_{mi,\omega_q} \equiv \mathcal{A}_{miq} \exp(\alpha_q z/2)$, and $\phi_{mi,\omega_q} \equiv \phi_{miq}$; we obtain from Eq. (A4.11) the following coupled local-mode equation for the PCM ax in the q-th optical carrier:

$$\begin{aligned} j\left(\partial_z + \widehat{\mathrm{D}}^{(\mathrm{eq})}_{axq} + \frac{\alpha_q}{2}\right)\mathcal{A}_{axq} = {} & m_{axq,ayq} \exp\left(-j\Delta\phi_{ayq,axq}\right)\mathcal{A}_{ayq} \\ & + \sum_{m\neq a}^{N} \kappa_{axq,mxq} \exp\left(-j\Delta\phi_{mxq,axq}\right)\mathcal{A}_{mxq} \\ & + \sum_{n,s,p}^{R_q} q_{axq,nsp}\mathcal{A}_{axn}\mathcal{A}_{axs}\mathcal{A}^{*}_{axp} \exp\left(-j\left(\phi_{axn}+\phi_{axs}-\phi_{axp}-\phi_{axq}\right)\right) \\ & + \frac{2}{3} g_{axq,nsp}\mathcal{A}_{axn}\mathcal{A}_{ays}\mathcal{A}^{*}_{ayp} \exp\left(-j\left(\phi_{axn}+\phi_{ays}-\phi_{ayp}-\phi_{axq}\right)\right) \\ & + \frac{1}{3} g_{axq,nsp}\mathcal{A}_{ayp}\mathcal{A}_{ays}\mathcal{A}^{*}_{axn} \exp\left(-j\left(\phi_{ayp}+\phi_{ays}-\phi_{axn}-\phi_{axq}\right)\right), \end{aligned} \tag{A4.15}$$

where $\Delta\phi_{ayq,axq} := \phi_{ayq} - \phi_{axq}$, $\Delta\phi_{mxq,axq} := \phi_{mxq} - \phi_{axq}$, and the MCCs are defined as:

$$m_{axq,ayq}(z,\omega_q;t) := \frac{k_q^2}{2\beta^{(\mathrm{eq})}_{ax,\omega_q} N_{axq}} \iint \sigma_{\omega_q} F_{ay,\omega_q} F_{ax,\omega_q} \mathrm{d}x\mathrm{d}y; \tag{A4.16}$$

$$\kappa_{axq,mxq}(z,\omega_q;t) := \frac{k_q^2}{2\beta^{(\mathrm{eq})}_{ax,\omega_q} N_{axq}} \iint \Delta\varepsilon_{\mathrm{r},ax,\omega_q} F_{bx,\omega_q} F_{ax,\omega_q} \mathrm{d}x\mathrm{d}y; \tag{A4.17}$$

$$q_{axq,nsp}(z,\omega_q;t) := \frac{k_q^2}{2\beta^{(\mathrm{eq})}_{ax,\omega_q} N_{axq}} \iint \gamma_{\mathrm{I},\omega_q} F_{ax,\omega_n} F_{ax,\omega_s} F_{ax,\omega_p} F_{ax,\omega_q} \mathrm{d}x\mathrm{d}y; \tag{A4.18}$$

$$g_{axq,nsp}(z,\omega_q;t) := \frac{k_q^2}{2\beta^{(\mathrm{eq})}_{ax,\omega_q} N_{axq}} \iint \gamma_{\mathrm{I},\omega_q} F_{ax,\omega_n} F_{ay,\omega_s} F_{ay,\omega_p} F_{ax,\omega_q} \mathrm{d}x\mathrm{d}y, \tag{A4.19}$$

with $N_{axq}(z,\omega_q;t) := \iint F^2_{ax,\omega_q} \mathrm{d}x\mathrm{d}y$. In this case, the CLMT is completed by $2N \times C^{(3)} - 1$ additional coupled equations for the PCMs $mis \neq axq$, which can be obtained just by exchanging the corresponding subindexes in Eq. (A4.15) and in the MCCs.

Appendix B4: Slowly-varying envelope approximation

In this appendix, we will discuss in more detail the approximation $\partial_z^2\mathcal{A} \simeq 0$ usually assumed in the literature to describe the propagation of optical pulses [139, 149, 150, 159]. To this end, let us first discuss the own concept of the slowly-varying envelope approximation (SVEA).

The most extended approach to describe the propagation of an optical pulse in a dielectric medium is based on using a *heuristic* modification of an exact solution of Maxwell's equations in the monochromatic regime. The exact solution will be referred to as the fundamental wave. Specifically, this approach considers an optical pulse, that is a quasi-monochromatic wave, as a *slowly-varying longitudinal and temporal modulation* of the envelope of the fundamental wave. This slow modulation of the envelope is mathematically described by using the SVEA.

As a basic example, let us consider a plane wave as the fundamental wave of a linear, isotropic, homogeneous, time-invariant, and non-dispersive dielectric medium. Moreover, we will also assume that the plane wave is propagated in the $+\hat{u}_z$ direction. In such a scenario, the real representation of the electric field strength can be written of the form $\boldsymbol{\mathcal{E}}(z,t) = \mathrm{Re}\{\mathcal{A}\exp(j(\omega_0 t - kz))\}\hat{u}_x$, where $\mathcal{A}$ is a complex constant, $k = 2\pi/\lambda = n\omega_0/c_0$, and n is the refractive index of the optical medium at $\omega = \omega_0$. From the above fundamental wave, an optical pulse can be modeled as a *pulsed plane wave* with an electric field strength of the form:

$$\boldsymbol{\mathcal{E}}(z,t) = \mathrm{Re}\{\mathcal{A}(z,t)\exp(j(\omega_0 t - kz))\}\hat{u}_x, \tag{B4.1}$$

where now $\mathcal{A}$ is a function named the *complex envelope* which describes the slowly-varying longitudinal and temporal variations of the optical pulse. By replacing the above ansatz in the wave equation $\left(\triangle - \left(n^2/c_0^2\right)\partial_t^2\right)\boldsymbol{\mathcal{E}}(z,t) = \mathbf{0}$, it is straightforward to verify that Eq. (B4.1) is an exact solution of Maxwell's equations *if and only if* the complex envelope obeys the following relation:

$$\partial_z^2\mathcal{A} - j2k\partial_z\mathcal{A} - k^2\mathcal{A} = \frac{n^2}{c_0^2}\left(\partial_t^2\mathcal{A} + j2\omega_0\partial_t\mathcal{A} - \omega_0^2\mathcal{A}\right). \tag{B4.2}$$

Equation (B4.2) indicates that not all the functions $\mathcal{A}$ can be exact solutions of Maxwell's equations. However, the heuristic proposal given by Eq. (B4.1) will be able to describe *approximately* an exact non-monochromatic solution of Maxwell's equations (i.e. the optical pulse) if we assume that the complex envelope is a slowly-varying function in space and time in comparison with the wavelength and the period of the optical carrier. Mathematically, the above condition can be rigorously expressed as $\delta_z\mathcal{A} \ll |\mathcal{A}|$ in $\delta z \sim \lambda$ and $\delta_t\mathcal{A} \ll |\mathcal{A}|$ in $\delta t \sim T_0 = 2\pi/\omega_0$, where $\delta_z\mathcal{A} := |\mathcal{A}(z,t) - \mathcal{A}(z+\delta z,t)|$ and $\delta_t\mathcal{A} := |\mathcal{A}(z,t) - \mathcal{A}(z,t+\delta t)|$. From the above statement, we find the order criteria of the SVEA:

$$\left|\partial_z^2\mathcal{A}\right| \ll k\left|\partial_z\mathcal{A}\right| \ll k^2\left|\mathcal{A}\right|; \quad \left|\partial_t^2\mathcal{A}\right| \ll \omega_0\left|\partial_t\mathcal{A}\right| \ll \omega_0^2\left|\mathcal{A}\right|, \tag{B4.3}$$

which is in line with our Eq. (1.5.10) in Chapter 1. As a result, we can omit the terms $\partial_z^2\mathcal{A}$, $2k\partial_z\mathcal{A}$, $\partial_t^2\mathcal{A}$ and $2\omega_0\partial_t\mathcal{A}$ in Eq. (B4.2) obtaining the identity $k^2\mathcal{A} = (n^2/c_0^2)\omega_0^2\mathcal{A}$, which is always satisfied for any function $\mathcal{A} \in \mathcal{F}\left(\mathbb{R}^2, \mathbb{C}\right)$.

Remarkably, Eq. (B4.3) is the *true* approximation proposed by the SVEA. In other words, we are imposing that Maxwell's equations must be locally satisfied in spatial and temporal variations of the optical carrier, i.e., $\delta z \sim \lambda$ and $\delta t \sim T_0$. Nonetheless, given that $\left|\partial_z^2\mathcal{A}\right| \ll k^2\left|\mathcal{A}\right|$ in the wave equation of $\boldsymbol{\mathcal{E}}$, the term $\partial_z^2\mathcal{A}$ is usually omitted in the classical literature of optics and photonics by assuming $\partial_z^2\mathcal{A} \simeq 0$ during the derivation of the pulse propagation equation [139, 149, 150, 159]. Unfortunately, this point has not been rigorously discussed in the aforementioned works when femtosecond optical pulses are involved in the electromagnetic propagation. For this reason, we include in this appendix a personal discussion about this approximation in the third transmission window ($\lambda_0 = n\lambda = 1550$ nm).

From the above lines, it is noticeable that we can test the accuracy of $\partial_z^2\mathcal{A} \simeq 0$ by analyzing if the ratio $\left|\partial_z^2\mathcal{A}\right|/k^2\left|\mathcal{A}\right|$ is lower than the unity in $\delta z \sim \lambda$ when varying the pulse width T_P. Thus, let us consider two different unchirped optical pulses: a Gaussian pulse (G) and a fundamental bright soliton (BS), described by the following real envelopes at $z = 0$ [139]:

$$a_{\mathrm{G}}(t) = a_0 \exp\left(-\frac{1}{2}\frac{t^2}{T_0^2}\right) \simeq a_0 \exp\left(-3.39\frac{t^2}{T_{\mathrm{P}}^2}\right); \tag{B4.4}$$

$$a_{\mathrm{BS}}(t) = a_0 \operatorname{sech}\left(\frac{t}{T_0}\right) \simeq a_0 \operatorname{sech}\left(2.98\frac{t}{T_{\mathrm{P}}}\right). \tag{B4.5}$$

In the above equations, we have introduced our parameter T_{P}, defined as the full-width at $1/(2e)$ of the peak power. Interestingly, a silica fiber is analogous to the dielectric medium previously considered when omitting its dispersive nature. In such circumstances, the phase and group velocities are found to be the same ($v_{\mathrm{G}} = v_{\mathrm{PH}} = c_0/n$) and the envelope of the optical pulses can be expressed at any z point as:

$$\mathcal{A}_{\mathrm{G}}(z,t) = a_{\mathrm{G}}\left(t - \frac{n}{c_0}z\right) = a_0 \exp\left(-3.39\frac{(t-(n/c_0)\,z)^2}{T_{\mathrm{P}}^2}\right); \tag{B4.6}$$

$$\mathcal{A}_{\mathrm{BS}}(z,t) = a_{\mathrm{BS}}\left(t - \frac{n}{c_0}z\right) = a_0 \operatorname{sech}\left(2.98\frac{(t-(n/c_0)\,z)}{T_{\mathrm{P}}}\right). \tag{B4.7}$$

Note that the envelopes are real functions because we have omitted the chirp and any phase reference at $z = 0$ of the form $\exp(j\varphi_a(z=0))$. Using Eqs. (B4.6) and (B4.7), we can analyze the behavior of the ratio $\left|\partial_z^2\mathcal{A}\right|/k^2\left|\mathcal{A}\right|$ in $\delta z \sim \lambda$ when varying T_{P}. Figure B4.1 shows this ratio with $z_{\mathrm{N}} := z/\lambda$, $z \in [0,\lambda]$, $\lambda = \lambda_0/n$, $n = 1.452$, $T_{\mathrm{P}} \in [0.01, 100]$ fs, and taking $t \equiv 0$ and $a_0 \equiv 1$ for simplicity. As seen, $\left|\partial_z^2\mathcal{A}\right| \sim k^2\left|\mathcal{A}\right|$ when $z_{\mathrm{N}} = 1$ and $T_{\mathrm{P}} \sim 10$ fs or shorter. For this reason, in Subsection 4.2.3, we retained the terms $\partial_z^2\mathcal{A}_{mi}$. In any case, this term is irrelevant in the final expression of the coupled local-mode equations given that it appears in the LHS of the form:

$$j\left(\partial_z + \frac{j}{2\beta_{mi,\omega_0}^{(\mathrm{eq})}}\partial_z^2 + \widehat{\mathrm{D}}_{mi}^{(\mathrm{eq})} + \frac{1}{2}\widehat{\alpha}\right)\mathcal{A}_{mi}(z,t), \tag{B4.8}$$

with $\left|\partial_z^2\mathcal{A}_{mi}\right| / \left(2\beta_{mi,\omega_0}^{(\mathrm{eq})}\right) \ll \left|\partial_z\mathcal{A}_{mi}\right|$. Hence, we can omit $\partial_z^2\mathcal{A}_{mi}$ in the CLMT.

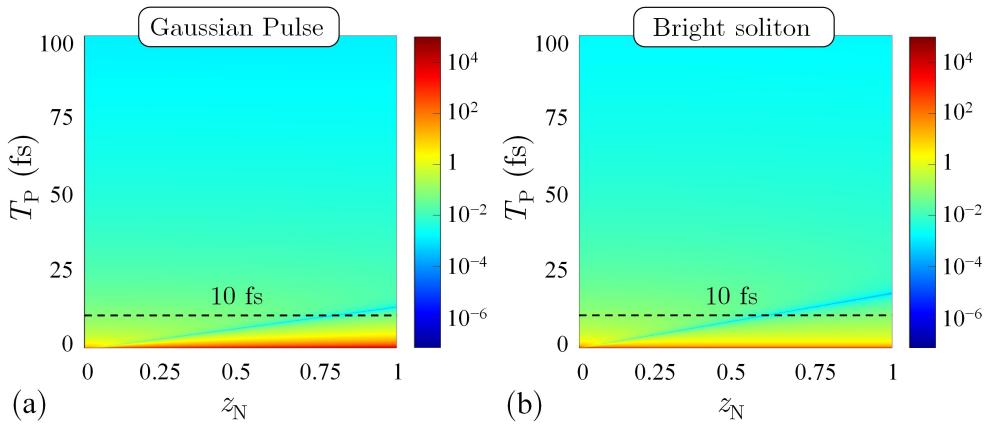

Figure B4.1. Numerical analysis of the ratio $\left|\partial_z^2\mathcal{A}\right|/k^2\left|\mathcal{A}\right|$ as a function of the normalized length $z_{\mathrm{N}} = z/\lambda$ and the pulse width T_{P} by considering an envelope accounting for: (a) a Gaussian pulse and (b) a bright soliton.

If we now analyze the second-order time derivative, the order criterion $\left|\partial_t^2\mathcal{A}\right| \ll \omega_0^2\left|\mathcal{A}\right|$ is also violated with $t \sim T_0$ at $\lambda_0 = 1550$ nm when $T_{\mathrm{P}} \leq 10$ fs. Therefore, from these results, we conclude that the own concept of the complex envelope (and the complex amplitude) itself becomes unclear in the third transmission window if $T_{\mathrm{P}} \leq 10$ fs, which sets the lower limit of applicability of the ansatz [Eq. (B4.1) in this appendix and Eq. (4.2.1) in the main text] to pulses wider than 10 fs, as was pointed out in Subsection 4.2.1. In conclusion, the lower limit of the CLMT can be tested as indicated on page 99 or in this appendix.

Additional note 1

An interesting question which emerges from the above discussion is why $\partial_z^2\mathcal{A}$ is neglected and $\partial_t^2\mathcal{A}$ is retained when deriving the CLMT or the nonlinear Schrödinger equation (NLSE) in the literature (see e.g. [139,159]). The answer is simpler than initially foreseen. Starting from Maxwell's equations, at the beginning of the mathematical derivation, we are using longitudinal and temporal orders of reference of $\delta z \sim \lambda$ and $\delta t \sim T_0$, respectively. In addition, note that the term $\partial_t^2\mathcal{A}$ does not appear at this point of our mathematical discussions because we usually work in the frequency domain. Therefore, we can only neglect the term $\partial_z^2\mathcal{A}$, provided that Eq. (B4.3) is fulfilled. Next, $\partial_t^2\mathcal{A}$ appears when obtaining the final equations in the time domain. At this point, the information of the rapid temporal oscillations of the optical carrier has dissapeared and the coupled local-mode equations (or the NLSE) only give information about the evolution of the complex envelopes. Hence, the temporal and longitudinal orders of reference have changed to $\delta t \sim T_\mathrm{P}$ and $\delta z \sim v_\mathrm{G} T_\mathrm{P}$ and, consequently, we cannot assume that $\partial_t^2\mathcal{A} \simeq 0$ in $\delta t \sim T_\mathrm{P}$.

Additional note 2

Note that Eq. (B4.2) is satisfied $\forall\ \mathcal{A} \in \mathcal{F}\left(\mathbb{R}^2, \mathbb{C}\right)$ when omitting the dispersive nature of the dielectric medium. In such a case, the independent variables z and t are simply connected by the expression $z = (c_0/n)\, t$ and, therefore, $\partial_z^2 \equiv \left(n^2/c_0^2\right)\partial_t^2$ and $2k\partial_z \equiv 2\left(n^2/c_0^2\right)\omega_0\partial_t$. Nonetheless, the SVEA is a sufficient condition to guarantee that Eq. (B4.2) is fulfilled in dispersive media.

Additional note 3

The reader can find a more detailed discussion about the SVEA in [193–196].

Appendix C4: Numerical model, local split-step Fourier method

The numerical simulations of the coupled local-mode equations have been performed in MATLAB by combining the ERIM of Chapter 3 and the split-step Fourier method [139] in each local birefringent segment. Both methods allow us to simulate the MCF perturbations and the linear and nonlinear propagation employing a low computational time. According to the split-step Fourier method, Eq. (4.2.66) should be rewritten as:

$$\left(\partial_z + \widehat{\mathrm{D}}_{ax}^{(\mathrm{eq})} + \frac{1}{2}\widehat{\alpha}\right)\mathcal{A}_{ax}(z,t) + j\widehat{\mathrm{M}}_{ax,ay}^{(\mathrm{eq})}\mathcal{A}_{ay}(z,t) + j\sum_{m\neq a}^{N}\widehat{\mathrm{K}}_{ax,mx}^{(\mathrm{eq})}\mathcal{A}_{mx}(z,t) = \widehat{\mathrm{N}}_{ax}^{(\mathrm{eq})}\mathcal{A}_{ax}(z,t), \tag{C4.1}$$

where $\widehat{\mathrm{N}}_{ax}^{(\mathrm{eq})}$ is the operator modeling the nonlinear propagation of the PCM ax:

$$\begin{aligned}
\widehat{\mathrm{N}}_{ax}^{(\mathrm{eq})} =& -j\widetilde{q}_{ax}^{(\mathrm{I})(0)}\left|\mathcal{A}_{ax}(z,t)\right|^2 - \frac{\widetilde{q}_{ax}^{(\mathrm{I})(1)}}{\mathcal{A}_{ax}(z,t)}\partial_t\left(\left|\mathcal{A}_{ax}(z,t)\right|^2\mathcal{A}_{ax}(z,t)\right)\\
&-j\frac{2}{3}\widetilde{g}_{ax,ay}^{(\mathrm{I})(0)}\left|\mathcal{A}_{ay}(z,t)\right|^2 - \frac{2}{3}\frac{\widetilde{g}_{ax,ay}^{(\mathrm{I})(1)}}{\mathcal{A}_{ax}(z,t)}\partial_t\left(\left|\mathcal{A}_{ay}(z,t)\right|^2\mathcal{A}_{ax}(z,t)\right)\\
&-\frac{1}{3}\frac{\exp\left(-j2\Delta\phi_{ay,ax}^{(0)}(z;t)\right)}{\mathcal{A}_{ax}(z,t)}\left[j\widetilde{g}_{ax,ay}^{(\mathrm{I})(0)}\mathcal{A}_{ax}^{*}(z,t)\,\mathcal{A}_{ay}^{2}(z,t) + \widetilde{g}_{ax,ay}^{(\mathrm{I})(1)}\partial_t\left(\mathcal{A}_{ax}^{*}(z,t)\,\mathcal{A}_{ay}^{2}(z,t)\right)\right]\\
&-j\widetilde{q}_{ax}^{(\mathrm{R})(0)}\left(f(t)*\left|\mathcal{A}_{ax}(z,t)\right|^2\right) - \frac{\widetilde{q}_{ax}^{(\mathrm{R})(1)}}{\mathcal{A}_{ax}(z,t)}\partial_t\left[\left(f(t)*\left|\mathcal{A}_{ax}(z,t)\right|^2\right)\mathcal{A}_{ax}(z,t)\right]\\
&-j\widetilde{g}_{ax,ay}^{(\mathrm{R})(0)}\left(h(t)*\left|\mathcal{A}_{ay}(z,t)\right|^2\right) - \frac{\widetilde{g}_{ax,ay}^{(\mathrm{R})(1)}}{\mathcal{A}_{ax}(z,t)}\partial_t\left[\left(h(t)*\left|\mathcal{A}_{ay}(z,t)\right|^2\right)\mathcal{A}_{ax}(z,t)\right]\\
&-j\frac{1}{2}\frac{\widetilde{g}_{ax,ay}^{(\mathrm{R})(0)}}{\mathcal{A}_{ax}(z,t)}\left\{\left[u(t)*\left(\mathcal{A}_{ax}(z,t)\,\mathcal{A}_{ay}^{*}(z,t)\right)\right]\mathcal{A}_{ay}(z,t)\right\}\\
&-\frac{1}{2}\frac{\widetilde{g}_{ax,ay}^{(\mathrm{R})(1)}}{\mathcal{A}_{ax}(z,t)}\partial_t\left\{\left[u(t)*\left(\mathcal{A}_{ax}(z,t)\,\mathcal{A}_{ay}^{*}(z,t)\right)\right]\mathcal{A}_{ay}(z,t)\right\}\\
&-j\frac{1}{2}\exp\left(-j2\Delta\phi_{ay,ax}^{(0)}(z;t)\right)\frac{\widetilde{g}_{ax,ay}^{(\mathrm{R})(0)}}{\mathcal{A}_{ax}(z,t)}\left\{\left[u(t)*\left(\mathcal{A}_{ax}^{*}(z,t)\,\mathcal{A}_{ay}(z,t)\right)\right]\mathcal{A}_{ay}(z,t)\right\}\\
&-\frac{1}{2}\exp\left(-j2\Delta\phi_{ay,ax}^{(0)}(z;t)\right)\frac{\widetilde{g}_{ax,ay}^{(\mathrm{R})(1)}}{\mathcal{A}_{ax}(z,t)}\partial_t\left\{\left[u(t)*\left(\mathcal{A}_{ax}^{*}(z,t)\,\mathcal{A}_{ay}(z,t)\right)\right]\mathcal{A}_{ay}(z,t)\right\}.
\end{aligned} \tag{C4.2}$$

As can be seen in Fig. C4.1, each core m is assumed to be composed by different birefringent segments with a random orientation of the local principal axes. In addition, each birefringent segment (denoted by the subindex $l \in \{1,\ldots,N_m\}$) is divided in several small fiber segments where the split-step Fourier method is applied. This method obtains an approximate solution of Eq. (C4.1) by considering that in each small fiber segment, the linear and nonlinear propagation can be decoupled [139]. The LHS of Eq. (C4.1), accounting for the linear propagation and the linear mode-coupling, is simulated in the frequency domain; and the RHS, which describes the nonlinear propagation and the nonlinear mode-coupling, is simulated in the time domain. A further description of the split-step Fourier method can be found on page 47 in [139].

However, additional remarks of the MCCs and the real phase functions $\phi_{mi}(z,\omega;t)$ should be indicated to complete the description of the numerical model. Specifically, we will describe in detail how to extend the ERIM of Chapter 3 to work in the frequency domain.

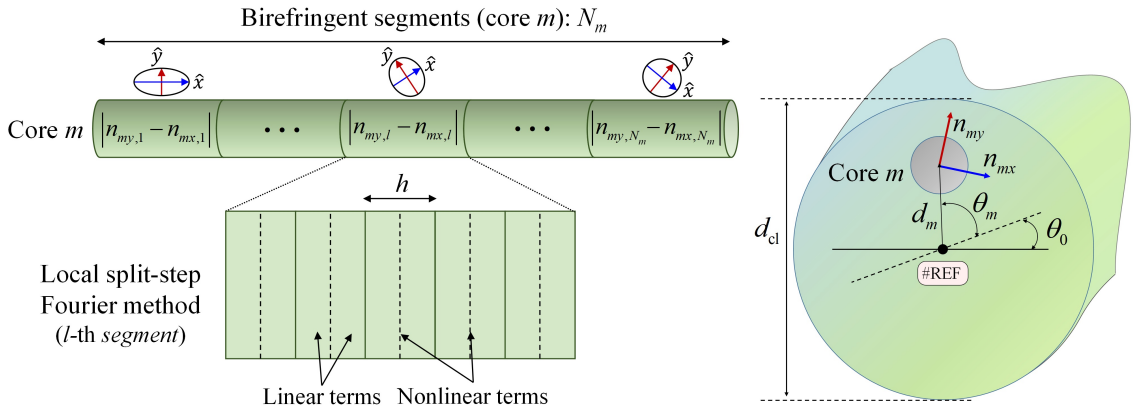

Figure C4.1. Multi-core fiber simulation model. Each core m is divided in different birefringent segments (N_m) and local modes with a different time-varying retardation and random orientation of the local principal axes. Each birefringent segment is composed by small short distances (h) where the split-step Fourier method is applied [116].

Let us consider a short MCF distance h in a given l-th birefringent segment of the PCM mi, as depicted in Fig. C4.1. We assume to be homogeneous along the l-th segment length: the bending radius $R_{\mathrm{B},l}(t)$, the twist rate $f_{\mathrm{T},l}(t)$ and the intrinsic linear birefringence $|n_{my,l}(t)-n_{mx,l}(t)|$. It should be noted that these parameters are found to be temporal dependent when simulating MCFs with time-varying conditions, in line with Chapter 3. However, in order to simplify the description of the ERIM in the frequency domain, we will not use the *discrete* birefringence temporal changes (BTCs) defined on page 67. Now, the time-varying fluctuations induced by floor vibrations and temperature excursions will be modeled by the continuous variable t in this chapter. Moreover, in contrast to Chapter 3, note that a Monte Carlo simulation is not required given that we are not interested in calculating the mean of the crosstalk. Therefore, the phase function $\phi_{mi,l}$ can be written in each short MCF distance h as:

$$\phi_{mi,l}(z,\omega;t)=\int_{\langle h\rangle}\beta_{mi,l}^{(\mathrm{eq})}(z,\omega;t)\,\mathrm{d}z\simeq\beta_{mi,l}^{(\mathrm{eq})}(z,\omega;t)\,h=\left[\beta_{mi}(\omega)+\beta_{mi,l}^{(\mathrm{B+S})}(z,\omega;t)\right]h. \tag{C4.3}$$

The ideal phase constant $\beta_{mi}(\omega)$ can be approximated by a third-order Taylor series expansion as follows:

$$\beta_{mi}(\omega)\simeq\beta_{mi}(\omega_0)+\sum_{k=1}^{3}\frac{1}{k!}(\omega-\omega_0)^k\beta_{mi,\omega_0}^{(k)}\simeq\frac{\omega_0}{c_0}n_{mi}(\omega_0)+\sum_{k=1}^{3}\frac{1}{k!}(\omega-\omega_0)^k\beta_{mi,\omega_0}^{(k)}, \tag{C4.4}$$

being $n_{mi}(\omega_0)$ a principal refractive index of core m at the center of the pulse bandwidth, which includes the intrinsic linear birefringence in HB-cores. In LB cores, $n_{mx}=n_{my}\equiv n_m$. In addition, the longitudinal and temporal perturbations of the l-th segment are calculated as follows:[24]

$$\beta_{mi,l}^{(\mathrm{B+S})}(z,\omega;t)\simeq\frac{\omega}{c_0}n_{mi,l}^{(\mathrm{B+S})}(z,\omega_0;t)=\frac{\omega}{c_0}\left(n_{mi,l}^{(\mathrm{eq})}(z,\omega_0;t)-n_{mi}(\omega_0)\right); \tag{C4.5}$$

$$n_{mi,l}^{(\mathrm{eq})}(z,\omega_0;t)\simeq n_{mi,l}(\omega_0;t)\left[1+\frac{d_m}{R_{\mathrm{B},l}(t)}\cos\left(2\pi f_{\mathrm{T},l}(t)\,z+\theta_0+\theta_m\right)\right]. \tag{C4.6}$$

In Eq. (C4.6), $n_{mi,l}(\omega_0;t)$ describes the temporal fluctuation of the intrinsic linear birefringence in the l-th birefringent segment, θ_0 is the offset of the twist angle of the MCF reference axis at $z=0$, θ_m is the offset of the twist angle of the core m measured from the MCF reference axis, and d_m is the Euclidean distance of the core m to the MCF center. The temporal birefringence fluctuation

[24]The subindex l indicates the discrete longitudinal evolution of the corresponding function. Nevertheless, the z variable is retained when a continuous longitudinal evolution is also involved.

$|n_{my,l}(\omega_0;t) - n_{mx,l}(\omega_0;t)|$ is modeled along the MCF length by the same Gaussian random process $\mathrm{N}\left(\mu(\omega_0;t), \sigma^2(z,\omega_0;t)\right)$ described by Eq. (3.3.6), repeated here for convenience. The mean $\mu(\omega_0;t) = \Delta n_m(\omega_0;t)$ is the longitudinal average value of the intrinsic linear birefringence of the core m at $\omega = \omega_0$, and it is assumed temporal dependent. The variance $\sigma^2(z,\omega_0;t) = \delta n_{m,l}(\omega_0;t)$ describes the photo-elastic effect in the l-th segment:

$$\delta n_{m,l}(\omega_0;t) \simeq \xi + 0.011 n_m^3 d_{\mathrm{cl}}^2 / R_{\mathrm{B},l}^2(t), \tag{C4.7}$$

where $\xi = 10^{-8}$, d_{cl} is the cladding diameter, and $n_m := (n_{mx} + n_{my})/2$. Finally, $n_{mi,l}(\omega_0;t)$ is found from the expression:

$$n_{mi,l}(\omega_0;t) \sim n_{mi}(\omega_0) \pm \frac{1}{2}\mathrm{N}\left(\Delta n_m(\omega_0;t), \delta n_{m,l}(\omega_0;t)\right), \tag{C4.8}$$

with '+' if $i = y$ and '−' if $i = x$.

It is noticeable that $\beta_{mi,l}^{(\mathrm{B+S})}$ is calculated from $n_{mi,l}^{(\mathrm{eq})}$ at $\omega = \omega_0$ to reduce the computational time of the CLMT. As an additional option, we may increase the accuracy of $\beta_{mi,l}^{(\mathrm{B+S})}$ by including the frequency dependence of $n_{mi}(\omega)$ via the Sellmeier equation in Eqs. (C4.5), (C4.6) and (C4.8). Remarkably, Eq. (C4.5) allows us to describe, not only the external linear birefringence induced by the fiber bending and twisting conditions, but also the intrinsic linear birefringence induced by manufacturing imperfections in the l-th segment. Moreover, although R_{B} and f_{T} should be regarded as time-dependent random processes, note that we have not considered temporal changes of these fiber parameters in the numerical simulations to facilitate the analysis of the main results.

On the other hand, the MCCs can be numerically calculated from Eqs. (4.2.52)-(4.2.55) by using Eqs. (3.3.7)-(3.3.11) replacing ω_0 by ω. In other words, the F_{mi} function should be calculated from the modal parameters $u_{mi}(z,\omega;t)$ and $w_{mi}(z,\omega;t)$, which depend on the normalized frequency $V_{mi}(z,\omega;t)$. This function should be written in the frequency domain and in the l-th segment as:

$$V_{mi,l}(z,\omega;t) = \frac{\omega}{c_0} R_{0,m} C_{\mathrm{F},m} \sqrt{\left(n_{mi,l}^{(\mathrm{eq})}(z,\omega_0;t)\right)^2 - n_{\mathrm{cl}}^2}. \tag{C4.9}$$

Likewise, the MCCs can be calculated in SI-MCFs from Eqs. (3.3.13)-(3.3.15) replacing ω_0 by ω. In particular, the following expressions can be employed to calculate the MCCs in each l-th birefringent segment (we omit the independent variables for the sake of simplicity):

$$\widetilde{m}_{ax,ay,l}(z,\omega;t) \simeq \frac{\pi}{2}\frac{\omega}{c_0}|p_{11} - p_{12}| f_{\mathrm{T},l} R_{0,a} \frac{n_a^4}{n_{ax,l}^{(\mathrm{eq})}}; \tag{C4.10}$$

$$\widetilde{\kappa}_{ax,bx,l}(z,\omega;t) \simeq 2\frac{\omega}{c_0}\left(n_{ax,l}^{(\mathrm{eq})} - n_{\mathrm{cl}}\right) \frac{J_0(u_{ax,l}) J_1(u_{ax,l})}{u_{ax,l}\left[J_0^2(u_{ax,l}) + J_1^2(u_{ax,l})\right]} \frac{K_0(w_{bx,l} d_{ab}/R_{0,b})}{K_0(w_{bx,l})}; \tag{C4.11}$$

$$\widetilde{q}_{ax,l}^{(\mathrm{S})}(z,\omega;t) \simeq \widetilde{g}_{ax,ay}^{(\mathrm{S})}(z,\omega;t) \simeq \frac{1}{8}\frac{\omega}{c_0}\frac{\gamma_{\mathrm{S}}}{n_{ax,l}^{(\mathrm{eq})}}\frac{H_{ax,l}^2}{R_{0,a}^2}\frac{\left[1 - \exp\left(-4R_{0,a}^2/H_{ax,l}^2\right)\right]}{J_0^2(u_{ax,l})\left[J_0^2(u_{ax,l}) + J_1^2(u_{ax,l})\right]}, \tag{C4.12}$$

where the main parameters involved in the above expressions were defined in Chapter 3 (see page 70), and the nonlinear parameters $\gamma_{\mathrm{I}}(\omega)$ and $\gamma_{\mathrm{R}}(\omega)$ were defined in Subsection 4.2.3.

In order to reduce the computational complexity of the nonlinear terms in the time domain and taking into account the low nonlinear nature of silica fibers, the nonlinear MCCs are approximated by a first-order Taylor series approximation in the operator $\widehat{\mathrm{N}}_{ax}^{(\mathrm{eq})}$. In particular, this approximation implies that we are omitting higher-order effects of the nonlinear PMD in Eq. (4.2.58). However, the first-order nonlinear PMD seems to be sufficiently accurate in very-high data rate transmission systems and particularly in those that employ solitons [197].

Furthermore, as discussed on page 70, the orientation of the local principal axes of each birefringent segment is changed along the MCF length as a consequence of the longitudinal fluctuations of the twist rate. For large MCF distances of several kilometers, the orientation of the principal axes should be adequately randomized along the MCF length by increasing the variance of the f_{T} distribution to describe accurately the intrinsic circular birefringence of the fiber, or by inserting phase plates between adjacent segments (see Ref. [155] for more details). In the second case, the computational time of the coupled local-mode equations could maybe be reduced.

Finally, we include in Tables C4.1 and C4.2 the MCF parameters employed in the numerical calculations. Additional fiber parameters employed in these simulations are listed below:[25]

- Fiber length: $L = 40$ m
- Optical carrier wavelength: $\lambda_0 = 1550$ nm
- Cut-off wavelength of cores a and b (*): $\lambda_{\mathrm{C},a} = \lambda_{\mathrm{C},b} = 1410$ nm
- Core radius of cores a and b (*): $R_{0,a} = R_{0,b} = 4$ μm
- Core-to-core distance: $d_{ab} = 26$ μm
- Distance of core a and b to the MCF center: $d_a = d_b = d_{ab}/\sqrt{2}$
- Cladding diameter (*): $d_{\mathrm{cl}} = 125$ μm
- Cladding refractive index (*): $n_{\mathrm{cl}} = 1.444$
- Nonlinear refractive index: $n_{\mathrm{NL}}(\omega) \simeq n_{\mathrm{NL}}^{(0)} + (\omega - \omega_0)\, n_{\mathrm{NL}}^{(1)}$, with $n_{\mathrm{NL}}^{(0)} = 2.6 \cdot 10^{-20}$ m^2/W and $n_{\mathrm{NL}}^{(1)} = 8.3 \cdot 10^{-24}$ ps $\cdot$ m^2/W
- Nonlinear parameters: $\gamma_{\mathrm{I}}(\omega) \simeq \gamma_{\mathrm{I}}^{(0)} + (\omega - \omega_0)\, \gamma_{\mathrm{I}}^{(1)}$ and $\gamma_{\mathrm{R}}(\omega) \simeq \gamma_{\mathrm{R}}^{(0)} + (\omega - \omega_0)\, \gamma_{\mathrm{R}}^{(1)}$; with $\gamma_{\mathrm{I}}^{(0)} = 1.5 \cdot 10^{-22}$ m^2/V^2, $\gamma_{\mathrm{I}}^{(1)} = 4.8 \cdot 10^{-26}$ ps $\cdot$ m^2/V^2, $\gamma_{\mathrm{R}}^{(0)} = 3.2 \cdot 10^{-23}$ m^2/V^2, and $\gamma_{\mathrm{R}}^{(1)} = 1.1 \cdot 10^{-26}$ ps $\cdot$ m^2/V^2
- Attenuation coefficient (*): $\alpha^{(0)} = 0.44$ dB/km $= 0.051$ Np/km, $\alpha^{(1)} = 3.7 \cdot 10^{-4}$ ps $\cdot$ Np/km
- Peak Power: P_0
- Pulse width [full-width at $1/(2e)$ of the peak power]: $T_{\mathrm{P}} \simeq 1.56 \cdot T_{\mathrm{FWHM}}$ for Gaussian pulses and $T_{\mathrm{P}} \simeq 1.7 \cdot T_{\mathrm{FWHM}}$ for Hyperbolic-Secant pulses (FWHM: Full Width at Half Maximum)
- Material refractive index of cores a and b: n_a, n_b
- Intrinsic linear birefringence in the l-th birefringent segment: $|n_{my,l}(\omega_0; t) - n_{mx,l}(\omega_0; t)| \sim \mathrm{N}(\Delta n_m(\omega_0; t), \delta n_{m,l}(\omega_0; t))$. Mean included in Table C4.1. Variance given by Eq. (C4.7).
- Number of birefringent segments in each core: $N_a = N_b \equiv N_{\mathrm{S}}$
- Number of small fiber segments in each birefringent segment: N_h
- Bending radius: R_{B}
- Twist rate: f_{T}

[25] The symbol (*) indicates the fiber parameters retrieved from the Fibercore SM-4C1500(8.0/125) datasheet.

Simulation	T_{P}	P_0	Pulse	n_a	n_b	Δn_a	Δn_b	N_{S}	N_h	R_{B}	f_{T}
(units)	(fs)	(dBm)								(cm)	(turns/m)
Fig. 4.3(a)	350	0	G	1.452	1.452	0	0	1	200	∞	0
Fig. 4.3(b)	350	0	G	1.452	1.452	0	0	1	200	10	0
Fig. 4.3(c)	350	0	G	1.452	1.452	0	0	1	200	1	0
Fig. 4.4(a)	250	0	G	1.452	1.452	0	0	50	10	N(100,40)	0
Fig. 4.4(b)	250	0	G	1.452	1.452	0	0	50	10	N(10,2)	0
Fig. 4.5(a)	200	0	G	1.452	1.452	0	0	50	10	N(100,40)	0
Fig. 4.5(b)	200	0	G	1.454	1.452	0	0	50	10	N(100,40)	0
Fig. 4.6	600	40.7	HS	1.452	1.452	$2 \cdot 10^{-7}$	$2 \cdot 10^{-7}$	50	10	N(100,40)	N(0.1,0.01)
Fig. 4.7	150	0	G	1.452	1.452	Fig. (a)	Fig. (a)	50	10	100	0
Fig. D4.1	350	0	G	1.452	1.452	0	0	1	200	∞	0
Fig. D4.2(a)	250	0	G	1.452	1.452	0	0	50	10	N(100,40)	N(0.1,0.01)
Fig. D4.2(b)	250	0	G	1.452	1.452	0	0	50	10	N(10,2)	N(0.1,0.01)
Fig. D4.3	200	0	G	1.452	1.452	$4 \cdot 10^{-7}$	$2 \cdot 10^{-6}$	50	10	N(100,40)	N(0.1,0.01)
Fig. D4.4	200	0	G	1.454	1.452	$4 \cdot 10^{-7}$	$2 \cdot 10^{-6}$	50	10	N(100,40)	N(0.1,0.01)

Table C4.1. Simulation parameters employed in the numerical calculations. $\mathrm{N}(\mu, \sigma^2)$ is the Normal distribution of mean μ and variance σ^2. (G: Gaussian, HS: Hyperbolic-Secant) [116].

Simulation	GVD	$\mathrm{GVD}_{\mathrm{comp}}$	$\Delta\beta^{(1)}_{bx,ax}$	$\beta^{(2)}_{ax}$	$\beta^{(3)}_{ax}$	$\beta^{(2)}_{bx}$	$\beta^{(3)}_{bx}$
(units)			(ps/km)	(ps^2/km)	(ps^3/km)	(ps^2/km)	(ps^3/km)
Fig. 4.3(a)	OFF	–	0	−21.75	0.16	−21.75	0.16
Fig. 4.3(b)	OFF	–	0	−21.75	0.16	−21.75	0.16
Fig. 4.3(c)	OFF	–	0	−21.75	0.16	−21.75	0.16
Fig. 4.4(a)	OFF	–	0	−21.75	0.16	−21.75	0.16
Fig. 4.4(b)	OFF	–	0	−21.75	0.16	−21.75	0.16
Fig. 4.5(a)	ON	ON	0.28	−21.75	0.16	−21.95	0.16
Fig. 4.5(b)	ON	ON	6.5	−21.75	0.16	−22.75	0.26
Fig. 4.6	ON	OFF	0.2	−1	0.1	−1.1	0.1
Fig. 4.7	ON	ON	0.28	−21.75	0.16	−21.95	0.16
Fig. D4.1	OFF	–	0	−21.75	0.16	−21.75	0.16
Fig. D4.2(a)	OFF	–	0	−21.75	0.16	−21.75	0.16
Fig. D4.2(b)	OFF	–	0	−21.75	0.16	−21.75	0.16
Fig. D4.3	ON	ON	0.28	−21.75	0.16	−21.95	0.16
Fig. D4.4	ON	ON	6.5	−21.75	0.16	−22.75	0.26

Table C4.2. Dispersive parameters employed in the numerical calculations. GVD: ON/OFF indicates whether the chromatic dispersion is included in the simulation (ON) or not (OFF). $\mathrm{GVD}_{\mathrm{comp}}$: ON/OFF indicates whether the chromatic dispersion is compensated (ON) or not (OFF) along the MCF propagation in each PCM using the GVD parameters of the PCM ax as a reference. That is, assuming $\beta^{(r)}_{ax} = 0$ and $\beta^{(r)}_{bx} \equiv \Delta\beta^{(r)}_{bx,ax}$ with $r \in \{2, 3\}$. Dispersive parameters are assumed similar for the y-polarization (lowly-birefringent cores). The time domain is normalized using $\beta^{(1)}_{ax}$ as a reference. Hence, the relative group delay between the PCMs bx and ax only depends on $\Delta\beta^{(1)}_{bx,ax}$ but not on $\beta^{(1)}_{ax}$, i.e., $\beta^{(1)}_{ax}$ is just an arbitrary parameter in the numerical simulations [116].

Appendix D4: Additional numerical examples

In this appendix, we present additional numerical examples of the IMCD effects for completeness the main discussions performed in Section 4.4. In order to achieve a better comprehension of the IMCD, we omit the optical power attenuation and the nonlinear effects. However, the chromatic dispersion [also known as the group-velocity dispersion (GVD)] and the PMD (induced by the circular birefringence along with the intrinsic linear birefringence of the fiber) will only be considered when is specified. In all the analyzed cases, the MCF comprises a fiber length of $L = 40$ m and two cores a and b distributed in a square lattice with a core-to-core distance $d_{ab} = 26$ μm and a core radius $R_0 = 4$ μm, as depicted in Fig. 4.1. Moreover, the wavelength of the optical carrier (λ_0) was selected in the third transmission window at $\lambda_0 = 1550$ nm, the peak power[26] of the optical pulses was taken to be 0 dBm, and the time domain was normalized by using the group delay of the PCM ax as a reference with $t_{\mathrm{N}} = (t - \beta_{ax}^{(1)} z)/T_{\mathrm{P}}$, where T_{P} is the full-width at $1/(2e)$ ($\sim 18\%$) of the peak power. The specific parameters of each simulation are detailed in Tables C4.1 and C4.2 included on previous page.

D4.1 Ideal homogeneous multi-core fiber: first- and higher-order CCD

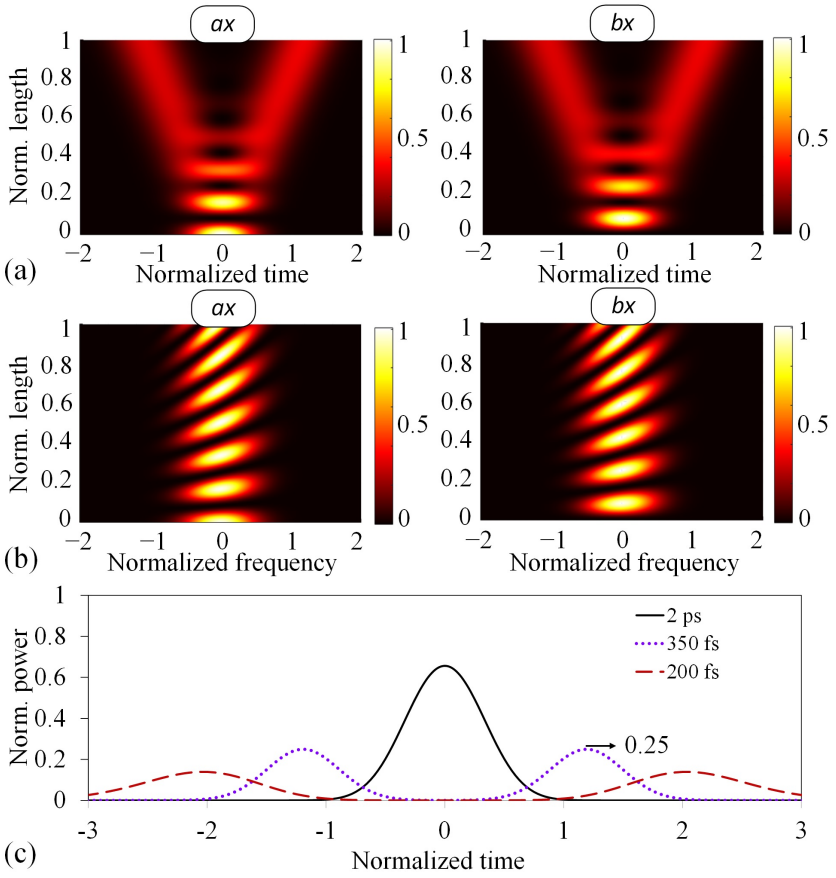

Figure D4.1. Coupling-coefficient dispersion in ideal homogeneous MCFs. Simulation results of ultra-short optical pulses through a 40-m ideal homogeneous 2-core MCF. Longitudinal evolution of a 350-fs Gaussian optical pulse propagated through the polarized core modes (PCMs) ax and bx in: (a) time domain, and (b) frequency domain. (c) Pulse splitting comparison at the MCF output in the PCM ax considering three different pulse widths of 2 ps, 350 fs and 200 fs. [Colorbar: normalized power] [116].

[26] As indicated before, to perform realistic numerical simulations, the power of the optical pulses should be calculated as $P_{mi}(z,t) = \mathscr{C}_{mi}^{(\mathrm{P})} |\mathcal{A}_{mi}(z,t)|^2$, with the exact value of $\mathscr{C}_{mi}^{(\mathrm{P})}$ given by Eq. (1.5.12).

As a first investigation of the IMCD, let us now analyze numerically the effects of the CCD when considering an ideal homogeneous MCF without fiber perturbations. We compare the propagation of an optical pulse with three different temporal pulse widths omitting the longitudinal and temporal fiber perturbations. Figure D4.1 shows the simulation results. Figure D4.1(a) depicts the longitudinal evolution in the time domain of a 350-fs Gaussian optical pulse along the MCF length in the PCMs ax and bx. It can be noted that the initial pulse launched into the PCM ax splits in four identical optical pulses (25% of the initial peak power) propagated by the PCMs ax and bx of the fiber. These results are in line with Eq. (4.3.12) and the observations reported in [175]. Moreover, Fig. D4.1(b) shows the longitudinal evolution of the optical spectrum as a function of the normalized frequency.[27] From these results, we conclude that each spectral component presents a different coupling length induced by the first-order CCD (as a direct consequence of the frequency dependence of the power confinement ratio of the LP_{01} mode in each core). Finally, we compare in Fig. D4.1(c) the pulse splitting in the PCM ax after the MCF propagation of three different Gaussian optical pulses of $T_P = 2$ ps, 350 fs and 200 fs. Note that the pulse splitting increases when the temporal pulse width is reduced, and remarkably, the complex envelope of the 200-fs optical pulse is additionally distorted by the second and higher-order CCD (inducing a linear and nonlinear chirp, respectively).

D4.2 Linear and circular birefringence perturbations: first-order IMCD

A very interesting example is to evaluate a real MCF perturbed by random linear and circular birefringence fluctuations. As discussed in Section 4.3, we know that the random fiber perturbations induce a stochastic group delay in the optical pulse due to the first-order IMCD. In this case, the effect of the first-order PhMD along with the CCD can also be observed when considering a high number of MCF birefringent segments, where the bending radius and the twist rate fluctuate between adjacent segments with a Normal distribution of $R_B = N(\mu = 100, \sigma^2 = 40)$ cm and $f_T = N(\mu = 0.1, \sigma^2 = 0.01)$ turns/m. We simulate the homogeneous MCF of the first example considering a 250-fs Gaussian optical pulse and 50 birefringent segments.

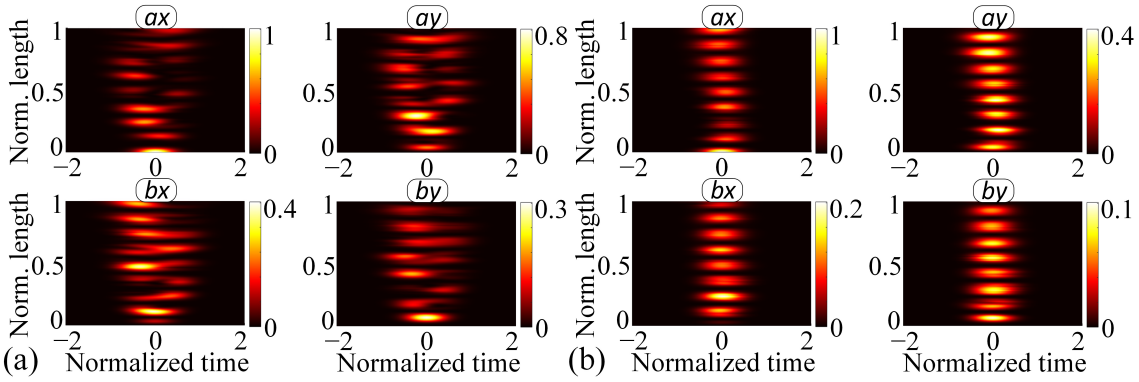

Figure D4.2. First-order IMCD with random bending and twisting conditions. Simulation results of a 250-fs Gaussian optical pulse considering a homogeneous 2-core MCF with a random twist rate (f_T) and a random bending radius (R_B) which fluctuate along the MCF length comprising 50 birefringent segments with Normal distributions $f_T = N(\mu = 0.1, \sigma^2 = 0.01)$ turns/m and: (a) $R_B = N(\mu = 100, \sigma^2 = 40)$ cm, and (b) $R_B = N(\mu = 10, \sigma^2 = 2)$ cm. [Colorbar: normalized power] [116].

It should be noted from Fig. D4.2(a) that the pulse splitting induced by the CCD is reduced in both PCMs as a direct consequence of the average value of $R_B = 100$ cm reducing the mode-coupling between the cores a and b. Now, the group delay and the pulse width present a random evolution in each PCM due to the random nature of the MCF perturbations inducing a stochastic

[27] Here, the normalized frequency is the ratio $\Omega/\mathfrak{B}_{\tilde{A}}$, where $\mathfrak{B}_{\tilde{A}}$ is the bandwidth of the complex envelope in baseband. Note that this parameter is different from the parameter V_{mi} given by Eq. (C4.9).

group velocity. Therefore, the effects of the IMCD can be observed as a distortion of the complex envelope when considering multiple random MCF birefringent segments. Moreover, the circular birefringence only induces power exchange between orthogonal polarizations. Remarkably, we cannot observe an additional pulse distortion induced by the PMD considering that the differential group delay between orthogonal polarizations can be neglected in both cores when the intrinsic linear birefringence is omitted in the numerical simulation. Here, the linear birefringence is only induced by the fiber bending conditions, which modify the equivalent refractive index of each PCM [see Eq. (C4.6)] without significantly changing the differential group delay between the PCMs *ax*-*ay* and *bx*-*by* in this case.

In order to minimize the effects of the IMCD in homogeneous MCFs, we can reduce the average value of the bending radius. To verify this statement, we compare the propagation of the same 250-fs optical pulse considering a bending radius distribution $R_{\mathrm{B}} = \mathrm{N}(\mu = 10, \sigma^2 = 2)$ cm. We can note from Fig. D4.2(b) that, the lower the average value of the bending radius is, the lower the pulse distortion induced by the IMCD is as a direct consequence of the mode-coupling reduction between the PCMs. In general, we can also reduce the mode-coupling inducing external stress in different points along the MCF length or manufacturing MCFs with: trench- or hole-assisted cladding, heterogeneous cores, higher core-to-core distances, or elliptical cores with random orientation of the ellipse. In the same way, the IMCD can also be reduced by using disordered MCFs based on the transverse Anderson localization, allowing for the absence of diffusive wave propagation [93].

D4.3 Higher-order IMCD

In this section, we analyze the higher-order effects of the IMCD. We also include the intrinsic linear birefringence of the medium along with the linear and circular birefringence induced by the fiber bending and twisting conditions. To this end, two different 40-m 2-core MCFs are compared comprising homogeneous and heterogeneous cores. In the homogeneous case, higher-order PhMD effects are induced considering $\Delta\beta^{(1)}_{bx,ax} = 0.28$ ps/km, $\Delta\beta^{(2)}_{bx,ax} = 0.2$ ps^2/km, $\Delta\beta^{(3)}_{bx,ax} = 0$ ps^3/km; and in the heterogeneous case $\Delta n = n_a - n_b = 0.002$, $\Delta\beta^{(1)}_{bx,ax} = 6.5$ ps/km, $\Delta\beta^{(2)}_{bx,ax} = 1$ ps^2/km, and $\Delta\beta^{(3)}_{bx,ax} = 0.1$ ps^3/km. In order to illustrate the higher-order IMCD effects, the GVD is compensated in each PCM along the MCF propagation using the dispersive parameters of a given PCM as a reference, in this case the PCM *ax* (see Table C4.2 in Appendix C4). Furthermore, we also consider 50 birefringent segments along the MCF length, where the linear and circular birefringence fluctuate between adjacent segments. The circular birefringence is induced by a random twist rate f_{T} given by the Normal distribution $f_{\mathrm{T}} = \mathrm{N}(\mu = 0.1, \sigma^2 = 0.01)$ turns/m. The linear birefringence is induced by two different effects: (*i*) the random bending conditions with $R_{\mathrm{B}} = \mathrm{N}(\mu = 100, \sigma^2 = 40)$ cm; and (*ii*) the intrinsic linear birefringence of each core, fixed to $4 \cdot 10^{-7}$ and $2 \cdot 10^{-6}$ in the cores *a* and *b*, respectively. In this case, the intrinsic linear birefringence will induce a differential group delay between the principal axes of each birefringent segment.

Figures D4.3 and D4.4 depict the numerical calculations of the CLMT when a 200-fs Gaussian optical pulse is launched into the PCM *ax* of the homogeneous and heterogeneous MCF, respectively. In the homogeneous case (Fig. D4.3), we can observe the additional chirp induced on the optical pulse by the second-order PhMD along with the PMD. As expected, we can also observe a higher pulse distortion than omitting the PMD when comparing these results with Fig. 4.5(a). Nevertheless, as verified in Fig. D4.4, the pulse distortion induced by the second-order PhMD is reduced in the heterogeneous case given that the mode-coupling is minimized due to a higher intrinsic material index mismatching Δn between the cores *a* and *b*. As seen from Eq. (4.3.15), H_{ax} tends to 1 when the phase-mismatching between the cores *a* and *b* is much higher than the MCCs, which verifies that the mode-coupling reduction allows us to minimize the effects of the IMCD in both cores. In the same way as in Fig. D4.3, note that the additional pulse distortion observed in Fig. D4.4 in the PCMs *bx* and *by* when comparing these results with Fig. 4.5(b) is induced by the PMD of the core *b*. Furthermore, it should be noticed that the optical power oscillates in the core *a* between the PCMs *ax* and *ay* because of the external circular birefringence induced by f_{T}.

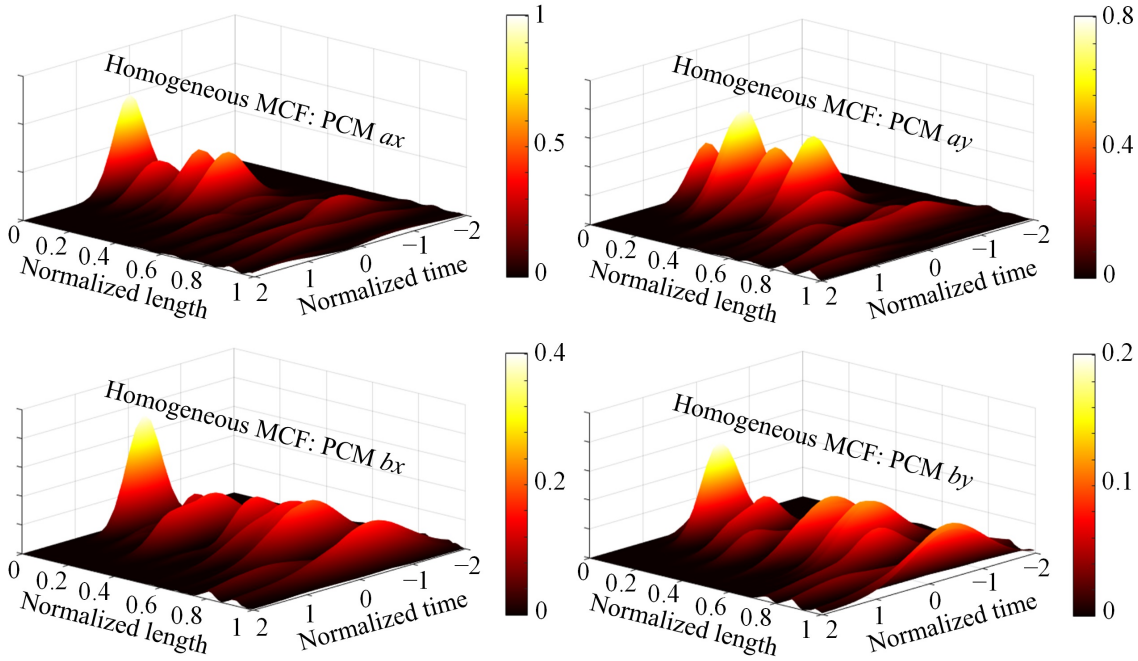

Figure D4.3. Higher-order IMCD in homogeneous MCF. 200-fs Gaussian optical pulse propagated along a 40-m 2-core homogeneous MCF considering higher-order PhMD effects and a random linear and circular birefringence given by the bending radius and twist rate distributions $R_{\mathrm{B}} = \mathrm{N}(\mu = 100, \sigma^2 = 40)$ cm and $f_{\mathrm{T}} = \mathrm{N}(\mu = 0.1, \sigma^2 = 0.01)$ turns/m along 50 birefringent segments. [Colorbar: normalized power] [116].

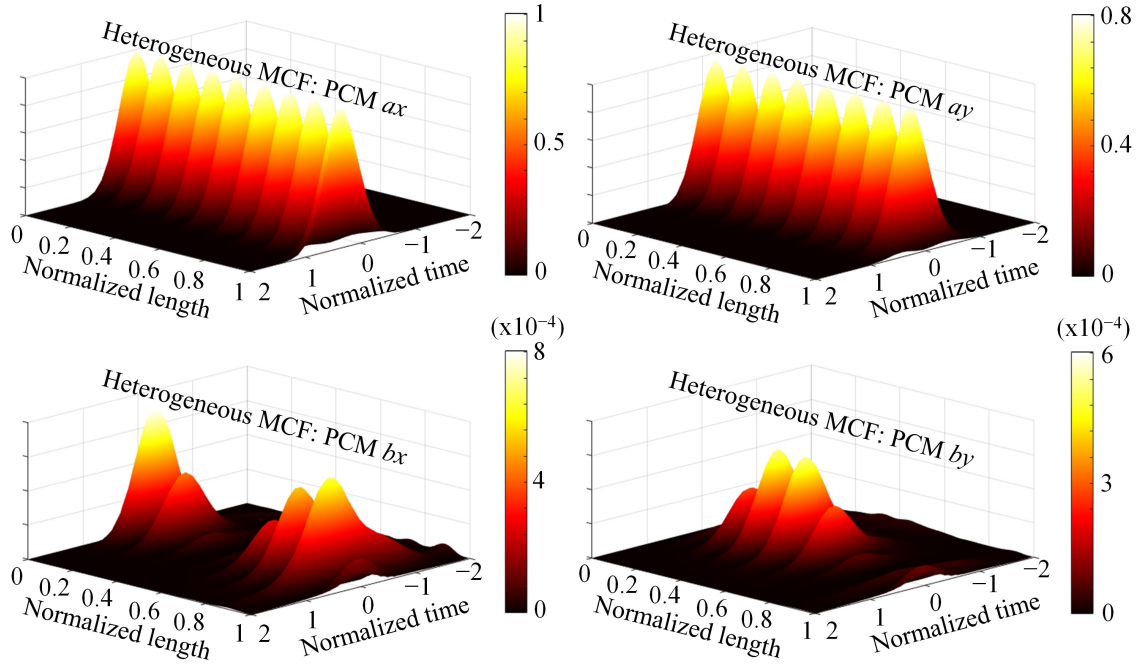

Figure D4.4. Higher-order IMCD in heterogeneous MCF. 200-fs Gaussian optical pulse propagated along a 40-m 2-core heterogeneous MCF considering higher-order PhMD effects and a random linear and circular birefringence given by the bending radius and twist rate distributions $R_{\mathrm{B}} = \mathrm{N}(\mu = 100, \sigma^2 = 40)$ cm and $f_{\mathrm{T}} = \mathrm{N}(\mu = 0.1, \sigma^2 = 0.01)$ turns/m along 50 birefringent segments. [Colorbar: normalized power] [116].

On the other hand, in the homogeneous case, we can also induce an external perturbation (e.g. reducing the average value of the bending radius) to increase the equivalent index mismatching between the PCMs reducing the higher-order effects of the IMCD. Additional strategies as trench-assisted MCFs or disordered MCFs based on the transverse Anderson localization [93] can also be employed to reduce the pulse distortion induced by the first- and higher-order effects of the IMCD, as mentioned before.

D4.4 IMCD length

Finally, once we know in general terms the effects of the IMCD in ultra-short optical pulses, it is natural to ask about the fiber length scales over which the dispersive effects of the IMCD should be considered in the pulse propagation phenomena when comparing this optical dispersion with the first-order GVD. So far, we have discussed that the IMCD is reduced when inducing random perturbations on the optical medium. Therefore, the IMCD and the GVD should be compared in MCFs without including birefringence effects. To this end, we analyze the GVD and the IMCD lengths, defined as the fiber length scales over which their dispersive effects should be considered. The GVD length is defined in [139] as a function of the pulse half-width at $1/e$ of the peak power. Nonetheless, in this work we have investigated the IMCD using the full-width at $1/(2e)$ of the peak power (T_{P}). Thus, in order to compare the GVD with the IMCD, we define the GVD length in terms of T_{P}:

$$L_{\mathrm{GVD}} := T_{\mathrm{P}}^2 / \left|\beta_{ax}^{(2)}\right| . \tag{D4.1}$$

In the same way, the CCD length is defined as the minimum fiber length over which the pulse splitting can be observed. Hence, considering the PCMs ax and bx, it is straightforward to conclude from Eq. (4.3.12) that the CCD length should be defined as:

$$L_{\mathrm{CCD}} := T_{\mathrm{P}} / \left(2\left|\widetilde{\kappa}_{ax,bx}^{(1)}\right|\right) . \tag{D4.2}$$

Furthermore, taking into account that the second-order PhMD induces a linear chirp between the PCMs ax and bx when $\Delta\beta_{bx,ax}^{(2)} \neq 0$, the PhMD length is defined in a similar way as the GVD length:

$$L_{\mathrm{PhMD}} := T_{\mathrm{P}}^2 / \left|\Delta\beta_{bx,ax}^{(2)}\right| . \tag{D4.3}$$

All in all, the IMCD length should be defined by considering the predominant physical impairment, the CCD or the PhMD:

$$L_{\mathrm{IMCD}} := \min\left\{L_{\mathrm{CCD}}, L_{\mathrm{PhMD}}\right\} . \tag{D4.4}$$

Appendix E4: Multi-mode regime

In this appendix, we will extend the CLMT [Eq. (4.2.66)] to the multi-mode regime. To this end, let us consider a real weakly-guiding M-core MCF with each core supporting N LP modes ($n \in \{1,\ldots,N\}$). In addition, we consider two orthogonal polarizations $i \in \{x,y\}$ and a single optical carrier with angular frequency ω_0. Thus, each core propagates $2N$ PCMs.[28] Following the same mathematical strategy as in the single-mode regime, we assume the electric field strength of the MCF ($\boldsymbol{\mathcal{E}}$) as a linear combination of the PCMs of each core $m \in \{1,\ldots,M\}$. In addition, we separate the rapid and the slow temporal and longitudinal variations of $\boldsymbol{\mathcal{E}}$ by using respectively the slowly-varying amplitude (E_{mni,ω_0}) and envelope ($\widetilde{\mathtt{A}}_{mni}$) functions of each PCM mni:

$$\boldsymbol{\mathcal{E}}(\boldsymbol{r},t) \simeq \sum_{m=1}^{M}\sum_{n=1}^{N}\sum_{i=x,y} \mathcal{E}_{mni}(\boldsymbol{r},t)\,\hat{u}_i \simeq \sum_{m=1}^{M}\sum_{n=1}^{N}\sum_{i=x,y} \mathrm{Re}\left\{E_{mni,\omega_0}(\boldsymbol{r},t)\exp(j\omega_0 t)\right\}\hat{u}_i, \tag{E4.1}$$

with:

$$E_{mni,\omega_0}(\boldsymbol{r},t) = \frac{1}{2\pi}\int_{\mathfrak{B}_{\widetilde{\mathtt{A}}}} \widetilde{\mathtt{A}}_{mni}(z,\omega-\omega_0;t)\,F_{mni}(x,y,\omega;z,t)\times \\ \times \exp(-j\Phi_{mni}(z,\omega;t))\exp(j(\omega-\omega_0)t)\,\mathrm{d}\omega; \tag{E4.2}$$

$$\Phi_{mni}(z,\omega;t) = \phi_{mni}(z,\omega;t) - j\frac{1}{2}\alpha_{mn}(\omega)\,z = \int_0^z \beta_{mni}^{(\mathrm{eq})}(\xi,\omega;t)\,\mathrm{d}\xi - j\frac{1}{2}\alpha_{mn}(\omega)\,z. \tag{E4.3}$$

The description of each function included in the above equations is similar to the single-mode regime (see Section 4.2). Now, however, the transversal eigenfunction F_{mni} is a complex function which includes the azimuthal variation of the corresponding LP mode group of the PCM mni, and the power attenuation coefficient α_{mn} is assumed to be different in each core m and each mode n to describe the mode-dependent losses (MDL) in the SDM transmission [198].

Inserting Eqs. (E4.1)-(E4.3) in Maxwell's equations, we derive the following coupled local-mode equation for the PCM $a1x$ in the time domain:[29]

$$\begin{aligned} j\left(\partial_z + \widehat{\mathrm{D}}_{a1x}^{(\mathrm{eq})} + \frac{1}{2}\widehat{\alpha}_{a1}\right)\mathcal{A}_{a1x}(z,t) = &-j\sum_{n=2}^{N}\widehat{\mathrm{X}}_{a1x,anx}^{(\mathrm{eq})}\left(\partial_z + \widehat{\mathrm{D}}_{anx}^{(\mathrm{eq})} + \frac{1}{2}\widehat{\alpha}_{an}\right)\mathcal{A}_{anx}(z,t) \\ &+ \sum_{n=1}^{N}\widehat{\mathrm{M}}_{a1x,any}^{(\mathrm{eq})}\mathcal{A}_{any}(z,t) + \sum_{m\neq a}^{M}\sum_{n=1}^{N}\widehat{\mathrm{K}}_{a1x,mnx}^{(\mathrm{eq})}\mathcal{A}_{mnx}(z,t) \\ &+ \hat{\mathrm{q}}_{a1x}^{(\mathrm{I})}\left(|\mathcal{A}_{a1x}(z,t)|^2\,\mathcal{A}_{a1x}(z,t)\right) \\ &+ \frac{2}{3}\hat{\mathrm{g}}_{a1x,a1y}^{(\mathrm{I})}\left(|\mathcal{A}_{a1y}(z,t)|^2\,\mathcal{A}_{a1x}(z,t)\right) \\ &+ \frac{1}{3}\exp\left(-j2\Delta\phi_{a1y,a1x}^{(0)}(z;t)\right)\hat{\mathrm{g}}_{a1x,a1y}^{(\mathrm{I})}\left(\mathcal{A}_{a1x}^{*}(z,t)\,\mathcal{A}_{a1y}^{2}(z,t)\right) \\ &+ \hat{\mathrm{q}}_{a1x}^{(\mathrm{R})}\left[\left(f(t)*|\mathcal{A}_{a1x}(z,t)|^2\right)\mathcal{A}_{a1x}(z,t)\right] \\ &+ \hat{\mathrm{g}}_{a1x,a1y}^{(\mathrm{R})}\left[\left(h(t)*|\mathcal{A}_{a1y}(z,t)|^2\right)\mathcal{A}_{a1x}(z,t)\right] \\ &+ \frac{1}{2}\hat{\mathrm{g}}_{a1x,a1y}^{(\mathrm{R})}\left\{\left[u(t)*\left(\mathcal{A}_{a1x}(z,t)\,\mathcal{A}_{a1y}^{*}(z,t)\right)\right]\mathcal{A}_{a1y}(z,t)\right\} \\ &+ \frac{1}{2}\exp\left(-j2\Delta\phi_{a1y,a1x}^{(0)}(z;t)\right)\hat{\mathrm{g}}_{a1x,a1y}^{(\mathrm{R})}\times \\ &\times\left\{\left[u(t)*\left(\mathcal{A}_{a1x}^{*}(z,t)\,\mathcal{A}_{a1y}(z,t)\right)\right]\mathcal{A}_{a1y}(z,t)\right\}. \end{aligned} \tag{E4.4}$$

[28] The number of LP modes (N) and PCMs per core ($2N$) can be calculated from the sum of the degeneracy factors $d_{\mathrm{F}}^{(lp)}$ of the propagated LP_{lp} mode groups as $N = 0.5\sum_{lp} d_{\mathrm{F}}^{(lp)}$. As an example, if each core supports the LP_{01} and LP_{11} mode groups, with $d_{\mathrm{F}}^{(01)} = 2$ and $d_{\mathrm{F}}^{(11)} = 4$, then, $N = 3$.

[29] We have assumed a core-to-core distance (d_{ab}) between two cores a and b of the MM-MCF satisfying the condition $d_{ab} > R_{0,a} + R_{0,b} + \max\{R_{0,a}, R_{0,b}\}$, where $R_{0,a(b)}$ is the radius of the core $a(b)$.

The theoretical model is completed by $2N \times M - 1$ additional coupled local-mode equations for the PCMs $mni \neq a1x$, which can be obtained just by exchanging the corresponding subindexes in the above equation. As can be seen, the LHS of Eq. (E4.4) describes the linear propagation of the PCM $a1x$ and the RHS includes the *sources* of the linear and nonlinear MCD (also referred to as intermodal dispersion in the literature). Specifically, we find new terms in the multi-mode regime when comparing Eqs. (4.2.66) and (E4.4). Let us discuss in detail these new terms by analyzing the linear and nonlinear MCD in the next lines.

E4.1 Linear MCD (linear regime)

The mode-coupling dispersion (MCD) can be observed in an MM-MCF between the PCMs of a given core [intra-core MCD (iMCD)] and between the PCMs of different cores [inter-core MCD (IMCD)]. If the iMCD (IMCD) concerns the mode-coupling between PCMs with the same polarization, we will refer to *direct* iMCD (IMCD). In contrast, if the iMCD (IMCD) involves the mode-coupling between PCMs with orthogonal polarizations, we will refer to *cross* iMCD (IMCD). Each MCD type is described in Eq. (E4.4) by the following terms of the RHS:

- **Direct iMCD.** Intermodal dispersion between the PCMs $a1x$ and anx with $n \geq 2$. This effect is modeled by the term:

$$-j\sum_{n=2}^{N}\widehat{\mathrm{X}}_{a1x,anx}^{(\mathrm{eq})}\left(\partial_z+\widehat{\mathrm{D}}_{anx}^{(\mathrm{eq})}+\frac{1}{2}\widehat{\alpha}_{an}\right)\mathcal{A}_{anx}\left(z,t\right), \tag{E4.5}$$

  where $\widehat{\mathrm{X}}_{a1x,anx}^{(\mathrm{eq})}$ is the linear operator modeling the frequency dependence of the mode overlapping between the PCMs $a1x$ and anx:

$$\widehat{\mathrm{X}}_{a1x,anx}^{(\mathrm{eq})}\left(z;t\right):=\sum_{n=0}^{\infty}\frac{\left(-j\right)^n}{n!}\widetilde{X}_{a1x,anx}^{(\mathrm{eq})(n)}\partial_t^n, \tag{E4.6}$$

  with $\widetilde{X}_{a1x,anx}^{(\mathrm{eq})(n)}\left(z;t\right):=\partial_\omega^n\widetilde{X}_{a1x,anx}^{(\mathrm{eq})}\left(z,\omega=\omega_0;t\right)$. In particular, the complex function $\widetilde{X}_{a1x,anx}^{(\mathrm{eq})}$ describes the linear operator $\widehat{\mathrm{X}}_{a1x,anx}^{(\mathrm{eq})}$ in the frequency domain as:

$$\widetilde{X}_{a1x,anx}^{(\mathrm{eq})}\left(z,\omega;t\right):=\exp\left(-j\Delta\phi_{anx,a1x}\left(z,\omega_0;t\right)\right)\widetilde{\chi}_{a1x,anx}\left(z,\omega;t\right), \tag{E4.7}$$

  where $\widetilde{\chi}_{a1x,anx}$ is the MCC defined as:

$$\widetilde{\chi}_{a1x,anx}\left(z,\omega;t\right):=\frac{\beta_{anx,\omega_0}^{(\mathrm{eq})}}{\beta_{a1x,\omega_0}^{(\mathrm{eq})}N_{a1x}}\iint F_{anx}F_{a1x}^{*}\mathrm{d}x\mathrm{d}y, \tag{E4.8}$$

  and $N_{a1x}\left(z,\omega;t\right):=\iint\left|F_{a1x}\right|^2\mathrm{d}x\mathrm{d}y$. Note that in absence of fiber perturbations we find that $\iint F_{anx}F_{a1x}^{*}\mathrm{d}x\mathrm{d}y=0$ due to the orthogonal condition between the LP modes [124]. Moreover, $\widehat{\mathrm{D}}_{anx}^{(\mathrm{eq})}$ is the equivalent dispersion operator of the PCM anx accounting for the frequency dependence of the ideal phase constant $\beta_{anx}\left(\omega\right)$ and the MCF perturbations $\beta_{anx}^{(\mathrm{B+S})}\left(z,\omega;t\right)$:

$$\widehat{\mathrm{D}}_{anx}^{(\mathrm{eq})}\left(z;t\right):=\sum_{n=1}^{\infty}\frac{\left(-j\right)^{n-1}}{n!}\beta_{anx,\omega_0}^{(\mathrm{eq})(n)}\partial_t^n, \tag{E4.9}$$

  $\beta_{anx,\omega_0}^{(\mathrm{eq})(n)}\left(z;t\right):=\partial_\omega^n\beta_{anx}^{(\mathrm{eq})}\left(z,\omega=\omega_0;t\right)$ and $\widehat{\alpha}_{an}$ describes the temporal dispersion induced by the frequency dependence of $\alpha_{an}\left(\omega\right)$. Interestingly, note that the CCD of the direct iMCD is modeled by the MCCs $\widetilde{\chi}_{a1x,anx}$ and $\widetilde{\chi}_{anx,a1x}$, and the PhMD by the phase-mismatching function $\Delta\phi_{anx,a1x}$, both dispersive effects modeled by the linear operators $\widehat{\mathrm{X}}_{a1x,anx}^{(\mathrm{eq})}$, $\widehat{\mathrm{X}}_{anx,a1x}^{(\mathrm{eq})}$, $\widehat{\mathrm{D}}_{a1x}^{(\mathrm{eq})}$, and $\widehat{\mathrm{D}}_{anx}^{(\mathrm{eq})}$.

- **Cross iMCD.** Intermodal dispersion between the PCMs $a1x$ and any with $n \geq 1$. This effect is modeled by the term:

$$\sum_{n=1}^{N} \widehat{\mathrm{M}}_{a1x,any}^{(\mathrm{eq})} \mathcal{A}_{any}(z,t), \tag{E4.10}$$

where the linear operator $\widehat{\mathrm{M}}_{a1x,any}^{(\mathrm{eq})}$ accounts for the frequency dependence of the mode overlapping between the PCMs $a1x$ and any:

$$\widehat{\mathrm{M}}_{a1x,any}^{(\mathrm{eq})}(z;t) := \sum_{n=0}^{\infty} \frac{(-j)^n}{n!} \widetilde{M}_{a1x,any}^{(\mathrm{eq})(n)} \partial_t^n, \tag{E4.11}$$

with $\widetilde{M}_{a1x,any}^{(\mathrm{eq})(n)}(z;t) := \partial_\omega^n \widetilde{M}_{a1x,any}^{(\mathrm{eq})}(z,\omega=\omega_0;t)$. The complex function $\widetilde{M}_{a1x,any}^{(\mathrm{eq})}$ is defined as $\widetilde{M}_{a1x,any}^{(\mathrm{eq})}(z,\omega;t) := \exp\left(-j\Delta\phi_{any,a1x}(z,\omega_0;t)\right) \widetilde{m}_{a1x,any}(z,\omega;t)$, where $\widetilde{m}_{a1x,any}$ is the MCC given by the expression:

$$\widetilde{m}_{a1x,any}(z,\omega;t) := \frac{\omega^2}{2c_0^2 \beta_{a1x,\omega_0}^{(\mathrm{eq})} N_{a1x}} \iint \widetilde{\sigma} F_{any} F_{a1x}^* \mathrm{d}x\mathrm{d}y. \tag{E4.12}$$

In ideal conditions, $\widetilde{\sigma} = 0$. Along these lines, it should be taken into account that the cross iMCD is described not only by the linear operators $\widehat{\mathrm{M}}_{a1x,any}^{(\mathrm{eq})}$ and $\widehat{\mathrm{M}}_{any,a1x}^{(\mathrm{eq})}$, but also by the linear operators $\widehat{\mathrm{D}}_{a1x}^{(\mathrm{eq})}$ and $\widehat{\mathrm{D}}_{any}^{(\mathrm{eq})}$ of the coupled local-mode equations.

- **Direct IMCD.** Intermodal dispersion between the PCMs $a1x$ and mnx with $m \neq a$ and $n \geq 1$. This effect is modeled in Eq. (E4.4) by the term:

$$\sum_{m\neq a}^{M} \sum_{n=1}^{N} \widehat{\mathrm{K}}_{a1x,mnx}^{(\mathrm{eq})} \mathcal{A}_{mnx}(z,t). \tag{E4.13}$$

The linear operator $\widehat{\mathrm{K}}_{a1x,mnx}^{(\mathrm{eq})}$, defined as:

$$\widehat{\mathrm{K}}_{a1x,mnx}^{(\mathrm{eq})}(z;t) := \sum_{n=0}^{\infty} \frac{(-j)^n}{n!} \widetilde{K}_{a1x,mnx}^{(\mathrm{eq})(n)} \partial_t^n, \tag{E4.14}$$

with $\widetilde{K}_{a1x,mnx}^{(\mathrm{eq})(n)}(z;t) := \partial_\omega^n \widetilde{K}_{a1x,mnx}^{(\mathrm{eq})}(z,\omega=\omega_0;t)$, describes the temporal dispersion induced by the frequency dependence of the complex function $\widetilde{K}_{a1x,mnx}^{(\mathrm{eq})}$:

$$\widetilde{K}_{a1x,mnx}^{(\mathrm{eq})}(z,\omega;t) := \exp\left(-j\Delta\phi_{mnx,a1x}(z,\omega_0;t)\right) \widetilde{\kappa}_{a1x,mnx}(z,\omega;t), \tag{E4.15}$$

where $\widetilde{\kappa}_{a1x,mnx}$ is the MCC:

$$\widetilde{\kappa}_{a1x,mnx}(z,\omega;t) := \frac{\omega^2}{2c_0^2 \beta_{a1x,\omega_0}^{(\mathrm{eq})} N_{a1x}} \iint \Delta\widetilde{\varepsilon}_{\mathrm{r},ax} F_{mnx} F_{a1x}^* \mathrm{d}x\mathrm{d}y. \tag{E4.16}$$

Hence, the direct IMCD (CCD+PhMD) is modeled in the time domain by the linear operators $\widehat{\mathrm{K}}_{a1x,mnx}^{(\mathrm{eq})}$, $\widehat{\mathrm{K}}_{mnx,a1x}^{(\mathrm{eq})}$, $\widehat{\mathrm{D}}_{a1x}^{(\mathrm{eq})}$, and $\widehat{\mathrm{D}}_{mnx}^{(\mathrm{eq})}$.

- **Cross IMCD.** Intermodal dispersion between the PCMs $a1x$ and mny with $m \neq a$ and $n \geq 1$. Specifically, the mode overlapping between these PCMs is modeled in the frequency domain by the MCC:

$$\widetilde{\eta}_{a1x,mny}(z,\omega;t) := \frac{\omega^2}{2c_0^2 \beta_{a1x,\omega_0}^{(\mathrm{eq})} N_{a1x}} \iint \widetilde{\sigma} F_{mny} F_{a1x}^* \mathrm{d}x\mathrm{d}y. \tag{E4.17}$$

Nevertheless, the longitudinal and temporal average value of the ratio $\widetilde{\eta}_{a1x,mny}/\widetilde{\kappa}_{a1x,mnx}$ is of the order of 10^{-3} (or lower) for a realistic average value of the fiber twist rate lower than 6 turns/m. Consequently, we have neglected this term in Eq. (E4.4). Thus, it is natural to ask how the cross IMCD is modeled in the CLMT. As demonstrated in Chapter 3 [see Fig. 3.2(b)], in the monochromatic regime, the XIC-XT depends directly on the iC-XT and the DIC-XT of both cores. Remarkably, given that a non-monochromatic wave can be expressed as a linear combination of multiple monochromatic waves, we can extrapolate the above result to the non-monochromatic regime. Therefore, we conclude that the cross IMCD depends directly on the iMCD and the direct IMCD, modeled via the linear operators $\widehat{\mathrm{X}}^{(\mathrm{eq})}$, $\widehat{\mathrm{M}}^{(\mathrm{eq})}$, $\widehat{\mathrm{K}}^{(\mathrm{eq})}$, and $\widehat{\mathrm{D}}^{(\mathrm{eq})}$.

In spite of the fact that there are additional MCCs modeling the *linear* iMCD and IMCD in Eq. (E4.4), in general, these MCCs can be neglected when assuming a core-to-core distance satisfying the condition indicated in footnote 29. Specifically, in Eq. (E4.4), we have retained the predominant linear operators. Otherwise, the linear self-coupling effect must be included in this equation generalizing the MCC given by Eq. (3.2.26) to the frequency domain.

Interestingly, in the multi-mode regime, we can perform the same theoretical discussion of the linear MCD as in the single-mode regime (see Section 4.3). Along this line, it should be noted that the LTIs given by Eqs. (4.3.15) and (4.3.16) can also be employed to analyze the impact of the intermodal dispersion between higher-order LP modes of the same core or different cores, but calculating the appropriate value of the corresponding MCCs and phase-mismatching functions. This finding will be of special interest to us in Chapter 7.

E4.2 Nonlinear MCD (nonlinear regime)

In the nonlinear regime, assuming a core-to-core distance satisfying the aforementioned condition in footnote 29, the nonlinear IMCD can be neglected. Consequently, the predominant nonlinear MCD is the iMCD, and more specifically, the nonlinear iMCD between degenerate ($\Delta\phi = 0$) or quasi-degenerate ($\Delta\phi \simeq 0$) PCMs. In this scenario, the iMCD between non-degenerate PCMs is suppressed when the *ideal* differential mode group delay[30] (DMGD), calculated as $\left|\Delta\beta^{(1)}\right|$ by omitting the medium perturbations, is higher than 50 ps/km [199]. This condition is usually satisfied in few-mode fibers and multi-mode fibers with a classical step-index profile operating in the third transmission window [8, 18]. In such circumstances, the predominant nonlinear MCD in Eq. (E4.4) arises from the nonlinear interaction between the PCMs $a1x$-$a1x$ and $a1x$-$a1y$.

However, an additional consideration should be pointed out for future works. The coupled local-mode equations modeling in their LHS the linear propagation of a PCM associated with an LP mode group with azimuthal variation will have new nonlinear MCCs. In such a case, note that we should distinguish between the nonlinear terms $|E_{i,\omega_0}|^2 E_{j,\omega_0}$ and $E_{i,\omega_0}^2 E_{j,-\omega_0}$ [$\forall\ (i,j) \in \{x,y\}^2$ and $i \neq j$] in the coupled-wave equations when F_{mni} is a complex function because $|F_{mni}|^2 \neq F_{mni}^2$.

E4.3 Multi-mode ERIM

Finally, we discuss the extension of the equivalent refractive index model (ERIM) to the multi-mode regime. In order to calculate the exact value of the equivalent refractive index $n_{mni}^{(\mathrm{eq})}$ of each PCM mni, now, we should use the *effective* principal refractive index $n_{mni}^{(\mathrm{eff})}$ instead of the MCF principal refractive index n_{mi}. Therefore, Eqs. (C4.3)-(C4.8) should be restated as:

[30] We must clarify here the difference between the differential mode group delay (DMGD) and the differential group delay (DGD). In the photonics literature, the DMGD is usually employed to indicate the difference between the group delay of PCMs of different LP mode groups (e.g., $\mathrm{LP}_{01,x}$ and $\mathrm{LP}_{02,x}$). In contrast, the DGD is usually employed to indicate the difference between the group delay of PCMs of the same LP mode group (e.g., $\mathrm{LP}_{01,x}$ and $\mathrm{LP}_{01,y}$). As seen, both parameters represent the same concept and can be found in the literature defined: (*i*) as a function of the absolute value of the difference between the group delays of the PCMs under analysis (in ps), or (*ii*) as a function of the absolute value of the difference between the group delays *per unit of length* of the PCMs under analysis (in ps/km). In this appendix, we use the latter definition.

$$\phi_{mni,l}(z,\omega;t)=\int_{\langle h\rangle}\beta_{mni,l}^{(\mathrm{eq})}(z,\omega;t)\,\mathrm{d}z\simeq\left[\beta_{mni}(\omega)+\beta_{mni,l}^{(\mathrm{B+S})}(z,\omega;t)\right]h; \tag{E4.18}$$

$$\beta_{mni}(\omega)\simeq\frac{\omega_0}{c_0}n_{mni}^{(\mathrm{eff})}(\omega_0)+\sum_{k=1}^{3}\frac{1}{k!}(\omega-\omega_0)^k\beta_{mni,\omega_0}^{(k)}; \tag{E4.19}$$

$$\beta_{mni,l}^{(\mathrm{B+S})}(z,\omega;t)\simeq\frac{\omega}{c_0}n_{mni,l}^{(\mathrm{B+S})}(z,\omega_0;t)=\frac{\omega}{c_0}\left(n_{mni,l}^{(\mathrm{eq})}(z,\omega_0;t)-n_{mni}^{(\mathrm{eff})}(\omega_0)\right); \tag{E4.20}$$

$$n_{mni,l}^{(\mathrm{eq})}(z,\omega_0;t)\simeq n_{mni,l}^{(\mathrm{eff})}(\omega_0;t)\left[1+\frac{d_m}{R_{\mathrm{B},l}(t)}\cos\left(2\pi f_{\mathrm{T},l}(t)\,z+\theta_0+\theta_m\right)\right]; \tag{E4.21}$$

$$n_{mni,l}^{(\mathrm{eff})}(\omega_0;t)\sim n_{mni}^{(\mathrm{eff})}(\omega_0)\pm\frac{1}{2}\mathrm{N}\left(\Delta n_m(\omega_0;t),\delta n_{mn,l}(\omega_0;t)\right), \tag{E4.22}$$

with '+' if $i=y$ and '−' if $i=x$. The temporal fluctuation of the intrinsic linear birefringence of the PCM mni in the l-th birefringent segment $[n_{mni,l}^{(\mathrm{eff})}(\omega_0;t)]$ is calculated from the Gaussian random process given by Eq. (E4.22). Note that we can estimate the mean $[\Delta n_m(\omega_0;t)]$ of this random process as in the single-mode regime [page 134], i.e., assuming the same mean of the linear birefringence for all the LP modes of a given core. Nonetheless, the variance $[\delta n_{mn,l}(\omega_0;t)]$, which includes the photo-elastic effect in the l-th birefringent segment, should be calculated as:

$$\delta n_{mn,l}(\omega_0;t)\simeq\xi+0.011n_{mn}^3d_{\mathrm{cl}}^2/R_{\mathrm{B},l}^2(t), \tag{E4.23}$$

where $n_{mn}:=\left(n_{mnx}^{(\mathrm{eff})}+n_{mny}^{(\mathrm{eff})}\right)/2$. It can be noted that $n_{mni}^{(\mathrm{eff})}$ can be calculated numerically by using a mode solver. In the case of step-index and LB cores, we can easily estimate analytically $n_{mni}^{(\mathrm{eff})}$ from [32], with $n_{mnx}^{(\mathrm{eff})}=n_{mny}^{(\mathrm{eff})}\equiv n_{mn}^{(\mathrm{eff})}$. In the case of HB cores, with $n_{mnx}^{(\mathrm{eff})}\neq n_{mny}^{(\mathrm{eff})}$, $n_{mni}^{(\mathrm{eff})}$ can be estimated from [161].

Chapter 5

Multi-core fiber in the optical fronthaul

5.1 Introduction

Once we have investigated the fundamentals of the linear and nonlinear propagation in MCFs, we will be able to investigate the suitability of the MCF technology in different branches of science (see Section 1.4 for more details). Specifically, in this chapter, we will study the use of MCF media to perform space-division multiplexing (SDM) transmissions in optical transport networks.

SDM systems using MCFs along with additional peripheral devices for optical connection have been extensively investigated in recent years as a potential solution to cover the exponential growth of data traffic demand in optical networks [8, 12]. Cloud radio-access network (C-RAN) systems should also deal with this huge future capacity demand in the next-generation wireless systems: 5G cellular technology and Beyond-5G [56, 57]. According to some telecom equipment manufacturers, it is expected that 5G cellular networks will be required to provide 1000 times higher mobile data traffic in 2025 as compared with 2013, including flexibility and adaptability solutions to maximize the energy efficiency of the network [58, 59]. A new radio-access model supporting massive data uploading will be required considering additional transport facilities provided by the physical layer [56–59].

Fronthaul connectivity performed by radio-over-fiber (RoF) transmission using single-input single-output (SISO), multiple-input multiple-output (MIMO), sub-Nyquist sampling, and ultra-wideband signals exceeding 400 MHz bandwidth has been proposed for the 5G cellular generation [57, 60–62]. The required channel capacity is further extended in the case of Beyond-5G systems, where a massive number of antennas operating in MIMO configuration should be connected by using RoF. To overcome the massive increment in the data capacity demand, MCF has been recently proposed as a suitable medium for LTE-Advanced (LTE-A) MIMO fronthaul systems [63, 64].

MCF technology opens up attractive possibilities in RoF systems: different wireless signals can be transmitted simultaneously over the same optical wavelengths and electrical frequencies in different cores of the optical waveguide to provide multi-wireless service using a single laser at the transmitter. Thus, MCF can be proposed as an alternative to the standard SM-SCF, termed in the literature as the standard single-mode fiber (SSMF), providing fronthaul connectivity using multiple wavelength channels with multiple lasers. Additionally, MCFs with a high core density are suitable for connecting large phase array antennas performing multi-user MIMO (MU-MIMO) processing [200]. Furthermore, network operators can offer a dynamic and scalable capacity in the next cellular generation due to the aggregated channel capacity provided by the MCF technology. Along this line, the possibility of combining MCF-RoF transmissions with additional multiplexing techniques as wavelength-division multiplexing (WDM), time-division multiplexing (TDM), optical polarization-division multiplexing (PDM) and mode-division multiplexing (MDM)

should be considered. Figure 5.1 depicts the proposed fronthaul provision applied to converged fiber-wireless passive optical networks (PON) and including PDM to provide connectivity between the SSMF and MCF media. In such a scenario, MCF transmissions should also deal with the IC-XT as one of the majors physical impairments, which presents a stochastic nature due to the fiber perturbations, as investigated in Chapters 2, 3 and 4.

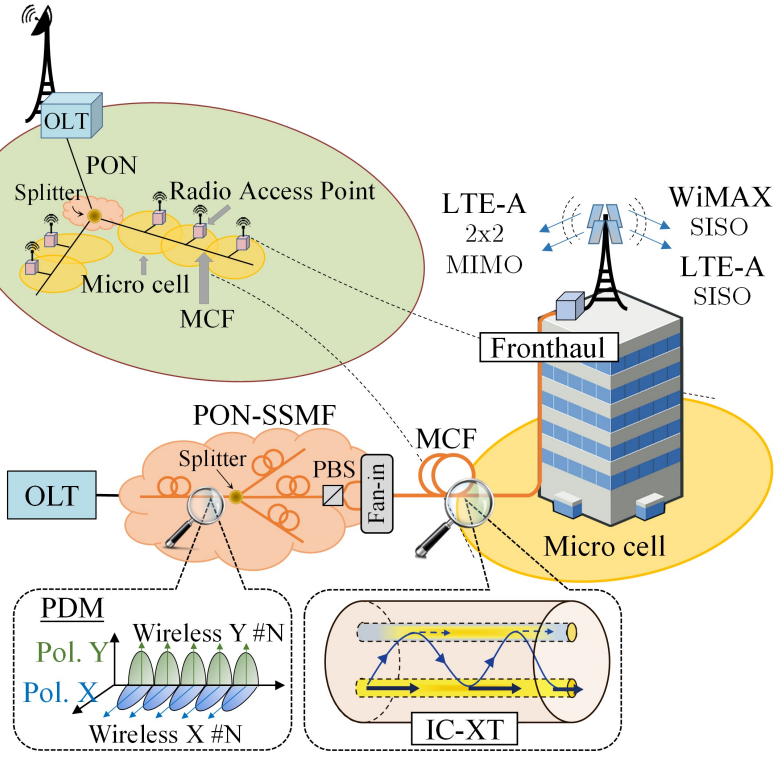

Figure 5.1. Next-generation optical fronthaul system using MCF media operating with a converged fiber-wireless PON and including optical polarization-division multiplexing (PDM) transmission [65].

In order to investigate the suitability of using the MCF technology in the next-generation RoF fronthaul systems, this chapter reports the experimental evaluation of the tolerance of fully-standard LTE-A signals in MIMO and SISO configurations to the IC-XT. In addition, we report the demonstration of fronthaul provision of both LTE-A and WiMAX signals by performing SDM using a commercial MCF. Interestingly, the error vector magnitude (EVM) will have a stochastic behavior induced by the random nature of the MCF perturbations. In such circumstances, we investigate the EVM random performance in these wireless standards and its impact on the next-generation of MCF-RoF systems.

The chapter is structured as follows. In Section 5.2, we demonstrate experimentally the provision of multi-wireless service fronthaul connectivity in MCF media by simultaneously using RoF transmission of LTE-A and WiMAX signals. Considering the inter-operability between both wireless standards [201], WiMAX is proposed as fallback option to provide connectivity in wireless scenarios where LTE-A service is overloaded [202]. In addition, the impact of IC-XT impairment over the RoF transmission is evaluated in a homogeneous 4-core fiber (4CF) when operating in the linear and nonlinear optical power regimes. The EVM performance is evaluated in both power regimes to investigate the impact of the inter-core and intra-core nonlinear effects. The effective advantage of stimulating the Kerr effect to reduce the EVM fluctuations is proposed and demonstrated. In Section 5.3, we demonstrate the use of PDM of LTE-A and WiMAX signals as an extension of the channel capacity of the optical access network by using additional MCF fronthaul provision. Next, in Section 5.4, the MCF-RoF fronthaul transmission is evaluated by using 2x2 MIMO built-in processing in LTE-A standard signals. In order to investigate the toler-

ance of SISO and MIMO configurations to the IC-XT impairment when transmitted in RoF using an MCF, the EVM degradation due to in-band crosstalk of both configurations is analyzed and compared. Later, MCF evaluation of MIMO and SISO LTE-A RoF transmissions is performed by operating in both linear and nonlinear regimes. Finally, in Section 5.5, the main conclusions of this work are highlighted.

5.2 Multi-wireless LTE-A and WiMAX fronthaul RoF provision using MCF

Most of the recent RoF research for next 5G networks is based on current wireless services such as 4G 3GPP LTE-A for evolved universal terrestrial radio access (E-UTRA) and IEEE 802.16 WiMAX orthogonal frequency-division multiplexing access (OFDMA) for local and metropolitan area networks [203]. The simultaneous transmission of LTE-A signals with additional wireless standards facilitates delivering fixed, portable and mobile wireless services providing the new required multimedia services based on scalable video distribution or massive data uploading [203, 204]. In this scenario WiMAX service could also be used as LTE fallback option to provide reliable service even with overloading throughput. In order to demonstrate the compatibility of LTE-A signals with additional wireless standards, we propose in this section the experimental demonstration of multiservice fronthaul provision using both LTE-A and WiMAX signals in 150-m of a commercial 4CF operating in the linear and nonlinear optical power regimes.

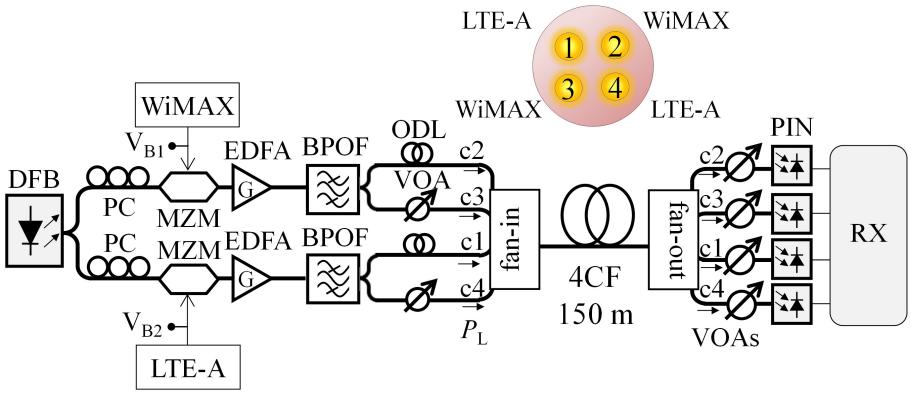

Figure 5.2. Experimental set-up employed for the performance evaluation of LTE-A and WiMAX RoF transmission in 4CF [65].

Figure 5.2 shows the experimental set-up where full-standard wireless LTE-A and WiMAX signals are transmitted using the same optical carrier generated by a continuous-wave (CW) distributed feedback laser (DFB) at 1550.12 nm and splitted by a 3-dB optical coupler. Two external single-drive Mach-Zehnder modulators (MZMs) operating at quadrature bias (QB) point modulate the LTE-A and WiMAX signals in its native frequency and modulation format for RoF transmission. In order to operate in the linear or in the nonlinear power regime of the MCF, the optical power level launched into each core is modified by using two erbium-doped fiber amplifiers (EDFAs) along with two band-pass optical filters (BPOFs) previously to the MCF signal injection. Four independent data signals, transmitted one in each core of the 4CF, are generated by employing two optical delay lines (ODLs). In addition, two variable optical attenuators (VOAs) are inserted to balance the optical power level launched into each core. The mode field diameter of the 4CF employed in the RoF transmissions (Fibercore SM-4C1500-8.0/125) is ~ 8.4 μm, the numerical aperture is 0.15 and the cut-off wavelength is 1410 nm. The MCF was spooled on a reel with an average value of the bending radius and twist rate of 67 cm and 4 turns/m, respectively.

The optical signals are injected and extracted from each core with a 3D fan-in/fan-out with an insertion loss of 4.5 dB. After the MCF-RoF transmission, four independent PIN photodiodes with 0.8 A/W responsivity are used to perform direct detection of the received signals, which are sampled with a real-time oscilloscope DSO91304A and demodulated with Agilent 89600B VSA software.

The LTE-A and WiMAX signals are generated by Agilent ESG 4438C generators following each wireless standard. The 3GPP LTE-A signal comprises two frequency division duplex (FDD) channels of 20 MHz each one with 100 resource blocks (RBs) centered at 2.633 and 2.655 GHz frequencies in the 3GPP band 7, respectively. In addition, the WiMAX signal comprises three IEEE 802.16 FDD channels of 20 MHz bandwidth centered at 3.478, 3.5 and 3.522 GHz, respectively. The LTE-A signals are configured with normal cyclic prefix and the WiMAX signals with 1/8 cyclic prefix. Four LTE-A frames of 10 ms and five WiMAX frames of 5 ms each one are generated by using 64 quadrature amplitude modulation (64QAM) in each OFDM subcarrier.

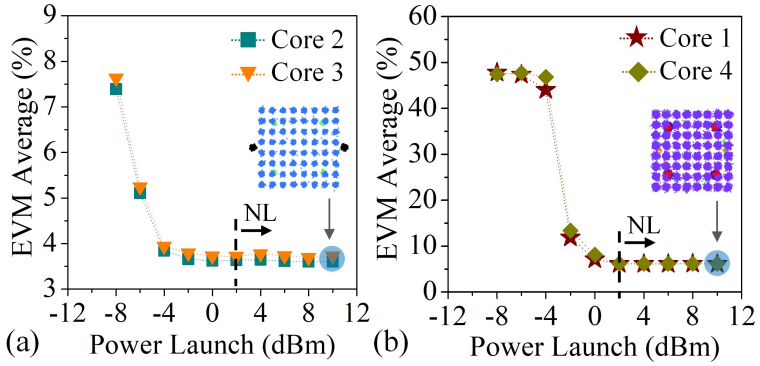

Figure 5.3. Measured EVM average value *vs* optical power level launched into the cores of the 4CF for: (a) WiMAX MCF-RoF transmission in cores 2 and 3, (b) LTE-A MCF-RoF transmission in cores 1 and 4. NL: nonlinear regime [65].

The EVM performance of WiMAX and LTE-A MCF-RoF transmission in the linear and nonlinear power regime is depicted in Fig. 5.3 (including some examples of the received 64QAM constellations). The EVM average values were measured as a function of the optical power launch level. It can be noted that the optimal EVM average performance is achieved with a power launch level higher than 0 dBm for WiMAX signals and 2 dBm for LTE-A signals. In addition, we verified that the EVM performance of both LTE-A and WiMAX channels is not degraded when operating in the nonlinear regime with an optical power launch level higher than 2 dBm, which was found as the critical power of silica MCFs, as detailed in Chapter 2 [Eq. (2.5.35)]. Moreover, it should be remarked that the IC-XT mean increases as the bending radius increases in homogeneous MCFs [Eq. (2.5.14)]. However, it is expected a similar EVM performance when using a bending radius with an average value ($\overline{R}_{\mathrm{B}}$) higher than 67 cm in the 4CF taking into account that the maximum IC-XT mean was estimated around -40 dB from Eq. (2.5.15) with $\overline{R}_{\mathrm{B}} \to \infty$ and $l_c = 4.9$ mm.[1]

As can be seen from Fig. 5.4, the stimulation of the nonlinear regime may be an attractive strategy in MCF-RoF systems to reduce the EVM time fluctuation induced by the IC-XT. Let us remember that the IC-XT has a random nature in both linear and nonlinear power regimes due to the random longitudinal and temporal perturbations of MCF (see Chapters 2 and 3). Therefore, we can also observe stochastic temporal fluctuations in the EVM performance induced by the temporal fluctuations of the optical power exchanged among cores.[2] However, when stimulating a single core with a high optical power level, the Kerr effect mismatches the phase constant of the core modes reducing the IC-XT mean and variance, as demonstrated in Chapter 2. As a result, the temporal fluctuation of the EVM is reduced in both LTE-A and WiMAX signals when operating with high optical power launch levels in a single core of each wireless standard.

[1] The value of l_c was experimentally estimated by using a large bending radius in the MCF reel and fitting Eq. (2.5.15) to the measured value of the IC-XT mean.

[2] In Appendix A5, page 161, we indicate how to calculate the temporal EVM fluctuations induced by the IC-XT.

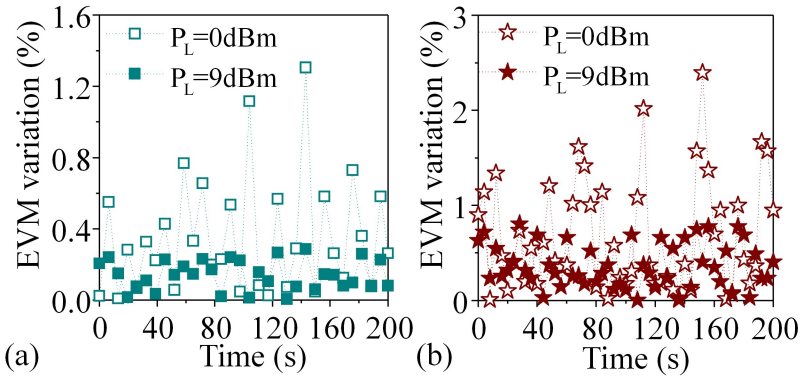

Figure 5.4. Time EVM fluctuation measured for: (a) WiMAX in core 3 and (b) LTE-A in core 1. Optical MCF-RoF transmission operating in the linear (hollow symbols) and nonlinear regime (solid symbols) [65].

Figures 5.4(a) and 5.4(b) show the percentage of the temporal EVM fluctuation induced by the IC-XT (see page 161 for more details) measured in cores 1 and 3 for WiMAX and LTE-A signals, respectively, when injecting an optical power of 0 dBm and 9 dBm in both cores. As a result, the phase constants of the LP_{01} mode between cores 1-4 and 2-3 are mismatched reducing the power exchange between cores carrying the same wireless standard. The experimental results indicate that the EVM time fluctuation is reduced in WiMAX and LTE-A MCF-RoF transmissions when mismatching cores 1-4 and 2-3 stimulating the fiber Kerr nonlinearities.

Moreover, an additional consideration should be pointed out in the fronthaul system proposed in this section. As can be noted from Fig. 5.2, a single DFB laser was employed to minimize the energy consumption in the RoF transmission. However, an alternative approach can also be proposed by using four independent DFBs with four different optical carriers providing more tolerance to hardware failures. In this way, the in-band crosstalk induced by the IC-XT becomes out-band crosstalk reducing the EVM performance degradation in more critical scenarios as in coupled-core MCFs.

5.3 Pol-Mux PON extension capacity using RoF and MCF fronthaul provision

Converged fiber-wireless access using RoF in PON have been proposed and developed in the last decade to connect the base station (BS) to the remote radio head (RRH) [205]. As expected in next 5G networks, a large number of RRHs providing high wireless capacity will be required. Therefore, converged fiber-wireless PON systems using RoF transmissions should also be developed to meet this huge capacity demand [56]. In order to confirm the suitability of the MCF fronthaul system proposed in the previous section when is applied to converged fiber-wireless PON systems using SSMF, we evaluate in this section the transmission of LTE-A and WiMAX signals over a PDM-PON followed by MCF-RoF optical fronthaul. The laboratory set-up employed to evaluate the PDM-PON and the MCF RoF fronthaul is depicted in Fig. 5.5. The proposed RoF system maximizes the PON capacity by aggregating three wireless carriers over two orthogonal optical polarizations followed by MCF-RoF fronthaul connectivity. Three 20-MHz LTE-A carriers are transmitted using polarization A (Pol. A) and three 20-MHz WiMAX carriers are transmitted using the orthogonal polarization (Pol. B) of the same wavelength centered at 1555.75 nm.

The RoF performance is evaluated under the worst-case of in-band interference by selecting the same radio-frequency band centered at 2.5 GHz in both wireless standards, as commercially available in 4G multi-wireless service devices [203]. The 1555.75 nm optical carrier is generated by a CW-DFB and splitted by a 3-dB optical splitter in two paths. RoF transmission is achieved by modulating the full-standard LTE-A and WiMAX signals with MZMs at QB point in the upper and the lower path, respectively. A polarization beam combiner (PBC) is employed to inject both polarizations in a 25.2-km of SSMF.

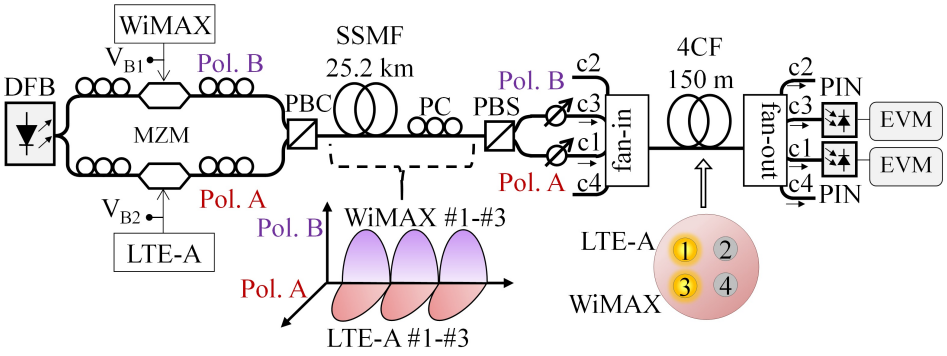

Figure 5.5. Laboratory set-up for the experimental demonstration of PON extension capacity by using optical polarization-division multiplexing (PDM) of LTE-A and WiMAX signals in 25.2-km SSMF (the standard SM-SCF) and optical fronthaul provision in 150-m 4CF [65].

After PON transmission both polarizations are demultiplexed with a polarization beam splitter (PBS) and each wireless standard is transmitted over a different core of the same MCF employed in Section 5.2. Two adjacent cores, specifically cores 1 and 3, were employed to maximize the IC-XT mean around −43 dB.[3] The optical power level launched into each core from the PON was changed from −13 to −6 dBm using two VOAs. At the optical receiver, direct detection was performed using two PIN photodetectors and each RF signal was sampled and demodulated as in Section 5.2. The measured EVM was compared with the wireless standard recommendations at the transmitter antenna for each subcarrier modulation order: $\mathrm{EVM}_{16\mathrm{QAM}} < 12.5\%$ and $\mathrm{EVM}_{64\mathrm{QAM}} < 8\%$ for 3GPP LTE-A, and $\mathrm{EVM}_{16\mathrm{QAM}} < 6\%$ and $\mathrm{EVM}_{64\mathrm{QAM}} < 5\%$ for IEEE 802.16 WiMAX.

The measured spectra at the input of both cores with the presence of the orthogonal polarization is shown in Fig. 5.6. Figure 5.6(a) indicates that a maximum cross-polarization crosstalk[4] of 4.6 dB is detected in core 1 (LTE-A transmission in Pol. A) induced by the interference from Pol. B (WiMAX transmission) generated in the SSMF and in the PBS due to manufacturing imperfections. The crosstalk measured in core 3 for the WiMAX receiver (Pol. B) is 9.2 dB induced by the interference from Pol. A, also generated in the SSMF and PBS [Fig. 5.6(b)].

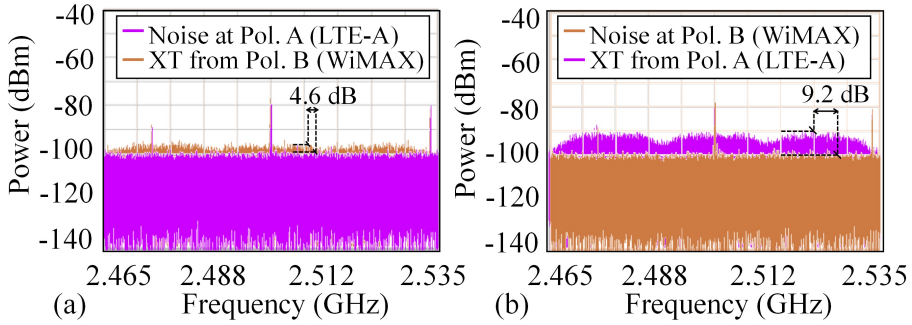

Figure 5.6. Measured electrical spectra of cross-polarization crosstalk *vs* noise floor after 25.2-km SSMF PON and 150-m 4CF transmission for: (a) polarization A carrying three 20-MHz LTE-A carriers and (b) polarization B with three 20-MHz WiMAX carriers [65].

Figure 5.7 shows the measured EVM for both LTE-A and WiMAX signals after the MCF-RoF fronthaul provision as a function of the optical power level launched into each core. We should note the successful transmission for the three LTE-A and WiMAX channels carried by each polarization and each core in the SSMF and 4CF. 3GPP LTE-A antenna limit is satisfied for the three LTE-A channels carried by Pol. A and core 1 when injecting into core 1 an optical power higher than −9 dBm for the 64QAM subcarrier modulation. The required optical power launch is reduced

[3]The IC-XT mean between cores 1 and 3 is detailed in Chapter 2 for different values of $\overline{R}_{\mathrm{B}}$.
[4]The cross-polarization crosstalk is referred to as the iC-XT in Chapter 3.

to −11 dBm when using 16QAM subcarrier modulation over the same bandwidth in the carrier-aggregated RoF transmission. Moreover, in the WiMAX RoF transmission carried by Pol. B and core 3, the optical power launch required in core 3 to meet the IEEE 802.16 WiMAX antenna limit is increased to −7 dBm for both 16QAM and 64QAM subcarrier modulations. It should be noted that WiMAX requires a higher optical power operation level due to the higher cross-polarization interference observed in Pol. B.

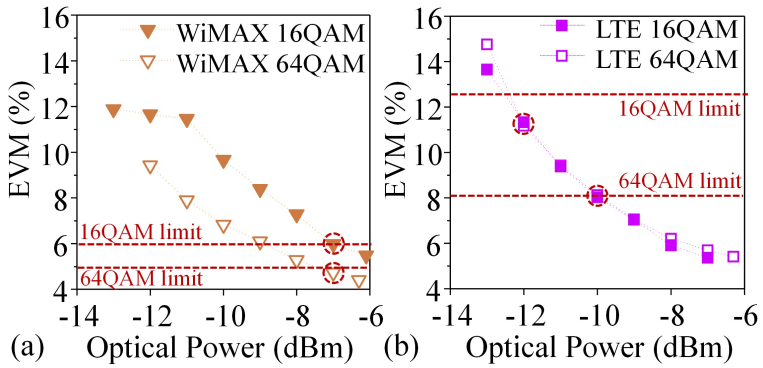

Figure 5.7. Measured EVM at the receiver *vs* optical power launched into cores 1 and 3 for: (a) WiMAX and (b) LTE-A RoF transmission [65].

5.4 Fronthaul extension capacity in MCF-RoF: improvement using MIMO processing

As commented before, MCF fronthaul capacity can be extended by using RoF transmission and MIMO processing. However, in this kind of fibers, the random power exchange among core modes and its impact on the additional signal processing of MIMO MCF-RoF transmissions should be investigated and compared with SISO configuration. The 2x2 MIMO processing algorithm used in this experimental evaluation is implemented in current LTE-A devices meeting 3GPP standard for wireless multipath compensation.

Employing different wavelengths in each excited core of the MCF, the IC-XT generates out-band crosstalk minimizing the EVM degradation due to mode-coupling among cores. Nonetheless, in order to reduce the energy consumption in the RoF transmission, a single optical carrier is employed to illuminate the cores of the MCF and, hence, the IC-XT becomes in-band crosstalk. In this section, we first analyze the tolerance of LTE-A RoF transmissions to in-band crosstalk comparing both MIMO and SISO configurations, and later, the performance of MIMO and SISO LTE-A is investigated in an MCF by using a single optical carrier to illuminate the different cores of the fiber.

5.4.1 Tolerance of LTE-A RoF transmissions to in-band crosstalk

In-band crosstalk is referred to as the interference between two different signals using the same central frequency. In the same way, IC-XT can be classified as in-band crosstalk when using the same optical carrier in each core. The experimental evaluation of the LTE-A RoF tolerance to in-band crosstalk becomes necessary to understand the propagation performance of LTE-A RoF transmissions in MCF media.

If we consider a 2x2 MIMO LTE-A transmission performing SDM, we refer to crosstalk induced by internal interference to the crosstalk between the master and slave signals containing different data that compose the 2x2 MIMO LTE-A [206]. In contrast, the crosstalk induced by external interference refers to the crosstalk between different signals, e.g. the 2x2 MIMO signal interfering with other external source. In this case, in order to evaluate the worst-case scenario, we use different signals with the same central frequency and bandwidth to have in-band interference.

Consequently, in RoF transmissions using MCF media, the IC-XT of a 2x2 MIMO transmitter is referred to as internal IC-XT, while the external IC-XT can be observed among cores carrying signals from different transmitters.

The evaluation of the impact of in-band crosstalk in LTE-A RoF transmissions should be performed by considering different crosstalk levels. In uncoupled-core MCFs, IC-XT presents a random nature with a reduced crosstalk mean and variance (see Chapter 2). Therefore, the in-band crosstalk evaluation in LTE-A RoF transmissions should be performed by using optical couplers and SSMF in order to force higher crosstalk levels than in an uncoupled-core MCF.

The LTE-A signals evaluated in this experiment are generated as in the previous sections, with a 2.655 GHz central frequency using the maximum LTE channel bandwidth of 20 MHz. In this case, we compare the RoF performance by using both SISO and MIMO transmissions. LTE-A 2x2 MIMO transmission is configured with SDM considering 2 layers without cyclic delay diversity.

In both in-band crosstalk cases (internal and external interference), it should be remarked that the experimental evaluation is performed with the same LTE-A SISO signals using the same modulation order and bandwidth as the MIMO configuration. The comparison of the crosstalk tolerance of MIMO and SISO RoF transmission should be additionally performed to evaluate the capability of the 3GPP MIMO algorithms to deal with the in-band crosstalk impairment when using MCF-RoF. Furthermore, it should be noted that using 2x2 MIMO configuration, two layers of different data are spatially multiplexed in comparison with SISO transmission. Hence, almost double bit rate is provided in MIMO compared with SISO configuration over the same bandwidth and with the same modulation order.

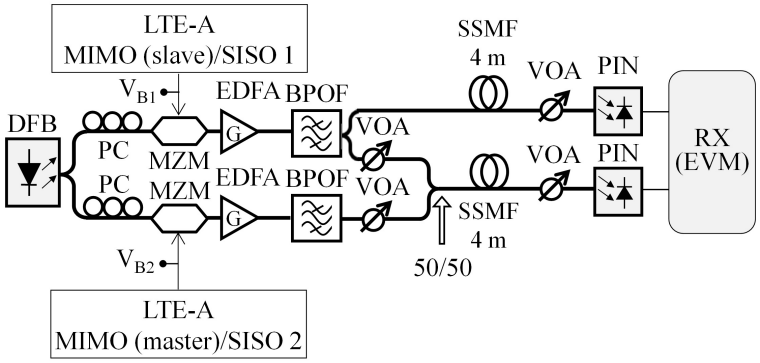

Figure 5.8. Experimental set-up employed for the evaluation of the in-band crosstalk induced by internal interference in RoF LTE-A MIMO and SISO transmissions [65].

The tolerance of 2x2 MIMO LTE-A RoF transmissions to internal interference between the master and slave signals is evaluated by using the experimental set-up depicted in Fig. 5.8. The optical system emulates a 2x2 MIMO transmission using a single optical carrier at 1550.12 nm and splitted in two paths with a 3-dB optical splitter. Each path is modulated by the LTE-A signal using a single-drive MZM operating at QB point. Additional EDFAs, BPOFs and VOAs are included in the laboratory set-up to induce high crosstalk levels in the optical signals. Two short SSMF patch cords with 4-m length were employed to emulate an MCF propagation scenario with tunable IC-XT mean. The internal interference is extracted from the upper path and injected into the lower path with a 3 dB optical coupler. The VOAs at the transmitter are used to control the in-band crosstalk level induced in the lower path and the VOAs at the receiver are used to keep balanced the received optical power in each photodiode.

The internal interference in MIMO and the external interference in SISO are evaluated by modifying the crosstalk level from -45 to -30 dB in the lower path. The experimental measurements depicted in Figs. 5.9 and 5.12 correspond to the lower optical path of each laboratory set-up. The crosstalk tolerance of both scenarios is analyzed by calculating the EVM penalty as a function of the induced crosstalk level. The EVM penalty is calculated as the difference between the EVM (in %) obtained with the minimum crosstalk level (XT $= -\infty$ dB) and the EVM (in %) measured with the current crosstalk level induced with the VOAs and the optical coupler.

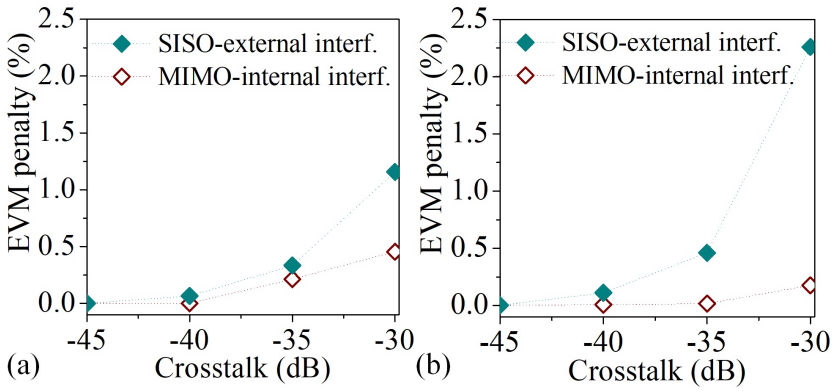

Figure 5.9. Measured RoF LTE-A EVM penalty: (a) 16QAM and (b) 64QAM subcarrier modulation [65].

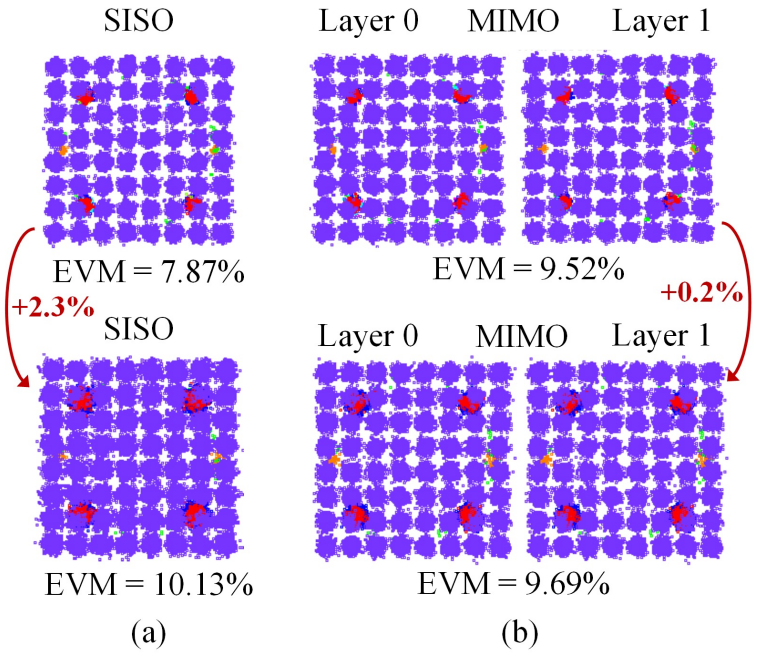

Figure 5.10. Measured constellations of SISO and 2x2 MIMO 64QAM LTE-A with: (a) $EVM_{penalty} = 2.3\%$ and (b) $EVM_{penalty} = 0.2\%$ [65].

Figures 5.9(a) and (b) show the measured EVM penalty as a function of the internal crosstalk level when using 16QAM and 64QAM subcarrier modulations, respectively. It can be observed that the EVM penalty in MIMO has a lower slope than in SISO. Therefore, the EVM performance of SISO configuration presents a higher degradation than MIMO for each in-band crosstalk level. As a result, we conclude that MIMO transmission has a better tolerance than SISO configuration to in-band crosstalk. These results confirm the successful tolerance of MIMO LTE-A transmission to in-band crosstalk induced by internal interference. In addition, Fig. 5.10 shows the impact on the received 64QAM constellations of -30 dB of in-band crosstalk generated by internal interference in MIMO and external interference in SISO. The digital constellations confirm that 2x2 MIMO LTE-A shows a better tolerance than SISO when the in-band crosstalk level is increased. Consequently, it is expected that LTE-A RoF transmission will present a better performance in coupled-core MCFs using MIMO than using SISO over the same bandwidth.

On the other hand, the tolerance analysis of the MIMO and SISO LTE-A signals to in-band crosstalk induced by an external interference is performed by using the experimental set up depicted in Fig. 5.11. Please note that the difference between Fig. 5.8 and Fig. 5.11 is based on the use of

an external interfering signal in the latter case. The external interference is generated by an arbitrary waveform generator (AWG) with the same electrical bandwidth (20 MHz) and in the same frequency band (at 2.655 GHz center frequency). In addition, it should be remarked that no EDFAs were included in this set-up because it is not necessary to preserve the optical power budget between the two paths considering that the power level injected into the lower path is not extracted from the upper path in this case.

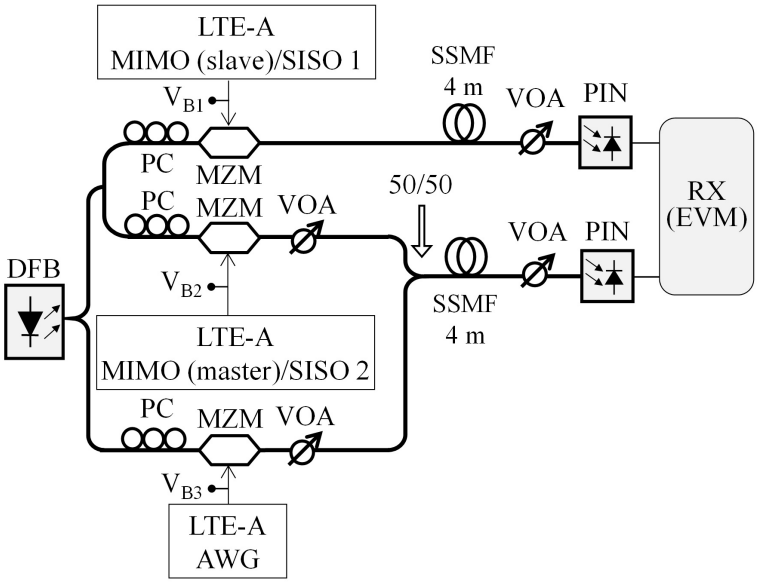

Figure 5.11. Experimental set-up used for the evaluation of in-band crosstalk induced by external interference in RoF LTE-A MIMO and SISO transmissions [65].

Figures 5.12(a) and (b) show the EVM penalty as a function of the crosstalk level induced by external interference considering 16QAM and 64QAM subcarrier modulations, respectively. In both cases, MIMO presents a lower EVM penalty than SISO for any in-band crosstalk level induced by the external interfering signal. It should be noted that the EVM penalty evolution presents a lower slope in MIMO than in SISO. Hence, the EVM performance has a lower degradation in MIMO for each crosstalk value induced by the external interference. Consequently, MIMO configuration can be an interesting option to perform SDM optical transmissions in MCF media with high IC-XT levels when using higher-order modulation formats. Furthermore, Fig. 5.13 depicts the degradation of digital constellations of the received 64QAM LTE-A signals in SISO and MIMO configurations when the power of the external interfering signal is increased. It can also be observed from Fig. 5.13 that SISO constellation is more degraded than MIMO, in line with Fig. 5.12(b).

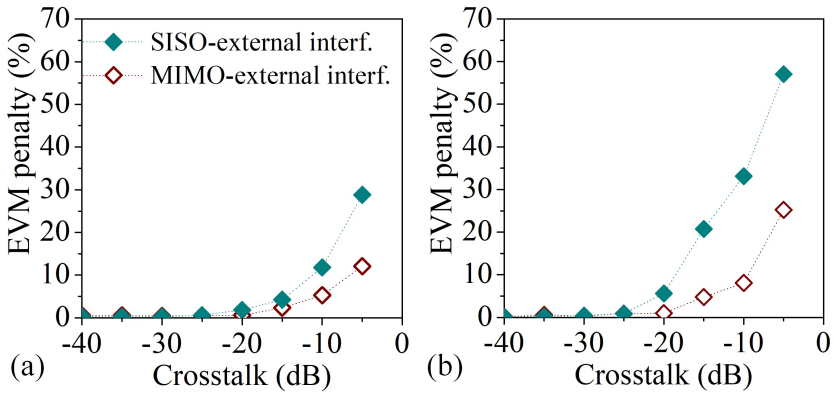

Figure 5.12. Measured RoF LTE-A EVM penalty: (a) 16QAM and (b) 64QAM subcarrier modulation [65].

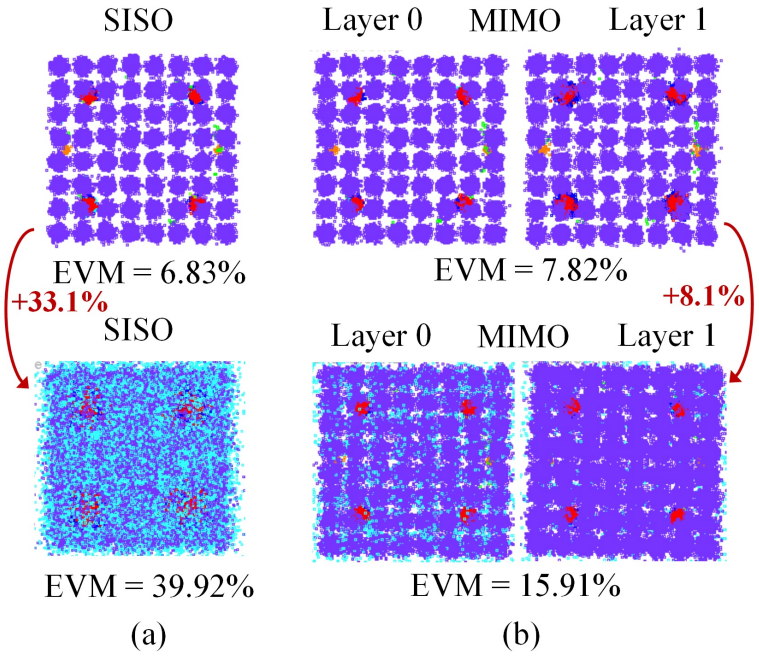

Figure 5.13. Measured constellations of SISO and 2x2 MIMO 64QAM LTE-A with: (a) $EVM_{penalty} = 33.1\%$ and (b) $EVM_{penalty} = 8.1\%$ [65].

5.4.2 MCF-RoF fronthaul evaluation

MCF fronthaul capacity can additionally be extended by using RoF transmission of full standard LTE-A signals in MIMO configuration. However, the power exchange among the excited cores and its impact on the additional signal processing of MIMO transmissions should be investigated and compared with SISO configuration. In this section, MIMO and SISO configurations of LTE-A signals are experimentally evaluated and compared in a homogeneous 4CF. The impact of the linear and nonlinear IC-XT in the EVM performance is investigated reporting the effective advantage of stimulating the Kerr effect in both MIMO and SISO configurations.

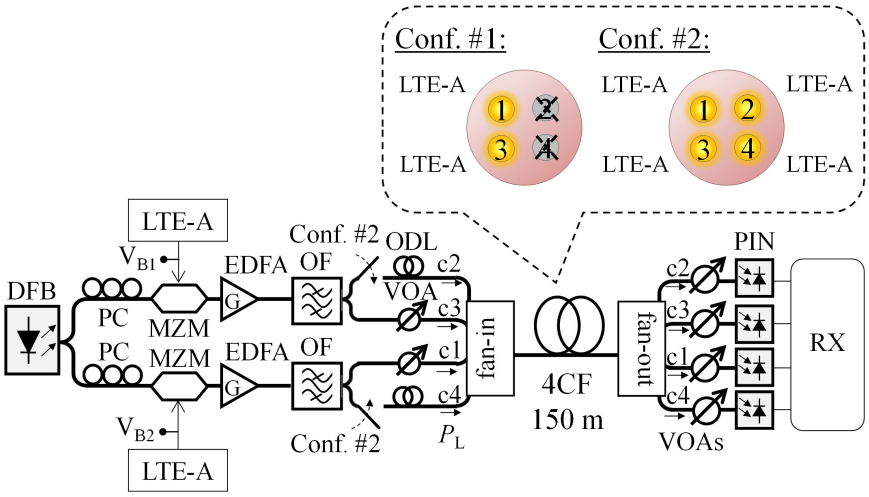

Figure 5.14. Experimental set-up for LTE-A 2x2 MIMO and SISO MCF-RoF transmission using a homogeneous 4CF. Two different MCF-RoF configurations are employed: (#1) using only cores 1 and 3, and (#2) using the four cores of the 4CF [65].

The experimental set-up employed in this section using LTE-A signals is shown in Fig. 5.14. A single carrier is generated at 1550.12 nm and splitted in two branches for optical external modulation. The optimum modulation index of the signal was selected in each case as performed in [63]. Two EDFAs and BPOFs are included previously to the MCF signal injection to stimulate the linear and nonlinear MCF regimes, the same fiber as in the previous sections and spooled on a reel with an average value of the bending radius and twist rate of 67 cm and 4 turns/m, respectively.

Two different MCF-RoF configurations have been used to evaluate the EVM fluctuation of the LTE-A signals induced by the IC-XT in the linear and nonlinear regimes: (#1) comparison of MCF-RoF performance using SISO and 2x2 MIMO configurations for the evaluation of the EVM fluctuation when varying the optical power launched into the cores 1 and 3. And (#2) MCF-RoF transmission of four independent SISO LTE-A signals for the evaluation of EVM fluctuation in the spectral domain using the four cores of the 4CF. Optical decorrelation of the four SISO LTE-A signals is performed using two ODLs and two VOAs to balance the optical power injected in each core. In both MCF-RoF configurations #1 and #2 the full-standard LTE-A wireless signals are centered at 2.633 and 2.655 GHz frequencies in the 3GPP band 7.

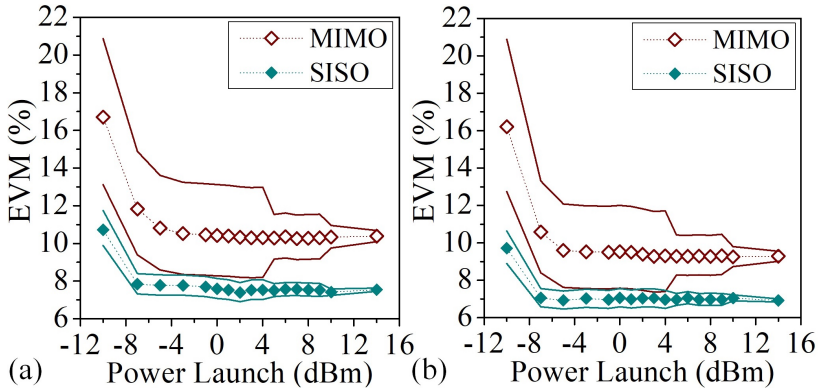

Figure 5.15. Measured EVM average value (dots) and EVM fluctuation margins (solid lines) for 2x2 MIMO and SISO LTE-A MCF-RoF configuration #1 considering: (a) 16QAM and (b) 64QAM subcarrier modulations [65].

The experimental measurements of MCF-RoF configuration #1 for SISO and MIMO transmissions are depicted in Fig. 5.15. The LTE-A EVM performance was measured as a function of the optical power level launched into each core. The MIMO and SISO signals are transmitted in adjacent cores 1 and 3 to evaluate the RoF performance considering the highest IC-XT conditions. The EVM average value (dots) and the maximum and minimum EVM excursion (solid lines) were measured for different optical power levels launched into the cores 1 and 3. In the linear regime, the optical power was increased from −10 dBm to 2 dBm in both cores. In the nonlinear regime, in order to mismatch the phase constant of the core modes, the optical power launch was kept constant 2 dBm in core 3 and was increased from 2 to 14 dBm in core 1.

As can be seen, MIMO configuration has a higher EVM fluctuation than SISO and worse EVM average performance. In MCF media with uncoupled cores and low IC-XT mean, a better EVM performance can be achieved with SISO configuration for the same modulation order, but MIMO achieves higher data rate. Furthermore, stimulating a single core with high power levels, the index mismatching between cores 1 and 3 increases, which reduces the EVM fluctuation in both SISO and MIMO MCF-RoF configurations. This is confirmed in the EVM fluctuation margins depicted in Fig. 5.15. The higher the power level injected into core 1 (keeping constant the power level launched into core 3), the lower the EVM fluctuation in MIMO and SISO configurations due to the variance reduction of the IC-XT in the nonlinear regime (see Fig. 2.10, on page 51). Additionally, as detailed on page 51, the IC-XT mean is also reduced in the nonlinear regime, but the EVM average value is not improved due to the absence of crosstalk penalty in the linear regime (the IC-XT mean is lower than −40 dB in such a case). In addition, it should be remarked that, in general, if

we operate with data rates below 1-Gb/s, the EVM performance is not degraded in OFDM-RoF transmissions when the intra- and inter-core Kerr nonlinearities are stimulated in a silica MCF, as was numerically verified using the OptiSystem software in combination with the CLMT reported in Chapter 4. Consequently, the Kerr nonlinearities can be stimulated in MCF-RoF transmissions to reduce the mean and variance of the IC-XT without EVM penalty.

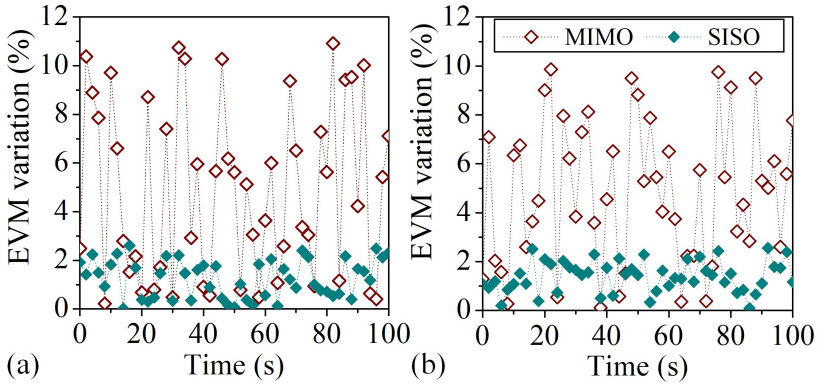

Figure 5.16. Time EVM fluctuation for 2x2 MIMO and SISO LTE-A MCF RoF configuration #1 considering: (a) 16QAM and (b) 64QAM subcarrier modulations [65].

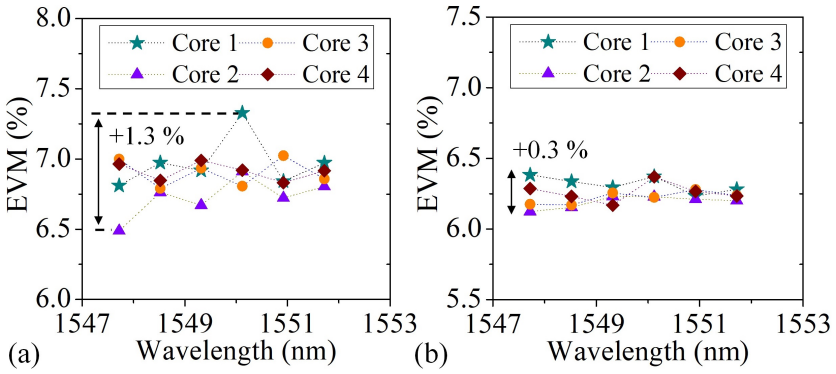

Figure 5.17. Spectral EVM fluctuation measured in SISO LTE-A MCF-RoF configuration #2 injecting an optical power launch level in cores 1 and 4 of: (a) 0 dBm and (b) 9 dBm, with a fixed power launch level of 0 dBm in cores 2 and 3 [65].

For completeness, we investigate the temporal EVM fluctuations induced by the IC-XT in both MIMO and SISO transmissions (MCF-RoF configuration #1). The specific details about the calculation of these temporal EVM fluctuations are indicated in Appendix A5, on page 161. Specifically, the difference of these temporal EVM fluctuations between MIMO and SISO was investigated when operating in the linear regime, where this difference is expected to be maximized, as indicated by Fig. 5.15. Figure 5.16 shows the EVM percentage variation calculated respect to the EVM average level for 100 seconds considering 0 dBm of power launch per core. It is verified from the experimental measurements that the EVM fluctuation is higher in MIMO than in SISO. MIMO has a maximum EVM excursion of 11%, while the maximum excursion in SISO is around 3%. In our personal opinion, we believe that MIMO has a higher EVM fluctuation than SISO because the refreshing period of the MIMO channel matrix [in our case every 42 LTE symbols ($\sim$ 2.8 ms)] may be slower than the rapidly-varying temporal fluctuations of the IC-XT induced by the floor vibrations (see Fig. 3.9 on page 76). Nevertheless, additional experimental work is required to improve our understanding about this question.

Finally, in the MCF-RoF configuration #2, the EVM fluctuation was evaluated in the frequency domain. Given that the phase constant of the core modes is randomized when the wavelength of the optical carrier is modified, the EVM RoF performance is also randomized in the optical spectrum.

We can observe this random behavior in Fig. 5.17(a). The EVM performance varies significantly up to +1.3% with the wavelength in the linear regime. Nevertheless, stimulating the nonlinear regime in cores 1 and 4 with a power launch level of 9 dBm and operating simultaneously in cores 2 and 3 in the linear regime injecting 0 dBm, the phase constant of the LP_{01} mode is mismatched between adjacent cores. This is confirmed with a reduction in the EVM fluctuation between optical carriers from +1.3% to +0.3%, as shown in Fig. 5.17(b). In both power regimes, all cores have an EVM below the EVM 3GPP limit ($EVM_{16QAM} < 12.5\%$), meeting the standard recommendation.

More broadly, in long-reach WDM systems, the EVM fluctuation in the frequency domain should be considered as some optical channels could satisfy the requirements while others could be deeply affected. In such a scenario, the stimulation of adjacent cores carrying the same wireless standard with different optical power launch levels, strategy referred to as the core interleaving nonlinear stimulation (CINLS), is pointed out as an interesting technique to avoid this limitation. In particular, the CINLS induces a phase-mismatching between adjacent cores of the MCF by using different optical power launch levels in each core. Hence, the CINLS proposes to use the Kerr effect to reduce the mean and variance of the IC-XT in order to minimize the temporal and spectral EVM fluctuations between adjacent cores of the MCF.

5.5 Conclusions

In this chapter, we have investigated the use of MCF in next-generation optical fronthaul systems applied to 5G-cellular networks. We have demonstrated the multi-wireless service fronthaul provision using LTE-A and WiMAX signals in MCF to guarantee reliable services connectivity. The experimental investigation of the MCF-RoF performance confirms that the optimal EVM average performance is achieved with a power launch level higher than 0 dBm for WiMAX signals and 2 dBm for LTE-A signals over 150-m of a commercial 4CF. The EVM performance of LTE-A and WiMAX MCF-RoF transmissions is not degraded when operating in the nonlinear MCF regime. The experimental results uncover that we can operate in the nonlinear regime to reduce the temporal EVM fluctuation induced by the IC-XT between cores carrying the same wireless standard. Furthermore, we have proposed the suitability of the MCF fronthaul systems applied to converged fiber-wireless PDM-PONs. LTE-A and WiMAX signals were transmitted over a PDM-PON using a 25.2-km SSMF preceding the MCF fronthaul system.

Considering that the IC-XT mean between two given cores of the 4CF is much lower than the iC-XT in SSMF, MCF technology is proposed to provide fronthaul connectivity as an evolution of the conventional RoF systems. The suitability of in-built 3GPP LTE-A MIMO processing for MCF-RoF transmission was also experimentally evaluated. The tolerance of the LTE-A RoF transmissions to in-band crosstalk was evaluated considering both internal and external interferences in SISO and 2x2 MIMO LTE-A RoF transmissions. It was observed that MIMO processing supports high levels of in-band crosstalk induced by internal and external interference. Therefore, MIMO processing provides better tolerance than SISO to the IC-XT impairment. Finally, SISO and MIMO LTE-A MCF-RoF transmissions were compared when operating in both linear and nonlinear optical power regimes. Although MIMO has a better tolerance to the IC-XT than SISO, lower temporal EVM fluctuations were observed in SISO LTE-A RoF transmission over the MCF medium. Finally, the CINLS strategy was proposed to mismatch the phase constant of adjacent core modes reducing the temporal and spectral EVM fluctuations of SISO and 2x2 MIMO LTE-A MCF-RoF transmissions.

The low IC-XT mean observed between adjacent cores of the 4CF indicates that the major physical impairment in MCF-RoF transmissions may be induced by the power insertion losses of the 3D fan-in/fan-out device. It is expected that the optimal EVM average performance of LTE-A and WiMAX signals may change when considering other MCF types, with different length and IC-XT levels. In this respect, additional investigations should be performed in future works. Along this line, note that the theoretical models reported in previous chapters can be employed to analyze numerically the EVM performance of MCF-RoF transmissions.

Appendix A5: Temporal EVM fluctuations in MCF media

In this appendix, we detail the calculation of the temporal EVM fluctuations (in %) induced by the temporal excursions of the IC-XT (Figs. 5.4 and 5.16). It is worth mentioning that this calculation should take into account the temporal EVM fluctuations induced by the experimental set-up without the presence of the MCF, which will be referred to as the *back-to-back* (B2B) transmission.[5]

Our approach is simple. Let us consider an *end-to-end* (E2E) MCF-RoF transmission with an EVM parameter exhibiting temporal excursions induced by the IC-XT and the B2B transmission. In this scenario, the measured EVM in the E2E transmission ($\mathrm{EVM_{E2E}}$) is found to be:

$$\mathrm{EVM_{E2E}}\left(t\right) = \mathrm{EVM_{E2E}^{(ideal)}} + \Delta\mathrm{EVM_{B2B}}\left(t\right) + \Delta\mathrm{EVM_{IC\text{-}XT}}\left(t\right), \tag{A5.1}$$

where $\mathrm{EVM_{E2E}^{(ideal)}}$ is the ideal EVM performance of the E2E transmission, $\Delta\mathrm{EVM_{B2B}}$ is the temporal excursion of the $\mathrm{EVM_{E2E}}$ induced by the B2B transmission, and $\Delta\mathrm{EVM_{IC\text{-}XT}}$ is the temporal excursion of the $\mathrm{EVM_{E2E}}$ induced by the IC-XT. In particular, we are interested in estimating the term $\Delta\mathrm{EVM_{IC\text{-}XT}}$. To this end, we perform the following steps:

1. First, we measure the term $\Delta\mathrm{EVM_{B2B}}\left(t\right)$. This requires to measure the temporal evolution of the EVM performance in the B2B transmission $[\mathrm{EVM_{B2B}}\left(t\right)]$ in a time interval much higher than the period of the floor vibrations in our laboratory room (e.g. 100 seconds). Then, we calculate $\Delta\mathrm{EVM_{B2B}}\left(t\right)$ as $\Delta\mathrm{EVM_{B2B}}\left(t\right) = \mathrm{EVM_{B2B}}\left(t\right) - \langle\mathrm{EVM_{B2B}}\left(t\right)\rangle$.

2. Second, we estimate the term $\mathrm{EVM_{E2E}^{(ideal)}}$ in the following way. We measure the temporal fluctuations of the EVM in an E2E connection in a time interval of the same duration as in the previous step, i.e., we measure the temporal random process $\mathrm{EVM_{E2E}}\left(t\right)$. Next, we approximate the parameter $\mathrm{EVM_{E2E}^{(ideal)}}$ as $\mathrm{EVM_{E2E}^{(ideal)}} \simeq \langle\mathrm{EVM_{E2E}}\left(t\right)\rangle$.[6]

3. Finally, we calculate the percentage of $\Delta\mathrm{EVM_{IC\text{-}XT}}\left(t\right)$ as:[7]

$$\Delta\mathrm{EVM_{IC\text{-}XT}}\left(t;\%\right) := \frac{\mathrm{EVM_{E2E}}\left(t\right) - \left(\mathrm{EVM_{E2E}^{(ideal)}} + \Delta\mathrm{EVM_{B2B}}\left(t\right)\right)}{\mathrm{EVM_{E2E}^{(ideal)}} + \Delta\mathrm{EVM_{B2B}}\left(t\right)} \times 100. \tag{A5.2}$$

[5] The temporal EVM fluctuations in the B2B transmission can be induced by different reasons, for instance, by the temporal excursions of the QB point in the MZMs.

[6] As an additional option, we could also estimate the value of $\mathrm{EVM_{E2E}^{(ideal)}}$ via numerical simulations of the CLMT by considering a single core.

[7] Another possible *definition* of the percentage $\Delta\mathrm{EVM_{IC\text{-}XT}}\left(t;\%\right)$ could be similar to Eq. (A5.2) but replacing the denominator by $\mathrm{EVM_{E2E}}\left(t\right)$.

This page was intentionally left blank.

Part II

Optical Supersymmetry: Analysis and Synthesis of Fibers and Devices

Chapter 6

Supersymmetry

Preface The close connection between the physics laws of quantum mechanics and classical electromagnetism becomes a fascinating opportunity to explore novel design strategies of MCFs. In this context, the mathematics of supersymmetric quantum mechanics are explored in the second part of this thesis. This approach will allow us to expand the basic functionalities of the MCF technology and, by extension, uncover ground-breaking photonic devices.

6.1 Introduction

A *theory of everything* encompassing a coherent mathematical framework of physics laws that fully explains all physical interactions of the universe is one of the major unsolved problems in physics. In this regard, supersymmetry (SUSY) was originally introduced in 1971 within the context of string and quantum field theory (QFT) as a necessary property of the theoretical models to unify the fundamental interactions known in nature: strong, electroweak, and gravitational interactions [207–209].

For particle theorists, SUSY also offers a potential mathematical framework upon which to propose different dark matter particle candidates [210–214]. Despite these interesting features of supersymmetric models, there has been no experimental evidence of SUSY in nature so far [215]. Nevertheless, the ideas of SUSY have been profitably extended to diverse areas of physics and engineering [216–242], with applications to, e.g., quantum cascade lasers [225], graphene field theory [227], or matter-wave circuits [231].

In particular, one-dimensional (1D) SUSY has attracted special attention in non-relativistic quantum mechanics (QM) and photonics [216,228]. The algebra underneath 1D SUSY allows us to relate two different quantum or optical potentials with identical spectra and scattering properties in the Helmholtz regime. Furthermore, the ideas of 1D SUSY can also be applied to three-dimensional (3D) potentials [241]. Thanks to these interesting features, new quantum potentials have been found analytically solvable [216–221], and a novel class of supersymmetric 1D and 3D optical devices has been recently proposed with unexpected properties for mode-division multiplexing, mode conversion and cloaking applications [228–230, 232–239, 241].

Motivated by these results, we present in this chapter a detailed review of 1D SUSY in QM. The chapter is structured following a similar table of contents as in [243]. In Section 6.2, we perform a historical survey of SUSY in theoretical physics. In Section 6.3, we briefly review a few mathematical concepts that will be fundamental to understand the rich toolbox of 1D SUSY. In Sections 6.4 - 6.12, we describe the theoretical formulation of 1D SUSY in detail revolving around the time-independent Schrödinger equation. In Section 6.13, we discuss the possibility of extrapolating the ideas of 1D SUSY to other fields of physics governed by equations that are formally equal to the time-independent Schrödinger equation. Finally, in Section 6.14, we discuss some fundamental limitations of applying 1D SUSY in other branches of physics and we include a brief description of some omitted topics in this chapter.

6.2 Historical survey

Supersymmetry was born in 1971 within the context of string theory and QFT by means of three independent works: Golfand and Likhtman [207], Ramond [208], and Neveu and Schwarz [209] (see Fig. 6.1). While the first two works gave rise to an immediate breakthrough in string theory, the work of Golfand and Likhtman was simply unnoticed in the literature of QFT during the next years.

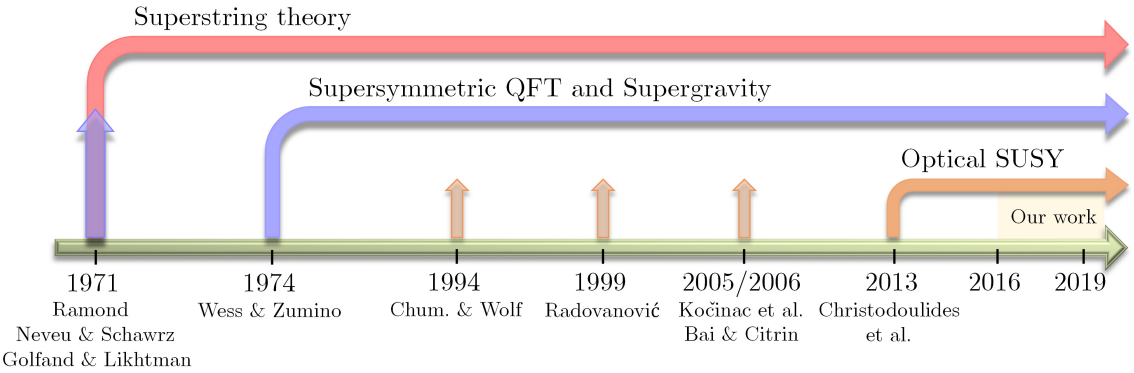

Figure 6.1. Chronology of supersymmetry in theoretical physics. The semi-transparent arrows indicate fundamental unnoticed works in the respective fields during several years.

SUSY in string theory, quantum field theory and general relativity The work of Ramond [208] was received as a breath of fresh air in the first years of string theory. The first version of string theory (1968-1971) was only able to describe *bosonic* strings [244]. In this scenario, Ramond constructed a stringy analog of the Dirac equation describing a *fermionic* string. Few months later, Neveu and Schwarz [209] proposed a new interacting bosonic string theory, the dual pion model, and remarkably, with a similar structure to the fermionic string of Ramond. Subsequently, the Neveu-Schwarz bosons and Ramond fermions could be combined by Neveu, Schwarz, and Thorn in [245], giving rise to the unification of the bosonic and fermionic string models. These works were the origin of *superstring theory*.

In parallel, the origin of SUSY in QFT can also be dated in 1971. The four-dimensional (4D) *super*-Poincaré algebra was introduced with the work of Golfand and Likhtman [207]. Specifically, the authors proposed constructing a 4D QFT using this algebra. Unfortunately, this paper was forgotten by the scientific community in the following years.[1] Nonetheless, the development of *supersymmetric quantum field theories* was launched thanks to the paper of Wess and Zumino three years later, in 1974 [246]. Wess and Zumino reported a new class of 4D supersymmetric gauge theories which became the real birth of SUSY in QFT. In the second half of the 1970s and in the next decades, the study of supersymmetric theories became the major effort, not only in string theory and QFT, but also in gravity [247]. Interestingly, general relativity seems to be a necessary consequence of a supersymmetric gauge theory. As a result, SUSY provides a natural mathematical framework for the *unification* of the four fundamental interactions known in nature.

SUSY experimental status One of the fundamental and exciting predictions of SUSY in QFT is the existence of supersymmetric particles of fermions and bosons of the Standard Model with the same masses as their SUSY counterparts. Nonetheless, there has been no experimental evidence of these SUSY particles in the Large Hadron Collider (LHC) [215]. The fact that no SUSY particles have been experimentally observed in the LHC implies that, if SUSY really plays a role in nature, it certainly must be explicitly broken and, therefore, the mass of SUSY particles must be much higher than the particles of the Standard Model. In fact, it is now widely felt that the energy level required to observe all these new hypothetical particles could be much higher than the current energy level available in the LHC (~ 1 PeV in November 2015).

[1] In fact, the celebrated paper of Wess and Zumino in 1974 [246] omits the work of Golfand and Likhtman [207].

SUSY in non-relativistic quantum mechanics Aimed to clarify fundamental outstanding questions of SUSY breaking in 4D QFT, Edward Witten analyzed SUSY in the simplest case of 1D non-relativistic quantum mechanics with two exceptional papers published in 1981 [248] and 1982 [249]. Thus, once the scientific community started studying various fundamental aspects of SUSY in this scenario, it was clearly observed the potential of 1D SUSY QM to solve other outstanding problems in QM. Remarkably, 1D SUSY QM emerged as a mathematical tool to obtain new quantum potentials analytically solvable [216]. In the next two decades, a vast number of works of 1D SUSY QM were reported in the quantum-mechanical literature.

Optical SUSY On the other hand, the mathematical framework of 1D SUSY QM has been profitably extended to diverse areas of physics and engineering in the last decades [222–242]. Concretely, in photonics, the ideas of 1D SUSY QM have stimulated the emergence of a new field in recent years: the *optical supersymmetry*.

The origin of optical SUSY can be found in 1994 with the work of Chumakov and Wolf [222]. In this paper, the authors studied the unbroken SUSY regime in 1D planar waveguides with the refractive index profile varying along the x-axis. Surprisingly, in the first part of this work, it was observed that the fundamental mode of the "bosonic" waveguide can be removed in the "fermionic" waveguide.[2] Despite the enormous potential of this result for mode filtering and mode conversion applications, in the second part of this work the authors focused their efforts on connecting two different beams of a given waveguide via SUSY transformations to obtain a periodic interference pattern. In any case, these results were unnoticed for the photonics community during the next decade.

From 1994 to 2013 appear three additional works in the photonics literature using the mathematical framework of 1D SUSY QM as an optimization tool [223–225]. Unfortunately, the unique features and the enormous potential underneath SUSY algebra also remained unexplored.

The breakthrough appears in 2013 with a paper published in Physical Review Letters by Prof. Demetrios Christodoulides and coworkers [228]. In this work, the authors reported the fundamentals of optical SUSY to design a new class of 1D optical structures with unprecedented applications for mode filtering, mode conversion and scattering engineering. These results provided a starting point to design novel 1D optical devices during the next years [229, 230, 232–239, 241, 242]. In addition, Christodoulides et al. also reported in [228] the possibility of applying unbroken SUSY transformations to 3D devices such as optical fibers, with interesting applications for angular momentum multiplexing. However, this study was limited to the unbroken SUSY regime, while many aspects of SUSY theory remained unexplored in the context of optical fibers.

In this scenario, our findings appear since 2016, the year when we started to develop the main results of the second part of this thesis. Two years later, we published our first work in optical SUSY [241]. Specifically, in this paper, we have analyzed the rich toolbox of the 1D SUSY formalism and its application in 3D optical, acoustic and quantum systems with axially-symmetric potentials, which entails a series of steps and assumptions whose range of validity has not been previously assessed. As a byproduct, a variety of applications for mode filtering, mode conversion, mode multiplexing, supermode generation, dispersion engineering and pulse shaping have been proposed (see Chapter 7).

Finally, in 2019, we introduce in [250] a paradigm shift demonstrating how the basic ideas of 1D SUSY QM, restricted to the space domain to understand why SUSY QFT may be broken in nature, can also be extended to the time domain in photonics. Outstandingly, we demonstrate that Maxwell's equations possess an underlying temporal supersymmetry. As a result, we obtain a simple analytic relation between the scattering coefficients of a large variety of time-varying optical systems and uncover a wide new class of non-reflecting, three-dimensional, all-dielectric, isotropic, omnidirectional, polarization-independent, non-complex media. These unprecedented features define a promising design platform for free-space and integrated photonics, enabling the creation of a number of novel reconfigurable transparent devices (see Chapter 8).

[2] We use here the concept of *bosonic* and *fermionic* waveguides in coherence with the SUSY QM literature. In this way, we explicitly indicate the optical waveguides that are connected via SUSY transformations.

6.3 Preliminary concepts

The mathematical formalism described in this chapter revolves around the following ordinary differential equation (ODE):

$$\widehat{\mathrm{H}}\psi\left(x\right)=\lambda\psi\left(x\right), \tag{6.3.1}$$

where $x\in[a,b]\subseteq\overline{\mathbb{R}}$, $\widehat{\mathrm{H}}$ is a linear operator defined as:

$$\widehat{\mathrm{H}}:=-\alpha\frac{\mathrm{d}^{2}}{\mathrm{d}x^{2}}+V\left(x\right), \tag{6.3.2}$$

and $(\psi,V,\lambda,\alpha)\in\mathcal{F}(\overline{\mathbb{R}},\overline{\mathbb{R}})\times\mathcal{F}(\overline{\mathbb{R}},\overline{\mathbb{R}})\times\mathbb{R}\times\mathbb{R}^{+}$. It should be noted that Eq. (6.3.1) is an eigenvalue equation, where ψ is the eigenfunction and λ is the eigenvalue (assumed to be finite). More specifically, Eq. (6.3.1) is a particularization of the Sturm-Liouville eigenvalue problem (SL-EVP), provided that the specific boundary conditions are included in this scenario [251]. In this context, we will say that the SL-EVP has a discrete or continuous spectrum depending on the discrete or continuous nature of the set of eigenvalues.

Interestingly, Eq. (6.3.1) serves as a master equation that allows us to describe the dynamics of waves in different branches of physics provided that an adequate physical interpretation of ψ, V and λ is performed. For instance, in quantum mechanics, Eq. (6.3.1) can be identified with the one-dimensional time-independent Schrödinger equation replacing $\alpha\equiv\hbar^{2}/2m$. Hence, λ, V and ψ describe the particle's discrete energy levels, the quantum potential and the probability amplitude, respectively. In such a scenario, the linear operator $\widehat{\mathrm{H}}$ is known as the Hamiltonian operator and represents the total energy of the system. Moreover, as we will see in Section 6.13, Eq. (6.3.1) can also model the propagation of waves in other fields of physics, such as in photonics or acoustics. Before delving into the theory of SUSY, let us perform in the next lines a brief review of some basic concepts of algebra and Sturm-Liouville's theory.

Probability density function In a 1D quantum system, the probability (P) of finding a particle located at the x-position is given by the expression $P\left(x\right)=\int_{-\infty}^{x}\left|\psi\left(\alpha\right)\right|^{2}\mathrm{d}\alpha$. Thus, the square absolute value of the wave function $\left|\psi\right|^{2}$ can be interpreted as the probability density function (p.d.f.) of the particle's location.

Vector space and dual vector space Consider a vector space $(\mathcal{V},+_{\mathcal{V}},\cdot_{\mathbb{K}\mathcal{V}})$ defined over a field $(\mathbb{K},+_{\mathbb{K}},\cdot_{\mathbb{K}})$, where $+_{\mathcal{V}}$ and $\cdot_{\mathbb{K}\mathcal{V}}$ are respectively the internal and external operations of the vector space, and $+_{\mathbb{K}}$ and $\cdot_{\mathbb{K}}$ are the internal operations of the field. The dual vector space $\mathcal{V}^{*}$ is defined as the set of all linear maps $\mathcal{V}\rightarrow\mathbb{K}$. Specifically, $\mathcal{V}^{*}$ is the vector space of homomorphisms $\mathscr{L}(\mathcal{V},\mathbb{K})$ defined over the same field. In order to complete the definition of $\mathcal{V}^{*}$, an internal operation $+_{\mathcal{V}^{*}}$ and an external operation $\cdot_{\mathbb{K}\mathcal{V}^{*}}$ must be defined.

In general, the internal and external operations of a vector space or a field are usually related with an operation of addition (e.g., $+_{\mathcal{V}}$, $+_{\mathcal{V}^{*}}$ and $+_{\mathbb{K}}$) and multiplication (e.g., $\cdot_{\mathbb{K}\mathcal{V}}$, $\cdot_{\mathbb{K}\mathcal{V}^{*}}$ and $\cdot_{\mathbb{K}}$). For the sake of simplicity, we will relax the notation by omitting the subindexes in each operation from now on. The context should avoid any confusion.

Inner product Consider a vector space $(\mathcal{V},+,\cdot)$ over the field of the complex numbers $(\mathbb{C},+,\cdot)$. An *inner product* is a function $\langle\cdot,\cdot\rangle:\mathcal{V}\times\mathcal{V}\rightarrow\mathbb{C}$ satisfying the following properties:

- Positive-definiteness: $\langle\mathbf{x},\mathbf{x}\rangle\geq0$ with $\langle\mathbf{x},\mathbf{x}\rangle=0\Leftrightarrow\mathbf{x}=\mathbf{0}$, $\forall\mathbf{x}\in\mathcal{V}$
- Linearity in the first argument: $\langle\alpha_{1}\mathbf{x}_{1}+\alpha_{2}\mathbf{x}_{2},\mathbf{y}\rangle=\alpha_{1}\langle\mathbf{x}_{1},\mathbf{y}\rangle+\alpha_{2}\langle\mathbf{x}_{2},\mathbf{y}\rangle$, $\forall\left(\mathbf{x}_{1},\mathbf{x}_{2},\mathbf{y}\right)\in\mathcal{V}^{3}$, $\forall\left(\alpha_{1},\alpha_{2}\right)\in\mathbb{C}^{2}$
- Conjugate symmetry: $\langle\mathbf{x},\mathbf{y}\rangle=\overline{\langle\mathbf{y},\mathbf{x}\rangle}$, $\forall\left(\mathbf{x},\mathbf{y}\right)\in\mathcal{V}^{2}$

In general, $\langle \mathbf{x}, \mathbf{y} \rangle \in \mathbb{C}$. Nevertheless, note that the definition of the inner product requires that $\langle \mathbf{x}, \mathbf{x} \rangle \in \mathbb{R}^+ \cup \{0\}$.

Alternatively, we can also define an inner product by requiring linearity in the *second* argument. This definition is usually employed in the *bra-ket* notation (see below Dirac notation) and the inner product is written as $\langle \mathbf{x}|\mathbf{y} \rangle$. Both definitions are connected via the relation $\langle \mathbf{x}|\mathbf{y} \rangle = \langle \mathbf{y}, \mathbf{x} \rangle$. As an example, the usual inner product for the vector space of complex-valued differentiable functions defined on $[a, b] \subseteq \overline{\mathbb{R}}$ is defined as:

$$\langle f, g \rangle := \int_a^b f(x)\, \overline{g(x)} \mathrm{d}x \equiv \langle g|f \rangle . \tag{6.3.3}$$

Norm Consider a vector space $(\mathcal{V}, +, \cdot)$ over the field of the complex numbers $(\mathbb{C}, +, \cdot)$. A *norm* is a nonsingular function $\|\cdot\| : \mathcal{V} \to \mathbb{R}$ satisfying the following properties:

- Positive-definiteness: $\|\mathbf{x}\| \geq 0$ with $\|\mathbf{x}\| = 0 \Leftrightarrow \mathbf{x} = \mathbf{0}$, $\forall \mathbf{x} \in \mathcal{V}$
- Triangle inequality: $\|\mathbf{x} + \mathbf{y}\| \leq \|\mathbf{x}\| + \|\mathbf{y}\|$, $\forall (\mathbf{x}, \mathbf{y}) \in \mathcal{V}^2$
- $\|\alpha \mathbf{x}\| = |\alpha| \, \|\mathbf{x}\|$, $\forall (\alpha, \mathbf{x}) \in \mathbb{C} \times \mathcal{V}$ where $|\alpha|$ is the module of α

As an example, the usual norm for the vector space of complex-valued differentiable functions on $[a, b] \subseteq \overline{\mathbb{R}}$ is defined via the inner product given by Eq. (6.3.3):

$$\|f\| := \sqrt{\langle f|f \rangle}. \tag{6.3.4}$$

Hilbert space Consider a vector space $(\mathcal{V}, +, \cdot)$ over the field of the complex numbers $(\mathbb{C}, +, \cdot)$. Defining an inner product $\langle \cdot|\cdot \rangle$, the 2-tuple $(\mathcal{V}, \langle \cdot|\cdot \rangle)$ constitutes a *pre-Hilbert space*. From the inner product, we will be able to define a norm in line with Eq. (6.3.4). If the norm is complete (i.e. any Cauchy sequence of vectors lying in $\mathcal{V}$ always converges to a well-defined limit lying within the same vector space) the 3-tupla $(\mathcal{V}, \langle \cdot|\cdot \rangle, \|\cdot\|)$ defines a *Hilbert space*. As an example, the vector space of the square-integrable functions $\mathcal{L}^2([a, b])$ is a Hilbert space. Nonetheless, there exists solutions that do not belong to this Hilbert space that are extremely useful for theoretical purposes, such as the plane waves or the Dirac delta function. Consequently, aimed to include this kind of functions in $\mathcal{L}^2([a, b])$, the aforementioned Hilbert space is usually extended in quantum mechanics leading to the concept of *rigged Hilbert space*.

Dirac notation Consider a Hilbert space $(\mathcal{V}, \langle \cdot|\cdot \rangle, \|\cdot\|)$ over the field $\mathbb{C}$ (the internal and external operations of both algebraic structures are omitted for simplicity). Let us define the dual vector space $\mathcal{V}^* = \mathscr{L}(\mathcal{V}, \mathbb{C})$ where $\forall \mathbf{x} \in \mathcal{V}$, $\exists \mathbf{x}^* \in \mathcal{V}^*$ referred to as the dual vector of $\mathbf{x}$ defined as:

$$\mathbf{x}^* : \mathcal{V} \to \mathbb{C}, \quad \mathbf{x}^*(\mathbf{y}) := \langle \mathbf{x}|\mathbf{y} \rangle , \quad \forall (\mathbf{x}, \mathbf{y}) \in \mathcal{V}^2. \tag{6.3.5}$$

In such a scenario, the notation can be recast as $\mathbf{x}^* \equiv \langle \mathbf{x}|$, $\mathbf{x} \equiv |\mathbf{x} \rangle$ and $\mathbf{y} \equiv |\mathbf{y} \rangle$. The dual vectors $\langle \mathbf{x}| \in \mathcal{V}^*$ and $|\mathbf{x} \rangle \in \mathcal{V}$ are referred to as *bra* and *ket*, respectively. In this way, the above equation can be rewritten as:

$$\mathbf{x}^*(\mathbf{y}) \equiv \langle \mathbf{x}| (|\mathbf{y} \rangle) := \langle |\mathbf{x} \rangle \, | \, |\mathbf{y} \rangle \rangle \equiv \langle \mathbf{x}|\mathbf{y} \rangle . \tag{6.3.6}$$

The bra-ket notation was introduced in 1939 by Paul Dirac and it is known as the Dirac notation.

Linear operators Consider two different vector spaces $(\mathcal{V}, +, \cdot)$ and $(\mathcal{W}, +, \cdot)$ over a field $(\mathbb{K}, +, \cdot)$. Remember that the operations $+$ and $\cdot$ of each algebraic structure may be defined in a different way. From both vector spaces, we can define a linear operator $\widehat{\mathrm{A}}$ as a linear mapping $\widehat{\mathrm{A}} : \mathcal{V} \to \mathcal{W}$, $\mathbf{x} \to \widehat{\mathrm{A}}(\mathbf{x}) := \widehat{\mathrm{A}}\mathbf{x}$, satisfying that:

$$\widehat{\mathrm{A}}(\alpha_1 \mathbf{x}_1 + \alpha_2 \mathbf{x}_2) = \alpha_1 \widehat{\mathrm{A}}\mathbf{x}_1 + \alpha_2 \widehat{\mathrm{A}}\mathbf{x}_2, \tag{6.3.7}$$

$\forall (\mathbf{x}_1, \mathbf{x}_2) \in \mathcal{V}^2$ and $\forall (\alpha_1, \alpha_2) \in \mathbb{K}^2$. In other words, $\widehat{\mathrm{A}}$ is a homomorphisms from $\mathcal{V}$ to $\mathcal{W}$. The set of linear operators from $\mathcal{V}$ to $\mathcal{W}$ will be referred to as $\mathscr{L}(\mathcal{V}, \mathcal{W})$.

In order to provide an algebraic structure to $\mathscr{L}(\mathcal{V},\mathcal{W})$, we should define the internal and external operations. Specifically, the internal operation $\cdot : \mathscr{L}(\mathcal{V},\mathcal{W}) \times \mathscr{L}(\mathcal{V},\mathcal{W}) \to \mathscr{L}(\mathcal{V},\mathcal{W})$ is defined in the same way as the composition of homomorphisms, i.e., $\forall(\widehat{\mathrm{A}},\widehat{\mathrm{B}}) \in \mathscr{L}(\mathcal{V},\mathcal{W})^2$ and $\forall \mathbf{x} \in \mathcal{V}$, $\left(\widehat{\mathrm{A}} \cdot \widehat{\mathrm{B}}\right)(\mathbf{x}) := \widehat{\mathrm{A}}(\widehat{\mathrm{B}}(\mathbf{x}))$. Therefore, the definition of this internal operation has as a necessary condition that $\mathcal{W} \subseteq \mathcal{V}$. For simplicity, we will assume that $\mathcal{V} = \mathcal{W}$, i.e., we will work with *endomorphisms*. In QM, if we consider the Hilbert space $\mathcal{V} = \mathcal{L}^2([a,b])$, the set of linear operators $\mathscr{L}(\mathcal{V},\mathcal{V})$ along with the corresponding internal and external operations of addition and multiplication define a noncommutative algebra (see below) over the field $\mathbb{C}$.

Adjoint, self-adjoint and positive operators The definition of *adjoint* operator does not require that $\mathcal{W} \subseteq \mathcal{V}$. However, each vector space must be a pre-Hilbert space, i.e., an inner product must be defined in $\mathcal{V}$ and $\mathcal{W}$. Thus, let us consider two different pre-Hilbert spaces $(\mathcal{V}, \langle\cdot|\cdot\rangle_{\mathcal{V}})$ and $(\mathcal{W}, \langle\cdot|\cdot\rangle_{\mathcal{W}})$. Given a linear operator $\widehat{\mathrm{A}} \in \mathscr{L}(\mathcal{V},\mathcal{W})$, the operator $\widehat{\mathrm{A}}^{\dagger} \in \mathscr{L}(\mathcal{W},\mathcal{V})$ is the adjoint operator of $\widehat{\mathrm{A}}$ if and only if:

$$\left\langle \widehat{\mathrm{A}}\mathbf{x}|\mathbf{y}\right\rangle_{\mathcal{W}} = \left\langle \mathbf{x}|\widehat{\mathrm{A}}^{\dagger}\mathbf{y}\right\rangle_{\mathcal{V}}, \quad \forall(\mathbf{x},\mathbf{y}) \in \mathcal{V}\times\mathcal{W}. \tag{6.3.8}$$

The operator $\widehat{\mathrm{A}}$ is *self-adjoint* if and only if $\mathcal{V} = \mathcal{W}$ and:

$$\widehat{\mathrm{A}} = \widehat{\mathrm{A}}^{\dagger}. \tag{6.3.9}$$

Along this line, consider the EVP $\widehat{\mathrm{A}}\mathbf{x} = \lambda\mathbf{x}$. If the field $\mathbb{K} = \mathbb{C}$ and $\widehat{\mathrm{A}}$ is self-adjoint, the following remarks are in order:

- All the eigenvalues are real, i.e., the spectrum of λ is a subset of $\mathbb{R}$
- The eigenvectors are orthogonal and constitute a basis of the solution space

These remarks can be inferred from the fact that the vector space $\mathscr{L}(\mathcal{V},\mathcal{V})$ is isomorphic to the matrix vector space $M_n(\mathbb{C})$ with $n = \dim(\mathcal{V})$.

Finally, given a pre-Hilbert space $(\mathcal{V}, \langle\cdot|\cdot\rangle)$ over the field $\mathbb{C}$, a linear operator $\widehat{\mathrm{A}} \in \mathscr{L}(\mathcal{V},\mathcal{V})$ is *positive* if and only if:

$$\left\langle \widehat{\mathrm{A}}\mathbf{x}|\mathbf{x}\right\rangle \geq 0, \quad \forall\mathbf{x} \in \mathcal{V}. \tag{6.3.10}$$

A positive operator is self-adjoint as a necessary condition when $\mathbb{K} = \mathbb{C}$. The converse is not always true. Furthermore, note that in such a case all the eigenvalues of the EVP $\widehat{\mathrm{A}}\mathbf{x} = \lambda\mathbf{x}$ are non-negative.

Algebra For the sake of clarity, let us retrieve the subindex notation in this paragraph to define the internal and external operations. Consider a field $(\mathbb{K}, +_{\mathbb{K}}, \cdot_{\mathbb{K}})$ and a set $\mathcal{V}$ with two internal operations $(+_{\mathcal{V}}, \cdot_{\mathcal{V}})$ and an external operation $\cdot_{\mathbb{K}\mathcal{V}}$. If the 3-tuplas $(\mathcal{V}, +_{\mathcal{V}}, \cdot_{\mathcal{V}})$ and $(\mathcal{V}, +_{\mathcal{V}}, \cdot_{\mathbb{K}\mathcal{V}})$ define respectively a ring and a vector space over the field $\mathbb{K}$, we say that $\mathcal{V}$ is an algebra. A closed algebra is an algebra defined on a closed field. The field $(\mathbb{K}, +_{\mathbb{K}}, \cdot_{\mathbb{K}})$ is closed if $\forall p \in \mathcal{F}(\mathbb{K},\mathbb{K})$: $p(x) = \sum_{m=0}^{g\geq 1} a_m x^m$ with $a_m \in \mathbb{K}$, $\exists\alpha \in \mathbb{K}$ satisfying that $p(\alpha) = e_{(+_{\mathbb{K}})}$, where $e_{(+_{\mathbb{K}})}$ is the neutral element for the operation $+_{\mathbb{K}}$. For instance, the field $\mathbb{C}$ is closed but $\mathbb{R}$ cannot be considered a closed field because the polynomial $x^2 + 1$ does not have any zero (the neutral element for the operation $+_{\mathbb{R}}$) lying in $\mathbb{R}$.

Lie algebras A Lie algebra is an algebra including the *Lie bracket* (also termed as commutator) as an additional internal operation. As an example, consider the Hilbert space $\mathcal{V} = \mathcal{L}^2([a,b])$ and the set of linear operators $\mathscr{L}(\mathcal{V},\mathcal{V})$. We know that $\mathscr{L}(\mathcal{V},\mathcal{V})$ along with the corresponding internal and external operations of addition and multiplication define a noncommutative algebra over the field $\mathbb{C}$. At this point, we will be able to obtain a Lie algebra if we include an additional internal operation, the Lie bracket $[\cdot,\cdot] : \mathscr{L}(\mathcal{V},\mathcal{V}) \times \mathscr{L}(\mathcal{V},\mathcal{V}) \to \mathscr{L}(\mathcal{V},\mathcal{V})$, $(\widehat{\mathrm{A}},\widehat{\mathrm{B}}) \to [\widehat{\mathrm{A}},\widehat{\mathrm{B}}]$, satisfying the anticommutative and Jacobi properties:

1. Anticommutative: $[\widehat{\mathrm{A}},\widehat{\mathrm{B}}]=-[\widehat{\mathrm{B}},\widehat{\mathrm{A}}]$
2. Jacobi: $[\widehat{\mathrm{A}},[\widehat{\mathrm{B}},\widehat{\mathrm{C}}]]+[\widehat{\mathrm{B}},[\widehat{\mathrm{C}},\widehat{\mathrm{A}}]]+[\widehat{\mathrm{C}},[\widehat{\mathrm{A}},\widehat{\mathrm{B}}]]=\widehat{0}$

The Lie bracket is usually defined as $[\widehat{\mathrm{A}},\widehat{\mathrm{B}}]:=\widehat{\mathrm{A}}\cdot\widehat{\mathrm{B}}-\widehat{\mathrm{B}}\cdot\widehat{\mathrm{A}}$. Moreover, an additional internal operation, called the anticommutator $\{\cdot,\cdot\}$, is usually included and defined as $\{\widehat{\mathrm{A}},\widehat{\mathrm{B}}\}:=\widehat{\mathrm{A}}\cdot\widehat{\mathrm{B}}+\widehat{\mathrm{B}}\cdot\widehat{\mathrm{A}}$. The reader can find an extensive bibliography about the Lie algebras in [252].

Lie superalgebras Consider an algebra $\mathcal{V}$ and an Abelian group $\mathbb{M}$ (the corresponding internal and external operations are omitted for simplicity). The algebra $\mathcal{V}$ is $\mathbb{M}$-graded if we can decompose $\mathcal{V}$ into a *direct sum* of vector subspaces $\mathcal{V}=\bigoplus_{k\in\mathbb{M}}\mathcal{V}_k$ satisfying that $\mathcal{V}_k\mathcal{V}_j\subseteq\mathcal{V}_{k+j}$.[3] If $\mathbf{x}\in\mathcal{V}_k$, we say that the vector $\mathbf{x}$ is homogeneous of degree k writing $\deg(\mathbf{x})=k$.

Now, let us consider the Abelian group $(\mathbb{Z}_2,+)$ with the binary elements $\overline{0}$ and $\overline{1}$ and $+$ the mod-2 addition.[4] A *superalgebra* is a $\mathbb{Z}_2$-graded algebra $\mathcal{V}=\mathcal{V}_{\overline{0}}\oplus\mathcal{V}_{\overline{1}}$. The elements of $\mathcal{V}_{\overline{0}}$ and $\mathcal{V}_{\overline{1}}$ are termed as even and odd, respectively. In SUSY QFT, the even elements are the bosons and the odd elements are the fermions.

A Lie superalgebra is a superalgebra $\mathcal{V}=\mathcal{V}_{\overline{0}}\oplus\mathcal{V}_{\overline{1}}$ which includes the Lie superbracket, an internal operation $[\cdot,\cdot]:\mathcal{V}\times\mathcal{V}\to\mathcal{V}$, $(\mathbf{x},\mathbf{y})\to[\mathbf{x},\mathbf{y}]$ satisfying the anticommutative and Jacobi properties, now redefined as:

1. Anticommutative: $[\mathbf{x},\mathbf{y}]=-(-1)^{\deg(\mathbf{x})\deg(\mathbf{y})}[\mathbf{x},\mathbf{y}]$
2. Jacobi: $[\mathbf{x},[\mathbf{y},\mathbf{z}]]=[[\mathbf{x},\mathbf{y}],\mathbf{z}]+(-1)^{\deg(\mathbf{x})\deg(\mathbf{y})}[\mathbf{y},[\mathbf{x},\mathbf{z}]]$

See [253] for a more detailed discussion about the Lie superalgebras.

Transformation physics: virtual and physical space As we will demonstrate in the next section, SUSY allows us to connect mathematically two different EVPs with Hamiltonians $\widehat{\mathrm{H}}_1$ and $\widehat{\mathrm{H}}_2$ with the *same* spectrum of eigenvalues. Hence, we can start from $\widehat{\mathrm{H}}_1$ to calculate $\widehat{\mathrm{H}}_2$ or vice versa. According to the transformation physics literature [243], the starting and final systems will be referred to as the *virtual* and *physical* spaces, respectively. As an example, if we calculate $\widehat{\mathrm{H}}_2$ from $\widehat{\mathrm{H}}_1$, the virtual space is $\widehat{\mathrm{H}}_1$ and the physical space is $\widehat{\mathrm{H}}_2$.

Notes on Sturm-Liouville's theory In the following, we include additional discussions on the Sturm-Liouville theory [251] in the mathematical framework of QM, photonics and acoustics:

- As commented at the beginning of this section, we initially assumed in Eq. (6.3.1) that $(\psi,V,\lambda,\alpha)\in\mathcal{F}(\overline{\mathbb{R}},\overline{\mathbb{R}})\times\mathcal{F}(\overline{\mathbb{R}},\overline{\mathbb{R}})\times\mathbb{R}\times\mathbb{R}^+$ to connect this EVP with the Sturm-Liouville theory. Concretely, if we focus our attention on *physical systems*, we will work with two different vector spaces over the field $\mathbb{C}$ (although we restrict the eigenvalues to $\mathbb{R}$ to use the Sturm-Liouville theory): $\mathcal{L}^2([a,b])$ and $\mathscr{L}(\mathcal{L}^2([a,b]),\mathcal{L}^2([a,b]))$ with $[a,b]\subseteq\overline{\mathbb{R}}$. Thus, a *physical eigenfunction* $\psi\in\mathcal{L}^2([a,b])$ and a *physical quantum system* $\widehat{\mathrm{H}}\in\mathscr{L}(\mathcal{L}^2([a,b]),\mathcal{L}^2([a,b]))$. In such a scenario, we can obtain a Hilbert space from the vector space $\mathcal{L}^2([a,b])$ by defining an inner product $\langle\cdot|\cdot\rangle$ and a norm $\|\cdot\|$ following the same definition as that of Eqs. (6.3.3) and (6.3.4).
- A wave function with a finite norm is referred to as a *normalizable wave function*. In QM, any physical eigenfunction of Eq. (6.3.1) is found to be normalizable by definition because its physical nature guarantees that lies in $\mathcal{L}^2([a,b])$. In particular, in QM ψ represents a probability amplitude and $|\psi|^2$ a p.d.f. Hence, it is required that:

$$\|\psi\|=\sqrt{\langle\psi|\psi\rangle}=\sqrt{\int_a^b|\psi(x)|^2\,\mathrm{d}x}=1. \tag{6.3.11}$$

[3] Here, note that the subindex operation $k+j$ is performed by using the addition operation of $\mathbb{M}$.
[4] The group $\mathbb{Z}_2$ is usually termed as $\mathbb{Z}/\mathbb{Z}_2$. Actually, they are different groups but are isomorphic.

This does not hold for non-normalizable wave functions, which are thus considered as having no physical meaning. In photonics or acoustics, the norm of a physical eigenfunction is not required to be the unity, but it must be finite.

- A *spatial bound state* is an eigenfunction ψ continuous, normalizable and usually satisfying the condition $\psi_{\pm} = 0$, where $\psi_{-} := \lim_{x \to a} \psi(x)$ and $\psi_{+} := \lim_{x \to b} \psi(x)$.[5] If the region of allowed particle positions $x \in [a, b]$ is the full line, then $a = -\infty$ and $b = \infty$. Otherwise, $-\infty < a \leq x \leq b < \infty$ and $\psi(x \notin [a, b]) = 0$ (e.g. the infinite square well potential). Remarkably, a spatial bound state is required to be continuous as a necessary condition to have a finite derivative. In QM, the linear momentum is proportional to the first-order spatial derivative ($\widehat{\mathrm{p}} = -j\hbar\nabla$) and, therefore, it must be finite to provide a physical meaning to the quantum system. In photonics or acoustics, the concept of spatial bound state is replaced by the concept of *spatial guided mode* and usually requires to satisfy the same conditions as a spatial bound state of quantum mechanics.

- A nontrivial solution of Eq. (6.3.1) is called *oscillatory* if it has an infinite number of *zeros*. Thus, in general, an oscillatory function cannot be a spatial bound state. A spatial bound state is usually a non-oscillatory solution. To summarize:[6]

$$\text{bound state} \Rightarrow \text{non-oscillatory solution;} \tag{6.3.12}$$

$$\text{oscillatory solution} \Rightarrow \text{no bound state.} \tag{6.3.13}$$

- It is worthy to note the difference between *eigenenergies* and *eigenvalues*. An eigenvalue λ is a real constant with an associated eigenfunction ψ_{λ}, both satisfying the EVP. However, only the continuous eigenfunctions of $\mathcal{L}^2([a, b])$ and their corresponding eigenvalues are possible physical solutions of a quantum system. In particular, these eigenvalues are referred to as the eigenenergies of the system, and they will be denoted by using the symbol E instead of λ. The set of eigenenergies is called the energy spectrum, a subset of the spectrum of all possible eigenvalues. From now on, when talking about an *energy level* of the system, we will refer to an eigenenergy, associated with an eigenfunction of our Hilbert space $\mathcal{L}^2([a, b])$.

- *Non-degeneracy theorem in 1D QM*: Eq. (6.3.1) is a second-order ODE. Thus, it has two linearly-independent solutions (eigenfunctions) for each eigenvalue, whose linear combination constitutes the general solution of the equation for this eigenvalue. Interestingly, in 1D QM, only one of these eigenfunctions is an element of $\mathcal{L}^2([a, b])$. This implies that the energy spectrum is non-degenerate, i.e., there is only a single physical eigenfunction associated with each energy level (see page 60 of [122]).[7]

- The SL-EVP is completed by including the adequate *explicit boundary conditions* to Eq. (6.3.1). More specifically, an SL-EVP is subjected to the following explicit boundary conditions (also termed as separated boundary conditions in the Sturm-Liouville theory):

$$\alpha_1 \psi(a) + \alpha_2 \psi'(a) = 0, \quad |\alpha_1| + |\alpha_2| > 0; \tag{6.3.14}$$

$$\beta_1 \psi(b) + \beta_2 \psi'(b) = 0, \quad |\beta_1| + |\beta_2| > 0, \tag{6.3.15}$$

  with $(\alpha_1, \alpha_2, \beta_1, \beta_2) \in \mathbb{R}^4$. Usually, the SL-EVP also has *implicit boundary conditions* in $x \in [a, b]$ emerged from the normalization and continuity of ψ.

- In an SL-EVP, the linear operator $\widehat{\mathrm{H}} \in \mathscr{L}(\mathcal{L}^2([a, b]), \mathcal{L}^2([a, b]))$ is *self-adjoint*. Consequently, the eigenvalues are real and the eigenfunctions are orthogonal and constitute a basis of the solution space.

[5] It is possible to construct counterexamples, for instance, in radially-symmetric potentials with $a = 0$, $b = \infty$, $\psi_{-} = \lim_{r \to 0} \psi(r) = \infty$ and $\psi_{+} = \lim_{r \to \infty} \psi(r) = 0$ [254].

[6] There are *exotic* bound states in QM that do not fulfill these statements, see e.g. Fig. 6.9 in Subsection 6.11.3. Nonetheless, these are particular cases. In most cases, Eqs. (6.3.12) and (6.3.13) are usually satisfied.

[7] The proof of the non-degeneracy theorem in 1D QM given by Landau in [122] has been extensively discussed in the literature leading to the possibility of constructing *exotic* 1D quantum systems supporting degenerate bound states, see e.g. [312]. These scenarios are out of the scope of this thesis.

- *Discrete vs continuous energy spectrum.* In QM, we can observe bound states if we have a discrete energy spectrum:

$$\text{discrete energy spectrum} \Rightarrow \text{bound states}, \tag{6.3.16}$$

and using the contrapositive:

$$\text{no bound states} \Rightarrow \text{continuous energy spectrum}. \tag{6.3.17}$$

Note that the converse of these statements is not always true (e.g. we can observe bound states in the continuum, see Subsection 6.11.3). It seems intuitively plausible that a *necessary condition* to support bound states could be to have an energy valley in the potential, i.e., $E \leq V(x)$ at least in a subset of $[a,b]$. Remarkably, the Sturm-Liouville theory provides a rigorous proof of this statement, as detailed on page 53 of [251]. Here, we only include a brief review of this reference. To this end, let us rewrite Eq. (6.3.1) in its quantum-mechanical version:

$$\left(\frac{\mathrm{d}^2}{\mathrm{d}x^2} + E - V(x)\right)\psi(x) = 0, \tag{6.3.18}$$

setting $\alpha = \hbar^2/2m \equiv 1$ for simplicity. As demonstrated in [251], the solutions of this second-order ODE are non-oscillatory if $E \leq V(x)$. However, if $E > V(x)$, then any solution of Eq. (6.3.18) is oscillatory in $[a,b]$. Hence, using the contrapositive of both statements, we conclude that:

$$E > V(x) \Leftrightarrow \psi \text{ oscillatory}; \tag{6.3.19}$$

$$E \leq V(x) \Leftrightarrow \psi \text{ non-oscillatory}. \tag{6.3.20}$$

Thus, combining Eqs. (6.3.13), (6.3.17) and (6.3.19), we find that in general:

$$E > V(x) \Rightarrow \text{no bound states} \Rightarrow \text{continuous energy spectrum}, \tag{6.3.21}$$

and using the contrapositive or combining Eqs. (6.3.12), (6.3.16) and (6.3.20), we infer that in general:

$$\text{discrete energy spectrum} \Rightarrow \text{bound states} \Rightarrow E \leq V(x). \tag{6.3.22}$$

Finally, from the Sturm-Liouville separation theorem [251] we can also conclude that if the interval $[a,b] = \overline{\mathbb{R}}$ and one solution of Eq. (6.3.18) oscillates, then all its solutions oscillate.

- In a discrete SL-EVP, the energy spectrum of $\widehat{\mathrm{H}}$, given by the set of energies $\{E_n\}_{n=0}^{\infty}$, is *bounded from below*. Specifically, $\min\{E_n\}_{n=0}^{\infty} = E_0$ and $E_0 < E_1 < E_2 < \ldots$ Moreover, the eigenfunction $\psi_n \in \mathcal{L}^2([a,b])$ with energy E_n has exactly n zeros (see page 60 of [122]). These zeros are termed as the *nodes* of the wave function in the quantum-mechanical literature.

6.4 SUSY Hamiltonian factorization

Once we have reviewed the preliminary mathematical concepts, we will be able to describe in detail the SUSY QM formalism. We start from a quantum system with Hamiltonian $\widehat{\mathrm{H}}_1$ described by the 1D time-independent Schrödinger equation, i.e., Eq. (6.3.1) replacing $\alpha \equiv \hbar^2/2m$:

$$\left(-\frac{\hbar^2}{2m}\frac{\mathrm{d}^2}{\mathrm{d}x^2} + V_1(x)\right)\psi^{(1)}(x) = \lambda^{(1)}\psi^{(1)}(x), \tag{6.4.1}$$

with $x \in [a,b] \subseteq \overline{\mathbb{R}}$. In line with the previous section, we describe the eigenvalue with $\lambda^{(1)}$ instead of $E^{(1)}$ to consider the normalizable and non-normalizable eigenfunctions $\psi^{(1)}$ of this EVP. The basic idea of SUSY QM is to factorize $\widehat{\mathrm{H}}_1$ as:

$$\widehat{\mathrm{H}}_1 = \widehat{\mathrm{A}}^{+}\widehat{\mathrm{A}}^{-}, \tag{6.4.2}$$

where:

$$\widehat{\mathrm{A}}^{\pm} := \mp \frac{\hbar}{\sqrt{2m}} \frac{\mathrm{d}}{\mathrm{d}x} + W(x), \tag{6.4.3}$$

are the so-called *SUSY operators* and the function W is known as the *superpotential*. From the previous Hamiltonian factorization, we can infer the relation between V_1 and W:

$$V_1(x) = W^2(x) - \frac{\hbar}{\sqrt{2m}} W'(x), \tag{6.4.4}$$

which is the well-known *Riccati equation*, a nonlinear first-order ODE.

SUSY QM proposes to construct a second quantum system $\widehat{\mathrm{H}}_2$, termed as the supersymmetric system, by inverting the order of the Hamiltonian factorization:

$$\widehat{\mathrm{H}}_2 := \widehat{\mathrm{A}}^{-} \widehat{\mathrm{A}}^{+}, \tag{6.4.5}$$

which corresponds to a linear operator of the form of $\widehat{\mathrm{H}}_1$, but with a potential:

$$V_2(x) = W^2(x) + \frac{\hbar}{\sqrt{2m}} W'(x). \tag{6.4.6}$$

In the SUSY QM literature, V_1 and V_2 are referred to as the SUSY partners potentials, also termed as superpartners. In this way, we have two different quantum systems described by the EVPs $\widehat{\mathrm{H}}_{1,2}\psi^{(1,2)} = \lambda^{(1,2)}\psi^{(1,2)}$ which are connected via the Riccati equation. Concretely, the power of this factorization resides in the fact that the eigenfunctions and eigenvalues of both EVPs are connected by the following simple relations:

$$\psi^{(2)} = \widehat{\mathrm{A}}^{-}\psi^{(1)}; \quad \psi^{(1)} = \widehat{\mathrm{A}}^{+}\psi^{(2)}; \quad \lambda^{(1)} = \lambda^{(2)}. \tag{6.4.7}$$

Surprisingly, both systems have the *same* eigenvalues. The proof of these expressions is straightforward. Consider the second EVP and the ansatz $\psi^{(2)} = \widehat{\mathrm{A}}^{-}\psi^{(1)}$. Thus, replacing this expression in $\widehat{\mathrm{H}}_2\psi^{(2)} = \lambda^{(2)}\psi^{(2)}$ we observe that:

$$\begin{aligned} \widehat{\mathrm{H}}_2\psi^{(2)} &= \widehat{\mathrm{H}}_2\left(\widehat{\mathrm{A}}^{-}\psi^{(1)}\right) = \left(\widehat{\mathrm{A}}^{-}\widehat{\mathrm{A}}^{+}\right)\left(\widehat{\mathrm{A}}^{-}\psi^{(1)}\right) = \widehat{\mathrm{A}}^{-}\left(\widehat{\mathrm{A}}^{+}\widehat{\mathrm{A}}^{-}\right)\psi^{(1)} \\ &= \widehat{\mathrm{A}}^{-}\left(\widehat{\mathrm{H}}_1\psi^{(1)}\right) = \widehat{\mathrm{A}}^{-}\left(\lambda^{(1)}\psi^{(1)}\right) = \lambda^{(1)}\left(\widehat{\mathrm{A}}^{-}\psi^{(1)}\right) \equiv \lambda^{(2)}\psi^{(2)}. \end{aligned} \tag{6.4.8}$$

That is, the ansatz $\psi^{(2)} = \widehat{\mathrm{A}}^{-}\psi^{(1)}$ is an *exact* solution of the second EVP and $\lambda^{(1)} = \lambda^{(2)}$. The expression $\psi^{(1)} = \widehat{\mathrm{A}}^{+}\psi^{(2)}$ can be demonstrated in a similar manner. Therefore, if both $\psi^{(1,2)} \neq 0$, we can see that the SUSY operators connect the eigenfunctions of $\widehat{\mathrm{H}}_1$ and $\widehat{\mathrm{H}}_2$ preserving the same eigenvalue spectrum, but not always the same energy spectrum. In particular, the energy spectrum will be exactly the same in both systems if the transformation $\psi^{(2,1)} = \widehat{\mathrm{A}}^{\mp}\psi^{(1,2)}$ is continuous (to have a finite linear momentum) and lies in $\mathcal{L}^2([a,b]) - \{0\}$. Interestingly, this is the *SUSY degeneracy theorem*, also termed as the boson-fermion degeneracy in SUSY QFT and superstring theory. In SUSY QM, it is usually described via the commutation of the superhamiltonian with the supercharges (see next section). Along these lines, we include some interesting remarks to close this section:

1. In QM, $\left\|\psi^{(1,2)}\right\| = 1$. Thus, Eq. (6.4.7) must be rewritten as $\psi^{(2,1)} = N^{(2,1)}\widehat{\mathrm{A}}^{\mp}\psi^{(1,2)}$, with $N^{(2,1)}$ real constants accounting for the normalization of $\psi^{(2,1)}$. From the condition $\left\|\psi^{(1,2)}\right\| = 1$, we obtain that:

$$N^{(2,1)} = \left[E^{(1,2)}\right]^{-1/2}. \tag{6.4.9}$$

   In photonics or acoustics, despite the fact that the norm of $\psi^{(1,2)}$ is not required to be 1, we should retain the normalization constant to guarantee that $\left\|\psi^{(1)}\right\| = \left\|\psi^{(2)}\right\|$.

2. From Eq. (6.4.6) we can note that the potential V_2 can be directly calculated from V_1 as:

$$V_2(x) = V_1(x) + \frac{2\hbar}{\sqrt{2m}} W'(x). \tag{6.4.10}$$

In line with the transformation physics literature, $\widehat{\mathrm{H}}_1$ is the virtual space and $\widehat{\mathrm{H}}_2$ is the physical space. In SUSY QM, the physical space is designed from the virtual space by using a field transformation, in particular, an autoBäcklund transformation (see [243] for a more detailed discussion about this point).

3. It is worth mentioning that:

$$\left(V_{1,2} \in \mathcal{F}\left(\overline{\mathbb{R}}, \overline{\mathbb{R}}\right)\right) \wedge (V_1 \neq V_2) \Longleftrightarrow W \in \mathcal{F}\left(\overline{\mathbb{R}}, \overline{\mathbb{R}}\right). \tag{6.4.11}$$

Proof. The demonstration of $\Leftarrow$ is straightforward by using the Riccati equations [Eqs. (6.4.4) and (6.4.6)]. The demonstration of $\Rightarrow$ can be performed by using the *reductio ad absurdum*. Let us assume that $(V_{1,2} \in \mathcal{F}(\overline{\mathbb{R}}, \overline{\mathbb{R}})) \wedge (V_1 \neq V_2)$ is true and $W \in \mathcal{F}(\overline{\mathbb{R}}, \mathbb{C})$ is of the form $W = W_{\mathrm{R}} + jW_{\mathrm{I}}$, with $W_{\mathrm{R(I)}} \in \mathcal{F}(\overline{\mathbb{R}}, \overline{\mathbb{R}})$. Given that[8] $V_{1,2} = W^2 \mp W' \in \mathcal{F}(\overline{\mathbb{R}}, \overline{\mathbb{R}})$ and $V_1 \neq V_2$ in line with the hypothesis, we find that $2W_{\mathrm{R}}W_{\mathrm{I}} \mp W_{\mathrm{I}}' = 0$. Hence:

$$W_{\mathrm{I}}(x) = D \exp\left(\pm 2 \int^x W_{\mathrm{R}}(y)\, \mathrm{d}y\right), \tag{6.4.12}$$

with D a non-vanishing real constant. In order to satisfy both Riccati equations, the following relation must be fulfilled:

$$\exp\left(2 \int^x W_{\mathrm{R}}(y)\, \mathrm{d}y\right) = \exp\left(-2 \int^x W_{\mathrm{R}}(y)\, \mathrm{d}y\right), \tag{6.4.13}$$

that is, $\int^x W_{\mathrm{R}}(y)\, \mathrm{d}y = 0,\ \forall x \in [a, b]$. Therefore, $W_{\mathrm{R}} = 0$ and $W(x) = jD$ concluding that $V_1 = V_2$ in contrast to the initial hypothesis. Consequently, $W \notin \mathcal{F}(\overline{\mathbb{R}}, \mathbb{C})$.

4. In a problem defined on the full line ($[a, b] = \overline{\mathbb{R}}$), Barbalat's lemma could be of great utility (see Section 6.10). This demonstrates that given a differentiable function W with $|W(x \to \pm\infty)| < \infty$ and W' uniformly continuous, then $W'(x \to \pm\infty) = 0$.

5. The Riccati equation cannot always be solved numerically by using finite-difference methods. As an example, the Riccati equation $W'(x) + bW^2(x) = cx^m$ with $(b, c) \in (\mathbb{R} - \{0\})^2$ can only be solved by finite-difference methods if and only if $m = -2$ or $m = -4k/(2k+1)$ with $k \in \mathbb{Z}$ (see page 23 of [255]).

6. The SUSY operators are adjoint operators:

$$\widehat{\mathrm{A}}^+ = \left(\widehat{\mathrm{A}}^-\right)^\dagger, \tag{6.4.14}$$

if and only if the superpotential is a real-valued function and $|\psi(a)| = |\psi(b)|, \forall \psi \in \mathcal{L}^2([a, b])$.[9] In such a case, $\widehat{\mathrm{H}}_1$ and $\widehat{\mathrm{H}}_2$ are positive operators:

$$\begin{aligned} \left\langle \widehat{\mathrm{H}}_{1,2}\psi^{(1,2)} | \psi^{(1,2)} \right\rangle &= \left\langle \widehat{\mathrm{A}}^{\pm}\widehat{\mathrm{A}}^{\mp}\psi^{(1,2)} | \psi^{(1,2)} \right\rangle \\ &= \left\langle \widehat{\mathrm{A}}^{\mp}\psi^{(1,2)} | \widehat{\mathrm{A}}^{\mp}\psi^{(1,2)} \right\rangle = \left\langle \psi^{(2,1)} | \psi^{(2,1)} \right\rangle \geq 0. \end{aligned} \tag{6.4.15}$$

Then, their eigenvalues cannot be negative, that is, the minimum possible eigenenergy is zero. Note that this does not apply when considering a *rigged* Hilbert space, with non-normalizable wave functions such as plane waves.

[8] Without loss of generality, let us take $\hbar/\sqrt{2m} \equiv 1$ for simplicity.
[9] This can be demonstrated by applying integration by parts at the LHS of Eq. (6.3.8).

6.5 SUSY algebra

In the previous section, we have introduced the basic ideas of SUSY QM connecting the EVPs $\widehat{\mathrm{H}}_1\psi^{(1)} = \lambda^{(1)}\psi^{(1)}$ and $\widehat{\mathrm{H}}_2\psi^{(2)} = \lambda^{(2)}\psi^{(2)}$. Nonetheless, the fundamental physical consequences of SUSY QM arise more clearly from the analysis of the algebraic structure of the matrix EVP which involves both EVPs:

$$\mathrm{H}\,|\psi\rangle = E\,|\psi\rangle\,, \tag{6.5.1}$$

with:

$$\mathrm{H} := \begin{bmatrix} \widehat{\mathrm{H}}_1 & \widehat{0} \\ \widehat{0} & \widehat{\mathrm{H}}_2 \end{bmatrix}; \quad |\psi\rangle := \begin{bmatrix} \psi^{(1)} \\ \psi^{(2)} \end{bmatrix}, \tag{6.5.2}$$

where H is known as the *superhamiltonian*. Note that: (i) we use the same eigenvalue for both SUSY systems given that $\lambda^{(1)} = \lambda^{(2)}$, and (ii) we use here the symbol E (energy in its quantum-mechanical sense) to describe only the physical eigenfunctions $|\psi\rangle$ by assuming that $\psi^{(1,2)}$, connected by Eq. (6.4.7), are continuous normalizable functions. At this point, we introduce the matrices:

$$\mathrm{Q}^- := \begin{bmatrix} \widehat{0} & \widehat{0} \\ \widehat{\mathrm{A}}^- & \widehat{0} \end{bmatrix}; \quad \mathrm{Q}^+ := \begin{bmatrix} \widehat{0} & \widehat{\mathrm{A}}^+ \\ \widehat{0} & \widehat{0} \end{bmatrix}, \tag{6.5.3}$$

known as the *supercharges*. Remarkably, the following commutation and anticommutation relations define the algebra of SUSY:

1. *Intertwining relation*:
$$\left[\mathrm{H}, \mathrm{Q}^{\pm}\right] = 0. \tag{6.5.4}$$

2. *Hamiltonian factorization*:
$$\mathrm{H} = \left\{\mathrm{Q}^{\pm}, \mathrm{Q}^{\mp}\right\}. \tag{6.5.5}$$

3. *Nilpotency of the supercharges*:
$$\left\{\mathrm{Q}^{\pm}, \mathrm{Q}^{\pm}\right\} = 0. \tag{6.5.6}$$

The underlying algebra of QM is a closed Lie algebra over the field $\mathbb{C}$. Now, if we include the previous commutation and anticommutation relations, the algebra of QM becomes a closed Lie superalgebra over the field $\mathbb{C}$, and more specifically, the closed Lie superalgebra $\mathfrak{sl}(2,\mathbb{C})$. In this context, the supercharges are also referred to as generators, Grassmann variables or Grassmann directions taking into account that we can generate a basis of the vector space $\mathfrak{sl}(2,\mathbb{C})$ of the form $B = \left(\mathrm{H}, \mathrm{Q}^+, \mathrm{Q}^-\right)$ with $\mathrm{H} = \left\{\mathrm{Q}^-, \mathrm{Q}^+\right\}$. Along these lines, it should be remarked that we construct the algebra of SUSY over the field $\mathbb{C}$. Nevertheless, we will only consider real eigenvalues (a subset of our field) to connect the EVP of Eq. (6.5.1) with the Sturm-Liouville theory.

Now, let us take a closer look at the SUSY commutation and anticommutation relations. The first property, the intertwining relation, is the *heart* of SUSY. From this property, we find that the matrix EVP is invariant when applying the supercharges to the eigenfunction $|\psi\rangle$:

$$\mathrm{H}\left(\mathrm{Q}^{\pm}\,|\psi\rangle\right) = \left(\mathrm{H}\mathrm{Q}^{\pm}\right)|\psi\rangle = \left(\mathrm{Q}^{\pm}\mathrm{H}\right)|\psi\rangle = \mathrm{Q}^{\pm}\left(\mathrm{H}\,|\psi\rangle\right) = \mathrm{Q}^{\pm}\left(E\,|\psi\rangle\right) = E\left(\mathrm{Q}^{\pm}\,|\psi\rangle\right). \tag{6.5.7}$$

That is, the supercharges generate a new eigenfunction of the EVP *without changing the energy*. To facilitate the physical interpretation and gain insight into this statement, consider the vector spaces $\mathcal{V}_1$ and $\mathcal{V}_2$ of the eigenfunctions of the EVPs $\widehat{\mathrm{H}}_1\psi_E^{(1)} = E\psi_E^{(1)}$ and $\widehat{\mathrm{H}}_2\psi_E^{(2)} = E\psi_E^{(2)}$, with basis $B_1 = \{\psi_E^{(1)}\}_{E\in I}$ and $B_2 = \{\psi_E^{(2)}\}_{E\in I}$ ($I \subset \mathbb{R}^+ \cup \{0\}$). Here, we explicitly indicate the eigenvalue-eigenvector relation by including the subindex E in the eigenvector for clarity. In such a scenario, assume that the elements of $\mathcal{V}_1$ are bosons and the elements of $\mathcal{V}_2$ are fermions. Bearing in mind that $\mathfrak{sl}(2,\mathbb{C})$ is a superalgebra, then we have a $\mathbb{Z}_2$ graduation. The $\mathbb{Z}_2$ graduation becomes clearer using as subindexes in $\mathcal{V}_1$ and $\mathcal{V}_2$ the elements of $\mathbb{Z}_2$, i.e., performing the relabeling $\mathcal{V}_{1\to\overline{0}}$ and $\mathcal{V}_{2\to\overline{1}}$. This implies that the vector space $\mathcal{V}$ of all the eigenfunctions of the matrix EVP $\mathrm{H}\,|\psi_E\rangle = E\,|\psi_E\rangle$

can be decomposed into a direct sum of $\mathcal{V}_{\overline{0}}$ and $\mathcal{V}_{\overline{1}}$, i.e., $\mathcal{V} = \mathcal{V}_{\overline{0}} \oplus \mathcal{V}_{\overline{1}}$. Consequently, we can construct a basis of $\mathcal{V}$ of the form $B = B_1 \cup B_2 = \left\{ \left|\psi_E^{(1)}\right\rangle, \left|\psi_E^{(2)}\right\rangle \right\}_{E\in I}$ with:

$$\left|\psi_E^{(1)}\right\rangle := \begin{bmatrix} \psi_E^{(1)} \\ 0 \end{bmatrix}; \quad \left|\psi_E^{(2)}\right\rangle := \begin{bmatrix} 0 \\ \psi_E^{(2)} \end{bmatrix}. \tag{6.5.8}$$

In this way, we can observe that Eq. (6.5.7) indicates that *the supercharges connect a boson to a fermion with the same energy*:

$$\mathrm{Q}^- \left|\psi_E^{(1)}\right\rangle = \begin{bmatrix} \widehat{0} & \widehat{0} \\ \widehat{\mathrm{A}}^- & \widehat{0} \end{bmatrix} \begin{bmatrix} \psi_E^{(1)} \\ 0 \end{bmatrix} = \begin{bmatrix} 0 \\ \widehat{\mathrm{A}}^- \psi_E^{(1)} \end{bmatrix} = \begin{bmatrix} 0 \\ \psi_E^{(2)} \end{bmatrix} = \left|\psi_E^{(2)}\right\rangle; \tag{6.5.9}$$

$$\mathrm{Q}^+ \left|\psi_E^{(2)}\right\rangle = \begin{bmatrix} \widehat{0} & \widehat{\mathrm{A}}^+ \\ \widehat{0} & \widehat{0} \end{bmatrix} \begin{bmatrix} 0 \\ \psi_E^{(2)} \end{bmatrix} = \begin{bmatrix} \widehat{\mathrm{A}}^+ \psi_E^{(2)} \\ 0 \end{bmatrix} = \begin{bmatrix} \psi_E^{(1)} \\ 0 \end{bmatrix} = \left|\psi_E^{(1)}\right\rangle. \tag{6.5.10}$$

This is the boson-fermion degeneracy predicted by all SUSY theories. Furthermore, the commutation of the superhamiltonian with the supercharges implies that we can connect two different systems $\widehat{\mathrm{H}}_1$ and $\widehat{\mathrm{H}}_2$ with degenerate eigenvalue spectra, and degenerate energy spectra provided that $\psi_E^{(2,1)} = \widehat{\mathrm{A}}^{\mp} \psi_E^{(1,2)}$ is continuous and lies in $\mathcal{L}^2([a,b]) - \{0\}$. This is the SUSY degeneracy theorem commented in the previous section.

The second property [Eq. (6.5.5)] describes in matrix notation the Hamiltonian factorization of the previous section ($\widehat{\mathrm{H}}_1 = \widehat{\mathrm{A}}^+ \widehat{\mathrm{A}}^-$ and $\widehat{\mathrm{H}}_2 = \widehat{\mathrm{A}}^- \widehat{\mathrm{A}}^+$) and allows us to demonstrate that SUSY is unbroken (see below) if and only if the energy level of the ground state (the bound state of minimum energy E_0) is zero. We will discuss this point in more detail in the next section.

The third property [Eq. (6.5.6)] indicates the nilpotency of the supercharges, i.e., $\left(\mathrm{Q}^{\pm}\right)^2 = 0$. This property guarantees that the supercharges cannot create a bosonic (fermionic) particle from a bosonic (fermionic) particle with the same energy. In other words, Q^+ annihilates the bosonic solutions and Q^- annihilates the fermionic solutions of the EVP:

$$\mathrm{Q}^+ \left|\psi_E^{(1)}\right\rangle = \mathrm{Q}^+ \left(\mathrm{Q}^+ \left|\psi_E^{(2)}\right\rangle\right) = \left(\mathrm{Q}^+\mathrm{Q}^+\right) \left|\psi_E^{(2)}\right\rangle = |0\rangle; \tag{6.5.11}$$

$$\mathrm{Q}^- \left|\psi_E^{(2)}\right\rangle = \mathrm{Q}^- \left(\mathrm{Q}^- \left|\psi_E^{(1)}\right\rangle\right) = \left(\mathrm{Q}^-\mathrm{Q}^-\right) \left|\psi_E^{(1)}\right\rangle = |0\rangle. \tag{6.5.12}$$

6.6 Unbroken SUSY

Small perturbations of the superhamiltonian might induce an explicit breakdown of the SUSY degeneracy theorem ($\left[\mathrm{H}, \mathrm{Q}^{\pm}\right] \neq 0$). In that case, there is not a boson-fermion correspondence (i.e. the energy levels of the bosonic and fermionic systems are unpaired) and, consequently, we will say that SUSY is *explicitly broken* [216]. Obviously, this scenario is not of interest to us in the present framework. We are only interested in physical systems fulfilling Eq. (6.5.4).

In such a situation, we will say by definition that SUSY is *unbroken* if and only if the ground state $|\psi_0\rangle$ is *supersymmetrically invariant*, i.e., the bosonic or fermionic nature of the ground state must remain invariant under the symmetry operation "$\mathfrak{boson} \leftrightarrow \mathfrak{fermion}$" performed by the supercharges [248]. This definition can be fulfilled via two different possibilities: $(i)\ \mathrm{Q}^{\pm} |\psi_0\rangle = |\psi_0\rangle$ or $(ii)\ \mathrm{Q}^{\pm} |\psi_0\rangle = |0\rangle$. The former implies that the supercharges must be the identity matrix and, therefore, this possibility must be discarded. Consequently, we infer that only the latter possibility satisfies the definition of unbroken SUSY. That is, SUSY is unbroken if and only if the supercharges annihilate the ground state. Otherwise, we will say that SUSY is *spontaneously broken* and we will have two different ground states (bosonic and fermionic) at energy E_0 related by the supercharges (see next section).

From the Hamiltonian factorization property of SUSY [Eq. (6.5.5)], we can demonstrate that:

$$\mathrm{Q}^{\pm}\left|\psi_0\right\rangle = \left|0\right\rangle \Longleftrightarrow E_0 = 0. \tag{6.6.1}$$

In other words, SUSY is unbroken *if and only if* the energy of the ground state is exactly zero. In SUSY QFT this biconditional implication is usually formulated as [248]: SUSY is unbroken if and only if the energy of the vacuum is exactly zero. Contrariwise, SUSY is broken if and only if $E_0 \neq 0$. In QM, it is straightforward to know when SUSY is explicitly or spontaneously broken by analyzing the energy spectrum of both superpartners, as discussed later in Section 6.8. However, in QFT it is quite hard to determine if SUSY is explicitly or spontaneously broken. In this scenario, Edward Witten proposed an index in [249] to solve this question, the Witten index, defined as $\triangle := \mathrm{Tr}\,(-1)^F$, where F is the fermion number. The technical details of the Witten index are out of the scope of this chapter.

Proof. The direct conditional statement ($\Rightarrow$) of Eq. (6.6.1) is straightforward to demonstrate by taking into account that $\mathrm{H} = \left\{\mathrm{Q}^{\pm}, \mathrm{Q}^{\mp}\right\}$ and the ground state $\left|\psi_0\right\rangle$ is a non-vanishing normalizable solution ($\left|\psi_0\right\rangle \neq \left|0\right\rangle$):

$$\begin{aligned}\mathrm{H}\left|\psi_0\right\rangle = E_0\left|\psi_0\right\rangle &\Rightarrow \left(\mathrm{Q}^{\pm}\mathrm{Q}^{\mp} + \mathrm{Q}^{\mp}\mathrm{Q}^{\pm}\right)\left|\psi_0\right\rangle = E_0\left|\psi_0\right\rangle \\ &\Rightarrow \mathrm{Q}^{\pm}\left(\mathrm{Q}^{\mp}\left|\psi_0\right\rangle\right) + \mathrm{Q}^{\mp}\left(\mathrm{Q}^{\pm}\left|\psi_0\right\rangle\right) = E_0\left|\psi_0\right\rangle \Rightarrow \left|0\right\rangle = E_0\left|\psi_0\right\rangle \Rightarrow E_0 = 0.\end{aligned} \tag{6.6.2}$$

The converse conditional statement ($\Leftarrow$) can also be demonstrated from Eq. (6.5.5):

$$\begin{aligned}\mathrm{H}\left|\psi_0\right\rangle = 0\left|\psi_0\right\rangle &\Rightarrow \left(\mathrm{Q}^{\pm}\mathrm{Q}^{\mp} + \mathrm{Q}^{\mp}\mathrm{Q}^{\pm}\right)\left|\psi_0\right\rangle = \left|0\right\rangle \\ &\Rightarrow \left(\mathrm{Q}^{\pm}\mathrm{Q}^{\mp}\right)\left|\psi_0\right\rangle + \left(\mathrm{Q}^{\mp}\mathrm{Q}^{\pm}\right)\left|\psi_0\right\rangle = \left|0\right\rangle.\end{aligned} \tag{6.6.3}$$

Now, applying the dual vector $\left\langle\psi_0\right|$ to the LHS and RHS of the above equation:

$$\left\langle\psi_0\right|\mathrm{Q}^{\pm}\mathrm{Q}^{\mp}\left|\psi_0\right\rangle + \left\langle\psi_0\right|\mathrm{Q}^{\mp}\mathrm{Q}^{\pm}\left|\psi_0\right\rangle = 0 \Rightarrow \left\langle\mathrm{Q}^{\mp}\psi_0\,\middle|\,\mathrm{Q}^{\mp}\psi_0\right\rangle + \left\langle\mathrm{Q}^{\pm}\psi_0\,\middle|\,\mathrm{Q}^{\pm}\psi_0\right\rangle = 0. \tag{6.6.4}$$

Thus, $\left\langle\mathrm{Q}^{\pm}\psi_0\,\middle|\,\mathrm{Q}^{\pm}\psi_0\right\rangle = 0$. Hence, using the positivity property of the scalar product we finally find that $\mathrm{Q}^{\pm}\left|\psi_0\right\rangle = \left|0\right\rangle$. □

Otherwise, note that in the unbroken SUSY case there is only a single ground state in the matrix EVP of Eq. (6.5.1). The ground state must be bosonic (derived from $\mathrm{Q}^{-}\left|\psi_0\right\rangle = \left|0\right\rangle$):

$$\left|\psi_0\right\rangle = \begin{bmatrix} \psi_0^{(1)}(x) \\ 0 \end{bmatrix} = \begin{bmatrix} N^{(1)}\exp\left(-\frac{\sqrt{2m}}{\hbar}\int^x W(y)\,\mathrm{d}y\right) \\ 0 \end{bmatrix}, \tag{6.6.5}$$

or fermionic (derived from $\mathrm{Q}^{+}\left|\psi_0\right\rangle = \left|0\right\rangle$):

$$\left|\psi_0\right\rangle = \begin{bmatrix} 0 \\ \psi_0^{(2)}(x) \end{bmatrix} = \begin{bmatrix} 0 \\ N^{(2)}\exp\left(\frac{\sqrt{2m}}{\hbar}\int^x W(y)\,\mathrm{d}y\right) \end{bmatrix}. \tag{6.6.6}$$

Both Eqs. (6.6.5) and (6.6.6) are mathematical solutions of the EVP at the zero energy level, but only one of them lies in $\mathcal{L}^2([a,b])$. Remember that, at the end of Section 6.3, we defined a spatial bound state as a continuous normalizable eigenfunction satisfying the condition $\psi_{\pm} = 0$, where $\psi_- := \lim_{x\to a}\psi(x)$, $\psi_+ := \lim_{x\to b}\psi(x)$ and $[a,b] \subseteq \overline{\mathbb{R}}$ is the region of allowed particle positions, that is, the interval where is defined our problem. Therefore, taking into account that $\psi_0^{(2)} \propto 1/\psi_0^{(1)}$ and the ground state is a bound state, if $\psi_{0,\pm}^{(1)} = 0$ then $\left|\psi_{0,\pm}^{(2)}\right| = \infty$ and vice versa. For this reason, only one of the solutions is normalizable, i.e., the ground state must be either bosonic or fermionic. In any case, the equations $\mathrm{Q}^{-}\left|\psi_0\right\rangle = \left|0\right\rangle$ and $\mathrm{Q}^{+}\left|\psi_0\right\rangle = \left|0\right\rangle$ are always simultaneously satisfied: if the ground state is bosonic (fermionic), the equation $\mathrm{Q}^{-}\left|\psi_0\right\rangle = \left|0\right\rangle$ ($\mathrm{Q}^{+}\left|\psi_0\right\rangle = \left|0\right\rangle$) is satisfied by definition, but the condition $\mathrm{Q}^{+}\left|\psi_0\right\rangle = \left|0\right\rangle$ ($\mathrm{Q}^{-}\left|\psi_0\right\rangle = \left|0\right\rangle$) is also fulfilled due to the nilpotency of the supercharges, as discussed in the previous section. From now on, let us suppose that the ground state is bosonic, without loss of generality in the remaining discussions of this chapter.

Under this assumption, let us discuss the form of the superpotential when SUSY is unbroken. To this end, we should first reformulate the biconditional implication given by Eq. (6.6.1) as:

$$\widehat{\mathrm{A}}^{-}\psi_0^{(1)} = 0 \Longleftrightarrow E_0^{(1)} = 0. \tag{6.6.7}$$

Thus, since $\widehat{\mathrm{A}}^{-}\psi_0^{(1)} = 0$, the superpotential must be of the form:

$$W(x) = -\frac{\hbar}{\sqrt{2m}}\frac{\mathrm{d}}{\mathrm{d}x}\ln\psi_0^{(1)}(x), \tag{6.6.8}$$

and the asymptotic behavior of the superpotential can be inferred from Eq. (6.6.5). Since we have assumed that the ground state is bosonic, then $\psi_{0,\pm}^{(1)} = 0$. Hence, we have as a necessary condition that $\lim_{x\to a,b}\int^x W(y)\,\mathrm{d}y = \infty$. From this relation, we can infer the behavior of $W_- := W(x \to a)$ and $W_+ := W(x \to b)$:

- If $a = -\infty$, then $W_- < 0$ and finite. Otherwise, if $-\infty < a < 0$, then $W_- = -\infty$.
- If $b = \infty$, then $W_+ > 0$ and finite. Otherwise, if $0 < b < \infty$, then $W_+ = \infty$.

On the other hand, remember that $\widehat{\mathrm{H}}_{1,2}$ are positive operators ($E_n^{(1,2)} \geq 0$) and the supercharges annihilate the ground state when SUSY is unbroken ($\widehat{\mathrm{A}}^{-}\psi_0^{(1)} = 0$). Hence, there is not SUSY counterpart of $\psi_0^{(1)}$ in $\widehat{\mathrm{H}}_2$ at the zero energy level, i.e., $\widehat{\mathrm{H}}_2$ has no zero-energy state ($E_0^{(2)} > 0$). Accordingly, Eq. (6.4.7) should be recast as:

$$E_n^{(2)} = E_{n+1}^{(1)}, \qquad E_0^{(1)} = 0; \tag{6.6.9}$$

$$\psi_n^{(2)} = \left[E_{n+1}^{(1)}\right]^{-1/2}\widehat{\mathrm{A}}^{-}\psi_{n+1}^{(1)}; \tag{6.6.10}$$

$$\psi_{n+1}^{(1)} = \left[E_n^{(2)}\right]^{-1/2}\widehat{\mathrm{A}}^{+}\psi_n^{(2)}, \tag{6.6.11}$$

including the normalization constants given by Eq. (6.4.9) in Eqs. (6.6.10) and (6.6.11). Figure 6.2 depicts the energy spectrum of the infinite square well and its SUSY potential. As seen, $E_0^{(1)} = 0$ and, then, SUSY is unbroken. Consequently, we cannot observe a zero-energy wave function in $\widehat{\mathrm{H}}_2$. In addition, note that the asymptotic behavior of W satisfies the conditions discussed above.

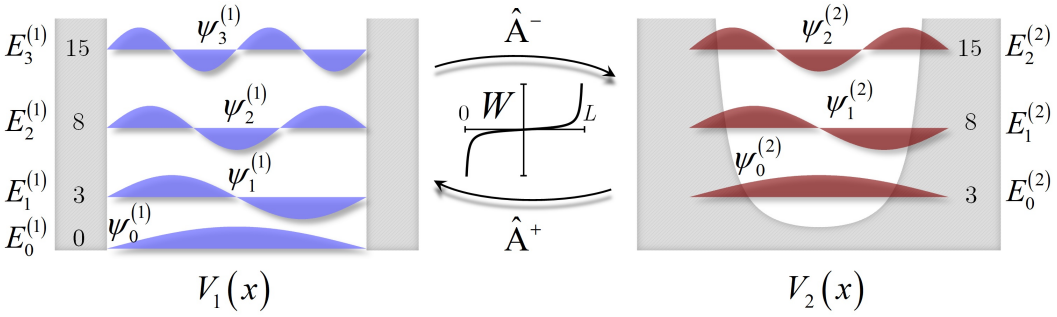

Figure 6.2. Unbroken SUSY. Energy spectra and wave functions of the infinite square well potential and its supersymmetric partner potential.

Furthermore, we could deal with the necessity of calculating an unbroken SUSY partner of $\widehat{\mathrm{H}}_1$ with $E_0^{(1)} \neq 0$. Obviously, we cannot generate $\widehat{\mathrm{H}}_2$ by directly factorizing $\widehat{\mathrm{H}}_1$. In such a case, it is useful to start from a shifted Hamiltonian $\widehat{\mathrm{H}}_{1,\mathrm{eq}} := \widehat{\mathrm{H}}_1 - E_0^{(1)}$ with zero-energy ground state,[10] calculate its superpartner $\widehat{\mathrm{H}}_{2,\mathrm{eq}}$, and undo the energy shift by building a Hamiltonian

[10]It is easy to demonstrate that the ground states of $\widehat{\mathrm{H}}_1$ ($\psi_0^{(1)}$) and $\widehat{\mathrm{H}}_{1,\mathrm{eq}}$ ($\psi_{0,\mathrm{eq}}^{(1)}$) are exactly the same wave function. Combining $\widehat{\mathrm{H}}_{1,\mathrm{eq}}\psi_{0,\mathrm{eq}}^{(1)} = 0$ and $\widehat{\mathrm{H}}_{1,\mathrm{eq}} = \widehat{\mathrm{H}}_1 - E_0^{(1)}$, we find that $\widehat{\mathrm{H}}_1\psi_{0,\mathrm{eq}}^{(1)} = E_0^{(1)}\psi_{0,\mathrm{eq}}^{(1)}$. Thus, from the non-degeneracy theorem in 1D QM (see Section 6.3), we conclude that $\psi_{0,\mathrm{eq}}^{(1)} = \psi_0^{(1)}$.

$\widehat{\mathrm{H}}_2 := \widehat{\mathrm{H}}_{2,\mathrm{eq}} + E_0^{(1)}$. The SUSY potentials V_1 and V_2 of the original Hamiltonians $\widehat{\mathrm{H}}_1$ and $\widehat{\mathrm{H}}_2$ are now related by the Riccati equation:

$$V_{1,2}(x) = W^2(x) \mp \frac{\hbar}{\sqrt{2m}} W'(x) + E_0^{(1)}. \tag{6.6.12}$$

Therefore, V_2 can be calculated from V_1 by using Eq. (6.6.8):

$$V_2(x) = V_1(x) - \frac{\hbar^2}{m}\frac{\mathrm{d}^2}{\mathrm{d}x^2} \ln \psi_0^{(1)}(x). \tag{6.6.13}$$

Interestingly, $\widehat{\mathrm{H}}_1$ and $\widehat{\mathrm{H}}_2$ have the same eigenfunctions and eigenvalues as $\widehat{\mathrm{H}}_{1,\mathrm{eq}}$ and $\widehat{\mathrm{H}}_{2,\mathrm{eq}}$, connected by an unbroken SUSY transformation, except for an energy shift $E_0^{(1)}$ of their eigenvalues. That is, $\psi_n^{(1,2)} = \psi_{n,\mathrm{eq}}^{(1,2)}$ and $E_n^{(1,2)} = E_{n,\mathrm{eq}}^{(1,2)} + E_0^{(1)}$.

Using this approach, we can easily construct a new Hamiltonian $\widehat{\mathrm{H}}_3$ by factorizing $\widehat{\mathrm{H}}_2$ using an unbroken SUSY transformation. Figure 6.3 illustrates the energy spectra of this scenario. In this vein, one can start from am exactly solvable EVP with Hamiltonian $\widehat{\mathrm{H}}_1$ and solve the eigenenergies and the physical eigenfunctions for the entire hierarchy of Hamiltonians $\left\{\widehat{\mathrm{H}}_k\right\}_{k\geq 2}$ built from iterative unbroken SUSY transformations. Conversely, if we know the ground states of the Hamiltonian chain, we can reconstruct the entire spectrum of $\widehat{\mathrm{H}}_1$. Specifically, the Hamiltonians $\widehat{\mathrm{H}}_{k-1}$ and $\widehat{\mathrm{H}}_k$ are factorized as (from now on we assume $\hbar^2/2m \equiv 1$ for simplicity):

$$\widehat{\mathrm{H}}_{k-1} = \widehat{\mathrm{A}}_{k-1}^{+}\widehat{\mathrm{A}}_{k-1}^{-} + E_0^{(k-1)}; \tag{6.6.14}$$

$$\widehat{\mathrm{H}}_{k} = \widehat{\mathrm{A}}_{k-1}^{-}\widehat{\mathrm{A}}_{k-1}^{+} + E_0^{(k-1)}, \tag{6.6.15}$$

with:

$$\widehat{\mathrm{A}}_{k-1}^{\pm} := \mp\frac{\mathrm{d}}{\mathrm{d}x} + W_{k-1}(x). \tag{6.6.16}$$

From an iterative process, we can generalize Eqs. (6.6.9), (6.6.10) and (6.6.13) for the unbroken SUSY Hamiltonian chain with k systems:

$$V_k(x) = V_1(x) - 2\frac{\mathrm{d}^2}{\mathrm{d}x^2} \ln\left(\prod_{i=1}^{k-1} \psi_0^{(i)}(x)\right); \tag{6.6.17}$$

$$E_n^{(k)} = E_{n+1}^{(k-1)} = \ldots = E_{n+k-1}^{(1)}; \tag{6.6.18}$$

$$\psi_n^{(k)} \propto \left(\prod_{i=1}^{k-1} \widehat{\mathrm{A}}_{k-i}^{-}\right)\psi_{n+k-1}^{(1)}, \tag{6.6.19}$$

and omitting the constants accounting for the normalization of the wave functions for clearness.

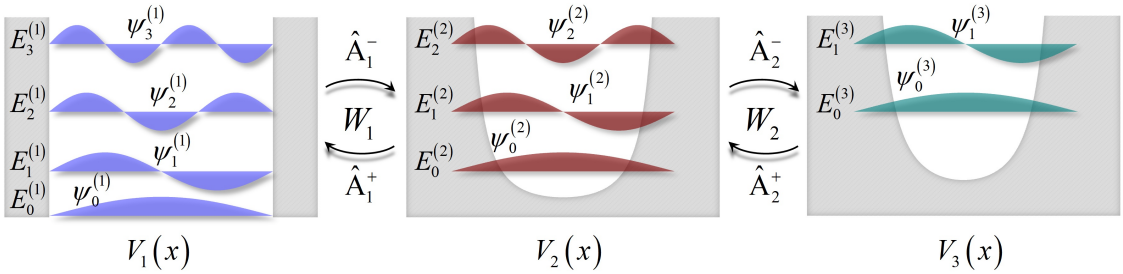

Figure 6.3. Unbroken SUSY Hamiltonian chain. Energy spectra and wave functions using the infinite square well potential as the initial system.

6.7 Spontaneously broken SUSY

SUSY is spontaneously broken when all the energy levels of the bosonic and fermionic systems are paired. This occurs when the ground state is not supersymmetrically invariant, that is, when the supercharges do not annihilate the ground state ($\mathrm{Q}^{\pm}|\psi_0\rangle \neq |0\rangle$). In such a scenario, we have two different ground states (bosonic and fermionic) at energy $E_0 > 0$ related by the supercharges. In terms of the SUSY operators, this implies that $\widehat{\mathrm{A}}^{-}\psi_0^{(1)}$ generates a non-vanishing normalizable solution $\psi_0^{(2)}$ of $\widehat{\mathrm{H}}_2$ at energy $E_0^{(2)} = E_0^{(1)} > 0$. Therefore, the spectra of the SUSY partners are found to be completely degenerate and Eq. (6.4.7) can be rewritten as:

$$E_n^{(2)} = E_n^{(1)}, \qquad E_0^{(1)} > 0; \tag{6.7.1}$$

$$\psi_n^{(2)} = \left[E_n^{(1)}\right]^{-1/2} \widehat{\mathrm{A}}^{-}\psi_n^{(1)}; \tag{6.7.2}$$

$$\psi_n^{(1)} = \left[E_n^{(2)}\right]^{-1/2} \widehat{\mathrm{A}}^{+}\psi_n^{(2)}. \tag{6.7.3}$$

In general, the constraints on SUSY breaking have a far richer scope in QFT than the implications previously described [249]. However, the aforementioned features of SUSY breaking seem to be sufficient for our purposes.

In Section 6.6, we discussed a method to calculate an unbroken SUSY partner from a Hamiltonian $\widehat{\mathrm{H}}_1$ with $E_0^{(1)} \neq 0$. Nonetheless, in some circumstances, we could have interest in building SUSY partners preserving exactly the same energy spectrum in both systems. In such a case, we can factorize $\widehat{\mathrm{H}}_1$ without performing the energy shift described in the previous section, i.e., $\widehat{\mathrm{H}}_1 = \widehat{\mathrm{A}}^{+}\widehat{\mathrm{A}}^{-}$ and $\widehat{\mathrm{H}}_2 = \widehat{\mathrm{A}}^{-}\widehat{\mathrm{A}}^{+}$. We illustrate an example of this scenario in Fig. 6.4. The SUSY partners have been calculated by using a Pöschl-Teller I superpotential. A detailed analytical description of this problem can be found in [243].

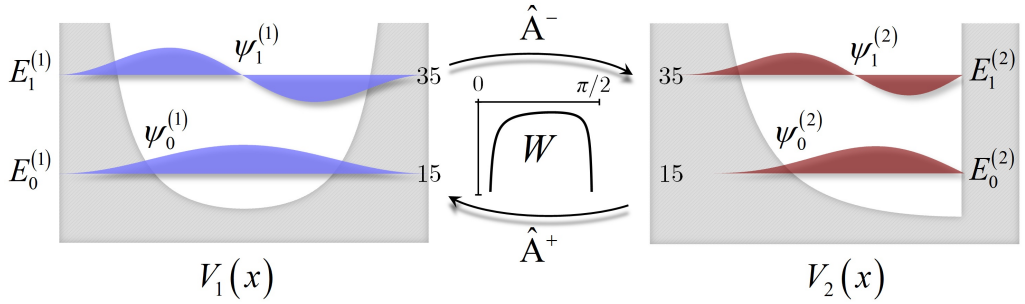

Figure 6.4. Spontaneously broken SUSY. Energy spectra and wave functions of the SUSY partner potentials associated with the Pöschl-Teller I superpotential.

In a similar way as in the unbroken SUSY case, we can generalize the broken SUSY transformation by generating a Hamiltonian chain with k systems connected by the following expressions:

$$V_k(x) = V_1(x) + 2\sum_{i=1}^{k-1} W_i'(x); \tag{6.7.4}$$

$$E_n^{(k)} = E_n^{(k-1)} = \ldots = E_n^{(1)}; \tag{6.7.5}$$

$$\psi_n^{(k)} \propto \left(\prod_{i=1}^{k-1} \widehat{\mathrm{A}}_{k-i}^{-}\right)\psi_n^{(1)}. \tag{6.7.6}$$

Note that Eq. (6.7.4) allows us to describe, not only the broken SUSY Hamiltonian chain, but also the unbroken case [Eq. (6.6.17)] by writing $W_i(x) = -(\ln\psi_0^{(i)}(x))'$.

6.8 Explicitly broken SUSY: singular superpotentials

So far, we have only considered to create SUSY partners by using nonsingular superpotentials in $x \in (a,b)$. For instance, in the unbroken SUSY transformation, we used a superpotential of the form $W(x) = -(\psi_0^{(1)})'(x)/\psi_0^{(1)}(x)$. This superpotential yields from the direct factorization $\widehat{\mathrm{H}}_1 = \widehat{\mathrm{A}}^+\widehat{\mathrm{A}}^-$ when $E_0^{(1)} = 0$, or from the energy-shifted factorization $\widehat{\mathrm{H}}_{1,\mathrm{eq}} = \widehat{\mathrm{H}}_1 - E_0^{(1)} = \widehat{\mathrm{A}}^+\widehat{\mathrm{A}}^-$ when $E_0^{(1)} \neq 0$. In both cases, W is nonsingular in $x \in (a,b)$ because $\psi_0^{(1)}$ has no nodes.

In this section, we discuss the possibility of performing a Hamiltonian factorization of the virtual space $\widehat{\mathrm{H}}_1$ as follows:

$$\widehat{\mathrm{H}}_{1,\mathrm{eq}} = \widehat{\mathrm{H}}_1 - E_{m>0}^{(1)} = \widehat{\mathrm{A}}^+\widehat{\mathrm{A}}^-, \tag{6.8.1}$$

that is, performing an energy shift $E_m^{(1)} > E_0^{(1)}$ of $\widehat{\mathrm{H}}_1$. This Hamiltonian factorization involves a superpotential of the form:[11]

$$W_{(m)}(x) = -\frac{(\psi_m^{(1)})'(x)}{\psi_m^{(1)}(x)} = -\frac{\mathrm{d}}{\mathrm{d}x}\ln\psi_m^{(1)}(x). \tag{6.8.2}$$

Then, the superpartner of $\widehat{\mathrm{H}}_{1,\mathrm{eq}}$ is calculated as $\widehat{\mathrm{H}}_{2,\mathrm{eq}} = \widehat{\mathrm{A}}^-\widehat{\mathrm{A}}^+$ and, finally, the physical space is found to be $\widehat{\mathrm{H}}_2 = \widehat{\mathrm{H}}_{2,\mathrm{eq}} + E_m^{(1)}$.

In this scenario, it should be noted that the SUSY relation between $\widehat{\mathrm{H}}_{1,\mathrm{eq}}$ and $\widehat{\mathrm{H}}_{2,\mathrm{eq}}$ is *broken* (explicitly or spontaneously, see below) because $\widehat{\mathrm{H}}_{1,\mathrm{eq}}$ has a non-zero ground state energy level. Concretely, $\widehat{\mathrm{H}}_{1,\mathrm{eq}}$ has m negative energy states of value $E_k^{(1)} - E_m^{(1)} < 0$ ($k \in \{0,\ldots,m-1\}$). In spite of the fact that $\widehat{\mathrm{H}}_1$ is a positive operator, $\widehat{\mathrm{H}}_{1,\mathrm{eq}}$ becomes a non-positive operator when performing an energy shift with $E_m^{(1)} > E_0^{(1)}$. Furthermore, it is noticeable that $W_{(m)}$ has m singularities induced by the m nodes of the bound state $\psi_m^{(1)}$. In particular, these singularities can also be observed in V_2. Consequently, depending on the *kind* of singularity [216], new implicit[12] boundary conditions may appear in the second EVP arising from the normalization and continuity of $\psi_n^{(2)}$. If a singularity of V_2 in $x = x_\mathrm{s}$ is of the *strong* type [216], $\left\{\psi_n^{(2)}\right\}_{n=0}^{\infty}$ are forced to vanish at $x = x_\mathrm{s}$. In such a case, if $\exists n \in \mathbb{N}\cup\{0\}$ with $\psi_n^{(2)}(x = x_\mathrm{s}) \neq 0$, then $\psi_n^{(2)}$ cannot be considered a bound state and its corresponding eigenvalue $E_n^{(2)}$ will not be an allowed energy level of $\widehat{\mathrm{H}}_2$. Along this line, note that the energy level $E_m^{(1)}$ is also annihilated in $\widehat{\mathrm{H}}_2$ given that $\widehat{\mathrm{A}}^-\psi_m^{(1)} = 0$. For these reasons, we indicated in Section 6.4 that: the SUSY operators connect the eigenfunctions of $\widehat{\mathrm{H}}_1$ and $\widehat{\mathrm{H}}_2$ preserving the same eigenvalue spectrum, but not always the same energy spectrum.

On the other hand, we could also generate SUSY partners by using a singular superpotential different from Eq. (6.8.2), but satisfying the Riccati equation:

$$V_{1,2}(x) = W^2(x) \mp W'(x) + \alpha, \tag{6.8.3}$$

with $\alpha > E_0^{(1)}$. In such circumstances, we could avoid to annihilate any bound state of $\widehat{\mathrm{H}}_1$ if the condition $\widehat{\mathrm{A}}^-\psi_n^{(1)} \neq 0$ is fulfilled $\forall n \in \mathbb{N}\cup\{0\}$. In addition, despite the fact that we are using a singular superpotential, if $\psi_n^{(2)} \propto \widehat{\mathrm{A}}^-\psi_n^{(1)}$ are also found to be bound states, then the degeneracy of the energy spectra will be totally preserved. Consequently, singular superpotentials may destruct partially, totally or not the degeneracy of the energy spectra. In the first and second cases, SUSY is *explicitly broken* because there are unpaired energy levels $E_{n>0}^{(1,2)}$ between the bosonic and fermionic systems. Contrariwise, in the third case, SUSY is *spontaneously broken*. All levels are paired.

[11] Note that $\widehat{\mathrm{H}}_{1,\mathrm{eq}}\psi_m^{(1)} = 0$. Thus, using the non-degeneracy theorem in 1D QM we know that if $\psi_m^{(1)} \in \mathcal{L}^2([a,b])$:

$$\widehat{\mathrm{H}}_{1,\mathrm{eq}}\psi_m^{(1)} = 0 \Longleftrightarrow \widehat{\mathrm{A}}^-\psi_m^{(1)} = 0.$$

From $\widehat{\mathrm{A}}^-\psi_m^{(1)} = 0$ the superpotential $W_{(m)}$ is finally derived. As we will see in the next section, a SUSY transformation with a superpotential of the form given by Eq. (6.8.2) can be regarded as a Darboux transformation.

[12] See the description of explicit and implicit boundary conditions of an SL-EVP in Section 6.3.

As an example, consider as a virtual space $\widehat{\mathrm{H}}_1$ the infinite square well of Fig. 6.2. Now, let us construct the superpotential $W_{(1)}(x) = -(\psi_1^{(1)})'(x)/\psi_1^{(1)}(x) = -2\cot(2\pi x/L)$ with $L = \pi/2$. The superpotential has a strong singularity at $x = L/2$. This singularity breaks the interval $[0, L]$ into two disjoint pieces in $V_2(x) = W_{(1)}^2(x) + W'_{(1)}(x) + E_1^{(1)}$, which do not *see* each other (Fig. 6.5). In other words, an additional implicit boundary condition is included in the second EVP forcing the eigenfunctions $\psi_n^{(2)} \propto \widehat{\mathrm{A}}^- \psi_n^{(1)}$ to vanish at $x = L/2$. As a result, only the continuous normalizable eigenfunctions $\psi_n^{(2)}$ satisfying that $\psi_n^{(2)}(x = L/2) = 0$ are found to be bound states and the corresponding eigenvalues $E_n^{(2)}$ will be allowed energy levels in $\widehat{\mathrm{H}}_2$. In this case, SUSY is *explicitly broken* because we can observe unpaired energy levels between both superpartners at energy levels higher than $E_0^{(1)}$.

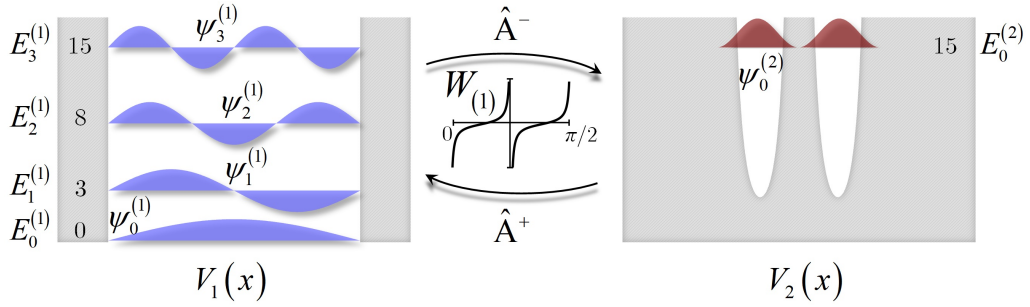

Figure 6.5. Singular superpotential. SUSY partners and energy spectra connected by a singular superpotential. In this example, we can observe a partial degeneracy. The energy levels are unpaired and, therefore, SUSY is explicitly broken.

6.9 Darboux transformation

The French mathematician Jean Gaston Darboux introduced in the second half of the XIX century a transformation connecting two EVPs of the form ($x \in [a, b] \subseteq \overline{\mathbb{R}}$):

$$-\frac{\mathrm{d}^2}{\mathrm{d}x^2}\psi_\lambda^{(1)}(x) + u(x)\,\psi_\lambda^{(1)}(x) = \lambda\psi_\lambda^{(1)}(x)\,; \tag{6.9.1}$$

$$-\frac{\mathrm{d}^2}{\mathrm{d}x^2}\psi_\lambda^{(2)}(x) + v(x)\,\psi_\lambda^{(2)}(x) = \lambda\psi_\lambda^{(2)}(x)\,, \tag{6.9.2}$$

both sharing the same eigenvalues (except for a selected $\lambda = \lambda_0$, see below). The main result, the so-called Darboux transformation, is given by the following theorem.

Theorem (Darboux transformation) *Consider an ODE of the form depicted by Eq.* (6.9.1) *with solutions* $\psi_\lambda^{(1)} \in C^2([a, b])$. *Now, consider the solution* $f = \psi_{\lambda_0}^{(1)}$ *at a fixed* $\lambda = \lambda_0$ *and its logarithmic derivative* $L_f = (\ln f)' = f'/f$. *Define the Darboux transformation as:*

$$\begin{array}{rccc} \mathfrak{D}_{\lambda_0}: & \mathcal{F}\left([a,b],\overline{\mathbb{R}}\right) & \longrightarrow & \mathcal{F}\left([a,b],\overline{\mathbb{R}}\right) \\ & \psi_\lambda^{(1)} & \longrightarrow & \mathfrak{D}_{\lambda_0}\left(\psi_\lambda^{(1)}\right) \end{array} \tag{6.9.3}$$

with:

$$\mathfrak{D}_{\lambda_0}\left(\psi_\lambda^{(1)}\right) := (\psi_\lambda^{(1)})' - L_f\,\psi_\lambda^{(1)}. \tag{6.9.4}$$

Then, the function $\psi_\lambda^{(2)} = \mathfrak{D}_{\lambda_0}(\psi_\lambda^{(1)})$ *satisfies the ODE Eq.* (6.9.2) *with:*

$$v(x) = u(x) - 2\frac{\mathrm{d}}{\mathrm{d}x}L_f(x)\,. \tag{6.9.5}$$

It is directly to verify that $\mathfrak{D}_{\lambda_0}(\psi^{(1)}_{\lambda_0}) = 0$. Hence, the Darboux transformation connects two EVPs of the form of Eqs. (6.9.1) and (6.9.2) with the same eigenvalues expect for the selected λ_0 eigenvalue. This behavior of the Darboux transformation reminds us the behavior of the SUSY operator $\widehat{\mathrm{A}}^{-}$ in previous sections. Concretely, we can identify the superpotential W with $-L_f$, and λ_0 with $E^{(1)}_0$ in Section 6.6 or with $E^{(1)}_{m>0}$ in Section 6.8. In this way, the unbroken SUSY transformation [Eq. (6.6.10)] can be rewritten in terms of the Darboux transformation as:

$$\psi^{(2)}_n \propto \widehat{\mathrm{A}}^{-}\psi^{(1)}_{n+1} = \mathfrak{D}_{E^{(1)}_0}\left(\psi^{(1)}_{n+1}\right). \tag{6.9.6}$$

In such a scenario, we can also identify $u \equiv V_1$ (our virtual space) and $v \equiv V_2$ (our physical space). Therefore, we can notice the intimate relation between 1D SUSY QM and the Darboux theorem.[13]

From now on, we will use the terminology Darboux transformation to refer to any SUSY transformation involving a superpotential of the form $W = -L_f$ with λ_0 an eigenvalue different from the ground state energy level of our virtual space [e.g. the transformation of Eq. (6.8.2)]. Later, in Section 6.11, we will use the terminology *Darboux procedure* to indicate that a Darboux transformation is involved in one of the SUSY transformations.

6.10 Continuous spectrum: spatial scattering

An interesting problem to analyze in QM is the probability that a free particle (plane wave) moving on a constant potential will be reflected or transmitted as a result of its interaction with a localized potential variation. As we will see later in Section 6.13, this problem is analogous to the spatial scattering in photonics.

Clearly, the scattering problem requires to focus our attention on potentials with continuous spectrum. In this scenario, the commutation and anticommutation relations which define the SUSY algebra [Eqs. (6.5.4)-(6.5.6)] are equally valid. As a result, SUSY will allow us to connect the spatial scattering problem of both superpartners, that is, we will be able to relate the reflected and transmitted probability amplitudes of a free particle moving in V_1 and V_2.

In order to have a well-defined scattering problem in $V_{1,2}$, now defined on the full line ($x \in \overline{\mathbb{R}}$), we require to observe an incident wave and at least one reflected or transmitted wave, that is:[14]

$$\psi^{(1,2)}(x \to -\infty) \neq 0 \quad \vee \quad \psi^{(1,2)}(x \to \infty) \neq 0. \tag{6.10.1}$$

A sufficient condition to satisfy Eq. (6.10.1) is to consider $V_{1,2}(x \to \pm\infty) < \infty$, which is fulfilled by assuming: (i) $W_\pm := W(x \to \pm\infty)$ exists and is finite, and (ii) W' is uniformly continuous on the full line. Thus, from Barbalat's lemma (see page 175) and Riccati's equation ($V_{1,2} = W^2 \mp W'$), we can infer that $W'_\pm = 0$ and $V_{1,\pm} = V_{2,\pm} = W^2_\pm < \infty$. To summarize, we will have a well-defined scattering problem in both superpartners with:

$$\left.\begin{array}{c} |W_\pm| < \infty \\ W' \text{ unif. cont.} \end{array}\right\} \Rightarrow V_\pm \equiv V_{1,\pm} = V_{2,\pm} = W^2_\pm < \infty \Rightarrow \psi^{(1,2)}(x \to \pm\infty) \neq 0. \tag{6.10.2}$$

Now, let us consider a free particle moving in each superpartner from the left with energy E. After the interaction with the potential variations $V_{1,2}(x)$, a reflected and a transmitted plane wave are generated. Thus, the asymptotic behavior of $\psi^{(1,2)}$ at $x \to \pm\infty$ is found to be:[15,16]

$$\psi^{(1,2)}(x) \underset{x\to-\infty}{\sim} \psi^{(1,2)}_-(x) = \exp(-jk_- x) + R_{1,2}\exp(jk_- x); \tag{6.10.3}$$

$$\psi^{(1,2)}(x) \underset{x\to+\infty}{\sim} \psi^{(1,2)}_+(x) = T_{1,2}\exp(-jk_+ x), \tag{6.10.4}$$

[13] In the transformation physics literature, the unbroken SUSY and Darboux transformations belong to the class of autoBäcklund transformations [243].

[14] The spatial scattering problem is well-defined when we can observe an incident wave and at least one reflected or transmitted wave. If the incident and reflected waves can be observed at $x \to -\infty$ ($x \to \infty$), then the transmitted wave is found at $x \to \infty$ ($x \to -\infty$).

[15] The results are analogous for a free particle moving from the right.

[16] We use here a different sign convention from [216] to denote the forward and backward propagation of the plane wave. Nonetheless, the conclusions are found to be the same.

with $R_{1,2}$ and $T_{1,2}$ being respectively the reflected and transmitted probability amplitudes,[17] and $k_\pm$ the particle wave number at $x \to \pm\infty$ given by the expression:

$$k_\pm = \sqrt{E - V_\pm}. \tag{6.10.5}$$

The reader can easily demonstrate that the wave functions given by Eqs. (6.10.3) and (6.10.4) are solutions of the Schrödinger equation with energy E and constant potentials V_- and V_+. In such a scenario, using the SUSY connection $\psi^{(2)} = N\widehat{\mathrm{A}}^{-}\psi^{(1)}$ (with N being a complex constant considering that $\psi^{(1,2)}$ are now complex-valued functions) we can relate the asymptotic behavior of the free particle in both systems as:

$$\psi_\pm^{(2)}(x) = N\left(\frac{\mathrm{d}}{\mathrm{d}x} + W_\pm\right)\psi_\pm^{(1)}(x). \tag{6.10.6}$$

Thus, we have at $x \to -\infty$:

$$\begin{aligned}\exp(-jk_-x) + R_2\exp(jk_-x) = N(-jk_- + W_-)\exp(-jk_-x)\\ + NR_1(jk_- + W_-)\exp(jk_-x),\end{aligned} \tag{6.10.7}$$

and at $x \to \infty$:

$$T_2\exp(-jk_+x) = N(-jk_+ + W_+)T_1\exp(-jk_+x). \tag{6.10.8}$$

Finally, equating terms with the same exponent in Eqs. (6.10.7) and (6.10.8), we find:

$$\frac{R_2}{R_1} = \frac{W_- + jk_-}{W_- - jk_-}; \quad \frac{T_2}{T_1} = \frac{W_+ - jk_+}{W_- - jk_-}. \tag{6.10.9}$$

These relations between the scattering amplitudes can be used to *analyze* the reflection and transmission coefficients of non-analytically solvable potentials or to *design* potentials with desired scattering properties, both functionalities (analysis & synthesis) without the necessity of solving numerically the Schrödinger equation. Outstandingly, these ideas can be directly extrapolated to the spatial scattering problem of photonics and acoustics, as we will see later in Section 6.13. For completeness, let us take a closer look at the above equations. In particular, the following remarks are in order:

1. The SUSY partners have identical reflection and transmission probabilities:

$$|R_1|^2 = |R_2|^2; \quad |T_1|^2 = |T_2|^2, \tag{6.10.10}$$

   as a direct consequence of the fact that the energy $E = k_\pm^2 + W_\pm^2$ is the same in both systems.

2. Using the SUSY relation $\psi^{(1)} = M\widehat{\mathrm{A}}^{+}\psi^{(2)}$ (with M being a complex constant), the ratio of the transmitted amplitudes can also be expressed as $T_2/T_1 = (W_- + jk_-)/(W_+ + jk_+)$. From the relation $E = k_\pm^2 + W_\pm^2$, it is directly to verify that this expression and Eq. (6.10.9) are in good agreement.

3. It should be noted that $|W_+| = |W_-| \Leftrightarrow V_+ = V_- \Leftrightarrow k_+ = k_-$. Such a situation can be observed:

   - If $W_+ = -W_-$, in which case SUSY is unbroken provided that the superpartners support bound states.[18] Here, we observe that $R_2/R_1 = -T_2/T_1$.
   - If $W_+ = W_-$, in which case SUSY is broken provided that the superpartners support bound states. Here, we observe that $T_1 = T_2$.

[17] The reflected and transmitted probability amplitudes are equal to the reflection and transmission coefficients when the amplitude of the incident wave is set to 1.

[18] Note that a potential with continuous spectrum can also support bound states, as commented in Section 6.3. This situation leads to the concept of bound states in the continuum, see Subsection 6.11.3.

4. When $W_- = 0$, thus $R_1 = -R_2$. If the superpartners support bound states, then SUSY may be unbroken or broken. Both SUSY states are possible taking into account that a solution for the ground state of the form given by Eqs. (6.6.5) or (6.6.6) could be normalizable or not.

5. In general, $\left|\psi^{(1,2)}\left(x \to -\infty\right)\right| \neq \left|\psi^{(1,2)}\left(x \to \infty\right)\right|$ and, therefore, $\widehat{\mathrm{A}}^{+} \neq \left(\widehat{\mathrm{A}}^{-}\right)^{\dagger}$. Along this line, it should also be taken into account that we are operating with non-normalizable complex-valued functions. Hence, we work in a *rigged* Hilbert space over the field $\mathbb{C}$.

6. Despite the fact that we consider complex-valued wave functions, the superpotential and the potentials must be assumed real-valued functions to guarantee identical reflection and transmission probabilities between superpartners. Otherwise, the scattering probabilities could be found different in both systems [235].

7. In a SUSY Hamiltonian chain $\left\{\widehat{\mathrm{H}}_s\right\}_{s=1}^{m}$ where the scattering problem is well-defined, the value of the potentials $\{V_s\}_{s=1}^{m}$ and superpotentials $\{W_s\}_{s=1}^{m-1}$ at $x \to \pm\infty$ is the same:

$$V_{1,\pm} = V_{2,\pm} = \ldots = V_{m,\pm} = W_{1,\pm}^2, \tag{6.10.11}$$

with $W_{1,\pm} = W_{2,\pm} = \ldots = W_{m-1,\pm} \equiv W_{\pm}$. Thus, the scattering coefficients of $\widehat{\mathrm{H}}_m$ and $\widehat{\mathrm{H}}_1$ are related by the following expressions:

$$\frac{R_m}{R_1} = \left(\frac{W_- + jk_-}{W_- - jk_-}\right)^{m-1}; \quad \frac{T_m}{T_1} = \left(\frac{W_+ - jk_+}{W_- - jk_-}\right)^{m-1}. \tag{6.10.12}$$

8. R_1 and R_2 have the same poles in the complex k-plane except that R_1 (R_2) has an additional pole at $k_- = jW_-$ ($k_- = -jW_-$). If the superpartners support bound states, the ground state lies in $\widehat{\mathrm{H}}_1$ ($\widehat{\mathrm{H}}_2$) and SUSY is unbroken, then $W_- < 0$ and $W_+ > 0$ ($W_- > 0$ and $W_+ < 0$). Consequently, the extra pole of R_1 (R_2) is on the negative imaginary axis. This case corresponds with a reflected wave that exists in the absence of the incident wave. Specifically, the reflected wave is the *tail* of the bosonic (fermionic) ground state. To clarify this scenario, it is interesting to highlight that:

   - Despite the fact that $k_- \in \mathbb{C}$, note that $V_- = E - k_-^2 \in \mathbb{R}$.
   - If SUSY is unbroken the energy must be zero. Clearly, we find that $E = k_-^2 + W_-^2 = 0$ when $k_- = \pm jW_-$.
   - $k_- \in \mathbb{C} \Rightarrow E < V_-$. This implies that a non-oscillatory behavior of the wave functions can be observed at $x \to -\infty$ [see Eq. (6.3.20)]. This is one of the characteristics features of a bound state. In particular, the reflected wave is $\exp(jk_-x) = \exp(|W_-|\,x)$ for the extra poles of R_1 and R_2, which decays exponentially as $x \to -\infty$. This is the tail of the bosonic (fermionic) ground state given by Eq. (6.6.5) [Eq. (6.6.6)]. As commented before, the reflected wave exists in the absence of the incident wave. This is the reason underlying the fact that we observe a pole in the reflection coefficient.
   - The extra poles of T_1 and T_2 admit a similar discussion.

As an interesting example, consider a constant potential $V_1(x) = A^2$, with $A \in \mathbb{R}^+$ and $x \in \overline{\mathbb{R}}$. It is clear that this potential is reflectionless because we cannot observe any localized potential variation ($R_1 = 0$). Then, the superpartner will be necessarily reflectionless ($R_2 = 0$). Concretely, the superpotential is:

$$W(x) = -A\tanh(Ax), \tag{6.10.13}$$

and the partner potential is of the form:

$$V_2(x) = A^2 - 2A^2\mathrm{sech}^2(Ax). \tag{6.10.14}$$

Outstandingly, a reflectionless quantum-mechanical potential can be employed in photonics and acoustics to design a reflectionless (optical or acoustical) refractive index profile. This result will be of great interest to us in Chapter 8.

6.11 Isospectral transformations

In this section, we will discuss the possibility of using 1D SUSY QM to construct, from a given potential V_1, an n-parameter family of isospectral potentials $\widetilde{V}_1(\eta_1, \ldots, \eta_n)$, that is, potentials with exactly the same spectrum and scattering properties (in module and phase) as the original one. Although there are other methods to generate an isospectral family of potentials (e.g. the Gelfand-Levitan method [256]), the use of SUSY allows us to reduce the complexity of these methods. In this way, the supersymmetric isospectral transformations will be revealed as an interesting and simple strategy to analyze and design new potentials with desired spectrum and scattering properties.

The section is organized as follows. In Subsection 6.11.1, we will describe how to construct the one-parameter family. The generalization to obtain a multi-parameter family is described in Subsection 6.11.2. Finally, in Subsection 6.11.3, we will discuss the possibility of generating bound states in the continuum by applying supersymmetric isospectral transformations starting from a potential V_1 without bound states.

6.11.1 One-parameter family

In this subsection, we describe two different procedures to build the one-parameter isospectral family $\widetilde{V}_1(\eta_1)$ of a given potential V_1. The first approach is based on finding a general solution of the Riccati equation. The second approach is based on the Darboux transformation, discussed in Section 6.9.

General solution of the Riccati equation

The first approach follows from a general solution of the nonlinear Riccati ODE. Suppose that V_1 and V_2 are superpartners connected by a superpotential W. In such a scenario, note that W is only a particular solution of the ODE $V_2(x) = W^2(x) + W'(x)$. Now, we ask about the general solution of the above equation. From [255], we know that given a particular solution of the Riccati equation (W), the general solution ($\widetilde{W}$) is of the form $\widetilde{W} = W + 1/g$, where g is a real-valued function satisfying the Bernoulli equation $g' = 1 + 2Wg$. Solving this ODE [255], we find the general solution of the Riccati equation:

$$\widetilde{W}(x;\eta_1) = W(x) + \frac{\mathrm{d}}{\mathrm{d}x}\ln\left[\eta_1 + \int^x \exp\left(-2\int^\alpha W(\beta)\,\mathrm{d}\beta\right)\mathrm{d}\alpha\right], \tag{6.11.1}$$

with η_1 a real constant of integration, i.e., a degree of freedom of our problem. Thus, we have obtained a superpotential family $\widetilde{W}(\eta_1)$ satisfying the Riccati equation for the potential V_2, that is, $V_2(x) = \widetilde{W}^2(x;\eta_1) + \widetilde{W}'(x;\eta_1)$.

Along this line, note that we have other Riccati equation, the Riccati equation for the original potential $V_1(x) = W^2(x) - W'(x)$. Hence, if we generate the family $\widetilde{V}_1(\eta_1)$ by using the superpotential family $\widetilde{W}(\eta_1)$:

$$\begin{aligned}\widetilde{V}_1(x;\eta_1) &= \widetilde{W}^2(x;\eta_1) - \widetilde{W}'(x;\eta_1)\\ &= V_1(x) - 2\frac{\mathrm{d}^2}{\mathrm{d}x^2}\ln\left[\eta_1 + \int^x \exp\left(-2\int^\alpha W(\beta)\,\mathrm{d}\beta\right)\mathrm{d}\alpha\right],\end{aligned} \tag{6.11.2}$$

we obtain an isospectral family of V_1 with η_1 being the parameter of the family. In other words, we have found a family of potentials $\widetilde{V}_1(\eta_1)$ sharing the same SUSY partner V_2 and connected via the Riccati equations:

$$\widetilde{V}_1(x;\eta_1) = \widetilde{W}^2(x;\eta_1) - \widetilde{W}'(x;\eta_1); \tag{6.11.3}$$

$$V_2(x) = \widetilde{W}^2(x;\eta_1) + \widetilde{W}'(x;\eta_1). \tag{6.11.4}$$

Figure 6.6 illustrates this scenario. It is interesting to mention that, in contrast to the Darboux procedure (see below), the SUSY relation between $\widetilde{V}_1$ and V_2 may be unbroken or broken in this method. In any case, in order to guarantee degenerate spectra, the superpotential family must be nonsingular (sufficient condition but not necessary). To this end, the parameter η_1 must satisfy the condition:

$$\eta_1 + \int^x \exp\left(-2\int^\alpha W(\beta)\,\mathrm{d}\beta\right)\mathrm{d}\alpha \neq 0, \quad \forall x \in [a,b]\,. \tag{6.11.5}$$

If SUSY is unbroken $W(x) = -(\ln\psi_0^{(1)}(x))'$ and, therefore, $\eta_1 \notin [-1,0]$.

As a direct consequence of sharing the same SUSY partner, the family $\widetilde{V}_1(\eta_1)$ must be isospectral: the same spectrum and the same scattering properties [$R_1 = R_1(\eta_1)$ and $T_1 = T_1(\eta_1)$] given that $\widetilde{W}_\pm(\eta_1) = W_\pm$. Furthermore, it should be noted that the families $\widetilde{V}_1(\eta_1)$ and $\widetilde{W}(\eta_1)$ contain the original potential and superpotential with $V_1 \equiv \widetilde{V}_1(\eta_1 \to \pm\infty)$ and $W \equiv \widetilde{W}(\eta_1 \to \pm\infty)$.

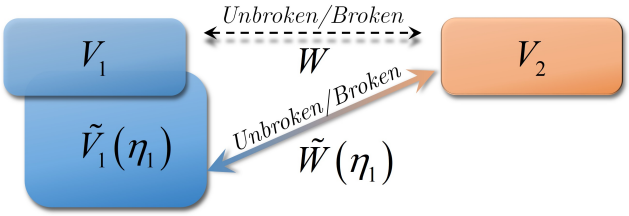

Figure 6.6. Schematic unbroken/broken SUSY relation between the isospectral family $\widetilde{V}_1(\eta_1)$ and V_2.

Darboux procedure

The second approach, the so-called Darboux procedure, is schematically depicted in Fig. 6.7 for the one-parameter case. In essence, it consists of first deleting the ground state $\psi_0^{(1)}$ of V_1 with an unbroken SUSY transformation obtaining the potential $V_2(x) = V_1(x) - 2(\ln\psi_0^{(1)}(x))''$ and, secondly, applying a Darboux transformation using a non-normalizable solution $\Phi_1(\eta_1) \propto 1/\psi_0^{(1)}$ of $\widehat{\mathrm{H}}_2$ at energy $E_0^{(1)}$ to obtain the isospectral family $\widetilde{V}_1(x;\eta_1) = V_2(x) - 2(\ln\Phi_1(x;\eta_1))''$. The method is called the Darboux procedure because it involves two different Darboux transformations: firstly using the physical eigenfunction $\psi_0^{(1)}$ of $\widehat{\mathrm{H}}_1$ at energy $E_0^{(1)}$, and secondly using the non-physical eigenfunction $\Phi_1(\eta_1)$ of $\widehat{\mathrm{H}}_2$ at energy $E_0^{(1)}$.

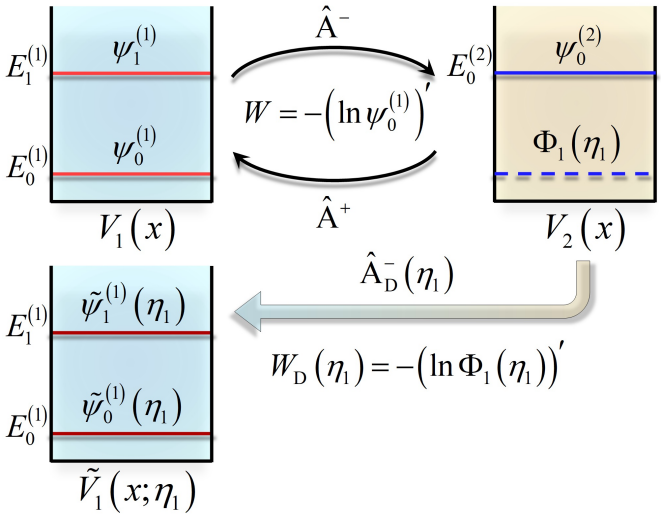

Figure 6.7. Flowchart of transformations of the one-parameter Darboux procedure.

In order to gain insight into this procedure, let us be more precise, specifically in the second Darboux transformation. It is worth mentioning that, although the potential V_2 does not have an allowed energy level $E_0^{(1)}$ (due to the unbroken SUSY transformation performed in the first step) the EVP $\widehat{\mathrm{H}}_2\psi_\lambda^{(2)} = \lambda\psi_\lambda^{(2)}$ has at $\lambda = E_0^{(1)}$ a general solution of the form:[19]

$$\psi^{(2)}_{\lambda=E_0^{(1)}}(x) \equiv \Phi_1(x;\eta_1) = \frac{\mathcal{I}_1(x)+\eta_1}{\psi_0^{(1)}(x)}, \tag{6.11.6}$$

where:

$$\mathcal{I}_1(x) := \int^x \left(\psi_0^{(1)}\right)^2(\alpha)\,\mathrm{d}\alpha. \tag{6.11.7}$$

Concretely, $\Phi_1(\eta_1)$ is a non-normalizable function because $1/\psi_0^{(1)}$ does not lie in $\mathcal{L}^2([a,b])$. Nevertheless, applying a Darboux transformation in $\widehat{\mathrm{H}}_2$ taking as eigenvalue of reference $\lambda_0 = E_0^{(1)}$ (see Section 6.9), or equivalently, applying an unbroken SUSY transformation in $\widehat{\mathrm{H}}_2$ by using $\Phi_1(\eta_1)$ as a *virtual* ground state, we obtain the sought isospectral family $\widetilde{V}_1(\eta_1)$:

$$\begin{aligned}\widetilde{V}_1(x;\eta_1) &= V_2(x) - 2\frac{\mathrm{d}^2}{\mathrm{d}x^2}\ln\Phi_1(x;\eta_1)\\ &= V_1(x) - 2\frac{\mathrm{d}^2}{\mathrm{d}x^2}\ln\left(\psi_0^{(1)}(x)\,\Phi_1(x;\eta_1)\right) = V_1(x) - 2\frac{\mathrm{d}^2}{\mathrm{d}x^2}\ln\left(\mathcal{I}_1(x)+\eta_1\right),\end{aligned} \tag{6.11.8}$$

which is in line with Eq. (6.11.2) taking into account that $\mathcal{I}_1$ can be expressed as a function of W by using the relation $W(x) = -(\ln\psi_0^{(1)}(x))'$. Along these lines, the following remarks require our attention:

- Note that the first isospectral method is more general than the Darboux procedure. In the former case, the SUSY relation between $\widetilde{V}_1$ and V_2 may be unbroken or broken (Fig. 6.6). However, in the latter case, the SUSY relation between $\widetilde{V}_1$ and V_2 is always unbroken (Fig. 6.7).
- As commented before, the second Darboux transformation can be regarded as an unbroken SUSY transformation. In particular, it involves a superhamiltonian and supercharges of the form:

$$\mathrm{H}_\mathrm{D} = \begin{bmatrix}\widehat{\mathrm{H}}_2 & \widehat{0}\\ \widehat{0} & \widehat{\widetilde{\mathrm{H}}}_1(\eta_1)\end{bmatrix};\quad \mathrm{Q}_\mathrm{D}^- = \begin{bmatrix}\widehat{0} & \widehat{0}\\ \widehat{\mathrm{A}}_\mathrm{D}^-(\eta_1) & \widehat{0}\end{bmatrix};\quad \mathrm{Q}_\mathrm{D}^+ = \begin{bmatrix}\widehat{0} & \widehat{\mathrm{A}}_\mathrm{D}^+(\eta_1)\\ \widehat{0} & \widehat{0}\end{bmatrix}, \tag{6.11.9}$$

[19] From the *reduction of order* method [255], we know that the general solution of the ODE $y''+p(x)y'+q(x)y=0$ is of the form $y_\mathrm{G} = c_1y_1 + c_2y_2$, where $c_{1,2}$ are real constants, $y_1 = f_1(x)$ is a particular solution and:

$$y_2 = f_1(x)\int^x \frac{1}{f_1^2(\alpha)}\exp\left(-\int^\alpha p(\beta)\,\mathrm{d}\beta\right)\mathrm{d}\alpha,$$

with y_1 and y_2 linearly independent solutions, that is, $\mathcal{W}(y_1,y_2) = y_1y_2' - y_1'y_2 \neq 0$, where $\mathcal{W}$ is the Wronskian. In our problem $y'' + (E_0^{(1)} - V_2(x))y = 0$, we find that $y_1 = 1/\psi_0^{(1)}(x)$ and $y_2 = \mathcal{I}_1(x)/\psi_0^{(1)}(x)$. Thus, the general solution [Eq. (6.11.6)] must be written as:

$$y_\mathrm{G} = \Phi_1(x;c_1,c_2) = \frac{c_1 + c_2\mathcal{I}_1(x)}{\psi_0^{(1)}(x)},$$

with two degrees of freedom described by the constants c_1 and c_2. Nonetheless, note that we can only observe a single degree of freedom in the isospectral family of potentials given that:

$$\begin{aligned}\widetilde{V}_1(x;c_1,c_2) &= V_1(x) - 2\frac{\mathrm{d}^2}{\mathrm{d}x^2}\ln\left(c_2\mathcal{I}_1(x)+c_1\right) = V_1(x) - 2\frac{\mathrm{d}^2}{\mathrm{d}x^2}\ln\left[c_2\left(\mathcal{I}_1(x)+\frac{c_1}{c_2}\right)\right]\\ &= V_1(x) - 2\frac{\mathrm{d}^2}{\mathrm{d}x^2}\ln(c_2) - 2\frac{\mathrm{d}^2}{\mathrm{d}x^2}\ln\left(\mathcal{I}_1(x)+\frac{c_1}{c_2}\right) = V_1(x) - 2\frac{\mathrm{d}^2}{\mathrm{d}x^2}\ln\left(\mathcal{I}_1(x)+\frac{c_1}{c_2}\right),\end{aligned}$$

which matches to Eq. (6.11.8) renaming $c_1/c_2 \equiv \eta_1$. For this reason, we write Eq. (6.11.6) with only one degree of freedom from the beginning.

with $\widehat{\mathrm{H}}_2 = -\mathrm{d}^2/\mathrm{d}x^2 + V_2(x)$ being the virtual space, $\widehat{\widetilde{\mathrm{H}}}_1(\eta_1) = -\mathrm{d}^2/\mathrm{d}x^2 + \widetilde{V}_1(x;\eta_1)$ the physical space and:

$$\widehat{\mathrm{A}}_{\mathrm{D}}^{\pm}(\eta_1) = \mp\frac{\mathrm{d}}{\mathrm{d}x} + W_{\mathrm{D}}(x;\eta_1); \quad W_{\mathrm{D}}(x;\eta_1) = -\frac{\mathrm{d}}{\mathrm{d}x}\ln\Phi_1(x;\eta_1). \tag{6.11.10}$$

- Using the new SUSY operators $\widehat{\mathrm{A}}_{\mathrm{D}}^{\pm}(\eta_1)$, the bound states of the isospectral family $\widetilde{V}_1(\eta_1)$ can be calculated as:

$$\widetilde{\psi}_0^{(1)}(x;\eta_1) \propto 1/\Phi_1(x;\eta_1) = \psi_0^{(1)}(x)/(\mathcal{I}_1(x) + \eta_1); \tag{6.11.11}$$

$$\widetilde{\psi}_n^{(1)}(x;\eta_1) \propto \widehat{\mathrm{A}}_{\mathrm{D}}^{-}(\eta_1)\,\widehat{\mathrm{A}}^{-}\psi_n^{(1)}(x), \quad (n>0). \tag{6.11.12}$$

  Hence, it is easily to verify that the bound states $\widetilde{\psi}_n^{(1)}(\eta_1)$ are found to be normalizable if $\eta_1 \notin [-1, 0]$, in line with the first isospectral method when the SUSY relation between $\widetilde{V}_1(\eta_1)$ and V_2 is unbroken [Eq. (6.11.5)].

- The original potential and superpotential can be retrieved from the families $\widetilde{V}_1(\eta_1)$ and $\widetilde{W}(\eta_1)$ taking $\eta_1 \to \pm\infty$.

Additional notes on the one-parameter isospectral methods

- In the first isospectral procedure, instead of finding a general solution to the Riccati equation $V_2(x) = W^2(x) + W'(x)$, we could propose to find the general solution of the Riccati equation $V_1(x) = W^2(x) - W'(x)$. Hence, proceeding in a similar way as in the first method, we will be able to calculate an isospectral family $\widetilde{V}_2(\eta_1)$ of the form:

$$\widetilde{V}_2(x;\eta_1) = V_2(x) - 2\frac{\mathrm{d}^2}{\mathrm{d}x^2}\ln\left[\eta_1 - \int^x \exp\left(2\int^\alpha W(\beta)\,\mathrm{d}\beta\right)\mathrm{d}\alpha\right], \tag{6.11.13}$$

  sharing the same superpartner V_1 and connected by the family of superpotentials $\widetilde{W}(\eta_1)$:

$$\widetilde{W}(x;\eta_1) = W(x) - \frac{\mathrm{d}}{\mathrm{d}x}\ln\left[\eta_1 - \int^x \exp\left(2\int^\alpha W(\beta)\,\mathrm{d}\beta\right)\mathrm{d}\alpha\right]. \tag{6.11.14}$$

  Remarkably, the family $\widetilde{V}_2(\eta_1)$ will have the same spectrum and scattering properties as V_2, provided that η_1 satisfies the condition:

$$\eta_1 - \int^x \exp\left(2\int^\alpha W(\beta)\,\mathrm{d}\beta\right)\mathrm{d}\alpha \neq 0, \quad \forall x \in [a,b]. \tag{6.11.15}$$

- Consider two superpartners V_1 and V_2 supporting both continuous spectra with absence of bound states. In this scenario, the first isospectral method can be directly employed in the continuum. Nevertheless, the second method is not straightforward to apply given that it will require to use oscillatory functions in the Darboux transformations (i.e., states in the continuum, eigenfunctions with nodes). As a result, $\widetilde{W}(\eta_1)$ could have singularities that could break the degeneracy of the family $\widetilde{V}_1(\eta_1)$. In any case, surprisingly, the Darboux procedure has attracted special attention in such a scenario as an interesting strategy, not only to construct an isospectral family of potentials, but also to generate bound states in the continuum (see Subsection 6.11.3).

- Consider an infinite broken SUSY Hamiltonian chain and an isospectral family of potentials $\widetilde{V}_1(\eta_1)$. It should be noted that they are different isospectral families. The former is an infinite countable set with the same cardinality as that of the natural numbers ($\aleph_0$). In contrast, the latter is an infinite uncountable set with the same cardinality as that of the real numbers ($\aleph_1$).

6.11.2 Multi-parameter family

Interestingly, the one-parameter Darboux procedure can be extended to an n-parameter family of isospectral potentials by first deleting all n bound states of a given potential V_1 using an unbroken SUSY Hamiltonian chain, and later reinserting them with a series of Darboux transformations. In order to gain clarity, let us detail the procedure for the two-parameter family. Figure 6.8 depicts the flowchart of transformations.

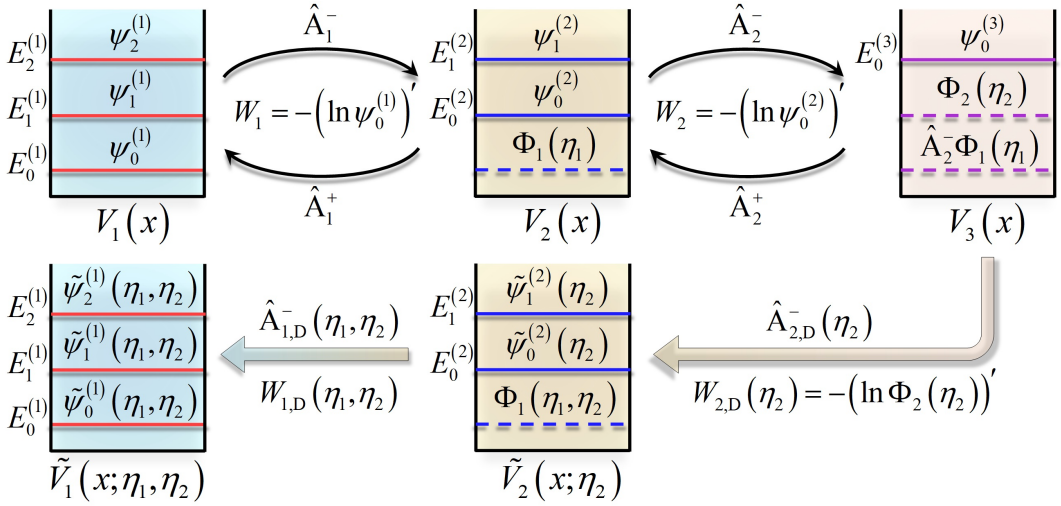

Figure 6.8. Flowchart of transformations of the two-parameter Darboux procedure.

Firstly, we start by generating an unbroken SUSY Hamiltonian chain of three systems deleting the first two bound states of V_1:

$$V_3(x) = V_1(x) - 2\frac{\mathrm{d}^2}{\mathrm{d}x^2}\ln\left(\psi_0^{(1)}(x)\,\psi_0^{(2)}(x)\right). \tag{6.11.16}$$

As seen, V_2 has a non-normalizable solution $\Phi_1(\eta_1)$ at $E_0^{(1)}$ of the form depicted by Eq. (6.11.6), and V_3 has a non-normalizable solution at $E_0^{(1)}$ and $E_1^{(1)}$ of the form $\widehat{\mathrm{A}}_2^-\Phi_1(\eta_1)$ and $\Phi_2(\eta_2)$, respectively, where:

$$\widehat{\mathrm{A}}_2^- = \frac{\mathrm{d}}{\mathrm{d}x} + W_2(x) = \frac{\mathrm{d}}{\mathrm{d}x} - \left(\ln\psi_0^{(2)}(x)\right)'; \tag{6.11.17}$$

$$\Phi_2(x;\eta_2) = \frac{\mathcal{I}_2(x) + \eta_2}{\psi_0^{(2)}(x)};\quad \mathcal{I}_2(x) := \int^x \left(\psi_0^{(2)}\right)^2(\alpha)\,\mathrm{d}\alpha, \tag{6.11.18}$$

and $\eta_2 \notin [-1, 0]$.

Secondly, we should reinsert the annihilated energy levels $E_0^{(1)}$ and $E_1^{(1)}$. To this end, we first reinsert $E_1^{(1)}$ by constructing the one-parameter isospectral family $\widetilde{V}_2(\eta_2)$ from V_3 using a Darboux transformation taking as eigenvalue of reference $\lambda_0 = E_1^{(1)}$ [or equivalently, we can say that we apply an unbroken SUSY transformation in V_3 by using $\Phi_2(\eta_2)$ as a virtual ground state]:

$$\widetilde{V}_2(x;\eta_2) = V_3(x) - 2\frac{\mathrm{d}^2}{\mathrm{d}x^2}\ln\Phi_2(x;\eta_2). \tag{6.11.19}$$

Note that the SUSY operators connecting the eigenfunctions of V_3 and $\widetilde{V}_2(\eta_2)$ are of the form:

$$\widehat{\mathrm{A}}_{2,\mathrm{D}}^{\pm}(\eta_2) = \mp\frac{\mathrm{d}}{\mathrm{d}x} - \left(\ln\Phi_2(x;\eta_2)\right)'. \tag{6.11.20}$$

Hence, the non-normalizable solution of V_3 at $E_0^{(1)}$ $[\widehat{\mathrm{A}}_2^- \Phi_1(\eta_1)]$ becomes a non-normalizable solution of $\widetilde{V}_2(\eta_2)$ at the same energy level by applying the operator $\widehat{\mathrm{A}}_{2,\mathrm{D}}^-(\eta_2)$. That is, $\widetilde{V}_2(\eta_2)$ has a non-normalizable solution at $E_0^{(1)}$ of the form:

$$\Phi_1(x;\eta_1,\eta_2) = \widehat{\mathrm{A}}_{2,\mathrm{D}}^-(\eta_2)\,\widehat{\mathrm{A}}_2^-\,\Phi_1(x;\eta_1)\,. \tag{6.11.21}$$

Finally, we will be able to reinsert $E_0^{(1)}$ by applying an additional Darboux transformation in $\widetilde{V}_2(\eta_2)$ taking as eigenvalue of reference $\lambda_0 = E_0^{(1)}$. As a result, we obtain the two-parameter isospectral family $\widetilde{V}_1(\eta_1,\eta_2)$ as a function of the original potential V_1 by using Eqs. (6.11.16) and (6.11.19):

$$\begin{aligned}\widetilde{V}_1(x;\eta_1,\eta_2) &= \widetilde{V}_2(x;\eta_2) - 2\frac{\mathrm{d}^2}{\mathrm{d}x^2}\ln\Phi_1(x;\eta_1,\eta_2)\\ &= V_3(x) - 2\frac{\mathrm{d}^2}{\mathrm{d}x^2}\ln\left(\Phi_2(x;\eta_2)\,\Phi_1(x;\eta_1,\eta_2)\right)\\ &= V_1(x) - 2\frac{\mathrm{d}^2}{\mathrm{d}x^2}\ln\left(\psi_0^{(1)}(x)\,\psi_0^{(2)}(x)\,\Phi_2(x;\eta_2)\,\Phi_1(x;\eta_1,\eta_2)\right).\end{aligned} \tag{6.11.22}$$

Proceeding in a similar manner, the multi-parameter family $\widetilde{V}_1(\eta_1,\ldots,\eta_n)$ can be calculated from V_1 as:

$$\widetilde{V}_1(x;\eta_1,\ldots,\eta_n) = V_1(x) - 2\frac{\mathrm{d}^2}{\mathrm{d}x^2}\ln\left[\prod_{i=1}^{n}\psi_0^{(i)}(x)\,\Phi_i(x;\eta_i,\ldots,\eta_n)\right], \tag{6.11.23}$$

where:

$$\Phi_i(x;\eta_i,\ldots,\eta_n) = \left(\prod_{j=i+1}^{n}\widehat{\mathrm{A}}_{j,\mathrm{D}}^-(\eta_j,\ldots,\eta_n)\right)\left(\prod_{q=1}^{n-i}\widehat{\mathrm{A}}_{n-q+1}^-\right)\Phi_i(r;\eta_i)\,; \tag{6.11.24}$$

$$\widehat{\mathrm{A}}_{i,\mathrm{D}}^-(\eta_i,\ldots,\eta_n) = \frac{\mathrm{d}}{\mathrm{d}x} - (\ln\Phi_i(x;\eta_i,\ldots,\eta_n))'\,;\quad \widehat{\mathrm{A}}_i^- = \frac{\mathrm{d}}{\mathrm{d}x} - \left(\ln\psi_0^{(i)}(x)\right)'\,; \tag{6.11.25}$$

$$\Phi_i(x;\eta_i) = \frac{\mathcal{I}_i(x)+\eta_i}{\psi_0^{(i)}(x)};\quad \mathcal{I}_i(x) := \int^x\left(\psi_0^{(i)}\right)^2(\alpha)\,\mathrm{d}\alpha;\quad \eta_i \notin [-1,0]\,. \tag{6.11.26}$$

In particular, $\widehat{\mathrm{A}}_{i,\mathrm{D}}^-(\eta_i,\ldots,\eta_n)$ reinserts the ground state energy level $E_0^{(i)}$ in $\widetilde{V}_i(\eta_i,\ldots,\eta_n)$ from V_{i+1} by using a Darboux transformation with the non-normalizable solution $\Phi_i(\eta_i)$ as eigenfunction of reference [or equivalently, by applying an unbroken SUSY transformation in V_{i+1} considering $\Phi_i(\eta_i)$ as a virtual ground state of V_{i+1} at energy $E_0^{(i)}$]. Note that this operator is related with the SUSY operator $\widehat{\mathrm{A}}_i^\dagger(\eta_i,\ldots,\eta_n)$ defined in [257] as $\widehat{\mathrm{A}}_{i,\mathrm{D}}^-(\eta_i,\ldots,\eta_n) = -\widehat{\mathrm{A}}_i^\dagger(\eta_i,\ldots,\eta_n)$. In any case, the multi-parameter isospectral family given by Eq. (6.11.23) is found to be the same when using $\widehat{\mathrm{A}}_{i,\mathrm{D}}^-(\eta_i,\ldots,\eta_n)$ or $\widehat{\mathrm{A}}_i^\dagger(\eta_i,\ldots,\eta_n)$ in Eq. (6.11.24). Outstandingly, the previous expressions allow us to *analyze* and *design* isospectral potentials, not only with identical spectra, but also with the same scattering probabilities. This will be of great interest to us to investigate new reflectionless potentials in Chapter 8.

6.11.3 Bound states in the continuum

Bound states in the continuum (BICs) are localized waves coexisting with a continuous spectrum of radiating waves carrying energy away. The idea of BICs was first introduced by Von Neumann and Wigner in 1929 in the framework of quantum mechanics [258]. These authors realized that it was possible to construct quantum potentials supporting bound states in the classical energy continuum. In this topic, further works have been reported extrapolating this idea to different branches of physics, such as in photonics and acoustics [259]. As a byproduct, a variety of applications have

been demonstrated for atomic systems [260], water waves [261], elastic waves in solids [262], optical waves [263] and acoustic waves in air [264].[20]

Motivated by these results, we show in this subsection a mechanism to construct BICs in the framework of quantum mechanics inspired by SUSY transformations, and more specifically, by the Darboux procedure. Obviously, this method can also be extended to other branches of physics to construct BICs by using quantum-mechanical analogies.

The basic idea is to start from a potential supporting a continuous spectrum and calculate an isospectral family of potentials by applying the Darboux procedure. However, in contrast to the previous subsections, we will apply the Darboux transformations starting from states in the continuum, i.e., oscillatory functions with nodes. The method will preserve the spectrum of the original potential, but adding BICs at the eigenvalues of reference (energies) selected in the Darboux transformations.

In order to illustrate this method, consider for simplicity a spherical potential $V_1^{(3D)}$ with radial symmetry. The three-dimensional (3D) time-independent Schrödinger equation can be reduced to (see Subsection 6.14.2 for more details):

$$\left(-\frac{\mathrm{d}^2}{\mathrm{d}r^2}+V_1\left(r\right)\right)u\left(r\right)=E\,u\left(r\right);\quad r\geq 0, \tag{6.11.27}$$

where V_1 and $V_1^{(3D)}$ are related as indicated by Eq. (6.14.16). In such a scenario, let us assume a potential V_1 supporting a continuous positive energy spectrum *without* bound states.

Now, consider a nonsingular oscillatory function u_0 (a state in the continuum) associated with an arbitrary energy $E_0>0$ and satisfying that $u_0\left(r=0\right)=0$. In particular, this eigenfunction will be used in the Darboux procedure to generate an isospectral family of potentials $\widetilde{V}_1(\eta_1)$. Bearing in mind that u_0 has nodes, the first step of the Darboux procedure gives rise to a singular superpotential and a singular superpartner V_2. Nonetheless, when E_0 is reinserted in the second step, the resulting isospectral family $\widetilde{V}_1(\eta_1)$ will be nonsingular. Surprisingly:

$$\widetilde{V}_1\left(r;\eta_1\right)=V_1\left(r\right)-2\frac{\mathrm{d}^2}{\mathrm{d}x^2}\ln\left(\mathcal{I}_1\left(r\right)+\eta_1\right), \tag{6.11.28}$$

with:

$$\mathcal{I}_1\left(r\right):=\int^r u_0^2\left(\alpha\right)\mathrm{d}\alpha, \tag{6.11.29}$$

is a nonsingular isospectral family of potentials and supports a family of BICs of the form:

$$\widetilde{u}_0\left(r;\eta_1\right)=\frac{u_0\left(r\right)}{\mathcal{I}_1\left(r\right)+\eta_1};\quad \eta_1>0. \tag{6.11.30}$$

The following remarks are in order from the previous relations:

- We set $u_0\left(r=0\right)=0$ as a sufficient condition to guarantee that the future candidate to BIC Eq. (6.11.30) fulfills one of the required boundary conditions of a bound state with:[21]

$$\widetilde{u}_{0,-}\left(\eta_1\right):=\widetilde{u}_0\left(r\to 0;\eta_1\right)=0. \tag{6.11.31}$$

- Clearly, u_0 oscillates and u_0^2 always increases as $r\to\infty$. As a result, we can observe that:

$$\widetilde{u}_{0,+}\left(\eta_1\right):=\widetilde{u}_0\left(r\to\infty;\eta_1\right)=0. \tag{6.11.32}$$

  Furthermore, note that $\widetilde{u}_0(\eta_1)$ is now a normalizable function, provided that $\eta_1>0$ to prevent singularities in $\widetilde{V}_1(\eta_1)$ and $\widetilde{u}_0(\eta_1)$.

[20] As an example, in photonics, a BIC can be observed when two identical resonators radiate into the same radiation channel and each resonator acts as a perfect *mirror* at the resonance frequency generating an optical standing wave (e.g., see Fig. 3 of [259]).

[21] Let us remember that, as indicated in Section 6.3, a spatial bound state is an eigenfunction ψ continuous, normalizable and usually satisfying the condition $\psi_\pm=0$. However, in radially-symmetric potentials, it is possible to observe 1D regular bound states with $\psi_-\neq 0$ and finite [122], or 1D singular bound states with $\psi_-=\infty$ [254]. In our example, for simplicity, we will consider 1D regular bound states satisfying that $\widetilde{u}_{0,\pm}\left(\eta_1\right)=0$.

- From these previous remarks, we conclude that all the potentials $\widetilde{V}_1(\eta_1)$ have a BIC $\widetilde{u}_0(\eta_1)$ at energy E_0.
- Consider other nonsingular state in the continuum u_1 of V_1 at energy E_1 (the order criterion between E_0 and E_1 is irrelevant). The function:[22]

$$\widetilde{u}_1(r;\eta_1) = (E_1 - E_0)\, u_1(r) + \widetilde{u}_0(r;\eta_1)\, \mathcal{W}[u_0(r), u_1(r)], \tag{6.11.33}$$

  is a state in the continuum at energy E_1 of the family $\widetilde{V}_1(\eta_1)$ [216]. In other words, $\widetilde{u}_1(\eta_1)$ satisfies the 1D time-independent Schrödinger equation:

$$\left(-\frac{\mathrm{d}^2}{\mathrm{d}r^2} + \widetilde{V}_1(r;\eta_1)\right) \widetilde{u}_1(r;\eta_1) = E_1\, \widetilde{u}_1(r;\eta_1). \tag{6.11.34}$$

- We can apply the Darboux procedure iteratively to generate an n-parameter isospectral family of potentials supporting n BICs at different arbitrary energies $E_0, E_1, \ldots, E_{n-1}$.
- The 3D spherical eigenfunctions $\widetilde{\Psi}_0(\eta_1)$ associated with the spherical potentials $\widetilde{V}_1^{(3\mathrm{D})}(\eta_1)$ which arise from the family $\widetilde{V}_1(\eta_1)$ via Eq. (6.14.16) are of the form:

$$\widetilde{\Psi}_0(r,\theta,\phi;\eta_1) = \frac{1}{r}\widetilde{u}_0(r;\eta_1)\,\Theta(\theta,\phi). \tag{6.11.35}$$

  Thus, $\widetilde{\Psi}_0(\eta_1)$ is a 3D BIC family if it is found to be a normalizable function for each η_1 value. To this end, we must check the necessary condition:

$$\widetilde{\Psi}_{0,+}(\eta_1) := \widetilde{\Psi}_0(r\to\infty,\theta,\phi;\eta_1) = 0. \tag{6.11.36}$$

  which is directly satisfied taking into account that $\widetilde{u}_{0,+}(\eta_1) = 0$. However, note that the condition $\widetilde{\Psi}_{0,-}(\eta_1) := \widetilde{\Psi}_0(r\to 0,\theta,\phi;\eta_1) = 0$ is not required in spherical potentials to guarantee the normalization criterion in the 3D bound states [122].

As a representative example, consider a free particle on the half line with $V_1(r) = 0$ for $r \geq 0$. Now, we select a nonsingular oscillatory state $u_0(r) = \sin(kr)$ corresponding to an energy $E_0 = k^2$. Applying the one-parameter Darboux procedure, we generate an isospectral family of potentials:

$$\widetilde{V}_1(r;\eta_1) = \frac{32k^2\sin^4(kr)}{(2kr - \sin(2kr) + 4k\eta_1)^2} - \frac{8k^2\sin(2kr)}{2kr - \sin(2kr) + 4k\eta_1}, \tag{6.11.37}$$

supporting each one a BIC at energy E_0 of the form:

$$\widetilde{u}_0(r;\eta_1) = \frac{4k\sin(kr)}{2kr - \sin(2kr) + 4k\eta_1}; \quad \eta_1 > 0. \tag{6.11.38}$$

Figure 6.9 shows the potential $\widetilde{V}_1(\eta_1)$ and the BIC $\widetilde{u}_0(\eta_1)$ for $k = 5$ and $\eta_1 = 0.5$. As can be seen, the original potential V_1 and the eigenfunction u_0 have become an oscillatory potential $\widetilde{V}_1(\eta_1)$ and an oscillatory eigenfunction $\widetilde{u}_0(\eta_1)$ with an envelope proportional to $1/r$. Surprisingly, despite the oscillatory nature of $\widetilde{u}_0(\eta_1)$, this envelope makes $\widetilde{u}_0(\eta_1)$ and $\widetilde{\Psi}_0(\eta_1)$ normalizable wave functions and, consequently, satisfying Eqs. (6.11.31), (6.11.32) and (6.11.36). As a result, the new oscillatory potential $\widetilde{V}_1(\eta_1)$ has the possibility of keeping a particle trapped at the energy level $E_0 = k^2$. In other words, we have created a BIC.

[22] $\mathcal{W}$ is the Wronskian, $\mathcal{W}[u_0(r), u_1(r)] = u_0(r)\,u_1'(r) - u_0'(r)\,u_1(r)$.

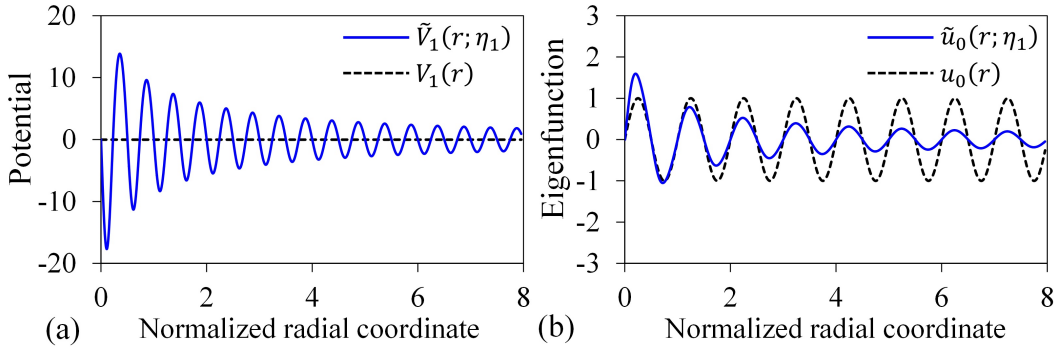

Figure 6.9. (a) Potential V_1 of the free particle and isospectral potential of the one-parameter family $\widetilde{V}_1(\eta_1)$ with $\eta_1 = 0.5$. (b) Oscillatory eigenfunction u_0 of V_1 corresponding to $k = 5$ m^{-1} and BIC $\widetilde{u}_0(\eta_1)$ of $\widetilde{V}_1(\eta_1)$ with $\eta_1 = 0.5$. The radial coordinate has been normalized as $r_{\mathrm{N}} := kr/2\pi$. The BIC has not been normalized to $\|\widetilde{u}_0(\eta_1)\|^2 = 1$ in this figure.

6.12 Shape invariant potentials and SUSY

Shape invariant potentials (SIP) are of great interest in quantum mechanics to find new analytically solvable potentials [265]. In the framework of SUSY QM, SIP allows us to: (*i*) calculate the spectrum of a given potential and its (unbroken or broken) SUSY Hamiltonian chain in a simple and elegant way, and (*ii*) analyze and design new potentials with desired scattering properties.

In general, we will say that two different potentials are *shape invariant* if they are similar in shape and differ only in the parameters that appear in them. In this vein, two SUSY partner potentials $V_{1,2}$ are shape invariant if their shape is preserved when applying the SUSY transformation to one of them to obtain its superpartner. More precisely, $V_{1,2}$ are said to be shape invariant if obey the relation:

$$V_2\left(x;\boldsymbol{a}_1\right) = V_1\left(x;\boldsymbol{a}_2\right) + M\left(\boldsymbol{a}_1\right), \tag{6.12.1}$$

where $(\boldsymbol{a}_1, \boldsymbol{a}_2) \in \mathbb{R}^p \times \mathbb{R}^p$ are a set of parameters related by a multivariate function $\boldsymbol{f} \in \mathcal{F}(\mathbb{R}^p, \mathbb{R}^p)$ of the form $\boldsymbol{a}_2 = \boldsymbol{f}\left(\boldsymbol{a}_1\right)$, and $M \in \mathcal{F}(\mathbb{R}^p, \mathbb{R})$. In most cases, we will have $p = 1$.

Figure 6.10 shows the energy relation established by Eq. (6.12.1) between superpartners for discrete and continuous spectra. In discrete spectra [Fig. 6.10(a)], Eq. (6.12.1) can be rewritten in terms of the n-th discrete energy level of each system as:

$$E_n^{(2)}\left(\boldsymbol{a}_1\right) = E_n^{(1)}\left(\boldsymbol{a}_2\right) + M\left(\boldsymbol{a}_1\right), \tag{6.12.2}$$

with $E_n^{(2)}\left(\boldsymbol{a}_{1,2}\right) = E_{n+1}^{(1)}\left(\boldsymbol{a}_{1,2}\right)$ if SUSY is unbroken [i.e., $m = n+1$ and $l = n-1$ in Fig. 6.10(a)], or $E_n^{(2)}\left(\boldsymbol{a}_{1,2}\right) = E_n^{(1)}\left(\boldsymbol{a}_{1,2}\right)$ if SUSY is spontaneously broken [i.e., $m = n = l$ in Fig. 6.10(a)]. In the continuum [Fig. 6.10(b)], $E^{(1)}\left(\boldsymbol{a}_{1,2}\right) = E^{(2)}\left(\boldsymbol{a}_{1,2}\right)$ and, consequently, we can omit the superindex by writing $E^{(1)}\left(\boldsymbol{a}_{1,2}\right) = E^{(2)}\left(\boldsymbol{a}_{1,2}\right) \equiv E\left(\boldsymbol{a}_{1,2}\right)$. In such a scenario, Eq. (6.12.1) establishes an energy relation of the form:

$$E\left(\boldsymbol{a}_1\right) = E\left(\boldsymbol{a}_2\right) + M\left(\boldsymbol{a}_1\right). \tag{6.12.3}$$

Discrete spectra Now, let us take a closer look at the SIP relation when the superpartners support discrete spectra. As we will see, the most interesting results appear when SUSY is unbroken. In such circumstances, one can easily calculate the energy levels of the original potential $V_1\left(\boldsymbol{a}_1\right)$.

To clarify this point, consider an unbroken SUSY relation between both superpartners. It is fundamental to note that the state of SUSY does not depend on the parameters of our problem, they are only *degrees of freedom*. That is, if we assume an unbroken SUSY scenario, the relation between $V_1\left(\boldsymbol{a}_i\right)$ and $V_2\left(\boldsymbol{a}_i\right)$ is unbroken $\forall i \in \{1, 2\}$. Obviously, this implies that $E_0^{(1)}\left(\boldsymbol{a}_1\right) = E_0^{(1)}\left(\boldsymbol{a}_2\right) = 0$.

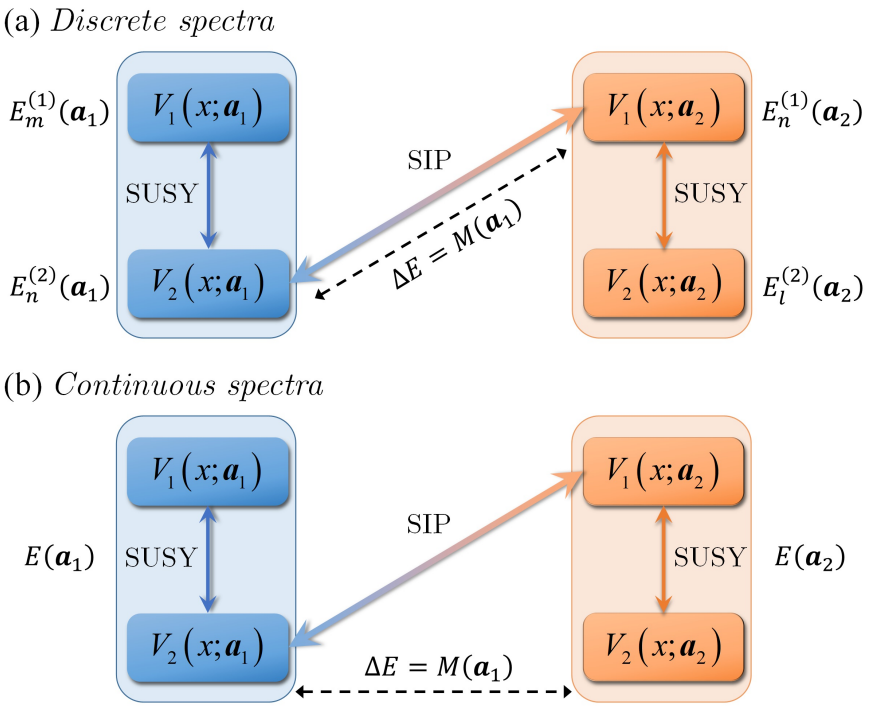

Figure 6.10. Energy relation between SIP superpartners with (a) discrete and (b) continuous spectra.

Hence, we start by factorizing the Hamiltonian $\widehat{\mathrm{H}}_1(\boldsymbol{a}_1) = \widehat{\mathrm{A}}^+(\boldsymbol{a}_1)\widehat{\mathrm{A}}^-(\boldsymbol{a}_1)$ as a function of the SUSY operators:

$$\widehat{\mathrm{A}}^{\pm}(\boldsymbol{a}_1) = \mp\frac{\mathrm{d}}{\mathrm{d}x} + W(x;\boldsymbol{a}_1)\,, \tag{6.12.4}$$

and constructing the superpartner:

$$\widehat{\mathrm{H}}_2(\boldsymbol{a}_1) = \widehat{\mathrm{A}}^-(\boldsymbol{a}_1)\,\widehat{\mathrm{A}}^+(\boldsymbol{a}_1) \equiv -\frac{\mathrm{d}^2}{\mathrm{d}x^2} + V_2(x;\boldsymbol{a}_1)\,, \tag{6.12.5}$$

with $V_2(x;\boldsymbol{a}_1)$ given by the SIP relation [Eq. (6.12.1)]. Thus, it is directly to see that:

$$\widehat{\mathrm{H}}_2(\boldsymbol{a}_1) = \widehat{\mathrm{H}}_1(\boldsymbol{a}_2) + M(\boldsymbol{a}_1)\,, \tag{6.12.6}$$

which is in line with the energy relation given by Eq. (6.12.2). From both results [Eqs. (6.12.2) and (6.12.6)] and bearing in mind that $E_0^{(1)}(\boldsymbol{a}_2) = 0$, it is directly to infer that:

$$E_1^{(1)}(\boldsymbol{a}_1) = E_0^{(2)}(\boldsymbol{a}_1) = M(\boldsymbol{a}_1)\,. \tag{6.12.7}$$

Furthermore:

$$\begin{aligned}\widehat{\mathrm{H}}_2(\boldsymbol{a}_1)\,\psi_0^{(1)}(x;\boldsymbol{a}_2) &= \widehat{\mathrm{H}}_1(\boldsymbol{a}_2)\,\psi_0^{(1)}(x;\boldsymbol{a}_2) + M(\boldsymbol{a}_1)\,\psi_0^{(1)}(x;\boldsymbol{a}_2)\\ &= E_0^{(1)}(\boldsymbol{a}_2)\,\psi_0^{(1)}(x;\boldsymbol{a}_2) + M(\boldsymbol{a}_1)\,\psi_0^{(1)}(x;\boldsymbol{a}_2) = M(\boldsymbol{a}_1)\,\psi_0^{(1)}(x;\boldsymbol{a}_2)\,.\end{aligned} \tag{6.12.8}$$

Since $E_0^{(2)}(\boldsymbol{a}_1) = M(\boldsymbol{a}_1)$, we can infer that the bound state $\psi_0^{(1)}(\boldsymbol{a}_2)$ is the same as $\psi_0^{(2)}(\boldsymbol{a}_1)$. Thus, $\psi_0^{(1)}(x;\boldsymbol{a}_2) = \psi_0^{(2)}(x;\boldsymbol{a}_1) \propto \widehat{\mathrm{A}}^-(\boldsymbol{a}_1)\,\psi_1^{(1)}(x;\boldsymbol{a}_1)$, or conversely:

$$\psi_1^{(1)}(x;\boldsymbol{a}_1) \propto \widehat{\mathrm{A}}^+(\boldsymbol{a}_1)\,\psi_0^{(1)}(x;\boldsymbol{a}_2)\,. \tag{6.12.9}$$

To summarize, note that in the original potential $V_1(\boldsymbol{a}_1)$, we have been able to calculate its second energy level $E_1^{(1)}(\boldsymbol{a}_1)$ from the value $M(\boldsymbol{a}_1)$ and its corresponding bound state $\psi_1^{(1)}(\boldsymbol{a}_1)$ from the ground state $\psi_0^{(1)}(\boldsymbol{a}_2)$, which can be directly found from $\psi_0^{(1)}(\boldsymbol{a}_1)$ by replacing the parameters $\boldsymbol{a}_1$ by $\boldsymbol{a}_2 = \boldsymbol{f}(\boldsymbol{a}_1)$.

In a similar way, we can repeat iteratively the above procedure to solve the first n energy levels $\left\{E_k^{(1)}\right\}_{k=0}^{n}$ and the corresponding bound states $\left\{\psi_k^{(1)}(\boldsymbol{a}_1)\right\}_{k=0}^{n}$ of $V_1(\boldsymbol{a}_1)$. To this end, we should construct an unbroken SUSY Hamiltonian chain with $n+1$ shape invariant potentials with Hamiltonians related as:

$$\widehat{\mathrm{H}}_{n+1}(\boldsymbol{a}_1) = \widehat{\mathrm{H}}_1(\boldsymbol{a}_{n+1}) + \sum_{i=1}^{n} M(\boldsymbol{a}_i), \tag{6.12.10}$$

with $\boldsymbol{a}_i = (\mathring{\boldsymbol{f}})^{i-1}(\boldsymbol{a}_1)$ [e.g., $\boldsymbol{a}_3 = (\mathring{\boldsymbol{f}})^2(\boldsymbol{a}_1) = (\boldsymbol{f}\circ\boldsymbol{f})(\boldsymbol{a}_1) = \boldsymbol{f}(\boldsymbol{f}(\boldsymbol{a}_1))$] and keeping in mind that $E_0^{(1)}(\boldsymbol{a}_i) = 0$, $\forall i \in \{1,\ldots,n+1\}$. The above equation establishes an energy relation for the k-th energy level of $\widehat{\mathrm{H}}_{n+1}(\boldsymbol{a}_1)$ and $\widehat{\mathrm{H}}_1(\boldsymbol{a}_{n+1})$ obeying the relation:

$$E_k^{(n+1)}(\boldsymbol{a}_1) = E_k^{(1)}(\boldsymbol{a}_{n+1}) + \sum_{i=1}^{n} M(\boldsymbol{a}_i). \tag{6.12.11}$$

Moreover, from Eq. (6.12.11) we can infer the following relation between bound states:[23]

$$\psi_{k+n}^{(1)}(x;\boldsymbol{a}_1) \propto \widehat{\mathrm{A}}_1^{+}(\boldsymbol{a}_1)\,\widehat{\mathrm{A}}_2^{+}(\boldsymbol{a}_1)\ldots\widehat{\mathrm{A}}_n^{+}(\boldsymbol{a}_1)\,\psi_k^{(1)}(x;\boldsymbol{a}_{n+1}). \tag{6.12.12}$$

As a result, we can calculate the n-th energy level $E_n^{(1)}(\boldsymbol{a}_1)$ and its corresponding bound state $\psi_n^{(1)}(\boldsymbol{a}_1)$ in the original potential $V_1(\boldsymbol{a}_1)$ only using the parameters and the ground state of the own system. Specifically, taking $k=0$ in Eqs. (6.12.11) and (6.12.12) we find that:

$$E_n^{(1)}(\boldsymbol{a}_1) = \sum_{i=1}^{n} M(\boldsymbol{a}_i); \tag{6.12.13}$$

$$\psi_n^{(1)}(x;\boldsymbol{a}_1) \propto \widehat{\mathrm{A}}_1^{+}(\boldsymbol{a}_1)\,\widehat{\mathrm{A}}_2^{+}(\boldsymbol{a}_1)\ldots\widehat{\mathrm{A}}_n^{+}(\boldsymbol{a}_1)\,\psi_0^{(1)}(x;\boldsymbol{a}_{n+1}), \tag{6.12.14}$$

with $\boldsymbol{a}_{n+1} = (\mathring{\boldsymbol{f}})^n(\boldsymbol{a}_1)$. The general case with $E_0^{(1)}(\boldsymbol{a}_i) \neq 0$ can be solved by performing an adequate energy shift of the Hamiltonian $\widehat{\mathrm{H}}_1(\boldsymbol{a}_i)$ of the form $\widehat{\mathrm{H}}_{1,\mathrm{eq}}(\boldsymbol{a}_i) := \widehat{\mathrm{H}}_1(\boldsymbol{a}_i) - E_0^{(1)}(\boldsymbol{a}_i)$ and later applying the aforementioned procedure. As an illustrative example, in [266] is detailed how to calculate the spectrum of the hydrogen atom by using this method. Likewise, it is worthy to mention that we can directly calculate the (unbroken or broken) SUSY Hamiltonian chain of shape invariant superpartners by using Eq. (6.12.10). This result will be retrieved in Chapter 8.

[23] It can be noted that:

$$\begin{aligned}
\widehat{\mathrm{H}}_{n+1}(\boldsymbol{a}_1)\,\psi_k^{(1)}(x;\boldsymbol{a}_{n+1}) &= \widehat{\mathrm{H}}_1(\boldsymbol{a}_{n+1})\,\psi_k^{(1)}(x;\boldsymbol{a}_{n+1}) + \sum_{i=1}^{n} M(\boldsymbol{a}_i)\,\psi_k^{(1)}(x;\boldsymbol{a}_{n+1}) \\
&= E_k^{(1)}(\boldsymbol{a}_{n+1})\,\psi_k^{(1)}(x;\boldsymbol{a}_{n+1}) + \sum_{i=1}^{n} M(\boldsymbol{a}_i)\,\psi_k^{(1)}(x;\boldsymbol{a}_{n+1}) \\
&= \left[E_k^{(1)}(\boldsymbol{a}_{n+1}) + \sum_{i=1}^{n} M(\boldsymbol{a}_i)\right]\psi_k^{(1)}(x;\boldsymbol{a}_{n+1}) \\
&= E_k^{(n+1)}(\boldsymbol{a}_1)\,\psi_k^{(1)}(x;\boldsymbol{a}_{n+1}) \equiv E_k^{(n+1)}(\boldsymbol{a}_1)\,\psi_k^{(n+1)}(x;\boldsymbol{a}_1),
\end{aligned}$$

that is, $\psi_k^{(1)}(x;\boldsymbol{a}_{n+1}) = \psi_k^{(n+1)}(x;\boldsymbol{a}_1) \propto \widehat{\mathrm{A}}_n^{-}(\boldsymbol{a}_1)\,\widehat{\mathrm{A}}_{n-1}^{-}(\boldsymbol{a}_1)\ldots\widehat{\mathrm{A}}_1^{-}(\boldsymbol{a}_1)\,\psi_{k+n}^{(1)}(x;\boldsymbol{a}_1)$, or conversely, using the SUSY operators $\widehat{\mathrm{A}}_i^{+}(\boldsymbol{a}_1)$ ($i \in \{1,\ldots,n\}$) we find Eq. (6.12.12).

Continuous spectra In the continuum, the SIP relation given by Eq. (6.12.1) will allow us to analyze an design new potentials with specific scattering properties. In such a scenario, we will revisit the scattering relations given by Eq. (6.10.9) and we will demonstrate that the particle wave number $k_\pm$ does not depend on the SIP parameters.

Consider two SUSY partners potentials V_1 and V_2 in the continuum satisfying the SIP relation indicated by Eq. (6.12.1). From this equation we can infer the following remarks in the spatial scattering problem discussed in Section 6.10:

- The energy relation given by Eq. (6.12.3) must be satisfied in the continuum, with $E(\boldsymbol{a}_i)$ being the energy spectrum of the SUSY partners $V_{1,2}(\boldsymbol{a}_i)$ and $i \in \{1,2\}$ [see Fig. 6.10(b)].

- Since $V_{i,\pm}(\boldsymbol{a}_j) = W_\pm^2(\boldsymbol{a}_j)\ \forall (i,j) \in \{1,2\}^2$, then:

$$W_\pm^2(\boldsymbol{a}_1) = W_\pm^2(\boldsymbol{a}_2) + M(\boldsymbol{a}_1). \tag{6.12.15}$$

  Consequently, the superpotential depends on the SIP parameters at $x \to \pm\infty$.

- From the SIP theory applied to discrete spectra, we know that:

$$\psi^{(2)}(x;\boldsymbol{a}_1) = \psi^{(1)}(x;\boldsymbol{a}_2). \tag{6.12.16}$$

- Interestingly, the particle wave number (or equivalently, the phase constant of the reflected and transmitted plane waves) does not depend on the SIP parameters at $x \to \pm\infty$. Using Eqs. (6.10.5), (6.12.3) and (6.12.15) we observe that:

$$\begin{aligned} k_\pm^2(\boldsymbol{a}_1) &= E(\boldsymbol{a}_1) - W_\pm^2(\boldsymbol{a}_1) = E(\boldsymbol{a}_2) + M(\boldsymbol{a}_1) - W_\pm^2(\boldsymbol{a}_2) - M(\boldsymbol{a}_1) \\ &= E(\boldsymbol{a}_2) - W_\pm^2(\boldsymbol{a}_2) = k_\pm^2(\boldsymbol{a}_2). \end{aligned} \tag{6.12.17}$$

- From Eq. (6.12.16), we can infer that $R_2(\boldsymbol{a}_1) = R_1(\boldsymbol{a}_2)$ and $T_2(\boldsymbol{a}_1) = T_1(\boldsymbol{a}_2)$. As a result, Eq. (6.10.9) can be restated as:

$$\frac{R_1(\boldsymbol{a}_2)}{R_1(\boldsymbol{a}_1)} = \frac{W_-(\boldsymbol{a}_1) + jk_-}{W_-(\boldsymbol{a}_1) - jk_-}; \quad \frac{T_1(\boldsymbol{a}_2)}{T_1(\boldsymbol{a}_1)} = \frac{W_+(\boldsymbol{a}_1) - jk_+}{W_-(\boldsymbol{a}_1) - jk_-}. \tag{6.12.18}$$

- In a SUSY Hamiltonian chain with m shape invariant potentials in the continuum, Eq. (6.12.1) can be generalized to:

$$V_m(x;\boldsymbol{a}_1) = V_1(x;\boldsymbol{a}_m) + \sum_{i=1}^{m-1} M(\boldsymbol{a}_i), \tag{6.12.19}$$

  with $\boldsymbol{a}_i = (\mathring{\boldsymbol{f}})^{i-1}(\boldsymbol{a}_1)$ as commented before. Hence, Eqs. (6.12.3), (6.12.15) and (6.12.16) become:

$$E(\boldsymbol{a}_1) = E(\boldsymbol{a}_m) + \sum_{i=1}^{m-1} M(\boldsymbol{a}_i); \tag{6.12.20}$$

$$W_\pm^2(\boldsymbol{a}_1) = W_\pm^2(\boldsymbol{a}_m) + \sum_{i=1}^{m-1} M(\boldsymbol{a}_i); \tag{6.12.21}$$

$$\psi^{(m)}(x;\boldsymbol{a}_1) = \psi^{(1)}(x;\boldsymbol{a}_m). \tag{6.12.22}$$

  Thus, $R_m(\boldsymbol{a}_1) = R_1(\boldsymbol{a}_m)$, $T_m(\boldsymbol{a}_1) = T_1(\boldsymbol{a}_m)$ and the scattering relations given by Eq. (6.10.12) can be recast as:

$$\frac{R_1(\boldsymbol{a}_m)}{R_1(\boldsymbol{a}_1)} = \left(\frac{W_-(\boldsymbol{a}_1) + jk_-}{W_-(\boldsymbol{a}_1) - jk_-}\right)^{m-1}; \quad \frac{T_1(\boldsymbol{a}_m)}{T_1(\boldsymbol{a}_1)} = \left(\frac{W_+(\boldsymbol{a}_1) - jk_+}{W_-(\boldsymbol{a}_1) - jk_-}\right)^{m-1}. \tag{6.12.23}$$

Classification of shape invariant potentials A fundamental problem within the context of SUSY QM is to perform a classification of different solutions to the shape invariance condition. Once such a classification is available, then one can discover new SIPs which are solvable by purely algebraic methods. Although the general case is an outstanding problem in quantum mechanics, two main classes of solutions have been discovered in the literature. In the first class, the set of parameters $\boldsymbol{a}_1$ and $\boldsymbol{a}_2$ are real numbers (i.e., $\boldsymbol{a}_{1,2} \equiv a_{1,2}$) related by a translation operation ($a_2 = a_1 + \alpha$). In the second class, the set of parameters are also real numbers related by scaling ($a_2 = qa_1$). There are other class of solutions combining translation and scaling [216], but they are out of the scope of this chapter.

Along this line, it is interesting to highlight the possibility of constructing superpartners connected by a SIP relation of scaling when using an *even* superpotential [$W(x) = W(-x)$]. In such a case, we can infer from the Riccati equation that:

$$V_2(x) = W^2(x) + W'(x) = W^2(-x) - W'(-x) = V_1(-x). \tag{6.12.24}$$

Rewriting Eq. (6.12.24) as $V_2(\boldsymbol{a}_1 x) = V_1(\boldsymbol{a}_2 x)$ and comparing this expression with the SIP condition [Eq. (6.12.1)], we find that $M = 0$ and the set of parameters $\boldsymbol{a}_1$ and $\boldsymbol{a}_2$ are real numbers connected as $a_2 = -a_1 = -1$, i.e., we have a scaling SIP relation between superpartners.[24]

6.13 SUSY in optics, acoustics and thermodynamics

In previous sections, we have presented the formalism of supersymmetry in quantum mechanics. Interestingly, the time-independent Schrödinger equation upon which the SUSY QM theory was constructed is formally equal to the Helmholtz equation that appears in different optical, acoustic and thermodynamic problems. In this way, the ideas of SUSY can be extrapolated to other areas of physics, allowing for the possibility of presenting SUSY as a general tool of analysis and synthesis. As a result, new physical phenomena and applications can be investigated in these aforementioned branches of physics. In the following, we first discuss some interesting examples in the optical case as an illustrative vehicle, and at the end of this section, we indicate how to extrapolate these ideas to acoustics and thermodynamics.

6.13.1 Optical SUSY

As a first and basic example, let us consider a dielectric slab waveguide [Fig. 6.11(a)]. Without loss of generality, the refractive index profile $n_1(x)$ can be assumed symmetric (even function) or asymmetric. The propagation in the linear regime is governed by the following wave equation in the frequency domain:[25]

$$\left(\triangle + \frac{\omega^2}{c_0^2} n_1^2(x)\right) \widetilde{\boldsymbol{\mathcal{E}}}^{(1)}(\boldsymbol{r}, \omega) = \boldsymbol{0}, \tag{6.13.1}$$

where ω is the angular frequency, c_0 is the speed of light at the vacuum and $\widetilde{\boldsymbol{\mathcal{E}}}^{(1)}$ is the Fourier transform of the electric field strength of the slab.

In this example, we are interested in guided modes (≡bound modes). If we restrict the modal analysis to the transverse electric (TE) modes [propagation in the xz plane assuming the electric field strength of the form $\widetilde{\boldsymbol{\mathcal{E}}}^{(1)}(\boldsymbol{r}, \omega) = \widetilde{\mathcal{E}}^{(1)}(x, z, \omega)\, \hat{u}_y$], the above equation is reduced to:

$$\left(\partial_x^2 + \partial_z^2 + \frac{\omega^2}{c_0^2} n_1^2(x)\right) \widetilde{\mathcal{E}}^{(1)}(x, z, \omega) = 0, \tag{6.13.2}$$

[24] On the contrary, we cannot directly obtain a SIP relation between superpartners from an *odd* superpotential [$W(x) = -W(-x)$]. In such a case, we only find that V_1 and V_2 are even functions by using the Riccati equation:

$$V_1(x) = W^2(x) - W'(x) = W^2(-x) - W'(-x) = V_1(-x);$$
$$V_2(x) = W^2(x) + W'(x) = W^2(-x) + W'(-x) = V_2(-x),$$

but we do not infer a SIP relation between V_1 and V_2 as in the even superpotential.

[25] We omit the material dispersion ($\partial_\omega n_1 = 0$) for simplicity.

where:

$$\widetilde{\mathcal{E}}^{(1)}(x,z,\omega)=\sum_{n=0}^{\infty}\psi_n^{(1)}(x)\exp\left(-jk_n^{(1)}z\right), \tag{6.13.3}$$

and $k_n^{(1)}$ is the z-component of the wave vector of the n-th TE mode, which can be expressed as a function of the effective index as $k_n^{(1)}=(\omega/c_0)n_{\mathrm{eff},n}^{(1)}$. Along this line, note that here ω is not considered a variable, it is just a parameter of our problem. Now, combining Eqs. (6.13.2) and (6.13.3) we find that:

$$\left(-\frac{\mathrm{d}^2}{\mathrm{d}x^2}-\frac{\omega^2}{c_0^2}n_1^2(x)\right)\psi_n^{(1)}(x)=-\frac{\omega^2}{c_0^2}\left(n_{\mathrm{eff},n}^{(1)}\right)^2\psi_n^{(1)}(x), \tag{6.13.4}$$

which is formally equal to the 1D time-independent Schrödinger equation by identifying:

$$V_1(x)\equiv-\frac{\omega^2}{c_0^2}n_1^2(x); \qquad E_n^{(1)}\equiv-\frac{\omega^2}{c_0^2}\left(n_{\mathrm{eff},n}^{(1)}\right)^2. \tag{6.13.5}$$

Therefore, we can construct a supersymmetric slab from the original one with totally or partially degenerate TE modes by using the different SUSY transformations discussed in previous sections. As an example, we show in Fig. 6.11(b) the refractive index profiles and the spectra (TE modes) of two unbroken SUSY-connected slabs. In both cases, the ground state of each slab has the highest effective index and, consequently, the lowest energy [see Eq. (6.13.5)]. In a similar way, broken SUSY and isospectral constructions can also be investigated in this scenario. Prof. Demetrios Christodoulides and coworkers reported the fundamentals of SUSY applied to optical waveguides in [228]. As a byproduct, unprecedented mode filtering and mode conversion applications were demonstrated. These results provided a starting point to design novel 1D optical devices [229, 230, 232–239, 241, 242].

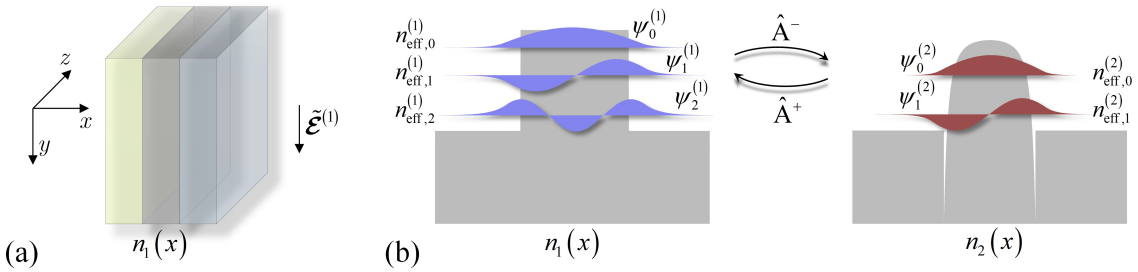

Figure 6.11. (a) Schematic representation of an optical slab waveguide with refractive index profile $n_1(x)$, which can be assumed symmetric or asymmetric. (b) Supersymmetric slab waveguides and associated spectra (TE modes) connected by an unbroken SUSY transformation. As can be seen, the ground state of the bosonic slab (left) has not SUSY counterpart in the fermionic slab (right) because SUSY is unbroken.

In a second example, we focus our attention on analyzing the scattering properties of a 1D heterogeneous optical medium with refractive index profile $n_1(x)$ (e.g., the slab waveguide of the previous example). That is, we are now interested in the reflection and transmission amplitudes associated with a plane wave impinging onto the optical medium from the left, as depicted in Fig. 6.12(a). This scenario is exactly described by the same wave equation as in the previous example [Eq. (6.13.1)]. Nonetheless, the electric field strength associated with the *incident* (I), *reflected* (R) and *transmitted* (T) plane waves at the angular frequency ω_0 is of the form:

$$\widetilde{\boldsymbol{\mathcal{E}}}_{\mathrm{I}}^{(1)}(\boldsymbol{r},\omega_0)\underset{x\to-\infty}{\sim}\exp\left(-jk_{x,-}^{(1)}x\right)\exp\left(jk_z^{(1)}z\right)\hat{u}_y; \tag{6.13.6}$$

$$\widetilde{\boldsymbol{\mathcal{E}}}_{\mathrm{R}}^{(1)}(\boldsymbol{r},\omega_0)\underset{x\to-\infty}{\sim}R_1\exp\left(jk_{x,-}^{(1)}x\right)\exp\left(jk_z^{(1)}z\right)\hat{u}_y; \tag{6.13.7}$$

$$\widetilde{\boldsymbol{\mathcal{E}}}_{\mathrm{T}}^{(1)}(\boldsymbol{r},\omega_0)\underset{x\to+\infty}{\sim}T_1\exp\left(-jk_{x,+}^{(1)}x\right)\exp\left(jk_z^{(1)}z\right)\hat{u}_y, \tag{6.13.8}$$

where R_1 and T_1 are the scattering amplitudes of the reflected and transmitted plane waves, $k_z^{(1)}$ is the z-component of the wave vector of the plane waves,[26] and $k_{x,\pm}^{(1)}$ is the x-component of the wave vector of the plane waves at the beginning ($x \to -\infty$) and at the end ($x \to \infty$) of the problem. Along this line, it should be noted that the following relation must be fulfilled [$n_{1,\pm} := n_1(x \to \pm\infty)$]:

$$n_{1,\pm}^2 k_0^2 = \left(k_{x,\pm}^{(1)}\right)^2 + \left(k_z^{(1)}\right)^2, \tag{6.13.9}$$

with:

$$k_{x,\pm}^{(1)} = n_{1,\pm} k_0 \cos\theta_\pm; \qquad k_z^{(1)} = n_{1,\pm} k_0 \sin\theta_\pm, \tag{6.13.10}$$

and $k_0 = \omega_0/c_0$ is the free-space wave number.

This scenario is formally equal to the spatial scattering problem of the free particle discussed in Section 6.10. Assuming the global electric field strength in the frequency domain of the form:

$$\widetilde{\boldsymbol{\mathcal{E}}}^{(1)}(\boldsymbol{r},\omega) = \pi\left[\psi^{(1)}(x)\exp\left(jk_z^{(1)}z\right)\delta(\omega-\omega_0) + \text{c.c.}\right]\hat{u}_y, \tag{6.13.11}$$

with $\psi^{(1)}$ including the variations of $k_x^{(1)}$ on the full line and the abbreviation c.c. indicating the complex conjugate term, we derive the following equation from Eq. (6.13.1) at $\omega = \omega_0$:

$$\left(-\frac{\mathrm{d}^2}{\mathrm{d}x^2} - k_0^2 n_1^2(x)\right)\psi^{(1)}(x) = -\left(k_z^{(1)}\right)^2\psi^{(1)}(x), \tag{6.13.12}$$

which matches the 1D time-independent Schrödinger equation by identifying:

$$V_1(x) \equiv -k_0^2 n_1^2(x); \qquad E^{(1)} \equiv -\left(k_z^{(1)}\right)^2. \tag{6.13.13}$$

From this quantum-optical analogy we infer that:

- In contrast to the first example of optical SUSY, note that we have now a continuous spectrum given that $k_z^{(1)}$ ranges in a continuous interval $[0, k_0 n_{1,-}]$. The value of the energy can be changed by modifying the angle of incidence θ_-.
- Bearing in mind that $V_{1,\pm} = V_{2,\pm} \equiv V_\pm$ and assuming all-dielectric media, we infer that $n_{1,\pm} = n_{2,\pm} \equiv n_\pm$. Consequently, $k_{x,\pm}^{(1)} = k_{x,\pm}^{(2)} \equiv k_{x,\pm}$, which plays the same role as that of the particle wave number $k_\pm$ in the spatial scattering of QM. Moreover, note that $k_z^{(1)} = k_z^{(2)}$ since $E^{(1)} = E^{(2)}$.

From these remarks, it is obvious that the results of Section 6.10 can be directly extrapolated to this scenario. Hence, the scattering amplitudes in $n_1(x)$ and $n_2(x)$ are connected by Eq. (6.10.9). Remarkably, these relations can be used to analyze the reflection and transmission coefficients of complicated refractive index profiles *without the necessity* of solving Maxwell's equations. Furthermore, specific refractive index profiles with desired scattering properties can also be designed by using Eq. (6.10.9) [232]. As an interesting example, we can design a reflectionless refractive index profile using the superpotential given by Eq. (6.10.13):[27]

$$n_2(x) = \sqrt{1 + 2\text{sech}^2(k_0 x)}. \tag{6.13.14}$$

The non-reflecting behavior of n_2 is illustrated in Fig. 6.12(c).

[26] Note that $k_z^{(1)}$ is assumed to be constant to guarantee the continuity of the tangential component of $\boldsymbol{\mathcal{E}}$ and $\boldsymbol{\mathcal{H}}$. This yields to the well-known Snell's law $n_{1,-}\sin\theta_- = n_{1,+}\sin\theta_+$, where $n_{1,\pm} := n_1(x \to \pm\infty)$.

[27] From the superpotential given by Eq. (6.10.13) we can construct the reflectionless SUSY partners $V_1(x) = A^2$ and $V_2(x) = A^2 - 2A^2\text{sech}^2(Ax)$. Therefore, the shifted potentials $\overline{V}_{1,2}(x) = V_{1,2}(x) - 2A^2$ will exhibit the same scattering properties, i.e., they will be reflectionless. Finally, from the relation $\overline{V}_2(x) = -k_0^2 n_2^2(x)$ and taking $A = k_0$ we obtain Eq. (6.13.14).

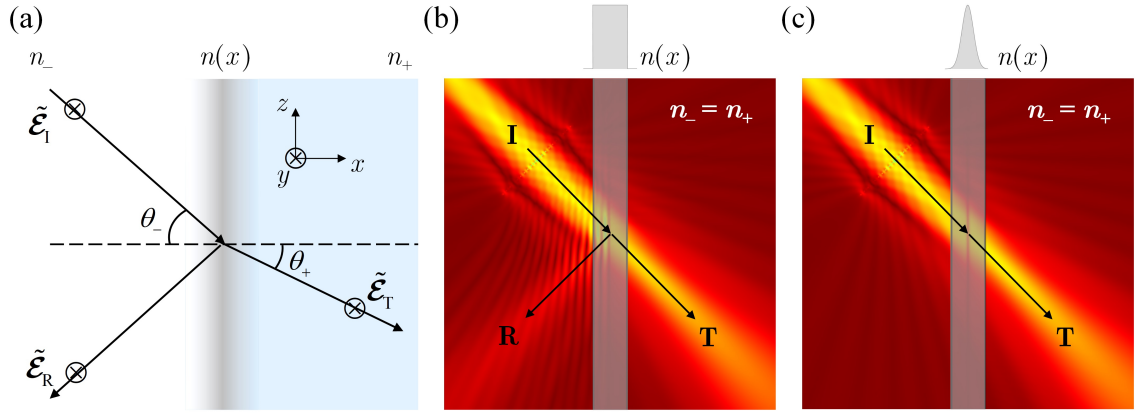

Figure 6.12. (a) Scattering of an electromagnetic plane wave in an optical medium with a refractive index profile $n(x)$. Scattering behavior of an incident optical beam in: (b) a step-index slab and (c) a slab with a refractive index profile given by Eq. (6.13.14), a SUSY partner of a constant refractive index. As seen, in contrast to the step-index slab, the *sech* profile does not generate a reflected wave. The numerical simulations have been performed by using COMSOL Multiphysics.

6.13.2 Extension to acoustics and thermodynamics

The use of the ideas of 1D SUSY QM in different branches of physics requires to obtain a Helmholtz equation. This possibility can be done in a variety of scenarios and it is almost impossible to cover all the possibilities in this subsection. Therefore, we only included some basic examples in optics, acoustics and thermodynamics. Specifically, in these areas of physics, we usually deal with wave and diffusion equations of a scalar field $\mathcal{U}(\boldsymbol{r},t)$ which admits separation of variables of the form $\mathcal{U}(\boldsymbol{r},t)=U(\boldsymbol{r})\mathcal{T}(t)$. In such a case, the wave and diffusion equations can usually be reduced to a partial differential equation of the form:

$$A^{-1}(\boldsymbol{r})\nabla\cdot(B(\boldsymbol{r})\nabla U(\boldsymbol{r}))+\xi U(\boldsymbol{r})=0, \tag{6.13.15}$$

with $\partial_t^2\mathcal{T}/\mathcal{T}=-\xi=-\omega_0^2$ for wave equations and $\partial_t\mathcal{T}/\mathcal{T}=-\xi$ for diffusion equations. The physical meaning of A, B and U is shown in Table 6.1 for each branch of physics. In the cases where:[28] (i) B is constant or presents a slow variation in comparison with the spatial period of U, (ii) A is a function of one variable [e.g., let us assume $A(x)$], and (iii) the above equation admits a solution of the form:

$$U(\boldsymbol{r})=\psi(x)\exp(\pm jk_y y)\exp(\pm jk_z z), \tag{6.13.16}$$

we will be able to reduce Eq. (6.13.15) to a Helmholtz equation:

$$\left(-\frac{\mathrm{d}^2}{\mathrm{d}x^2}-\xi B^{-1}A(x)\right)\psi(x)=-\left(k_y^2+k_z^2\right)\psi(x), \tag{6.13.17}$$

which is formally equal to the 1D time-independent Schrödinger equation with an equivalent potential $V(x)\equiv-\xi B^{-1}A(x)$ and equivalent energy $E\equiv-\left(k_y^2+k_z^2\right)$. As a result, the application of 1D SUSY transformations to Eq. (6.13.17) is then straightforward.[29]

[28] Other possible scenarios are discussed in the next section.

[29] Interestingly, the mathematical strategies of 1D SUSY QM can also be employed in other branches of physics such as in *black hole perturbation theory* [267]. However, the technical details of this work are out of the scope of this introduction to supersymmetry.

Physics	U	$A(x)$	B	$V(x) = -\xi B^{-1} A(x)$
Optics ($\mu_{\mathrm{r}} = 1$)	E_{T}	$c_0^{-2}\varepsilon_{\mathrm{r}}(x)$	1	$-\left(\omega_0^2/c_0^2\right)\varepsilon_{\mathrm{r}}(x)$
Optics ($\varepsilon_{\mathrm{r}} = 1$)	H_{T}	$c_0^{-2}\mu_{\mathrm{r}}(x)$	1	$-\left(\omega_0^2/c_0^2\right)\mu_{\mathrm{r}}(x)$
Pressure acoustics	P	$\rho^{-1}c_{\mathrm{S}}^{-2}(x)$	ρ^{-1}	$-\omega_0^2 c_{\mathrm{S}}^{-2}(x)$
Potential acoustics	ϕ	$\rho c_{\mathrm{S}}^{-2}(x)$	ρ	$-\omega_0^2 c_{\mathrm{S}}^{-2}(x)$
Thermodynamics	T	$\rho(x)\,C(x)$	K	$-\xi K^{-1}\rho(x)\,C(x)$

Table 6.1. Application of supersymmetry to different branches of physics. In optics, E_{T}, H_{T}, ε_{r}, μ_{r}, c_0 and ω_0 are respectively the electric field strength, the magnetic field strength, the electric permittivity, the magnetic permeability, the speed of light in vacuum and the angular frequency of the electromagnetic wave.[30] In acoustics, P, ϕ, ρ, c_{S} and ω_0 are respectively the acoustic pressure, the velocity potential, the background or static mass density, the speed of sound in the medium and the angular frequency of the acoustic wave. In thermodynamics, T, ρ, C and K are respectively the temperature distribution, the mass density of the material, the specific heat capacity and the thermal conductivity [243].

6.14 Further reading

So far, SUSY has been revealed as a potential bridge to extrapolate the ideas of quantum mechanics to other fields of physics. Unfortunately, 1D SUSY requires to work with a 1D Helmholtz equation, which gives rise to several important limitations:

- In some cases, in photonics, acoustics and thermodynamics we should deal with a Sturm-Liouville eigenvalue equation similar to Eq. (6.3.1):

$$\widehat{\mathrm{H}}\psi(x) = \lambda\psi(x); \quad x \in [a,b] \subseteq \overline{\mathbb{R}}, \tag{6.14.1}$$

  but with a linear operator $\widehat{\mathrm{H}}$ of the form:

$$\widehat{\mathrm{H}} := -\sigma(x)\frac{\mathrm{d}^2}{\mathrm{d}x^2} - \tau(x)\frac{\mathrm{d}}{\mathrm{d}x} + V(x), \tag{6.14.2}$$

  where $(\sigma, \tau, V, \psi) \in \mathcal{F}(\overline{\mathbb{R}}, \overline{\mathbb{R}})^4$ and $\lambda \in \mathbb{R}$. As an example, this occurs when B presents a rapid variation in the previous section [Eq. (6.13.15)]. Hence, in order to exploit the ideas of 1D SUSY, we must reduce Eq. (6.14.1) to a Helmholtz equation or perform a general factorization of the Sturm-Liouville operator [268, 269].

- 1D SUSY is restricted to scalar systems. Therefore, the possibility of including more dimensions or some fundamental properties such as the polarization of light in photonics is not straightforward.

In the following, we propose different possibilities to deal with these limitations. In Subsection 6.14.1, we propose a method to reduce Eq. (6.14.1) to a Helmholtz equation. In Subsection 6.14.2, we discuss the possibility of applying 1D SUSY to three-dimensional (3D) potentials exhibiting radial or axial symmetry. In Subsection 6.14.3, we present the basic concepts of two-dimensional (2D) SUSY QM. Finally, in Subsection 6.14.4, we include a brief description of some of the omitted topics in the SUSY QM literature.

6.14.1 From a general second-order ODE to a Helmholtz equation

How can we convert Eq. (6.14.1) to a Helmholtz equation? To solve this question, let us generalize the problem by considering the ODE [$y = g(x)$]:

$$a_0(x)\,y'' + a_1(x)\,y' + a_2(x)\,y = a_3(x), \tag{6.14.3}$$

[30] In optics, E_{T} and H_{T} represent a transversal component of the complex amplitude (phasor) of the electric and magnetic field strength, respectively. We have employed here the complex amplitude instead of using the Fourier transform $\widetilde{\mathcal{E}}_{\mathrm{T}}$ and $\widetilde{\mathcal{H}}_{\mathrm{T}}$ (as in the previous subsection) given that we have particularized the optical wave equation to a single angular frequency $\omega = \omega_0$. This remark is also found to be valid for the acoustic case.

with $g \in \mathcal{F}(\mathbb{R},\mathbb{C})$ and $a_i \in \mathcal{F}(\mathbb{R},\mathbb{C})$, $\forall i \in \{0,1,2,3\}$. It should be noted that Eq. (6.14.3) is reduced to Eq. (6.14.1) identifying $a_0(x) \equiv -\sigma(x)$, $a_1(x) \equiv -\tau(x)$, $a_2(x) \equiv V(x) - \lambda$ and $a_3(x) \equiv 0$. Thus, our initial question can be solved if we are able to eliminate the first-order derivative term in Eq. (6.14.3). To this end, we should firstly rewrite Eq. (6.14.3) as:

$$y'' + b_1(x)\, y' + b_2(x)\, y = b_3(x)\,, \tag{6.14.4}$$

with $b_i := a_i/a_0$, $\forall i \in \{1,2,3\}$. At this point, we should analyze the possible singularities that can appear in the b_i functions.

Secondly, we introduce in Eq. (6.14.4) the function f defined as $b_1 := 2f'/f$. In this way, Eq. (6.14.4) becomes:

$$y'' + 2\frac{f'(x)}{f(x)}y' + b_2(x)\, y = b_3(x)\,, \tag{6.14.5}$$

where:

$$f(x) = A\exp\left(\frac{1}{2}\int^x b_1(\tau)\,\mathrm{d}\tau\right), \tag{6.14.6}$$

and A is a constant of integration.

Thirdly, defining the complex number $z = h(x)$ with $h \in \mathcal{F}(\mathbb{R},\mathbb{C})$, we perform the transformation $y = f^{\alpha}(x)\, z^{\beta}$ in Eq. (6.14.5), with $(\alpha,\beta) \in \mathbb{R}^2$. After some algebra, it is straightforward to demonstrate that the terms in z' can be eliminated by taking $\alpha = -1$ and $\beta = 1$. As a result, Eq. (6.14.5) becomes a non-homogeneous Helmholtz equation with variable coefficients:

$$z'' + \left(b_2(x) - \frac{1}{2}b_1'(x) - \frac{1}{4}b_1^2(x)\right) z = b_3(x)\, f(x)\,. \tag{6.14.7}$$

If $b_3 = 0$ ($\equiv a_3 = 0$), Eq. (6.14.3) can be transformed into a homogeneous Helmholtz equation with variable coefficients using this procedure and, therefore, it can be connected with the time-independent Schrödinger equation of quantum mechanics.

6.14.2 SUSY in radially- and axially-symmetric potentials

Along this chapter, we have extensively discussed the ideas of 1D SUSY QM on the full line ($x \in \overline{\mathbb{R}}$). However, the unique features of 1D SUSY can also be exploitable in n-dimensional potentials [216]. In this subsection, we show how we can reduce the 3D time-independent Schrödinger equation:

$$\left(-\triangle + V^{(3\mathrm{D})}(\boldsymbol{r})\right)\Psi(\boldsymbol{r}) = E^{(3\mathrm{D})}\Psi(\boldsymbol{r})\,, \tag{6.14.8}$$

to a 1D equation in physical systems with radial or axial symmetry.

6.14.2.1 Radially-symmetric potentials

We start by assuming a spherical potential with radial symmetry and a discrete energy spectrum in Eq. (6.14.8):

$$\Psi(\boldsymbol{r}) \equiv \Psi_{nlm}(r,\theta,\phi)\,; \quad V^{(3\mathrm{D})}(\boldsymbol{r}) \equiv V^{(3\mathrm{D})}(r)\,; \quad E^{(3\mathrm{D})} \equiv E^{(3\mathrm{D})}_{nlm}. \tag{6.14.9}$$

In this scenario, Eq. (6.14.8) can be reduced to:

$$\left[-\frac{1}{r^2}\partial_r\left(r^2\partial_r\right) + \frac{\widehat{\boldsymbol{l}}^2}{r^2} + V^{(3\mathrm{D})}(r) - E^{(3\mathrm{D})}_{nlm}\right]\Psi_{nlm}(r,\theta,\phi) = 0, \tag{6.14.10}$$

where $\widehat{\boldsymbol{l}}^2$ is the square of the angular momentum operator:

$$\widehat{\boldsymbol{l}}^2 = -\left[\frac{1}{\sin\theta}\partial_\theta\left(\sin\theta\;\partial_\theta\right) + \frac{1}{\sin^2\theta}\partial_\phi^2\right]. \tag{6.14.11}$$

The dimensional reduction of Eq. (6.14.10) can be performed by applying the following separation of variables to Ψ_{nlm}:

$$\Psi_{nlm}(r,\theta,\phi) = \frac{1}{r} u_{nl}(r)\,\Theta_{lm}(\theta,\phi), \tag{6.14.12}$$

satisfying that:

$$\widehat{\boldsymbol{l}}^2 u_{nl} = l(l+1)\,u_{nl}; \quad \widehat{\boldsymbol{l}}^2 \Theta_{lm} = l(l+1)\,\Theta_{lm}. \tag{6.14.13}$$

In this way, Eq. (6.14.10) becomes:

$$\left(-\frac{\mathrm{d}^2}{\mathrm{d}r^2} + V^{(3\mathrm{D})}(r) + \frac{l(l+1)}{r^2}\right) u_{nl}(r) = E^{(3\mathrm{D})}_{nlm} u_{nl}(r). \tag{6.14.14}$$

Interestingly, the above equation matches the 1D Schrödinger equation (defined on the half line $x \geq 0$):

$$\left(-\frac{\mathrm{d}^2}{\mathrm{d}x^2} + V^{(1\mathrm{D})}(x)\right) \psi_n(x) = E^{(1\mathrm{D})}_n \psi_n(x), \tag{6.14.15}$$

by performing the relabeling $x \to r$ and identifying:

$$V^{(1\mathrm{D})}(r) \equiv V^{(3\mathrm{D})}(r) + \frac{l(l+1)}{r^2}; \quad E^{(1\mathrm{D})}_n \equiv E^{(3\mathrm{D})}_{nlm}; \quad \psi_n \equiv u_{nl}, \tag{6.14.16}$$

assuming a constant value of the parameters l and m, accounting for the angular order of the spherical bound states Ψ_{nlm}. Consequently, using 1D SUSY we will be able to connect radially-symmetric spherical potentials supporting bound states Ψ_{nlm} with the same (different) radial order using a broken (unbroken) SUSY transformation. In this scenario, note that the SUSY functions $u^{(1)}$ and $u^{(2)}$ could have a different l parameter in each superpartner. That is, we should assume $V^{(1\mathrm{D})}_1$ and $V^{(1\mathrm{D})}_2$ of the form:

$$V^{(1\mathrm{D})}_i(r) = V^{(3\mathrm{D})}_i(r) + \frac{l_i(l_i+1)}{r^2}; \quad i \in \{1,2\}. \tag{6.14.17}$$

On the other hand, in spite of the fact that we have assumed a discrete EVP in Eq. (6.14.9), we could also consider 3D potentials with continuum energy spectrum to engineer radially-symmetric potentials with the same scattering properties by using 1D SUSY transformations involving real superpotentials.

6.14.2.2 Axially-symmetric potentials

Now, let us focus our attention on cylindrical potentials with axial symmetry. Once again, our starting point is Eq. (6.14.8) assuming a discrete energy spectrum of the form:

$$\Psi(\boldsymbol{r}) \equiv \Psi_{mn}(r,\varphi,z); \quad V^{(3\mathrm{D})}(\boldsymbol{r}) \equiv V^{(3\mathrm{D})}(r); \quad E^{(3\mathrm{D})} \equiv E^{(3\mathrm{D})}_{mn}. \tag{6.14.18}$$

In such circumstances, Eq. (6.14.8) can be expressed as:

$$\left[-\partial_r^2 - \frac{1}{r}\partial_r - \frac{1}{r^2}\partial_\varphi^2 - \partial_z^2 + V^{(3\mathrm{D})}(r) - E^{(3\mathrm{D})}_{mn}\right] \Psi_{mn}(r,\varphi,z) = 0. \tag{6.14.19}$$

At this point, the dimensional reduction of the above equation can be performed by applying the following separation of variables to Ψ_{mn}:

$$\Psi_{mn}(r,\varphi,z) = \frac{1}{\sqrt{r}} u_{mn}(r) \exp(jm\varphi) \exp(-j\beta_{mn} z). \tag{6.14.20}$$

As a result, Eq. (6.14.19) can be reduced to:

$$\left(-\frac{\mathrm{d}^2}{\mathrm{d}r^2} + V^{(3\mathrm{D})}(r) + \frac{m^2}{r^2} - \frac{1}{4r^2}\right) u_{mn}(r) = \left(E^{(3\mathrm{D})}_{mn} - \beta^2_{mn}\right) u_{mn}(r). \tag{6.14.21}$$

We can observe that the above equation matches the 1D Schrödinger equation defined on the half line $x \geq 0$ [Eq. (6.14.15)] by performing the relabeling $x \to r$ and identifying:

$$V^{(1\mathrm{D})}(r) \equiv V^{(3\mathrm{D})}(r) + \frac{m^2}{r^2} - \frac{1}{4r^2}; \quad E_n^{(1\mathrm{D})} \equiv E_{mn}^{(3\mathrm{D})} - \beta_{mn}^2; \quad \psi_n \equiv u_{mn}, \tag{6.14.22}$$

assuming a constant value of the parameter m, accounting for the azimuthal order of the cylindrical bound states Ψ_{mn}. Accordingly, 1D SUSY allows us to connect axially-symmetric cylindrical potentials supporting bound states Ψ_{mn} with the same (different) radial order using a broken (unbroken) SUSY transformation (see Chapter 7). In such a case, it should be noted that the SUSY functions $u^{(1)}$ and $u^{(2)}$ could have a different m parameter in each superpartner. In other words, we should assume $V_1^{(1\mathrm{D})}$ and $V_2^{(1\mathrm{D})}$ of the form:

$$V_i^{(1\mathrm{D})}(r) = V_i^{(3\mathrm{D})}(r) + \frac{m_i^2}{r^2} - \frac{1}{4r^2}; \quad i \in \{1,2\}. \tag{6.14.23}$$

In a similar way as in the previous subsection, it is worth mentioning that, operating with continuum spectra, SUSY will allow us to design axially-symmetric potentials with the same scattering properties, provided that we use a real-valued superpotential.

6.14.2.3 Degeneracy breaking

Crucially, the dimensional reduction of the previous subsections may alter the degeneracy between the 3D superpartners $V_1^{(3\mathrm{D})}$ and $V_2^{(3\mathrm{D})}$. This possibility has not been analyzed so far and will be essential for some of the most interesting results derived from our study in Chapter 7. In particular, the following considerations are in order:

- From Eqs. (6.14.17) and (6.14.23), inverse-square potentials $V^{(1\mathrm{D})}$ appear for a nonsingular potential $V^{(3\mathrm{D})}$. The corresponding 1D eigenvalue problem [Eq. (6.14.15)] may be ill-defined if it is not possible to choose a unique basis of eigenfunctions based on square integrability and boundary conditions (see [254] for more details of such a situation).

- Inverse-square SUSY potentials $V_{1,2}^{(1\mathrm{D})}$ may be connected by a singular superpotential. As a consequence, the degeneracy between $V_{1,2}^{(3\mathrm{D})}$ will only be preserved if the 3D SUSY functions $\Psi^{(2)}$, calculated from the bound states $\Psi^{(1)}$ by combining $u^{(2)} \propto \widehat{\mathrm{A}}^{-} u^{(1)}$ with Eqs. (6.14.12) and (6.14.20), are found to be bound states.

In this context, the work of T. D. Imbo and U. P. Sukhatme [270] could be of extreme utility to elucidate if SUSY is broken. Remarkably, the authors demonstrated the following statement:

$$\lim_{r \to 0} r\,|W(r)| < 0.5 \Longrightarrow \text{SUSY is broken.} \tag{6.14.24}$$

6.14.3 Two-dimensional (2D) SUSY QM

The natural strategy to include two dimensions and the polarization of light in optical SUSY is to use 2D SUSY QM [271]. In the following, we will perform a brief review about the construction of the 2D SUSY QM theory. To simplify the discussion, we will use a more economical notation by employing the Einstein summation convention over the repeated subindexes.

Interestingly, 2D SUSY QM connects two scalar systems with Hamiltonians $\widehat{\mathrm{H}}^{(1)}$ and $\widehat{\mathrm{H}}^{(3)}$ to a vector system with Hamiltonian $\widehat{\mathrm{H}}_{ik}^{(2)}$, all of them described by the time-independent Schrödinger equations $[(i,k) \in \{1,2\}^2]$:

$$\widehat{\mathrm{H}}^{(1,3)} \psi^{(1,3)}(\boldsymbol{x}) = E^{(1,3)} \psi^{(1,3)}(\boldsymbol{x}); \tag{6.14.25}$$

$$\widehat{\mathrm{H}}_{ik}^{(2)} \psi_k^{(2)}(\boldsymbol{x}) = E^{(2)} \psi_i^{(2)}(\boldsymbol{x}), \tag{6.14.26}$$

where $\widehat{\mathrm{H}}^{(1,3)} := -\triangle + V^{(1,3)}(\boldsymbol{x})$, $\widehat{\mathrm{H}}^{(2)}_{ik} := -\delta_{ik}\triangle + V^{(2)}_{ik}(\boldsymbol{x})$, δ_{ik} is the Kronecker delta function and $\boldsymbol{x} = x_1\hat{u}_1 + x_2\hat{u}_2$. The basic idea of 2D SUSY QM is to factorize the above Hamiltonians by using the following linear operators:[31]

$$\widehat{\mathrm{A}}^{\pm}_i := \mp\partial_i + W_i(\boldsymbol{x}) = \mp\partial_i + (\partial_i M)(\boldsymbol{x}); \tag{6.14.27}$$

$$\widehat{\mathrm{B}}^{\pm}_i := \epsilon_{ik}\widehat{\mathrm{A}}^{\mp}_k, \tag{6.14.28}$$

where $\boldsymbol{W} = W_i\hat{u}_i \in \mathcal{F}(\overline{\mathbb{R}}^2, \overline{\mathbb{R}}^2)$ is the superpotential, $M \in \mathcal{F}(\overline{\mathbb{R}}^2, \overline{\mathbb{R}})$ is an auxiliary scalar function and ϵ_{ik} is the Levi-Civita tensor:

$$[\epsilon_{ik}] := \begin{bmatrix} 0 & 1 \\ -1 & 0 \end{bmatrix}. \tag{6.14.29}$$

Thus, $\widehat{\mathrm{B}}^{\pm}_1 = \widehat{\mathrm{A}}^{\mp}_2$ and $\widehat{\mathrm{B}}^{\pm}_2 = -\widehat{\mathrm{A}}^{\mp}_1$. In this scenario, the mutual orthogonal condition:

$$\widehat{\mathrm{A}}^{\pm}_i\widehat{\mathrm{B}}^{\mp}_i = \widehat{0}, \tag{6.14.30}$$

emerges as a necessary condition of the nilpotency of the supercharges [see below Eq. (6.14.38)].

The *first* and the *third* systems are factorized as:

$$\widehat{\mathrm{H}}^{(1)} = \widehat{\mathrm{A}}^{+}_i\widehat{\mathrm{A}}^{-}_i; \quad \widehat{\mathrm{H}}^{(3)} = \widehat{\mathrm{B}}^{+}_i\widehat{\mathrm{B}}^{-}_i = \widehat{\mathrm{A}}^{-}_i\widehat{\mathrm{A}}^{+}_i. \tag{6.14.31}$$

Hence, $V^{(1,3)}$ and $\boldsymbol{W}$ are connected via the equation:

$$V^{(1,3)}(\boldsymbol{x}) = W^2_i(\boldsymbol{x}) \mp \partial_i W_i(\boldsymbol{x}) = (\partial_i M)^2(\boldsymbol{x}) \mp \partial^2_i M(\boldsymbol{x}). \tag{6.14.32}$$

Moreover, the *second* system is factorized as:

$$\widehat{\mathrm{H}}^{(2)}_{ik} = \widehat{\mathrm{A}}^{-}_i\widehat{\mathrm{A}}^{+}_k + \widehat{\mathrm{B}}^{-}_i\widehat{\mathrm{B}}^{+}_k = \delta_{ik}\widehat{\mathrm{H}}^{(1)} + \left[\widehat{\mathrm{A}}^{-}_i, \widehat{\mathrm{A}}^{+}_k\right], \tag{6.14.33}$$

which yields the following relation between $V^{(2)}_{ik}$ and $V^{(1)}$:

$$V^{(2)}_{ik}(\boldsymbol{x}) = \delta_{ik}V^{(1)}(\boldsymbol{x}) + \left[\widehat{\mathrm{A}}^{-}_i, \widehat{\mathrm{A}}^{+}_k\right] = \delta_{ik}V^{(1)}(\boldsymbol{x}) + 2\partial_{ik}M(\boldsymbol{x}), \tag{6.14.34}$$

provided that $\psi^{(2)}_i \in C^2(I)$, where $I \subset \overline{\mathbb{R}}^2$ is the subset where the potentials are defined.

In a similar way as in 1D SUSY QM, the three quantum systems can be described by a matrix EVP of the form:

$$\mathrm{H}|\psi\rangle = E|\psi\rangle, \tag{6.14.35}$$

with the superhamiltonian and the eigenfunctions defined as:

$$\mathrm{H} := \begin{bmatrix} \widehat{\mathrm{H}}^{(1)} & \widehat{0} & \widehat{0} & \widehat{0} \\ \widehat{0} & \widehat{\mathrm{H}}^{(2)}_{11} & \widehat{\mathrm{H}}^{(2)}_{12} & \widehat{0} \\ \widehat{0} & \widehat{\mathrm{H}}^{(2)}_{21} & \widehat{\mathrm{H}}^{(2)}_{22} & \widehat{0} \\ \widehat{0} & \widehat{0} & \widehat{0} & \widehat{\mathrm{H}}^{(3)} \end{bmatrix}; \quad |\psi\rangle := \begin{bmatrix} \psi^{(1)} \\ \psi^{(2)}_1 \\ \psi^{(2)}_2 \\ \psi^{(3)} \end{bmatrix}. \tag{6.14.36}$$

Note that: (i) we use the same eigenvalue for the three systems given that $E^{(1)} = E^{(2)} = E^{(3)}$ (see below), and (ii) we use here the symbol E (energy in its quantum-mechanical sense) to describe only the physical eigenfunctions $|\psi\rangle$ by assuming that $\psi^{(1,3)}$ and $\psi^{(2)}_i$ are continuous normalizable functions. At this point, we introduce the supercharges:

[31] Note that the linear operator $\widehat{\mathrm{A}}^{\pm}_1$ matches to the linear operator $\widehat{\mathrm{A}}^{\pm}$ of 1D SUSY QM, i.e., $\widehat{\mathrm{A}}^{\pm}_1 \equiv \widehat{\mathrm{A}}^{\pm}$.

$$\mathrm{Q}^{-}:=\begin{bmatrix}\widehat{0} & \widehat{0} & \widehat{0} & \widehat{0}\\ \widehat{\mathrm{A}}_1^{-} & \widehat{0} & \widehat{0} & \widehat{0}\\ \widehat{\mathrm{A}}_2^{-} & \widehat{0} & \widehat{0} & \widehat{0}\\ \widehat{0} & \widehat{\mathrm{B}}_1^{+} & \widehat{\mathrm{B}}_2^{+} & \widehat{0}\end{bmatrix};\quad \mathrm{Q}^{+}:=\begin{bmatrix}\widehat{0} & \widehat{\mathrm{A}}_1^{+} & \widehat{\mathrm{A}}_2^{+} & \widehat{0}\\ \widehat{0} & \widehat{0} & \widehat{0} & \widehat{\mathrm{B}}_1^{-}\\ \widehat{0} & \widehat{0} & \widehat{0} & \widehat{\mathrm{B}}_2^{-}\\ \widehat{0} & \widehat{0} & \widehat{0} & \widehat{0}\end{bmatrix}, \tag{6.14.37}$$

satisfying the commutation and anticommutation relations:

$$\left[\mathrm{H},\mathrm{Q}^{\pm}\right]=0;\quad \mathrm{H}=\left\{\mathrm{Q}^{\pm},\mathrm{Q}^{\mp}\right\};\quad \left\{\mathrm{Q}^{\pm},\mathrm{Q}^{\pm}\right\}=0, \tag{6.14.38}$$

which define the algebra of 2D SUSY QM, the closed Lie superalgebra $\mathfrak{sl}(4,\mathbb{C})$.

From $\left[\mathrm{H},\mathrm{Q}^{\pm}\right]=0$, we can derive the *intertwining relations* between the Hamiltonians and their corresponding wave functions:

$$\left[\mathrm{H},\mathrm{Q}^{+}\right]=0\equiv \widehat{\mathrm{H}}^{(1)}\widehat{\mathrm{A}}_i^{+}=\widehat{\mathrm{A}}_k^{+}\widehat{\mathrm{H}}_{ki}^{(2)}\quad\wedge\quad \widehat{\mathrm{H}}_{ik}^{(2)}\widehat{\mathrm{B}}_k^{-}=\widehat{\mathrm{B}}_i^{-}\widehat{\mathrm{H}}^{(3)} \tag{6.14.39}$$

$$\equiv \psi^{(1)}\propto \widehat{\mathrm{A}}_i^{+}\psi_i^{(2)}\quad\wedge\quad \psi_i^{(2)}\propto \widehat{\mathrm{B}}_i^{-}\psi^{(3)}; \tag{6.14.40}$$

$$\left[\mathrm{H},\mathrm{Q}^{-}\right]=0\equiv \widehat{\mathrm{H}}_{ik}^{(2)}\widehat{\mathrm{A}}_k^{-}=\widehat{\mathrm{A}}_i^{-}\widehat{\mathrm{H}}^{(1)}\quad\wedge\quad \widehat{\mathrm{H}}^{(3)}\widehat{\mathrm{B}}_i^{+}=\widehat{\mathrm{B}}_k^{+}\widehat{\mathrm{H}}_{ki}^{(2)} \tag{6.14.41}$$

$$\equiv \psi_i^{(2)}\propto \widehat{\mathrm{A}}_i^{-}\psi^{(1)}\quad\wedge\quad \psi^{(3)}\propto \widehat{\mathrm{B}}_i^{+}\psi_i^{(2)}. \tag{6.14.42}$$

Using these intertwining relations in Eqs. (6.14.25) and (6.14.26), it is straightforward to verify that $E^{(1)}=E^{(2)}=E^{(3)}$. Nonetheless, in spite of the fact that $E^{(1)}=E^{(3)}$, note that the eigenfunctions $\psi^{(1)}$ and $\psi^{(3)}$ are not connected due to the mutual orthogonality condition [Eq. (6.14.30)] imposed by the nilpotency of the supercharges [Eq. (6.14.38)]:

$$\psi^{(3)}\propto \widehat{\mathrm{B}}_i^{+}\psi_i^{(2)}\propto \widehat{\mathrm{B}}_i^{+}\widehat{\mathrm{A}}_i^{-}\psi^{(1)}=0. \tag{6.14.43}$$

Outstandingly, 2D SUSY QM could emerge as an attractive tool to relate isotropic and anisotropic optical systems by including the polarization of light in the second system.

6.14.4 Omitted topics

An extensive literature covers the area of SUSY QM in the last decades. Given that it is impossible to review all the topics in this chapter, we include in the next lines some of the omitted topics providing the most relevant references in each one.

1. Pauli equation and 1D SUSY [272]. In contrast to 2D SUSY QM, the ideas of 1D SUSY QM can also be applied to 2D problems by using the Pauli equation. Interestingly, the polarization of light can also be included in the quantum-optical analogy by using this strategy.

2. Darboux transformations in two variables [273]. An additional option to extend the ideas of SUSY to two dimensions.

3. Supermathematics [274]. In this topic, it is interesting to highlight the work of Rodríguez-Lara and coworkers [275] about the group theory underlying Parity-Time ($\mathcal{PT}$) and SUSY in optics.

4. Combination of $\mathcal{PT}$ and SUSY in the linear and nonlinear Schrödinger equations [229, 276, 277].

5. SUSY and new soliton solutions (see Section 7.3 of [216]).

6. Quasi-solvable potentials [278].

7. Modified SUSY factorizations [279, 280].

8. General factorization of the Sturm-Liouville operator [269].

9. SUSY in condensed matter and statistical physics [281, 282].
10. SUSY in nuclear physics [283].
11. SUSY and WKB approximation (see Section 6 of [216]).

This page was intentionally left blank.

Chapter 7

Supersymmetric optical fibers

7.1 Introduction

One-dimensional supersymmetry (1D SUSY) has recently emerged as a tool to design unique optical structures with degenerate spectra and similar scattering properties [228]. Remarkably, as discussed in the previous chapter in Subsection 6.14.2, the ideas of 1D SUSY can also be applied to n-dimensional potentials. This enables us to benefit from the unique features of 1D SUSY, for instance, in axially-symmetric systems. Physical systems with axial symmetry present particular interest not only in quantum mechanics [284, 285], but also in other branches of physics, such as acoustics and photonics. In acoustics, cylindrical ducts are of special interest for pressure wave propagation and turbocharger applications [286–289]. In photonics, axially-symmetric media can be found in single- and multi-core optical fibers, optical couplers, laser arrays, modulators and Bragg gratings [28, 32, 78, 137, 149].

Along this line, Miri et al. reported a theoretical SUSY relation between the azimuthal Bessel modes of two optical fibers [228] and its potential application to angular momentum multiplexing [290]. However, the study was limited to the unbroken SUSY regime, while many aspects of SUSY theory still remain unexplored in this context. Firstly, the different spectral features of SUSY axially-symmetric optical systems have not been studied so far. Secondly, the SUSY formalism encompasses a rich toolbox, including, e.g., unbroken SUSY chains, broken SUSY transformations, and isospectral deformations, which have not been analyzed within the frame of axially-symmetric media. Thirdly, the application of SUSY to this kind of systems entails a series of steps and assumptions whose range of validity has not yet been assessed: the dimensional reduction of the Helmholtz equation from 3D to 1D, the subsequent appearance of singularities in the superpotential relating the superpartners, and the accuracy of the required slowly-varying index (SVI) and paraxial approximations in the photonic case.

For instance, a singular superpotential can give rise to a breakdown of the degeneracy theorem between superpartners (see Section 6.8) and, therefore, its impact on the corresponding mode multiplexing applications should be critically investigated. Moreover, as we will show, the paraxial approximation is no longer valid (except for some energy levels) in broken SUSY and isospectral constructions, leading to unexpected effects and novel functionalities.

In this chapter, we study all these points within the context of photonics. Our results define a new class of optical fibers with unprecedented applications for mode filtering, mode conversion, mode multiplexing, supermode generation (linear combination of degenerate modes of close-packed waveguides), dispersion engineering and pulse shaping. Specifically, using unbroken SUSY transformations, we design a multi-core fiber (MCF) incorporating mode conversion, mode filtering, and pulse shaping functionalities spanning the S+C+L optical bands (1460-1625 nm), as well as a photonic lantern supporting broadband heterogeneous supermodes generated from the linear combination of degenerate fiber modes with different azimuthal and radial order. In addition, we show that the partial degeneracy associated with isospectral SUSY fibers can be used to build a broad-

band all-fiber *true* mode (de)multiplexer requiring no mode conversion and that, interestingly, this approach offers a dimension-independent design control over the group delay of the fiber modes. To verify and illustrate these utilities, extensive numerical simulations are performed using a 3D electromagnetic mode solver (CST Microwave Studio and COMSOL Multiphysics).

The chapter is structured as follows. In Section 7.2, we describe the transformation method proposed to apply 1D SUSY to 3D axially-symmetric optical potentials. In Section 7.3, we explore unbroken and broken 1D SUSY transformations of these systems. The construction of isospectral potentials via the Darboux procedure is investigated in Section 7.4. Finally, in Section 7.5, the main conclusions and applications of this work are highlighted, including the extension of the presented theory to acoustics and quantum mechanics.

7.2 SUSY in axially-symmetric optical potentials

We are interested in the guided modes (corresponding to a discrete spectrum of energy levels) of an axially-symmetric linear isotropic all-dielectric optical medium with a refractive index profile $n(r)$ (with variations confined to a finite spatial region). Such a system is described by the following exact 3D wave equation [we use cylindrical coordinates (r, φ, z)]:[1]

$$\nabla \times \nabla \times \widetilde{\boldsymbol{\mathcal{E}}}_{m,n}(\boldsymbol{r}, \omega) - \frac{\omega^2}{c_0^2} n^2(r)\, \widetilde{\boldsymbol{\mathcal{E}}}_{m,n}(\boldsymbol{r}, \omega) = \mathbf{0}, \tag{7.2.1}$$

where ω is the angular frequency, c_0 is the speed of light at the vacuum, and $\widetilde{\boldsymbol{\mathcal{E}}}_{m,n}$ is the Fourier transform of the electric field strength of the guided mode mn, with $m \in \mathbb{N} \cup \{0\}$ and $n \in \mathbb{N}$ indicating respectively the azimuthal and radial order. Note that Eq. (7.2.1) allows us to work with dispersive media just by using the proper frequency-dependent expression for the refractive index, although we only considered non-dispersive media ($\partial_\omega n = 0$) to facilitate the analysis.

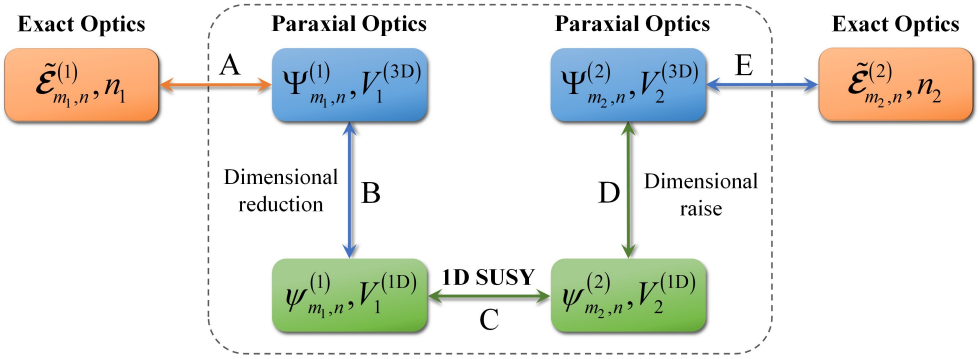

Figure 7.1. Flowchart of transformations to apply 1D SUSY to optical fibers [241].

In particular, we focus on the possibility of applying 1D SUSY to Eq. (7.2.1) through the scheme shown in Fig. 7.1. We start from a virtual space[2] $[\widetilde{\boldsymbol{\mathcal{E}}}^{(1)}_{m_1,n}, n_1]$ satisfying Eq. (7.2.1). For an SVI medium [i.e., with $\delta_r n \ll n$ in $\delta r \sim \lambda_0/n$, where $\delta_r n := |n(r) - n(r + \delta r)|$ and $\lambda_0 = 2\pi c_0/\omega$ is the free-space wavelength] and under the paraxial approximation,[3] for which the longitudinal component of $\widetilde{\boldsymbol{\mathcal{E}}}^{(1)}_{m_1,n}$ can be neglected, Eq. (7.2.1) reduces to (step A):

[1] Equation (7.2.1) is derived from Maxwell's equations by combining exclusively Faraday's and Ampère's laws, which are found to be a system of independent and complete coupled PDEs in all-dielectric media with $\omega \neq 0$. In such a case, the Gauss laws $\nabla \cdot \widetilde{\boldsymbol{\mathcal{D}}}_{m,n} = 0$ and $\nabla \cdot \widetilde{\boldsymbol{\mathcal{B}}}_{m,n} = 0$ can be respectively inferred from Ampère's and Faraday's laws. Hence, any solution of Eq. (7.2.1) automatically satisfies the four Maxwell equations.

[2] According to the transformation optics literature, the starting and final systems will be referred to as the *virtual* and *physical* spaces, respectively.

[3] In the photonics literature, the paraxial and the weakly-guiding approximations are usually considered equivalent approaches. Unfortunately, this equivalence is incorrect. In the former, the longitudinal component of the electromagnetic fields must be much lower than the transversal component as a necessary and sufficient condition. However, in the latter, this is only a necessary condition, but not sufficient.

$$\left[\triangle + E_{m,n}^{(3D)} - V^{(3D)}(r)\right]\Psi_{m,n}(\boldsymbol{r}) = 0, \tag{7.2.2}$$

where $\triangle$ is the Laplacian operator, $E_{m,n}^{(3D)} - V^{(3D)}(r) \equiv (\omega^2/c_0^2)n^2(r)$, and $\Psi_{m,n}$ is the linear combination of the transversal component of the quasi-degenerate true modes of the optical medium. For instance, in a weakly-guiding optical fiber, this corresponds to the transversal component of the linearly polarized $\mathrm{LP}_{m,n}$ mode group.[4] Since there is a degree of freedom in the mathematical identification of $E_{m,n}^{(3D)} - V^{(3D)}(r)$ with the refractive index profile, we set $E_{m,n}^{(3D)} \equiv 0$ for simplicity (it will be nonzero in quantum systems, see Table 7.1 in Section 7.5). Therefore, it is important to bear in mind that $E_{m,n}^{(3D)}$ is just an auxiliary mathematical quantity different from the physical field energy. In Appendix A7 (on page 231), we include a more detailed discussion of Eq. (7.2.2).

At this point, we perform a dimensional reduction from the 3D system $[\Psi_{m_1,n}^{(1)}, V_1^{(3D)}]$ to the 1D system $[\psi_{m_1,n}^{(1)}, V_1^{(1D)}]$ (step B, see below). Then, we transform $[\psi_{m_1,n}^{(1)}, V_1^{(1D)}]$ into $[\psi_{m_2,n}^{(2)}, V_2^{(1D)}]$ using a 1D SUSY transformation (step C). Proceeding in a similar manner as in the previous dimensional reduction, we calculate the 3D system $[\Psi_{m_2,n}^{(2)}, V_2^{(3D)}]$ from $[\psi_{m_2,n}^{(2)}, V_2^{(1D)}]$ (step D). Finally, $\Psi_{m_2,n}^{(2)}$ can be identified with the transversal component of the true modes of a second optical system (our physical space) $[\widetilde{\boldsymbol{\mathcal{E}}}_{m_2,n}^{(2)}, n_2]$ SUSY-connected with $[\widetilde{\boldsymbol{\mathcal{E}}}_{m_1,n}^{(1)}, n_1]$, provided that the SVI and the paraxial approximations are preserved (step E).

The dimensional reduction of Eq. (7.2.2) can be performed in axially-symmetric potentials as indicated in Subsection 6.14.2 of the previous chapter. We repeat here this discussion for clarity. Concretely, the dimensional reduction of the above equation can be performed by applying the following separation of variables to $\Psi_{m,n}$:

$$\Psi_{m,n}(\boldsymbol{r}) = R_{m,n}(r)\exp(jm\varphi)\exp(-j\beta_{m,n}z), \tag{7.2.3}$$

with $R_{m,n}$ the function describing the radial dependence and $\beta_{m,n}$ the phase constant of the eigenmode. Now, using the transformation:

$$R_{m,n}(r) := \frac{1}{\sqrt{r}}\psi_{m,n}(r), \tag{7.2.4}$$

Eq. (7.2.2) is reduced to:

$$\left(\frac{\mathrm{d}^2}{\mathrm{d}r^2} + E_{m,n}^{(3D)} - \beta_{m,n}^2 - V^{(3D)}(r) - \frac{m^2}{r^2} + \frac{1}{4r^2}\right)\psi_{m,n}(r) = 0. \tag{7.2.5}$$

The above equation matches the 1D time-independent Schrödinger equation:

$$\left(\frac{\mathrm{d}^2}{\mathrm{d}r^2} + E_n^{(1D)} - V^{(1D)}(r)\right)\psi_{m,n}(r) = 0, \tag{7.2.6}$$

with the identification:

$$E_n^{(1D)} - V^{(1D)}(r) \equiv E_{m,n}^{(3D)} - \beta_{m,n}^2 - V^{(3D)}(r) - \frac{m^2}{r^2} + \frac{1}{4r^2}. \tag{7.2.7}$$

In order to obtain a well-defined eigenvalue problem, an adequate expression for $E_n^{(1D)}$ and $V^{(1D)}(r)$ must be selected. Obviously, the spatially-dependent terms of the RHS of Eq. (7.2.7) should be identified with $V^{(1D)}(r)$ assuming a constant value of m. With this consideration in mind, a possible choice is (other options are accounted for by introducing a free-parameter α, see below):

$$E_n^{(1D)} \equiv E_{m,n}^{(3D)} - \beta_{m,n}^2; \tag{7.2.8}$$

$$V^{(1D)}(r) \equiv V^{(3D)}(r) + \frac{m^2}{r^2} - \frac{1}{4r^2}. \tag{7.2.9}$$

[4] As discussed in Chapter 1 (on page 13), remember that an LP_{mn} mode group includes one (two) LP mode(s) and two (four) different polarized core modes (PCMs) when $m = 0$ ($m > 0$). As an example, the LP_{11} mode group has two LP modes ($\mathrm{LP}_{11}^{(+)}$ and $\mathrm{LP}_{11}^{(-)}$) and four different PCMs ($\mathrm{LP}_{11,x}^{(+)}$, $\mathrm{LP}_{11,y}^{(+)}$, $\mathrm{LP}_{11,x}^{(-)}$ and $\mathrm{LP}_{11,y}^{(-)}$). However, in this chapter, we do not differentiate between different LP modes and PCMs in a given LP mode group. We will simply refer to an LP_{mn} mode group as an LP_{mn} mode from now on.

Crucially, the various steps and approximations of the described method may alter the ideal SUSY relation between the virtual and physical spaces $[\widetilde{\boldsymbol{\mathcal{E}}}^{(1)}_{m_1,n}, n_1]$ and $[\widetilde{\boldsymbol{\mathcal{E}}}^{(2)}_{m_2,n}, n_2]$, respectively. This possibility has been previously discussed on page 206 for radially- and axially-symmetric potentials. Here, we will perform a more detailed discussion focusing our efforts on real-valued axially-symmetric potentials. The following remarks will be essential for some of the most interesting results derived from our study (especially in isospectral constructions, in Section 7.4):

- From Eq. (7.2.9), inverse-square potentials $V^{(1\mathrm{D})}$ appear for a nonsingular potential $V^{(3\mathrm{D})}$ (as will be our case). The corresponding 1D eigenvalue problem [Eq. (7.2.6)] may be ill-defined if it is not possible to choose a unique basis of eigenfunctions based on square integrability and boundary conditions [291]. Fortunately, this is never the case for $m \geq 0$ [254], guarantying the validity of the mapping between Eqs. (7.2.2) and (7.2.6) established in step B.
- As we will see later, inverse-square potentials relate to a singular superpotential in the SUSY transformations. As a consequence, the degeneracy between $V_1^{(1\mathrm{D})}$ and $V_2^{(1\mathrm{D})}$ will only be preserved if the SUSY eigenfunctions $\psi^{(2)}_{m_2,n}$ (calculated from the bound states $\psi^{(1)}_{m_1,n}$ of $V_1^{(1\mathrm{D})}$ using the SUSY operators $\widehat{\mathrm{A}}^{\pm}$) are bound states of $V_2^{(1\mathrm{D})}$ (see Chapter 6, page 182).
- The transformation depicted by Eq. (7.2.4) may give rise to a breakdown of the degeneracy between $V_1^{(3\mathrm{D})}$ and $V_2^{(3\mathrm{D})}$ if the optical boundary conditions are violated, that is, if $R^{(2)}_{m_2,n}$ becomes singular at $r = 0$ after step D.
- The degeneracy between $V_1^{(3\mathrm{D})}$ and $V_2^{(3\mathrm{D})}$ may also be broken if the index profiles $n_1(r)$ or $n_2(r)$ do not approximately satisfy the SVI criterion or their true modes do not meet the paraxial approximation.

We will check all these points in the considered SUSY transformations. To simplify the discussion, we will use a more economical notation $V^{(1\mathrm{D})}(r) \equiv V(r)$ and $E_n^{(1\mathrm{D})} \equiv E_n$ from now on. Along this line, note that $n \geq 1$ in this scenario. Therefore, in this chapter, the ground state of a given potential V_i will be denoted as $\psi^{(i)}_{m_i,1}$, that is, employing the subindex $n = 1$ instead of using $n = 0$ as in the previous chapter.

7.3 Unbroken and broken SUSY optical fibers

As was extensively discussed in Chapter 6, for a given potential V_1 with energy levels $E_n^{(1)}$, SUSY provides a systematic way for generating a superpartner V_2 with energy levels $E_n^{(2)}$ equal to those of V_1, with the possible exception of the ground state energy level $E_1^{(1)}$. If SUSY is unbroken, the SUSY operator $\widehat{\mathrm{A}}^{-}$ annihilates the ground state of V_1, i.e., $\widehat{\mathrm{A}}^{-}\psi^{(1)}_{m_1,1} = 0$, which corresponds with the case $E_1^{(1)} = 0$ (see page 178). In this scenario, V_2 has the same energy levels as V_1 except for $E_1^{(1)}$, i.e., $E_n^{(2)} = E_{n+1}^{(1)}$. On the contrary, SUSY is spontaneously broken when $\widehat{\mathrm{A}}^{-}\psi^{(1)}_{m_1,1}$ generates a ground state in V_2, in which case $E_1^{(1)} \neq 0$ and both spectra are found to be completely degenerate, that is, $E_n^{(2)} = E_n^{(1)}$.

In our case, $E_1^{(1)} = -\beta^2_{m_1,1} \neq 0$. Therefore, instead of directly calculating a SUSY potential V_2 of V_1, it is useful to start from a potential $V_{1,\mathrm{eq}} := V_1 - \alpha$ (associated with the energy-shifted Hamiltonian $\widehat{\mathrm{H}}_{1,\mathrm{eq}} = \widehat{\mathrm{H}}_1 - \alpha = -\mathrm{d}^2/\mathrm{d}r^2 + V_1 - \alpha$ with zero-energy ground state), calculate its SUSY potential $V_{2,\mathrm{eq}}$ (with a corresponding Hamiltonian $\widehat{\mathrm{H}}_{2,\mathrm{eq}} = \widehat{\mathrm{H}}_2 - \alpha = -\mathrm{d}^2/\mathrm{d}r^2 + V_2 - \alpha$), and undo the energy shift to find the potential V_2 as $V_2 = V_{2,\mathrm{eq}} + \alpha$. This allows us to choose between unbroken SUSY or different broken SUSY transformations by selecting $\alpha = E_1^{(1)}$ or $\alpha \neq E_1^{(1)}$, respectively. Hence, assuming V_1 and V_2 of the form:

$$V_i(r) = -\frac{\omega^2}{c_0^2} n_i^2(r) + \frac{m_i^2}{r^2} - \frac{1}{4r^2}; \quad i \in \{1, 2\}, \tag{7.3.1}$$

both superpartners are related by the Riccati equation:

$$V_{1,2}(r) = W^2(r) \mp W'(r) + \alpha, \tag{7.3.2}$$

where W is the superpotential. The underlying connection given by the Riccati equation is derived from the properties of the SUSY algebra (see Section 6.5). In our case, the superhamiltonian and the supercharges take the form:

$$\mathrm{H} = \begin{bmatrix} \widehat{\mathrm{H}}_{1,\mathrm{eq}} & \widehat{0} \\ \widehat{0} & \widehat{\mathrm{H}}_{2,\mathrm{eq}} \end{bmatrix}; \quad \mathrm{Q}^- := \begin{bmatrix} \widehat{0} & \widehat{0} \\ \widehat{\mathrm{A}}^- & \widehat{0} \end{bmatrix}; \quad \mathrm{Q}^+ := \begin{bmatrix} \widehat{0} & \widehat{\mathrm{A}}^+ \\ \widehat{0} & \widehat{0} \end{bmatrix}, \tag{7.3.3}$$

with:

$$\widehat{\mathrm{A}}^{\pm} := \mp \frac{\mathrm{d}}{\mathrm{d}r} + W(r), \tag{7.3.4}$$

and $\widehat{\mathrm{A}}^+ = (\widehat{\mathrm{A}}^-)^\dagger$ when the superpotential is a real-valued function (this will be not the case in Subsection 7.3.2). Thus, the commutation and anticommutation relations given by Eqs. (6.5.4)-(6.5.6) define the closed Lie superalgebra $\mathfrak{sl}(2,\mathbb{C})$ of 1D SUSY QM. The degeneracy of the spectra is a direct consequence of the fact that the supercharges commute with the superhamiltonian when a nonsingular superpotential is involved.

7.3.1 Unbroken SUSY fibers

As mentioned before, the unbroken SUSY transformation allows us to connect the spectra of V_1 and V_2 through a relation of the form $E_n^{(2)} = E_{n+1}^{(1)}$. In addition, since $\widehat{\mathrm{A}}^- \psi_{m_1,1}^{(1)} = 0$ and the energy levels are related to the phase constant of the LP modes as indicated by Eq. (7.2.8), we will be able to annihilate the ground state $\mathrm{LP}_{m_1,1}^{(1)}$ and establish a perfect phase-matching between the $\mathrm{LP}_{m_2,n}^{(2)}$ and $\mathrm{LP}_{m_1,n+1}^{(1)}$ modes at λ_0. In this vein, outstanding optical applications such as the mode filtering of the $\mathrm{LP}_{m_1,1}^{(1)}$ mode, mode conversion between a great number of LP modes of different azimuthal (if $m_1 \neq m_2$) and radial order, and supermode generation, can be investigated using the unbroken SUSY procedure. In this context, pulse shaping applications can also be proposed by exploiting the spectral behavior of V_1 and V_2 at different wavelengths. Finally, some previous works on 1D SUSY suggest that all these interesting features might have a broadband nature, which is an additional motivation to carry out the present study [232, 237]. Before exploring these possibilities, let us first describe the unbroken SUSY transformation in more detail.

A well-known solution of Eq. (7.3.2) with $\alpha = E_1^{(1)}$ can be expressed in terms of the ground state wave function $\psi_{m_1,1}^{(1)}$ of $\widehat{\mathrm{H}}_1$ as $W(r) = -(\ln \psi_{m_1,1}^{(1)}(r))'$. From the relation $\psi_{m_1,1}^{(1)}(r) = \sqrt{r} R_{m_1,1}^{(1)}(r)$:

$$W(r) = -\frac{\mathrm{d}}{\mathrm{d}r} \ln \psi_{m_1,1}^{(1)}(r) = -\frac{\left(R_{m_1,1}^{(1)}\right)'(r)}{R_{m_1,1}^{(1)}(r)} - \frac{1}{2r}. \tag{7.3.5}$$

In spite of the fact that Q^+ and Q^- commute with H at $r = 0$, the singularity of W at this point might break the degeneracy between the 1D potentials V_1 and V_2 (see Appendix B7, on page 233). We analytically studied this possibility, finding that any bound state of V_1 has a SUSY bound state in V_2 (with the exception of the ground state $\psi_{m_1,1}^{(1)}$) via the transformation $\psi_{m_2,n}^{(2)} = \widehat{\mathrm{A}}^- \psi_{m_1,n+1}^{(1)}$. In other words, $\psi_{m_2,n}^{(2)}$ is found to be a continuous normalizable solution satisfying that $\psi_{m_2,n,\pm}^{(2)} = 0$, where $\psi_{m_2,n,-}^{(2)} := \psi_{m_2,n,-}^{(2)}(r \to 0)$ and $\psi_{m_2,n,+}^{(2)} := \psi_{m_2,n,+}^{(2)}(r \to \infty)$. This implies that degeneracy between V_1 and V_2 is preserved in all cases, which is consistent with the numerical results obtained via the mode solver of CST Microwave Studio (see below). That is, step C always yields unbroken SUSY-related 1D systems.

On the other hand, an expression for $n_2(r)$ can be derived by combining Eqs. (7.3.1), (7.3.2) and (7.3.5):

$$n_2(r) = \sqrt{n_1^2(r) + 2\frac{c_0^2}{\omega^2}\frac{\mathrm{d}^2}{\mathrm{d}r^2}\ln\left(r^{\frac{m_1^2-m_2^2+1}{2}}R^{(1)}_{m_1,1}(r)\right)}. \tag{7.3.6}$$

From the above equation, the considered SUSY procedure may also introduce a singularity in n_2 at $r = 0$. Although singular potentials have been extensively discussed in the quantum-mechanical literature with interesting physical implications and properties [291,292], singular refractive indexes pose physical and technological complications in photonics. To avoid this potential hindrance, we search for nonsingular refractive indexes by selecting an appropriate value of m_1 and m_2. From the equivalence:

$$R^{(1)}_{m_1,1}(r) \propto J_{m_1}(r) \underset{r\to 0}{\sim} \frac{(r/2)^{m_1}}{\Gamma(m_1+1)}; \quad m_1 \geq 0, \tag{7.3.7}$$

where J_{m_1} is the Bessel function of the first kind and order m_1, and Γ is the Gamma function, we can deduce that the singularity at $r = 0$ is avoided *if and only if* n_1 is nonsingular and $m_2 = m_1+1$, with $m_1 \geq 0$. This was already pointed out in [228], although only the case $m_1 = 1$ was analyzed. However, LP modes without azimuthal variation ($m_1 = 0$) are of paramount importance in optical communications, so we will pay particular attention to them in this work.

In addition, it should be noted that Eq. (7.3.6) is frequency dependent, not only as a result of the possible frequency changes of n_1, but also of the c_0/ω term and the frequency dependence of $R^{(1)}_{m_1,1}$. Consequently, the mentioned phase-matching of SUSY axially-symmetric potentials will be band limited, a fundamental feature that has not been pointed out so far and the implications of which will be carefully studied in this work. Finally, a third parameter that has not yet been analyzed within the framework of optical SUSY is the group delay, i.e., the first-order derivative of the phase constant as a function of the angular frequency.

As an illustrative example that allows us to study all these features (modes without azimuthal variation, band-limited phase-matching, and group delay), we consider an optical fiber (core radius $R_0 = 25$ μm) with a step-index profile n_1 [$n_1(r \leq R_0) = n_{\mathrm{co}}$, $n_1(r > R_0) = n_{\mathrm{cl}}$, see Fig. 7.2(a)], as the original system. For this configuration, the SVI and paraxial approximations are very accurate, ensuring that, after step A, $\Psi^{(1)}_{m_1,n}$ is related to $\widetilde{\boldsymbol{\mathcal{E}}}^{(1)}_{m_1,n}$ as described above. The same initial index profile will be considered in all the examples analyzed in this chapter. Figure 7.2(a) shows the profiles of n_2 and W for two different free-space wavelengths ($\lambda_0 = 2\pi c_0/\omega$): 1550 nm and 3000 nm. As expected, n_2 and W are wavelength-dependent, and so will be the phase-matching predicted by Eq. (7.3.11).

In the classical modal analysis of step- and gradual-index optical fibers, the spectral features are analyzed from the dispersion and group delay diagrams, which respectively depict the phase constant and the group delay of the LP modes as a function of the angular frequency. In weakly-guiding optical fibers, the above parameters are usually normalized by using the step-index profile as a reference [18]. The normalized phase constant $b_{m,n}$, normalized frequency ν and normalized group delay $\tau_{m,n}$ are defined as:[5]

$$b_{m,n} := \frac{(\beta_{m,n}/k)^2 - n_{\mathrm{cl}}^2}{n_{\mathrm{co}}^2 - n_{\mathrm{cl}}^2} \simeq \frac{(\beta_{m,n}/k) - n_{\mathrm{cl}}}{n_{\mathrm{co}} - n_{\mathrm{cl}}}; \tag{7.3.8}$$

$$\nu := kR_0\sqrt{n_{\mathrm{co}}^2 - n_{\mathrm{cl}}^2}; \tag{7.3.9}$$

$$\tau_{m,n} := b_{m,n} + \nu\frac{\mathrm{d}b_{m,n}}{\mathrm{d}\nu}, \tag{7.3.10}$$

[5]The approximation of Eq. (7.3.8) can be performed by assuming weakly-guiding optical fibers. Moreover, in order to avoid any confusion with the quantum potential (V), note that we use here a typography different from the typography employed in Chapters 2, 3 and 4 to denote the normalized frequency (ν).

with $k = \omega/c_0$. In this way, the spectral features of the unbroken SUSY procedure can be analyzed by calculating numerically (via CST Microwave Studio) the aforementioned diagrams for the index profiles $n_1(r)$ and $n_2(r)$.

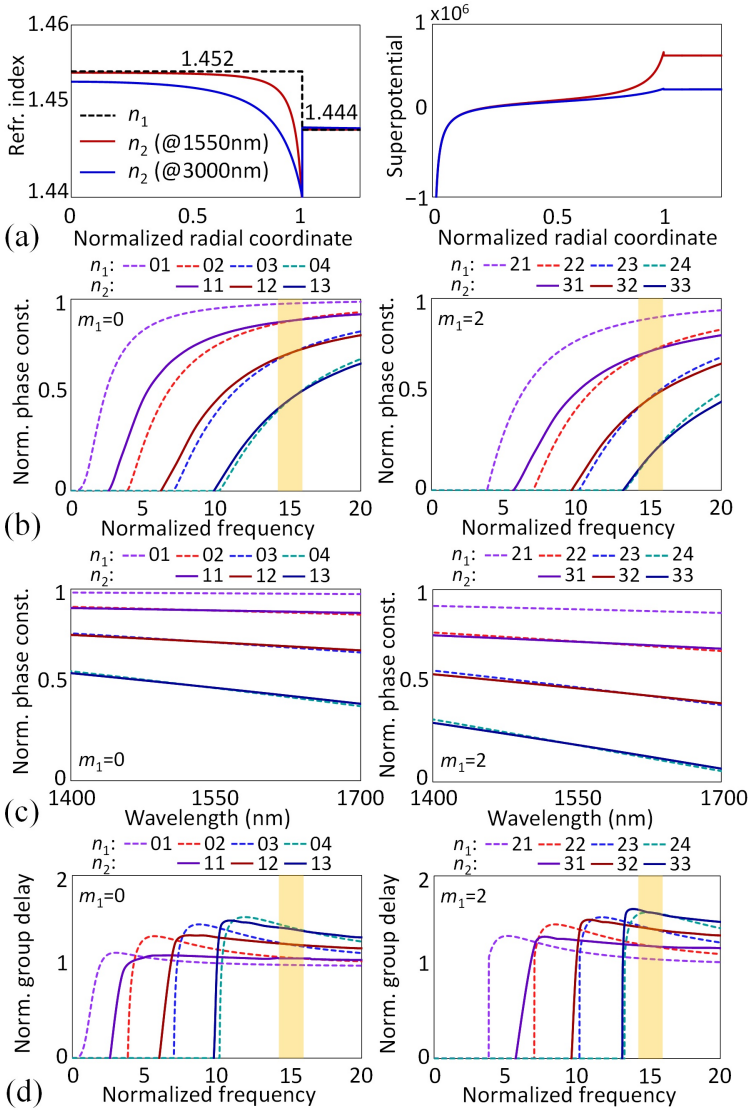

Figure 7.2. Modal analysis of two supersymmetric refractive indexes. (a) SUSY partner for the step-index profile and the corresponding superpotential as a function of the normalized radial coordinate (r/R_0). (b) Normalized dispersion diagram of the LP modes as a function of the normalized frequency, and (c) the wavelength comprising the S + C + L optical bands. (d) Normalized group delay as a function of the normalized frequency [241].

Figures 7.2(b)-(d) depict the normalized dispersion and normalized group delay diagrams of the $\mathrm{LP}^{(1)}_{m_1,n}$ and $\mathrm{LP}^{(2)}_{m_2,n}$ modes for the cases $m_1 \in \{0,2\}$, $m_2 = m_1 + 1$ and n varying from 1 to 4 ($\lambda_0 = 1550$ nm). The cases $m_1 = 1$ and $m_1 = 3$ are also included in Appendix B7 for completeness (see page 233). As seen, in spite of using a singular superpotential, degeneracy between the expected LP modes of both optical systems is present in this case. This inherently implies that step D does not generate unphysical functions $R^{(2)}_{m_2,n}$ and that the SVI and paraxial approximations are valid for n_2. Therefore, the unbroken SUSY procedure establishes a perfect phase-matching at λ_0 between the $\mathrm{LP}^{(2)}_{m_1+1,n}$ and $\mathrm{LP}^{(1)}_{m_1,n+1}$ optical modes, with $m_1 \geq 0$ and $n \geq 1$. More specifically, the corresponding $R_{m,n}$ and $\beta_{m,n}$ are connected by the expressions:

$$\beta^{(2)}_{m_1+1,n} = \beta^{(1)}_{m_1,n+1}; \tag{7.3.11}$$

$$R^{(2)}_{m_1+1,n}(r) = \frac{\xi^{(2)}}{\sqrt{r}}\widehat{\mathrm{A}}^{-}\left(\sqrt{r}R^{(1)}_{m_1,n+1}(r)\right); \tag{7.3.12}$$

$$R^{(1)}_{m_1,n+1}(r) = \frac{\xi^{(1)}}{\sqrt{r}}\widehat{\mathrm{A}}^{+}\left(\sqrt{r}R^{(2)}_{m_1+1,n}(r)\right), \tag{7.3.13}$$

with $\xi^{(1,2)}$ non-vanishing real constants accounting for the normalization of the LP modes.

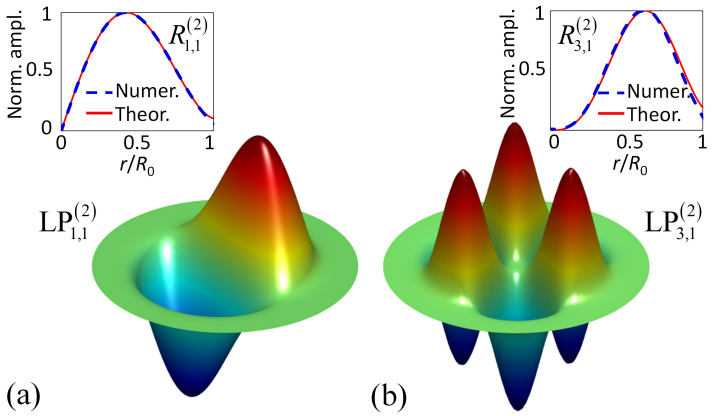

Figure 7.3. Ground state wave function $\psi^{(2)}_{m_2,1}$ of the SUSY refractive index n_2 for the cases: (a) $m_1 = 0$ and (b) $m_1 = 2$. The comparison between the numerical calculation using the 3D mode solver and Eq. (7.3.12) is inset in the top of the figure [241].

In order to validate Eqs. (7.3.12) and (7.3.13) in the analyzed example, we compare in Fig. 7.3 the theoretical results of $R^{(2)}_{m_2,1}$ for the cases $m_1 = 0$ and $m_1 = 2$ with the numerical results obtained from the 3D mode solver of CST Microwave Studio, finding that both results are in excellent agreement. Notably, an almost perfect phase-matching ($\Delta b \leq 0.02$) is achieved between LP modes in an optical bandwidth higher than 300 nm [see Fig. 7.2(c)]. The above bandwidth is defined as the phase-matching bandwidth (PMBW), which gives information about the range of optical frequencies for which the LP modes of both superpartners are found to be approximately degenerate according to the aforementioned criterion. In real optical fibers, in which the frequency dependence of n_1 and n_2 should also be taken into account, the PMBW could be slightly reduced with respect to the ideal case shown in Fig. 7.2.

Furthermore, Fig. 7.2(d) reveals a very interesting feature: the normalized group delay of the LP modes in n_2 presents a weaker frequency dependence than in n_1, which indicates that the supersymmetric optical fiber is less dispersive than the original one. Consequently, the differential mode group delay (DMGD) between the LP mode groups of n_2 [calculated here as the absolute value of the difference between the group delays per unit of length (in ps/km)] is approximately constant within the PMBW.[6]

[6]For the sake of clarity, let us remember here the concept of the differential mode group delay (DMGD) and the difference with the differential group delay (DGD), discussed in Chapter 4 (Appendix E4). In the photonics literature, the DMGD is usually employed to indicate the difference between the group delay of PCMs of different LP mode groups (e.g., $\mathrm{LP}_{01,x}$ and $\mathrm{LP}^{(+)}_{11,x}$). In contrast, the DGD is usually employed to indicate the difference between the group delay of PCMs of the same LP mode group (e.g., $\mathrm{LP}_{01,x}$ and $\mathrm{LP}_{01,y}$). Both parameters can be found in the literature defined: (*i*) as a function of the absolute value of the difference between the group delays of the PCMs under analysis (in ps), or (*ii*) as a function of the absolute value of the difference between the group delays *per unit of length* of the PCMs under analysis (in ps/km). As an example, in Chapter 3 we used the former definition to calculate the DGD. Nonetheless, in this chapter, we will use the latter definition to calculate the DMGD.

We next construct an unbroken SUSY chain comprising N supersymmetric refractive index profiles $\{n_1(r),\ldots,n_N(r)\}$. A given index profile $n_q(r)$ $[q\in\{2,\ldots,N\}]$ can be calculated from the original profile $n_1(r)$ as (see Appendix B7 for more details):

$$n_q(r)=\sqrt{n_1^2(r)+2\frac{c_0^2}{\omega^2}\frac{\mathrm{d}^2}{\mathrm{d}r^2}\ln\left(r^{\frac{m_1^2-m_{q+1}^2}{2}}\prod_{i=1}^{q-1}R_{m_i,1}^{(i)}(r)\right)}, \tag{7.3.14}$$

with $m_i=m_1+i-1$. The phase constants and the wave functions of the q-th system satisfy:

$$\beta_{m_1+q-1,n}^{(q)}=\beta_{m_1,n+q-1}^{(1)}; \tag{7.3.15}$$

$$R_{m_1+q-1,n}^{(q)}(r)=\frac{\xi^{(2)}}{\sqrt{r}}\left(\prod_{i=1}^{q-1}\widehat{\mathrm{A}}_{q-i}^{-}\right)\left(\sqrt{r}R_{m_1,n+q-1}^{(1)}(r)\right), \tag{7.3.16}$$

where $\widehat{\mathrm{A}}_{q-i}^{-}:=\mathrm{d}/\mathrm{d}r+W_{q-i}(r)$ and W_{q-i} is the superpotential connecting the indexes n_{q-i} and n_{q-i+1}. Concretely, W_{q-i} can be calculated from the corresponding ground state of the $q-i$ system $\psi_{m_{q-i},1}^{(q-i)}$ as $W_{q-i}(r)=-(\ln\psi_{m_{q-i},1}^{(q-i)}(r))'$.

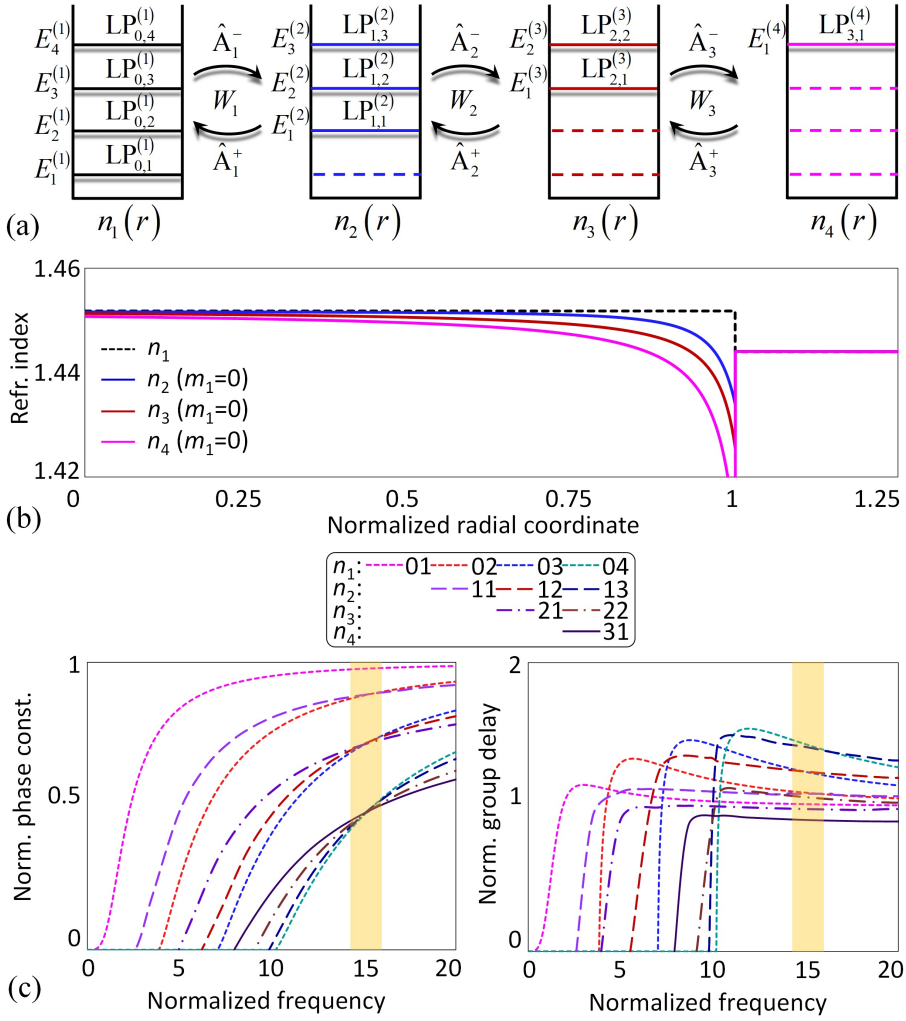

Figure 7.4. Modal analysis of the unbroken SUSY Hamiltonian chain. (a) Symbolic representation of the SUSY chain. (b) Supersymmetric refractive indexes calculated from Eq. (7.3.14). (c) Normalized dispersion diagram and normalized group delay of the LP modes in the SUSY chain [241].

As an example, we perform a modal analysis of an unbroken SUSY Hamiltonian chain with $N = 4$ and $m_1 = 0$. The numerical results are shown in Fig. 7.4. All refractive index profiles are nonsingular, thanks to the choice $m_i = m_1 + i - 1$ [see Fig. 7.4(b)]. As before, it can be theoretically shown that the SUSY eigenfunctions $\psi^{(i)}_{m_i,n}$ of each system with index n_i are bound states, that is, continuous normalizable eigenfunctions satisfying that $\psi^{(i)}_{m_i,n,\pm} = 0$ (see Appendix B7). This is further confirmed through numerical simulations [Fig. 7.4(c)], which evidence that degeneracy is present throughout the whole chain (implicitly validating the application of step D and the SVI and paraxial approximations for all systems).

Although the PMBW is slightly reduced in the fourth system, the group delay of higher-order modes (specially the $\mathrm{LP}^{(4)}_{3,1}$) is lower than that of the fundamental mode of the first system, the $\mathrm{LP}^{(1)}_{0,1}$. This opens up the possibility of enabling privileged optical transmissions in higher-order LP modes. Moreover, the unexpected flexibility provided by SUSY in the design of exotic propagation properties (such as weak dispersion or low group delay) can be combined with the mode-coupling phenomenon to design MCFs with special features for, e.g., mode conversion, mode filtering, dispersion engineering and pulse shaping.

In order to illustrate these potential applications, we perform a pulse propagation simulation using a beam propagation method (BPM) based on Eq. (E4.4) in a 2.7-km MCF comprising two cores a and b with $R_0 = 25$ μm, $\lambda_0 = 1550$ nm and index profiles $n_a = n_1$ and $n_b = n_4$. For simplicity, we employ the notation $\mathrm{LP}^{(a)}_{m,n} \equiv \mathrm{LP}^{(1)}_{m,n}$ and $\mathrm{LP}^{(b)}_{m,n} \equiv \mathrm{LP}^{(4)}_{m,n}$. The core-to-core distance d_{ab} (measured from the center of the cores) is fixed to 75 μm. A Gaussian optical pulse with a temporal width of 20-ns [at $1/(2e)$ of the peak power] excites the $\mathrm{LP}^{(a)}_{0,1}$ and $\mathrm{LP}^{(a)}_{0,4}$ modes with a peak power of 0 dBm in order to guarantee that we are operating in the linear regime of the MCF. For this value of peak power, the pulse distortion induced by the nonlinear effects of the optical medium can be neglected (as demonstrated in Chapter 4).

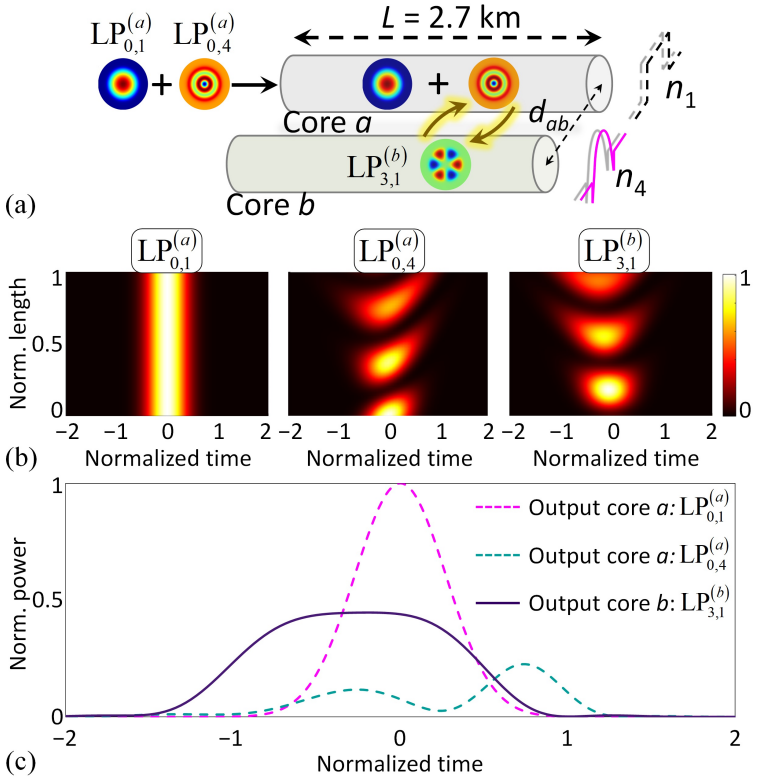

Figure 7.5. (a) Pulse propagation in a 3-km 2-core SUSY MCF. (b) Simulation results of a 20-ns Gaussian optical pulse propagating through the MCF length when the $\mathrm{LP}^{(a)}_{0,1}$ and $\mathrm{LP}^{(a)}_{0,4}$ modes are stimulated at the MCF input (colorbar: normalized power). (c) Pulse shaping at the MCF output [241].

Figure 7.5 depicts the simulated pulse propagation for the $\mathrm{LP}_{0,1}^{(a)}$, $\mathrm{LP}_{0,4}^{(a)}$ and $\mathrm{LP}_{3,1}^{(b)}$ modes. The time was normalized with respect to the (non-normalized) group delay of the $\mathrm{LP}_{0,1}^{(a)}$ mode ($\tau_{\mathrm{G},01}^{(a)}$) as $t_{\mathrm{N}} := (t - \tau_{\mathrm{G},01}^{(a)} z)/T_{\mathrm{P}}$, where T_{P} is the full-width at $1/(2e)$ of the peak power. The z-coordinate was normalized to the MCF length, i.e., $z_{\mathrm{N}} := z/L$. Figure 7.5(b) shows that the pulse propagating through the $\mathrm{LP}_{0,1}^{(a)}$ retains its shape along the MCF length as a direct consequence of the phase-mismatching of this mode, not only with the $\mathrm{LP}_{3,n}^{(b)}$ modes, but also with any $\mathrm{LP}_{m,n}^{(b)}$ mode (it was numerically tested that $\beta_{0,1}^{(a)} > \beta_{m,n}^{(b)}$ at $\lambda_0 = 1550$ nm).

However, the shape of an optical pulse launched to the $\mathrm{LP}_{0,4}^{(a)}$ mode is modified along the MCF due to the intermodal dispersion between the degenerate $\mathrm{LP}_{0,4}^{(a)}$ and $\mathrm{LP}_{3,1}^{(b)}$ modes [see Fig. 7.4(c)]. Figure 7.5(c) shows the pulse shape observed at the MCF output for each mode. As demonstrated in Chapter 4, the first-order intermodal dispersion[7] between two different phase-matched LP core modes [$\Delta b(\lambda_0) = 0$] can be modeled by two linear and time-invariant systems with impulse response approximately proportional to $\delta(t - \Delta\tau_{\mathrm{G}} z) + \delta(t + \Delta\tau_{\mathrm{G}} z)$ in core a and $\delta(t - \Delta\tau_{\mathrm{G}} z) - \delta(t + \Delta\tau_{\mathrm{G}} z)$ in core b, where $\Delta\tau_{\mathrm{G}}$ is the DMGD between the LP modes (see page 115). That is, the input pulse is transformed into the sum of two pulses with a relative delay of $2\Delta\tau_{\mathrm{G}} L$ at the fiber output. In particular, the first-order intermodal dispersion length $L_{\mathrm{ID}}^{(1)} := T_{\mathrm{P}}/(2\Delta\tau_{\mathrm{G}})$ indicates the MCF length scales over which the dispersive effects of the first-order intermodal dispersion should be considered. Since $L > L_{\mathrm{ID}}^{(1)} = 0.4$ km, the first-order intermodal dispersion between the $\mathrm{LP}_{0,4}^{(a)}$ and $\mathrm{LP}_{3,1}^{(b)}$ modes allows us to generate different pulse shapes by optimizing L. For instance, in the example of Fig. 7.5, L was chosen so that the two pulses into which the initial pulse launched into the $\mathrm{LP}_{0,4}^{(a)}$ mode is transformed, add up to form a flat-top pulse with a broadened temporal width and a lower group delay than the original one. Likewise, note that the $\mathrm{LP}_{0,1}^{(a)}$ mode is filtered at the output of the core a.

Along these same lines, it should be noted that the group-velocity dispersion (GVD) — also referred to as chromatic dispersion in the photonics literature — can be neglected in each LP mode. The GVD should only be considered in a given $\mathrm{LP}_{m,n}$ mode when $L > L_{\mathrm{GVD}} := T_{\mathrm{P}}^2/\beta_{m,n}^{(2)}$, where $\beta_{m,n}^{(2)} := \mathrm{d}^2\beta_{m,n}/\mathrm{d}\omega^2$ at λ_0. Typically, $\beta_{m,n}^{(2)}$ is of the order of -20 ps^2/km or lower in weakly-guiding silica fibers [139]. Thus, since $L \ll L_{\mathrm{GVD}} \sim 2 \cdot 10^7$ km, we can neglect the pulse distortion induced by the GVD in Fig. 7.5(c).

The unbroken SUSY procedure and its intriguing features and applications can also be exploited by using planar waveguides [228–230]. In this context, a planar SUSY mode converter has been experimentally demonstrated in [234] by Heinrich et al. by performing a discrete representation of the refractive index profile using photonic lattices. In contrast to SUSY optical fibers, a SUSY mode converter with planar structure would be of special interest for signal processing applications in integrated photonics [293, 294]. However, the device demonstrated in Fig. 7.5 could be of extreme utility in applications requiring an all-fiber design, especially, for a fully integrated realization of angular momentum multiplexing [290]. Along this line, novel pulse shaping and dispersion management applications based on unbroken SUSY fiber chains can be explored within the framework of microwave photonics and radio-over-fiber transmissions for the next-generation 5G cellular networks [56, 65]. Furthermore, in contrast to the classical mode conversion and mode filtering strategies based on rectangular waveguides and optical fibers with different width [295–298], the unbroken SUSY procedure allows us to perform these functionalities in an extremely high optical bandwidth (see Figs. 7.2 and 7.4).

Moreover, the singular features of the unbroken SUSY chain allows us to design MCFs and selective photonic lanterns with unique broadband intra- and intermodal dispersion properties [Fig. 7.4(c)] that would be difficult to obtain with classical step-index or gradual-index profiles [299–304]. The concept of photonic lantern was originally conceived in the field of astrophotonics

[7] Let us remember that in Chapter 4 the intermodal dispersion was referred to as mode-coupling dispersion (MCD). In general, the MCD is induced by two different dispersive effects: the phase-mismatching dispersion (PhMD) and the coupling-coefficient dispersion (CCD). Specifically, in this case, the first-order intermodal dispersion observed in Fig. 7.5 is only induced by the first-order PhMD.

to couple the light between a multi-mode single-core fiber and individual single-mode single-core fibers [299]. In recent years, this device has been extensively developed to inject (extract) light to (from) optical fibers in space-division multiplexing transmissions, as well as for other applications [305].

The photonic lanterns considered in these previous works (based on classical step-index and gradual-index profiles) support homogeneous supermodes, i.e., supermodes generated from the linear combination of degenerate LP modes with the same azimuthal and radial order. Typically, these supermodes are constructed through the linear combination of the LP_{01} mode of different cores in an MCF, which requires a high number of cores to obtain supermodes with large effective area [33]. This is of special interest to increase the tolerance of the signal-to-noise ratio to the fiber Kerr nonlinearities in space-division multiplexing systems. In such a scenario, the advantage of SUSY would be that it allows us to construct photonic lanterns with heterogeneous supermodes, generated from the linear combination of different LP mode groups. In this vein, supermodes with large effective area can be designed using an MCF with a reduced number of SUSY cores.

As a specific example, we designed an MCF comprising two cores a and b with $R_0 = 9$ μm, $d_{ab} = 2R_0$, $n_a = n_1$ and $n_b = n_2(m_1 = 0, \lambda_0 = 1550$ nm). Figures 7.6(a)-7.6(c) show the intensity mode profile $I(x, y)$ of different hybrid modes of the MCF calculated with the 3D mode solver of CST Microwave Studio at $\lambda_0 = 1550$ nm. As can be seen, this structure supports both isolated LP modes [Fig. 7.6(a) and 7.6(b)] and supermodes [Fig. 7.6(c)], depending on the stimulated hybrid modes. Remarkably, the supermode of Fig. 7.6(c) is generated in the MCF from the almost perfect phase-matching between LP modes of different azimuthal order ($\mathrm{LP}_{0,2}^{(a)} \pm \mathrm{LP}_{1,1}^{(b)}$ in this case). As a result, SUSY allows us to generate designer heterogeneous supermodes with large effective area:

$$A_{\mathrm{eff}} := \frac{\left(\iint I\,(x,y)\,\mathrm{d}x\mathrm{d}y\right)^2}{\iint I^2\,(x,y)\,\mathrm{d}x\mathrm{d}y}, \tag{7.3.17}$$

in a high optical bandwidth and using only two cores [Fig. 7.6(d)].

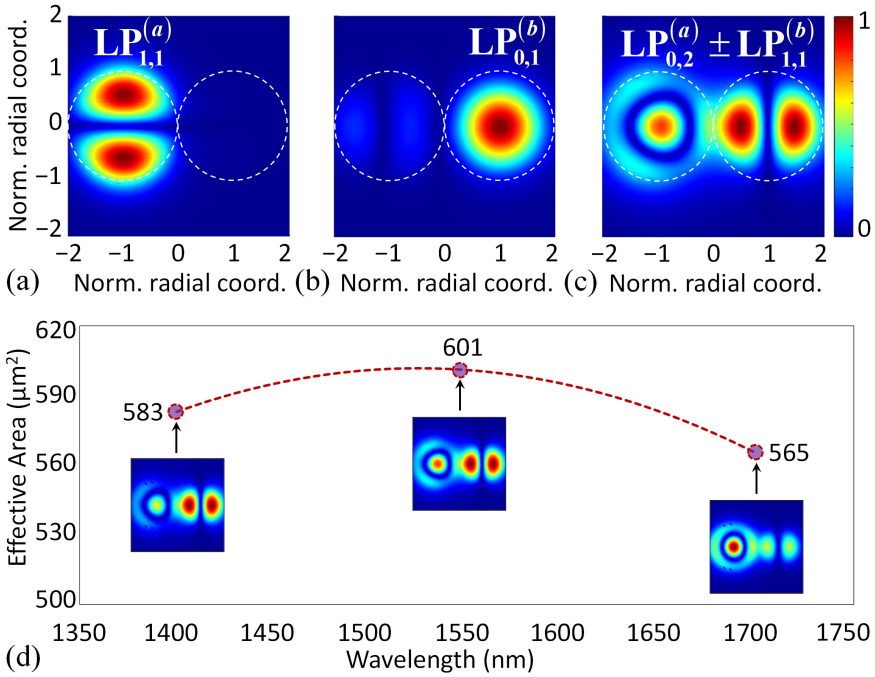

Figure 7.6. Calculated intensity mode profiles of different hybrid modes of the SUSY coupled-core MCF at 1550 nm: (a) 6-th hybrid mode, (b) 8-th hybrid mode and (c) 15-th hybrid mode. (d) Effective area of the supermode $\mathrm{LP}_{0,2}^{(a)} \pm \mathrm{LP}_{1,1}^{(b)}$ as a function of the wavelength. (Colorbar: normalized intensity) [241].

7.3.2 Broken SUSY fibers

Broken and isospectral (see next section) SUSY transformations relate the spectra of the original (V_1) and transformed potentials (V_2) through the relation $E_n^{(2)} = E_n^{(1)}$. In this way, we will be able to establish a perfect phase-matching between the $\mathrm{LP}_{m_1,n}^{(1)}$ and $\mathrm{LP}_{m_2,n}^{(2)}$ modes at λ_0, provided that the conditions for the degeneracy between the optical systems $[\widetilde{\boldsymbol{\mathcal{E}}}_{m_1,n}^{(1)}, n_1]$ and $[\widetilde{\boldsymbol{\mathcal{E}}}_{m_2,n}^{(2)}, n_2]$ are satisfied (see Section 7.2). In such circumstances, mode conversion applications between LP modes with the same radial order could be explored by using the broken (and isospectral) SUSY procedure. On the other hand, if degeneracy were not preserved (which will turn out to be the case for the broken transformations analyzed in this section), the corresponding SUSY transformation could be employed as a mathematical strategy to design gradual-index MCFs with a high core density and a low mode-coupling between the LP modes of different cores (also termed in the literature as inter-core crosstalk, see Chapter 2) within a large bandwidth. Finally, a partial degeneracy (which will be the case for the isospectral constructions studied in next section) could be used to achieve unprecedented selective mode filtering configurations without mode conversion provided that $m_1 = m_2$.

The SUSY relation between V_1 and V_2 is broken if $\alpha \neq E_1^{(1)}$. In this work, we focus on the case $\alpha < E_1^{(1)}$. Redefining the auxiliary constant as $\alpha \equiv -k^2 n_\alpha^2$, where $k = \omega/c_0$, we find that SUSY is broken if n_α is higher than the effective refractive index of the ground state $\mathrm{LP}_{m_1,1}^{(1)}$, i.e., $n_\alpha > \beta_{m_1,1}^{(1)}/k$. The previous condition is guaranteed by selecting $n_\alpha > \max\{n_1(r)\}$, in which case, the solution to Eq. (7.3.2) for the step-index profile is:

$$W(r) = jX(r)\left[\frac{J'_{m_1}(-jrX(r)) + Y'_{m_1}(-jrX(r))}{J_{m_1}(-jrX(r)) + Y_{m_1}(-jrX(r))}\right] - \frac{1}{2r}, \tag{7.3.18}$$

where $X(r) = k\sqrt{n_\alpha^2 - n_1^2(r)}$. The index n_2 is calculated from the superpotential as:

$$n_2(r) = \sqrt{n_1^2(r) - 2\frac{c_0^2}{\omega^2}\frac{\mathrm{d}}{\mathrm{d}r}\left(\frac{m_2^2 - m_1^2}{2r} + W(r)\right)}. \tag{7.3.19}$$

As in the previous section, W is found to be singular. However, W and n_2 are now *complex* functions. This means that n_2 includes local gain or loss (via its imaginary part), as in some transformation optics approaches [306–308]. At this point, let us analyze under which conditions n_2 will be nonsingular, depending on the relation between m_1 and m_2:

- $m_1 = m_2$: n_2 will not be singular only for a nonsingular W, which cannot be the case.
- $m_1 < m_2$: n_2 is bounded at $r = 0$ if $W_- = -\infty$. Nevertheless, from Eq. (7.3.18), we found that $W_- = \infty$.
- $m_1 > m_2$: As $W(r) \propto (2m_1 - 1)/2r$ when $r \to 0$ and $m_1 > 0$, n_2 becomes nonsingular if $m_2 = m_1 - 1$.

Thus, we focus on the last case in what follows. A particular example with $m_1 = 2$, $m_2 = 1$, $\lambda_0 = 1550$ nm, and $n_\alpha = 1.452$ is considered. In this case, in order to simulate a complex refractive index profile, we use the 3D electromagnetic mode solver of COMSOL. Figures 7.7(a) and 7.7(b) depict the real (blue line) and imaginary (red line) parts of the broken SUSY index n_2 and W. As expected, W presents a singularity at $r = 0$, but n_2 is nonsingular. Surprisingly, in this case both optical systems are found to be non-degenerate concerning the SUSY modes $\mathrm{LP}_{m_1,n}^{(1)}$ and $\mathrm{LP}_{m_2,n}^{(2)}$ [Fig. 7.7(c)]. Nonetheless, as can be seen from Fig. B7.4 in Appendix B7 (on page 237), additional LP modes are found to be degenerate at different frequencies in the third transmission optical window (normalized frequency between 14.2 and 16). Furthermore, the imaginary part of n_2 induces at 1550 nm a mode-dependent loss per unit of length of 1.46 Np/m, 1.34 Np/m and 1.07 Np/m for the $\mathrm{LP}_{1,1}^{(2)}$, $\mathrm{LP}_{1,2}^{(2)}$ and $\mathrm{LP}_{1,3}^{(2)}$ modes, respectively [1 Np $\equiv 10\log(e)$ dB $\simeq 4.34$ dB].

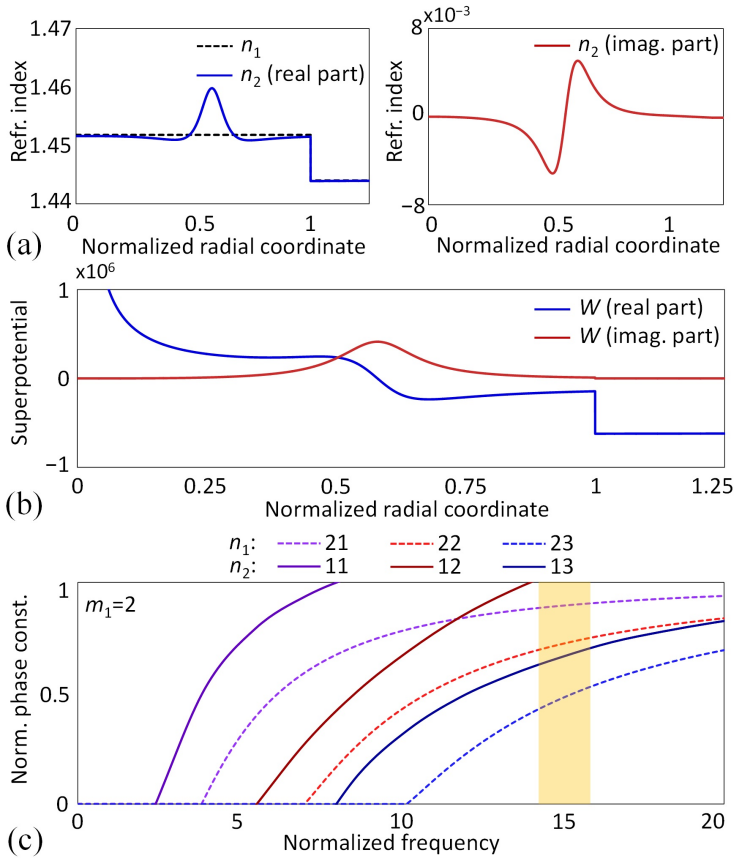

Figure 7.7. Broken SUSY 1D. (a) SUSY partner for the step-index profile, (b) superpotential (blue line: real part, red line: imaginary part), and (c) normalized dispersion diagram of the broken SUSY pattern of the step-index profile assuming $m_1 = 2$ and $m_2 = 1$ in Eq. (7.3.19) [241].

We investigated the different possible origins for the non-degeneracy between $[\widetilde{\boldsymbol{\mathcal{E}}}^{(1)}_{m_1,n}, n_1]$ and $[\widetilde{\boldsymbol{\mathcal{E}}}^{(2)}_{m_2,n}, n_2]$. Firstly, we verified that the singularity of W involved in step C is not behind this unusual behavior, since the SUSY eigenfunctions $\psi^{(2)}_{m_2,n} = \widehat{\mathrm{A}}^{-}\psi^{(1)}_{m_1,n}$ are again continuous normalizable eigenfunctions satisfying that $\psi^{(2)}_{m_2,n,\pm} = 0$ (see Appendix B7). Then, we checked whether the absence of degeneracy may come from a violation of the optical boundary condition at $r = 0$ by the SUSY modes of $V_2^{(3\mathrm{D})}$ after step D. This is not the case either, since $R^{(2)}_{m_2,n}(r = 0) = 0$ in the analyzed case. By process of elimination, the non-degeneracy must be induced by step E. In fact, although we found that the SVI criterion is fulfilled ($\delta n_2 \leq 0.01 \ll n_2$ in $\delta r \sim \lambda_0/n_2$), the paraxial approximation is strongly degraded for $V_2^{(3\mathrm{D})}$. As analyzed in Appendix B7, on page 236, although the true modes of the n_2 profile are quasi-degenerate and their linear combination shows a quasi-linearly polarized nature similar to [32], i.e. we observe quasi-LP modes, their longitudinal component $\widetilde{\mathcal{E}}_z$ cannot be neglected with respect to the transversal one $\widetilde{\mathcal{E}}_{\mathrm{T}}$ ($\widetilde{\mathcal{E}}_z/\widetilde{\mathcal{E}}_{\mathrm{T}} \simeq 0.1$). Hence, as the bound states of $V_2^{(3\mathrm{D})}$ do not approximately satisfy Eq. (7.2.2), the degeneracy between both spectra is broken.

This exclusive feature of broken SUSY in axially-symmetric optical media can be used to design MCFs with a high density of cores propagating non-degenerate modes with low inter-core crosstalk levels. The ever decreasing core-to-core distance in MCFs (aiming at increasing the core density and hence the fiber capacity) significantly enhances the inter-core crosstalk (IC-XT) [16]. In this scenario, gradual-index MCFs comprising a high core density with low IC-XT can be designed with the broken SUSY procedure. For completeness, in Appendix B7 we also analyze additional strategies as the inverse SUSY transformation.

So far, we have analyzed SUSY transformations by considering $\alpha \leq E_1^{(1)}$. The reason for not having discussed the case $\alpha > E_1^{(1)}$ is that it is related to a superpotential of the form:

$$W_{(n)}(r) = -\frac{\mathrm{d}}{\mathrm{d}r} \ln \psi_{m_1,n}^{(1)}(r), \tag{7.3.20}$$

with $n > 1$ and $\psi_{m_1,n}^{(1)}$ a bound state with n nodes. Hence, $W_{(n)}$ and V_2 will have $n-1$ singularities at $r > 0$ in this case, and so will the corresponding SUSY refractive index. Nevertheless, a superpotential $W_{(n)}$ could be an interesting alternative in complex cylindrical potentials involving: (*i*) a discrete spectrum and exhibiting parity-time symmetry, e.g. to remove arbitrary modes [229], or (*ii*) a continuum spectrum, for instance, to generate bound states in the continuum [259].

7.4 Isospectral optical fibers

In the context of quantum mechanics, it is well-known that one can start from a given 1D potential and use SUSY transformations to construct single- and multi-parameter families of isospectral potentials, i.e., potentials with exactly the same energy levels and scattering properties as the original one. In this section, we investigate the application of these isospectral transformations to axially-symmetric optical potentials. As we will demonstrate, such transformations provide a privileged procedure to construct families of refractive index distributions supporting degenerate LP modes with a dimension-independent design control over their group delay. Furthermore, as mentioned above, selective mode filtering may also be performed if degeneracy is only partially preserved.

As detailed in Section 6.11, there exist different approaches to construct a one-parameter family of isospectral potentials. For its intuitive character, we use here the Darboux procedure, particularized in Fig. 7.8(a) for axially-symmetric potentials. At this point, let us remember that the Darboux method involves two different Darboux transformations: firstly using the normalizable eigenfunction $\psi_{m_1,1}^{(1)}$ of V_1 at energy $E_1^{(1)}$ (which can be regarded as an unbroken SUSY transformation), and secondly using the non-normalizable eigenfunction $\Phi_1(\eta_1)$ of V_2 at energy $E_1^{(1)}$. Remarkably, although the potential V_2 does not have an allowed energy level $E_1^{(1)}$ (due to the unbroken SUSY transformation performed in the first step) the EVP $\widehat{\mathrm{H}}_2\psi_\lambda^{(2)} = \lambda\psi_\lambda^{(2)}$ has at $\lambda = E_1^{(1)}$ a general (and non-normalizable) solution of the form (see Appendix C7 for more details):

$$\psi_{\lambda=E_1^{(1)}}^{(2)} \equiv \Phi_1(r;\eta_1) = \frac{\mathcal{I}_1(r) + \eta_1}{\sqrt{r} R_{m_1,1}^{(1)}(r)}; \quad \mathcal{I}_1(r) := \int^r \alpha \left(R_{m_1,1}^{(1)}\right)^2 (\alpha)\, \mathrm{d}\alpha. \tag{7.4.1}$$

Thus, in the second step, we apply a Darboux transformation in V_2 taking as eigenvalue of reference $\lambda_0 = E_1^{(1)}$, or equivalently, we can say that we apply an unbroken SUSY transformation in V_2 by using $\Phi_1(\eta_1)$ as a *virtual* ground state, i.e., using a superpotential of the form:

$$W_{\mathrm{D}}(r;\eta_1) = -\frac{\mathrm{d}}{\mathrm{d}r} \ln \Phi_1(r;\eta_1). \tag{7.4.2}$$

The resulting partner potential $\widetilde{V}_1(\eta_1)$ will have a solution $1/\Phi_1(\eta_1)$ at energy $E_1^{(1)}$, which will be normalizable if $\eta_1 \notin [-\mathcal{I}_{1,+}, 0]$, where $\mathcal{I}_{1,+} := \mathcal{I}_1(r \to \infty)$. In contrast to quantum mechanics, the condition $\mathcal{I}_{1,+} = 1$ is not required in photonics. In this second transformation, a ground state $\widetilde{\psi}_{m_1,1}^{(1)}(\eta_1)$ has been reinserted at energy $E_1^{(1)}$ obtaining the sought isospectral family $\widetilde{V}_1(\eta_1)$. Finally, the corresponding refractive index profiles $\widetilde{n}_1(r;\eta_1)$ and ground state functions $\widetilde{R}_{m_1,1}^{(1)}(\eta_1)$ are found to be:

$$\widetilde{n}_1(r;\eta_1) = \sqrt{n_1^2(r) + 2\frac{c_0^2}{\omega^2}\frac{\mathrm{d}^2}{\mathrm{d}r^2} \ln\left(\mathcal{I}_1(r) + \eta_1\right)}; \tag{7.4.3}$$

$$\widetilde{R}_{m_1,1}^{(1)}(r;\eta_1) = R_{m_1,1}^{(1)}(r) / \left(\mathcal{I}_1(r) + \eta_1\right). \tag{7.4.4}$$

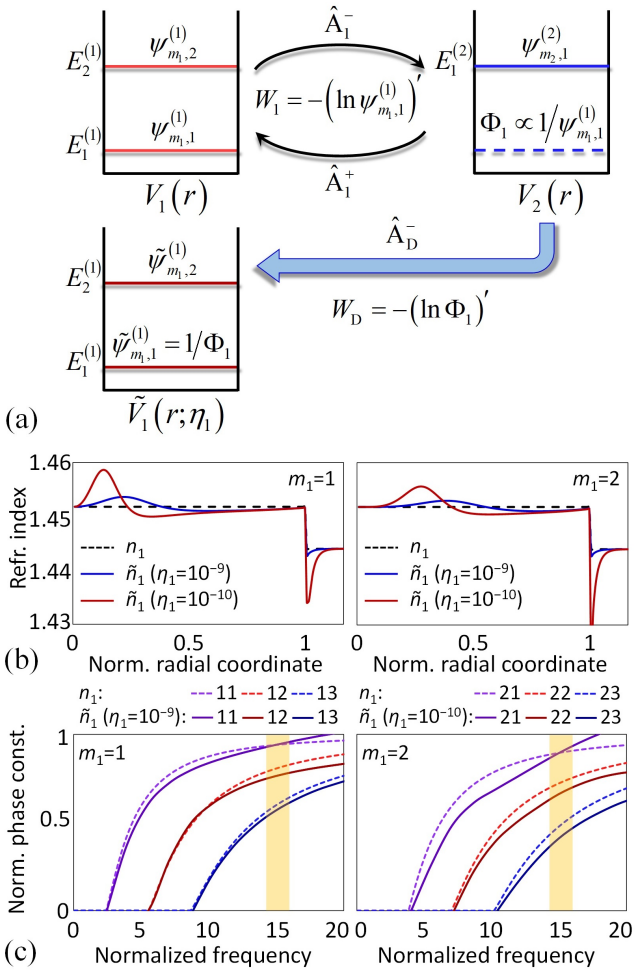

Figure 7.8. One-parameter isospectral cylindrical potentials. (a) Flowchart of the one-parameter Darboux procedure. (b) Isospectral refractive indexes. (c) Normalized dispersion diagram [241].

Concretely, the Darboux procedure involves a singular superpotential in the first and second step, W_1 and $W_{\mathrm{D}}\,(\eta_1)$, respectively [see Fig. 7.8(a)]. While the singular nature of W_1 does not break the degeneracy between V_1 and V_2 (as verified in Subsection 7.3.1), we ask about the possibility of the degeneracy breaking between V_2 and $\widetilde{V}_1(\eta_1)$ when performing the second step. In order to elucidate whether degeneracy is also preserved in this second step, we study the cases $m_1 = 1$ and $m_1 = 2$ for two different values of η_1 (we include additional examples in Appendix C7, on page 239). The resulting profiles for $\widetilde{n}_1(m_1, \eta_1)$ are shown in Fig. 7.8(b). A closer look at the dispersion diagram (calculated with the 3D mode solver of CST Microwave Studio) for the cases $\widetilde{n}_1(m_1 = 1, \eta_1 = 10^{-9})$ and $\widetilde{n}_1(m_1 = 2, \eta_1 = 10^{-10})$ reveals an interesting and unexpected result: the Darboux procedure gives rise to optical media for which only the ground states of the selected isospectral family are degenerate [see Fig. 7.8(c)]. As in the broken SUSY case, we found that this occurs as a result of a degradation of the paraxial approximation (step E). In particular, we observed that $\widetilde{\mathcal{E}}_z/\widetilde{\mathcal{E}}_{\mathrm{T}} \simeq 0.01$ in the ground state of $\widetilde{n}_1(m_1, \eta_1)$, but in the remaining bound states, which are found to be quasi-LP modes, $\widetilde{\mathcal{E}}_z/\widetilde{\mathcal{E}}_{\mathrm{T}} \simeq 0.1$. A further description of the LP and quasi-LP modes of Fig. 7.8(c) can be found in Appendix C7, on page 241.

In contrast to the unbroken SUSY procedure and classical mode filtering strategies based on using optical waveguides with different width [295–298], this unique property allows us to perform a *true* mode (de)multiplexing of any (fundamental) $\mathrm{LP}_{m_1,1}$ mode, i.e., without having mode conversion between optical waveguides. A second advantage of the proposed isospectral construction is

that the slope of the normalized propagation constant b associated with $\widetilde{R}^{(1)}_{m_1,1}$ increases as $\eta_1 \to 0$ [see Fig. 7.8(c) and Fig. C7.1 in Appendix C7]. Consequently, we have full control over the group delay of the SUSY ground state through this free parameter. These singular features open new paths for mode filtering, dispersion engineering and pulse shaping applications in photonics.

Aimed to illustrate these results, we propose an all-fiber mode demultiplexer (M-DEMUX) of the first three LP mode groups ($\mathrm{LP}_{0,1}$, $\mathrm{LP}_{1,1}$ and $\mathrm{LP}_{2,1}$) based on the presented theory. The M-DEMUX is designed using a 60-cm MCF comprising three cores a, b and c with a core-to-core distance $d_{ab} = d_{ac} = 55$ μm, $R_0 = 25$ μm, and $\lambda_0 = 1550$ nm [Fig. 7.9(a)]. The index profiles of cores a and c are calculated from Eq. (7.4.3) as $n_a = \widetilde{n}_1(m_1 = 1, \eta_1 = 10^{-9})$ and $n_c = \widetilde{n}_1(m_1 = 2, \eta_1 = 10^{-10})$. The index profile of core b is taken to be the previous step-index profile, with $n_b = n_1$. A 10-ps Gaussian optical pulse is launched to the $\mathrm{LP}_{0,1}$, $\mathrm{LP}_{1,1}$ and $\mathrm{LP}_{2,1}$ modes of the central core b with a peak power of 0 dBm to operate in the linear regime of the device. Figure 7.9(b) shows the BPM numerical results for the optical pulse propagating through each LP mode in the M-DEMUX. The time and length were normalized with respect to the group delay of the $\mathrm{LP}^{(b)}_{0,1}$ mode and the MCF length, respectively. As desired, at the device output, the pulse launched into the $\mathrm{LP}^{(b)}_{1,1}$ has hoped to the $\mathrm{LP}^{(a)}_{1,1}$, the pulse launched into the $\mathrm{LP}^{(b)}_{0,1}$ remains at core b, and the pulse launched into the $\mathrm{LP}^{(b)}_{2,1}$ has been transferred to the $\mathrm{LP}^{(c)}_{2,1}$.

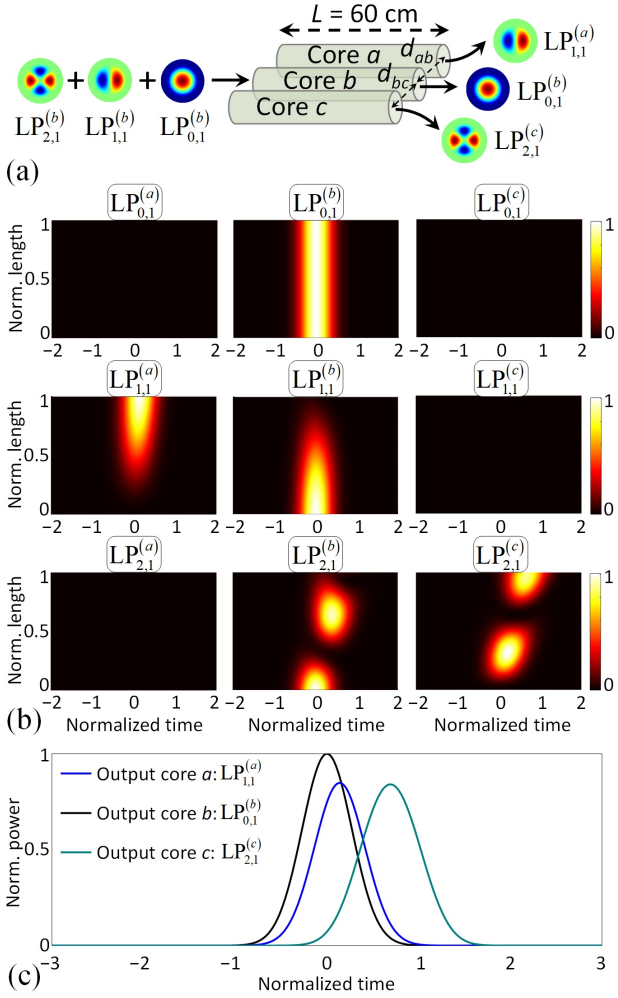

Figure 7.9. M-DEMUX based on a 3-core MCF. (a) Schematic structure of the device with refractive index profiles $n_a = \widetilde{n}_1(m_1 = 1, \eta_1 = 10^{-9})$, $n_b = n_1$ and $n_c = \widetilde{n}_1(m_1 = 2, \eta_1 = 10^{-10})$. (b) 10-ps Gaussian optical pulse propagating through the: LP_{01}, LP_{11} and LP_{21} modes of cores a, b and c (colorbar: normalized power). (c) Optical pulse at the M-DEMUX output [241].

In addition, Fig. 7.9(c) shows that, in this case, the modification of the pulse shape induced by the first-order intermodal dispersion of the M-DEMUX (i.e. the first-order mode-coupling dispersion studied in Chapter 4) is quite low given that the length of the M-DEMUX is of the order of the first-order intermodal dispersion length, which is found to be $L_{\mathrm{ID}}^{(1)} \simeq 1.4$ m and 0.3 m between the $\mathrm{LP}_{1,1}^{(a)}$-$\mathrm{LP}_{1,1}^{(b)}$ and $\mathrm{LP}_{2,1}^{(c)}$-$\mathrm{LP}_{2,1}^{(b)}$ modes, respectively. As a result, a true modal demultiplexing (or modal multiplexing considering the reciprocal nature of the device) with a reduced pulse dispersion is demonstrated.

Nonetheless, in contrast with the unbroken SUSY case (Fig. 7.5), the Darboux procedure allows us to engineer the first-order intermodal dispersion of an MCF just by adjusting η_1. This provides us with a much higher design flexibility, as we can tailor this parameter even for fixed MCF length, core-to-core distance and core diameters. In this fashion, pulse shaping and dispersion engineering functionalities can be incorporated to the M-DEMUX. As an example, Fig. 7.10 depicts the behavior of the M-DEMUX now taking $\eta_1 = 10^{-10}$ and $\eta_1 = 10^{-11}$ for the cores a and c, respectively. These values were chosen so as to increase the intermodal dispersion with respect to the previous case and produce broadened and flat-top pulses at the M-DEMUX output. [Fig. 7.10(b)]. Now, we found that $L_{\mathrm{ID}}^{(1)} \simeq 0.14$ m and 0.11 m between the $\mathrm{LP}_{1,1}^{(a)}$-$\mathrm{LP}_{1,1}^{(b)}$ and $\mathrm{LP}_{2,1}^{(c)}$-$\mathrm{LP}_{2,1}^{(b)}$ modes, respectively. Moreover, since the M-DEMUX length is much lower than the GVD length in the $\mathrm{LP}_{0,1}$, $\mathrm{LP}_{1,1}$ and $\mathrm{LP}_{2,1}$ modes of each core ($L_{\mathrm{GVD}} \sim 5$ km), the pulse dispersion induced by the GVD can be neglected when propagating optical pulses in the picosecond regime (or higher temporal widths) in our M-DEMUX.

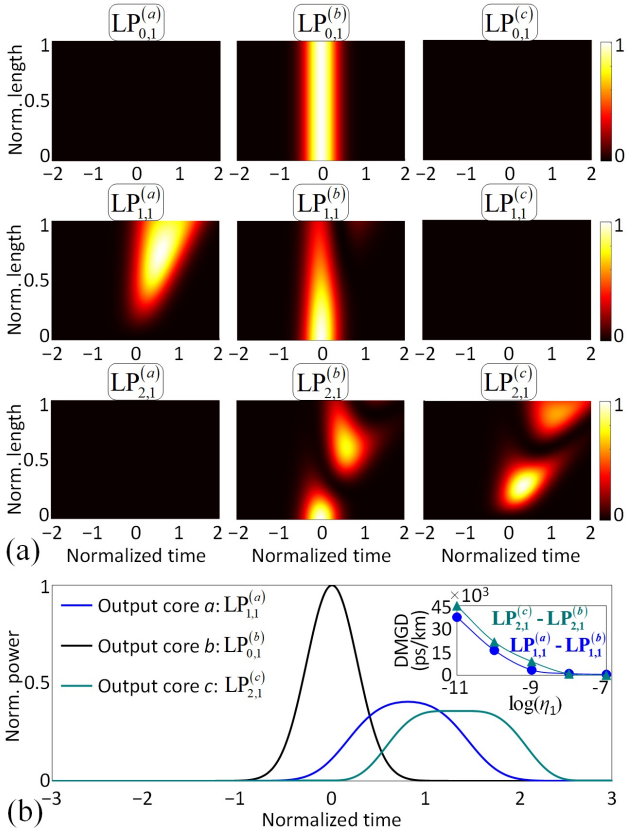

Figure 7.10. (a) 10-ps Gaussian pulse propagating through the LP_{01}, LP_{11} and LP_{21} modes of cores a, b and c of the M-DEMUX with $n_a = \widetilde{n}_1(m_1 = 1, \eta_1 = 10^{-10})$, $n_b = n_1$ and $n_c = \widetilde{n}_1(m_1 = 2, \eta_1 = 10^{-11})$ (colorbar: normalized power). (b) Pulse shaping at the M-DEMUX output. The inset shows the DMGD between the $\mathrm{LP}_{2,1}^{(c)}$-$\mathrm{LP}_{2,1}^{(b)}$ modes and between the $\mathrm{LP}_{1,1}^{(a)}$-$\mathrm{LP}_{1,1}^{(b)}$ modes as a function of η_1 [241].

Because of the partial degeneracy observed in the isospectral family, novel photonic devices can be designed for next-generation optical networks based on MDM transmissions. In spite of the fact that the proposed M-DEMUX is not scalable to a higher number of modes if the number of cores (three in this case) is kept constant, we can achieve such a scalability by including additional adjacent cores around core b and optimizing the MCF length to extract higher-order modes from this core, e.g., the $\mathrm{LP}_{3,1}$ and $\mathrm{LP}_{4,1}$ modes. As an important example, an all-fiber add-drop mode multiplexer can be designed by using an MCF with a hexagonal close-packed structure [300] along with isospectral constructions. In this way, the surrounding cores will inject and extract the $\mathrm{LP}_{m,1}$ modes from the central core (at the corresponding λ_0 wavelength), which can be used to distribute the different multiplexed signals in the MDM system.

In addition, the Darboux procedure can also be generalized to obtain an n-parameter isospectral family of cylindrical potentials. In Appendix C7, we investigate the multi-parameter case and include an illustrative example of the two-parameter family for the step-index profile.

7.5 Conclusions

In this chapter, we have applied different 1D SUSY transformations to cylindrical potentials exhibiting axial symmetry, focusing our efforts on optical potentials, but with direct extrapolation of the results to quantum mechanics (see below). As SUSY transformations involve inverse-square 1D potentials and singular superpotentials, we investigated numerically and theoretically whether these features may produce a degeneracy between the corresponding 3D optical superpartners. Our results show that, while degeneracy is present in unbroken SUSY transformations, it is indeed violated in broken and isospectral SUSY transformations. Notably, this violation does not occur due to the aforementioned reasons, but it is actually induced at the energy levels for which the bound states of the SUSY optical medium do not satisfy the paraxial approximation. These results provide us with a recipe to construct axially-symmetric potentials with total, partial, or no degeneracy using unbroken, isospectral, or broken SUSY constructions, respectively. Outstandingly, the unbroken and isospectral SUSY transformations share an extremely large phase-matching bandwidth.

Building on these interesting modal properties of optical superpartners, we have proposed and demonstrated a variety of applications for mode filtering, mode conversion, mode multiplexing, supermode generation, pulse shaping and dispersion engineering. These include SUSY multi-core fibers, mode-selective photonic lanterns and true all-fiber mode (de)multiplexers. Specifically, the true mode (de)multiplexer is designed using optical potentials with partial degeneracy induced by the violation of the paraxial approximation. Remarkably, this concept has not been previously observed in the optical SUSY literature [222–226, 228–230, 232–239, 241, 242]. In this vein, these results could be extrapolated to SUSY planar waveguides, which may open new possibilities for signal processing applications in integrated photonics [293, 294].

The SUSY transformation method depicted in Fig. 7.1 can be generalized by analyzing additional factorization procedures of the superhamiltonian given by Eq. (7.3.3) [279, 280]. As such, SUSY fiber transformations can likewise be employed to study new degenerate axially-symmetric potentials with a different azimuthal relation from those for the unbroken and broken SUSY cases. The proposed idea builds a bridge to investigate novel mode conversion and mode filtering strategies in all-fiber devices.

On the other hand, it is worth mentioning the possibility of extrapolating the proposed transformation method to acoustics and quantum mechanics when axially-symmetric potentials are involved. Interestingly, Eq. (7.2.2) serves as a master equation that allows us to describe the dynamics of waves in these branches of physics, provided that an adequate mathematical identification of $E_{m,n}^{(3\mathrm{D})}$, $V^{(3\mathrm{D})}$ and $\Psi_{m,n}$ is performed. We include in Table 7.1 a possible choice of the physical meaning of these parameters in each of the aforementioned fields [other options are accounted for by introducing a free-parameter in $E_{m,n}^{(3\mathrm{D})}$ and $V^{(3\mathrm{D})}$ for the photonic and acoustic cases, e.g., $E_{m,n}^{(3\mathrm{D})} \equiv \gamma$ and $V^{(3\mathrm{D})}(r) \equiv \gamma - (\omega^2/c_0^2)n^2(r)$]. In non-relativistic quantum mechanics,

the wave equation is given by the time-independent Schrödinger equation. Hence, $E_{m,n}^{(3D)}$, $V^{(3D)}$ and $\Psi_{m,n}$ describe respectively the particle's discrete energy levels, the quantum potential, and the probability amplitude. Moreover, Eq. (7.2.2) models the propagation of sound in acoustic media with slowly-varying mass density, provided that we use the identifications of the third column of Table 7.1. In this case, $\Psi_{m,n}$ may represent the acoustic velocity potential or the acoustic pressure.

The applicability of 1D SUSY in these fields is straightforward by employing Table 7.1 and Eqs. (7.2.8), (7.2.9). Given that the degeneracy between $V_1^{(3D)}$ and $V_2^{(3D)}$ is present in all the analyzed cases (unbroken, broken and isospectral deformations), one would expect the same behavior for the case in which $V_1^{(3D)}$ and $V_2^{(3D)}$ represent acoustic or quantum systems, as they involve no paraxial approximations. However, this should be confirmed through further numerical analyses in future works. If degeneracy is indeed preserved, our results for unbroken SUSY can be directly extrapolated to these fields. Hence, multi-core acoustic ducts or cylindrical quantum potentials with axial symmetry may be engineered with the same modal properties as unbroken SUSY MCFs. Furthermore, it would be interesting to explore broken SUSY transformations within the context of quantum mechanics as a theoretical procedure to generate complex $V_2^{(3D)}$ potentials from a given $V_1^{(3D)}$ real analytically solvable potential. This may present interesting practical applications in Bose-Einstein condensates [309]. Finally, proceeding in a similar way as in Section 7.4, isospectral deformations may also be proposed as a strategy to construct acoustic and quantum axially-symmetric potentials with similar spectra.

Physics	$E_{m,n}^{(3D)}$	$V^{(3D)}(r)$	$\Psi_{m,n}(\boldsymbol{r})$
Photonics	0	$-(\omega^2/c_0^2)n^2(r)$	$\widetilde{\mathcal{E}}_{m,n}(\boldsymbol{r},\omega)$ $\widetilde{\mathcal{H}}_{m,n}(\boldsymbol{r},\omega)$
Quantum Mechanics	$\widetilde{E}_{m,n}$	$\widetilde{V}(r)$	$\widetilde{\psi}_{m,n}(\boldsymbol{r})$
Acoustics	0	$-\omega^2/c_{\mathrm{S}}^2(r)$	$\widetilde{\phi}_{m,n}(\boldsymbol{r},\omega)$ $\widetilde{P}_{m,n}(\boldsymbol{r},\omega)$

Table 7.1. Physical interpretation of the eigenvalue, potential and wave function of Eq. (7.2.2) in photonics, quantum mechanics and acoustics. The speed of light in a vacuum is denoted as c_0, while c_{S} represents the speed of sound in the acoustic medium. Note that here ω is not a variable, it is just a parameter [241].

Appendix A7: Linear wave equation in weakly-guiding fiber

Here, we will show in more detail the derivation of the linear wave equation Eq. (7.2.2), which emerges from Maxwell's equations when assuming an optical fiber under the slowly-varying index (SVI) and paraxial approximations. For completeness, we will also demonstrate that Eq. (7.2.2) serves as a master wave equation that allows us to describe the dynamics of waves in photonics, acoustics and quantum mechanics by performing an adequate mathematical identification of $E_{m,n}^{(3\mathrm{D})}$, $V^{(3\mathrm{D})}(r)$ and $\Psi_{m,n}(\boldsymbol{r})$ in axially-symmetric systems.

Let us consider a weakly-guiding gradual-index optical fiber with *axial symmetry* operating in the linear regime. The above optical medium can be regarded as a dielectric linear, isotropic, time-invariant and non-magnetic medium with a refractive index profile $n(r)$. As indicated in the main text, we also assume a non-dispersive medium to facilitate the comprehension of the main conclusions of this work. The corresponding wave equation can be derived from the macroscopic Maxwell equations in the frequency domain:

$$\nabla \times \widetilde{\boldsymbol{\mathcal{E}}}(\boldsymbol{r},\omega) = -j\omega\widetilde{\boldsymbol{\mathcal{B}}}(\boldsymbol{r},\omega); \tag{A7.1}$$

$$\nabla \times \widetilde{\boldsymbol{\mathcal{H}}}(\boldsymbol{r},\omega) = j\omega\widetilde{\boldsymbol{\mathcal{D}}}(\boldsymbol{r},\omega); \tag{A7.2}$$

$$\nabla \cdot \widetilde{\boldsymbol{\mathcal{D}}}(\boldsymbol{r},\omega) = 0; \tag{A7.3}$$

$$\nabla \cdot \widetilde{\boldsymbol{\mathcal{B}}}(\boldsymbol{r},\omega) = 0, \tag{A7.4}$$

where the fields involved in the previous equations were described in Chapter 1 (see Section 1.5). Specifically, in this case, $\widetilde{\boldsymbol{\mathcal{D}}}$ and $\widetilde{\boldsymbol{\mathcal{H}}}$ can be expressed as:

$$\widetilde{\boldsymbol{\mathcal{D}}}(\boldsymbol{r},\omega) = \varepsilon_0 n^2(r)\,\widetilde{\boldsymbol{\mathcal{E}}}(\boldsymbol{r},\omega); \quad \widetilde{\boldsymbol{\mathcal{H}}}(\boldsymbol{r},\omega) = (1/\mu_0)\,\widetilde{\boldsymbol{\mathcal{B}}}(\boldsymbol{r},\omega). \tag{A7.5}$$

Combining Faraday's and Ampère's laws [Eqs. (A7.1) and (A7.2)] by applying the curl operator and using the above constitutive relations [Eq. (A7.5)], we find the following exact wave equation:

$$\nabla \times \nabla \times \widetilde{\boldsymbol{\mathcal{E}}}(\boldsymbol{r},\omega) - \frac{\omega^2}{c_0^2} n^2(r)\,\widetilde{\boldsymbol{\mathcal{E}}}(\boldsymbol{r},\omega) = \mathbf{0}. \tag{A7.6}$$

The global electric field strength can be expressed as a function of the hybrid modes (also referred to as true modes) of the optical fiber $\widetilde{\boldsymbol{\mathcal{E}}}_{m,n}$, i.e., $\widetilde{\boldsymbol{\mathcal{E}}} = \sum_{m,n}\widetilde{\boldsymbol{\mathcal{E}}}_{m,n}$, with m and n indicating respectively the azimuthal and radial order. In this way, Eq. (7.2.1) is directly found:

$$\nabla \times \nabla \times \widetilde{\boldsymbol{\mathcal{E}}}_{m,n}(\boldsymbol{r},\omega) - \frac{\omega^2}{c_0^2} n^2(r)\,\widetilde{\boldsymbol{\mathcal{E}}}_{m,n}(\boldsymbol{r},\omega) = \mathbf{0}. \tag{A7.7}$$

For gradual-index fibers satisfying the SVI criterion (see page 212), $\nabla\cdot\widetilde{\boldsymbol{\mathcal{D}}}_{m,n} \simeq \varepsilon_0 n^2(r)\,\nabla\cdot\widetilde{\boldsymbol{\mathcal{E}}}_{m,n} = 0$ and, consequently, we can approximate:

$$\nabla \times \nabla \times \widetilde{\boldsymbol{\mathcal{E}}}_{m,n} = \nabla(\nabla \cdot \widetilde{\boldsymbol{\mathcal{E}}}_{m,n}) - \triangle\widetilde{\boldsymbol{\mathcal{E}}}_{m,n} \simeq -\triangle\widetilde{\boldsymbol{\mathcal{E}}}_{m,n}. \tag{A7.8}$$

Hence, Eq. (A7.7) is reduced to:

$$\triangle\widetilde{\boldsymbol{\mathcal{E}}}_{m,n}(\boldsymbol{r},\omega) + \frac{\omega^2}{c_0^2} n^2(r)\,\widetilde{\boldsymbol{\mathcal{E}}}_{m,n}(\boldsymbol{r},\omega) = \mathbf{0}. \tag{A7.9}$$

In weakly-guiding fibers, the paraxial approximation is automatically satisfied. In such a scenario, the linearly polarized $\mathrm{LP}_{m,n}$ mode groups emerge as the linear combination of the quasi-degenerate hybrid modes and the longitudinal component of each mode group can be neglected [32]. Moreover, bearing in mind the isotropic nature of the medium, we can describe $\widetilde{\boldsymbol{\mathcal{E}}}_{m,n}$ by a single transverse component (e.g. the x-polarization), that is, $\widetilde{\boldsymbol{\mathcal{E}}}_{m,n} \simeq \widetilde{\mathcal{E}}_{m,n}\hat{u}_x$. Thus, the above equation becomes:

$$\triangle\widetilde{\mathcal{E}}_{m,n}(\boldsymbol{r},\omega) + \frac{\omega^2}{c_0^2} n^2(r)\,\widetilde{\mathcal{E}}_{m,n}(\boldsymbol{r},\omega) = 0. \tag{A7.10}$$

In a similar way, we can also derive the scalar wave equation in terms of the magnetic field strength, which takes the form ($\widetilde{\boldsymbol{\mathcal{H}}}_{m,n} \simeq \widetilde{\mathcal{H}}_{m,n}\hat{u}_y$):

$$\triangle\widetilde{\mathcal{H}}_{m,n}\left(\boldsymbol{r},\omega\right)+\frac{\omega^2}{c_0^2}n^2\left(r\right)\widetilde{\mathcal{H}}_{m,n}\left(\boldsymbol{r},\omega\right)=0. \tag{A7.11}$$

In acoustics and quantum mechanics, we can also find a Helmholtz equation formally equal to Eqs. (A7.10) and (A7.11) when axially-symmetric potentials are involved. In acoustics, the following equations (c_{S} is the speed of sound in the acoustic medium):

$$\triangle\widetilde{\phi}_{m,n}\left(\boldsymbol{r},\omega\right)+\frac{\omega^2}{c_{\mathrm{S}}^2\left(r\right)}\widetilde{\phi}_{m,n}\left(\boldsymbol{r},\omega\right)=0; \tag{A7.12}$$

$$\triangle\widetilde{P}_{m,n}\left(\boldsymbol{r},\omega\right)+\frac{\omega^2}{c_{\mathrm{S}}^2\left(r\right)}\widetilde{P}_{m,n}\left(\boldsymbol{r},\omega\right)=0, \tag{A7.13}$$

model the propagation of sound in axially-symmetric acoustic media with slowly-varying mass density as a function of the acoustic velocity potential ($\widetilde{\phi}$) or the acoustic pressure ($\widetilde{P}$) [310]. In quantum mechanics, the wave equation is given by the time-independent Schrödinger equation (we set $\hbar^2/2m \equiv 1$ for simplicity):

$$-\triangle\widetilde{\psi}_{m,n}\left(\boldsymbol{r}\right)+\widetilde{V}\left(r\right)\widetilde{\psi}_{m,n}\left(\boldsymbol{r}\right)=\widetilde{E}_{m,n}\widetilde{\psi}_{m,n}\left(\boldsymbol{r}\right), \tag{A7.14}$$

where $\widetilde{E}_{m,n}$, $\widetilde{V}$ and $\widetilde{\psi}_{m,n}$ describe respectively the particle's discrete energy levels, the quantum potential and the probability amplitude.

In spite of the fact that we focus our efforts on the photonic case, we can easily extrapolate the transformation method depicted in Fig. 7.1 to acoustics and quantum mechanics by using a master wave equation of the form given by Eq. (7.2.2). Remarkably, this equation allows us to describe Eqs. (A7.10)-(A7.14) by performing an adequate mathematical identification of $E_{m,n}^{(3\mathrm{D})}$, $V^{(3\mathrm{D})}$ and $\Psi_{m,n}$, see Table 7.1.

Appendix B7: Unbroken and broken SUSY (discussion)

In this appendix, we discuss theoretically if the singular superpotentials involved in the unbroken and broken SUSY transformations break the degeneracy between the one-dimensional potentials $V_{1,2}$ and we also include additional numerical examples and discussions to complete our work in Section 7.3.

B7.1 Unbroken SUSY

The commutation of the supercharges with the superhamiltonian $\left[\mathrm{H},\mathrm{Q}^{\pm}\right]=0$, the normalization and the continuity of the wave functions $\psi^{(1)}_{m_1,n+1}$ and $\psi^{(2)}_{m_2,n}$ are sufficient conditions to guarantee the degeneracy between superpartners. In this way, a singular superpotential may give rise to a breakdown of the SUSY degeneracy theorem if a singularity of W induces a violation of one of the above conditions. Along this line, bearing in mind that the reduction of the 3D Helmholtz equation to 1D introduces a singular superpotential in the unbroken SUSY transformations, we should verify if the aforementioned sufficient conditions are fulfilled.

Firstly, let us investigate if the relation $\left[\mathrm{H},\mathrm{Q}^{\pm}\right]=0$ is satisfied at the singularity ($r=0$). Specifically, the condition $\left[\mathrm{H},\mathrm{Q}^{\pm}\right]=0$ can be rewritten in terms of the following intertwining relations:

$$\widehat{\mathrm{H}}_{2,\mathrm{eq}}\widehat{\mathrm{A}}^{-}=\widehat{\mathrm{A}}^{-}\widehat{\mathrm{H}}_{1,\mathrm{eq}};\qquad \widehat{\mathrm{H}}_{1,\mathrm{eq}}\widehat{\mathrm{A}}^{+}=\widehat{\mathrm{A}}^{+}\widehat{\mathrm{H}}_{2,\mathrm{eq}},\tag{B7.1}$$

where:

$$\widehat{\mathrm{H}}_{1,2,\mathrm{eq}}=-\frac{\mathrm{d}^2}{\mathrm{d}r^2}+V_{1,2}\left(r\right)-\alpha;\qquad \widehat{\mathrm{A}}^{\pm}=\mp\frac{\mathrm{d}}{\mathrm{d}r}+W\left(r\right).\tag{B7.2}$$

Thus, our goal is to verify if Eqs. (B7.1) are satisfied at $r=0$. Let us first discuss the former intertwining relation. To this end, we should check if this relation is satisfied for any eigenfunction of the form $\psi^{(1)}_{m_1,n}(r)=\sqrt{r}R^{(1)}_{m_1,n}(r)$. The LHS and the RHS of $\widehat{\mathrm{H}}_{2,\mathrm{eq}}\widehat{\mathrm{A}}^{-}\psi^{(1)}_{m_1,n}=\widehat{\mathrm{A}}^{-}\widehat{\mathrm{H}}_{1,\mathrm{eq}}\psi^{(1)}_{m_1,n}$ are respectively:

$$\widehat{\mathrm{H}}_{2,\mathrm{eq}}\widehat{\mathrm{A}}^{-}\psi^{(1)}_{m_1,n}(r)=\left(-\frac{\mathrm{d}^2}{\mathrm{d}r^2}+V_2\left(r\right)-\alpha\right)\left(\frac{\mathrm{d}}{\mathrm{d}r}-\frac{\left(R^{(1)}_{m_1,1}\left(r\right)\right)'}{R^{(1)}_{m_1,1}\left(r\right)}-\frac{1}{2r}\right)\left(\sqrt{r}R^{(1)}_{m_1,n}\left(r\right)\right);\tag{B7.3}$$

$$\widehat{\mathrm{A}}^{-}\widehat{\mathrm{H}}_{1,\mathrm{eq}}\psi^{(1)}_{m_1,n}(r)=\left(\frac{\mathrm{d}}{\mathrm{d}r}-\frac{\left(R^{(1)}_{m_1,1}\left(r\right)\right)'}{R^{(1)}_{m_1,1}\left(r\right)}-\frac{1}{2r}\right)\left(-\frac{\mathrm{d}^2}{\mathrm{d}r^2}+V_1\left(r\right)-\alpha\right)\left(\sqrt{r}R^{(1)}_{m_1,n}\left(r\right)\right).\tag{B7.4}$$

Now, taking into account that ($i\in\{1,2\}$):

$$V_i\left(r\right)=-\frac{\omega^2}{c_0^2}n_i^2\left(r\right)+\frac{m_i^2}{r^2}-\frac{1}{4r^2},\tag{B7.5}$$

our initial question is solved by calculating the limit:

$$\lim_{r\to 0}\left(\widehat{\mathrm{H}}_{2,\mathrm{eq}}\widehat{\mathrm{A}}^{-}\psi^{(1)}_{m_1,n}\left(r\right)-\widehat{\mathrm{A}}^{-}\widehat{\mathrm{H}}_{1,\mathrm{eq}}\psi^{(1)}_{m_1,n}\left(r\right)\right).\tag{B7.6}$$

Notifying that:

$$R^{(1)}_{m_1,n}\left(r\right)\sim J_{m_1}\left(\frac{u_{m_1,n}}{R_0}r\right)=\sum_{k=0}^{\infty}\frac{(-1)^k}{k!\left(m_1+k\right)!}\left(\frac{u_{m_1,n}}{2R_0}r\right)^{m_1+2k},\tag{B7.7}$$

where $u_{m_1,n}$ is a modal parameter of the $\mathrm{LP}^{(1)}_{m_1,n}$ mode, it is tedious but straightforward to verify that Eq. (B7.6) is found to be null for any m_1 value. We also found the same result when analyzing $\widehat{\mathrm{H}}_{1,\mathrm{eq}}\widehat{\mathrm{A}}^{+}=\widehat{\mathrm{A}}^{+}\widehat{\mathrm{H}}_{2,\mathrm{eq}}$ at the singularity.

Secondly, we discuss if the eigenfunctions $\psi^{(2)}_{m_2,n}$ of the SUSY potential V_2 are continuous normalizable functions. Specifically, $\psi^{(2)}_{m_2,n}$ are generated from the SUSY relation $\psi^{(2)}_{m_2,n} \propto \widehat{\mathrm{A}}^{-}\psi^{(1)}_{m_1,n+1}$, with $m_2 = m_1 + 1$. That is:

$$\psi^{(2)}_{m_2,n}(r) \propto \sqrt{r}\left[\left(R^{(1)}_{m_1,n+1}\right)'(r) - R^{(1)}_{m_1,n+1}(r)\frac{\left(R^{(1)}_{m_1,1}\right)'(r)}{R^{(1)}_{m_1,1}(r)}\right]. \tag{B7.8}$$

From the above expression we can infer that:

- Behavior at $r = 0$. $\psi^{(2)}_{m_2,n}$ is nonsingular with $r \geq 0$. Concretely, at $r = 0$, we can verify that $\psi^{(2)}_{m_2,n}(r \to 0) \equiv \psi^{(2)}_{m_2,n,-} = 0$ by using Eqs. (B7.7) and (B7.8).
- Behavior at $r \to \infty$. It is easy to verify that $\psi^{(2)}_{m_2,n}(r \to \infty) \equiv \psi^{(2)}_{m_2,n,+} = 0$ taking into account that $\psi^{(1)}_{m_1,n+1,+} = 0$, $(\psi^{(1)}_{m_1,n+1,+})' = 0$ and $|W_+| < \infty$.
- Continuity. Equation (B7.8) is found to be a continuous function with $r \geq 0$. Note that Eq. (B7.8) involves sums and products of continuous functions.

The same conclusions are found for the functions $\left|\psi^{(2)}_{m_2,n}\right|$ and $\left|\psi^{(2)}_{m_2,n}\right|^2$. All in all, we infer that $\int_0^r \left|\psi^{(2)}_{m_2,n}(x)\right|^2 \mathrm{d}x$ is bounded and, therefore, $\int_0^\infty \left|\psi^{(2)}_{m_2,n}(r)\right|^2 \mathrm{d}r$ is convergent. Consequently, $\psi^{(2)}_{m_2,n}$ is a bound state of $\widehat{\mathrm{H}}_{2,\mathrm{eq}}$. Thus, we conclude that the singular superpotential does not break the degeneracy between superpartners.[8]

For completeness, the cases $m_1 = 1$ and $m_1 = 3$ were also numerically analyzed. The normalized dispersion diagram, normalized group delay and the ground state wave function of the SUSY refractive index profile $n_2(r)$ are shown in Figs. B7.1, B7.2 and B7.3, respectively.

Finally, we analyze an unbroken SUSY Hamiltonian chain comprising N supersymmetric axially-symmetric potentials V_1,...,V_N. The relations between the potentials V_1 and V_q ($q \in \{2, \ldots, N\}$), their energy levels and wave functions are given by the same expressions as on the full line (see Chapter 6, Section 6.6):

$$V_q(r) = V_1(r) - 2\frac{\mathrm{d}^2}{\mathrm{d}r^2}\ln\left(\prod_{i=1}^{q-1}\psi^{(i)}_{m_i,1}(r)\right); \tag{B7.9}$$

$$E^{(q)}_n = E^{(1)}_{n+q-1}; \tag{B7.10}$$

$$\psi^{(q)}_{m_q,n}(r) = \xi^{(2)}\left(\prod_{i=1}^{q-1}\widehat{\mathrm{A}}^{-}_{q-i}\right)\psi^{(1)}_{m_1,n+q-1}(r), \tag{B7.11}$$

where:

$$\widehat{\mathrm{A}}^{-}_{q-i} = \frac{\mathrm{d}}{\mathrm{d}r} - \left(\ln\psi^{(q-i)}_{m_{q-i},1}(r)\right)', \tag{B7.12}$$

and $\psi^{(i)}_{m_i,1}(r) = \sqrt{r}R^{(i)}_{m_i,1}(r)$ is the ground state of the i-th Hamiltonian. Thus, using Eq. (B7.5) and the azimuthal relation $m_i = m_1 + i - 1$ in each system, Eqs. (7.3.14)-(7.3.16) of the main text are derived.

In spite of the fact that the superpotential $W_i(r) = -(\ln\psi^{(i)}_{m_i,1}(r))'$ connecting the Hamiltonians $\widehat{\mathrm{H}}_{i,\mathrm{eq}}$ and $\widehat{\mathrm{H}}_{i+1,\mathrm{eq}}$ is found to be singular at $r = 0$, the degeneracy of the spectra is preserved. Following a similar discussion as before, it is straightforward to demonstrate that $\left[\mathrm{H}_i, \mathrm{Q}^{\pm}_i\right] = 0$ and the eigenfunctions $\psi^{(i+1)}_{m_{i+1},n}$ [given by Eq. (B7.11) taking $q = i + 1$] are bound states of $\widehat{\mathrm{H}}_{i+1,\mathrm{eq}}$.

[8] The normalization criterion of $\psi^{(2)}_{m_2,n}$ was also numerically verified with Mathematica software.

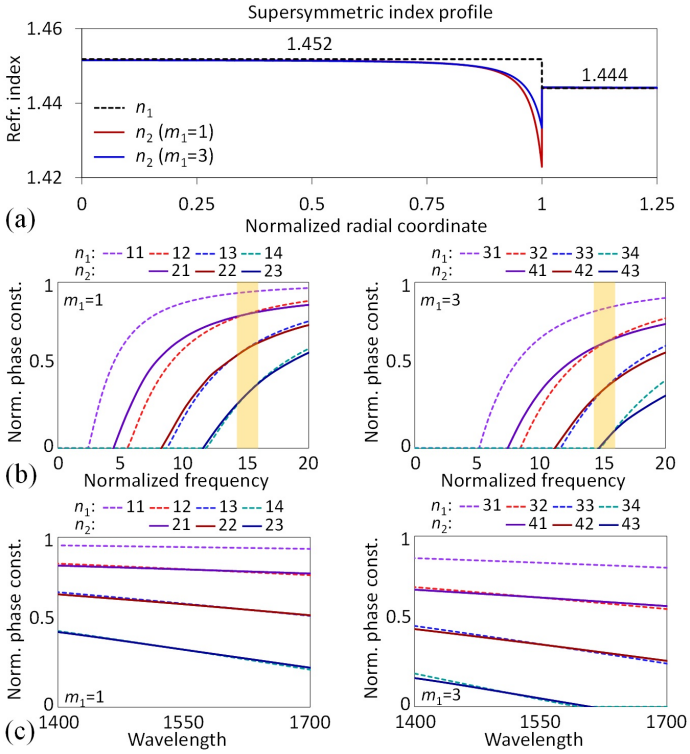

Figure B7.1. Modal analysis of two SUSY optical refractive indexes with $m_1 = 1$ and $m_1 = 3$. (a) SUSY partner for the step-index profile. Normalized dispersion diagram as a function of: (b) the normalized frequency, and (c) the wavelength comprising the S + C + L optical bands [241].

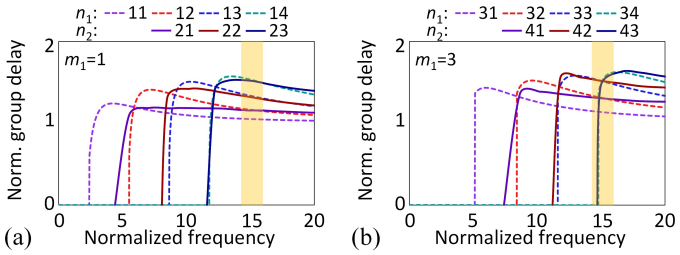

Figure B7.2. Normalized group delay diagram for the $m_1 = 1$ and $m_1 = 3$ cases [241].

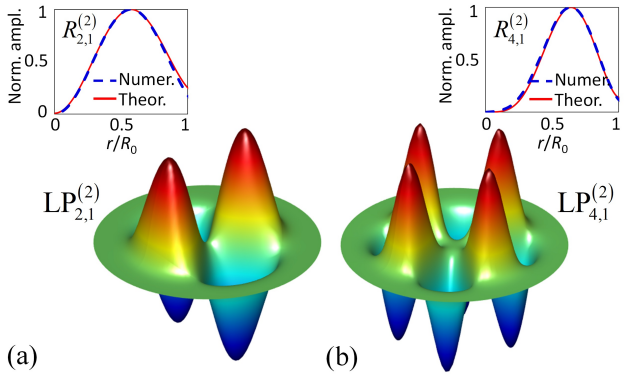

Figure B7.3. Ground state wave function $\psi^{(2)}_{m_2,1}$ of the SUSY refractive index n_2 for the cases: (a) $m_1 = 1$ and (b) $m_1 = 3$. The comparison between the numerical calculation using the 3D mode solver and Eq. (7.3.12) is inset in the top of the figure [241].

B7.2 Broken SUSY

Firstly, we verify if the singularity of W given by Eq. (7.3.18) is not behind the rupture of the degeneracy between the $\mathrm{LP}^{(1)}_{m_1,n}$ and $\mathrm{LP}^{(2)}_{m_2,n}$ modes ($m_2 = m_1 - 1$). Since the commutation of the superhamiltonian and the supercharges is also preserved in this case (the property $\left[\mathrm{H}, \mathrm{Q}^{\pm}\right] = 0$ was numerically verified with Mathematica software), we investigate if the SUSY eigenfunctions $\psi^{(2)}_{m_2,n}$ are bound states of $\widehat{\mathrm{H}}_{2,\mathrm{eq}}$:

- Behavior at $r = 0$. Considering that $W(r) \underset{r\to 0}{\propto} (2m_1 - 1)/2r$ and $\psi^{(1)}_{m_1,n}(r) \underset{r\to 0}{\sim} r^{m_1+1/2}$, we find that:

$$R^{(2)}_{m_2,n}(r) \underset{r\to 0}{\sim} \begin{cases} a, & m_2 = 0 \\ 0, & m_2 > 0 \end{cases} \quad \Rightarrow \quad \psi^{(2)}_{m_2,n,-} = \lim_{r\to 0} \sqrt{r} R^{(2)}_{m_2,n}(r) = 0, \tag{B7.13}$$

  where a is a non-vanishing real constant.

- Behavior at $r \to \infty$. We note that $\psi^{(2)}_{m_2,n,+} = 0$, as deduced from the fact that $\psi^{(1)}_{m_1,n,+} = 0$, $(\psi^{(1)}_{m_1,n,+})' = 0$ and $|W_+| < \infty$.

- Continuity. Since $\psi^{(2)}_{m_2,n}(r) \propto (\psi^{(1)}_{m_1,n}(r))' + W(r)\,\psi^{(1)}_{m_1,n}(r)$ with $\psi^{(1)}_{m_1,n}$, $(\psi^{(1)}_{m_1,n})'$ and W continuous functions in $r \geq 0$, then $\psi^{(2)}_{m_2,n}$ is also found to be a continuous function in $r \geq 0$.

Once again, we can infer the same conclusions for the functions $\left|\psi^{(2)}_{m_2,n}\right|$ and $\left|\psi^{(2)}_{m_2,n}\right|^2$. Thus, $\int_0^r \left|\psi^{(2)}_{m_2,n}(x)\right|^2 \mathrm{d}x$ is bounded, $\int_0^\infty \left|\psi^{(2)}_{m_2,n}(r)\right|^2 \mathrm{d}r$ is convergent and, therefore, $\psi^{(2)}_{m_2,n}$ are bound state of $\widehat{\mathrm{H}}_{2,\mathrm{eq}}$. As a result, $\widehat{\mathrm{H}}_{1,\mathrm{eq}}$ and $\widehat{\mathrm{H}}_{2,\mathrm{eq}}$ have degenerate spectra.

Nonetheless, as discussed in Subsection 7.3.2, the non-degeneracy between $V_1^{(3\mathrm{D})}$ and $V_2^{(3\mathrm{D})}$ is induced by a degradation of the paraxial approximation in the SUSY modes $\mathrm{LP}^{(2)}_{m_2,n}$. Table B7.1 shows the ratio $\widetilde{\mathcal{E}}_z/\widetilde{\mathcal{E}}_\mathrm{T}$ and the phase-mismatching ($\Delta\beta$) of the true modes which compose the LP and quasi-LP mode groups in the SUSY fibers. As seen, the true modes of each LP group of n_2 are found to be quasi-degenerate, with $\Delta\beta$ much lower than the phase-mismatching between different LP mode groups, but $\widetilde{\mathcal{E}}_z$ cannot be neglected with respect to $\widetilde{\mathcal{E}}_\mathrm{T}$ in this case. In addition, we have verified with CST Microwave Studio that the linear combination of the quasi-degenerate true modes shows approximately a linearly polarized nature.

LP mode group	True modes	β_{av} rad/m	$\Delta\beta$ rad/m	$\widetilde{\mathcal{E}}_z/\widetilde{\mathcal{E}}_\mathrm{T}$
$\mathrm{LP}^{(1)}_{2,1}$	$\mathrm{EH}_{11} \pm \mathrm{HE}_{31}$	5777946	2	0.01
$\mathrm{LP}^{(1)}_{2,2}$	$\mathrm{EH}_{12} \pm \mathrm{HE}_{32}$	5772568	5	0.02
$\mathrm{LP}^{(1)}_{2,3}$	$\mathrm{EH}_{13} \pm \mathrm{HE}_{33}$	5764932	6	0.02
$\mathrm{LP}^{(2)}_{1,1}$	$\mathrm{TE}_{01} \pm \mathrm{TM}_{01} \pm \mathrm{HE}_{21}$	5788827	52	0.09
$\mathrm{LP}^{(2)}_{1,2}$	$\mathrm{TE}_{02} \pm \mathrm{TM}_{02} \pm \mathrm{HE}_{22}$	5782934	61	0.12
$\mathrm{LP}^{(2)}_{1,3}$	$\mathrm{TE}_{03} \pm \mathrm{TM}_{03} \pm \mathrm{HE}_{23}$	5770742	77	0.14

Table B7.1. Comparison of the degeneracy of the true modes for the n_1 and n_2 index profiles. β_{av} and $\Delta\beta$ are respectively the average value of the phase constant and the phase-mismatching of the true modes in each LP or quasi-LP mode group at $\lambda_0 = 1550$ nm [241].

For completeness, we show in Fig. B7.4 the normalized dispersion diagram of the broken SUSY fibers depicted in Fig. 7.7(c). Here, we only include the first twelve LP mode groups of n_1 and n_2. As discussed in Fig. 7.7(c), n_1 and n_2 comprise non-degenerate SUSY modes $\mathrm{LP}_{2,n}^{(1)}$ and $\mathrm{LP}_{1,n}^{(2)}$. Nevertheless, additional LP mode groups are found to be degenerate between both superpartners at different frequencies in the third transmission optical window ($\nu \in [14.2, 16]$).

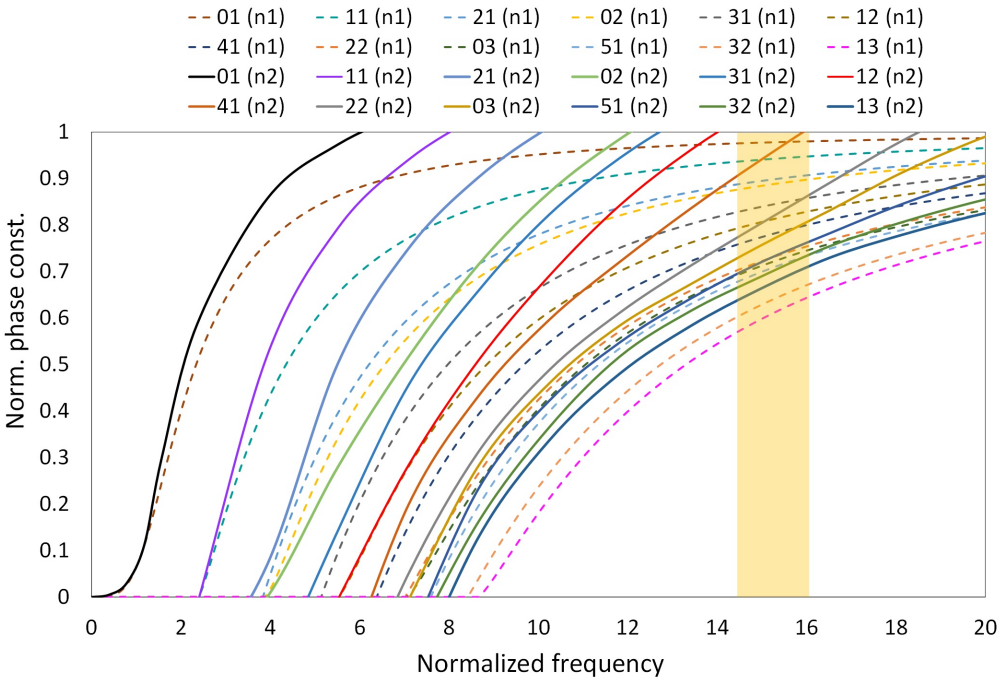

Figure B7.4. Normalized dispersion diagram of the n_1 and n_2 index profiles shown in Fig. 7.7 (only the first twelve LP mode groups have been simulated) [241].

B7.3 A brief discussion on the Riccati equation

From a closer look at the Riccati equation, we can derive the order relation between m_1 and m_2 for the unbroken and broken SUSY transformations. Combining the ODEs:

$$V_1(r) = W^2(r) - W'(r) + \alpha; \quad V_2(r) = W^2(r) + W'(r) + \alpha, \tag{B7.14}$$

we obtain the relation:

$$W_+ - W_- = \frac{1}{2}\int_0^\infty (V_2(r) - V_1(r))\,\mathrm{d}r, \tag{B7.15}$$

with $W_+ := W(r \to \infty)$ and $W_- := W(r \to 0)$. Solving the above equation using Eq. (B7.5) and assuming nonsingular refractive index profiles n_1 and n_2, we find that:

$$W_+ - W_- = \mathrm{sgn}\left(m_2^2 - m_1^2\right) \cdot \infty. \tag{B7.16}$$

Therefore, it is straightforward to conclude that ($\alpha \equiv -k_0^2 n_\alpha^2$):

$$\begin{cases} \text{UNBROKEN:} & W_+ = +k_0\sqrt{n_\alpha^2 - n_{\mathrm{cl}}^2} \ \wedge \ W_- = -\infty \Rightarrow m_2 > m_1 \\ \text{BROKEN:} & W_+ = -k_0\sqrt{n_\alpha^2 - n_{\mathrm{cl}}^2} \ \wedge \ W_- = +\infty \Rightarrow m_2 < m_1 \end{cases}, \tag{B7.17}$$

in line with the order relation between m_1 and m_2 detailed in Section 7.3.

B7.4 Inverse SUSY

In contrast to the unbroken and broken SUSY transformations of Section 7.3 (direct SUSY), one can start from a given cylindrical potential V_1 and calculate a V_0 potential via the relations:

$$V_0(r) = W^2(r) - W'(r) + \alpha; \qquad V_1(r) = W^2(r) + W'(r) + \alpha. \tag{B7.18}$$

In the same way as in direct SUSY transformations, α is an auxiliary constant of the problem which accounts for the energy shift of the Hamiltonians $\widehat{\mathrm{H}}_{0,1,\mathrm{eq}} = \widehat{\mathrm{H}}_{0,1} - \alpha = -\mathrm{d}^2/\mathrm{d}r^2 + V_{0,1}(r) - \alpha$. If $\alpha = E_1^{(0)}$ SUSY is unbroken. Otherwise, SUSY is broken. In the former case, a bound state will be added to the newly derived cylindrical potential V_0. Once the superpotential is calculated numerically from Eq. (B7.18), the refractive index profile $n_0(r)$ is found as:

$$n_0(r) = \sqrt{n_1^2(r) + 2\frac{c_0^2}{\omega^2}\frac{\mathrm{d}}{\mathrm{d}r}\left(\frac{m_1^2 - m_0^2}{2r} + W(r)\right)}. \tag{B7.19}$$

Appendix C7: Isospectral transformations (discussion)

In this appendix, we include additional comments, discussions and numerical examples of the one-parameter and multi-parameter isospectral Darboux procedure applied to axially-symmetric potentials.

C7.1 One-parameter family

As detailed in Sections 6.11 and 7.4, the second step of the Darboux procedure requires to use a non-normalizable solution $\Phi_1(\eta_1)$ of V_2 at energy $E_1^{(1)}$ of the form given by Eq. (7.4.1). Along this line, note that Eq. (7.4.1) has a singularity at $r = 0$. This singularity is responsible for the singular nature of the superpotential $W_{\rm D}(\eta_1)$ [Eq. (7.4.2)], which gives rise to the isospectral family of potentials:

$$\widetilde{V}_1\left(r;\eta_1\right) = V_1\left(r\right) - 2\frac{\mathrm{d}^2}{\mathrm{d}r^2}\ln\left(\mathcal{I}_1\left(r\right)+\eta_1\right). \tag{C7.1}$$

Combining this equation with Eq. (7.3.1), then Eq. (7.4.3) is derived. In this scenario, in the same way as $1/\psi_{m_1,1}^{(1)}$ is an eigenfunction of V_2 at energy $E_1^{(1)}$, $1/\Phi_1(\eta_1)$ is found to be an eigenfunction of $\widetilde{V}_1(\eta_1)$. Concretely, $1/\Phi_1(\eta_1)$ is normalizable if $\mathcal{I}_1\left(r\right)+\eta_1 \neq 0$, $\forall r \geq 0$. That is:

$$\widetilde{\psi}_{m_1,1}^{(1)}\left(r;\eta_1\right) = \frac{1}{\Phi_1\left(r;\eta_1\right)} = \frac{\psi_{m_1,1}^{(1)}\left(r\right)}{\mathcal{I}_1\left(r\right)+\eta_1}, \tag{C7.2}$$

describes the ground state family of $\widetilde{V}_1(\eta_1)$ if $\eta_1 \notin [-\mathcal{I}_{1,+},0]$, where $\mathcal{I}_{1,+} := \mathcal{I}_1\left(r\to\infty\right)$. From Eq. (C7.2) we obtain Eq. (7.4.4). Note that in QM $\mathcal{I}_{1,+} = \int_0^\infty \left|\psi_{m_1,1}^{(1)}\left(r\right)\right|^2 \mathrm{d}r = 1$. However, in photonics the condition $\mathcal{I}_{1,+} = 1$ is not required. Consequently, we can use a ground state of the form $\sqrt{\xi}\psi_{m_1,1}^{(1)}$, with ξ a real constant accounting for the power of the optical mode. Hence, $\mathcal{I}_{1,+}$ is found in photonics as $\mathcal{I}_{1,+} = \xi$. Nonetheless, it should be noted that only a single degree of freedom appears in Eq. (C7.2) taking into account that:

$$\frac{\mathrm{d}^2}{\mathrm{d}r^2}\ln\left(\xi\mathcal{I}_1\left(r\right)+\eta_1\right) = \frac{\mathrm{d}^2}{\mathrm{d}r^2}\left[\ln\left(\xi\right)+\ln\left(\mathcal{I}_1\left(r\right)+\frac{\eta_1}{\xi}\right)\right] = \frac{\mathrm{d}^2}{\mathrm{d}r^2}\ln\left(\mathcal{I}_1\left(r\right)+\frac{\eta_1}{\xi}\right), \tag{C7.3}$$

with the degree of freedom given by the real constant η_1/ξ.

C7.2 Superpotential, supercharges and bound states in the second step

Using Eq. (B7.7) in Eq. (7.4.2), we verify that the superpotential $W_{\rm D}(\eta_1)$ has a singularity at $r = 0$:

$$\lim_{r\to 0} W_{\rm D}\left(r;\eta_1\right) = \lim_{r\to 0}\left(-\frac{ar^{4m_1+2}+\eta_1 r^{2m_1}}{br^{4m_1+3}+\eta_1 r^{2m_1+1}}\right) = \mathrm{sgn}\left(-a/b\right)\cdot\infty, \tag{C7.4}$$

with a and b non-vanishing real constants. As mentioned before, the singular nature of $W_{\rm D}(\eta_1)$ is induced by the singularity of $\Phi_1(\eta_1)$ at $r = 0$. Therefore, we should now analyze if the sufficient conditions for the degeneracy between V_2 and $\widetilde{V}_1\left(\eta_1\right)$ are fulfilled: (*i*) the commutation of the supercharges with the superhamiltonian, and (*ii*) the normalization and the continuity of the wave functions $\widetilde{\psi}_{m_1,n}^{(1)}(\eta_1)$.

Firstly, we check if the singular nature of $W_{\rm D}(\eta_1)$ may break the commutation of the supercharges $\mathrm{Q}_{\rm D}^{\pm}$ with the superhamiltonian $\mathrm{H}_{\rm D}$ in the second step of the Darboux procedure, where:

$$\mathrm{H}_{\rm D} = \begin{bmatrix} \widehat{\mathrm{H}}_{2,\mathrm{eq}} & \widehat{0} \\ \widehat{0} & \widehat{\widetilde{\mathrm{H}}}_{1,\mathrm{eq}}\left(\eta_1\right) \end{bmatrix}; \quad \mathrm{Q}_{\rm D}^{-} = \begin{bmatrix} \widehat{0} & \widehat{0} \\ \widehat{\mathrm{A}}_{\rm D}^{-}\left(\eta_1\right) & \widehat{0} \end{bmatrix}; \quad \mathrm{Q}_{\rm D}^{+} = \begin{bmatrix} \widehat{0} & \widehat{\mathrm{A}}_{\rm D}^{+}\left(\eta_1\right) \\ \widehat{0} & \widehat{0} \end{bmatrix}, \tag{C7.5}$$

and ($\alpha = E_1^{(1)}$):

$$\widehat{\mathrm{H}}_{2,\mathrm{eq}} = -\frac{\mathrm{d}^2}{\mathrm{d}r^2} + V_2\left(r\right) - \alpha; \quad \widehat{\widetilde{\mathrm{H}}}_{1,\mathrm{eq}}\left(\eta_1\right) = -\frac{\mathrm{d}^2}{\mathrm{d}r^2} + \widetilde{V}_1\left(r;\eta_1\right) - \alpha; \quad \widehat{\mathrm{A}}_{\mathrm{D}}^{\pm}\left(\eta_1\right) = \mp\frac{\mathrm{d}}{\mathrm{d}r} + W_{\mathrm{D}}\left(r;\eta_1\right). \tag{C7.6}$$

The commutation relation $\left[\mathrm{H}_{\mathrm{D}}, \mathrm{Q}_{\mathrm{D}}^{\pm}\right] = 0$ can also be expressed in terms of the following Hamiltonian intertwining relations:

$$\widehat{\widetilde{\mathrm{H}}}_{1,\mathrm{eq}}\left(\eta_1\right)\widehat{\mathrm{A}}_{\mathrm{D}}^{-}\left(\eta_1\right) = \widehat{\mathrm{A}}_{\mathrm{D}}^{-}\left(\eta_1\right)\widehat{\mathrm{H}}_{2,\mathrm{eq}}; \qquad \widehat{\mathrm{H}}_{2,\mathrm{eq}}\widehat{\mathrm{A}}_{\mathrm{D}}^{+}\left(\eta_1\right) = \widehat{\mathrm{A}}_{\mathrm{D}}^{+}\left(\eta_1\right)\widehat{\widetilde{\mathrm{H}}}_{1,\mathrm{eq}}\left(\eta_1\right). \tag{C7.7}$$

Taking the former intertwining relation, we must check the limit ($\forall n \geq 1$):

$$\lim_{r\to 0}\left[\left(\widehat{\widetilde{\mathrm{H}}}_{1,\mathrm{eq}}\left(\eta_1\right)\widehat{\mathrm{A}}_{\mathrm{D}}^{-}\left(\eta_1\right)\right)\left(\widehat{\mathrm{A}}^{-}\psi_{m_1,n}^{(1)}\left(r\right)\right)\right] = \lim_{r\to 0}\left[\left(\widehat{\mathrm{A}}_{\mathrm{D}}^{-}\left(\eta_1\right)\widehat{\mathrm{H}}_{2,\mathrm{eq}}\right)\left(\widehat{\mathrm{A}}^{-}\psi_{m_1,n}^{(1)}\left(r\right)\right)\right], \tag{C7.8}$$

with the LHS and RHS of the form:

$$\mathrm{LHS} \equiv \left(-\frac{\mathrm{d}^2}{\mathrm{d}r^2} + \widetilde{V}_1\left(r;\eta_1\right) - \alpha\right)\left(\frac{\mathrm{d}}{\mathrm{d}r} - \frac{\Phi_1'\left(r;\eta_1\right)}{\Phi_1\left(r;\eta_1\right)}\right)\left(\frac{\mathrm{d}}{\mathrm{d}r} - \frac{\left(R_{m_1,1}^{(1)}\left(r\right)\right)'}{R_{m_1,1}^{(1)}\left(r\right)} - \frac{1}{2r}\right)\left(\sqrt{r}R_{m_1,n}^{(1)}\left(r\right)\right); \tag{C7.9}$$

$$\mathrm{RHS} \equiv \left(\frac{\mathrm{d}}{\mathrm{d}r} - \frac{\Phi_1'\left(r;\eta_1\right)}{\Phi_1\left(r;\eta_1\right)}\right)\left(-\frac{\mathrm{d}^2}{\mathrm{d}r^2} + V_2\left(r\right) - \alpha\right)\left(\frac{\mathrm{d}}{\mathrm{d}r} - \frac{\left(R_{m_1,1}^{(1)}\left(r\right)\right)'}{R_{m_1,1}^{(1)}\left(r\right)} - \frac{1}{2r}\right)\left(\sqrt{r}R_{m_1,n}^{(1)}\left(r\right)\right). \tag{C7.10}$$

Using Eq. (B7.7) and after some algebraic work, we found that Eq. (C7.8) is satisfied. Proceeding in a similar manner, the second intertwining relation was also verified.

Secondly, we discuss if the eigenfunctions $\widetilde{\psi}_{m_1,n}^{(1)}(\eta_1)$ of the isospectral family $\widetilde{V}_1\left(\eta_1\right)$ are found to be continuous normalizable functions. The ground state ($n = 1$) is given by Eq. (C7.2) and its bound state nature was discussed before. The additional eigenfunctions ($n > 1$) which can be possible bound states are found from the relation $\widetilde{\psi}_{m_1,n}^{(1)}(\eta_1) \propto \widehat{\mathrm{A}}_{\mathrm{D}}^{-}(\eta_1)\widehat{\mathrm{A}}^{-}\psi_{m_1,n}^{(1)}$. From this expression, the following considerations are in order:

- Behavior at $r = 0$. We have tested the limit of $\widetilde{R}_{m_1,n}^{(1)}(\eta_1)$ at $r \to 0$ using Eq. (B7.7):

$$\lim_{r\to 0}\widetilde{R}_{m_1,1}^{(1)}\left(r;\eta_1\right) = \begin{cases} 1/\eta_1; & m_1 = 0 \\ 0; & m_1 > 0 \end{cases} \tag{C7.11}$$

$$\lim_{r\to 0}\widetilde{R}_{m_1,n}^{(1)}\left(r;\eta_1\right) = \begin{cases} \left(u_{0,1}^2 - u_{0,n}^2\right)/R_0^2; & m_1 = 0 \\ 0; & m_1 > 0 \end{cases} \tag{C7.12}$$

  Bearing in mind that $\widetilde{\psi}_{m_1,n}^{(1)}(r;\eta_1) = \sqrt{r}\widetilde{R}_{m_1,n}^{(1)}(r;\eta_1)$, we infer that $\widetilde{\psi}_{m_1,n,-}^{(1)}(\eta_1) = 0$.

- Behavior at $r \to \infty$. Note that $\widetilde{\psi}_{m_1,n,+}^{(1)}(\eta_1) = 0$, as deduced from the fact that $\psi_{m_1,n,+}^{(1)} = 0$, $|W_{1,+}| < \infty$ and $|W_{\mathrm{D},+}(\eta_1)| < \infty$, where W_1 is the superpotential employed in the first step of the Darboux procedure [see Fig. 7.8(a)].

- Continuity. The relations given by Eq. (C7.2) and $\widetilde{\psi}_{m_1,n}^{(1)}(\eta_1) \propto \widehat{\mathrm{A}}_{\mathrm{D}}^{-}(\eta_1)\widehat{\mathrm{A}}^{-}\psi_{m_1,n}^{(1)}$ do not introduce any discontinuity in $r \geq 0$.

As in the unbroken and broken SUSY transformations, we found the same conclusions for the functions $\left|\widetilde{\psi}_{m_1,n}^{(1)}(\eta_1)\right|$ and $\left|\widetilde{\psi}_{m_1,n}^{(1)}(\eta_1)\right|^2$, which allows us to conclude that $\int_0^r \left|\widetilde{\psi}_{m_1,n}^{(1)}(x;\eta_1)\right|^2 \mathrm{d}x$ is bounded with $r \geq 0$ and, therefore, $\int_0^\infty \left|\widetilde{\psi}_{m_1,n}^{(1)}(r;\eta_1)\right|^2 \mathrm{d}r$ is convergent. Consequently, $\widetilde{\psi}_{m_1,n}^{(1)}(\eta_1)$ are bound state of $\widetilde{V}_1\left(\eta_1\right)$.

C7.3 Additional numerical examples

For completeness, we include in Fig. C7.1 the normalized dispersion diagram of the refractive indexes calculated from Eq. (7.4.3) by assuming: n_1 as the step-index profile of previous examples, $m_1 \in \{0, 1, 2, 3\}$, and taking two different values of the η_1 parameter in each case.

Next, we show in Table C7.1 a comparison at 1550 nm of the phase-mismatching $\Delta\beta$ and the ratio $\widetilde{\mathcal{E}}_z/\widetilde{\mathcal{E}}_{\mathrm{T}}$ of the true modes which compose the LP and quasi-LP mode groups depicted in Fig. 7.8(c) and Fig. C7.1. Despite the fact that all the bound states (emerged from the linear combination of the quasi-degenerate true modes) show a linearly or quasi-linearly polarized nature similar to [32], as was verified with CST Microwave Studio, only the ground state $\mathrm{LP}_{m_1,1}^{(\widetilde{n}_1)}$ meets the paraxial approximation, where $\widetilde{\mathcal{E}}_z$ can be neglected ($\widetilde{\mathcal{E}}_z/\widetilde{\mathcal{E}}_{\mathrm{T}} \sim 0.01$). Nevertheless, the additional bound states operate in the quasi-paraxial regime ($\widetilde{\mathcal{E}}_z/\widetilde{\mathcal{E}}_{\mathrm{T}} \sim 0.1$), where $\widetilde{\mathcal{E}}_z$ should be retained in Maxwell's equations. These bound states do not approximately satisfy Eq. (7.2.2) and, therefore, the degeneracy in these energy levels is broken between n_1 and $\widetilde{n}_1$.

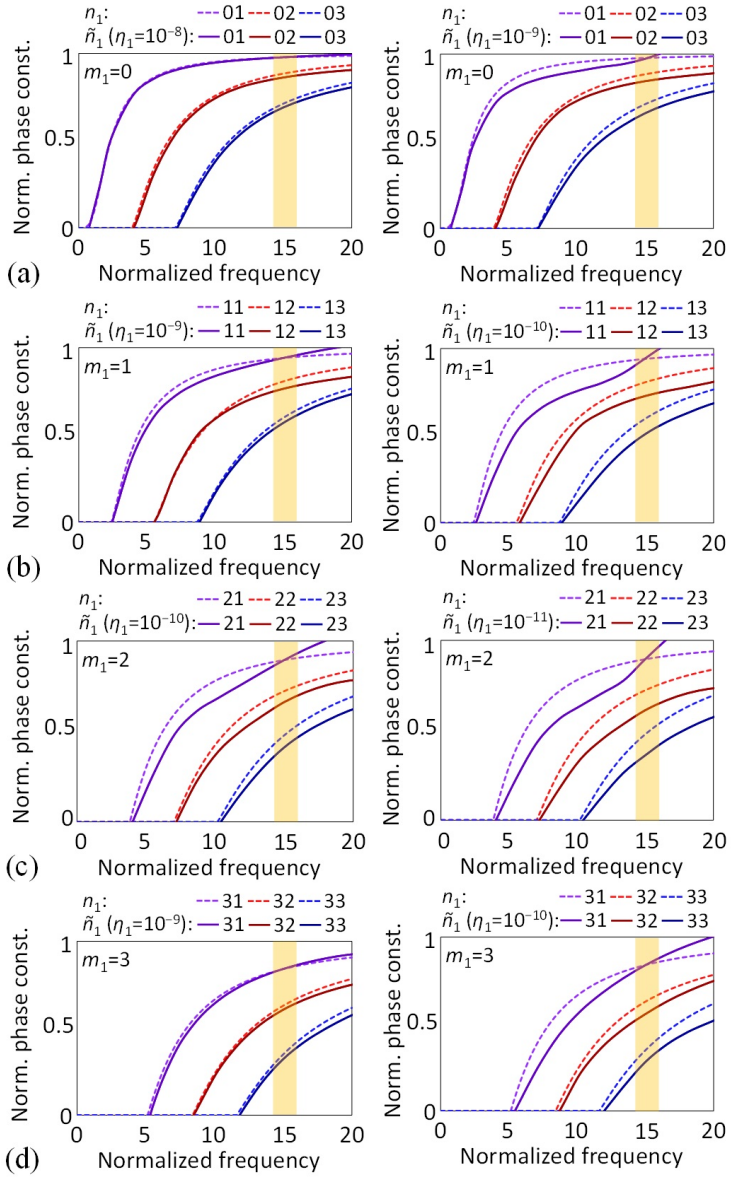

Figure C7.1. Normalized dispersion diagram of the refractive index profiles calculated using the 1-param. Darboux procedure for the step-index case. (a) $m_1 = 0$, (b) $m_1 = 1$, (c) $m_1 = 2$ and (d) $m_1 = 3$ [241].

LP mode group	True modes	$\beta_{\rm av}$ rad/m	$\Delta\beta$ rad/m	$\widetilde{\mathcal{E}}_z/\widetilde{\mathcal{E}}_{\rm T}$
$\mathrm{LP}_{0,1}^{(n_1)}$ [✠]	HE_{11}	5780535	0	0.008
$\mathrm{LP}_{0,2}^{(n_1)}$	HE_{12}	5777612	0	0.01
$\mathrm{LP}_{0,3}^{(n_1)}$	HE_{13}	5772252	0	0.01
$\mathrm{LP}_{0,1}^{(\widetilde{n}_1,\eta_1=1\mathrm{e}-8)}$ [✠]	HE_{11}	5780532	0	0.009
$\mathrm{LP}_{0,2}^{(\widetilde{n}_1,\eta_1=1\mathrm{e}-8)}$	HE_{12}	5777242	0	0.10
$\mathrm{LP}_{0,3}^{(\widetilde{n}_1,\eta_1=1\mathrm{e}-8)}$	HE_{13}	5771893	0	0.10
$\mathrm{LP}_{0,1}^{(\widetilde{n}_1,\eta_1=1\mathrm{e}-9)}$ [✠]	HE_{11}	5780536	0	0.01
$\mathrm{LP}_{0,2}^{(\widetilde{n}_1,\eta_1=1\mathrm{e}-9)}$	HE_{12}	5776365	0	0.14
$\mathrm{LP}_{0,3}^{(\widetilde{n}_1,\eta_1=1\mathrm{e}-9)}$	HE_{13}	5770649	0	0.15
$\mathrm{LP}_{1,1}^{(n_1)}$ [✠]	$\mathrm{TE}_{01}\pm\mathrm{TM}_{01}\pm\mathrm{HE}_{21}$	5779387	2	0.009
$\mathrm{LP}_{1,2}^{(n_1)}$	$\mathrm{TE}_{02}\pm\mathrm{TM}_{02}\pm\mathrm{HE}_{22}$	5775189	2	0.02
$\mathrm{LP}_{1,3}^{(n_1)}$	$\mathrm{TE}_{03}\pm\mathrm{TM}_{03}\pm\mathrm{HE}_{23}$	5768687	6	0.04
$\mathrm{LP}_{1,1}^{(\widetilde{n}_1,\eta_1=1\mathrm{e}-9)}$ [✠]	$\mathrm{TE}_{01}\pm\mathrm{TM}_{01}\pm\mathrm{HE}_{21}$	5779382	3	0.01
$\mathrm{LP}_{1,2}^{(\widetilde{n}_1,\eta_1=1\mathrm{e}-9)}$	$\mathrm{TE}_{02}\pm\mathrm{TM}_{02}\pm\mathrm{HE}_{22}$	5773888	17	0.10
$\mathrm{LP}_{1,3}^{(\widetilde{n}_1,\eta_1=1\mathrm{e}-9)}$	$\mathrm{TE}_{03}\pm\mathrm{TM}_{03}\pm\mathrm{HE}_{23}$	5767792	16	0.11
$\mathrm{LP}_{1,1}^{(\widetilde{n}_1,\eta_1=1\mathrm{e}-10)}$ [✠]	$\mathrm{TE}_{01}\pm\mathrm{TM}_{01}\pm\mathrm{HE}_{21}$	5779386	4	0.02
$\mathrm{LP}_{1,2}^{(\widetilde{n}_1,\eta_1=1\mathrm{e}-10)}$	$\mathrm{TE}_{02}\pm\mathrm{TM}_{02}\pm\mathrm{HE}_{22}$	5772760	41	0.13
$\mathrm{LP}_{1,3}^{(\widetilde{n}_1,\eta_1=1\mathrm{e}-10)}$	$\mathrm{TE}_{03}\pm\mathrm{TM}_{03}\pm\mathrm{HE}_{23}$	5765952	46	0.16
$\mathrm{LP}_{2,1}^{(n_1)}$ [✠]	$\mathrm{EH}_{11}\pm\mathrm{HE}_{31}$	5777946	2	0.01
$\mathrm{LP}_{2,2}^{(n_1)}$	$\mathrm{EH}_{12}\pm\mathrm{HE}_{32}$	5772568	5	0.02
$\mathrm{LP}_{2,3}^{(n_1)}$	$\mathrm{EH}_{13}\pm\mathrm{HE}_{33}$	5764932	6	0.02
$\mathrm{LP}_{2,1}^{(\widetilde{n}_1,\eta_1=1\mathrm{e}-10)}$ [✠]	$\mathrm{EH}_{11}\pm\mathrm{HE}_{31}$	5777950	4	0.02
$\mathrm{LP}_{2,2}^{(\widetilde{n}_1,\eta_1=1\mathrm{e}-10)}$	$\mathrm{EH}_{12}\pm\mathrm{HE}_{32}$	5772305	27	0.10
$\mathrm{LP}_{2,3}^{(\widetilde{n}_1,\eta_1=1\mathrm{e}-10)}$	$\mathrm{EH}_{13}\pm\mathrm{HE}_{33}$	5763807	27	0.11
$\mathrm{LP}_{2,1}^{(\widetilde{n}_1,\eta_1=1\mathrm{e}-11)}$ [✠]	$\mathrm{EH}_{11}\pm\mathrm{HE}_{31}$	5777948	10	0.03
$\mathrm{LP}_{2,2}^{(\widetilde{n}_1,\eta_1=1\mathrm{e}-11)}$	$\mathrm{EH}_{12}\pm\mathrm{HE}_{32}$	5770676	40	0.12
$\mathrm{LP}_{2,3}^{(\widetilde{n}_1,\eta_1=1\mathrm{e}-11)}$	$\mathrm{EH}_{13}\pm\mathrm{HE}_{33}$	5762860	45	0.17
$\mathrm{LP}_{3,1}^{(n_1)}$ [✠]	$\mathrm{EH}_{21}\pm\mathrm{HE}_{41}$	5776254	3	0.009
$\mathrm{LP}_{3,2}^{(n_1)}$	$\mathrm{EH}_{22}\pm\mathrm{HE}_{42}$	5769643	5	0.01
$\mathrm{LP}_{3,3}^{(n_1)}$	$\mathrm{EH}_{23}\pm\mathrm{HE}_{43}$	5760907	7	0.02
$\mathrm{LP}_{3,1}^{(\widetilde{n}_1,\eta_1=1\mathrm{e}-9)}$ [✠]	$\mathrm{EH}_{21}\pm\mathrm{HE}_{41}$	5776250	5	0.02
$\mathrm{LP}_{3,2}^{(\widetilde{n}_1,\eta_1=1\mathrm{e}-9)}$	$\mathrm{EH}_{22}\pm\mathrm{HE}_{42}$	5769103	21	0.10
$\mathrm{LP}_{3,3}^{(\widetilde{n}_1,\eta_1=1\mathrm{e}-9)}$	$\mathrm{EH}_{23}\pm\mathrm{HE}_{43}$	5760234	20	0.11
$\mathrm{LP}_{3,1}^{(\widetilde{n}_1,\eta_1=1\mathrm{e}-10)}$ [✠]	$\mathrm{EH}_{21}\pm\mathrm{HE}_{41}$	5776252	8	0.03
$\mathrm{LP}_{3,2}^{(\widetilde{n}_1,\eta_1=1\mathrm{e}-10)}$	$\mathrm{EH}_{22}\pm\mathrm{HE}_{42}$	5767426	26	0.13
$\mathrm{LP}_{3,3}^{(\widetilde{n}_1,\eta_1=1\mathrm{e}-10)}$	$\mathrm{EH}_{23}\pm\mathrm{HE}_{43}$	5758839	33	0.14

Table C7.1. Comparison at 1550 nm of the degeneracy of the true modes for the isospectral refractive indexes calculated with the one-parameter Darboux procedure. $\beta_{\rm av}$ and $\Delta\beta$ are respectively the average value of the phase constant and the phase-mismatching of the true modes in each LP and quasi-LP mode group. ([✠]: ground state) [241].

C7.4 Multi-parameter family

The one-parameter Darboux procedure can be extended to an N-parameter isospectral family of cylindrical potentials with axial symmetry in a similar way as detailed in Chapter 6 (on page 191) on the full line. Deleting all N bound states of a given cylindrical potential V_1 using an unbroken SUSY Hamiltonian chain and reinserting them with a series of Darboux transformations, we obtain:

$$\widetilde{V}_1\left(r;\eta_1,\ldots,\eta_N\right)=V_1\left(r\right)-2\frac{\mathrm{d}^2}{\mathrm{d}r^2}\ln\left[r^{N/2}\prod_{i=1}^{N}R^{(i)}_{m_i,1}\left(r\right)\Phi_i\left(r;\eta_i,\ldots,\eta_N\right)\right], \tag{C7.13}$$

where:

$$\Phi_i\left(r;\eta_i,\ldots,\eta_N\right)=\left(\prod_{j=i+1}^{N}\widehat{\mathrm{A}}^{-}_{j,\mathrm{D}}\left(\eta_j,\ldots,\eta_N\right)\right)\left(\prod_{q=1}^{N-i}\widehat{\mathrm{A}}^{-}_{N-q+1}\right)\Phi_i\left(r;\eta_i\right); \tag{C7.14}$$

$$\widehat{\mathrm{A}}^{-}_{i,\mathrm{D}}\left(\eta_i,\ldots,\eta_N\right)=\frac{\mathrm{d}}{\mathrm{d}r}-\left(\ln\Phi_i\left(r;\eta_i,\ldots,\eta_N\right)\right)';\quad \widehat{\mathrm{A}}^{-}_{i}=\frac{\mathrm{d}}{\mathrm{d}r}-\left(\ln\sqrt{r}R^{(i)}_{m_i,1}\left(r\right)\right)'; \tag{C7.15}$$

$$\Phi_i\left(r;\eta_i\right)=\frac{\mathcal{I}_i\left(r\right)+\eta_i}{\sqrt{r}R^{(i)}_{m_i,1}\left(r\right)};\quad \mathcal{I}_i\left(r\right)=\int^{r}\alpha\left(R^{(i)}_{m_i,1}\right)^2\left(\alpha\right)\mathrm{d}\alpha;\quad \eta_i\notin\left[-\mathcal{I}_{i,+},0\right]. \tag{C7.16}$$

In photonics and acoustics, the refractive index can be calculated from Eq. (C7.13) as:

$$\widetilde{n}_1\left(r;\eta_1,\ldots,\eta_N\right)=\sqrt{n_1^2\left(r\right)+2\frac{c_0^2}{\omega^2}\frac{\mathrm{d}^2}{\mathrm{d}r^2}\ln\left[r^{N/2}\prod_{i=1}^{N}R^{(i)}_{m_i,1}\left(r\right)\Phi_i\left(r;\eta_i,\ldots,\eta_N\right)\right]}. \tag{C7.17}$$

As in the one-parameter family, the multi-parameter Darboux procedure also gives rise to singular superpotentials when axially-symmetric potentials are involved in the theoretical work. Thus, the degeneracy is only preserved at energy levels where the corresponding eigenfunctions $\widetilde{\psi}_{m_1,n}(\eta_1,\ldots,\eta_N)$ are found to be bound states of the isospectral family of potentials $\widetilde{V}_1(\eta_1,\ldots,\eta_N)$. In the cases where the degeneracy is preserved, Eqs. (C7.13)-(C7.16) could be of extreme utility within the context of quantum mechanics. In this branch of physics, the previous expressions may allow us to construct real cylindrical potentials with identical spectra and scattering properties. As an example, it would be of great interest to investigate simple expressions for the pure multi-soliton solutions of the Korteweg-de Vries (KdV) equation, following a similar mathematical discussion as in [216] for the 1D potential $V(x)=-n(n+1)\mathrm{sech}^2(x)$ on the full line $(-\infty<x<\infty)$.

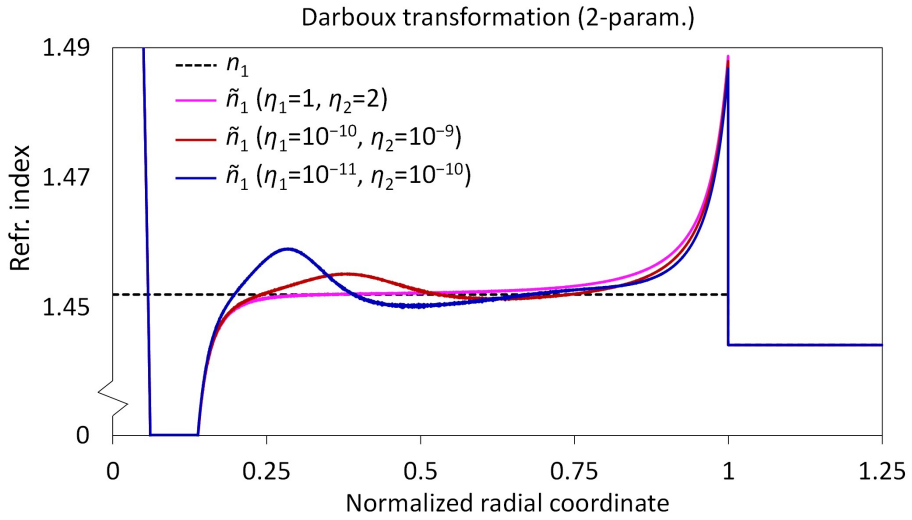

Figure C7.2. Two-parameter refractive index family of the step-index profile [241].

On the other hand, in photonics and acoustics, the multi-parameter family is found to be less attractive than the one-parameter case. As a simple example, we show in Fig. C7.2 the two-parameter family $\widetilde{n}_1(\eta_1, \eta_2)$ of the n_1 step-index profile when assuming $R_0 = 25$ μm, $\lambda_0 = 1550$ nm, $N = 2$ and $m_1 = 3$ in Eq. (C7.17). As seen, $\widetilde{n}_1$ exhibits a zero-index region at $r/R_0 \sim 0.1$ and a singularity at $r = 0$. Although zero-index media are hardly found in naturally-occurring materials, both photonic and sonic near-zero-index media can be synthesized with current metamaterial technology [311]. Nonetheless, due to the singular behavior of $\widetilde{n}_1$, the multi-parameter Darboux procedure does not present an apparent practical utility within the context of photonics or acoustics for wave propagation purposes. Specifically, in photonics, the degeneracy of the isospectral family will not be preserved. The SVI and the paraxial approximations will not be satisfied due to the high index contrast induced by the singularity.

Chapter 8

Optical supersymmetry in the time domain

Preface Originally emerged within the context of string and quantum field theory as a means to achieve a theory of everything, the mathematical framework of supersymmetry was restricted to the *space domain* in non-relativistic quantum mechanics to clarify fundamental outstanding questions in physics. In this chapter, we introduce a paradigm shift demonstrating how the foundations of the non-relativistic supersymmetry can also be extended to the *time domain*, at least within the realm of photonics and acoustics. Dr. Carlos García-Meca is acknowledged for conceiving the idea of temporal SUSY. The main work was developed in equal contribution by Carlos and Andrés Macho Ortiz. We also thank Prof. Demetrios Christodoulides and Dr. Rodrigo Amezcua-Correa from CREOL, The College of Optics & Photonics, for their thoughtful discussions that greatly contributed to the results of this chapter.

8.1 Introduction

Supersymmetry (SUSY) emerged in 1971 within the context of string and quantum field theory as a coherent mathematical framework for the unification of the strong, electroweak, and gravitational interactions [207–209]. Attempting to solve fundamental questions about SUSY, scientists subsequently created the field of SUSY quantum mechanics (SUSY QM), a non-relativistic model for testing the aforementioned theories [216]. Essentially, the one-dimensional (1D) version of SUSY QM considers two different QM systems described by the eigenvalue problems:

$$\widehat{\mathrm{H}}_{1,2}\psi^{(1,2)}(x) = \Omega^{(1,2)}\psi^{(1,2)}(x), \tag{8.1.1}$$

with $\widehat{\mathrm{H}}_{1,2} = -\alpha \mathrm{d}^2/\mathrm{d}x^2 + V_{1,2}(x)$ and $\alpha \in \mathbb{R}^+$. As discussed in Chapter 6, the basic idea of SUSY QM is to factorize $\widehat{\mathrm{H}}_1$ as $\widehat{\mathrm{H}}_1 = \widehat{\mathrm{A}}^+\widehat{\mathrm{A}}^-$, where $\widehat{\mathrm{A}}^\pm := \mp\sqrt{\alpha}\mathrm{d}/\mathrm{d}x + W(x)$ are known as the SUSY operators and W is the superpotential, and then construct a second (supersymmetric) system $\widehat{\mathrm{H}}_2$ by inverting the order of the factorization $\widehat{\mathrm{H}}_2 := \widehat{\mathrm{A}}^-\widehat{\mathrm{A}}^+$. The power of SUSY QM lies in the fact that both systems exhibit almost identical eigenvalue spectra and scattering properties. For this reason, while evidence of SUSY in nature remains elusive [215], SUSY QM became of great interest in itself, leading to the discovery of new analytically-solvable potentials, explaining intriguing aspects of quantum mechanics (such as the energy spectrum equality shared by very different systems or the existence of non-trivial reflectionless potentials), and offering a unique way to generate new families of isospectral and reflectionless systems [216]. Remarkably, under specific circumstances, Eq. (8.1.1) also describes the dynamics of electromagnetic waves (and of any physical phenomenon governed by Helmholtz's equation), enabling a straightforward application of SUSY QM theory in optics. As a result, notions of this formalism have been very recently utilized to design ground-breaking photonic devices [228–230, 232, 234–239, 241].

Interestingly, in optics, there is a vast number of scenarios governed by a wave equation involving second-order spatial derivatives over which we can apply the spatial factorization of SUSY QM. As an illustrative example of the optical SUSY literature, consider the following wave equation that allows us to describe the propagation of light in diverse optical systems:[1]

$$\left(\triangle - \frac{n^2 (\boldsymbol{r}, t)}{c_0^2} \partial_t^2 \right) \boldsymbol{F} (\boldsymbol{r}, t) = \boldsymbol{0}, \tag{8.1.2}$$

where $\triangle = \partial_i^2$ is the Laplacian operator, c_0 is the speed of light in vacuum, n is the refractive index profile defined as $n^2 (\boldsymbol{r}, t) := \varepsilon_{\mathrm{r}} (\boldsymbol{r}, t) \mu_{\mathrm{r}} (\boldsymbol{r}, t)$, ε_{r} is the relative electric permittivity, μ_{r} is the relative magnetic permeability, and $\boldsymbol{F}$ is the *analytic*[2] representation of the electric ($\boldsymbol{D}$) or magnetic ($\boldsymbol{B}$) flux density. In the above wave equation, the application of SUSY QM is straightforward by factorizing the Laplacian operator and omitting the temporal dependence of n [222–225, 228–230, 232–239, 241]. However, time-varying optical systems are crucial for a broad range of applications, including optical modulation [313, 314], isolation and non-reciprocity [315, 316], signal processing [317–319], quantum information [320], and reconfigurable photonics [321]. Thus, it is certainly surprising that the main studies on optical SUSY are only valid for time-invariant systems.

Here, we lift this important restriction demonstrating that Maxwell's equations also possess an underlying *temporal supersymmetry* (T-SUSY) in a large variety of time-varying systems. In our example, this implies that the SUSY QM factorization can be moved from the Laplacian operator to the second-order time derivative by redefining the SUSY operators as $\widehat{\mathrm{A}}^{\pm} := \mp\sqrt{\alpha}\partial_t + W(t)$. This paradigm shift will allow us to extend the unique properties of SUSY QM to the time domain, adding an unprecedented degree of control over time-varying optical systems and opening the door to a myriad of new applications.

It is worthy to note that the factorization proposed by T-SUSY is completely different from the factorization employed in SUSY QM with a time-dependent potential [322–324], where the SUSY operators are also defined using a first-order spatial derivative. The underlying problem of using SUSY operators based on spatial derivatives is that we are restricted to reduce multidimensional optical problems to one dimension obtaining polarization-dependent applications (see e.g. [228, 232]). However, in our proposal, we can benefit from the 1D nature of the time domain to elude these restrictions by introducing time operators. As a result, we will be able to extend the notions of SUSY in a wide variety of scenarios in photonics guaranteeing omnidirectional and polarization-independent applications, sketched in Fig. 8.1.

Outstandingly, T-SUSY will allow us to explore the fundamentals of the temporal scattering giving rise to unprecedented optical devices. Exploiting the intimate relationship between supersymmetric time-varying refractive index profiles, we uncover a general relation between their scattering amplitudes. This result can be used to analyze the reflection and transmission coefficients of a large number of time-varying media or to design temporal modulations of the refractive index with desired scattering properties, both functionalities (analysis & synthesis) without the necessity of solving numerically Maxwell's equations. As a byproduct, a new class of omnidirectional, isotropic, polarization-independent and transparent (i.e. non-reflecting, lossless and gainless) media is found, valid for all-dielectric, all-magnetic materials or a combination of both [Fig. 8.1(a)]. Using this result, we build an ultra-compact reconfigurable transparent phase shifter with frequency-independent phase response [Fig. 8.1(b)], and a broadband optical isolator [Fig. 8.1(c)]. Next, we extend the possibilities of T-SUSY by considering time-varying dispersive media. To unfold the potential of dispersive T-SUSY media, we design supersymmetric temporal waveguides, which could be crucial for all-optical signal processing applications based on mode filtering and mode conversion of temporal bound states.[3] As a corollary of our findings, we introduce the concept of the *temporal photonic lantern* (a dispersive time-varying device which generates temporal supermodes

[1] Imposing specific necessary conditions on the refractive index profile, this wave equation is *exact* and may describe the propagation of light in dielectric (or magnetic), linear, isotropic, heterogeneous, time-varying, and non-dispersive optical media. See Appendix A8, on page 258.

[2] The definition of the analytic representation of a field is detailed on page 2.

[3] By analogy with a spatial bound state, a *temporal* bound state can be defined as a time-dependent eigenfunction ψ continuous, normalizable and satisfying the condition $\psi (t \to \pm\infty) = 0$.

from the linear combination of degenerate bound states of close-packed temporal waveguides) and we extend its applications for pulse shaping devices by applying T-SUSY [Fig. 8.1(d)]. Finally, we discuss the possibility of extrapolating our results to acoustics.

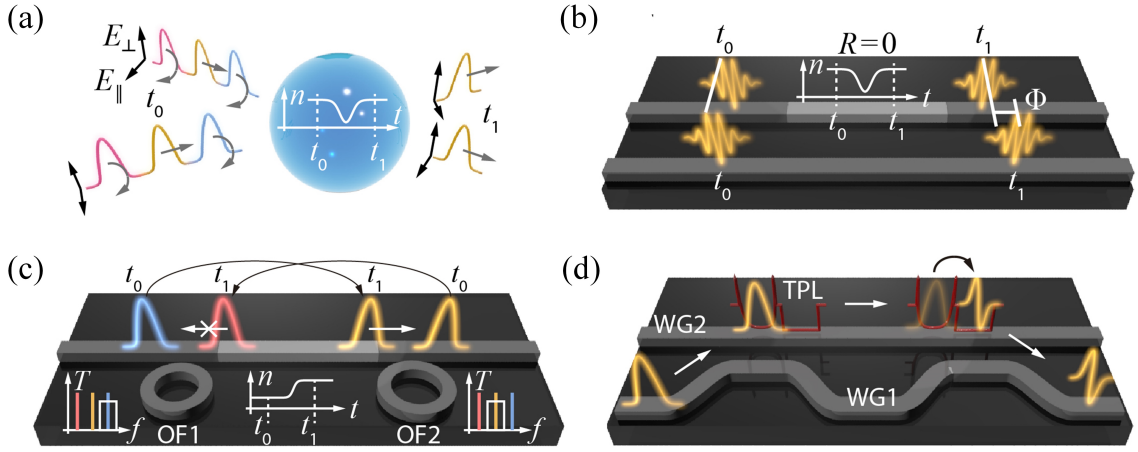

Figure 8.1. Optical applications and devices demonstrated in this chapter using T-SUSY. (a) All-dielectric (all-magnetic), omnidirectional, isotropic, polarization-independent and transparent medium with real positive permittivity (permeability). (b) Ultra-compact, reconfigurable, polarization-independent and transparent phase shifter with frequency-independent phase response Φ. (c) Polarization-independent optical isolator based on frequency down-conversion of the input signal using a reflectionless time-varying refractive index $n(t)$ implemented, e.g., on a planar waveguide. Two band-pass optical filters OF1 and OF2 of frequency $\omega_{\mathrm{OF1}} = \omega_-$ and $\omega_{\mathrm{OF2}} = \omega_+ = (n_-/n_+)\omega_-$, with $n_\pm := n(t \to \pm\infty)$, are included at the input and at the output of the device to protect the light source from external reflections. (d) Pulse-shape transformer using a temporal photonic lantern (TPL) constructed with two close-packed T-SUSY temporal waveguides (red line) moving through the longitudinal axis of a spatial waveguide WG2. The spatial waveguide WG1 is employed to insert (extract) the initial (final) pulse into (from) the TPL.

8.2 Temporal SUSY and temporal scattering

Aimed to highlight the power of our idea, let us consider as an initial example an all-dielectric, linear, isotropic, homogeneous, time-varying and non-dispersive medium. This scenario is exactly described by Eq. (8.1.2) taking $\boldsymbol{F} = \boldsymbol{D}$ and $n^2(t) = \varepsilon_{\mathrm{r}}(t)$. In such conditions, the isotropic and homogeneous nature of the medium guarantee that $\boldsymbol{D}$ is transversal to the propagation direction of the electromagnetic energy (e.g. $\hat{u}_x$), the wave vector is parallel to $\hat{u}_x$, and the temporal scattering is polarization-independent. Hence, without loss of generality, we can safely assume a single component in $\boldsymbol{D}$ and, consequently, Eq. (8.1.2) can be reduced to the scalar wave equation:

$$\left(\triangle - \frac{n^2(t)}{c_0^2}\partial_t^2\right) D(\boldsymbol{r}, t) = 0. \tag{8.2.1}$$

Applying separation of variables $D(\boldsymbol{r}, t) = \phi(\boldsymbol{r})\,\psi(t)$, we find that the temporal solution ψ obeys the 1D temporal Helmholtz equation:

$$\left(\frac{\mathrm{d}^2}{\mathrm{d}t^2} + \omega_0^2 N^2(t)\right)\psi(t) = 0, \tag{8.2.2}$$

where $N^2(t) := n_-^2/n^2(t)$, $n_- := n(t \to -\infty)$, and ω_0 is the angular frequency (central angular frequency) of the electromagnetic fields at $t \to -\infty$ in the monochromatic (non-monochromatic) regime. The same equation is obtained for homogeneous time-varying all-magnetic materials $[n^2(t) = \mu_{\mathrm{r}}(t)]$, homogeneous time-varying dielectric and magnetic materials $[n^2(t) = \varepsilon_{\mathrm{r}}(t)\,\mu_{\mathrm{r}}(t)]$, and also in the heterogeneous case $[n^2(\boldsymbol{r}, t)]$ (see Appendix A8, on page 258).[4]

[4]Moreover, although it is out of the scope of this work, it can also be demonstrated that Eq. (8.2.2) also follows in the case of non-dispersive anisotropic and conductive media (see Appendix A8.4, on page 260).

Interestingly, Eq. (8.2.2) matches Eq. (8.1.1) taking $\alpha \equiv 1$, performing the relabeling $x \to t$, and identifying $\Omega - V(x \to t) \equiv \omega_0^2 N^2(t)$. In this way, assuming Ω as a degree of freedom, we will be able to use the algebraic transformations of SUSY QM in the time domain, which will give rise to time-varying optical media $n_1(t)$ and $n_2(t)$ with similar scattering properties, provided that we use real $V_{1,2}$ potentials [235].

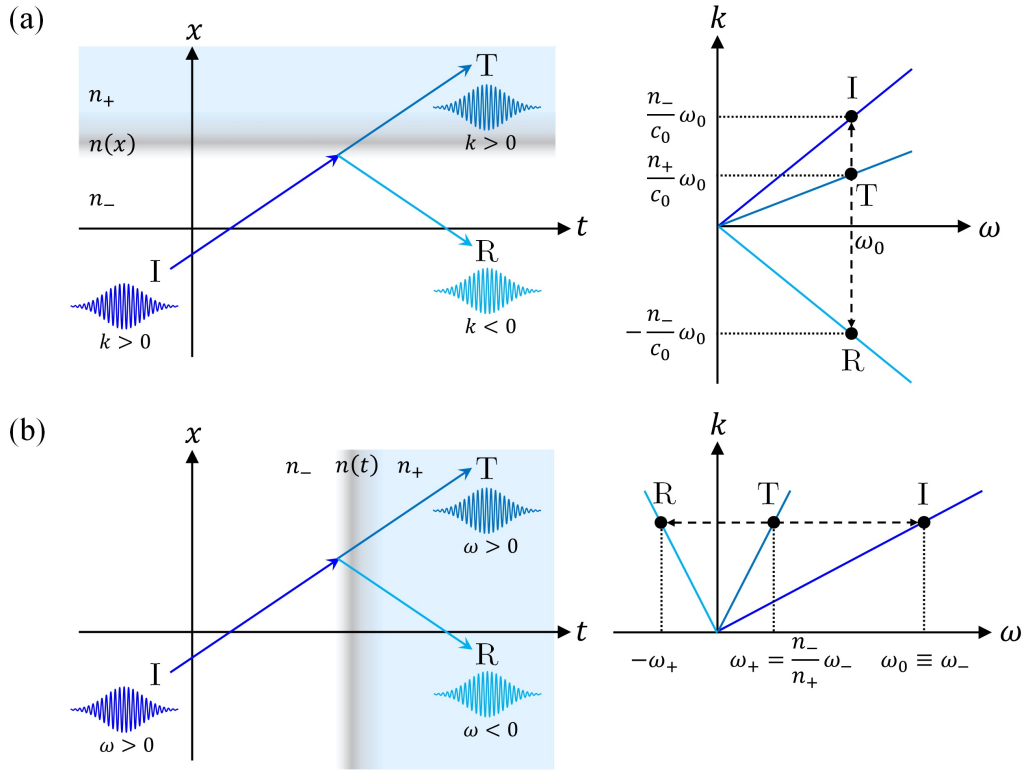

Figure 8.2. Wave propagation through heterogeneous time-invariant *vs* homogeneous time-varying media. (a) Incident (I), reflected (R) and transmitted (T) waves propagating in the x-axis in a heterogeneous time-invariant medium and dispersion diagram of such a situation. The frequency is found to be constant and the reflected wave has a negative wave number. (b) Incident, reflected and transmitted waves propagating in the x-axis in a homogeneous time-varying medium and dispersion diagram of this scenario. In such a case, the wave number is constant and we can observe a negative frequency in the reflected wave.

For the sake of clarity, before delving into the theory of T-SUSY in the temporal scattering problem, we should discuss the main differences between the spatial and temporal scattering in optics. To this end, consider an incident (I) plane wave of angular frequency ω_0 propagating in the x-axis from the left within two different media: (a) a heterogeneous time-invariant medium with refractive index $n(x)$, and (b) a homogeneous time-varying medium with refractive index $n(t)$. In both cases, the refractive index profile tends to a positive constant $n_\pm$ at the beginning and at the end of the problem ($x \to \pm\infty$ and $t \to \pm\infty$). A schematic of both scenarios is shown in Fig. 8.2. In both cases, a reflected (R) and a transmitted (T) wave can be observed as a result of the interaction of the incident wave with a localized refractive index variation in space or in time. In the former case [Fig. 8.2(a)], the frequency (or equivalently, the photon energy) is found to be constant and the wave number (or equivalently, the photon momentum) changes. Specifically, the wave number of the incident ($k_\mathrm{I} \equiv k_-$), reflected (k_R) and transmitted ($k_\mathrm{T} \equiv k_+$) waves fulfills the relations $k_\mathrm{R} = -k_-$ and $k_-/n_- = k_+/n_+$, which is a particularization of the well-known Snell law.[5] Along this line, note that the reflected wave has a negative wave number, as depicted in the

[5]The Snell law reads as $n_- \sin\theta_- = n_+ \sin\theta_+$, where $\sin\theta_+ = k_y/k_\pm$ and k_y is the component of the wave vector which is tangential to the spatial refractive index variations $n(x)$. Taking into account that k_y is constant, the Snell law can be recast as $k_-/n_- = k_+/n_+$.

dispersion diagram k-ω of Fig. 8.2(a). In the latter case [Fig. 8.2(b)], the wave number is constant and the frequency changes. This is an open system, that is, we can observe an energy transfer with the outer medium. The frequency of the incident ($\omega_{\mathrm{I}} \equiv \omega_- = \omega_0$), reflected ($\omega_{\mathrm{R}}$) and transmitted ($\omega_{\mathrm{T}} \equiv \omega_+$) waves obeys the relations $\omega_{\mathrm{R}} = -\omega_+$ and $n_+\omega_+ = n_-\omega_-$, which is the Snell law of the temporal scattering [325, 326]. In such a scenario, it is worth mentioning that the reflected wave has a negative frequency, in particular the opposite of the transmitted wave, whilst the wave number is found to be the same. Hence, as demonstrated in Appendix B8.2 (see page 266), an inversion of the dispersion diagram leads to a time-reversal operation of light: the reflected wave is the time-reversed version of the transmitted wave.

The existence of negative-frequency waves is a striking and controversial concept which has been exhaustively discussed in optics, gravity and for water waves [105, 327–330]. In this work, the introduction of negative frequencies is not a mere sign convention to describe the backward propagation. The use of negative frequencies is a necessary ingredient that allows us, firstly, to describe adequately the temporal scattering, as shown in Fig. 8.2 and we discuss in more detail in Appendix B8 (on page 263) and, secondly, to relate the reflection and transmission coefficients of the T-SUSY refractive index profiles $n_{1,2}(t)$. Otherwise, the reflection and transmission coefficients of $n_{1,2}(t)$ cannot be decoupled [see Eq. (C8.24) in Appendix C8]. Concretely, Eq. (8.2.2) admits an asymptotic solution for the incident, reflected and transmitted waves in $n_{1,2}(t)$ of the form:

$$\psi_{\mathrm{I}}^{(1,2)}(t) \underset{t\to-\infty}{\sim} \exp(j\omega_0 t); \tag{8.2.3}$$

$$\psi_{\mathrm{R}}^{(1,2)}(t) \underset{t\to\infty}{\sim} R_{1,2}\exp(-jN_+\omega_0 t); \tag{8.2.4}$$

$$\psi_{\mathrm{T}}^{(1,2)}(t) \underset{t\to\infty}{\sim} T_{1,2}\exp(jN_+\omega_0 t), \tag{8.2.5}$$

where $N_+ := n_{1,-}/n_{1,+} = n_{2,-}/n_{2,+}$, $n_{1,2,\pm} := n_{1,2}(t\to\pm\infty)$, and $R_{1,2}$ and $T_{1,2}$ are respectively the reflection and transmission coefficients of the electric flux density. The T-SUSY formalism then relates the SUSY refractive index profiles as (see Appendix C8, on page 270):

$$n_2(t) = \frac{n_{2,-}}{\sqrt{\frac{n_{1,-}^2}{n_1^2(t)} - \frac{2}{\omega_0^2}W'(t)}}, \tag{8.2.6}$$

and their scattering coefficients in the following way:

$$R_2 = \frac{W_- - j\omega_0}{W_+ + jN_+\omega_0}R_1; \qquad T_2 = \frac{W_- - j\omega_0}{W_+ - jN_+\omega_0}T_1, \tag{8.2.7}$$

where $W_\pm := W(t\to\pm\infty)$, W is found from the Riccati equation $V_{1,2}(t) = W^2(t) \mp W'(t)$, and $V_{1,2}(t) = \Omega - \omega_0^2 N_{1,2}^2(t)$. The first important consequence of Eq. (8.2.7) is that it can be employed to obtain the reflection and transmission coefficients of a large number of non-trivial time-varying optical media without solving Maxwell's equations (specifically, of any supersymmetric partner of a medium with a known response). As a second important consequence, since n_1 and n_2 share the same eigenvalue Ω, then $|R_1| = |R_2|$ and $|T_1| = |T_2|$. This allows us to readily generate families of temporal index profiles exhibiting the same scattering intensity as another medium, synthesizable over the same ($n_{1,-} = n_{2,-}$) or different ($n_{1,-} \neq n_{2,-}$) background materials, opening up a variety of applications.

8.2.1 Transparent phase shifter

As an initial application of these findings, let us consider the simplest example: a constant refractive index $n_1(t) = n_{1,-}$, which has a T-SUSY refractive index of the form:

$$n_2(t) = \frac{n_{2,-}}{\sqrt{1 + \frac{2}{\omega_0^2}(\Omega-\omega_0^2)\operatorname{sech}^2\left(\sqrt{\Omega-\omega_0^2}\,t\right)}}; \quad \left(\Omega > \omega_0^2\right), \tag{8.2.8}$$

where $n_{2,-}$ and Ω are degree of freedoms of the problem. The former allows us to change the material preserving the same intensity scattering properties as $n_1(t)$, and the latter can be employed to tailor the temporal width (Δt) and the index modulation contrast (Δn) of $n_2(t)$ (see Appendix C8, on page 275). The T-SUSY partner $n_2(t)$ is shown in Fig. 8.3(a) with $n_{2,-} = 2$ and $\Omega = 2\omega_0^2$. Moreover, we select $\omega_0 = 38$ rad/s to guarantee a low computational time of the numerical simulations of Eq. (8.2.1) (see Subsection 8.2.4). Nonetheless, the conclusions detailed below and in the next numerical example (Fig. 8.4) are found to be valid for any angular frequency.

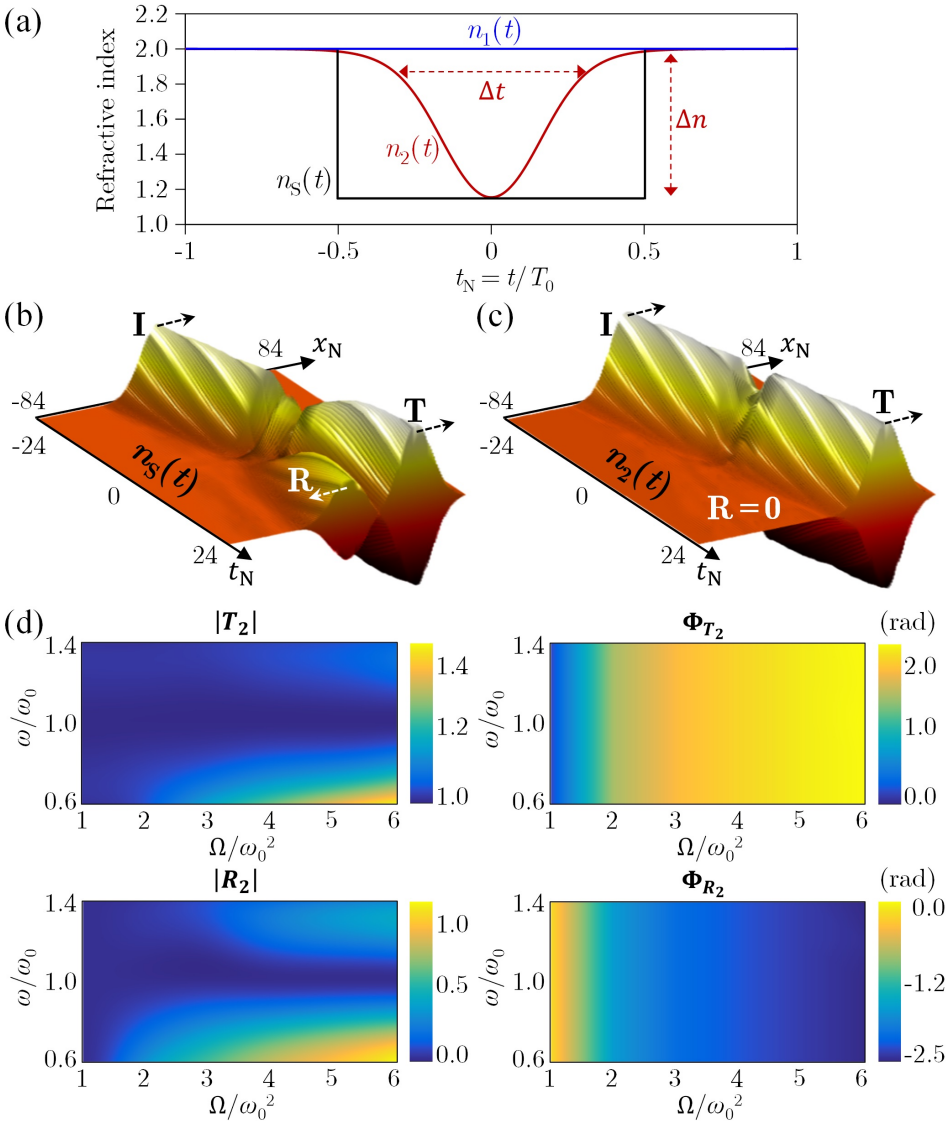

Figure 8.3. Transparent all-dielectric (all-magnetic) time-varying optical medium. (a) Reflecting step-index profile $n_S(t)$ and non-reflecting T-SUSY refractive index profiles $n_1(t)$ and $n_2(t)$. The temporal axis is normalized as $t_N = t/T_0$ with $T_0 = 2\pi/\omega_0$. (b,c) Spatio-temporal evolution of a Gaussian pulse propagated at $\omega = \omega_0$ through the time-varying medium described by (b) $n_S(t)$ and (c) $n_2(t)$. The x-axis is normalized as $x_N = x/\lambda$ with $\lambda = \lambda_0/n_{2,-}$ and $\lambda_0 = 2\pi c_0/\omega_0$. In contrast to (b), the absence of any reflected wave and the invariant amplitude of the transmitted wave in (c) demonstrate the transparent nature of $n_2(t)$. (d) Scattering coefficients $T_2 = |T_2|\exp(j\Phi_{T_2})$ and $R_2 = |R_2|\exp(j\Phi_{R_2})$ of $n_2(t)$ as a function of ω/ω_0 and Ω/ω_0^2.

It is clear that being n_1 constant, $R_1 = 0$. Thus, n_2 will also be reflectionless as demonstrated in Fig. 8.3(b,c) for a quasi-monochromatic optical pulse. Since T-SUSY is uncoupled from space, n_2 represents a new class of all-dielectric (all-magnetic), omnidirectional, isotropic, polarization-independent, and *transparent* media with real positive permittivity (permeability). This is illustrated in Fig. 8.1(a). To the best of our knowledge, no known spatially-varying material possesses all these features, including transformation media [331], complex-parameter materials [332], and spatial SUSY media [232]. The only previously reported time-varying reflectionless media required simultaneously time-varying permittivity and permeability values [325]. Our T-SUSY proposal is completely different, since it is valid for all-magnetic and all-dielectric materials, as demonstrated in Appendix A8 (see page 258). The latter are particularly important, as implementing temporal permittivity variations is extremely easier than implementing permeability ones. Another general feature of T-SUSY is that it is only exact for the design frequency $\omega = \omega_0$. Therefore, n_2 will be transparent ($|R_2| = 0$ and $|T_2| = 1$) for all directions and polarizations at ω_0, while a reflected wave will appear for $\omega \neq \omega_0$. Moreover, the spectral span for which n_2 is almost transparent ($|R_2| \simeq 0$ and $|T_2| \simeq 1$) can also be tailored via Ω (being considerably wide around $\Omega = \omega_0^2$), enabling us to generate custom-made transparent temporal windows within n_2 only for desired bands [Fig. 8.3(d)]. Notably, out of the transparent band, all waves are (partially) retroreflected along the input path, in contrast to spatial retroreflectors, in which the reflected path is parallel to, but different from, the input one [333].

Additionally, n_2 presents an outstanding unexpected property: the phases Φ_{R_2} and Φ_{T_2} of the reflection and transmission coefficients $R_2 = |R_2| \exp(j\Phi_{R_2})$, $T_2 = |T_2| \exp(j\Phi_{T_2})$ show a frequency-independent response, also tunable through Ω, as depicted in Fig. 8.3(d) and Fig. C8.3 (see page 276). This makes n_2 a perfect dynamically-reconfigurable phase shifter: polarization-independent, flat-frequency, reflectionless, and requiring a short time variation (allowing a dramatically reduced device length), paving the way to *ideal* ultra-compact modulators, e.g., at microwave frequencies. Contrariwise, optical-path-based phase shifters demand slow index variations (and therefore long devices) to be reflectionless, and are inherently frequency-dependent [334, 335]. In contrast, the T-SUSY device can simultaneously introduce the same phase shift over many spectral channels, which could be useful in, e.g., wavelength-division multiplexing and frequency combs. Furthermore, the nonlinear behavior of Φ_{T_2} may be employed to implement pulse shaping operations (see page 277). There exist additional media connectable to a constant index via T-SUSY (and thus reflectionless), such as the hyperbolic Rosen-Morse II (HRMII) potential, which has the advantage of allowing independent design control over Δn for a fixed $\Delta t \sim 20T_0$, enabling a technology-oriented adjustment of the index modulation contrast (see page 281).

8.2.2 Optical isolator

The analysis and synthesis functionalities of T-SUSY in the temporal scattering problem can be outstandingly extended by using isospectral transformations and shape invariant potentials (SIP). The theoretical details of both strategies are detailed in Appendix C8 (see pages 272 and 274). Specifically, isospectral constructions provide a powerful tool to obtain a multi-parameter family of time-varying refractive index profiles $\widetilde{n}(t; \eta_1, \ldots, \eta_m)$ with exactly the same scattering properties in module and phase as those of the original modulation $n(t)$. As an illustrative example, in Appendix C8 (page 278) we calculate an isospectral two-parameter family $\widetilde{n}(t; \eta_1, \eta_2)$ of a transparent refractive index profile $n(t)$ different from the case shown in Fig. 8.3. In this way, we demonstrate the possibility of building infinite transparent refractive index profiles in a simple and elegant way. On the other hand, the SIP strategy allows us to construct two T-SUSY refractive index profiles of the form $n_2(t; \boldsymbol{a}_1) \propto n_1(t; \boldsymbol{a}_2)$, where $\boldsymbol{a}_1$ and $\boldsymbol{a}_2$ are a set of real parameters ($\boldsymbol{a}_{1,2} \in \mathbb{R}^p$) related by a multivariate function $\boldsymbol{f} \in \mathcal{F}(\mathbb{R}^p, \mathbb{R}^p)$ of the form $\boldsymbol{a}_2 = \boldsymbol{f}(\boldsymbol{a}_1)$ (in our numerical examples, we will consider $p = 1$). As a result, the scattering coefficients are connected as $R_2(\boldsymbol{a}_1) = R_1(\boldsymbol{a}_2)$ and $T_2(\boldsymbol{a}_1) = T_1(\boldsymbol{a}_2)$. Likewise, the T-SUSY refractive index chain $\{n_i(t; \boldsymbol{a}_1)\}_{i=1}^m$ can be easily solved as $n_m(t; \boldsymbol{a}_1) \propto n_1(t; \boldsymbol{a}_m)$, with $R_m(\boldsymbol{a}_1) = R_1(\boldsymbol{a}_m)$, $T_m(\boldsymbol{a}_1) = T_1(\boldsymbol{a}_m)$ and $\boldsymbol{a}_m = (\mathring{\boldsymbol{f}})^{m-1}(\boldsymbol{a}_1)$ [e.g., $\boldsymbol{a}_3 = (\mathring{\boldsymbol{f}})^2(\boldsymbol{a}_1) = (\boldsymbol{f} \circ \boldsymbol{f})(\boldsymbol{a}_1) = \boldsymbol{f}(\boldsymbol{f}(\boldsymbol{a}_1))$]. As seen, we can directly analyze and design the temporal scattering problem of a large number of time-varying media.

As an example to demonstrate the benefits of SIP, consider the HRMII refractive index:

$$n_1\left(t;a_1\right)=\frac{n_{1,-}\left(a_1\right)}{\sqrt{1-\frac{2B}{\omega_0^2}+\frac{a_1(a_1+\alpha)}{\omega_0^2}\operatorname{sech}^2\left(\alpha t\right)-\frac{2B}{\omega_0^2}\tanh\left(\alpha t\right)}}, \tag{8.2.9}$$

with a_1, B and α real parameters. Equation (8.2.9) is shown in Fig. 8.4(a) with $a_1=40$, $B=a_1^2/10$, $\alpha=10$, $\omega_0=38$ rad/s and $n_{1,-}\left(a_1\right)=2$. Taking into account that $n_{1,-}\neq n_{1,+}$, we infer that $\omega_-\neq\omega_+$ from the Snell law. That is, we have a *non-reciprocal* system which performs a frequency down-conversion of the input signal as $\omega_+=(n_{1,-}/n_{1,+})\omega_-$. In addition, analyzing the scattering coefficients $R_1(a_1)$ and $T_1(a_1)$ [Fig. 8.4(b,c)], we observe that $n_1(t;a_1)$ is also reflectionless in a wide spectral band. Consequently, from this result emerges the possibility of constructing a polarization-independent optical isolator with an extremely large optical bandwidth. The principle of operation of the device is illustrated in Fig. 8.1(c). Unfortunately, the exotic shape of $n_1(t;a_1)$ and its maximal excursion (Δn) hampers its experimental implementation. In this context, T-SUSY allows us to overcome this drawback by using SIP. Concretely, Eq. (8.2.9) satisfies the SIP condition with $a_m=a_1-(m-1)\alpha$. In this way, we can generate different refractive index profiles with the same intensity scattering behavior and the same reflectionless spectral band as the original one, but with a smoother index variation and lower Δn. Taking $m=6$, we find a T-SUSY refractive index of the form $n_6(t;a_1)=\left(n_{6,-}\left(a_1\right)/n_{1,-}\left(a_6\right)\right)n_1(t;a_6)$ which provides a smooth index variation and minimizes Δn by using the same background material setting $n_{6,-}\left(a_1\right)=n_{1,-}\left(a_6\right)$. Along this line, note that: (*i*) the optical isolator can be implemented in different background media by selecting $n_{6,-}\left(a_1\right)\neq n_{1,-}\left(a_6\right)$, and (*ii*) the frequency down-conversion can be engineered with ω_0 and B. In Appendix C8 (page 282), we discuss in more detail the theory of the optical isolator and we include additional interesting SIP examples.

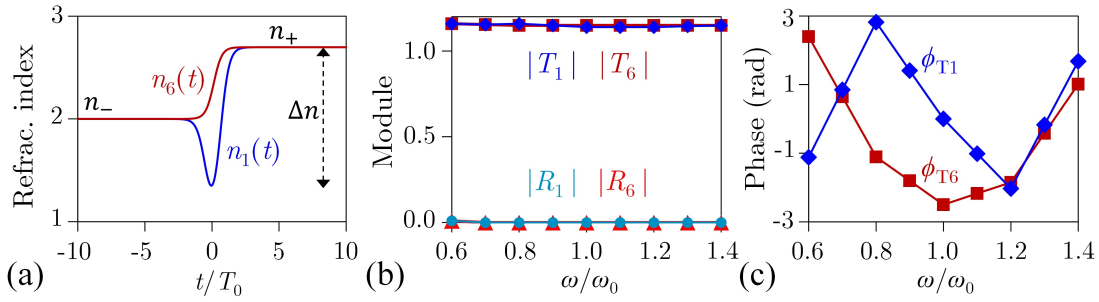

Figure 8.4. Polarization-independent optical isolator. (a) Supersymmetric refractive index profiles $n_1(t;a_1)$ and $n_6(t;a_1)$ calculated using Eq. (8.2.9) and SIP, respectively. The temporal axis is normalized as t/T_0, with $T_0=2\pi/\omega_-$ and $\omega_-\equiv\omega_0$. (b) Module and (c) phase of the scattering coefficients of $n_1(t;a_1)$ and $n_6(t;a_1)$ as a function of the frequency. The phase of $R_1(a_1)$ and $R_6(a_1)$ could not be numerically estimated because the non-reflecting behavior of $n_1(t;a_1)$ and $n_6(t;a_1)$ has a flat frequency response in an extremely large optical bandwidth. We could not observed any reflected wave in the numerical simulation when propagating wide-band optical pulses through the above time-varying media.

8.2.3 Heterogeneous media

In time-varying heterogeneous media, we will be able to decouple the spatial and temporal scattering problems by assuming as a necessary condition that the spatial and temporal evolution of n can be decoupled as $n\left(\boldsymbol{r},t\right)=n_{\mathrm{S}}\left(\boldsymbol{r}\right)n_{\mathrm{T}}\left(t\right)$. In such circumstances, the spatial and temporal evolution of the electromagnetic field involved in the initial wave equation ($\boldsymbol{D}$ or $\boldsymbol{B}$) is governed by decoupled wave equations and decoupled boundary conditions (see Appendix A8.2, page 258). Interestingly, this implies that: (*i*) the phase shifter and the optical isolator discussed before can be implemented in optical waveguides [as depicted in Figs. 8.1(b,c)], and (*ii*) any transparent $n_{\mathrm{T}}\left(t\right)$ temporal modulation *preserves* the intensity spatial scattering properties of $n_{\mathrm{S}}\left(\boldsymbol{r}\right)$ in the global system $n\left(\boldsymbol{r},t\right)$. Figure 8.5 illustrates this second remark: a heterogeneous medium perturbed by

a transparent time-varying modulation $n_{\mathrm{T}}(t)$ of the form $n(\boldsymbol{r},t) = n_{\mathrm{S}}(\boldsymbol{r})\, n_{\mathrm{T}}(t)$. As an example, consider the phase shifter of Fig. 8.1(b) operating at $\omega = \omega_0$. In such a case, the decoupling of the wave equations and boundary conditions of the spatial and temporal scattering, along with the transparent nature of $n_{\mathrm{T}}(t)$ at $\omega = \omega_0$, guarantee that the intensity of the reflected and transmitted waves, generated from the interaction of the incident wave with $n_{\mathrm{S}}(\boldsymbol{r})$, is time-invariant. However, the phase of the incident, reflected and transmitted waves can be temporally modified by the extra-phase induced by $n_{\mathrm{T}}(t)$.

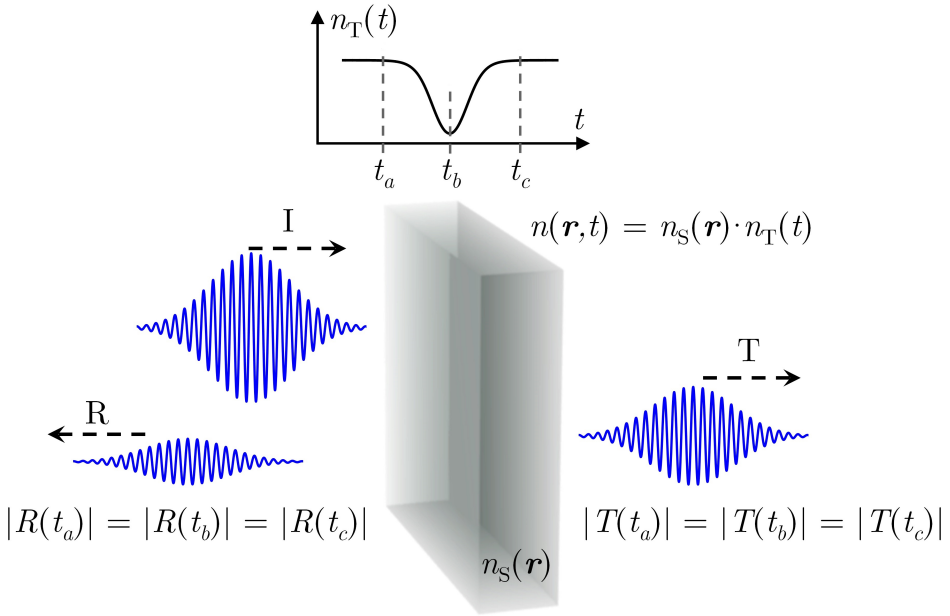

Figure 8.5. Transparent T-SUSY modulation $n_{\mathrm{T}}(t)$ preserving the intensity spatial scattering properties of heterogeneous media.

8.2.4 Methods

Numerical simulations of the temporal scattering (Figs. 8.3 and 8.4) have been performed by solving Eq. (8.2.1) with COMSOL Multiphysics taking $\omega_0 = 38$ rad/s and $c_0 = 1$ m/s to guarantee a low computational time. However, the conclusions derived from Figs. 8.3 and 8.4 are found to be valid for any value of ω_0 and c_0. Concretely, the results of the phase shifter (Fig. 8.3) are independent on the value of ω_0 and only depend on the ratio Ω/ω_0^2. Accordingly, they can be directly extrapolated to the range of THz. Furthermore, if we are interested in synthesizing the optical isolator (Fig. 8.4) with $\omega_0/2\pi$ in the range of THz, we must select an adequate value of the B parameter in Eq. (8.2.9) that preserves the ratio n_-/n_+ (see page 282 in Appendix C8 for more details).

8.3 Temporal SUSY and temporal waveguide

So far, we have extensively discussed the application of T-SUSY in time-varying non-dispersive optical media. Now, for the sake of completeness, we will analyze the consequences of T-SUSY in time-varying dispersive media. In the following, we will discuss the temporal dispersion case, whilst the spatial dispersion scenario will be analyzed in Appendix C8, on page 286.

8.3.1 Supersymmetric temporal waveguides

In this regard, consider a time-varying temporally dispersive medium such a temporal waveguide (TWG): two adjacent temporal index boundaries defining a (position-dependent) temporal index window, which can confine and carry optical pulses by temporal total internal reflection [336–338].

A TWG can be constructed, for instance, over a single-mode spatial waveguide inducing a moving temporal perturbation of the effective refractive index (n_{eff}) of its fundamental mode of the form $\Delta n_{\text{eff}}(t - z/v_{\text{B}})$, where v_{B} is the speed of the temporal perturbation propagating through the longitudinal axis of the spatial waveguide (e.g. the z-axis). In a co-moving reference frame, described by the coordinate transformation $\tau := t - z/v_{\text{B}}$, the propagation of an optical pulse inside the TWG is described by the time-domain equation (see Appendix D8):

$$\left(\partial_z + \Delta\beta_1\partial_\tau - j\frac{1}{2}\beta_2\partial_\tau^2 + j\beta_{\text{B}}(\tau)\right) A(z,\tau) = 0, \tag{8.3.1}$$

where A is the slowly-varying complex envelope of the optical pulse, β_1 and β_2 are respectively the inverse of the group velocity and the group-velocity dispersion of the fundamental mode, $\Delta\beta_1 := \beta_1 - 1/v_{\text{B}}$, $\beta_{\text{B}}(\tau) = k_0\Delta n_{\text{eff}}(\tau)$, $k_0 = \omega_0/c_0$, and ω_0 is the angular frequency of the optical carrier. In Appendix D8, on page 290, we include a detailed discussion about the *controversial* theory of TWGs reported in [336–338] starting from Maxwell's equations.

Interestingly, a TWG supports *temporal bound states*: continuous normalizable eigenfunctions ψ_n satisfying that $\psi_n(\tau \to \pm\infty) = 0$. These temporal bound states emerge from the above equation by assuming a modal solution of the form (see Appendix D8, page 298):

$$A(z,\tau) = \sum_{n=0}^{\infty} \psi_n(\tau) \exp\left(-j\frac{\Delta\beta_1}{\beta_2}\tau\right) \exp(-jK_n z), \tag{8.3.2}$$

which leads to the following eigenvalue equation with *discrete* spectrum ($n = 0, 1, 2, \ldots$):

$$\left(-\frac{\mathrm{d}^2}{\mathrm{d}\tau^2} + 2\frac{\beta_{\text{B}}(\tau)}{\beta_2}\right)\psi_n(\tau) = \left(2\frac{K_n}{\beta_2} + \frac{\Delta\beta_1^2}{\beta_2^2}\right)\psi_n(\tau). \tag{8.3.3}$$

Equation (8.3.3) matches Eq. (8.1.1) taking $\alpha = 1$, performing the relabeling $x \to \tau$, and identifying $V(x \to \tau) \equiv 2\beta_{\text{B}}(\tau)/\beta_2$ and $\Omega_n \equiv 2K_n/\beta_2 + \Delta\beta_1^2/\beta_2^2$. Therefore, we can apply T-SUSY to Eq. (8.3.3), which will give rise to a new class of TWGs with unprecedented potential functionalities such as mode conversion, mode filtering and dispersion engineering of temporal bound states, as well as for pulse shaping applications.

In order to illustrate these applications, we start by assuming, for simplicity, an analytically solvable TWG with a step-index temporal perturbation β_{B1} defined on a temporal window of width $2T_{\text{B}} = 660$ ps, and dispersion parameters $|\Delta\beta_1| = 10^{-3}$ ps/m and $\beta_2 = 0.06$ ps^2/m. Next, we calculate its unbroken T-SUSY TWG, defined by a temporal perturbation of the form:

$$\beta_{\text{B2}}(\tau) = \beta_{\text{B1}}(\tau) - \beta_2\frac{\mathrm{d}^2}{\mathrm{d}\tau^2}\ln\psi_0^{(1)}(\tau), \tag{8.3.4}$$

where $\psi_0^{(1)}$ is the ground state of β_{B1} (see Appendix D8, page 301). The temporal profile of β_{B1} and β_{B2} is depicted in Fig. 8.6(a). An unbroken T-SUSY relation between TWGs demands that $\widehat{\text{A}}^-$ annihilates $\psi_0^{(1)}$ in β_{B2} (i.e. $\widehat{\text{A}}^-\psi_0^{(1)} = 0$) and, accordingly, their bound states are connected as $\psi_n^{(2)} \propto \widehat{\text{A}}^-\psi_{n+1}^{(1)}$, with $\widehat{\text{A}}^- := \mathrm{d}/\mathrm{d}\tau - (\ln\psi_0^{(1)}(\tau))'$. As the modal analysis of both TWGs clearly shows in Figs. 8.6(b,c), $\psi_0^{(1)}$ has no SUSY counterpart in the eigenvalue spectrum of β_{B2}, i.e., $\psi_0^{(1)}$ is not phase-matched with any temporal bound state $\psi_n^{(2)}$. On the other hand, the temporal bound states $\psi_{n+1}^{(1)}$ are perfectly phase-matched with the temporal bound states $\psi_n^{(2)}$ in an extremely large optical bandwidth ($\Delta\nu \sim 0.5$, where $\nu \propto 1/\beta_2$ is the normalized frequency), provided that both TWGs are built on a dispersion-flattened spatial waveguide ($\mathrm{d}\beta_2/\mathrm{d}\omega \simeq 0$). Furthermore, Fig. 8.6(b) reveals that all the states $\psi_n^{(2)}$ have a normalized phase constant with a lower slope than $\psi_n^{(1)}$, which indicates that the T-SUSY TWG is less dispersive than the original one. Hence, T-SUSY allows us to engineer the dispersion properties of TWGs.

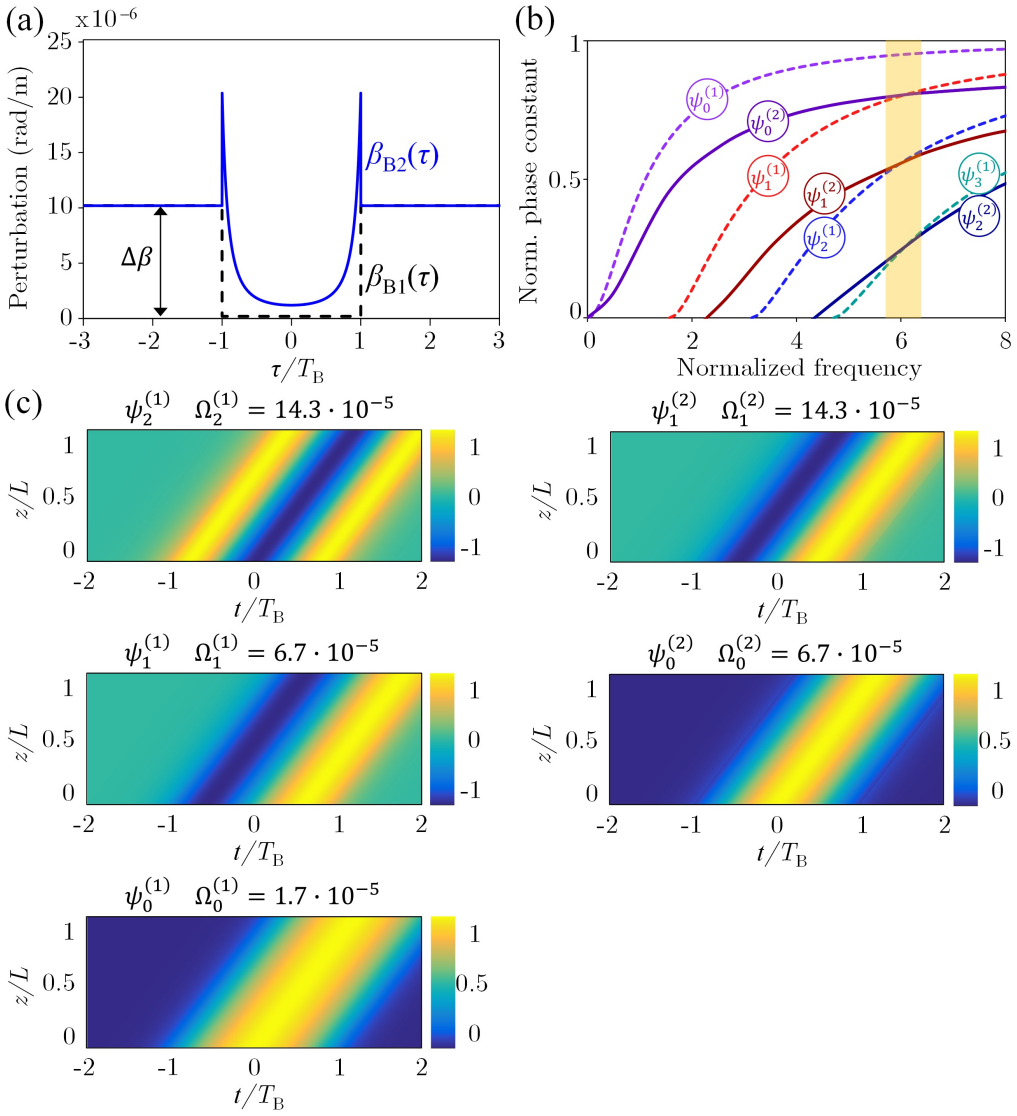

Figure 8.6. T-SUSY temporal waveguides (TWG). (a) Temporal perturbation profile of two T-SUSY TWGs. (b) Normalized dispersion diagram b-ν of the temporal bound states $\psi_n^{(1)}$ and $\psi_n^{(2)}$ of both TWGs, where b and ν are respectively the normalized phase constant and normalized frequency, defined as $b_n := 1 - K_n/\Delta\beta - \Delta\beta_1^2/(2\beta_2\Delta\beta)$ and $\nu^2 := 2T_B^2\Delta\beta/\beta_2$. Both TWGs operate at $\nu \simeq 6$. The orange area depicts the normalized phase-matching bandwidth $\Delta\nu \sim 0.5$, defined as the normalized frequency interval where $\Delta b_n \leq 0.2$ between T-SUSY bound states. (c) Spatio-temporal evolution of $\psi_n^{(1,2)}(t - z/v_B)$ and corresponding eigenvalue $\Omega_n^{(1,2)} = 2K_n^{(1,2)}/\beta_2 + \Delta\beta_1^2/\beta_2^2$ in Eq. (8.3.3). The temporal and spatial axes are normalized as t/T_B and z/L, where L is the length of the spatial waveguide over which the TWGs are propagated. Note that v_B and L are arbitrary parameters in the numerical simulation. (Colorbar: normalized amplitude).

Remarkably, a single-mode TWG can carry a soliton-like (shape-invariant) optical pulse in a dispersive medium, with the advantage of allowing an arbitrary pulse amplitude and duration, as well as a tunable propagation speed.[6] However, the pulse shape is that of the TWG fundamental mode, which has no nodes and is therefore strongly restricted. Using $\psi_m^{(1)}$ instead of $\psi_0^{(1)}$ to generate β_{B2} in Eq. (8.3.4), we could have the possibility of building a T-SUSY single-mode TWG

[6]Working with multi-mode TWGs poses the risk of unintentionally exciting multiple modes, deteriorating the pulse shape, e.g., due to multi-mode interference [337, 338].

with an m-node fundamental mode (provided that β_{B2} is free of singularities), widening the range of achievable soliton shapes. Moreover, single-mode TWGs reshape the profile of any exciting pulse until matching the fundamental mode [337]. Thus, T-SUSY TWGs are versatile and robust shape-protecting pulse carriers with profile conversion capabilities.

8.3.2 The temporal photonic lantern

Moreover, combining close-packed T-SUSY TWGs moving with the same speed in a given spatial waveguide, the above features can be exploited for mode conversion and mode filtering of temporal bound states, as well as for pulse shaping applications. The idea is illustrated in Fig. 8.7(a), where two parallel T-SUSY TWGs of width $2T_B = 660$ ps and separated in time $T_B/4$ can perform all the aforementioned applications. Such a device will be referred to as a temporal photonic lantern (TPL): a dispersive time-varying device which generates temporal supermodes from the linear combination of degenerate temporal bound states of close-packed TWGs.

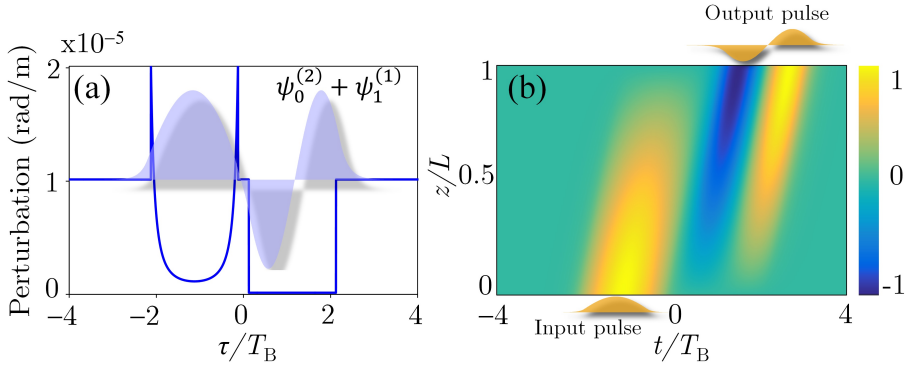

Figure 8.7. Temporal photonic lantern (TPL). (a) Temporal perturbation profile $\beta_B(\tau) = k_0 \Delta n_{eff}(\tau)$ of the TPL (constructed using two T-SUSY TWGs) and its temporal supermode (blue area) generated from the perfect phase-matching between the temporal bound states $\psi_0^{(2)}$ and $\psi_1^{(1)}$ of both TWGs. (b) Pulse shape transformation inspired by a mode conversion between degenerate temporal bound states of the T-SUSY TWGs. (Colorbar: normalized amplitude).

In our example [Fig. 8.7(a)], we can observe a temporal supermode emerging from the perfect phase-matching between the isolated bound states $\psi_0^{(2)}$ and $\psi_1^{(1)}$. Consequently, if we stimulated this supermode, we would obtain an optical pulse of width $4T_B + T_B/4$ exhibiting the exotic shape shown in Fig. 8.7(a). In a similar way, we could stimulate other supermodes of the TPL to construct optical pulses with new exotic shapes arising from the linear combination $\psi_n^{(2)} \pm \psi_{n+1}^{(1)}$. This could be of great interest for optical wavelet transforms, coherent laser control of physicochemical and quantum-mechanical processes, and spectrally selective nonlinear microscopy among other application areas [339–341].

In this scenario, we can also benefit from the mode conversion functionality of the TPL to build a robust pulse-shape transformer [Fig. 8.1(d)]. As demonstrated in Appendix D8 (see page 301) using a coupled-mode theory (CMT) specifically developed for parallel TWGs, the power of the temporal bound state $\psi_0^{(2)}$ of the T-SUSY TWG can be completely transferred to the temporal bound state $\psi_1^{(1)}$ of the step-index TWG. Hence, as we have numerically verified using this CMT [Fig. 8.7(b)], if an external optical pulse launched into the T-SUSY TWG is able to stimulate exclusive the $\psi_0^{(2)}$ bound state,[7] then this will be transformed into an optical pulse with shape $\psi_1^{(1)}$ at the TPL output. Achieving the required perfect phase-matching between bound states of

[7] To this end, in Fig. 8.1(d), we propose to use a parallel single-mode spatial waveguide WG1 with a propagation constant of its fundamental mode matched to the propagation constant of $\psi_0^{(2)}$. In such a scenario, if WG1 propagates an optical pulse with the same shape and spectrum of $\psi_0^{(2)}$, then we will be able to stimulate exclusively the ground state of the T-SUSY TWG propagated by WG2.

different order without T-SUSY typically demands multi-mode adjacent TWGs of different width, whilst T-SUSY permits an independent control over this parameter and generally presents a much larger normalized phase-matching bandwidth $\Delta\nu$ (in the same way as in the unbroken SUSY mode converter reported in Fig. 7.5 of Chapter 7). This inherently implies a higher tolerance to fluctuations in T_{B} and Δn_{eff} in TPLs constructed on T-SUSY TWGs.

8.3.3 Methods

The modal analysis of the TWGs and the TPL shown in Fig. 8.6 and Fig. 8.7(a) has been calculated with CST Microwave Studio and MATLAB by using the analogy reported in [337] between a dielectric slab waveguide and a TWG. On the other hand, the numerical simulation of Fig. 8.7(b), based on the CMT derived in Appendix D8 for parallel TWGs, was performed in MATLAB. In addition, in Appendix D8, we include a detailed discussion about the numerical methods employed in Figs. 8.6 and 8.7 (see pages 299 and 304).

8.4 Conclusions

Overall, these results generalize the foundations of SUSY QM to the time domain, unveiling the temporal supersymmetric nature of Maxwell's equations and, consequently, leading to the emergence of an entire field of research within optics, as well as to a new photonic design toolbox.

Interestingly, since T-SUSY is uncoupled from space, all the results presented herein are found to be omnidirectional and polarization-independent. In particular, using Eq. (8.2.7), we find a simple strategy to calculate the reflection and transmission coefficients of time-varying media which can also be used to design temporal modulations of the refractive index with desired scattering coefficients. Remarkably, this finding is found to be valid for all-dielectric, all-magnetic materials or a combination of both. As a byproduct, we demonstrate a new class of transparent media which can be employed, for instance, to design a reconfigurable transparent phase shifter with frequency-independent phase response and a broadband optical isolator.

In view of the growing interest in photonic integrated circuits, we expect that these results will aid the development of ultra-compact optical modulators using high refractive index excursions, which may reduce the phase shifter length to a few micrometers. In practice, in contrast to the spatial SUSY applications reported in previous works, the results outlined above relax the need for controlling the polarization state of the input signal and the refractive index profile in space, which always involves complex fabrication process [228,229,234]. However, the technological difficulties associated with the implementation of high refractive index excursions in time can be circumvented by using dynamically reconfigurable refractive index materials such as germanium-antimony-tellurium, indium antimonide and vanadium dioxide [342, 343], large optical nonlinear media such as indium tin oxide [344], or metamaterials [345, 346]. Along this line, note that Eq. (8.2.7) allows us to engineer the scattering properties of time-varying media by using different background materials.

In addition, the application of T-SUSY in temporal waveguides and temporal photonic lanterns builds a bridge to develop new optical devices implementing pulse shaping functionalities, as well as mode conversion and mode filtering of temporal bound states generated, e.g., from the pulse-to-pulse interaction during the cross-phase modulation (XPM) effect [347]. A traveling-wave electro-optic phase modulator driven by microwave pulses or, alternatively, the XPM process can be used in the laboratory to generate the moving temporal perturbations required by such devices [336,337].

Finally, it is worth mentioning the possibility of extrapolating our results to acoustics. A temporal Helmholtz equation formally equal to Eq. (8.2.2) can be found in acoustics by replacing respectively the electric or magnetic flux density by the sound pressure (see Appendix E8, on page 306). Consequently, the scattering results presented in this work can be directly transferred to this branch of physics. Moreover, acoustic temporal waveguides and temporal acoustic lanterns can also be designed with T-SUSY in the same way as in photonics, i.e., considering a moving temporal perturbation of the speed of sound propagating through an acoustic spatial waveguide.

Appendix A8: Time-varying optical systems

In this appendix, we include some fundamentals notes on time-varying optical systems which are crucial to gain clarity in the main results of this chapter.

A8.1 Optical wave equations

The theory of T-SUSY applied to the temporal scattering problem revolves around the optical wave equation given by Eq. (8.1.2), which accounts for the propagation of electromagnetic waves in the materials specified in the main text provided that we assume specific necessary conditions on the constitutive parameters, i.e., the electric permittivity ε_{r} and the magnetic permeability μ_{r}. Concretely, as we will see in this subsection, Eq. (8.1.2) describes the propagation of light in dielectric (or magnetic), linear, isotropic, heterogeneous, time-varying, non-dispersive media; and leads to the temporal Helmholtz Eq. (8.2.2) in all these cases.

Let us start by discussing the *homogeneous* time-varying all-dielectric case ($\mu_{\mathrm{r}} = 1$). In such media, it is straightforward to demonstrate by combining Faraday's, Ampère's and Gauss's laws (applying the curl operator in Faraday's law) that the exact time-domain vector wave equation for the analytic representation of the electric flux density $\boldsymbol{D}$ takes the form:

$$\left(\triangle - \frac{n^2\left(t\right)}{c_0^2} \partial_t^2 \right) \boldsymbol{D}\left(\boldsymbol{r},t\right) = \boldsymbol{0}, \tag{A8.1}$$

with $n^2\left(t\right) = \varepsilon_{\mathrm{r}}\left(t\right)$. Note that Eq. (A8.1) is a specific case of Eq. (8.1.2) and is reduced to Eq. (8.2.1) when assuming a single component in the electric flux density.

The analysis of homogeneous time-varying all-magnetic materials ($\varepsilon_{\mathrm{r}} = 1$) can be carried out by the same exact wave equation as Eq. (A8.1) replacing $\boldsymbol{D}$ by the magnetic flux density $\boldsymbol{B}$ and taking $n^2\left(t\right) = \mu_{\mathrm{r}}\left(t\right)$. However, the case of homogeneous time-varying dielectric and magnetic materials $[n^2\left(t\right) = \varepsilon_{\mathrm{r}}\left(t\right)\mu_{\mathrm{r}}\left(t\right)]$ requires to assume a slowly-varying temporal evolution in μ_{r} (ε_{r}) to obtain an approximate wave equation formally equal to Eq. (A8.1) for $\boldsymbol{D}$ ($\boldsymbol{B}$).[8]

On the other hand, we will be able to apply T-SUSY to *heterogeneous* time-varying all-dielectric (all-magnetic) media, with $n^2\left(\boldsymbol{r},t\right) = \varepsilon_{\mathrm{r}}\left(\boldsymbol{r},t\right)$ (with $n^2\left(\boldsymbol{r},t\right) = \mu_{\mathrm{r}}\left(\boldsymbol{r},t\right)$), starting from an exact wave equation for $\boldsymbol{D}$ ($\boldsymbol{B}$) of the form of Eq. (8.1.2), but assuming as necessary conditions: (i) the spatial and temporal evolution of n must be decoupled as $n\left(\boldsymbol{r},t\right) = n_{\mathrm{S}}\left(\boldsymbol{r}\right) n_{\mathrm{T}}\left(t\right)$, and (ii) n_{S} must vary in the same direction as the direction of $\boldsymbol{D}$ ($\boldsymbol{B}$) or, otherwise, we must start from the exact wave equation (which also applies to $\boldsymbol{B}$):

$$\nabla \times \nabla \times \left(\frac{1}{n^2\left(\boldsymbol{r},t\right)} \boldsymbol{D}\left(\boldsymbol{r},t\right) \right) + \frac{1}{c_0^2} \partial_t^2 \boldsymbol{D}\left(\boldsymbol{r},t\right) = \boldsymbol{0}. \tag{A8.2}$$

A8.2 Spatial and temporal solution

In all the aforementioned media, assuming the electromagnetic field under analysis $\boldsymbol{F} \in \{\boldsymbol{D},\boldsymbol{B}\}$ of the form:

$$\boldsymbol{F}\left(\boldsymbol{r},t\right) = \psi\left(t\right) \boldsymbol{\Phi}\left(\boldsymbol{r}\right), \tag{A8.3}$$

and decoupling the refractive index as $n^2\left(\boldsymbol{r},t\right) = n_{\mathrm{S}}^2\left(\boldsymbol{r}\right) n_{\mathrm{T}}^2\left(t\right) = n_{\mathrm{S}}^2\left(\boldsymbol{r}\right)\left[n_{-}^2 + \Delta n_{\mathrm{T}}^2\left(t\right)\right]$, with $n_{\mathrm{S}}^2\left(\boldsymbol{r} \to -\infty\right) := 1$ and $\Delta n_{\mathrm{T}}^2\left(t \to -\infty\right) := 0$, we can infer from the starting wave equation [Eq. (8.1.2) or Eq. (A8.2)] that $n_{\mathrm{T}}^2\left(t\right)\psi''\left(t\right)/\psi\left(t\right) = \gamma^2 \in \mathbb{C},\ \forall t \in \overline{\mathbb{R}}$. Evaluating the above expression at $t \to -\infty$, we find that $\gamma = jn_{-}\omega_0$, yielding Eq. (8.2.2) of the main text.

[8] The slowly-varying temporal evolution in a constitutive parameter, e.g. μ_{r}, requires to assume that $\delta_t \mu_{\mathrm{r}} \ll \mu_{\mathrm{r}}\left(t\right)$ in $\delta t \sim 2\pi/\omega_0$, where $\delta_t \mu_{\mathrm{r}} := |\mu_{\mathrm{r}}\left(t+\delta t\right) - \mu_{\mathrm{r}}\left(t\right)|$. In a similar way, the slowly-varying spatial evolution requires to assume that $\delta_{\boldsymbol{r}} \mu_{\mathrm{r}} \ll \mu_{\mathrm{r}}\left(\boldsymbol{r},t\right)$ in $|\delta \boldsymbol{r}| \sim \lambda_0$, where $\delta_{\boldsymbol{r}} \mu_{\mathrm{r}} := |\mu_{\mathrm{r}}\left(\boldsymbol{r}+\delta\boldsymbol{r},t\right) - \mu_{\mathrm{r}}\left(\boldsymbol{r},t\right)|$ and λ_0 is the maximum wavelength of the problem. Along this line, also note that we assume positive-real constitutive parameters.

Since ψ must be twice differentiable, ψ and ψ' must be necessarily continuous functions. These are the intrinsic *boundary conditions* of the temporal scattering and note that: (i) are invariant to changes in the polarization, which demonstrates that the temporal scattering is polarization-independent in all the analyzed cases, and (ii) are decoupled from the spatial solution $\boldsymbol{\Phi}$ and its corresponding boundary conditions (see below).

Specifically, $\boldsymbol{\Phi}$ is governed by different wave equations depending on the analyzed case. In homogeneous media, starting from a wave equation formally equal to Eq. (A8.1) for $\boldsymbol{F}$ and assuming propagation along the $\hat{u}_x$ direction, we find that $\boldsymbol{\Phi}$ satisfies the ODE $(\mathrm{d}^2/\mathrm{d}x^2 + k_0^2 n_-^2)\boldsymbol{\Phi}(x) = \mathbf{0}$. Thus, $\boldsymbol{\Phi}(x) = \exp(-jk_0 n_- x)\,\hat{u}_y$. In heterogeneous media, we contemplate two different scenarios:

1. If n_{S} varies in the same direction as the direction of $\boldsymbol{F}$, the separation of variables must be applied to Eq. (8.1.2), which leads to the PDE $(\triangle + k_0^2 n_-^2 n_{\mathrm{S}}^2(\boldsymbol{r}))\boldsymbol{\Phi}(\boldsymbol{r}) = \mathbf{0}$. This scenario corresponds, for instance, with an optical waveguide propagating a TE (TM) mode when $\boldsymbol{F} = \boldsymbol{D}$ ($\boldsymbol{F} = \boldsymbol{B}$). Hence, assuming non-conductive media, the spatial boundary conditions emerge from the continuity of $\boldsymbol{\Phi}$ in the interface that separates the core and cladding regions of the waveguide.

2. Otherwise, the separation of variables must be applied to Eq. (A8.2). In such a case, $\boldsymbol{\Phi}$ is governed by the wave equation:

$$\triangle\left(\frac{1}{n_{\mathrm{S}}^2(\boldsymbol{r})}\boldsymbol{\Phi}(\boldsymbol{r})\right) - \nabla\left(\nabla\left(\frac{1}{n_{\mathrm{S}}^2(\boldsymbol{r})}\right)\cdot\boldsymbol{\Phi}(\boldsymbol{r})\right) + k_0^2 n_-^2\,\boldsymbol{\Phi}(\boldsymbol{r}) = \mathbf{0}, \tag{A8.4}$$

   This case corresponds, e.g., with Fig. 8.5, where we can observe a spatial scattering problem coexisting with the temporal scattering. The boundary conditions of the spatial scattering are the spatial continuity of the tangential component of $\boldsymbol{E}$ and $\boldsymbol{H}$ at the spatial interfaces of the problem. In terms of the $\boldsymbol{\Phi}$ function, this implies to evaluate the continuity of the tangential component of $\boldsymbol{\Phi}/n_{\mathrm{S}}^2$.

Finally, it is worth mentioning that T-SUSY systems share the same spatial solution ($\boldsymbol{\Phi}^{(2)} = \boldsymbol{\Phi}^{(1)}$), but possess a different temporal evolution ($\psi^{(2)} \neq \psi^{(1)}$). Consequently, the eigenvalue degeneracy and the scattering properties between both optical systems are preserved *if and only if* both $\psi^{(1)}$ and $\psi^{(2)}$ fulfill the aforementioned temporal boundary conditions. Later, on page 278, we will see a numerical example where this necessary and sufficient condition is violated.

A8.3 Lorentz oscillator model

The optical wave equations discussed before are derived from Faraday's and Ampère's laws by using a *heuristic* proposal of the constitutive relations. For instance, in the homogeneous all-dielectric case, we heuristically assume that the relation between the electric field strength and the electric flux density is of the form $[n^2(t) = \varepsilon_{\mathrm{r}}(t)]$:

$$\boldsymbol{D}(\boldsymbol{r},t) = \varepsilon_0 n^2(t)\,\boldsymbol{E}(\boldsymbol{r},t). \tag{A8.5}$$

However, in this subsection, we argue about the possibility of inferring the constitutive relations from a microscopic model, such as the naive (yet fortunate) Lorentz oscillator model, accounting for the light-matter interactions circumventing the complex quantum-mechanical treatment [348].

Let us illustrate this for the constitutive relation given by Eq. (A8.5). In its purely classical-mechanical interpretation, the Abraham-Lorentz equation can be recast in isotropic time-varying homogeneous dielectric media as:

$$m\partial_t^2 d(\boldsymbol{r},t) = q\mathcal{E}(\boldsymbol{r},t) - k(t)\,d(\boldsymbol{r},t) - \zeta\partial_t d(\boldsymbol{r},t), \tag{A8.6}$$

where d is the magnitude of the displacement vector $\boldsymbol{d}$ of the electric dipole (pointing from the negative charge to the positive charge), q is the positive charge of the dipole, m is the mass of the positive or negative charge of the dipole (assumed to be equal), $\mathcal{E}$ is the magnitude of the *incident* electric field strength (real representation) impinging onto the optical medium, ζ is a real constant introduced *ad hoc* in the model to describe the dielectric losses, and k is the elastic constant of the restoring force, which is assumed to be homogeneous and time-varying in line with our scenario.

Bearing in mind that we have considered in Section 8.2 non-dispersive media, we can neglect the dispersive terms of the above equation, emerged from the time-derivative terms. In this way, Eq. (A8.6) is reduced to $k(t)\, d(\boldsymbol{r},t) = q\mathcal{E}(\boldsymbol{r},t)$, which becomes in the frequency domain when using the Fourier transform:

$$\widetilde{k}(\omega) * \widetilde{d}(\boldsymbol{r},\omega) = 2\pi q \widetilde{\mathcal{E}}(\boldsymbol{r},\omega). \tag{A8.7}$$

Now, consider the inverse element of $\widetilde{k}$ in the unitary and commutative ring $(\mathcal{F}(\mathbb{R},\mathbb{C}),+,*)$ with zero divisors. That is, consider the element $\widetilde{k}^{-1}$ satisfying that $\widetilde{k}^{-1} * \widetilde{k} = \delta$, where δ is the Dirac delta function, i.e., the identity element of the ring for the second internal operation.[9] Thus, applying $\widetilde{k}^{-1}$ to both sides of the above equation, we find that:

$$\widetilde{d}(\boldsymbol{r},\omega) = 2\pi q \widetilde{k}^{-1}(\omega) * \widetilde{\mathcal{E}}(\boldsymbol{r},\omega). \tag{A8.8}$$

The electric polarization density $\widetilde{\boldsymbol{\mathcal{P}}}(\boldsymbol{r},\omega)$ measures the quantity and strength of the dipoles induced by the incident field. Therefore, idealizing the material as a collection of electric dipoles having a dipole moment $q\widetilde{\boldsymbol{d}}(\boldsymbol{r},\omega)$, we can write:

$$\widetilde{\boldsymbol{\mathcal{P}}}(\boldsymbol{r},\omega) = Nq\widetilde{\boldsymbol{d}}(\boldsymbol{r},\omega) = 2\pi N q^2 \widetilde{k}^{-1}(\omega) * \widetilde{\boldsymbol{\mathcal{E}}}(\boldsymbol{r},\omega) \equiv \frac{1}{2\pi}\varepsilon_0 \widetilde{\chi}^{(1)}(\omega) * \widetilde{\boldsymbol{\mathcal{E}}}(\boldsymbol{r},\omega), \tag{A8.9}$$

where N is the density of dipoles (in m^{-3}) and is homogeneous in our case. Finally, in the time domain, we find a constitutive relation of the desired form:[10]

$$\boldsymbol{\mathcal{D}}(\boldsymbol{r},t) = \varepsilon_0 \boldsymbol{\mathcal{E}}(\boldsymbol{r},t) + \boldsymbol{\mathcal{P}}(\boldsymbol{r},t) = \varepsilon_0 \left(1 + \chi^{(1)}(t)\right) \boldsymbol{\mathcal{E}}(\boldsymbol{r},t) \equiv \varepsilon_0 n^2(t)\, \boldsymbol{\mathcal{E}}(\boldsymbol{r},t), \tag{A8.10}$$

which is in line with Eq. (A8.5) when using the analytic representation of the fields. Proceeding in a similar manner, we can also derive the constitutive relation for the heterogeneous case. In all-magnetic and dielectric&magnetic materials, the constitutive relations can also be discussed from the corresponding microscopic models [349, 350] instead of using heuristic proposals.

A8.4 Anisotropic and conductive media

In the main text, we have not considered anisotropic or conductive media for the sake of simplicity. Nonetheless, it is interesting to highlight that it is also plausible to apply T-SUSY in these media. In this subsection we discuss about this possibility.

Firstly, let us consider an anisotropic case. The wave equations of Appendix A8.1 can be generalized to non-dispersive anisotropic media by replacing the scalar constitutive parameters by tensors. In the all-dielectric case $[\boldsymbol{\mu}_{\mathrm{r}}(\boldsymbol{r},t) = \mathbf{I}_3]$, the most general expression of the exact wave equation is similar to Eq. (A8.2) but replacing $n^2(\boldsymbol{r},t)$ by the relative electric permittivity tensor $\boldsymbol{\epsilon}_{\mathrm{r}}(\boldsymbol{r},t)$:

$$\nabla \times \nabla \times \left(\boldsymbol{\epsilon}_{\mathrm{r}}^{-1}(\boldsymbol{r},t)\, \boldsymbol{D}(\boldsymbol{r},t)\right) + \frac{1}{c_0^2}\partial_t^2 \boldsymbol{D}(\boldsymbol{r},t) = \mathbf{0}. \tag{A8.11}$$

The same wave equation applies to all-magnetic media $[\boldsymbol{\epsilon}_{\mathrm{r}}(\boldsymbol{r},t) = \mathbf{I}_3]$ if $\boldsymbol{D}$ is replaced by $\boldsymbol{B}$ and $\boldsymbol{\epsilon}_{\mathrm{r}}(\boldsymbol{r},t)$ by the relative magnetic permeability tensor $\boldsymbol{\mu}_{\mathrm{r}}(\boldsymbol{r},t)$. The temporal Helmholtz equation over which we apply T-SUSY to study the temporal scattering in the main text [Eq. (8.2.2)] emerges

[9] The function $\widetilde{k}^{-1}$ can be straightforwardly found from the relation $\widetilde{k}^{-1}(\omega) * \widetilde{k}(\omega) = \delta(\omega)$. Applying the inverse Fourier transform, we find that $k^{-1}(t) \cdot k(t) = 1/(2\pi)$. Hence, $k^{-1}(t) \propto 1/k(t)$. In addition, it should be noticed that k^{-1} is a nonsingular function if we assume that k has no zeros.

[10] The refractive index profile is derived from Eq. (A8.9) of the form $n(t) = \sqrt{1 + 2\pi N q^2/(\varepsilon_0 k(t))}$.

from the above wave equation when: (i) applying separation of variables in the electromagnetic field under analysis $\boldsymbol{F} \in \{\boldsymbol{D}, \boldsymbol{B}\}$ as indicated by Eq. (A8.3) and, (ii) assuming that $\boldsymbol{\epsilon}_{\mathrm{r}}(\boldsymbol{r}, t)$ and $\boldsymbol{\mu}_{\mathrm{r}}(\boldsymbol{r}, t)$ can be decoupled as:

$$\boldsymbol{\epsilon}_{\mathrm{r}}(\boldsymbol{r}, t) = \varepsilon_{\mathrm{T}}(t)\, \boldsymbol{\epsilon}_{\mathrm{S}}(\boldsymbol{r}); \tag{A8.12}$$

$$\boldsymbol{\mu}_{\mathrm{r}}(\boldsymbol{r}, t) = \mu_{\mathrm{T}}(t)\, \boldsymbol{\mu}_{\mathrm{S}}(\boldsymbol{r}), \tag{A8.13}$$

with ε_{T} and μ_{T} being scalar functions. Under the previous assumptions, note that the temporal solution of the electromagnetic fields is completely uncoupled from space (as well as their corresponding intrinsic boundary conditions), which demonstrates that the temporal scattering is polarization-independent in any optical medium with a nontensorial nature of ε_{T} and μ_{T}.

Now, let us focus our attention on conductive media with constitutive relations of the form:

$$\boldsymbol{D}(\boldsymbol{r}, t) = \varepsilon_0 \varepsilon_{\mathrm{r}}(t)\, \boldsymbol{E}(\boldsymbol{r}, t); \quad \boldsymbol{B}(\boldsymbol{r}, t) = \mu_0 \boldsymbol{H}(\boldsymbol{r}, t); \quad \boldsymbol{J}_{\mathrm{c}}(\boldsymbol{r}, t) = \sigma(t)\, \boldsymbol{E}(\boldsymbol{r}, t), \tag{A8.14}$$

where $\boldsymbol{J}_{\mathrm{c}}$ is the conduction current density associated with the free electric charges. Here, the macroscopic Maxwell equations [Eqs. (1.5.1)-(1.5.4)] must be restated as:[11]

$$\nabla \times \boldsymbol{E}(\boldsymbol{r}, t) = -\partial_t \boldsymbol{B}(\boldsymbol{r}, t); \tag{A8.15}$$

$$\nabla \times \boldsymbol{H}(\boldsymbol{r}, t) = \boldsymbol{J}_{\mathrm{c}}(\boldsymbol{r}, t) + \partial_t \boldsymbol{D}(\boldsymbol{r}, t); \tag{A8.16}$$

$$\nabla \cdot \boldsymbol{D}(\boldsymbol{r}, t) = \rho_{\mathrm{c}}(\boldsymbol{r}, t); \tag{A8.17}$$

$$\nabla \cdot \boldsymbol{B}(\boldsymbol{r}, t) = 0, \tag{A8.18}$$

where ρ_{c} is the electric charge density connected with $\boldsymbol{J}_{\mathrm{c}}$ via the law of charge conservation $\nabla \cdot \boldsymbol{J}_{\mathrm{c}} + \partial_t \rho_{\mathrm{c}} = 0$. From this equation, we find that ρ_{c} is homogeneous:

$$\rho_{\mathrm{c}}(t) \propto \exp\left(-\int_{-\infty}^{t} \frac{\sigma(\tau)}{\varepsilon_0 \varepsilon_{\mathrm{r}}(\tau)} \mathrm{d}\tau\right). \tag{A8.19}$$

Hence, taking into account that $\nabla \rho_{\mathrm{c}} = \boldsymbol{0}$, the following *exact* wave equation emerges when combining Faraday's and Ampère's laws:

$$\left[\triangle - \frac{\varepsilon_{\mathrm{r}}(t)}{c_0^2}\partial_t^2 - \frac{\sigma(t)}{\varepsilon_0 c_0^2}\partial_t - \frac{\varepsilon_{\mathrm{r}}(t)}{\varepsilon_0 c_0^2}\left(\frac{\sigma(t)}{\varepsilon_{\mathrm{r}}(t)}\right)'\right] \boldsymbol{D}(\boldsymbol{r}, t) = \boldsymbol{0}. \tag{A8.20}$$

Without loss of generality, assuming that the electromagnetic energy propagates in the direction $\hat{u}_x$, we can apply separation of variables of the form $\boldsymbol{D}(\boldsymbol{r}, t) = \phi(x)\, \varphi(t)\, \hat{u}_y$. The spatial solution is found to be $\phi(x) = \exp(-jk_0\sqrt{\varepsilon_{\mathrm{r},-}}\, x)$, and the temporal solution obeys the relation:

$$\left[\frac{\mathrm{d}^2}{\mathrm{d}t^2} + \frac{\sigma(t)}{\varepsilon_0 \varepsilon_{\mathrm{r}}(t)}\frac{\mathrm{d}}{\mathrm{d}t} + \omega_0^2 \frac{\varepsilon_{\mathrm{r},-}}{\varepsilon_{\mathrm{r}}(t)} + \frac{1}{\varepsilon_0}\left(\frac{\sigma(t)}{\varepsilon_{\mathrm{r}}(t)}\right)'\right] \varphi(t) = 0, \tag{A8.21}$$

with $\varepsilon_{\mathrm{r},-} := \varepsilon_{\mathrm{r}}(t \to -\infty)$. Interestingly, this second-order ODE can be transformed into a temporal Helmholtz equation by using the transformation method detailed in Subsection 6.14.1. Using this procedure, we find the following temporal Helmholtz equation:

$$\left[\frac{\mathrm{d}^2}{\mathrm{d}t^2} + b_2(t) - \frac{1}{2}b_1'(t) - \frac{1}{4}b_1^2(t)\right] \psi(t) = 0, \tag{A8.22}$$

[11] Equations (A8.15)-(A8.18) are found from Eqs. (1.5.1)-(1.5.4) using the analytic representation of the fields and the constitutive relations Eq. (1.5.5). Along this line, we should also take into account that the total charge and current densities must be separated in free and bound charges and currents, i.e., $\rho = \rho_{\mathrm{f}} + \rho_{\mathrm{b}}$ and $\boldsymbol{\mathcal{J}} = \boldsymbol{\mathcal{J}}_{\mathrm{f}} + \boldsymbol{\mathcal{J}}_{\mathrm{b}}$. In this context, the free current density $\boldsymbol{\mathcal{J}}_{\mathrm{f}}$ is related to the conduction current density $\boldsymbol{\mathcal{J}}_{\mathrm{c}}$ as $\boldsymbol{\mathcal{J}}_{\mathrm{f}} = \boldsymbol{\mathcal{J}}_{\mathrm{c}} + \nabla \times \boldsymbol{\mathcal{M}}$. Moreover, from the law of charge conservation, it should be noticed that:

$$\rho_{\mathrm{f}}(\boldsymbol{r}, t) = -\int_{-\infty}^{t} \nabla \cdot \boldsymbol{\mathcal{J}}_{\mathrm{f}}(\boldsymbol{r}, \tau)\, \mathrm{d}\tau = -\int_{-\infty}^{t} \nabla \cdot \boldsymbol{\mathcal{J}}_{\mathrm{c}}(\boldsymbol{r}, \tau)\, \mathrm{d}\tau \equiv \rho_{\mathrm{c}}(\boldsymbol{r}, t).$$

where:

$$b_1(t) = \frac{\sigma(t)}{\varepsilon_0 \varepsilon_{\mathrm{r}}(t)}; \quad b_2(t) = \omega_0^2 \frac{\varepsilon_{\mathrm{r},-}}{\varepsilon_{\mathrm{r}}(t)} + \frac{1}{\varepsilon_0}\left(\frac{\sigma(t)}{\varepsilon_{\mathrm{r}}(t)}\right)', \tag{A8.23}$$

and:

$$\psi(t) = \varphi(t) \exp\left(-\frac{1}{2}\int^t b_1(\tau)\,\mathrm{d}\tau\right). \tag{A8.24}$$

A similar temporal Helmholtz equation can also be obtained for heterogeneous time-varying anisotropic conductive media with an electric conductivity of the form $\boldsymbol{\sigma}(\boldsymbol{r}, t) = \sigma_{\mathrm{T}}(t)\,\boldsymbol{\sigma}_{\mathrm{S}}(\boldsymbol{r})$ and an electric permittivity and magnetic permeability given by Eqs. (A8.12) and (A8.13). Remarkably, Eq. (A8.22) is formally equal to Eq. (8.2.2) by restating $\omega_0^2 N^2(t) = b_2(t) - b_1'(t)/2 - b_1^2(t)/4$. Consequently, Eq. (A8.22) matches Eq. (8.1.1) taking $\alpha = 1$, performing the relabeling $x \to t$, and identifying $\Omega - V(x \to t) \equiv \omega_0^2 N^2(t)$. That is:

$$\Omega - V(t) = \omega_0^2 \frac{\varepsilon_{\mathrm{r},-}}{\varepsilon_{\mathrm{r}}(t)} + \frac{1}{2}\left(\frac{\sigma(t)}{\varepsilon_0 \varepsilon_{\mathrm{r}}(t)}\right)' - \frac{1}{4}\left(\frac{\sigma(t)}{\varepsilon_0 \varepsilon_{\mathrm{r}}(t)}\right)^2. \tag{A8.25}$$

If ε_{r} is time-varying, we find a T-SUSY problem supporting continuous spectra. In such a case, we will be able to analyze and design time-varying conductive optical systems $[\varepsilon_{\mathrm{r}1}(t), \sigma_1(t)]$ and $[\varepsilon_{\mathrm{r}2}(t), \sigma_2(t)]$ with the same intensity scattering behavior using T-SUSY. Otherwise, if ε_{r} is time-invariant $[\varepsilon_{\mathrm{r}}(t) = \varepsilon_{\mathrm{r},-}]$, we can obtain a well-defined eigenvalue problem (in the sense of the Sturm-Liouville theory, see Section 6.3) by decoupling Ω and V as:

$$\Omega = \omega_0^2; \;\; V(t) = \frac{1}{4}\left(\frac{\sigma(t)}{\varepsilon_0 \varepsilon_{\mathrm{r},-}}\right)^2 - \frac{1}{2}\left(\frac{\sigma(t)}{\varepsilon_0 \varepsilon_{\mathrm{r},-}}\right)'. \tag{A8.26}$$

The eigenvalue problem will support a discrete spectrum of eigenvalues $\{\Omega_n = \omega_n^2\}_{n\in\mathbb{N}}$ if V holds bound states. Consequently, time-varying conductive media can provide a fertile ground to observe *true* temporal bound states in photonics.[12]

[12] These temporal bound states are different from the temporal bound states observed in a temporal waveguide (see Appendix D8), which are localized not only in time, but also in space. Here, the concept of temporal bound state is more restrictive and exotic: an eigenfunction $D_n(x,t) = \varphi_n(t)\exp(-jk_0\sqrt{\varepsilon_{\mathrm{r},-}}\,x)$ of the optical system which is only localized in time, provided that φ_n fulfills the condition $\varphi_n(t \to \pm\infty) = 0$.

Appendix B8: Negative-frequency waves

"*The definition of insanity is doing the same thing over and over again, but expecting different results*"

Albert Einstein

The existence of negative-frequency waves is a controversial concept which has been discussed in different branches of physics, such as in optics or in gravity [105, 327–330]. In particular, in optics, the axis of negative frequencies is usually neglected, or even considered meaningless, in the dispersion diagram k-ω taking into account that it can be related with the positive-frequency axis via the conjugation operation.[13] Nevertheless, as we will show here, the use of negative-frequency waves is not a mere sign convention to differentiate the forward and backward propagation in the temporal scattering. Outstandingly, negative-frequency waves are of physical relevance to describe the time-reversal operation of light that can be observed in the reflected wave of the temporal scattering. In the following, let us first describe three different alternative views about the introduction of negative-frequency waves in optics, and latter we will analyze the necessity of using negative frequencies to describe the time-reversal of light.

B8.1 Different alternative views

Consider an all-dielectric, linear, isotropic, non-dispersive, homogeneous, time-invariant optical medium. The *exact* wave equation for the electric field strength is (we use the analytic representation):

$$\left(\triangle - \frac{n^2}{c_0^2}\partial_t^2\right)\boldsymbol{E}\left(\boldsymbol{r},t\right) = \boldsymbol{0}, \tag{B8.1}$$

where n is the refractive index and is found to be constant. In addition, let us consider an electromagnetic wave propagating through the above medium in the $\hat{u}_x$ direction of the form:[14]

$$\boldsymbol{E}\left(\boldsymbol{r},t\right) = \phi\left(x\right)\psi\left(t\right)\hat{u}_y. \tag{B8.2}$$

Replacing our ansatz in the above wave equation we find that:

$$\underbrace{\frac{\phi''\left(x\right)}{\phi\left(x\right)}}_{\gamma^2} = \underbrace{\frac{n^2}{c_0^2}\frac{\psi''\left(t\right)}{\psi\left(t\right)}}_{\gamma^2}, \tag{B8.3}$$

with $\gamma \in \mathbb{C}$. In other words, the LHS and RHS must be space- and time-independent. The LHS leads to the constant-coefficient ODE:

$$\phi''\left(x\right) - \gamma^2\phi\left(x\right) = 0, \tag{B8.4}$$

which yields a solution of the form $\phi\left(x\right) = \exp\left(\pm\gamma x\right)$. The nature of our optical medium indicates that the solution cannot have any gain or loss. This implies that γ must be a purely imaginary number $\gamma = jk$ and, then, the spatial solution ϕ must be a periodic function with k accounting for the spatial frequency. Therefore, the spatial solution is $\phi\left(x\right) = \exp\left(\pm jkx\right)$ and k is defined as the *wave number*. On the other hand, from the RHS emerges the ODE:

$$\frac{n^2}{c_0^2}\psi''\left(t\right) - \gamma^2\psi\left(t\right) = 0, \tag{B8.5}$$

[13] That is, $\boldsymbol{\mathcal{E}}^- = (\boldsymbol{\mathcal{E}}^+)^*$ where $\boldsymbol{\mathcal{E}}^+$ ($\boldsymbol{\mathcal{E}}^-$) is the real wave function of the electric field strength involving the positive (negative) frequencies of the spectrum. See page 2 for more details.

[14] Obviously, assuming an ansatz of the form given by Eq. (B8.2) we omit different possible solutions to the wave equation. A more general ansatz would be of the form $\boldsymbol{E}\left(\boldsymbol{r},t\right) = \psi\left(t\right)\boldsymbol{\Phi}\left(\boldsymbol{r}\right)$. However, Eq. (B8.2) will allow us to introduce the concept of negative-frequency waves in our discussions in a simple way.

which is found to be the same as the spatial ODE by setting $n^2/c_0^2 \equiv 1$. Consequently, it is straightforward to find the temporal solution as $\psi(t) = \exp(\pm(c_0/n)\gamma t)$, with $\gamma = jk$ and the constant $(c_0/n)k$ accounting for the temporal frequency. This temporal frequency, usually denoted as ω, is defined as the *angular frequency* of the wave and is connected to the wave number via the relation $\omega = c_0 k/n$. Hence, the temporal solution is found as $\psi(t) = \exp(\pm j\omega t)$. All in all, the *general* solution of the wave equation is of the form:

$$\boldsymbol{E}(\boldsymbol{r}, t) = A_0 \exp(\pm jkx) \exp(\pm j\omega t)\, \hat{u}_y, \tag{B8.6}$$

with A_0 a complex constant accounting for the power of the wave ($P \propto |A_0|^2$). In any case, the main terms are the exponential functions, which describe the photon momentum ($\boldsymbol{p} = \hbar k \hat{u}_x$) and the photon energy ($\mathscr{E} = \hbar\omega$).

First interpretation

Given that we have four different possible solutions, encoded in the different combinations of the spatial and temporal exponential functions, it is natural to ask how the forward and backward propagation should be described. The answer is not unique. We should take into account that we must describe two spatial directions ($\hat{u}_x$ and $-\hat{u}_x$) and only one temporal direction ($\hat{u}_t$). We can envision this scenario as a mathematical problem with three *degrees of freedom*. These degrees of freedom can be mathematically described via three different *variables* (x_1, x_2, x_3) which can be defined in different ways. For instance, we can select $(x_1, x_2, x_3) \equiv (x, -x, t)$ or $(x_1, x_2, x_3) \equiv (x, t, -t)$ among other possibilities. Note that the three degrees of freedom are perfectly defined in these two examples. The former example implies to retain the double sign $\pm$ in the spatial exponent leading to the use of negative wave numbers as a means to describe the propagation direction via the sign of the speed of light in the medium ($c = c_0/n$). The forward ($+c$) and backward ($-c$) directions are respectively described by $\pm c = \omega/\pm k$. In contrast, the latter example requires to retain the double sign $\pm$ in the temporal exponent leading to the use of negative frequencies. In this fashion, the propagation direction is also described via the sign of c. The forward ($+c$) and backward ($-c$) directions are respectively described by $\pm c = \pm\omega/k$.

Hence, in this first interpretation, a change in the sign of the frequency of a wave corresponds to a *reversal* of the phase velocity, provided that we use a positive wave number. Therefore, from the relation $\mathscr{E} = \hbar\omega$, we infer that a photon with positive energy apparently becomes a photon with negative energy. Remarkably, this can be associated with various exotic physical effects, such as the Cherenkov radiation [351], quantum friction [352], and the Hawking radiation [353]. For instance, the Hawking radiation, originated from the change in the sign of the frequency of a wave as it crosses the event horizon, has been experimentally evaluated in an optical fiber by using analogue gravity [105], leading to the identification of new pulse propagation phenomena [327].

Second interpretation

Using a more rigorous mathematical approach, we should note that the general solution of the second-order ODE Eq. (B8.4) must be written as a linear combination of two linearly independent solutions $\phi^{\pm}$:

$$\phi(x) = \phi^+(x) + \phi^-(x) = A_1 \exp(jkx) + A_2 \exp(-jkx), \tag{B8.7}$$

with the Wronskian $\mathcal{W}(\phi^+, \phi^-) = \phi^+(\phi^-)' - (\phi^+)'\phi^- \neq 0$. In the same way, the general solution of the second-order ODE Eq. (B8.5) must also be written as a linear combination of two linearly independent solutions $\psi^{\pm}$:

$$\psi(t) = \psi^+(t) + \psi^-(t) = A_3 \exp(j\omega t) + A_4 \exp(-j\omega t), \tag{B8.8}$$

with $\mathcal{W}(\psi^+, \psi^-) \neq 0$. Therefore, the general solution Eq. (B8.6) must be written of the form:

$$\begin{aligned}\boldsymbol{E}(\boldsymbol{r}, t) &= \left(\phi^+(x) + \phi^-(x)\right)\left(\psi^+(t) + \psi^-(t)\right)\hat{u}_y \\ &= \{A_1 A_3 \exp(jkx)\exp(j\omega t) + A_1 A_4 \exp(jkx)\exp(-j\omega t) \\ &+ A_2 A_3 \exp(-jkx)\exp(j\omega t) + A_2 A_4 \exp(-jkx)\exp(-j\omega t)\}\, \hat{u}_y.\end{aligned} \tag{B8.9}$$

These four terms are linearly independent.[15] Nevertheless, working with the real representation of the electric field strength, only two terms are linearly independent. Concretely, the real part of the first and fourth terms is linearly independent to the real part of the second and third terms. Consequently, we must describe the forward and backward waves by selecting two terms whose real parts are linearly independent, e.g., the third and fourth terms. Hence, we conclude that we have only two degrees of freedom (and not three as discussed before), in line with the number of variables in $\boldsymbol{E}$. However, using this approach, the negative frequencies do not possess any physical meaning. In this case, negative-frequency waves emerge from a sign convention.

Third interpretation

In the third alternative view, we will see that the use of negative frequencies is necessary to perform a complete description of the propagation of the electromagnetic fields when assuming positive wave numbers. Note that this conclusion is in line with the first interpretation. Let us start by considering the real solution $\boldsymbol{\mathcal{E}} = \mathrm{Re}\{\boldsymbol{E}\}$ of the initial wave equation [Eq. (B8.1)], which can be written using the two-dimensional Fourier transform as follows:[16]

$$\boldsymbol{\mathcal{E}}(\boldsymbol{r},t) = \frac{1}{4\pi^2}\int_{-\infty}^{\infty}\int_{-\infty}^{\infty}\widetilde{\boldsymbol{\mathcal{E}}}(k,\omega;\boldsymbol{r}_{\mathrm{T}})\exp(-jkx)\exp(j\omega t)\,\mathrm{d}k\mathrm{d}\omega; \tag{B8.10}$$

$$\widetilde{\boldsymbol{\mathcal{E}}}(k,\omega;\boldsymbol{r}_{\mathrm{T}}) = \int_{-\infty}^{\infty}\int_{-\infty}^{\infty}\boldsymbol{\mathcal{E}}(\boldsymbol{r},t)\exp(jkx)\exp(-j\omega t)\,\mathrm{d}x\mathrm{d}t. \tag{B8.11}$$

It can be noted that this solution is more general than the plane wave discussed before and includes both forward and backward propagation directions. From Eq. (B8.11) it is easy to see that, if $\boldsymbol{\mathcal{E}}$ is real (as is the case for an electromagnetic field), then $\widetilde{\boldsymbol{\mathcal{E}}}$ is a Hermitian function:

$$\widetilde{\boldsymbol{\mathcal{E}}}(k,\omega;\boldsymbol{r}_{\mathrm{T}}) = \widetilde{\boldsymbol{\mathcal{E}}}^{*}(-k,-\omega;\boldsymbol{r}_{\mathrm{T}}). \tag{B8.12}$$

This property allows us to express $\boldsymbol{\mathcal{E}}(\boldsymbol{r},t)$ in terms of its inverse Fourier transform as [we use the polar form $\widetilde{\boldsymbol{\mathcal{E}}} = \left|\widetilde{\boldsymbol{\mathcal{E}}}\right|\exp(j\phi_{\widetilde{\boldsymbol{\mathcal{E}}}})$]:[17]

$$\begin{aligned}
\boldsymbol{\mathcal{E}}(\boldsymbol{r},t) &= \frac{1}{4\pi^2}\int_{\omega=-\infty}^{\infty}\left[\int_{k=-\infty}^{0}\widetilde{\boldsymbol{\mathcal{E}}}(k,\omega;\boldsymbol{r}_{\mathrm{T}})\,e^{-jkx}e^{j\omega t}\mathrm{d}k + \int_{k=0}^{\infty}\widetilde{\boldsymbol{\mathcal{E}}}(k,\omega;\boldsymbol{r}_{\mathrm{T}})\,e^{-jkx}e^{j\omega t}\mathrm{d}k\right]\mathrm{d}\omega \\
&= \frac{1}{4\pi^2}\int_{\omega=-\infty}^{\infty}\left[\int_{k=-\infty}^{0}\widetilde{\boldsymbol{\mathcal{E}}}^{*}(-k,-\omega;\boldsymbol{r}_{\mathrm{T}})\,e^{-jkx}e^{j\omega t}\mathrm{d}k + \int_{k=0}^{\infty}\widetilde{\boldsymbol{\mathcal{E}}}(k,\omega;\boldsymbol{r}_{\mathrm{T}})\,e^{-jkx}e^{j\omega t}\mathrm{d}k\right]\mathrm{d}\omega \\
&= \frac{1}{4\pi^2}\int_{\omega=-\infty}^{\infty}\left[\int_{k=0}^{\infty}\widetilde{\boldsymbol{\mathcal{E}}}^{*}(k,\omega;\boldsymbol{r}_{\mathrm{T}})\,e^{jkx}e^{-j\omega t}\mathrm{d}k + \int_{k=0}^{\infty}\widetilde{\boldsymbol{\mathcal{E}}}(k,\omega;\boldsymbol{r}_{\mathrm{T}})\,e^{-jkx}e^{j\omega t}\mathrm{d}k\right]\mathrm{d}\omega \\
&= \frac{1}{4\pi^2}\int_{\omega=-\infty}^{\infty}\left[\int_{k=0}^{\infty}\left|\widetilde{\boldsymbol{\mathcal{E}}}(k,\omega;\boldsymbol{r}_{\mathrm{T}})\right|\left(e^{j\left(kx-\omega t-\phi_{\widetilde{\boldsymbol{\mathcal{E}}}}(k,\omega;\boldsymbol{r}_{\mathrm{T}})\right)} + e^{-j\left(kx-\omega t-\phi_{\widetilde{\boldsymbol{\mathcal{E}}}}(k,\omega;\boldsymbol{r}_{\mathrm{T}})\right)}\right)\mathrm{d}k\right]\mathrm{d}\omega \\
&= \frac{1}{4\pi^2}\int_{\omega=-\infty}^{\infty}\int_{k=0}^{\infty}2\left|\widetilde{\boldsymbol{\mathcal{E}}}(k,\omega;\boldsymbol{r}_{\mathrm{T}})\right|\cos\left(kx-\omega t-\phi_{\widetilde{\boldsymbol{\mathcal{E}}}}(k,\omega;\boldsymbol{r}_{\mathrm{T}})\right)\mathrm{d}k\mathrm{d}\omega.
\end{aligned} \tag{B8.13}$$

[15] These four vectors $\{\Phi_i\}_{i=1}^{4} = \{\phi^{+}\psi^{+}, \phi^{+}\psi^{-}, \phi^{-}\psi^{+}, \phi^{-}\psi^{-}\}$ are linearly independent because they are mutually orthogonal. It is straightforward to verify that:

$$\langle\Phi_i|\Phi_k\rangle = \int_{\langle 2\lambda\rangle}\int_{\langle 2T\rangle}\Phi_i^{*}(x,t)\,\Phi_k(x,t)\,\mathrm{d}x\mathrm{d}t = 4\lambda T\delta_{ik},$$

where $\lambda = 2\pi/k$ and $T = 2\pi/\omega$ are the spatial and temporal periods, respectively. Also note that, taking into account the periodic nature of our general solution [Eq. (B8.9)], the inner product must be defined as in the Fourier series, i.e., involving a finite number of spatial and temporal periods in the integration limits.

[16] The two-dimensional Fourier transform was defined on page 4.

[17] We have performed a double dummy variable transformation $k \to -k$ and $\omega \to -\omega$ between the second and third lines.

That is, the wave $\boldsymbol{\mathcal{E}}$ is a superposition of cosines of different frequency ω and wave number k [each with a different amplitude $\left|\widetilde{\boldsymbol{\mathcal{E}}}(k,\omega;\boldsymbol{r}_{\mathrm{T}})\right|$ and phase offset $\phi_{\widetilde{\boldsymbol{\mathcal{E}}}}(k,\omega;\boldsymbol{r}_{\mathrm{T}})$], where $\omega \in (-\infty,\infty)$ whilst $k \in [0,\infty)$. In other words, the Hermiticity of $\widetilde{\boldsymbol{\mathcal{E}}}$ halves the interval of relevant wave numbers and requires the use of negative frequencies to perform a complete description of $\boldsymbol{\mathcal{E}}$. Conversely, the symmetry of the inverse Fourier transform in k and ω implies that we can also reduce the range of frequencies instead of that of wave numbers. This is the reason underlying the fact that only positive frequencies are usually considered in optics.

Discussion

The first and third interpretations indicate that the use of negative-frequency waves is not a mere *sign* convention to describe the the forward and backward waves. Nonetheless, the three interpretations suggest that we can arbitrarily choose to work either with positive values of ω or with positive values of k. This incorrectly implies that we could use only-positive frequencies to describe the temporal scattering. Unfortunately, as we will see below, positive-frequency waves cannot describe the time-reversal of light that takes place in the reflected wave of the temporal scattering.

B8.2 Time-reversal of light

Let us consider an optical pulse described by a complex envelope $\mathcal{A}(x,t)$ satisfying the SVEA (see Chapter 4, page 129) which is propagated through the x-axis of an optical system of length L. Hence, the pulse is described at the input and at the output of the system by the functions $A_{\mathrm{IN}}(t) := \mathcal{A}(x=0,t)$ and $A_{\mathrm{OUT}}(t) := \mathcal{A}(x=L,t)$, respectively. By definition, we will say that the optical system performs a time-reversal operation of the pulse when [314]:

$$A_{\mathrm{OUT}}(t) = A_{\mathrm{IN}}(-t+\tau_{\mathrm{G}}) = \mathcal{A}(x=0,-t+\tau_{\mathrm{G}}), \tag{B8.14}$$

where τ_{G} is the group delay of the system. Thus, at a given x point, the time-reversed version of the pulse $\mathcal{A}(x,t)$ involves a complex envelope of the form $\mathcal{A}(x,-t)$. Taking into account that we can describe the original envelope by means of the two-dimensional inverse Fourier transform:

$$\mathcal{A}(x,t) = \frac{1}{4\pi^2}\int_{-\infty}^{\infty}\int_{-\infty}^{\infty}\widetilde{\mathcal{A}}(k,\omega)\exp(-jkx)\exp(j\omega t)\,\mathrm{d}k\mathrm{d}\omega, \tag{B8.15}$$

the time-reversed pulse can be written of the form:[18]

$$\begin{aligned}\mathcal{A}(x,-t) &= \frac{1}{4\pi^2}\int_{-\infty}^{\infty}\int_{-\infty}^{\infty}\widetilde{\mathcal{A}}(k,\omega)\exp(-jkx)\exp(-j\omega t)\,\mathrm{d}k\mathrm{d}\omega \\ &= \frac{1}{4\pi^2}\int_{-\infty}^{\infty}\int_{-\infty}^{\infty}\widetilde{\mathcal{A}}(k,-\omega)\exp(-jkx)\exp(j\omega t)\,\mathrm{d}k\mathrm{d}\omega.\end{aligned} \tag{B8.16}$$

As seen, a time-reversal optical system has to deal with negative frequencies as a necessary condition given that the dispersion diagram must be inverted: $(k,\omega) \to (k,-\omega)$. For instance, this can be observed in the reflected wave of the temporal scattering, where the wave number is constant and the frequency of the reflected wave is the opposite of the transmitted wave. As depicted in Fig. 8.2(b), the dispersion diagram of the transmitted wave has been inverted in the reflected wave $(k,\omega_+) \to (k,-\omega_+)$. As a result the reflected optical pulse is the time-reversed version of the transmitted pulse. Furthermore, it is obvious to infer from this discussion that positive-frequency waves cannot describe the time-reversal effect of the temporal scattering. Therefore, a complete description of the temporal scattering *requires* the use of negative frequencies.

[18] We have performed a simple transformation ($\omega \equiv -\Omega$) and relabeling ($\Omega \to \omega$) of dummy variables between the first and second lines.

For completeness, we verify the time-reversal effect of the temporal scattering by performing a numerical simulation of the exact wave equation (8.2.1) considering the step-index profile of Fig. B8.1(a). The incident, reflected and transmitted pulses are shown in Fig. B8.1(b). We can see that the reflected pulse is the time-reversed version of the transmitted pulse as a direct consequence of the inversion of the dispersion diagram. Interestingly, the time-reversed pulse could be guided to the $+\hat{u}_x$ direction by using the scheme shown in Fig. B8.1(c). An optical circulator would recover the reflected wave, which would be guided to the same direction as the transmitted pulse. Finally, at the device output, we would find the original pulse and its time-reversed version in both parallel waveguides.

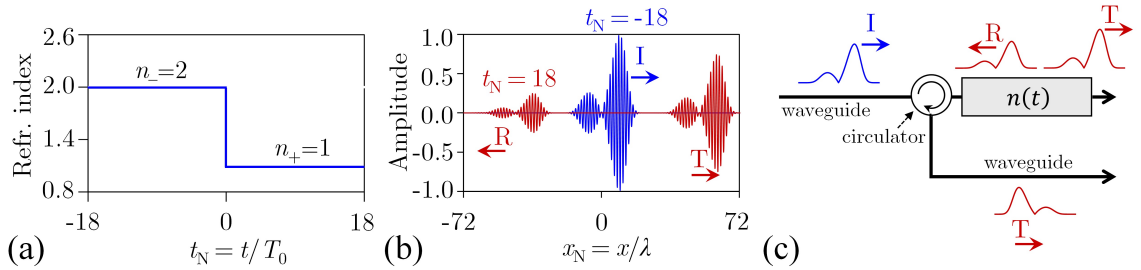

Figure B8.1. Time-reversal of light in the temporal scattering. (a) Simulated temporal step-index profile. The temporal axis has been normalized as $t_N = t/T_0$, with $T_0 = 2\pi/\omega_0$ and $\omega_0 = 38$ rad/s (see Methods). (b) Incident (I), transmitted (T) and reflected (R) pulses at the beginning ($t_N = -18$) and at the end of the simulation ($t_N = 18$). The x-axis has been normalized as $x_N = x/\lambda$, with $\lambda = \lambda_0/n_-$ and $\lambda_0 = 2\pi c_0/\omega_0$. The amplitude has also been normalized. (c) Proposed scheme to recover the time-reversed pulse generated by $n(t)$ in reflection using an optical circulator.

B8.3 Conclusion

The temporal scattering problem must be described by using negative frequencies and positive wave numbers. Consequently, the analytic representation of the electromagnetic fields must be defined in a different way in the spatial and temporal scattering problems. In the latter scenario, the analytic representation must be defined by including only the positive wave numbers of the real representation of the fields, as detailed on page 4.

Appendix C8: Temporal scattering

In this appendix, we explain the main theory of Section 8.2 in detail and we include additional numerical examples for completeness our findings.

C8.1 Fundamentals of the temporal scattering

Let us start by including some fundamental notes on the temporal scattering in optics. This will allow us to understand more in depth the theory and numerical examples of T-SUSY in the next subsections. First, we will analyze in more detail the mathematical solution of a wave equation of a time-varying optical system. As a byproduct, we will be able to infer the fundamental physical concepts enclosed in this kind of systems.

In this regard, consider as a basic example an all-dielectric, linear, isotropic, non-dispersive, homogeneous, time-varying optical medium. From Appendix A8, we know that the exact wave equation for the electric flux density is given by Eq. (A8.1), reproduced here for clarity:

$$\left(\triangle - \frac{n^2(t)}{c_0^2}\partial_t^2\right)\boldsymbol{D}(\boldsymbol{r},t) = \boldsymbol{0}. \tag{C8.1}$$

In such a scenario, the isotropic and homogeneous nature of the medium guarantees that $\boldsymbol{D}$ is transversal to the propagation direction of the electromagnetic energy (e.g. $\hat{u}_x$) and the temporal scattering is polarization-independent (see Appendix A8.2). Therefore, assuming an ansatz of the form $\boldsymbol{D}(\boldsymbol{r},t) = \phi(x)\,\psi(t)\,\hat{u}_y$, we infer from the wave equation that:[19]

$$\underbrace{\frac{\phi''(x)}{\phi(x)}}_{\gamma^2} = \underbrace{\frac{n^2(t)}{c_0^2}\frac{\psi''(t)}{\psi(t)}}_{\gamma^2}. \tag{C8.2}$$

That is, the LHS and RHS must be space- and time-independent ($\gamma \in \mathbb{C}$). From the LHS, we find the ODE $\phi''(x) - \gamma^2\phi(x) = 0$, which yields a solution of the form $\phi(x) = \exp(\pm\gamma x)$, with $\gamma = jk$ a purely imaginary number to avoid a lossy term which would be independent on the temporal variation of the refractive index. Let us be more specific. A complex constant of the form $\gamma = \alpha + jk$ leads to a spatial solution with a lossy term $\exp(\pm\alpha x)$.[20] Therefore, in such a case we would have an *intrinsic* absorption or amplification in the solution which would be independent on the temporal variation of the refractive index. This incorrectly implies that we would observe absorption or amplification, for instance, in a non-dispersive medium with a constant refractive index profile $n(t) = n_-$. Specifically, the non-dispersive nature initially assumed in our medium allows us to infer via the Kramers-Kronig relations that the solution cannot involve an intrinsic lossy term of the form $\exp(\pm\alpha x)$. Consequently, γ must be a purely imaginary number.[21] In other words, the spatial solution ϕ must be a periodic function with k accounting for the spatial frequency. We have found the so-called wave number parameter, and must be constant. Then:

The wave vector $\boldsymbol{k} = k\hat{u}_x$, or equivalently the photon momentum $\boldsymbol{p} = \hbar\boldsymbol{k}$, is a conserved quantity

[19] Actually, the theory of T-SUSY of the temporal scattering emerges from Eq. (C8.2) but rewriting this equation as $(c_0^2/n_-^2)\phi''(x)/\phi(x) = (n^2(t)/n_-^2)\psi''(t)/\psi(t)$ to introduce n_- as a degree of freedom of the problem. In this way, we have the possibility of changing the background material in the supersymmetric system.

[20] The lossy term describes absorption or amplification depending on the sign of α.

[21] Nonetheless, in spite of the fact that we have discarded a lossy term of the form $\exp(\pm\alpha x)$, a time-varying system can amplify or attenuate the incident wave. The electromagnetic fields are propagating in an *open* system, i.e., any loss or gain is *extrinsic* to the system and is induced by the energy transfer with the outer medium. Concretely, this is modeled by the reflection and transmission coefficients of the temporal scattering when $|R| \neq 1$ and $|T| \neq 1$.

Otherwise, from the RHS of Eq. (C8.2), we find the ODE $\psi''(t) + (c_0^2/n^2(t))\gamma^2\psi(t) = 0$. For simplicity in our discussions, let us assume a slowly-varying temporal evolution in $n(t)$ satisfying that $n''(t) \simeq n'(t) \simeq 0$ in $\delta t \sim T_0$, where T_0 is the temporal period of the electromagnetic fields at the beginning of the problem, at $t \to -\infty$.[22] In such circumstances, we can approximate the solution to $\psi(t) \simeq \exp[\pm(c_0/n(t))\gamma t]$, with $(c_0/n(t))k$ accounting for the temporal frequency.[23] Despite the fact that the above solution is not exact, we can infer with this simple example that the temporal frequency must vary in time. Rewriting the temporal solution as $\psi(t) \simeq \exp(\pm j\omega(t)\, t)$, we find that:

$$\omega(t) \simeq c_0 k/n(t). \tag{C8.3}$$

Then:

The angular frequency ω, or equivalently the photon energy $\mathscr{E} = \hbar\omega$, is not constant

It is worth mentioning that Eq. (C8.3) is exact at $t \to \pm\infty$ bearing in mind that the refractive index is constant at the beginning and at the end of the problem [$n_\pm := n(t \to \pm\infty)$]. That is, at $t \to \pm\infty$, the temporal ODE with variable coefficients becomes a constant-coefficient ODE and the above approximate solution of $\psi(t)$ is exact. Concretely, the initial and final angular frequencies are $\omega_\pm := \omega(t \to \pm\infty) = c_0 k/n_\pm$. Therefore, taking into account the conservation of the photon momentum, the Snell law of the temporal scattering is finally derived:

$$n_-\omega_- = n_+\omega_+. \tag{C8.4}$$

Next, let us solve the temporal scattering for an analytical case. Consider a temporal sudden change of the refractive index given by the step-index function ($n_\pm > 0$):

$$n(t) = \begin{cases} n_-, & t \le 0 \\ n_+, & t > 0 \end{cases} \tag{C8.5}$$

As illustrated in Fig. 8.2(b), the interaction of an incident (I) plane wave with a localized temporal variation of the refractive index generates a reflected (R) and a transmitted (T) wave. In this scenario, as discussed in Section 8.2 and in Appendix B8, the use of negative frequencies is required to describe adequately the variation of the angular frequency in the temporal scattering problem. Hence, a double (single) sign must be retained in ψ (ϕ). In this vein, the asymptotic solution of Eq. (C8.1) for the incident, reflected and transmitted waves can be written as:

$$\boldsymbol{D}_{\mathrm{I}}(\boldsymbol{r}, t) \underset{t\to-\infty}{\sim} \exp(-jkx)\exp(j\omega_- t)\,\hat{u}_y; \tag{C8.6}$$

$$\boldsymbol{D}_{\mathrm{R}}(\boldsymbol{r}, t) \underset{t\to\infty}{\sim} R\exp(-jkx)\exp(-j\omega_+ t)\,\hat{u}_y; \tag{C8.7}$$

$$\boldsymbol{D}_{\mathrm{T}}(\boldsymbol{r}, t) \underset{t\to\infty}{\sim} T\exp(-jkx)\exp(j\omega_+ t)\,\hat{u}_y. \tag{C8.8}$$

Using the boundary conditions of the temporal scattering ($\boldsymbol{D}$ and $\partial_t\boldsymbol{D}$ must be necessarily continuous functions at $t = 0$) we obtain the equations $T + R = 1$ and $T - R = n_+/n_-$. This system of linear equations leads to the following scattering coefficients:

$$R = \frac{n_- - n_+}{2n_-}; \tag{C8.9}$$

$$T = \frac{n_- + n_+}{2n_-}. \tag{C8.10}$$

[22] Note that assuming a slowly-varying temporal evolution in $n(t)$ we are considering the temporal ODE as an ODE with constant coefficients in $\delta t \sim T_0$.

[23] Optionally, we can find a more rigorous approximated solution for the slowly-varying index scenario [354]:

$$\psi(t) \simeq \exp\left[\pm j\frac{\omega_-}{2}\left(t + \int^t \frac{n_-^2}{n^2(\tau)}\mathrm{d}\tau\right)\right],$$

by assuming an ansatz of the form $\psi(t) \simeq R(t)\exp(\pm j\omega_- t)$, with R a complex envelope satisfying the SVEA in the time domain (see page 129).

These are the equivalent to Fresnel's formulas for the step-index profile.[24] As commented before in footnote 21, we can observe that our system amplifies or attenuates the incident wave when $|R| \neq 1$ and $|T| \neq 1$.

C8.2 Temporal scattering and T-SUSY: theory

In all the optical media discussed in Appendix A8.1, the temporal evolution of $\boldsymbol{\mathcal{D}}$ ($\boldsymbol{\mathcal{B}}$), encoded by the ψ function, obeys Eq. (8.2.2), reproduced here for clarity:

$$\left(\frac{\mathrm{d}^2}{\mathrm{d}t^2} + \omega_0^2 N^2(t)\right)\psi(t) = 0, \tag{C8.11}$$

where $N^2(t) := n_-^2/n^2(t)$, $n_- := n(t \to -\infty)$, and ω_0 is the angular frequency (central angular frequency) of the electromagnetic fields at the beginning of the problem, i.e. $\omega_0 \equiv \omega_-$, in the monochromatic (non-monochromatic) regime. In heterogeneous media $n(t) \equiv n_{\mathrm{T}}(t)$.

As discussed in the main text, Eq. (C8.11) matches the 1D time-independent Schrödinger equation [Eq. (8.1.1)] taking $\alpha = 1$, performing the relabeling $x \to t$, and identifying:

$$\Omega - V(x \to t) \equiv \omega_0^2 N^2(t). \tag{C8.12}$$

In this way, assuming Ω [the eigenvalue in Eq. (8.1.1)] as a degree of freedom of the problem, we will be able to use the algebraic transformations of 1D SUSY in the time domain, which will give rise to time-varying refractive index profiles $n_{1,2}(t)$ with similar scattering properties, provided that we use real $V_{1,2}$ potentials.

In order to have a well-defined *temporal* scattering problem in both superpartners, defined on the full line ($t \in \overline{\mathbb{R}}$), we require that:[25]

$$\psi^{(1,2)}(t \to \pm\infty) \neq 0. \tag{C8.13}$$

A sufficient condition to satisfy Eq. (C8.13) is to consider $V_{1,2}(t \to \pm\infty) < \infty$, which is fulfilled by assuming: (*i*) $W_\pm := W(t \to \pm\infty)$ exists and is finite, and (*ii*) W' is uniformly continuous on the full line. Thus, from Barbalat's lemma (see page 175) and Riccati's equation ($V_{1,2} = W^2 \mp W'$), we can infer that $W'_\pm = 0$ and $V_{1,\pm} = V_{2,\pm} = W_\pm^2 < \infty$. To summarize, we will have a well-defined scattering problem in both superpartners with:

$$\left.\begin{array}{c} |W_\pm| < \infty \\ W' \text{ unif. cont.} \end{array}\right\} \Rightarrow V_\pm \equiv V_{1,\pm} = V_{2,\pm} = W_\pm^2 < \infty \Rightarrow \psi^{(1,2)}(t \to \pm\infty) \neq 0. \tag{C8.14}$$

Hence, combining Eqs. (C8.12) and (C8.14), keeping in mind that both superpartners share the same eigenvalue Ω, we infer that:

$$N_1^2(t \to \pm\infty) = N_2^2(t \to \pm\infty) \equiv N_\pm^2, \tag{C8.15}$$

with $N_- = 1$ by definition. From the above equation, the following remarks are in order:

- In spite of the fact that $N_{1,+}^2 = N_{2,+}^2$, note that $n_{1,+}^2 \neq n_{2,+}^2$ when $n_{1,-}^2 \neq n_{2,-}^2$, that is, when the T-SUSY systems are implemented in different background materials.
- If we assume positive-real constitutive parameters, $N_{1,\pm} = N_{2,\pm} \equiv N_\pm$, and then:

$$\frac{n_{1,-}}{n_{1,+}} = \frac{n_{2,-}}{n_{2,+}}. \tag{C8.16}$$

In order to connect the temporal scattering problem between both superpartners, consider a plane wave in each system at $t \to -\infty$. Next, after the interaction with the refractive index variations $n_{1,2}(t)$, a reflected and a transmitted plane wave will be found at $t \to \infty$. Thus, the asymptotic behavior at $t \to \pm\infty$ of $\psi^{(1,2)}$ is found to be [$\psi^{(1,2)}(t) \underset{t\to\pm\infty}{\sim} \psi_\pm^{(1,2)}(t)$]:

[24] The scattering coefficients of the electric field strength ($\mathcal{R}$ and $\mathcal{T}$) can be calculated from the scattering coefficients of the electric flux density (R and T) as $\mathcal{R} = N_+^2 R$ and $\mathcal{T} = N_+^2 T$, where $N_+ = n_-/n_+$.

[25] A spatial or temporal scattering problem is well-defined when we can observe an incident wave and at least one reflected or transmitted wave. In the temporal scattering, the incident wave is always defined at $t \to -\infty$ and the reflected and transmitted waves are found at $t \to \infty$. Thus, we require a non-vanishing wave function at $t \to \pm\infty$.

$$\psi_{-}^{(1,2)}(t) = \exp(jN_{-}\omega_0 t); \tag{C8.17}$$

$$\psi_{+}^{(1,2)}(t) = R_{1,2}\exp(-jN_{+}\omega_0 t) + T_{1,2}\exp(jN_{+}\omega_0 t), \tag{C8.18}$$

$R_{1,2}$ and $T_{1,2}$ being respectively the reflection and transmission coefficients, and $\omega_0^2 N_{\pm}^2 = \Omega - W_{\pm}^2$. Using the SUSY relation $\psi^{(1)} = \xi\widehat{\mathrm{A}}^{+}\psi^{(2)}$, where $\xi \in \mathbb{C}$, $\widehat{\mathrm{A}}^{\pm} := \mp\mathrm{d}/\mathrm{d}t + W(t)$ are the T-SUSY operators, and W is the superpotential (a real-valued function in our case), we can relate the asymptotic behaviors as:

$$\psi_{\pm}^{(1)}(t) = \xi\left(-\frac{\mathrm{d}}{\mathrm{d}t} + W_{\pm}\right)\psi_{\pm}^{(2)}(t). \tag{C8.19}$$

Thus, we have at $t \to -\infty$:

$$\exp(j\omega_0 t) = \xi(-j\omega_0 + W_{-})\exp(j\omega_0 t), \tag{C8.20}$$

and at $t \to \infty$:

$$\begin{aligned} R_1\exp(-jN_{+}\omega_0 t) + T_1\exp(jN_{+}\omega_0 t) = {} & \xi R_2(jN_{+}\omega_0 + W_{+})\exp(-jN_{+}\omega_0 t) \\ & + \xi T_2(-jN_{+}\omega_0 + W_{+})\exp(jN_{+}\omega_0 t). \end{aligned} \tag{C8.21}$$

Finally, equating terms with the same exponent in Eqs. (C8.20) and (C8.21), we find:

$$\frac{R_1}{R_2} = \frac{W_{+} + jN_{+}\omega_0}{W_{-} - j\omega_0}; \quad \frac{T_1}{T_2} = \frac{W_{+} - jN_{+}\omega_0}{W_{-} - j\omega_0}. \tag{C8.22}$$

Let us take a closer look at the above equations. In particular, it should be remarked that:

1. The T-SUSY refractive index profiles have identical intensity scattering behavior:

$$|R_1|^2 = |R_2|^2; \quad |T_1|^2 = |T_2|^2, \tag{C8.23}$$

because both systems share the same eigenvalue $\Omega = \omega_0^2 N_{\pm}^2 + W_{\pm}^2$.

2. Although we consider complex-valued wave functions, the superpotential and the potentials must be assumed real-valued functions to guarantee Eq. (C8.23). Otherwise, the intensity scattering behavior could be found different in both systems [235].

3. Equation (C8.22) does not depend on $n_{1,2,-}$. Consequently, we can engineer time-varying refractive index profiles exhibiting the same intensity scattering behavior using the same ($n_{1,-} = n_{2,-}$) or different ($n_{1,-} \neq n_{2,-}$) background materials.

4. Bearing in mind that $N_{-} = 1$, we find that $\Omega = \omega_0^2 + W_{-}^2$. Hence, $\Omega \geq \omega_0^2$.

5. The use of negative frequencies in Eq. (C8.21) allows us, not only to describe adequately the temporal scattering (as discussed in Fig. 8.2), but also to decouple the ratios R_1/R_2 and T_1/T_2. If we used only positive frequencies, we would find a coupled scattering relation of the form:

$$\frac{R_1 + T_1}{R_2 + T_2} = \frac{W_{+} - jN_{+}\omega_0}{W_{-} - j\omega_0}. \tag{C8.24}$$

6. The ratios of the scattering coefficients $\mathcal{R}_i$ and $\mathcal{T}_i$ of the electric (magnetic) field strength are exactly the same as Eq. (C8.22) taking into account that $\mathcal{R}_i = N_{+}^2 R_i$ and $\mathcal{T}_i = N_{+}^2 T_i$. Therefore, we find that $\mathcal{R}_1/\mathcal{R}_2 = R_1/R_2$ and $\mathcal{T}_1/\mathcal{T}_2 = T_1/T_2$.

7. Note that $|W_{+}| = |W_{-}| \Leftrightarrow N_{+} = N_{-} = 1 \Leftrightarrow n_{i,+} = n_{i,-}$. Such a situation takes place:

   - If $W_{+} = -W_{-}$, in which case T-SUSY is said to be unbroken, provided that the SUSY QM potentials support bound states. Here, we observe that $R_1 = -R_2$. The reflected wave has an extra phase shift of π rad in the T-SUSY system.
   - If $W_{+} = W_{-}$, in which case T-SUSY is said to be broken, provided that the SUSY QM potentials support bound states. Here, we find that $T_1 = T_2$.

8. In general, $\left|\psi^{(1,2)}\left(t\rightarrow-\infty\right)\right|\neq\left|\psi^{(1,2)}\left(t\rightarrow\infty\right)\right|$ and, therefore, $\widehat{\mathrm{A}}^{+}\neq\left(\widehat{\mathrm{A}}^{-}\right)^{\dagger}$. Along this line, it should also be taken into account that we are operating with non-normalizable complex-valued functions. Hence, we work in a *rigged* Hilbert space over the field $\mathbb{C}$.

9. In a T-SUSY refractive index chain $\{n_s\left(t\right)\}_{s=1}^{m}$ where the scattering problem is well-defined, the value of the potentials $\{V_s\}_{s=1}^{m}$ and superpotentials $\{W_s\}_{s=1}^{m-1}$ at $t\rightarrow\pm\infty$ is the same. That is:

$$V_{1,\pm}=V_{2,\pm}=\ldots=V_{m,\pm}=W_{1,\pm}^{2}, \tag{C8.25}$$

and $W_{1,\pm}=W_{2,\pm}=\ldots=W_{m-1,\pm}\equiv W_{\pm}$. Consequently, the scattering coefficients of n_m and n_1 can be related by the following expressions:

$$\frac{R_1}{R_m}=\left(\frac{W_{+}+jN_{+}\omega_0}{W_{-}-j\omega_0}\right)^{m-1};\quad\frac{T_1}{T_m}=\left(\frac{W_{+}-jN_{+}\omega_0}{W_{-}-j\omega_0}\right)^{m-1}. \tag{C8.26}$$

10. In contrast to the spatial scattering discussed within the framework of quantum mechanics (see page 186), the poles of $R_{1,2}$ and $T_{1,2}$ cannot correspond with a tail of a temporal bound state. In this case, the poles of the scattering coefficients involve a complex value of ω_0 or N_+ and, consequently, these situations are directly discarded (we have assumed positive-real constitutive parameters).

On the other hand, given a time-varying refractive index profile $n_1\left(t\right)=n_{1,-}/N_1\left(t\right)$, its T-SUSY profile $n_2\left(t\right)=n_{2,-}/N_2\left(t\right)$ can be directly found by combining Eq. (C8.12) and Riccati's equation ($V_{1,2}=W^2\mp W'$):

$$n_2\left(t;\Omega,n_{2,-}\right)=\frac{n_{2,-}}{\sqrt{\frac{n_{1,-}^2}{n_1^2(t)}-\frac{2}{\omega_0^2}W'\left(t;\Omega\right)}}, \tag{C8.27}$$

where the semicolon symbol is used to separate explicitly the system parameters ($\equiv$ degrees of freedom) from the time variable. Specifically, as mentioned above, $n_{2,-}$ allows us to change the background material preserving the same intensity scattering properties as the original modulation $n_1\left(t\right)$, and the Ω parameter can be employed to tailor different features of $n_2\left(t\right)$, e.g., its maximal excursion (see next subsection).

Shape Invariant Potentials (SIP)

As introduced in Chapter 6 (see Section 6.12), two different potentials are *shape invariant* if they are similar in shape and differ only in the parameters that appear in them. In our case, two T-SUSY potentials $V_{1,2}$ are also said to be shape invariant if obey the relation:

$$V_2\left(t;\boldsymbol{a}_1\right)=V_1\left(t;\boldsymbol{a}_2\right)+M\left(\boldsymbol{a}_1\right), \tag{C8.28}$$

where $(\boldsymbol{a}_1,\boldsymbol{a}_2)\in\mathbb{R}^p\times\mathbb{R}^p$ are a set of parameters related by a multivariate function $\boldsymbol{f}\in\mathcal{F}(\mathbb{R}^p,\mathbb{R}^p)$ of the form $\boldsymbol{a}_2=\boldsymbol{f}\left(\boldsymbol{a}_1\right)$, and $M\in\mathcal{F}(\mathbb{R}^p,\mathbb{R})$. In our numerical examples, we take $p=1$.

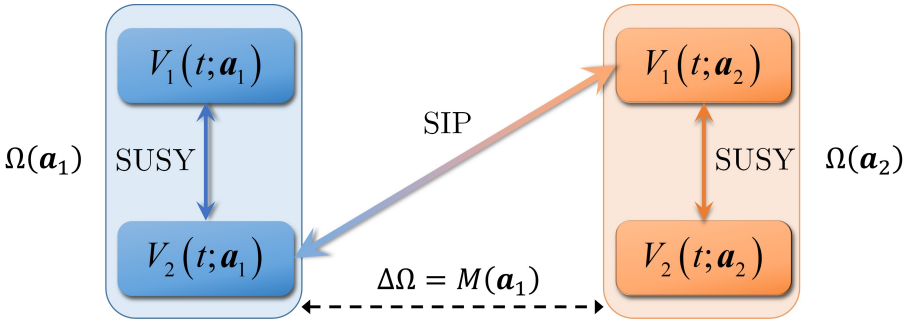

Figure C8.1. Eigenvalue relation between SIP temporal superpartners supporting continuous spectra.

From the above equation, we can infer the following properties of the temporal scattering problem, with the superpartners supporting a continuous spectrum:

- Eq. (C8.28) establishes an eigenvalue relation between superpartners of the form (see Fig. C8.1):

$$\Omega\left(\boldsymbol{a}_1\right)=\Omega\left(\boldsymbol{a}_2\right)+M\left(\boldsymbol{a}_1\right), \tag{C8.29}$$

  where $\Omega\left(\boldsymbol{a}_i\right)\in I_i\subset\mathbb{R}$ and I_i is the eigenvalue spectrum of the SUSY partners $V_{1,2}\left(\boldsymbol{a}_i\right)$.

- Since $V_{i,\pm}\left(\boldsymbol{a}_j\right)=W_{\pm}^2\left(\boldsymbol{a}_j\right)\ \forall\left(i,j\right)\in\left\{1,2\right\}^2$, then:

$$W_{\pm}^2\left(\boldsymbol{a}_1\right)=W_{\pm}^2\left(\boldsymbol{a}_2\right)+M\left(\boldsymbol{a}_1\right). \tag{C8.30}$$

  Consequently, the superpotential depends on the SIP parameters at $t\rightarrow\pm\infty$.

- As demonstrated on page 198, the wave functions are connected as:

$$\psi^{(2)}\left(t;\boldsymbol{a}_1\right)=\psi^{(1)}\left(t;\boldsymbol{a}_2\right). \tag{C8.31}$$

- Combining Eqs. (C8.28) and (C8.29) in $\Omega\left(\boldsymbol{a}_1\right)-V_2\left(t;\boldsymbol{a}_1\right)=\omega_0^2N_2^2\left(t;\boldsymbol{a}_1\right)$ we find that $N_2\left(t;\boldsymbol{a}_1\right)=N_1\left(t;\boldsymbol{a}_2\right)$ and, therefore:

$$n_2\left(t;\boldsymbol{a}_1\right)=\frac{n_{2,-}\left(\boldsymbol{a}_1\right)}{n_{1,-}\left(\boldsymbol{a}_2\right)}n_1\left(t;\boldsymbol{a}_2\right), \tag{C8.32}$$

  with $n_{2,-}\left(\boldsymbol{a}_1\right)$ a degree of freedom of the problem.

- Interestingly, $N_{\pm}$ does not depend on the SIP parameters at $t\rightarrow\pm\infty$. Using Eqs. (C8.29) and (C8.30):

$$\begin{aligned}\omega_0^2N_{\pm}^2\left(\boldsymbol{a}_1\right)&=\Omega\left(\boldsymbol{a}_1\right)-W_{\pm}^2\left(\boldsymbol{a}_1\right)=\Omega\left(\boldsymbol{a}_2\right)+M\left(\boldsymbol{a}_1\right)-W_{\pm}^2\left(\boldsymbol{a}_2\right)-M\left(\boldsymbol{a}_1\right)\\&=\Omega\left(\boldsymbol{a}_2\right)-W_{\pm}^2\left(\boldsymbol{a}_2\right)=\omega_0^2N_{\pm}^2\left(\boldsymbol{a}_2\right),\end{aligned} \tag{C8.33}$$

  we verify that $N_{\pm}\left(\boldsymbol{a}_1\right)=N_{\pm}\left(\boldsymbol{a}_2\right)$.

- From Eq. (C8.31), we can infer that $R_2\left(\boldsymbol{a}_1\right)=R_1\left(\boldsymbol{a}_2\right)$ and $T_2\left(\boldsymbol{a}_1\right)=T_1\left(\boldsymbol{a}_2\right)$. As a result, Eq. (C8.22) can be restated as:

$$\frac{R_1\left(\boldsymbol{a}_1\right)}{R_1\left(\boldsymbol{a}_2\right)}=\frac{W_+\left(\boldsymbol{a}_1\right)+jN_+\omega_0}{W_-\left(\boldsymbol{a}_1\right)-j\omega_0};\quad\frac{T_1\left(\boldsymbol{a}_1\right)}{T_1\left(\boldsymbol{a}_2\right)}=\frac{W_+\left(\boldsymbol{a}_1\right)-jN_+\omega_0}{W_-\left(\boldsymbol{a}_1\right)-j\omega_0}. \tag{C8.34}$$

- In a T-SUSY refractive index chain with m shape invariant potentials in the continuum, Eq. (C8.28) can be generalized to:

$$V_m\left(t;\boldsymbol{a}_1\right)=V_1\left(t;\boldsymbol{a}_m\right)+\sum_{i=1}^{m-1}M\left(\boldsymbol{a}_i\right), \tag{C8.35}$$

  with $\boldsymbol{a}_i=(\mathring{\boldsymbol{f}})^{i-1}\left(\boldsymbol{a}_1\right)$ [e.g., $\boldsymbol{a}_3=(\mathring{\boldsymbol{f}})^2\left(\boldsymbol{a}_1\right)=\left(\boldsymbol{f}\circ\boldsymbol{f}\right)\left(\boldsymbol{a}_1\right)=\boldsymbol{f}(\boldsymbol{f}(\boldsymbol{a}_1))$]. Hence, Eqs. (C8.29)-(C8.32) become:

$$\Omega\left(\boldsymbol{a}_1\right)=\Omega\left(\boldsymbol{a}_m\right)+\sum_{i=1}^{m-1}M\left(\boldsymbol{a}_i\right); \tag{C8.36}$$

$$W_{\pm}^2\left(\boldsymbol{a}_1\right)=W_{\pm}^2\left(\boldsymbol{a}_m\right)+\sum_{i=1}^{m-1}M\left(\boldsymbol{a}_i\right); \tag{C8.37}$$

$$\psi^{(m)}\left(t;\boldsymbol{a}_1\right)=\psi^{(1)}\left(t;\boldsymbol{a}_m\right); \tag{C8.38}$$

$$n_m\left(t;\boldsymbol{a}_1\right)=\frac{n_{m,-}\left(\boldsymbol{a}_1\right)}{n_{1,-}\left(\boldsymbol{a}_m\right)}n_1\left(t;\boldsymbol{a}_m\right). \tag{C8.39}$$

Thus, $R_m(\boldsymbol{a}_1) = R_1(\boldsymbol{a}_m)$, $T_m(\boldsymbol{a}_1) = T_1(\boldsymbol{a}_m)$ and the scattering relations given by Eq. (C8.26) can be recast as:

$$\frac{R_1(\boldsymbol{a}_1)}{R_1(\boldsymbol{a}_m)} = \left(\frac{W_+(\boldsymbol{a}_1) + jN_+\omega_0}{W_-(\boldsymbol{a}_1) - j\omega_0}\right)^{m-1}; \quad \frac{T_1(\boldsymbol{a}_1)}{T_1(\boldsymbol{a}_m)} = \left(\frac{W_+(\boldsymbol{a}_1) - jN_+\omega_0}{W_-(\boldsymbol{a}_1) - j\omega_0}\right)^{m-1}. \quad \text{(C8.40)}$$

Isospectral Transformations

In the next lines, we will discuss the possibility of using SUSY transformations in the time domain to construct, from a given refractive index $n_1(t)$, an m-parameter family of isospectral refractive index profiles $\widetilde{n}_1(t;\eta_1,\ldots,\eta_m)$, that is, time-varying optical systems with exactly the same scattering properties in module and phase as the original one.

The *one-parameter* isospectral family $\widetilde{V}_1(x;\eta_1)$ of a given potential $V_1(x)$ can be calculated as indicated in Chapter 6, Subsection 6.11.1. In this vein, using our quantum-optical analogy [Eq. (C8.12)], we find the one-parameter isospectral family $\widetilde{n}_1(t;\eta_1)$ of the refractive index $n_1(t)$:

$$\widetilde{n}_1(t;\eta_1) = \frac{\widetilde{n}_{1,-}(\eta_1)}{\sqrt{\frac{n_{1,-}^2}{n_1^2(t)} + \frac{2}{\omega_0^2}\frac{\mathrm{d}^2}{\mathrm{d}t^2}\ln\left[\eta_1 + \int^t \exp\left(-2\int^\alpha W(\beta)\,\mathrm{d}\beta\right)\mathrm{d}\alpha\right]}}, \quad \text{(C8.41)}$$

with η_1 and $\widetilde{n}_{1,-}(\eta_1)$ degrees of freedom of the problem. Interestingly, the above family has exactly the same scattering coefficients as the original modulation, provided that we use a nonsingular superpotential family, which is fulfilled with $\eta_1 > 0$. It is straightforward to prove this statement. Let us denote the scattering coefficients of $\widetilde{n}_1(t;\eta_1)$ as $R_1(\eta_1)$ and $T_1(\eta_1)$. The ratios $R_1(\eta_1)/R_2$ and $T_1(\eta_1)/T_2$ can be expressed in the same form as Eq. (C8.22), but replacing $W_\pm$ by $\widetilde{W}_\pm(\eta_1)$ and $N_\pm$ by $\widetilde{N}_\pm(\eta_1)$, with $\widetilde{N}_\pm(\eta_1) := \widetilde{N}_1(t\to\pm\infty;\eta_1) = \widetilde{n}_{1,-}(\eta_1)/\widetilde{n}_1(t\to\pm\infty;\eta_1)$ and:

$$\widetilde{W}_\pm(\eta_1) := \widetilde{W}(t\to\pm\infty;\eta_1) = \lim_{t\to\pm\infty}\left\{W(t) + \frac{\mathrm{d}}{\mathrm{d}t}\ln\left[\eta_1 + \int^t \exp\left(-2\int^\alpha W(\beta)\,\mathrm{d}\beta\right)\mathrm{d}\alpha\right]\right\}. \quad \text{(C8.42)}$$

Concretely, $\widetilde{W}(t;\eta_1)$ is the family of superpotentials connecting $\widetilde{V}_1(t;\eta_1)$ and $V_2(t)$ via the Riccati equation. In order to preserve the scattering properties between both superpartners, the superpotential family must be nonsingular (sufficient condition but not necessary). To this end, we set $\eta_1 > 0$. Finally, taking into account that $\widetilde{W}_\pm(\eta_1) = W_\pm$ and $\widetilde{N}_\pm(\eta_1) = N_\pm$, we demonstrate that $R_1(\eta_1) = R_1$ and $T_1(\eta_1) = T_1$.

In addition, it is worth highlighting the possibility of combining the one-parameter isospectral transformation along with SIP. More specifically, given two potentials $V_i(t;\boldsymbol{a}_1)$ and $V_{i+1}(t;\boldsymbol{a}_1)$ of a SUSY chain calculated respectively with SIP from $V_1(t;\boldsymbol{a}_i)$ and $V_1(t;\boldsymbol{a}_{i+1})$ by using Eq. (C8.35), we can obtain the superpotential $W_i(t;\boldsymbol{a}_1)$ from:

$$W_i(t;\boldsymbol{a}_1) = W_-(\boldsymbol{a}_1) + \frac{1}{2}\int_{-\infty}^t \left[V_1(\tau;\boldsymbol{a}_{i+1}) - V_1(\tau;\boldsymbol{a}_i) + M(\boldsymbol{a}_i)\right]\mathrm{d}\tau, \quad \text{(C8.43)}$$

and later calculate the family $\widetilde{W}_i(t;\boldsymbol{a}_1,\eta_1)$ to construct the isospectral family $\widetilde{n}_i(t;\boldsymbol{a}_1,\eta_1)$ with the same scattering properties in module and phase as those of $n_i(t;\boldsymbol{a}_1)$. As seen, the temporal scattering can be analyzed and designed in a large number of time-varying optical systems by combining both SUSY transformations.

On the other hand, the *multi-parameter* isospectral family $\widetilde{n}_1(t;\eta_1,\ldots,\eta_m)$ can be calculated from the multi-parameter Darboux procedure detailed in Chapter 6, Subsection 6.11.2. Here, we only describe the different steps of this procedure when is applied to time-varying optical systems:

1. We start from a given refractive index profile $n_1(t)$ associated with a QM potential $V_1(t\to x)$ via Eq. (C8.12). This potential must support bound states and must satisfy the sufficient conditions detailed at the beginning of this section to guarantee that the temporal scattering problem is well-defined [Eq. (C8.14)].

2. Next, we generate the family $\widetilde{V}_1(x;\eta_1,\ldots,\eta_m)$ from $V_1(x)$ by using the multi-parameter Darboux procedure.

3. Finally, performing the relabeling $\widetilde{V}_1\left(x \to t; \eta_1, \ldots, \eta_m\right)$ we obtain the sought family:

$$\widetilde{n}_1\left(t; \eta_1, \ldots, \eta_m\right) = \frac{\widetilde{n}_{1,-}\left(\eta_1, \ldots, \eta_m\right)}{\sqrt{1 + \frac{1}{\omega_0^2}\left[V_{1,-} - \widetilde{V}_1\left(t; \eta_1, \ldots, \eta_m\right)\right]}}, \tag{C8.44}$$

where $\{\eta_1, \ldots, \eta_m\} \subset \mathbb{R}^+$ and $\widetilde{n}_{1,-}\left(\eta_1, \ldots, \eta_m\right)$ are degrees of freedom in the above equation.

C8.3 Temporal scattering and T-SUSY: numerical examples

In this subsection, we include additional numerical examples of the temporal scattering problem in T-SUSY optical systems.

Transparent hyperbolic secant modulation

In the main text, we analyzed the T-SUSY refractive index profile $n_2\left(t\right)$ of a constant and, therefore, transparent refractive index $n_1\left(t\right) = n_{1,-}$. In such a case, using Eq. (C8.12), we infer that the original potential is:

$$V_1\left(t\right) = \Omega - \omega_0^2, \tag{C8.45}$$

which leads to a superpotential of the form:

$$W\left(t; \Omega\right) = -\sqrt{\Omega - \omega_0^2}\tanh\left(\sqrt{\Omega - \omega_0^2}\, t\right). \tag{C8.46}$$

Finally, using Eq. (C8.27), we find the T-SUSY refractive index:

$$n_2\left(t; \Omega, n_{2,-}\right) = \frac{n_{2,-}}{\sqrt{1 + \frac{2}{\omega_0^2}\left(\Omega - \omega_0^2\right)\operatorname{sech}^2\left(\sqrt{\Omega - \omega_0^2}\, t\right)}}, \tag{C8.47}$$

with $\Omega \geq \omega_0^2$, as discussed on page 271. In the following, we will first discuss the case $\Omega > \omega_0^2$, and later, we will analyze the case $\Omega = \omega_0^2$.

Considering $\Omega > \omega_0^2$, we observe two degrees of freedom in Eq. (C8.47): $n_{2,-}$ and Ω. The former allows us to implement the above refractive index modulation in different background materials, and the latter can be employed to tailor its maximal excursion (Δn) and its temporal width (Δt).[26] Figure C8.2 shows the refractive index $n_2\left(t; \Omega, n_{2,-}\right)$ for different values of the ratio Ω/ω_0^2. As seen, the higher the value of Ω/ω_0^2 is, the higher Δn and the lower Δt are. Along this line, it can be noted that the value of Ω/ω_0^2 also allows us to select the phase shifting performed by n_2. Specifically, bearing in mind that $R_1 = 0$ and $T_1 = 1$, we find from Eq. (C8.22) that $R_2 = 0$ and:

$$T_2 = \left|T_2\right| \exp\left(j\Phi_{T_2}\right) = \exp\left[-j\left(\pi + 2\arctan\frac{1}{\sqrt{\Omega/\omega_0^2 - 1}}\right)\right]. \tag{C8.48}$$

Figure C8.3 compares Eq. (C8.48) with the numerical results calculated with COMSOL solving the exact wave equation (8.2.1) taking $n_{2,-} = 2$, $\omega_0 = 38$ rad/s and $c_0 = 1$ m/s to guarantee a low computational time of the numerical simulations.[27] We can note that the transmitted amplitude T_2 calculated with T-SUSY is in good agreement with the numerical results of the wave equation.

These graphics, along with Fig. 8.3, could be of great interest to design and synthesize an *ideal* omnidirectional, polarization-independent, transparent and reconfigurable optical phase shifter using, e.g., electro-optic modulators at microwave frequencies ($T_0 \in [3, 3000]$ ps), where the required index modulation speed may be implementable with current technology [355]. From the selected value Ω/ω_0^2, we can directly estimate the performed phase shifting (Fig. C8.3), the required Δn

[26] The parameter Δn is defined as $\Delta n := n_{2,-} - \min\left\{n_2\left(t; \Omega, n_{2,-}\right)\right\}$ and the parameter Δt is defined as the full-width at $1/\left(2e\right)$ maximum of the temporal profile $n_{2,-} - n_2\left(t; \Omega, n_{2,-}\right)$.

[27] The conclusions detailed below and in the next numerical examples are valid for any value of ω_0 and c_0.

and Δt (Fig. C8.2), and the spectral band of transparency (Fig. 8.3). Remarkably, these results can be implemented in all-dielectric, all-magnetic materials, or a combination of both. In the latter case, despite the fact that we must assume a slowly-varying temporal evolution in one of the constitutive parameters (see Appendix A8.1), n_2 may also present rapidly-varying temporal fluctuations. Moreover, note that these results are independent of the value of ω_0 and only depend on the ratio Ω/ω_0^2. Accordingly, they can be directly extrapolated to the range of THz.

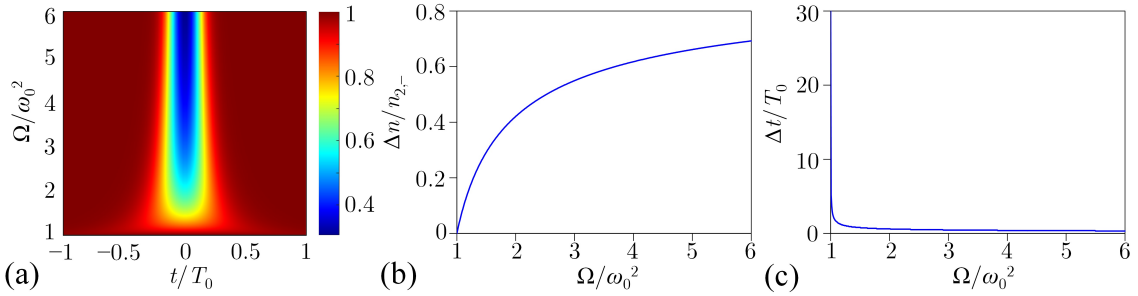

Figure C8.2. Hyperbolic secant temporal index modulation Eq. (C8.47). (a) Normalized refractive index profile $n_2(t;\Omega,n_{2,-})/n_{2,-}$, (b) normalized maximal excursion $\Delta n/n_{2,-}$, and (c) normalized temporal width $\Delta t/T_0$, with $T_0 = 2\pi/\omega_0$. All graphics have been normalized to guarantee the same results for any value of ω_0 and $n_{2,-}$.

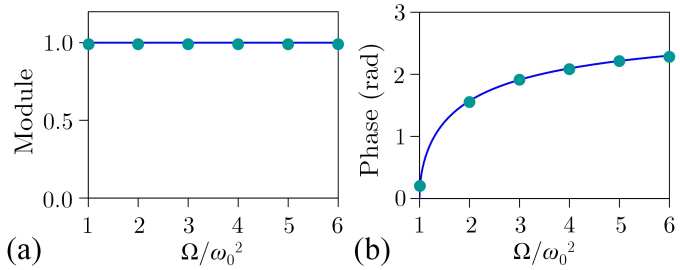

Figure C8.3. Scattering coefficient T_2 given by Eq. (C8.48) (blue line) and calculated numerically from Eq. (8.2.1) using COMSOL Multiphysics (dots). (a) Module and (b) phase as a function of the ratio Ω/ω_0^2.

In addition, as discussed in Fig. 8.3(c), Φ_{T_2} shows a flat frequency response. Consequently, in our phase shifter, the reconfigurable and frequency-independent response of the phase could be of extreme utility for wavelength-division multiplexing (WDM) transmissions of *narrow-band* signals to generate the same phase shifting in each WDM channel minimizing the distortion of the optical pulses induced by the nonlinear behavior of Φ_{T_2}. In such a scenario, if we use electro-optic modulators with a reduced Δn excursion ($\Delta n \sim 10^{-3}$), we must operate in the range $\Omega/\omega_0^2 < 1.01$, where $\Phi_{T_2} < 1$ rad. In these circumstances, it would be of interest to us to concatenate a chain of non-reflecting hyperbolic secant modulations to increase the phase shifting induced by a single hyperbolic secant. Concretely, the hyperbolic secant chain (HSC) can be described as:

$$n_{\mathrm{HSC}}(t) = \sum_{k=0}^{N_{\mathrm{HSC}}-1} n_2\left(t + \left(\frac{N_{\mathrm{HSC}}-1}{2} - k\right)\mathcal{T}_{\mathrm{HSC}};\Omega,n_{2,-}\right) - (N_{\mathrm{HSC}}-1)\,n_{2,-}, \tag{C8.49}$$

where $\mathcal{T}_{\mathrm{HSC}}$ is the fundamental period of the chain and N_{HSC} is the number of fundamental periods [see Fig. C8.4(a)]. In order to analyze the scattering behavior of $n_{\mathrm{HSC}}(t)$, we numerically calculate the scattering coefficients R_{HSC} and T_{HSC} as a function of the ratio $\mathcal{T}_{\mathrm{HSC}}/\mathcal{T}_{\mathrm{P}}$, where $\mathcal{T}_{\mathrm{P}}$ is the full-width at $1/(2e)$ of the peak power of the incident pulse. Figure C8.4 shows the numerical results of R_{HSC} and T_{HSC} taking: $\Omega/\omega_0^2 = 1.01$ [Fig. C8.4(b)] and $\Omega/\omega_0^2 = 6$ [Fig. C8.4(c)] in Eq. (C8.49), $N_{\mathrm{HSC}} \in \{2,3,4\}$, $\mathcal{T}_{\mathrm{HSC}}/\mathcal{T}_{\mathrm{P}} \in (0,2]$, and $\mathcal{T}_{\mathrm{P}} = 1$ s. We can observe that the module and phase of R_{HSC} and T_{HSC} have a flat behavior as a function of $\mathcal{T}_{\mathrm{HSC}}/\mathcal{T}_{\mathrm{P}}$, even if $\mathcal{T}_{\mathrm{HSC}} < \mathcal{T}_{\mathrm{P}}$. Hence, as expected, we can use an HSC to increase the phase shifting of the original hyperbolic secant [$\Phi_{T_{\mathrm{HSC}}}(N_{\mathrm{HSC}}) = N_{\mathrm{HSC}}\Phi_{T_2}$] maintaining its non-reflecting nature.

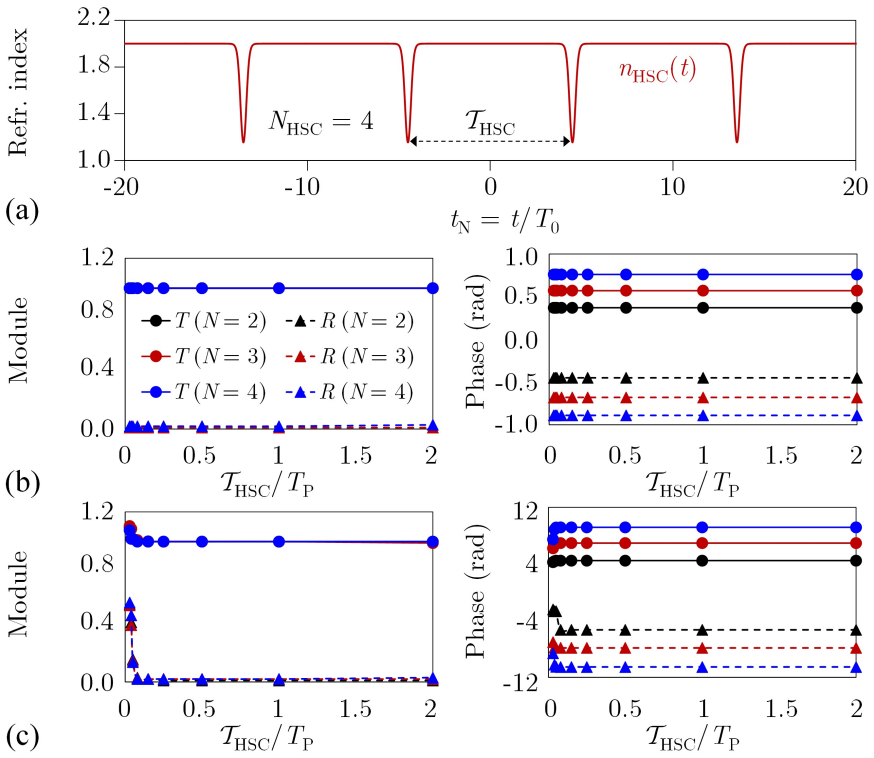

Figure C8.4. Chain of non-reflecting hyperbolic secant refractive index profiles. (a) Refractive index profile $n_{\mathrm{HSC}}(t)$. Scattering coefficients T_{HSC} and R_{HSC} calculated numerically as a function of the ratio $\mathcal{T}_{\mathrm{HSC}}/T_{\mathrm{P}}$, where T_{P} is the full-width at $1/(2e)$ of the peak power of the incident pulse for: (b) $\Omega/\omega_0^2 = 1.01$ and (c) $\Omega/\omega_0^2 = 6$. The number of fundamental periods N_{HSC} of the chain ranges from 2 to 4. The legend of (b) also applies to (c). We omit the subindexes of T_{HSC}, R_{HSC} and N_{HSC} in the legend due to space constraints.

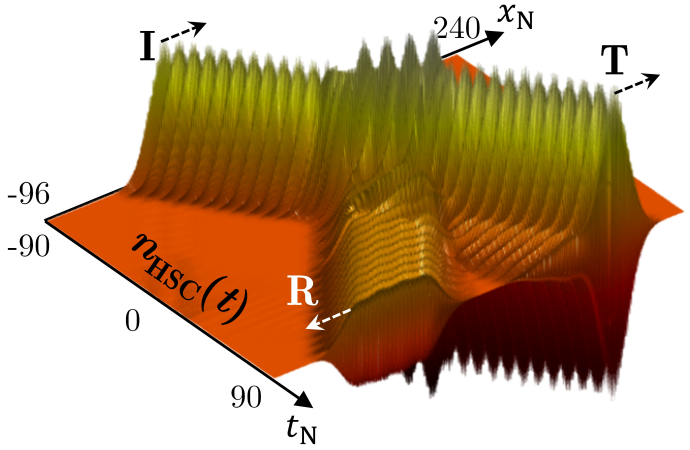

Figure C8.5. Spatio-temporal evolution of a Gaussian pulse propagated at $\omega = 1.4\omega_0$ through the time-varying medium described by the hyperbolic secant chain $n_{\mathrm{HSC}}(t)$ of Fig. C8.4(a). A reflected (R) and a transmitted (T) optical pulse are generated from the interaction of the incident (I) pulse with $n_{\mathrm{HSC}}(t)$. As a result of this interaction, we can observe a flat-top optical pulse in reflection and a distorted Gaussian pulse in transmission. Note that the transmitted pulse has a higher peak power than the incident pulse because the energy is not conserved in a time-varying system (I $\neq$ R + T). The temporal axis is normalized as $t_{\mathrm{N}} = t/T_0$ with $T_0 = 2\pi/\omega_0$. The x-axis is normalized as $x_{\mathrm{N}} = x/\lambda$, with $\lambda = \lambda_0/n_{2,-}$ and $\lambda_0 = 2\pi c_0/\omega_0$.

On the other hand, the reflecting behavior of $n_2(t)$ at $\omega \neq \omega_0$ and the nonlinear nature of $\Phi_{T_2}(\omega)$ [see Fig. 8.3(c)] can be exploited to implement pulse shaping operations in reflection and transmission. Specifically, in reflection, we can build a flat-top optical pulse using the HSC. The chain generates N_{HSC} reflected pulses of temporal width T_{P} and separated $\mathcal{T}_{\text{HSC}}$ in time. Hence, selecting $T_{\text{P}} \sim \mathcal{T}_{\text{HSC}}$, we will obtain a flat-top optical pulse emerging from the superposition of all the reflected pulses. Figure C8.5 illustrates this basic idea. We build an HSC with $\Omega/\omega_0^2 = 6$, $\omega = 1.4\omega_0$, $\mathcal{T}_{\text{HSC}}/T_{\text{P}} = 1.2$, $T_{\text{P}} = 1\,\text{s}$ and $N_{\text{HSC}} = 4$. As seen, a flat-top optical pulse can be observed in reflection at the end of the chain. Moreover, the tail of the transmitted pulse has been distorted due to the nonlinear nature of $\Phi_{T_2}(\omega)$.[28] This can be further investigated in future works to generate transmitted optical pulses with an exotic shape, e.g., for optical wavelet transforms, coherent laser control of physicochemical processes or spectrally selective nonlinear microscopy among other application areas [339–341]. On the contrary, the pulse distortion induced by the nonlinear frequency response of $\Phi_{T_2}(\omega)$ can be reduced if we operate with narrow-band incident optical pulses.

So far, we have extensively evaluated the T-SUSY refractive index of $n_1(t) = n_{1,-}$ by taking $\Omega > \omega_0^2$. Now, we focus our attention on the case $\Omega = \omega_0^2$. In such circumstances, $V_1(t) = 0$, $W(t) = 1/(C-t)$ and:

$$n_2(t; C, n_{2,-}) = \frac{n_{2,-}}{\sqrt{1 - \frac{2}{\omega_0^2 (C-t)^2}}}, \tag{C8.50}$$

where C is an integration constant arising from Riccati's equation. Figure C8.6 illustrates the T-SUSY refractive index profile given by the above equation. Now, it is fundamental to note that we have a singular superpotential that may break the degeneracy of the eigenvalue spectra between both superpartners ($\Omega^{(1)} \neq \Omega^{(2)}$). More precisely, note that $\boldsymbol{D}^{(2)} \propto (\partial_t + W(t))\,\boldsymbol{D}^{(1)}$ is not a continuous function at $t = C$. Therefore, $\boldsymbol{D}^{(2)}$ cannot be a solution of Maxwell's equations. The boundary conditions of the temporal scattering are not satisfied ($\boldsymbol{D}^{(2)}$ and $\partial_t \boldsymbol{D}^{(2)}$ must be necessarily continuous functions in the temporal variable). As a result, in this case, we cannot guarantee the same intensity scattering properties for n_1 and n_2.

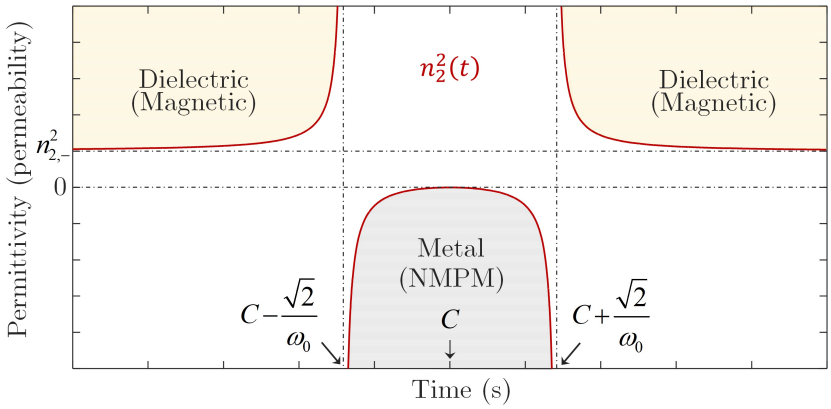

Figure C8.6. T-SUSY permittivity (permeability) n_2^2 [Eq. (C8.50)] of a constant permittivity (permeability) $n_{1,-}^2$ when $\Omega = \omega_0^2$. (NMPM: negative magnetic permeability material).

Isospectral two-parameter family

As an application of the isospectral theory detailed in Appendix C8.2, let us consider the Hyperbolic Rosen-Morse II (HRMII) refractive index:

$$n_1(t; m) = \frac{\omega_0 n_{1,-}(m)}{\sqrt{\omega_0^2 + m(m+1)\,\text{sech}^2 t}}, \tag{C8.51}$$

[28] The nonlinear frequency dependence of the phase $\Phi_{T_2}(\omega)$ implies that each spectral component of $\boldsymbol{D}_{\text{I}}^{(2)}(\boldsymbol{r}, t)$ is phase shifted by a different quantity. Consequently, the envelope of an incident wide-band optical pulse will be distorted in transmission.

where $m \in \mathbb{Z}$. Remarkably, the above refractive index profile is transparent (see below page 281). Taking $\Omega = \omega_0^2$ in Eq. (C8.12), the corresponding quantum potential is of the form (step 1 of the isospectral theory, see page 274):

$$V_1(t \to x) = \Omega - \omega_0^2 \frac{n_{1,-}^2}{n_1^2(t \to x; m)} = -m(m+1)\,\mathrm{sech}^2 x. \tag{C8.52}$$

In particular, V_1 holds m bound states and the scattering problem is well-defined ($V_{1,\pm} < \infty$). For the case $m = 2$, the two-parameter isospectral family $\widetilde{V}_1(x; \eta_1, \eta_2)$ can be calculated from $V_1(x)$ by using the multi-parameter Darboux procedure (step 2):

$$\widetilde{V}_1(x; \eta_1, \eta_2) = -12 \frac{3 + 4\cosh(2x - 2\Lambda_2) + \cosh(4x - 2\Lambda_1)}{[\cosh(3x - \Lambda_2 - \Lambda_1) + 3\cosh(x + \Lambda_2 - \Lambda_1)]^2}, \tag{C8.53}$$

with $\Lambda_{1,2} = -0.5\ln(1 + 1/\eta_{1,2})$ and $\eta_{1,2} > 0$. Finally, performing the relabeling $\widetilde{V}_1(x \to t; \eta_1, \eta_2)$ and using Eq. (C8.44), we obtain the two-parameter isospectral family of time-varying optical systems (step 3):

$$\widetilde{n}_1(t; \eta_1, \eta_2) = \frac{\widetilde{n}_{1,-}(\eta_1, \eta_2)}{\sqrt{1 - \frac{1}{\omega_0^2}\widetilde{V}_1(t; \eta_1, \eta_2)}}. \tag{C8.54}$$

Figure C8.7 shows the refractive index profile of different time-varying optical systems of the family taking $\widetilde{n}_{1,-}(\eta_1, \eta_2) = n_{1,-} = 2$. We have numerically calculated the scattering coefficients of these refractive index profiles and we have found the same reflection and transmission coefficients in module and phase as those of the original modulation $n_1(t; m = 2)$ at $\omega = \omega_0$: $R_1(\eta_1, \eta_2) = 0$ and $T_1(\eta_1, \eta_2) = \exp(j0.23)$. Thus, we have constructed infinite transparent refractive index profiles in a simple and elegant way.

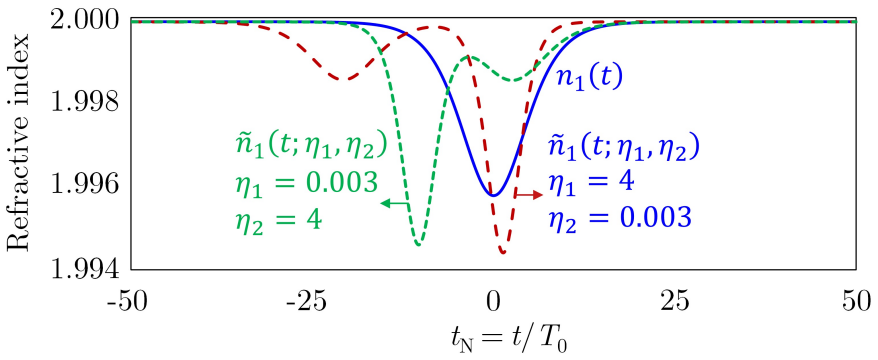

Figure C8.7. Two-parameter isospectral family of the transparent refractive index $n_1(t; m = 30)$ [Eq. (C8.51)].

Hyperbolic Rosen-Morse II potential: general relations

In the next two numerical examples, we will analyze the T-SUSY refractive index profiles emerging from the shape invariant HRMII potentials, described by the following equations:

$$W(t) = A\tanh(\alpha t) + B/A; \tag{C8.55}$$

$$V_1(t) = A^2 + B^2/A^2 - A(A + \alpha)\,\mathrm{sech}^2(\alpha t) + 2B\tanh(\alpha t); \tag{C8.56}$$

$$V_2(t) = A^2 + B^2/A^2 - A(A - \alpha)\,\mathrm{sech}^2(\alpha t) + 2B\tanh(\alpha t), \tag{C8.57}$$

with A, B and α real parameters and $B < A^2$. From the above expressions, we can verify that the SIP condition [Eq. (C8.28)] is fulfilled with $a_1 \equiv A$, $a_2 = f(a_1) = a_1 - \alpha$ and $M(a_1) = a_1^2 - (a_1 - \alpha)^2 + B^2[1/a_1^2 - 1/(a_1 - \alpha)^2]$. Taking $\Omega(a_1) = \omega_0^2 + W_-^2 = \omega_0^2 + (B/a_1 - a_1)^2$, the corresponding refractive index profiles are:

$$n_1(t;a_1) = \frac{\omega_0 n_{1,-}(a_1)}{\sqrt{\omega_0^2 - 2B + a_1(a_1+\alpha)\operatorname{sech}^2(\alpha t) - 2B\tanh(\alpha t)}}; \tag{C8.58}$$

$$n_2(t;a_1) = \frac{\omega_0 n_{2,-}(a_1)}{\sqrt{\omega_0^2 - 2B + a_1(a_1-\alpha)\operatorname{sech}^2(\alpha t) - 2B\tanh(\alpha t)}}. \tag{C8.59}$$

Equation (C8.58) is Eq. (8.2.9) of the main text. We also observe that $|W_-| = |W_+|$ ($|W_-| \neq |W_+|$) if $B = 0$ ($B \neq 0$). Hence, we have the ability of constructing reciprocal (non-reciprocal) time-varying optical systems with $\omega_{i,-} = \omega_{i,+}$ ($\omega_{i,-} \neq \omega_{i,+}$) and $i \in \mathbb{N}$. In the case $B \neq 0$, we should take into account that:

- The scattering coefficients of the electric (magnetic) flux density R_i and T_i are found to be different from the scattering coefficients of the electric (magnetic) field strength $\mathcal{R}_i$ and $\mathcal{T}_i$. More precisely, $\mathcal{R}_i = N_+^2 R_i$ and $\mathcal{T}_i = N_+^2 T_i$, with $N_+^2 = 1 - 4B/\omega_0^2 \in (0,1)$. Nonetheless, $\mathcal{R}_1/\mathcal{R}_2 = R_1/R_2$ and $\mathcal{T}_1/\mathcal{T}_2 = T_1/T_2$.
- From the previous point, we deduce that $0 < N_+ < 1$, $n_{i,-} < n_{i,+}$ and $B < \omega_0^2/4$.
- From the temporal version of Snell's law, we infer that the frequency of the transmitted signal is lower than that of the incident signal, with $\omega_{i,+} = N_+ \omega_{i,-}$.

In both cases ($B = 0$ and $B \neq 0$), the scattering relations [Eq. (C8.22)] become:

$$\frac{R_1(a_1)}{R_2(a_1)} = \frac{R_1(a_1)}{R_1(a_2)} = \frac{a_1 + B/a_1 + j\sqrt{\omega_0^2 - 4B}}{-a_1 + B/a_1 - j\omega_0}; \tag{C8.60}$$

$$\frac{T_1(a_1)}{T_2(a_1)} = \frac{T_1(a_1)}{T_1(a_2)} = \frac{a_1 + B/a_1 - j\sqrt{\omega_0^2 - 4B}}{-a_1 + B/a_1 - j\omega_0}. \tag{C8.61}$$

Figure C8.8 shows the above ratios as a function of ω_0 and a_1 setting $B = 0.4a_1^2$. As seen, the module is equal to 1 when $N_+ \in \mathbb{R}$ and the phase has a low dependence on ω_0. Furthermore, the lower the value of a_1 is, the lower the frequency dependence of the phase and the area where $N_+ \in \mathbb{C}$ are.

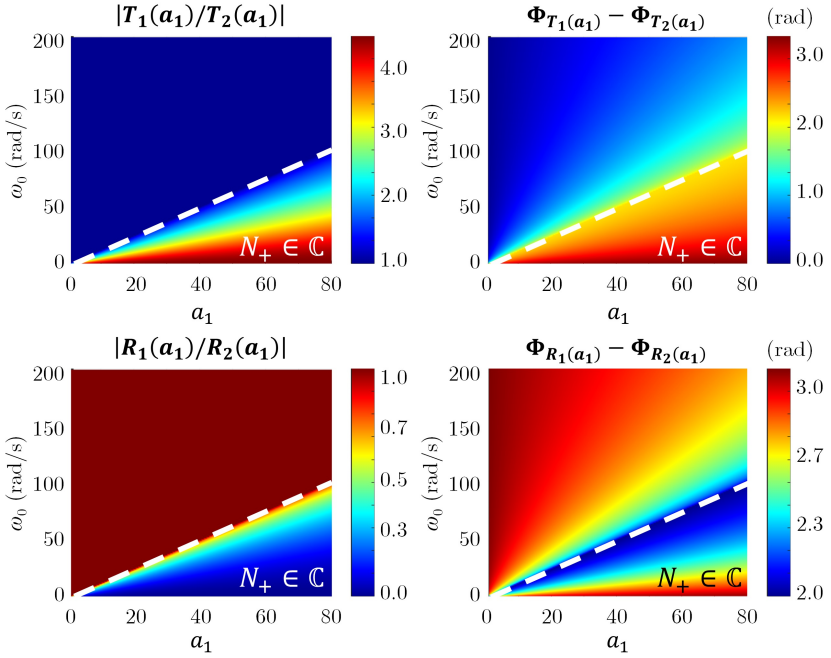

Figure C8.8. Ratios of the scattering coefficients in the hyperbolic Rosen-Morse II potential. The dashed white line separates the allowed ($N_+ \in \mathbb{R}$, top) and forbidden ($N_+ \in \mathbb{C}$, bottom) regions.

Hyperbolic Rosen-Morse II potential: case $B = 0$

The case $B = 0$ leads to reciprocal, omnidirectional, polarization-independent and transparent phase shifters such as the hyperbolic secant profile of the first numerical example. Specifically, taking $\alpha = a_1$ in Eq. (C8.58), we retrieve the aforementioned refractive index profile [Eq. (C8.47)]. Nevertheless, considering $\alpha = 1$ and $a_1 = m \in \mathbb{Z}$, we will find new refractive index modulations with an extremely large transparent optical bandwidth. In such a scenario, Eqs. (C8.58) and (C8.59) are reduced to:

$$n_1(t;m) = \frac{\omega_0 n_{1,-}(m)}{\sqrt{\omega_0^2 + m(m+1)\,\mathrm{sech}^2 t}}; \tag{C8.62}$$

$$n_2(t;m) = \frac{\omega_0 n_{2,-}(m)}{\sqrt{\omega_0^2 + m(m-1)\,\mathrm{sech}^2 t}}, \tag{C8.63}$$

obeying the SIP relation Eq. (C8.32), which can be rewritten as:

$$n_2(t;m) = \frac{n_{2,-}(m)}{n_{1,-}(m-1)} n_1(t;m-1)\,. \tag{C8.64}$$

From this recurrence relation as a function of the m parameter, we can infer the transparent behavior of these systems taking into account that they are SUSY-connected with the potential of the free particle ($m = 1$). Nevertheless, in contrast to the first numerical example [Eq. (C8.47)], we can note that the HRMII index has the advantage of allowing independent design control over $\Delta n \sim n_{1,2,-}\left|1 - \omega_0/\sqrt{\omega_0^2 + m(m \pm 1)}\right|$ for a fixed $\Delta t \sim 20T_0$, enabling a technology-oriented adjustment of the index modulation contrast. Figure C8.9(a) shows the T-SUSY refractive index profiles for the case $m = 30$, and Fig. C8.9(b) depicts their scattering coefficients as a function of the frequency. As commented before, we can observe an extremely large spectral band of transparency.

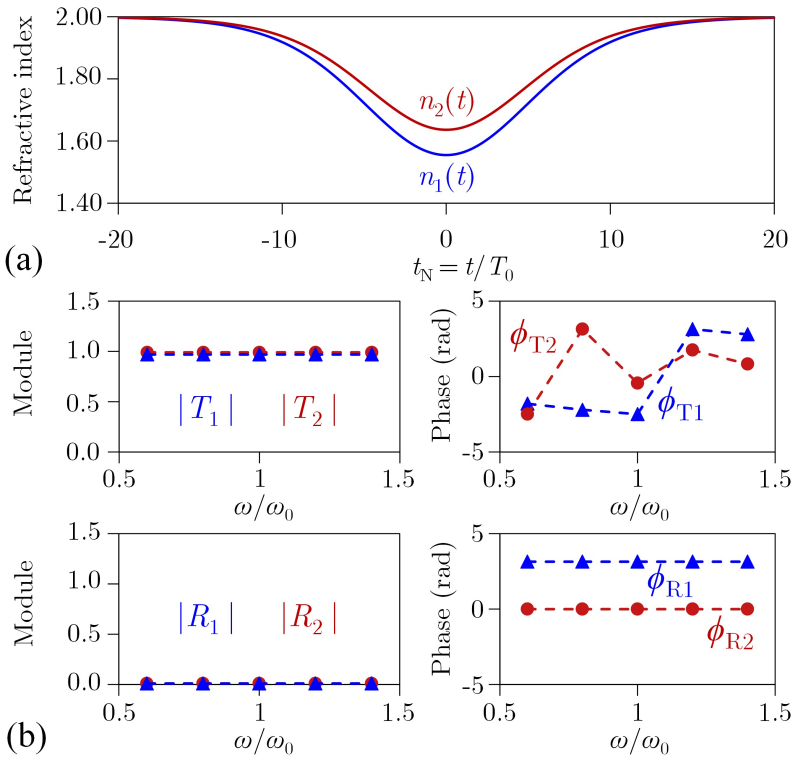

Figure C8.9. (a) T-SUSY refractive index profiles Eqs. (C8.62) and (C8.63) with $m = 30$. (b) Scattering coefficients calculated numerically as a function of the ratio ω/ω_0.

On the other hand, in this case we can report an analytic solution for $T_1(m)$, which can be calculated in the same way as the transmitted probability amplitude of the quantum-mechanical potential $V_1(x;m) = m^2 + \omega_0^2[1 - N_1^2(t \to x;m)]$ (see page 299 of [216]):

$$T_1(m) = \frac{\Gamma(-m - j\omega_0)\,\Gamma(m + 1 - j\omega_0)}{\Gamma(-j\omega_0)\,\Gamma(1 - j\omega_0)}, \tag{C8.65}$$

where Γ is the Gamma function. Figure C8.10 indicates an excellent fitting between the theoretical and numerical transmission coefficient associated with $n_1(t;m)$. Strikingly, Eq. (C8.65) can be combined with Eq. (C8.61) to solve straightforwardly the temporal scattering problem in this family of time-varying systems without using Maxwell's equations. Furthermore, it can be noted that we can select the desired phase of the transmitted wave via the m parameter.

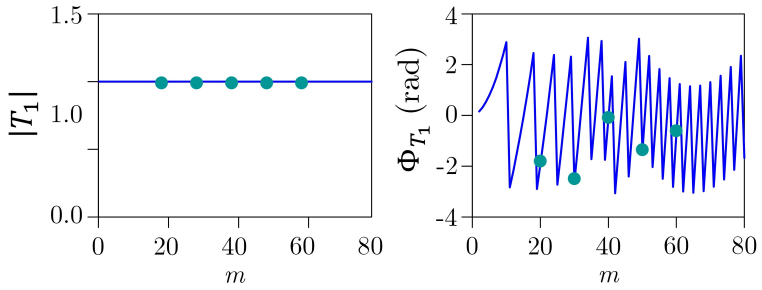

Figure C8.10. Transmission coefficient associated with the refractive index profile given by Eq. (C8.62) as a function of m. [Solid line: Eq. (C8.65). Dots: numerical results].

Hyperbolic Rosen-Morse II potential: case $B \neq 0$ (optical isolator)

The case $B \neq 0$ is of great interest to us given that builds a bridge to design non-reciprocal optical systems using time-varying refractive index modulations, as commented before and in the main text. In particular, the optical isolator demonstrated in Subsection 8.2.2 [the hyperbolic step-index profile of Fig. 8.4(a)] emerges from Eq. (C8.58) replacing a_1 by $a_6 = a_1 - 5\alpha$. The frequency down-conversion between the incident and transmitted waves, with angular frequencies $\omega_0 \equiv \omega_{6,-}$ and $\omega_{6,+}$, respectively, can be calculated from the Snell law as $\omega_{6,-}n_{6,-} = \omega_{6,+}n_{6,+}$. Hence, the ratio $\omega_{6,+}/\omega_{6,-}$ obeys the relation:

$$\frac{\omega_{6,+}}{\omega_{6,-}} = \frac{n_{6,-}}{n_{6,+}} = N_+ = \sqrt{1 - 4B/\omega_0^2}. \tag{C8.66}$$

Figure C8.11 depicts the ratio $\omega_{6,+}/\omega_{6,-}$ for different values of ω_0 and B. The dashed line separates the allowed ($N_+ \in \mathbb{R}$) and forbidden ($N_+ \in \mathbb{C}$) areas. In our case, we operate at $\omega_{6,+}/\omega_{6,-} \simeq 0.7$ with $\omega_0 \equiv \omega_{6,-} = 38$ rad/s. However, if we are interested in synthesizing the optical isolator of Fig. 8.1(c) using an angular frequency of the order of THz, we must select an adequate value of B that preserves the same value in Eq. (C8.66).

On the other hand, the ratios $R_1(a_1)/R_6(a_1)$ and $T_1(a_1)/T_6(a_1)$ can be calculated by combining Eq. (C8.40) with Eqs. (C8.60) and (C8.61). In particular, we find that:

$$\frac{T_1(a_1)}{T_6(a_1)} = \frac{T_1(a_1)}{T_1(a_6)} = \left(\frac{a_1 + B/a_1 - j\sqrt{\omega_0^2 - 4B}}{-a_1 + B/a_1 - j\omega_0}\right)^5 = \exp(j2.55), \tag{C8.67}$$

which is in good agreement with Fig. 8.4(b,c) at $\omega = \omega_0$. The ratio $R_1(a_1)/R_6(a_1)$ could not be numerically estimated because the non-reflecting behavior of $n_1(t;a_1)$ and $n_6(t;a_1)$ has a flat frequency response in an extremely large optical bandwidth (see Fig. 8.4). We could not observe any reflected wave in the numerical simulation when propagating wide-band optical pulses through the above media.

Interestingly, for the hyperbolic step-index profile with $\alpha = A = B^{1/2}$, we can find an analytic expression for the scattering coefficients (the mathematical derivation is detailed below):

$$R = -\frac{1}{N_+}\frac{\Gamma\left(j\omega_0/\alpha\right)\Gamma\left(1-j\omega_0 N_+/\alpha\right)}{\Gamma\left(j\omega_0\left(1-N_+\right)/2\alpha\right)\Gamma\left(1+j\omega_0\left(1-N_+\right)/2\alpha\right)}; \tag{C8.68}$$

$$T = \frac{1}{N_+}\frac{\Gamma\left(j\omega_0/\alpha\right)\Gamma\left(1+j\omega_0 N_+/\alpha\right)}{\Gamma\left(j\omega_0\left(1+N_+\right)/2\alpha\right)\Gamma\left(1+j\omega_0\left(1+N_+\right)/2\alpha\right)}. \tag{C8.69}$$

Figure C8.12 demonstrates a perfect fitting between the above expressions and the numerical results for a particular value of α. In this example, we can observe the non-reflecting behavior of the hyperbolic step-index profile when $\omega_0 > 10$ rad/s. In conclusion, we can combine the theoretical tools provided by T-SUSY, SIP and Eqs. (C8.68) and (C8.69) to design broadband polarization-independent optical isolators.

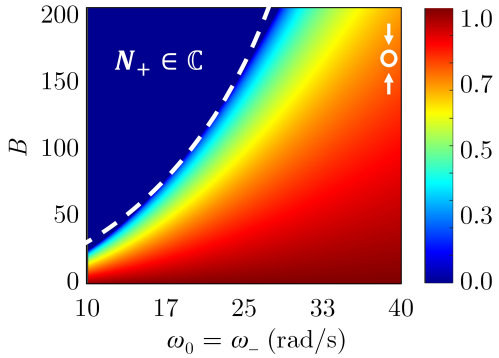

Figure C8.11. Frequency down-conversion $\omega_{6,+}/\omega_{6,-}$ as a function of ω_0 and B. The dashed line separates the allowed ($N_+ \in \mathbb{R}$) and forbidden ($N_+ \in \mathbb{C}$) areas. The hollow circle indicates the operation point of the optical isolator of the main text.

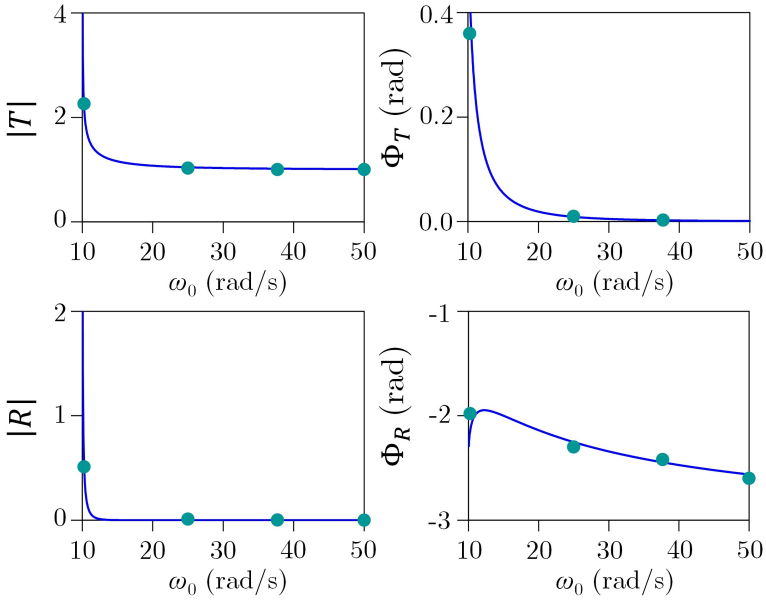

Figure C8.12. Scattering coefficients of the hyperbolic step-index profile [Eq. (C8.58) taking $\alpha = A = B^{1/2}$] as a function of ω_0 for the case $\alpha = 5$. [Solid line: Eqs. (C8.68) and (C8.69). Dots: numerical results].

***Derivation of Eqs.* (C8.68) *and* (C8.69).** Following a similar strategy as in [356], our first goal is to analyze the asymptotic behavior of the general solution of the time-independent Schrödinger equation when considering the hyperbolic step potential:

$$V(x) = \frac{1}{2}V_0\left[1 + \tanh\left(\frac{x}{2\widetilde{\alpha}}\right)\right], \tag{C8.70}$$

with $V_0 > 0$ and $\widetilde{\alpha} > 0$. The general solution to the equation $\psi''(x) + (E - V(x))\,\psi(x) = 0$ is given by Eq. (9) of [356], where $k = \sqrt{E}$ and $k' = \sqrt{E - V_0}$. Thus, using the asymptotic behavior of the hypergeometric functions, we find that [$\psi(x) \underset{x\to-\infty}{\sim} \psi_-(x)$ and $\psi(x) \underset{x\to\infty}{\sim} \psi_+(x)$]:

$$\begin{aligned}\psi_-(x) &= (C\Gamma_1(\mu,\nu) + D\Gamma_2(\mu,\nu))\exp(jkx) + (C\Gamma_3(\mu,\nu) + D\Gamma_4(\mu,\nu))\exp(-jkx)\\ &\equiv A\exp(jkx) + B\exp(-jkx);\end{aligned} \tag{C8.71}$$

$$\psi_+(x) = C\exp(jk'x) + D\exp(-jk'x), \tag{C8.72}$$

with C and D integration constants. The functions $\Gamma_i(\mu,\nu)$ can be found by identifying our Eq. (C8.71) with Eq. (11) of [356].

Along these lines, it is important to note that the sign convention employed in [356] is the same as that in Cooper's tutorial [216], and it is analogous to the sign convention employed in the temporal scattering problem for the forward and backward plane waves. In this way, one could expect that relabeling $k \to \omega_0$ and $k' \to N_+\omega_0$ in the expressions of R and T of [356], we would be able to obtain the reflection and transmission coefficients of the temporal scattering. Unfortunately, this procedure does not allow us to derive the closed-form expressions of R and T in the temporal scattering because the equations connecting R_1 (T_1) and R_2 (T_2) in spatial SUSY and T-SUSY are not analogous. Specifically, the *spatial scattering* is SUSY-connected in [216] as:

$$\exp(jkx) + R_1\exp(-jkx) = \xi\left(-\frac{\mathrm{d}}{\mathrm{d}x} + W_-\right)(\exp(jkx) + R_2\exp(-jkx)); \tag{C8.73}$$

$$T_1\exp(jk'x) = \xi\left(-\frac{\mathrm{d}}{\mathrm{d}x} + W_+\right)T_2\exp(jk'x). \tag{C8.74}$$

In contrast, the *temporal scattering* is SUSY-connected as:

$$\exp(j\omega_0 t) = \xi\left(-\frac{\mathrm{d}}{\mathrm{d}t} + W_-\right)\exp(j\omega_0 t); \tag{C8.75}$$

$$R_1\exp(-jN_+\omega_0 t) + T_1\exp(jN_+\omega_0 t) = \xi\left(-\frac{\mathrm{d}}{\mathrm{d}t} + W_+\right)(R_2\exp(-jN_+\omega_0 t) + T_2\exp(jN_+\omega_0 t)). \tag{C8.76}$$

If $R_1 = R_2 = 0$, both systems are analogous and we can perform the previous relabeling to find the reflection and transmission coefficients of the temporal scattering. For instance, we calculated Eq. (C8.65) using this procedure. Nevertheless, $R_{1,2} \neq 0$ in this case (see Fig. C8.12). Consequently, we should recalculate the scattering coefficients for the temporal problem from the beginning.

Considering that $\psi_-(t) = \exp(j\omega_0 t)$ and $\psi_+(t) = R\exp(-jN_+\omega_0 t) + T\exp(jN_+\omega_0 t)$, we infer from Eqs. (C8.71) and (C8.72) that $A = 1$, $B = 0$, $C = T$ and $D = R$. Now, using Eq. (14) of [356], we find that $C = t_{11}$ and $D = t_{21}$, where the transfer matrix t_{ij} is given by Eq. (16) of the aforementioned reference. Therefore, performing the transformation of parameters $\alpha = 1/(2\widetilde{\alpha})$ to match the definition of the hyperbolic step potential of [356] with our definition of the hyperbolic step-index profile [Eq. (C8.58) taking $\alpha = A = B^{1/2}$], we finally obtain Eqs. (C8.68) and (C8.69).

Supersymmetric time-reversal modulations

Interestingly, an *even* superpotential $W(t) = W(-t)$ allows us to construct T-SUSY time-reversal refractive index profiles of the form $n_2(t) = n_1(-t)$ with the same intensity scattering behavior, certainly an unexpected result taking into account that, in general, $n_1(-t)$ has different scattering properties from those of the original modulation $n_1(t)$ (consider, e.g., the step-index case [326]).

Let us analyze this scenario in more detail. To this end, consider a given W with even symmetry. In such a case, we can infer from Riccati's equation that:

$$V_2(t) = W^2(t) + W'(t) = W^2(-t) - W'(-t) = V_1(-t), \tag{C8.77}$$

and then, we find that $n_2(t) = n_1(-t)$ by setting $n_{2,-} = n_{1,-}$. Now, rewriting Eq. (C8.77) as $V_2(\boldsymbol{a}_1 t) = V_1(\boldsymbol{a}_2 t)$ and comparing this expression with the SIP condition [Eq. (C8.28)], we find that $M = 0$ and the set of parameters $\boldsymbol{a}_1$ and $\boldsymbol{a}_2$ are real numbers related as $a_2 = -a_1 = -1$, i.e., we have a scaling SIP relation between superpartners. In this way, T-SUSY and SIP allow us to find time-reversal refractive index modulations with the same intensity scattering properties. As an example, consider an even superpotential of the form:[29]

$$W(t) = B\,\mathrm{sech}(\alpha t), \tag{C8.78}$$

where B and α are real parameters. The T-SUSY refractive index profiles $n_{1,2}(t)$ can be calculated by combining Riccati's equation and Eq. (C8.12) bearing in mind that $\Omega = \omega_0^2 + W_-^2 = \omega_0^2$. The corresponding profiles are shown in Fig. C8.13(a), and the behavior of the scattering coefficients as a function of the frequency [numerically calculated from the wave equation Eq. (8.2.1)] is depicted in Fig. C8.13(b). Outstandingly, we can see that both time-reversal refractive index profiles have the same intensity scattering properties, not only at $\omega = \omega_0$, but also at $\omega \neq \omega_0$. In other words, the ratios R_1/R_2 and T_1/T_2 have a flat frequency response. In any case, T-SUSY only provides control at the design frequency.[30]

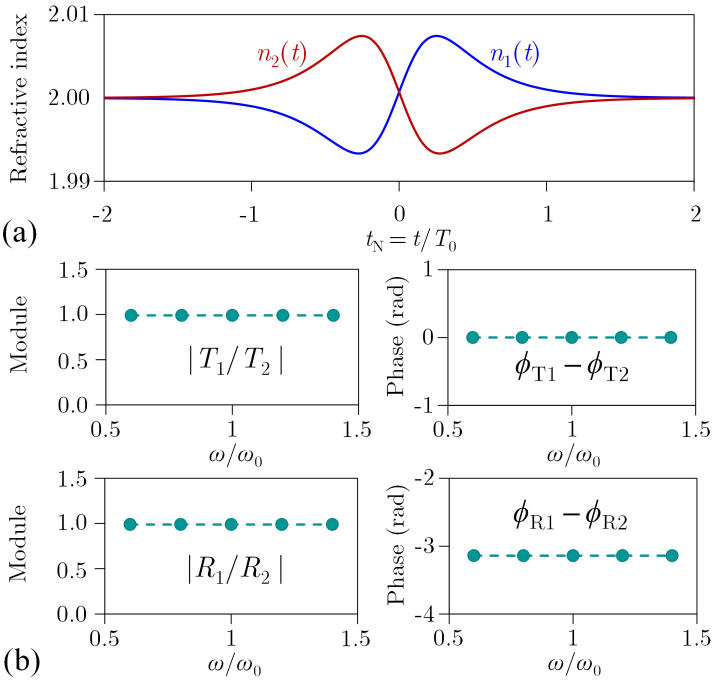

Figure C8.13. (a) T-SUSY time-reversal refractive index profiles associated with the superpotential of Eq. (C8.78) and (b) ratios of the corresponding scattering coefficients R_1/R_2 and T_1/T_2 as a function of the ratio ω/ω_0.

[29] Equation (C8.78) is a particular case of the hyperbolic Scarf II superpotential $W(t) = A\tanh(\alpha t) + B\,\mathrm{sech}(\alpha t)$.

[30] We analyzed other even superpotentials and we found that R_1/R_2 and T_1/T_2 also presented a flat frequency response. Nevertheless, we cannot extrapolate this singular feature as a general rule in T-SUSY time-reversal modulations. At least, the demonstration is not straightforward.

C8.4 Temporal scattering and T-SUSY: spatially dispersive systems

In this subsection, we discuss about the possibility of applying T-SUSY in time-varying spatially dispersive media (also termed as non-local media in the optical literature). Firstly, we include some notes on the spatial Fourier transform and, secondly, we derive a temporal Helmholtz equation for linear, isotropic, time-varying and spatially dispersive media considering the homogeneous and heterogeneous case of all-dielectric, all-magnetic, and dielectric&magnetic materials.

C8.4.1 Spatial Fourier transform

In non-local media, the analysis of Maxwell's equations can be alleviate via the three-dimensional spatial Fourier transform (SFT). Considering, for instance, the real electric field strength $\boldsymbol{\mathcal{E}}(\boldsymbol{r},t)$, the pair of SFTs is defined as:

$$\widetilde{\boldsymbol{\mathcal{E}}}(\boldsymbol{k},t)=\mathcal{F}_{\mathrm{S}}\left[\boldsymbol{\mathcal{E}}(\boldsymbol{r},t)\right]:=\int_{-\infty}^{\infty}\boldsymbol{\mathcal{E}}(\boldsymbol{r},t)\exp\left(j\boldsymbol{k}\cdot\boldsymbol{r}\right)\mathrm{d}^3r; \tag{C8.79}$$

$$\boldsymbol{\mathcal{E}}(\boldsymbol{r},t)=\mathcal{F}_{\mathrm{S}}^{-1}\left[\widetilde{\boldsymbol{\mathcal{E}}}(\boldsymbol{k},t)\right]:=\frac{1}{8\pi^3}\int_{-\infty}^{\infty}\widetilde{\boldsymbol{\mathcal{E}}}(\boldsymbol{k},t)\exp\left(-j\boldsymbol{k}\cdot\boldsymbol{r}\right)\mathrm{d}^3k, \tag{C8.80}$$

with $\mathrm{d}^3r\equiv\mathrm{d}x\mathrm{d}y\mathrm{d}z$ and $\mathrm{d}^3k\equiv\mathrm{d}k_x\mathrm{d}k_y\mathrm{d}k_z$ to use a more economical notation.[31] From the above definitions, it is straightforward to demonstrate that $\forall i\in\{x,y,z\}$:

$$\mathcal{F}_{\mathrm{S}}\left[\partial_i\boldsymbol{\mathcal{E}}(\boldsymbol{r},t)\right]=-jk_i\widetilde{\boldsymbol{\mathcal{E}}}(\boldsymbol{k},t). \tag{C8.81}$$

Proof:

$$\begin{aligned}\partial_i\boldsymbol{\mathcal{E}}(\boldsymbol{r},t)&=\partial_i\left[\frac{1}{8\pi^3}\int_{-\infty}^{\infty}\widetilde{\boldsymbol{\mathcal{E}}}(\boldsymbol{k},t)\exp\left(-j\boldsymbol{k}\cdot\boldsymbol{r}\right)\mathrm{d}^3k\right]=\frac{1}{8\pi^3}\int_{-\infty}^{\infty}\widetilde{\boldsymbol{\mathcal{E}}}(\boldsymbol{k},t)\,\partial_i\left[\exp\left(-j\boldsymbol{k}\cdot\boldsymbol{r}\right)\right]\mathrm{d}^3k\\&=\frac{1}{8\pi^3}\int_{-\infty}^{\infty}-jk_i\widetilde{\boldsymbol{\mathcal{E}}}(\boldsymbol{k},t)\exp\left(-j\boldsymbol{k}\cdot\boldsymbol{r}\right)\mathrm{d}^3k.\end{aligned} \tag{C8.82}$$

Hence, using the SFT, Faraday's and Ampère's laws can be recast in the wave number domain as:

$$-j\boldsymbol{k}\times\widetilde{\boldsymbol{\mathcal{E}}}(\boldsymbol{k},t)=-\partial_t\widetilde{\boldsymbol{\mathcal{B}}}(\boldsymbol{k},t); \tag{C8.83}$$

$$-j\boldsymbol{k}\times\widetilde{\boldsymbol{\mathcal{H}}}(\boldsymbol{k},t)=\widetilde{\boldsymbol{\mathcal{J}}}_{\mathrm{c}}(\boldsymbol{k},t)+\partial_t\widetilde{\boldsymbol{\mathcal{D}}}(\boldsymbol{k},t). \tag{C8.84}$$

C8.4.2 Derivation of the temporal Helmholtz equation with the SFT

Homogeneous all-dielectric media. The constitutive relations read as follows:

$$\boldsymbol{\mathcal{D}}(\boldsymbol{r},t)=\varepsilon_0\int_{-\infty}^{\infty}\varepsilon_{\mathrm{r}}(\boldsymbol{r}-\boldsymbol{r}',t)\,\boldsymbol{\mathcal{E}}(\boldsymbol{r}',t)\,\mathrm{d}^3r'; \tag{C8.85}$$

$$\boldsymbol{\mathcal{B}}(\boldsymbol{r},t)=\mu_0\boldsymbol{\mathcal{H}}(\boldsymbol{r},t), \tag{C8.86}$$

and applying $\mathcal{F}_{\mathrm{S}}$:

$$\widetilde{\boldsymbol{\mathcal{D}}}(\boldsymbol{k},t)=\varepsilon_0\widetilde{\varepsilon_{\mathrm{r}}}(\boldsymbol{k},t)\,\widetilde{\boldsymbol{\mathcal{E}}}(\boldsymbol{k},t); \tag{C8.87}$$

$$\widetilde{\boldsymbol{\mathcal{B}}}(\boldsymbol{k},t)=\mu_0\widetilde{\boldsymbol{\mathcal{H}}}(\boldsymbol{k},t). \tag{C8.88}$$

Next, starting from Eq. (C8.83):

$$-j\boldsymbol{k}\times\left(\frac{\widetilde{\boldsymbol{\mathcal{D}}}(\boldsymbol{k},t)}{\varepsilon_0\widetilde{\varepsilon_{\mathrm{r}}}(\boldsymbol{k},t)}\right)=-\partial_t\widetilde{\boldsymbol{\mathcal{B}}}(\boldsymbol{k},t), \tag{C8.89}$$

[31] We work in Cartesian coordinates to guarantee the linear property of the 3D-SFT when using vector functions. Otherwise, note that $\mathcal{F}_{\mathrm{S}}\left[\mathcal{E}_i(\boldsymbol{r},t)\,\hat{u}_i\right]\neq\mathcal{F}_{\mathrm{S}}\left[\mathcal{E}_i(\boldsymbol{r},t)\right]\hat{u}_i$ if the vector basis of $\mathbb{R}^3$ is not invariant to d^3r.

we find:

$$j\boldsymbol{k}\times\widetilde{\boldsymbol{\mathcal{D}}}\left(\boldsymbol{k},t\right)=\frac{\widetilde{n}^{2}\left(\boldsymbol{k},t\right)}{c_{0}^{2}}\partial_{t}\widetilde{\boldsymbol{\mathcal{H}}}\left(\boldsymbol{k},t\right), \tag{C8.90}$$

where $\widetilde{n}^{2}\left(\boldsymbol{k},t\right):=\widetilde{\varepsilon}_{\mathrm{r}}\left(\boldsymbol{k},t\right)$. Now, multiplying by $-j\boldsymbol{k}\times$ and combining with Eq. (C8.84) taking $\widetilde{\boldsymbol{\mathcal{J}}}_{\mathrm{c}}=\boldsymbol{0}$ (we omit the independent variables for simplicity):

$$-j\boldsymbol{k}\times j\boldsymbol{k}\times\widetilde{\boldsymbol{\mathcal{D}}}=\frac{\widetilde{n}^{2}}{c_{0}^{2}}\partial_{t}\left(-j\boldsymbol{k}\times\widetilde{\boldsymbol{\mathcal{H}}}\right)\Rightarrow\boldsymbol{k}\times\boldsymbol{k}\times\widetilde{\boldsymbol{\mathcal{D}}}=\frac{\widetilde{n}^{2}}{c_{0}^{2}}\partial_{t}^{2}\widetilde{\boldsymbol{\mathcal{D}}}, \tag{C8.91}$$

with $(\boldsymbol{k}\perp\widetilde{\boldsymbol{\mathcal{D}}})$:

$$\boldsymbol{k}\times\boldsymbol{k}\times\widetilde{\boldsymbol{\mathcal{D}}}=\begin{vmatrix}\boldsymbol{k} & \widetilde{\boldsymbol{\mathcal{D}}}\\ \boldsymbol{k}\cdot\boldsymbol{k} & \boldsymbol{k}\cdot\widetilde{\boldsymbol{\mathcal{D}}}\end{vmatrix}=\underbrace{\left(\boldsymbol{k}\cdot\widetilde{\boldsymbol{\mathcal{D}}}\right)}_{0}\boldsymbol{k}-\left(\boldsymbol{k}\cdot\boldsymbol{k}\right)\widetilde{\boldsymbol{\mathcal{D}}}=-k^{2}\widetilde{\boldsymbol{\mathcal{D}}}. \tag{C8.92}$$

From Eq. (C8.91), we obtain the *exact* vector wave equation for the electric flux density:

$$k^{2}\widetilde{\boldsymbol{\mathcal{D}}}\left(\boldsymbol{k},t\right)+\frac{\widetilde{n}^{2}\left(\boldsymbol{k},t\right)}{c_{0}^{2}}\partial_{t}^{2}\widetilde{\boldsymbol{\mathcal{D}}}\left(\boldsymbol{k},t\right)=\boldsymbol{0}. \tag{C8.93}$$

Finally, applying separation of variables of the form $\widetilde{\boldsymbol{\mathcal{D}}}\left(\boldsymbol{k},t\right)=\psi\left(t\right)\widetilde{\boldsymbol{\Phi}}\left(\boldsymbol{k}\right)$ and decoupling the refractive index as $\widetilde{n}^{2}\left(\boldsymbol{k},t\right)=\widetilde{n}_{\mathrm{S}}^{2}\left(\boldsymbol{k}\right)n_{\mathrm{T}}^{2}\left(t\right)=\widetilde{n}_{\mathrm{S}}^{2}\left(\boldsymbol{k}\right)\left[n_{-}^{2}+\Delta n_{\mathrm{T}}^{2}\left(t\right)\right]$, with $\widetilde{n}_{\mathrm{S}}^{2}\left(\boldsymbol{k}\rightarrow-\infty\right):=1$ and $\Delta n_{\mathrm{T}}^{2}\left(t\rightarrow-\infty\right):=0$, we can infer from Eq. (C8.93) that ψ fulfills the same temporal Helmholtz equation as the local media analyzed in the main text, i.e., Eq. (8.2.2) with $N^{2}\left(t\right):=n_{-}^{2}/n_{\mathrm{T}}^{2}\left(t\right)$ and $n_{-}:=n_{\mathrm{T}}\left(t\rightarrow-\infty\right)$.

Homogeneous all-magnetic media. Now, the constitutive relations are:

$$\widetilde{\boldsymbol{\mathcal{D}}}\left(\boldsymbol{k},t\right)=\varepsilon_{0}\widetilde{\boldsymbol{\mathcal{E}}}\left(\boldsymbol{k},t\right); \tag{C8.94}$$

$$\widetilde{\boldsymbol{\mathcal{B}}}\left(\boldsymbol{k},t\right)=\mu_{0}\widetilde{\mu}_{\mathrm{r}}\left(\boldsymbol{k},t\right)\widetilde{\boldsymbol{\mathcal{H}}}\left(\boldsymbol{k},t\right), \tag{C8.95}$$

and the refractive index is defined as $\widetilde{n}^{2}\left(\boldsymbol{k},t\right):=\widetilde{\mu}_{\mathrm{r}}\left(\boldsymbol{k},t\right)$. Hence, repeating the above procedure starting in this case from Ampère's laws [Eq. (C8.84)] taking $\widetilde{\boldsymbol{\mathcal{J}}}_{\mathrm{c}}=\boldsymbol{0}$, we find an *exact* vector wave equation for the magnetic flux density of the form:

$$k^{2}\widetilde{\boldsymbol{\mathcal{B}}}\left(\boldsymbol{k},t\right)+\frac{\widetilde{n}^{2}\left(\boldsymbol{k},t\right)}{c_{0}^{2}}\partial_{t}^{2}\widetilde{\boldsymbol{\mathcal{B}}}\left(\boldsymbol{k},t\right)=\boldsymbol{0}. \tag{C8.96}$$

Finally, applying separation of variables as $\widetilde{\boldsymbol{\mathcal{B}}}\left(\boldsymbol{k},t\right)=\psi\left(t\right)\widetilde{\boldsymbol{\Phi}}\left(\boldsymbol{k}\right)$ and decoupling the refractive index in the same way as in the all-dielectric case, we find the sought temporal Helmholtz equation Eq. (8.2.2).

Homogeneous dielectric&magnetic media. The constitutive relations are found to be:

$$\widetilde{\boldsymbol{\mathcal{D}}}\left(\boldsymbol{k},t\right)=\varepsilon_{0}\widetilde{\varepsilon}_{\mathrm{r}}\left(\boldsymbol{k},t\right)\widetilde{\boldsymbol{\mathcal{E}}}\left(\boldsymbol{k},t\right); \tag{C8.97}$$

$$\widetilde{\boldsymbol{\mathcal{B}}}\left(\boldsymbol{k},t\right)=\mu_{0}\widetilde{\mu}_{\mathrm{r}}\left(\boldsymbol{k},t\right)\widetilde{\boldsymbol{\mathcal{H}}}\left(\boldsymbol{k},t\right), \tag{C8.98}$$

and the refractive index is defined as $\widetilde{n}^{2}\left(\boldsymbol{k},t\right):=\widetilde{\varepsilon}_{\mathrm{r}}\left(\boldsymbol{k},t\right)\widetilde{\mu}_{\mathrm{r}}\left(\boldsymbol{k},t\right)$. Thus, Faraday's and Ampère's laws can be recast as:

$$j\boldsymbol{k}\times\widetilde{\boldsymbol{\mathcal{D}}}\left(\boldsymbol{k},t\right)=\varepsilon_{0}\widetilde{\varepsilon}_{\mathrm{r}}\left(\boldsymbol{k},t\right)\partial_{t}\widetilde{\boldsymbol{\mathcal{B}}}\left(\boldsymbol{k},t\right); \tag{C8.99}$$

$$j\boldsymbol{k}\times\widetilde{\boldsymbol{\mathcal{B}}}\left(\boldsymbol{k},t\right)=-\mu_{0}\widetilde{\mu}_{\mathrm{r}}\left(\boldsymbol{k},t\right)\partial_{t}\widetilde{\boldsymbol{\mathcal{D}}}\left(\boldsymbol{k},t\right). \tag{C8.100}$$

At this point, in order to obtain an *approximate* wave equation formally equal to Eq. (C8.93) (Eq. (C8.96)) for the electric (magnetic) flux density, we should assume a slowly-varying temporal evolution in $\widetilde{\mu}_{\mathrm{r}}$ ($\widetilde{\varepsilon}_{\mathrm{r}}$) starting from Faraday's (Ampère's) law. Finally, applying separation of variables in $\widetilde{\boldsymbol{\mathcal{D}}}$ ($\widetilde{\boldsymbol{\mathcal{B}}}$), we find the same temporal Helmholtz equation as in previous cases.

Heterogeneous media. Let us first consider the heterogeneous all-dielectric case. In such a scenario, Eq. (C8.85) must be rewritten as:

$$\boldsymbol{\mathcal{D}}(\boldsymbol{r},t)=\varepsilon_0\int_{-\infty}^{\infty}\varepsilon_{\mathrm{r}}(\boldsymbol{r},\boldsymbol{r}',t)\,\boldsymbol{\mathcal{E}}(\boldsymbol{r}',t)\,\mathrm{d}^3r'. \tag{C8.101}$$

As seen, the constitutive relation is described by a more complicated expression than in the previous examples.[32] However, we will be able to derive a wave equation similar to Eq. (C8.93) if we assume a slowly-varying spatial evolution in ε_{r}. In such circumstances, we can approximate the above constitutive relation as:

$$\boldsymbol{\mathcal{D}}(\boldsymbol{r},t)\simeq\varepsilon_0\int_{|\delta\boldsymbol{r}|\sim\lambda_0}\varepsilon_{\mathrm{r}}(\boldsymbol{r}-\boldsymbol{r}',t)\,\boldsymbol{\mathcal{E}}(\boldsymbol{r}',t)\,\mathrm{d}^3r', \tag{C8.102}$$

where λ_0 is the maximum wavelength of the problem. In other words, we are assuming that the medium is approximately homogeneous at $|\delta\boldsymbol{r}|\sim\lambda_0$. Next, performing the same discussion as in homogeneous all-dielectric media, we obtain the *approximate* vector wave equation:

$$k^2\widetilde{\boldsymbol{\mathcal{D}}}(\boldsymbol{k},t;\boldsymbol{r})+\frac{\widetilde{n}^2(\boldsymbol{k},t;\boldsymbol{r})}{c_0^2}\partial_t^2\widetilde{\boldsymbol{\mathcal{D}}}(\boldsymbol{k},t;\boldsymbol{r})=\boldsymbol{0}, \tag{C8.103}$$

where $\widetilde{n}^2(\boldsymbol{k},t;\boldsymbol{r}):=\widetilde{\varepsilon}_{\mathrm{r}}(\boldsymbol{k},t;\boldsymbol{r})$. Here, $\widetilde{\varepsilon}_{\mathrm{r}}$ and $\widetilde{\boldsymbol{\mathcal{D}}}$ are the *short-length spatial Fourier transform* (SL-SFT) of ε_{r} and $\boldsymbol{\mathcal{D}}$, respectively. For instance, the SL-SFT of ε_{r} is defined as:

$$\widetilde{\varepsilon}_{\mathrm{r}}(\boldsymbol{k},t;\boldsymbol{r}):=\int_{W_{\mathrm{S}}(\boldsymbol{r})}\varepsilon_{\mathrm{r}}(\boldsymbol{r},t)\exp(j\boldsymbol{k}\cdot\boldsymbol{r})\,\mathrm{d}^3r, \tag{C8.104}$$

where $W_{\mathrm{S}}(\boldsymbol{r})$ is a 3D spatial window of length $\sim\lambda_0$ in each spatial direction. It should be noted that we introduce space-dependent integration limits in the definition of the SL-SFT to retain the space-varying nature of ε_{r} and $\boldsymbol{\mathcal{D}}$ in the Fourier transformed domain. Finally, applying separation of variables in $\widetilde{\boldsymbol{\mathcal{D}}}(\boldsymbol{k},t;\boldsymbol{r})=\psi(t)\,\widetilde{\boldsymbol{\Phi}}(\boldsymbol{k};\boldsymbol{r})$ and decoupling the refractive index as:

$$\widetilde{n}^2(\boldsymbol{k},t;\boldsymbol{r})=\widetilde{n}_{\mathrm{S}}^2(\boldsymbol{k};\boldsymbol{r})\,n_{\mathrm{T}}^2(t)=\widetilde{n}_{\mathrm{S}}^2(\boldsymbol{k};\boldsymbol{r})\left[n_-^2+\Delta n_{\mathrm{T}}^2(t)\right], \tag{C8.105}$$

with $\Delta n_{\mathrm{T}}^2(t\to-\infty):=0$, we obtain the same temporal Helmholtz equation as in the homogeneous case. Heterogeneous all-magnetic media can be analyzed in a similar way but replacing $\widetilde{\boldsymbol{\mathcal{D}}}$ by $\widetilde{\boldsymbol{\mathcal{B}}}$ in Eq. (C8.103), assuming a slowly-varying spatial evolution in μ_{r} and defining the refractive index as $\widetilde{n}^2(\boldsymbol{k},t;\boldsymbol{r}):=\widetilde{\mu}_{\mathrm{r}}(\boldsymbol{k},t;\boldsymbol{r})$. Finally, the non-local heterogeneous dielectric&magnetic scenario requires to consider the slowly-varying spatial evolution in both constitutive parameters and the slowly-varying temporal evolution in $\widetilde{\mu}_{\mathrm{r}}$ ($\widetilde{\varepsilon}_{\mathrm{r}}$) if we derive the temporal Helmholtz equation from the wave equation of $\widetilde{\boldsymbol{\mathcal{D}}}$ ($\widetilde{\boldsymbol{\mathcal{B}}}$).

C8.4.3 Derivation of the temporal Helmholtz equation without the SFT

Despite the fact that the SFT alleviates the analysis of the general solution of Maxwell's equations in non-local media, we can also apply T-SUSY to this kind of media without requiring the use of the SFT. The basic idea is to apply separation of variables in all the electromagnetic fields and decouple the non-local and time-varying nature of the constitutive parameters. As an advantage of using this approach, we will not require to consider a slowly-varying spatial evolution in ε_{r} or μ_{r} to apply T-SUSY in non-local heterogeneous media.

As an example, consider the non-local heterogeneous all-dielectric case. Assuming, respectively, the electric field strength and the electric flux density of the form $\boldsymbol{\mathcal{E}}(\boldsymbol{r},t)=\psi_{\mathcal{E}}(t)\,\boldsymbol{\Phi}_{\mathcal{E}}(\boldsymbol{r})$ and $\boldsymbol{\mathcal{D}}(\boldsymbol{r},t)=\psi_{\mathcal{D}}(t)\,\boldsymbol{\Phi}_{\mathcal{D}}(\boldsymbol{r})$, and decoupling the non-local and time-varying nature of the relative electric permittivity as:

[32] The constitutive relation Eq. (C8.101) describes an input-output relation of the form $\boldsymbol{\mathcal{D}}(\boldsymbol{r},t)=\widehat{\mathcal{O}}(\boldsymbol{r},t)\,\boldsymbol{\mathcal{E}}(\boldsymbol{r},t)$, where $\widehat{\mathcal{O}}$ is a heterogeneous time-varying linear operator accounting for the non-local response of the medium to the input $\boldsymbol{\mathcal{E}}(\boldsymbol{r},t)$. Specifically, $\varepsilon_0\varepsilon_{\mathrm{r}}(\boldsymbol{r},\boldsymbol{r}',t)$ is the impulse response of the system, i.e., $\varepsilon_0\varepsilon_{\mathrm{r}}(\boldsymbol{r},\boldsymbol{r}',t)=\widehat{\mathcal{O}}(\boldsymbol{r},t)\,\delta(\boldsymbol{r}-\boldsymbol{r}')$.

$$\varepsilon_{\mathrm{r}}\left(\boldsymbol{r},\boldsymbol{r}',t\right)=\varepsilon_{\mathrm{S}}\left(\boldsymbol{r},\boldsymbol{r}'\right)\varepsilon_{\mathrm{T}}\left(t\right), \tag{C8.106}$$

the constitutive relation Eq. (C8.101) can be separated in the following relations:

$$\psi_{\mathcal{D}}\left(t\right)=\varepsilon_{0}\varepsilon_{\mathrm{T}}\left(t\right)\psi_{\mathcal{E}}\left(t\right); \tag{C8.107}$$

$$\boldsymbol{\Phi}_{\mathcal{D}}\left(\boldsymbol{r}\right)=\int_{-\infty}^{\infty}\varepsilon_{\mathrm{S}}\left(\boldsymbol{r},\boldsymbol{r}'\right)\boldsymbol{\Phi}_{\mathcal{E}}\left(\boldsymbol{r}'\right)\mathrm{d}^{3}r'. \tag{C8.108}$$

Hence, the exact time-domain vector wave equation $\nabla\times\nabla\times\boldsymbol{\mathcal{E}}\left(\boldsymbol{r},t\right)=-\mu_{0}\partial_{t}^{2}\boldsymbol{\mathcal{D}}\left(\boldsymbol{r},t\right)$ becomes:

$$\nabla\times\nabla\times\left(\psi_{\mathcal{E}}\left(t\right)\boldsymbol{\Phi}_{\mathcal{E}}\left(\boldsymbol{r}\right)\right)=-\mu_{0}\partial_{t}^{2}\left(\psi_{\mathcal{D}}\left(t\right)\boldsymbol{\Phi}_{\mathcal{D}}\left(\boldsymbol{r}\right)\right). \tag{C8.109}$$

Next, from Eqs. (C8.107) and (C8.108), the above equation is reduced to:

$$-c_{0}^{2}\nabla\times\nabla\times\left(\boldsymbol{\Phi}_{\mathcal{E}}\left(\boldsymbol{r}\right)\right)=\varepsilon_{\mathrm{T}}\left(t\right)\frac{\psi_{\mathcal{D}}''\left(t\right)}{\psi_{\mathcal{D}}\left(t\right)}\boldsymbol{\Phi}_{\mathcal{D}}\left(\boldsymbol{r}\right). \tag{C8.110}$$

Therefore, we must have:

$$\varepsilon_{\mathrm{T}}\left(t\right)\frac{\psi_{\mathcal{D}}''\left(t\right)}{\psi_{\mathcal{D}}\left(t\right)}=\gamma^{2}, \tag{C8.111}$$

where $\gamma^{2}\in\mathbb{C},\ \forall\, t\in\overline{\mathbb{R}}$. Defining $n_{\mathrm{T}}^{2}\left(t\right):=\varepsilon_{\mathrm{T}}\left(t\right)$ and evaluating the above expression at $t\to-\infty$, we find that $\gamma=jn_{-}\omega_{0}$, yielding Eq. (8.2.2) of the main text.[33] We can also proceed in a similar way for non-local all-magnetic and dielectric&magnetic media.

C8.4.4 Conclusion

An *exact* temporal Helmholtz equation formally equal to Eq. (8.2.2) is derived from Maxwell's equations for time-varying spatially dispersive homogeneous and heterogeneous media. Consequently, the extrapolation of the scattering results of Section 8.2 to non-local media is then straightforward.

C8.5 Extrapolation of the results to the spatial scattering

In complete analogy with the temporal scattering, the one-dimensional spatial scattering can be described in photonics by a Helmholtz equation formally equal to our Eq. (8.2.2), as discussed in Chapter 6, in Subsection 6.13.1 [see Eq. (6.13.12)]. Consequently, the main results of this chapter can be extrapolated to the spatial scattering.[34] Despite the fact that the transparent spatial hyperbolic secant modulation is a well-known result in photonics [332], the non-reflecting hyperbolic step-index profile of Subsection 8.2.2 has not been investigated in the space domain, to the best of our knowledge. This opens up a great opportunity to explore new transparent heterogeneous optical media.

[33] Actually, we should work with the *analytic* representation of the electromagnetic fields to be coherent with the theory of the main text. Nevertheless, we have employed the real representation of the electromagnetic fields, in line with the notation used in Subsection C8.4.2.

[34] Nevertheless, remember that in the space domain the results are found to be polarization-dependent.

Appendix D8: Temporal waveguide

The concept of *temporal waveguide* has been recently introduced in the literature in [336–338]. In this appendix, we perform a detailed discussion about the fundamental concepts enclosed in this new kind of optical systems starting from Maxwell's equations. As a result, we will see that the pulse propagation equation (2) of [336] cannot correctly describe the interaction of light with a moving "temporal" boundary due to the absence of boundary conditions in this equation. However, the modal analysis of a temporal waveguide can be correctly performed starting from this equation, provided that the corresponding boundary conditions are incorporated to the modal solution.

The appendix is structured as follows. In Subsection D8.1, we define the concept of temporal waveguide. In Subsection D8.2, we detail some inconsistencies and open questions in the literature. In Subsections D8.3 and D8.4 we attempt to solve these questions. In Subsection D8.5, we include some notes on the theory of T-SUSY applied to temporal waveguides. In Subsection D8.6, we derive a coupled-mode theory for parallel temporal waveguides. In Subsection D8.7, we discuss in more detail the concept of temporal photonic lantern presented on page 256. Finally, in Subsection D8.8, we solve an outstanding question formulated in Subsection D8.2.

D8.1 Preliminary concepts

A temporal waveguide (TWG) is a *time-varying* and *temporally dispersive* medium which can confine and carry optical pulses inside a moving temporal perturbation $\Delta n_{\text{eff}}(t - z/v_{\text{B}})$ of the effective refractive index (n_{eff}) of a guided mode of a spatial waveguide. Figure D8.1 illustrates this scenario. As seen, the perturbation is finite and is defined by two *moving temporal boundaries* separated in time $2T_{\text{B}}$ and in space $2T_{\text{B}}v_{\text{B}}$. Actually, a moving temporal boundary is a spatial change of n_{eff} which is moving along the z-axis. However, in coherence with [336–338], we will use the naive and unfortunate term "temporal boundary" to describe the spatial limits of the TWG.

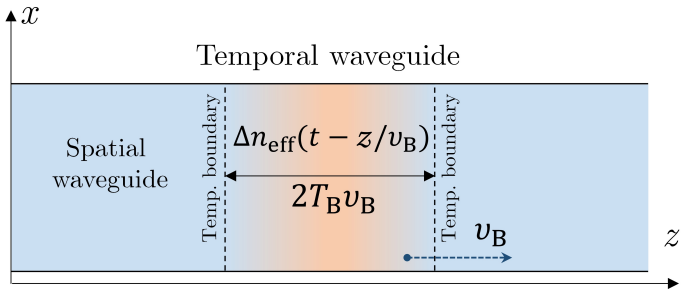

Figure D8.1. Temporal waveguide: moving temporal perturbation of the effective refractive index (n_{eff}) of a guided mode of a spatial waveguide (blue area) of the form $\Delta n_{\text{eff}}(t - z/v_{\text{B}})$, where v_{B} is the speed of the temporal perturbation propagating through the longitudinal axis of the spatial waveguide.

Surprisingly, the double temporal boundary which defines the TWG leads to an eigenvalue equation with a discrete set of eigenvalues and eigenfunctions $\{\psi_n\}_{n=0}^{\infty}$ [Eq. (8.3.3)]. Performing the coordinate transformation $\tau := t - z/v_{\text{B}}$, the eigenfunctions $\psi_n(t - z/v_{\text{B}})$ can be considered as *temporal bound states* at a given z point, that is, time-dependent continuous normalizable eigenfunctions satisfying the condition $\psi(\tau \to \pm\infty) = 0$. A static external observer located at a given z point can only see the eigenfunctions in a time interval $2T_{\text{B}}$. For this reason, these eigenfunctions are referred to as temporal bound states.[35] Interestingly, these temporal bound states can be stimulated by an external optical pulse if $v_{\text{B}} < 1/\beta_1$, where β_1 is the inverse of the group velocity of the guided mode of the spatial waveguide over which the TWG is constructed.

[35] Nevertheless, strictly speaking, the concept of temporal bound state is more restrictive than the concept mentioned herein because it must be a continuous, normalizable eigenfunction which is only localized in time. Here, the eigenfunctions of a TWG are localized not only in time, but also in space. However, using the coordinate transformation $\tau := t - z/v_{\text{B}}$, we can consider these eigenfunctions as temporal bound states at a given z point.

D8.2 Open questions in previous works

The theory of the interaction of an electromagnetic field with a moving temporal boundary and the modal analysis of TWGs revolve around the following equation [336–338]:[36]

$$\left(\partial_z + \beta_1 \partial_t - j\frac{1}{2}\beta_2 \partial_t^2 + j\beta_{\mathrm{B}}\left(t - z/v_{\mathrm{B}}\right)\right)\mathcal{A}\left(z,t\right) = 0. \tag{D8.1}$$

As indicated in these previous works, this equation emerges from Maxwell's equations and attempts to describe the propagation of an optical pulse in the scenario shown in Fig. D8.1. In particular, $\mathcal{A}$ is the slowly-varying complex envelope of an optical pulse propagating in the perturbed guided mode of the spatial waveguide through the $+\hat{u}_z$ direction, β_1 and β_2 are respectively the inverse of the group velocity and the group-velocity dispersion of the guided mode, $\beta_{\mathrm{B}} := k_0 \Delta n_{\mathrm{eff}}$, $k_0 = \omega_0/c_0$, and ω_0 is the angular frequency of the light source which stimulates the guided mode of the spatial waveguide at $z = 0$.

It is worth mentioning that the concept of moving temporal boundary of [336] clearly involves a moving spatial boundary. Thus, it is natural to expect that the interaction of an electromagnetic wave with this kind of boundary can generate a reflected and a transmitted wave. Along this line, the following fundamental questions emerge:

1. Can Eq. (D8.1) describe both forward and backward propagations?

2. As seen in Fig. 1(a) of [336], it is not observed a *real* reflection when an optical pulse interacts with a moving temporal boundary of the order of $\Delta n_{\mathrm{eff}} \sim 10^{-8}$. Concretely, it is observed a deceleration of the incident optical pulse. This *virtual* reflection, emerging from the numerical simulation of Eq. (D8.1), is of the order of -20 dB, much lower than the expected value of a real reflected wave with $|R| \sim \Delta n_{\mathrm{eff}} \sim -8$ dB. Hence, we wonder whether Eq. (D8.1) is derived from Maxwell's equations taking into account the corresponding boundary conditions of the spatial scattering problem: continuity of the tangential components of $\boldsymbol{\mathcal{E}}$ and $\boldsymbol{\mathcal{H}}$. Therefore, the question is: can Eq. (D8.1) correctly describe the spatial scattering in this scenario?

3. In the case of a negative answer to question 2, that is, absence of boundary conditions in Eq. (D8.1), can we correctly perform a modal analysis of a TWG starting from Eq. (D8.1)?

4. The perturbation of the optical medium modifies the phase velocity (c_0/n_{eff}), but the group velocity ($1/\beta_1$) is assumed time-invariant. This situation is analogous to omit the self-steepening effect in an optical fiber operating in the nonlinear regime, which strongly depends on the order of Δn_{eff}, ω_0 and the pulse width [139]. However, we wonder whether the modal analysis of the TWGs and the T-SUSY theory of Section 8.3 must be revisited when this initial consideration is not fulfilled.

Questions 1-3 will be answered in the next subsection and question 4 will be discussed at the end of this appendix, in Subsection D8.8.

D8.3 Time-domain pulse propagation equation

How can we describe the propagation of an optical pulse through a time-varying and temporally dispersive medium? In the same way as in a real multi-core fiber with spatial and temporal perturbations, which is found to be a time-varying and temporally dispersive medium. Therefore, the coupled local-mode theory (CLMT) presented in Chapter 4 can be retrieved to describe the scenario of Fig. D8.1 by assuming a single core and a single polarized core mode (e.g. $\mathrm{LP}_{01,x}$).

[36] Note that Eq. (D8.1) is the same as Eq. (2) of [336] when performing the coordinate transformation $\tau := t - z/v_{\mathrm{B}}$. However, the terms β_2 and β_{B} have the opposite sign in Eq. (D8.1) in comparison with Eq. (2) of [336] because we used a different sign convention in the Fourier transform to derive Eq. (D8.1) from Maxwell's equations (see Subsection D8.3 for more details). Obviously, the results do not depend on this sign convention.

Nonetheless, questions 1-3 require to revisit the derivation of the CLMT. In Chapter 4, we omitted the power reflected generated by the spatial and temporal perturbations of the medium because these perturbations were assumed to be slowly-varying in comparison with the space and time interval where is located the propagated optical pulse. Unfortunately, this assumption does not hold in Fig. D8.1. Now, the medium perturbations can have a rapidly-varying nature (e.g. a step-index TWG) and, therefore, the reflected wave and the corresponding boundary conditions of the spatial scattering must be included in the theoretical model. Consequently, we must revisit the four steps of perturbation theory (described in Fig. 1.9, see page 23) starting from Maxwell's equations to derive a time-domain pulse propagation equation suitable for TWGs.

First step: Ansatz of the electric field strength of the optical medium

In the first step, we should propose the ansatz of the global electric field strength ($\boldsymbol{\mathcal{E}}$) of the optical medium depicted in Fig. D8.1. This ansatz will be replaced later in Maxwell's equations. Thus, it is a fundamental point of our theoretical discussions. Here, we will consider an optical pulse with a temporal width $T_{\mathrm{P}} \gg 1$ ps [full-width at $1/(2e)$ of the peak power] generated from a laser radiating an optical carrier of angular frequency ω_0. The pulse is launched into a guided mode of a dielectric waveguide where the longitudinal component of $\boldsymbol{\mathcal{E}}$ is zero or can be neglected (e.g. a TE mode of a planar waveguide or an LP mode of a weakly-guiding optical fiber). In addition, for the sake of simplicity, we will omit any birefringent effect of the spatial waveguide. Consequently, we can assume $\boldsymbol{\mathcal{E}} = \mathcal{E}\hat{u}_{\mathrm{T}}$, where $\hat{u}_{\mathrm{T}}$ is a unit vector transverse to the propagation direction of the electromagnetic energy ($\hat{u}_{\mathrm{T}} \perp \hat{u}_z$).

In order to describe correctly the propagation of the optical pulse, we should decouple the rapidly- and the slowly-varying temporal and longitudinal changes of $\boldsymbol{\mathcal{E}}$. The rapidly-varying *temporal* changes are decoupled by using the slowly-varying complex amplitude approximation:

$$\boldsymbol{\mathcal{E}}(\boldsymbol{r},t) \simeq \mathrm{Re}\left\{E_{\omega_0}(\boldsymbol{r},t)\exp(j\omega_0 t)\right\}\hat{u}_{\mathrm{T}}, \tag{D8.2}$$

where E_{ω_0} is the complex amplitude of the electric field strength satisfying that $\delta_t E_{\omega_0} \ll |E_{\omega_0}|$ in $\delta t \sim 2\pi/\omega_0$, where $\delta_t E_{\omega_0} := |E_{\omega_0}(\boldsymbol{r},t+\delta t) - E_{\omega_0}(\boldsymbol{r},t)|$. In addition, the rapidly- and the slowly-varying *longitudinal* variations can be decoupled by introducing the complex envelope in our ansatz. However, this step is not as straightforward as initially foreseen. The reader can find in [357] a detailed discussion about this question in a simpler scenario than in a TWG. Using the same approach as in [357] and in Chapter 4, we should assume the complex amplitude of the form:

$$E_{\omega_0}(\boldsymbol{r},t) = \frac{1}{2\pi}\int_{\mathfrak{B}_{\widetilde{\mathtt{A}}}} \widetilde{\mathtt{A}}(\omega-\omega_0;t)\,F(x,y,\omega;z,t)\exp(\mp j\Phi(z,\omega;t))\exp(j(\omega-\omega_0)t)\,\mathrm{d}\omega, \tag{D8.3}$$

where:

- $\widetilde{\mathtt{A}}(\Omega;t)$ is the short-time Fourier transform (STFT) of the complex envelope in baseband (see below) and $\mathfrak{B}_{\widetilde{\mathtt{A}}}$ is the bandwidth of $\widetilde{\mathtt{A}}$. Specifically, the STFT allows us to encode the time-varying nature of the medium in $\widetilde{\mathtt{A}}$, which is found to be temporal dependent. On the other hand, in contrast to Chapter 4, we do not have to describe mode-coupling and, therefore, $\widetilde{\mathtt{A}}$ must be assumed invariant along the z-axis. Unfortunately, $\widetilde{\mathtt{A}}$ is only able to describe the slowly-varying *temporal* evolution of the electric field because it is the shape of the optical pulse at $z = 0$. To include the description of the slowly-varying *longitudinal* evolution of E_{ω_0} at any z point, we should perform a mathematical transformation in $\widetilde{\mathtt{A}}$. Nevertheless, this step previously requires to describe adequately the phase function Φ (see below).

- $F(x,y,\omega;z,t)$ is the transversal function of the guided mode. In line with Chapter 4, F is assumed to be longitudinal and temporal dependent to describe the changes in the transversal area of the guided mode induced by $\Delta n_{\mathrm{eff}}(t - z/v_{\mathrm{B}})$. The semicolon symbol is used to denote explicitly these longitudinal and temporal changes.

- The forward $(-)$ and backward $(+)$ propagations are described by the double sign $\mp$ in $\exp\left(\mp j\Phi\left(z,\omega;t\right)\right)$, where Φ is the complex phase function of the guided mode involving: (i) the equivalent real phase function $\beta_{\mathrm{eq}}\left(z,\omega;t\right)$, which accounts for the ideal phase constant $\beta\left(\omega\right)$ of the guided mode and the dynamical evolution of the optical medium $\beta_{\mathrm{B}}\left(z,\omega;t\right)$ (see below the relation with Δn_{eff}), and (ii) the power attenuation coefficient $\alpha\left(\omega\right)$. Specifically, Φ is assumed of the form:

$$\begin{aligned}\Phi\left(z,\omega;t\right) :&= \int_0^z \beta_{\mathrm{eq}}\left(\xi,\omega;t\right)\mathrm{d}\xi - j\frac{1}{2}\underbrace{\alpha\left(\omega\right)}_{\simeq 0}z = \int_0^z \left[\beta\left(\omega\right)+\beta_{\mathrm{B}}\left(\xi,\omega;t\right)\right]\mathrm{d}\xi \\ &\simeq \int_0^z \sum_{k=0}^{2}\frac{1}{k!}\left(\omega-\omega_0\right)^k\left[\beta_k+\beta_{\mathrm{B},k}\left(\xi;t\right)\right]\mathrm{d}\xi \\ &= \int_0^z \sum_{k=0}^{2}\frac{1}{k!}\left(\omega-\omega_0\right)^k\left[\beta_k+\beta_{\mathrm{B},k}\left(t-\xi/v_{\mathrm{B}}\right)\right]\mathrm{d}\xi \\ &\simeq \left\{\sum_{k=0}^{2}\frac{1}{k!}\left(\omega-\omega_0\right)^k\left[\beta_k+\beta_{\mathrm{B},k}\left(t-z/v_{\mathrm{B}}\right)\right]\right\}z, \end{aligned} \tag{D8.4}$$

  with $\beta_k := \mathrm{d}^k\beta\left(\omega=\omega_0\right)/\mathrm{d}\omega^k$ and $\beta_{\mathrm{B},k}\left(z;t\right) := \partial_\omega^k\beta_{\mathrm{B}}\left(z,\omega=\omega_0;t\right)$. Here, the following remarks are in order:

  - In contrast to Chapters 2, 3 and 4, we denote the order of the dispersion parameters of the optical medium in the subindex to avoid any confusion with the SUSY superindex notation. That is, now $\beta_{\omega_0}^{(k)} \equiv \beta_k$.
  - We have considered that we are operating far from the resonant frequencies of the dielectric medium and $T_{\mathrm{P}} \gg 1$ ps. In this way, the dielectric losses (encoded by α) and the higher-order dispersive terms $\beta_{k\geq 3}$ can been omitted.
  - The dynamical perturbation of the medium is moving with a constant speed v_{B}. In this vein, we have rewritten the dispersive terms $\beta_{\mathrm{B},k}$ of the medium perturbation β_{B} as $\beta_{\mathrm{B},k}\left(z;t\right) \equiv \beta_{\mathrm{B},k}(t-z/v_{\mathrm{B}})$. Along this line, it should be noticed that writing $\beta_{\mathrm{B},k}\left(z;t\right)$ and $\beta_{\mathrm{B},k}(t-z/v_{\mathrm{B}})$ simultaneously is a "sloppy" notation because we are using the same function for two different functions. However, let us relax the notation for simplicity.
  - In coherence with [336–338], we assume $\beta_{\mathrm{B},1} \simeq \beta_{\mathrm{B},2} \simeq 0$. As commented before, the approximation $\beta_{\mathrm{B},1} \simeq 0$ is analogous to omit the self-steepening effect in an optical fiber operating in the nonlinear regime, where a high-power pulse which stimulates the Kerr effect plays the role of the moving temporal perturbation of the medium $\Delta n_{\mathrm{eff}}(t-z/v_{\mathrm{B}})$. Later, in Subsection D8.8, we will revisit this point. Otherwise, the approximation $\beta_{\mathrm{B},2} \simeq 0$ can be perfectly performed if we assume a weak perturbation, $n_{\mathrm{eff}} \gg |\Delta n_{\mathrm{eff}}|$.
  - The approximation in the last line of Eq. (D8.4) was performed as a direct consequence of assuming $n_{\mathrm{eff}} \gg |\Delta n_{\mathrm{eff}}|$.
  - Note that $\beta_{\mathrm{B},0} = k_0\Delta n_{\mathrm{eff}}$. For simplicity, we will omit the subindex "0" in $\beta_{\mathrm{B},0}$ from now on to use a more economical notation.
  - All in all, Eq. (D8.4) is reduced to:

$$\Phi\left(z,\omega;t\right) \simeq \left\{\underbrace{\beta_{\mathrm{B}}\left(t-z/v_{\mathrm{B}}\right)}_{=k_0\Delta n_{\mathrm{eff}}(t-z/v_{\mathrm{B}})} + \sum_{k=0}^{2}\frac{1}{k!}\left(\omega-\omega_0\right)^k\beta_k\right\}z. \tag{D8.5}$$

- Once we have described the phase function Φ, we can decouple the rapidly- and the slowly-varying *longitudinal* variations in E_{ω_0} by performing the aforementioned mathematical transformation of $\widetilde{\mathtt{A}}$. To this end, we should subtract the rapidly-varying longitudinal variations of the optical carrier $\exp(\mp j\beta_0 z)$ from $\exp\left(\mp j\Phi\left(z,\omega;t\right)\right)$ as follows:

$$\widetilde{\mathcal{A}}\left(z,\omega-\omega_0;t\right) := \widetilde{\mathtt{A}}\left(\omega-\omega_0;t\right)\exp\left[\mp j\left(\Phi\left(z,\omega;t\right)-\beta_0 z\right)\right]$$
$$\simeq \widetilde{\mathtt{A}}\left(\omega-\omega_0;t\right)\exp\left[\mp j\left(\beta_{\mathrm{B}}\left(t-z/v_{\mathrm{B}}\right)+\sum_{k=1}^{2}\frac{1}{k!}\left(\omega-\omega_0\right)^k\beta_k\right)z\right]. \quad \text{(D8.6)}$$

Note that the subtraction $\Phi\left(z,\omega;t\right)-\beta_0 z$ in the spatial exponential function is analogous to the subtraction $(\omega-\omega_0)t$ in the temporal exponential function of Eq. (D8.3). Remarkably, the new complex envelope $\widetilde{\mathcal{A}}$ describes, in the frequency domain, the slowly-varying *longitudinal* and *temporal* evolution of $\boldsymbol{\mathcal{E}}$. Thus, our goal is to obtain a partial differential equation accounting for the longitudinal and temporal evolution of $\mathcal{A}$, a complex-valued function satisfying the SVEA (see page 129) which is found to be the *analytic* representation of the optical pulse in the time domain. Specifically, $\mathcal{A}$ and $\widetilde{\mathcal{A}}$ are connected via the STFT, defined as in Chapter 4:

$$\widetilde{\mathcal{A}}\left(z,\Omega;t\right)=\mathcal{F}_{\mathrm{T}}\left[\mathcal{A}\left(z,t\right)\right]:=\int_{t-T_{\mathrm{P}}/2}^{t+T_{\mathrm{P}}/2}\mathcal{A}\left(z,\tau\right)\exp\left(-j\Omega\tau\right)\mathrm{d}\tau, \quad \text{(D8.7)}$$

with the time interval of integration describing a moving temporal window function where the STFT is performed.[37]

Second step: Wave equation of the spatial guided mode

From Chapter 4 [Eq. (4.2.11)], we know that the spatial guided mode must satisfy the Helmholtz equation in each spectral component ω:

$$\left(\triangle+\frac{\omega^2}{c_0^2}\widetilde{n}^2\left(\boldsymbol{r},\omega;t\right)\right)F\left(x,y,\omega;z,t\right)\exp\left(\mp j\Phi\left(z,\omega;t\right)\right)=0, \quad \text{(D8.8)}$$

where $\widetilde{n}^2:=\mathcal{F}_{\mathrm{T}}\left[1+\chi^{(1)}(\boldsymbol{r},t)\right]$ and $\chi^{(1)}$ is the first-order electric susceptibility of the perturbed spatial waveguide, which involves the ideal first-order electric susceptibility (i.e. when $\Delta n_{\mathrm{eff}}=0$) and the fluctuation of the material properties of the spatial waveguide induced by Δn_{eff}. Thus, at this point, the theoretical analysis requires to know the perturbation induced by Δn_{eff} in $\chi^{(1)}$ along the z-axis to find the function $\widetilde{n}\left(\boldsymbol{r},\omega;t\right)$:

$$\widetilde{n}\left(\boldsymbol{r},\omega;t\right)=\begin{cases}\widetilde{n}_{\mathrm{TWG}}\left(x,y,\omega;z,t\right) & ;\ |t-z/v_{\mathrm{B}}|\leq T_{\mathrm{B}}\\ \widetilde{n}_{\mathrm{SWG}}\left(x,y,\omega\right) & ;\ |t-z/v_{\mathrm{B}}|>T_{\mathrm{B}}\end{cases} \quad \text{(D8.9)}$$

If the modal perturbation is induced in a weakly-guiding spatial waveguide with a step-index profile $\widetilde{n}_{\mathrm{SWG}}$, we can safely assume that $\widetilde{n}\simeq\left(c_0/\omega\right)\beta_{\mathrm{eq}}$. In particular, Eq. (D8.8) is step 2 depicted in Fig. 1.9. This will be employed later in the fourth step to simplify the algebraic work.

Third step: Wave equation of the optical medium

In the third step, we should derive the wave equation of the time-varying and temporally dispersive medium of Fig. D8.1. As in Chapter 4, we start by combining Faraday's and Ampère's laws applying the curl operator in the former, which leads to the wave equation:

$$\triangle\boldsymbol{\mathcal{E}}\left(\boldsymbol{r},t\right)-\frac{1}{c_0^2}\partial_t^2\boldsymbol{\mathcal{E}}\left(\boldsymbol{r},t\right)=\mu_0\partial_t^2\boldsymbol{\mathcal{P}}^{(1)}\left(\boldsymbol{r},t\right), \quad \text{(D8.10)}$$

[37] The STFT must be rigorously defined as:

$$\widetilde{\mathcal{A}}\left(z,\Omega;t\right):=\int_{-\infty}^{\infty}\mathcal{A}\left(z,\tau\right)\mathscr{W}\left(\tau-t\right)\exp\left(-j\Omega\tau\right)\mathrm{d}\tau,$$

with $\mathscr{W}$ a temporal window function of width T_{P}. However, in order to use a more economical notation, we describe the moving window function in the time interval of integration, i.e., $\tau\in[t-T_{\mathrm{P}}/2,t+T_{\mathrm{P}}/2]$.

where $\boldsymbol{\mathcal{P}}^{(1)}$ is the linear polarization density. We have neglected the third-order nonlinear polarization density by omitting the nonlinear nature of the dielectric waveguide to simplify the problem. Furthermore, we have neglected the term $\nabla(\nabla\cdot\boldsymbol{\mathcal{P}}^{(1)})$ in the above equation by considering that we will separate the problem in different dielectric regions where n_{eff} can be assumed approximately constant: the unperturbed spatial waveguide and the TWG (see below Fig. D8.2).

The constitutive relation $\boldsymbol{\mathcal{P}}^{(1)}$-$\boldsymbol{\mathcal{E}}$ is the key of the striking results of [336–338] and will allow us to clarify questions 2 and 3 of Subsection D8.2. Concretely, the relation $\boldsymbol{\mathcal{P}}^{(1)}$-$\boldsymbol{\mathcal{E}}$ should describe the linear response of the polarization density to an electric field impinging onto a dielectric medium: isotropic, heterogeneous, spatially non-dispersive, time-varying and temporally dispersive. In such circumstances, the aforementioned constitutive relation should be written of the form:[38]

$$\boldsymbol{\mathcal{P}}^{(1)}(\boldsymbol{r},t)=\varepsilon_0\int_{-\infty}^{\infty}\chi^{(1)}(\boldsymbol{r},t,\tau)\,\boldsymbol{\mathcal{E}}(\boldsymbol{r},\tau)\,\mathrm{d}\tau. \tag{D8.11}$$

At this point, if we wish to obtain a pulse propagation equation of the form of Eq. (2) of [336], we must perform the following approximation as a *necessary* condition: the time-varying optical medium must be considered as a time-invariant system in $\delta t\sim T_{\text{P}}$. In other words, the constitutive relation must be approximated to:

$$\boldsymbol{\mathcal{P}}^{(1)}(\boldsymbol{r},t)\simeq\varepsilon_0\int_{\langle T_{\text{P}}\rangle}\chi^{(1)}(\boldsymbol{r},t-\tau)\,\boldsymbol{\mathcal{E}}(\boldsymbol{r},\tau)\,\mathrm{d}\tau. \tag{D8.12}$$

Otherwise, we could not derive Eq. (2) of [336] from Maxwell's equations. In MCF media, the above approximation does not involve any incoherence given that we assumed slowly-varying temporal perturbations in $\delta t\sim T_{\text{P}}$. Unfortunately, as commented before, this assumption does not hold in Fig. D8.1. Our medium can be perturbed by rapidly-varying temporal fluctuations of $\chi^{(1)}$ in $\delta t<T_{\text{P}}$ (induced by Δn_{eff}), as can be observed, for instance, in a step-index TWG. In fact, in general, Eq. (D8.12) cannot correctly describe the interaction of an optical pulse with a moving temporal boundary.

Therefore, if we require to employ the above approximation to derive a time-domain pulse propagation equation of the desired form [Eq. (D8.1)], how can we correctly model the propagation of a pulse in the scenario illustrated in Fig. D8.1? The solution is found by considering the following fundamental remarks:

- Bearing in mind that a moving temporal boundary is actually a moving spatial boundary, a different linear polarization must be assumed at the left and at the right of the temporal boundary. In this way, in Fig. D8.1, we must assume two different linear polarizations $\boldsymbol{\mathcal{P}}^{(1)}_{\text{SWG}}$ and $\boldsymbol{\mathcal{P}}^{(1)}_{\text{TWG}}$ to describe the two different dielectric regions observed in a TWG (see Fig. D8.2).

- In such a scenario, $\boldsymbol{\mathcal{P}}^{(1)}_{\text{SWG}}$ and $\boldsymbol{\mathcal{P}}^{(1)}_{\text{TWG}}$ can be written of the form of Eq. (D8.12), provided that we assume a slowly-varying evolution of $\Delta n_{\text{eff}}(\tau)$ in $\delta\tau\sim T_{\text{P}}$, where $\tau=t-z/v_{\text{B}}$ and considering z as a parameter in this discussion. Specifically, we are assuming that a gradual-index TWG, with temporal profile $\beta_{\text{B}}(\tau)=k_0\Delta n_{\text{eff}}(\tau)$, satisfies that $\delta_\tau\beta_{\text{B}}\ll|\beta_{\text{B}}|$ in $\delta\tau\sim T_{\text{P}}$, where $\delta_\tau\beta_{\text{B}}:=|\beta_{\text{B}}(\tau+\delta\tau)-\beta_{\text{B}}(\tau)|$. This is analogous to the slowly-varying condition imposed in the refractive index profile of gradual-index optical fibers. Moreover, note that a step-index TWG automatically fulfills this condition given that β_{B} is constant between the temporal boundaries.

- The linear polarizations $\boldsymbol{\mathcal{P}}^{(1)}_{\text{SWG}}$ and $\boldsymbol{\mathcal{P}}^{(1)}_{\text{TWG}}$ must be connected by imposing the corresponding boundary conditions of the spatial scattering: the tangential component of $\boldsymbol{\mathcal{E}}$ and $\boldsymbol{\mathcal{H}}$ must be continuous at the interfaces that separate each dielectric region in Fig. D8.2.

[38] Let us remember that in a linear and time-varying system the general input-output relation is of the form $y(t)=\int_{-\infty}^{\infty}h(t,\tau)\,x(\tau)\,\mathrm{d}\tau$, where $h(t,\tau)$ is the time-varying impulse response of the system, i.e., the response of the system at time t for an input at time τ of the form $x(t)=\delta(t-\tau)$ [358]. In our case, $x\equiv\boldsymbol{\mathcal{E}}$, $y\equiv\boldsymbol{\mathcal{P}}^{(1)}$ and $h\equiv\varepsilon_0\chi^{(1)}$.

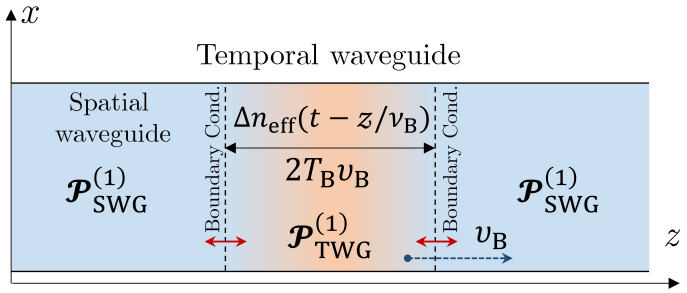

Figure D8.2. Different responses of the linear polarization $\boldsymbol{\mathcal{P}}^{(1)}$ in a TWG: $\boldsymbol{\mathcal{P}}^{(1)}_{\mathrm{SWG}}$ and $\boldsymbol{\mathcal{P}}^{(1)}_{\mathrm{TWG}}$. Specifically, $\boldsymbol{\mathcal{P}}^{(1)}_{\mathrm{SWG}}$ is the linear polarization which describes the medium response in the unperturbed region of the spatial waveguide (blue area), and $\boldsymbol{\mathcal{P}}^{(1)}_{\mathrm{TWG}}$ is the linear polarization which describes the medium response inside the TWG. The three regions are connected by the following boundary conditions (red arrows): the tangential component of $\boldsymbol{\mathcal{E}}$ and $\boldsymbol{\mathcal{H}}$ must be continuous at the interfaces that separate each dielectric region.

Consequently, we find a different wave equation for each dielectric region connected by the aforementioned boundary conditions. Using the refractive index profile calculated in the second step [Eq. (D8.9)], the global wave equation of our scenario (Fig. D8.2) can be expressed in the frequency domain following the same formalism as in Chapter 4:

$$\triangle \widetilde{E}_{\omega_0}\left(\boldsymbol{r}, \omega - \omega_0; t\right) + \frac{\omega^2}{c_0^2}\widetilde{n}^2\left(\boldsymbol{r}, \omega; t\right)\widetilde{E}_{\omega_0}\left(\boldsymbol{r}, \omega - \omega_0; t\right) = 0, \tag{D8.13}$$

with:

$$\begin{aligned}\widetilde{E}_{\omega_0}\left(\boldsymbol{r}, \omega - \omega_0; t\right) :&= \mathcal{F}_{\mathrm{T}}\left[E_{\omega_0}\left(\boldsymbol{r}, t\right)\exp\left(j\omega_0 t\right)\right] \\ &= \widetilde{\mathcal{A}}\left(z, \omega - \omega_0; t\right) F\left(x, y, \omega; z, t\right)\exp\left(\mp j\beta_0 z\right). \end{aligned}\tag{D8.14}$$

Fourth step: Pulse propagation equation

Replacing our ansatz [Eq. (D8.14)] into the wave equation [Eq. (D8.13)], we find after some algebraic work the following time-domain pulse propagation equation:[39]

$$\left(\pm\partial_z + \beta_1\partial_t - j\frac{1}{2}\beta_2\partial_t^2 + j\beta_{\mathrm{B}}\left(t - z/v_{\mathrm{B}}\right)\right)\mathcal{A}\left(z, t\right) = 0, \tag{D8.15}$$

with the sign "+" to describe the forward propagation and the sign "−" to describe the backward propagation. The theoretical model is completed by *including* the boundary conditions of the spatial scattering that allow us to calculate the reflected and transmitted complex envelopes $\mathcal{A}_{\mathrm{R}}$ and $\mathcal{A}_{\mathrm{T}}$ generated from the interaction of the incident pulse $\mathcal{A}_{\mathrm{I}}$ with the moving temporal boundaries described by β_{B}.

[39] The algebra of the fourth step requires to use the second step to simplify the mathematical discussion. In particular, from the second step [Eq. (D8.8)], we find using Eq. (D8.5) $[\partial_z F \simeq \partial_z^2 F \simeq 0$ in $\delta z \sim 2\pi/\beta_{\mathrm{eq}}\left(z, \omega_0; t\right)]$:

$$\left(\triangle_{\mathrm{T}} + \frac{\omega^2}{c_0^2}\widetilde{n}^2\left(\boldsymbol{r}, \omega; t\right)\right)F\left(x, y, \omega; z, t\right) = \left[\beta_0^2 - j2\beta_0\mathfrak{D}_{\mathrm{eq}}\left(z, \omega; t\right)\right]F\left(x, y, \omega; z, t\right),$$

where $\triangle_{\mathrm{T}} = \partial_x^2 + \partial_y^2$ is the transverse Laplacian operator and:

$$\mathfrak{D}_{\mathrm{eq}}\left(z, \omega; t\right) := j\beta_{\mathrm{B}}\left(t - z/v_{\mathrm{B}}\right) + \sum_{k=1}^{2}\frac{j}{k!}\left(\omega - \omega_0\right)^k\beta_k \equiv \sum_{k=0}^{2}\frac{j}{k!}\left(\omega - \omega_0\right)^k\gamma_k\left(z; t\right),$$

where $\gamma_0\left(z; t\right) := \beta_{\mathrm{B}}\left(t - z/v_{\mathrm{B}}\right)$ and $\gamma_{k>0}\left(z; t\right) := \beta_{k>0}$. The function $\mathfrak{D}_{\mathrm{eq}}$ can be expressed in the time domain via the linear operator:

$$\widehat{\mathrm{D}}_{\mathrm{eq}}\left(z; t\right) = \sum_{k=0}^{2}\frac{\left(-j\right)^{k-1}}{k!}\gamma_k\left(z; t\right)\partial_t^k,$$

and repeating the same discussion as in Chapter 4, we find a PDE of the form $\left(\pm\partial_z + \widehat{\mathrm{D}}_{\mathrm{eq}}\right)\mathcal{A} = 0$, that is, our Eq. (D8.15).

Open questions 1-3

Once we have performed a rigorous discussion about the propagation of an optical pulse in the time-varying and temporally dispersive medium shown in Fig. D8.1, we will be able to answer the questions 1-3 detailed on page 291:

Question 1 Equation (D8.1) cannot simultaneously describe both forward and backward propagation directions.

Question 2 Equation (D8.1) cannot correctly describe the spatial scattering in a moving temporal boundary. This requires to: (*i*) consider different polarization densities in each dielectric region, leading to different pulse propagation equations, and (*ii*) include boundary conditions to connect the solution of each region.

Question 3 We can correctly perform a modal analysis of a TWG starting from Eq. (D8.1), despite the fact that the backward propagation and the boundary conditions are omitted. The modal analysis only requires to consider a single propagation direction (e.g. the forward propagation) and the boundary conditions can be included in the problem once we have calculated the eigenfunctions of each dielectric region from Eq. (D8.1) by using the profile β_{B} of each region.

D8.4 Modal analysis

In this subsection, we indicate how to perform the modal analysis of a TWG and we include some basic notes about the numerical methods employed to calculate the eigenvalues and eigenfunctions of this new class of optical systems.

D8.4.1 Coordinate transformation

The modal analysis of a TWG can by simplified by using a reference system in which the temporal boundaries are stationary for an external observer. To this end, we should perform the coordinate transformations $\mathrm{z} := z$ and $\tau := t - z/v_{\mathrm{B}}$.

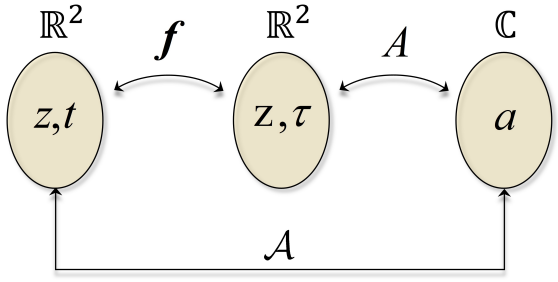

Figure D8.3. Flowchart of coordinate transformations.

Figure D8.3 depicts the flowchart of coordinate transformations. Applying the chain rule we find:

$$\frac{\partial \mathcal{A}\left(z,t\right)}{\partial z} \equiv \frac{\partial a}{\partial z} = \frac{\partial a}{\partial \mathrm{z}}\frac{\partial \mathrm{z}}{\partial z} + \frac{\partial a}{\partial \tau}\frac{\partial \tau}{\partial z} = \frac{\partial a}{\partial \mathrm{z}} - \frac{1}{v_{\mathrm{B}}}\frac{\partial a}{\partial \tau}; \tag{D8.16}$$

$$\frac{\partial \mathcal{A}\left(z,t\right)}{\partial t} \equiv \frac{\partial a}{\partial t} = \frac{\partial a}{\partial \mathrm{z}}\frac{\partial \mathrm{z}}{\partial t} + \frac{\partial a}{\partial \tau}\frac{\partial \tau}{\partial t} = \frac{\partial a}{\partial \tau}, \tag{D8.17}$$

that is, $\partial_z = \partial_{\mathrm{z}} - (1/v_{\mathrm{B}})\partial_\tau$ and $\partial_t = \partial_\tau$. Hence, Eq. (D8.1) becomes:

$$\left[(\partial_{\mathrm{z}} - (1/v_{\mathrm{B}})\partial_\tau) + \beta_1\partial_\tau - j\frac{1}{2}\beta_2\partial_\tau^2 + j\beta_{\mathrm{B}}\left(\tau\right)\right] a = 0. \tag{D8.18}$$

Now, defining $\Delta\beta_1 := \beta_1 - 1/v_{\mathrm{B}}$, we find the equation [$a = A(\mathrm{z},\tau)$]:

$$\left(\partial_{\mathrm{z}} + \Delta\beta_1\partial_\tau - j\frac{1}{2}\beta_2\partial_\tau^2 + j\beta_{\mathrm{B}}\left(\tau\right)\right) A\left(\mathrm{z},\tau\right) = 0. \tag{D8.19}$$

D8.4.2 Helmholtz equation

Applying separation of variables in the complex envelope A of the form:

$$A(\mathrm{z},\tau)=\sum_{n=0}^{\infty}\Theta_n(\mathrm{z})\,\Psi_n(\tau)\,, \tag{D8.20}$$

Eq. (D8.19) becomes:

$$\frac{\Theta_n'(\mathrm{z})}{\Theta_n(\mathrm{z})}=-\Delta\beta_1\frac{\Psi_n'(\tau)}{\Psi_n(\tau)}+j\frac{1}{2}\beta_2\frac{\Psi_n''(\tau)}{\Psi_n(\tau)}-j\beta_{\mathrm{B}}(\tau)\,. \tag{D8.21}$$

Taking into account that we have omitted the dielectric losses of the optical medium on page 293, the LHS and the RHS of the above equation must be a purely imaginary constant $\pm jK_n$, which leads to a spatial modal solution of the form $\Theta_n(\mathrm{z})=\exp(\pm jK_n\mathrm{z})$. Given that we have only considered the forward propagation, we select the sign "$-$" to be coherent with the sign convention selected in Subsection D8.3. Then:

$$\Theta_n(\mathrm{z})=\exp(-jK_n\mathrm{z})\,. \tag{D8.22}$$

It should be noted that the spatial solution is a periodic function with fundamental period $2\pi/K_n$.

Furthermore, from the RHS of Eq. (D8.21) we find the ODE:

$$\left[\frac{\mathrm{d}^2}{\mathrm{d}\tau^2}+j2\frac{\Delta\beta_1}{\beta_2}\frac{\mathrm{d}}{\mathrm{d}\tau}+2\frac{K_n}{\beta_2}-2\frac{\beta_{\mathrm{B}}(\tau)}{\beta_2}\right]\Psi_n(\tau)=0, \tag{D8.23}$$

which can be transformed into a Helmholtz equation by using the transformation method detailed in Chapter 6, in Subsection 6.14.1. In this way, Eq. (D8.23) becomes an eigenvalue equation:

$$\left(-\frac{\mathrm{d}^2}{\mathrm{d}\tau^2}+2\frac{\beta_{\mathrm{B}}(\tau)}{\beta_2}\right)\psi_n(\tau)=\Omega_n\psi_n(\tau)\,, \tag{D8.24}$$

with a discrete set of eigenfunctions $\{\psi_n\}_{n=0}^{\infty}$ and eigenvalues $\{\Omega_n\}_{n=0}^{\infty}$:

$$\psi_n(\tau)=\Psi_n(\tau)\exp\left(j\frac{\Delta\beta_1}{\beta_2}\tau\right); \tag{D8.25}$$

$$\Omega_n=2\frac{K_n}{\beta_2}+\frac{\Delta\beta_1^2}{\beta_2^2}. \tag{D8.26}$$

Concretely, the above Helmholtz equation is Eq. (8.3.3) of the main text over which we apply T-SUSY to design supersymmetric TWGs.

Consequently, the modal solution of the TWG is of the form:

$$A(\mathrm{z},\tau)=\sum_{n=0}^{\infty}\psi_n(\tau)\exp\left(-j\frac{\Delta\beta_1}{\beta_2}\tau\right)\exp(-jK_n\mathrm{z})\,, \tag{D8.27}$$

which is Eq. (8.3.2) of the main text. Once we have calculated the eigenfunctions ψ_n in each dielectric region of the TWG, we must impose the continuity of ψ_n to fulfill the boundary conditions of our system: continuity of the tangential components of $\boldsymbol{\mathcal{E}}$ and $\boldsymbol{\mathcal{H}}$ at the temporal boundaries. In addition, we must verify that A satisfies the SVEA[40] for the selected value of $\Delta\beta_1/\beta_2$ and the set of phase constants $\{K_n\}_{n=0}^{\infty}$ calculated from the modal analysis. However, note that ω_0 is a degree of freedom of the problem and, therefore, we can always select a value of ω_0 that guarantees that the SVEA is fulfilled.

[40] See page 129.

D8.4.3 Numerical analysis

The modal analysis of a step-index or gradual-index TWG can be numerically calculated with CST Microwave Studio and MATLAB by using the analogy reported in [337], discussed here for the sake of clarity of the results presented in Section 8.3.

Analogy	**Spatial slab (TE modes)**	**Temporal waveguide**
Helmholtz equation	$\left[\frac{\mathrm{d}^2}{\mathrm{d}x^2} + \underbrace{(-\beta_n^2)}_{\Omega_n} - \underbrace{\left(-\frac{\omega^2}{c_0^2}n^2(x)\right)}_{V(x)}\right]\psi_n(x) = 0$	$\left[\frac{\mathrm{d}^2}{\mathrm{d}\tau^2} + \underbrace{\frac{2}{\beta_2}K_n + \left(\frac{\Delta\beta_1}{\beta_2}\right)^2}_{\Omega_n} - \underbrace{\frac{2}{\beta_2}\beta_\mathrm{B}(\tau)}_{V(\tau)}\right]\psi_n(\tau) = 0$
Waveguide profile	$n(x) = \begin{cases} n_\mathrm{cl} & \lvert x\rvert > a \\ n_\mathrm{co} & \lvert x\rvert \le a \end{cases}$	$\beta_\mathrm{B}(\tau) = \begin{cases} \beta_\mathrm{cl} & \lvert\tau\rvert > T_\mathrm{B} \\ \beta_\mathrm{co} & \lvert\tau\rvert \le T_\mathrm{B} \end{cases}$; $\sqrt{2\beta_2(\beta_\mathrm{cl}-\beta_\mathrm{co})} > \lvert\Delta\beta_1\rvert$
Eigenmodes	$\psi_n(x) = \begin{cases} B\exp\left(-\frac{w_n}{a}(\lvert x\rvert - a)\right) & \lvert x\rvert > a \\ A\cos\left(\frac{u_n}{a}x - \frac{n\pi}{2}\right) & \lvert x\rvert \le a \end{cases}$	$\psi_n(\tau) = \begin{cases} B\exp\left(-\frac{w_n}{T_\mathrm{B}}(\lvert\tau\rvert - T_\mathrm{B})\right) & \lvert\tau\rvert > T_\mathrm{B} \\ A\cos\left(\frac{u_n}{T_\mathrm{B}}\tau - \frac{n\pi}{2}\right) & \lvert\tau\rvert \le T_\mathrm{B} \end{cases}$
Eigenvalue equation	$\nu\sqrt{1-b_n} = \frac{n\pi}{2} + \arctan\left(\sqrt{\frac{b_n}{1-b_n}}\right)$; $n = 0,1,2,\ldots$	$\nu\sqrt{1-b_n} = \frac{n\pi}{2} + \arctan\left(\sqrt{\frac{b_n}{1-b_n}}\right)$; $n = 0,1,2,\ldots$
Dispersion diagram	$b_n = f_n(\nu)$	$b_n = f_n(\nu)$

Table D8.1. Analogy between a step-index spatial dielectric slab waveguide [124] and a step-index temporal waveguide [337]. The constants A and B fulfill the relation $B = A\cos(u_n - n\pi/2)\,\mathrm{sign}(\tau)^n$, which arises from the continuity boundary condition of the eigenmodes ψ_n at $|x| = a$ and $|\tau| = T_\mathrm{B}$.[41]

Table D8.1 summarizes the analogy reported in [337] between a step-index spatial dielectric slab waveguide and a step-index TWG. Concretely, the analogy only applies to the TE modes of the slab. As seen, the spatial and temporal Helmholtz equations are analogous with an effective potential V and eigenvalue Ω_n of the form:

$$V(x) = -\frac{\omega^2}{c_0^2}n^2(x) \equiv \frac{2}{\beta_2}\beta_\mathrm{B}(\tau \to x); \tag{D8.28}$$

$$\Omega_n = -\beta_n^2 \equiv \frac{2}{\beta_2}K_n + \left(\frac{\Delta\beta_1}{\beta_2}\right)^2. \tag{D8.29}$$

It can be seen that the modal analysis of both structures involves the same eigenvalue equation, where b_n and ν are respectively the normalized phase constant and normalized frequency, given by the expressions:[42]

$$\nu^2 = u^2 + w^2 = \frac{\omega^2}{c_0^2}a^2\left(n_\mathrm{co}^2 - n_\mathrm{cl}^2\right) \equiv \frac{2}{\beta_2}T_\mathrm{B}^2(\beta_\mathrm{cl} - \beta_\mathrm{co}); \tag{D8.30}$$

$$u_n = \nu\sqrt{1-b_n}; \qquad w_n = \nu\sqrt{b_n}; \tag{D8.31}$$

$$b_n = \frac{\beta_n^2/\left(\omega^2/c_0^2\right) - n_\mathrm{cl}^2}{n_\mathrm{co}^2 - n_\mathrm{cl}^2} \equiv \frac{\beta_\mathrm{cl} - K_n - (\beta_2/2)\left(\Delta\beta_1/\beta_2\right)^2}{\beta_\mathrm{cl} - \beta_\mathrm{co}}. \tag{D8.32}$$

In the gradual-index case, the analogy is only preserved if the slowly-varying condition of $n(x)$ is satisfied.[43] Otherwise, the TE solutions of the spatial slab, calculated from Maxwell's equations, do not obey the spatial Helmholtz equation depicted in Table D8.1 and, then, the analogy is broken.

[41] The condition $\sqrt{2\beta_2(\beta_\mathrm{cl}-\beta_\mathrm{co})} > |\Delta\beta_1|$ is required to guarantee total internal reflection inside the TWG, provided that the results of [336] are found to be valid. This should be revisited in future works taking into account the discussion performed on page 291.

[42] Here, in order to avoid any confusion with the quantum potential (V), we use a typography different from the typography employed in the first part of this thesis to denote the normalized frequency (ν).

[43] The slowly-varying condition of $n(x)$ requires that $\delta_x n \ll n(x)$ in $\delta x \sim \lambda_0/\overline{n}$, where $\delta_x n := |n(x+\delta x) - n(x)|$, λ_0 is the wavelength in vacuum and $\overline{n}$ is the average value of $n(x)$ in $\delta x = 2a$.

Hence, in step- and gradual-index TWGs, the eigenfunctions ψ_n and eigenvalues Ω_n of the temporal Helmholtz equation can be calculated from the spatial Helmholtz equation of Table D8.1, provided that the slowly-varying condition of the analogous $n(x)$ profile is satisfied (which is the case in all TWGs analyzed in this work). It is important to note that the analogy should be established by selecting values of ω and a that guarantee the same normalized frequency in the spatial slab and in the TWG [Eq. (D8.30)]. In this work, we have solved the spatial Helmholtz equation of the analogous slab with CST Microwave Studio. In particular, this software allows us to calculate numerically the TE modes of interest directly from Maxwell's equations, which are connected with the spatial Helmholtz equation via the slowly-varying condition, as mentioned above. Once we calculated the normalized dispersion diagram[44] of the TE modes with CST, we verified in MATLAB that the corresponding eigenfunctions and eigenvalues fulfill the temporal Helmholtz equation of the TWG under analysis.

Note on the numerical analysis with CST Microwave Studio

The modal analysis of the TE modes of a step- or gradual-index spatial dielectric slab waveguide can be estimated with a high degree of accuracy from a rectangular waveguide with $\mathfrak{b} \gg \mathfrak{a}$ (see Fig. D8.4) and a refractive index profile $n(x,y)$ with $\partial_y n(x,y) = 0$. Setting $\mathfrak{b} = 20\mathfrak{a}$, we have observed an error in $\{b_n\}_{n=0}^{3}$ around $\sim 1\%$ for the ideal step-index slab in comparison with its analytic solution [124]. Specifically, b_n can be calculated from β_n by using Eq. (D8.32) and β_n can be estimated in MATLAB as:

$$\beta_n = \sqrt{-\frac{\langle\psi_n|\,\widehat{\mathrm{H}}\,|\psi_n\rangle}{\langle\psi_n\,|\psi_n\,\rangle}} = \sqrt{-\frac{\int \psi_n^*(x)\,\widehat{\mathrm{H}}\psi_n(x)\,\mathrm{d}x}{\int \psi_n^*(x)\,\psi_n(x)\,\mathrm{d}x}}, \tag{D8.33}$$

where $\widehat{\mathrm{H}} = -\mathrm{d}^2/\mathrm{d}x^2 + V(x)$ and $\psi_n(x)$ is the 1D mode profile calculated with CST in the $y = 0$ plane of the rectangular waveguide from the 2D mode profile $\Psi_n(x,y)$ satisfying the condition $\partial_y \Psi_n(x,y) \simeq 0$.

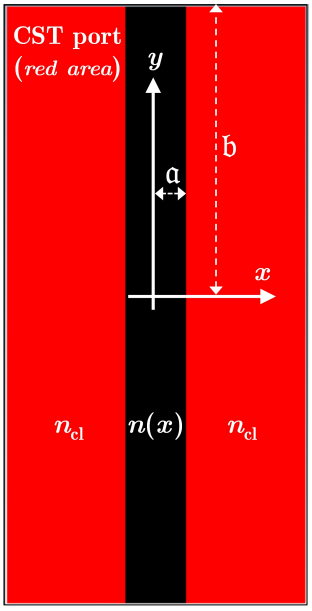

Figure D8.4. Screenshot of the rectangular dielectric waveguide simulated with CST setting $\mathfrak{b} \gg \mathfrak{a}$.

[44]The normalized dispersion diagram of the n-th TE mode is the function $b_n = f_n(\nu)$.

D8.5 T-SUSY in temporal waveguides

We know from Chapter 6 that the unbroken SUSY relation between two quantum-mechanical superpartners $V_{1,2}$ is given by the expression (we assume $\hbar^2/2m \equiv 1$ for simplicity):

$$V_2(x) = V_1(x) - 2\frac{\mathrm{d}^2}{\mathrm{d}x^2}\ln\psi_0^{(1)}(x), \tag{D8.34}$$

where $\psi_0^{(1)}$ is the ground state of V_1. As detailed in the main text, we can identify an effective potential in a TWG of the form ($i \in \{1,2\}$):

$$V_i(x \to \tau) \equiv \frac{2}{\beta_2}\beta_{\mathrm{B}i}(\tau), \tag{D8.35}$$

by comparing the time-independent Schrödinger equation of quantum mechanics with Eq. (8.3.3). Hence, combining Eqs. (D8.34) and (D8.35) we infer that:

$$\beta_{\mathrm{B}2}(\tau) = \beta_{\mathrm{B}1}(\tau) - \beta_2\frac{\mathrm{d}^2}{\mathrm{d}\tau^2}\ln\psi_0^{(1)}(\tau), \tag{D8.36}$$

where $\psi_0^{(1)}$ is the ground state (fundamental mode) of $\beta_{\mathrm{B}1}$ in this case. This expression is Eq. (8.3.4) of this chapter. Crucially, the above transformation may alter the degeneracy between the temporal bound states of T-SUSY TWGs if:

- The T-SUSY profiles $\beta_{\mathrm{B}1}$ and $\beta_{\mathrm{B}2}$ are related by a singular superpotential W. Nonetheless, this is not the case given that $W(\tau) = -(\ln\psi_0^{(1)}(\tau))'$ and $\psi_0^{(1)}$ has no nodes.
- $\beta_{\mathrm{B}2}(\tau)$ does not have a slowly-varying temporal profile. In such a case, the pulse propagation equation (D8.1) would not fulfill Maxwell's equations. Nevertheless, in our case, the T-SUSY TWG shown in Fig. 8.6(a) satisfies the slowly-varying criterion with $T_{\mathrm{P}} < T_{\mathrm{B}}/4 \sim 80$ ps. In such circumstances, we find that $\beta'_{\mathrm{B}2}(\tau) \ll \beta_{\mathrm{B}2}(\tau)/T_{\mathrm{P}}$ in $\delta\tau \sim T_{\mathrm{P}}$.

D8.6 Parallel temporal waveguides: coupled-mode theory

Consider two parallel TWGs a and b constructed from two different temporal perturbations $\beta_{\mathrm{B},a}(t - z/v_{\mathrm{B}})$ and $\beta_{\mathrm{B},b}(t - z/v_{\mathrm{B}})$ of temporal width $2T_{\mathrm{B},a}$ and $2T_{\mathrm{B},b}$. Furthermore, both TWGs are moving with the same speed v_{B} through the longitudinal z-axis of a given spatial waveguide and are separated T_{ab} in time and $v_{\mathrm{B}}T_{ab}$ in space. Figure D8.5 illustrates this scenario.

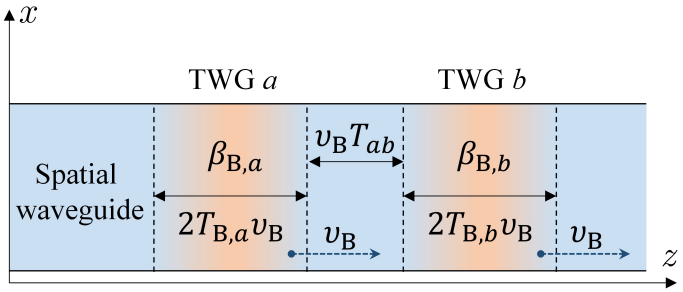

Figure D8.5. Parallel temporal waveguides (TWGs) a and b moving with the same speed v_{B} through the longitudinal axis of a given spatial waveguide (blue area).

For the sake of simplicity, let us first assume that both TWGs are operating in the single-mode regime. The fundamental mode of each TWG will be denoted with the subindex a or b. In such a scenario, the complex envelope of the global electric field of this optical structure can be approximated using perturbation theory as:

$$A(\mathrm{z},\tau) \simeq \sum_{m=a,b} \mathscr{A}_m(\mathrm{z})\,\psi_m(\tau)\exp\left(-j\frac{\Delta\beta_1}{\beta_2}\tau\right)\exp(-jK_m\mathrm{z}), \tag{D8.37}$$

where $\mathscr{A}_m$ is the complex amplitude of each mode. In isolated conditions (i.e., when each TWG is uncoupled from the other one), we find that $\mathrm{d}\mathscr{A}_m/\mathrm{d}z = 0$ and ψ_m must fulfill the temporal Helmholtz equation:

$$\left[\frac{\mathrm{d}^2}{\mathrm{d}\tau^2} + 2\frac{K_m}{\beta_2} + \left(\frac{\Delta\beta_1}{\beta_2}\right)^2 - 2\frac{\beta_{\mathrm{B},m}(\tau)}{\beta_2}\right]\psi_m(\tau) = 0. \tag{D8.38}$$

Nevertheless, if the two TWGs are in close proximity, the longitudinal dependence of $\mathscr{A}_m$ accounts for the power exchange between modes,[45] ψ_m also fulfills Eq. (D8.38), and the complex envelope A given by Eq. (D8.37) must satisfy the time-domain pulse propagation equation:

$$\left(\partial_{\mathrm{z}} + \Delta\beta_1\partial_\tau - j\frac{1}{2}\beta_2\partial_\tau^2 + j\beta_{\mathrm{B}}(\tau)\right)A(\mathrm{z},\tau) = 0, \tag{D8.39}$$

with $\beta_{\mathrm{B}}(\tau) = \beta_{\mathrm{B},a}(\tau) + \beta_{\mathrm{B},b}(\tau)$. Note that the above equation plays the same role as the wave equation in optical couplers based on parallel spatial waveguides. Hence, substituting Eq. (D8.37) into Eq. (D8.39) and using Eq. (D8.38), we find after some algebra (we omit the independent variables for simplicity):

$$\sum_{m=a,b}\frac{\mathrm{d}\mathscr{A}_m}{\mathrm{dz}}\psi_m\exp(-jK_m\mathrm{z}) + j\left(\beta_{\mathrm{B}} - \beta_{\mathrm{B},m}\right)\mathscr{A}_m\psi_m\exp(-jK_m\mathrm{z}) = 0. \tag{D8.40}$$

From the above equation, we can find the coupled-mode equations describing the power exchange between modes of both parallel TWGs. As an example, the coupled-mode equation governing the mode-coupling from mode b to mode a is found: (*i*) multiplying Eq. (D8.40) by $\psi_a\exp(jK_a\mathrm{z})$, (*ii*) integrating in $\tau\in(-\infty,\infty)$, and (*iii*) writing the first-order derivative of $\mathscr{A}_{a(b)}$ at the LHS. In this way, we obtain:

$$j\frac{\mathrm{d}\mathscr{A}_a}{\mathrm{dz}} = c_a\mathscr{A}_a + \exp(-j\Delta K_{b,a}\mathrm{z})\left(\kappa_{a,b} - j\chi_{a,b}\frac{\mathrm{d}}{\mathrm{dz}}\right)\mathscr{A}_b, \tag{D8.41}$$

where $\Delta K_{b,a} := K_b - K_a$. A similar coupled-mode equation describing the coupled power from mode a to mode b can be found by exchanging the subindexes in the above equation. The mode-coupling coefficients (MCCs), accounting for the mode overlapping between ψ_a and ψ_b, are defined as:

$$\chi_{a,b} := \frac{1}{N_a}\int_{-\infty}^{\infty}\psi_b(\tau)\,\psi_a(\tau)\,\mathrm{d}\tau; \tag{D8.42}$$

$$c_a := \frac{1}{N_a}\int_{-\infty}^{\infty}\beta_{\mathrm{B},b}(\tau)\,\psi_a^2(\tau)\,\mathrm{d}\tau = \frac{1}{N_a}\int_{\langle 2T_{\mathrm{B},b}\rangle}\beta_{\mathrm{B},b}(\tau)\,\psi_a^2(\tau)\,\mathrm{d}\tau; \tag{D8.43}$$

$$\kappa_{a,b} := \frac{1}{N_a}\int_{-\infty}^{\infty}\beta_{\mathrm{B},a}(\tau)\,\psi_b(\tau)\,\psi_a(\tau)\,\mathrm{d}\tau = \frac{1}{N_a}\int_{\langle 2T_{\mathrm{B},a}\rangle}\beta_{\mathrm{B},a}(\tau)\,\psi_b(\tau)\,\psi_a(\tau)\,\mathrm{d}\tau, \tag{D8.44}$$

with $N_a := \int_{-\infty}^{\infty}\psi_a^2(\tau)\,\mathrm{d}\tau$.

It is worth mentioning the complete analogy between the CMT of parallel spatial waveguides [see the linear terms of Eq. (2.2.5), in Chapter 2] and the CMT of parallel TWGs [Eq. (D8.41)]. As demonstrated on page 31, $\chi_{a,b}$ can usually be neglected in the spatial case. However, in parallel TWGs, the MCC $\chi_{a,b}$ is generally higher than the MCCs c_a and $\kappa_{a,b}$ and, therefore, all the MCCs should be retained to guarantee a complete description of the mode-coupling phenomenon. Along this line, note that Eq. (D8.41) can be rewritten as:

[45] The mode-coupling between temporal modes of parallel TWGs takes place through their evanescent tails.

$$j\frac{\mathrm{d}\mathscr{A}_a(\mathrm{z})}{\mathrm{dz}} = c_a^{(\mathrm{eq})}\mathscr{A}_a(\mathrm{z}) + \kappa_{a,b}^{(\mathrm{eq})}\exp\left(-j\Delta K_{b,a}\mathrm{z}\right)\mathscr{A}_b(\mathrm{z}), \tag{D8.45}$$

where $c_a^{(\mathrm{eq})} := (c_a - \chi_{a,b}\kappa_{b,a})/(1-\chi_{a,b}\chi_{b,a})$ and $\kappa_{a,b}^{(\mathrm{eq})} := (\kappa_{a,b} - \chi_{a,b}c_b)/(1-\chi_{a,b}\chi_{b,a})$. A similar equation for $\mathrm{d}\mathscr{A}_b(z)/\mathrm{d}z$ can be obtained by exchanging the subindexes a and b in Eq. (D8.45). Finally, for completeness, the following considerations are in order:

- If we solve the CMT assuming that only the mode a is excited at $\mathrm{z}=0$ [$\mathscr{A}_b(0)=0$], we find that:

$$\mathscr{A}_b(\mathrm{z}) = -j\frac{\kappa_{b,a}^{(\mathrm{eq})}}{\eta}\exp\left(j\frac{\Delta K_{b,a}}{2}\mathrm{z}\right)\sin(\eta\mathrm{z})\,\mathscr{A}_a(0), \tag{D8.46}$$

  where:

$$\eta = \sqrt{\kappa_{a,b}^{(\mathrm{eq})}\kappa_{b,a}^{(\mathrm{eq})} + \frac{\left(\Delta K_{b,a} + c_b^{(\mathrm{eq})} - c_a^{(\mathrm{eq})}\right)^2}{4}}. \tag{D8.47}$$

  Bearing in mind that $\psi_0^{(2)}$ and $\psi_1^{(1)}$ are degenerate modes in the TPL shown in Fig. 8.7(a) of the main text ($\Delta K_{b,a}=0$), we conclude from Eqs. (D8.46) and (D8.47) that they must exchange their optical power periodically along the z-axis with a coupling length[46] $L_{\mathrm{C}} = \pi/2\eta$ and a coupling efficiency $\left|\mathscr{A}_b(z=L_{\mathrm{C}})/\mathscr{A}_a(0)\right|^2 = \left|\kappa_{b,a}^{(\mathrm{eq})}/\eta\right|^2$.

- In the multi-mode regime, the modes $\{a_n\}_{n=1}^N$ of TWG a exchange optical power with the modes $\{b_n\}_{n=1}^N$ of TWG b. In order to describe this situation, Eq. (D8.37) must be restated as:

$$A(\mathrm{z},\tau) \simeq \sum_{m=a,b}\sum_{n=1}^{N}\mathscr{A}_{mn}(\mathrm{z})\,\psi_{mn}(\tau)\exp\left(-j\frac{\Delta\beta_1}{\beta_2}\tau\right)\exp\left(-jK_{mn}\mathrm{z}\right), \tag{D8.48}$$

  and, consequently, the mode-coupling from the modes $\{b_n\}_{n=1}^N$ to a given mode a_i is governed by the coupled-mode equation:

$$j\frac{\mathrm{d}\mathscr{A}_{ai}(\mathrm{z})}{\mathrm{dz}} = c_{ai}\mathscr{A}_{ai}(\mathrm{z}) + \sum_{n=1}^{N}\exp\left(-j\Delta K_{bn,ai}\mathrm{z}\right)\left(\kappa_{ai,bn} - j\chi_{ai,bn}\frac{\mathrm{d}}{\mathrm{dz}}\right)\mathscr{A}_{bn}(\mathrm{z}). \tag{D8.49}$$

  We cannot observe internal mode-coupling among the modes of a given TWG m if we assume that its temporal perturbation profile $\beta_{\mathrm{B},m}(\tau)$ is invariant during the propagation of the TWG along the longitudinal axis of the spatial waveguide.[47] In practice, the temporal profile $\beta_{\mathrm{B},m}$ may experience dispersion along the z-axis. The precise longitudinal evolution of $\beta_{\mathrm{B},m}$ depends on the exact physical mechanism used to generate the temporal perturbation in the spatial waveguide. For example, using the XPM with a pump-probe set-up, the shape of the pump pulse will generally be affected by dispersion during propagation [337]. We could overcome this drawback: (*i*) using an optical soliton as a pump pulse or, (*ii*) selecting the pump wavelength at the zero-dispersion wavelength of the spatial waveguide, provided that the higher-order dispersion terms are negligible. This second scenario requires to use, e.g., microstructured optical fibers to tailor the material dispersion properties of the spatial waveguide.

- In parallel TWGs with different speed or different propagation directions, the MCCs are found to be space-dependent. Nevertheless, this scenario is out of the scope of this work.

[46] The coupling length L_{C} is the length that maximizes the sinusoidal term of Eq. (D8.46).

[47] An internal mode-coupling among the modes of a TWG requires a temporal perturbation $\beta_{\mathrm{B},m}$ with a varying shape along the longitudinal axis. This can be modeled by a profile of the form $\beta_{\mathrm{B},m}(\tau;\mathrm{z})$. The τ variable describes the ideal temporal profile of the TWG, and the z variable accounts for the fluctuation of its shape during the propagation of the TWG along the longitudinal axis of the spatial waveguide. This is analogous to an optical fiber with a refractive index profile $n(r;z)$ which fluctuates along the z-axis due to manufacturing imperfections, which induce intra-core mode-coupling between different fiber modes.

Note on the numerical analysis of the temporal photonic lantern using the CMT

Figure 8.7(b) depicts the function (we retrieve the original reference system by using the variables z and t):

$$|\mathscr{A}_a(z)|\,\psi_a(t-z/v_{\mathrm{B}})+|\mathscr{A}_b(z)|\,\psi_b(t-z/v_{\mathrm{B}}), \tag{D8.50}$$

where $\psi_a \equiv \psi_0^{(2)}$ and $\psi_b \equiv \psi_1^{(1)}$. The longitudinal evolution of $\mathscr{A}_a$ and $\mathscr{A}_b$ has been numerically calculated in MATLAB by using the CMT derived in this subsection. Along this line, note that v_{B} and L (the length of the spatial waveguide over which the TPL propagates) are arbitrary parameters in the numerical simulation. Aimed to facilitate the comprehension of the results, we have taken $L = L_{\mathrm{C}}$, which can be calculated as indicated before.

D8.7 The temporal photonic lantern

The concept of *temporal photonic lantern* (TPL) is analogous to the concept of the spatial photonic lantern extensively discussed in [305]: a device which generates temporal (spatial) supermodes from the linear combination of degenerates modes of close-packed temporal (spatial) waveguides. Thus, in the same way as a spatial photonic lantern, we can use a TPL constructed from two identical single-mode TWGs to generate supermodes with a temporal profile $\psi(\tau)$ similar to a higher-order mode of a multi-mode TWG.

However, in Fig. 8.7, we used a different approach. We designed a TPL by using *non-identical* multi-mode TWGs, specifically supersymmetric TWGs, to generate temporal supermodes arising from the linear combination of SUSY temporal bound states, that is, $\psi(\tau) = \psi_n^{(2)}(\tau) \pm \psi_{n+1}^{(1)}(\tau)$. This allows us to: (*i*) obtain optical pulses exhibiting an exotic shape [Fig. 8.7(a)], and (*ii*) build pulse-shape transformers [Fig. 8.7(b)].

On the other hand, in complete analogy with a spatial photonic lantern, we can introduce a figure-of-merit to characterize the temporal supermodes of a TPL. Concretely, the role of the effective area of a spatial supermode can be covered by the *effective temporal width* of a temporal supermode, which is defined as:

$$T_{\mathrm{eff}} := \frac{\left(\int_{-\infty}^{\infty}|\psi(\tau)|^2\,\mathrm{d}\tau\right)^2}{\int_{-\infty}^{\infty}|\psi(\tau)|^4\,\mathrm{d}\tau}, \tag{D8.51}$$

where $\psi(\tau)$ is the temporal profile of the supermode under analysis. In particular, the supermode shown in Fig. 8.7(a) has an effective temporal width of $T_{\mathrm{eff}} = 1065$ ps.

D8.8 Time-varying group velocity

Here, we study question 4 of Subsection D8.2. So far, we have extensively discussed the theory of TWGs by assuming that the phase velocity c_0/n_{eff} is modified by the medium perturbation, but the group velocity $1/\beta_1$ is invariant. Now, let us consider that the perturbation also modifies the group velocity. In such a case, Eq. (D8.4) is reduced to ($\beta_{\mathrm{B},2} \simeq 0$):

$$\Phi(z,\omega;t) \simeq \left\{\beta_0 + \beta_{\mathrm{B},0}(t-z/v_{\mathrm{B}}) + (\omega-\omega_0)\left[\beta_1 + \beta_{\mathrm{B},1}(t-z/v_{\mathrm{B}})\right] + \frac{1}{2}(\omega-\omega_0)^2\beta_2\right\} z. \tag{D8.52}$$

As a result, Eq. (D8.19) becomes:

$$\left(\partial_{\mathrm{z}} + \Delta\beta_1(\tau)\,\partial_\tau - j\frac{1}{2}\beta_2\partial_\tau^2 + j\beta_{\mathrm{B}}(\tau)\right) A(\mathrm{z},\tau) = 0, \tag{D8.53}$$

where $\Delta\beta_1(\tau) := \beta_1 + \beta_{\mathrm{B},1}(\tau) - 1/v_{\mathrm{B}}$ and $\beta_{\mathrm{B},0}$ is redefined as $\beta_{\mathrm{B},0} \equiv \beta_{\mathrm{B}}$ to use a more economical notation. Obviously, the modal analysis of the TWG and the T-SUSY theory previously detailed in Subsections D8.4 and D8.5 should be revisited starting from the new version of the pulse propagation equation.

Modal analysis

Applying the separation of variables of Subsection D8.4, $A(\mathrm{z},\tau)=\sum_{n=0}^{\infty}\Theta_n(\mathrm{z})\,\Psi_n(\tau)$, we find the same spatial modal solution $\Theta_n(\mathrm{z})=\exp(-jK_n\mathrm{z})$, but the temporal modal solution is governed by a different eigenvalue equation. In particular, Eq. (D8.24) becomes:

$$\left[-\frac{\mathrm{d}^2}{\mathrm{d}\tau^2}+2\frac{\beta_{\mathrm{B}}(\tau)}{\beta_2}+j\frac{(\Delta\beta_1)'(\tau)}{\beta_2}-\left(\frac{\Delta\beta_1(\tau)}{\beta_2}\right)^2\right]\psi_n(\tau)=\Omega_n\psi_n(\tau), \tag{D8.54}$$

with a discrete set of eigenfunctions $\{\psi_n\}_{n=0}^{\infty}$ and eigenvalues $\{\Omega_n\}_{n=0}^{\infty}$:

$$\psi_n(\tau)=\Psi_n(\tau)\exp\left(j\int^{\tau}\frac{\Delta\beta_1(\zeta)}{\beta_2}\mathrm{d}\zeta\right); \tag{D8.55}$$

$$\Omega_n=2\frac{K_n}{\beta_2}. \tag{D8.56}$$

Therefore, the modal solution of the TWG is now of the form:

$$A(\mathrm{z},\tau)=\sum_{n=0}^{\infty}\psi_n(\tau)\exp\left(-j\int^{\tau}\frac{\Delta\beta_1(\zeta)}{\beta_2}\mathrm{d}\zeta\right)\exp(-jK_n\mathrm{z}). \tag{D8.57}$$

As seen, the temporal evolution is governed by a time-varying frequency, i.e., we can observe a time-varying spectral shift of the optical pulse $A(\mathrm{z},\tau)$. Consequently, the modal analysis and the main results of [337, 338] are found to be radically different in these circumstances. In the same vein, the CMT of Subsection D8.6 must also be revisited when $\partial_t\beta_1\neq 0$. However, this is out of the scope of this work.

T-SUSY theory

Now, we can identify an effective potential from Eq. (D8.54) of the form ($i\in\{1,2\}$):

$$V_i(\tau)\equiv 2\frac{\beta_{\mathrm{B}i}(\tau)}{\beta_2}+j\frac{\left(\Delta\beta_1^{(i)}\right)'(\tau)}{\beta_2}-\left(\frac{\Delta\beta_1^{(i)}(\tau)}{\beta_2}\right)^2, \tag{D8.58}$$

which directly depends on $\beta_{\mathrm{B}i}(\tau)$ and $\Delta\beta_1^{(i)}(\tau)$. Thus, we will be able to explore new types of supersymmetric TWGs by engineering the effective potential varying the perturbation $\beta_{\mathrm{B}i}$, the group velocity $1/\beta_1^{(i)}$, or both parameters. In other words, we can relate the virtual and physical spaces in different manners. Interestingly, we can observe a complex-valued potential with a real set of eigenvalues. In such a scenario, we can combine T-SUSY with $\mathcal{PT}$ symmetry in TWGs in the same way as in spatial waveguides [229].

Appendix E8: Temporal SUSY in acoustics

In this section, a temporal Helmholtz equation formally equal to Eq. (8.2.2) of the main text is derived for acoustic systems characterized by space- and time-varying properties. Particularly, in the case of pressure acoustics, the spatio-temporal evolution of the acoustic pressure $P(\boldsymbol{r},t)$ is governed by the following wave equation [359]:

$$-\partial_t^2 P(\boldsymbol{r},t) + B(\boldsymbol{r},t)\,\nabla\cdot\left(\rho^{-1}(\boldsymbol{r},t)\,\nabla P(\boldsymbol{r},t)\right) = 0, \tag{E8.1}$$

where the medium bulk modulus $B(\boldsymbol{r},t)$ and static mass density $\rho(\boldsymbol{r},t)$ are, in general, functions of space and time. Taking a medium for which ρ depends only on time (a similar result could be obtained for a medium with a slowly-varying spatial dependence of ρ), it is possible to rewrite Eq. (E8.1) as:

$$-\partial_t^2 P(\boldsymbol{r},t) + \frac{B(\boldsymbol{r},t)}{\rho(t)}\triangle P(\boldsymbol{r},t) = 0. \tag{E8.2}$$

Furthermore, if the bulk modulus can be expressed as $B(\boldsymbol{r},t) = B_{\mathrm{S}}(\boldsymbol{r})\,B_{\mathrm{T}}(t)$, and applying separation of variables to the pressure as $P(\boldsymbol{r},t) = P_{\mathrm{S}}(\boldsymbol{r})\,P_{\mathrm{T}}(t)$, the previous equation can be recast as:

$$\frac{\rho(t)}{B_{\mathrm{T}}(t)}\frac{P_{\mathrm{T}}''(t)}{P_{\mathrm{T}}(t)} = B_{\mathrm{S}}(\boldsymbol{r})\,\frac{\triangle P_{\mathrm{S}}(\boldsymbol{r})}{P_{\mathrm{S}}(\boldsymbol{r})}. \tag{E8.3}$$

Once again, this is satisfied if and only if both sides of the equation are equal to a constant. In analogy with the electromagnetic case, defining $n_{\mathrm{T}}^2(t) := \rho(t)/B_{\mathrm{T}}(t)$ and $n_- := n_{\mathrm{T}}(t\to-\infty)$, the following temporal Helmholtz equation is readily obtained:

$$\left(\frac{\mathrm{d}^2}{\mathrm{d}t^2} + \omega_0^2\frac{n_-^2}{n_{\mathrm{T}}^2(t)}\right)P_{\mathrm{T}}(t) = 0, \tag{E8.4}$$

that is, Eq. (8.2.2) of the main text.

Chapter 9

Conclusions and further work

The research work reported in this thesis combines two complementary topics: *multi-core fiber* and *optical supersymmetry*. Given the whirlwind of exotic ideas surrounding other branches of physics, such as supersymmetric quantum mechanics, we initially believed that such a thesis could take advantage of using these ideas to explore novel applications and functionalities in multi-core fibers that have remained hidden. Moreover, fascinated by the potential applications of supersymmetry, not only in multi-core fibers, but also in photonics in general, we finally decided to focus our efforts on optical supersymmetry in the second part of the thesis. It is worthy to note that the "engine" of our research work has always been the scientific curiosity in combination with our intuition.

In this chapter, we highlight the main results of this thesis. In addition, aimed to cover a broadband audience, we discuss the possibility of extrapolating these results to other branches of physics such as acoustics and quantum mechanics. Finally, for the sake of completeness, we detail the ongoing and future work.

9.1 Conclusions

Here, we detail the main objectives and conclusions achieved in this thesis:

1. A fundamental propagation phenomenon of multi-core fibers (MCFs) is the inter-core crosstalk (IC-XT), i.e., light coupling between optical modes of different cores. In Chapter 2, we have UNIFIED the theoretical description of the IC-XT in single-mode MCFs operating in the linear and nonlinear regimes, i.e., with low and high power levels, respectively. The linear coupled-mode and coupled-power theories of [128] have been extended to the nonlinear regime including the spatial perturbations of the medium: macrobends, microbends, fiber twisting and manufacturing imperfections. Both theories allow us to: (*i*) reduce the computational time of Maxwell's equations based on FDTD (finite-differences in the time-domain) methods, and (*ii*) unify the statistical analysis of the linear and nonlinear IC-XT. The spatial distribution of the IC-XT has been identified as a chi-squared distribution with 4 degrees of freedom in both power regimes. These degrees of freedom may be increased when multiple cores are excited at the MCF input.

2. In Chapter 3, we have reported the theoretical and experimental analysis of the IC-XT in single-mode MCFs by including POLARIZATION EFFECTS along with spatial and also temporal medium perturbations. The temporal perturbations are induced by external environmental factors, such as floor vibrations due to human activity and temperature variations. The theoretical model, the so-called coupled local-mode theory (CLMT), is able to describe this complicated scenario with a higher degree of accuracy than the coupled-mode theory of Chapter 2 and exhibiting a lower computational time than FDTD simulations of Maxwell's equations. Interestingly, the CLMT can be used to analyze and design the IC-XT in lowly- and highly-birefringent MCFs. Concretely, in highly-birefringent MCFs, the IC-XT can be

straightforwardly engineered by using the coupled local-power theory (CLPT) without the necessity of performing numerical simulations (see Appendix B3, page 88).

3. The benefits of the CLMT have also been employed to describe the optical propagation of ULTRA-SHORT pulses (minimum pulse width of the order of few femtoseconds) in real MCFs, which include the aforementioned spatial and temporal medium perturbations. New dispersive effects emerge when considering these fibers perturbations, which should be considered in future real-deployed MCF systems. In addition, the CLMT can be used to design MCFs comprising cores of different manufacturing characteristics: homogeneous, heterogeneous, coupled, uncoupled, lowly- or highly-birefringent, trench- or hole-assisted, step- or gradual-index. On the other hand, it is important to remark that, in contrast to our PAPER 6, where only the single-mode regime was reported, we have also discussed in Chapter 4 the multi-mode regime of the fiber (Appendix E4) and MCF transmissions comprising several optical carriers (Appendix A4). To highlight these new contributions to the CLMT, we show in Table 9.1 a schematic comparison of our model with previous pulse propagation models in the literature, not only in single-mode MCFs (depicted in Fig. 4.9), but also in optical fibers in general. Outstandingly, note that our model is able to describe the anisotropic Raman response, overlooked so far in the literature.

	CLMT	**Chiang**	**Mecozzi**	**Mumtaz**	**Poletti**	**Mamyshev**
[References]	Chapter 4	[181]	[153]	[155]	[186]	[185]
Polarization effects	✓		✓	✓	✓	
Spatial birefringence	✓		✓	✓	✓	
Temporal birefringence	✓					
Isotropic Raman	✓	✓			✓	✓
Anisotropic Raman	✓					
Fiber Type	MCFs	MCFs	SCFs	MCFs	SCFs	SCFs
Single-mode regime	✓	✓	✓	✓	✓	✓
Multi-mode regime	✓		✓	✓	✓	
Multiple carriers	✓		✓	✓	✓	

Table 9.1. Schematic comparison of our model reported in Chapter 4 with previous short (∼ps) and ultra-short (∼fs) pulse propagation models in single-core fibers (SCFs) and multi-core fibers (MCFs).

Likewise, the CLMT can also be used to describe the propagation of pulses in weakly-guiding single- and multi-core planar waveguides. Therefore, the CLMT could be of great utility in integrated photonics to analyze the pulse dispersion induced by the waveguide perturbations which may appear when the waveguide is integrated in ultra-compact optical devices.

4. The comprehension of the main propagation impairments of MCFs has allowed us to study the suitability of the MCF technology in optical transport networks. In Chapter 5, we have investigated the use of this new kind of optical fibers in the NEXT-GENERATION of optical fronthaul systems proposed to 5G-cellular networks. Concretely, we have observed that the average performance of these systems is not degraded when using high signal powers but, remarkably, the temporal performance fluctuations (induced by the random behavior of the IC-XT) are significantly reduced. Moreover, despite the fact that we have used signal standards (LTE-A and WiMAX) maybe different from the standards which will be employed in future real-deployed 5G and Beyond-5G cellular systems, our results could be of great utility taking into account that we have analyzed a potential common platform: OFDM modulation formats.

5. In order to explore hidden applications and functionalities of MCFs, we exploited in Chapter 7 the close connection between the laws of electromagnetism and quantum mechanics to design a new type of MCFs using the mathematical framework of supersymmetry. As a result, we conceived the supersymmetric MCFs, which allow us not only to increment the capacity of current optical networks, but also to implement a variety of signal processing applications: mode filtering, mode conversion, mode multiplexing, supermode generation, dispersion engineering and pulse shaping. As a byproduct, we have also demonstrated the possibility of performing TRUE mode (de)multiplexing using these fibers, an outstanding problem in optics.

6. Despite the fact that in non-relativistic quantum mechanics the spatial ($\sum_i \partial^2/\partial x_i^2$) and temporal ($\partial/\partial t$) operators of the Schrödinger equation are not symmetric (i.e., they involve partial derivatives of different order), in photonics we can find wave equations describing a vast number of scenarios where the spatial ($\sum_i \partial^2/\partial x_i^2$) and temporal ($\partial^2/\partial t^2$) operators are symmetric. In this way, in Chapter 8, we have proposed the possibility of extending the foundations of the non-relativistic supersymmetric quantum mechanics, only conceived in the space domain, to the TIME DOMAIN, at least within the framework of photonics. As a result, we have demonstrated that Maxwell's equations possess an underlying temporal supersymmetry. This can be used to straightforwardly analyze and design the scattering properties of time-varying optical systems without the necessity of solving the corresponding wave equation, which alleviates the numerical analysis of complicated scenarios. Especially, this result builds a bridge to design a new class of omnidirectional and polarization-independent transparent media. These unprecedented features define a promising platform for integrated photonics. To illustrate this, we have designed an ultra-compact reconfigurable transparent phase shifter with frequency-independent phase response, and a broadband optical isolator with tunable frequency down-conversion of the input signal. Finally, we have also shown that the temporal supersymmetry of Maxwell's equations may serve as a unique tool to judiciously design versatile pulse shaping devices based on optical systems supporting temporal modes.

9.2 Extrapolation to acoustics and quantum mechanics

The mathematical analogy between the laws of electromagnetism, acoustic and quantum mechanics in the Helmholtz regime entails the fascinating possibility of extrapolating the main results of this thesis to these branches of physics. This has already been explored in Sections 4.5, 6.13, 7.5 and 8.4. Here, for completeness, we include some interesting notes that facilitate the use of our models and results in acoustics and quantum mechanics.

The main results of the first part of this thesis are enclosed in the CLMT reported in Chapter 4 taking into account that the electromagnetic phenomena studied in Chapters 2 and 3 can also be numerically simulated using this theory. As discussed in Section 4.5, the CLMT may play an essential role in any physical system in which the underlying wave propagation phenomena are governed by coupled nonlinear Schrödinger equations (CNLSEs). For instance, we can highlight fundamental quantum and acoustic systems such as coupled Bose-Einstein condensates (BECs) [114] or ion-acoustic waves [190,191]. In the same way, nonlinear systems based on the CNLSEs are also of special interest in mathematics to study strongly interacting dynamical systems [360–363].

Interestingly, the CNLSEs are formally equal to our coupled local-mode equations when higher-order nonlinear terms are neglected in our equations (see below). Nevertheless, it is worthy to note that our theory posses a basic feature that is difficult to observe in the literature of the CNLSEs: the coupling coefficients and the exponential terms are found to be *space*- and *time*-dependent. This could be fundamental to analyze the impact of spatial and temporal perturbations on the aforementioned systems [364–367].

In order to guarantee a direct extrapolation of the results among the different branches of physics and mathematics where the CLMT can be applied, it is more convenient to work with *dimensionless* coupled local-mode equations. To this end, Eq. (4.2.66) should be restated as:

$$\partial_1 \psi_i(\boldsymbol{x}) = \sum_{n=1}^{N} \widehat{\mathrm{L}}_n^{(i)} \psi_n(\boldsymbol{x}) + \sum_{q,r,s}^{R^{(i)}} \exp\left(j\phi_{qrs}^{(i)}(\boldsymbol{x})\right) \widehat{\mathrm{N}}_{qrs}^{(i)} \psi_q(\boldsymbol{x}) \psi_r(\boldsymbol{x}) \psi_s^*(\boldsymbol{x}), \tag{9.2.1}$$

where $i \in \{1, \ldots, N\}$ and:

$$\widehat{\mathrm{L}}_n^{(i)} := \sum_{k=0}^{l_n^{(i)}} \mathcal{L}_{n,k}^{(i)}(\boldsymbol{x}) \partial_2^k; \quad \widehat{\mathrm{N}}_{qrs}^{(i)} := \sum_{k=0}^{n_{qrs}^{(i)}} \mathcal{N}_{qrs,k}^{(i)}(\boldsymbol{x}) \partial_2^k, \tag{9.2.2}$$

$\boldsymbol{x} = x_1\hat{u}_1 + x_2\hat{u}_2$, $\partial_1 \equiv \partial/\partial x_1$ and $\partial_2^k \equiv \partial^k/\partial x_2^k$. All functions appearing in Eq. (9.2.1) are complex-valued functions, except $\phi_{qrs}^{(i)}$, which can be assumed a real-valued function. Furthermore, the following considerations are in order:

- In photonics, x_1 and x_2 are usually related with a spatial and a temporal variable, respectively. In contrast, in quantum mechanics and acoustics, x_1 usually describes a temporal variable and x_2 accounts for a spatial variable.
- We have omitted the Raman terms of Eq. (4.2.66) in Eq. (9.2.1) given that these higher-order nonlinear terms do not usually appear in the CNLSEs.
- We have included the XPM and FWM terms of Appendix A4 [see Eq. (A4.15)] in Eq. (9.2.1) to describe important strongly nonlinear interactions studied in mathematics [360–363].
- The parameter $R^{(i)}$ indicates the number of nonlinear terms of the form $\psi_q\psi_r\psi_s^*$ which interact with the wave of the LHS, in this case ψ_i, when varying $(q, r, s) \in \{1, \ldots, N\}^3$. Here, we cannot write the summation of these nonlinear terms starting from $q = r = s = 1$ if $|\psi_1|^2 \psi_1$ does not interact with ψ_i. For this reason, we have omitted the initial value of the dummy indexes q, r, s in Eq. (9.2.1).
- The parameters $l_n^{(i)}$ and $n_{qrs}^{(i)}$ indicate respectively the order of the linear operators $\widehat{\mathrm{L}}_n^{(i)}$ and $\widehat{\mathrm{N}}_{qrs}^{(i)}$, which are usually of third-order or lower. In general, $l_n^{(i)} \leq 3$ and $n_{qrs}^{(i)} \leq 1$.
- The split-step Fourier method can be employed to solve numerically Eq. (9.2.1), provided that the linear and nonlinear terms can be decoupled (see page 132 for more details).

On the other hand, the results of optical SUSY reported in the second part of this thesis can be directly extrapolated to acoustic and quantum mechanics, as detailed in Sections 7.5 and 8.4. Special mention is required in the fact that the results of Chapter 7 could be of extreme importance in axially-symmetric quantum systems given that this class of symmetry has been overlooked so far in the literature of SUSY QM [216]. Moreover, this thesis could lead to a breakthrough in acoustics. The unique and exotic ideas of SUSY are introduced in this branch of physics for the first time to the best of our knowledge.

9.3 Further work

Many of the research topics in this thesis support and inspire the work in others [368–433] and allow for future work and further results.

1. The spatial distribution of the crosstalk reported in Chapter 2 should be further investigated in *coupled-core* MCFs. In this topic, a mathematical formalism similar to [148] could be of great utility.
2. The theoretical models of Chapters 2 and 3 can be extended to the *multi-mode* regime to investigate the spatial and temporal distribution of the IC-XT in MCFs guiding several LP mode groups in each core.

3. The *time scale* over which the linear birefringence of an MCF can be assumed to be constant and its impact on the temporal evolution of the IC-XT should be investigated in different geographic regions with diverse climatic conditions. In such a scenario, the works reported in [371,375] by T. M. F. Alves and A. V. T. Cartaxo could be of valuable interest to analyze the crosstalk statistics in homogeneous uncoupled-core MCFs with a lower computational time than that of the CLMT.

4. The mathematical formalism of the CLMT reported in Chapter 4 can be generalized to describe the propagation of pulses in different scenarios of nonlinear optics, for instance, in unguided dielectric media [357] and non-paraxial fibers (see our PAPER 9, on page 313). In this way, complicated scenarios such as the *white-light continuum generation* in gases [434] can be numerically simulated without the necessity of using FDTD calculations of Maxwell's equations, which usually require a large computational time.

5. In the same spirit as [105], new fiber-optical analogies of *gravitational phenomena* could be investigated in MCFs using the CLMT. In particular, it is interesting to note that the presence of parallel cores can be envisioned as perturbations of the virtual space-time geometry created by an optical pulse propagating in a given core of an MCF.

6. The analysis about the suitability of the MCF technology for the next-generation of optical fronthaul systems (Chapter 5) can be completed by using *ultra-wideband* (UWB) signals.

7. Novel all-fiber mode conversion and mode filtering devices can be further investigated by analyzing factorization methods different from the SUSY factorization reported in Chapter 7. In this vein, we can mention interesting alternatives such as the Sturm-Liouville factorization [269] or the combination of SUSY with *parity-time symmetry* [229, 277].

8. The scattering analysis of SUSY optical fibers builds a bridge to unveil novel *invisible* optical media with axial symmetry. In such a scenario, it would be interesting to analyze the SUSY optical fiber $n_2(r)$ of a constant refractive index profile $n_1(r) = n$. This opens an alternative to complete the work of Stefano Longhi recently published in Optics Letters [435].

9. The *experimental* validation of the results reported in Chapter 8 may pave the way for a real implementation of ultra-compact optical devices such as Mach-Zehnder modulators in the required scale by the future photonic integrated circuits in the next decades [436–444].

This page was intentionally left blank.

Publications

Journal papers

[PAPER 1] **A. Macho**, M. Morant, and R. Llorente, "Experimental evaluation of nonlinear crosstalk in multi-core fiber," Optics Express **23**, 18712 (OSA 2015).

[PAPER 2] M. Morant, **A. Macho**, and R. Llorente, "On the suitability of multicore fiber for LTE-advanced MIMO optical fronthaul systems," Journal of Lightwave Technology **34**, 676 (IEEE/OSA 2016).

[PAPER 3] **A. Macho**, M. Morant, and R. Llorente, "Unified model of linear and nonlinear crosstalk in multi-core fiber," Journal of Lightwave Technology **34**, 3035 (IEEE/OSA 2016).

[PAPER 4] **A. Macho**, C. García-Meca, F. J. Fraile-Peláez, M. Morant, and R. Llorente, "Birefringence effects in multi-core fiber: coupled local-mode theory," Optics Express **24**, 21415 (OSA 2016).

[PAPER 5] **A. Macho**, M. Morant, and R. Llorente, "Next-generation optical fronthaul systems using multicore fiber media," Journal of Lightwave Technology **34**, 4819 (IEEE/OSA 2016).

[PAPER 6] **A. Macho**, C. García-Meca, F. J. Fraile-Peláez, F. Cortés-Juan, and R. Llorente, "Ultra-short pulse propagation model for multi-core fibers based on local modes," Nature Scientific Reports **7**, 16457 (Springer Nature 2017).

[PAPER 7] **A. Macho**, R. Llorente, and C. García-Meca, "Supersymmetric transformations in optical fibers," Physical Review Applied **9**, 014024 (APS 2018).

[PAPER 8] C. García-Meca*, **A. Macho***, and R. Llorente, "Optical supersymmetry in the time domain," submitted (2019). [**Equal contribution*]

[PAPER 9] **A. Macho** and R. Llorente, "Generalized method to describe the propagation of pulses in classical and specialty optical fibers," submitted to IEEE Photonics Journal (IEEE 2019). [*Invited paper*]

[PAPER 10] **A. Macho**, R. Llorente, and C. García-Meca, "Supersymmetric space- and time-reversed potentials and their application to photonics," submitted (2019).

Pre-print submissions

[PRE-PRINT 1] A. Macho and R. Llorente, Ultra-short pulse propagation in nonlinear optics, arXiv:1806.11434 (2018).

[PRE-PRINT 2] C. García-Meca*, A. Macho*, and R. Llorente, Optical supersymmetry in the time domain, arXiv:1903.12639 (2019). [**Equal contribution*]

Book chapters

[BOOK 1] A. Macho and R. Llorente, "Multi-Core Optical Fibers: Theory, Applications and Opportunities," in *Selected Topics on Optical Fiber Technologies and Applications*, F. Xu and C. Mou (Editors), (InTech 2018), Chap. 4.

Conferences

[CONF 1] R. Llorente, M. Morant, M. Beltrán, and A. Macho, "Deep optical access on multi-core and multi-mode fiber for integrated wireless applications," in Proc. of SPIE 9387, Broadband Access Communication Technologies IX, paper 938708 (2015).

[CONF 2] M. Morant, A. Macho, and R. Llorente, "Optical fronthaul of LTE-Advanced MIMO by spatial multiplexing in multicore fiber," in Optical Fiber Communication Conference (OFC), paper W1F.6 (2015).

[CONF 3] A. Macho, M. Morant, and R. Llorente, "Experimental analysis of multicore crosstalk impact on MIMO LTE-A radio-over-fibre optical systems," in IEEE International Conference on Communications Workshop (ICCW), p. 329 (2015).

[CONF 4] R. Llorente, M. Morant, A. Macho, D. G.-Rodríguez, and J. L. Corral, "Demonstration of a spatially multiplexed multicore fibre-based next-generation radio-access cellular network," in International Conference on Transparent Optical Networks (ICTON), paper Th.A1.4 (2015).

[CONF 5] M. Morant, A. Macho, and R. Llorente, "Multicore optical-wireless extended-range fronthaul by polarization-multiplexing in passive optical networks," in European Conference on Optical Communication (ECOC), paper 0554 (2015).

[CONF 6] A. Macho, M. Morant, and R. Llorente, "Impact of inter-core crosstalk in radio-over-fiber transmission on multi-core optical media," in Proc. SPIE 9772, Broadband Access Communication Technologies X, paper 97720O (2016).

[CONF 7] R. Llorente, M. Morant, and A. Macho, "Multicore fronthaul and backhaul provision in next-generation optical access networks," in Proc. SPIE 9772, Broadband Access Communication Technologies X, paper 97720M (2016).

[CONF 8] R. Llorente, A. Macho, D. G.-Rodríguez, A. Zainullin, M. Morant, and J. L. Corral, "Towards multidimensional multiplexing in multicore fiber optical data links," in International Conference on Transparent Optical Networks (ICTON), paper Mo.C1.4 (2016).

[CONF 9] A. Zainullin, B. Vidal, A. Macho, and R. Llorente, "Multicore fiber beamforming network for broadband satellite communications," in Proc. of SPIE 10103, Terahertz, RF, Millimeter, and Submillimeter-Wave Technology and Applications X, paper 1010310 (2017).

[CONF 10] A. Macho and R. Llorente, "Experimental characterization of first-order polarization-mode dispersion in multi-core fiber," in Proc. of SPIE 10559, Broadband Access Communication Technologies XII, paper 105590P (2018).

[CONF 11] A. Macho, R. Llorente, and C. García-Meca, "Supersymmetry-inspired true optical mode (de)multiplexing," in XGEFES, División de Física de la Materia Condensada de la Real Sociedad Española de Física (2018).

Invited talks

[TALK 1] R. Llorente, M. Morant, and A. Macho, "Multi-core optical fibre transmission in optical fronthaul and backhaul: challenges and opportunities," in Microstructured Optical Fibers Topical Workshop, IEEE Photonics Society Sweden, Stockholm, Sweden (2016).

[TALK 2] R. Llorente, M. Morant, and A. Macho, "Multiservice SDM-based 5G C-RAN: Architecture and performance analysis," in European Conference on Optical Communication (ECOC), Gothenburg, Sweden (2017).

This page was intentionally left blank.

Bibliography

[1] S. L. Hahn, "The history of applications of analytic signals in electrical and radio engineering," in The International Conference on Computer as a Tool (EUROCON), 2627 (2007).

[2] M. A. AL-Jawary and L. C. Wrobel, "Numerical solution of the two-dimensional Helmholtz equation with variable coefficients by the radial integration boundary integral and integro-differential equation methods," International Journal of Computer Mathematics **89**, 1463 (2012).

[3] E.Turkel, D. Gordon, R. Gordon, and Semyon Tsynkov, "Compact 2D and 3D sixth order schemes for the Helmholtz equation with variable wave number," Journal of Computational Physics **232**, 272 (2013).

[4] L. Marin, L. Elliott, P. J. Heggs, D .B. Ingham, D. Lesnic, and X. Wen, "Dual reciprocity boundary element method solution of the Cauchy problem for Helmholtz-type equations with variable coefficients," J. Sound Vib. **297**, 89 (2006).

[5] W. Shouxin, L. Xiping, P. Tianguo, Z. Zhongshcng, and Z. Suh, "The BEM for solving the nonhomogeneous Helmholtz equation with variable coefficients," Appl. Math. Mech. **17**, 85 (1996).

[6] B. Perthame and L. Vega, "Morrey-Campanato estimates for Helmholtz equations," Journal of Functional Analysis **164**, 340 (1999).

[7] N. S. Kapany, *Fiber optics. Principles and applications*. (Academic Press, New York, 1967).

[8] P. J. Winzer, D. T. Neilson, and A. R. Chraplyvy, "Fiber-optic transmission and networking: the previous 20 and the next 20 years," Optics Express **26**, 24190 (2018).

[9] J. Hecht, *City of Light, The Story of Fiber Optics*. (Oxford University Press, New York, 1999).

[10] J. M. Senior, *Optical Fiber Communications Principles and Practice*, 3rd ed. (Prentice Hall, Harlow, 2009).

[11] P. J. Winzer and R.-J. Essiambre, "Advanced modulation formats for high-capacity optical transport networks," J. Lightwave Technol. **24**, 4711 (2006).

[12] R.-J. Essiambre, G. Kramer, P. J. Winzer, G. J. Foschini, and B. Goebel, "Capacity limits of optical fiber networks," J. Lightwave Technol. **28**, 662 (2010).

[13] D. J. Richardson, J. M. Fini, and L. E. Nelson, "Space-division multiplexing in optical fibres," Nature Photonics **7**, 354 (2013).

[14] S. Inao, T. Sato, S. Sentsui, T. Kuroha, and Y. Nishimura, "Multi-core optical fiber," in Optical Fiber Communication Conference (OFC), paper WB1 (1979).

[15] J. Yamamoto, T. Yajima, Y. Kinoshita, F. Ishii, M. Yoshida, T. Hirooka, M. Nakazawa, "Fabrication of multi-core fiber by using slurry casting method," in Optical Fiber Communication Conference (OFC), paper Th1H.5 (2017).

[16] T. Mizuno, H. Takara, A. Sano, and Y. Miyamoto, "Dense space-division multiplexed transmission systems using multi-core and multi-mode fiber," J. Lightwave Technol. **34**, 582 (2016).

[17] P. J. Winzer, R. Ryf, and S. Randel, "Spatial multiplexing using multiple-input multiple-output signal processing," in *Optical Fiber Telecommunications VIB: Components and Subsystems*, I. P. Kaminow, T. Li, and A. E. Willner (Eds), 6th ed. (Elsevier, 2013), Chap. 10.

[18] D. W. Peckham, Y. Sun, A. McCurdy, and R. Lingle, "Few-mode fiber technology for spatial multiplexing," in *Optical Fiber Telecommunications VIA: Components and Subsystems*, I. P. Kaminow, T. Li, and A. E. Willner (Eds), 6th ed. (Elsevier, 2013), Chap. 8.

[19] S. Randel, S. Corteselli, D. Badini, D. Pilori, S. Caelles, S. Chandrasekhar, J. Gripp, H. Chen, N. K. Fontaine, R. Ryf, and P. J. Winzer, "First real-time coherent MIMO-DSP for six coupled mode transmission," in IEEE Photonics Conference (IPC15), 15600579 (2015).

[20] P. M. Krummrich, "Optical amplifiers for multi-mode/multi-core transmission," in Optical Fiber Communication Conference (OFC), paper OW1D.1 (2012).

[21] R. S. Luís, B. J. Puttnam, J. Mendinueta, W. Klaus, Y. Awaji, and N. Wada, "Comparing inter-core skew fluctuations in multi-core and single-core fibers," in IEEE Conference on Lasers and Electro-Optics (CLEO), paper SM2L.5 (2015).

[22] INSPACE project, www.ict-inspace.eu.

[23] H. Yuan, M. Furdek, A. Muhammad, A. Saljoghei, L. Wosinska, G. Zervas, "Space-division multiplexing in data center networks: on multi-core fiber solutions and crosstalk-suppressed resource allocation," J. Optical Comm. and Networking **10**, 272 (2018).

[24] B. J. Puttnam, T. A. Eriksson, J.-M. Delgado Mendinueta, R. S. Luís, Y. Awaji, N. Wada, M. Karlsson, and E. Agrell, "Modulation formats for multi-core fiber transmission," Optics Express **22**, 32457 (2014).

[25] Fibercore seven-core fiber, www.fibercore.com/product/multicore-fiber.

[26] T. Hayashi, Y.Tamura, T. Hasegawa, T. Taru, "125-μm-cladding coupled multi-core fiber with ultra-low loss of 0.158 dB/km and record-low spatial mode dispersion of 6.1 ps/km," in Optical Fiber Communication Conference (OFC), paper Th5A.1 (2016).

[27] B. J. Puttnam, R. S. Luís, W. Klaus, J. Sakaguchi, J.-M. Delgado Mendinueta, Y. Awaji, N. Wada, Y. Tamura, T. Hayashi, M. Hirano, and J. Marciante, "2.15 Pb/s transmission using a 22 core homogeneous single-mode multi-core fiber and wideband optical comb," in European Conference on Optical Communication (ECOC), paper PDP 3.1 (2015).

[28] R. G. H. van Uden, R. A. Correa, E. A. López, F. M. Huijskens, C. Xia, G. Li, A. Schülzgen, H. de Waardt, A. M. J. Koonen, and C. M. Okonkwo, "Ultra-high-density spatial division multiplexing with a few-mode multi-core fibre," Nature Photonics **8**, 865 (2014).

[29] A. V. Newkirk, J. E. A.-López, G. S.-Delgado, M. U. Piracha, R. A.-Correa, and A. Schülzgen, "Multicore fiber sensors for simultaneous measurement of force and temperature," IEEE Photonics Technology Letters **27**, 1523 (2015).

[30] H. F. Wei, H. W. Chen, S. P. Chen, P. G. Yan, T. Liu, L. Guo, Y. Lei, Z. L. Chen, J. Li, X. B. Zhang, G. L. Zhang, J. Hou, W. J. Tong, J. Luo, J. Y. Li, and K. K. Chen, "A compact seven-core photonic crystal fiber supercontinuum source with 42.3 W output power," Laser Physics Letters **10**, 045101 (2013).

[31] T. Hayashi, "Multi-core optical fibers," in *Optical Fiber Telecommunications VIA: Components and Subsystems*, I. P. Kaminow, T. Li, and A. E. Willner (Eds), 6th ed. (Elsevier, 2013), Chap. 9.

[32] D. Gloge, "Weakly guiding fibers," Applied Optics **10**, 2252 (1971).

[33] C. Xia, N. Bai, I. Ozdur, X. Zhou, and G. Li, "Supermodes for optical transmissions," Optics Express **19**, 16653 (2011).

[34] R. Ryf, N. K. Fontaine, M. Montoliu, S. Randel, S. H. Chang, H. Chen, S. Chandrasekhar, A. Gnauck, R. Essiambre, P. J. Winzer, T. Taru, T. Hayashi, and T. Sasaki, "Space-division multiplexed transmission over 3×3 coupled-core multicore fiber," in Optical Fiber Communication Conference (OFC), paper Tu2J.4 (2014).

[35] T. Hayashi, R. Ryf, N. K. Fontaine, C. Xia, S. Randel, R.-J. Essiambre, P. J. Winzer, and T. Sasaki, "Coupled-core multi-core fibers: high-spatial-density optical transmission fibers with low differential modal properties," in European Conference on Optical Communication (ECOC), paper 0318 (2015).

[36] J. M. Stone, F. Yu and J. C. Knight, "Highly birefringent 98-core fiber," Optics Letters **39**, 4568 (2014).

[37] Y. Kim, S. C. Warren, J. M. Stone, J. C. Knight, M. A. A. Neil, C. Paterson, C. W. Dunsby, and P. M. W. French, "Adaptive multiphoton endomicroscope incorporating a polarization-maintaining multicore optical fibre," IEEE J. of Selected Topics in Quantum Electronics **22**, 171 (2016).

[38] S. García and I. Gasulla, "Dispersion-engineered multicore fibers for distributed radiofrequency signal processing," Optics Express **24**, 20641 (2016).

[39] I. Gasulla, D. Barrera, J. Hervás, and S. Sales, "Spatial division multiplexed microwave signal processing by selective grating inscription in homogeneous multicore fibers," Nature Scientific Reports **7**, 41727 (2017).

[40] J. E. A.-López, Z. S. Eznaveh, P. L. LiKamWa, A. Schülzgen, and R. A.-Correa, "Multicore fiber sensor for high-temperature applications up to 1000ºC," Optics Letters **39**, 4309 (2014).

[41] T. Hayashi, T. Taru, O. Shimakawa, T. Sasaki, and E. Sasaoka, "Design and fabrication of ultra-low crosstalk and low-loss multi-core fiber," Optics Express **19**, 16576 (2011).

[42] G. A. Mahdiraji, F. Amirkhan, D. M. Chow, Z. Kakaie, P. S. Yong, K. D. Dambul, and F. R. M. Adikan, "Multicore flat fiber: a new fabrication technique," IEEE Photonics Technology Letters **26**, 1972 (2014).

[43] I. Ishida, T. Akamatsu, Z. Wang, Y. Sasaki, K. Takenaga, and S. Matsuo, "Possibility of stack and draw process as fabrication technology for multi-core fiber," in Optical Fiber Communication Conference (OFC), paper OTu2G.1 (2013).

[44] B. Zhu, T. Taunay, M. Yan, J. Fini, M. Fishteyn, and E. M. Monberg, "Seven-core multi-core fibre transmissions for passive optical network," Optics Express **18**, 11117 (2010).

[45] S. Chandrasekhar, A. H. Gnauck, X. Liu, P. J. Winzer, Y. Pan, E. C. Burrows, T. F. Taunay, B. Zhu, M. Fishteyn, M. F. Yan, J. M. Fini, E.M. Monberg, and F. V. Dimarcello, "WDM/SDM transmission of 10×128-Gb/s PDM-QPSK over 2688-km 7-core fiber with a per-fiber net aggregate spectral-efficiency distance product of 40.320 km·b/s/Hz," in European Conference on Optical Communication (ECOC), paper Th13.C.4 (2011).

[46] H. Takara, A. Sano, T. Kobayashi, H. Kubota, H. Kawakami, A. Matsuura, Y. Miyamoto, Y. Abe, H. Ono, K. Shikama, Y. Goto, K. Tsujikawa, Y. Sasaki, I. Ishida, K. Takenaga, S. Matsuo, K. Saitoh, M. Koshiba, and T. Morioka, "1.01-Pb/s (12 SDM/222 WDM/456 Gb/s) crosstalk-managed transmission with 91.4-b/s/Hz aggregate spectral efficiency," in European Conference on Optical Communication (ECOC), paper Th3.C.1 (2012).

[47] J. Sakaguchi, B. Puttnam, W. Klaus, Y. Awaji, N. Wada, A. Kanno, T. Kawanishi, K. Imamura, H. Inaba, K. Mukasa, R. Sugizaki, T. Kobayashi, and M. Watanabe, "305 Tb/s space division multiplexed transmission using homogeneous 19-core fibre," J. Lightwave Technol. **31**, 554 (2013).

[48] B. J. Puttnam, J.-M. Delgado Mendinueta, J. Sakaguchi, R. S. Luís, W. Klaus, Y. Awaji, N. Wada, A. Kanno, and T. Kawanishi, "210Tb/s self-homodyne PDM-WDM-SDM transmission with DFB Lasers in a 19-Core Fibre," in European Conference on Optical Communication (ECOC), paper TuC1.2 (2013).

[49] K. Takeshima, T. Tsuritani, Y. Tsuchida, K. Maeda, T. Saito, K. Watanabe, T. Sasa, K. Imamura, R. Sugizaki, K. Igarashi, I. Morita, and M.Suzuki, "51.1-Tbit/s MCF transmission over 2520 km using cladding pumped 7-core EDFAs," in Optical Fiber Communication Conference (OFC), paper W3G.1 (2015).

[50] J. Sakaguchi, W. Klaus, J.-M. D. Mendinueta, B. J. Puttnam, R. S. Luís, Y. Awaji, N. Wada, T. Hayashi, T. Nakanishi, T. Watanabe, Y. Kokubun, T. Takahata, and T. Kobayashi, "Realizing a 36-core, 3-mode fibre with 108 spatial channels," in Optical Fiber Communication Conference (OFC), paper Th5C.2 (2015).

[51] K. Shibahara, T. Mizuno, H. Takara, A. Sano, H. Kawakami, D. Lee, Y. Miyamoto, H. Ono, M. Oguma, Y. Abe, T. Kobayashi, T. Matsui, R. Fukumoto, Y. Amma, T. Hosokawa, S. Matsuo, K. Saito, H. Nasu, and T. Morioka, "Dense SDM (12-core×3-mode) transmission over 527 km with 33.2 ns mode-dispersion employing low-complexity parallel MIMO frequency-domain equalization," in Optical Fiber Communication Conference (OFC), paper Th5C.3 (2015).

[52] K. Igarashi, D. Souma, Y. Wakayama, K. Takeshima, Y. Kawaguchi, T. Tsuritani, I. Morita, and M. Suzuki, "114 space-division-multiplexed transmission over 9.8-km weakly-coupled-6-mode uncoupled-19-core fibers," in Optical Fiber Communication Conference (OFC), paper Th5C.4 (2015).

[53] K. Igarashi, D. Soma, Y. Wakayama, K. Takeshima, Y. Kawaguchi, N. Yoshikane, T. Tsuritani, I. Morita, and M. Suzuki, "Ultra-dense spatial-division-multiplexed optical fiber transmission over 6-mode 19-core fibers," Optics Express **24**, 10213 (2016).

[54] T. Kobayashi, M. Nakamura, F. Hamaoka, K. Shibahara, T. Mizuno, A. Sano, H. Kawakami, A. Isoda, M. Nagatani, H. Yamazaki, Y. Miyamoto, Y. Amma, Y. Sasaki, K. Takenaga, K. Aikawa, K. Saitoh, Y. Jung, D. J. Richardson, K. Pulverer, M. Bohn, M. Nooruzzaman, and T. Morioka, "1-Pb/s (32 SDM/46 WDM/768 Gb/s) C-band dense SDM transmission over 205.6-km of single-mode heterogeneous multi-core fiber using 96-Gbaud PDM-16QAM channels," in Optical Fiber Communication Conference (OFC), paper Th5B.1 (2017).

[55] D. Soma, Y. Wakayama, S. Beppu, S. Sumita, T. Tsuritani, T. Hayashi, T. Nagashima, M. Suzuki, M. Yoshida, K. Kasai, M. Nakazawa, H. Takahashi, K. Igarashi, I. Morita, and M.

Suzuki, "10.16-Peta-b/s dense SDM/WDM transmission over 6-mode 19-core fiber across the C+L band," J. Lightwave Technol. **36**, 1362 (2018).

[56] K. Tanaka and A. Agata, "Next-generation optical access networks for C-RAN," in Optical Fiber Communication Conference (OFC), paper Tu2E.1 (2015).

[57] N. Cvijetic, "Optical network evolution for 5G mobile applications and SDN-based control," in IEEE Proc. International Telecomm. Network Strategy and Planning Symposium, 14771595 (2014).

[58] T. S. Rappaport, "Millimeter wave wireless communications for 5G cellular: it will work!," in IEEE Personal, Indoor, and Mobile Radio Communications Conference, 13528376 (2014).

[59] Ericsson, "5G Energy Performance," white paper (2015).

[60] M. Zhu, X. Liu, N. Chard, F. Effenberger, and G.-K. Chang, "High-capacity mobile fronthaul supporting LTE-Advanced carrier aggregation and 8×8 MIMO," in Optical Fiber Communication Conference (OFC), paper M2J.3 (2015).

[61] L. Cheng, X. Liu, N. Chard, F. Effenberger, and G.-K. Chang, "Experimental demonstration of sub-Nyquist sampling for bandwidth- and hardware-efficient mobile fronthaul supporting 128×128 MIMO with 100-MHz OFDM signals," in Optical Fiber Communication Conference (OFC), paper W3C.3 (2016).

[62] N. Wang, E. Hossain, and V. K. Bhargava, "Backhauling 5G small cells: A radio resource management perspective," IEEE Wireless Communications **22**, 41 (2015).

[63] M. Morant, A. Macho, and R. Llorente, "Optical fronthaul of LTE-Advanced MIMO by spatial multiplexing in multicore fiber," in Optical Fiber Communication Conference (OFC), paper W1F.6 (2015).

[64] M. Morant, A. Macho, and R. Llorente, "On the suitability of multicore fiber for LTE-advanced MIMO optical fronthaul systems," J. Lightwave Technol. **34**, 676 (2016).

[65] A. Macho, M. Morant, and R. Llorente, "Next-generation optical fronthaul systems using multicore fiber media," J. Lightwave Technol. **34**, 4819 (2016).

[66] I. Gasulla and J. Capmany, "Microwave photonics applications of multicore fibers," IEEE Photonics Journal **4**, 877 (2012).

[67] S. Yu, T. Jiang, J. Li, R. Zhang, G. Wu, and W. Gu, "Linearized frequency doubling for microwave photonics links using integrated parallel Mach–Zehnder modulator," IEEE Photonics Journal **5**, 5501108 (2013).

[68] I. Gasulla, D. Barrera, and S. Sales, "Microwave photonic devices based on multicore fibers," in International Conference on Transparent Optical Networks (ICTON), 1 (2014).

[69] S. García and I. Gasulla, "Design of heterogeneous multicore fibers as sampled true-time delay lines," Optics Letters, **40**, 621 (2015).

[70] R. C. Lawrence, "Silicon photonics for microwave photonics applications," in Optical Fiber Communication Conference (OFC), paper M2B.4 (2016).

[71] A. Zainullin, B. Vidal, A. Macho, and R. Llorente, "Multicore fiber beamforming network for broadband satellite communications," in Proc. of SPIE 10103, Terahertz, RF, Millimeter, and Submillimeter-Wave Technology and Applications X, paper 1010310 (2017).

[72] M. Dine, *Supersymmetry and String Theory.* (Cambridge University Press, Cambridge, 2007).

[73] M.-A. Miri, M. Heinrich, R. El-Ganainy, and D. N. Christodoulides, "Supersymmetric optics: SUSY fibers for integrated angular momentum multiplexing," in Conf. on Lasers and Electro-Optics (CLEO), paper QM1E.8 (2013).

[74] A. Macho, R. Llorente, and C. García-Meca, "Supersymmetry-inspired true optical mode (de)multiplexing," in XGEFES, División de Física de la Materia Condensada de la Real Sociedad Española de Física (2018). Available in: ResearchGate.

[75] K. Y. Song, I. K. Hwang, S. H. Yun, and B. Y. Kim, "High performance fused-type mode-selective coupler using elliptical core two-mode fiber at 1550 nm," IEEE Photonics Technology Letters **14**, 501 (2002).

[76] N. Hanzawa, K. Saitoh, T. Sakamoto, T. Matsui, K. Tsujikawa, M. Koshiba, and F. Yamamoto, "Mode multi/demultiplexing with parallel waveguide for mode division multiplexed transmission," Optics Express **22**, 29321 (2014).

[77] S. H. Chang, H. S. Chung, R. Ryf, N. K. Fontaine, C. Han, K. J. Park, K. Kim, J. C. Lee, J. H. Lee, B. Y. Kim, and Y. K. Kim, "Mode- and wavelength-division multiplexed transmission using all-fiber mode multiplexer based on mode selective couplers," Optics Express **23**, 7164 (2015).

[78] L. Michaille, C. R. Bennet, D. M. Taylor, and T. J. Shepherd, "Multicore photonic crystal fiber lasers for high power/energy applications," IEEE J. of Selected Topics in Quantum Electronics **15**, 328 (2009).

[79] J. Anderson, C. Jollivet, A. Van Newkirk, K. Schuster, S. Grimm, and A. Schülzgen, "Multicore fiber lasers," in Frontiers in Optics/Laser Science, paper LTu2H.2 (2015).

[80] W. Chuncan, Z. Fan, L. Chu, and J. Shuiseng, "Microstructured optical fiber for in-phase mode selection in multicore fiber lasers," Optics Express **16**, 5505 (2008).

[81] C. Jollivet, A. Mafi, D. Flamm, M. Duparré, K. Schuster, S. Grimm, and A. Schülzgen, "Mode-resolved gain analysis and lasing in multisupermode multi-core fiber laser," Optics Express **22**, 30377 (2014).

[82] L. Li, A. Schülzgen, S. Chen, and V. I. Témyanko, "Phase locking and in-phase supermode selection in monolithic multicore fiber lasers," Optics Letters **31**, 2577 (2006).

[83] P. M. Krummrich and S. Akhtari, "Selection of energy optimized pump concepts for multi-core and multi-mode erbium doped fiber amplifiers," Optics Express **22**, 30267 (2014).

[84] K. S. Abedin, J. M. Fini, T. F. Thierry, V. R. Supradeepa, B. Zhu, M. F. Yan, L. Bansal, E. M. Monberg, and D. J. DiGiovanni, "Multicore Erbium doped fiber amplifiers for space division multiplexing systems," J. Lightwave Technol. **32**, 2800 (2014).

[85] Y. Mizuno, N. Hayashi, H. Tanaka, Y. Wada, and K. Nahamura, "Brillouin scattering in multi-core optical fibers for sensing applications," Nature Scientific Reports **5**, 11388 (2015).

[86] J. E. A.-López, Z. S. Eznaveh, P. L. LiKamWa, A. Schülzgen, and R. A.-Correa, "Multicore fiber sensor for high-temperature applications up to 1000^{o}C," Optics Letters **39**, 4309 (2014).

[87] A. V. Newkirk, J. E. A.-López, G. S.-Delgado, M. U. Piracha, R. A.-Correa, and A. Schülzgen, "Multicore fiber sensors for simultaneous measurement of force and temperature," IEEE Photonics Technology Letters **27**, 1523 (2015).

[88] A. V. Newkirk, Z. S. Eznaveh, J. E. A.-López, G. S.-Delgado, A. Schülzgen, and R. A.-Correa, "High temperature sensor based on supermode interference in multicore fiber," in Conference on Lasers and Electro-Optics (CLEO), paper SM2N.7 (2014).

[89] A. J. Thompson, C. Paterson, M. A. A. Neil, C. Dunsby, and P. M. W. French, "Adaptive phase compensation for ultracompact laser scanning endomicroscopy," Optics Letters **36**,1707 (2011).

[90] E. R. Andresen, G. Bouwmans, S. Monneret, and H. Rigneault, "Toward endoscopes with no distal optics: video-rate scanning microscopy through a fiber bundle," Optics Letters **38**, 609 (2013).

[91] E. R. Andresen, G. Bouwmans, S. Monneret, and H. Rigneault, "Two-photon lensless endoscope," Optics Express **21**,20713 (2013).

[92] E. R. Andresen, S. Sivankutty, G. Bouwmans, L. Gallais, S. Monneret, and H. Rigneault, "Measurement and compensation of residual group delay in a multi-core fiber for lensless endoscopy," J. Opt. Soc. Am. B. **32**, 1221 (2015).

[93] S. Karbasi, R. J. Frazier, K. W. Koch, T. Hawkins, J. Ballato, and A. Mafi, "Image transport through a disordered optical fibre mediated by transverse Anderson localization," Nature Communications **5**, 3362 (2014).

[94] J. C. Roper, S. Yerolatsitis, T. A. Birks, B. J. Mangan, C. Dunsby, P. M. W. French, and J. C. Knight, "Minimizing group index variations in a multicore endoscope fiber," IEEE Photonics Technology Letters **27**, 2359 (2015).

[95] Y. Kim, S. C. Warren, J. M. Stone, J. C. Knight, M. A. A. Neil, C. Paterson, C. W. Dunsby, and P. M. W. French, "Adaptive multiphoton endomicroscope incorporating a polarization-maintaining multicore optical fibre," IEEE Journal of Selected Topics in Quantum Electronics **22**, 6800708 (2015).

[96] S. Sivankutty, V. Tsvirkun, G. Bouwmans, D. Kogan, D. Oron, E. R. Andresen, and H. Rigneault, "Extended field-of-view in a lensless endoscope using an aperiodic multicore fiber," Optics Letters **41**, 3531 (2016).

[97] D. B. Conkey, N. Stasio, E. E. Morales-Delgado, M. Romito, C. Moser, and Demetri Psaltis, "Lensless two-photon imaging through a multicore fiber with coherence-gated digital phase conjugation," J. Biomedical Optics **21**, 045002 (2016).

[98] N. Stasio, C. Moser, and D. Psaltis, "Calibration-free imaging through a multicore fiber using speckle scanning microscopy," Optics Letters **41**, 3078 (2016).

[99] E. R. Andresen, S. Sivankutty, V. Tsvirkun, G. Bouwmans, and H. Rigneault, "Ultrathin endoscopes based on multicore fibers and adaptive optics: a status review and perspectives," J. Biomedical Optics **21**, 121506 (2016).

[100] F. Helmchen and F. Denk, "Deep tissue two-photon microscopy," Nature Methods **2**, 932 (2005).

[101] T. Schwartz, G. Bartal, S. Fishman, and M. Segev, "Transport and Anderson localization in disordered two-dimensional photonic lattices," Nature **446**, 52 (2007).

[102] W. Wan, S. Jia, and J. W. Fleischer, "Dispersive superfluid-like shock waves in nonlinear optics," Nature Physics **3**, 46 (2007).

[103] J. Fatome, C. Finot, G. Millot, A. Armaroli, and S. Trillo, "Observation of optical undular bores in multiple four-wave mixing," Physical Review X **4**, 021022 (2014).

[104] F. Dreisow, M. Heinrich, R. Keil, A. Tünnermann, S. Nolten, S. Longui, and A. Szameit, "Classical simulation of relativistic Zitterbewegung in photonic lattices," Physical Review Letters **105**, 143902 (2010).

[105] T. G. Philbin, C. Kuklewicz, S. Robertson, S. Hill, F. König, and U. Leonhardt, "Fiber-optical analog of the event horizon," Science **319**, 1367 (2008).

[106] M. F. Saleh, A. Armaroli, T. X. Tran, A. Marini, F. Belli, A. Abdolvand, and F. Biancalana, "Raman induced temporal condensed matter physics in a gas-filled photonic crystal fibers," Optics Express **23**, 11879 (2015).

[107] L. G. Wright, Z. Liu, D. A. Nolan, M.-J. Li, D. N. Christodoulides, and F. W. Wise, "Self-organized instability in graded-index multimode fibres," Nature Photonics **10**, 771 (2016).

[108] C. Kharif and E. Pelinovsky, "Physical mechanisms of the rogue wave phenomenon," European Journal of Mechanics - B/Fluids **22**, 603 (2003).

[109] J. M. Dudley, F. Dias, M. Erkintalo, and G. Genty, "Instabilities, breathers and rogue waves in optics," Nature Photonics **8**, 755 (2014).

[110] N. N. Akhmediev and V. I. Korneev, "Modulation instability and periodic solutions of the nonlinear Schrödinger equation," Theoret. and Math. Phys. **69**, 1089 (1986).

[111] C. F. Wu, R. H. Grimshaw, K. W. Chow, and H. N. Chan, "A coupled 'AB' system: rogue waves and modulation instabilities," Chaos **25**, 103113 (2015).

[112] W.-P. Zhong, M. Belić, and B. A. Malomed, "Rogue waves in a two-component Manakov system with variable coefficients and an external potential," Physical Review E **92**, 053201 (2015).

[113] K. Manikandan, M. Senthilvelan, and R. A. Kraenkel, "On the characterization of vector rogue waves in two-dimensional two coupled nonlinear Schrödinger equations with distributed coefficients," The European Physical Journal B **89**, 218 (2016).

[114] R. B. Mareeswaran and T. Kanna, "Superposed nonlinear waves in coherently coupled Bose-Einstein condensates," Physics Letters A **380**, 3244 (2016).

[115] H. Rämmal and J. Lavrentjev, "Sound reflection at an open end of a circular duct exhausting hot gas," Noise Control Eng. Journal **56**, 107 (2008).

[116] A. Macho, C. García-Meca, F. J. Fraile-Peláez, F. Cortés-Juan, and R. Llorente, "Ultra-short pulse propagation model for multi-core fibers based on local modes," Nature Scientific Reports **7**, 16457 (2017).

[117] N. Jovanovic, O. Guyon, H. Kawahara, and T. Kotani, "Application of multicore optical fibers in astronomy," in Optical Fiber Communication Conference (OFC), paper W3H.3 (2017).

[118] S. M. Croom, J. S. Lawrence, J. B.-Hawthorn, J. J. Bryant, L. Fogarty, S. Richards, M. Goodwin, T. Farrell, S. Miziarski, R. Heald, D. H. Jones, S. Lee, M. Colless, S. Brough, A. M. Hopkins, A. E. Bauer, M. N. Birchall, S. Ellis, A. Horton, S. L.-Saval, G. Lewis, A. R. L.-Sánchez, S.-S. Min, C. Trinh, and H. Trowland, "The Sydney-AAO multi-object integral field spectrograph," Monthly Notices of the Royal Astronomical Society **421**, 872 (2012).

[119] K. Cho, *Reconstruction of Macroscopic Maxwell equations. A Single Susceptibility Theory.* (Springer, Berlin, 2010).

[120] J. D. Jackson, *Classical Electrodynamics.* (John Wiley & Sons, New York, 1998).

[121] W. E. Wiesel, *Modern Astrodynamics.* (CreateSpace Independent Publishing Platform, 2010).

[122] L. D. Landau and L. M. Lifshitz, *Quantum Mechanics: Non-Relativistic Theory.* (Pergamon Press, Oxford, 1977).

[123] M. B. Green, J. Schwarz, and E. Witten, *Superstring Theory*. (Cambridge University Press, Cambridge, 1987).

[124] K. Okamoto, *Fundamentals of Optical Waveguides*, 2nd ed. (Elsevier, Burlington, 2006).

[125] W.-P. Huang, "Coupled-mode theory for optical waveguides: an overview," J. Opt. Soc. Am. **11**, 963 (1994).

[126] J. D. Joannopoulos, S. G. Johnson, J. N. Winn, and R. D. Meade, *Photonic Crystals: Molding the Flow of Light*. (Princeton University Press, New Jersey, 2008).

[127] S. Fan, W. Suh, and J. D. Joannopoulos, "Temporal coupled-mode theory for the Fano resonance in optical resonators," J. of the Optical Society of America A **20**, 569 (2003).

[128] M. Koshiba, K. Saitoh, K. Takenaga, and S. Matsuo, "Multi-core fiber design and analysis: coupled-mode theory and coupled-power theory," Optics Express **19**, B102 (2011).

[129] T. Hayashi, T. Sasaki, E. Sasaoka, K. Saitoh, and M. Koshiba, "Physical interpretation of intercore crosstalk in multicore fiber: effects of macrobend, structure fluctuation, and microbend," Optics Express **21**, 5401 (2013).

[130] T. Hayashi, T. Taru, O. Shimakawa, T. Sasaki, and E. Sasaoka, "Characterization of crosstalk in ultra-low crosstalk multi-core fiber," J. Lightwave Technol. **30**, 583 (2012).

[131] A. Macho, C. García-Meca, F. J. Fraile-Peláez, M. Morant, and R. Llorente, "Birefringence effects in multi-core fiber: coupled local-mode theory," Optics Express **24**, 21415 (2016).

[132] J. M. Fini, B. Zhu, T. F. Taunay, and M. F. Yan, "Statistics of crosstalk in bent multicore fibers," Optics Express **18**, 15122 (2010).

[133] T. Hayashi, T. Taru, O. Shimakawa, T. Sasaki, and E. Sasaoka, "Design and fabrication of ultra-low crosstalk and low-loss multi-core fiber," Optics Express **19**, 16576 (2011).

[134] M. Koshiba, K. Saitoh, K. Takenaga, and S. Matsuo, "Analytical expression of average power-coupling coefficients for estimating intercore crosstalk in multicore fibers," IEEE Photonics Journal **4**, 1987 (2012).

[135] J. M. Fini, B. Zhu, T. F. Taunay, M. F. Yan, and K. S. Abedin, "Statistical models of multicore fiber crosstalk including time delays," J. Lightwave Technol. **30**, 2003 (2012).

[136] J. M. Fini, B. Zhu, T. F. Taunay, M. F. Yan, and K. S. Abedin, "Crosstalk in multicore fibers with randomness: gradual drift vs. short-length variations," Optics Express **21**, 30739 (2013).

[137] A. W. Snyder, "Coupled-mode theory for optical fibers," J. Opt. Soc. Am. **62**, 1267 (1972).

[138] S. M. Jensen, "The nonlinear coherent coupler," IEEE Trans. Microwave Theory and Techniques **30**, 1568 (1982).

[139] G. P. Agrawal, *Nonlinear Fiber Optics*, 5th ed. (Elsevier, 2013).

[140] F. J. Fraile-Peláez and G. Assanto, "Coupled-mode equations for nonlinear directional couplers," Applied Optics **29**, 2216 (1990).

[141] M. Abramowitz and I. A. Stegun, *Handbook of Mathematical Functions*. (Dover Publications, New York, 1965).

[142] A. Macho, M. Morant, and R. Llorente, "Experimental evaluation of nonlinear crosstalk in multi-core fiber," Optics Express **23**, 18712 (2015).

[143] A. Macho, M. Morant, and R. Llorente, "Unified model of linear and nonlinear crosstalk in multi-core fiber," J. Lightwave Technol. **34**, 3035 (2016).

[144] D. Marcuse, "Derivation of coupled power equations," The Bell System Technical Journal **51**, 229 (1972).

[145] H. P. Hsu, *Probability, Random Variables, & Random Processes*. (McGraw-Hill, New York, 1997).

[146] D. Marcuse, *Theory of Dielectric Optical Waveguides*. (Academic Press Elsevier, New York, 1974).

[147] T. Hayashi, "Design of multi-core and coupled-core fibers," in IEEE Photonics Society Summer Topical Meeting Series (SUM), 173 (2018).

[148] T. Sakamoto, T. Mori, M. Wada, T. Yamamoto, F. Yamamoto, and K. Nakajima, "Fiber twisting- and bending-induced adiabatic/nonadiabatic super-mode transition in coupled multicore fiber," J. Lightwave Technol. **34**, 1228 (2016).

[149] B. E. A. Saleh and M. C. Teich, *Fundamentals of Photonics*, 2nd ed. (Wiley, New Jersey, 2007).

[150] R. W. Boyd, *Nonlinear Optics*, 3rd ed. (Academic Press Elsevier, New York, 2008).

[151] F. Ye, J. Tu, K. Saitoh, and T. Morioka, "Simple analytical expression for crosstalk estimation in homogeneous trench-assisted multi-core fibers," Optics Express **22**, 23007 (2014).

[152] Y. Guo, C. K. Kao, E. H. Li, and K. S. Chiang, *Nonlinear Photonics: Nonlinearities in Optics, Optoelectronics and Fiber Communications*. (Springer, Berlin, 2002), Chap. 9.

[153] A. Mecozzi, C. Antonelli, and M. Shtaif, "Coupled Manakov equations in multimode fibers with strongly coupled groups of modes," Optics Express **20**, 23436 (2012).

[154] A. Mecozzi, C. Antonelli, and M. Shtaif, "Nonlinear propagation in multi-mode fibers in the strong coupling regime," Optics Express **20**, 11673 (2012).

[155] S. Mumtaz, R. J. Essiambre, and G. P. Agrawal, "Nonlinear propagation in multimode and multicore fibers: generalization of the manakov equations," J. Lightwave Technol. **31**, 398 (2013).

[156] S. Mumtaz, R.-J. Essiambre, and G. P. Agrawal, "Birefringence effects in space-division multiplexed fiber transmission systems: Generalization of Manakov equation," in IEEE Photonics Society Summer Topical Meeting Series, paper MC3.5 (2012).

[157] J. M. Fini, B. Zhu, T. F. Taunay, M. F. Yan, and K. S. Abedin, "Statistical models of multicore fiber crosstalk including time delays," J. Lightwave Technol. **30**, 2003 (2012).

[158] R. S. Luís, B. J. Puttnam, A. V. T. Cartaxo, W. Klaus, J. M. D. Mendinueta, Y. Awaji, N. Wada, T. Nakanishi, T. Hayashi, and T. Sasaki, "Time and modulation frequency dependence of crosstalk in homogeneous multi-core fibers," J. Lightwave Technol. **34**, 441 (2016).

[159] A. M. Weiner, *Ultrafast Optics*. (John Wiley & Sons, New Jersey, 2009).

[160] R. B. Dyott, *Elliptical Fiber Waveguides*. (Artech House, London, 1995).

[161] A. Antikainen, R.-J. Essiambre, and G. P. Agrawal, "Determination of modes of elliptical waveguides with ellipse transformation perturbation theory," Optica **4**, 1510 (2017).

[162] S. Huard, *Polarization of Light*, 1st ed. (John Wiley & Sons, Paris, 1997), Chap. 2.

[163] M. J. Weber, *Handbook of Optical Materials*. (CRC Press, New York, 2003).

[164] K. Iizuka, *Elements of Photonics Volume I.* (Wiley-Interscience, New York, 2002), Chap. 6.

[165] P. Drexler and F. Pavel, "Optical Fiber Birefringence Effects – Sources, Utilization and Methods of Suppression," in *Recent Progress in Optical Fiber Research*, M. Yasin, S. Harun, and H. Arof (Eds.), (InTech, 2011), Chap. 7.

[166] P. K. A. Wai and C. R. Menyuk, "Polarization decorrelation in optical fibers with randomly varying birefringence," Optics Letters **19**, 1517 (1994).

[167] P. K. A.Wai and C. R. Menyuk, "Polarization mode dispersion, decorrelation, and diffusion in optical fibers with randomly varying birefringence," J. Lightwave Technol. **14**, 148 (1997).

[168] H. Bachman and W. Amman, *Vibration in Structures Induced by Man and Machines.* (IABSE-AIPC-IVBH, Zurich, 1987).

[169] R. Hui and M. O'Sullivan, *Fiber Optic Measurement Techniques.* (Academic Press Elsevier, London, 2009), Chap. 4.

[170] S. Randel, R. Ryf, A. Sierra, P. J. Winzer, A. H. Gnauck, C. A. Bolle, R.-J. Essiambre, D. W. Peckham, A. McCurdy, and R. Lingle, "6×56-Gb/s mode-division multiplexed transmission over 33-km few-mode fiber enabled by 6×6 MIMO equalization," Optics Express **19**, 16697 (2011).

[171] R. Ryf, S. Randel, N. K. Fontaine, M. Montoliu, E. Burrows, S. Corteselli, S. Chandrasekhar, A. H. Gnauck, C. Xie, R.-J. Essiambre, P. J. Winzer, R. Delbue, P. Pupalaikis, A. Sureka, Y. Sun, L. Grüner-Nielsen, R. V. Jensen, and R. Lingle, "32-bit/s/Hz spectral efficiency WDM transmission over 177-km few-mode fiber," in Optical Fiber Communication Conference (OFC), paper PDP5A.1 (2013).

[172] R. Ryf, S. Randel, A. H. Gnauck, C. Bolle, A. Sierra, S. Mumtaz, M. Esmaeelpour, E. C. Burrows, R.-J. Essiambre, P. J. Winzer, D. W. Peckham, A. H. McCurdy, R. Lingle, "Mode-division multiplexing over 96 km of few-mode fiber using coherent 6×6 MIMO processing," J. Lightwave Technol. **30**, 521 (2012).

[173] S. T. Cundiff and A. M. Weiner, "Optical arbitrary waveform generation," Nature Photonics **4**, 760 (2010).

[174] J. Pfeifle, V. Brasch, M. Lauermann, Y. Yu, D. Wegner, T. Herr, K. Hartinger, P. Schindler, J. Li, D. Hillerkuss, R. Schmogrow, C. Weimann, R. Holzwarth, W. Freude, J. Leuthold, T. J. Kippenberg, and C. Koos, "Coherent terabit communications with microresonator Kerr frequency combs," Nature Photonics **8**, 375 (2014).

[175] K. S. Chiang, "Coupled-mode equations for pulse switching in parallel waveguides," IEEE J. of Quantum Electronics **33**, 950 (1997).

[176] C. G. Someda and F. Cauduro, "Propagation in a decoupled twin-core waveguide: a frequency-domain analysis," IEEE Photonics Journal **4**, 422 (2012).

[177] M. Liu and K. S. Chiang, "Pulse propagation in a decoupled two-core fiber," Optics Express **18**, 21261 (2010).

[178] Y. V. Kartashov, V. V. Konotop, and B. A. Malomed, "Dark solitons in dual-core waveguides with dispersive coupling," Optics Letters **40**, 4126 (2015).

[179] Y. V. Kartashov, B. A. Malomed, V. V. Konotop, V. E. Lobanov, and L. Torner, "Stabilization of spatiotemporal solitons in Kerr media by dispersive coupling," Optics Letters **40**, 1045 (2015).

[180] J. H. Li, K. S. Chiang, and K. W. Chow, "Suppression of pulse splitting in two-core optical fibers with Kerr nonlinearity," J. Opt. Soc. Am. B **30**, 460 (2013).

[181] M. Liu and K. S. Chiang, "Effects of intrapulse stimulated Raman scattering on short pulse propagation in a nonlinear two-core fiber," Applied Physics B **87**, 45 (2007).

[182] P. Shum and M. Liu, "Effects of intermodal dispersion on two-nonidentical-core coupler with different radii," IEEE Photonics Technology Letters **14**, 1106 (2002).

[183] Q. Li, Y. Xie, Y. Zhu, and Z. Zhao, "Effects of second-order coupling coefficient dispersion on short-pulse propagation and switching in an active two-core nonlinear fiber coupler," J. Lightwave Technol. **27**, 2933 (2009).

[184] K. S. Chiang, "Propagation of short optical pulses in directional couplers with Kerr nonlinearity," J. Opt. Soc. Am. B **14**, 1437 (2007).

[185] P. V. Mamyshev and S. V. Chernikov, "Ultrashort-pulse propagation in optical fibers," Optics Letters **15**, 1076 (1990).

[186] F. Poletti and P. Horak, "Description of ultrashort pulse propagation in multimode optical fibers," J. Opt. Soc. Am. B **25**, 1645 (2008).

[187] Q. Lin and G. Agrawal, "Raman response function for silica fibers," Optics Letters **31**, 3086 (2006).

[188] P. J. Mosley, I. Gris-Sánchez, J. M. Stone, R. J. A. Francis-Jones, D. J. Ashton, and T. A. Birks, "Characterizing the variation of propagation constants in multicore fiber," Optics Express **22**, 25689 (2014).

[189] M. Koshiba, K. Saitoh, and Y. Kokubun, "Heterogeneous multi-core fibers: proposal and design principle," IEICE Electronics Express **6**, 98 (2009).

[190] B. Som, M. R. Gupta, and B. Dasgupta, "Coupled nonlinear Schrödinger equation for Langmuir and dispersive ion acoustic waves," Physics Letters A **72**, 111 (1979).

[191] S. V. Vladimirov and M. Y. Yu, "Coupled Langmuir and nonlinear ion-acoustic waves in collisional plasmas," Physical Review E **49**, 1569 (1994).

[192] G. P. Agrawal, *Lightwave Technology: Telecommunication Systems*. (Wiley, 2005).

[193] B. Crosignani, P. D. Porto, and A. Yariv, "Coupled-mode theory and slowly-varying approximation in guided-wave optics," Optics Communications **78**, 237 (1990).

[194] K. D. Shaw, "On the slowly varying envelope approximation in coupled-wave theory," Optics Communications **85**, 191 (1991).

[195] B. Crosignani, P. D. Porto, and A. Yariv, "Slowly-varying approximation and coupled-mode equations in guiding structures," Optics Communications **91**, 341 (1992).

[196] J. K. Ranka and A. L. Gaeta, "Breakdown of the slowly varying envelope approximation in the self-focusing of ultrashort pulses," Optics Letters **23**, 534 (1998).

[197] P. K. A. Wai, W. I. Kath, C. R. Menyuk, and J. W. Zhang, "Nonlinear polarization-mode dispersion in optical fibers with randomly varying birefringence," J. Opt. Soc. Am. B **24**, 2967 (1997).

[198] K.-Po Ho and J. M. Kahn, "Mode-dependent loss and gain: statistics and effect on mode-division multiplexing," Optics Express **19**, 16612 (2011).

[199] K. Koebel, M. Salsi, G. Charlet, and S. Bigo, "Nonlinear effects in mode-division-multiplexed transmission over few-mode optical fiber," IEEE Photonics Technology Letters **23**, 1316 (2011).

[200] A. Karadimitrakis, A. L. Moustakas, and P. Vivo, "Outage capacity for the optical MIMO channel," IEEE Transactions on Information Theory **60**, 4370 (2014).

[201] J. T. J. Penttinen, *The LTE-Advanced Deployment Handbook*. (Wiley, 2015), Chap. 7.

[202] X. Ligeret, "Mobile terminating network failure forwarding for LTE circuit-switched fallback", US 20150271711 A1, US 14/224044 patent (2015).

[203] U. Kohn, "Fronthaul networks - a key enabler for LTE-Advanced," ADVA Optical Networking technology white paper (2014).

[204] P. Öhlén, B. Skubic, A. Rostami, K. Laraqui, F. Cavaliere, B. Varga, and N. Fonseca, "Flexibility in 5G transport network: the key to meeting the demand for connectivity," Ericsson Technology Review (2015).

[205] A. G. Sarigiannidis, M. Iloridou, P. Nicopolitidis, G. Papadimitriou, F. N. Pavlidou, P. G. Sarigiannidis, M. D. Louta, and V. Vitsas, "Architectures and bandwidth allocation schemes for hybrid wireless-optical networks", IEEE Communications Surveys&Tutorials **17**, 427 (2015).

[206] M. Morant, J. Prat, and R. Llorente, "Radio-Over-fiber optical polarization-multiplexed networks for 3GPP wireless carrier-aggregated MIMO provision," J. Lightwave Technol. **32**, 3721 (2014).

[207] Y. A. Gol'fand and E. P. Likhtman, "Extension of the algebra of Poincare group generators and violation of P invariance," JETP Lett. **13**, 452 (1971).

[208] P. Ramond, "Dual theory for free fermions," Physical Review D **3**, 2415 (1971).

[209] A. Neveu and J. H. Schwarz, "Factorizable dual model of pions," Nuclear Physics B **31**, 86 (1971).

[210] F. Takayama and M. Yamaguchi, "Gravitino dark matter without R-parity," Physics Letters B **485**, 388 (2000).

[211] H. Goldberg, "Constrain on the photino mass from cosmology," Physical Review Letters **50**, 1419 (1983).

[212] M. Throm, R. Thornberry, J. Killough, B. Sun, G. Abdulla, and R. E. Allen, "Two natural scenarios for dark matter particles coexisting with supersymmetry," Modern Physics Letters A **34**, 1930001 (2019).

[213] M. Hirsch, W. Porod, and D. Restrepo, "Collider signals of gravitino dark matter in bilinearly broken R-parity," J. High Energy Physics **3**, 062 (2005).

[214] L. M. Krauss, "New constraints on 'INO' masses from cosmology (I). Supersymmetric 'inos'," Nuclear Physics B **227**, 556 (1983).

[215] K. A. Ulmer, Supersymmetry: experimental status, arXiv:1601.03774.

[216] F. Cooper, A. Khare, and U. Sukhatme, "Supersymmetry and quantum mechanics," Physics Reports **251**, 267 (1995).

[217] A. A. Andrianov and A. V. Sokolov, Nonlinear supersymmetry in quantum mechanics: algebraic properties and differential representation, arXiv:hep-th/0301062.

[218] B. Bagchi, F. Cannata, and C. Quesne, "PT-symmetric sextic potentials," Physics Letters A **269**, 79 (2000).

[219] M. Znojil, F. Cannata, B. Bagchi, and R. Roychoudhury, "Supersymmetry without hermiticity within PT symmetric quantum mechanics," Physics Letters B **483**, 284 (2000).

[220] F. Cannata, M. Ioffe, R. Roychoudhury, and P. Roy, "A new class of PT-symmetric Hamiltonians with real spectra," Physics Letters A **281**, 305 (2001).

[221] B. F. Samsonov, "Spectral singularities of non-hermitian Hamiltonians and SUSY transformations," J. Phys. A 38, L571−L579 (2005).," J. Phys. A **38**, L571 (2005).

[222] S. M. Chumakov and K. B. Wolf, "Supersymmetry in Helmholtz optics," Physics Letters A **193**, 51 (1994).

[223] J. Radovanović, V. Milanović, Z. Ikonić, and D. Indjin, "Quantum-well shape optimization for intersubband-related electro-optic modulation properties," Physical Review B **59**, 5637 (1999).

[224] S. Kočinac, V. Milanović, Z. Ikonić, D. Indjin, J. Radovanović, and P. Harrison, "SUSY transformation of guided modes in semiconductor waveguides," Phys. Stat. Solid **2**, 3552 (2005).

[225] J. Bai and D. Citrin, "Supersymmetric optimization of second-harmonic generation in mid-infrared quantum cascade lasers," Optics Express **14**, 4043 (2006).

[226] Y. Yu and K. Yang, "Simulating the Wess-Zumino supersymmetry model in optical lattices," Physical Review Letters **105**, 150605 (2010).

[227] E. M. C. Abreu, M. A. De Andrade, L. P. G. De Assis, J. A. Helayël-Neto, A. L. M. A. Nogueira, and R. C. Paschoal, "A supersymmetric model for graphene," J. High Energy Physics **5**, 1 (2011).

[228] M.-A. Miri, M. Heinrich, R. El-Ganainy, and D. N. Christodoulides, "Supersymmetric optical structures," Physical Review Letters **110**, 233902 (2013).

[229] M.-A. Miri, M. Heinrich, and D. N. Christodoulides, "Supersymmetry-generated complex optical potentials with real spectra," Physical Review A **87**, 043819 (2013).

[230] H. P. Laba and V. M. Tkachuk, "Quantum-mechanical analogy and supersymmetry of electromagnetic wave modes in planar waveguides," Physical Review A **89**, 033826 (2014).

[231] A. del Campo, M. G. Boshier, and A. Saxena, "Bent waveguides for matter-waves: supersymmetric potentials and reflectionless geometries," Nature Scientific Reports **4**, 5274 (2014).

[232] M.-A. Miri, M. Heinrich, and D. N. Christodoulides, "SUSY-inspired one-dimensional transformation optics," Optica **1**, 89 (2014).

[233] S. Dehdashti, R. Li, X. Liu, M. Raoofi, and H. Chen, "Role of intertwined Hamiltonian in two dimensional classical optics," Laser Physics **25**, 075201 (2015).

[234] M. Heinrich, M.-A. Miri, S. Stützer, R. El-Ganainy, S. Nolte, A. Szameit, and D. N. Christodoulides, "Supersymmetric mode converters," Nature Communications **5**, 3698 (2014).

[235] B. Midya, "Supersymmetry-generated one-way-invisible PT-symmetric optical crystals," Physical Review A **89**, 032116 (2014).

[236] S. Longhi, "Supersymmetric Bragg gratings," Journal of Optics **17**, 045803 (2015).

[237] S. Longhi, "Supersymmetric transparent optical intersections," Optics Letters **40**, 463 (2015).

[238] M. Principe, G. Castaldi, M. Consales, A. Cusano, and V. Galdi, "Supersymmetry-inspired non-hermitian optical couplers," Nature Scientific Reports **5**, 8568 (2015).

[239] G. Queralto, V. Ahufinger, and J. Mompart, "Mode-division (de)multiplexing using adiabatic passage and supersymmetric waveguides," Optics Express **25**, 27396 (2017).

[240] F. Correa, "Darboux-Crum transformations, Jordan States and PT-Symmetry," Physics of Particles and Nuclei Letters **14**, 395 (2017).

[241] A. Macho, R. Llorente, and C. García-Meca, "Supersymmetric transformations in optical fibers," Physical Review Applied **9**, 014024 (2018).

[242] A. C.-Astorga and V. Jakubský, Photonic systems with two-dimensional landscapes of complex refractive index via time-dependent supersymmetry, arXiv:1808.08225.

[243] C. García-Meca, *Transformation Physics: From Invisibility to Supersymmetry.* (Pan Stanford Publishing, Forthcoming 2019). Chap. 3.

[244] J. H. Schwarz, The early history of string theory and supersymmetry, arXiv:1201.0981.

[245] A. Neveu, J. H. Schwarz, and C. B. Thorn, "Reformulation of the dual pion model," Physics Letters B **35**, 529 (1971).

[246] J. Wess and B. Zumino, "Supergauge transformations in four dimensions," Nuclear Physics B **70**, 39 (1974).

[247] D. Z. Freedman, P. van Nieuwenhuizen, and S. Ferrara, "Progress toward a theory of supergravity," Physical Review D **13**, 3214 (1976).

[248] E. Witten, "Dynamical breaking of supersymmetry," Nuclear Physics B **188**, 513(1981).

[249] E. Witten, "Constraints on supersymmetry breaking," Nuclear Physics B **202**, 253 (1982).

[250] C. García-Meca, A. Macho, and R. Llorente, Optical supersymmetry in the time domain, arXiv:1903.12639.

[251] M. A. Al-Gwaiz, *Sturm-Liouville Theory and its Applications.* (Springer, London, 2008).

[252] B. C. Hall, *Lie Groups, Lie Algebras, and Representations.* (Springer, New York, 2003).

[253] V. C. Kac, "Lie superalgebras," Advances in Mathematics **26**, 8 (1977).

[254] A. Gangopadhyaya, P. K. Panigrahi, and U. P. Sukhatme, "Analysis of inverse-square potentials using supersymmetric quantum mechanics," J. Phys. A: Math. Gen. **27**, 4295 (1994).

[255] J. L. V. Malumbres, *Métodos Clásicos de Resolución de Ecuaciones Diferenciales Ordinarias.* (Universidad de la Rioja, Logroño, 1996).

[256] K. Chadan and P.C. Sabatier, *Inverse Problems in Quantum Scattering Theory.* (Springer, Verlag, 1977).

[257] W.-Y. Keung, U. P. Sukhatme, Q. Wang, and T. D. Imbo, "Families of strictly isospectral potentials," J. Phys. A **22**, 987 (1989).

[258] J. von Neumann and E. Wigner, "Uber merkwürdige diskrete Eigenwerte. Uber das verhalten von eigenwerten bei adiabatischen prozessen," Physikalische Zeitschrift **30**, 467 (1929).

[259] C. W. Hsu, B. Zhen, A. D. Stone, J. D. Joannopoulos, and M. Soljačić, "Bound states in the continuum," Nature Reviews **1**, 16048 (2016).

[260] F. H. Stillinger and D. R. Herrick, "Bound states in the continuum," Physical Review A **11**, 446 (1975).

[261] P. J. Cobelli, V. Pagneux, A. Maurel, and P. Petitjeans, "Experimental study on water-wave trapped modes," J. Fluid Mech. **666**, 445 (2011).

[262] A. G. Every, "Guided elastic waves at a periodic array of thin coplanar cavities in a solid," Physical Review B **78**, 174104 (2008).

[263] Y. Plotnik, O. Peleg, F. Dreisow, M. Heinrich, S. Nolte, A. Szameit, and M. Segev, "Experimental observation of optical bound states in the continuum," Physical Review Letters **107**, 183901 (2011).

[264] N. A. Cumpsty and D. S. Whitehead, "The excitation of acoustic resonances by vortex shedding," J. Sound Vib. **18**, 353 (1971).

[265] L. E. Gendenshtein, "Derivation of exact spectra of the Schrödinger equation by means of supersymmetry," JETP Lett. **38**, 356 (1983).

[266] E. Nygren, "Supersymmetric Quantum Mechanics," Bachelor Thesis (2010).

[267] K. Glampedakis, A. D. Johnson, and D. Kennefick, "Darboux transformation in black hole perturbation theory," Physical Review D **96**, 024036 (2017).

[268] M. Humi, "New types of factorizable equations," Mathematical Proceedings of the Cambridge Philosophical Society **68**, 439 (1970).

[269] M. N. Hounkonnou, K. Sodoga, and E. S. Azatassou, "Factorization of Sturm-Liouville operators: solvable potentials and underlying algebraic structure," J. Phys. A: Math. Gen. **38**, 371 (2005).

[270] T. D. Imbo and U. P. Sukhatme, "Conditions for nondegeneracy in supersymmetric quantum mechanics," Physical Review D **33**, 3147 (1986).

[271] M. V. Ioffe, J. Mateos Guilarte, P. A. Valinevich, Two-dimensional supersymmetry: from SUSY quantum mechanics to integrable classical models, arXiv:hep-th/0603006.

[272] M. V. Ioffe and A. I. Neelov, Pauli equation and the method of supersymmetric factorization, arXiv:hep-th/0302004.

[273] M. Humi, "Darboux transformations for Schrödinger equations in two variables," J. of Math. Physics **46**, 083515 (2005).

[274] L. Caston and R. Fioresi, Mathematical foundations of supersymmetry, arXiv:0710.5742.

[275] B. M. Rodríguez-Lara, R. El-Ganainy, and J. Guerrero, "Symmetry in optics and photonics: a group theory approach," Science Bulletin **63**, 244 (2018).

[276] A. A. Andrianov and M. V. Ioffe, Nonlinear supersymmetric quantum mechanics: concepts and realizations, arXiv:1207.6799.

[277] F. Cooper, A. Khare, A. Comech, B. Mihaila, J. F. Dawson, A. Saxena, "Stability of exact solutions of the nonlinear Schrödinger equation in an external potential having supersymmetry and parity-time symmetry," J. of Physics A: Mathematical and Theoretical **50**, 015301 (2017).

[278] V. M. Tkachuk, Supersymmetric method for constructing quasi-exactly solvable potentials, arXiv:quant-ph/9806030.

[279] M. S. Berger and N. S. Ussembayev, "Isospectral potentials from modified factorization," Physical Review A **82**, 022121 (2010).

[280] D. Dutta and P. Roy, "Generalized factorization and isospectral potentials," Physical Review A **83**, 054102 (2011).

[281] V.A. Kostelecky and D.K. Campbell, *Supersymmetry in Physics.* (Elsevier Science, 1985).

[282] N. Sourlas, "Introduction to supersymmetry in condensed matter physics," Physica D: Nonlinear Phenomena **15**, 115 (1985).

[283] A.B. Balantekin, Symmetry and supersymmetry in nuclear physics, arXiv:0711.0710.

[284] F. Buonocore, G. Iadonisi, D. Ninno, and F. Ventriglia, "Polarons in cylindrical quantum wires," Physical Review B **65**, 205415 (2002).

[285] D. C. Dillen, K. Kim, E.-S. Liu, and E. Tutuc, "Radial modulation doping in core-shell nanowires," Nature Nanotech. **9**, 116 (2014).

[286] H. Esfahlani, H. Lissek, and J. R. Mosig, "Generation of acoustic helical wavefronts using metasurfaces," Physical Review B **95**, 024312 (2017).

[287] H. Rämmal and J. Lavrentjev, "Sound reflection at an open end of a circular duct exhausting hot gas," Noise Control Eng. Journal **56**, 107 (2008).

[288] S. W. Rienstra, "A classification of duct modes based on surface waves," Wave Motion **37**, 119 (2003).

[289] E. J. Brambley and N. Peake, "Classification of aeroacoustically relevant surface modes in cylindrical lined ducts," Wave Motion **43**, 301 (2006).

[290] J. Wang, J. Y. Yang, I. M. Fazal, N. Ahmed, Y. Yan, H. Huang, Y. Ren, Y. Yue, S. Dolinar, M. Tur, and A. E. Willner, "Terabit free space data transmission employing orbital angular momentum multiplexing," Nature Photonics **6**, 488 (2012).

[291] W. M. Frank, D. J. Land, and R. M. Spector, "Singular potentials," Rev. Mod. Phys. **43**, 36 (1971).

[292] A. Jevicki and J. Rodrigues, "Singular potentials and supersymmetry breaking," Physics Letters B **146**, 55 (1984).

[293] C. García-Meca, S. Lechago, A. Brimont, A. Griol, S. Mas, L. Sánchez, L. Bellieres, N. S. Losilla, and J. Martí, "On-chip wireless silicon photonics: from reconfigurable interconnects to lab-on-chip devices," Light: Science&Applications **6**, e17053 (2017).

[294] D. Pérez, I. Gasulla, L. Crudgington, D. J. Thomson, A. Z. Khokhar, K. Li, W. Cao, G. Z. Mashanovich, and J. Capmany, "Multipurpose silicon photonics signal processor core," Nature Communications **8**, 636 (2017).

[295] J. L. Corral, D. G.-Rodríguez, and R. Llorente, "Mode-selective couplers for two-mode transmission at 850 nm in standard SMF," IEEE Photonics Technology Letters **28**, 425 (2016).

[296] K. Y. Song, I. K. Hwang, S. H. Yun, and B. Y. Kim, "High performance fused-type mode-selective coupler using elliptical core two-mode fiber at 1550 nm," IEEE Photonics Technology Letters **14**, 501 (2002).

[297] N. Hanzawa, K. Saitoh, T. Sakamoto, T. Matsui, K. Tsujikawa, M. Koshiba, and F. Yamamoto, "Mode multi/demultiplexing with parallel waveguide for mode division multiplexed transmission," Optics Express **22**, 29321 (2014).

[298] S. H. Chang, H. S. Chung, R. Ryf, N. K. Fontaine, C. Han, K. J. Park, K. Kim, J. C. Lee, J. H. Lee, B. Y. Kim, and Y. K. Kim, "Mode- and wavelength-division multiplexed transmission using all-fiber mode multiplexer based on mode selective couplers," Optics Express **23**, 7164 (2015).

[299] S. G. Leon-Saval, T. A. Birks, J. B.-Hawthorn, and M. Englund, "Multimode fiber devices with single-mode performance," Optics Letters **30**, 2545 (2005).

[300] Y. Sasaki, K. Takenaga, S. Matsuo, K. Aikawa, and K. Saitoh, "Few-mode multicore fibers for long-haul transmission line," Optical Fiber Technol. **35**, 19 (2017).

[301] T. Sakamoto, T. Mori, M. Wada, T. Yamamoto, and F. Yamamoto, "Coupled multicore fiber design with low intercore differential mode delay for high-density space division multiplexing," J. Lightwave Technol. **33**,1175 (2015).

[302] N. K. Fontaine, R. Ryf, J. B.-Hawthorn, and S. G. L.-Saval, "Geometric requirements for photonic lanterns in space division multiplexing," Optics Express **20**, 27123 (2012).

[303] S. G. L.-Saval, N. K. Fontaine, J. R. S.-Gil, B. Ercan, R. Ryf, and J. B.-Hawthorn, "Mode-selective photonic lanterns for space-division multiplexing," Optics Express **22**, 1 (2014).

[304] Z. S. Eznaveh, J. E. Antonio-Lopez, J. C. A. Zacarias, A. Schülzgen, C. M. Okonkwo, and R. A. Correa, "All-fiber few-mode multicore photonic lantern mode multiplexer," Optics Express **25**, 16701 (2017).

[305] T. A. Birks, I. Gris-Sánchez, S. Yerolatsitis, S. G. Leon-Saval, and R. R. Thomson, "The photonic lantern," Advances in Optics and Photonics **7**, 107 (2015).

[306] B.-I. Popa and S. A. Cummer, "Complex coordinates in transformation optics," Physical Review A **84**, 063837 (2011).

[307] M. Moccia, G. Castaldi, V. Galdi, A. Alù, and N. Engheta, "Dispersion engineering via nonlocal transformation optics," Optica **3**, 179 (2016).

[308] C. García-Meca and C. Barceló, "Nontensorial transformation optics," Physical Review Applied **5**, 064008 (2016).

[309] S. Schmid, A. Härter, and J. H. Denschlag, "Dynamics of a cold trapped ion in a Bose-Einstein condensate," Physical Review Letters **105**, 133202 (2010).

[310] C. García-Meca, S. Carloni, C. Barcelo, G. Jannes, J. Sanchez-Dehesa, and A. Martínez, "Transformational acoustic metamaterials based on pressure gradients," Physical Review B **90**, 024310 (2014).

[311] I. Liberal, A. M. Mahmoud, Y. Li, B. Edwards, and N. Engheta, "Photonic doping of epsilon-near-zero media," Science **355**, 1058 (2017).

[312] S. Kar and R. R. Parwani, Can degenerate bound states occur in one dimensional quantum mechanics?, arXiv:0706.1135v2.

[313] G. T. Reed, G. Mashanovich, F. Y. Gardes, and D. J. Thomson, "Silicon optical modulators," Nature Photonics **4**, 518 (2010).

[314] M. F. Yanik and S. Fan, "Time reversal of light with linear optics and modulators," Physical Review Letters **93**, 173903 (2004).

[315] D. L. Sounas and A. Alù, "Non-reciprocal photonics based on time modulation," Nature Photonics **11**, 774 (2017).

[316] T. T. Koutserimpas and R. Fleury, "Nonreciprocal gain in non-hermitian time-Floquet systems," Physical Review Letters **120**, 087401 (2018).

[317] A. E. Willner, S. Khaleghi, M. R. Chitgarha, and O. F. Yilmaz, "All-optical signal processing," J. Lightwave Technol. **32**, 660 (2014).

[318] S. Vezzoli, V. Bruno, C. DeVault, T. Roger, V. M. Shalaev, A. Boltasseva, M. Ferrera, M. Clerici, A. Dubietis, and D. Faccio, "Optical time reversal from time-dependent epsilon-near-zero media," Physical Review Letters **120**, 043902 (2018).

[319] E. Lustig, Y. Sharabi, and M. Segev, "Topological aspects of photonic time crystals," Optica **5**, 1390 (2018).

[320] C. K. Law, "Effective Hamiltonian for the radiation in a cavity with a moving mirror and a time-varying dielectric medium," Physical Review A **49**, 433 (1994).

[321] A. Kord, D. L. Sounas, and A. Alù, "Magnet-less circulators based on spatiotemporal modulation of bandstop filters in a delta topology," IEEE Transactions on Microwave Theory and Techniques **66**, 911 (2018).

[322] V. A. Kostelecký, V. I. Man'ko, M. M. Nieto, and D. R. Truax, "Supersymmetry and time-dependent Landau systems," Physical Review A **48**, 951 (1993).

[323] V. G. Baggrov and B. F. Samsonov, "Supersymmetry of a nonstationary Schrödinger equation," Physics Letters A **210**, 60 (1996).

[324] A. S.-Halberg and J. M. C. Jimenez, "Supersymmetry of generalized linear Schrödinger equations in (1+1) dimensions," Symmetry **1**, 115 (2009).

[325] J. T. Mendonça and P. K. Shukla, "Time refraction and time reflection: two basic concepts," Physica Scripta **65**, 160 (2002).

[326] Y. Xiao, D. N. Maywar, and G. P. Agrawal, "Reflection and transmission of electromagnetic waves at a temporal boundary," Optics Letters **39**, 574 (2014).

[327] E. Rubino, J. McLenaghan, S. C. Kehr, F. Belgiorno, D. Townsend, S. Rohr, C. E. Kuklewicz, U. Leonhardt, F. König, and D. Faccio, "Negative-frequency resonant radiation," Physical Review Letters **108**, 253901 (2012).

[328] S. A. R. Horsley and S. Bugler-Lamb, "Negative frequencies in wave propagation: a microscopic model," Physical Review A **93**, 063828 (2016).

[329] G. Rousseaux, C. Mathis, P. Maïssa, T. G Philbin, and U. Leonhardt, "Observation of negative-frequency waves in a water tank: a classical analogue to the Hawking effect?," New Journal of Physics **10**, 053015 (2008).

[330] C. Barceló, S. Liberati, and M. Visser, "Analogue gravity," Living Reviews in Relativity **14**, 3 (2011).

[331] U. Leonhardt and T. Philbin, *Geometry and Light: The Science of Invisibility.* (Dover Publications, New York, 2010).

[332] S. A. R. Horsley, M. Artoni, and G. C. La Rocca, "Spatial Kramers-Kronig relations and the reflection of waves," Nature Photonics **9**, 436 (2015).

[333] Y. G. Ma, C. K. Ong, T. Tyc, and U. Leonhardt, "An omnidirectional retroreflector based on the transmutation of dielectric singularities," Nature Materials **8**, 639 (2009).

[334] C. Wang, M. Zhang, X. Chen, M. Bertrand, A. S.-Ansari, S. Chandrasekhar, P. Winzer, and Marko Lončar, "Integrated lithium niobate electro-optic modulators operating at CMOS-compatible voltages," Nature **562**, 101 (2018).

[335] C. Haffner, W. Heni, Y. Fedoryshyn, J. Niegemann, A. Melikyan, D. L. Elder, B. Baeuerle, Y. Salamin, A. Josten, U. Koch, C. Hoessbacher, F. Ducry, L. Juchli, A. Emboras, D. Hillerkuss, M. Kohl, L. R. Dalton, C. Hafner, and J. Leuthold, "All-plasmonic Mach-Zehnder modulator enabling optical high-speed communication at the microscale," Nature Photonics **9**, 525 (2015).

[336] B. W. Plansinis, W. R. Donaldson, and G. P. Agrawal, "What is the temporal analog of reflection and refraction of optical beams?," Physical Review Letters **115**, 183901 (2015).

[337] B. W. Plansinis, W. R. Donaldson, and G. P. Agrawal, "Temporal waveguides for optical pulses," J. Opt. Soc. Am. B **33**, 1112 (2016).

[338] J. Zhou, G. Zheng, and J. Wu, "Comprehensive study on the concept of temporal optical waveguides," Physical Review A **93**, 063847 (2016).

[339] J. M. Vázquez, M. Mazilu, A. Miller, and I. Galbraith, "Wavelet transforms for optical pulse analysis," J. Opt. Soc. Am. A **22**, 2890 (2005).

[340] M. Dantus and V. V. Lozovoy, "Experimental coherent laser control of physicochemical processes," Chem. Rev. **104**, 1813 (2004).

[341] A. Weiner, "Ultrafast optical pulse shaping: a tutorial review," Optics Communications **284**, 3669 (2011).

[342] Z. Yang and S. Ramanathan, "Breakthroughs in photonics 2014: phase change materials for photonics," IEEE Photonics Journal **7**, 070030 (2015).

[343] W. J. Wang, L. P. Shia, R. Zhao, K. G. Lim, H. K. Lee, T. C. Chong, and Y. H. Wu, "Fast phase transitions induced by picosecond electrical pulses on phase change memory cells," Appl. Phys. Lett. **93**, 043121 (2008).

[344] M. Z. Alam, I. De Leon, and R. W. Boyd, "Large optical nonlinearity of indium tin oxide in its epsilon-near-zero region," Science **352**, 6287 (2016).

[345] Q. Wang, E. T. F. Rogers, B. Gholipour, C.-M. Wang, G. Yuan, J. Teng, and N. I. Zheludev, "Optically reconfigurable metasurfaces and photonic devices based on phase change materials," Nature Photonics **10**, 60 (2016).

[346] E. Petronijevic and C. Sibilia, "All-optical tuning of EIT-like dielectric metasurfaces by means of chalcogenide phase change materials," Optics Express **24**, 30411 (2016).

[347] B. W. Plansinis, W. R. Donaldson, and G. P. Agrawal, "Cross-phase-modulation-induced temporal reflection and waveguiding of optical pulses," J. Opt. Soc. Am. B **35**, 436 (2018).

[348] R. Loudon, "The propagation of electromagnetic energy through an absorbing dielectric," J. Phys. A: Math. Gen. **3**, 233 (1970).

[349] R. Ruppin, "Electromagnetic energy density in a dispersive absorptive material," Physics Letters A **299**, 309 (2002).

[350] A. D. Boardman and K. Marinov, "Electromagnetic energy in a dispersive metamaterial," Physical Review B **73**, 165110 (2006).

[351] P. A. Cherenkov, "Visible emission of clean liquids by action of γ radiation," Doklady Akademii Nauk SSSR **2**, 451 (1934).

[352] J. B. Pendry, "Shearing the vacuum - quantum friction," Journal of Physics: Condensed Matter **9**, 10301 (1997).

[353] S. W. Hawking, "Black hole explosions?," Nature **248**, 30 (1974).

[354] M. F. Yanik and S. Fan, "Dynamic photonic structures: stopping, storage, and time reversal of light," Studies in Applied Mathematics **115**, 233 (2005).

[355] A. R. Escutia, *High-efficient electrodes for novel optoelectronic devices in silicon photonics.* (Ph.D. Dissertation, 2018).

[356] M. Gadella, Ş. Kurub, and J. Negroa, "The hyperbolic step potential: anti-bound states, SUSY partners and Wigner time delays," Annals of Physics **379**, 86-101 (2017).

[357] A. Macho and R. Llorente, Ultra-short pulse propagation in nonlinear optics, arXiv:1806.11434.

[358] E. W. Kamen, "Fundamentals of linear time-varying systems," in *The Control Systems Handbook: Control System Advanced Methods*, W. S. Levine (Ed), 2nd ed. (CRC Press, Boca Raton, 2010), Chap. 3.

[359] L. D. Landau and L. M. Lifshitz, *Fluids Mechanics: Course of Theoretical Physics*. (Pergamon Press, Oxford, 1959).

[360] S. Bhattarai, Stability of normalized solitary waves for three coupled nonlinear Schrödinger equations, arXiv:1509.00425.

[361] S. Bhattarai, "Stability of solitary-wave solutions of coupled NLS equations with power-type nonlinearities," Adv. Nonlinear Anal. **4**, 73 (2015).

[362] J. Bona, "On the stability theory of solitary waves," Proc. Roy. Soc. London Ser. A **344**, 363 (1975).

[363] T. Cazenave and P. L. Lions, "Orbital stability of standing waves for some nonlinear Schrödinger equations," Comm. Math. Phys. **85**, 549 (1982).

[364] P. N.-Boltyk, *Coherence and Perturbed Dynamics in Magnon Bose-Einstein Condensates*. (Ph.D. Dissertation, 2014).

[365] T. Harko, "Evolution of cosmological perturbations in Bose-Einstein condensate dark matter," Monthly Notices of the Royal Astronomical Society **413**, 3095 (2011).

[366] M. Shahmansouri and E. Astaraki, "Transverse perturbation on three-dimensional ion acoustic waves in electron-positron-ion plasma with high-energy tail electron and positron distribution," Journal of Theoretical and Applied Physics **8**, 189 (2014).

[367] E. Kengne and W. M. Liu, "Management of matter-wave solitons in Bose-Einstein condensates with time-dependent atomic scattering length in a time-dependent parabolic complex potential," Physical Review E **98**, 012204 (2018).

[368] A. V. T. Cartaxo and T. M. F. Alves, "Discrete changes model of inter-core crosstalk of real homogeneous multi-core fibers," J. Lightwave Technol. **35**, 2398 (2017).

[369] H. H. Diamandi, Y. London, and A. Zadok, "Opto-mechanical inter-core cross-talk in multicore fibers," Optica **4**, 289 (2017).

[370] Q. Yao, H. Yang, Y. Zhao, R. Zhu, J. Zhang, and J. Wu, "Crosstalk-aware routing, spectrum, and core assignment in elastic optical networks with multi-core fibers," in Asia Communications and Photonics Conference, paper ATh2C.1 (2016).

[371] T. M. F. Alves and A. V. T. Cartaxo, "Characterization of the stochastic time evolution of short-term average intercore crosstalk in multicore fibers with multiple interfering cores," Optics Express **26**, 4605 (2018).

[372] S. García, D. Barrera, J. Hervás, S. Sales, and I. Gasulla, "Microwave signal processing over multicore fiber," Photonics **4**, 49 (2017).

[373] H. H. Diamandi, Y. London, and A. Zadok, "Guided acoustic waves Brillouin scattering in multi-core fibers," 25th International Conference on Optical Fiber Sensors, paper 103236Y (2017).

[374] I. A. Alimi, A. L. Teixeira, and P. P. Monteiro, "Toward an efficient C-RAN optical fronthaul for the future networks: a tutorial on technologies requirements challenges and solutions," Communications Surveys & Tutorials **20**, 708 (2018).

[375] T. M. F. Alves and A. V. T. Cartaxo, "Intercore crosstalk in homogeneous multicore fibers: theoretical characterization of stochastic time evolution," J. Lightwave Technol. **35**, 4613 (2017).

[376] M. Morant and R. Llorente, "Performance analysis of carrier-aggregated multiantenna 4 x 4 MIMO LTE-A fronthaul by spatial multiplexing on multicore fiber," J. Lightwave Technol. **36**, 594 (2018).

[377] R. Llorente, M. Morant, J. S. Bruno, V. Almenar, J. L. Corral, J. M. Fuster, J. Valls, "Multidimensional multiplexing in multicore fibre for hybrid optical backhaul provision: the XCORE approach," in 20th International Conference on Transparent Optical Networks (ICTON), paper We.A3.1 (2018).

[378] L. Gan, L. Shen, M. Tang, C. Xing, Y. Li, C. Ke, W. Tong, B. Li, S. Fu, and D. Liu, "Investigation of channel model for weakly coupled multicore fiber," Optics Express **26**, 5182 (2018).

[379] M. Morant and R. Llorente, "Experimental demonstration of LTE-A M×4×4 MIMO radio-over-multicore fiber fronthaul," in Optical Fiber Communication Conference (OFC), paper Th4E.4 (2017).

[380] Y. Lei, J. Li, Z. Meng, R. Wu, Z. Wan, Y. Fan, W. Zhang, F. Yin, Y. Dai, and K. Xu, "Feasibility of space-division-multiplexed transmission of IEEE 802.11 n/ac-compliant wireless MIMO signals over OM3 multimode fiber," J. Lightwave Technol. **36**, 2076 (2018).

[381] J. He, B. Li, L. Deng, M. Tang, L. Gan, S. Fu, P. Ping Shum, and D. Liu, "Experimental demonstration of bidirectional OFDM/OQAM-MIMO signal over a multicore fiber system," IEEE Photonics Journal **8**, 1 (2016).

[382] R. M. Nejad, F. Tavakoli, L. Wang, X. Guan, S. LaRochelle, and L. A. Rusch, "RoF data transmission using four linearly polarized vector modes of a polarization maintaining elliptical ring core fiber," J. Lightwave Technol. **36**, 3794 (2018).

[383] F. P. Guiomar, I. A. Alimi, P. P. Monteiro, and A. Gameiro, "Flexible infrastructure for the development and integration of access/fronthauling solutions in future wireless systems," in IEEE 19th International Workshop on Signal Processing Advances in Wireless Communications (SPAWC), pp. 1-5 (2018).

[384] J. He, B. Li, L. Deng, M. Tang, L. Gan, S. Fu, P. Ping Shum, and D. Liu, "Experimental investigation of inter-core crosstalk tolerance of MIMO-OFDM/OQAM radio over multicore fiber system," Optics Express **24**, 13418 (2016).

[385] Y. Lei, J. Li, Y. Fan, D. Yu, S. Fu, F. Yin, Y. Dai, and K. Xu, "Space-division-multiplexed transmission of 3×3 multiple-input multiple-output wireless signals over conventional graded-index multimode fiber," Optics Express **24**, 28372 (2016).

[386] J. Zhang, Y. Ji, H. Yu, X. Huang, and H. Li, "Experimental demonstration of fronthaul flexibility for enhanced CoMP service in 5G radio and optical access networks," Optics Express **25**, 21247 (2017).

[387] T. M. F. Alves, A. V. T. Cartaxo, R. S. Luís, B. J. Puttnam, Y. Awaji, and N. Wada, "Intercore crosstalk in direct-detection homogeneous multicore fiber systems impaired by laser phase noise," Optics Express **25**, 29417 (2017).

[388] Y. Lei, J. Li, R. Wu, Y. Fan, S. Fu, F. Yin, Y. Dai, and K. Xu, "Experimental study on the statistic characteristics of a 3x3 RF MIMO channel over a single conventional multimode fiber," Optics Letters **42**, 2217 (2017).

[389] R. O. J. Soeiro, T. M. F. Alves, and A. V. T. Cartaxo, "Impact of longitudinal variation of the coupling coefficient due to bending and twisting on inter-core crosstalk in weakly-coupled MCFs," J. Lightwave Technol. **36**, 3898 (2018).

[390] J. H. Li, H. Xu, T. T. Sun, S. X. Pei, and H. D. Ren, "Effects of intermode nonlinearity and intramode nonlinearity on modulation instability in randomly birefringent two-mode optical fibers," Optics Communications **415**, 74 (2018).

[391] G. Bellanca, P. Orlandi, and P. Bassi, "Assessment of the orthogonal and non-orthogonal coupled-mode theory for parallel optical waveguide couplers," Journal of the Optical Society of America A **35**, 577 (2018).

[392] R. O. J. Soeiro, T. M. F. Alves, and A. V. T. Cartaxo, "Dual polarization discrete changes model of inter-core crosstalk in multi-core fibers," IEEE Photonics Technology Letters **29**, 1395 (2017).

[393] T. Ahmed and J. Atai, "Bragg solitons in systems with separated nonuniform Bragg grating and nonlinearity," Physical Review E **96**, 032222 (2017).

[394] N.-P. Diamantopoulos, Y. Yoshida, and K.-I. Kitayama, "Seamless wireless/optical MIMO transmission via radio-over-FMF," in IEEE Photonics Society Summer Topical Meeting Series (SUM), pp. 223-224 (2018).

[395] G. Wang, R. Gu, H. Li, and Y. Ji, "Efficient resource allocation for passive optical fronthaul-based coordinated multipoint transmission," EURASIP Journal on Wireless Communications and Networking **2016**, 225 (2016).

[396] S. Watanabe, K. Sekine, K. Wada, S. Owaki, and M. Nakamura, "Area-efficient analog FIR filter for multi-level optical transmission," IEEE J. Transactions on Electronics, Information and Systems **138**, 774 (2018).

[397] L. Gan, J. Zhou, S. Fu, M. Tang, and D. Liu, Efficient channel model for homogeneous weakly coupled multicore fiber, arXiv:1811.07666.

[398] T. X. Tran and D. Pompili, "Octopus: a cooperative hierarchical caching strategy for cloud radio access networks," in IEEE 13th International Conference on Mobile Ad Hoc and Sensor Systems (MASS), pp. 154-162 (2016).

[399] S. Rommel, L. C. P. Cavalcante, J. J. V. Olmos, I. T. Monroy, and A. K. Mishra, "Requirements for bend insensitive fiber in millimeter-wave fronthaul systems," in International Topical Meeting on Microwave Photonics (MWP), pp. 1-4 (2015).

[400] N. P. Diamantopoulos, Y. Takami, Y. Yoshida, A. Maruta, A. Kanno, N. Yamamoto, T. Kawanishi, R. Maruyama, N. Kuwaki, S. Matsuo, and K. Kitayama, "Mitigation of modal crosstalk-induced power fading in mode division multiplexed W-band RoF links," in Optical Fiber Communications Conference (OFC), pp. 1-3 (2016).

[401] C. Lim, Y. Tian, C. Ranaweera, A. Nirmalathas, E. Wong, and K.-L. Lee, "Evolution of radio-over-fiber technologies: past and present," in European Conference on Optical Communication (ECOC), pp. 1-3 (2018).

[402] I. C.-Lin and J. Huang, "RAN revolution with NGFI (xHaul) for 5G," in Optical Fiber Communications Conference (OFC), paper W1C.7 (2017).

[403] R. L. Aguiar, "Vision Document for B5G Research," Technical Report (5G-Infrasturcture-Association).

[404] D. Kiesewetter and V. Malyugin, "The crosstalk compensator for fiber-optic data transmission systems with division multiplexing," in IEEE 10th International Conference on Application of Information and Communication Technologies (AICT), paper 17061681 (2016).

[405] N. J. Muga, G. M. Fernandes, M. J. N. Lima, A. N. Pinto, P. S. André, M. Facão, and A. M. Rocha, "Optical and digital key enabling techniques for SDM-based optical networks," in 20th International Conference on Transparent Optical Networks (ICTON), paper We.D1.2 (2018).

[406] M. H. M. Nor, T. Kanesan, F. Maskuriy, A. Yusof, F. A. Fatah, and S. B. A. Anas, "Experimental realization of multi-service RoF system using OCS-PolMux techniques," in 19th International Conference on Advanced Communication Technology (ICACT), p. 148 (2017).

[407] J. D. Marconi, M. L. F. Abbade, E. A. de Mello Fagotto, C. M. S.-Imbett, P. F. P. Neto, and I. Aldaya, "Network performance of optical parametric amplifiers based on tellurite waveguides," in 19th International Conference on Transparent Optical Networks (ICTON), paper We.C5.3 (2017).

[408] G. Queraltó, V. Ahufinger, and J. Mompart, Continuous supersymmetric transformations in optical waveguides, arXiv:1806.00418.

[409] W. Walasik, B. Midya, L. Feng, and N. M. Litchinitser, "Supersymmetry-guided method for mode selection and optimization in coupled systems," Optics Letters **43**, 3758 (2018).

[410] B. Midya, W. Walasik, N. M. Litchinitser, and L. Feng, "Supercharge optical arrays," Optics Letters **43**, 4927 (2018).

[411] G. D. Valle, "Ultracompact low-pass modal filters based on shortcuts to adiabaticity," Physical Review A **98**, 053861 (2018).

[412] G. Queraltó, V. Ahufinger, and J. Mompart, "Integrated photonic devices based on adiabatic transitions between supersymmetric structures," Optics Express **26**, 33797 (2018).

[413] J. Yammine, A. Tandjè, Michel Dossou, L. Bigot, and E. R. Andresen, "Time-dependence of the transmission matrix of a specialty few-mode fiber," APL Photonics **4**, 022904 (2019).

[414] M. Waqar, A. Kim, and P. K. Cho, "A study of fronthaul networks in CRANs - requirements and recent advancements," KSII Transactions on Internet and Information Systems (TIIS) **12**, 4618 (2018).

[415] J. Zhang, S. Chen, X. Guo, J. Shi, and L. Hanzo, Boosting fronthaul capacity: global optimization of power sharing for centralized radio access network, arXiv:1812.11413.

[416] R. O. J. Soeiro, T. M. F. Alves, and A. V. T. Cartaxo, "Inter-core crosstalk in weakly coupled MCFs with arbitrary core layout and the effect of bending and twisting on the coupling coefficient," Optics Express **27**, 74 (2019).

[417] Y. Yoshida, "Mobile xhaul evolution: enabling tools for a flexible 5G xhaul network," in Optical Fiber Communications Conference (OFC), paper Tu2K.1 (2018).

[418] L. Gan, M. Tang, L. Shen, C. Xing, C. Ke, C. Yang, W. Tong, S. Fu, and D. Liu, "Realistic model for frequency-dependent crosstalk in weakly-coupled multicore fiber," in Optical Fiber Communication Conference (OFC), paper Tu3B.6 (2018).

[419] T. M. F. Alves, R. O. J. Soeiro, and A. V. T. Cartaxo, "Statistical distribution and correlation properties of intercore crosstalk in weakly-coupled MCFs," in IEEE Asia Communications and Photonics Conference (ACP), 8595897 (2018).

[420] J. Yammine, A. Tandjè, M. Dossou, L. Bigot, and E. R. Andresen, "Time-dependence of the transmission matrix of a specialty few-mode fiber," in Proc. of SPIE 10947, Next-Generation Optical Communication: Components, Sub-Systems, and Systems VIII, paper 1094702 (2019).

[421] J. L. Rebola, A.V. T. Cartaxo, and A. S. Marques, "10 Gbps CPRI signals transmission impaired by intercore crosstalk in 5G network fronthauls with multicore fibers," Photonic Network Communications **1**, 1 (2019).

[422] C. Liu, L. Deng, J. He, D. Li, S. Fu, M. Tang, M. Cheng, and D. Liu, "Experimental demonstration of high spectral efficient 4×4 MIMO SCMA-OFDM/OQAM radio over multi-core fiber system," Optics Express **25**, 18431 (2017).

[423] S. Doddikrinda, A. Marotta, D. Cassioli, C. Antonelli, K. Kondepu, and L. Valcarenghi, "Exploiting core-switching to minimize fronthaul degradation using multicore fiber," in IEEE Asia Communications and Photonics Conference (ACP), 8595797 (2018).

[424] J. L. Rebola, T. M. F. Alves, A. V. T. Cartaxo, and A. S. Marques, "5G fronthauls with multicore fibers: CPRI signals performance degradation induced by intercore crosstalk," in Proc. of SPIE 10945, Broadband Access Communication Technologies XIII, paper 109450D (2019).

[425] M. Morant, J. S. Bruno, V. Almenar, and R. Llorente, "Performance evaluation of OFDM and SC-QAM backhaul provision on FTTH optical access networks including multi-core fiber riser," in Proc. of SPIE 10945, Broadband Access Communication Technologies XIII, paper 1094509 (2019).

[426] D. J. T. Elson, *Maximising Achievable Rates of Experimental Nonlinear Optical Fibre Transmission Systems*. (Ph.D. Dissertation, 2018).

[427] S. Rommel, D. P.-Galacho, J. M. Fabrega, R. Muñoz, S. Sales, and I. T. Monroy, "High-capacity 5G fronthaul networks based on optical space division multiplexing," accepted to be published in IEEE Transactions on Broadcasting (2019).

[428] A. A. Andrianov and M. V. Ioffe, Supersymmetrization of the Lindblad-Franke-GKS equation, arXiv:1901.03848.

[429] Z. Zakrzewski and J. Majewski, "Multi-core optical fibers in FTTH/FTTA/FTTS solutions supporting IoT," in Proc. SPIE 11045, Optical Fibers and Their Applications 2018, paper 110450N (2019)

[430] T. M. F. Alves, R. O. J. Soeiro, and A. V. T. Cartaxo, "Probability distribution of intercore crosstalk in weakly coupled MCFs with multiple interferers," IEEE Photonics Technology Letters **31**, 651 (2019)

[431] C. Lim, Y. Tian, C. Ranaweera, T. A. Nirmalathas, E. Wong, and K.-L. Lee, "Evolution of radio-over-fiber technology," J. Lightwave Technol. **37**, 1647 (2019).

[432] T. M. F. Alves and A. V. T. Cartaxo, "Decorrelation bandwidth of intercore crosstalk in weakly coupled multicore fibers with multiple interfering cores," J. Lightwave Technol. **37**, 744 (2019).

[433] M. P. Hokmabadi, N. S. Nye, R. El-Ganainy, D. N. Christodoulides, and M. Khajavikhan, "Supersymmetric laser arrays" Science **363**, 623 (2019).

[434] N. Múnera, *Optimization of broadband white light continuum in gases for Z-scan and other nonlinear applications*. (Ph.D. Dissertation, 2018).

[435] S. Longhi, "Reflectionless and invisible potentials in photonic lattices," Optics Letters **42**, 3229 (2017).

[436] W. Bogaerts, M. Fiers, and P. Dumon, "Design challenges in silicon photonics," IEEE J. Sel. Top. Quantum Electron. **20**, 8202008 (2014).

[437] Editorial, "Birth of the programmable optical chip," Nature Photonics **10**, 1 (2016).

[438] D. Pérez, *Integrated Microwave Photonic Processors using Waveguide Mesh Cores.* (Ph.D. Dissertation, 2017).

[439] J. Capmany, I. Gasulla, and D. Pérez, "Microwave photonics: the programmable processor," Nature Photonics (News&Views) **10**, 6 (2016).

[440] D. Marpaung, "On-chip microwave photonics," in Asia Communications and Photonics Conference (OSA), paper Su1E.1 (2017).

[441] N. C. Harris, J. Carolan, D. Bunandar, M. Prabhu, M. Hochberg, T. B.-Jones, M. L. Fanto, A. M. Smith, C. C. Tison, P. M. Alsing, and D. Englund, "Linear programmable nanophotonic processors," Optica **5**, 1623 (2018).

[442] D. Pérez and J. Capmany, "Scalable analysis for arbitrary photonic integrated waveguide meshes," Optica **6**, 19 (2019).

[443] N. C. Harris, J. Carolan, D. Bunandar, M. Prabhu, M. Hochberg, T. B.-Jones, M. L. Fanto, A. M. Smith, C. C. Tison, P. M. Alsing, and D. Englund, "Linear programmable nanophotonic processors," Optica **5**, 1623 (2018).

[444] D. Marpaung, J. Yao, and J. Capmany, "Integrated microwave photonics," Nature Photonics **13**, 80 (2019).

List of Acronyms

3GPP	3rd Generation Partnership Project
AB	Akhmediev Breather
ACF	Autocorrelation Function
ASE	Amplified Spontaneous Emission
AWG	Arbitrary Waveform Generator
B2B	Back-to-Back
BEC	Bose-Einstein Condensate
BER	Bit Error Rate
BIC	Bound State in the Continuum
BPM	Beam Propagation Method
BPOF	Band-Pass Optical Filter
BS	Base Station
BTC	Birefringence Temporal Change
c.c.	complex conjugate
c.d.f.	cumulative distribution function
CCD	Coupling-Coefficient Dispersion
CC-MCF	Coupled-Core Multi-Core Fiber
CINLS	Core Interleaving Nonlinear Stimulation
CLMT	Coupled Local-Mode Theory
CLPT	Coupled Local-Power Theory
CMT	Coupled-Mode Theory
CNLSE	Coupled Nonlinear Schrödinger Equation
CPT	Coupled-Power Theory
C-RAN	Cloud Radio-Access Network
CW	Continuous-Wave

d.f.	degree of freedom
DFB	Distributed Feedback Laser
DGD	Differential Group Delay
DIC-XT	Direct Inter-Core Crosstalk
DMGD	Differential Mode Group Delay
DSP	Digital Signal Processing
E2E	End-to-End
ECL	External Cavity Laser
EDFA	Erbium Doped Fiber Amplifier
ERIM	Equivalent Refractive Index Model
E-UTRA	Evolved Universal Terrestrial Radio Access
EVM	Error Vector Magnitude
EVP	Eigenvalue Problem
FDD	Frequency Division Duplex
FDM	Frequency-Division Multiplexing
FDTD	Finite-Difference Time-Domain
FEC	Forward Error Correction
FMF	Few-Mode Fiber
FM-MCF	Few-Mode Multi-Core Fiber
FTTH	Fiber-to-the-Home
FWHM	Full Width at Half Maximum
FWM	Four-Wave Mixing
GI-MCF	Gradual-Index Multi-Core Fiber
GVD	Group-Velocity Dispersion
HA-MCF	Hole-Assisted Multi-Core Fiber
HB	Highly-Birefringent
HE-MCF	Heterogeneous Multi-Core Fiber
HO-MCF	Homogeneous Multi-Core Fiber
HR-FBG	Highly-Reflective Fiber Bragg Grating
HRMII	Hyperbolic Rosen-Morse II
HSC	Hyperbolic Secant Chain
IC-XT	Inter-Core Crosstalk
iC-XT	intra-Core Crosstalk

IMCD	Inter-core Mode-Coupling Dispersion
iMCD	intra-core Mode-Coupling Dispersion
KdV	Korteweg-de Vries
KM	Kuznetsov-Ma
LB	Lowly-Birefringent
LHC	Large Hadron Collider
LHS	Left-Hand Side
LP	Linearly Polarized
LR-FBG	Lowly-Reflective Fiber Bragg Grating
LTE-A	Long-Term Evolution Advanced
LTI	Linear Time-Invariant
M2M	Machine-to-Machine
MCC	Mode-Coupling Coefficient
MCD	Mode-Coupling Dispersion
MCF	Multi-Core Fiber
M-DEMUX	Mode Demultiplexer
MDL	Mode-Dependent Loss
MDM	Mode-Division Multiplexing
MIMO	Multiple-Input Multiple-Output
MMF	Multi-Mode Fiber
MMI	Multi-Mode Interference
MM-MCF	Multi-Mode Multi-Core Fiber
MM-SCF	Multi-Mode Single-Core Fiber
M-MUX	Mode Multiplexer
MU-MIMO	Multi-User Multiple-Input Multiple-Output
MWP	Microwave Photonics
MZM	Mach-Zehnder Modulator
NLDC	Nonlinear Directional Coupler
NLSE	Nonlinear Schrödinger Equation
NMPM	Negative Magnetic Permeability Material
ODE	Ordinary Differential Equation
ODL	Optical Delay Line
OFDMA	Orthogonal Frequency-Division Multiplexing Access

OOK	On-Off Keying
p.d.f.	probability density function
PBC	Polarization Beam Combiner
PBS	Polarization Beam Splitter
PC	Polarization Controller
PCM	Polarized Core Mode
PDE	Partial Differential Equation
PDM	Polarization-Division Multiplexing
PhMD	Phase-Mismatching Dispersion
PMBW	Phase-Matching Bandwidth
PMD	Polarization-Mode Dispersion
PON	Passive Optical Network
PS	Peregrine Soliton
PSD	Power Spectral Density
$\mathcal{PT}$	Parity-Time
QAM	Quadrature Amplitude Modulation
QB	Quadrature Bias
QFT	Quantum Field Theory
QM	Quantum Mechanics
r.v.	random variable
RB	Resource Block
RHS	Right-Hand Side
RIFS	Raman-Induced Frequency Shift
RoF	Radio-over-Fiber
RRH	Remote Radio Head
SAMI	Sydney-AAO Multi-object IFS
SBS	Stimulated Brillouin Scattering
SC	Single Carrier
SCF	Single-Core Fiber
SDM	Space-Division Multiplexing
SE	Spectral Efficiency
SFB	Soliton on a Finite Background
SFT	Spatial Fourier Transform

SI	Step-Index
SI-MCF	Step-Index Multi-Core Fiber
SIP	Shape Invariant Potential
SISO	Single-Input Single-Output
SL-EVP	Sturm-Liouville Eigenvalue Problem
SLM	Spatial Light Modulator
SL-SFT	Short-Length Spatial Fourier Transform
SMF	Single-Mode Fiber
SM-MCF	Single-Mode Multi-Core Fiber
SM-SCF	Single-Mode Single-Core Fiber
SSMF	Standard Single-Mode Fiber
STFT	Short-Time Fourier Transform
SUSY	Supersymmetry
SVEA	Slowly-Varying Envelope Approximation
SVI	Slowly-Varying Index
TA-MCF	Trench-Assisted Multi-Core Fiber
TDM	Time-Division Multiplexing
TE	Transverse Electric
TM	Transverse Magnetic
TMC	Tapered MCF Connector
TPEF	Two Photon Excited Fluorescence
TPL	Temporal Photonic Lantern
T-SUSY	Temporal Supersymmetry
TTDL	True-Time Delay Line
TWG	Temporal Waveguide
UC-MCF	Uncoupled-Core Multi-Core Fiber
UWB	Ultra-Wideband
VOA	Variable Optical Attenuator
WDM	Wavelength-Division Multiplexing
WiMAX	Worldwide interoperability for Microwave Access
WKB	Wentzel-Kramers-Brillouin
XIC-XT	Cross Inter-Core Crosstalk
XPM	Cross-Phase Modulation
XT	Crosstalk

This page was intentionally left blank.

List of Figures

List of Tables

This page was intentionally left blank.

List of Symbols

Preface Here, we include a list with the main symbols used in this thesis. The symbols which are not included in the following list (e.g. appendix's symbols) are detailed in the main text.

Roman symbols

A

a	Core. Also, real number. Also, width of a dielectric slab waveguide
a_m	Real envelope of $\mathcal{E}_m$. Also, an arbitrary scalar. Also, scalar SIP parameter with m an integer. Also, complex-valued function with m an integer
$\boldsymbol{a}_m$	Vector SIP parameter with m an integer
A	Complex envelope. Also, real-valued function. Also, real constant
$\mathbf{A}$	Matrix of complex envelopes
A_{eff}	Effective area
A_i	Complex constant, with i an integer
A_m	Complex envelope of $\mathcal{E}_m$
A_{mi}	Complex envelope of $\mathcal{E}_{mi}$
$\widetilde{A}_{mi}$	Fourier transform of A_{mi}
$\mathcal{A}$	Complex envelope of $\mathcal{E}$
$\widetilde{\mathcal{A}}$	Fourier transform of $\mathcal{A}$
$\mathcal{A}_{\text{I}}$	Incident complex envelope
$\mathcal{A}_{\text{R}}$	Reflected complex envelope
$\mathcal{A}_{\text{T}}$	Transmitted complex envelope
$\mathcal{A}_{mi}$	Complex envelope of $\mathcal{E}_{mi}$
$\widetilde{\mathcal{A}}_{mi}$	Fourier transform of $\mathcal{A}_{mi}$
$\mathscr{A}_m$	Amplitude of the m-th temporal bound state of a TWG
$\mathtt{A}$	Complex envelope including only the slowly-varying temporal evolution of the electric field strength

$\widetilde{\mathtt{A}}$	Fourier transform of $\mathtt{A}$
$\mathtt{A}_{mi}$	Complex envelope including only the slowly-varying temporal evolution of the electric field strength associated to PCM mi
$\widetilde{\mathtt{A}}_{mi}$	Fourier transform of $\mathtt{A}_{mi}$
$\widehat{\mathrm{A}}$	Arbitrary linear operator used to introduce the preliminary mathematical concepts of SUSY in Chapter 6
$\widehat{\mathrm{A}}^{\dagger}$	Adjoint operator of $\widehat{\mathrm{A}}$
$\widehat{\mathrm{A}}^{\pm}$	SUSY operators
$\widehat{\mathrm{A}}_1^{\mp}$	SUSY operators connecting $\widehat{\mathrm{H}}_1$ and $\widehat{\mathrm{H}}_2$ in 1D SUSY QM. Also, SUSY operators in 2D SUSY QM
$\widehat{\mathrm{A}}_2^{\mp}$	SUSY operators connecting $\widehat{\mathrm{H}}_2$ and $\widehat{\mathrm{H}}_3$ in 1D SUSY QM. Also, SUSY operators in 2D SUSY QM
$\widehat{\mathrm{A}}_{k-1}^{\pm}$	SUSY operators connecting $\widehat{\mathrm{H}}_{k-1}$ and $\widehat{\mathrm{H}}_k$ in a SUSY chain
$\widehat{\mathrm{A}}^{\pm}(\boldsymbol{a}_m)$	SUSY operators connecting SIP superpartners
$\widehat{\mathrm{A}}_{\mathrm{D}}^{\pm}(\eta_1)$	SUSY operators associated to the second step of the one-parameter Darboux procedure
$\widehat{\mathrm{A}}_{2,\mathrm{D}}^{\pm}(\eta_2)$	SUSY operators associated to the two-parameter Darboux procedure
$\widehat{\mathrm{A}}_{i,\mathrm{D}}^{\pm}(\eta_i,\ldots,\eta_n)$	SUSY operators associated to the multi-parameter Darboux procedure

B

b	Core. Also, real number
b_i	Complex or real-valued function, with i an integer
$b_{m,n}$	Normalized phase constant of the LP_{mn} mode group
$\mathbf{b}^{(\mathrm{eq})}$	Matrix of equivalent phase constants
B	Modulus of $\boldsymbol{B}$. Also, basis of a vector space. Also, real-valued function. Also, free-parameter. Also, medium bulk modulus
B_1	Basis of a vector space accounting for bosonic wave functions
B_2	Basis of a vector space accounting for fermionic wave functions
B_{S}	Spatial evolution of the medium bulk modulus
B_{T}	Temporal evolution of the medium bulk modulus
$\boldsymbol{B}$	Analytic representation $\boldsymbol{\mathcal{B}}$
$\boldsymbol{\mathcal{B}}$	Real representation (or real wave function) of the magnetic induction
$\widetilde{\boldsymbol{\mathcal{B}}}$	Fourier transform of $\boldsymbol{\mathcal{B}}$
$\widetilde{\boldsymbol{\mathcal{B}}}_{m,n}$	Fourier transform of $\boldsymbol{\mathcal{B}}$ associated to the LP_{mn} mode group
$\mathfrak{B}_{\widetilde{\mathtt{A}}}$	Bandwidth of $\widetilde{\mathtt{A}}$

$\widehat{\mathrm{B}}$	Arbitrary linear operator used to introduce the preliminary mathematical concepts of SUSY in Chapter 6
$\widehat{\mathrm{B}}_1^{\pm}$	SUSY operators in 2D SUSY QM
$\widehat{\mathrm{B}}_2^{\pm}$	SUSY operators in 2D SUSY QM

C

c	Speed of light in a medium different from the vacuum. Also, it may represent a core of an MCF. Also, real number
c_0	Speed of light in vacuum
c_a	Linear MCC describing linear coupling in core a
$c_a^{(\mathrm{eq})}$	Equivalent linear MCC of c_a
c_{ax}	Linear MCC describing linear coupling in PCM ax
c_i	Real number, with i an integer
c_{S}	Speed of sound
cn	Jacobi elliptic function
C	Specific heat capacity
$C_{\mathrm{F},m}$	Correction factor of core m
$C^{(k)}$	Number of optical carriers which can be observed when operating in the linear ($k = 1$) and nonlinear ($k = 3$) regimes
$C^2([a,b])$	The set of complex-valued functions with continuous second-order derivatives within the interval $[a,b] \subseteq \overline{\mathbb{R}}$
$\mathscr{C}_a^{(\mathrm{P})}$	Constant to calculate the optical power propagated in core a
$\mathscr{C}_b^{(\mathrm{P})}$	Constant to calculate the optical power propagated in core b
$\mathscr{C}_{mi}^{(\mathrm{P})}$	Constant to calculate the optical power propagated in PCM mi
$\mathbb{C}$	The set of complex numbers

D

d	Magnitude of the displacement vector
$\boldsymbol{d}$	Displacement vector
$\widetilde{d}$	Fourier transform of the magnitude of the displacement vector
d_{ab}	Core-to-core distance between cores a and b
d_{cl}	Cladding diameter
d_m	Euclidean distance of core m to the MCF center
$d_{\mathrm{F}}^{(lp)}$	Degeneracy factor of the LP_{lp} mode group
deg	Degree of a vector

D	Modulus of $\boldsymbol{D}$. Also, subset of real numbers. Also, non-vanishing real constant
$\boldsymbol{D}$	Analytic representation of $\boldsymbol{\mathcal{D}}$
$\boldsymbol{D}_{\mathrm{I}}$	Incident $\boldsymbol{D}$
$\boldsymbol{D}_{\mathrm{R}}$	Reflected $\boldsymbol{D}$
$\boldsymbol{D}_{\mathrm{T}}$	Transmitted $\boldsymbol{D}$
$\boldsymbol{D}^{(1)}$	Analytic representation of the electric displacement in the first T-SUSY system
$\boldsymbol{D}^{(2)}$	Analytic representation of the electric displacement in the second T-SUSY system
$\boldsymbol{\mathcal{D}}$	Real representation (or real wave function) of the electric displacement
$\widetilde{\boldsymbol{\mathcal{D}}}$	Fourier transform of $\boldsymbol{\mathcal{D}}$
$\widetilde{\boldsymbol{\mathcal{D}}}_{m,n}$	Fourier transform of $\boldsymbol{\mathcal{D}}$ associated to the LP_{mn} mode group
$\mathfrak{D}_{\mathrm{eq}}$	Complex-valued function accounting for the GVD along with the medium perturbations in frequency domain
$\mathfrak{D}_{mi}^{(\mathrm{eq})}$	Complex-valued function of PCM mi accounting for the GVD along with the medium perturbations in frequency domain
$\mathfrak{D}_{\lambda_0}$	Darboux transformation using λ_0 as eigenvalue of reference
$\mathfrak{D}_{E_0^{(1)}}$	Darboux transformation using $E_0^{(1)}$ as eigenvalue of reference
$\widehat{\mathrm{D}}_{\mathrm{eq}}$	Equivalent dispersion operator accounting for the GVD along with the medium perturbations
$\widehat{\mathrm{D}}_{mi}^{(\mathrm{eq})}$	Equivalent dispersion operator of PCM mi accounting for the GVD along with the medium perturbations

E

$e_{(+_{\mathbb{K}})}$	Neutral element for the operation $+_{\mathbb{K}}$
E	Energy in quantum mechanics. Also, expectation operator
$\boldsymbol{E}$	Analytic representation of $\boldsymbol{\mathcal{E}}$
$\widetilde{\boldsymbol{E}}$	Fourier transform of $\boldsymbol{E}$
E_0	Ground state energy level of a quantum system. Also, arbitrary energy level in the continuum
E_1	Arbitrary energy level in the continuum
E_n	n-th energy level of a quantum system
E_{T}	Transversal component of the complex amplitude of the electric field strength
E_{ω_0}	Modulus of $\boldsymbol{E}_{\omega_0}$
$\boldsymbol{E}_{\omega_0}$	Complex amplitude of the electric field strength
$\widetilde{\boldsymbol{E}}_{\omega_0}$	Fourier transform of $\boldsymbol{E}_{\omega_0}$
E_{i,ω_0}	i-th component of the complex amplitude of the electric field strength

$\widetilde{E}_{i,\omega_0}$	Fourier transform of E_{i,ω_0}
E_{m,ω_0}	Complex amplitude of the electric field strength associated to core m
E_{mi,ω_0}	Complex amplitude of the electric field strength associated to PCM mi
$\widetilde{E}_{mi,\omega_0}$	Fourier transform of E_{mi,ω_0}
$\widetilde{E}_{m,n}$	Quantum energy level
$E^{(1)}$	Eigenenergy of the first SUSY system
$E^{(2)}$	Eigenenergy of the second SUSY system
$E_n^{(1)}$	n-th energy level of the first SUSY system
$E_n^{(2)}$	n-th energy level of the second SUSY system
$E_0^{(1)}$	Ground state energy level of the first SUSY system
$E_0^{(2)}$	Ground state energy level of the second SUSY system
$E_{n,\mathrm{eq}}^{(1)}$	n-th energy level of $\widehat{\mathrm{H}}_{1,\mathrm{eq}}$
$E_{n,\mathrm{eq}}^{(2)}$	n-th energy level of $\widehat{\mathrm{H}}_{2,\mathrm{eq}}$
$E^{(\mathrm{3D})}$	Energy associated to $V^{(\mathrm{3D})}$
$E_{nlm}^{(\mathrm{3D})}$	Energy level associated to Ψ_{nlm}
$E_{mn}^{(\mathrm{3D})}$	Energy level associated to Ψ_{mn}
$E_n^{(k)}$	n-th energy level of $\widehat{\mathrm{H}}_k$
$E\left(\boldsymbol{a}_m\right)$	Energy associated to SIP superpartners in the continuum
$E_k^{(n)}\left(\boldsymbol{a}_m\right)$	k-th energy level of the n-th system of a SUSY chain constructed using SIP
$\mathcal{E}_{\mathrm{A}}$	Characteristic atomic electric field strength
$\mathcal{E}_{\mathrm{T}}$	Transversal component of $\boldsymbol{\mathcal{E}}$
$\widetilde{\mathcal{E}}_{\mathrm{T}}$	Fourier transform of $\mathcal{E}_{\mathrm{T}}$
$\boldsymbol{\mathcal{E}}$	Real representation (or real wave function) of the electric field strength
$\widetilde{\boldsymbol{\mathcal{E}}}$	Fourier transform of $\boldsymbol{\mathcal{E}}$
$\check{\boldsymbol{\mathcal{E}}}$	Hilbert transform of $\boldsymbol{\mathcal{E}}$
$\boldsymbol{\mathcal{E}}^{+}$	Real representation (or real wave function) of the electric field strength including exclusively the positive frequencies of the spectrum
$\boldsymbol{\mathcal{E}}^{-}$	Real representation (or real wave function) of the electric field strength including exclusively the negative frequencies of the spectrum
$\mathcal{E}_z$	z component of $\boldsymbol{\mathcal{E}}$
$\widetilde{\mathcal{E}}_z$	Fourier transform of $\mathcal{E}_z$
$\widetilde{\mathcal{E}}_i$	i-th component of $\widetilde{\boldsymbol{\mathcal{E}}}$

$\widetilde{\mathcal{E}}^{(1)}$ Modulus of $\widetilde{\boldsymbol{\mathcal{E}}}^{(1)}$

$\widetilde{\boldsymbol{\mathcal{E}}}^{(1)}$ Fourier transform of the real representation of the electric field strength in the first SUSY optical system

$\widetilde{\boldsymbol{\mathcal{E}}}_{\mathrm{I}}^{(1)}$ Incident $\widetilde{\boldsymbol{\mathcal{E}}}^{(1)}$

$\widetilde{\boldsymbol{\mathcal{E}}}_{\mathrm{R}}^{(1)}$ Reflected $\widetilde{\boldsymbol{\mathcal{E}}}^{(1)}$

$\widetilde{\boldsymbol{\mathcal{E}}}_{\mathrm{T}}^{(1)}$ Transmitted $\widetilde{\boldsymbol{\mathcal{E}}}^{(1)}$

$\mathcal{E}_m$ Modulus of $\boldsymbol{\mathcal{E}}_m$

$\boldsymbol{\mathcal{E}}_m$ Real representation (or real wave function) of the electric field strength in core m

$\mathcal{E}_{mi}$ Modulus of $\boldsymbol{\mathcal{E}}_{mi}$

$\boldsymbol{\mathcal{E}}_{mi}$ Real representation (or real wave function) of the electric field strength in PCM mi

$\widetilde{\boldsymbol{\mathcal{E}}}_{m,n}$ Fourier transform of $\boldsymbol{\mathcal{E}}$ associated to the LP_{mn} mode group

$\widetilde{\boldsymbol{\mathcal{E}}}_{m_i,n}^{(i)}$ Fourier transform of $\boldsymbol{\mathcal{E}}$ associated to the $\mathrm{LP}_{m_i n}$ mode group in the i-th SUSY optical system

$\mathscr{E}$ Photon energy

$\mathrm{EVM}_{\mathrm{B2B}}$ EVM (error vector magnitude) in the B2B (back-to-back) transmission

$\mathrm{EVM}_{\mathrm{E2E}}$ EVM (error vector magnitude) in the E2E (end-to-end) transmission

$\mathrm{EVM}_{\mathrm{E2E}}^{(\mathrm{ideal})}$ Ideal EVM (error vector magnitude) in the E2E (end-to-end) transmission

F

f Arbitrary real or complex-valued function. Also, frequency

$\boldsymbol{f}$ Vector-valued function connecting the SIP parameters

$f_{b,a}$ Spatial random process describing the longitudinal random perturbations of the MCF

f_i Real or complex-valued function. Also, real constant associated to Raman response. In both cases, the subindex i is an integer

f_{R} Fractional contribution of the delayed Raman response to the nonlinear polarization

f_{T} Twist rate in an MCF

$\overline{f}_{\mathrm{T}}$ Average value of f_{T}

$f_{\mathrm{T},l}$ Twist rate in the l-th birefringent segment of the MCF

$f_{\mathrm{T},l,s}$ Twist rate in the l-th birefringent segment and s-th Monte Carlo iteration

f_U p.d.f. associated to random variable U

$f_{X_{a,b}^{\mathrm{L}}}$ p.d.f. associated to random variable $X_{a,b}^{\mathrm{L}}$

$f_{X_{a,b}^{\mathrm{NL}}}$ p.d.f. associated to random variable $X_{a,b}^{\mathrm{NL}}$

$f_{X_{i,j}}$ p.d.f. associated to random variable $X_{i,j}$

f_Y p.d.f. associated to random variable Y

$f_{Z_{i,j}}$ p.d.f. associated to random variable $Z_{i,j}$

F Elliptic integral of the first kind. Also, fermion number. Also, transversal eigenfunction of the LP_{01} mode

$\boldsymbol{F}$ Arbitrary vector-valued function

F_m Transversal eigenfunction of the LP_{01} mode in core m

F_{mi} Transversal eigenfunction of the LP_{01} mode in PCM mi

$F_{X^{\mathrm{L}}_{a,b}}$ c.d.f. associated to random variable $X^{\mathrm{L}}_{a,b}$

$F_{X^{\mathrm{NL}}_{a,b}}$ c.d.f. associated to random variable $X^{\mathrm{NL}}_{a,b}$

$\mathcal{F}$ Fourier transform operator. Also, a set of functions

$\mathcal{F}^{-1}$ Inverse Fourier transform operator

$\mathcal{F}_{\mathrm{S}}$ Spatial Fourier transform operator

$\mathcal{F}_{\mathrm{S}}^{-1}$ Inverse spatial Fourier transform operator

$\mathcal{F}_{\mathrm{T}}$ Short-time Fourier transform operator

$\mathcal{F}_{\mathrm{T}}^{-1}$ Inverse short-time Fourier transform operator

G

g Arbitrary real or complex-valued function. Also, an integer

g_{B} Gain of the stimulated Brillouin scattering

$g^{(1)}$ Nonlinear MCC describing nonlinear intra-core coupling between different polarization axes. The super-index (1) indicates the intra-core nature of the mode-coupling and g indicates that the mode-coupling takes place between different polarization axes

$g^{(2,\ldots,6)}$ Nonlinear MCCs describing nonlinear inter-core coupling between different polarization axes. The super-index ($i > 1$) indicates the inter-core nature of the mode-coupling and g indicates that the mode-coupling takes place between different polarization axes

$\widetilde{g}^{(\mathrm{I,R})}$ Nonlinear MCC $g^{(1)}$ in frequency domain. The super-index (I) indicates the instantaneous nature of the nonlinear effects, and the super-index (R) indicates that the nonlinear effects are related to Raman response of the optical medium

$\hat{\mathrm{g}}^{(\mathrm{I,R})}$ Linear operator associated to $\widetilde{g}^{(\mathrm{I,R})}$ in time domain

H

h Bijective and positive-real function connecting the random variables $X^{\mathrm{L}}_{a,b}$ and $X^{\mathrm{NL}}_{a,b}$. Also, complex-valued function. Also, isotropic Raman response. Also, impulse response of an LTI or LTV system

h_a Nonlinear power-coupling coefficient describing self-coupling in core a

$h_{a,b}$ Linear power-coupling coefficient describing linear coupling from core b to core a

$h^{(\mathrm{eq})}_{a,b}$ Equivalent power-coupling coefficient describing power coupling from core b to core a

h_{ax}	Impulse response of H_{ax}
h_{bx}	Impulse response of H_{bx}
$\hbar$	Reduced Planck's constant (or Dirac's constant)
H_a	Modal field radius associated to the LP_{01} mode in core a
H_b	Modal field radius associated to the LP_{01} mode in core b
H_{ax}	Transfer function of PCM ax. Also, modal field radius associated to the LP_{01} mode in PCM ax
H_{bx}	Transfer function of PCM bx. Also, modal field radius associated to the LP_{01} mode in PCM bx
H_{T}	Transversal component of the complex amplitude of the magnetic field strength
$\boldsymbol{H}$	Analytic representation of $\boldsymbol{\mathcal{H}}$
$\mathcal{H}_{\mathrm{T}}$	Transversal component of $\boldsymbol{\mathcal{H}}$
$\widetilde{\mathcal{H}}_{\mathrm{T}}$	Fourier transform of $\mathcal{H}_{\mathrm{T}}$
$\boldsymbol{\mathcal{H}}$	Real representation (or real wave function) of the magnetic field strength
$\widetilde{\boldsymbol{\mathcal{H}}}$	Fourier transform of $\boldsymbol{\mathcal{H}}$
$\boldsymbol{\mathcal{H}}_{mi}$	Real representation (or real wave function) of the magnetic field strength in PCM mi
H	Superhamiltonian
H_{D}	Superhamiltonian associated to the second step of the one-parameter Darboux procedure
$\widehat{\mathrm{H}}$	Hamiltonian operator
$\widehat{\mathrm{H}}_0$	Hamiltonian associated to V_0 potential
$\widehat{\mathrm{H}}_1$	Hamiltonian of the first SUSY system
$\widehat{\mathrm{H}}_2$	Hamiltonian of the second SUSY system
$\widehat{\mathrm{H}}_3$	Hamiltonian of the third system in a SUSY chain
$\widehat{\mathrm{H}}_k$	Hamiltonian of the k-th system in a SUSY chain
$\widehat{\mathrm{H}}_{0,\mathrm{eq}}$	Energy-shifted Hamiltonian of $\widehat{\mathrm{H}}_0$
$\widehat{\mathrm{H}}_{1,\mathrm{eq}}$	Energy-shifted Hamiltonian of $\widehat{\mathrm{H}}_1$
$\widehat{\mathrm{H}}_{2,\mathrm{eq}}$	Energy-shifted Hamiltonian of $\widehat{\mathrm{H}}_2$
$\widehat{\mathrm{H}}_n(\boldsymbol{a}_m)$	n-th Hamiltonian of a SUSY chain constructed using SIP
$\widehat{\mathrm{H}}_{n,\mathrm{eq}}(\boldsymbol{a}_m)$	Energy-shifted Hamiltonian of $\widehat{\mathrm{H}}_n(\boldsymbol{a}_m)$
$\widehat{\mathrm{H}}^{(1)}$	Hamiltonian of the first SUSY system in 2D SUSY QM
$\widehat{\mathrm{H}}^{(3)}$	Hamiltonian of the third SUSY system in 2D SUSY QM
$\widehat{\mathrm{H}}_{ik}^{(2)}$	Component of the Hamiltonian matrix of the second SUSY system in 2D SUSY QM
$\widehat{\widetilde{\mathrm{H}}}_1(\eta_1)$	Hamiltonian associated to $\widetilde{V}_1(\eta_1)$ potential

I

i	Integer
I	Subset of real numbers. Also, intensity mode profile distribution
$\mathbf{I}$	Identity matrix
$\mathbf{I}_3$	Identity matrix of third-order
$I_{\mathrm{cl}}^{(k,s)}$	Mode overlapping in cladding region
$\mathcal{I}_1$	Primitive function of $\left(\psi_0^{(1)}\right)^2$. Also, primitive function of u_0^2
$\mathcal{I}_{1,+}$	Limit of $\mathcal{I}_1$ at $x \to \infty$, $r \to \infty$ or $t \to \infty$
$\mathcal{I}_2$	Primitive function of $\left(\psi_0^{(2)}\right)^2$
$\mathcal{I}_i$	Primitive function of $\left(\psi_0^{(i)}\right)^2$

J

j	Imaginary unit $j := \sqrt{-1}$. Also, it may represent an integer
J_0	Zero-order Bessel function of the first kind
J_1	First-order Bessel function of the first kind
$\boldsymbol{J}$	Analytic representation of $\boldsymbol{\mathcal{J}}$
$\boldsymbol{J}_{\mathrm{c}}$	Analytic representation of $\boldsymbol{\mathcal{J}}_{\mathrm{c}}$
$\boldsymbol{\mathcal{J}}$	Real representation (or real wave function) of the total current density
$\widetilde{\boldsymbol{\mathcal{J}}}$	Fourier transform of $\boldsymbol{\mathcal{J}}$
$\boldsymbol{\mathcal{J}}_{\mathrm{b}}$	Real representation (or real wave function) of the current density associated to the bound charges
$\boldsymbol{\mathcal{J}}_{\mathrm{c}}$	Real representation (or real wave function) of the conduction current density
$\widetilde{\boldsymbol{\mathcal{J}}}_{\mathrm{c}}$	Fourier transform of $\boldsymbol{\mathcal{J}}_{\mathrm{c}}$
$\boldsymbol{\mathcal{J}}_{\mathrm{f}}$	Real representation (or real wave function) of the current density associated to the free charges

K

k	Electromagnetic wave number. Also, real number, integer or arbitrary scalar-valued function. Also, particle wave number. Also, elastic constant of the restoring force in Lorentz oscillator model. Also, it may indicate a given core of an MCF
k_0	Wave number of the optical carrier in vacuum
$\widetilde{k}$	Fourier transform of the elastic constant of the restoring force in Lorentz oscillator model
$\boldsymbol{k}$	Wave vector
$\mathbf{k}$	Matrix of linear MCCs

k_m	Wave number of the optical carrier in core m
k_y	y-component of the wave vector
k_z	z-component of the wave vector
$k_\pm$	Limit of the particle or electromagnetic wave number $k(x)$ at $x \to \pm\infty$
$k_n^{(1)}$	z-component of the wave vector of the n-th TE mode in a bosonic dielectric slab
$k_x^{(1)}$	x-component of the wave vector in the first SUSY optical system
$k_z^{(1)}$	z-component of the wave vector in the first SUSY optical system
$k_{x,\pm}^{(1)}$	Limit of $k_x^{(1)}$ at $x \to x_\pm$, with $x \in [x_-, x_+] \subseteq \overline{\mathbb{R}}$. In the main text, x_- and x_+ are usually denoted by the symbols a and b, respectively.
K	Complete elliptic integral of the first kind. Also, thermal conductivity
K_0	Zero-order modified Bessel function of the second kind
K_1	First-order modified Bessel function of the second kind
K_n	Phase constant of the n-th guided mode of a TWG
$K_{a,b}$	Linear MCC describing quasi-discrete changes of linear IC-XT from core b to core a
$\widetilde{K}_{ax,bx}^{(\mathrm{eq})}$	Equivalent inter-core mode-coupling function
$\widehat{\mathrm{K}}_{ax,bx}^{(\mathrm{eq})}$	Linear operator describing the function $\widetilde{K}_{ax,bx}^{(\mathrm{eq})}$ in time domain
$\mathbb{K}$	Arbitrary field

L

l	Integer
l_c	Correlation length
l_i	Angular order of the i-th SUSY system
$l_n^{(i)}$	Order of the linear operator $\widehat{\mathrm{L}}_n^{(i)}$
$\widehat{\boldsymbol{l}}$	Angular momentum operator
L	MCF length. Also, width of the infinite square well potential
L_C	Coupling length
L_f	Logarithmic derivative of f function
L_{l-1}	MCF length in the l-th MCF segment
$L_{N_\mathrm{NL}-1}$	MCF length between the last two phase-matching points
L_eff	Effective interaction length
L_CCD	MCF length scale over which the dispersive effects of the CCD should be considered
L_GVD	Fiber length scale over which the dispersive effects of the GVD should be considered

$L_{\mathrm{ID}}^{(1)}$	Fiber length scale over which the dispersive effects of the first-order intermodal dispersion should be considered
L_{IMCD}	MCF length scale over which the dispersive effects of the IMCD should be considered
L_{NL}	MCF length scale over which the nonlinear IC-XT can be observed
L_{PhMD}	MCF length scale over which the dispersive effects of the PhMD should be considered
$\widehat{\mathrm{L}}_n^{(i)}$	Linear operator accounting for linear mode-coupling from ψ_n to ψ_i
$\mathcal{L}_{n,k}^{(i)}$	Complex-valued function describing k-th order linear mode-coupling effects from ψ_n to ψ_i
$\mathcal{L}^2\left([a,b]\right)$	The vector space of square-integrable functions in $[a,b] \subseteq \overline{\mathbb{R}}$
$\mathscr{L}(\mathcal{V},\mathbb{K})$	The set of homomorphisms from $\mathcal{V}$ to $\mathbb{K}$
$\mathrm{LP}_{01,a}$	LP_{01} mode associated to core a
$\mathrm{LP}_{01,b}$	LP_{01} mode associated to core b
$\mathrm{LP}_{m_i,n}^{(i)}$	LP group associated to the i-th SUSY optical fiber with azimuthal order m_i and radial order n

M

m	Integer. Also, it may indicate a given core of an MCF. Also, auxiliary parameter of the NLDC. Also, mass of a quantum particle. Also, mass of the positive or negative charge of the dipole
mi	$\mathrm{LP}_{01,mi}$ mode, where m indicates the core and i the polarization axis
m_i	Azimuthal order of the i-th SUSY system
$m_{ax,ay}$	Linear MCC describing linear coupling from PCM ay to PCM ax
$\widetilde{m}_{ax,ay}$	Linear MCC describing linear coupling from PCM ay to PCM ax in frequency domain
M	Integer. It may represent different parameters: number of cores or number of LP modes, among other examples. Also, it may represent a complex constant or a real-valued function (e.g. to connect supersymmetric shape invariant potentials or refractive index profiles)
$\mathbf{M}$	Auxiliary Matrix accounting for the linear and nonlinear mode-coupling
$M_n\left(\mathbb{C}\right)$	Vector space of square matrices of dimension $n \times n$ with complex numbers
$\widetilde{M}_{ax,ay}^{(\mathrm{eq})}$	Equivalent intra-core mode-coupling function
$\boldsymbol{\mathcal{M}}$	Real representation of the magnetization field
$\widehat{\mathrm{M}}_{ax,ay}^{(\mathrm{eq})}$	Linear operator describing the function $\widetilde{M}_{ax,ay}^{(\mathrm{eq})}$ in time domain
$\mathbb{M}$	Arbitrary Abelian group

N

n Refractive index. Also, it may represent an integer (e.g. order of the radial variation of an LP mode)

$\widetilde{n}$ Isospectral refractive index. Also, Fourier transform of n

n_0 Inverse SUSY refractive index of n_1

n_1 Refractive index of the first SUSY optical system

n_2 Refractive index of the second SUSY optical system

n_{cl} Material refractive index of the cladding

n_{co} Material refractive index of the core

n_{eff} Effective refractive index

$n_{\mathrm{eff},n}^{(1)}$ Effective refractive index of the n-th TE mode in a bosonic dielectric slab

n_{HSC} Refractive index profile of the hyperbolic secant chain

n_m Refractive index of the m-th SUSY optical system in a SUSY chain. Also, material refractive index of core m. Also, refractive index profile of core m $[n_m(\boldsymbol{r})]$. Also, average value of the MCF principal refractive indexes

$\overline{n}_m$ Average value of the refractive index profile $n_m(\boldsymbol{r})$ in gradual-index cores

n_{mi} Principal refractive index associated to core m and principal axis i

$n_{mi,l,j,s}$ Principal refractive index n_{mi} in the l-th birefringent segment, j-th BTC and s-th Monte Carlo iteration

n_{MCF} Average value of the material refractive index of an MCF

n_{NL} Nonlinear changes induced in n_{MCF} by the nonlinear polarization

n_{S} Step-index profile. Also, spatial evolution of the refractive index profile of a heterogeneous time-varying optical medium

$\widetilde{n}_{\mathrm{S}}$ Fourier transform of n_{S}

n_{T} Temporal evolution of the refractive index profile of a heterogeneous time-varying optical medium

n_α Auxiliary refractive index

$n_\pm$ Limit of n at $x \to x_\pm$, with $x \in [x_-, x_+] \subseteq \overline{\mathbb{R}}$. In the main text, x_- and x_+ are usually denoted by the symbols a and b, respectively. These limits also apply to the time domain

$n_{1,\pm}$ Limit of n_1 at $x \to x_\pm$, with $x \in [x_-, x_+] \subseteq \overline{\mathbb{R}}$. In the main text, x_- and x_+ are usually denoted by the symbols a and b, respectively. These limits also apply to the time domain

$n_{2,\pm}$ Limit of n_2 at $x \to x_\pm$, with $x \in [x_-, x_+] \subseteq \overline{\mathbb{R}}$. In the main text, x_- and x_+ are usually denoted by the symbols a and b, respectively. These limits also apply to the time domain

$n_{m,\pm}$ Limit of n_m at $x \to x_\pm$, with $x \in [x_-, x_+] \subseteq \overline{\mathbb{R}}$. In the main text, x_- and x_+ are usually denoted by the symbols a and b, respectively. These limits also apply to the time domain

$n_m^{(\mathrm{eq})}$ Equivalent refractive index associated to core m

$n_{mi}^{(\mathrm{eq})}$ Equivalent refractive index associated to PCM mi

$n_{mi,l,j,s}^{(\mathrm{eq})}$ Equivalent refractive index $n_{mi}^{(\mathrm{eq})}$ in the l-th birefringent segment, j-th BTC and s-th Monte Carlo iteration

$n_{mni}^{(\mathrm{eff})}$ Effective principal refractive index of PCM mni, where m indicates the core, n is the n-th LP mode supported by core m, and i is a principal axis of core m

$n_{qrs}^{(i)}$ Order of the linear operator $\widehat{\mathrm{N}}_{qrs}^{(i)}$

$\widetilde{n}_1(\eta_1)$ One-parameter isospectral family of n_1

$\widetilde{n}_1(m_1,\eta_1)$ One-parameter isospectral family of n_1 generated from the $\mathrm{LP}_{m_1,n}^{(1)}$ mode using the one-parameter Darboux procedure

$\widetilde{n}_{1,\pm}(\eta_1)$ Limit of $\widetilde{n}_1(\eta_1)$ at $t \to \pm\infty$

$\widetilde{n}_1(\eta_1,\ldots,\eta_m)$ Multi-parameter isospectral family of n_1

$\widetilde{n}_{1,-}(\eta_1,\ldots,\eta_m)$ Limit of $\widetilde{n}_1(\eta_1,\ldots,\eta_m)$ at $t \to -\infty$ or $r \to 0$

$\widetilde{n}_{1,+}(\eta_1,\ldots,\eta_m)$ Limit of $\widetilde{n}_1(\eta_1,\ldots,\eta_m)$ at $t \to \infty$ or $r \to \infty$

N Integer. It may represent different parameters: number of cores, number of LP modes, or number of linear coupling terms in the dimensionless coupled local-mode equations, among other examples. Also, it may represent a complex constant. Also, ratio $n_-/n(t)$. Also, density of dipoles

$N_\pm$ Limit of $N(t)$ at $t \to \pm\infty$

$N^{(1)}$ Real constant accounting for the normalization of $\psi^{(1)}$

$N^{(2)}$ Real constant accounting for the normalization of $\psi^{(2)}$

N Normal distribution

N_a Integral of self-overlapping in core a

N_{ax} Integral of self-overlapping in PCM ax

N_{HSC} Number of fundamental periods in the hyperbolic secant chain

N_{L} Number of phase-matching points in the linear regime

N_m Number of birefringent segments in core m

N_{NL} Number of phase-matching points in the nonlinear regime

$\widetilde{N}_1(\eta_1)$ Function defined as the ratio $\widetilde{n}_{1,-}(\eta_1)/\widetilde{n}_1(\eta_1)$

$\mathcal{N}_{qrs,k}^{(i)}$ Complex-valued function describing k-th order nonlinear mode-coupling effects from ψ_q, ψ_r and ψ_s to ψ_i

$\widehat{\mathrm{N}}_{ax}^{(\mathrm{eq})}$ Linear operator modeling nonlinear propagation in PCM ax

$\widehat{\mathrm{N}}_{qrs}^{(i)}$ Linear operator accounting for nonlinear mode-coupling from ψ_q, ψ_r and ψ_s to ψ_i

$\aleph_0$ Aleph-zero

$\aleph_1$ Aleph-one

$\mathbb{N}$	The set of natural numbers
NA_a	Numerical aperture of core a
NA_b	Numerical aperture of core b

O

$\widehat{\mathcal{O}}$	Arbitrary linear operator

P

p	Arbitrary function. Also, arbitrary polynomial. Also, integer
p_{11}	Component of the photo-elastic tensor
p_{12}	Component of the photo-elastic tensor
$\boldsymbol{p}$	Photon linear momentum
$\widehat{\mathrm{p}}$	Linear momentum operator
P	Probability. Also, acoustic pressure
$\boldsymbol{P}$	Analytic representation of $\boldsymbol{\mathcal{P}}$
$\mathbf{P}$	Matrix of optical power
P_a	Optical power propagated in core a
$\overline{P}_a$	Average optical power propagated in core a
P_b	Optical power propagated in core b
$\overline{P}_b$	Average optical power propagated in core b
P_{C}	Critical power of the MCF or NLDC
P_i	Optical power propagated in core i
$P_{i,j}$	Coupled power from core j to core i
$P^{(1)}_{i,\omega_0}$	i-th component of the complex amplitude of $\boldsymbol{\mathcal{P}}^{(1)}$
$\widetilde{P}^{(1)}_{i,\omega_0}$	Fourier transform of $P^{(1)}_{i,\omega_0}$
$P^{(3)}_{i,\omega_0}$	i-th component of the complex amplitude of $\boldsymbol{\mathcal{P}}^{(3)}$
$\widetilde{P}^{(3)}_{i,\omega_0}$	Fourier transform of $P^{(3)}_{i,\omega_0}$
$P^{(3\mathrm{I})}_{i,\omega_0}$	Instantaneous (I) contribution of $P^{(3)}_{i,\omega_0}$
$P^{(3\mathrm{R})}_{i,\omega_0}$	Raman (R) contribution of $P^{(3)}_{i,\omega_0}$
P_j	Optical power propagated in core j
P_{L}	Power launched to the MCF
$P_{\mathrm{L},max}$	Maximum value of P_{L} where the nonlinear CPT provides a non-divergent solution
P_{mi}	Optical power propagated in PCM mi

$\widetilde{P}_{m,n}$	Acoustic pressure
P_{S}	Spatial evolution of the acoustic pressure
P_{T}	Total optical power propagated by the MCF. Also, temporal evolution of the acoustic pressure
$P_{\mathrm{TH}}^{(\mathrm{SBS})}$	Threshold power of the stimulated Brillouin scattering
$P_{\omega_0}^{(1)}$	Complex amplitude of $\boldsymbol{\mathcal{P}}^{(1)}$
$P_{\omega_0}^{(3)}$	Complex amplitude of $\boldsymbol{\mathcal{P}}^{(3)}$
$\boldsymbol{P}^{(1)}$	Analytic representation of $\boldsymbol{\mathcal{P}}^{(1)}$
$\boldsymbol{P}^{(3)}$	Analytic representation of $\boldsymbol{\mathcal{P}}^{(3)}$
$\boldsymbol{\mathcal{P}}$	Real representation of the polarization density
$\widetilde{\boldsymbol{\mathcal{P}}}$	Fourier transform of $\boldsymbol{\mathcal{P}}$
$\boldsymbol{\mathcal{P}}^{(1)}$	Real representation (or real wave function) of the linear polarization density
$\widetilde{\boldsymbol{\mathcal{P}}}^{(1)}$	Fourier transform of $\boldsymbol{\mathcal{P}}^{(1)}$
$\boldsymbol{\mathcal{P}}^{(3)}$	Real representation (or real wave function) of the third-order nonlinear polarization density
$\widetilde{\boldsymbol{\mathcal{P}}}^{(3)}$	Fourier transform of $\boldsymbol{\mathcal{P}}^{(3)}$
$\widetilde{\mathcal{P}}_a$	Spatial Fourier transform of the random process $\overline{P}_a$
$\widetilde{\mathcal{P}}_i^{(1)}$	i-th component of $\widetilde{\boldsymbol{\mathcal{P}}}^{(1)}$
$\widetilde{\mathcal{P}}_i^{(3)}$	i-th component of $\widetilde{\boldsymbol{\mathcal{P}}}^{(3)}$

Q

q	Nonlinear MCC $q^{(1)}$ [the super-index (1) is omitted when the MCCs $q^{(2,3,4)}$ can be neglected]. Also, arbitrary function. Also, arbitrary polynomial. Also, arbitrary real number. Also, integer. Also, elementary charge, i.e., magnitude of the electric charge carried by a single proton or electron
$\mathbf{q}$	Matrix of nonlinear MCCs
$q^{(1)}$	Nonlinear MCC describing nonlinear intra-core coupling in the same polarization axis. The super-index (1) indicates the intra-core nature of the mode-coupling and q indicates that the mode-coupling takes place in the same polarization axis
$q^{(2,3,4)}$	Nonlinear MCCs describing nonlinear inter-core coupling in the same polarization axis. The super-index ($i > 1$) indicates the inter-core nature of the mode-coupling and q indicates that the mode-coupling takes place in the same polarization axis
q_a	Nonlinear MCC $q^{(1)}$ associated to core a. The super-index (1) is omitted when the MCCs $q^{(2,3,4)}$ can be neglected
$\widetilde{q}^{(\mathrm{I,R})}$	Nonlinear MCC $q^{(1)}$ in frequency domain. The super-index (I) indicates the instantaneous nature of the nonlinear effects, and the super-index (R) indicates that the nonlinear effects are related to Raman response of the optical medium
$\hat{\mathrm{q}}^{(\mathrm{I,R})}$	Linear operators associated to $\widetilde{q}^{(\mathrm{I,R})}$ in time domain

Q	Number of optical carriers injected into the MCF at $z = 0$
$\mathrm{Q}^{\pm}$	Supercharges
$\mathrm{Q}_{\mathrm{D}}^{\pm}$	Supercharges associated to the second step of the one-parameter Darboux procedure

R

r	Radial coordinate in spherical or cylindrical coordinates
$\boldsymbol{r}$	Position vector
r_{L}	Modulus of $\boldsymbol{r}_{\mathrm{L}}$
$\boldsymbol{r}_{\mathrm{L}}$	Position vector parallel to the propagation direction of the electromagnetic energy
r_{N}	Normalized radial coordinate
$\boldsymbol{r}_{\mathrm{T}}$	Position vector transversal to the propagation direction of the electromagnetic energy
R_0	Core radius
$R_{0,a}$	Radius of core a
$R_{0,b}$	Radius of core b
$R_{0,mi}$	Length of the principal axis mi, where m indicates the core and i the principal axis
R_1	Reflection coefficient of the first SUSY system
$R_1(\eta_1)$	Reflection coefficient of $\widetilde{V}_1(\eta_1)$ potential
R_2	Reflection coefficient of the second SUSY system
R_a	Autocorrelation function of random process P_a
R_{B}	Bending radius
$\overline{R}_{\mathrm{B}}$	Average value of the bending radius
$R_{\mathrm{B},l}$	Bending radius in the l-th birefringent segment of the MCF
$R_{\mathrm{B},l,s}$	Core radius in the l-th birefringent segment and s-th Monte Carlo iteration
$R_{\mathrm{BT},m}$	Bending radius induced by the MCF twisting in core m
R_{HSC}	Reflection coefficient of the hyperbolic secant chain
R_m	Reflection coefficient of the m-th system in a SUSY chain
$R_{m_i,n}^{(i)}$	Radial dependence of $\Psi_{m_i,n}^{(i)}$
$R_n\left(\boldsymbol{a}_m\right)$	Reflection coefficient of $\widehat{\mathrm{H}}_n(\boldsymbol{a}_m)$
R_{pk}	Threshold value of the bending radius to separate the phase-matching and phase-mismatching regions
$\widetilde{R}_{m_i,n}^{(i)}\left(\eta_1\right)$	One-parameter isospectral family of $R_{m_i,n}^{(i)}$
$R^{(i)}$	Number of nonlinear terms which interact with the wave ψ_i
$R^{(X)}$	Autocorrelation function of random process X
$R_{b,a}^{(f)}$	Autocorrelation function of random process $f_{b,a}$

$\mathcal{R}_i$ Reflection coefficient associated to the electric or magnetic field strength of the i-th SUSY optical system

$\mathcal{R}^{(1)}$ Real-valued function to study the impact of the term $\nabla(\nabla\cdot\boldsymbol{\mathcal{P}}^{(1)})$ on the nonlinear wave equation of an SCF or MCF

$\mathcal{R}^{(3)}$ Real-valued function to study the impact of the term $\nabla(\nabla\cdot\boldsymbol{\mathcal{P}}^{(3)})$ on the nonlinear wave equation of an SCF or MCF

$\mathbb{R}$ The set of real numbers

$\overline{\mathbb{R}}$ The set of extended real numbers. Specifically, $\overline{\mathbb{R}} := \mathbb{R} \cup \{-\infty, +\infty\}$

$\mathbb{R}^+$ The set of positive real numbers. Specifically, $\mathbb{R}^+ := \{x \in \mathbb{R}/x > 0\}$

$\mathbb{R}^n$ n-ary Cartesian product of $\mathbb{R}$

S

sd Jacobi elliptic function

sgn Sign function

$\mathfrak{sl}\,(n, \mathbb{K})$ Special linear group of degree n over the field $\mathbb{K}$

S_a Cross-sectional area of core a. Also, power spectral density of random process P_a

S_b Cross-sectional area of core b

S_k Cross-sectional area of a given core k

S_{cl} Cross-sectional area of cladding

S_{T} Total cross-sectional area of an MCF

$S^{(X)}$ Power spectral density of random process X

$S_{b,a}^{(f)}$ Power spectral density of random process $f_{b,a}$

$\boldsymbol{\mathcal{S}}_{mi}$ Poynting vector associated to PCM mi

T

t Time variable

t_{N} Normalized time variable

T Subset of real numbers. Also, fundamental period of a wave. Also, temperature distribution

$\mathbf{T}$ Auxiliary Matrix accounting for the longitudinal evolution of $\mathbf{A}$ in a short MCF segment

$T_{a,a}$ Element of $\mathbf{T}$ matrix

$T_{a,b}$ Element of $\mathbf{T}$ matrix

T_{ab} Temporal separation between parallel TWGs

$T_{b,a}$ Element of $\mathbf{T}$ matrix

$T_{b,b}$ Element of $\mathbf{T}$ matrix

T_{B} Temporal width of a TWG

$T_{\mathrm{B},m}$ Temporal width of TWG m

T_1 Transmission coefficient of the first SUSY system

T_2 Transmission coefficient of the second SUSY system

T_m Transmission coefficient of the m-th system in a SUSY chain

$T_1(\eta_1)$ Transmission coefficient of $\widetilde{V}_1(\eta_1)$ potential

$T_n\left(\boldsymbol{a}_m\right)$ Transmission coefficient of $\widehat{\mathrm{H}}_n(\boldsymbol{a}_m)$

T_0 Fundamental period of the optical carrier

T_{eff} Effective temporal width

T_{FWHM} Full temporal width at half maximum of the peak power of an optical pulse

T_{HSC} Transmission coefficient of the hyperbolic secant chain

T_{P} Pulse width, defined in this work as the full-width at $1/\left(2e\right)$ of the peak power

Tr Trace of a matrix

$\mathcal{T}$ Temporal evolution of $\mathcal{U}$

$\mathcal{T}_i$ Transmission coefficient associated to the electric or magnetic field strength of the i-th SUSY optical system

$\mathcal{T}_{\mathrm{HSC}}$ Fundamental period of the hyperbolic secant chain

U

u Heaviside step function. Also, anisotropic Raman response. Also, independent variable associated to U random variable. Also, complex-valued function used to introduce the Darboux transformation and the concept of bound states in the continuum in Chapter 6

u_0 Oscillatory function at energy E_0

$\widetilde{u}_0\left(\eta_1\right)$ Bound state in the continuum generated from u_0 at energy E_0 by using the Darboux procedure

$\widetilde{u}_{0,\pm}\left(\eta_1\right)$ Limit of $\widetilde{u}_0\left(\eta_1\right)$ at $x \to x_{\pm}$, with $x \in [x_-, x_+] \subseteq \overline{\mathbb{R}}$. In the main text, x_- and x_+ are usually denoted by the symbols a and b, respectively. These limits also apply to the time domain

u_1 Oscillatory function at energy E_1

$\widetilde{u}_1(\eta_1)$ Bound state in the continuum generated from u_1 at energy E_1 by using the Darboux procedure

u_{mi} Modal parameter associated to PCM mi

$u_{mi,l,j,s}$ Modal parameter associated to PCM mi in the l-th birefringent segment, j-th BTC and s-th Monte Carlo iteration

u_{mn} Radial evolution of Ψ_{mn}

u_n Modal parameter of core n. Also, modal parameter of a TWG

u_{nl} Radial evolution of Ψ_{nlm}

$u^{(1)}$ Wave function of the first SUSY system

$u^{(2)}$ Wave function of the second SUSY system

$\hat{u}_i$ Unit vector associated to the i axis

$\hat{u}_{\mathrm{L}}$ Unit vector parallel to the propagation direction of the electromagnetic energy

U Auxiliary random variable to study the linear and nonlinear IC-XT with the MCF operating in multi-core excitation. Also, spatial evolution of $\mathcal{U}$

$\mathcal{U}$ Arbitrary scalar field

V

v Complex- or real-valued function used to introduce the Darboux transformation in Chapter 6

v_{B} Speed of a TWG

V Normalized frequency in Part I. Quantum potential in Part II

$V^{(3\mathrm{D})}$ Three-dimensional quantum potential

V_0 Inverse SUSY potential of V_1

V_1 Quantum potential of the first SUSY system

$V_1^{(3\mathrm{D})}$ Three-dimensional potential

$\widetilde{V}_1$ Family of isospectral potentials of V_1

$\widetilde{V}_1(\eta_1)$ One-parameter isospectral family of V_1

$\widetilde{V}_1(\eta_1, \eta_2)$ Two-parameter isospectral family of V_1

$\widetilde{V}_1(\eta_1, \ldots, \eta_n)$ Multi-parameter isospectral family of V_1

$\widetilde{V}_1^{(3\mathrm{D})}(\eta_1)$ One-parameter isospectral family of $V_1^{(3\mathrm{D})}$

V_2 Quantum potential of the second SUSY system

$\widetilde{V}_2(\eta_1)$ One-parameter isospectral family of V_2

$\widetilde{V}_2(\eta_2)$ One-parameter isospectral family of V_2 generated in the two-parameter Darboux procedure (see Fig. 6.8)

$V_i^{(1\mathrm{D})}$ One-dimensional potential associated to the i-th SUSY system

$V_i^{(3\mathrm{D})}$ Three-dimensional potential associated to the i-th SUSY system

$V_{ik}^{(2)}$ Quantum potential associated to $\widehat{\mathrm{H}}_{ik}^{(2)}$

V_k Quantum potential of the k-th system in a SUSY chain

$V_{k,\pm}$ Limit of V_k function at $x \to x_\pm$, with $x \in [x_-, x_+] \subseteq \overline{\mathbb{R}}$. In the main text, x_- and x_+ are usually denoted by the symbols a and b, respectively. These limits also apply to the time domain

$\overline{V}_k$ Energy-shifted potential of V_k

V_{mi} Normalized frequency in PCM mi

$V_n\left(\boldsymbol{a}_m\right)$ n-th potential of a SUSY chain constructed using SIP

$V_{n,\pm}\left(\boldsymbol{a}_m\right)$ Limit of $V_n\left(\boldsymbol{a}_m\right)$ at $x \to x_\pm$, with $x \in [x_-, x_+] \subseteq \overline{\mathbb{R}}$. In the main text, x_- and x_+ are usually denoted by the symbols a and b, respectively. These limits also apply to the time domain

$\mathcal{V}$ Arbitrary vector space

$\mathcal{V}^*$ Dual vector space of $\mathcal{V}$

$\mathcal{V}_{\overline{0}}$ Vector space of bosons

$\mathcal{V}_{\overline{1}}$ Vector space of fermions

W

w Independent variable associated to random variable W

$w_{mi,l,j,s}$ Modal parameter associated to PCM mi in the l-th birefringent segment, j-th BTC and s-th Monte Carlo iteration

w_n Modal parameter of core n. Also, modal parameter of a TWG

W Superpotential. Also, auxiliary random variable to study the linear and nonlinear IC-XT with the MCF operating in multi-core excitation

$W_\pm$ Limit of W function at $x \to x_\pm$, with $x \in [x_-, x_+] \subseteq \overline{\mathbb{R}}$. In the main text, x_- and x_+ are usually denoted by the symbols a and b, respectively. These limits also apply to the time domain

$W\left(\boldsymbol{a}_m\right)$ Superpotential connecting SIP superpartners

$W_\pm\left(\boldsymbol{a}_m\right)$ Limit of $W\left(\boldsymbol{a}_m\right)$ at $x \to x_\pm$, with $x \in [x_-, x_+] \subseteq \overline{\mathbb{R}}$. In the main text, x_- and x_+ are usually denoted by the symbols a and b, respectively. These limits also apply to the time domain

$W_{\mathrm{D}}\left(\eta_1\right)$ Superpotential associated to the second step of the one-parameter Darboux procedure

W_{k-1} Superpotential connecting $\widehat{\mathrm{H}}_{k-1}$ and $\widehat{\mathrm{H}}_k$ in a SUSY chain. Also, component of $\boldsymbol{W}$ in 2D SUSY QM

$W_{k-1,\pm}$ Limit of W_{k-1} function at $x \to x_\pm$, with $x \in [x_-, x_+] \subseteq \overline{\mathbb{R}}$. In the main text, x_- and x_+ are usually denoted by the symbols a and b, respectively. These limits also apply to the time domain

$W_{(m)}$ Superpotential connecting the SUSY systems $\widehat{\mathrm{H}}_1 - E_m^{(1)}$ and $\widehat{\mathrm{H}}_2 - E_m^{(1)}$

$\boldsymbol{W}$ Vector superpotential in 2D SUSY QM

W_{I} Imaginary part of the superpotential

W_{R} Real part of the superpotential

$\widetilde{W}$ Family of superpotentials

$\widetilde{W}(\eta_1)$ Superpotential connecting $\widetilde{V}_1(\eta_1)$ and V_2

$\widetilde{W}_\pm(\eta_1)$ Limit of $\widetilde{W}(\eta_1)$ at $x \to x_\pm$, with $x \in [x_-, x_+] \subseteq \overline{\mathbb{R}}$. In the main text, x_- and x_+ are usually denoted by the symbols a and b, respectively. These limits also apply to the time domain

$\mathcal{W}$ Arbitrary vector space. Also, Wronskian

$\mathscr{W}$ Temporal window function

X

x	Position coordinate
$\boldsymbol{x}$	Arbitrary vector. Also, position vector in Cartesian coordinates
$\mathbf{x}$	Arbitrary vector used to introduce the preliminary mathematical concepts of SUSY in Chapter 6
$\mathbf{x}^*$	Dual vector of $\mathbf{x}$
x_1	Independent variable associated to dimensionless coupled local-mode equations
x_2	Independent variable associated to dimensionless coupled local-mode equations
$\mathbf{x}_1$	Arbitrary vector used to introduce the preliminary mathematical concepts of SUSY in Chapter 6
$\mathbf{x}_2$	Arbitrary vector used to introduce the preliminary mathematical concepts of SUSY in Chapter 6
$x_{i,j}$	Independent variable associated to $X_{i,j}$
x_{L}	Independent variable associated to $X_{a,b}^{\mathrm{L}}$
x_{N}	Normalized x coordinate
x_{NL}	Independent variable associated to $X_{a,b}^{\mathrm{NL}}$
x_{R}	Positive-real value of reference
x_{s}	Singular point of a quantum potential
X	Random variable or random process. Also, auxiliary function
X_i	Auxiliary random variable
$X_{i,j}$	Random variable accounting for the linear and nonlinear IC-XT from core j to core i
$X_{a,b}^{\mathrm{L}}$	Random variable accounting for the linear IC-XT from core b to core a
$X_{a,b}^{\mathrm{NL}}$	Random variable accounting for the nonlinear IC-XT from core b to core a
$XT_{a,b}$	Crosstalk from core b to core a

Y

y	Position coordinate. Also, independent variable associated to random variable Y. Also, real or complex number
$\mathbf{y}$	Arbitrary vector used to introduce the preliminary mathematical concepts of SUSY in Chapter 6
y_1	Particular solution of a second-order ODE
y_2	Particular solution of a second-order ODE
y_{G}	General solution of a second-order ODE
Y	Random variable accounting for the linear and nonlinear IC-XT with the MCF operating in multi-core excitation
Y_m	m-order Bessel function of the second kind

Z

z	Position coordinate. Also, real or complex number
z	Position coordinate which describes the longitudinal evolution of an optical pulse inside a TWG using a co-moving reference frame
$\mathbf{z}$	Arbitrary vector used to introduce the preliminary mathematical concepts of SUSY in Chapter 6
z_0	Point of the z axis
z_1	Point of the z axis
z_2	Point of the z axis
z_l	Point of the z axis
z_{l+1}	Point of the z axis
z_{N}	Normalized z coordinate
$\mathrm{z_P}$	Discrete variable accounting for the phase-matching points along the MCF length. Also, location of a fiber perturbation in the z axis
z_{PM}	Point of the z axis where $\Delta n_{b,a}^{(\mathrm{eq})} = 0$
$z_{i,j}$	Independent variable associated to random variable $Z_{i,j}$
$Z_{i,j}$	Auxiliary random variable to study the linear and nonlinear IC-XT with the MCF operating in multi-core excitation
$\mathbb{Z}$	The set of integer numbers
$\mathbb{Z}_2$	Group of integers modulo 2
$\mathbb{Z}/\mathbb{Z}_2$	Finite cyclic group modulo 2

Greek Symbols

α

α	Power attenuation coefficient of the MCF. Also, positive real number. Also, arbitrary scalar. Also, energy shift
α_1	Arbitrary scalar used to introduce the preliminary mathematical concepts of SUSY in Chapter 6
α_2	Arbitrary scalar used to introduce the preliminary mathematical concepts of SUSY in Chapter 6
$\alpha^{(0)}$	Power attenuation coefficient at the angular frequency of the optical carrier
$\alpha^{(1)}$	First-order derivative of the power attenuation coefficient as a function of the angular frequency
$\widehat{\alpha}$	Linear operator associated to the power attenuation coefficient α in time domain

$\boldsymbol{\beta}$

β	Phase constant. Also, arbitrary scalar
β_{av}	Average value of the phase constant of the quasi-degenerate true modes in a given LP mode group
β_{B}	Perturbation of the phase constant β over which a TWG is constructed
$\beta_{\mathrm{B},m}$	Temporal profile of TWG m
β_{B1}	Temporal perturbation associated to a bosonic T-SUSY TWG
β_{B2}	Temporal perturbation associated to a fermionic T-SUSY TWG
$\beta_{\mathrm{B},k}$	k-th partial derivative of β_{B} as a function of the angular frequency
β_{cl}	Phase constant of the fundamental mode of a spatial waveguide in the cladding region
β_{co}	Phase constant of the fundamental mode of a spatial waveguide in the core region
β_m	In Part I, ideal phase constant of $\mathcal{E}_m$. In Part II, this symbol indicates the m-th partial derivative of the phase constant β as a function of the angular frequency
$\beta^{(m)}$	m-th partial derivative of the phase constant β as a function of the angular frequency (the order of the partial derivative is indicated using a superindex in Part I)
$\beta_m^{(\mathrm{B+S})}$	Perturbation of the ideal phase constant of $\mathcal{E}_m$
$\beta_m^{(\mathrm{eq})}$	Equivalent phase constant of $\mathcal{E}_m$
β_{mi}	Ideal phase constant of $\mathcal{E}_{mi}$
$\beta_{mi}^{(\mathrm{B+S})}$	Perturbation of the ideal phase constant of $\mathcal{E}_{mi}$
$\beta_{mi}^{(\mathrm{eq})}$	Equivalent phase constant of $\mathcal{E}_{mi}$
$\beta_{mi,l,j,s}^{(\mathrm{eq})}$	Equivalent phase constant $\beta_{mi}^{(\mathrm{eq})}$ in the l-th birefringent segment, j-th BTC and s-th Monte Carlo iteration
$\beta_{mi,\omega_0}^{(\mathrm{eq})}$	Equivalent phase constant of $\mathcal{E}_{mi}$ at the angular frequency of the optical carrier ω_0
$\beta_{mi,\omega_0}^{(\mathrm{eq})(k)}$	k-th partial derivative of $\beta_{mi,\omega_0}^{(\mathrm{eq})}$ as a function of the angular frequency
$\beta_{m,n}$	Phase constant of the $\mathrm{LP}_{m,n}$ group
β_{mn}	Phase function of Ψ_{mn}
$\beta_{m_i,n}^{(i)}$	Phase constant of the $\mathrm{LP}_{m_i,n}$ group in the i-th SUSY optical system

$\boldsymbol{\gamma}$

γ	Nonlinear coefficient of the MCF. Also, free-parameter associated to $E_{m,n}^{(\mathrm{3D})}$ and $V^{(\mathrm{3D})}$. Also, separation constant
γ_{I}	Nonlinear parameter associated to the instantaneous (I) response of the nonlinear polarization
γ_{R}	Nonlinear parameter associated to the Raman (R) response of the nonlinear polarization
Γ	Auxiliary parameter of the NLDC. Also, Gamma function

δ

δ	Dirac delta function. Also, incremental operator
δ_{ij}	Kronecker delta function
δn	Increment of the refractive index
$\delta n_{m,l,s}$	Variance of the intrinsic linear birefringence in core m, l-th birefringent segment and s-th Monte Carlo iteration
δt	Increment of the t variable
δ_t	Linear operator performing an increment of a function in the t variable
δx_i	Increment of the x_i variable
δz	Increment of the z variable
δ_z	Linear operator performing an increment of a function in the z variable
Δ	Incremental operator
Δb_n	Increment of the normalized phase constant
ΔE	Energy shift
$\Delta\mathrm{EVM}_{\mathrm{B2B}}$	Excursion of the $\mathrm{EVM}_{\mathrm{E2E}}$ induced by the B2B (back-to-back) transmission
$\Delta\mathrm{EVM}_{\mathrm{IC\text{-}XT}}$	Excursion of the $\mathrm{EVM}_{\mathrm{E2E}}$ induced by the IC-XT
$\Delta K_{b,a}$	Phase-mismatching between the ground states of TWG a and TWG b
Δn	Intrinsic linear birefringence
$\Delta n_{b,a}$	Material refractive index difference between core a and b
$\Delta n_{b,a}^{(\mathrm{eq})}$	Equivalent refractive index difference between core a and b
Δn_{eff}	Increment of n_{eff}
$\Delta n_{m,j}$	Longitudinal average value of the intrinsic linear birefringence in core m the j-th BTC
$\langle \Delta n_{m,j} \rangle$	Temporal average value of $\Delta n_{m,j}$
Δt	Temporal increment or temporal width of an event
$\Delta T_{m,\omega_0}^{(\mathrm{G})}$	DGD of the LP_{01} mode in core m at ω_0
$\Delta\beta$	Phase-mismatching
$\Delta\beta_1$	Design parameter of a TWG defined as $\Delta\beta_1 := \beta_1 - 1/v_{\mathrm{B}}$
$\Delta\beta_1^{(i)}$	Design parameter $\Delta\beta_1$ of the i-th T-SUSY TWG
$\Delta\beta_{b,a}$	Ideal phase-mismatching between the fundamental mode of cores a and b
$\Delta\beta_{b,a}^{(\mathrm{B+S})}$	Phase-mismatching between the fundamental mode of cores a and b induced by the MCF perturbations
$\Delta\beta_{b,a}^{(\mathrm{eq})}$	Equivalent phase-mismatching between the fundamental mode of cores a and b
$\Delta\beta_{b,a}^{(\mathrm{S})}$	Phase-mismatching between the fundamental mode of cores a and b induced by the structural perturbations of the MCF

$\Delta\beta_{bx,ax}^{(\mathrm{eq})(k)}$	k-th partial derivative of the equivalent phase-mismatching $\Delta\beta_{bx,ax}^{(\mathrm{eq})}$ as a function of the angular frequency
$\Delta\varepsilon_{\mathrm{r},a}$	Electric permittivity difference between core a and cladding
$\Delta\varepsilon_{\mathrm{r},b}$	Electric permittivity difference between core b and cladding
$\Delta\varepsilon_{\mathrm{r},mi}$	Electric permittivity difference between PCM mi and cladding
$\Delta\widetilde{\varepsilon}_{\mathrm{r},mi}$	Fourier transform of $\Delta\varepsilon_{\mathrm{r},mi}$
$\Delta\phi_{b,a}$	Phase-mismatching between the fundamental mode of cores a and b including the medium perturbations
$\Delta\phi_{mi,nj}$	Phase-mismatching between PCM mi and PCM nj, where $(mi,nj) \in \{ax,ay,bx,by\}^2$
$\Delta\phi_{mi,nj}^{(0)}$	Phase-mismatching at ω_0 between PCM mi and PCM nj, where $(mi,nj) \in \{ax,ay,bx,by\}^2$
$\Delta\nu$	Normalized phase-matching bandwidth
$\Delta\tau_{\mathrm{G}}$	DMGD between different LP modes groups
$\Delta\chi^{(1)}$	Increment in the first-order electric susceptibility

ϵ

ε_0	Electric permittivity in vacuum
ε_{r}	Relative electric permittivity of MCF
$\varepsilon_{\mathrm{r},\pm}$	Limit of ε_{r} at $x \to \pm\infty$ or $t \to \pm\infty$
$\widetilde{\varepsilon}_{\mathrm{r}}$	Fourier transform of the relative electric permittivity
$\varepsilon_{\mathrm{r},c}$	Relative electric permittivity in cladding
$\varepsilon_{\mathrm{r},ci}$	Relative electric permittivity in cladding and polarization i
$\widetilde{\varepsilon}_{\mathrm{r},ci}$	Fourier transform of $\varepsilon_{\mathrm{r},ci}$
$\varepsilon_{\mathrm{r},i}$	Relative electric permittivity in polarization i of the MCF
$\widetilde{\varepsilon}_{\mathrm{r},i}$	Fourier transform of $\varepsilon_{\mathrm{r},i}$
$\varepsilon_{\mathrm{r},m}$	Relative electric permittivity in core m
$\varepsilon_{\mathrm{r},mi}$	Relative electric permittivity in core m and polarization i
$\widetilde{\varepsilon}_{\mathrm{r},mi}$	Fourier transform of $\varepsilon_{\mathrm{r},mi}$
ε_{T}	Temporal evolution of $\boldsymbol{\epsilon}_{\mathrm{r}}$
ϵ_{ik}	Levi-Civita tensor
$\boldsymbol{\epsilon}_{\mathrm{r}}$	Relative electric permittivity tensor
$\boldsymbol{\epsilon}_{\mathrm{S}}$	Spatial evolution of $\boldsymbol{\epsilon}_{\mathrm{r}}$

ζ

ζ	Real constant accounting for the dielectric losses in Lorentz's model

$\boldsymbol{\eta}$

η	Auxiliary parameter of the CMT of parallel TWGs
$\widetilde{\eta}$	Auxiliary complex-valued function associated to H_{ax} and H_{bx}
η_0	Intrinsic impedance in vacuum
η_1	Isospectral parameter
$\widetilde{\eta}^{(1)}$	First-order derivative of $\widetilde{\eta}$ as a function of the angular frequency in baseband
η_m	Intrinsic impedance in core m. Also, m-th isospectral parameter
$\eta_{ax,by}$	Linear MCC describing linear coupling from PCM by to PCM ax

$\boldsymbol{\theta}$

θ	Angle in a spherical coordinate system
θ_+	Angle of the transmitted wave
θ_-	Angle of the incident wave
θ_0	Offset of the twist angle of the MCF reference axis at $z = 0$
θ_m	Offset of the twist angle of core m measured from the MCF reference axis
Θ	Complex-valued function accounting for the angular dependence of $\widetilde{\Psi}_0(\eta_1)$. Also, misalignment angle between $\boldsymbol{P}^{(1)}_{\omega_0}$ and $\boldsymbol{E}_{\omega_0}$
Θ_{lm}	Angular evolution of Ψ_{nlm}
Θ_n	Spatial evolution of an optical pulse propagating inside a TWG

$\boldsymbol{\kappa}$

κ	Linear MCC describing inter-core linear coupling
$\kappa_{a,b}$	Linear MCC describing linear coupling from core b to core a
$\kappa^{(\mathrm{eq})}_{a,b}$	Equivalent linear MCC of $\kappa_{a,b}$
$\kappa_{ax,bx}$	Linear MCC describing linear coupling from PCM bx to PCM ax
$\widetilde{\kappa}_{ax,bx}$	Linear MCC describing linear coupling from PCM bx to PCM ax in frequency domain

$\boldsymbol{\lambda}$

λ	Wavelength. Also, eigenvalue in Part II
λ_0	Wavelength of the optical carrier in vacuum. Also, eigenvalue of reference associated to the Darboux transformation
$\lambda^{(1)}$	Eigenvalue of the first SUSY system
$\lambda^{(2)}$	Eigenvalue of the second SUSY system
$\lambda_{\mathrm{C},m}$	Cut-off wavelength of core m
λ_m	Wavelength of the optical carrier in core m
$\overline{\lambda}_m$	Wavelength of the optical carrier associated to $\overline{n}_m$

$\boldsymbol{\mu}$

μ	Mean
μ_0	Magnetic permeability in vacuum
μ_{L}	Mean of the linear IC-XT
μ_{NL}	Mean of the nonlinear IC-XT
$\mu_{\nu,\xi}$	Crosstalk mean from PCM ξ to PCM ν, with $(\nu,\xi) \in \{ax, ay, bx, by\}^2$
$\widetilde{\mu}_{\mathrm{r}}$	Fourier transform of the relative magnetic permeability
μ_{T}	Temporal evolution of $\boldsymbol{\mu}_{\mathrm{r}}$
$\boldsymbol{\mu}_{\mathrm{r}}$	Relative magnetic permeability tensor
$\boldsymbol{\mu}_{\mathrm{S}}$	Spatial evolution of $\boldsymbol{\mu}_{\mathrm{r}}$

$\boldsymbol{\nu}$

ν	Normalized frequency in Part II

$\boldsymbol{\xi}$

ξ	MCF parameter accounting for the average value of $\delta n_{m,l,s}$ due to manufacturing imperfections. Also, real constant
$\xi^{(1,2)}$	Non-vanishing real constants accounting for the normalization of the LP modes in SUSY fibers

$\boldsymbol{\rho}$

ρ	Real and analytic representation of the total charge density (the context should avoid any confusion between the real and analytic representation). Also, auxiliary parameter of the NLDC. Also, positive-real constant used to estimate the nonlinear IC-XT. Also, static mass density in acoustics
$\widetilde{\rho}$	Fourier transform of ρ
ρ_{b}	Real and analytic representation of the bound charges. The context should avoid any confusion between the real and analytic representation
ρ_{c}	Real and analytic representation of the electric charge density associated to $\boldsymbol{J}_{\mathrm{c}}$. The context should avoid any confusion between the real and analytic representation
ρ_{f}	Real and analytic representation representation of the free charges. The context should avoid any confusion between the real and analytic representation

$\boldsymbol{\sigma}$

σ	Electric conductivity. Also, auxiliary parameter of the NLDC. Also, circular birefringence of the MCF. Also, real function
$\widetilde{\sigma}$	Fourier transform of the MCF circular birefringence
σ^2	Variance
σ_c	Circular birefringence in cladding

$\widetilde{\sigma}_c$ Fourier transform of σ_c

σ_{L}^2 Variance of the linear IC-XT

σ_m Circular birefringence in core m

$\widetilde{\sigma}_m$ Fourier transform of σ_m

σ_{NL}^2 Variance of the nonlinear IC-XT

σ_{T} Temporal evolution of $\boldsymbol{\sigma}$

$\boldsymbol{\sigma}$ Electric conductivity tensor

$\boldsymbol{\sigma}_{\mathrm{S}}$ Spatial evolution of $\boldsymbol{\sigma}$

$\boldsymbol{\tau}$

τ Time variable. Also, real function. Also, position coordinate which describes the temporal evolution of an optical pulse inside a TWG using a co-moving reference frame

$\tau_{\mathrm{G},01}^{(a)}$ Group delay of the LP_{01} mode in core a

τ_i Constant associated to Raman response. The subindex i is an integer

$\tau_{m,n}$ Normalized group delay of the LP_{mn} mode group

$\boldsymbol{\upsilon}$

υ Spatial frequency

$\boldsymbol{\phi}$

ϕ Scalar-valued function. Also, angle in a spherical coordinate system. Also, acoustic potential

ϕ_0 Auxiliary parameter of the NLDC

$\phi_{\widetilde{\boldsymbol{\mathcal{E}}}}$ Phase of $\widetilde{\boldsymbol{\mathcal{E}}}$

ϕ_m Real phase function involving the longitudinal and temporal medium perturbations in core m

ϕ_{mi} Real phase function involving the longitudinal and temporal medium perturbations in core m and polarization i

ϕ_{mi,ω_0} Phase function ϕ_{mi} at the angular frequency of the optical carrier ω_0

$\phi_{mi,l,j,s}$ Real phase function ϕ_{mi} in the l-th birefringent segment, j-th BTC and s-th Monte Carlo iteration

$\widetilde{\phi}_{m,n}$ Fourier transform of the acoustic velocity potential associated to an acoustic mode with azimuthal order m and radial order n

$\phi_{qrs}^{(i)}$ Real-valued phase function

Φ Phase shift. Also, complex phase function including the power attenuation and the fiber perturbations

$\boldsymbol{\Phi}$ Vector-valued function accounting for the spatial evolution of an electromagnetic field

$\boldsymbol{\Phi}_{\mathcal{D}}$ Spatial evolution of $\boldsymbol{\mathcal{D}}$

$\boldsymbol{\Phi}_{\mathcal{E}}$ Spatial evolution of $\boldsymbol{\mathcal{E}}$

Φ_{T_2} Phase of T_2

Φ_{R_2} Phase of R_2

Φ_{mi} Complex phase function including the real phase function ϕ_{mi} and the power attenuation coefficient of the MCF

$\Phi_{T_{\mathrm{HSC}}}$ Phase of T_{HSC}

$\Phi_1(\eta_1)$ Non-normalizable solution of $\widehat{\mathrm{H}}_2$ at energy $E_0^{(1)}$

$\Phi_2(\eta_2)$ Non-normalizable solution of $\widehat{\mathrm{H}}_3$ at energy $E_0^{(2)}$

$\Phi_i(\eta_i)$ Non-normalizable solution of $\widehat{\mathrm{H}}_{i+1}$ at energy $E_0^{(i)}$

$\Phi_i(\eta_i, \ldots, \eta_n)$ Non-normalizable solution of $\widetilde{V}_{i+1}(\eta_{i+1}, \ldots, \eta_n)$ at energy $E_0^{(i)}$

$\Phi_1(\eta_1, \eta_2)$ Non-normalizable solution of $\widetilde{V}_2(\eta_2)$ at energy $E_0^{(1)}$

φ

φ Temporal evolution of an electromagnetic field

φ_m Phase of A_m

χ

$\chi^{(1)}$ First-order electric susceptibility tensor

$\chi_{a,b}$ Linear MCC describing linear coupling from core b to core a

$\chi_{ax,bx}$ Linear MCC describing linear coupling from PCM bx to PCM ax

$\widetilde{\chi}^{(1)}$ Fourier transform of the first-order electric susceptibility

$\chi_{xx}^{(1)}$ Element of the first-order electric susceptibility tensor

$\chi_{ij}^{(1)}$ Element of the first-order electric susceptibility tensor

$\widetilde{\chi}_{ij}^{(1)}$ Fourier transform of $\chi_{ij}^{(1)}$

χ_{NL} Nonlinear coefficient

χ_4^2 Chi-squared distribution

$\chi_{xxxx}^{(3)}$ Element of the third-order electric susceptibility tensor

$\chi_{ijkl}^{(3)}$ Element of the third-order electric susceptibility tensor

$\chi_{ijkl}^{(3\mathrm{I})}$ Element of the third-order electric susceptibility tensor associated to the instantaneous (I) response of the nonlinear polarization

$\chi_{ijkl}^{(3\mathrm{R})}$ Element of the third-order electric susceptibility tensor associated to the Raman (R) response of the nonlinear polarization

$\boldsymbol{\chi}^{(1)}$ First-order electric susceptibility tensor

$\widetilde{\boldsymbol{\chi}}^{(1)}$ Fourier transform of $\boldsymbol{\chi}^{(1)}$

$\boldsymbol{\psi}$

ψ	Wave function. Also, scalar-valued function
$\psi_{\pm}$	Limit of ψ function at $x \to x_{\pm}$, with $x \in [x_-, x_+] \subseteq \overline{\mathbb{R}}$. In the main text, x_- and x_+ are usually denoted by the symbols a and b, respectively. These limits also apply to the time domain
$\psi_{\mathcal{D}}$	Temporal evolution of $\boldsymbol{\mathcal{D}}$
$\psi_{\mathcal{E}}$	Temporal evolution of $\boldsymbol{\mathcal{E}}$
ψ_E	Wave function of a quantum system with energy E
ψ_i	Arbitrary wave function associated to dimensionless coupled local-mode equations
ψ_n	n-th bound state of a quantum potential, spatial waveguide or temporal waveguide. Also, arbitrary wave function associated to dimensionless coupled local-mode equations
ψ_q	Arbitrary wave function associated to dimensionless coupled local-mode equations
ψ_r	Arbitrary wave function associated to dimensionless coupled local-mode equations
ψ_s	Arbitrary wave function associated to dimensionless coupled local-mode equations
$\psi_{\mathrm{I}}^{(1,2)}$	Incident wave of the temporal scattering problem in both superpartners
$\psi_{\mathrm{R}}^{(1,2)}$	Reflected wave of the temporal scattering problem in both superpartners
$\psi_{\mathrm{T}}^{(1,2)}$	Transmitted wave of the temporal scattering problem in both superpartners
ψ_0	Ground state wave function
$\psi^{(1)}$	Wave function of the first SUSY system
$\psi^{(2)}$	Wave function of the second SUSY system
$\psi^{(3)}$	Wave function associated to $\widehat{\mathrm{H}}^{(3)}$ in 2D SUSY QM
$\psi_0^{(1)}$	Ground state of the first SUSY system
$\psi_0^{(2)}$	Ground state of the second SUSY system
$\psi_n^{(1)}$	Bound state of the first SUSY system with n nodes
$\psi_n^{(2)}$	Bound state of the second SUSY system with n nodes
$\psi_{0,\pm}^{(1)}$	Limit of $\psi_0^{(1)}$ function at $x \to x_{\pm}$, with $x \in [x_-, x_+] \subseteq \overline{\mathbb{R}}$. In the main text, x_- and x_+ are usually denoted by the symbols a and b, respectively. These limits also apply to the time domain
$\psi_{0,\pm}^{(2)}$	Limit of $\psi_0^{(2)}$ function at $x \to x_{\pm}$, with $x \in [x_-, x_+] \subseteq \overline{\mathbb{R}}$. In the main text, x_- and x_+ are usually denoted by the symbols a and b, respectively. These limits also apply to the time domain
$\psi_{0,\mathrm{eq}}^{(1)}$	Ground state of $\widehat{\mathrm{H}}_{1,\mathrm{eq}}$
$\psi_{0,\mathrm{eq}}^{(2)}$	Ground state of $\widehat{\mathrm{H}}_{2,\mathrm{eq}}$
$\psi_{n,\mathrm{eq}}^{(1)}$	Bound state of $\widehat{\mathrm{H}}_{1,\mathrm{eq}}$ with n nodes

$\psi_{n,\mathrm{eq}}^{(2)}$	Bound state of $\widehat{\mathrm{H}}_{2,\mathrm{eq}}$ with n nodes
$\psi_0^{(i)}$	Ground state of the i-th system in a SUSY chain
$\psi_n^{(k)}$	Bound state of $\widehat{\mathrm{H}}_k$ with n nodes
$\psi_\lambda^{(1)}$	Eigenfunction of an EVP associated to the eigenvalue λ
$\psi_\lambda^{(2)}$	Eigenfunction of an EVP associated to the eigenvalue λ
$\psi_{\lambda_0}^{(1)}$	Eigenfunction of an EVP associated to the eigenvalue λ_0
$\psi_E^{(1)}$	Wave function of the first SUSY system with energy E
$\psi_E^{(2)}$	Wave function of the second SUSY system with energy E
$\psi_{m_i,n}^{(i)}$	Radial dependence of $\Psi_{m_i,n}^{(i)}$ connected to $R_{m_i,n}^{(i)}$ as $\psi_{m_i,n}^{(i)}(r) := \sqrt{r} R_{m_i,n}^{(i)}(r)$
$\psi_{m_i,n,-}^{(i)}$	Limit of $\psi_{m_i,n}^{(i)}$ at $r \to 0$
$\psi_{m_i,n,+}^{(i)}$	Limit of $\psi_{m_i,n}^{(i)}$ at $r \to \infty$
$\psi_k^{(n)}(\boldsymbol{a}_m)$	k-th bound state of the n-th system of a SUSY chain constructed using SIP
$\psi^{(n)}(\boldsymbol{a}_m)$	Wave function of the n-th system of a SUSY chain constructed using SIP
$\widetilde{\psi}_0^{(1)}(\eta_1)$	Ground state of $\widetilde{V}_1(\eta_1)$
$\widetilde{\psi}_n^{(1)}(\eta_1)$	Bound state of $\widetilde{V}_1(\eta_1)$ with n nodes
$\widetilde{\psi}_{m,n}$	Quantum wave function
Ψ	Three-dimensional quantum wave function
Ψ_n	Two-dimensional mode profile distribution of a guided mode of a rectangular waveguide. Also, temporal evolution of an optical pulse propagating inside a TWG
Ψ_{mn}	Three-dimensional bound state associated to a 3D potential with axial symmetry
Ψ_{nlm}	Three-dimensional bound state associated to a 3D potential with radial symmetry
$\Psi_{m_i,n}^{(i)}$	Transversal component of $\widetilde{\boldsymbol{\mathcal{E}}}_{m_i,n}^{(i)}$
$\widetilde{\Psi}_0(\eta_1)$	Three-dimensional BIC associated with the spherical potential $\widetilde{V}_1^{(\mathrm{3D})}(\eta_1)$
$\widetilde{\Psi}_{0,\pm}(\eta_1)$	Limit of $\widetilde{\Psi}_0(\eta_1)$ at $x \to x_\pm$, with $x \in [x_-, x_+] \subseteq \overline{\mathbb{R}}$. In the main text, x_- and x_+ are usually denoted by the symbols a and b, respectively. These limits also apply to the time domain

ω

ω	Angular frequency
$\omega_{\pm}$	Limit of $\omega\,(t)$ at $t \to \pm\infty$
ω_i	Angular frequency of the i-th T-SUSY system in a SUSY chain
$\omega_{i,\pm}$	Initial $(-)$ and final $(+)$ angular frequency of the i-th T-SUSY system
ω_0	Angular frequency of the optical carrier. Also, angular frequency of the acoustic carrier
ω_n	Angular frequency of an optical carrier different from the central optical carrier
ω_{I}	Incident angular frequency
ω_{R}	Reflected angular frequency
ω_{T}	Transmitted angular frequency
ω_{OF}	Central angular frequency of a band-pass optical filter
Ω	Eigenvalue. Also, free-parameter
Ω_n	n-th eigenvalue of an EVP
$\Omega^{(1)}$	Eigenvalue of the first SUSY system
$\Omega^{(2)}$	Eigenvalue of the second SUSY system

Mathematical Symbols

$\overline{0}$	Binary element of $\mathbb{Z}_2$
$\overline{1}$	Binary element of $\mathbb{Z}_2$
$\cap$	Intersection operation (set theory)
$\cup$	Union operation (set theory)
$\underset{x\to a}{\sim}$	Equivalence of functions at $x \to a$. By definition, $f \underset{x\to a}{\sim} g$ iff $\lim_{x\to a} f(x)/g(x) = 1$
$+_{\mathbb{K}}$	Internal operation of $\mathbb{K}$
$\cdot_{\mathbb{K}}$	Internal operation of $\mathbb{K}$
$+_{\mathcal{V}}$	Internal operation of $\mathcal{V}$
$\cdot_{\mathbb{K}\mathcal{V}}$	External operation of $\mathcal{V}$ with the field $\mathbb{K}$
$+_{\mathcal{V}^*}$	Internal operation of $\mathcal{V}^*$
$\cdot_{\mathbb{K}\mathcal{V}^*}$	External operation of $\mathcal{V}^*$ with the field $\mathbb{K}$
$\lvert\ \rvert$	Absolute value of a real number or modulus of a complex number
$\lVert\ \rVert$	Norm
$[\ ,\ ]$	Lie bracket, also termed as commutator
$\{\ ,\ \}$	Anticommutator
$\bigoplus$	Direct sum

$\langle\ \rangle$	Ensemble average operator
$\langle\ ,\ \rangle$	Inner product
$\langle\ \vert\ \rangle$	Inner product
$\langle\ \vert\ \rangle_{\mathcal{V}}$	Inner product of the vector space $\mathcal{V}$
$\langle\ \vert\ \rangle_{\mathcal{W}}$	Inner product of the vector space $\mathcal{W}$
$\langle\ \vert$	Bra
$\vert\ \rangle$	Ket
∂_i^n	n-th order partial derivative in the $\hat{u}_i$ direction
∂_t^n	n-th order time derivative (partial derivative)
∇	Nabla operator. Also, gradient operator
$\nabla\cdot$	Divergence operator
$\nabla\times$	Curl operator
$\triangle$	Laplacian operator
$\triangle_{\mathrm{T}}$	Transverse Laplacian operator